Vol. 22, No. 1, March, 2023
ISSN (Print): 0972-6268; ISSN (Online) : 2395-3454

# Nature Environment & Pollution Technology

*A Multidisciplinary, International Journal on Diverse Aspects of Environment*

Technoscience Publications
website: www.neptjournal.com

Technoscience Publications
A-504, Bliss Avenue, Balewadi,
Opp. SKP Campus, Pune-411 045
Maharashtra, India

www.neptjournal.com

# Nature Environment and Pollution Technology

**(An International Quarterly Scientific Research Journal)**

## EDITORS



**Published by :** Mrs. T. P. Goel, Technoscience Publications, A-504, Bliss Avenue, Balewadi, Pune-411 045, Maharashtra, India

**E-mail :** contact@neptjournal.com; operations@neptjournal.com

## INSTRUCTIONS TO AUTHORS

### Scope of the Journal

The Journal publishes original research/review papers covering almost all aspects of environment like monitoring, control and management of air, water, soil and noise pollution; solid waste management; industrial hygiene and occupational health hazards; biomedical aspects of pollution; conservation and management of resources; environmental laws and legal aspects of pollution; toxicology; radiation and recycling etc. Reports of important events, environmental news, environmental highlights and book reviews are also published in the journal.

### Format of Manuscript

- The manuscript (*mss*) should be typed in double space leaving wide margins on both the sides.
- First page of mss should contain only the title of the paper, name(s) of author(s) and name and address of Organization(s) where the work has been carried out along with the affiliation of the authors.

*Continued on back inner cover...*

# Nature Environment and Pollution Technology

**Vol. 22, No. (1), March 2023**

## CONTENTS

# The Journal is Currently Abstracted and Indexed in:

CNKI Scholar (China National Knowledge Infrastructure)

Scopus CiteScore (2021) 0.70

Scopus®, SJR (0.169) 2021

Chemical Abstracts, U.S.A.

Pollution Abstracts, U.S.A.

Paryavaran Abstract, New Delhi, India

Electronic Social and Science Citation Index (ESSCI)

CrossRef (DOI)

Google Scholar

Environment Abstract, U.S.A.

WorldCat (OCLC)

Indian Science

SHERPA/RoMEO

Index Copernicus (2021) = 111.68

Indian Science Abstracts, New Delhi, India

Elsevier Bibliographic Databases

Zoological Records

Indian Citation Index (ICI)

EBSCO: Environment Index™

DOAJ

ProQuest, U.K.

British Library

JournalSeek

Directory of Science

CAB Abstracts, U.K.

Ulrich's (Refereed) database

Zetoc

J-Gate

Centre for Research Libraries

Connect Journals (India)

Research Bible (Japan)

Elektronische Zeitschriftenbibliothek (EZB)

CSA: Environmental Sciences and Pollution Management

CNKI Scholar (China National Knowledge Infrastructure)

Access to Global Online Research in Agriculture (AGORA)

AGRIS (UN-FAO)

Present in UGC-CARE List (Group II)

UDL-EDGE (Malaysia) Products like *i*-Journals, *i*-Focus and *i*-Future

**www.neptjournal.com**

# Nature Environment and Pollution Technology

Nature Environment and Pollution Technology
An International Quarterly Scientific Journal

p-ISSN: 0972-6268
(Print copies up to 2016)
e-ISSN: 2395-3454

Vol. 22 | No. 1 | pp. 1-13 | 2023

Original Research Paper

https://doi.org/10.46488/NEPT.2023.v22i01.001

Open Access Journal

# Spatial Distribution of $PM_{10}$ and $NO_2$ in Ambient Air Quality in Cape Town CBD, South Africa

**O. Ndletyana*, B. S. Madonsela* and T. Maphanga*†**

*Cape Peninsula University of Technology, Faculty of Applied Sciences, Department of Environmental and Occupational Studies, Corner of Hanover and Tennant Street, Zonnebloem, Cape Town 8000, RSA

†Corresponding author: T. Maphanga; maphangat@cput.ac.za

**Nat. Env. & Poll. Tech.**
**Website: www.neptjournal.com**

*Received:* 28-07-2022
*Revised:* 12-09-2022
*Accepted:* 15-09-2022

**Key Words:**
Air quality
$PM_{10}$
$NO_2$
Spatial distribution
Seasonal variation
Geographic information system

## ABSTRACT

Fixed air quality monitoring stations generally monitor the air quality in developing countries. However, this practice, in addition to being costly, inherently contains drawbacks associated with the inability to capture the spatial distribution of air pollutants. Against this limitation, it is necessary to employ flexible and dynamic monitoring techniques that are fundamental and influential in comprehending the spatial distribution of pollutants. Because of this, in recent times, the application of GIS as a monitoring technique has proved to be more efficient than using fixed monitoring stations. Therefore, to this end, the current study mapped the spatial distribution of $PM_{10}$ and $NO_2$ pollutants in Cape Town CBD using the GIS technique. Subsequently, the GIS monitoring technique revealed that both pollutants had high spatial distribution between 2017 and 2018, irrespective of the season. Furthermore, high exposure concentrations of $PM_{10}$ were generally observed across the CBD in contrast to $NO_2$ exposure levels, which were relatively low. To contextualize the findings, compared with other studies, the current research discovered that spatial distribution of air pollution is associated with meteorological conditions, such as wind speed and temperature, that traditional techniques of monitoring exposure can't capture.

## INTRODUCTION

Air pollution is one of the most important environmental problems, mainly concentrated in cities. Monitoring atmospheric pollution is a difficult problem, especially for particulate matter and nitrogen oxides. Southern Africa faces difficulty in measuring air quality, and as a result, South Africa is the only country with more advanced ambient air quality monitoring equipment (Coker & Kizito 2018). Mainly because South Africa's spheres of government are entrusted with exposure assessment of ambient air pollutants (DEADP 2017). Therefore, to fulfill this mandate, the different spheres of government have erected automated fixed-air quality monitoring stations across the country (Gwaze & Mashele 2018). The fixed monitoring stations are designed to collect regulatory pollutants, such as nitrogen oxides ($NO_x$, NO, $NO_2$) and particulate matter ($PM_{10}$, $PM_{2.5}$), which have been internationally recognized as environmental priority air pollutants since they can constitute a threat to human health and the Environment (Mustafić et al. 2012, Castell et al. 2017). These fixed monitoring stations capture accurate measurements that are used to understand long-term air quality levels and indicate the status of compliance with prescribed national ambient air quality standards. The policymakers must take the necessary and suitable actions to lower the level of air pollution for the citizens' welfare in light of the detected air quality concentrations. In essence, monitoring presents the air quality data contributing to understanding air pollution exposure levels and potential health risks.

For this reason, monitoring air pollution is fundamental in ensuring compliance with prescribed air quality standards that seek to mitigate the risks of exposure. Hence air pollution exposure monitoring efforts are associated with protecting human health and the environment (Zheng et al. 2015). Given that monitoring ensures that management of air quality is adequate and the potential negative impacts to the Environment and human health linked with poor air quality are understood and mitigated as early as possible (Forbes 2016).

However, in as much as the South African government is proactive in managing air quality by monitoring exposure through continuous assessment, they should be conscious that fixed monitoring stations only measure air pollution at a shallow spatial resolution (Sajani et al. 2004). Due to the limited number of available monitoring stations (Castell et al. 2017). This is due to the exuberant costs associated with

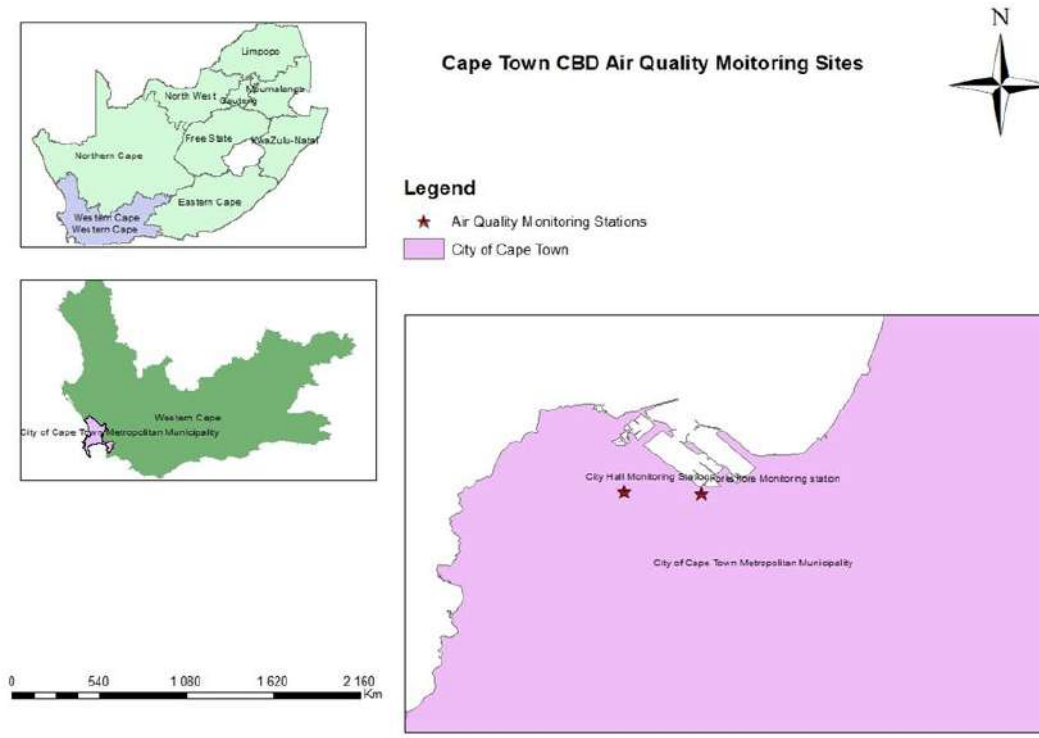


Fig. 1: The study area map of Cape Town monitoring stations in the CBD.

installing, operating, and maintaining fixed monitoring stations. These drawbacks influence the conventional fixed air quality monitoring station's ability to capture the spatial variability of pollutants. Even though understanding spatial and temporal variability in pollutants concentration is essential to air quality management and health risk assessment (Marshall et al. 2008, Wei et al. 2020).

To this end, Pavani & Rao (2017) substantiate that conventional fixed air quality monitoring systems cannot provide air pollution data of high spatiotemporal resolution due to non-scalability and limited data availability. Hence, the gaps in monitoring the spatial variability of pollutants. Therefore because of the limitation in monitoring techniques such as the fixed stations, the application of GIS has been introduced to alternate the traditional monitoring methods. The use of GIS as a monitoring system is advantageous in estimating the spatial distribution of air quality rather than relying on conventional methods, i.e., fixed monitoring station that limits the understanding of the spatial distribution of pollutants. As Somvanshi et al. (2019) state, GIS has proved to be a crucial tool for monitoring, serving various purposes, from spatially monitoring a region's air quality to creating spatial models for predicting future air quality conditions of the region of study. Considering the above, it makes sense that in recent times, a small but growing number of scientists have started experimenting with the use of GIS in monitoring air quality, and others have looked at the spatial distribution of air pollution in Beijing (Li et al. 2019) and Weifang (Song et al. 2019). Keeping this in view, the current study aimed to map the spatial distribution of PM and $NO_2$ pollutants in Cape Town CBD using GIS. The following objectives were pursued: (a) investigate and map the spatial distribution of $PM_{10}$ and $NO_2$ in the CBD; (b) determine the spatial behavior of $PM_{10}$ and $NO_2$ concentration in the CBD and (c) assess the seasonal (summer and winter) distribution of $PM_{10}$ and $NO_2$.

## MATERIALS AND METHODS

### Study Area

Cape Town is one of SA's capital cities which falls under the legislative capital. It is normally referred to as the Mother City. Cape Town is the largest city on the western cape, situated southwest coast beneath the imposing Table Mountain with GPS coordinates -33°55'29.64" S and 18°25'26.75" E. The city occupies an area of about 2461 $km^2$ with an average elevation of 1590.4 m above sea level. It is bordered by the Table Mountain range along the west coast, influencing airflow within the region. The Cape Town climate is the Mediterranean, with warm, dry summers and mild, moist winters. It has a wind force called "Cape doctor," which helps blow away smog and impurities to clear

the skies and provide fresh air (World Weather and Climate Information 2019). According to Census (2011), the Cape Town population is about 374,0026. Increased urbanization and economic activities have resulted in many people in the area. This has consequently increased the number of potential users of public transport (taxis, buses, and trains); private transport is also included (Walton 2005). According to CoCT (2002), the CBD experiences massive traffic congestion during peak hours, i.e., in the morning and afternoon. Thus, Cape Town experiences high pollution levels from motor vehicle exhaust emissions, which is characterized as the primary contributor to the formation of brown haze (Walton 2005). The brown haze is noticeable from April to September due to strong temperature inversions and calm conditions experienced during this period. The haze extends over most of the City of Cape Town (CCT) and shifts according to the prevailing wind direction (Keen & Altier 2016, Wicking-Baird et al. 1997).

### Air Pollution Monitoring Stations

The City of Cape Town (CoCT) municipality monitors the Cape Town CBD's ambient air quality through a network of 2 Air Quality Monitoring (AQM) Stations (DEADP 2016) (Fig. 1). Therefore, these two monitoring stations have been selected to analyze the spatial distribution of air quality in Cape Town CBD. The first monitoring station is located at City Hall CBD. As the name suggests, it is in the central business district on the grand parade west of the Castle of Good Hope center.

### Data Collection

The ambient air quality data was retrieved from the City of Cape Town Municipality air quality monitoring stations. These stations are located in Cape Town CBD to measure ambient air quality exposure concentrations. Amongst the measured pollutants substances are Particulate Matter ($PM_{10}$) and Nitrogen Dioxide ($NO_2$), which are pollutants of concern since they are associated with traffic emissions. To this end, each station is designed to collect data on a particular pollutant. For instance, the Foreshore monitoring station is designated to measure PM pollutants, while the City Hall monitoring station measures the ($NO_2$) pollutants. However, these stations collected data intermittently. As a result, the current data obtained from the CoCT municipality mostly covered the years 2017 to 2018 for both pollutants.

### Data Analysis

GIS spatial analysis was used in this study to determine the distribution of ambient air quality levels in Cape Town CBD. Therefore, the results of this research were presented and analyzed using ArcGIS 10.8 pro, a product of ESRI. This software can be used in mapping and analytics application to examine spatial relationships, predicts outcomes, and make better data-driven decisions. Moreover, this software handles multiple tables and easily relates them to each other. Additionally, the study used ArcGIS for statistical purposes to model the pollution surface based on measurements at air quality monitoring sites. IDW modeling technique was deployed as it provides heat maps of pollution surfaces based on point measurements. IDW was more suitable for this study as it uses the existing monitoring station data. Therefore, the development of a regression model and testing of a regression-mapping approach was carried out in all three centers using ArcGIS pro-10.8. In each center, a GIS was established, containing four main sets of data: main roads (e.g., road network, road type), altitude monitored data $NO_2$ and $PM_{10}$ concentrations. The geostatistical analysis functions in ArcMap pro 10.8 database development are either non-spatial (tubular) or spatial (containing locations). Therefore, graphs and heat maps were produced using the mean concentration of geostatistical analysis called the IDW interpolation method. The conceptual model below outlines the methodology adopted for exploring the spatial patterns of air pollution.

## RESULTS AND DISCUSSION

### Seasonal Spatial Behaviour Concentration of $PM_{10}$ and $NO_2$ in Cape Town CBD, 2017-2018

During the rapid development of Cape Town's economy and society, urbanization has accelerated, and energy consumption has increased steadily. As a result, air pollution in cities has become a significant threat to both physical and mental health. The seasonal spatial behavior analysis for the concentration of $PM_{10}$ and $NO_2$ in Cape Town CBD is represented in bar and line graphs. The bar graphs in Fig. 2 and 3 show the seasonal (winter and summer months) dataset of monthly average concentration (Tables 1 and 2) of Cape Town CBD from 2017 to 2018. The line graphs in Fig. 4 and 5 show the daily concentration exposure level of $PM_{10}$ and $NO_2$ during the winter and summer months of 2017 and 2018. The x-axis in the graphs shows the seasonal variation (winter and summer months), while the y-axis demonstrates the pollutant concentration exposure level. The seasonal behavior concentration demonstrates high levels of $PM_{10}$ and $NO_2$ pollutants during winter, which might be influenced and exacerbated by meteorological conditions such as low temperatures and low wind speed.

### Seasonal Spatial Behavior Concentration of $PM_{10}$ at Cape Town CBD

Despite the importance of understanding and controlling air pollution in highly populated areas, interpreting levels of gaseous pollutants and particulates in the

atmosphere is complicated by several factors, including dominant natural and anthropogenic emissions, micro-meteorological processes, and chemical reactions that occur directly in the atmosphere. Therefore, to better explore and determine the seasonal (winter and summer) spatial distribution and behavior characteristics of $PM_{10}$ in Cape Town CBD during 2017- 2018, table 1 and Fig. 2 were used to show the concentration exposure levels. Both Fig. 2 and Table 2 illustrate readings from Foreshore AQM, which display the seasonal spatial behavior of $PM_{10}$ pollutants during winter (Jun, Jul, and Aug) and summer (Dec, Jan, and Feb) months within the years 2017 and 2018.

Fig. 2 demonstrated that the high concentration exposure levels of $PM_{10}$ in 2017 peaked in Jun (winter) at 38.9 $\mu g.m^{-3}$. While in 2018, during the same season, the concentration of the pollutant peaked in July at 40.91 $\mu g.m^{-3}$. The occurrence of high concentration levels of $PM_{10}$ in different months of the year might be influenced by a couple of factors, for example, the type of climate, changing state of the weather, and anthropogenic activities in that particular year. This resulted in a distinct variation of $PM_{10}$ concentration in ascending order from 2017 to 2018. Moreover, the seasonal variation concentration of $PM_{10}$ in Fig. 6 shows that high concentration levels were observed in winter and low concentrations in summer months. Thus,

Table 1: Seasonal concentration variation of $PM_{10}$ for Foreshore monitoring station.

| Monthly average concentration data of Foreshore AQM for $PM_{10}$ ($\mu g.m^{-3}$), 2017-2018 | | | | |
|---|---|---|---|---|
| Air Quality Monitoring station | Year | Season | Months | Average concentration |
| **Foreshore AQM** | 2017 | Winter | Jun | 38.92 |
| | | | Jul | 33.83 |
| | | | Aug | 29.00 |
| | | Summer | Jan | 26.61 |
| | | | Feb | 30.32 |
| | | | Dec | 28.06 |
| | 2018 | Winter | Jun | 32.35 |
| | | | Jul | 40.91 |
| | | | Aug | 23.08 |
| | | Summer | Jan | 29.56 |
| | | | Feb | 33.87 |
| | | | Dec | 0.00 |

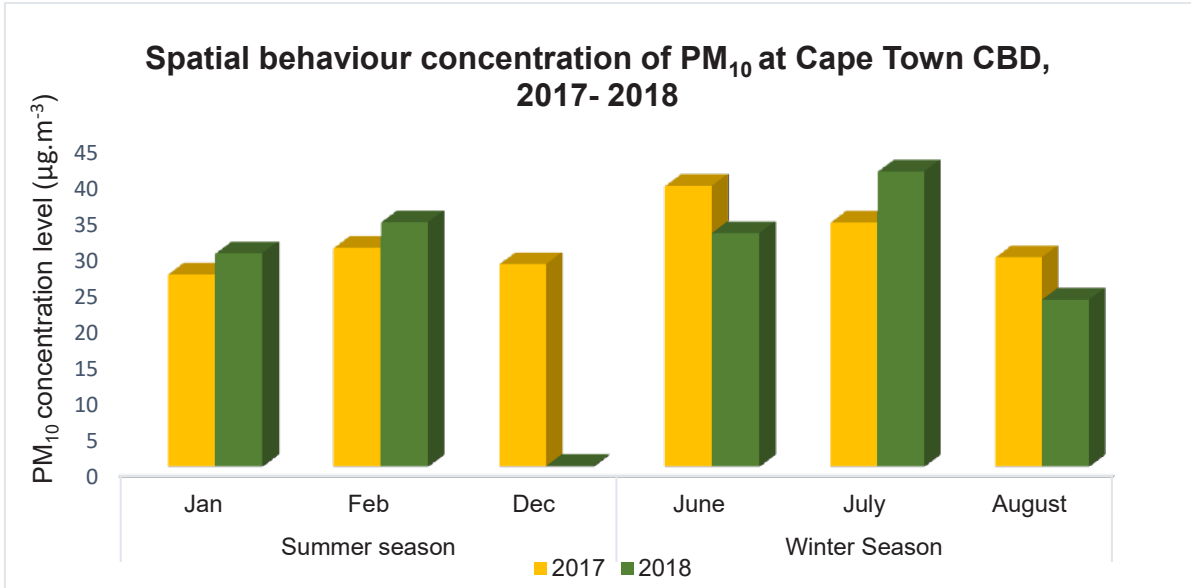


Fig. 2: Seasonal spatial behavior concentration of $PM_{10}$, 2017-2018.

the strong temperature inversion during the winter combined with prevailing windless conditions is attributed to the high concentration levels of $PM_{10}$ Kelly et al. (2012). The findings of this study are consistence with previous studies done in cities in China which included Beijing (Jiang & Bai 2018), Weifang (Li et al. 2019), and Jiangsu (Song et al. 2019), observed high concentration levels during the winter season and low concentration levels during the summer season. The studies further demonstrated that low temperatures and windless conditions worsened the high concentration levels observed in winter. Cichowicz et al. (2017) corroborate the findings that the high concentration levels of $PM_{10}$ in winter may be exacerbated by an increase in emission from local furnaces and the inversion temperature that may result in smog events in most cities around the world. Literature has supported that meteorological conditions such as temperature during the winter season may result in air pollutants not being easily dispersed, which might lead to high concentration levels of PM (Wei et al. 2020, Jiang & Bai 2018, Li et al. 2019, Song et al. 2019).

### Seasonal Spatial Behavior Concentration of $NO_2$ at Cape Town CBD

Increasing ambient $NO_2$ concentrations can have significant effects on respiratory health, particularly for children, the elderly, and individuals who are susceptible to asthma, pneumonia, bronchitis, etc. It can even cause death at extremely high levels and long-term exposure. Table 2 and Fig. 3 shows the seasonal concentration variation behavior of $NO_2$ pollutant during winter (June, July, and August) and summer (Jan, Feb, and Dec) months within the years 2017 and 2018.

Fig. 3 shows a seasonal variation in the concentration behavior of $NO_2$ from 2017 to 2018. It was noted that the winter season in both years recorded the highest concentration of $NO_2$, 38.41 $\mu g.m^{-3}$ (2017) and 35.61 $\mu g.m^{-3}$ (2018), all for the month of August. Furthermore, the results illustrate that the average concentration of $NO_2$ was low for the summer period (2017 and 2018) compared to the winter average this might be attributed to Cape Town's dry summer subtropical climate (Mediterranean). More people use private cars as opposed to summer as winter is characterized by heavy wind and rainfall. It was also observed that during summer, the maximum concentration level peaked in February, reaching a concentration level of 33.51 $\mu g.m^{-3}$ in 2017 and 32.65 $\mu g.m^{-3}$ in 2018. This study's findings align with the results of the study done in Jiangsu city, where high concentrations of $NO_2$ were reported during the winter season, reaching 54 $\mu g.m^{-3}$ concentration and low in the summer season with an average of 40 $\mu g.m^{-3}$ (Wang et al. 2021). The study further discussed that Jiangsu's climate influenced the high concentration levels of $NO_2$ during winter; in winter, the city experiences a strong vertical temperature inversion layer which makes air pollutants not easily dispersed.

### Daily Concentration Exposure Level of $PM_{10}$ and $NO_2$ at Cape Town, 2017-2018

To make predictions, selecting the appropriate time series models for the data is important. Using these time series models, environmental quality managers can estimate parameters according to evolving information needs. As well as providing early warnings to the respective population, related bodies can also use the developed models. Fig. 4 and Fig. 5 demonstrate the daily time series dataset for $PM_{10}$ and $NO_2$ pollutants during winter (Jun, Jul, and Aug) and summer (Jan, Feb, and Dec) months at Cape Town CBD within the years 2017 to 2018. Specifically, it shows the

Table 2: Seasonal concentration variation of $NO_2$ for City Hall monitoring station.

| Monthly average concentration data of City Hall AQM for $NO_2$ ($\mu g.m^{-3}$), 2017-2018 | | | | |
|---|---|---|---|---|
| Air Quality Monitoring Station | Year | Season | Months | Average concentration |
| **City Hall AQM** | 2017 | Winter | Jun | 34.43 |
| | | | Jul | 37.37 |
| | | | Aug | 38.41 |
| | | Summer | Jan | 29.64 |
| | | | Feb | 33.51 |
| | | | Dec | 24.94 |
| | 2018 | Winter | Jun | 20.74 |
| | | | Jul | 31.65 |
| | | | Aug | 35.61 |
| | | Summer | Jan | 26.97 |
| | | | Feb | 32.65 |
| | | | Dec | 21.36 |

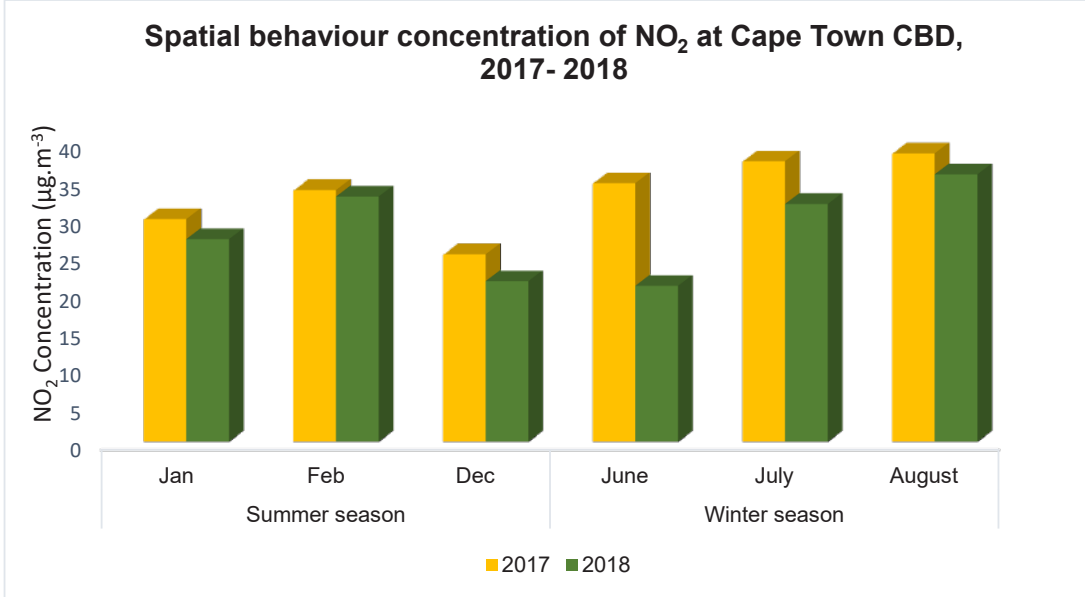


Fig. 3: Seasonal spatial behavior concentration of $NO_2$, 2017-2018.

daily concentration exposure levels of Cape Town CBD from foreshore AQM ($PM_{10}$) and City Hall AQM ($NO_2$) measurements from 2017 to 2018.

According to Fig. 4, the $PM_{10}$ pollutant has high concentration exposure levels that reach 140 µg.m$^{-3}$ during the winter months (Jul 2018). On other months and days, the concentration levels of $PM_{10}$ and $NO_2$ almost behave the same, with the lowest concentration levels of less than 20 µg.m$^{-3}$. In corroboration with the results found by Tui et al. (2021), similar behavior was found; the variation of the daily concentration of $PM_{10}$ and $NO_2$ fluctuated significantly and had a high degree of similarity. In comparison with the winter months (Fig. 4), $NO_2$ pollutant has high concentration exposure levels that reach 94 µg.m$^{-3}$ during the summer season (Jan 2017). Notably, the high concentration exposure level of $NO_2$ was more severe in 2017 during the summer compared to 2018. Although the $NO_2$ pollutant concentration peaked during summer days in 2017, the observation indicates that summer (Fig. 5) concentration exposure levels are low compared to winter concentration readings (Fig. 4). Additionally, according to observation (Fig. 5), during summer, some days the concentration exposure level on $NO_2$ and $PM_{10}$ have similar behavior with the lowest readings of less than 10 µg.m$^{-3}$. This indicates better air quality in summer, while the levels in winter imply risky air pollution levels in the CBD. Moreover, the observations (Fig.4 and 5) indicate that $PM_{10}$ is the main pollutant of concern, with high concentrations recorded in the CBD, particularly during winter. The above results can collaborate with the previous results from Fig. 2 and Fig. 3, which depicted that winter had higher concentration levels.

## Spatial Distribution of $PM_{10}$ and $NO_2$ During Summer and Winter Seasons in Cape Town CBD, 2017 To 2018

Considering the spatial characteristics of air pollution in cities can give us a better understanding of how the city as a whole is affected by air pollution, help identify the sources of urban air pollution, and help develop practical policies to control air pollution. As a result, such research has a significant impact on urban sustainability. Spatial interpolation maps were used to illustrate the air pollution exposure to $PM_{10}$ and $NO_2$. The heat maps show how pollutants varied across the CBD of Cape town during the summer and winter months of 2017 and 2018. An elevated concentration of the pollutant of concern indicates the hazardous zones, indicated by the color red on the heat maps. In contrast, yellow indicates an exposure level of an average to middle concentration, whereas green indicates a low concentration of a pollutant, which identifies a zone that does not constitute a hazardous situation.

## Spatial Distribution of $PM_{10}$ During the Summer Season in Cape Town CBD

High traffic volume and excessive pollutant emissions have been associated with the rapid development of Cape Town's economy and urbanization process, resulting in serious air pollution issues and hindering sustainable development. Fig. 6 shows that the seasonal variations in $PM_{10}$ concen-

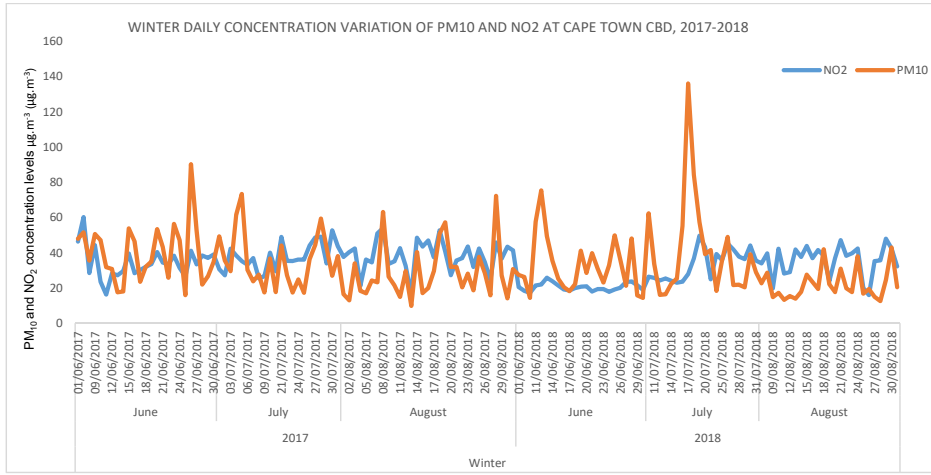


Fig. 4: Daily concentration of $PM_{10}$ and $NO_2$ pollutants during winter months at Cape Town CBD.

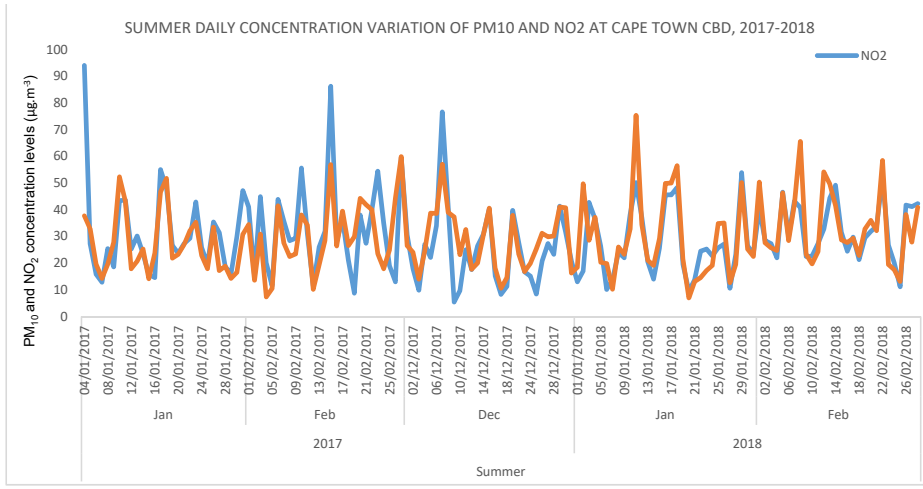


Fig. 5: Daily concentration of PM10 and $NO_2$ pollutants during summer months at Cape Town CBD.

trations are essentially similar, and the seasonal variations' characteristics are as follows.

Fig. 6 demonstrate mapping of the spatial distribution of $PM_{10}$ concentration recorded at Foreshore AQM station within the Cape Town CBD from 2017 to 2018. The mapping outcome of summer $PM_{10}$ pollutants generally indicates variability in spatial distribution. According to Fig. 6, the Foreshore monitoring station recorded low exposure concentrations (23.94 $\mu g.m^{-3}$) of $PM_{10.}$ It was observed that there was an increase in concentration when moving the north and eastern parts of the map. It was also noted that the high concentration of $PM_{10}$ was found close to national highways and traffic intersections entering CBD, which recorded 37.78 $\mu g.m^{-3}$. This demonstrates that the national freeways, main roads, and traffic intersections entering CBD can be described as hazardous delineated zones. The findings of this study are in line with a study conducted in the areas of Bengaluru City, where it was established that national highways and traffic intersections recorded high spatial distribution concentrations of $PM_{10}$ due to high traffic volume (Begum et al. 2006, Song et al. 2020, Cichowicz et al. 2020).

A similar observation was found in a study done at Coimbatore City by Tharani et al. (2021) that $PM_{10}$ pollutants were spatially distributed nearby of major roads. The study further demonstrated the spatial distribution of high $PM_{10}$ concentration was mostly accredited to increased vehicular movement and the presence of high buildings. Tshehla &

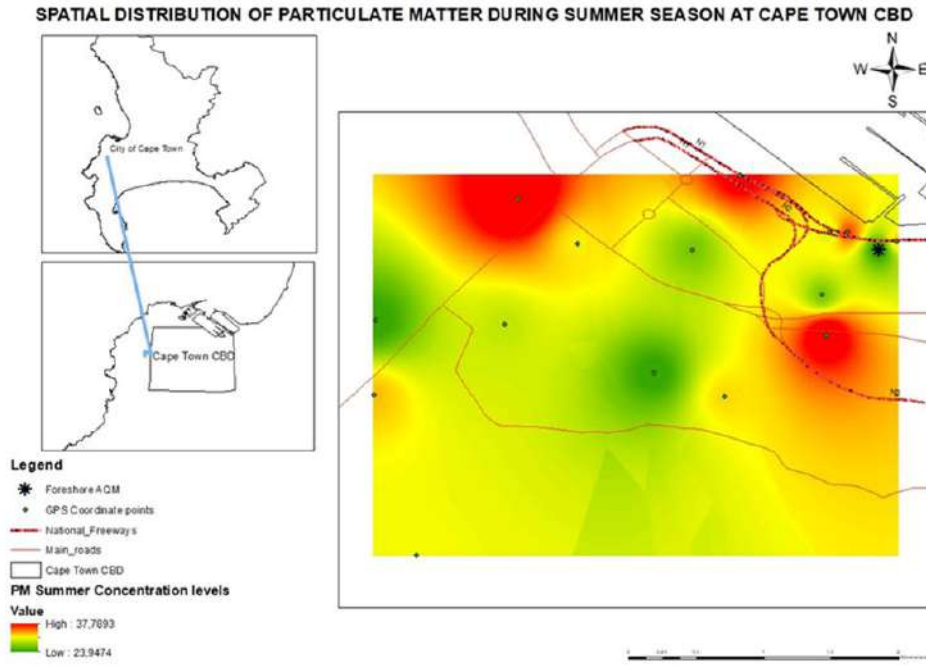


Fig. 6: Spatial distribution of $PM_{10}$ during the summer season.

Wright (2019) did a study on the spatiotemporal distribution of air pollutants and corroborated that the high concentration levels of $PM_{10}$ were observed closer to the source of pollution. According to CoCT (2012), approximately 60% of vehicular traffic movements from Cape Metropolitan Areas are heading to Cape Town CBD. Thus, traffic emissions might be the source of air pollution in the CBD because of the ongoing and coming traffic congestion (Kandlikar 2007, Khan et al. 2020). As presented, for instance, by the analysis in Fig. 6, the hazardous delineated zone is found near the traffic intersection and national highway entering the CBD.

Moreover, Cape Town experiences a wind force called 'Cape Doctor' during the period that is said to clear all air pollutants in the city, offering an amazingly clear sky (World Weather and Climate Information 2019). The direction of this wind force is from South to East ('South Eastern wind') during warm summer seasons (Kelly et al. 2012). Therefore, wind can be a factor that spatially distributes the air pollutants due to the wind force and direction that blows from False Bay and funnels through Cape Town City Bowl to Blouberg. Consequently, Kandlikar (2007) corroborates that meteorological factors such as wind speed and direction have the aptitude to spatially disperse air pollutants. Thus, the variability in the spatial distribution of pollutants at Foreshore AQM.

## Spatial Distribution of $PM_{10}$ During the Winter Season in Cape Town CBD

The spatial distribution analysis in air quality studies is essential and helpful in predicting seasonal variations in the concentration of air pollutants due to changes in meteorology. Mapping the spatial distribution will help us understand the distributed pollutants across the city and the investigation of movement and their influential factors. Fig. 7 shows the winter seasonal variation characteristics of $PM_{10}$ concentration.

The Fig. 7 shows the analysis of the winter spatial distribution of $PM_{10}$. The heat map illustrates the outcome of the pollutant that the Foreshore monitoring station recorded during the winter months from 2017 to 2018. The Winter spatial distribution of $PM_{10}$ shows a distinctive spatial distribution compared to the summer season. In this season, the pollutant maximum concentration exposure level increase is almost double (46.81 $\mu g.m^{-3}$) the records of the summer season. Chen et al. (2013) reported a similar trend whereby particulate matter significantly increased over the winter seasonal period. Another recent study undertaken in the Western Cape neighborhoods observed that the change of season generally affects pollution exposure levels (Madonsela et al. 2022). The results from this current study indicate that in contrast to summer observations, the maximum concentration levels were relatively higher

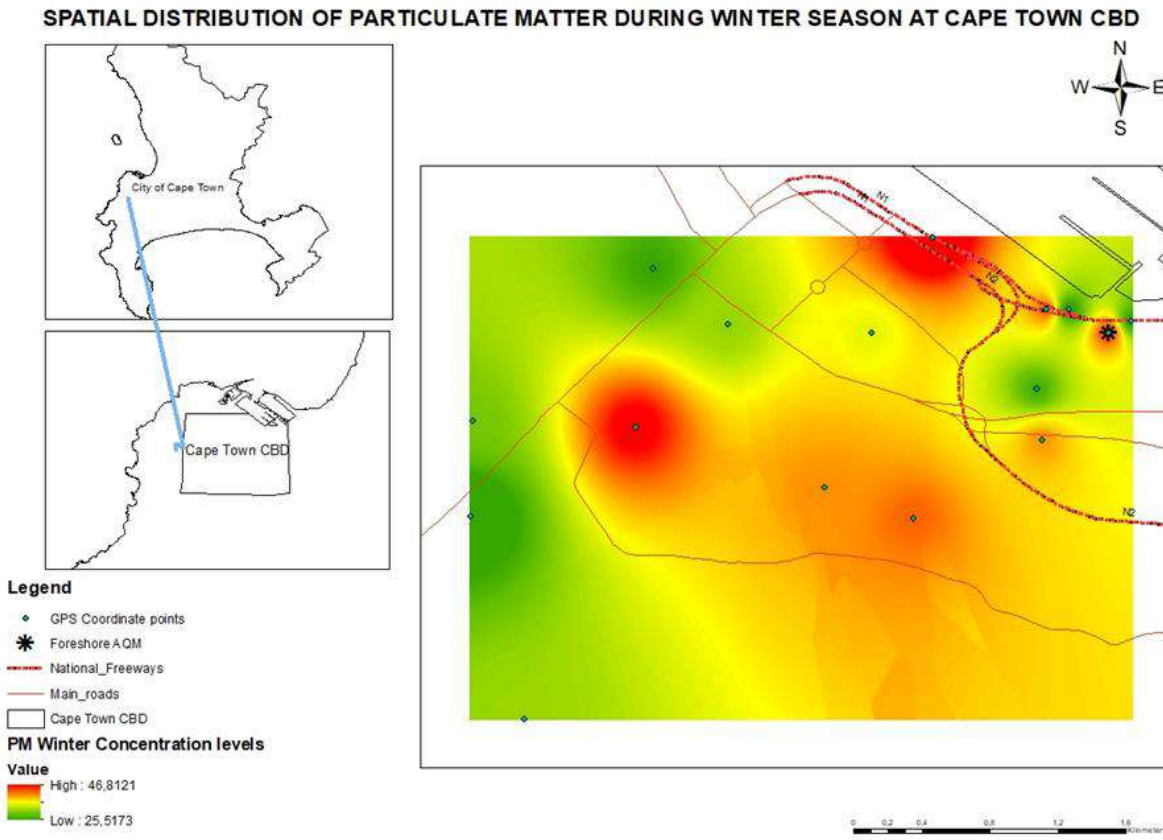


Fig. 7: Spatial distribution of $PM_{10}$ during the winter season.

in the Foreshore air quality monitoring station during the winter season, with an increase observed when moving to the southeastern side of the map. Thus, in winter, the $PM_{10}$ high concentration exposure levels are spatially distributed on the inland side closer to residential and high buildings. Song et al. (2019) studied the spatiotemporal distribution of air pollution characteristics in Jiangsu Province, China; the results showed a similar trend of the highest readings of $PM_{10}$ pollutants on the inland side.

The study corroborated that the northwest wind prevails in winter can be attributed to the spatial distribution of the air pollutants in the northern part of Jiangsu, which is close to the inland. Furthermore, Jiangsu has rainy conditions during the winter season, which results in a strong vertical temperature inversion layer, making air pollutants difficult to disperse (Song et al. 2019). Thus, Jiangsu's winter condition is similar to Cape Town's winter conditions, with strong temperature inversion that combines with prevailing windless conditions that prevent air pollutants from dispersing upwards (Kelly et al. 2012). These high levels of air pollution are primarily responsible for brown haze episodes in the CBD, resulting in poor visibility. The distribution of pollutants can be attributed to low wind speed and direction, favoring the accumulation of pollutants mostly experienced during winter (Cichowicz et al. 2020). In the summer, the opposite situation occurred where the temperature was high with a high wind speed called "cape doctor' therefore, the $PM_{10}$ pollutant was also reduced and behaved differently compared to the winter season. In a nutshell, the high concentration levels of $PM_{10}$ during winter in the CBD are likely to be influenced by pollution from motor vehicles as source pollution and meteorological factors (i.e., wind speed and temperature).

## Spatial Distribution of $NO_2$ During the Summer Season in Cape Town CBD

Considering the location of the air quality monitoring station, $NO_2$ concentrations are lower in the west and higher in the east, as illustrated in the Fig. 8. It shows that the seasonal $NO_2$ concentrations are essentially similar to $PM_{10}$, and the seasonal variations' characteristics are as follows.

Fig. 8 shows the spatial distribution of $NO_2$ during the summer season in Cape Town CBD from 2017 to 2018. Among two monitoring stations within the Cape Town CBD, one monitored the nitrogen dioxide pollutant for only

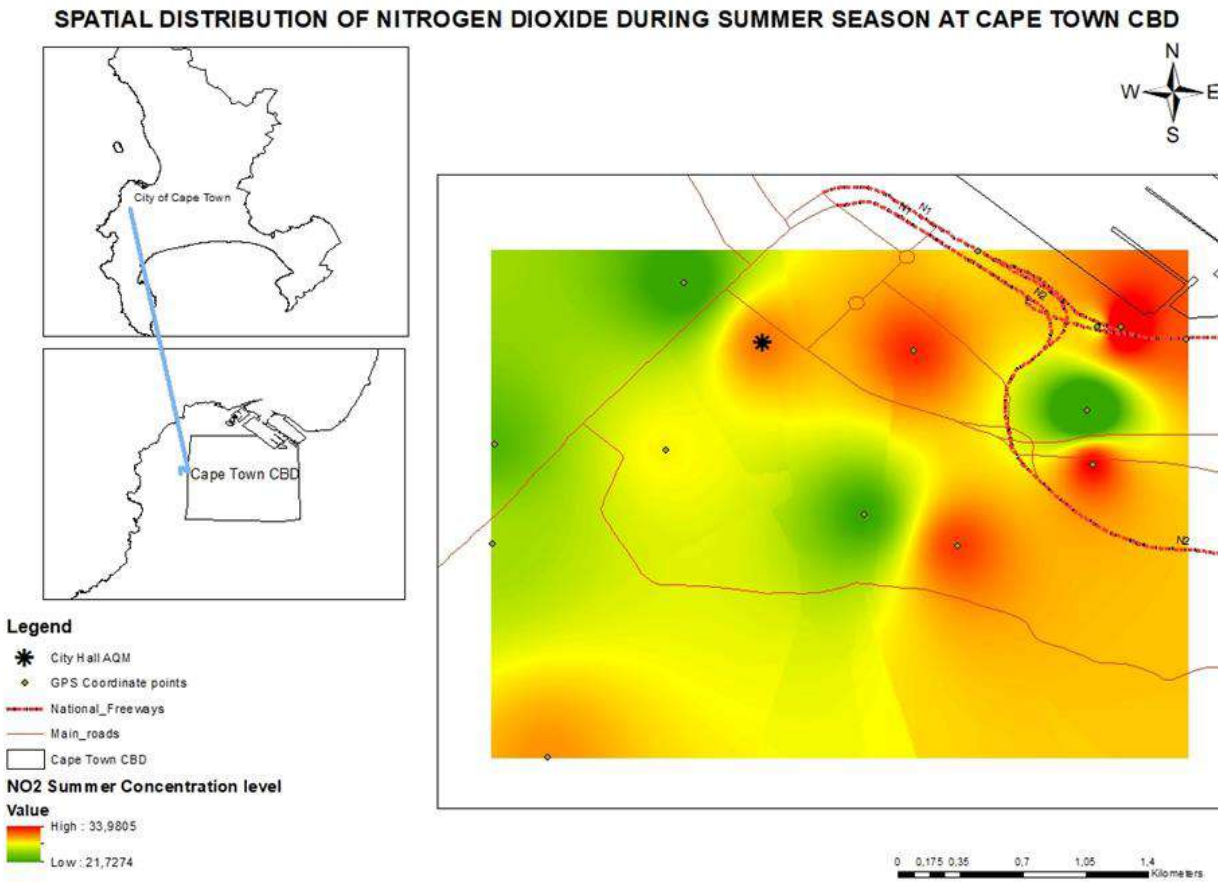


Fig. 8: Spatial distribution of $NO_2$ during the summer season.

January 2017 to December 2018. Therefore, the study used the measurements between these years for data accuracy for the winter and summer seasons. The heat map in Fig. 8 illustrates the outcome of the summer seasonal distribution of $NO_2$ concentration at City Hall AQM station within Cape Town CBD. The City Hall monitoring station recorded high exposure concentrations (33.98 $\mu g.m^{-3}$) of $NO_2$, with an increase in exposure concentration observed when the distance increases towards the northeastern and southeastern side of the monitoring station close to national highways and traffic intersections. The findings are similar to a study conducted by Adedeji (2016) in Nigeria, Metropolis, where the highest concentration of $NO_2$ was observed in the southeastern part near major roads that are attributed to high traffic volume. Nevertheless, in a study done in Jinan City determining the spatial characteristics of environmental air quality, the $NO_2$ pollutant was higher in the Northeastern and central parts of the map (Wang et al. 2021). The study further demonstrated that the direction of the pollutant distribution might be related to industrial production located in the northeastern part of the city.

In comparison with the $PM_{10}$ summer spatial distribution demonstrated in Fig. 7, the spatial distribution of $NO_2$ (Fig. 8) almost behaves similarly to $PM_{10}$ towards the national highways, traffic intersections, and main roads. That is, these two pollutants are both concentrated toward the traffic intersections. The discovery of a correlation reflected in similar behavior between $PM_{10}$ and $NO_2$ pollutants validates a long-standing relationship between the two pollutants (Pineda & Cano 2021, Madonsela 2019). The observed correlation might be engendered by the fact that $NO_2$ has been identified as a secondary precursor for particulate matter (Pineda & Cano 2021, Madonsela et al. 2022), and these pollutants are both associated with traffic-related emissions primarily emitted from the combustion of motor engines (Keen & Altieri 2006). According to Fig. 8, national highways and major roads can be identified as hotspot areas during the summer season; the results of this study corroborate this finding.

Moreover, the south-easterly wind force is known as the 'Cape Doctor' that blows during the summer months and can

be credited for spatially distributing the pollutants of $PM_{10}$ and $NO_2$. Given the above, numerous scholars suggest that the most important constraints on air pollution dispersion throughout the summer are meteorological variables such as wind speed and topographically induced flows (Wei et al. 2021, Jiang & Bai 2018, Wang et al. 2021).

### Spatial Distribution of $NO_2$ During the Winter Season in Cape Town CBD

The spatial distribution of transport emissions is of key concern. The meteorological patterns, high buildings, and street canyons will likely affect the concentration and spatial distribution of air pollution emissions from mobile sources.

Fig. 9 shows the results of the winter seasonal spatial distribution of $NO_2$ in the Cape Town CBD for the period of 2017 to 2018. The heat map outcome of winter $NO_2$ pollutants from the City Hall AQM station generally indicates variability in spatial distribution. Fig. 9 shows that the City Hall monitoring station recorded high exposure concentrations (38.59 $\mu g.m^{-3}$) of $NO_2$. It was observed that the is an increase in concentration when moving to the southwestern side of the map. Subsequently, high concentration exposure levels were also observed near the national highway (N1) and traffic intersections entering the CBD on the northeastern side of the map. The findings of this study are in line with a study done by Moja et al. (2019), which was conducted in the City of Tshwane, which identified that poor air quality is not evenly distributed throughout the city but localized in a few large residential areas and commercial activities, particularly in winter. Similarly, observations made by Moja et al. (2019) in Fig. 9 indicate that the hazardous delineated zones are mostly marked close to residential areas (Southwest side of the map) and the harbour industrial areas (Northeastern side of the map). This is partly because stable meteorological conditions in winter do not promote the distribution of pollutants (Lourens et al. 2011).

These high concentration levels close to the harbour commercial areas may be influenced by the presence of shipping emissions and other sources, such as heavy-duty vehicles associated with port activities. A study by Tularam et al. (2020) in Durban, South Africa, highlighted the importance of the harbor variable, which serves as a proxy

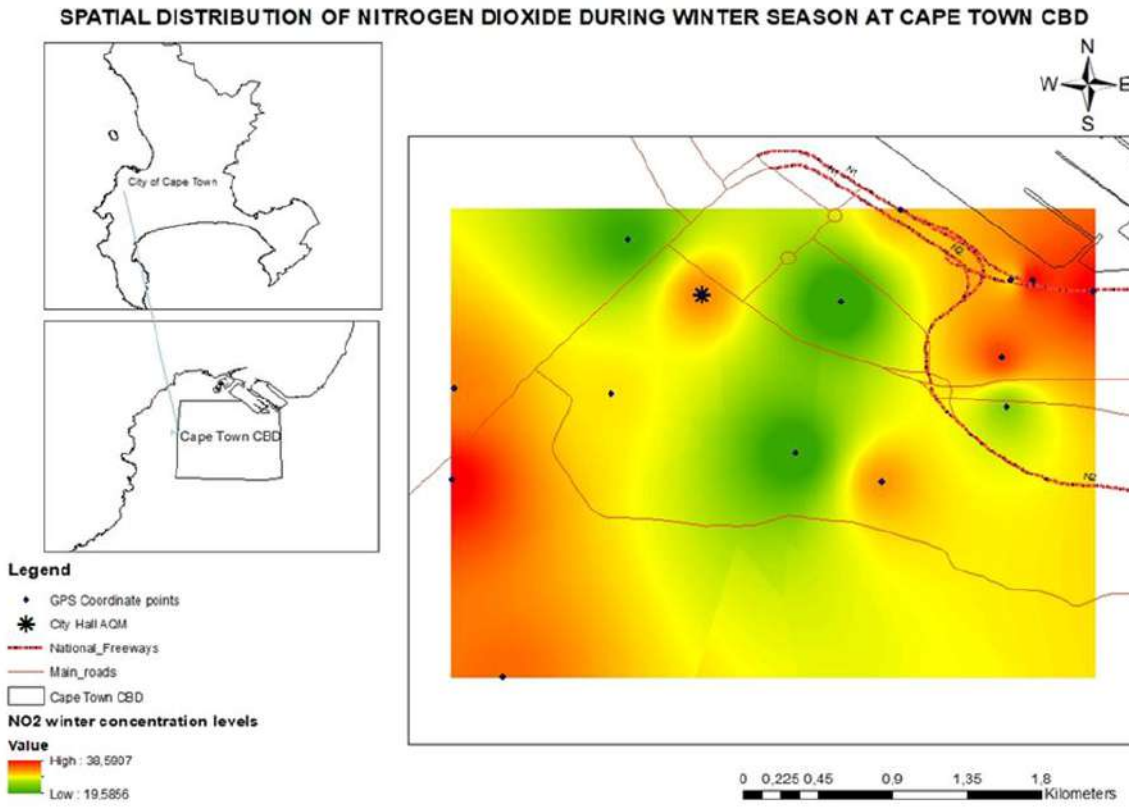


Fig. 9: Spatial distribution of $NO_2$ during the winter season.

for $NO_2$ concentration. In addition, the analysis in Fig. 8 indicated that the maximum concentration of ambient $NO_2$ levels was relatively higher in winter (38.59 $\mu g.m^{-3}$) than in summer (33.98 $\mu g.m^{-3}$). This can be attributed to the Table Mountain shielding properties and the climatic factors in winter that influence the accumulation and distribution of air pollutants Jury et al. (1990). Likewise, Kelly et al. (2012) substantiate that stable meteorological conditions contribute to pollutant level increases during the cold (winter) seasons.

The maximum concentration level results indicate that the $NO_2$ concentration level trend is comparable to results obtained elsewhere, where high exposure levels of $NO_2$ were discovered during the winter compared to the summer season (Levy et al. 2014, Rabiei-Dastjerdi et al. 2022). A study by Zheng et al. (2018, 2015) emphasized that in the winter, the pollutants are not easily washed away; hence some cities experience brown-haze smog episodes. Correspondingly, in a study of spatiotemporal variation characteristics of air pollutants in Shijiazhuang City, the distribution of $NO_2$ was more severe in the northeastern part of the map (Tui et al. 2021). The reason being in the north-eastern side, they are industrial activity sources and large vehicles.

## CONCLUSION

The spatial distribution and behavior characteristics of ambient air quality ($PM_{10}$ and $NO_2$) at Cape Town CDB were investigated utilizing ArcGIS to map spatial distribution. The study's findings show a distinct spatial variation in that $PM_{10}$ was the main pollutant in the CBD, with a high concentration between summer and winter in 2017 and 2018, and the $NO_2$ pollutant was lighter. A large number of studies have shown that there are obvious seasonal differences in the distribution of air pollutants. The finding of this study indicated that meteorological conditions such as wind speed and temperature have a correlation close with the ambient air pollutants and play an important role in the spatial distribution of $PM_{10}$ and $NO_2$. Although the meteorological factors are not studied in this study, the findings were comparable with others studies conducted globally. Moreover, the national traffic roads entering the CBD, industrial harbor, and dense residential areas with high buildings were considered the pollution hotspot in the CBD.

The monthly variation of atmospheric pollutant concentrations in Cape Town CBD's main urban area has obvious seasonal characteristics. The worse pollution was in winter, especially in August, which is in winter, and light (medium) pollution was noted in summer. Therefore, this paper is important because it provides an in-depth understanding of the spatiotemporal characteristics of air quality and the primary pollutants that have affected the AQI in Cape Town CBD. The study sheds light on future urban development and pollution control. Furthermore, air quality is affected by various factors, including weather and human activities, and this paper lacks other influential factors in wind speed. Future research should combine remote-sensed and ground-monitored data to reduce extrapolation errors/bias and investigate relationships between other driving factors and air pollutants for more urban sites.

## ACKNOWLEDGEMENTS

We acknowledge Cape Peninsula, University of Technology for its support, and the City of Cape Town for providing us with raw data for analysis.

## DATA AVAILABILITY

Raw data from the City of Cape Town, air quality management, were used in the study. The information can be requested from https://www.capetown.gov.za/City-Connect/Environmental-health/Apply-for-an-atmospheric

## REFERENCES

Adedeji, O.H., Oluwafunmilayo, O. and Oluwaseun, T.A.O. 2016. Mapping of traffic-related air pollution using GIS techniques in Ijebu-Ode, Nigeria. Indones. J. Geogr., 48(1): 73.

Begum, B.A., Biswas, S.K. and Hopke, P.K. 2006. Temporal variations and spatial distribution of ambient PM2. 2 and PM10 concentrations in Dhaka, Bangladesh. Sci. Total Environ., 358(1-3): 36-45.

Castell, N., Dauge, F.R., Schneider, P., Vogt, M., Lerner, U., Fishbain, B., Broday, D. and Bartonova, A. 2017. Can commercial low-cost sensor platforms contribute to air quality monitoring and exposure estimates? Environ. Int., 99: 293-302.

Census. 2011. City of Cape Town Metropolitan Municipality. http://census2011.adrianfrith.com/place/199. [Accessed 13 July 2022].

Chen, R., Wang, X., Meng, X., Hua, J., Zhou, Z., Chen, B. and Kan, H. 2013. Communicating air pollution-related health risks to the public: An application of the Air Quality Health Index in Shanghai, China. Environ. Int., 51: 168-173.

Cichowicz, R., Wielgosiński, G. and Fetter, W. 2017. Dispersion of atmospheric air pollution in summer and winter seasons. Environ. Monit. Assess., 189(12): 1-10.

Cichowicz, R., Wielgosiński, G. and Fetter, W. 2020. Effect of wind speed on the level of particulate matter PM10 concentration in atmospheric air during winter season in vicinity of large combustion plant. J. Atmos. Chem., 77(1): 35-48.

City of Cape Town (CoCT). 2002. State of the Environment Report for the City of Cape Town: Year Five 2002, Cape Town.

Coker, E. and Kizito, S. 2018. A narrative review on the human health effects of ambient air pollution in Sub-Saharan Africa: an urgent need for health effects studies. Int. J. Environ. Res. Pub. Health, 15(3): 427.

Department of Environmental Affairs and Development Planning (DEADP). 2017. Western Cape State of Air Quality Management Report 2017. Western Cape Government, Cape Town.

Forbes, P.B. 2016. Novel Approaches to Environmental Monitoring. In International Conference on Pure and Applied Chemistry, 18-22 July 2016, Mauritius, Springer, Cham, pp. 345-354.

Gwaze, P. and Mashele, S.H. 2018. South African Air Quality Information

System (SAAQIS) mobile application tool: Bringing real time state of air quality to South Africans. Clean Air J., 28(1): 3-3.

Jiang, L. and Bai, L. 2018. Spatio-temporal characteristics of urban air pollutions and their causal relationships: Evidence from Beijing and its neighboring cities. Sci. Rep., 8(1): 1-12.

Jury, M., Tegen, A., Ngeleza, E. and Dutoit, M. 1990. Winter air pollution episodes over Cape Town. Bound. Lay. Meteorol., 53(1): 1-20.

Kandlikar, M. 2007. Air pollution at a hotspot location in Delhi: detecting trends, seasonal cycles and oscillations. Atmos. Environ., 41(28): 5934-5947.

Keen, S. and Altieri, K. 2016. The health benefits of attaining and strengthening air quality standards in Cape Town. Clean Air J., 26(2): 22-27.

Kelly, F.J., Fuller, G.W., Walton, H.A. and Fussell, J.C. 2012. Monitoring air pollution: Use of early warning systems for public health. Respirology, 17(1): 7-19.

Khan, J., Kakosimos, K., Jensen, S.S., Hertel, O., Sørensen, M., Gulliver, J. and Ketzel, M. 2020. The spatial relationship between traffic-related air pollution and noise in two Danish cities: Implications for health-related studies. Sci. Total Environ., 726: 138577.

Levy, I., Mihele, C., Lu, G., Narayan, J. and Brook, J.R. 2014. Evaluating multipollutant exposure and urban air quality: pollutant interrelationships, neighborhood variability, and nitrogen dioxide as a proxy pollutant. Environ. Health Persp., 122(1): 65-72.

Li, C., Dai, Z., Yang, L. and Ma, Z. 2019. Spatiotemporal characteristics of air quality across Weifang from 2014–2018. Int. J. Environ. Res. Pub. Health, 16(17). 3122.

Lourens, A.S., Fourie, G.D., Burger, J.W., Pienaar, J.J., Read, C.E., Jordaan, J.H., Van Zyl, P.G. and Beukes, J.P. 2011. Spatial and temporal assessment of gaseous pollutants in the Highveld of South Africa. S. Afr. J. Sci., 107(1): 1-8.

Madonsela, B.S. 2019. Assessment Of Environmental Exposure To Air Pollution Within Four Neighbourhoods Of The Western Cape, South Africa. Doctoral dissertation. Cape Peninsula University of Technology, Cape Town, SA.

Madonsela, B.S., Maphanga, T., Chidi, B.S., Shale, K. and Zungu, V. 2022. Assessment of air pollution in the informal settlements of the Western Cape, South Africa. J. Air Pollut. Health, 7(1): 1-14.

Marshall, J.D., Nethery, E. and Brauer, M. 2008. Within-urban variability in ambient air pollution: comparison of estimation methods. Atmos. Environ., 42(6): 1359-1369.

Moja, S.J., Godobedzha, T., Moja, S.J. and Godobedzha, T. 2019. Spatial and Temporal Assessment of PM10 Levels within the City of Tshwane, South Africa. Int. J. Environ. Sci. Nat. Resour., 17(5): 154-161.

Mustafić, H., Jabre, P., Caussin, C., Murad, M.H., Escolano, S., Tafflet, M., Périer, M.C., Marijon, E., Vernerey, D., Empana, J.P. and Jouven, X. 2012. Main air pollutants and myocardial infarction: a systematic review and meta-analysis. Jama, 307(7): 713-721.

Pavani, M. and Rao, P.T. 2017. Urban air pollution monitoring using wireless sensor networks: A comprehensive review. International J. Commun. Netw. Inform. Security, 9(3): 439-449.

Pineda, A.A.L. and Cano, J.A. 2021. Assessment of air quality in the Aburrá Valley (Colombia) using composite indices: Towards comprehensive sustainable development planning. Urban Clim., 39: 100942.

Rabiei-Dastjerdi, H., Mohammadi, S., Saber, M., Amini, S. and McArdle, G. 2022. Spatiotemporal analysis of NO2 production using TROPOMI time-series images and Google Earth Engine in a middle eastern country. Remote Sens., 14(7): 1725.

Sajani, S.Z., Scotto, F., Lauriola, P., Galassi, F. and Montanari, A. 2004. Urban air pollution monitoring and correlation properties between fixed-site stations. J. Air Waste Manag. Assoc., 54(10): 1236-1241.

Somvanshi, S.S., Vashisht, A., Chandra, U. and Kaushik, G. 2019. Delhi air pollution modeling using remote sensing technique. Hand. Environ. Mater. Manag., 16: 1-27.

Song, J., Qiu, Z., Ren, G. and Li, X. 2020. Prediction of pedestrian exposure to traffic particulate matters (PMs) at urban signalized intersection. Sustain. Cities Soc., 60,:.102153.

Song, R., Yang, L., Liu, M., Li, C. and Yang, Y. 2019. Spatiotemporal distribution of air pollution characteristics in Jiangsu Province, China. Adv. Meteorol., 61: 2119.

Tharani, T., Geethakarthi, A. and Prabakaran, P.A. 2021. Spatial distribution analysis of air pollutants and the impact of meteorological factor. In 2021 International Conference on Advancements in Electrical, Electronics, Communication, Computing and Automation (ICAECA) (pp. 1-6). IEEE.

Tshehla, C.E. and Wright, C.Y. 2019. Spatial and temporal variation of PM10 from industrial point sources in a rural area in Limpopo, South Africa. Int. J. Environ. Res. Pub. Health, 16(18),: 3455.

Tui, Y., Jiaxin, Q., Ju, W. and Chunsheng Fang. 2021. Analysis of spatio-temporal variation characteristics of main air pollutants in Shijiazhuang city. Sustainability, 941 :(2)13. https://doi.org/10.3390/su13020941

Tularam, H., Ramsay, L.F., Muttoo, S., Naidoo, R.N., Brunekreef, B., Meliefste, K. and de Hoogh, K. 2020. Harbor and intra-city drivers of air pollution: Findings from a land use regression model, Durban, South Africa. Int. J. Environ. Res. Pub. Health, 17(15): 5406.

Walton, N.M. 2005. Characterisation of Cape Town brown haze. Doctoral Dissertation. University of the Witwatersrand, Johannesburg, SA.

Wang, Y., Yao, L., Xu, Y., Sun, S. and Li, T. 2021. Potential heterogeneity in the relationship between urbanization and air pollution, from the perspective of urban agglomeration. J. Clean. Prod., 298: 126822.

Wei, J., Li, Z., Xue, W., Sun, L., Fan, T., Liu, L., Su, T. and Cribb, M. 2021. The ChinaHighPM10 dataset: generation, validation, and spatiotemporal variations from 2015 to 2019 across China. Environ. Int., 146: 106290.

Wei, W., Zhang, H., Cai, X., Song, Y., Bian, Y., Xiao, K. and Zhang, H. 2020. Influence of intermittent turbulence on air pollution and its dispersion in winter 2016/2017 over Beijing, China. J. Meteorol. Res., 34(1): 176-188.

Wicking-Baird, M.C., De Villiers, M.G. and Dutkiewicz, R.K. 1997. Cape Town brown haze study. J. Energy S. Afr., 8(4): 275

World Weather and Climate Information. 2019. Climate and Average Monthly Weather in Cape Town (Western Cape), South Africa. https://weather-and-climate.com/average-monthly-Rainfall-Temperature Sunshine,Cape_Town,South-Africa. [Accessed 13 July 2022].

Zheng, B., Tong, D., Li, M., Liu, F., Hong, C., Geng, G., Li, H., Li, X., Peng, L., Qi, J. and Yan, L. 2018. Trends in China's anthropogenic emissions since 2010 as the consequence of clean air actions. Atmos. Chem. Phys., 18(19): 14095-14111.

Zheng, Y., Yi, X., Li, M., Li, R., Shan, Z., Chang, E. and Li, T. 2015. Forecasting fine-grained air quality based on big data. In Proceedings of the 21th ACM SIGKDD International Conference On Knowledge Discovery And Data Mining, 10-13 August 2015, Sydney, Australia, ACM, NY, pp. 2267-2276.

Nature Environment and Pollution Technology
An International Quarterly Scientific Journal

p-ISSN: 0972-6268
(Print copies up to 2016)
e-ISSN: 2395-3454

Vol. 22 | No. 1 | pp. 15-28 | 2023

Original Research Paper

https://doi.org/10.46488/NEPT.2023.v22i01.002

Open Access Journal

# Pattern Characterization of Meteorological Drought Using Multivariate Drought Index Over Mirzapur in Middle Gangetic Plains of India

**Shivani Gond*†, Nitesh Gupta**, P. K. S. Dikshit* and Shyam Bihari Dwivedi***

*Department of Civil Engineering, Indian Institute of Technology (BHU), Varanasi, 221005, Uttar Pradesh, India

**Department of Civil Engineering, Sagar Institute of Research & Technology (SIRT), Bhopal, 462041, Madhya Pradesh, India

†Corresponding author: Shivani Gond; shivanigond@gmail.com

**Nat. Env. & Poll. Tech.**
**Website: www.neptjournal.com**

*Received:* 19-06-2022
*Revised:* 05-08-2022
*Accepted:* 10-08-2022

**Key Words:**
Multivariate drought index
Wet event
SPEI
Run theory
Pattern characterization
Variable-sized cluster analysis

## ABSTRACT

Droughts and floods have been occurring at a higher frequency in recent decades. The rapid transition between them magnifies the socio-economic consequences of these catastrophes relative to the effects of the individual occurrences of the extreme event. This study examines the temporal variability of meteorological drought and wet event characteristics occurring over Mirzapur (Uttar Pradesh), India. The Standardized Precipitation Evapotranspiration Index (SPEI) is applied to monthly water balance at scales 3, 6, 9, and 12 months to estimate the meteorological drought and wet events from 1971 to 2018. Drought and wet event characteristics such as the number of drought/wet events, severity, duration, and intensity are estimated using run theory over SPEI output. While characterizing the pattern of trends over the historical time period, variable-sized cluster analysis (VSCA) allows the detection of multiple change points as opposed to the Mann-Kendall (MK) test, which produces a monotonic trend for the entire time period. The VSCA technique accounts for drought variability and depicts the pattern's evolution across the period under consideration. Station-scale drought data from Mirzapur, Uttar Pradesh (UP), India, were used in the procedure. VSCA allows for the detection of many change points while describing the pattern of drought trend throughout a historical period, as opposed to the usual Mann-Kendall (MK) test, which provides a monotonic trend for the whole time. As a result, VSCA demonstrated the MK test compatibility.

## INTRODUCTION

There is growing evidence of increasing events of hydrologic extremes (drought and flood) becoming more regular due to the impact of recent warming, which significantly alters the global hydrologic cycle. The climate system comprises interdependent and dynamic mechanisms that fluctuate randomly within a fixed range of variability. The climate system consists of interdependent and dynamic mechanisms that fluctuate randomly within a static envelope of variability (Gupta et al. 2022). On the other hand, the precipitation and temperature characteristics alter with the anthropogenic changes in the earth (Omar et al. 2019a, 2020, Srinivas & Saral 2007). Heatwaves and humid heat stress in South Asia are expected to become more common and severe in the coming decades, according to the IPCC's Sixth Assessment Report (AR6). Increased yearly and summer monsoon precipitation variability means higher totals (Bhagawati et al. 2017, Varughese 2017). In most situations, water resources are examined separately for features related to wet and dry occurrences. Hydrologic and atmospheric dynamics are intertwined in a way that might exacerbate hydro-climatic variability under the impact of climate change (Omar et al. 2020, He et al. 2017). Drought is one of the hydrologic extremes that causes the most harm because it is so complicated and recurrent. Decreased precipitation for an extended period in a vast geographic region causes considerable damage to the environment and human livelihoods across the world (Subbiah et al. 2021). This increase in temperature exacerbates the severity of drought. Therefore, It is necessary to utilize a wide range of drought indicators to monitor a wide range of hydrologic cycles and processes due to a variety of different types of meteorological, agricultural, and hydrological droughts that have been seen in recent decades (Nabaei et al. 2019, Qutbudin et al. 2019, Rosalia & Hakim, 2021, Tan et al. 2015, Mishra & Singh 2010). SPI and SPEI are widely acknowledged for practical drought monitoring among the many drought indicators, as are the limits of each. The input parameters for SPI and SPEI are different, but the mathematical computations are equivalent. Climate

inputs used by SPI models include simply precipitation, whereas those of SPEI models also have information on climate water balance. Many studies recommend employing SPEI rather than SPI because of its relation to potential evapotranspiration (PET), which is more sensitive to global warming (Vicente-Serrano et al. 2010, Huang et al. 2017). Studying historical drought occurrences may be aided by understanding regional patterns in terms of drought severity, length, and geographical extent. Drought episodes and their effects can also be predicted more accurately (Mallya et al. 2015). Due to the varied geological and climatic conditions on the Indian subcontinent, Indian agriculture is too complex for irrigated and dry land areas (Omar et al. 2019b).

Various studies have evaluated the trend of drought variability over the considered period using the nonparametric Mann-Kendall (M.K.) test (Bacanli 2017, Dashtpagerdi et al. 2015). Guhathakurta et al. (2017) analyzed the trend variability of monthly SPI for the monsoon season using the M.K. test at a 95% significance level. They noted a significant rise in the drought occurrence over the districts of India (Pandey et al. 2021). Over the post-monsoon season, a substantial rise in drought severity and the event was found by conducting the M.K. test on SPI output in the Bundelkhand area. However, the monotonic trend of climatic parameter time series generally does not display monotonic behavior but rather nonperiodic alternating behavior at an intermediate period when using the Mann-Kendall (M.K.) approach. Typical parametric and nonparametric tests may miss real-time information that varies from the aggregation in aggregated data sets. Non-stationarity in hydrological systems leads to shifts in average precipitation, frequency of severe events, evapotranspiration amplitude, and river flow. The complex interconnectedness and dynamic dynamics of climatic variables continually update hydrometeorological processes and contribute to the non-stationarity of climatic variables. Gupta et al. (2021) introduce the methodology to assess the change in the trend pattern, which incorporates the intermediate variation of the climatic variable over the study period. Singh et al. (2019) advised that drought-resistant crops should be grown in Mirzapur (Uttar Pradesh) throughout the Ravi season, according to a study that examines the probability of dry and wet periods and the likelihood of successive dry and wet spells. The development of understandable maps of spatial rainfall patterns that depict temporal variations and highlight hazards related to water scarcity and drought, as well as the vulnerability assessment of ecosystems, agriculture, water resources, and socioeconomic contexts to drought risk, need to be the main focus of future research.

There must be early knowledge of the length and scope of the water scarcity if precautions against moisture stress in crops are to be taken. Using weather data from the past 30 years (1984-2013), scientists have come up with a way to predict how much water crops need each week in Mirzapur, District (Uttar Pradesh) in the Vindhya Zone of the Indo-Gangetic Plains (Singh et al. 2019). Gond et al. (2019) examined SPI and SPEI at multiscale for their temporal variability in the severity of drought, and their trend assessment by applying M.K. tests conducted in Mirzapur District revealed that SPEI accounts for a higher number of events with a higher magnitude of the district's droughts than SPI. The Theory of Runs is a time series analysis method that has been frequently employed in drought event identification (Zhang et al. 2015). Its fundamental challenge is determining the intercept level. Many earlier studies merely set a single intercept level in the Theory of Runs (Liu et al. 2016). This method was straightforward, but it tended to overidentify or under-identify drought characteristics, lowering the accuracy of the data. As a result, further optimizing the interception level of drought detection and testing more distinct drought index thresholds are required so that the drought events identified are consistent with the actual ones. There was a lack of attention paid to the wet event features in all the investigations in the aforesaid context.

Consequently, in this work, we aimed to examine the drought and wet parts of Mirzapur (Uttar Pradesh), India. The location's monthly means temperature and longitude are input variables in Thornthwaite's method to calculate potential evapotranspiration (PET) (Thornthwaite 1948). SPEI was used to estimate drought and wet occurrences over a period of three, six, nine, and twelve months from 1971 to 2018. The severity, duration, and intensity of dry and wet event characteristics were calculated by applying the run theory to the SPEI output. The VSCA technique was utilized to account for drought variability and depict the evolution of the pattern during the time period under consideration.

## Study Area and Data Used

The district of Mirzapur in Uttar Pradesh (India), located on the Vindhyan Plateau in the middle Gangetic plain and covering a total area of 4,521 $km^2$, is being studied for this present objective. Mirzapur stretches between 23°52′ to 25°32′ North latitude and 82°07′ to 83°33′ East longitude (Fig. 1). The Mirzapur district has two immediate reliefs, the Alluvial Ganga plains in the north and the Vindhyan Plateau in the south. Soil is available in various forms, from alluvial to sandy to red. Red and black soils predominate in plateau regions (Census of India 2011). The humid subtropical climate (Köppen classification Cwa) characterizes the weather in Mirzapur, which has dry winters. The average annual rainfall occurs at 997.40 mm a year, with 75 to

80 percent of the rainfall coming from the Bay of Bengal monsoonal system during the monsoon season (June to September). And the temperature extremes were observed during summer (42 to 45°C) and winter (8 to 10°C). The average relative humidity is 42.2 %, ranging from 42.2 to 70.5 %. In rainfed sections of the district, farmers plant paddy as a primary crop during the Kharif season (90 % of total farmed land) and mustard, lentil, chickpea, and pea during the rabi season on residual moisture.

SPEI index is adopted to evaluate the temporal pattern of meteorological drought and wet events over the research area. It requires monthly precipitation (P) and potential evapotranspiration (PET) as input climate variables to estimate drought and wet events at the timescale of 3 months, 6 months, 9 months, and 12 months. The Thornthwaite method was used to calculate potential evapotranspiration. From 1971 to 2018, the monthly weather data (rainfall and temperature) were obtained from the Indian Meteorological Department (IMD) and the Indian Water Portal (https://www.indiawaterportal.org/met_data).

## MATERIALS AND METHODS

### Potential Evapotranspiration (PET)

Potential evapotranspiration (PET) is the potential of the atmosphere to remove the maximum amount of water by evaporation and transpiration from the uniformly vegetated surface without any limitation's other atmospheric demands. The critical factors limiting the rate of potential evapotranspiration are the sun's radiative energy, wind, the vapors deficit of the air, and temperature. The Thornthwaite method, as given in equation 1, used to estimate PET requires only monthly average temperature as an input climatic variable (Thornthwaite 1948).

$$PET = 16d\left(\frac{10T}{I}\right)^{a} \quad \ldots(1)$$

Where $d$ is the correction factor, $T$ (°C) means monthly temperature, $I$ denote the annual thermal index, and $i$ is the monthly thermal index. These variables can be calculated as follows:

$$I = \sum_{j=i}^{12} i \quad \ldots(2)$$

$$i = \left(\frac{t}{5}\right)^{1.514} \quad \ldots(3)$$

$$a = 0.49 + 0.018I - 7.7x10^{-5} I^2 + 6.7x10^{-7} I^3 \quad \ldots(4)$$

### Standardized Precipitation Evapotranspiration Index (SPEI)

The standardized evapotranspiration index (SPEI) is a multivariate drought index established by Vicente-Serrano et al. (2010), which considers the impact of temperature

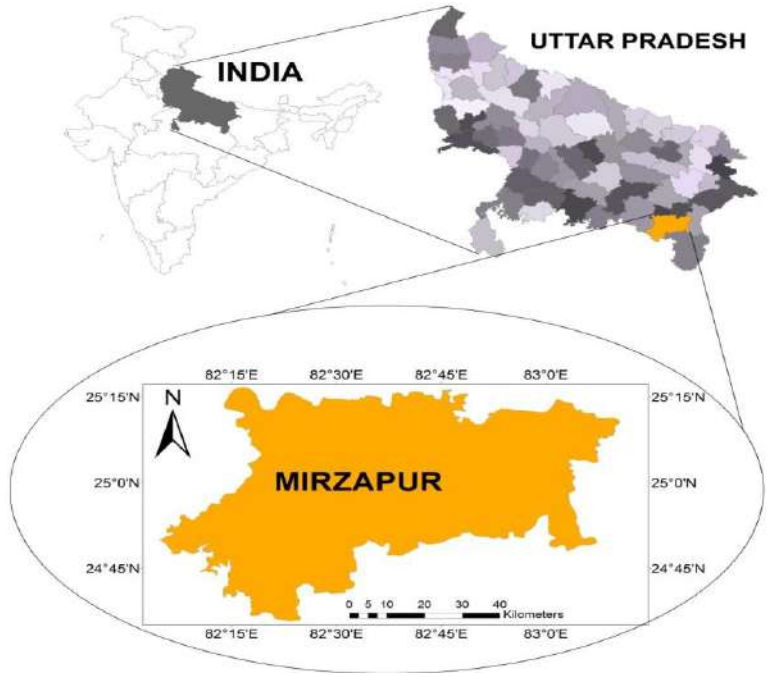


Fig. 1: Geographical map of the Mirzapur district of Uttar Pradesh, India.

Table 1: Categorization of the severity of drought and wet events based on SPEI values.

| SPEI | Severity | SPEI | Severity |
|---|---|---|---|
| Extreme drought | <-2 | Moderately Wet | 1.49 to 1.0 |
| Severe drought | -1.5 to 1.99 | Very Wet | 1.99 to 1.5 |
| Moderate drought | -1.0 to -1.49 | Extremely Wet | 2≤ |
| Near Normal | 0.99 to -0.99 | - | - |

variation on drought severity (Liu et al. 2021). Climate factors such as precipitation and temperature, which influence water availability and variability, are considered in the classification of drought severity. SPEI takes water balance (P-PET) as input climatic at different accumulation periods. The non-exceedance probability of water balance ($Di = P_i - PET_i$) (equation) determines the SPEI values. The method for calculating the SPEI value is described in detail (Pei et al. 2020, Polong et al. 2019, Tan et al. 2015).

The calculated D values are accumulated at different time scales

$$D_n^k = \sum_{i=0}^{k-1} P_{n-1} - (PET)_{n-1} \quad \ldots(5)$$

K is the timescale (months) of accumulation, and n is the calculation month.

The probability density function of a Log-logistic distribution is given as follows:

$$f(x) = \frac{\beta}{\gamma}\left(\frac{x-\gamma}{\alpha}\right)^{\beta-1}\left(1+\left(\frac{x-\gamma}{\alpha}\right)^{\beta}\right)^{-2} \quad \ldots(6)$$

where α, β, and γ are scale, shape, and origin parameters, respectively, for $\gamma > D < \infty$. The probability distribution function for the D series is given as follows:

$$F(x) = \left[1+\left(\frac{\alpha}{x}-y\right)^{\beta}\right]^{-1} \quad \ldots(7)$$

With f(x) the SPEI can be obtained as the standardized values of F(x):

Where, $SPEI = W - \frac{C_0+C_1W+C_2W^2}{1+d_1W+d_2W^2+d_3W^3}$ …(8)

$$W = \sqrt{-2\ln(P)} \text{ for } P \leq 0.5 \quad \ldots(9)$$

P is the probability of exceeding a determined $D_i$ value and is given as

$P = 1 - f(x)$ while the constants are:

$C_0 = 2.515517$, $C_1 = 0.802853$, $C_2 = 0.010328$, $d_1 = 1.432788$, $d_2 = 0.189269$, $d_3 = 0.001308$

## Characteristics of Drought and Wet Events

Drought and wet episode characteristics are defined by severity, intensity, and duration, determined by the run theory given by Yevjevich (1969). A run is a period in which all the index values fall below a predetermined threshold (Yevjevich 1969). Researchers in the literature have used various thresholds to estimate drought parameters (Mesbahzadeh et al. 2020, Pandey et al. 2021). Based on SPEI output, drought and wet event parameters were estimated at the threshold of SPEI <-1 to evaluate drought/ wet event characteristics. When SPEI values are consistently negative and reach a value of -1 or below, it is considered a drought event, and when SPEI value comes to 1 or above, it is considered a wet event (Table 1).

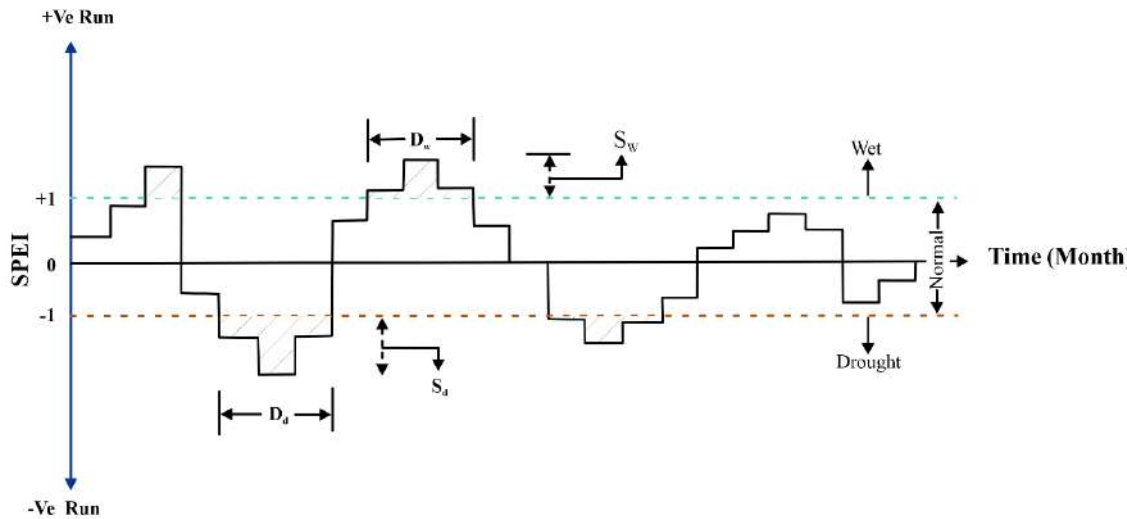


Fig. 2: Run theory-based drought and wet characterization (Malik et al. 2021).

***Drought and Wet Severity ($S_d$ and $S_w$)***

During droughts and wet events, severity is calculated as the absolute value of indices.

$$S_d = |\sum_{n=1}^{D} \text{SPEI}| \leq -1 \quad \ldots(10)$$

$$S_w = |\sum_{n=1}^{D} \text{SPEI}| \geq 1 \quad \ldots(11)$$

***Drought and Wet Duration ($D_d$ and $D_w$)***

It is defined as months between the start and end of a drought event when SPI/SPEI ≤ -1 and during wet during the event when SPEI ≥ 1.

***Drought and Wet Intensity ($I_d$ and $I_w$)***

During a drought and wet event, the ratio of the absolute value of drought and wet severity to the duration of the drought and the wet event is computed as drought and wet intensity ($I_d$ and $W_d$).

$$I_d = \frac{S_d}{D_d} \quad \ldots(12)$$

$$I_w = \frac{S_w}{D_w} \quad \ldots(13)$$

**Variable-Sized Cluster Analysis**

For trend analysis, rather than the traditional approach of using Pettitt Mann Whitney's method, which yields a single long-term trend, the provided form uses variable-size cluster analysis, which provides a visual representation of the changing trend pattern as well as hints to identify one or several change points and/or alternate trends (Gupta et al. 2021). Drought trend variation was clearly illustrated by 3-D figures created for Z-score variability with varied starting and ending periods. This was not apparent by a conventional M.K. test, including the whole historical dataset. Trend analysis based on station scale data was more accurate than grid-based data based on spatial averaging. A more accurate result may be drawn when numerous clusters were created by successively deleting data from the beginning of each year in the M.K. test.

It was necessary to apply the Mann-Kendall test many times to provide a reliable picture of the effect of drought in the Mirzapur area of Uttar Pradesh. Although it was first set to 5, 10, 15, and 20 to check if the results of the research were influenced, it was ultimately set at 10 for the repeated application of the Mann-Kendall trend test for all districts. The following equation was used to determine how many times the Mann-Kendall test would have to be run in a given district:

$$N = \frac{[(n-8).(n-9)]}{2} \quad \ldots(14)$$

The two-and three-dimensional planes were used to depict the Z values obtained from each MK test application. Z values are shown in 3-D for the first time in this study. Each of the graphs in this section shows the time at which each data cluster is picked for Z-value determination, as shown in Fig. 5(a)-8(a). Alternatively, the Z-statistic may be seen in various colors in the upper left triangle region of Images 5(b)-8(b) from the top viewpoint of Images 5(a)-8(a). As one goes across the graphical plane, the size of the data cluster is utilized to compute the Z-statistic changes. This is seen in Figs. 5(a)-8(a), where the Z statistic values correspond to variable-sized data clusters with varying starting and ending durations (a). These variable-sized data clusters may assess drought trend patterns using different Z-statistic values. The magnitude of the Z-statistic was depicted using a Z-axis normal to the X-Y plane; as a result, these images provide a 3-D graphical viewpoint of an erratic surface spread according to various Z-statistic values.

Z values are shown in 3-D in this work, which is a novel feature. The numbers indicate data clusters selected for Z value determination on the abscissa and ordinate axes in Figs. 5(a)-8(a). As Figs. 5(b)-8(b), the Z-statistic can be shown in various shades of color in the top left triangle of the figures. On the graphical plane, the size of the data cluster is utilized to compute the Z-statistic changes as illustrated in Fig. 5(a)-8(a), which shows the Z statistic values for variable-sized data clusters with varied beginning and ending durations. It is possible to calculate multiple Z-statistic values, which may then be displayed to study the drought pattern and trend. Using a Z-axis (Z-axis) normal to the X-Y plane, these images display a 3-D viewpoint of an erratic surface spread in accordance with shifting Z-statistic values, as seen in these images.

Z-values with fixed window size (data cluster size) but growing start time are depicted in Figs. 5b-8b by a line parallel to the hypotenuse of the right-angled triangle. There are 10 data points in this window, and parallel lines on the hypotenuse represent the following window sizes 11, 12, 13, 14, and so on. Data from the first to the tenth, first to the eleventh, first to the twelfth, etc., are represented by dots on perpendicular vertical lines to the abscissa. Color variations in Fig. 5(a-b)-8(a-b) represent significant shifts in the drought trend, which are seen in the figures. Change points with multimodal characteristics cannot be detected using the Pettitt-Mann-Whitney test because it relies on a single maximum value of Ut for the entire time period, whereas variable-sized cluster analysis allows for the detection of multiple change points that may have occurred over the course of a century. When one or more changes occur throughout the research, VSCA can identify them.

## RESULTS AND DISCUSSION

**Meteorological Drought and Wet Characterization**

A joint assessment of meteorological drought and wet period using SPEI at different accumulation periods of water balance

(P- PET) (3-month, 6-month,9- month, and 12-month) over Mirzapur (Uttar Pradesh) India for the period of years from 1971 to 2018. The negative value of SPEI indicates the drying condition from normal conditions, whereas the positive value of SPEI referred to as wet condition (Fig. 2). Meteorological drought characteristics, i.e., severity, intensity, and duration, and the number of drought occurrences estimated at the threshold of SPEI $\leq$ -1 similarly, wet event characteristics estimated at the threshold of SPEI $\geq$ 1. Fig. 4 indicate that a higher number of drought/ wet event of different categories recorded at a shorter time scale (SPEI-3, SPEI-6 ) indicate the seasonal variation of climatic water balance, which may cause an adverse impact on the crops of the study region. In contrast, at higher time scale (SPEI-9 and SPEI-12), the number of occurrence drought/wet event reduced but occurred with higher severity and persisted for a longer duration (Fig. 3 & Fig. 4), which indicate the SPEI's gradual and consistent response to changes in water balance annual scale. The study area dominantly experiences moderate drought-wet events during the study period. During the study period, a slightly higher number of meteorological drought events at every scale (SPEI-3=42, SPEI-6=30, SPEI-9=23, SPEI=20 ) were recorded in comparison with wet events (SPEI-3=40, SPEI-6=30, SPEI-9=24, SPEI12=11) Fig. 4 depicts the decadal shift in the occurrences of drought-wet events of various types, highlighting the most significant number of drought occurrences reported during the 2000s, followed by the 2000s. After 2000, the maximum number of wet occurrences was recorded throughout the 1970s and 1980s. As the decades progressed, the number of wet occurrences decreased, indicating drying up conditions over the study area.

The drought-wet event characteristics (severity, intensity, and duration) are summarized in Fig. 3 by combining a violine plot with a small box plot for different timescales for the study period, where the width of the violine denotes frequency, and the curve denotes the shape of the data. The thin black line represents the maximum and minimum value

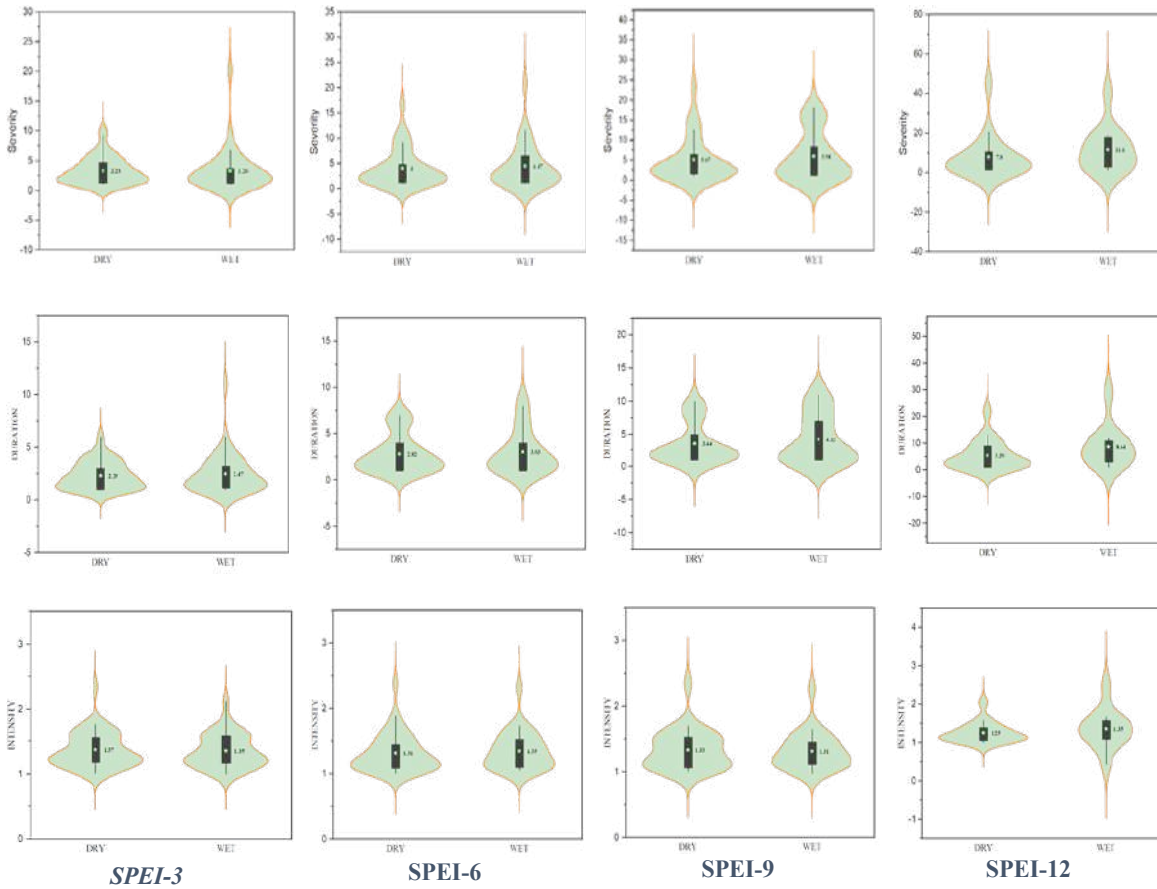


Fig. 3: Violine diagram with a small box plot explaining the drought and wet event characteristics (Severity, Duration, and Intensity) of SPEI-3, SPEI-6, SPEI-9, and SPEI-12 time series from 1971 to 2018. The density curve's width represents the data's frequency, and the small black box plot represents the first and third quartiles. The star sign in the center of the box plot represents the mean.

of drought-wet characteristics, and the star at the center of the box plot indicates the average of drought-wet characteristics. A greater of drought-wet events occurred as the timescale of SPEI progressed $S_w$ (SPEI-3)=3.26, $S_w$ (SPEI-6)=4.47, $S_w$ (SPEI-9)=5.94, and $S_w$ (SPEI-12)=11.6 which interestingly illustrates that wet event occurred with the severity of drought events $S_d$ (SPEI-3)=3.5, $S_d$ (SPEI-6)=5, $S_d$ (Spei-9)=6.93, $S_d$ (SPEI-12)=7.34. In contrast, the duration of the drought-wet event is $D_d$ (SPEI-3)=2.4, $D_d$ (SPEI-6)=3, $D_d$ (SPEI-9)=4.12, $D_d$ (SPEI-12) =2.2, $D_w$ (SPEI-6)=2.8, $D_w$ (SPEI-9)=3.4, and $D_w$ (SPEI-12)=5.3, indicating that the drought episode persisted for a longer duration. As demonstrated in Fig. 3, the intensity of drought-wet episodes does not vary significantly with the timescale. Drought and wet events occurred at roughly the same intensity.

**Pattern Characterization of Meteorological Drought**

3-D and 2-D images of the drought trend over Mirzapur

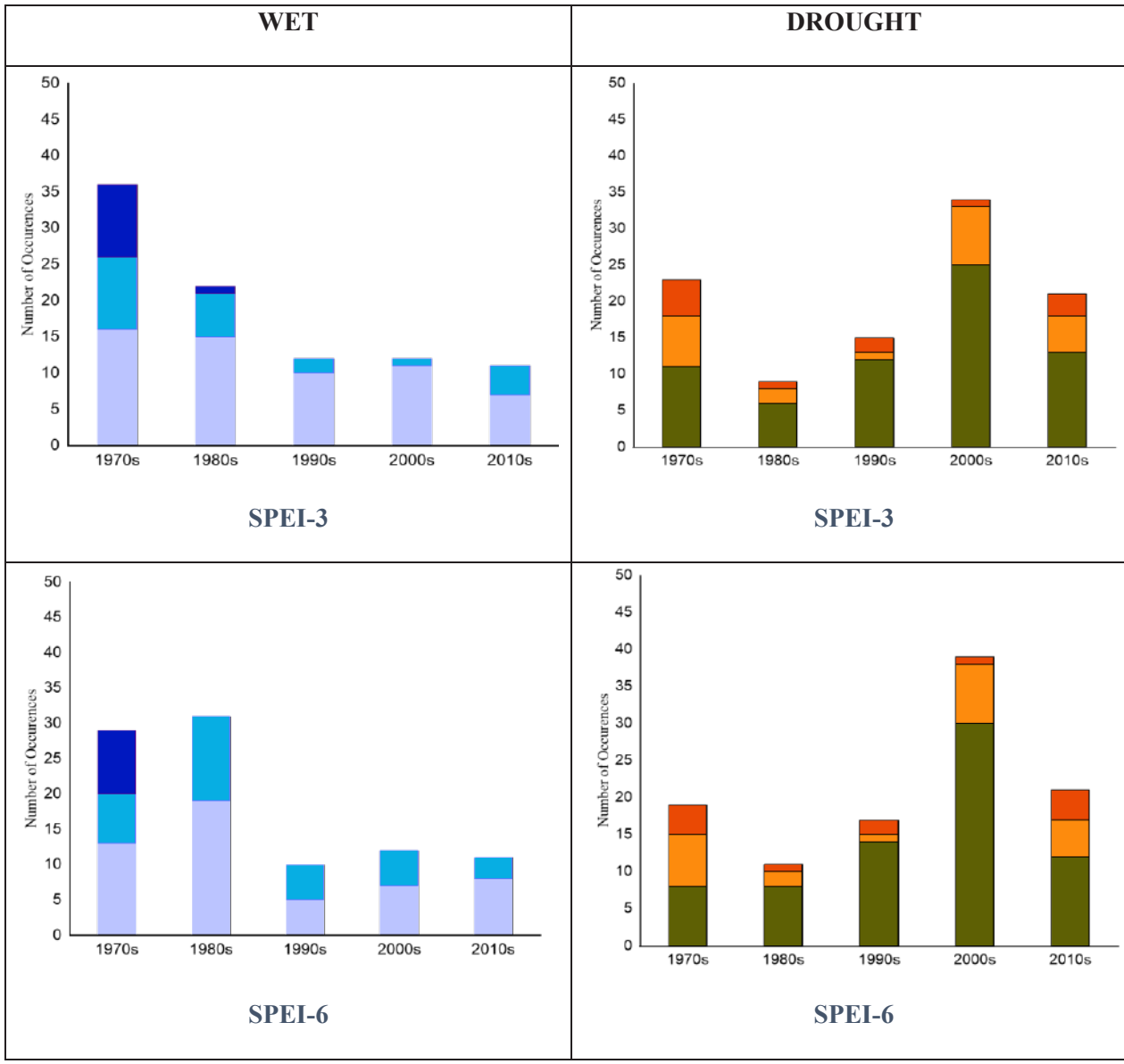


Fig. Cont....

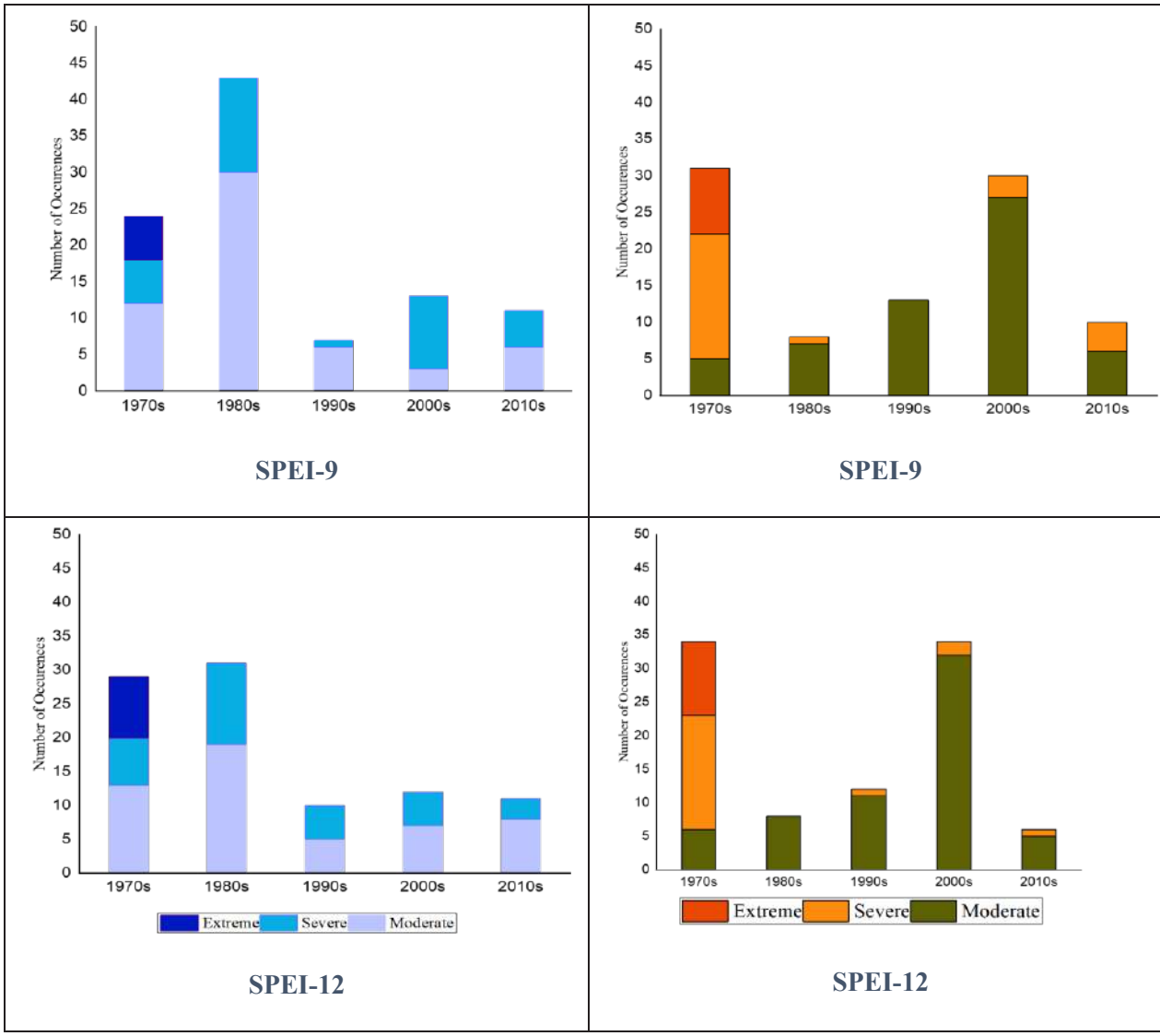


Fig. 4: Number of Drought and Wet events occurrences of different categories (Extreme, Severe, Moderate) of SPEI-3, SPEI-6, SPEI-9, and SPEI-12 during the last five decades, i.e., the 1970s, 1980s, 1990s, 2000s, and 2010s.

from 1971 to 2018 are shown in Figs. 5(a-b) and 8(a-b), respectively. There are many crests and troughs of different heights seen in Fig. 5a. The greater the height of the crests, the more intense and stronger the trend direction is. The trend's swings are reflected in the chart's many crests and troughs. Thus, the drought patterns in Mirzapur were shown to shift throughout time. There are basically three distinct zones in Fig. 5(a), each with a distinct set of troughs, crests, and low-amplitude troughs and high-amplitude crests (Zone-1, Zone-2, and Zone-3) (Zone-3). In Fig. 5(b), these zones are shown as patches of the same number. Zone-1 and patch-1 show a lessening tendency in drought conditions. Drought in Zone 2 and Patch 2 increased significantly during the 1960s compared to the previous decades. Zone-3, on the other hand, shows just a minor tendency for drought in either direction, with no notable characteristics.

The results of this cluster analysis with a range of cluster sizes can also be used to pinpoint the point(s) at which the drought pattern began to shift. As shown in Fig. 5(b), to draw a line separating Patches 1-2 from Patch 3, one must first project an imaginary straight line from Patches 1 and 2's maximum amplitude crest (see Fig. 5(a)) to Patch 3's least undulating surface (indicated along ending data 100). When these lines connect with the horizontal line, the tendency of drought undergoes a substantial shift over a number of years. Thus, the MK test-based VSCA anal-

ysis provided not only the drought trend but also a great capacity to pinpoint the time of change. The inflection line between zones 1 and 2 is the foundation for drawing the line separating patches 1 and 2 from each other. The difference in the drought trend might be considered a turning point in the differentiation of these zones. The increasing industrialization-induced urbanization is thought to be the cause.

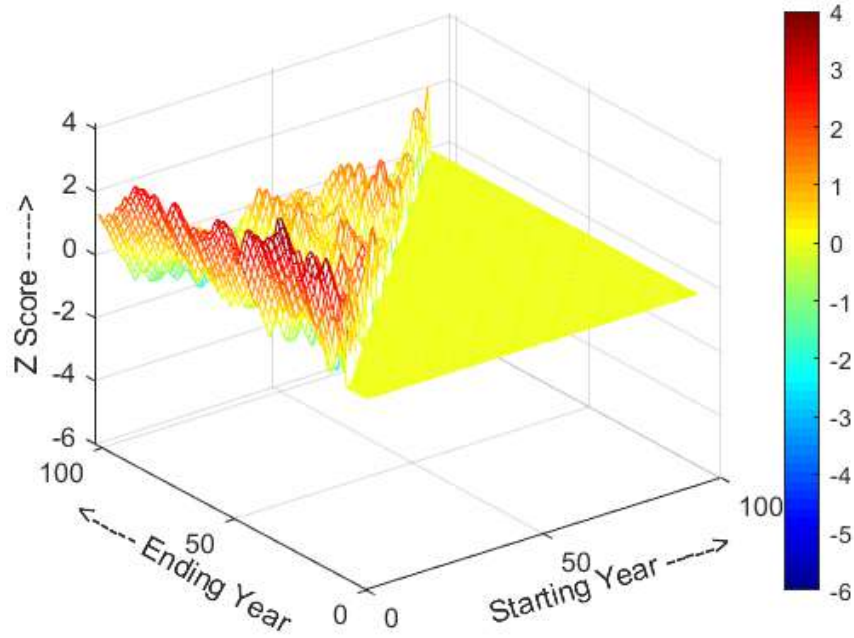


Fig. 5(a): 3-D characteristics of the pattern of drought trend at time scale 3 at significance level 0.05 for Mirzapur.

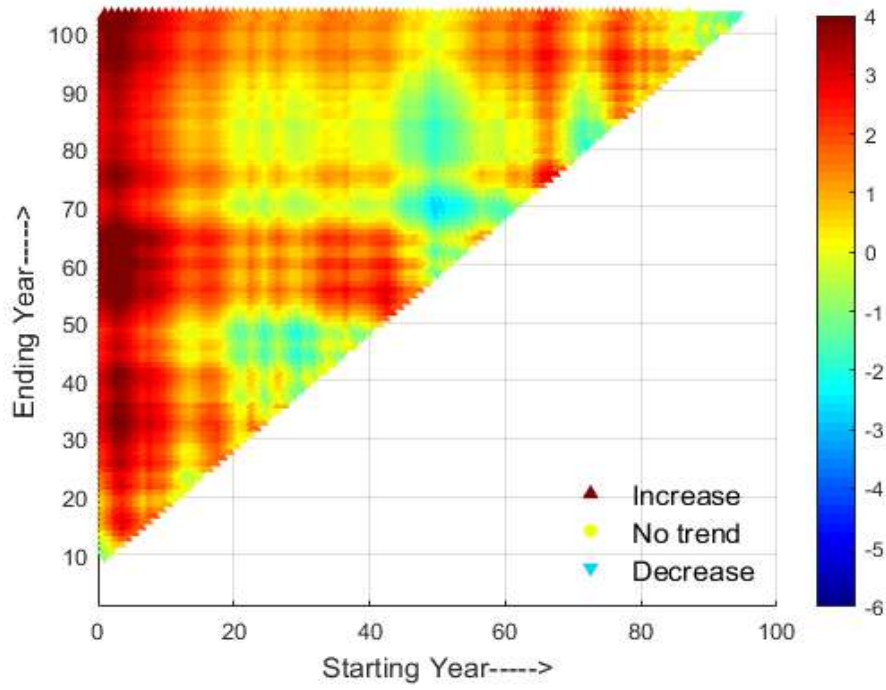


Fig. 5(b): 2-D characteristics of the pattern of drought trend at time scale 3 at significance level 0.05 for Mirzapur.

3D and 2D patterns of drought features for Mirzapur are shown in Figs. 6 (a-b). Several color shifts can be seen near the 100-point mark on the x-axis-parallel line that was drawn. The point at which something changes is called the change point. These spots around the 13th, 27th, 41st, and 73rd have disrupted drought patterns. Fig. 6(a) displays the trend's multimodal features, including two trough zones (equivalent to patches 1&3 in 2D Fig. 6(b)) and a crest zone (patch 2). The variable-sized cluster analysis may determine the various change points that may have happened in the provided historical drought data. As a result, if the research is lengthy enough, VSCA may be able to detect numerous

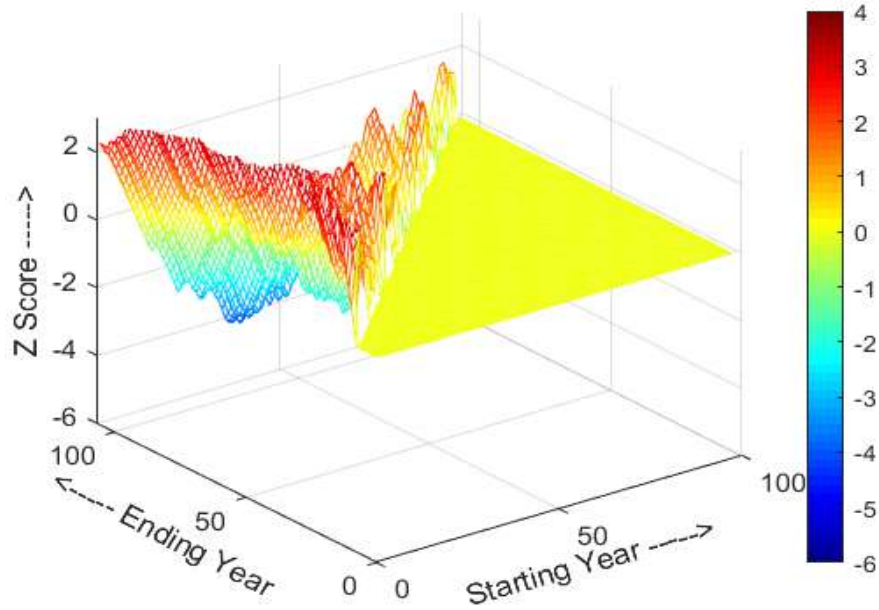


Fig. 6(a): 3-D characteristics of the pattern of drought trend at time scale 6 at a significance level of 0.05 for Mirzapur.

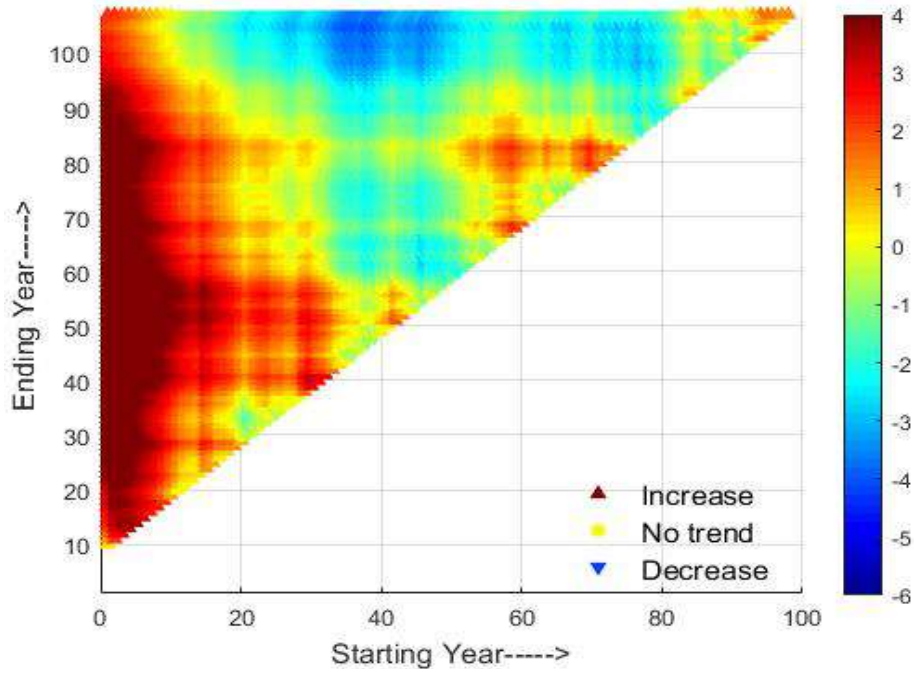


Fig. 6(b): 2-D characteristics of the pattern of drought trend at time scale 6 at significance level 0.05 for Mirzapur.

points of change. Fig. 6 and 7 show the same thing as in Fig.5(a) and (b).

Fig. 7 and 8 illustrate the 3D and 2D drought trends at time scale 9 for Mirzapur (a-b). As seen in 2D Fig 7(b), Fig 7(a) exhibits two troughs and one crest (patches 1 and 3). The multimodal trend pattern is clearly apparent in Fig 7(a). Comparing the data from the first decades of the drought series, a decrease in drought severity is seen in Zone 1

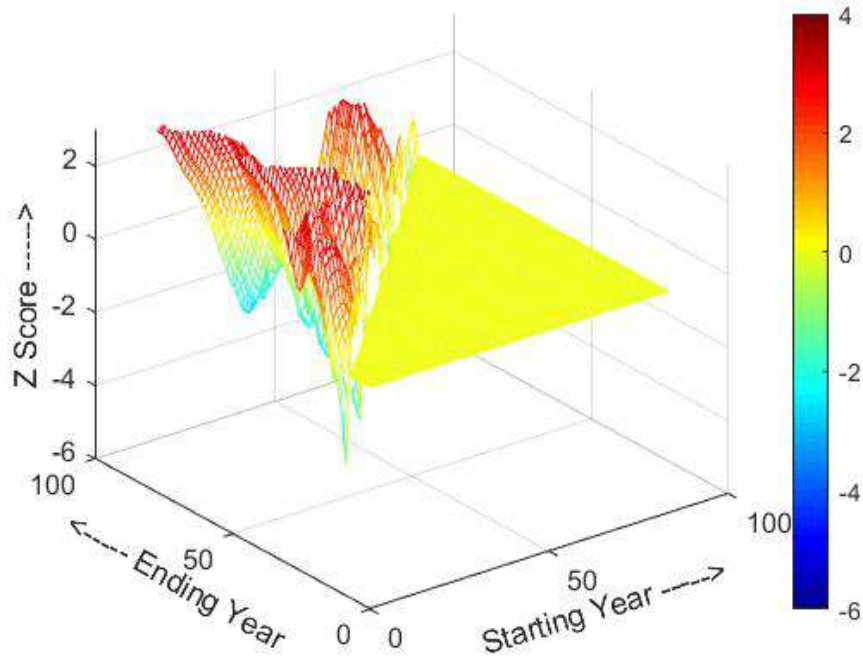


Fig. 7(a): 3-D characteristics of the pattern of drought trend at time scale 9 at a significance level of 0.05 for Mirzapur.

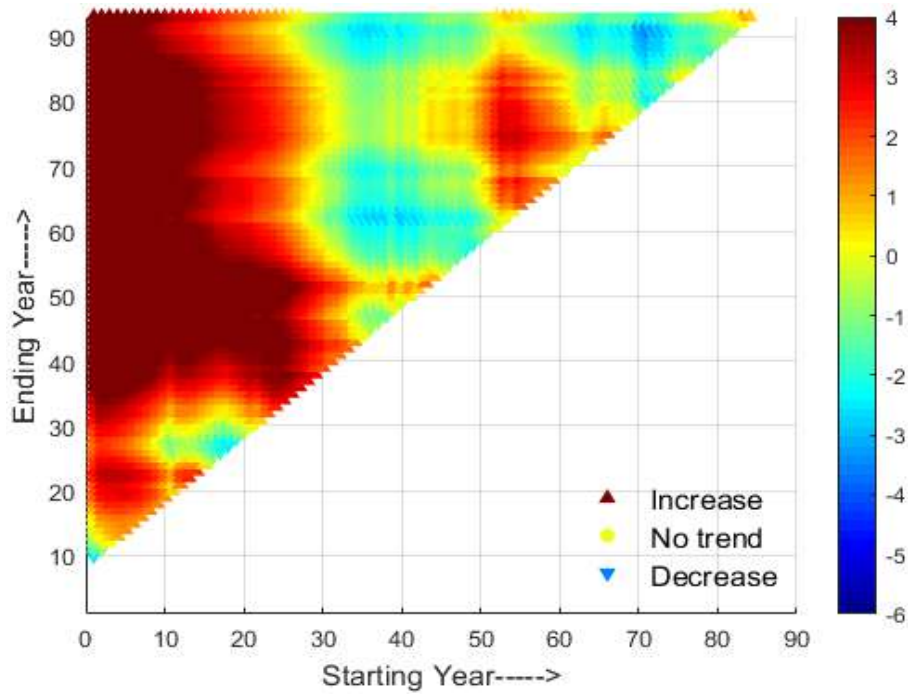


Fig. 7(b): 2-D characteristics of the pattern of drought trend at time scale 9 at a significance level of 0.05 for Mirzapur.

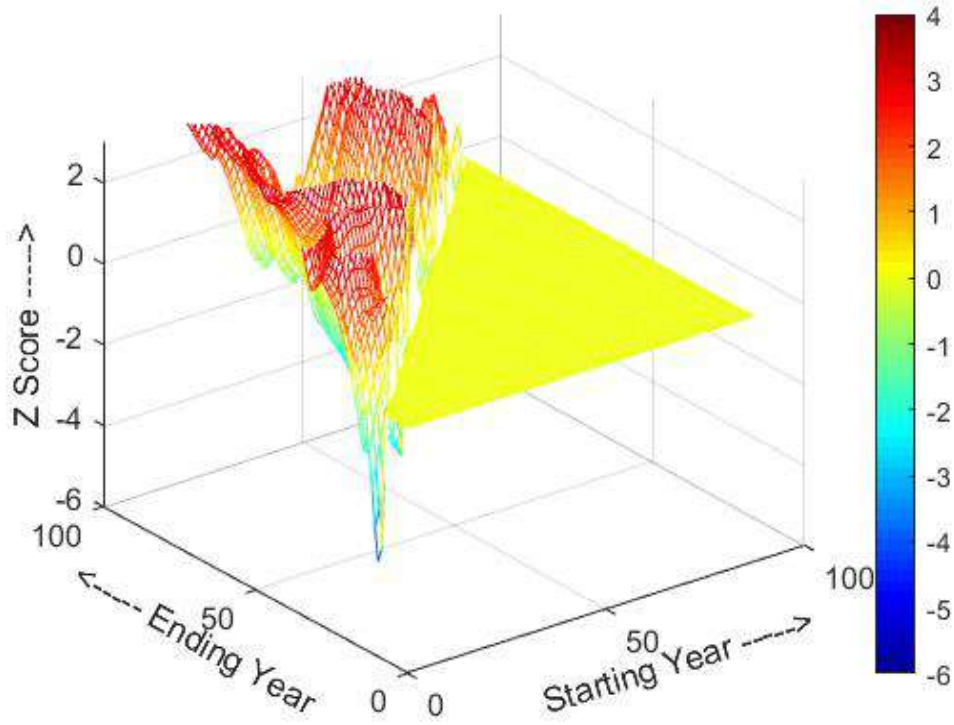


Fig. 8(a): 3-D characteristics of the pattern of drought trend at the time scale of 12 at a significance level of 0.05 for Mirzapur.

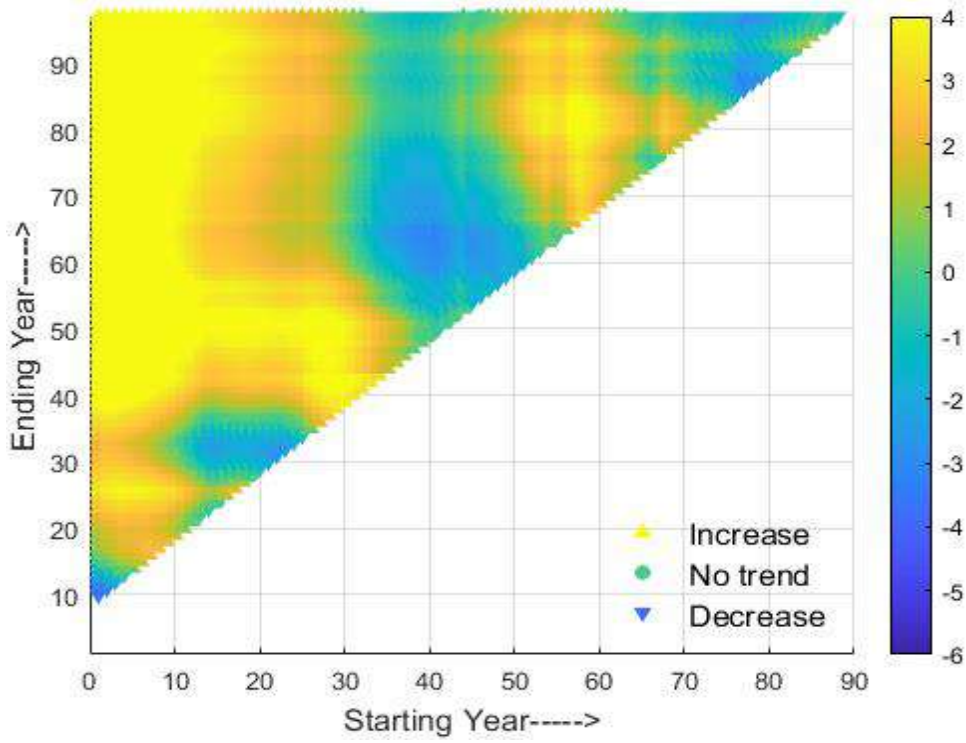


Fig. 8(b): 2-D characteristics of the pattern of drought trend at a time scale of 12 at a significance level of 0.05 for Mirzapur.

throughout the decades surrounding the 40th century. The line drawn parallel to the x-axis shows a significant break in the continuity of shades of hue. With regard to the total duration of the data series, this refers to a shift in the drought trend. In this case, the variable-sized cluster analysis could also show the trend pattern across multiple periods for a century's worth of data and identify the transition point. As a result, VSCA may be able to detect one or more change points if the research is long enough. Fig. 7 and 8 show the same thing as in Fig. 5(a) and (b).

For Mirzapur, 3D and 2D patterns of drought features are shown in Figs. 8(a-b). It is obvious that two patches 1-2, which split the two zones of crest and depression, may be seen in Fig. 8(a) and (b). Mirzapur's change sites were identified using the multimodal properties of the pattern of trend in Fig. 8(a) and the 2D pattern in Fig. 8(b). Ending time series data 100 is shown in the 2D Fig. 8 as an increase or decrease in color along a line drawn parallel to the x-axis (b). This is where a major shift in the trend has happened, according to the change in the continuity of colors. It's possible to see a change in trend around roughly data points 19 through 69 (On the x-axis). Fig. 8(a) clearly shows the crests and troughs that result from these many transition points. VSCA provided numerous change points to detect multiple change points.

## CONCLUSION

The present study provides a joint assessment of drought-wet event characteristics and their temporal variability over the study period. The SPEI is used as proxies to estimate the meteorological drought–wet event, which incorporates the impact of global warming over the hydrologic extremes. The monthly SPEI was estimated at different accumulation periods (3-month, 6-month, 9-month, and 12-month) for the period 1971 to 2018. The assessment of temporal variability of drought–wet event occurrence indicates that the study area was primarily impacted by moderate category drought and wet conditions, followed by severe category drought and wet conditions, and extreme category drought and wet conditions, which occurred only infrequently over the course of the research. The decadal analysis of dry and wet event occurrences reveals a considerable increase in drought events after the 2000s, indicating a shift in climatic conditions over Mirzapur, which poses a threat to agriculture. To better understand the characteristics of drought and wet event severity, intensity, and duration, a threshold of one was used to determine that as the timescale grows, the severity and duration of an event increase, and the drought event occurs with greater severity and lasts longer. There is no discernible variation in the intensity of drought and wet events over timescales. The above analysis revealed that Mirzapur experiences a higher number of meteorological droughts with higher severity and longer duration.

## REFERENCES

Bacanli, Ü.G. 2017. Trend analysis of precipitation and drought in the Aegean region, Turkey. Meteorol. Appl., 249: 239-249. https://doi.org/10.1002/met.1622

Bhagawati, R., Bhagawati, K., Jini, D., Alone, R.A., Singh, R., Chandra, A., Makdoh, B., Sen, A. and Shukla, K.K. 2017. Review on climate change and its impact on agriculture of Arunachal Pradesh in the Northeastern Himalayan region of India. Nat. Environ. Pollut. Technol., 6(2): 535-539.

Dashtpagerdi, M.M., Kousari, M.R., Vagharfard, H., Ghonchepour, D., Hosseini, M.E. and Ahani, H. 2015. An investigation of drought magnitude trend during 1975–2005 in arid and semi-arid regions of Iran. Environ. Earth Sci., 73(3): 1231-1244. https://doi.org/10.1007/s12665-014-3477-1

Gond, S., Gupta, N. and Gupta, S. 2019. Evaluation of Drought Severity Indices and their Trend for Mirzapur (Uttar Pradesh). December 2019. 24th International Conference on Hydraulics, Water Resources and Coastal Engineering (HYDRO 2019 International), 18-20 December 2019, Hyderabad, India, Osmania University & The Indian Society for Hydraulics, Hyderabad & Pune, pp. 2275-2283

Guhathakurta, P., Menon, P., Inkane, P.M., Krishnan, U. and Sable, S.T. 2017. Trends and variability of meteorological drought over the districts of India using standardized precipitation index. J. Earth Syst. Sci., 126(8): 1-18. https://doi.org/10.1007/s12040-017-0896-x

Gupta, N., Gond, S. and Gupta, S.K. 2022. Spatiotemporal trend characteristics of rainfall and drought jeopardy over Bundelkhand Region, India. Arab. J. Geosci., 15(12): 1155. https://doi.org/10.1007/s12517-022-10389-8

Gupta, S.K., Gupta, N. and Singh, V.P. 2021. Variable-sized cluster analysis for 3d pattern characterization of trends in precipitation and change-point detection. J. Hydrol. Eng., 26(1): 04020056. https://doi.org/10.1061/(asce)he.1943-5584.0002010

He, X., Wada, Y., Wanders, N. and Sheffield, J. 2017. Intensification of hydrological drought in California by human water management. Geophys. Res. Lett., 44(4): 1777-1785. https://doi.org/10.1002/2016GL071665

Huang, C., Zhang, Q., Singh, V.P., Gu, X. and Shi, P. 2017. Spatio-temporal variation of dryness/wetness across the Pearl River basin, China, and relation to climate indices. Int. J. Climatol., 37: 318-332. https://doi.org/10.1002/joc.5005

Liu, X.F., Wang, S.X., Zhou, Y., Wang, F.T., Yang, G. and Liu, W.L. 2016. Spatial analysis of meteorological drought return periods in China using Copulas. Natural Hazards, 80(1): 367-388. https://doi.org/10.1007/s11069-015-1972-7

Malik, A., Kumar, A., Kisi, O., Khan, N., Salih, S. Q. and Yaseen, Z. M. 2021. Analysis of dry and wet climate characteristics at Uttarakhand (India) using effective drought index. Natural Hazards, 105(2), 1643-1662. https://doi.org/10.1007/s11069-020-04370-5

Mallya, G., Mishra, V., Niyogi, D., Tripathi, S. and Govindaraju, R. S. 2015. Trends and variability of droughts over the Indian monsoon region. Weather Clim. Extremes, 12: 43-68. https://doi.org/10.1016/j.wace.2016.01.002

Mesbahzadeh, T., Mirakbari, M., Mohseni Saravi, M., Soleimani Sardoo, F. and Miglietta, M.M. 2020. Meteorological drought analysis using copula theory and drought indicators under climate change scenarios (RCP). Meteorol. Appl. 27(1): 1-20. https://doi.org/10.1002/met.1856

Mishra, A.K. and Singh, V.P. 2010. A review of drought concepts. J. Hydrol., 391(1-2): 202-216. https://doi.org/10.1016/j.jhydrol.2010.07.012

Nabaei, S., Sharafati, A., Yaseen, Z.M. and Shahid, S. 2019. Copula

based assessment of meteorological drought characteristics: Regional investigation of Iran. Agric. Forest Meteorol., 276-277:, 107611. https://doi.org/10.1016/j.agrformet.2019.06.010

Omar, P.J., Dwivedi, S.B. and Dikshit, P.K. 2019a. Temporal variability study in rainfall and temperature over Varanasi and adjoining areas. Disas. Adv., 12(1): 1-7.

Omar, P.J., Gaur, S., Dwivedi, S.B. and Dikshit, P.K.S. 2019b. Groundwater modelling using an analytic element method and finite difference method: An insight into Lower Ganga river basin. J. Earth Syst. Sci., 128(7): 195. https://doi.org/10.1007/s12040-019-1225-3.

Omar, P.J., Gaur, S., Dwivedi, S.B. and Dikshit, P.K.S. 2020. A modular three-dimensional scenario-based numerical modelling of groundwater flow. Water Resour. Manag., 34(6): 1913-1932. https://doi.org/10.1007/s11269-020-02538-z

Pandey, V., Srivastava, P. K., Singh, S.K., Petropoulos, G.P. and Mall, R.K. 2021. Drought identification and trend analysis using long-term chirps satellite precipitation product in Bundelkhand, India. Sustainability (Switzerland), 13(3): 1-20. https://doi.org/10.3390/su13031042

Pei, Z., Fang, S., Wang, L. and Yang, W. 2020. Comparative analysis of drought indicated by the SPI and SPEI at various timescales in inner Mongolia, China. Water, 12(7): 925. https://doi.org/10.3390/w12071925

Polong, F., Chen, H., Sun, S. and Ongoma, V. 2019. Temporal and spatial evolution of the standard precipitation evapotranspiration index (SPEI) in the Tana River Basin, Kenya. Theor. Appl. Climatol., 138(1-2): 777-792. https://doi.org/10.1007/s00704-019-02858-0

Qutbudin, I., Shiru, M.S., Sharafati, A., Ahmed, K., Al-Ansari, N., Yaseen, Z.M., Shahid, S. and Wang, X. 2019. Seasonal drought pattern changes due to climate variability: Case study in Afghanistan. Water, 11(5): 096. https://doi.org/10.3390/w11051096

Singh, G. 2019. Rainfall analysis for crop planning under rainfed condition at Mirzapur district in Vindhya plateau of Indo-Gangetic Plain Rainfall analysis for crop planning under rainfed condition at Mirzapur district in Vindhya plateau of Indo-Gangetic Plain. Indian J. Soil Conserv., 47(1): 1-8.

Singh, G., Soil, C. and Singh, R.M. 2019. Stochastic modeling of water deficit for crop planning under climatic conditions of Mirzapur district in Uttar Pradesh Stochastic modeling of water deficit for crop planning under climatic conditions of Mirzapur district in Uttar Pradesh. J. Agrometeorol., 21: 41-47.

Srinivas, P. and Sarala, C. 2007. Hydrological data analysis for the identification of droughts in Anantapur District, Andhra Pradesh. Nature Environ. Pollut. Technol., 6(4): 565-572.

Subbiah, T.S., Parthiban, P., Mahesh, R. and Das, A. 2021. Time series analysis of decadal precipitation pattern at selected cities of southern India. Nature Environ. Pollut. Technol., 20(3): 1201-1208. https://doi.org/10.46488/NEPT.2021.v20i03.028

Rosalia, A.C. and Hakim, L. 2021. Spatial analysis of the impact of flood and drought on food security index. Nature Environ. Pollut. Technol., 20(2): 721-727. https://doi.org/10.46488/NEPT.2021.v20i02.031

Tan, C., Yang, J. and Li, M. 2015. Temporal-spatial variation of drought indicated by SPI and SPEI in Ningxia Hui autonomous region, China. Atmosphere, 6(10): 1399-1421. https://doi.org/10.3390/atmos6101399

Thornthwaite, C.W. 1948. An approach toward a rational classification of climate. Geogr. Rev., 38(1): 55. https://doi.org/10.2307/210739

Varughese, A. 2017. Analysis of historical climate change trends in Bharathapuzha River Basin, Kerala, India. Nature Environ. Pollut. Technol., 16(1): 237-242.

Vicente-Serrano, S.M., Beguería, S. and López-Moreno, J.I. 2010. A multiscalar drought index sensitive to global warming: The standardized precipitation evapotranspiration index. J. Clim., 23(7): 1696-1718. https://doi.org/10.1175/2009JCLI2909.1

Yevjevich, V. 1969. An objective approach to definitions and investigations of continental hydrologic droughts. J. Hydrol., 7(3): 353. https://doi.org/10.1016/0022-1694(69)90110-3

Zhang, D.D., Yan, D.H., Lu, F., Wang, Y.C. and Feng, J. 2015. Copula-based risk assessment of drought in Yunnan province, China. Natural Hazards, 75(3): 2199-2220. https://doi.org/10.1007/s11069-014-1419-6

Nature Environment and Pollution Technology
An International Quarterly Scientific Journal

p-ISSN: 0972-6268
(Print copies up to 2016)
e-ISSN: 2395-3454

Vol. 22 | No. 1 | pp. 29-38 | 2023

Original Research Paper

https://doi.org/10.46488/NEPT.2023.v22i01.003

Open Access Journal

# Rethinking Waste Management in Indonesia Using Public-Private Partnership Framework: A Case Study of PET Bottle Waste Management

**Akhmad Amirudin*(**)†, Chihiro Inoue* and Guido Grause*(***)**

*Department of Environmental Studies for Advance Society, Graduate School of Environmental Studies, Tohoku University, Aramaki, Aoba 6-6-20 Aoba-ku, Sendai 980-8579, Japan

**Departement of Public Administration, Faculty of Administrative Science, Brawijaya University, Jl. MT. Haryono No.163, Ketawanggede, Kec. Lowokwaru, Kota Malang, Jawa Timur 65145, Indonesia

***School of Chemical Engineering, University of Birmingham, Edgbaston, Birmingham B15 2TT, UK

†Corresponding author: Akhmad Amirudin; akhmad.amirudin.r2@dc.tohoku.ac.jp

**Nat. Env. & Poll. Tech.**
**Website: www.neptjournal.com**

*Received:* 31-05-2022
*Revised:* 21-06-2022
*Accepted:* 22-06-2022

**Key Words:**
Plastic waste management
Role analysis
Stakeholder integration
Deposit refund system
Waste bank

## ABSTRACT

Municipal solid waste (MSW) continues to be a major challenge in almost every country. In Indonesia alone, approximately 64 million tons of MSW are produced on an annual basis. While polyethylene terephthalate (PET) bottles account for 12% of all plastic products, the waste is not well managed. Many stakeholders are involved in PET bottle waste recycling but no forum for stakeholders has been established. In this study, the aim is to identify an acceptable system for PET bottle waste, to determine the role and function of each stakeholder, and to propose a framework under the perspective of public-private partnerships. The study's novelty is the elaborate roles and schematic framework for various stakeholders in PET bottle waste. The aim is to identify an acceptable scheme for PET bottle waste and determine each stakeholder's role and function. Data was generated from electronic databases (2017 to December 2021) a systematic literature review methodology followed by Preferred Reporting Items for Systematic review. The data were analyzed by the Meta-Analysis (PRISMA) approach. This study found that the laws and regulations for waste management in Indonesia are not suitable for dealing with PET bottle waste, and the government carries out limited tasks and dedicates few resources to managing the waste. A public-private partnership framework was proposed to divide the role, commitment, goal, and activities of each stakeholder to properly manage PET bottle waste.

## INTRODUCTION

In Indonesia, PET bottle waste is mostly managed by multiple stakeholders in accordance with their own interests. The lack of integration between stakeholders has been acknowledged to lower the optimization of the recycling process in a number of ways: 1) the Indonesian government typically treats PET bottle waste as municipal solid waste; 2) waste collectors and waste pickers treat PET bottle waste as a valuable material that can be sold to industry or processed into other raw materials; 3) waste banks treat PET bottle waste as a valuable waste to obtain higher recycling profit; and 4) producers manage the PET bottle waste without considering the environmental impacts (Putri et al. 2018). Under Law No. 18 of 2008 on solid waste management, the government introduced a mandate to significantly reduce the negative impact on the environment and health. As yet, however, there is little evidence that the law is having an impact on the current conditions (Sondang Siagian et al. 2019).

It has been reported that the involvement of the private sector is likely to be more efficient in providing waste management services rather than relying on the government. By following a simpler administration protocol, the private sector functions more efficiently and flexibly (Adib & Mahapatro 2022, Amirudin et al. 2022). Several private companies in Indonesia, including Danone and Plastic Pay, have taken measures to address the problem related to PET bottle waste by developing a deposit system (Eloksari 2019). However, a lack of support from the government has complicated the management of PET bottle waste, and the system proposed by the private sector has not been well integrated into existing policies. Another major problem is the low collection rate and low awareness among authorities. Thus, in addressing these barriers and finding the best solution to the liabilities related to the environment, it is important to identify a better strategy to manage PET bottle waste.

Therefore, this study emphasizes the importance of public-private partnerships (PPP) to overcome the issues related to the management of PET bottle waste. In several developing countries, PPP has been implemented to strengthen the role of different sectors in waste management (Jotaworn et al. 2021, Sondang Siagian et al. 2019, Sukholthaman et al. 2017). Through this framework, different stakeholders are allowed to cooperate under long-term contractual models and shared risks (Batista et al. 2021). The parties involved are responsible for the planning, financing, construction, and management of government targets (Yang et al. 2013). The implementation of PPP can promote the engagement between private and public sectors to benefit each party in projects (Batista et al. 2021).

However, it has been reported that the implementation of PPP has not met the stated goals both from a theoretical perspective and a policy perspective (Sondang Siagian et al. 2019). For instance, the key infrastructure required to increase the effectiveness of waste collection was not provided by the public sector (Makamté Kakeu–Tardy & Véron, 2019). The unpacking problem of PET bottles shows the complexity of the various stakeholders involved in solving plastic bottle waste. Gerassimidou et al. (2022) evaluated the role of various stakeholders involved in PET bottle waste in the United Kingdom. At the same time, Putri et al. (2018) broke down the material flow in plastic bottle waste in Indonesia. However, little research describes the collaborative roles of these various stakeholders. Therefore, the research will explore roles and schematic frameworks for various stakeholders in PET bottle waste. Thus, the optimization of waste management remains low.

Public-private partnership research will help provide a clearer picture for policymakers to share the integrated roles of various stakeholders. It is urgent to do so that every

Table 1: Search results for combining keywords from the database.

| Search results for combining keyword | Boolean keywords | Base | Gross Result | Net Result |
|---|---|---|---|---|
| Public-private partnership waste management | "Public-private partnership" AND "waste management" | Science-direct | 142 | 104 |
| | | Plos-one | 71 | 71 |
| | | Taylor and Francis Social Sciences | 86 | 86 |
| | | Wiley Online Library | 68 | 50 |
| Public-private partnership solid waste management | "Public-private partnership" AND "solid waste management" | Science-direct | 44 | 31 |
| | | Plos-one | 21 | 21 |
| | | Taylor and Francis Social Sciences | 28 | 28 |
| | | Wiley Online Library | 20 | 19 |
| Public-private partnership project for waste | "Public-private partnership" AND "project for waste" | Science-direct | 4 | 2 |
| | | Plos-one | 69 | 63 |
| | | Taylor and Francis Social Sciences | 0 | 0 |
| | | Wiley Online Library | 0 | 0 |
| Public-private partnership plastic waste | "Public-private partnership" AND "plastic waste" | Science-direct | 9 | 6 |
| | | Plos-one | 9 | 9 |
| | | Taylor and Francis Social Sciences | 7 | 7 |
| | | Wiley Online Library | 9 | 7 |
| Public-private partnership plastic bottle waste | "Public-private partnership" AND "plastic bottle waste" | Science-direct | 1 | 1 |
| | | Plos-one | 0 | 0 |
| | | Taylor and Francis Social Sciences | 0 | 0 |
| | | Wiley Online Library | 0 | 0 |
| Management PET bottle waste | "Management" AND "PET bottle waste" | Science-direct | 37 | 16 |
| | | Plos-one | 3 | 3 |
| | | Taylor and Francis Social Sciences | 0 | 0 |
| | | Wiley Online Library | 3 | 3 |
| | | other relevant sources | 5 | 5 |
| Total | | | 636 | 532 |

Source: Science-direct, Plos-One, Taylor and Francis Social Sciences, and Wiley Online Library database

stakeholder's interest can be fulfilled and still pay attention to environmental protection. This study aims to identify an acceptable scheme for PET bottle waste, to determine the role and function of each stakeholder in the management of PET bottle waste, and to propose a framework for public-private partnerships to improve the management of PET bottle waste.

## MATERIALS AND METHODS

This study adopted a systematic literature review (SLR) method to generate information related to the management of PET bottle waste. Through this method, all of the relevant studies that meet the pre-identified inclusion criteria are identified, appraised, and synthesized. The results are extracted to address the specific research questions. An electronic database was employed to identify all relevant prior studies. Inclusion/exclusion criteria were used for specified types of publications: 1) searches in subject indexes were specified to the index of Science-direct, Taylor and Francis Social Sciences, Plos-One, and Wiley Online Library; 2) literature from the reference list of relevant articles was added; 3) the search was centered on the period between December 2017 and December 2021; and 4) only selected scientific articles were investigated, and all proceedings and conferences with multidisciplinary focus outside PPP related to waste management were removed. The study lists the combinations of Booleans with keywords. The gross results were defined as all types of articles (articles, conference, and book chapters) and the net results include the referred articles only.

By using pre-identified keywords, this study yielded 532 articles from selected publishers as population, and the sampling is 27 studies included in the review (detailed data in Table 1). After removing duplicate documents in searches, the screening process was begun by reading the title and abstract. At the end of the eligibility steps, only articles that met the inclusion criteria remained in the literature review.

### Studies Categorization

This study retained 27 articles from the SLR method. Predominately, the most-discussed topic was the role of actors and stakeholders related to waste management (n = 14 or 54%), followed by disposal techniques (n = 7 or 27%), and existing legal policy (n = 5 or 19%). The greatest number of publications (n = 10 publications) was observed in the year 2020. Out of the 26 studies, there were 3 studies conducted in developed countries (n=3), only one study was cross-country research, and most studies were conducted in developing countries, more detailed categorization can be seen in Fig. 1.

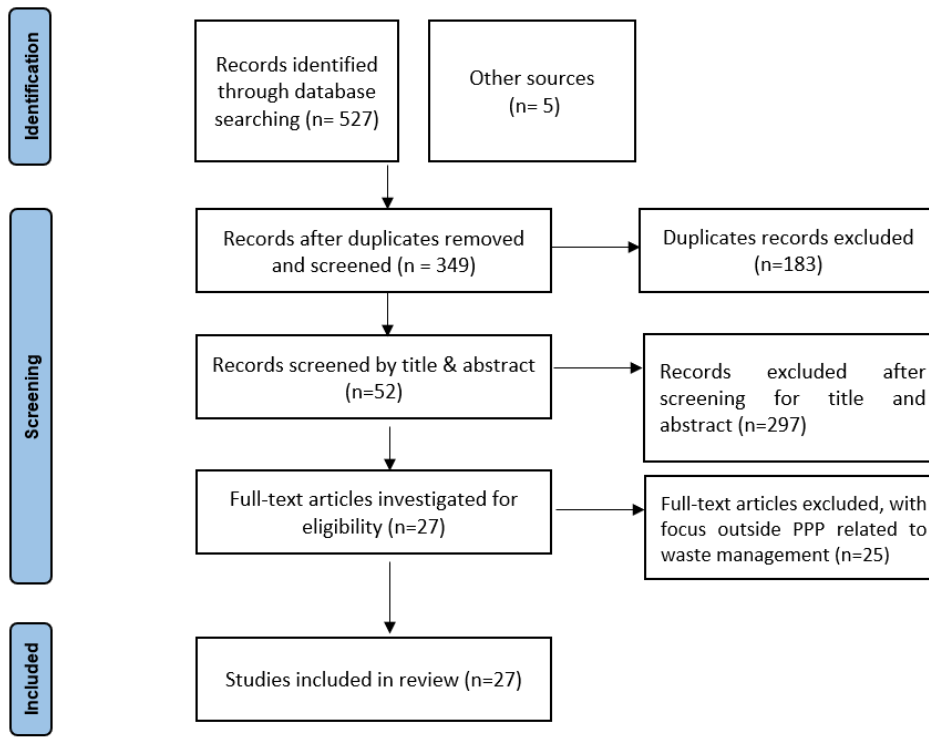


Fig. 1: Data extraction according to the PRISMA guidelines

### Role of Actors and Stakeholders Related to Waste Management

In multiple studies conducted in developing countries, the focus was on the involvement of the government, the private sector, the public sector, and individual households in managing municipal solid waste. Under the route of PPP, the central and local governments are the most essential stakeholders that play a role as accountable regulators and environmental factors (Makamté Kakeu-Tardy & Véron 2019). The public sector is responsible as the facilitator while the private sector is authorized to handle the significant responsibilities and risks transferred from the public sector (Dolla & Laishram 2019). Another important factor in the success of solid waste management is the participation of households as key stakeholders in the waste collection (Dolla & Laishram 2019, Makamté Kakeu-Tardy & Véron 2019, Phonchi-Tshekiso et al. 2020). The potential for households to contribute to the costs of solid waste collection was also discussed (1). The focus of research in Indonesia is associated with the formation of waste-pickers with the role of collecting and transacting recyclables (Colombijn & Morbidini 2017, Sasaki et al. 2018).

The research design was developed to get good research. Following the problems described in the background, the research design begins with identifying problems in PET bottle waste management, namely various stakeholders who manage it according to their interests without having an integrated framework. The systematic literature review method is used to get the right literature to be used as the basis for analysis and developing research solutions. The literature obtained is specified on public-private partnerships, especially on the division of roles, obligations, targets, and activities of each stakeholder. Finally, an elaboration of the Schematic of public-private partnership for Stakeholders in PET bottle waste. For more details, the research design is presented in Fig. 2.

## RESULTS AND DISCUSSION

### Laws and Regulations Relating to Waste Management in Indonesia

To ensure the optimization of waste management in every process from their formation to disposal, it is necessary to investigate the existing laws and regulations, especially the regulation related to plastic bottles. Government, business

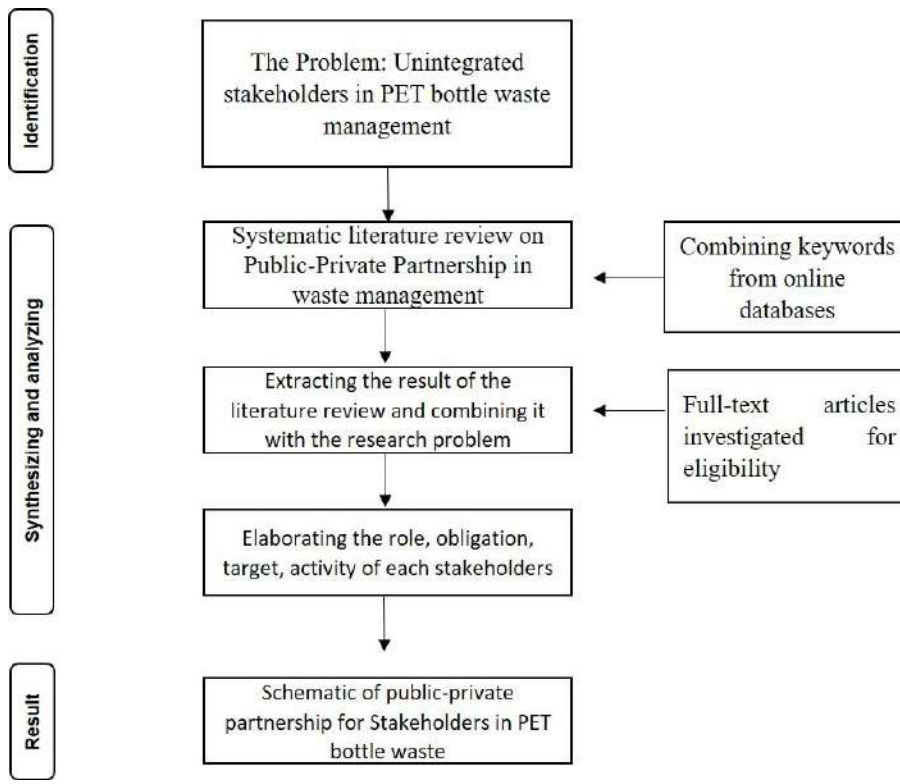


Fig. 2: Research design.

actors, and members of society, in general, are required to comply with the policy. This section will discuss the laws and regulations of waste management in Indonesia at a national level, consisting of government regulations, presidential regulations, and ministerial regulations (see Table 2).

A review of the 12 laws and regulations on waste management revealed that PET bottle waste management was only mentioned in Decree No. P.75/2019 of the Ministry of Environment and Forestry on a Roadmap for Waste Reduction by Manufacturers. Through this regulation, manufacturers are instructed to use transparent material for bottles, use 100% recyclable material, ensure a 50% yield of raw material should come from the recycling process, and implement closed or open loops. However, several problems have arisen since the manufacturers are not able to meet all the requirements. This is due to several stages in the decree which are not the responsibility of manufacturers, including the immediate collection of PET bottle waste from customers and households.

## Policy Recommendation

Xevgenos et al. (2015) discussed several options for PET bottle waste management and distinguished three main instruments to improve its management. As shown in Fig. 3, they include technical instruments, economic instruments, and legal instruments. By considering these instruments, the

Table 2: Laws and regulations of waste management in Indonesia.

| National Law | Law No. 18/2008 about Solid Waste Management | Law No. 32/2009 about Environmental Protection and Management | | |
|---|---|---|---|---|
| Government Regulation | Government Regulation No. 81/2012 about the Management of Household and Household-like Waste | Government Regulation No. 101/2014 about Hazardous Waste Management | Government regulation No 27/2020 about Specific Waste Management | Draft of Regulation about Plastic Tax |
| Presidential Regulation | President Regulation No. 97/2017 about National Policy and Management Strategy of Household Waste and Household-like Waste | President Regulation No. 83/2018 about Marine Debris Management | President Regulation No. 35/2018 about Acceleration of Development for Waste to Energy Installation using Environmental Technology | |
| Ministerial Regulation | Ministry of Trade Regulation No. 31/2016 about Non-Hazardous Waste Import | Ministry of Public Works Regulation NO. 3/2013 about the Implementation of Solid Waste Infrastructure and Facilities | Ministry of Environment and Forestry Regulation No. P.75/2019 about Roadmap to Waste Reduction by Producers | |

Source: Adopted from several sources by the researcher.

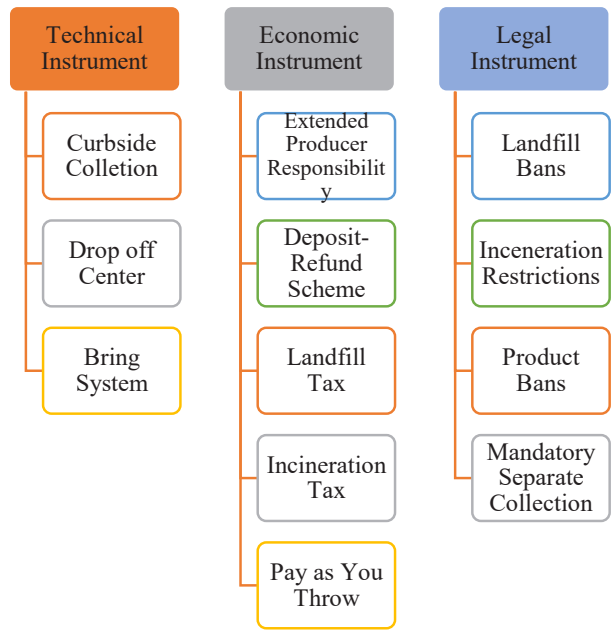


Fig. 3: Instruments to increase waste performance. Source: Adopted from (Xevgenos et al. 2015).

government may formulate new regulations with the support of many stakeholders to ensure better waste management.

Formally, plastic bottle waste management in Indonesia is equated with municipal solid waste management where municipalities and other local governments play a major role (Putri et al. 2018). Informal management is required to ensure that the waste collected by various types of waste collectors is sorted and that the valuable material is sent for recycling. That is, these materials need to be sent to factories that can use them as raw materials or to other processing plants. The first step in ensuring this process is to encourage householders to take the waste to a temporary collection point. At present, however, no waste segregation is the norm in the disposal of household waste (Kristanto et al. 2021). From this perspective, the waste disposal system in Indonesia suffers from the absence of a clear system, and this must be addressed as the first step in ensuring the recycling of PET bottle waste. Sharma and Jain (2019) emphasized that to achieve sustainability in waste management. It is mandatory to regulate all stakeholders involved, so waste management has the same goal and is more effective and efficient.

The implementation of PPP provides a framework for the interaction between private companies and public authorities. As pointed out in one study, this is especially important when obstacles related to time limitations of traditional procurement measures need to be overcome (Batista et al. 2021, Dawodu et al. 2021). In a study of the PPP approach to waste management in India, it was reported that project delivery times can be accelerated and creative and innovative solutions are delivered by the private sector (Dolla & Laishram 2021). The findings of this study are consistent with the finding that PPP has the potential to benefit many sectors as reported in many other studies (Dolla & Laishram 2021, Lee et al. 2021, Sondang Siagian et al. 2019). However, in the absence of strong policy implementation and sufficient funding, it is difficult to achieve the desired outcomes. Other problems which would make it difficult to ensure the success of a PPP for PET bottle waste management include poor task contributions, and the lack of a clear framework. For this reason, the study proposes a clear framework (Fig. 4) for the management of PET bottle waste in Indonesia, which stipulates the extent of the involvement of the actors.

To ensure that a public-private partnership for PET bottle waste management in Indonesia works efficiently, this study divides the roles, commitments, goals, and activities of each stakeholder. As shown in Table 3, seven stakeholders were identified in the system: government agencies, manufacturers, households, waste banks, landfill operators, retailers, and waste recyclers.

Government agencies are tasked with developing a framework based on mandatory separation in managing PET bottle waste that involves stakeholders in PET bottle waste management. Hosseini-Motlagh et al. (2022) emphasized the importance of the government's role in deciding the legal framework for specific types of waste. The results of this study indicate the requirement for binding legal regulations in the framework which must be followed by stakeholders. Pati & Dash (2022) specified the role of government in deciding the regulatory framework for waste and providing promoting the framework to all stakeholders, and Gerassimidou et al. (2022) divided the government role into national government should regulate and encourage the supply of PET drinks bottles and PET bottle waste management and local government is responsible for the collection of the waste. These regulations should clarify the roles, obligations, targets, and activities of each of the stakeholders, and serve as the basis of the establishment of the 'bring system'. The 'bring system' requires households to separate PET bottle waste and includes a "deposit-refund system" as an instrument in the transaction of various products using PET bottles. The framework of the 'bring system' will also provide requirements for the monitoring and evaluation its implementation.

Manufacturers apply PET bottle materials that can be recycled and minimize the use of waste in various products. Manufacturers can also implement a system where their products can be purchased by refilling PET containers or other types of containers. Singh & Ordoñez (2016) mentioned that manufacturers should avoid virgin extraction and support the raw material from the recycling process. It will encourage circularity in waste management. Gu et al. (2017) also suggested that manufacturers of plastic waste are responsible for purchasing the proceeds from the plastic waste recycling process. The implementation of the role will be extended the manufacturer's responsibility and behavior, and the manufacturer also could support further research in the development of recycling in the field of PET bottle waste which may contribute to further advancements in the technology of recycling or providing recycling technology.

In their study focused on the development of a PET recycling model, Egun & Evbayiro (2020) stress that households must be empowered in the recycling process since proper waste management potentially has both direct and indirect benefits to households. Amheka et al. (2015) point out that household behavior should support the recycling system because it plays a significant role in plastic waste management as a customer and main contributor to waste collection. To maximize compliance among households, governments can run media campaigns that stress the responsibility of householders to separate waste

Table 3: The schematic framework of the public-private partnership for PET Bottle Waste.

| | Government Agencies | Manufacturers | Household | Waste Bank | Retailer | Waste Recycler | Landfills Operator |
|---|---|---|---|---|---|---|---|
| Role | Designing a suitable framework for PET bottle waste. Monitor and evaluate PET bottle waste management | Apply PET bottle material that can be recycled, and accept the recycling material from the recycler and waste bank. | Separate and collect PET bottle waste and take it to the collection point | Provide collection points for the deposit refund scheme | Sell the PET bottle product with an added extra cost, as a deposit | Receive PET bottle waste from waste banks and convert it to raw material | Collect wrongly disposed PET bottle waste from landfill |
| Obligation | Control the negative Impact of PET bottle waste on the environment, human health, and biodiversity. | Avoid virgin PET bottle extraction. Provide research funds to develop recycling in PET bottle waste. Provide recycle technology | Ensure not to dispose of PET bottle waste | Compile PET bottle waste as much as possible and operate a deposit refund system. Operate modest technology in separation. | Manage deposit money and ensure it is returned to the household or waste picker | Convert PET bottles to valuable material | Separate PET bottle waste from solid waste |
| Target | Minimize the negative impact of PET bottle waste | Minimize virgin material to produce PET bottle waste | Minimize disposal of PET bottle waste in the wrong places | Increase the number of participants from household and waste picker | Promote the deposit refund scheme | Minimize the negative impact of converting the process | Minimize uncollected PET bottle waste |
| Activity | Conduct monitoring and evaluation regularly | Conduct a circular economy model in their business process. | Deliver PET bottle waste to the collection point | Quantify PET bottle waste regularly and convert the waste to money | Transfer the deposit to the waste bank regularly | Convert reproduced PET bottle waste regularly | Patrol to selected area |
| Reference | (Gerassimidou et al. 202, Hosseini-Motlagh et al. 2022, Pati & Dash 2022) | (Gu et al. 2017, Singh & Ordoñez 2016) | (Amheka et al. 2015, Egun & Evbayiro 2020) | (Sekito et al. 2019, Wijayanti & Suryani 2015) | (Numata 2009) | (Tong et al. 2021) | (Feil et al. 2017, Kieckhäfer et al. 2017) |

and include this message in the teaching of children in the school system. Another layer of encouragement to ensure the householders comply is to implement a "deposit-refund system" for the delivery of PET bottle waste to the retailer, who adds to the waste bank at this collection point. Increased public awareness and economic incentives are essential to increase the collection rate of PET bottle waste.

A study by Sekito et al. (2019) concludes that a waste bank can be a waste converter into income that connects households and recyclers. Meanwhile, Wijayanti & Suryani (2015) assert that the capacity of the waste bank can still be increased by managing a more modern recycling technology to support the recycling process. A system of collection points, which serve as waste banks, needs to be established in each region. Local government is responsible for establishing this type of network, which will serve as the bridge between the separation of PET bottle waste done by householders and the actual conversion of this step into monetary gain. That is, waste banks, as collection points for PET bottle waste, become the operators of the "deposit-refund system". Waste banks are also expected to be able to operate simple recycling technology, at least by separating PET bottle waste into labels caps and PET. Potentially, these waste banks could also engage in the more advanced steps in the recycling of PET, such as pelletizing and granulate production. In their study of the potential of waste banks, Sekito et al. (2019) showed the importance of ensuring that converting the waste becomes income for households and for these waste banks to engage in modest recycling technology.

In the "deposit-refund system", which is central to the success of the "bring system", the retailer plays a vital role as the connection point between the customer (householder), the waste bank, and the waste recycler. It is the retailer who is responsible for setting the price and providing a payment and collection schem e (Numata 2009). To maximize compliance with the "bring system", retailers are required to comply with and promote the "deposit-refund system" scheme. As such, the pricing system and the supporting facilities are the responsibility of the retailer. The role of the informal sector in waste management is significant in developing countries since it is this sector which fills the gap which exists because of the lack of formal institutional infrastructure and technology in the recycling of plastics (Tong et al. 2021). That is, the informal sector plays the role of waste recycler, and therefore is responsible for operating modern technology in the recycling of PET bottle waste. These local waste recyclers must have the capability of carrying out the glycolysis, hydrolysis, and methanolysis steps of PET waste recycling.

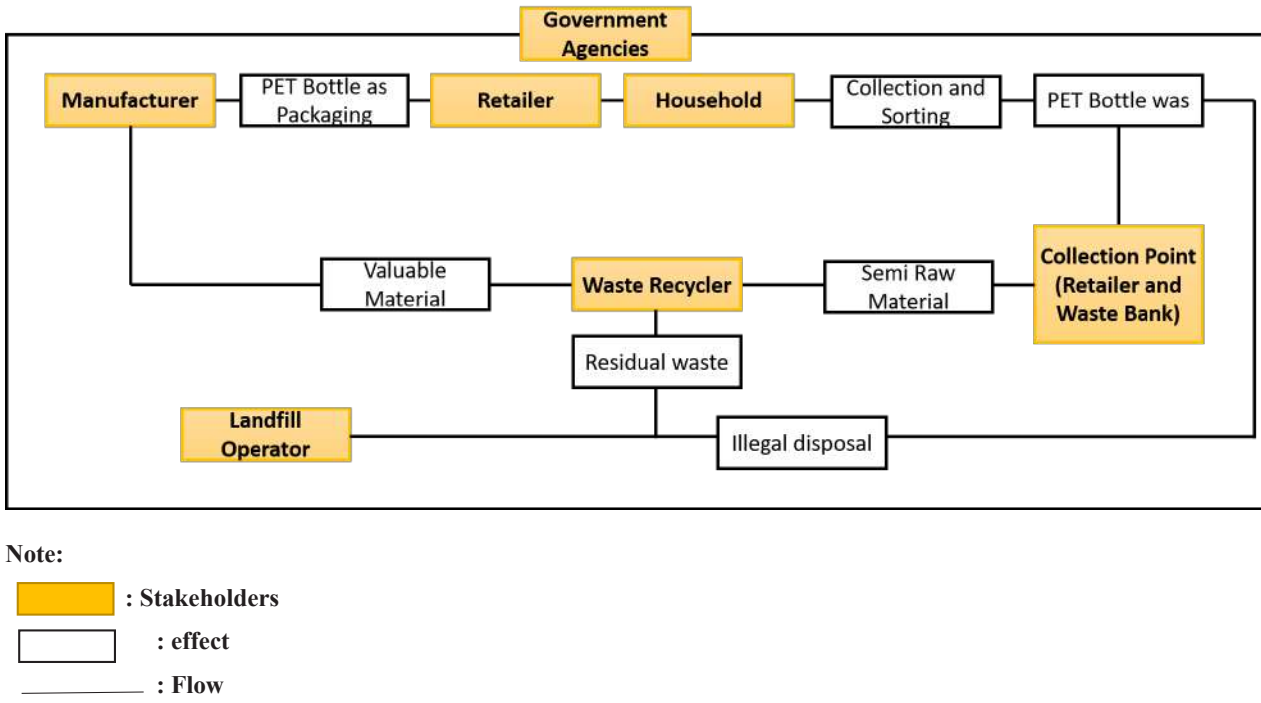


Fig. 4: Flow of PET waste management.

As a final resort, a landfill operator is a necessary disposal option. Feil et al. (2017) recommended a pre-double separation for plastic waste in landfills because there may still be households that do not comply with the separation process. Kieckhäfer et al. (2017)also recommended a landfill mining concept to tighten the waste that comes to the final disposal. PET recycling inevitably results in a residue that degrades the quality of PET at every recycling step. At some point, the PET would be considered unworthy of further recycling. In such cases, the only option available for the disposal of this PET is a landfill. In these cases, it is necessary for the PET bottle waste to be separated before the waste is buried.

The importance of the findings of this study cannot be understated. The PET bottle waste management situation in Indonesia at present is unsustainable and needs to be overhauled. The study by Amheka et al. (2015) concluded that a schema that can divide roles and responsibilities between stakeholders in management is very important to avoid overlapping roles and minimize waste from the recycling process. The schema proposed in this study includes scavengers, collectors, recycling firms, markets, and consumers' waste. This study finding is more complex and encourages the circularity of waste management compared to the previous study. To our knowledge, this is the first comprehensive study that is focused on PET bottle waste management in Indonesia. Based on the findings of numerous studies in the literature, the study was able to devise a framework for the public-private partnership management of PET bottle waste. The proposed framework details the roles and responsibilities of the stakeholders related to the management of PET bottle waste.

There are limits to this study that need to be acknowledged. This study is based solely on a systematic literature review to elaborate on the scope of the problem presented by the challenge to provide a better system for the management of PET bottle waste. Other factors, including the legal aspect and the potential to recover energy through the recycling of PET plastics, were not taken into consideration. While these are important considerations for further study, they are beyond the scope of this study.

## CONCLUSION

In this study, a comprehensive analysis of existing literature was conducted to reveal the details of the current waste management systems in place for PET bottle waste in many countries. The potential of public-private partnerships to address the issues related to PET bottle waste was also revealed through the literature review. These findings were then considered in the context of the need for a better waste management system for PET bottles in Indonesia. The main contributions of this study can be summarized as follows:

An effective PPP framework must clarify the role, commitments, goals, and activities of all stakeholders, including government, private sectors, public sectors, and individual households, and ensure cooperation among these stakeholders.

Laws and regulations for waste management with a focus on PET bottle waste are required in Indonesia. Recommendations to improve waste management in Indonesia included a requirement for the public to deliver their separated PET bottle waste for collection, with a deposit refund system as an economic incentive, and that mandatory separate collection is legally enforced.

The implementation of Public-private partnerships in waste management could be improved with information and technology, and it could be reached by more users and is effective in monitoring and evaluation. And waste can also contribute to the gross domestic product if it can be recycled optimally and reach the export market. The findings of this study are expected to assist policy-makers and local governments in Indonesia to strengthen the implementation of the PPP framework in managing PET bottle waste. They can also serve as a reference for other countries with poorly developed formal waste disposal and recycling infrastructure which face similar challenges with PET bottle waste management.

## REFERENCES

Adib, A. and Mahapatro, M. 2022. Private sector involvement in waste management of metropolises: Insights from Dhaka city. Waste Manag., 142: 143-151. https://doi.org/10.1016/j.wasman.2022.01.030

Amheka, A., Higano, Y., Mizunoya, T. and Yabar, H. 2015. An overview of current household waste management in Indonesia: Development of a new integrated strategy. I. J. Environ. Waste Manag., 15(1): 86. https://doi.org/10.1504/IJEWM.2015.066953

Amirudin, A., Inoue, C. and Grause, G. 2022. Analyzing polyethylene terephthalate bottle waste technology using an analytic hierarchy process for developing countries: a case study from Indonesia. Recycling, 7(4): 58. https://doi.org/10.3390/recycling7040058

Dolla, T. and Laishram, B. 2021. Effect of energy from waste technologies on the risk profile of public-private partnership waste treatment projects of India. J. Clean Prod., 284: 124726. https://doi.org/10.1016/j.jclepro.2020.124726

Egun, N.K. and Evbayiro, O.J. 2020. Beat the plastic: An approach to polyethylene terephthalate (PET) bottle waste management in Nigeria. Waste Disp. Sustain. Energy, 2(4): 313-320. https://doi.org/10.1007/s42768-020-00052-x

Eloksari, E.A. 2019. Indonesia's Top F&B Plastic Polluters join forces toward circular economy. https://www.thejakartapost.com/news/2019/11/25/indonesias-top-fb-plastic-polluters-join-forces-toward-circular-economy.html

Feil, A., Pretz, T., Jansen, M., Thoden, V. and Velzen, E.U. 2017. Is separate collection of plastic waste, better than technical sorting of municipal solid waste? Waste Manag. Res. J. Sustain. Circular Econ., 35(2): 172-180. https://doi.org/10.1177/0734242X16654978

Gerassimidou, S., Lovat, E., Ebner, N., You, W., Giakoumis, T., Martin, O.V. and Iacovidou, E. 2022. Unpacking the complexity of the UK plastic packaging value chain: A stakeholder perspective. Sustain. Prod. Consump., 30: 657-673. https://doi.org/10.1016/j.spc.2021.11.005

Gu, F., Guo, J., Zhang, W., Summers, P.A. and Hall, P. 2017. From waste plastics to industrial raw materials: A life cycle assessment of mechanical plastic recycling practice based on a real-world case study. Sci. Total Environ., 601; 1192-1207. https://doi.org/10.1016/j.scitotenv.2017.05.278

Hosseini-Motlagh, S.M., Jazinaninejad, M. and Nami, N. 2022. Coordinating a socially concerned reverse supply chain for pharmaceutical waste management considering government role. Environ. Dev. Sustain., 24(2): 1852-1877. https://doi.org/10.1007/s10668-021-01511-z

Jotaworn, S., Nitivattananon, V., Kusakabe, K. and Xue, W. 2021. Partnership towards synergistic municipal solid waste management services in a coastal tourism sub-region. Sustainability, 13(1): 397. https://doi.org/10.3390/su13010397

Kieckhäfer, K., Breitenstein, A. and Spengler, T.S. 2017. Material flow-based economic assessment of landfill mining processes. Waste Manag., 60: 748-764. https://doi.org/10.1016/j.wasman.2016.06.012

Kristanto, G.A., Kemala, D. and Nandhita, P. A. 2021. Challenges confronting waste pickers in Indonesia: An on-field analysis. Waste Mana & Research: The Journal for a Sustainable Circular Economy, 0734242X2110291. https://doi.org/10.1177/0734242X211029181

Lee, W.J., Juskenaite, I. and Mwebaza, R. 2021. Public–private partnerships for climate technology transfer and innovation: Lessons from the climate technology centre and network. Sustainability, 13(6): 3185. https://doi.org/10.3390/su13063185

Makamté Kakeu–Tardy, R. C. and Véron, R. 2019. Hunting for tonnage: Waste workers' incentives in a public-private partnership in Bafoussam, Cameroon. Inteelopment, 11(2): 154-171. https://doi.org/10.1080/19463138.2019.1604526

Numata, D. 2009. Economic analysis of deposit–refund systems with measures for mitigating negative impacts on suppliers. Resour., Conserv. Recycl., 53(4): 199-207. https://doi.org/10.1016/j.resconrec.2008.11.008

Pati, D.J. and Dash, S.P 2022. Strategy for promoting utilization of non-biodegradable wastes in affordable housing in India. Mater. Today Proceed., 60: 26-32. https://doi.org/10.1016/j.matpr.2021.11.026

Putri, A.R., Fujimori, T. and Takaoka, M. 2018. Plastic waste management in Jakarta, Indonesia: Evaluation of material flow and recycling scheme. J. Mater. Cycl. Waste Manag., 20(4): 2140-2149. https://doi.org/10.1007/s10163-018-0753-2

Sekito, T., Prayogo, T.B., Meidiana, C., Shimamoto, H. and Dote, Y. 2019. Estimating the flow of recyclable items and potential revenue at a waste bank: The case in Malang City, Indonesia. Environ. Dev. Sustain., 21(6): 2979-2995. https://doi.org/10.1007/s10668-018-0175-2

Sharma, K.D. and Jain, S. 2019. Overview of municipal solid waste generation, composition, and management in India. J. Environ. Eng., 145(3): 04018143. https://doi.org/10.1061/(ASCE)EE.1943-7870.0001490

Singh, J. and Ordoñez, I. 2016. Resource recovery from post-consumer waste: Important lessons for the upcoming circular economy. Journal of Cleaner Production, 134, 342-353. https://doi.org/10.1016/j.jclepro.2015.12.020

Sondang Siagian, E., Sumaryana, A., Widianingsih, I. and Nurasa, H. 2019. Public-private partnerships in solid waste management in Indonesia: The need for technical regulation. Asia Pac. J. Pub. Admin., 41(4): 246-250. https://doi.org/10.1080/23276665.2019.1694236

Sukholthaman, P., Shirahada, K. and Sharp, A. 2017. Toward effective multi-sector partnership: A case of municipal solid waste management service provider in Bangkok, Thailand. Kasetsart J. Social Sci., 38(3): 324-330. https://doi.org/10.1016/j.kjss.2017.05.004

Tong, Y.D., Huynh, T.D.X. and Khong, T.D. 2021. Understanding the role of the informal sector for sustainable development of municipal solid waste management system: A case study in Vietnam. Waste Manag., 124: 118-127. https://doi.org/10.1016/j.wasman.2021.01.033

Wijayanti, D.R. and Suryani, S. 2015. Waste bank as community-based environmental governance: A lesson learned from Surabaya. Proced. Social Behav. Sci., 184: 171-179. https://doi.org/10.1016/j.sbspro.2015.05.077

Xevgenos, D., Papadaskalopoulou, C., Panaretou, V., Moustakas, K. and Malamis, D. 2015. Success stories for recycling of MSW at municipal level: A review. Waste Biomass Valor., 6(5): 657-684. https://doi.org/10.1007/s12649-015-9389-9

Yang, Y., Hou, Y. and Wang, Y. 2013. On the development of public-private partnerships in transitional economies: An explanatory framework. Pub. Admin. Rev., 73(2): 301-310. https://doi.org/10.1111/j.1540-6210.2012.02672.x

Nature Environment and Pollution Technology
An International Quarterly Scientific Journal

p-ISSN: 0972-6268
(Print copies up to 2016)
e-ISSN: 2395-3454

Vol. 22 | No. 1 | pp. 39-61 | 2023

Review Research Paper

https://doi.org/10.46488/NEPT.2023.v22i01.004

Open Access Journal

# Advanced Synthetic and Bio-Based Sorbents for Oil Spill Clean-up: A Review of Novel Trends

**M. G. Gote*†, H. H. Dhila* and S. R. Muley****
*School of Chemistry, Dr. Vishwanath Karad MIT World Peace University, Pune, Maharashtra, India
**Nuvation Bio Inc., 1500 Broadway, New York, NY, USA
†Corresponding author: M. G. Gote; meghna.gote@mitwpu.edu.in

**Nat. Env. & Poll. Tech.**
**Website: www.neptjournal.com**

*Received:* 18-08-2022
*Revised:* 06-10-2022
*Accepted:* 19-10-2022

**Key Words:**
Oil/water mixtures
Sorbents
Surface modification
Polymers

## ABSTRACT

Due to immense population growth and economic development, the use of crude oil for various energy applications has escalated in the past few decades. This has led to the large-scale exploitation of oil reserves which has further resulted in the accidental release of large amounts of oil into our oceans. In recent years, significant emphasis has been placed on processes involving oil sorption by various natural and synthetic sorbents. Several sorbent materials based on synthetic polymers such as polypropylene, polyurethane, polystyrene, etc., possessing three-dimensional porous structure, large surface area, high mechanical strength, and exhibiting good oil recoverability and reusability, have been employed for oil-water separation processes. Conversely, many of these materials in their native or pristine form are amphipathic, which prevents their large-scale use in oil spill clean-up. This has led to researchers exploring surface modifications of commercially available sorbent polymeric materials to enhance their oleophilicity and hydrophobicity. This review article summarizes and discusses recent advances in the strategies for the fabrication of newer surface-modified synthetic polymeric materials and natural bio-based sorbents, and further highlights their effectiveness in dealing with the oil/water separation challenges.

## INTRODUCTION

Water is an essential component of all living beings on this planet. Earth's surface has 97% saline water, and only 3% fresh water is available for us to use. Therefore, water needs to be recycled and re-utilized in the best possible manner across the globe. In the last few decades, the rise in water pollution is seriously threatening the environment and one-third of all water pollution is due to oil spillage and untreated industrial discharge (Zhang et al. 2019). Crude oil is an important source of energy and is currently an indispensable component of industrial development and modernization. Several complex processes are involved in the extraction, refining, and transportation of oil to consumers (Speight 2006). However, accidental spillage of crude oil and oil distillate products occurs quite frequently in seas and oceans as a result of large offshore drilling and oil transportation (Rogowska & Namieśnik 2010). There are numerous reasons for the occurrence of these oil spills which include oil discharge near oil wells, pipelines and other equipment failures, land runoff, natural disasters, etc. Most of the accidents are due to human error and some may be due to natural disasters such as earthquakes and hurricanes which cause oil tanker ships to be damaged. The various oils that get mixed with water are mostly lipids, hydrocarbons, and fractions of petroleum products such as diesel oil, gasoline, kerosene, etc. In oil-containing wastewater, oils may be mainly present in three forms: free oil (oil droplet size > 150 μm), dispersed oil (20 μm < oil droplet size < 150 μm), and emulsified oil (oil droplet size < 20 μm). The amount of oil that is spilled during such accidents may range from a few hundred tons to several hundred thousand tons. A recent report from ITOPF 2020 indicated that the number of incidences with spills larger than 700 tonnes has decreased significantly over the last few decades. The annual average number of spills reported in the 2010s was 1.8 spills, which in comparison to the 1970s shows a 90% reduction in the number of average spills, with a loss of 164,000 tonnes of oil from tanker spills ≥ 7 tonnes in 2010s. These oil spills have a deteriorating effect on soil, water and air. The BP Deepwater Horizon disaster which occurred in 2010, is considered to be the worst and the largest oil spill ever (Middlebrook et al. 2012) recorded. Another recent mishap near the California

**ORCID details of the authors:**

**M. G. Gote**
https://orcid.org/0000-0002-7862-9621

coastline (2021) released 25,000 gallons of crude oil into the waters. Although there is a trend of decreasing the number and quantity of oil spilled due to better drilling technology and more safeguards against spills in recent years, there remains a significantly high risk of large oil spills causing environmental havoc.

Oil spills are a catastrophe for marine wildlife as it suffocates fish and other aquatic fauna. Oil-coated birds and marine mammals may die from hypothermia. Photosynthesis by marine plants is also hindered due to oil spills blocking sunlight from penetrating the water's surface. In addition, textile and chemical industries release a large amount of oily wastewater that contaminates aquatic bodies causing serious damage to the ecosystem. The cost of oil spills is very high in terms of both the economy and ecology. Oil spills are a serious environmental crisis that needs to be dealt with relentlessly to save our ecosystem. The remediation of oily wastewater is extremely critical and of paramount importance. Oil clean-up and recovery of oil from the spill is however, a complicated task that is influenced by numerous factors such as quantity and type of oil spilled, water temperature, air currents, waves, type of shorelines, etc., which may take a long time to clean up (Usman & Okoro 2017).

## CONVENTIONAL METHODS OF OIL-SPILL CLEAN UP

Many conventional techniques are in use to tackle the problem of oil-water separation. These methods include mechanical, chemical, thermal, and biological treatments (Fig. 1) (Padaki et al. 2015). Various devices such as skimmers, pumps, booms, etc. are being used as mechanical methods (Jamaly et al. 2015, Ramanathan et al. 2021). Additionally, chemicals such as detergents are employed to emulsify the spilled oils to enable their biodegradation. In-situ, localized burning of oil has also been carried out, but needless to say, this method can have devastating effects on the environment (Potter & Buist 2008). Biological remediation, wherein certain oil-eating bacteria are employed, causes the breakdown and further detoxification of dangerous chemicals or contaminants present in the polluted water (Atlas & Hazen 2011). Other technologies which have been developed include electrochemical methods specifically electrocoagulation and electroflotation, wherein by passing an electric current through an emulsion, oil-water separation can be achieved. Oily waste water treatment has also been conducted through membrane filtration which involves applying pressure to separate the liquids via a membrane usually made of ceramic and polymeric materials (Fingas 2012). These oil-water separation techniques are not very efficient due to ineffective oil/water separation, use of energy-intensive processes, high operations costs, time-consuming processes, the release of secondary pollutants, and various other challenges (Pavlatou 2020).

Sorbents for oil-spill clean-up, owing to their structure are materials capable of capturing a liquid primarily in their cavities, fibers, and surfaces. The word "sorbent" comes from the Latin word "sorbere" which means material that soaks with liquid. Liquid sorption occurs till the system

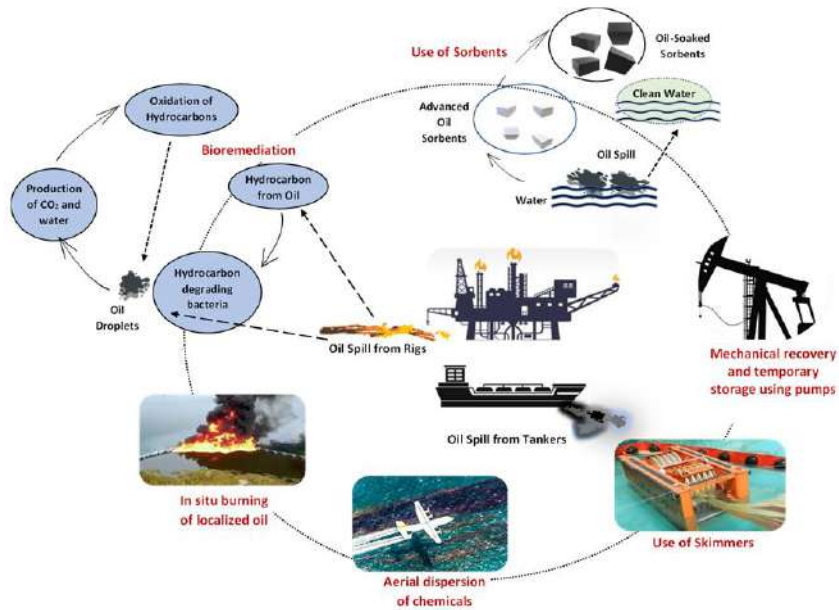


Fig. 1: Common methods used in oil spill clean up.

reaches the equilibrium or saturation point. In comparison with other conventional techniques, the application of sorbent materials has proven to be a more effective way of dealing with environmental concerns and recovering oil in preference to water (Wu et al. 2014, Zhang & Seeger 2011). The mode of action of these sorbents is either absorption or adsorption. Absorbents work like sponges and absorb oil by capillary action or suction and are useful for less viscous oils. On the other hand, adsorbents have a large surface area, high porosity, and high chemical affinity for spilled oil and work best for heavy, sticky oils. Some sorbents may use both modes of action to sequester oil. A wide array of techniques based on sorbent materials has recently been developed as promising solutions to the oil spill problem (Shang et al. 2016). These absorbing or adsorbing materials are generally easily available, inexpensive, and environmentally friendly (Singh et al. 2013, Yang et al. 2015). In addition, they also have high regeneration ability and the oil can be subsequently recovered and reused, making the sorbents crucial in the removal of oil from water.

Oil sorbents fall into three basic categories: organic, inorganic synthetic materials, and biomaterials available in nature. The carbon-based biomaterials include rice husk, sugarcane bagasse, sawdust, straw, cellulose, etc. (Yue et al. 2019). The natural inorganic sorbents include clay, perlite, glass wool, sand, zeolites, etc. (Ruan et al. 2014, Wang & Geng 2015, Zhang et al. 2019). However, these sorbents suffer from certain drawbacks such as being amphipathic i.e., absorbing both oil and water, poor oil recoverability, poor buoyancy, and poor recyclability.

## SYNTHETIC SORBENTS

Several novel synthetic sorbents have been developed in the form of foams, sponges, fibers, meshes, nanoparticles, etc. to achieve high absorption capacity, oil/water selectivity, and reusability for efficient separation and recovery of oil from water surfaces (Gui et al. 2013, Zhang et al. 2014). Recently, synthetic polymers such as polypropylene (PP), polystyrene (PS), and polyurethane (PU), have received a lot of attention as viable sorbent materials among others since they have reasonably good oil sorption capacity (Sarbatly et al. 2016, Zhang et al. 2018). They are substantiated by properties such as lower density, high porosity, larger surface area, and excellent mechanical strength. Polymers have several advantages in the manner in which they can be easily processed, molded, and functionalized in comparison with other materials (Guo et al. 2017, Zhou et al. 2013). However, certain drawbacks, such as poor recyclability, low oil retention, and poor oil recoverability still limit their performance in oil spill clean-up. Hence, it has become imperative to modify these polymeric materials to enhance their hydrophobicity and oleophilicity to improve their performance in oil/water separation (Khosravi & Azizian 2015, Li et al. 2018).

One of the research strategies has been to modify the surface of synthetic, polymeric sorbents by using certain low surface energy materials to enhance their surface roughness to convert them into more hydrophobic and oleophilic materials to achieve higher oil absorption capacity (Lü et al. 2016). Generally, if the water contact angle (WCA) is lower than 90°, the solid surface is considered to be hydrophilic, and if the WCA is greater than 90°, it is considered hydrophobic. Highly hydrophobic surfaces made of low surface energy materials may achieve WCA as high as $\approx$ 120°. Some of the materials with highly rough surfaces may achieve a static WCA greater than 150° and a dynamic WCA less than 10° due to the existence of air pockets under the liquid drops and have been termed superhydrophobic surfaces. Several reports have been published which illustrate the superior performance of superhydrophobic materials in oil-water separation applications due to their super-anti-wetting and self-cleaning properties. Extensive efforts have been dedicated in the last couple of decades to researching the preparation and synthesis of durable superhydrophobic materials for efficient separation of oil and water during the clean-up of global oil-spills. One of the disadvantages of the use of hydrophobic, highly porous polymeric materials in oil-spill clean-up is the tendency of highly viscous oil to be trapped in the pores of the material due to their low surface tension, resulting in decreased regeneration and reusability of the material to continue adsorbing the oil. Therefore, modification of polymeric materials to enhance their adsorption capacity, surface self-cleaning, and regeneration ability have to be evaluated in depth. In addition, challenges related to the decreased thermal stability of polymeric materials at high temperatures and low energy conversion efficiency need to be overcome. Future research should also aim at making the commercial manufacture of functional polymeric foams more efficient, economical, widely available, and easy to deploy and use.

Given the plethora of research in the field of environmental science in curbing the effects of aquatic pollution specifically due to oil spills, this review evaluates the latest advances in the strategies for modification of polymeric materials to make them more efficient in oil-spill clean-up and assesses their effectiveness and commercial applicability.

## STRATEGIES EMPLOYED IN THE FABRICATION OF MODIFIED SYNTHETIC SORBENTS

### Polyurethane

Polyurethane (PU) sorbents are some of the popular sorbents due to a combination of their characteristics including low

cost, high porosity, good elasticity, large internal surface area, smaller cross-linked structure, and excellent microstructure. PU polymers are usually synthesized by reacting a di- or tri-isocyanate with a polyol and are classified as alternating copolymers since PU monomers polymerize one after the other in a sequence. The possibilities for the preparation and modification of PUs are numerous, which combined with an extensive choice of additives and processing conditions available, make the use of PU very widespread. However, due to the presence of groups like carboxyl and amino groups in these polymers, PU is amphiphilic. Increasing the oil absorption capacity of PU sponge is therefore an essential requirement for its applicability in oil spill clean-up. The efficiency of PU sponges as sorbents is greatly enhanced when their wettability is improved upon modification of its surface with low surface energy hydrophobic materials. Surface-modified polyurethane has been shown to exhibit promising results in terms of oil/water separation owing to its good stability, high sorption capacity, and recyclability. Specifically, methods that generally involve the coating of various materials onto the sorbents should aim at transforming the surface functions and not alter their bulk properties. The following sections discuss various strategies for the modification of PU and other polymers to help improve their sorbent efficiency. A summary of modified polyurethane sorbents is given in Table 1.

In recent years, polymerization has been employed as a facile technique to construct superhydrophobic sponge surfaces. The polymerization reactions involve covering the surface of the sorbent with crosslinked polymer chains to produce oil-sorbing surfaces. This technique results in polymeric chains formed on the surface to facilitate the adhering of other hydrophobic materials. Graft copolymerization has been conducted with an oleophilic monomer as lauryl methacrylate (LMA) to modify PU using divinylbenzene as the cross-linker (Li et al. 2012) to get a highly oleophilic polyurethane. The sorption efficiency of LMA microspheres coated onto PU cubes was also evaluated. The surface roughness of the modified PU sorbents was observed to increase upon grafting or coating

Table 1: Modified Polyurethane Sorbents.

| Sorbent | Treatment Material | Method | Sorption Capacity (g/g) | Sorption Experimental Conditions | Reference |
|---|---|---|---|---|---|
| PU foam | Lauryl methacrylate (using DVB as a linker) | Graft copolymerization | 50–69 | Sorption conducted at 23 ± 4°C by immersing sorbent into oil | Li et al. 2012 |
| PU | Perfluorinated polydopamine-coated nanodiamonds | Controlled dripping/drying process | Diesel: 31.2 Gasoline: 20.5 | NDs-fPDA loading at 60%, highest sorption capacities observed at pH 1 and 13 | Cao et al. 2017 |
| PU | Polydopamine- hexamethyl disilazane (HMDS) | PU sponge coated with PDA nano-aggregates grafted with HMDS | Acetone: 36 Chloroform: 53 | Sorption conducted at room temperature (RT). No specific test conditions described | Liu et al. 2019 |
| PU | Acidified carbon nanotubes-Polydopamine | Electrospun PU nanofibers immersed in ACNTs followed by self-polymerization of dopamine | Separation Efficiency: 99.9% | Water Permeation Flux: 4195 – 7240 L $m^{-2}$ $h^{-1}$ at driving pressure 0.5 bar for heptane, toluene & cyclohexane; SDS used as emulsifier @ 0.001% w/w | Huang et al. 2020 |
| PU Foam Waste | Lauryl methacrylate & hexadecene, using crosslinkers like divinyl benzene (DVB) & 1,1,1-trimethylolpropane trimethacrylate (TPT) | Free radical polymerization | Diesel:132.4 Crude oil: 125.1 | Sorption with immersion for ~60 min at RT at 2% w/w nanoparticles loading | Keshawy et al. 2020 |
| PU | Poly(dimethylsiloxane) (PDMS)-$TiO_2$ | Sol-gel method followed by in-situ polymerization | Diesel & Pump Oil > 16.7 | Sponge size 1 × 1 × 2 $cm^3$, sorption determined at RT with $TiO_2$ sol-gel loading of 13.6g/mL | Shuai et al. 2015 |
| PU sponge | 1,3-oxazolidine, octadecyl trichlorosilane (OTS) self-assemblies | Solution immersion | Bean Oil: 25 Lubrication Oil: 23 | Oil absorption occurred within few seconds at RT | Liang et al. 2019 |
| PU sponge | PU@ZnO@Fe3O4@SA | Microwave and Dip-coating | Diesel: 81 Vacuum Oil: 110 | Evaluated on a round sponge, 7 cm diameter & 2 cm thick at RT | Tran & Lee 2017 |

| Sorbent | Treatment Material | Method | Sorption Capacity (g/g) | Sorption Experimental Conditions | Reference |
|---|---|---|---|---|---|
| PU sponge | $TiO_2$ nanoparticles | Immersion | Motor Oil: 105<br>Diesel: 90 | Sponge added to oil film 2-6 mm thick at 20 ± 2°C & stirred at 500 rpm for 1h. | Wu et al. 2014 |
| PU | $TiO_2$ nanoparticles coated PU followed by GO amidated with tetradecyl amine (TDA) | Immersion | Crude Oil: 26<br>Chloroform: 62 | Carbon content 69%; Maximum sorption occurred in <5 min at RT | Wei et al. 2018 |
| PU sponge | Asphaltene-capped hydrophobic silica nanoparticles | Emulsion technique | Crude Oil: 50 | PU: HSNP-2 at 1:1 ratio using sponge 2 cm thick | Atta et al. 2019 |
| PU sponge | Carbon nanofibers | Grafting | Hexane: 27<br>Toluene: 50 | Dynamic separation of oil by Pumping oil/water mixture through a pipe fitted with sponge | Baig et al. 2019 |
| PU sponge | Carbon nanofibers & methylene diphenyl diisocyanate oligomers | Grafting | Pure System: 5.25<br>Mixture: 2.56 | 1 $cm^3$ foam in contact with 50 mL water, diesel, or water/diesel mixture for 30 min | Visco et al. 2021 |
| PU sponge | Crosslinked reduced graphene oxide | Immersion | Not Available | Oil/water emulsion poured over sponge strip at RT | Zhu et al. 2016 |
| Graphene/ PU sponge | Graphene/N-methyl pyrrolidone | *In-situ* polymerization of polyols & diisocyanate in the presence of graphene/N-methyl pyrrolidone | Sorption Capacity: NA, Continuous collection of various oils | Engine oil and crude oil filtered through PU sponge at $8.9 \times 10^4$ and $6.4 \times 10^4$ $L*m^{-2}*h^{-1}$ respectively, at 30 kPa applied pressure | Kong et al. 2017 |
| PU | Octadecylamine coating using polydopamine-reduced graphene oxide for adhesion | Solution immersion | Crude Oil: 25<br>Silicone Oil: 30 | Sorbent foam in contact with oil dispersed on the water surface at RT | Oribayo et al. 2017 |
| PU sponge | Polydimethylsiloxane (PDMS) layer and carbon dots | Solar-mediated grafting | Castor Oil: 34<br>Kerosene: 52 | 3 mm thick sponges placed in oil/water mixtures and irradiated at 1 $kW/m^2$ (wavelength 350-1800 nm) at 25°C | Singh & Jelinek, 2020 |
| PU foam | Crosslinked siloxane | Immersion followed by pyrolysis | Pump Oil: 500 – 2500% wt. gain | Felt piece size $3 \times 1 \times 0.5$ $cm^3$, sorption determined @ 25°C | Biesuz et al. 2020 |
| PU sponge | $SiO_2$/GO nanohybrid | Dip-coating | 180 | Cubical sorbent specimen of $5 \times 5 \times 2$ $mm^3$ dipped in 20 ml oil for 5 min. | Lü et al. 2016 |
| PU foam | Zeolitic imidazolate (ZIF-8) framework (MOF) | In situ self-assembly method | Silicone Oil: 28<br>Methylbenzene: 33 | No specific test conditions described; sorption conducted at RT | Zhao et al. 2019 |

the PU surface with LMA. The grafting copolymerization with LMA was observed to be less efficient or incomplete compared to the coating of PU with LMA microspheres resulting in greater sorption of oil by PU-LMA microspheres in comparison to PU-g-LMA and blank PU cubes. A novel and promising PU sponge coated with superhydrophobic poly(dimethylsiloxane) (PDMS)-$TiO_2$ was reported (Shuai et al. 2015) for the treatment of oil spills. An easy fabrication was carried out on the surface of the PU sponge via sol-gel growth of $TiO_2$, followed by immersing the PU-$TiO_2$ construct in PDMS solution for in situ polymerization. The surface was found to be superhydrophobic as proven by the WCA of 154°. The sorption capacity was observed to increase to 16.7 $g.g^{-1}$. The rate of sorption and sorption selectivity was found to be greatest for diesel oil out of the various oils evaluated. The absorbed oil was recovered from the sponge by a mechanical extrusion process and the recovered sponge displayed excellent reusability of more than 60 times.

There has been a surge in the exploration of multifunctional polydopamine (PDA) nanocoatings on a variety of substrates due to their versatility. In addition, they are a practical and effective approach to transforming the surface properties of various materials (Zhang et al. 2019). Out of the several cross-linking agents, dopamine has been especially useful as it can self-polymerize and result in the fabrication of stable covalent and non-covalent bonds between the materials (Peng et al. 2019). Taking advantage of the adhesion

property of dopamine, a practical approach was developed by Cao et al. (2017) to fabricate stable superhydrophobic nanodiamond particles (NDs) coated with polydopamine which were subsequently perfluorinated. Nanodiamonds are a new class of carbonaceous material, which exhibit high surface area, non-reactivity, and extensive surface chemistry, and hence show great promise for a variety of applications. Self-polymerization of dopamine was first carried out on the surface of NDs. The catechol and amino groups present on the polydopamine film assisted in a facile Michael addition reaction of the -SH groups of 1H,1H,2H,2H-perfluoro-1-decanethiol (PFDT) to prepare superhydrophobic perfluorinated (NDs-fPDA) particles. The performance of the modified sponge was improved due to its superhydrophobicity, and high oil/water separation properties. The sponge shows an absorption capacity 15 to 60 times greater than its weight for a variety of solvents and oils. It also exhibited good recyclability and good oil recoverability. The low cost, easy fabrication method, and excellent performance of this superhydrophobic sponge make it a good candidate for oil spill clean-up.

A unique flame-retardant polydopamine (PDA) coated PU sponge was fabricated (Liu et al. 2019) via a one-step polymerization with further surface modification carried out using hexamethyl disilazane (HMDS). The PU-PDA-HMDS sponge demonstrated superhydrophobicity with a contact angle of 153°. Pristine PU sponges were dipped into dopamine solution which self-polymerized. The nano aggregates of PDA rendered the surface quite rough. However, due to the presence of hydroxyl groups on the PDA film, the sorbent was observed to be quite hydrophilic. Further grafting of HMDS on the PU-PDA surface was conducted which led to the attachment of methyl groups across the surface transforming the hydrophilic surface into an oleophilic surface. The surface modification led to an enhanced oil absorption capacity in the range of 21 to 53 $g.g^{-1}$ for various oils and organic solvents evaluated. Stable absorption performance was demonstrated by the surface-modified PU sponge with repeated absorption-desorption cycles. Measurements showed that the PU-PDA-HMDS sponges exhibited excellent heat stability and flame-retardancy in comparison with the original PU or PDA-coated PU. The flame-retardant property was attributed to the formation of a silica-hybrid char residue layer during the combustion process. The compact nature of the char residue layer can prevent flames from reaching the interior bulk of the sponge, thereby preserving the latter's structural integrity and exhibiting good flame-retardant capabilities during a real fire.

Membrane technology processes are rapidly emerging as highly viable solutions for treating oily wastewater due to the ease with which they can be used, as well as their high separation effectiveness. Other advantages of using membrane separation processes include reproducible product quality, lower operating costs, and a smaller carbon footprint, i.e., lower energy consumption over long durations required for oil-water separation processes (Karami et al. 2020). However, the hydrophobic properties of the membrane which make it an efficient oil-adsorbing agent can also shorten the life of the membrane due to increased membrane fouling. As a result, modification of membranes, specifically the enhancement of their hydrophilicity is also essential to improve the membrane performance. Superhydrophilic/underwater superoleophilic PU nanofibrous membranes decorated with acidified carbon nanotubes (ACNTs), and coated with polydopamine with a core/shell structure have been fabricated by (Huang et al. 2020). Excellent stretching ability and surface stability were achieved due to extensive interfacial hydrogen bonding between the various components of the nanofibres. Better anti-fouling properties and excellent oil-water separation with outstanding recyclability were exhibited by the fabricated nanofibres. Core/shell composites of PDA/ACNTs and polymer nanofiber exhibited great potential in oil spill clean-up.

Another pressing environmental pollution problem we are facing is the daunting task of dealing with an enormous quantity of plastic waste generated around the world. The usage of plastic waste as a feed for the fabrication of oil sorbents could therefore solve the dual problems of minimizing and management of plastic waste, as well as containment of oil spills. To further investigate this approach, Keshawy et al. (2020) evaluated the functionalization of the surface of polyurethane foam waste via a facile copolymerization of hydrophobic monomers, namely lauryl methacrylate & hexadecene, using crosslinkers as divinyl benzene (DVB) and 1,1,1-trimethylolpropane trimethacrylate (TPT). Furthermore, nano magnetite was incorporated into the coated PU foam waste which enhanced its oleophilicity. Increasing the nanoparticle concentrations also increased the sorption capacity for diesel and Egyptian crude oil to 132.4 g/g and 125.1 g/g respectively. Higher oil sorption was observed for DVB crosslinked coated samples compared to TPT crosslinked samples. It was inferred that a denser network could be achieved with TPT in comparison to DVB as the crosslinker.

Liang et al. (2019) have prepared via a facile, mild, and inexpensive process, 1,3-oxazolidine-modified polyurethane sponges were immersed in a solution of octadecyl trichlorosilane (OTS) to generate self-assemblies. Though the OTS functionalization could not alter the original structure of the PU sponge, it still made its surface quite rough, thus rendering it more hydrophobic. The sponge showed good

absorption ability for various oils and organic solvents, such as lubricating oil, bean oil, acetone, peanut oil, and n-hexane. High selectivity and absorption capacity of up to 25 times the original weight were observed for the modified sorbent in addition to oil retention of up to 92% with good recyclability.

**Surface Modification Using Nanomaterials**

In the pursuit of finding efficient sorbents to assuage the environmental pollution caused by the petroleum industry, newer technologies utilizing super oleophilic and superhydrophobic nanomaterials have been developed for modification of PU and other polymeric materials to improve the sorbents' oil sorption capacities. Sorbents have been functionalized by incorporating various nanoparticles along with low surface energy molecules containing long hydrophobic groups to impart them with superhydrophobic properties. These nanostructures have been shown to perform much better than conventional materials in resolving the issue of oil spillage. Tran & Lee (2017) investigated a novel, facile, and environmentally friendly method for the fabrication of a durable, magnetic, and superhydrophobic PU@ZnO@$Fe_3O_4$@stearic acid sponge. This work highlighted that the functionalized sponge had high surface roughness, low surface energy, and magnetic responsiveness necessary for high oil absorption capacity. A large static WCA of 161°, and a very low dynamic WCA of 7°, were exhibited by the fabricated sponge. Oils of varying densities and viscosities were absorbed to different extents by the fabricated and modified sponge. The efficiency of the fabricated sponge in oil-water separation exceeded 99%, and easy recoverability was observed upon simple squeezing of the sponge. The superhydrophobicity and oil absorbency of the fabricated sponge were unaltered after multiple rounds of stretching and compression.

The fabrication of PU sponges modified with $TiO_2$ sol has been reported (Wu et al. 2014). $TiO_2$ nanoparticles attached to the PU sponge were able to reduce the hydrophilicity of the sponge to a great extent. An oil absorption capacity of 95–110 $g.g^{-1}$ was achieved by $TiO_2$ -PU sponges with negligible uptake of water under both static and dynamic conditions. Good reusability of up to 12 cycles with a holding capacity of 70% was observed for the modified sponge compared to the uptake capacity of the original PU sponge. Similarly, the preparation of PU foam coated with $TiO_2$ nanoparticles (TPU), and its further treatment with graphene oxide (GO) amidated with tetradecyl amine (TDA) to obtain TPU-GO-TDA foam has been described (Wei et al. 2018) as depicted in Fig. 2. Due to an extensively interconnected three-dimensional pore structure in foams which are also supported by pore mesh to lend them good structural stability, the pores in these foams were able to store large amounts of absorbed oil. The authors hypothesized that the enhancement in the oil uptake capacity was probably due to the long hydrophobic chains of tetradecyl amine. The surface roughness was enabled by coating with $TiO_2$ nanoparticles and GO nanosheets. It was observed that the hydrophobicity


Fig. 2: Schematic illustration for the fabrication of TPU-GO-TDA foam sorbent. (Reprinted with permission from Wei et al. (2018). Copyright © 2018, American Chemical Society).

was achieved only after the treatment with GO-TDA since oil sorption increased in comparison to unmodified TPU foam. This was also evident from the high-WCA of around 140°.

Improved hydrophobicity of the PU sponge has also been achieved by coating asphaltene-capped hydrophobic silica nanoparticles onto the surface of the PU sponge. This modified PU sponge has been used for heavy Arabian crude oil spill clean-up (Atta et al. 2019). The PU sponge modification was conducted by emulsification technique, and it was hypothesized that the hydrophobicity of the PU sponge was due to the interaction between the PU sponge and the reactive groups of superhydrophobic silica. Excellent and rapid collection of oil by the sponge was enabled by the hydrophobic PU sponge, which was also reusable and exhibited an excellent recovery.

Biesuz et al. (2020) developed efficient oleophilic nanofelt by impregnating PU foams with a liquid pre-ceramic siloxane followed by controlled pyrolysis, wherein the siloxane converted into an amorphous SiOC foam at a temperature below 800°C, and at temperature ~ 1500°C it decomposed to give $Si_3N_4$ fibers. Oil separation from the water was easily achieved by the nanofelt. The results showed a 500% to 2500% increase in weight after oil absorption. Simple thermal treatment was able to clean the material. The fibers developed from small pore foams were found to be extremely stable even after repeated oil-absorption cycles.

**Carbon Materials**

Owing to their intrinsic hydrophobicity, carbon-based materials such as graphene-reduced GO, carbon nanotubes and carbon nanofibres have been explored for oil spill treatment. These carbon materials coated onto the sponge surface can render the original hydrophilic surface into a hydrophobic surface. Carbon nanofibres (CNFs) display exceptional hydrophobicity but have not been evaluated in detail for their application as PU modifiers for oil spill clean-up. The hydrophobic characteristics of CNFs and the adsorption properties of PU can be combined to improve the efficiency of the latter for oil sorption from oily wastewater. To leverage the hydrophobic nature of CNF, Baig et al. (2019) have investigated the grafting of CNF onto a PU surface using a dip-coating method. The formation of additional pores by the CNF on the surface of PU resulted in a decrease in the average pore size of the PU sponge, resulting in a significant increase in the surface area and a greater uptake of oil. The surface area of PU increased by about 31 times from 9 $m^2.g^{-1}$ to 276 $m^2.g^{-1}$ owing to the grafting process, which resulted in an increase in the oil absorption capacity by approximately 50 times its weight. The study demonstrated the CNF-PU sponge's repeated ability for oil absorption and its recoverability due to the improved flexibility and mechanical stability of the sorbent.

In a recent study, Visco et al. (2021) fabricated polyurethane-based nanocomposite foams by incorporating varying amounts of ball-milled carbon nanofibres and employed them for the selective recovery of oil from water. The fabrication of the grafted PU foams was carried out by mixing methylene diphenyl diisocyanate oligomers with carbonaceous filler followed by the addition of polyether polyols (PEP) to obtain the crosslinked polymer. CNFs were loaded on to PU foams up to 15% by weight. A contact angle greater than 90° was observed for nanocomposite sponges indicating low surface energy between liquid and solid. Water/diesel mixtures were used to study the efficiency of the sorbents. The absorption values for the sponges determined by Visco et al. (2021) contrasted significantly with those obtained by Baig et al. (2019) probably because the former evaluated a sponge structure possessing a larger pore size distribution (range of 130-190 μm) with oils which varied significantly in their chemical composition and viscosity. Maximum absorption of diesel from the oil/water mixture was demonstrated for a foam with 1% w/w loading of the carbonaceous filler as 1: 5.25, oil-water ratio.

Graphene aerogels and CNTs can significantly improve the hydrophobic-oleophilic wettability of a PU surface due to their porous interconnected structures. However, they suffer from a few disadvantages which limit their use as good PU surface modifiers, which include their high cost which makes large-scale manufacture of CNT and graphene-grafted PU more expensive, and poor stability of the grafted sorbent due to weak CNT/graphene-PU interactions which decrease their oil absorption capacity. Therefore, carbon derivatives that can bond more strongly with PU are required. One such derivative is the reduced graphene oxide which itself can be further modified appropriately to obtain a sorbent with greater oil absorption capacity. The presence of groups such as carboxyl, epoxy, and hydroxyl in the two-dimensional structure of graphene oxide (GO) makes it a good swelling material. Its applicability as a feasible sorbent for oil spill clean-up has been explored also because of its large specific surface area and excellent sorption capability (Junaidi et al. 2021). However, the hydrophilic nature of GO has to be chemically modified to render it more hydrophobic. Zhu et al. (2016) have fabricated a porous PU sponge cross-linked with reduced graphene oxide (rGO). This was achieved by the addition of calcium carbonate nanoparticles and graphene oxide nanoparticles during PU foam synthesis, which upon etching with a mild acid resulted in the formation of a PU sponge with a nanosized porous framework which is not present in a normal PU sponge. A thin layer of rGO was then coated onto the porous PU sponge

via a crosslinking procedure. The results indicated that PU@rGO sponge has excellent potential use in oil-water separation. The rGO surface coating in the porous PU@rGO structure was found to have good electrical conductivity which prompted the authors to evaluate the construct to disrupt the oil in water emulsion.

A microporous PU sponge coated with $SiO_2$/GO nanohybrid material displayed a flexible structure with an excellent oil sorption capacity of about 180 times its own weight and good recyclability (Lü et al. 2016). A high-performance graphene/PU sponge was prepared by in-situ polymerization of polyols and diisocyanate in the presence of graphene/N-methyl pyrrolidone (NMP) suspension (Kong et al. 2017). The strong dipole interactions between graphene sheets and NMP facilitated the introduction of graphene sheets into the framework of the PU sponge, which led to better physical and chemical strength of the graphene/PU sponge. Continuous oil removal from the water was achieved by using a vacuum pump. The graphene/PU sponge was found to have good filtration capabilities for continuous removal of oil due to its superior mechanical strength and oleophilicity as evidenced by its magnificent adsorption capacities up to 40 to 80 times its own weight.

A PU foam derived from lignin (LPU) a plant-based material, using green technology was subjected to surface modification by treating it with octadecyl amine (ODA) using adhesive polydopamine-reduced graphene oxide (rGO) (Oribayo et al. 2017). The synthetic methodology led to grafting long hydrophobic methylene chains and alkyl groups from ODA molecules onto the surface of LPU foam through an adhesive coating of polydopamine-rGO, resulting in a 3-D porous structure. GO contains distended structural hydrophilic groups such as hydroxyl, epoxy, and carboxyl groups which are responsible for its significant swelling, intercalating and ion-exchange capabilities. An outstanding oil sorption capacity of 26–68 times its own weight could be achieved with the LPU foam which was prepared by covalently attaching hydrophilic GO to LPU, followed by reducing it to hydrophobic rGO via oxidative self-polymerization of dopamine to polydopamine. This oil sorption capacity was found to be much higher than that of a non-woven commercial polypropylene sorbent. ODA along with the low surface energy and hydrophobic rGO rendered the foam with varying degrees of wettability for oil and water. rGO was responsible for introducing surface roughness which affected the interaction of the foam with a wetting or non-wetting liquid. LPU-rGO-ODA foam sorbent also showed good oil selectivity and reusability.

A new class of carbon nanoparticles called the carbon dots (C-dots) have been recently identified as having great potential in oil-spill containment due to their simple synthesis, unique optical properties, and environment-friendly characteristics. An innovative strategy was demonstrated involving the application of a composite material consisting of a PU sponge embedded with a polydimethylsiloxane (PDMS) layer and C-dots prepared from p-phenylenediamine for solar-mediated oil uptake from oil spills (Singh & Jelinek 2020). The combination of the high porosity of the PU sponge structure, hydrophobicity of PDMS, and the conversion of sunlight into heat by carbon dots, facilitates greater absorption of oil from the spills. C-dots absorb sunlight in the visible region. An excess of electrons on the C-dot surface results in a reduction of the HOMO-LUMO gap which further results in increased light absorption. The C-dots were immobilized in the PU-PDMS matrix such that the energy absorbed by them upon exposure to sunlight increased the temperature of the matrix which facilitated increased oil absorption. The carbon dot-PDMS-polyurethane composite sponge exhibited good chemical stability and recyclability.

**Surface Modification Using Metal-Organic Frameworks**

Metal-organic frameworks (MOFs) are porous materials composed of a metal ion or a cluster of metal ions and an organic molecule as a linker. They have large pores and open metal sites, thereby making them attractive for applications such as the adsorption of pollutants from water (Fig. 3). However, MOFs have certain drawbacks which include low mechanical strength and poor processability, which have been overcome by integrating them with more sturdy and inert materials to produce sorbents for efficient oil-water separation. Zeolitic imidazolate (ZIF-8) framework, a type of MOF grown on flexible PU foam (MFPU) was synthesized by Zhao et al. (2020) through an in situ self-assembly method. The increased surface roughness of MFPU foams resulted in a higher contact angle, which improved the hydrophobicity and lipophilicity of the parent MOF. Various types of oils and organic solvents could be absorbed into these foams quite efficiently with an extraordinary absorption capacity reaching 33 times its own weight. The ZIF-8 coating was also observed to significantly enhance the flame retardancy of MFPU foams, which was determined by cone calorimeter test, vertical burning test, and limited oxygen index test.

**Polystyrene**

Yu et al. (2016) have reported a durable and modified magnetic polystyrene foam (DMMPF), synthesized via an inexpensive two-step immersion method by using oleic acid coated $Fe_3O_4$ particles and PS microspheres which exhibited excellent superhydrophobicity, superoleophilicity, and

fast magnetic response. The modified magnetic PS foam exhibited an oil absorption capacity of nearly 40 times its original weight. Simple mechanical extrusion allowed recovery of absorbed oils and solvents from the DMMPF foam which was shown to retain its high oil absorption capacity even after 60 use cycles. Porous PS fibers work as effective oil sorbents by either adsorption or capillary action and promising prospective in wastewater remediation. Oils and solvents like diesel, lubricating oil, vegetable oil, DCM, cyclohexane, benzene, etc. were found to be absorbed by the as-fabricated foam. Authors claim that the absorption capacity of DMMPF is higher than magnetic graphene foam and cryogels based on graphene. Damavandi & Soares (2022) grafted polystyrene (PS) chains on the surface of silica-coated super magnetic iron oxide nanoparticles using a blending technique using SI-ATRP. The use of SI-ATRP conferred high hydrophobicity and oleophilicity to the PS graft. Oil was absorbed rapidly and to an extent of 5x in 5 minutes by a nanocomposite in which 90% of the PS-$SiO_2$-IONP was replaced with polystyrene. The fast oil absorption is explained by van der Waals forces, hydrophobic effects, and stacking interactions between polystyrene molecules grafted on PS-$SiO_2$-IONP and the oil molecules. Nanofibrous syndiotactic polystyrene (sPS) monoliths were fabricated and were demonstrated to possess superhydrophobicity by Gui et al. (2019). These fibers were prepared by solidifying non-aqueous high internal phase emulsions (HIPEs) through crystallization-induced gelation. The HIPEs were formed by dispersing glycerol in 1,2,4-trichlorobenzene (TCB), stabilizing with sulfonated sPS at a relatively high temperature of 120 °C. Cooling of HIPEs resulted in their solidification due to the crystallization of sPS within the continuous phase to produce porous sPS monoliths. The morphological study of the prepared sPS monoliths showed hierarchically porous structures (Fig. 4). They were found to exhibit a high specific surface area of approximately 420 $m^2.g^{-1}$ and also good mechanical strength with Young's moduli ranging from 157.7 to 2638.0 kPa. The sorbent material exhibited excellent oil absorbing capacities of up to 81.3, 44.4, and 41.9 $g.g^{-1}$ for chloroform, olive oil, and diesel, respectively.

A superhydrophobic sorbent was fabricated from PS foam waste via a high internal phase pickering emulsion (HIPPE) technique in a one-step process (Yu et al. 2019). Silica and Span 80 were used as surfactants for stabilizing the emulsion in which the PS packaging waste was introduced as the crosslinker due to its low surface energy, thereby making the process more facile. The as-fabricated $SiO_2$@PS sorbent had a high porosity which enabled good removal of oily contaminants from the water. The sorbent displayed a high adsorption capacity of 20.4–58.1 $g.g^{-1}$ and retained its recyclability for 10 clean-up cycles. Polymeric nanofibres owing to their properties such as layered structure have great potential to collect oil from oily wastewater. Such nanofibres are fabricated through various techniques such as electrospinning, melt-blowing, bicomponent spinning, and force spinning.

Out of the various techniques widely used for the construction of nanofibres, electrospinning (Sarbatly et al. 2016) has found its niche in the manufacture of sorbents for efficient oil-water separation. The process involves subjecting a jet of polymer solution to electrostatic forces to obtain the polymeric fibers with diameters in the range of 5 to 500 nm. Polystyrene-carbon nanotubes (PS-CNTs) prepared using the electrospinning technique were found to possess high oleophilicity (Wu et al. 2017). Studies indicated that the oil absorption occurred due to intra-particle diffusion. The super-hydrophobic-oleophilic PS-CNT sorbents showed reusable potential. These sorbents proved to be efficient sorption materials for the clean-up of oil spills. Various oils such as sunflower oil, peanut oil, and motor oils were

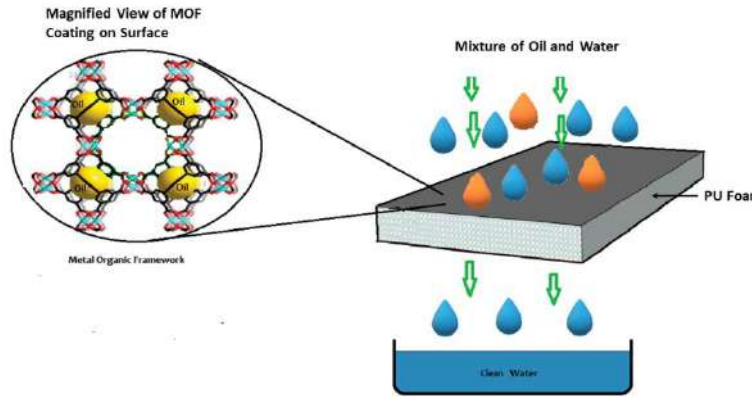


Fig. 3: Polyurethane foam coated with a metal-organic framework to trap oil.


Fig. 4: (a) Schematic Illustration of Fabricating Emulsion-Templated sPS Monoliths through Crystallization Induced Gelation, (b) Porous sPS Monoliths with Superhydrophobicity/Oleophilicity, Extremely Low Density, and Nanofibrous Structures, (c) Absorption of Oils on Water Surface, Underwater Oils and Emulsified Oils Using the sPS Monolith (Reprinted with permission from Gui et al. 2019. Copyright © 2019, American Chemical Society).

used to study the oil sorption capacity which was found to be 116, 123, and 112 $g.g^{-1}$, respectively. An increase of 65% in oil uptake capacity was observed for the composite in comparison to PS sorbent without CNTs. Alnaqbi et al. (2020) demonstrated that polymer blends have greatly enhanced properties and distinct advantages over original polymers as components of oil-sorbent materials. Their study highlighted the application of hydrophobic polymers prepared through polymer blending, wherein blends were prepared by using PS as the matrix polymer, to which poly (vinyl chloride) (PVC) and polyethylene (PE) were added individually at 5–20 % w/w. Electrospinning of the blends was carried out to obtain microfibers. Good removal of crude oil, diesel, and motor oil was achieved. In comparison to other commercially available polypropylene (PP) fibrous materials for oil absorption, the blended electrospun fibers were far more efficient for a wide range of oils.

The removal of various oils from aqueous solutions by PS nanofiber membranes synthesized by two methods namely electrospinning and impregnation filled up with different types of sawdust was demonstrated by Ghiasvand et al. (2021). The particle size of sawdust in the range of 40-60 mesh showed the highest sorption capacity. Separator pads were fabricated comprising of an outer covering made of PS nanofiber membranes sandwiching sawdust and used for the removal of oil spills from the surface of the water. An increase in temperature led to a decrease in the sorption capacity of the PS nanofiber membrane. The sorption capacity also decreased with an increase in pH up to neutral pH while increasing slightly with a further increase in pH above 7. These membranes prepared by the electrospinning technique offer better sorption capability than the ones prepared via impregnation. This variation in the performance of the membranes may be explained in terms of the process of impregnation that does not leave many pores open for the oil to be taken up since they are covered by polystyrene. A magnetic PS/$Fe_3O_4$ fibrous membrane fabricated by the electrospinning technique showed high selectivity and excellent oil adsorption. The magnetic response from $Fe_3O_4$ and superiority in hydrophobicity and oleophilicity of polystyrene combined to enhance the separation efficiency as well as adsorption capacity of magnetic fibrous sorbent in oil/water mixtures (Song et al. 2017). The highly porous structured PS fibrous sorbent shows a motor oil sorption capacity of 113.87 $g.g^{-1}$, approximately 3-4 times that of natural sorbents and nonwoven PP fibrous

membranes. Additionally, the nanoporous fiber sorbents also exhibited high sorption capacity for edible oils, such as bean oil (111.80 $g.g^{-1}$) and sunflower seed oil (96.89 $g.g^{-1}$) (Lin et al. 2012). Yadav et al. (2019) demonstrated the recyclability of thermoplastic PS using orange peel extract. The method involves extracting liquid from the outer rind of the peel (primary extract) which was further processed into three layers. PS was dissolved in the layers to get viscous solutions. These PS solutions were then processed into fibers that exhibited high contact angle. The oil sorption capacity was found to be higher for fibers obtained using the top layer of extract (TLF) compared to the ones obtained from using the primary extract (PEF), primarily due mainly to a greater surface area of TLF. Expanded polystyrene (EPS) waste was utilized as a sorbent to clean up a crude oil spill from an aquatic environment (Nasir & Hameed 2014). The sorption capacity of these sorbents increases with the increase in surface area and sorption time. It was also observed that the rough surface of EPS adsorbed more oil than the smooth surface. The punctured hole diameter in EPS sorbent (1.65 mm) also enhanced the oil sorption capacity.

Zhu et al. (2011) investigated the viability of fibers made from blended PVC-PS as a unique oil sorbent prepared by an electrospinning process. Up to a 9 times increase in the oil, uptake was noted for these sorbent fibers as compared to commercial PP sorbent due to the voids present in PS-PVC fibers. A one-step electrospinning process has been demonstrated for the fabrication of nanoporous polystyrene fibers by Lin et al. (2012). Due to the high porosity of PS fibers, a maximum oil sorption capacity of 113.87 $g.g^{-1}$ was obtained for motor oil. The uptake efficiency of certain edible oils was also found to be good with an oil absorption capacity of about 111.80 $g.g^{-1}$ achieved for bean oil.

### Melamine

Melamine sponges consist of formaldehyde-melamine-sodium bisulfite copolymer. Owing to the high porosity (>99%), extensive pore structure, large surface area, low density, and ease of chemical modification, they are finding application in the treatment of oily wastewater as sorbents (Wang et al. 2015). A highly oleophilic composite comprising melamine, MOF (HPU-13) crystals, and carboxymethyl cellulose (CMC) was prepared by Xu et al. (2019). CMC sodium-treated melamine sponge (MS) sponge was able to facilitate the attachment of HPU-13 onto the MS leading to the formation of an excellent hydrophobic material proven by its oil uptake capacity of up to 13000%. A hydrophilic cellulose polymer, carboxymethylcellulose sodium (CMC) was used to impart adequate coordination of functional groups on the surface of MS. CMC was envisioned to wrap the branches of the sponge with hydroxyl and carboxylic groups enabling greater interaction with metal ions to strongly link HPU-13 to MS. Feng et al. (2017) modified a commercially available melamine sponge with eco-friendly material, furfuryl alcohol. The MS was soaked in furfuryl alcohol solution followed by acidic polymerization to achieve surface modification. This method resulted in a reaction of furfuryl alcohol with MS along with polymerization of furfuryl alcohol onto the surface of MS, thereby making the sponge hydrophobic. The modified MS displayed excellent sorption capacities for various oils and organic solvents (75-160 $g.g^{-1}$), resulting in a good hydrophobic, environment-friendly modified melamine sponge. Xue et al. (2021) investigated a unique superhydrophobic and superoleophilic tetradecyl amine-MXene functionalized melamine sponge for effective oil/water separation through selective oil adsorption. The results showed an absorption capacity of 60-112 times the weight of the sorbent. The functionalized melamine sponge exhibited high mechanical strength, and chemical stability, as well as good reproducibility and recyclability for oil-water separation. Arunagiri et al. (2021) fabricated a chemically modified 3D porous MS with polycaprolactone and poly-D, L-Lactic acid via inexpensive freeze-drying. The sponge displayed high hydrophobicity with a water contact angle of 162°. The composite material showed an absorption capacity in the range of 3.3-8.7 $g.g^{-1}$ for several oils and organic solvents such as crude oil, soyabean oil, n-hexane, n-octane, etc.

## POLYMERIC SORBENTS AS SOLIDIFIERS

Conversion of spilled oil into a solid coherent mass using solidifiers could be a viable option for efficient oil-water separation. Though quite an attractive possibility, solidifiers have remained an underutilized approach to alleviate the effects of oil spills. Solidifiers can potentially help in oil-water separation by containing the oil spill, preventing it from spreading, and promoting its removal from the environment, as well as aiding the recovery of oil. Shojaei et al. (2021) demonstrated that oil spills can be solidified using polypropylene and polyethylene fibers and granules. The performance of these polymeric fibers and granules was analyzed by gravimetric and spectrophotometric methods. The results showed a high sorption capacity of 12.5 $g.g^{-1}$ for polypropylene fibers. The Freundlich isotherm model is consistent with the sorption characteristics of PP and PE granules owing to the heterogeneous surface of these two solidifiers. Oil adsorption tendency was attributed to the heterogeneous surface of polymeric granules with varying adsorption energies which resulted in enhanced oil uptake. Motta et al. (2019) demonstrated an inexpensive and

simple method for the fabrication of a bio-based subclass of solidifiers constructed from sorbent amylopectin-graft-poly (methyl acrylate) (AP-g-PMA) polymer. The results indicated that the rapid solidification of diluted bitumen in terms of contact time and solidifier-to-oil ratio could be achieved within a few minutes by AP-f-PMA. The combination of the biodegradability of amylopectin and the hydrophobicity of the synthetic polymer holds a lot of potential. Another recent study by (Lv et al. 2020) showed the application of polymer-grafted wheat bran for oil gelling capability. Vinyl tri ethoxy silane was used to introduce vinyl functionality onto the wheat bran, which was further polymerized with divinyl benzene monomer, using azo bis isobutyronitrile as the initiator. The methodology rendered the wheat bran with a large BET surface area of 176 $m^2.g^{-1}$ and a maximum absorption capacity of 12.0 $g.g^{-1}$ for various oily liquids. The sorbent material was found to exhibit excellent hydrophobicity and oleophilicity due to the presence of a multi-scale porous structure.

## SORBENT GELS FOR OIL SPILL CLEAN-UP

Unique and efficient oleophilic sorbent gels based on glycerol propoxylate, synthesized through a bulk polymerization technique without the use of an activator, an initiator, or a catalyst, have been reported by (Kizil & Sonmez 2017). Various organic solvents and oils were selected to study the absorption tendency of the synthesized gels. Varying concentrations of the crosslinkers were examined for their effect on the above-mentioned parameters wherein star-type propoxylate monomers were reacted with different concentrations of tris [3-(trimethoxysilyl) propyl] isocyanurate (ICS) crosslinker. For the PDMS sorbents, the capability to swell was found to depend on the amount of cross-linking in the polymers. Fully swollen material obtained after 24 h, was analyzed for the oil/solvent retention ability by determining the polymer weight loss avoiding the use of any external forces such as squeezing or exposing the sorbents to high temperatures. Janqamsari et al. (2021) developed ecofriendly sorbent aerogels based on recycled polyethylene terephthalate (PET) fibers chemically modified with the polymer polyvinyl alcohol (PVA) and further with carbon nanotubes (CNTs). The incorporation of CNTs in the structure of nanocomposite sorbent increases the oleophilicity and thereby increases the oil sorption capacity. The surface area, entanglements among the fibers and the hydrophobic interaction between the sorbents and oil droplets significantly affect the sorption capacity. The nanocomposite sorbent shows efficient oil sorption capacity and reusability even after four cycles. They investigated the efficiency of the sorbent aerogels for their density, porosity, and oil sorption capacity which were found to be 0.043-0.097 $g.cm^{-3}$, 92.93-96.87%, and ~ 12 $g.g^{-1}$ for kerosene oil respectively. In another study, Shen et al. (2021) demonstrated the applicability of superelastic and strong polyimide (PI) nanofiber-based aerogels (NFAs) aided by a three-dimensional (3D) structure and porosity that can also be altered. The aerogels were prepared by freeze-drying followed by solvent-vapor treatment as illustrated in Fig. 5. Silicone nanofilaments (SiNFs) were then formed on the surface of PI fibers upon treatment with trichloromethyl silane. SiNFs-coated NFAs exhibited very low density, high porosity, and very high oil sorption capacity of 159x its own weight. Separation of stable water-in-oil emulsions was also achieved indicating that the method was very energy efficient. Ali (2019) has synthesized and demonstrated the use of an oleophilic gel based on butyl acrylate polymer for the remediation of oily wastewater. The polymer, poly (n-butyl acrylate) was synthesized by solution polymerization and various parameters such as reaction time,

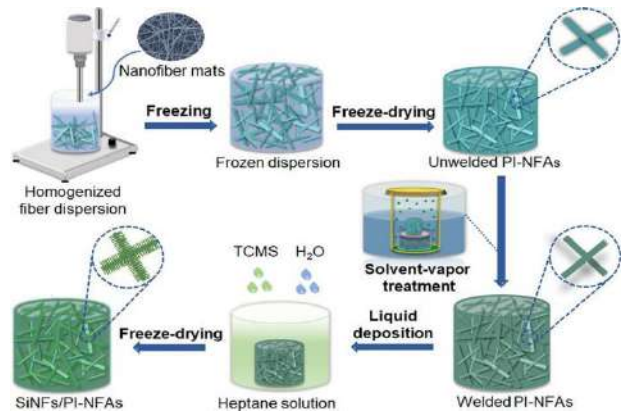


Fig. 5: Schematic illustration of the preparation of SiNFs/PI-NFAs. (Reprinted with permission from Shen et al. 2021. Copyright © 2021, American Chemical Society).

the concentration of the monomer, initiator, crosslinker, and the temperature were optimized for improved yield of the polymer sorbent. The sorption capacity of the sorbent under different conditions like dry system, static system, and the dynamic system was found to be quite promising for various oils such as gasoline, kerosene, diesel, xylene, octanol, and Mobil oil.

## MISCELLANEOUS SYNTHETIC SORBENTS

Fabrication of poly(dimethylsiloxane) based hydrophobic sorbents through the condensation reaction of poly(dimethylsiloxane) and tris[3-(trimethoxysilyl)propyl] isocyanurate cross-linker via bulk polymerization was demonstrated by Askin et al. (2021). High oil absorption capacity and a high rate of absorption-desorption were achieved. The sorbents could be easily reused many times without any major loss in the oil-uptake capacity. The hydrophobic polymeric sorbents have an additional advantage in that they selectively absorb oil from the water surface which increases their potential use in water clean-up applications. Additionally, Askin et al. (2021) also developed a unique hybrid sorbent via a bulk polymerization reaction between poly (dimethylsiloxane) and fluorinated alkyl silane. The highly hydrophobic structure of the material resulted in good oil uptake from both the surface and the bulk of water. High oil sorption capacity in the range of 500-1800% and fast uptake and release of oil were also observed indicating promising clean-up of oil spills. Krishnan et al. (2022) have recently demonstrated through in-situ one-step bulk copolymerization, the fabrication of a composite absorbent with a three-dimensional cross-linked network comprised of polystyrene-polymethyl methacrylate/divinyl benzene (PS-PMMA/DVB) copolymer and 2D-nanosheets of $BN_3$ (Boron Nitride)/graphene. The as-prepared composite material was found to efficiently remove various organic solvents and oils from the spills and showed good flexibility. The absorption capability was found to be dependent on the amount of DVB used. Interestingly, the PS-PMMA/DVB composites with $BN_3$ nanosheets exhibited higher absorption capacities in comparison to the ones with CG composites. The polymer composites with lower nanosheet content, i.e., 0.1 wt% were observed to have higher absorption capacities compared to the ones with higher nanosheet content (2.0 wt%).

The conversion of nonwoven polyester fibers into hydrophobic oil-absorbing material by treating the fibers with poly (methylhydrodimethyl) siloxane copolymers has been

Table 2: Other Modified Polymeric Sorbents.

| Sorbent | Treatment Material | Method | Sorption Capacity (g/g) | Sorption Experimental Conditions | Reference |
|---|---|---|---|---|---|
| PS foam | Oleic acid-coated $Fe_3O_4$ | Two-step immersion | 40 | Maximum absorption capacity reached in 60 s | Yu et al. 2016 |
| PS fibers | Silica-coated iron oxide nanoparticles | Grafting | Diesel: 3<br>Diluted Bitumen: 5 | 20 mg of the sorbent for 5 minutes at 23°C. | Damavandi & Soares 2022 |
| Syndiotactic PS (sPS) monoliths | Trichlorobenzene (TCB) & Glycerol | High internal phase emulsion crystallization-induced gelation | 41.9-81.3 | Cubic monoliths (≈1.0 × 1.0 × 1.0 $cm^3$) with known mass immersed in 20 mL of o/w emulsion for 12 hours. | Gui et al. 2019 |
| PS foam waste | Silica and Span 80 | High internal phase pickering emulsion (HIPPE) | 20.4-58.1 | 0.1 g cylindrical-shaped foam sample was immersed in oil at RT for 5 min. | Yu et al. 2019 |
| PS | Carbon nanotubes | Electrospinning | 111.45-122.82 | Sorbent immersed in pure oil for 90 min at RT. | Wu et al. 2017 |
| PS fibers | Blended with PVC and PE individually | Electrospinning | 112- 119 | 0.1 g of sorbent was placed onto the oil surface for 15 minutes. | Alnaqbi et al. 2020 |
| PS -PVC blended fibers | Not Applicable | Electrospinning | 81-146 | 1 g of sorbent was placed on top of 300 mL of oil at 23 ±4 °C for 60 min. and drained for 2 min before weighing. | Zhu et al. 2011 |
| PS nanoporous fibers | Not Applicable | Electrospinning | Motor oil: 113.87<br>Bean oil: 111.80<br>Sunflower seed oil: 96.89 | 0.1 g of sorbent was dropped onto the oil film and drained for 10 s. | Lin et al. 2012 |

Table cont....

| Sorbent | Treatment Material | Method | Sorption Capacity (g/g) | Sorption Experimental Conditions | Reference |
|---|---|---|---|---|---|
| PS nanofibres | Sawdust | Electrospinning | Motor oil: 1.41<br>Diesel oil: 1.4<br>Furnace oil: 1.5<br>Crude oil: 1.1 | Reaction temperature = 25°C, pH = 4, contact time = 1 min. | Ghiasvand et al. 2021 |
| | | Impregnation | Motor oil: 1.00<br>Diesel oil: 0.63<br>Furnace oil: 0.97<br>Crude oil: 0.59 | | |
| PS/$Fe_3O_4$ nanofibres | $Fe_3O_4$ nanoparticles | Electrospinning | Edible oil: 87<br>Saxoline: 65<br>Dimethicone: 94 | Sorbent drained for 2 minutes before weighing. | Song et al. 2017 |
| rPS fabric | Orange peel extract | Electrospinning | 40.5±3.6 | 0.2 g sorbent in 100 mL of oil for 60 min | Yadav et al. 2019 |
| Expanded PS waste | Mechanical modification with holes puncture | Mechanical Puncturing | Crude oil: 3.26<br>Lubricating oil: 4.9<br>Distilled water: 0.32 | 0.9 g of sorbent was placed on the surface of the oil/water mixture at RT | Nasir & Hameed 2014 |
| PS/PVC fabric | PVC | Electrospinning | Motor oil: 146<br>Peanut oil: 119<br>Diesel: 38<br>Ethylene Glycol: 81 | 1 g of sorbent was placed on the top layer of 300 ml oil at 23±4°C for 60 min and drained for 2 min before final weighing. | Zhu et al. 2011 |
| Melamine sponge | MOF crystals | Not Applicable | 13000% | Not Specified | Xu et al. 2019 |
| Melamine sponge | Furfuryl alcohol | Immersion followed by polymerization | 75-160 | Not Specified | Feng et al. 2017 |
| Melamine sponge | Tetradecylamine-MXene | Immersion | 60-112 | Sorbent immersed into oil/water mixture at RT. Thermal and chemical stability tested at pH range 2-11 for 24 hours. | Xue et al. 2021 |
| Melamine sponge | Polycaprolactone and poly-D, L-Lactic acid | Freeze drying | 3.3-8.7 | Not Specified | Arunagiri et al. 2021 |
| PP and PE fibers & granules | Not Applicable | Not Applicable | 12.5 | Crude oil (0.5 mL, 0.49 g) in 80 mL water. Volumes of crude oil and saline water were kept constant, while the solidifier mass varied depending on the SOR ratio. | Shojaei et al. 2021 |
| Poly(methyl acrylate) | Amylopectin | Not Applicable | Not Available | The sorbent was tested at RT on a 0.2 mm thick oil layer on top of fresh water by using a contact time of 8 min for crude oil while 32 min for diluted bitumen. | Motta et al. 2019 |
| Divinyl benzene-vinyltriethoxysilane | Wheat bran | Polymerization | 12 | Oil gelling experiment of the bran sample conducted for 10 min at RT | Lv et al. 2020 |
| Glycerol propoxylate | Tris[3-(trimethoxysilyl) propyl]isocyanurate (ICS) as crosslinker | Bulk Polymerization | Not Available | Wire mesh basket sorbent soaked in an organic solvent for sorption studies at RT. | Kizil & Sonmez 2017 |

Table cont....

| Sorbent | Treatment Material | Method | Sorption Capacity (g/g) | Sorption Experimental Conditions | Reference |
|---|---|---|---|---|---|
| Recycled polyethylene terephthalate fibers | Polyvinyl alcohol followed by carbon nanotubes | Not Applicable | 12 | Performance of rPET-based oil sorbents studied at RT | Janqamsari et al. 2021 |
| Polyimide aerogels | Silicone nanofilaments (SiNFs) formed on the surface of PI fibers | Freeze drying followed by solvent-vapor treatment | 159 | Surfactant (Span 80, 10 mg) dissolved in 100 mL of organic liquid and homogenized at 10,000 rpm for 5 min. | Shen et al. 2021 |
| Poly(n-butyl acrylate) | Not Applicable | Solution Polymerization | Not Available | Not Specified | Ali 2019 |
| Poly(dimethylsiloxane) | Tris[3-(trimethoxysilyl) propyl] isocyanurate cross-linker | Bulk Polymerization | Not Available | Maximum absorbancy of 85-90% achieved in 40 minutes. | Askin et al. 2021 |
| Polydimethylsiloxane | Fluorinated alkyl silane. | Bulk Polymerization | 500-1800% | Highest sorption capacity of 1800% observed for dichloromethane due to its high polarity | Askin et al. 2021 |
| PS-polymethyl methacrylate/ divinyl benzene | 2D-nanosheets of $BN_3$/ graphene | Bulk Polymerization | Not Available | Sorption efficiency depends upon the polarity of adsorbate and the study was conducted in the temperature range of 30-60 °C. | Krishnan et al. 2022 |
| Polyester fibers | Poly(methylhydrodimethyl) siloxane copolymers | Heterogeneous polymerization | Dodecane: 5.52<br>Motor oil: 10.03 | Square-shaped sorbent immersed in oil and reaches saturation in 15 min and drained for 30 s before weighing and tested at 23 ± 4 °C. | Cojocaru et al. 2017 |
| Polysiloxane | Viscose-maghemite/ goethite magnetic nanoparticles | Not Applicable | Liquid HC: 15-17<br>Motor oils: 35-37 | Sorbent sample (0.15-0.2 g) dipped in oil for 15 min till saturation and drained for 30 s before weighing. | Rotaru et al. 2019 |
| PP/polyester micro/ nanofibres | Not Applicable | Three-step process including blending, drawing and etching | 21.9 | $CCl_4$/water mixture was passed through the sorbent as a filter set between two glass tubes. $CCl_4$ passed through the filter in 60 s and water retained in the upper glass tube. | Zhang et al. 2020 |
| Polyether sulfone (PES) | Zeolitic imidazolate (ZIF-8) framework (MOF) | One-step phase inversion method | Paraffin Oil: 37.6% (v/v)<br>Olive Oil: 35.6% (v/v) | Sorption at RT for 30 min. | Abbasi et al. 2017 |

demonstrated by Cojocaru et al. (2017). Novel polysiloxane copolymers were synthesized which were then used to treat polyester fibers to make them more hydrophobic. The hydrophobic polyester fibers were evaluated for their oil-absorbing capacities, which were found to be 5.52 $g.g^{-1}$ and 10.03 $g.g^{-1}$ for dodecane and motor oil, respectively. Optical microscopy identified the presence of inter-fiber voids which were responsible for oil absorption. Good recyclability of the sorbent was achieved as demonstrated by centrifugation tests.

The technique of engraving or etching has been used to modify the surface morphology of micro- and nanofibres to improve their oil sorption capacity. Another hydrophobic modification of polysiloxane with viscose-maghemite/ goethite magnetic nanoparticles has been reported by Rotaru et al. (2019). The material was found to exhibit a sorption capacity of 15-17 $g.g^{-1}$ for liquid hydrocarbons and 35-37 $g.g^{-1}$ for motor oils uptake. A multi-step procedure was employed to obtain the polymeric composite. Groove-like rough morphology was engraved on nonwoven polypropylene/polyester microfibrous and nanofibrous material by Zhang et al. (2020), using a three-step process that involved blending, drawing and etching. The oil adsorption results revealed that the nonwoven nanofibres had oil-saturated adsorption of 21.9 $g.g^{-1}$ and an oil retention rate of 10.3 $g.g^{-1}$. An excellent oil/water separation efficiency of 99% was obtained driven solely by gravity. Coating of

the zeolitic imidazolate framework (ZIF-8) on polyether sulfone (PES) was successfully carried out by Abbasi et al. (2017) through a simple one-step phase inversion method. Phase inversion refers to the process in which a homogenous solution of a polymer (in solvent) is reverted from a single phase into a two-phase system. The two-phase system consists of a solid polymer phase which forms the membrane structure and a liquid (polymer-poor) phase which forms the pores in the final film. In the composite material, the ZIF-8 particles were held together by the PES, and the ZIF-8 was responsible for effectively absorbing oil. A summary of other modified polymeric sorbents is given in Table 2.

## CHEMICALLY MODIFIED NATURAL SORBENTS

Natural adsorbents used for oil spill cleanup have been reported as the most economical, eco-friendly, and cost-effective promising technique. Some of the bio-based sorbents used for crude oil removal include chitosan, bagasse from sugar cane and pith, cotton, dried straws, fibers of palm, banana trunk and vegetables, byproducts of cork, rice hulls and fibers, onion and garlic peels, kapok, coconut fibers, and shells of various nuts, etc. Chemical modifications of these bio-based sorbents by acid and alkaline treatments have been reported to increase their sorption capacity for various pollutants (Cao et al. 2017, Gheriany et al. 2020, Zamparas et al. 2020).

### Chitosan

Biobased aerogels/sorbents offer great advantages in terms of natural abundance, low cost, environment-friendly, and biodegradability as compared to synthetic polymers. Chitosan is a naturally abundant polymer that has attracted great attention worldwide due to its extraordinary properties as biodegradability and the presence of reactive functional groups (Vidal & Moraes 2019). Hu et al. (2020) successfully fabricated aerogels of graphene oxide-modified chitosan nanosheets, followed by freeze drying of the nanosheets with silicon particles and PDMS, to impart hydrophobicity to the modified aerogels for improved oil absorption. The composite aerogel showed promising adsorption capacity in the range of 18-45 $g.g^{-1}$ for various oils and solvents. Since the recovery of adsorbed oil is usually achieved through the mechanical extrusion of the oil-loaded sorbents, the aerogels with better compressibility and stability exhibited the highest oil recovery. In another study, Yi et al. (2020) constructed a chitosan aerogel composite in which methyl trimethoxy silane was bonded to the aerogel through chemical vapor deposition. The rapid absorption of various oils and solvents and oil absorption capacities in the range of 31-63 $g.g^{-1}$ were observed. The chitosan-based aerogel also displayed excellent reusability and recyclability, with rapid recovery of oil by mechanical squeezing. Li et al. (2018) investigated the applicability of a unique chitosan-cellulose aerogel which was prepared by oxidation, crosslinking, freeze-drying, and cold plasma modification for remediation of oily wastewater. A cellulosic aerogel was prepared by freeze drying, followed by oxidation with $NaIO_4$ and exposure to an acetic acid solution containing 2% w/w of chitosan. The amino groups from chitosan reacted with aldehydic groups of oxidized cellulose resulting in crosslinking between the two molecules, followed by treatment with trimethyl chlorosilane (TMCS) to enhance the aerogel's hydrophobicity. Due to the rapid absorption rate, high absorption capacity (13.77–28.20 $g.g^{-1}$), high oil/water selectivity, and good reusability demonstrated by the chitosan aerogel, it can be considered a promising sorbent for oil/water separation.

### Modified Celluloses

Cellulosic sorbents are natural plant-based materials and have been more widely used as effective sorbents due to their biodegradability compared to other synthetic materials. Cellulose and lignin materials have been hydrophobically modified by physical or chemical methods (Valdebenito et al. 2018). Physical modifications include cold plasma coating, surface crystal growth, grafting, and sol-gel conversion treatments (Galblaub et al. 2016, Koch & Barthlott 2009). Chemical modifications include hydrophobic modifications with nanomaterials and polymers. Cotton fabric was rendered superhydrophobic upon treating the fabric with dopamine in presence of $FeCl_3$, causing self-polymerization of dopamine (polydopamine (PDA)). The PDA-cotton fabric was then treated with octadecyl amine (ODA) (Yan et al. 2020) to form a nano construct that exhibited a 2x surface roughness with greater strength and robustness compared to untreated cotton fabric. The oil separation efficiency was observed to increase by 96% which could be attributed to the high adhesion capacity of PDA. An additional improvement in oil/water separation ability could be achieved by further wrapping the Fe/PDA/ODA fabric around the PU sponge to fabricate an adsorption bag.

A superhydrophobic magnetic cellulose sponge was fabricated by deposition of $Fe_3O_4$ nanoparticles on the cellulose sponge which was further modified by immersion in an ethanolic solution of hexadecyltrimethoxysilane (Peng et al. 2016). The oil sorption capacity and oil separation efficiency of natural cellulose were increased by more than 95% due to the acetylation of the modified sponge.

Modified and unmodified date palm fibers (PFs) were used as natural sorbent material for oil spill removal by Abdelwahab et al. (2017). Various oils such as diesel oil, crude

oil, and vegetable oil were chosen to study the efficacy of the sorbent fibers. Simple chemical modification was carried out on PFs by soaking them in 2% w/v NaOH and 2% v/v $H_2SO_4$ separately at room temperature overnight, followed by drying at 80°C. The acid-base treatment made the fiber surface rough which affected the interaction between the inner surface of the fibers and the oil such that high sorption efficiency was achieved. In another study by Neelamegan et al. (2020), chemical modification of cellulose and lignin was carried out in the presence of carbon nanotubes (CNT) under basic (NaOH) conditions using CNT-COCl. The material was further reinforced with iron oxide to enable its purification. The increased hydrophobicity of the sorbent was proven by an increased water contact angle in the range of 130□135°. Sorption capacities for CNT-g-Cellulose/$Fe_3O_4$ and CNT-g-Lignin/$Fe_3O_4$ were found to be 15-25 and 10-23 $g.g^{-1}$ for a variety of oils and organic solvents.

**Rice Husk**

Wang et al. (2020) demonstrated the biological delignification of cellulose derived from rice husk followed by acetylation to prepare a hydrophobic sorbent. Both fungi and bacteria were employed to conduct the delignification process. The fabricated cellulosic sorbent exhibited good hydrophobicity which was evident in a sorption capacity of 20 g/g. In this study, Langmuir and Freundlich isotherms were used to analyze the sorption capacity, which indicated that the oil sorption capacity of rice husk fit the Langmuir model better than the Freundlich model. Through simple acetylation of oil palm empty fruit bunch (OPEFB) and cocoa pod (CP) fibers under mild conditions, Onwuka et al. (2018) fabricated a sorbent material for the sequestration of oil from water. A comparison of the acetylated and unacetylated sorbents indicated that the differences in their sorption capacities were dependent on time and concentration. Acetylation improved the oil sorption capacity of CP fibers. Kinetic studies demonstrated that the oil sorption was diffusion-controlled for both physisorption and chemisorption.

Thermally enhanced rice husk montmorillonite combination (TRMC) was evaluated for handling crude oil pollution (Akpomie et al. 2018). Studies revealed that the modified sorbent (TRMC) was more efficient in treating oil-contaminated water compared to the unmodified sorbent. It was observed that the sorption efficiency was significantly dependent on pH, temperature, the concentration of crude oil, sorbent-oil contact time, and dosage of sorbent. TRMC exhibited the maximum sorption potential as compared to the other reported sorbents which have been used for remediation of the crude oil spill.

**Other Natural Sorbents**

Seashells and epoxy resins have been used to modify PU sponges to create eco-friendly, robust, superhydrophobic, and super oleophilic adsorbents for the removal of oil from polluted water (Jamsaz & Goharshadi 2020). The clean PU sponge was immersed in a suspension of treated seashell powder followed by the addition of epoxy resin. The modified PU sponge was then freeze dried resulting in a sorbent material that exhibited good recyclability and high oil adsorption capacity in the range of 28.03-42.17 $g.g^{-1}$.

Eze et al. (2019) have shown the use of a unique biomass i.e., *Dialium guineense* (velvet tamarind) seed husk (DGSH) chemically treated with ammonium sulfate (AS-DGHS) for the remediation of oily water collected from the Niger Delta region in Nigeria. The surface morphology of both modified and unmodified sorbents exhibited a certain degree of porosity, with AS-DGSH possessing a greater porosity than DGSH indicating that the chemical modification was able to alter the surface of the biomass material. Around 50% of oil sequestration was achieved from polluted water at a pH of 6.1. However, a significant decrease in sorption was observed for both DGSH (41.2 to 20.3%) and AS-DGSH (52.6 to 27.2%) with an increase in pH from 3.0 to 9.0.

The adsorption capacity of raw luffa fibers was evaluated for various oil/water emulsions (Abdelwahab et al. 2014). High selectivity was exhibited by luffa fibers for various oils along with excellent water repellency in its original form. The contact time and dose of adsorbent were observed to have a significant effect on the sorption capacity such that it decreased as the amount of adsorbent increased and vice versa. A maximum sorption capacity was observed at 40°C for diesel oil. Other parameters that affected the efficiency of the fibrous sorbent were surface properties, temperature, the concentration of the crude oil, and the amount of fiber used. Raw luffa fibers were not very reusable since their sorption efficiency was observed to decrease after three sorption trials.

The sorption capacity of raw and acetylated sugarcane bagasse was determined for crude oil (Behnood et al. 2016). It was observed that the sorption capacity of acetylated bagasse was 90% greater than that of raw bagasse mainly due to the oleophilicity of acetylated bagasse. A sorption capacity of 11.3 $g.g^{-1}$ of crude oil and 9.1 $g.g^{-1}$ of oil layer in an emulsion was observed. The sugarcane bagasse, therefore, offers a significantly improved, low-cost method for the treatment of hydrocarbon impurities in aqueous systems (Boni et al. 2016). The porous nature and fibrous network structure of natural luffa sponge were observed to assist in the removal of dye and other solvents through filtration and absorption mechanisms (Wang et al. 2017). Surface modification of

luffa with polyhedral oligomeric silsesquioxane (POSS) imparted superhydrophobicity to the luffa sponge and significantly enhanced its oil absorption capacity.

## CONCLUSIONS

This review article evaluates the advances made in oil spill clean-up techniques based on the use of modified polymeric and natural sorbents. The methods reported by various researchers show promising prospects in dealing with such a hard pressing problem as the remediation of oil spills and oily wastewater. The treatment of oily wastewater requires a great deal of research in developing cost-efficient, recyclable and effective materials that can be employed in cleaning oil spills. The sorption characteristics of polymeric or natural oil sorbents depend on material morphology, especially for sponge-type sorbents which have a three-dimensional porous structure. Therefore, an effort should be made to understand the structure-property relationships of porous materials with respect to the effect of pore size, shape, and porosity on the uptake capacity and kinetics of various oils and organic solvents. An assessment of the performance of various sorbent materials developed through innovative processes which function in more efficient ways as compared to other typical methods used for oil spill clean-up has been the focus of this article. Surface roughness and high porosity are some of the characteristics gained from the surface modification of polymeric sorbents which have resulted in an enhancement of their oil sorption capacities. In addition, the ability to recover the oil from the sorbent and its reusability have also been discussed. The recyclability of the sorbents in efficient and continued extraction and separation of oil from spills and wastewater which will allow the recovery of potentially lost oil are critical endeavors in oils/organic solvents cleanup applications.

Identification of materials with excellent separation efficiency, elasticity, recyclability, and durability is therefore imperative for the viability of these sorbents in large-scale usage for remediation of global oil spill disasters. The development of super-wetting materials that are highly stable and durable is necessary for continued advancement in spill-cleanup technology. Additionally, sorbents with flame-retardant properties will help minimize fire hazards that usually occur during an active oil spill and minimize the spread of flammable gas and the generation of toxic smoke.

Significant challenges still exist when it comes to practical applications for synthetic sorbents, such as the fabrication cost, environmental impact, the strength of absorbent materials, and the oil treatment after recovery. Efforts are therefore needed to make the sorbent modification processes and techniques for functionalization, inexpensive, and relatively easy to conduct on a large scale. Furthermore, the environmental and economic impact of the techniques used in the fabrication of various chemically modified sorbents should be thoroughly evaluated. The techniques discussed herein have so far been studied on a lab scale, and further evaluation at an industrial scale needs to be conducted. A combination of a variety of sorbent modification techniques may be considered in identifying a cost-effective solution for mitigating an oil spill, while also considering environmental and economic implications. Further advancements in this field will include the generation of new functional oil-absorbing materials which are suitable for optimized, low-cost, large-scale manufacture of sorbents that are themselves environment-friendly for widespread usage during oil spill containment and oily wastewater treatment. Extensive research and funding will be needed to achieve these goals.

## REFERENCES

Abbasi, Z., Shamsaei, E., Fang, X. Y., Ladewig, B. and Wang, H. 2017. Simple fabrication of zeolitic imidazolate framework ZIF-8/polymer composite beads by phase inversion method for efficient oil sorption. Journal of Colloid and Interface Science, 493: 150-161. https://doi.org/10.1016/j.jcis.2017.01.006

Abdelwahab, O. 2014. Assessment of raw luffa as a natural hollow oleophilic fibrous sorbent for oil spill cleanup. Alexandria Engineering Journal, 53(1): 213-218. https://doi.org/10.1016/j.aej.2013.11.001

Abdelwahab, O., Nasr, S. M. and Thabet, W. M. 2017. Palm fibers and modified palm fibers adsorbents for different oils. Alexandria Engineering Journal, 56(4): 749-755. https://doi.org/10.1016/j.aej.2016.11.020

Akpomie, K. G., Ezeofor, C. C., Olikagu, C. S., Odewole, O. A. and Ezeorah, C. J. 2018. Abstraction and regeneration potential of temperature-enhanced rice husk montmorillonite combo for oil spill. Environmental Science and Pollution Research, 25(34): 34711-34719. https://doi.org/10.1007/s11356-018-3425-9

Ali, S. 2019. Synthesis and characteristics of oleophilic gel polymer for oil spills cleanup. African Journal of Engineering Research, 7(3): 85-93. https://doi.org/10.30918/AJER.73.19.032

Alnaqbi, M. A., Al Blooshi, A. G. and Greish, Y. E. 2020. Polyethylene and polyvinyl chloride-blended polystyrene nanofibrous sorbents and their application in the removal of various oil spills. Advances in Polymer Technology, 1-12. https://doi.org/10.1155/2020/4097520

Arunagiri, V., Prasannan, A., Udomsin, J., Lai, J.Y., Wang, C.-F., Hong, P.-D. and Tsai, H. C. 2021. Facile fabrication of eco-friendly polycaprolactone (PCL)/Poly-D, L-Lactic acid (PDLLA) modified melamine sorbent for oil-spill cleaning and water/oil (W/O) emulsion separation. Separation and Purification Technology, 259: 118081. https://doi.org/10.1016/j.seppur.2020.118081

Askin, S., Kizil, S. and Bulbul Sonmez, H. 2021. Creating of highly hydrophobic sorbent with fluoroalkyl silane cross-linker for efficient oil-water separation. Reactive and Functional Polymers, 167: 105002. https://doi.org/10.1016/j.reactfunctpolym.2021.105002

Askin, S., Kizil, S. and Bulbul Sonmez, H. 2021. Hydrophobic cross‐linked poly(dimethylsiloxane)‐based sorbents for oil spill applications. Macromolecular Materials and Engineering, 306(2): 2000556. https://doi.org/10.1002/mame.202000556

Atlas, R. M. and Hazen, T. C. 2011. oil biodegradation and bioremediation: a tale of the two worst spills in U.S. history. Environmental Science and Technology, 45(16): 6709-6715. https://doi.org/10.1021/es2013227

Atta, A. M., Abdullah, M. M. S., Al-Lohedan, H. A. and Mohamed, N. H. 2019. Novel superhydrophobic sand and polyurethane sponge coated with silica/modified asphaltene nanoparticles for rapid oil spill cleanup. Nanomaterials, 9(2). https://doi.org/10.3390/nano9020187

Baig, N., Alghunaimi, F. I., Dossary, H. S. and Saleh, T. A. 2019. Superhydrophobic and superoleophilic carbon nanofiber grafted polyurethane for oil-water separation. Process Safety and Environmental Protection, 123: 327-334. https://doi.org/10.1016/j.psep.2019.01.007

Behnood, R., Anvaripour, B., Jaafarzadeh, N. and Farasati, M. 2016. Oil spill sorption using raw and acetylated sugarcane bagasse. Journal of Central South University, 23(7): 1618–1625. https://doi.org/10.1007/s11771-016-3216-8

Biesuz, M., Tomasi, M., Santhosh, B., Sglavo, V. M. and Sorarù, G. D. 2020. Polymer-derived Si3N4 nanofelts as a novel oil spills clean-up architecture. Journal of Environmental Chemical Engineering, 8(5): 104134. https://doi.org/10.1016/j.jece.2020.104134

Boni, H. T., de Oliveira, D., Ulson de Souza, A. A. and Ulson de Souza, S. M. A. G. 2016. Bioadsorption by sugarcane bagasse for the reduction in oil and grease content in aqueous effluent. International Journal of Environmental Science and Technology, 13(4): 1169-1176. https://doi.org/10.1007/s13762-016-0962-y

Cao, N., Yang, B., Barras, A., Szunerits, S. and Boukherroub, R. 2017. Polyurethane sponge functionalized with superhydrophobic nanodiamond particles for efficient oil/water separation. Chemical Engineering Journal, 307: 319-325. https://doi.org/10.1016/j.cej.2016.08.105

Cao, S., Dong, T., Xu, G. and Wang, F. 2017. Oil spill cleanup by hydrophobic natural fibers. Journal of Natural Fibres, 14(5): 727-735. https://doi.org/10.1080/15440478.2016.1277820

Cojocaru, C., Pricop, L., Samoila, P., Rotaru, R. and Harabagiu, V. 2017. Surface hydrophobization of polyester fibers with poly(methylhydrodimethyl)siloxane copolymers: Experimental design for testing of modified nonwoven materials as oil spill sorbents. Polymer Testing, 59: 377-389. https://doi.org/10.1016/j.polymertesting.2017.02.024

Damavandi, F. and Soares, J. B. P. 2022. Polystyrene magnetic nanocomposite blend: An effective, facile, and economical alternative in oil spill removal applications. Chemosphere, 286(April 2021). https://doi.org/10.1016/j.chemosphere.2021.131611

El Gheriany, I. A., Ahmad El Saqa, F., Abd El Razek Amer, A. and Hussein, M. 2020. Oil spill sorption capacity of raw and thermally modified orange peel waste. Alexandria Engineering Journal, 59(2): 925-932. https://doi.org/10.1016/j.aej.2020.03.024

Eze, S. I., Akpomie, K. G., Ezeofor, C. C., Mmadubuike, N. V. and Ojo, F. K. 2019. Remediation of oil spill polluted water from Niger Delta Nigeria by sorption onto ammonium sulfate modified Dialium guineense seed husk. Petroleum Science and Technology, 37(15): 1830-1838. https://doi.org/10.1080/10916466.2019.1608240

Feng, Y., Wang, Y., Wang, Y. and Yao, J. 2017. Furfuryl alcohol modified melamine sponge for highly efficient oil spill clean-up and recovery. J. Mater. Chem. A, 5(41): 21893-21897. https://doi.org/10.1039/C7TA06966A

Fingas, M. 2012. The Basics of Oil Spill Cleanup. CRC Press. https://doi.org/10.1201/b13686

Galblaub, O. A., Shaykhiev, I. G., Stepanova, S. V. and Timirbaeva, G. R. 2016. Oil spill cleanup of water surface by plant-based sorbents: Russian practices. Process Safety and Environmental Protection, 101: 88-92. https://doi.org/10.1016/j.psep.2015.11.002

Ghiasvand, S., Rahmani, A., Samadi, M., Asgari, G., Azizian, S. and Poormohammadi, A. 2021. Application of polystyrene nanofibres filled with sawdust as separator pads for separation of oil spills. Process Safety and Environmental Protection, 146: 161-168. https://doi.org/10.1016/j.psep.2020.08.044

Gui, H., Zhang, T. and Guo, Q. 2019. Nanofibrous, emulsion-templated syndiotactic polystyrenes with superhydrophobicity for oil spill cleanup. ACS Applied Materials and Interfaces, 11(39): 36063-36072. https://doi.org/10.1021/acsami.9b10467

Gui, X., Zeng, Z., Lin, Z., Gan, Q., Xiang, R., Zhu, Y., Cao, A. and Tang, Z. 2013. Magnetic and highly recyclable macroporous carbon nanotubes for spilled oil sorption and separation. ACS Applied Materials and Interfaces, 5(12): 5845-5850. https://doi.org/10.1021/am4015007

Guo, J., Wang, J., Zhang, S., Ma, X., Qiu, Z., Peng, X., Ying, J., Wang, Y. and Wu, G. 2017. One-step modification of PU sponges for selective absorption of oil–water mixtures. New Journal of Chemistry, 41(1): 90-96. https://doi.org/10.1039/C6NJ03239G

Hu, J., Zhu, J., Ge, S., Jiang, C., Guo, T., Peng, T., Huang, T. and Xie, L. 2020. Biocompatible, hydrophobic and resilience graphene/chitosan composite aerogel for efficient oil-water separation. Surface and Coatings Technology, 385: 125361. https://doi.org/10.1016/j.surfcoat.2020.125361

Huang, X., Zhang, S., Xiao, W., Luo, J., Li, B., Wang, L., Xue, H. and Gao, J. 2020. Flexible PDA@ACNTs decorated polymer nanofiber composite with superhydrophilicity and underwater superoleophobicity for efficient separation of oil-in-water emulsion. Journal of Membrane Science, 614: 118500. https://doi.org/10.1016/j.memsci.2020.118500

Jamaly, S., Giwa, A. and Hasan, S. W. 2015. Recent improvements in oily wastewater treatment: Progress, challenges, and future opportunities. Journal of Environmental Sciences, 37: 15-30. https://doi.org/10.1016/j.jes.2015.04.011

Jamsaz, A. and Goharshadi, E. K. 2020. An environmentally friendly superhydrophobic modified polyurethane sponge by seashell for the efficient oil/water separation. Process Safety and Environmental Protection, 139: 297-304. https://doi.org/10.1016/j.psep.2020.04.042

Janqamsari, Y., Ashjari, M. and Niazi, Z. 2021. Carbon nanotube promoted porous nanocomposite based on PVA and recycled PET fibers for efficient oil spills cleanup applications. Chemical Papers, 75(7): 3443-3456. https://doi.org/10.1007/s11696-021-01587-x

Junaidi, N. F. D., Othman, N. H., Fuzil, N. S., Mat Shayuti, M. S., Alias, N. H., Shahruddin, M. Z., Marpani, F., Lau, W. J., Ismail, A. F. and Aba, N. D. 2021. Recent development of graphene oxide-based membranes for oil–water separation: A review. Separation and Purification Technology, 258: 118000. https://doi.org/10.1016/j.seppur.2020.118000

Karami, P., Khorshidi, B., McGregor, M., Peichel, J. T., Soares, J. B. P. and Sadrzadeh, M. 2020. Thermally stable thin film composite polymeric membranes for water treatment: A review. Journal of Cleaner Production, 250. https://doi.org/10.1016/j.jclepro.2019.119447

Keshawy, M., Farag, R. K. and Gaffer, A. 2020. Egyptian crude oil sorbent based on coated polyurethane foam waste. Egyptian Journal of Petroleum, 29(1): 67-73. https://doi.org/10.1016/j.ejpe.2019.11.001

Khosravi, M. and Azizian, S. 2015. Synthesis of a novel highly oleophilic and highly hydrophobic sponge for rapid oil spill cleanup. ACS Applied Materials and Interfaces, 7(45): 25326-25333. https://doi.org/10.1021/acsami.5b07504

Kizil, S. and Sonmez, B. 2017. Oil loving hydrophobic gels made from glycerol propoxylate: Efficient and reusable sorbents for oil spill clean-up. Journal of Environmental Management, 196: 330-339. https://doi.org/10.1016/j.jenvman.2017.02.016

Koch, K. and Barthlott, W. 2009. Superhydrophobic and superhydrophilic plant surfaces: an inspiration for biomimetic materials. Philosophical Transactions of the Royal Society A: Mathematical, Physical and Engineering Sciences, 367(1893): 1487-1509. https://doi.org/10.1098/rsta.2009.0022

Kong, Z., Wang, J., Lu, X., Zhu, Y. and Jiang, L. 2017. In situ fastening graphene sheets into a polyurethane sponge for the highly efficient continuous cleanup of oil spills. Nano Research, 10(5): 1756-1766. https://doi.org/10.1007/s12274-017-1484-8

Krishnan, M. R., Aldawsari, Y. F. and Alsharaeh, E. H. 2022. 3D-poly (styrene-methyl methacrylate)/divinyl benzene-2D-nanosheet

composite networks for organic solvents and crude oil spill cleanup. Polymer Bulletin, 79(6): 3779-3802. https://doi.org/10.1007/s00289-021-03565-5

Li, D., Gou, X., Wu, D. and Guo, Z. 2018. A robust and stretchable superhydrophobic PDMS/PVDF@KNFs membrane for oil/water separation and flame retardancy. Nanoscale, 10(14): 6695-6703. https://doi.org/10.1039/C8NR01274A

Li, H., Liu, L. and Yang, F. 2012. Hydrophobic modification of polyurethane foam for oil spill cleanup. Marine Pollution Bulletin, 64(8): 1648-1653. https://doi.org/10.1016/j.marpolbul.2012.05.039

Li, Z., Shao, L., Hu, W., Zheng, T., Lu, L., Cao, Y. and Chen, Y. 2018. Excellent reusable chitosan/cellulose aerogel as an oil and organic solvent absorbent. Carbohydrate Polymers, 191: 183-190. https://doi.org/10.1016/j.carbpol.2018.03.027

Liang, L., Xue, Y., Wu, Q., Dong, Y. and Meng, X. 2019. Self-assembly modification of polyurethane sponge for application in oil/water separation. RSC Advances, 9(69): 40378-40387. https://doi.org/10.1039/c9ra05855a

Lin, J., Shang, Y., Ding, B., Yang, J., Yu, J. and Al-Deyab, S. S. 2012. Nanoporous polystyrene fibers for oil spill cleanup. Marine Pollution Bulletin, 64(2): 347-352. https://doi.org/10.1016/j.marpolbul.2011.11.002

Liu, C., Fang, Y., Miao, X., Pei, Y., Yan, Y., Xiao, W. and Wu, L. 2019. Facile fabrication of superhydrophobic polyurethane sponge towards oil-water separation with exceptional flame-retardant performance. Separation and Purification Technology, 229: 115801. https://doi.org/10.1016/j.seppur.2019.115801

Lü, X., Cui, Z., Wei, W., Xie, J., Jiang, L., Huang, J. and Liu, J. 2016. Constructing polyurethane sponge modified with silica/graphene oxide nanohybrids as a ternary sorbent. Chemical Engineering Journal, 284: 478-486. https://doi.org/10.1016/j.cej.2015.09.002

Lv, P., Yasin, A., Hao, B. and Ma, P.-C. 2020. Wheat bran/polymer composites as a solidifier to gel oil on water surface. Composites Communications, 22: 100471. https://doi.org/10.1016/j.coco.2020.100471

Middlebrook, A. M., Murphy, D. M., Ahmadov, R., Atlas, E. L., Bahreini, R., Blake, D. R., Brioude, J., de Gouw, J. A., Fehsenfeld, F. C., Frost, G. J., Holloway, J. S., Lack, D. A., Langridge, J. M., Lueb, R. A., McKeen, S. A., Meagher, J. F., Meinardi, S., Neuman, J. A., Nowak, J. B. and Ravishankara, A. R. 2012. Air quality implications of the deepwater horizon oil spill. Proceedings of the National Academy of Sciences, 109(50): 20280-20285. https://doi.org/10.1073/pnas.1110052108

Motta, F. L., Stoyanov, S. R. and Soares, J. B. P. 2019. Development and application of an amylopectin-graft-poly(methyl acrylate) solidifier for rapid and efficient containment and recovery of heavy oil spills in aqueous environments. Chemosphere, 236: 124352. https://doi.org/10.1016/j.chemosphere.2019.124352

Nasir, M. I. and Hameed, Z. M. 2014. Utilization of expanded polystyrene (EPS) Waste as sorbent for oil spill cleanup. Society of Petroleum Engineers - 30th Abu Dhabi International Petroleum Exhibition and Conference, ADIPEC 2014: Challenges and Opportunities for the Next 30 Years, 5, 3375-3385. https://doi.org/10.2118/172000-ms

Neelamegan, H., Yang, D.K., Lee, G.-J., Anandan, S. and Wu, J. J. 2020. Synthesis of magnetite nanoparticles anchored cellulose and lignin-based carbon nanotube composites for rapid oil spill cleanup. Materials Today Communications, 22: 100746. https://doi.org/10.1016/j.mtcomm.2019.100746

Onwuka, J. C., Agbaji, E. B., Ajibola, V. O. and Okibe, F. G. 2018. Treatment of crude oil-contaminated water with chemically modified natural fiber. Applied Water Science, 8(3): 86. https://doi.org/10.1007/s13201-018-0727-5

Oribayo, O., Feng, X., Rempel, G. L. and Pan, Q. 2017. Synthesis of lignin-based polyurethane/graphene oxide foam and its application as an absorbent for oil spill clean-ups and recovery. Chemical Engineering Journal, 323: 191-202. https://doi.org/10.1016/j.cej.2017.04.054

Padaki, M., Surya Murali, R., Abdullah, M. S., Misdan, N., Moslehyani, A., Kassim, M. A., Hilal, N. and Ismail, A. F. 2015. Membrane technology enhancement in oil–water separation. A review. Desalination, 357: 197-207. https://doi.org/10.1016/j.desal.2014.11.023

Pavlatou, E. A. 2020. Commercial sponges as a novel technology for crude oil removal from seawater and industrial wastewater: a review. Biomedical Journal of Scientific and Technical Research, 25(5). https://doi.org/10.26717/BJSTR.2020.25.004251

Peng, H., Wang, H., Wu, J., Meng, G., Wang, Y., Shi, Y., Liu, Z. and Guo, X. 2016. Preparation of superhydrophobic magnetic cellulose sponge for removing oil from water. Industrial and Engineering Chemistry Research, 55(3): 832-838. https://doi.org/10.1021/acs.iecr.5b03862

Peng, M., Zhu, Y., Li, H., He, K., Zeng, G., Chen, A., Huang, Z., Huang, T., Yuan, L. and Chen, G. 2019. Synthesis and application of modified commercial sponges for oil-water separation. Chemical Engineering Journal, 373: 213-226. https://doi.org/10.1016/j.cej.2019.05.013

Potter, S. and Buist, I. 2008. In-situ burning for oil spills in arctic waters: State-of-the-Art and Future Research Needs, 23-39. https://doi.org/10.1007/978-1-4020-8565-9_5

Ramanathan, R., Abdullah, L., Mohamed, S. and Fauadi, M.H.F.M. 2022. A review of user-centred design methods for designing a portable oil spill skimmer. Nat. Env. Poll. Tech., 21(4).

Rogowska, J. and Namieśnik, J. 2010. Environmental implications of oil spills from shipping accidents. Reviews of Environmental Contamination and Toxicology, 95-114. https://doi.org/10.1007/978-1-4419-6260-7_5

Rotaru, R., Fortuna, M. E., Cojocaru, C., Samoila, P., Pricop, L. and Harabagiu, V. 2019. Viscose-maghemite/goethite polymeric composite as sorbent for oil spill cleanup. Environmental Engineering and Management Journal, 18(6): 1193-1200. https://doi.org/10.30638/eemj.2019.114

Ruan, C., Ai, K., Li, X. and Lu, L. 2014. A superhydrophobic sponge with excellent absorbency and flame retardancy. Angewandte Chemie, 126(22): 5662-5666. https://doi.org/10.1002/ange.201400775

Sarbatly, R., Krishnaiah, D. and Kamin, Z. 2016. A review of polymer nanofibres by electrospinning and their application in oil–water separation for cleaning up marine oil spills. Marine Pollution Bulletin, 106(1-2): 8-16. https://doi.org/10.1016/j.marpolbul.2016.03.037

Shang, B., Wang, Y., Peng, B. and Deng, Z. 2016. Bioinspired polydopamine particles-assisted construction of superhydrophobic surfaces for oil/water separation. Journal of Colloid and Interface Science, 482: 240-251. https://doi.org/10.1016/j.jcis.2016.07.081

Shen, Y., Li, D., Wang, L., Zhou, Y., Liu, F., Wu, H., Deng, B. and Liu, Q. 2021. Superelastic polyimide nanofiber-based aerogels modified with silicone nanofilaments for ultrafast oil/water separation. ACS Applied Materials and Interfaces, 13(17): 20489-20500. https://doi.org/10.1021/acsami.1c01136

Shojaei, N., Aminsharei, F. and Abbastabar Ahangar, H. 2021. Application of hydrophobic polymers as solidifiers for oil spill cleanup. International Journal of Environmental Science and Technology, 18(6): 1419-1424. https://doi.org/10.1007/s13762-020-02882-y

Shuai, Q., Yang, X., Luo, Y., Tang, H., Luo, X., Tan, Y. and Ma, M. 2015. A superhydrophobic poly(dimethylsiloxane)-$TiO_2$ coated polyurethane sponge for selective absorption of oil from water. Materials Chemistry and Physics, 162: 94-99. https://doi.org/10.1016/j.matchemphys.2015.05.011

Singh, S. and Jelinek, R. 2020. Solar-mediated oil-spill cleanup by a carbon dot-polyurethane sponge. Carbon, 160: 196-203. https://doi.org/10.1016/j.carbon.2020.01.016

Singh, V., Kendall, R. J., Hake, K. and Ramkumar, S. 2013. Crude oil sorption by raw cotton. Industrial and Engineering Chemistry Research, 52(18): 6277-6281. https://doi.org/10.1021/ie4005942

Song, B., Zhu, J. and Fan, H. 2017. Magnetic fibrous sorbent for remote and efficient oil adsorption. Marine Pollution Bulletin, 120(1-2): 159-164.

https://doi.org/10.1016/j.marpolbul.2017.05.011
Speight, J. G. 2006. The Chemistry and Technology of Petroleum. CRC Press. https://doi.org/10.1201/9781420008388
Tran, V.-H. T. and Lee, B.K. 2017. Novel fabrication of a robust superhydrophobic PU@ZnO@Fe3O4@SA sponge and its application in oil-water separations. Scientific Reports, 7(1): 17520. https://doi.org/10.1038/s41598-017-17761-9
Usman, A. D. and Okoro, L. N. 2017. Chemical science review and letters innovations in oil spill clean-up techniques. Chem. Sci. Rev. Lett., 6(23): 1908-1916.
Valdebenito, F., García, R., Cruces, K., Ciudad, G., Chinga-Carrasco, G. and Habibi, Y. 2018. $CO_2$ adsorption of surface-modified cellulose nanofibril films derived from agricultural wastes. ACS Sustainable Chemistry and Engineering, 6(10): 12603-12612. https://doi.org/10.1021/acssuschemeng.8b00771
Vidal, R. R. L. and Moraes, J. S. 2019. Removal of organic pollutants from wastewater using chitosan: a literature review. International Journal of Environmental Science and Technology, 16(3): 1741-1754. https://doi.org/10.1007/s13762-018-2061-8
Visco, A., Quattrocchi, A., Nocita, D., Montanini, R. and Pistone, A. 2021. Polyurethane foams loaded with carbon nanofibres for oil spill recovery: Mechanical properties under fatigue conditions and selective absorption in oil/water mixtures. Nanomaterials, 11(3): 1-14. https://doi.org/10.3390/nano11030735
Wang, C.F., Huang, H.-C. and Chen, L.-T. 2015. Protonated melamine sponge for effective oil/water separation. Scientific Reports, 5(1): 14294. https://doi.org/10.1038/srep14294
Wang, J. and Geng, G. 2015. Highly recyclable superhydrophobic sponge suitable for the selective sorption of high viscosity oil from water. Marine Pollution Bulletin, 97(1-2): 118-124. https://doi.org/10.1016/j.marpolbul.2015.06.026
Wang, Z., Ma, H., Chu, B. and Hsiao, B. S. 2017. Super-hydrophobic modification of porous natural polymer "luffa sponge" for oil absorption. Polymer, 126: 470-476. https://doi.org/10.1016/j.polymer.2017.05.068
Wang, Z., Saleem, J., Barford, J. P. and McKay, G. 2020. Preparation and characterization of modified rice husks by biological delignification and acetylation for oil spill cleanup. Environmental Technology, 41(15): 1980-1991. https://doi.org/10.1080/09593330.2018.1552725
Wei, Q., Oribayo, O., Feng, X., Rempel, G. L. and Pan, Q. 2018. Synthesis of polyurethane foams loaded with tio2 nanoparticles and their modification for enhanced performance in oil spill cleanup. Industrial and Engineering Chemistry Research, 57(27): 8918-8926. https://doi.org/10.1021/acs.iecr.8b01037
Wu, D., Wu, W., Yu, Z., Zhang, C. and Zhu, H. 2014. Facile preparation and characterization of modified polyurethane sponge for oil absorption. Industrial and Engineering Chemistry Research, 53(52): 20139-20144. https://doi.org/10.1021/ie5032327
Wu, J., An, A. K., Guo, J., Lee, E. J., Farid, M. U. and Jeong, S. 2017. CNTs reinforced super-hydrophobic-oleophilic electrospun polystyrene oil sorbent for enhanced sorption capacity and reusability. Chemical Engineering Journal, 314: 526-536. https://doi.org/10.1016/j.cej.2016.12.010
Wu, L., Zhang, J., Li, B. and Wang, A. 2014. Magnetically driven super durable superhydrophobic polyester materials for oil/water separation. Polymer Chemistry, 5(7): 2382. https://doi.org/10.1039/c3py01478a
Xu, Z., Wang, J., Li, H. and Wang, Y. 2019a. Coating sponge with multifunctional and porous metal-organic framework for oil spill remediation. Chemical Engineering Journal, 370(April), 1181-1187. https://doi.org/10.1016/j.cej.2019.03.288
Xu, Z., Wang, J., Li, H. and Wang, Y. 2019b. Coating sponge with multifunctional and porous metal-organic framework for oil spill remediation. Chemical Engineering Journal, 370: 1181-1187. https://doi.org/10.1016/j.cej.2019.03.288
Xue, J., Zhu, L., Zhu, X., Li, H., Ma, C., Yu, S., Sun, D., Xia, F. and Xue, Q. 2021. Tetradecylamine-MXene functionalized melamine sponge for effective oil/water separation and selective oil adsorption. Separation and Purification Technology, 259: 118106. https://doi.org/10.1016/j.seppur.2020.118106
Yadav, S., Mattaparthi, S., Sreenivasulu, K., Khandelwal, M., Majumdar, S. and Sharma, C. S. 2019. Recycling of thermoplastic polystyrene waste using citrus peel extract for oil spill remediation. Journal of Applied Polymer Science, 136(33): 1-8. https://doi.org/10.1002/app.47886
Yan, X., Zhu, X., Ruan, Y., Xing, T., Chen, G. and Zhou, C. 2020. Biomimetic, dopamine-modified superhydrophobic cotton fabric for oil–water separation. Cellulose, 27(13): 7873-7885. https://doi.org/10.1007/s10570-020-03336-x
Yang, Y., Yi, H. and Wang, C. 2015. Oil absorbents based on melamine/lignin by a dip adsorbing method. ACS Sustainable Chemistry and Engineering, 3(12): 3012-3018. https://doi.org/10.1021/acssuschemeng.5b01187
Yi, L., Yang, J., Fang, X., Xia, Y., Zhao, L., Wu, H. and Guo, S. 2020. Facile fabrication of wood-inspired aerogel from chitosan for efficient removal of oil from Water. Journal of Hazardous Materials, 385: 121507. https://doi.org/10.1016/j.jhazmat.2019.121507
Yu, C., Lin, W., Jiang, J., Jing, Z., Hong, P. and Li, Y. 2019. Preparation of a porous superhydrophobic foam from waste plastic and its application for oil spill cleanup. RSC Advances, 9(65): 37759-37767. https://doi.org/10.1039/c9ra06848a
Yu, L., Hao, G., Zhou, S. and Jiang, W. 2016. Durable and modified foam for cleanup of oil contamination and separation of oil–water mixtures. RSC Advances, 6(29): 24773-24779. https://doi.org/10.1039/C5RA27370F
Yue, X., Li, Z., Zhang, T., Yang, D. and Qiu, F. 2019. Design and fabrication of superwetting fiber-based membranes for oil/water separation applications. Chemical Engineering Journal, 364: 292-309. https://doi.org/10.1016/j.cej.2019.01.149
Zamparas, M., Tzivras, D., Dracopoulos, V. and Ioannides, T. 2020. Application of sorbents for oil spill cleanup focusing on natural-based modified materials: a review. Molecules, 25(19): 4522. https://doi.org/10.3390/molecules25194522
Zhang, B., Matchinski, E. J., Chen, B., Ye, X., Jing, L. and Lee, K. 2019. Marine oil spills-oil pollution, sources and effects. In World Seas: an Environmental Evaluation (pp. 391-406). Elsevier. https://doi.org/10.1016/B978-0-12-805052-1.00024-3
Zhang, H., Zhen, Q., Cui, J.-Q., Liu, R.-T., Zhang, Y.-F., Qian, X.-M. and Liu, Y. 2020. Groove-shaped polypropylene/polyester micro/nanofibrous nonwoven with enhanced oil wetting capability for high oil/water separation. Polymer, 193, 122356. https://doi.org/10.1016/j.polymer.2020.122356
Zhang, Jiaoyuan, Chen, R., Liu, J., Liu, Q., Yu, J., Zhang, H., Jing, X., Zhang, M. and Wang, J. 2019. Construction of ZnO@$Co_3O_4$-loaded nickel foam with abrasion resistance and chemical stability for oil/water separation. Surface and Coatings Technology, 357: 244-251. https://doi.org/10.1016/j.surfcoat.2018.09.042
Zhang, Junping and Seeger, S. 2011. Polyester materials with superwetting silicone nanofilaments for oil/water separation and selective oil absorption. Advanced Functional Materials, 21(24): 4699-4704. https://doi.org/10.1002/adfm.201101090
Zhang, P., Hu, W., Wu, M., Gong, L., Tang, A., Xiang, L., Zhu, B., Zhu, L. and Zeng, H. 2019. Cost-effective strategy for surface modification via complexation of disassembled polydopamine with Fe(III) ions. Langmuir, 35(11): 4101-4109. https://doi.org/10.1021/acs.langmuir.9b00245
Zhang, X., Wang, X., Liu, X., Lv, C., Wang, Y., Zheng, G., Liu, H., Liu, C., Guo, Z. and Shen, C. 2018. Porous polyethylene bundles with enhanced hydrophobicity and pumping oil-recovery ability via skin-peeling. ACS Sustainable Chemistry and Engineering, 6(10): 12580-12585. https://doi.org/10.1021/acssuschemeng.8b03305

Zhang, Z., Sèbe, G., Rentsch, D., Zimmermann, T. and Tingaut, P. 2014. Ultralightweight and flexible silylated nanocellulose sponges for the selective removal of oil from water. Chemistry of Materials, 26(8): 2659-2668. https://doi.org/10.1021/cm5004164

Zhao, S., Yin, L., Zhou, Q., Liu, C. and Zhou, K. 2020. In situ self-assembly of zeolitic imidazolate frameworks on the surface of flexible polyurethane foam: Towards for highly efficient oil spill cleanup and fire safety. Applied Surface Science, 506: 144700. https://doi.org/10.1016/j.apsusc.2019.144700

Zhou, X., Zhang, Z., Xu, X., Men, X. and Zhu, X. 2013. Facile fabrication of superhydrophobic sponge with selective absorption and collection of oil from water. Industrial and Engineering Chemistry Research, 52(27): 9411-9416. https://doi.org/10.1021/ie400942t

Zhu, H., Chen, D., Yang, S., Li, N., Xu, Q., Li, H., Wang, L., He, J., Jiang, J. and Lu, J. 2016. A versatile and cost-effective reduced graphene oxide-crosslinked polyurethane sponge for highly effective wastewater treatment. RSC Advances, 6(44): 38350-38355. https://doi.org/10.1039/C6RA05450A

Zhu, H., Qiu, S., Jiang, W., Wu, D. and Zhang, C. 2011a. Evaluation of electrospun polyvinyl chloride/polystyrene fibers as sorbent materials for oil spill cleanup. Environmental Science and Technology, 45(10): 4527-4531. https://doi.org/10.1021/es2002343

Nature Environment and Pollution Technology
An International Quarterly Scientific Journal

p-ISSN: 0972-6268
(Print copies up to 2016)
e-ISSN: 2395-3454

Vol. 22 | No. 1 | pp. 63-72 | 2023

Original Research Paper

https://doi.org/10.46488/NEPT.2023.v22i01.005

Open Access Journal

# Water Quality Assessment of Wenyu River with Variable Weight Cloud Model

**Li Guojiao, Men Baohui† and Wang Lehao**
School of Water Resources and Hydropower Engineering, North China Electric Power University, Beijing 102206, China
†Corresponding author: Men Baohui; menbh@ncepu.edu.cn.com

**Nat. Env. & Poll. Tech.**
**Website: www.neptjournal.com**

*Received:* 29-05-2022
*Revised:* 30-06-2022
*Accepted:* 01-07-2022

**Key Words:**
Water quality evaluation
Combination weighting
Penalty variable weight
Cloud model
Wenyu river

## ABSTRACT

The water resource is an important guarantee of social and economic sustainable development. The improvement of water's ecological carbon sequestration ability is a direct response to the goal of "double carbon". Water quality directly affects its carbon sequestration capacity. So it is necessary to understand the water quality of rivers. In view of the fuzziness and uncertainty in water quality evaluation, this paper uses the cloud model to realize the qualitative to quantitative transformation of water quality in Wenyu River. By combining moment estimation theory with critic weight, AHM weight, and variable weight theory. A water quality evaluation method integrating a variable weight cloud model is constructed. And the temporal and spatial changes in water quality in Wenyu River are studied. The results show that the combined weights balance the influence of each index while retaining the advantages of subjective and objective weights. The results of the water quality evaluation are consistent with the practice, which verifies the feasibility and applicability of the method.

## INTRODUCTION

Water quality evaluation is of great significance to the survival and development of human beings. On the one hand, according to the results of the water quality evaluation, the corresponding water purification work is carried out to improve water quality and protect water resources. On the other hand, water resources can be developed within an appropriate range to maximize the utilization of resources (Zhao 2017). The water environment of the Wenyu River plays an important role in the development of the north Canal basin. With the social attention to water ecological protection, research on the Wenyu River has gradually increased in recent years. Cai et al. (2019) combined the fuzzy set theory method and coefficient of variation method to assign weight to the combination of water quality indicators and studied the water quality of Wenyu River in 2018 by attribute recognition method (Cai et al. 2019). Li et al. (2021) used the comprehensive pollution index method to analyze and study the water quality status and temporal and spatial variation trend of Wenyu River in 2019 (Li et al. 2021). Guo et al. (2019) analyzed the temporal and spatial variation of the water quality of the Wenyu River from 1998 to 2017 and concluded that the water quality of Wenyu River gradually improved after deterioration, but the ammonia nitrogen index was still poor (Guo et al. 2019). The research shows that the water quality of Wenyu River is not optimistic. So it is necessary to further study the law of water quality change. Analyze the causes of poor water quality, and put forward targeted measures to improve water quality.

Currently, the commonly used water quality evaluation methods include the single-factor evaluation method, Nemerow index method, water quality identification index method, fuzzy comprehensive analysis method, artificial neural network method, etc. Different methods apply to different environmental conditions. But they all have certain limitations (You et al. 2021, Yin et al. 2008). The single-factor evaluation method takes the maximum pollution index as the evaluation standard. And the evaluation result is conservative, which is not conducive to the development of water resources. The Neme-row index method can make the pollutant value fluctuate when choosing different evaluation factors. And it can't reflect the condition of exceeding the standard of pollutants. The fuzzy comprehensive analysis method can quantify some factors with unclear boundaries that are not easy to quantify. When there are too many indicators, the algorithm of taking large and small will often cause excessive information loss. Resulting in the homogenization of evaluation results and fuzzy failure (Luo et al. 2021). The artificial neural network evaluation method has a high calculation accuracy. But it requires too much data and the results are poorly interpretable (Wang et al. 2019). Cloud models can better deal with the uncertain factors

in the water environment assessment system. And many studies have confirmed the applicability of the cloud model in the field of water quality assessment. The cloud model can take into account the randomness and fuzziness of the water quality evaluation model (Li et al. 2004). Yang Wen confirmed the effectiveness and applicability of the cloud model in water quality evaluation (Yang 2013). Zhao et al. (2020) obtained accurate and stable water quality evaluation results by using the improved cloud model (Zhao et al. 2020). Kang Xiaobing obtained similar evaluation results of the cloud model with a combination of weighting and a fuzzy comprehensive evaluation method. It is proven to be scientific and feasible (Kang et al. 2019).

Weight has a great influence on the accuracy of evaluation results. So it is very important to choose a reasonable weight. At present, there are many methods to determine weight. Such as single weight is one-sided. There are partial subjective, light objective, or partial objective, light subjective defects. After that, there appeared many combination weight methods, such as linear combination weight, hybrid cross weight, genetic algorithm for combination weight, and game theory weight. Fusion weight can greatly improve the shortcomings of the single-weight method. Improve the accuracy of the weight. In this paper, the moment estimation theory is used to fuse the subjective weight and objective weight through the minimum deviation function. And then the cloud model is used to evaluate the water quality of Wenyu River.

## MATERIALS AND METHODS

### Study Area

Wenyu River is a water body carrying the middle water and rainwater of the sewage treatment plant along the coast. Which plays an important role in flood control and sewage discharge. At the same time, as originates in Beijing and flows through a wide range, it plays an ecological landscape role. In recent years, with the improvement of the discharge standards of sewage treatment plants, and the implementation of measures such as river bottom dredging, reclaimed water reuse, and wetland park construction (Chen et al. 2022), the water quality of Wenyu River has been greatly improved, and it reaches the water functional zone goal in many months (Beijing. gov. cn). In this paper, six areas, including Shahe Reservoir (section 1), Mafang (section 2), Lutuan Gate (section 3), Xinbao Gate (section 4), Sewage outlet (section 5), and Shaziying (section 6), are selected to set up monitoring sections. The monitoring sections' layout situation is shown in Fig. 1. And monthly sampling is carried out for each section. Liu et al. (2019) studied that the main source of river pollution was domestic sewage, and selected four water quality indexes of pH, DO, COD and $NH_3$-N as evaluation factors (Liu et al. 2019). Ren et al. (2021) selected three representative indicators: DO, COD and $NH_3$-N (Ren et al. 2021). This paper selects three water quality indexes of DO, COD, and $NH_3$-N to study the water quality of Wenyu River.

### Research Method

In this paper, the cloud model coupled with comprehensive weight is selected to evaluate and study the water quality of Wenyu River. The comprehensive weight is formed by combining the attribute hierarchical model (AHM) and penalized variable weight as subjective weight (Yang et al. 2009). The objective weight is calculated with CRITIC, and then the moment estimation theory is used to combine subjective weight and objective weight. The variable weight theory reflects the interaction between different indexes according to the balanced function. The value of one index meeting the high standard of water quality does not mean that the water quality of the whole water body belongs to a high standard. It is necessary to select the penalty equilibrium function to calculate the variable weight through the common judgment of all indexes. The combination of penalty variable weight based on the attribute hierarchical model (AHM) can compensate for the subjective arbitrariness of humans to some extent. The moment estimation theory (Wu et al. 2022) fuses all kinds of weights according to the minimum deviation function to find the optimal combination mode and retain the advantages of all kinds of weights, avoiding the amplification effect of multiplication, addition, combination, and weight assignment methods on weights. Cloud models can better reflect the uncertainty and randomness of water quality so that the evaluation results of water quality are objective and reliable. The process of integrating the variable cloud model is shown in Fig. 2.

### Determination of Weight

Weight is an important part of the evaluation system, so it is particularly important to determine an objective and reasonable weight. All kinds of indexes in water bodies interact with each other, so the penalized variable weight is integrated into the attribute analytic hierarchy process. So that the influence of each index tends to be balanced on the evaluation results of water quality. Reducing the effect of strong indexes, and enhancing the influence of weak indexes. The objective weight and subjective weight are fused together to form a combined weight-by-moment estimation theory. This not only keeps the objectivity of the critic method and the advantages of the AHM method but also avoids the multiplication phenomenon of simple linear weight fusion.

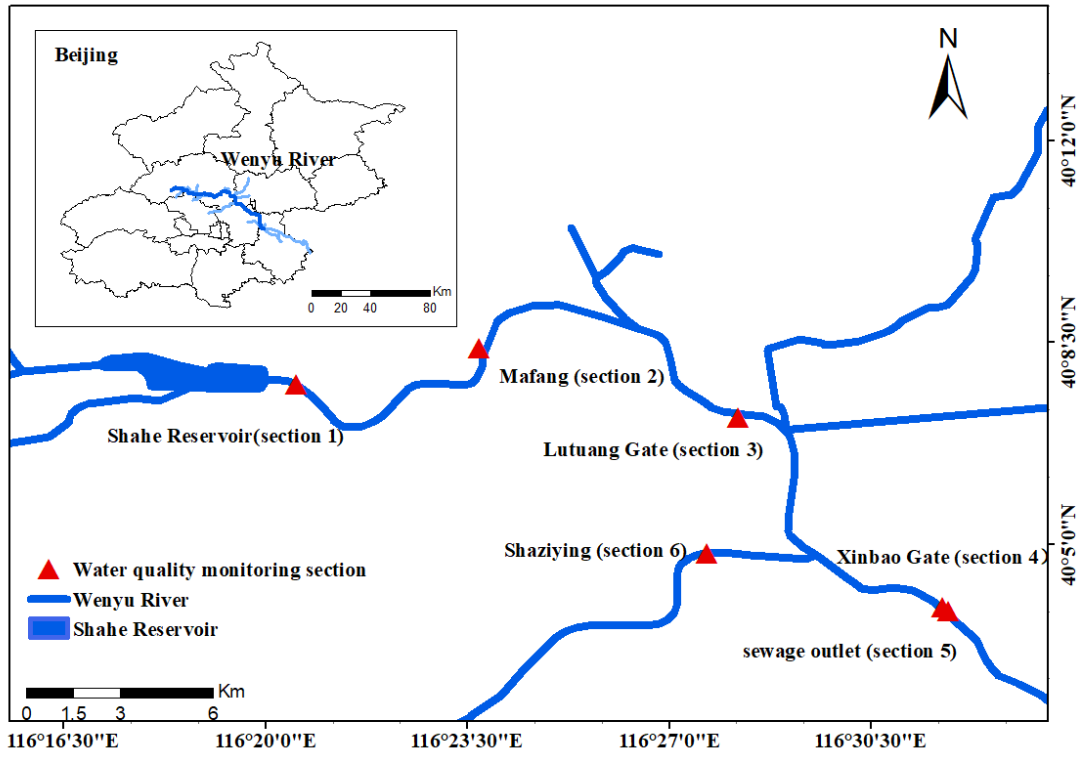


Fig. 1: Layout of monitoring section.

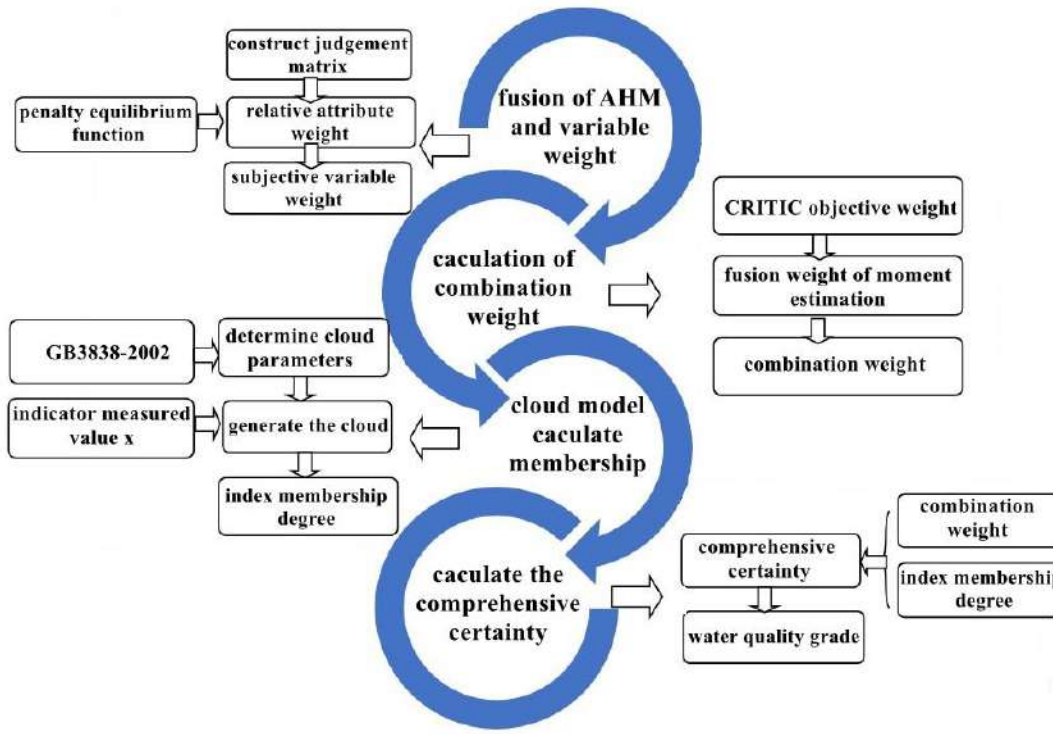


Fig. 2: Integrated evaluation system of the dynamic weight cloud model.

**CRITIC Objective Weight**

Diakoulaki et al. (1995) proposed the critic method to determine the objective weight. It contains the contrast intensity and conflict between different indicators in decision-making problems. And it can more comprehensively reflect the attribute information of the data itself. The standard deviation is used to represent the comparison intensity. The larger the standard deviation is, the greater the volatility is. And the larger the proportion is, the higher the correlation coefficient is. The smaller the conflict is and the smaller the weight is. The specific formula for determining the weight is as follows.

the j-th objective weight $W_j$ is:

$$W_j = \frac{C_j}{\sum_{j=1}^{p} C_j} \quad \ldots(1)$$

$$C_j = S_j \sum_{i=1}^{p}(1 - r_{ij}) = S_j \times R_j \quad \ldots(2)$$

$$R_j = \sum_{i=1}^{p}(1 - r_{ij}) \quad \ldots(3)$$

Among them, the $C_j$ said information, $R_j$ says index conflict, $S_j$ said the standard deviation of the j-th indicators.

$$S_j = \sqrt{\frac{\sum_{i=1}^{n}(Xij - Xj)^2}{n-1}} \quad \ldots(4)$$

$$X_j = \frac{1}{n\sum_{i=1}^{n} Xij} \quad \ldots(5)$$

**AHM Weight of Fused Variable Weight**

The attribute hierarchical model (AHM) is easier to calculate than AHP. It does not need to solve the eigenvector and eigenroot of the matrix and consistency test. It only needs a simple calculation to achieve the same effect as AHP. Each index does not exist in isolation but is interrelated. The overall water quality situation cannot be determined by the good or bad situation of one index, but the mutual influence of each index should be considered comprehensively. Therefore, the subjective weight and punishment equilibrium function are combined to form the AHM weight of the fusion variable weight theory.

Firstly, it should construct a judgment matrix *A*. In the evaluation index level, the target layer is set as water quality grade, and the criterion layer is DO, COD, and $NH_3$-N. In the criterion layer, according to the nine-scale method, the judgment matrix is obtained by comparing the importance of two elements

Secondly, it should calculate the relative attribute weight (Cheng 1997). Relative attribute $B_{ij}$ measure the conversion formula is:

$$B_{ij} = \begin{cases} \frac{\beta K}{\beta K+1}, A_{ij} = K(i < j) \\ \frac{2}{\beta K+2}, A_{ij} = 2/K(i > j) \\ 0, A_{ij} = 0(i = j) \end{cases} \quad \ldots(6)$$

$$\beta = 1$$

Then we can get the relative attribute judgment matrix B and the relative attribute weight $\omega_A$.

$$\omega_{Bi} = \frac{2}{m(m-1)}\sum_{j=1}^{m} B_{ij} \quad \ldots(7)$$

$$\omega_A = (\omega_{B1}, \omega_{B2}, \omega_{B3})^{\mathrm{T}}$$

Thirdly, it should fuse punishment type of variable weight. In the first step, we should get the weight state vector matrix X. Then we calculate the i-th term of the penalty variable weight vector in n-dimension according to the following formula (Yang et al. 2009).

$$\omega_i(x_1, x_2, \ldots, x_n) = \frac{\frac{\omega_i}{x_i}}{\sum_{j=1}^{m}\frac{\omega_i}{x_i}} \quad \ldots(8)$$

Finally, we can get the subjective weight after the fusion.

$$\omega = \left(\omega_{\mathrm{DO}}, \omega_{\mathrm{COD}}, \omega_{\mathrm{NH_3-N}}\right)^{\mathrm{T}}$$

**Combination Weight**

Combining subjective weight and objective weight with moment estimation theory can overcome the unreasonable phenomenon of linear weighted average and multiplication normalization while retaining the influence of subjective weight and objective weight.

Use $\alpha$ on behalf of the subjective weight proportion, use $\beta$ represents the proportion of objective weight, have a kind of subjective weight *x* and *y* kind of objective weight, m as an index number. The calculation formula (Ji et al. 2018) is as follows.

$$\begin{cases} minH(\omega_i) = \alpha_i \sum_{s=1}^{x}(\omega_i - \omega_{si})^2 + \beta_i \sum_{o=1}^{y}(\omega_i - \omega_{oi})^2 \\ s.t \qquad \sum_{i=1}^{m} \omega_i = 1, 0 \le \omega_i \le 1, 1 \le i \le m \end{cases} \quad \ldots(9)$$

$$\alpha_i = \frac{E(\omega_{si})}{E(\omega_{si}) + E(\omega_{oi})} \quad \ldots(10)$$

$$\beta_i = \frac{E(\omega_{oi})}{E(\omega_{si}) + E(\omega_{oi})} \quad \ldots(11)$$

$$\alpha = \frac{\sum_{i=1}^{m} \alpha_i}{m} \quad \ldots(12)$$

$$\beta = \frac{\sum_{i=1}^{m} \beta_i}{m} \quad \ldots(13)$$

The Lagrange multiplier method was used to solve the above optimization model.

$$\omega_i = \left(\alpha \sum_{s=1}^{x} \omega_{si} + \beta \sum_{o=1}^{y} \omega_{oi}\right)/(x+y) -$$

$$\left(\sum_{i=1}^{m}(\alpha \sum_{s=1}^{x} \omega_{si} + \beta \sum_{o=1}^{y} \omega_{oi}) - x - y\right)/(m*(x+y))$$

$$\omega = (\omega_1, \omega_2, \omega_3) \quad \ldots(14)$$

**Evaluation Methodology**

The cloud model coupled with comprehensive weight to calculate the comprehensive determination of the combined dynamic weight and the membership degree determined by the cloud model, and obtain the water quality grade according to the principle of maximum membership degree. Normal membership cloud was first proposed by Academician Li Deyi in 1995. It reflects the fuzziness and randomness of things and can realize the transformation between qualitative concepts and quantitative values. The normal cloud model is represented by three independent characteristic numbers, which are the expectation $E_x$, entropy $E_n$ and super-entropy $H_e$. The expectation is the most typical sample point for concept quantification. Entropy is the uncertainty of qualitative concepts. And super-entropy is the entropy of entropy, which reflects the randomness of the sample appearance of qualitative concept value and reveals the correlation between fuzziness and randomness. Many cloud droplets are generated by the forward cloud generator to form the cloud. The overall shape of the cloud model is outlined by the expectation curve, and the thickness of the cloud is determined by $H_e$.

**Calculation of Cloud Characteristic Parameters (Lei 2019)**

$$E_x = (B_{\min} + B_{\max})/2 \quad \ldots(15)$$

$$E_n = (B_{\max} - B_{\min})/2.355 \quad \ldots(16)$$

$$H_e = K\, E_n \quad \ldots(17)$$

Where, $B_{\max}$ and $B_{\min}$ are the total upper and lower limits of bilateral constraints of this index respectively. For the index standard with a single boundary, $B_{\max} = 2B_{\min}$ (Liu et al. 2014). $K$ takes the empirical value 0.1. According to the surface water quality standard, it is concluded that the indexes in all three parameters of the water quality grade size are as shown in Table 1. Take cloud drop N = 2000 to draw the cloud map of each indicator level, as shown in Fig. 3.

**Forward Normal Cloud Generator Algorithm Steps**

(1) Generate a normal random number $E_n'$ with $E_n$ as expectation and $H_e$ as a standard value.

(2) To generate an $E_x$ as expected, the absolute value of $E_n'$ as the standard deviation of the normal random number $x$.

(3) Calculate the membership of cloud droplet y corresponding to $x$. $y = \exp\left[-\frac{(x-Ex)^2}{2(En')^2}\right]$..

(4) Repeat n times to produce n cloud droplets to form the entire cloud.

**Calculation of Comprehensive Certainty**

Calculate the degree of certainty according to the steps in the b section.

**Evaluation Result**

The water quality evaluation level is determined according to the principle of maximum membership.

## RESULTS AND DISCUSSION

**The Evaluation Results**

According to the water quality monitoring data of Wenyu River in 2021. The weight of each section is calculated

Table 1: Cloud parameters of each indicator standard.

| | | I | II | III | IV | V | VI |
|---|---|---|---|---|---|---|---|
| DO | $E_x$ | 11.25 | 6.75 | 5.50 | 4.00 | 2.50 | 1.00 |
| | $E_n$ | 3.18 | 0.64 | 0.42 | 0.85 | 0.42 | 0.85 |
| | $H_e$ | 0.32 | 0.06 | 0.04 | 0.08 | 0.04 | 0.08 |
| COD | $E_x$ | 7.50 | 15.00 | 17.50 | 25.00 | 35.00 | 60.00 |
| | $E_n$ | 6.37 | 0.00 | 2.12 | 4.25 | 4.25 | 16.99 |
| | $H_e$ | 0.64 | 0.00 | 0.21 | 0.42 | 0.42 | 1.70 |
| $NH_3$-N | $E_x$ | 0.08 | 0.33 | 0.75 | 1.25 | 1.75 | 3.00 |
| | $E_n$ | 0.06 | 0.15 | 0.21 | 0.21 | 0.21 | 0.85 |
| | $H_e$ | 0.01 | 0.01 | 0.02 | 0.02 | 0.02 | 0.08 |

Table 2: Objective weight of each section.

| Monitoring section | DO | COD | $NH_3$-N |
|---|---|---|---|
| 1 | 0.359 | 0.349 | 0.292 |
| 2 | 0.323 | 0.358 | 0.318 |
| 3 | 0.315 | 0.370 | 0.315 |
| 4 | 0.258 | 0.516 | 0.225 |
| 5 | 0.384 | 0.374 | 0.242 |
| 6 | 0.293 | 0.500 | 0.207 |

Table 3: The combined weight of each section.

| Monitoring section | DO | COD | $NH_3$-N |
|---|---|---|---|
| 1 | 0.311 | 0.363 | 0.326 |
| 2 | 0.302 | 0.365 | 0.333 |
| 3 | 0.300 | 0.368 | 0.332 |
| 4 | 0.285 | 0.405 | 0.310 |
| 5 | 0.317 | 0.369 | 0.313 |
| 6 | 0.294 | 0.401 | 0.305 |

as shown in Table 2 and Table 3. The objective weight is calculated by the CRITIC method and the subjective weight is calculated by a fusion of AHM and variable weight theory. The combined weight is calculated by moment estimation theory.

The subjective weight after the fusion is

$$\omega=\left(\omega_{\mathrm{DO}}, \omega_{\mathrm{COD}}, \omega_{\mathrm{NH_3-N}}\right)^{\mathrm{T}} = (0.217,0.437,0.346)^{\mathrm{T}}$$

The results of calculating comprehensive certainty with different weights are shown in Table 4.

The water quality of Wenyu River in December 2021 was evaluated by using different weighted combined cloud model methods and single-factor methods. The evaluation results are shown in Table 5. According to the above steps, the combined weight cloud model is used to evaluate the water quality of six monitoring sections of Wenyu River from March to December 2021, and the results are shown in Fig. 4. The results of the single factor evaluation method are shown in Fig. 5.

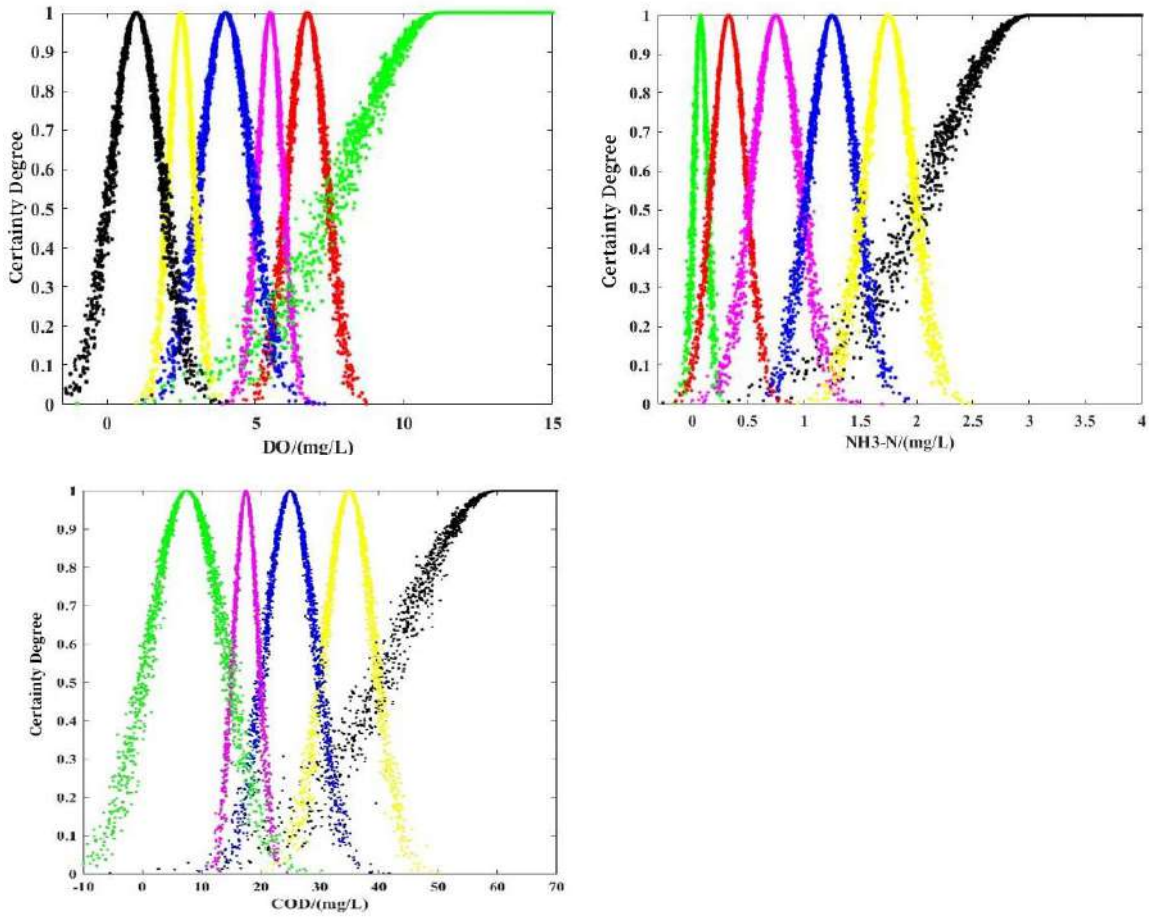


Fig. 3: Cloud view of each indicator water quality standard.

Table 4: Different weights to get comprehensive certainty of each section.

| Monitoring Section | Different weight | I | II | III | IV | V | VI |
|---|---|---|---|---|---|---|---|
| 1 | Combined weight | 0.0178 | 0.1302 | 0.2102 | 0.2652 | 0.0411 | 0.253 |
| | Critic weight | 0.0187 | 0.1092 | 0.1764 | 0.2772 | 0.0433 | 0.2833 |
| | AHM weight | 0.0185 | 0.1683 | 0.2718 | 0.2757 | 0.0411 | 0.1661 |
| | Penalty variable weight | 0.018 | 0.1634 | 0.2639 | 0.2679 | 0.0403 | 0.1834 |
| 2 | Combined weight | 0.2465 | 0.0027 | 0.0185 | 0.3536 | 0.0292 | 0.2977 |
| | Critic weight | 0.2384 | 0.0026 | 0.0165 | 0.3167 | 0.0266 | 0.331 |
| | AHM weight | 0.2627 | 0.0028 | 0.0234 | 0.4482 | 0.0358 | 0.2149 |
| | Penalty variable weight | 0.2553 | 0.0028 | 0.0227 | 0.4353 | 0.035 | 0.2319 |
| 3 | Combined weight | 0.2729 | 0.0003 | 0.0004 | 0.1023 | 0.2531 | 0.3876 |
| | Critic weight | 0.2589 | 0.0003 | 0.0003 | 0.091 | 0.2252 | 0.4315 |
| | AHM weight | 0.2926 | 0.0004 | 0.0005 | 0.1301 | 0.3217 | 0.2966 |
| | Penalty variable weight | 0.2844 | 0.0003 | 0.0004 | 0.1263 | 0.3125 | 0.3154 |
| 4 | Combined weight | 0.2846 | 0 | 0.02 | 0.333 | 0.0754 | 0.2545 |
| | Critic weight | 0.2309 | 0 | 0.0135 | 0.225 | 0.0938 | 0.3435 |
| | AHM weight | 0.3186 | 0 | 0.027 | 0.45 | 0.0594 | 0.1741 |
| | Penalty variable weight | 0.3097 | 0 | 0.0262 | 0.437 | 0.062 | 0.1866 |
| 5 | Combined weight | 0.1239 | 0.3469 | 0 | 0 | 0 | 0.6261 |
| | Critic weight | 0.1363 | 0.3817 | 0 | 0 | 0 | 0.5865 |
| | AHM weight | 0.1264 | 0.3539 | 0 | 0 | 0 | 0.6287 |
| | Penalty variable weight | 0.1228 | 0.3439 | 0 | 0 | 0 | 0.6369 |
| 6 | Combined weight | 0.2786 | 0 | 0 | 0.0003 | 0.1435 | 0.3955 |
| | Critic weight | 0.2496 | 0 | 0 | 0.0002 | 0.1211 | 0.428 |
| | AHM weight | 0.3033 | 0 | 0 | 0.0005 | 0.1668 | 0.3661 |
| | Penalty variable weight | 0.2948 | 0 | 0 | 0.0004 | 0.165 | 0.3736 |

Table 5: Water quality evaluation results of different methods.

| Evaluation method | 1 | 2 | 3 | 4 | 5 | 6 |
|---|---|---|---|---|---|---|
| Single factor | IV | VI | VI | VI | VI | VI |
| Combination weight-cloud | IV | IV | VI | IV | VI | VI |
| Critic-cloud | VI | VI | VI | VI | VI | VI |
| AHM-cloud | IV | IV | V | IV | VI | VI |
| Penalty variable weight-cloud | IV | IV | VI | IV | VI | VI |

## Temporal and Spatial Variation of Water Quality in Wenyu River in 2021

In terms of time, the water quality of Wenyu River in July, August, September, and December is worse than that of other months. Water quality is relatively good in November, March, and April. That is, the water quality in flood season is worse than that in non-flood season. It may be that the erosion effect of flood season rain on the ground will bring some surface pollution into the river, resulting in increased pollution. The value of the dissolved oxygen index in all sections from June to October is significantly lower than that in other months. And the dissolved oxygen content in other months meets the class I water standard. In summer, high temperatures lead to accelerated metabolism and rapid reproduction. So the consumption of dissolved oxygen increased. And the dissolved oxygen content in water decreased. The content of the COD index from August to November is lower than that of other months. It may be that the increase of microorganisms in water consumes a lot of organic matter, leading to the reduction of COD content in water. Which is consistent with the analysis of DO.

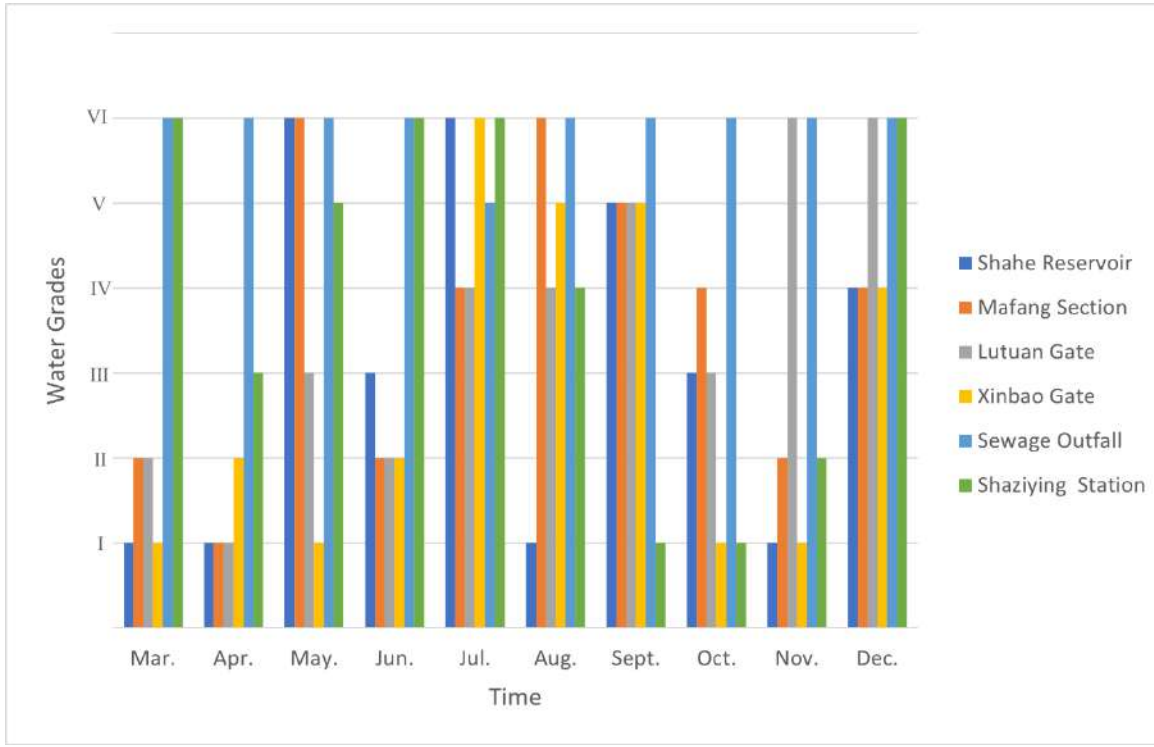


Fig. 4: Temporal and spatial variation of the combined weight cloud model of water quality in Wenyu River in 2021.

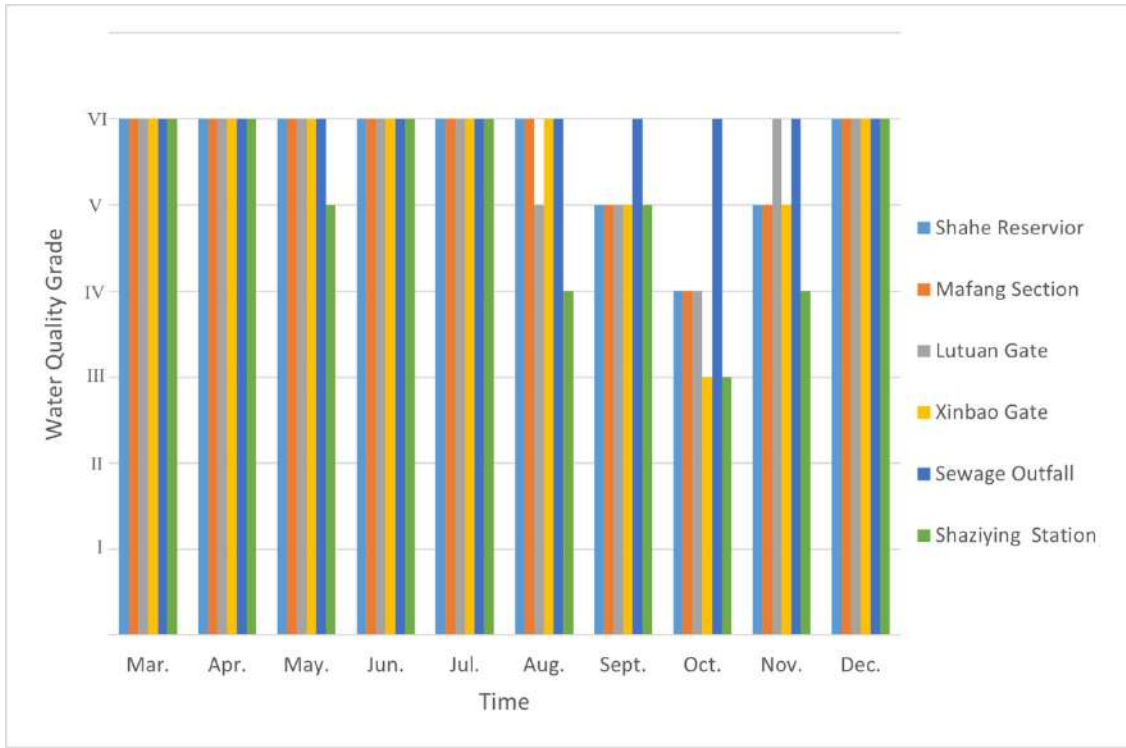


Fig. 5: Temporal and spatial changes of single-factor assessment method for water quality of Wenyu River in 2021.

Ammonia nitrogen indexes in May and July to September were worse than in other months. The reason may be that more nitrogen is washed into the river from the ground near the shore. Increases the amount of nitrogen in the water. Biological organic nitrogen produces ammonia nitrogen by consuming dissolved oxygen through ammonification. Thus the ammonia nitrogen content increases, and the dissolved oxygen content decreases. The reason for the decrease in dissolved oxygen in this period was further verified.

From the spatial dimension, the water quality of the sewage outlet section is the worst, all of which is inferior V water. The second is the sand camp section, with 5 months of water quality V and below; There were 6 months in the Mafang section with category IV water and below. 5 months of Lutuan gate section are IV type water and below. 4 months of the Shahe reservoir section and Xinbao section were classified as IV-type water or below. Except for August, September, and October, the COD of the sewage outlet section is in the standard of inferior V water, and the ammonia nitrogen is in the standard of VI water in all months. In a few months, the proportion of ammonia nitrogen exceeds the standard by more than 8 times. And COD exceeds the standard by more than three times. So it is inferred that there is still a direct discharge of wastewater in this section.

Cloud model the cloud map of various water quality standards is close to a normal distribution. When the index exceeds the standard seriously, that is, when the measured value X deviates far from the standard of each class. It is often reflected in the positive index greater than the I class water standard and the condition of the negative index is far less than the water V class standard. The membership degree of the cloud model will be full is 0. Then embodied in the index did not affect the results of the water quality evaluation. The evaluation result is too ideal. Especially when fewer indicators are selected, the impact on the results can even be decisive. Which is not in accordance with the actual situation. Therefore, when an index seriously exceeds the standard of class V water, the membership degree of inferior class V water of the index is given a number close to 1 from the left. Which can avoid the evaluation result error caused by the above situation.

### Comparison of Evaluation Results of Combined Weight and Other Single-Weight Combined Cloud Models

The results of the single-factor evaluation method show that the water quality of Wenyu River in December 2021 is inferior V class. Because the single factor takes the worst index as the basis of water quality evaluation. And the COD value of each monitoring section exceeds the standard of V-class water, so all is inferior V-class water. The evaluation result obtained by the objective weight critic method is also poor V. CRITIC method to determine the weight of objective data. in the three indicators, the weight of COD is relatively large, and COD seriously exceeds the V class water standard, so the impact of water quality evaluation results is relatively large. The evaluation result of AHM is the best. Which is greatly influenced by personal subjectivity. Because COD water quality is too bad. If a large weight is given, all the evaluation results of water quality will be poor V. So DO and ammonia nitrogen are given relatively large weights. Except for the section on sewage outlet, the value of ammonia nitrogen in December is basically around the class III water standard, so the evaluation result is more optimistic than other methods. The evaluation result of combination weight is consistent with that of penalty variable weight. The evaluation result is better than that of the single factor evaluation method and critic objective weight. But worse than that of AHM subjective weight. The moment estimation theory fuses subjective weight and objective weight through the minimum deviation function. So that the combined weight tends to be between them.

According to the single-factor evaluation method, the indexes that have a bad influence on water quality can be obtained. The results of water quality evaluation based on the worst indexes are conservative. Which cannot fully reflect the water quality of rivers and restrict the development and utilization of rivers. AHM is greatly influenced by personal subjectivity and lacks the support of objective data, so it cannot objectively reflect the water quality situation. The variable weight attribute hierarchical model is to adjust the weight of indicators according to the changes in index values to ensure some balance among indicators. For the water quality evaluation system, the relative importance of each index can be reflected more accurately by considering the mutual influence of each index. Moment estimation theory integrates variable weight attribute analytic hierarchy process and criticism. And combines the artificial experience of subjective weight with the reality of objective weight.

## CONCLUSIONS

1. Compared with single empowerment, the combined variable Kwon model can reflect the status of water quality of the real objective. And considering the interaction between the various indicators. A blend of human experience and objective data. Then the combination weights are more reasonable. the uncertainty of the cloud model to the water quality by the mapping of the quantitative representation method.

Let the water quality situation be more specific and intuitive.

2. According to the water quality measurement of Wenyu River in 2021, the indexes are closely related. This is reflected in the increase of organic nitrogen content in water from July to October due to rainfall erosion. Then the ammonia nitrogen content is increased by ammonification. After ammonification, ammonia nitrogen content increases, and plants can absorb ammonia nitrogen and COD as nutrients for their growth. Then COD goes down, the whole process consumes oxygen, so the dissolved oxygen in the water goes down.
3. From the perspective of spatial distribution, the water quality of six monitoring sections of Wenyu River in 2021 is as follows: Xinbao gate > Shahe reservoir> Mafang > Lutuan gate > Shaziying section > sewage outlet. The sewage outlet section is the most seriously polluted. Because COD and ammonia nitrogen seriously exceed the standard of poor V water, the water quality in 2021 is poor V. In terms of time distribution, the water quality in flood season was worse than that in non-flood season.
4. The determination of entropy and super entropy in the characteristic parameters of the cloud model needs further study. And for the standard indexes with no upper or lower bounds in GB 3838-2002, such as the water standard of DO. There is no upper limit. And the determination of boundaries also needs further study. There is no specific standard for water quality grade in GB 3838-2002, for example, pH is 6-9 in class I to V water. And turbidity has no corresponding standard. The calculation of these indicators needs to be studied.

## ACKNOWLEDGMENTS

This work was Supported by the funds for the undergraduate innovative experiment plan of North China Electric Power University. (Grant No. 202108009), and the National Key R and D Program of China (grant No. 2016YFC0401406).

## REFERENCES

Beijing Municipal Bureau of Ecology and Environment. River Water Quality in the City. OL. http://http/sthjj.beijing.gov.cn/bjhrb/

Cai, X., Men, B.H. and Liu, C.J. 2019. Water quality assessment of Wenyu River based on attribute recognition theory. Beij. Water, (03): 26-30.

Chen, Y.T., Wang, D.E. and Li, H.Y. 2022. Temporal and spatial evolution characteristics of indicator microorganisms in Wenyu River from 2009 to 2019. J. Environ. Sci., 42(3): 51-64.

Cheng, Q.S. 1997. AHP and attribute hierarchy model. J. Sys. Eng. Theory Pract., 15: 25-28.

Diakoulaki, G., Mavrotas, D. and Papayannakis, L. 1995. Determining objective weights in multiple criteria problems: An evaluation method for the critical value of computer shadow. J. Comp. Oper. Res., 22(7): 763-770.

Guo, J., Tian, Y. and Liang, Y.P. 2019. Characteristics of water quality change in Wenyu River basin from 1998 to 2017. J. China Environ. Monit., 35(4): 85-92.

Ji, C.M., Li, R.B. and Liu, D. 2018. Comprehensive evaluation of load adjustment scheme for cascade hydropower stations based on moment estimation grey target model. J. Syst. Eng. Theory Prac., 38(6): 1609-1617.

Kang, X.B., Li, K. and Zhu, Z.Q. 2019. Application of cloud model based on fusion weight to groundwater quality assessment in Xichang Area. J. Water Irrig., 22: 62-67.

Lei, L.P. 2019. Research on optimization of water quality evaluation method based on cloud model. Southwest Jiaotong Univ., 15: 65-98.

Li, D.Y. and Liu, C.Y. 2004. On the universality of normal cloud model. Eng. Sci., 6(8): 28-34.

Li, L.J., Men, B.H. and Peng, R. 2021. Water quality evaluation of Wenyu river based on single factor evaluation and comprehensive pollution index pollution characteristics and pollution characteristics of the soil. J. Environ. Sci. Technol., 20(3): 1041-1046.

Liu, C.J., Men, B.H. and Cai, C.X. 2019. Preliminary study on water quality assessment of Wenyu River based on matter element analysis. J. Water Resour. Dev. Manag., (10): 11-16.

Liu, D.F., Wang, D. and Ding, H. 2014. Entropy-cloud coupling model for water eutrophication evaluation. J. Hydraul. Eng., 45(10): 1214-1222.

Luo, P.P., Wu, Y. and Wang, S.T. 2021. Spatial and temporal comparison of water quality in Pei River Basin. J. Water Resour. Water Eng., 32(5): 35-41.

Ren, S.Q., Men, B.H. and Shen, Y.D. 2021. Water quality evaluation of Wenyu river in Beijing by matter element model. J. Nat. Environ. Pollut. Technol., 20(4): 1585-1591

Wang, F.Y. and Tang, Y.F. 2019. Application of artificial neural network method in water quality evaluation of Daqing River. Northeast Water Resour. Hydrop., 12: 25-26.

Wu, J.J., Xiang, Y.J. and Wang, Z.F. 2022. Research on reliability Allocation method of micro-robot based on combined weight. J. Manuf. Autom., 44(2): 93-97.

Yang, W. 2013. Evaluation of surface water environmental quality in Ninghai County based on cloud model. Water, 10(4): 510.

Yang, X.Y. and Zeng, L.X. 2009. An analytic hierarchy process model of reasonable variable weight. J. Quanzhou Univ., 27(32): 18-24.

Yin, H.L. and Xu, X.Z. 2008. Comparison of methods for comprehensive water quality assessment in rivers. Environ. Monit. Assess., 17(5): 729-733.

You, R.Y., Ao, T.Q. and Zhu, H. 2021. Comparative study on water quality assessment methods in small watershed. Int. J. Environ. Res. Pub. Health, 40(2): 73-81.

Zhao, M.T., Huang, X.F. and Jin, G.Y. 2020. Regional water quality assessment based on improved cloud model. J. Anhui Agric. Univ., 47(5): 778-783.

Zhao, Y. 2017. Discussion on the significance and content of water quality analysis. J. Sci. Technol. Innov. Appl., 06: 15-32

Nature Environment and Pollution Technology
An International Quarterly Scientific Journal

p-ISSN: 0972-6268
(Print copies up to 2016)
e-ISSN: 2395-3454

Vol. 22 | No. 1 | pp. 73-85 | 2023

Original Research Paper

https://doi.org/10.46488/NEPT.2023.v22i01.006

Open Access Journal

# A Novel Green Approach for Lead Adsorption and Isotherm Evaluation

**M. Dharsana* and J. Prakash Arul Jose*†**
*Department of Civil Engineering, Noorul Islam Centre for Higher Education, Thuckalay, Kanyakumari, Tamilnadu, India
†Corresponding author: J. Prakash Arul Jose; joseprakash1430@gmail.com

**Nat. Env. & Poll. Tech.**
**Website: www.neptjournal.com**

*Received:* 14-07-2022
*Revised:* 30-08-2022
*Accepted:* 04-10-2022

**Key Words:**
Green Approach
Lead adsorption
Isotherms
Bio-sorbents

## ABSTRACT

Environmental damage due to the discharge of organic pollutants and heavy metal toxins has become a major topic of concern for the past couple of years. Using just a natural adsorbent to solve wastewater concerns has lately gained popularity as an ecologically acceptable solution that encourages long-term growth. A range of approaches, including adsorption to the surface of agricultural leftovers, have been used to minimize heavy metals in an aqueous medium. Lead is amongst the most hazardous and widely discovered toxic substances in industrial waste. *Citrus limetta* peel powder, Banana peel powder, and Betel leaf powder were chosen as adsorbents in this study to absorb synthetic lead from an aqueous solution since they are low-cost materials. Our research aims to find natural bio-sorbents that can remove highly hazardous $Pb^{2+}$ ions from aqueous solutions. The importance of contact time, concentrations, adsorbent-based dose, and pH in the adsorption process is investigated. The adsorption rate for betel leaves, *Citrus limetta* peel, and banana peel was 5, 10, 15, 20, and 25 $g.L^{-1}$. *Citrus limetta* peel (10 $g.L^{-1}$), banana peel (5 $g.L^{-1}$), and betel leaf (5 $g.L^{-1}$) provide the highest lead adsorption. Material characterization is used to determine the lead nitrate process in lead adsorption. The capacity of the lead-adsorbing substances to achieve adsorption equilibrium was assessed and estimated using linear Freundlich and Langmuir isotherms, with the experimental data fitting the Freundlich isotherm models.

## INTRODUCTION

Heavy metal ions are employed in a wide range of industrial applications (Gunarathne et al. 2022). These businesses' wastewater discharges gradually leak some toxins into the atmosphere (Singh et al. 2022). Contamination by heavy metals water is a major ecological calamity due to its high toxicity and accumulation in food chains (Ashar et al. 2022). Unlike biological pollutants that are usually recyclable, heavy metals do not break down into safe end products. Heavy metals are hazardous to marine habitats, even at small concentrations (Brennecke et al. 2022). Heavy metals such as copper (Cu), chromium (Cr), mercury (Hg), and lead (Pb) are toxic to humans and the environment. Lead ($Pb^{2+}$) is a very hazardous heavy metal that can harm people and the environment (Ajiboye et al. 2021). It causes severe damage to both the nervous and immune systems (Munir et al. 2021) $Pb^{2+}$ is utilized in various industrial processes, including battery production (Otieno et al. 2022). Electroplating (Shittu et al. 2017), petroleum and chemical operations (Védrine 2016), printing inks (Näsström et al. 2022), and biofuel production (Sentanuhady et al. 2021). Hazardous residues from the process sector, energy storage, pesticides, and pharmaceutical mixtures used for flavoring and seasonings contribute to lead in water (Jarvis & Fawell 2021). Adsorption is the most effective method for removing hazardous or heavy metals, and it gives the best results since it can be used to remove a wide range of hazardous elements (Anselmo et al. 2022). Commercial activated carbon (CAC) is the most widely used technology for removing dangerous ions due to its effectiveness and increased adsorption capacity; however, its usage remains limited due to the increased operating costs (Jose & Dharsana 2022). CAC also raises concerns about the need for regeneration and the challenges of isolating it from the effluent after its use (Shahrokhi-Shahraki 2021). Several researchers have focussed on discovering non-traditional alternative adsorbents to reduce the cost of pollution treatment.

Although it is common, most agricultural residues are conveniently utilized and thus do not necessarily require an advanced processing stage or design that empowers before execution. Restoration of these absorbents may not be a requirement, and the procedure requires minimal supervision. Some researchers have concentrated on using waste material as a sorbent (Kim & Singh 2022). Heavy metals can be removed using precipitation, phase separation, electrochemical treatment, and membrane filtration (Xu et

al. 2022). However, only adsorption seems to become an economically feasible option at this time. The adsorbent is a unit process in residential and municipal sewage treatment operations and is becoming more common in today's plants (Kim et al. 2022). Contaminant adsorption has always been the subject of extensive research throughout the years, and it has been ongoing. Adsorbents such as chemical adsorbents (Hu et al. 2022, Alex et al. 2022a), zeolites (He et al. 2021), bio-adsorbent materials (Karimi et al. 2022), and nano-adsorbents (Janani et al. 2022), were suggested. However, due to isolation and regeneration costs, most recommended adsorbents have still yet to show cost-effectiveness; consequently, research into the best biosorbent metal ion removal continues. Several therapeutic approaches have been used in the past to eliminate lead from water. The use of cationic resin polite (Jose & Dharsana 2022), adsorbents using high alumina concentration bauxite, alkali ash particle permeable responsive barrier, use of particular lactic acid bacteria (Li et al. 2021), electro-coagulation process (Deng et al. 2021), adsorption using natural American bentonite (Gupt et al. 2022, Alex et al. 2021) and activated carbon (Hao et al. 2021), using iron nanoparticles (Vázquez-Guerrero et al. 2021), and using okra (Barasikina 2021), rice husk (Babazad et al. 2021), and sawdust are among these (Ibrahim et al. 2022).

Adsorption is the process of preventing adsorbents from moving around on the adsorbent. In the affluent approach, isotherm adsorption studies were used to predict the ability of specific adsorbents to remove contaminants. Water contamination arises from a lack of contemporary wastewater-treatment systems and a scarcity of competent workers, resulting in a shortage of drinkable water. The demand for low-cost wastewater treatment options prompted this research. Poor economic situations in several developing countries need low-cost water treatment options for afflicted areas, as traditional or advanced pollution removal, is impossible.

Plant-based compounds for water treatment are environmentally friendly, inexpensive, non-toxic, and simple to use, with the residual created being disposed of even though they are readily available (Rastogi et al. 2008). Numerous organic chemicals have been studied as low-cost water treatment coagulants. Using bio-sorbents in water filtering fits well with environmental stability since waste material is reused to lessen created in an environmentally advantageous manner (Giri et al. 2022). Adsorption was assumed to be a critical method for eliminating toxins whenever these biomass materials were used for water treatment. Even though many types of research conducted have concentrated on the use of natural materials as water treatment agents to remove various impurities, little is known about the mechanisms of operation in the method of treatment (Elkhaleefa et al. 2021, Thakare et al. 2021, Dineshkumar et al. 2022, Alex et al. 2022b). The removal process of one heavy metal may differ from that of others. As a result, instead of concentrating on biomass use, it is critical to comprehend the factors contributing to the removal of specific metal ions from an aqueous solution. Adsorption is a regularly used strategy for isolating and purifying lead ions due to its substantially improved metal-binding capacity. It could promote human health by improving the quality of treated wastewater quality.

Furthermore, the activation chemicals are easily recyclable and reusable (Zhang et al. 2022). Carbon activation using phosphoric acid is often used to saturate lignocellulose substances, including coir and timber, on a big scale. Phosphoric acid increases yield by modifying the pyrolysis process, which includes the disintegration of lignocellulosic materials, depolymerization, dryness, and component distribution (Mirmohammadmakki et al. 2022). Phosphoric acid has become extremely popular as the acid recovery duration has improved.

The goal of this study was to use organic substances such as *Citrus limetta* peel powder, Banana peel powder, and Betel leaves powder to remove $Pb^{2+}$ ions from an aqueous system via a biosorption method. These are organic resources with a large adsorption ability for heavy metal removal from wastewater (Chawla et al. 2022, Sharma et al. 2021). The purpose of this study was to see whether the existing adsorption isotherm technique could effectively define the behavior and therapeutic efficiency of *Citrus limetta* peel powder, Banana peel powder, and Betel leaves powder in removing Pb and to learn much

Table 1: Biosorbents for lead removal.

| Biosorbent | Metal removed | References |
|---|---|---|
| Spirogyra | Lead | (Kumar & Oommen 2012) |
| Red microalgae | Lead | (Anastopoulos & Kyzas 2015) |
| Caster leaf powder | Lead | (Al Rmalli et al, 2008) |
| Punica granatum L. peels | Lead | (Ay et al. 2012) |
| Green algae waste biomass | Lead | (Jalali et al. 2002) |
| Cucumis melo | Lead | (Akar et al. 2012) |
| A.Leucocephala bark | Lead | (Munagapati et al. 2010) |
| Maple sawdust | Lead | (Hossain et al. 2014) |
| Tea leaves | Lead | (Ahluwalia & Goyal 2005) |
| Waste tea leaves | Lead | (Mohammed et al. 2016) |
| Palm kernel husk | Lead | (Baby et al. 2019) |
| Rice husk and fly ash | Lead | (Syuhadah & Rohasliney 2012) |
| Trichoderma reesi | Lead | (Ng et al. 2013) |

about the adsorption mechanism of a particular heavy metal described by the ideas. Table 1 shows some research works which use biosorbents for lead removal.

## THE OBJECTIVES OF THE WORK

The main intentions of this research study are given below.

- To identify an efficient method to remove lead from synthetic and industrial wastewater.
- To carry out the experimental study using three adsorbents, namely *Citrus limetta* peel, Banana peel, and Betel Leaf, on both synthetic and industrial wastewater.
- To analyze the characterization of the bio adsorbents and identify the optimizing pH, contact time, and adsorbent dose.

## MATERIALS AND METHODS

### Green Adsorbents Used in This Study

This research uses natural adsorbents like *Citrus limetta* peel powder, Banana peel powder, and Betel leaves powder to absorb the synthetic lead from an aqueous solution. The technical details of the green absorbent materials used in this study are shown in Table 2.

### Preparation of Adsorbent

*Citrus limetta* peel, Betel leaf, and Banana peel were washed with distilled water and dried in the sun for 7 days. After sundried, it was dried in an oven for two hours at 150°C. After that, it was ground in the mill as a *Citrus limetta* peel powder, depicted in Fig. 1**.** The adsorbent dosage was selected as 5, 10, 15, 20, and 25 $g.L^{-1}$ for Betel leaf, banana peel, and *Citrus limetta* peel.

### Preparation of Stock Solution

The synthetic stock solution is prepared by dissolving the lead Nitrate salt in various concentrations in the range of 5 $g.L^{-1}$, 10 $g.L^{-1}$, and 15 $g.L^{-1}$ from the literature study, and the volume of the solution is made up to 1000 mL. The details of the salts and the amount used are tabulated in Table 3.

Table 2: Scientific details of green absorbents used.

| GREEN ADSORBENTS USED | | |
|---|---|---|
| Citrus limetta | Banana | Betel |
| • Kingdom: Plantae<br>• Order: Sapindales<br>• Family: Rutaceae<br>• Genus: *Citrus*<br>• Species: *C. limetta* | • Kingdom: Plantae<br>• Order: Zingiberales<br>• Family: Musaceae<br>• Genus: *Musa* | • Kingdom: Plantae<br>• Order: Piperales<br>• Family: Piperaceae<br>• Genus: *Piper*<br>• Species: *P. betel* |

Table 3: Preparation of stock solution.

| Metal | Complex salt | Formula | Molecular weight | Amount used [$g.L^{-1}$] |
|---|---|---|---|---|
| Lead | Lead Nitrate | $Pb(NO_3)_2$ | 331.2 $g.mol^{-1}$ | 5<br>10<br>15 |

### Methodology and Characterization

Characterization is performed to study the different attributes of created adsorbents from *Citrus limetta* peel powder, Banana peel powder, and Betel Leaf powder. Synthetic water is the stock solution prepared in the laboratory using lead Nitrate at various concentrations. Industrial water is collected from the river Cauvery, Karur District, Tamilnadu. The characterization is critical when another material is produced as an adsorbent for the expulsion of particular contamination, as depicted in Fig. 2.

### FTIR Analysis

The Fourier transforms infrared spectroscopy (FTIR), performed in the wavelength range of 4000-500$cm^{-1,}$ to analyze the available functional groups. The chemical nature of bio adsorbents and functional groups on the surface of


Fig. 1: (a) *Citrus limetta* peel powder, (b) Banana peel powder, and (c) Betel leaf powder.


Fig. 2. Methodology of study.

biosorbents were predicted using Fourier Transform Infrared spectroscopy (FTIR). The batch adsorption test information is utilized to assess different parameters with the assistance of various isotherm models accessible in the literature.

**Isotherm Models**

To comprehend the circulation of the metal particles in the fluid and solid stages at balance, the distinctive isotherm models must be fitted with experimental equilibrium data information. The present work fits the information with the Langmuir Freundlich isotherm model, depicted in Fig. 3.

**Langmuir Isotherm**

This model suggests monolayer coverage and continuous adsorbate-surface binding energy. The model is given by equation 1:

$$q_e = \frac{K \cdot Q_a^0 \cdot C_e}{1 + K \cdot C_e} \quad \ldots(1)$$

Where Ce is the equilibrium concentration of the adsorbate ($mg.L^{-1}$), qe is the amount of adsorbate adsorbed per unit mass of adsorbent ($mg.g^{-1}$), Qo and a are Langmuir constants related to adsorption capacity and rate of adsorption, respectively. Qao represents the maximal adsorption efficiency (g solute.$g^{-1}$ adsorbent). $L.mg^{-1}$ is the unit of measurement for K.

**BET (Brunauer, Emmett and Teller) Isotherm**

This is a multi-layer, more general model. It is assumed that each layer has a Langmuir isotherm and that no translocation happens between them. Apart from the first layer, this assumes that each layer has the same adsorption energy, as shown in equation 2.

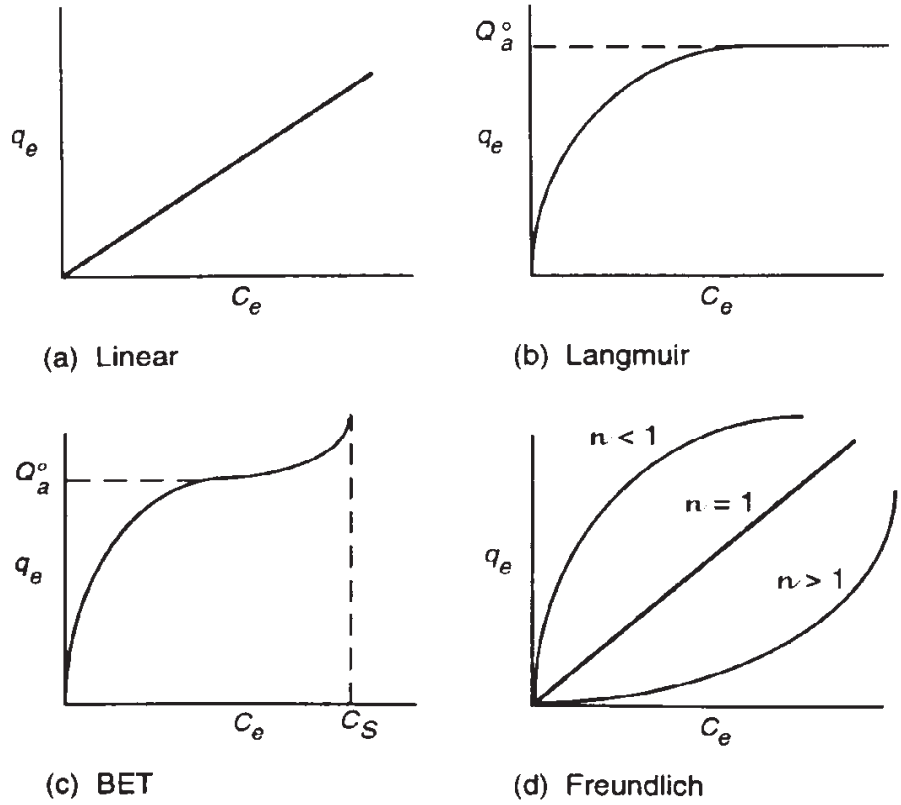


Fig. 3: Isotherm models.

$$q_e = \frac{K_B \cdot C_e \cdot Q_a^0}{(C_S - C_e)\{1 + (K_B - 1)(C_e / C_S)\}} \quad \ldots(2)$$

where qe is the measure of adsorbate adsorbed per unit mass of adsorbent ($mg.g^{-1}$), Ce is the equilibrium concentration of the adsorbate ($mg.L^{-1}$ ), Kf and *n* are Freundlich constants with *n* giving an indication of how suitable the adsorption process.

**Freundlich Isotherm**

The Freundlich model is used for the special case of multiple surface energies (particularly useful for contaminated materials) in which the frequency term, KF, fluctuates as a factor of surface coverage n, and $K_F$ is a specific constant, as shown in equation 3.

$$q_e = K_F * C_e^{1/n} \quad \ldots(3)$$

**Physicochemical Properties of the Adsorbents**

The adsorbents *Citrus limetta* peel, Banana peel, and Betel Leaf are characterized in terms of

- pH
- moisture content
- Ash content

**Determination of pH**

The standard analysis of pH for three adsorbents was tested. 1g of all three adsorbents was weighed and moved into a glass beaker. The adsorbent was mixed with 100mL of distilled water was measured and added to the sample of powdered adsorbents in the beaker, and stirred for one hour. The pH for all three adsorbents is represented in the graph.

**Determination of Moisture Content**

A crucible was dried out and cooled in a desiccator, and weighed. The powdered adsorbents were transferred into the crucible and weighed ($W_i$). The crucible and sample were then dried out in a hot air oven at 105°C, and it was considered as ($W_f$), as given in equation 4. The result is represented in the graph.

$$\text{Moisture content (\%)} = \frac{W_i - W_f}{W_i} * 100 \quad \ldots(4)$$

**Determination of Ash Content**

A crucible was preheated in a muffle furnace at 500°C, cooled in a desiccator, and 1g of adsorbents were transferred into the crucible and reweighed. Then the sample was kept in a muffle-shaped furnace and preheated to 500°C. It was

cooled in desiccators, and the weight was taken. The result is represented in the graph, and equation 5 represents it.

$$\text{Ash content (\%)} = \frac{\text{Ash weight on dry x 100}}{\text{Oven weight dry}} \quad ...(5)$$

## RESULT AND DISCUSSION

### Effect of Parameters in Synthetic Wastewater

Batch adsorption studies were directed to improve critical exploratory parameters which can influence the efficiency of containment removal. The activated biosorbents are pressed mechanically and applied in water treatment. Press cake was soaked with water overnight to get the remaining compounds, and the clean press cake was used in this experimental work. The moisture content was calculated to get the correct mass for the biosorbent added to water. The press cake of biosorbents was added to each beaker with the sample solution. The stirring speed was set at 200 rpm for 4 minutes and 40 rpm for 30 minutes. All treatments were done as triplicates, and at the end of each optimization, solutions were allowed 60 min for settling and filtered using filter papers. Finally, the remaining heavy metals concentration of each solution was measured using Thermo Fisher Scientific iCE 3500 AAS Atomic Absorption Spectrometer

### Effect of Initial Concentration

The impact of initial lead concentration in addition to the measure of adsorbate adsorbed per unit weight of adsorbent. From Fig. 4, it is demonstrated clearly that the removal efficiency of *Citrus limetta* is 77% at an initial concentration, Banana peel is 82.7% at an initial concentration, and Betel leaf is 52.98% at an initial concentration of 5 $g.L^{-1}$, as depicted in Fig. 4.

### Effect of Adsorbent Dosage

The impact of the adsorbent dose on the expulsion of lead is depicted in Fig. 5, with an initial concentration of 5 $g.L^{-1}$ for *Citrus limetta* peel and 7.5 $g.L^{-1}$ for Banana peel and Betel Leaf. It is seen that the maximum removal efficiency of lead is 73.4%, 81.7%, and 53%, which is found at an optimum dosage of 30 $g.L^{-1}$ for *Citrus limetta* peel, 15 $g.L^{-1}$ for Banana peel, and Betel Leaf.

### Effect of pH

The impact of pH on the adsorption of lead particles is shown in Fig. 6 with steady introductory fixation and adsorbent measurement. The proportion of adsorption was the least in the case of pH 2 anyway. It increased with expanding pH. The most extraordinary adsorption occurs at pH 6 for Banana peel and pH 7 for *Citrus limetta* peel and betel leaf.

### Effect of Contact Time

The impact of contact time on the expulsion of lead ions is shown in Fig. 7 by maintaining other optimization parameters at constant magnitude. The percentage removal of lead is attained within 100mins for *Citrus limetta* peel powder and Betel Leaf, while it takes about 140 mins for Banana peel powder. This data implies a better adsorption efficiency

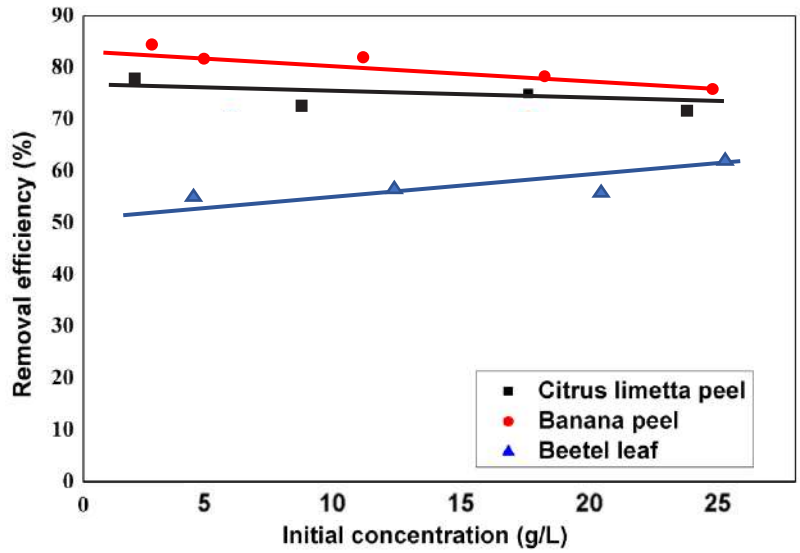


Fig. 4: Impact of initial concentration on the expulsion of lead by *Citrus limetta* peel powder, Banana peel powder, and Betel Leaf powder.

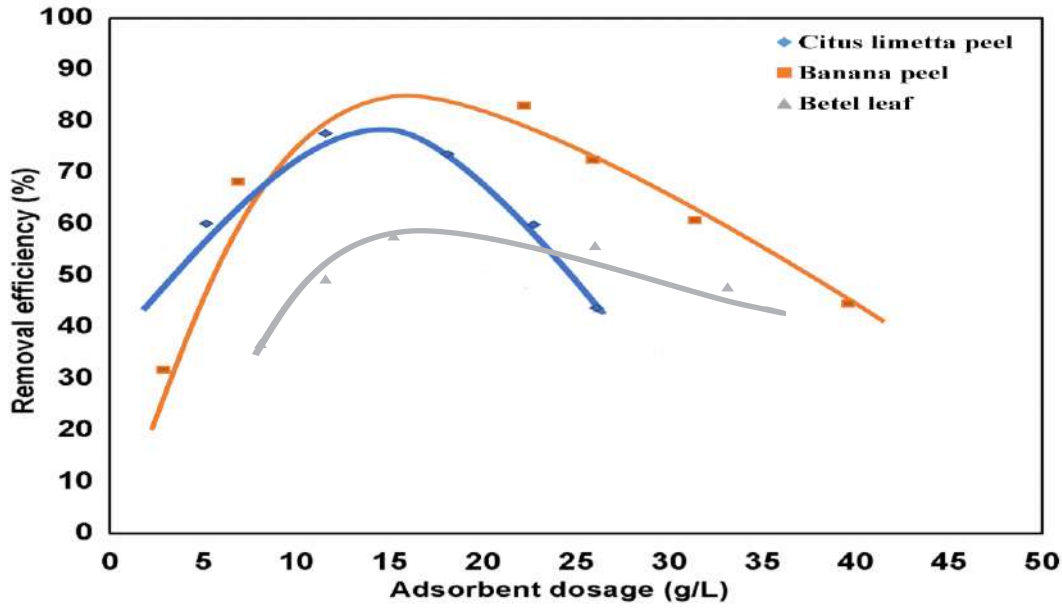


Fig. 5: Impact of adsorbent dose on the expulsion of lead by *Citrus limetta* peel powder, Banana peel powder, and Betel Leaf powder.

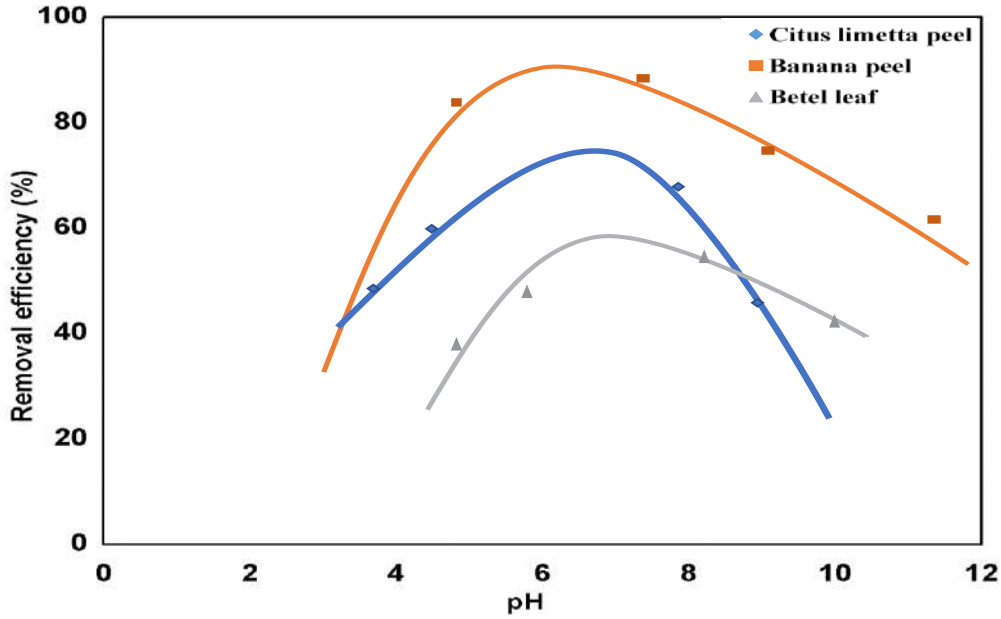


Fig. 6: Impact of pH on the expulsion of lead by *Citrus limetta* peel powder, Banana peel powder, and Betel Leaf powder.

for Banana peel when compared to *Citrus limetta* peel and Betel leaf powder.

### Adsorption Isothermal Studies

At equilibrium conditions, the adsorption isotherm is an equation depicting the transfer of adsorbed species from the liquid solution to the adsorption phase. Adsorption isotherm provides essential models in the description of adsorption behavior. It describes how the adsorbate interacts with the adsorbent and offers an explanation of the nature and mechanism of the adsorption process. When the adsorption reaction reaches an equilibrium state, the adsorption isotherm can indicate the distribution of adsorbate molecules between the solid phase and the liquid phase. Equilibrium

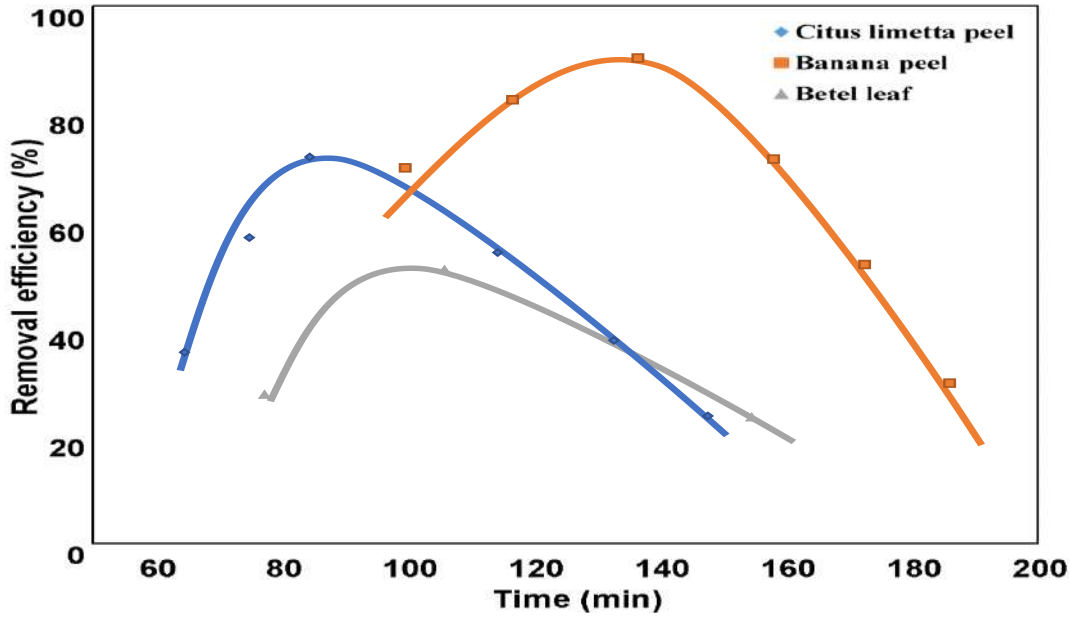


Fig. 7: Impact of contact time on the expulsion of lead by *Citrus limetta* peel powder, Banana peel powder, and Betel Leaf powder.

isotherm data obtained from the different models provide essential information on adsorption mechanisms and the surface properties and affinities of the adsorbent. Therefore, establishing the most appropriate correlation of equilibrium curves is essential to optimize the conditions for designing adsorption systems. In this present work, Langmuir and Freundlich's isotherms were employed to investigate the adsorption behavior.

The following characteristics, listed in Table 4, were used to evaluate the appropriateness of the equation given to explain the adsorption process.

### Adsorption Equilibrium Isotherm Result

#### *Freundlich Model*

The following results are obtained from experimental data of the Freundlich model

**(a) Freundlich model for Betel leaves:** The Freundlich isotherm model for the adsorption of lead by Betel leaves powder is expressed as $R^2$ =0.9873, n = 0.71, 1/n = 1.408, $K_f$ (1.mg$^{-1}$) = 0.132. Fig. 8 depicts the Freundlich isotherm model for the adsorption of lead by Betel leaves powder. It should be noted that the experimental values have a high coefficient of the relation between logarithmic values.

**(b) Freundlich model for Citrus limetta peel:** The Freundlich adsorption isotherm model of lead by *Citrus limetta* peel powder is expressed as $R^2$ = 0.9937, n = 5.052, 1/n = 0.198, $K_f$ (1.mg$^{-1}$) = 1.268, depicted in Fig. 9. It exposed that the experimental values have high logarithmic correlation coefficients.

**(c) Freundlich model for Banana peel**: The Freundlich adsorption isotherm model of lead by Banana peel powder is expressed as $R^2$ = 0.9866, n = 0.284, 1/n = 3.52, $K_f$(1.mg$^{-1}$) = 0.073, depicted in Fig. 10. It proved that the experimental values have a high correlation between logarithmic co-efficient.

#### *Langmuir Model*

The following results are obtained from experimental data of the Langmuir model

**(a) Langmuir model for Betel leaves:** The Langmuir isotherm model for adsorption of lead by Betel leaves powder is expressed as $R^2$ = 0.9891, $Q^O$ = 0.683, b = 0.544, depicted in Fig. 11. The experimental

Table 4: Adsorption isotherm studies.

| Isotherms | Parameters | *Citrus limetta* peel powder | Betel leaves powder | Banana peel powder |
|---|---|---|---|---|
| Langmuir | $R^2$ | 0.9877 | 0.9891 | 0.9966 |
| | $Q^0$ [mg.g$^{-1}$] | 1.994 | 0.683 | 2.704 |
| | b [1.mg$^{-1}$] | 2.863 | 0.544 | 5.116 |
| Freundlich | $R^2$ | 0.9937 | 0.9873 | 0.9865 |
| | N | 5.052 | 0.71 | 0.284 |
| | 1/n | 0.198 | 1.408 | 3.52 |
| | $K_f$[1.mg$^{-1}$] | 1.268 | 0.132 | 0.073 |

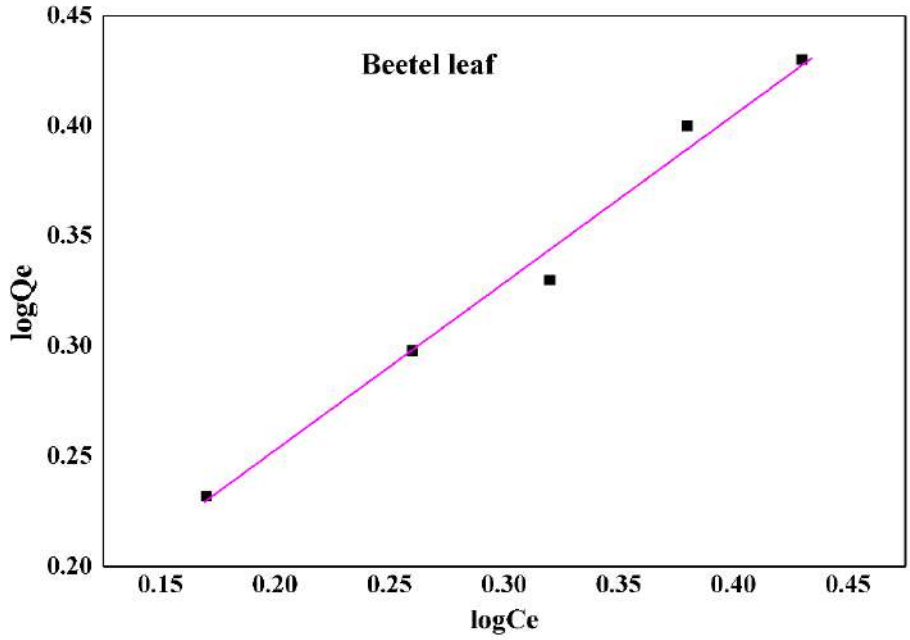


Fig. 8: Freundlich adsorption isotherm model of lead by Betel leaves powder.

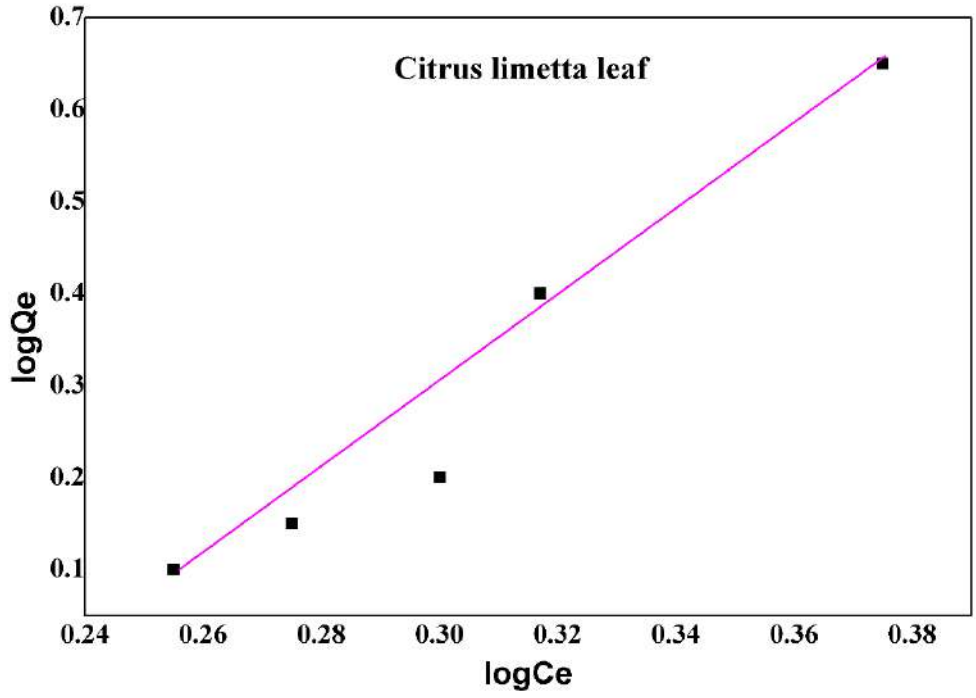


Fig. 9: Freundlich isotherm model for adsorption of lead by *Citrus limetta* peel powder.

values contain strong logarithmic ($C_e/Q_e$) correlation coefficients, which should be noted.

**(b) Langmuir model for Citrus limetta peel:** The Langmuir isotherm model for the adsorption of lead by *Citrus limetta* peel powder is expressed as $R^2 = 0.9$, $Q^O$ =, b=, depicted in Fig. 12. The $C_e/ Q_e$ values expose the same trend of betel leaves.

**(c) Langmuir model for Banana peel:** The Langmuir

isotherm model for the adsorption of lead by Banana peel powder is expressed as $R^2 = 0.9966$, $Q^O = 2.704$, b = 5.116, as depicted in Fig. 13. High logarithmic correlation ($C_e/Q_e$) coefficients between the experimental values should be noted.

## CONCLUSION

From this study, the following results can be concluded.

- In this work, the adsorption of lead from synthetic and industrial water was investigated using low-cost adsorbents such as *Citrus limetta* peel powder, Banana peel powder, and betel leaf powder were successfully developed.
- The adsorbent dosage was selected as 5, 10, 15, 20, and 25 $g.L^{-1}$ for Betel leaf, banana peel, and *Citrus limetta* peel.

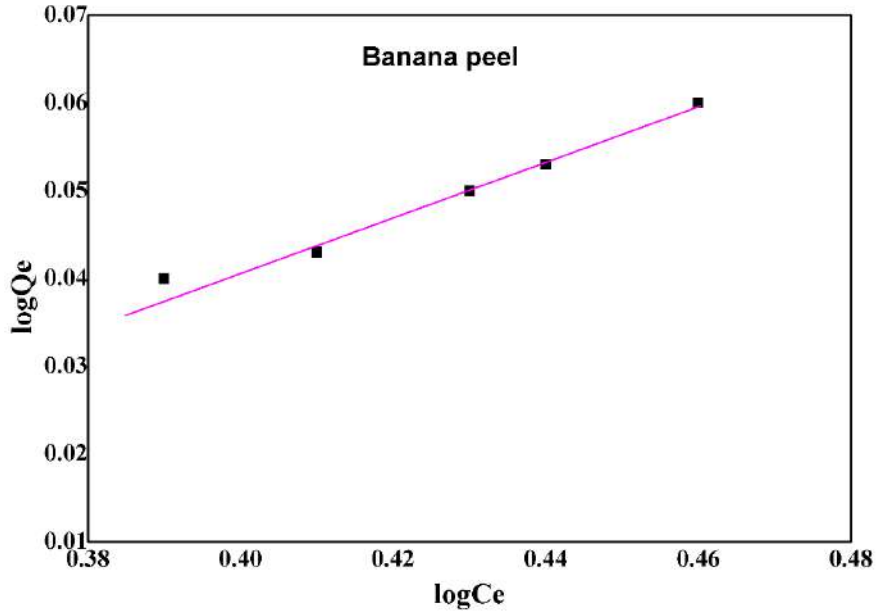


Fig. 10: Freundlich adsorption isotherm model of lead by Banana peel powder.

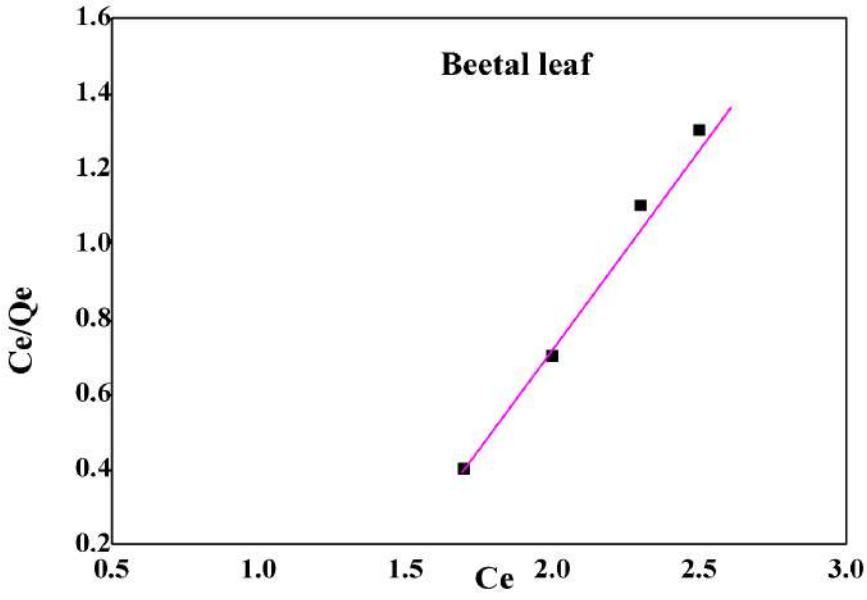


Fig. 11: Langmuir isotherm model for adsorption of lead by Betel leaves powder.

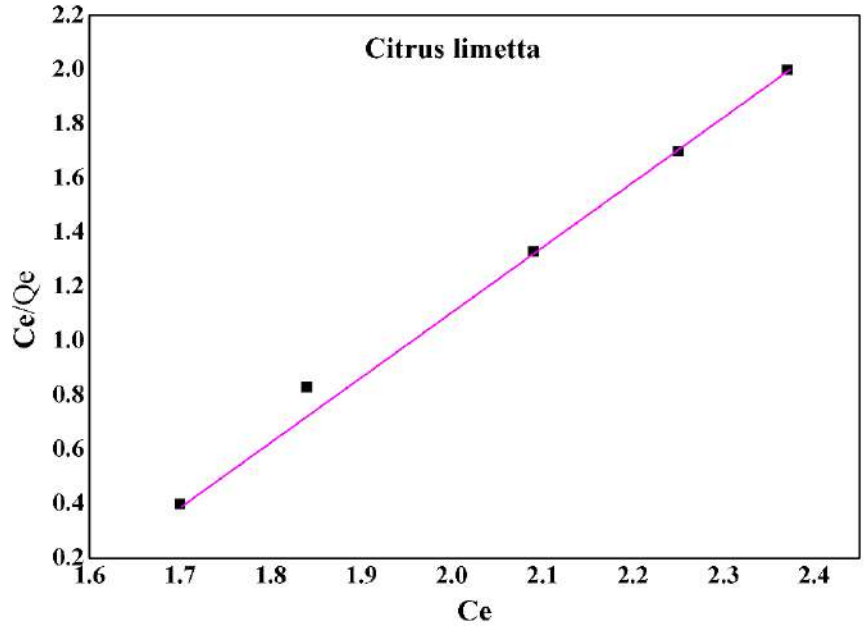


Fig. 12: Langmuir isotherm model for adsorption of lead by *Citrus limetta* peel.

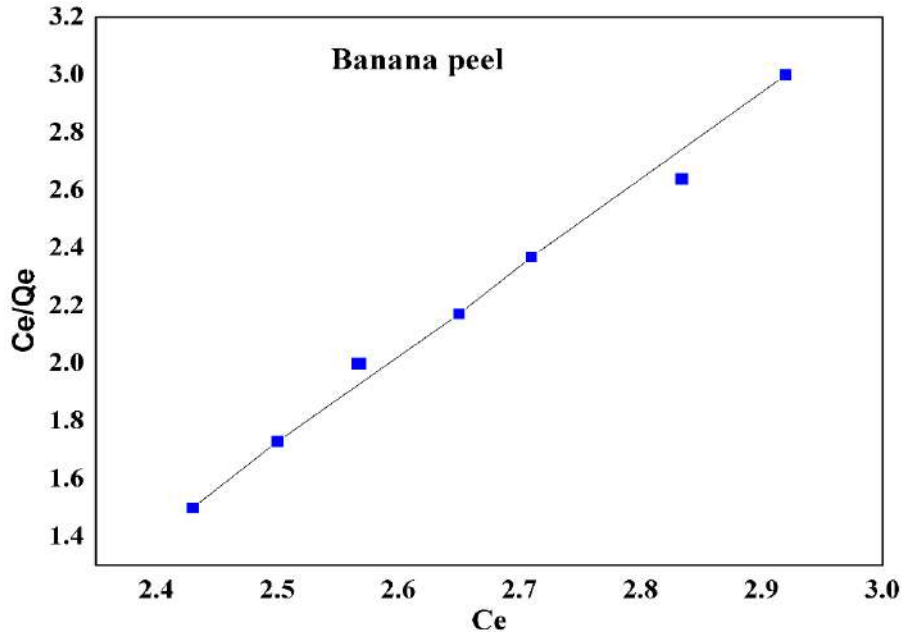


Fig. 13. Langmuir isotherm model for adsorption of lead by Banana peel.

- The result indicated that the percentage removal of lead was considerably affected by initial lead concentration, amount of adsorbent dose, pH value, and mixing contact time. The results showed that the removal percentage increased with an increasing amount of adsorbent dosage.
- The equilibrium adsorption of metal ion Lead was well-fitted by Langmuir and Freundlich's adsorption isotherm model.
- From these experimental results, the Langmuir is better fitted ($R^2 = 0.999$) for *Citrus limetta* peel powder, ($R^2 = 0.993$) Banana peel powder, and ($R^2 = 0.961$) betel leaf powder.

## FUTURE SCOPE

The research study can be continued to advance studies in the following fields. The developed adsorbent may be further utilized to eliminate lead from industrial wastewater, and their process parameters can be studied. The results of the adsorption activity of adsorbents can be compared with both synthetic and industrial wastewater can be done. This work can be further developed on a large scale for use in Industries, and a comparison can be made by adding two adsorbents simultaneously.

## REFERENCES


Ahluwalia, S. and Goyal, D. 2005. Removal of heavy metals by waste tea leaves from aqueous solution. Eng. Life Sci., 5: 158-162.

Ajiboye, O.A., Oyewo, T.O. and Onwudiwe, D.C. 2021. Simultaneous removal of organics and heavy metals from industrial wastewater: A review, Chemosphere, 262: 128379.

Akar, S., Arslan, T., Alp, D., Arslan, T. and Akar, S.T. 2012. Biosorption potential of the waste biomaterial obtained from Cucumis melo for the removal of Pb2+ ions from aqueous media: equilibrium, kinetic, thermodynamic and mechanism analysis, Chem. Eng. J., 185: 82-90.

Al Rmalli, A.A., Dahmani, M.M., Abuein, A.A. and Gleza, S.W. 2008. Biosorption of mercury from aqueous solutions by powdered leaves of castor tree (Ricinus communis L.). J. Hazard. Mater., 152: 955-959.

Alex, Z., Kemal, T., Gebrehiwet, S. and Getahun, G. 2022b. Effect of α: Phase nano $Al_2O_3$ and rice husk ash in cement mortar. Adv. Civ. Eng., 11: 202-222.

Alex, T., Gebrehiwet, Z. and Kemal, T. 2021. M-Sand cement mortar with partial replacement of alpha-phase nano alumina. J. Build. Pathol. Rehab., 6(1): 1-6.

Alex, T., Gebrehiwet, Z., Kemal, R.B. and Subramanian, A. 2022a. Structural performance of low-calcium fly ash geo-polymer reinforced concrete beam. Iran. J. Sci. Technol. Trans. Civ. Eng., 11: 1-12.

Anastopoulos, I. and Kyzas, G.Z. 2015. Progress in batch biosorption of heavy metals onto algae. J. Mol. Liq., 209: 77-86.

Anselmo, S., Cataldo, S., Avola, T., Sancataldo, G., D'Oca, M.C., Fiore, T., Muratore, N., Scopelliti, M., Pettignano, A. and Vetri, V. 2022. Lead (II) ions adsorption onto amyloid particulates: An in-depth study. J. Colloid Interface Sci., 610: 347-358,

Ashar, N., Naeem, N., Afshan, M., Mohsin, Z.A. and Bhutta, A. 2022. Remediation of Metal Pollutants in the Environment. In Deng, Y. and Zhao, R. (eds), Advanced Oxidation Processes for Wastewater Treatment, CRC Press, Boca Raton, Florida, pp. 223-234.

Ay, A.S., Özcan, Y., Erdoğan, A. and Özcan, C. 2012. Characterization of Punica granatum L. peels and quantitatively determination of its biosorption behavior towards lead (II) ions and Acid Blue 40. Colloids Surf. B Biointerf., 100: 197-204.

Babazad, F., Kaveh, M., Ebadi, R.Z., Mehrabian, M.H. and Juibari,. 2021. Efficient removal of lead and arsenic using macromolecule-carbonized rice husks. Heliyon, 7: e06631.

Baby, B., Saifullah, M.Z. and Hussein, S. 2019. Palm kernel shell as an effective adsorbent for the treatment of heavy metal contaminated water. Sci. Rep., 9: 1-11.

Barasikina, J.D.A. 2021. Evaluation of the efficiency of okra adsorbent for heavy metals removal from wastewater in natural gas production. Processes, 9(3): 559.

Brennecke, B., Duarte, F., Paiva, I., Caçador, D. and Canning-Clode, J. 2016. Microplastics as vector for heavy metal contamination from the marine environment, Estuar. Coast. Shelf Sci., 178: 189-195.

Chawla, P., Rai, T., Garain, S., Uday, C.M. and Hussain, M. 2022. Green carbon materials for the analysis of environmental pollutants. Trends Environ. Anal. Chem., 5: e00156.

Deng, N., Chen, W., Hu, H., Wang, P., Kuang, F. and Chen, Y. 2021. Treatment of old landfill leachate by persulfate enhanced electro-coagulation system: Improving organic matter removal and precipitates settling performance. Chem. Eng. J., 424: 130262.

Dineshkumar, M., Sowndariya, S., Kalaiselvi, G., Israth Rehana, M., Durai Murugan, M. and Abraham, R. 2022. Effective removal of lead (Pb) by natural biosorbent marine microalgae (Dunaliella salina) through batch experiment. Biom. Conv. Bioref., 15: 1-6.

Elkhaleefa, I.H., Ali, E.I., Brima, I., Shigidi, A., Elhag, B. and Karama, A. 2021. Evaluation of the adsorption efficiency on the removal of lead (II) Ions from aqueous solutions using Azadirachta indica leaves as an adsorbent. Processes, 9: 559.

Giri, A., Alhazmi, A., Mohammad, S., Haque, N., Srivastava, V.K. and Thakur, D. 2022. Lead removal from synthetic wastewater by biosorbents prepared from seeds of Artocarpus Heterophyllus and Syzygium Cumini. Chemosphere, 287: 132016.

Gunarathne, A.U., Rajapaksha, M., Vithanage, D.S., Alessi, R., Selvasembian, M. and Naushad, V. 2022. Hydrometallurgical processes for heavy metals recovery from industrial sludges. Crit. Rev. Environ. Sci. Technol., 52: 1022-1062.

Gupt, S., Sekharan, C. and Arnepalli, D. 2022. Impact of buffering agent on lead adsorption of bentonite: An appraisal. J. Environ. Eng., 148: 04021083.

Hao, J., Cao, J., Ye, C., Zhang, C., Li, B. and Bate, N. 2021.Content and morphology of lead remediated by activated carbon and biochar: A spectral induced polarization study. J. Hazard. Mater., 411: 124605.

He, Y., Zhang, X., Zhang, H. and Chen, Y. 2021. Diverse zeolites derived from a circulating fluidized bed fly ash-based geopolymer for the adsorption of lead ions from wastewater. J. Clean. Prod., 312: 127769.

Hossain, H.H., Ngo, W., Guo, J., Zhang, S. and Liang, M.A. 2014. A laboratory study using maple leaves as a biosorbent for lead removal from aqueous solutions. Water Qual. Res. J. Canad., 49: 195-209.

Hu, Y., Ding, Y., Shao, L.. Cai, Z.Y., Jin, Z. and Liu, Z.T. 2021. Banana peel biochar with a nanoflake-assembled structure for cross-contamination treatment in water: Interaction behaviors between lead and tetracycline. J. Chem. Eng., 420: 129807.

Ibrahim, F.H., Abdellatif, M.S., Hasanin, M.M. and Abdellatif, N.M. 2022. Fabrication, characterization, and potential application of modified sawdust sorbents for efficient removal of heavy metal ions and anionic dye from aqueous solutions. J. Clean Prod., 332: 130021.

Jalali, H., Ghafourian, Y., Asef, S., Davarpanah, S. and Sepehr, R. 2002. Removal and recovery of lead using nonliving biomass of marine algae. J. Hazard. Mater., 92:253-262.

Janani, B., Gurunathan, K., Sivakumar, S., Varjani, H.H.. Ngo, E. and Gnansounou, F. 2022. Advancements in heavy metals removal from effluents employing nano-adsorbents: Way towards cleaner production. Environ. Res., 203: 111815.

Jarvis, P. and Fawell, J. 2021. Lead in drinking water–an ongoing public health concern? Curr. Opin. Environ. Sci. Health, 20: 100239.

Jose, P.A. and Dharsana, M. 2022. Adsorption of lead from contaminated water using biosorbent. Mater. Technol., 56: 171-177.

Karimi, A., Ayati, B., Tanhaei, A.L., Sanati, S., Afshar, A. and Kardan, M. 2022. Removal of metal ions using a new magnetic chitosan nano-bio-adsorbent; A powerful approach in water treatment. Environ. Res. 203: 111753.

Kim, S.N., Nam, A., Jang, M., Jang, C.M., Park, A. and Son, M. 2022. Review of adsorption–membrane hybrid systems for water and wastewater treatment. Chemosphere, 286: 131916.

Kim, W. and Singh, R. 2022. Modified oyster waste shells as a value-added sorbent for lead removal from water. Bull. Environ. Contam. Toxicol., 108: 518-525.

Kumar, J.N. and Oommen, C. 2012. Removal of heavy metals by biosorption using freshwater alga Spirogyra hyalina. J. Environ. Biol., 33: 27.

Li, Y., Chen, T. and Wang, X. 2021. Cadmium biosorption by lactic acid bacteria Weissella viridescens ZY-6. Food Cont., 123: 107747.

Mirmohammadmakki, M., Gharachorloo, M., Ghavami, V., Abdossi, R. and Azizinezhad, F. 2022. The efficiency of almond shell (Amygdalus communis L.) bio-sorption in reduction of heavy metals (lead, cadmium, arsenic, and nickel) from parsley (Petroselinum crispum). Biom. Conv. Bioref., 1: 1-12.

Mohammed, F.I., Abed, T.J. and Al-Musawi, M.M. 2016. Biosorption of Pb (II) from aqueous solution by spent black tea leaves and separation by flotation. Desal. Water Treat., 57: 2028-2039.

Munagapati, V., Yarramuthi, S.K., Nadavala, S.R., Alla, K. and Abburi, V.S. 2010. Biosorption of Cu (II), Cd (II), and Pb (II) by Acacia leucocephala bark powder: kinetics, equilibrium, and thermodynamics. Chem. Eng. J., 157: 357-365.

Munir, M., Jahangeer, A., Bouyahya, N., El Omari, R., Ghchime, A. and Balahbib, N. 2021. Heavy metal contamination of natural foods is a serious health issue: A review. Sustainability, 14: 161.

Näsström, H., Shargaieva, O., Becker, P., Mathies, F., Zizak, I., Schröder, V.R., List-Kratochvil, E.J., Unold, T. and Unger, E. Combinatorial inkjet printing for compositional tuning of metal-halide perovskite thin films. J. Mater. Chem. A, 65: 1231

Ng, X., Wu, X., Yang, Y., Xie, Y., Lu, C. and Chen, I. 2013. Synergistic effect of Trichoderma reesei cellulases on agricultural tea waste for adsorption of heavy metal Cr (VI). Bioresour. Technol., 145: 297-301.

Otieno, P., Kowal, J. and Mąkinia, J. 2022. Monitoring lead concentration in the surrounding environmental components of a lead battery company: Plants, air and effluents: Case study, Kenya. Int. J. Environ. Res. Public Health, 19: 5195.

Rastogi, R., Kaushal, S., Tripathi, A.L., Sharma, I., Kaur, L.M. and Bharadwaj, R. 2008. Comparative study of carbon nanotube dispersion using surfactants. J. Colloid Interface Sci., 328: 421-428.

Sentanuhady, J., Saputro, W. and Muflikhun, M.A. 2021. Metals and chemical compounds contaminants in diesel engine lubricant with B20 and B100 biofuels for long-term operation. Sustain. Energy Technol. Assess., 45: 10116.

Shahrokhi-Shahraki, C., Benally, M.G., El-Din, J. and Park, R. 2021. High-efficiency removal of heavy metals using tire-derived activated carbon vs. commercial activated carbon: Insights into the adsorption mechanisms. Chemosphere, 264: 128455.

Sharma, R., Sharma, K., Parveen, D., Pant, P. and Malaviya, R. 2021. Comprehensive and critical appraisal of plant-based defluoridation from environmental matrices. Chemosphere, 281: 130892.

Shittu, O., Gara, T.Y. and Onyinye, I. 2022. Removal of contaminant in electroplating wastewater and its toxic effect using biosynthesized silver nanoparticles. SN Appl. Sci., 4: 266.

Singh, D.B., Pal, A., Mohammad, A., Alhazmi, S., Haque, T. and Yoon, D. 2022. Biological remediation technologies for dyes and heavy metals in wastewater treatment: New insight. Bioresour. Technol., 343: 126154.

Syuhadah, N. and Rohasliney, H. 2012. Rice husk as biosorbent: a review. Health Environ. J., 3: 89-95.

Thakare, H., Sarma, S., Datar, A., Roy, P., Pawar, K. and Gupta, M. 2021. Understanding the holistic approach to plant-microbe remediation technologies for removing heavy metals and radionuclides from the soil. Curr. Res. Biotechnol., 3: 84-98.

Vázquez-Guerrero, R. Cortés-Martínez, R., Alfaro-Cuevas-Villanueva, E.M., Rivera-Muñoz, R. and Huirache-Acuña, M. 2021. Cd (II) and Pb (II) adsorption using a composite obtained from Moringa oleifera Lam. cellulose nanofibrils impregnated with iron nanoparticles. Water, 13: 89.

Védrine, J.C. 2017.Heterogeneous catalysis on metal oxides. Catalysts, 7: 341.

Xu, S., Gu, D., Rana, T., Matsuura, C.Q. and Lan, Z. 2021. Chemical precipitation enabled UF and MF filtration for lead removal. J. Water Process. Eng., 41: 101987.

Zhang, I., Elsayed, R.O., Nayanathara, X., Song, R., Shmulsky, E.B. and Hassan, X. 2022. Biobased hierarchically porous carbon featuring micron-sized honeycomb architecture for $CO_2$ capture and water remediation. J. Environ. Chem. Eng., 10: 107460.

Nature Environment and Pollution Technology
An International Quarterly Scientific Journal

p-ISSN: 0972-6268
(Print copies up to 2016)
e-ISSN: 2395-3454

Vol. 22 | No. 1 | pp. 87-96 | 2023

Original Research Paper

https://doi.org/10.46488/NEPT.2023.v22i01.007

Open Access Journal

# Corrosion Behavior of Petroleum Pipeline Steel in the Sulfur Ion Enriched Solution with Quinoline

**Shanjian Li*(**)†, Guotao Cui***, Panfeng Wu*(**) and Yang Feng*****

*School of Chemistry and Chemical Engineering, Xi'an Shiyou University, Xi'an, 710065, PR of China

**Shaanxi Key Laboratory of Carbon Dioxide Sequestration and Enhanced Oil recovery, Xi'an 710065, Shaanxi, China

***No. 3 Gas production plant of Yanchang Gas Field of Shaanxi Yanchang Petroleum Co. Ltd., Yan'an, Shaanxi 716000, PR of China

†Corresponding author: Shanjian Li; lishanjian@xsyu.edu.cn

**Nat. Env. & Poll. Tech.**
**Website: www.neptjournal.com**

*Received:* 19-07-2022
*Revised:* 06-10-2022
*Accepted:* 18-10-2022

**Key Words:**
Local corrosion
Occluded battery
Quinoline corrosion inhibitor
Electrochemical behavior

## ABSTRACT

Localized corrosion is a serious, hazardous destroyer of steel petroleum pipelines meant for long-time use. However, previous studies on localized corrosion primarily focused on local corrosion morphology and corrosion rate of bulk metals because detecting the corrosion state of occlusive metals is difficult. Herein, we employ a simulating occluded battery unit to disclose the local corrosion behavior of the steel petroleum pipeline (N80 steel) in an occlusive $S^{2-}$-enriched solution. After simulating localized corrosion in the $S^{2-}$- containing corrosion solution using the occluded battery unit, the occlusive solution was acidified and the migration amount of $S^{2-}$ to the occluded area increased. Despite the increase of $S^{2-}$ concentration, the addition of quinoline corrosion inhibitor (0.8 wt%) still effectively impedes the corrosion of the occluded metal. Moderately raising the environmental temperature can stimulate the activity of the inhibitor and promote the inhibition effect. The quinoline corrosion inhibitor displays the maximum inhibition rate at an elevated temperature of 50°C. Meanwhile, a maximum over the temperature of 60°C-70°C will likely accelerate the failure of the inhibitor.

## INTRODUCTION

Amongst the various anti-corrosion methods for petroleum pipelines and equipment, the addition of corrosion inhibitors have been widely used due to their low cost, ease of operation, and convenience (Zong 2008, Wang 2017, Shi & Shi 2017, Jiao 2019, Xue & Liu 2018). Quinoline corrosion inhibitors are often used as acidizing corrosion inhibitors in petroleum exploitation to achieve a high corrosion inhibition rate, and satisfactory corrosion inhibition effect with low dosage (Puskullu et al. 2013, Ser et al. 2020, Chen et al. 2019, Dong et al. 2019). Previous reports confirmed that this type of corrosion inhibitor could effectively impede the uniform corrosion of metals (Huang et al. 2018, Lu et al. 2021, Yu & Zhen 2015). For instance, Wang et al. (2015) demonstrated the effect of 8-aminoquinoline and 8-nitroquinoline on the corrosion protection of AA5052 alloy in 3 wt% of NaCl solution using various experimental and computational methods. The 8-aminoquinoline and 8-NQ provided a protection efficiency of 89.5% and 87.0%, respectively. As anodic-type inhibitors, they can effectively enhance the value of charge transfer resistance to weaken the overall corrosion current on the metal at a concentration of 0.02 $mol.L^{-1}$. Upon a synergistic effect of 8-hydroxyquinoline with 0.4 wt% of KI, Obot et al. (2017) investigated the corrosion effect of 8-hydroxyquinoline on X60 steel in 15 wt% of HCl using loss-in-weight and electrochemical methods. The results showed satisfactory inhibition performance owing to the synergistically enhanced corrosion protection capability. Up till now, limited studies have been focused on the corrosion inhibition effect of quinoline corrosion inhibitors on the localized corrosion of metals.

Different from the above evaluation on uniform corrosion inhibition, herein, the corrosion inhibition of the quinoline corrosion inhibitor on the localized corrosion of N80 steel (a common material for oil pipelines) in $Na_2S$-containing oil and gas field mineralized water solution system is concentrated on by simulating the occluded battery method. $S^{2-}$- enriched and -acidized occlusive solutions are obtained, and their chemical state is analyzed in detail through the simulation method. The electrochemical corrosion behavior of N80 steel in the generated occluded solutions, along with changes in the chemical state of the occlusive solution, is explored. The corrosion state of this occlusive cell simulating the localized corrosion under elevated environmental temperature is

discussed to understand the quinoline-containing and $S^{2-}$-enriched systems further. This concentration on localized corrosion from the chemical state of the occlusive solution to the electrochemical corrosion state of the occlusive metal can provide a theoretical reference for the application of quinoline corrosion inhibitors to impede localized corrosion in the field of petroleum exploration and production.

## MATERIALS AND METHODS

### Materials

N80 steel used in this experiment is collected from Foshan Wenxian Electromechanical Control Company Limited. Analytical-grade sodium sulfide ($Na_2S$). The composition of mineralized water derived from oil and gas fields is listed in Table 1.

The corrosive medium is a mixed solution composed of 0, 1.0, 1.5, and 2.0 wt% $Na_2S$ in oil and gas field mineralized water and prepared by dissolving the designed amount of $Na_2S$ into the oil and gas field mineralized water.

### Analytical Methods

**Chemical evaluation of the occluded area:** The simulated occluded battery was prepared according to our previous works (Li et al. 2016). The solution in the occlusive area was taken out for chemical analysis after the simulation of localized corrosion in the corrosive solution environment with/without quinoline quaternary ammonium salt. Initially, its pH value was measured after cooling to room temperature. The concentration of $S^{2-}$ was then analyzed via titration. Before analysis, the same volume of sodium tetraphenylborate (7 $g.L^{-1}$) and potassium nitrate (7 $g.L^{-1}$) was added to the solution to remove the interference of quinoline quaternary ammonium salt.

The $S^{2-}$ concentration was examined using iodometric titration according to the Chinese national standard of GB/T223.68-1997. The occlusive solution (0.25 mL) was pipetted to achieve a dilution of 100 mL using deionized water and then placed in a 250 mL Erlenmeyer flask. Sodium hydroxide (2 $g.L^{-1}$) and nitric acid (1+300000 $mg.L^{-1}$) solutions were mixed with the diluted solution to adjust the pH value and ensure that the red color just becomes colorless after adding two drops of phenolphthalein indicator (10 $g.L^{-1}$ of ethanol solution). Iodine standard solution (10 mL, 0.01 $mol.L^{-1}$) was then added to the mixture. Hydrochloric acid solution (5 mL, 18 wt%) was added dropwise to the mixture under continuous stirring to form a uniform blend. The blend was placed in a dark environment for 10 min. After titrating with sodium thiosulphate standard solution (0.01 $mol.L^{-1}$), it transformed into a light yellow solution from its original colorless appearance. The blend began to demonstrate a dark blue color after adding 1 mL of starch indicator solution (1.0 wt%). Titration was continued until the blue disappeared to indicate the endpoint. The $S^{2-}$ concentration can be described in Equation 1.

$$\left[S^{2-}\right] = \frac{(V_0 - V_1) \times c}{V} \quad \ldots(1)$$

Where $V_1$ is the volume of sodium thiosulphate titrant consumed by the titration sample (mL), $V_0$ is the volume of sodium thiosulphate titrant consumed by the control sample (mL), V is the volume of the diluted occlusive solution (mL) and c is the molarity of the standard titration solution of sodium thiosulphate ($mol.L^{-1}$).

Table 1: Compositions of mineralized water.

| Parameter | Measured value [$mg.L^{-1}$] |
|---|---|
| $Ca^{2+}$ | 1824.00 |
| $Mg^{2+}$ | 169.59 |
| $Fe^{3+}$ | 0.5492 |
| $Fe^{2+}$ | 0.1727 |
| $Na^+$ with $K^+$ | 1419.28 |
| $HCO_3^-$ | 116.48 |
| $Cl^-$ | 5843.22 |
| $SO_4^{2-}$ | 7.56 |
| pH | 6.44 |

### Electrochemical Evaluation

The polarization curve and alternating current (AC) impedance measurement on N80 steel in oil and gas field mineralized aqueous solutions with different concentrations of $Na_2S$ and quinoline corrosion inhibitors were investigated using dynamic potential scanning and electrochemical impedance spectrum (EIS) methods. Based on these electrochemical evaluations, the uniform corrosion and localized corrosion behavior of N80 steel triggered by a specific corrosion medium and the inhibition effect of the corrosion inhibitor on the two corrosion forms are explored. Meanwhile, the corresponding corrosion inhibition mechanism of the corrosion inhibitor is analyzed. The corrosion inhibition rate derived from the polarization curve after testing is calculated as Equation 2, where $\eta$ is the inhibition efficiency (%), $I_{corr}$ is the corrosion current density without the corrosion inhibitor ($\mu A.cm^{-2}$) and $I'_{corr}$ is the corrosion current density with the corrosion inhibitor ($\mu A.cm^{-2}$).

$$\eta = \frac{(I_{corr} - I'_{corr})}{I_{corr}} \times 100\% \quad \ldots(2)$$

The corrosion inhibition rate based on the EIS method is expressed as follows:

$$\eta = \frac{(R_p - R_p^0)}{R_p} \times 100\% \quad \ldots(3)$$

Where $\eta$ is the inhibition efficiency (%), $R_p$ and $R_p^0$ represent the polarization resistance with and without the corrosion inhibitor ($\Omega.cm^{-2}$), respectively.

## RESULTS AND DISCUSSION

### Simulating the Constant Current Experiment in the Occluded Battery

After simulating the occlusive corrosion of N80 steel at 50°C for 8 h, changes in the $S^{2-}$ concentration and pH of the solution inside and outside the occlusion zone in different $Na_2S$ oil and gas field-mineralized water systems are presented in Table 2.

Data in Table 2 indicate that the $S^{2-}$ concentration in the occluded area is 1.05, 1.45, 1.38, and 1.16 times more concentrated than the original values in the oil and the gas field-mineralized water corrosion solution system with 0, 1.0, 1.5 and 2.0 wt% of $Na_2S$. Meanwhile, the pH value inside the occlusive solution drops sharply as the solution acidifies. A localized corrosion cell composed of an ultra-small anode (sample inside occluded area) interacting with a large cathode (sample outside occluded area) is formed when the anode current is applied to the simulated occlusion battery system. The anodic current accelerates the metal dissolution inside the occlusive area to generate high-concentration metal cations, which are hydrolyzed to produce a large amount of $H^+$. As a result, the pH value of the occlusive solution drops significantly. Due to the increased positive charge inside the occlusive area, $S^{2-}$ in the outside bulk solution continuously migrates to the occlusive zone to maintain the electric neutrality of the solution. After adding different concentrations of the quinoline corrosion inhibitor to diverse oil and gas field-mineralized water systems with various concentrations of $Na_2S$, changes in the $S^{2-}$ concentration and pH of the solution in the occluded area under the condition

Table 2: The composition changes of the solution inside/outside the occluded area in the oil and gas fields mineralized aqueous solution system with different concentrations of $Na_2S$.

| Current density | Solution system | Sampling | $S^{2-}$ concentration [mol.L$^{-1}$] | pH |
|---|---|---|---|---|
| $i$ = 1 mA.cm$^{-2}$ | 0 wt% $Na_2S$ + Oil and gas field mineralized water | Inside | 0.2400 | 4.63 |
| | | Outside | 0.2280 | 12.21 |
| | 1.0 wt% $Na_2S$ + Oil and gas field mineralized water | Inside | 0.3441 | 4.97 |
| | | Outside | 0.2360 | 12.38 |
| | 1.5 wt% $Na_2S$ + Oil and gas field mineralized water | Inside | 0.3522 | 5.67 |
| | | Outside | 0.2560 | 12.49 |
| | 2.0 wt% $Na_2S$ + Oil and gas field mineralized water | Inside | 0.3780 | 6.45 |
| | | Outside | 0.3241 | 12.66 |

Table 3: Changes in solution composition of the occluded solution with different concentrations of corrosion inhibitor-modified $Na_2S$ oil and gas field mineralization aqueous system.

| Current density | Solution system | Inhibitor concentration [wt%] | $S^{2-}$ concentration [mol.L$^{-1}$] | pH |
|---|---|---|---|---|
| $i$ = 1 mA.cm$^{-2}$ | 0 wt% $Na_2S$ + Oil and gas field mineralized water | 0.0 | 0.2400 | 4.63 |
| | | 0.2 | 0.0188 | 4.69 |
| | | 0.5 | 0.0100 | 4.73 |
| | | 0.8 | 0.0040 | 4.81 |
| | 1.0 wt% $Na_2S$ + Oil and gas field mineralized water | 0.0 | 0.3441 | 4.97 |
| | | 0.2 | 0.0320 | 5.20 |
| | | 0.5 | 0.0240 | 5.44 |
| | | 0.8 | 0.0064 | 5.59 |
| | 1.5 wt% $Na_2S$ + Oil and gas field mineralized water | 0.0 | 0.3522 | 5.67 |
| | | 0.2 | 0.0441 | 5.90 |
| | | 0.5 | 0.0323 | 6.09 |
| | | 0.8 | 0.0241 | 6.41 |
| | 2.0 wt% $Na_2S$ + Oil and gas field mineralized water | 0.0 | 0.3780 | 6.45 |
| | | 0.2 | 0.1400 | 6.83 |
| | | 0.5 | 0.1240 | 6.95 |
| | | 0.8 | 0.1000 | 7.13 |

of simulating the occlusive corrosion at 50°C for 8 h are presented in Table 3.

The $S^{2-}$ enrichment and solution acidification are alleviated by adding different concentrations of the quinoline corrosion inhibitor under the same corrosion current density. The trend curve of the $S^{2-}$ concentration versus the corrosion inhibitor concentration is depicted in Fig. 1(a). Compared with that of the controlled solution without the inhibitor, the $S^{2-}$ concentration decreases gradually with the increase of concentration of the corrosion inhibitor. This finding indicates that the corrosion of metals in the occlusive zone is mitigated and the dissolution of metal reduces. The $S^{2-}$ concentration in the occlusive zone still decreases rapidly when 2.0 wt% of the quinoline corrosion inhibitor is added. The downward trend of the $S^{2-}$ concentration slows down with the continued concentration increase of the corrosion inhibitor. The pH of the solution in the occlusive zone also clearly increases after adding a certain concentration of the corrosion inhibitor to the bulk solution, thereby showing an inverse trend to the $S^{2-}$ concentration (Fig. 1(b)). The pH value of the occlusive solution in the four $Na_2S$ oil and gas field mineralization aqueous systems gradually increases with the increase of the corrosion inhibitor concentration, thereby suggesting that the corrosion of the metal in the occlusive area is mitigated. Overall, this type of quinoline corrosion inhibitor can effectively reduce the migration of $S^{2-}$ to the occlusive area whilst inhibiting solution acidification. Hence, the dissolution of metal in the occlusive area is prevented from slow down the occurrence of local corrosion.

## Changes in the Electrochemical State of the Occluded Area

The simulated occluded battery unit in the four solution systems with different concentrations of corrosion inhibitors was operated at an anodic current density of 1 $mA.cm^{-2}$ for 8 h to generate the corresponding occlusive solutions before conducting the electrochemical measurement. The dynamic potential polarization curve was then obtained with the occluded sample of N80 petroleum special steel at 50°C in the formed occlusive environment (Fig. 2). The anodic polarization kinetic constant $\beta a$, cathodic polarization kinetic constant $\beta c$, self-corrosion current $I_0$, self-corrosion potential $E_{corr}$, corrosion rate fitted from Fig. 2(a)–2(d), and the calculated corrosion inhibition rate is listed in Table 3.

As illustrated in Fig. 2, the chemical state of the occluded area changes with the addition of the corrosion inhibitor. Upon adding corrosion inhibitors, the self-corrosion potential of N80 steel in the simulated occlusive solution shifts positively and both the self-corrosion current density and corrosion rate decrease significantly in the four solution systems. The metal corrosion rate in the occluded area decreases from 0.51 $mm.a^{-1}$ to 0.12 $mm.a^{-1}$ when 0.8 wt% of the quinoline corrosion inhibitor is added to the oil and gas field-mineralized aqueous solution system with 0 wt% of $Na_2S$. The corresponding corrosion inhibition rate is calculated at 77%. Similarly, the significantly reduced metal corrosion rate in the occluded area corresponds to a maximum corrosion inhibition rate of 83% and 86% in the oil and gas field mineralized aqueous solution systems with 1.0 and 1.5 wt% of $Na_2S$, respectively. The decrease of corrosion rate in the oil and gas field mineralization aqueous system containing 2.0 wt% of $Na_2S$ slows down from 0.98 $mm.a^{-1}$ to 0.41 $mm.a^{-1}$, corresponding to a corrosion inhibition rate rebound of 58%. Although the concentration of $S^{2-}$ in the solution system increases, the quinoline corrosion inhibitor can still inhibit the corrosion of the occluded area to a

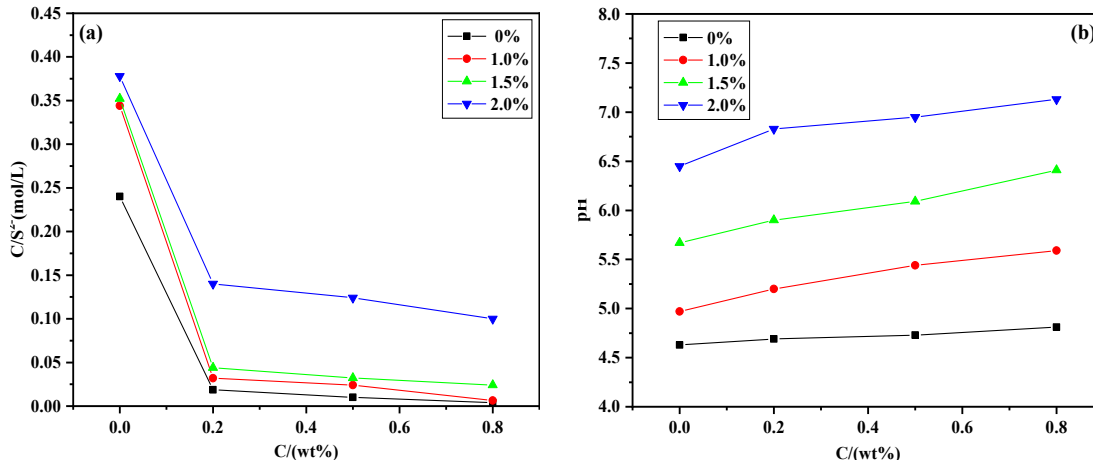


Fig. 1: (a) Trend curves of the change in $S^{2-}$ concentration of the occlusive solution as the concentration of the corrosion inhibitor increases. (b) Variation of the pH of the occlusive solution with the concentration of the corrosion inhibitor.

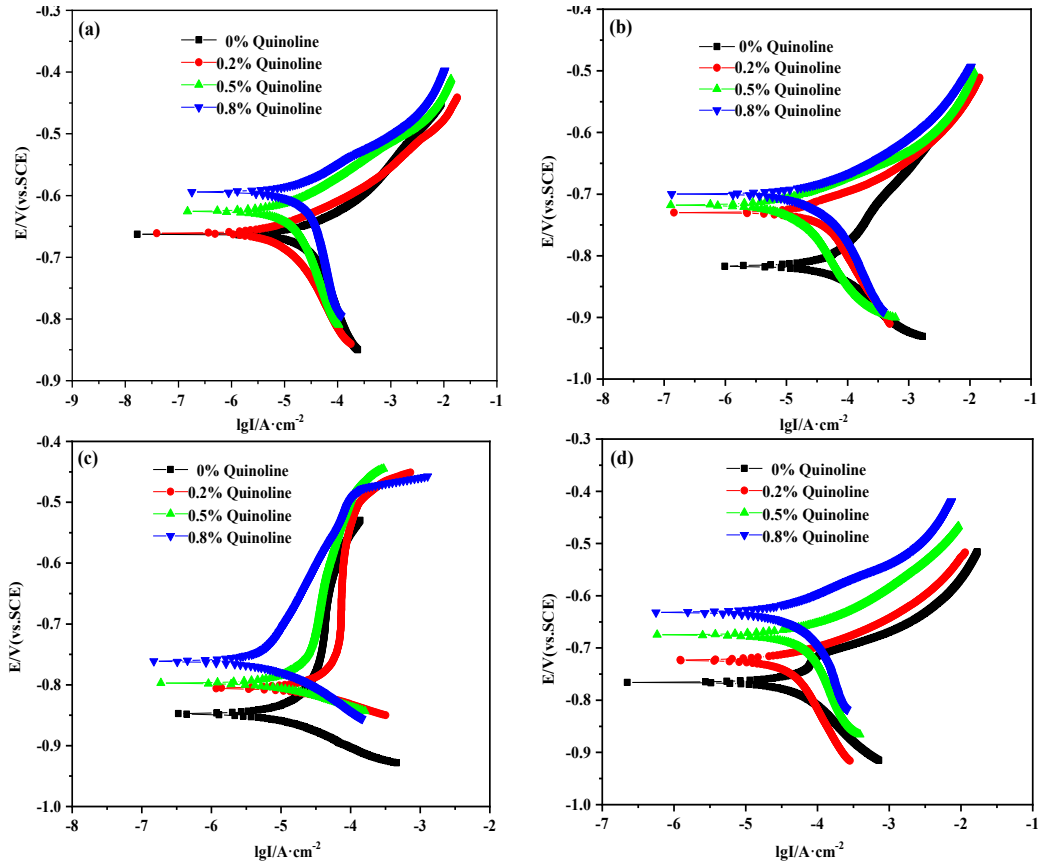


Fig. 2: Polarization curves tested in the occlusive area in oil and gas field-mineralized aqueous solution systems with (a) 0%, (b) 1.0%, (c) 1.5%, and (d) 2.0% of $Na_2S$ after different concentrations of the corrosion inhibitor modification.

Table 3: Electrochemical parameters fitted from the polarization curves through potentiodynamic scanning.

| Corrosion solution | Temperature [°C] | Inhibitor concentration [wt%] | Ba [mV] | Bc [mV] | $E_0$ [V] | $I_0$ [μA.cm$^{-2}$] | Corrosion rate [mm.a$^{-1}$] | Corrosion inhibition rate [%] |
|---|---|---|---|---|---|---|---|---|
| 0 wt% $Na_2S$+Oil and gas field mineralized water | 50 | 0.0 | 82.38 | 355.80 | -0.6627 | 42.90 | 0.5046 | --- |
| | | 0.2 | 57.15 | 236.96 | -0.6612 | 18.73 | 0.2204 | 56% |
| | | 0.5 | 60.04 | 213.82 | -0.6254 | 14.00 | 0.1654 | 67% |
| | | 0.8 | 55.75 | 149.50 | -0.5951 | 9.85 | 0.1158 | 77% |
| 1.0 wt% $Na_2S$+Oil and gas field mineralized water | 50 | 0.0 | 157.38 | 103.63 | -0.8162 | 79.67 | 0.9371 | --- |
| | | 0.2 | 67.79 | 180.12 | -0.7301 | 43.07 | 0.5066 | 46% |
| | | 0.5 | 58.73 | 129.43 | -0.7180 | 18.71 | 0.2201 | 77% |
| | | 0.8 | 54.05 | 148.53 | -0.7007 | 13.60 | 0.1599 | 83% |
| 1.5 wt% $Na_2S$+Oil and gas field mineralized water | 50 | 0.0 | 1709.90 | 63.74 | -0.8479 | 63.50 | 0.7467 | --- |
| | | 0.2 | 453.82 | 75.570 | -0.8056 | 22.78 | 0.2679 | 64% |
| | | 0.5 | 334.74 | 48.14 | -0.7982 | 16.19 | 0.1905 | 74% |
| | | 0.8 | 309.65 | 72.89 | -0.7620 | 8.67 | 0.1020 | 86% |
| 2.0 wt% $Na_2S$+Oil and gas field mineralized water | 50 | 0.0 | 86.54 | 386.70 | -0.7657 | 83.41 | 0.9812 | --- |
| | | 0.2 | 74.80 | 485.82 | -0.7239 | 69.16 | 0.8135 | 17% |
| | | 0.5 | 77.31 | 249.46 | -0.6757 | 53.70 | 0.6316 | 36% |
| | | 0.8 | 71.16 | 114.07 | -0.6315 | 35.03 | 0.4120 | 58% |

certain extent. The corrosion inhibition rate of the quinoline corrosion inhibitor (0.8 wt%) to the occluded area still reaches 58% when the $Na_2S$ content rises to a maximum of 2.0% in the solution system. These results indicate that the addition of the quinoline inhibitor to the bulk solution can highly benefit the electrochemical state of the occluded area by slowing down the corrosion of the metal in the occluded area to inhibit the occurrence and development of local corrosion.

The oil and gas field mineralized water system without $Na_2S$ is taken as an example to discuss the influence of temperature on the corrosion behavior of N80 steel in the occlusion area. Fig. 3(a) and 3(b) illustrate the polarization curve of N80 steel tested in the occlusion zone solution at 40°C–70°C after simulating the localized corrosion for 8 h in the oil and gas field mineralization aqueous system with and without the addition of 0.8 wt% of the quinoline inhibitor. The fitted Tafel parameters, including $\beta a$, $\beta c$, $I_{0,}$ and $E_{corr}$, are listed in Table 4.

As shown in Fig. 3(a) and Table 4, the self-corrosion potential of the polarization curve measured in the occlusive solution without corrosion inhibitor negatively shifts from 40°C to 70°C, whilst the corrosion current density increases gradually. Both the negative shift of corrosion potential and the increase of corrosion current density slow down after adding 0.8 wt% of the quinoline corrosion inhibitor to the bulk solution. This finding indicates that the corrosion acceleration effect on both the cathode and anode is significantly alleviated by the inhibitor at elevated temperatures (Fig. 3(b)).

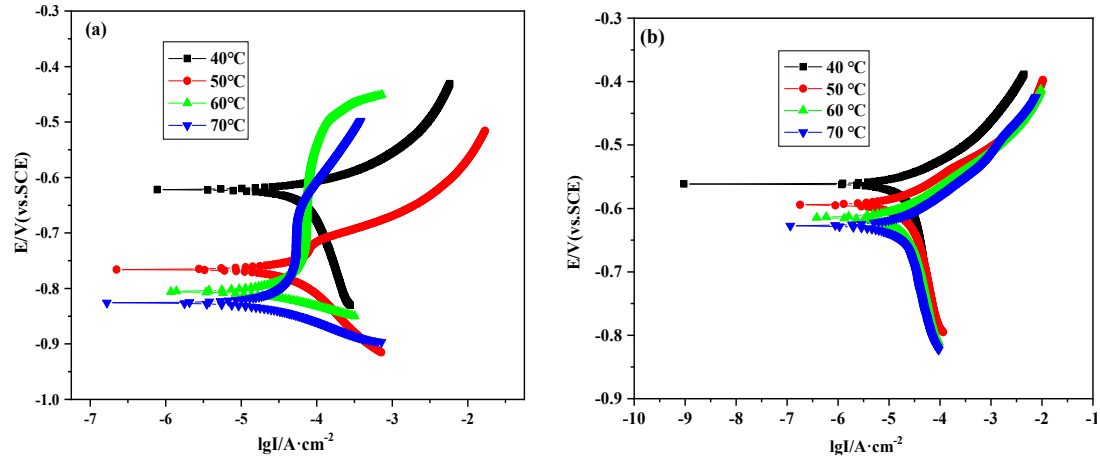


Fig. 3: Polarization curves tested in the occlusive solution of the oil and gas field mineralization aqueous solution system with 0 wt% of $Na_2S$ (a) in the absence of corrosion inhibitor and (b) in addition of the corrosion inhibitor (0.8 wt%) at 40°C-70°C.

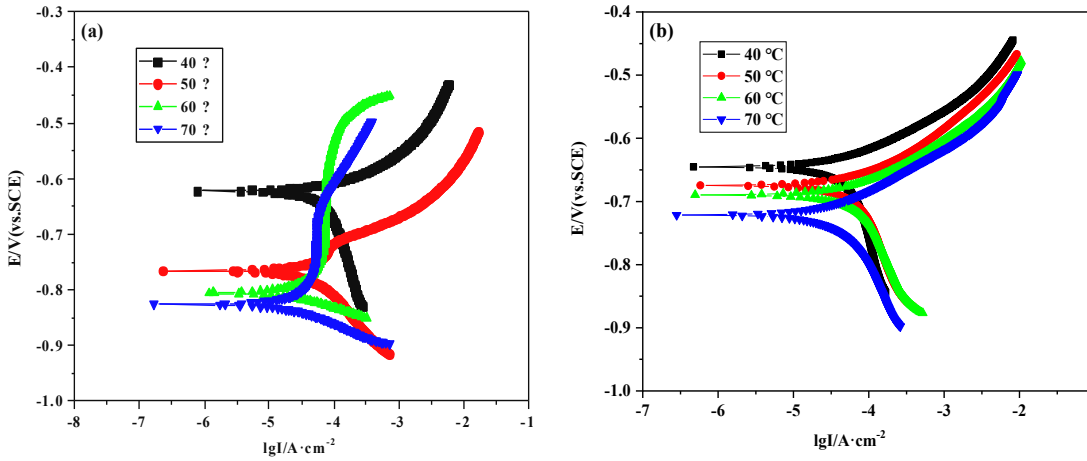


Fig. 4: Polarization curve tested in the occlusive solution in the oil and gas field mineralized aqueous solution system with 1.5 wt% of $Na_2S$ (a) in the absence of the corrosion inhibitor and (b) in addition of 0.8 wt% of the corrosion inhibitor at 40°C-70°C.

Table 4: Parameters fitted from the polarization curve tested in two kinds of corrosion solution systems without/without corrosion inhibitor at 40-70°C.

| Corrosion solution | Temperature [°C] | Inhibitor concentration [wt%] | $E_0$ [mV] | $I_0$ [μA.cm$^{-2}$] | Corrosion inhibition rate [%] |
|---|---|---|---|---|---|
| 0 wt% $Na_2S$+Oil and gas field mineralized water | 40 | 0.0 | -645.58 | 55.50 | |
| | | 0.8 | -561.59 | 19.51 | 65% |
| | 50 | 0.0 | -662.69 | 42.90 | |
| | | 0.8 | -595.11 | 9.85 | 77% |
| | 60 | 0.0 | -688.71 | 41.49 | |
| | | 0.8 | -614.27 | 24.69 | 41% |
| | 70 | 0.0 | -716.08 | 35.59 | |
| | | 0.8 | -627.46 | 23.63 | 34% |
| 1.5 wt% $Na_2S$+Oil and gas field mineralized water | 40 | 0.0 | -622.84 | 126.00 | |
| | | 0.8 | -645.50 | 64.33 | 49% |
| | 50 | 0.0 | -765.73 | 83.42 | |
| | | 0.8 | -631.49 | 35.03 | 58% |
| | 60 | 0.0 | -805.60 | 137.51 | |
| | | 0.8 | -690.55 | 77.27 | 44% |
| | 70 | 0.0 | -826.84 | 107.44 | |
| | | 0.8 | -721.29 | 67.23 | 37% |

Increasing the $Na_2S$ content to 1.5 wt% in the solution system, the inhibition effect of the quinoline corrosion inhibitor (0.8 wt%) is weakened slightly at elevated temperatures from 40°C to 70°C, as illustrated in Figs. 4(a) and 4(b). However, inhibition effectiveness, such as self-corrosion potential, corrosion current density, and corrosion inhibition rate, follows the same attenuation law as that in Figs. 3(a) and 3(b). Fitted parameters from the polarization curve of Fig. 4(a) and 4(b) shown in Table 4 0further reveal that the corrosion effect is inferior to that in the system without $Na_2S$ and with 0.8 wt% of the quinoline corrosion inhibitor under the same environmental temperature. The corrosion inhibition rate reduces to 37% when the temperature is increased to 70°C. These electrochemical analyses demonstrated that the addition of the quinoline corrosion inhibitor to the bulk solution could efficiently mitigate the corrosion of the occluded metal, even at an elevated temperature of 50°C regardless of the $Na_2S$ solution (0 or 1.5 wt%) used. Inhibition superiority is significantly impaired at a sufficiently higher temperature of 60°C–70°C. This finding indicates that an over temperature will likely accelerate the failure of the quinoline corrosion inhibitor.

**Electrochemical Impedance Spectroscopy Analysis**

Electrochemical impedance spectra measured in the occlusion zone solution after simulating the localized corrosion in the four corrosion solution systems at 50°C for 8 h are depicted in Fig. 5. Electrochemical impedance spectra (EIS) are fitted using the equivalent circuit model (Fig. 6), which is composed of a double-layer electric capacitance $C_{dl}$ parallel to the polarization resistance $R_p$, which is in series with the former solution resistance $R_s$. EIS parameters are fitted using the equivalent circuit (Table 5).

Compared with the impedance spectrum of the controlled solution without corrosion inhibitor, the fitted diameter of the semicircle representing the polarization resistance $R_p$ increases with the increase of the corrosion inhibitor concentration in the four solution systems, while the interface capacitance $C_{dl}$ decreases (Fig. 5). This variation tendency indicated that the quinoline corrosion inhibitor diffuses smoothly from the bulk solution into the occlusive area and competitively adsorbs onto the surface of the steel to form a protective film while replacing water molecules and corrosive anions on the steel surface after adding quinoline into the bulk solution.

As shown in Table 5, the polarization resistance of the corrosion system increases while the interface capacitance $C_{dl}$ decreases with the addition of the corrosion inhibitor at increasing concentrations to the bulk solution in the four solution systems due to the growing thickness of the adsorbed quinoline layer. Correspondingly, the calculated corrosion inhibition rate based on the polarization resistance increases gradually. The corrosion inhibitor still exerts an acceptable inhibitive effect on the occluded area with the increase of the $S^{2-}$ concentration from the perspective of the corrosion medium. The addition of quinoline (0.8 wt%) to the oil and

Table 5: Fitted electrochemical impedance spectroscopy parameters.

| Corrosion solution | Temperature [°C] | Inhibitor concentration [wt%] | $R_s$ | $C_{dl}$ | $R_p$ | Corrosion inhibition rate [η] |
|---|---|---|---|---|---|---|
| 0 wt% $Na_2S$+Oil and gas field mineralized water | 50 | 0.0 | 18.91 | $1.33 \times 10^{-3}$ | 230.5 | - |
| | | 0.2 | 7.51 | $5.77 \times 10^{-5}$ | 327.9 | 30% |
| | | 0.5 | 8.29 | $1.33 \times 10^{-5}$ | 712.5 | 68% |
| | | 0.8 | 4.65 | $3.31 \times 10^{-4}$ | 776.8 | 70% |
| 1.0 wt% $Na_2S$+Oil and gas field mineralized water | 50 | 0.0 | 7.21 | $2.50 \times 10^{-3}$ | 100.7 | - |
| | | 0.2 | 4.51 | $6.70 \times 10^{-3}$ | 150.1 | 33% |
| | | 0.5 | 3.84 | $1.27 \times 10^{-2}$ | 158.6 | 37% |
| | | 0.8 | 8.97 | $2.74 \times 10^{-3}$ | 256.7 | 61% |
| 1.5 wt% $Na_2S$+Oil and gas field mineralized water | 50 | 0.0 | 10.49 | $9.14 \times 10^{-4}$ | 132.0 | - |
| | | 0.2 | 4.88 | $4.2 \times 10^{-3}$ | 150.5 | 12% |
| | | 0.5 | 7.58 | $1.26 \times 10^{-3}$ | 211.8 | 38% |
| | | 0.8 | 17.34 | $9.14 \times 10^{-4}$ | 364.8 | 64% |
| 2.0 wt% $Na_2S$+Oil and gas field mineralized water | 50 | 0.0 | 7.62 | $2.48 \times 10^{-3}$ | 437.2 | - |
| | | 0.2 | 4.67 | $5.61 \times 10^{-4}$ | 718.7 | 39% |
| | | 0.5 | 3.25 | $1.45 \times 10^{-3}$ | 1521.0 | 71% |
| | | 0.8 | 7.91 | $1.73 \times 10^{-3}$ | 2094.0 | 79% |

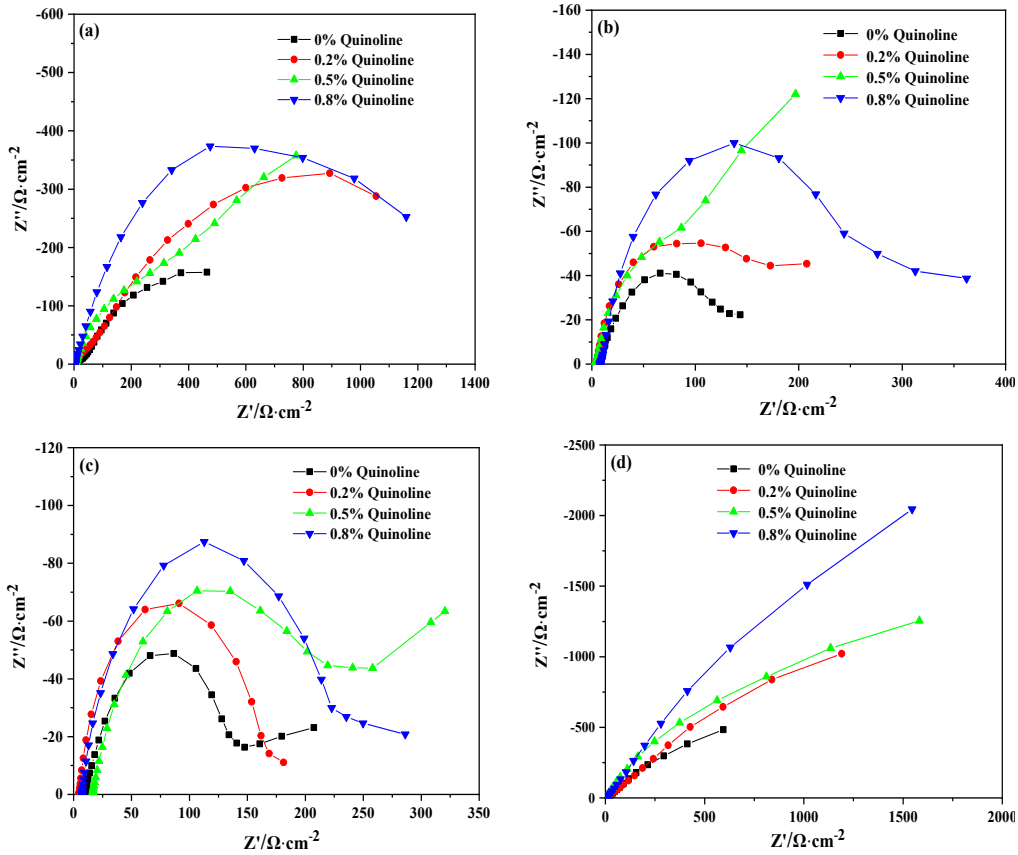


Fig. 5: EIS comparison in the blocked area of the oil and gas field mineralized aqueous solution systems with (a) 0 wt%, (b) 1.0 wt%, (c) 1.5 wt% and (d) 2.0 wt% of $Na_2S$ at different concentrations of the corrosion inhibitor.

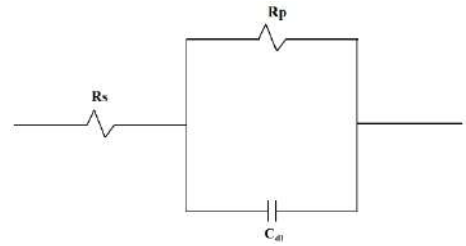


Fig. 6: Equivalent circuit diagram.
(Rs—solution resistance, Rp—polarization resistance, and Cdl—electric double-layer capacitance)

gas field mineralized water system with 2.0 wt% of $Na_2S$ can significantly slow down the corrosion of the occluded metal. The corrosion rate with 0.8 wt% of quinoline can still reach 79% even at a high temperature of 50°C, indicating that quinoline can effectively inhibit the formation and expansion of local corrosion. This finding is consistent with the results of the polarization curve measurement.

## CONCLUSIONS

In summary, the corrosion inhibition of the quinoline corrosion inhibitor on the localized corrosion of N80 steel in $Na_2S$-containing oil and gas field mineralized water solution system is investigated by simulating the occluded battery method. Through simulating the anodic polarization of the occluded battery in the corrosion solution, the solution in the occluded area is acidified as the pH drops sharply and an increasing amount of $S^{2-}$ concentrates migrate into the occluded area simultaneously. Correspondingly, the $S^{2-}$ concentrations in the occluded area of the oil and gas field mineralized water corrosion solution systems with 0, 1.0, 1.5, and 2.0 wt% of $Na_2S$ are 1.05, 1.45, 1.38, and 1.16 times higher than the original values. The addition of the quinoline corrosion inhibitor can mitigate the acidification of the occlusive solution and the migration of $S^{2-}$ to the occlusive zone. Hence, the dissolution of metal in the occlusive zone is alleviated against local corrosion. The electrochemical corrosion of N80 steel in the occluded area significantly slows down with the changes in the chemical state of the occlusive solution. The corrosion inhibitor can still effectively inhibit the corrosion of the occluded metal with an increase of the $S^{2-}$ concentration in the system. Moderately raising the environmental temperature is beneficial for stimulating the activity of the inhibitor and promoting the inhibition effect. The quinoline corrosion inhibitor displays the maximum inhibition rate at an elevated temperature of 50°C, while an over the temperature of 60°C–70°C will likely accelerate the failure of the quinoline corrosion inhibitor.

## ACKNOWLEDGEMENT

**Author contributions:** Shanjian Li was responsible for document preparation, data and statistical analyses, and figure generation. Guotao Cui, Panfeng Wu, and Yang Feng contributed to the study design, document framing, technical review, and editing.

**Funding:** This work was carried out with the financial support of the National Natural Science Foundation of China (21808182), Xi'an Science and Technology Plan Project Science and Technology Innovation Talent Service Enterprise Project (2020KJRC0096) and National Science Foundation of Shaanxi (2022GY-144). Open Foundation of Shaanxi Key Laboratory of Carbon Dioxide Sequestration and Enhanced Oil Recovery (No. YJSYZX22SKF0002)

**Data availability statement:** Data were presented in the main manuscript or the supplemental data and raw data were available on request from the corresponding author (lishanjian@xsyu.edu.cn).

## REFERENCES

Chen, S., Chen, S. and Li, W. 2019. Corrosion inhibition effect of a new quinoline derivative on Q235 steel in $H_2SO_4$ solution. Int. J. Electrochem. Sci., 14: 11419-11428.

Dong, Q.C., Zhang, G.H. and Zhang, W.B. 2019. Experimental and theoretical analysis of quinoline Gemini quaternary ammonium salt corrosion inhibitor. Chem. J. Chin. Univ., 40(10): 2195-2204.

Huang, P., Liu, W.J. and Zhang, Q.D. 2018. Preparation and performance evaluation of new quinoline corrosion inhibitors. China Petrol. Chem. Stand. Qual., 38(14): 102-103.

Jiao, D.W. 2019. Problems in the corrosion protection of petroleum pipelines and their solutions. Total Corr. Contr., 33(05): 96-98.

Li, S.J., Feng, L.J. and Zhang, J. 2016. Corrosion study of quinoline derivative corrosion inhibitor on tubing steel in simulated solution occlusion area. J. Appl. Basic Eng. Sci., 24(05): 1025-1033.

Lu, Y., Feng, H.X. and Tang, R.P. 2021. Summary of research and application of quinoline and its derivatives in metal corrosion inhibitors. Plast. Addit., 3: 6-10.

Obot, I.B., Ankah, N.K., Sorour, A.A., Gasem, Z.M. and Haruna, K. 2017. 8-Hydroxyquinoline as an alternative green and sustainable acidizing oilfield corrosion inhibitor. Sust. Mater. Technol., 14: 1-10.

Puskullu, M.O., Tekiner, B. and Suzen, S. 2013. Recent studies of antioxidant quinolone derivatives. Mini Rev. Med. Chem., 13(3): 365-372.

Ser, C.T., Žuvela, P. and Wong, M.W. 2020. Prediction of corrosion inhibition efficiency of pyridines and quinolines on an iron surface using machine learning-powered quantitative structure-property relationships. Appl. Surf. Sci., 512: 145612.

Shi, Y.H. and Shi, Y.K. 2017. Analysis of influence factors of pipeline corrosion. Petrochem. Technol., 24(12): 115.

Wang, D., Yang, D., Zhang, D.Q., Li, K., Gao, L.X. and Lin, T. 2015. Electrochemical and DFT studies of quinoline derivatives on corrosion inhibition of AA5052 aluminium alloy in NaCl solution. Appl. Surf. Sci., 357: 2176-2183.

Wang, Z.Y. 2017. Analysis of corrosion factors of petroleum pipelines and optimization measures for corrosion protection. Chem. Manag., 21(08): 126-127.

Xue, S.X. and Liu, C. 2018. The current situation of the corrosion work of petroleum pipelines and the countermeasures. Chem. Eng. Design Newslett., 44(07): 27.

Yu, H.L. and Zhen, H. 2015. Study on the synthesis and performance of a quinoline-type corrosion inhibitor. Sci. Technol. Eng., 15(19): 106-109.

Zong, P. 2008. Study on the synthesis of quaternary ammonium salt type acidizing corrosion inhibitor and its corrosion inhibition mechanism. China Univ. Petrol., 11: 56.

Nature Environment and Pollution Technology
An International Quarterly Scientific Journal

p-ISSN: 0972-6268
(Print copies up to 2016)
e-ISSN: 2395-3454

Vol. 22 | No. 1 | pp. 97-107 | 2023

Original Research Paper

https://doi.org/10.46488/NEPT.2023.v22i01.008

Open Access Journal

# Variability and Trend in Summer Monsoon Rainfall and its Correlation with Crop Yield in the Districts of Andhra Pradesh During 2011-2020

**Chandu Kavitha*†, A. Dharma Raju** and S.V.J. Kumar*****

*Department of Physics, GITAM Institute of Science, GITAM (deemed to be) University, Vishakhapatnam-530045, India
**India Meteorological Department, Ministry of Earth Sciences, Hyderabad-501218, India
***India Meteorological Department, Ministry of Earth Sciences, Vishakhapatnam-530017, India
†Corresponding author: Chandu Kavitha; kchandu@gitam.edu

**Nat. Env. & Poll. Tech.**
**Website: www.neptjournal.com**

*Received:* 06-06-2022
*Revised:* 15-07-2022
*Accepted:* 20-07-2022

**Key Words:**
Variability in Monsoon
Climate change
Rainfall
Crop yield

## ABSTRACT

In the context of climate change and its impact on agriculture, the paper analyses the trend of monsoon rainfall and its correlation with crop yield in Andhra Pradesh. The summer monsoon is the main rainy source of water for the state of Andhra Pradesh. The Kharif crops depend on the southwest monsoon rains to the extent that its adverse variability may lead to water stress and agrarian crisis. It has been observed from the study that in recent years the contribution of monsoon rainfall during September is increasing, and any harvest during the month is correspondingly affected, leading to a decline in the crop yield.

## INTRODUCTION

Andhra Pradesh (AP) is an agrarian state where about 62% of its population still depends on agriculture. Agriculture in the state is mainly dependent on rain-fed riverine systems and irrigation. The monsoon rains feed the rivers and hence help agriculture in the state. Of all the meteorological factors that have a bearing on agriculture and crop yield, rainfall has an indubitable influence, and its variability can cause water stress leading to an agrarian crisis in certain pockets of the farming-sensitive economy of the state.

As per the National Crime Records Bureau (NCRB), Andhra Pradesh recorded the third highest number of farmer suicides in India in 2019, with a total of 1,029 farmers taking their own lives in the state, against 664 in 2018. The data showed that 438 farmers in AP who owned farmland, 306 tenant farmers, and 401 agricultural laborers had died by suicide (https://www.thenewsminute.com/article/andhra-pradesh-records-third-highest-farmer-suicides-country-132140, https://www.newindianexpress.com/states/andhra-pradesh/2020/sep/02/1029-farmers-committed-suicide-in-andhra-pradesh-last-year-up-from-664-in-2018-2191296.html).

**ORCID details of the authors:**

**Chandu Kavitha**
https://orcid.org/0000-0003-1516-924X
**A. Dharma Raju**
https://orcid.org/0000-0002-3403-0609
**S.V.J. Kumar**
https://orcid.org/0000-0002-6402-7208

Andhra Pradesh is located between 12°41′ and 19.07°N latitude and 77° and 84°40′E longitude. It has a coastline of 974 km, with two major rivers (Godavari and Krishna) flowing across the state. The monsoon year is between June to September. The climate varies across the state. It is hot and humid in coastal districts, while it is mainly semi-arid in Rayalaseema districts. According to the standards of the Indian Meteorological Department (IMD), heavy rainfall is categorized into three categories- heavy, very heavy, and extremely heavy, if the rainfall is in the ranges of 64.5-115.5mm, 115.6-204.4 mm, and above 204.4 mm, respectively.

### The Problem

Ray et al. (2019) observed that during the recent decade (2007-2016) annual extreme rain events increased by 18%

when compared to the past decade (1997-2006). Goswami et al. (2006) and Mukherjee et al. (2005), pinpointed that there is a significantly increasing trend in the frequency and magnitude of extreme rain events and the frequency of heavy and very heavy rain events (while the frequency of moderate events decreased significantly) over central India.

Dash et al. (2009), reported that the frequency of long spells is decreasing, and the frequency of short rainy spells, dry spells, and prolonged dry spells are increasing. Krishna Kumar et al. (2004) and Mallick et al. (2007), observed that the crop yield during the Kharif season is low when monsoon rainfall is low.

Considering the rain gauge data of 1476 stations for the period 1901-2003, Guhathakurta & Rajeevan (2006), analyzed the spatial and temporal trend in rainfall over the country, the homogeneous regions, and its 36 subdivisions. Significantly, an increasing trend was observed in coastal Andhra Pradesh and Rayalaseema during the monsoon. The increasing trend in July and August is statistically significant while in September, the trend increased which is statistically not significant. Monsoon rain registered decreasing trend in June which again is statistically not significant. Over Rayalaseema, the trend was increasing with statistical significance during June and July. It also shows an increasing trend without significance in August but registered decreasing trend in September month, which is statistically not significant. Annual rainfall has been increasing in July and August months and decreasing in September over coastal Andhra Pradesh.

Rainfall data for 102 years analyzed using MK and Sen's slope estimator test by Rajwade et al. (2018), observed an increasing trend in annual rainfall in Andhra Pradesh and Telangana states. Specifically, an increasing trend of a magnitude ranging between 7 and 9% in mean annual rainfall in coastal Andhra Pradesh and Rayalaseema regions is observed by Vijay et al. (2010). Annual precipitation time-series data from 1991 to 2019 also indicated an increasing trend during June and monsoon seasons and a decreasing trend in the July and winter seasons (Significant at A 5% level) in the Prakasam district of AP. However, the trend and pattern of precipitation in coastal Andhra analyzed using daily and monthly rainfall data for 36 years from 1983 to 2018 by Baig et al. (2021), exhibited a decreasing trend. Climatic parameters and temperature impacted rainfall trends on a seasonal and annual scale as evidenced in an investigation by Aruna Jyothy et al. (2021). They reported that relative humidity, vapor pressure, and wind speed significantly impacted rainfall at Kurnool while vapor pressure impacted rainfall at Kakinada. At Machilipatnam, vapor pressure and temperature influenced rainfall considerably.

Rao et al. (2011) analyzed trends in rainfall over the districts of erstwhile Andhra Pradesh state using 1° X 1° gridded and rain gauge data. While the gridded data showed no trend over the state as a whole, the block level and gridded data showed a mismatch of increasing/decreasing trends in the districts.

It is evident from the above studies that rainfall has been mostly exhibiting an increasing trend in Andhra Pradesh. Most of the studies focused on the variability and trends in different rainfall events considering 30 or more years of data. However, the limitation of these studies is that they have not studied district-wise rainfall trends, which could vary with the corresponding impact. Further, recent data was not considered. Such an analysis is needed for policy-related decisions like mitigation and respite measures of the government in view of the climatic variations across the districts of Andhra Pradesh.

### Objectives of the Study

Against this backdrop, the present study focuses on analyzing rainfall trends for the period 2011-2020 across the districts of Andhra Pradesh for the summer monsoon season. The study also considered mean seasonal rainfall distribution and anomalies for the period 1991-2020 to understand inter-decadal variation during the recent climatological time strip.

## MATERIALS AND METHODS

A statistical analysis of rainfall for all the districts of Andhra Pradesh is carried out to identify the variability and trends in monthly rainfall in the monsoon season for the decade 2011-2021. The trend in the time-series rainfall data is observed using linear regression and the Mann-Kendall test. The monthly average rainfall is analyzed by computing the mean, standard deviation, and coefficient of variance. The correlation between crop yield and seasonal rainfall is carried out to understand the association between rainfall and yield at study locations for the reference period. Data collected from Indian Meteorological Department (IMD) was analyzed for this purpose.

The crop data has been garnered from the website https://aps.dac.gov.in/APY/Public_Report1.aspx. The data is extracted from "The Area and Production Statistics", Ministry of Agriculture and Farmers Welfare.

Rao et al. (2011) and some other studies observed that the gridded data has an inherent inadequacy in presenting rainfall as it is an area weighed average rainfall and hence is at variance with the point-location rainfall. In this study, the IMD 0.25 degree X 0.25 degree gridded-rainfall data is used only to analyze anomalies in the rainfall regime in

various districts during the recent climatology period and also to address the issue of the unavailability of data at various point locations. To address the issue of parity and correlation, rainfall at stations is used to reflect the district rainfall and crop yield in the district as a unit. This analysis helps in planning agricultural operations. A proper understanding of the trends in rainfall and its correlation with crop yield will help in foreseeing associated risks and thereby reduce spending on stimulus packages.

Fig. 1 depicts the study area with 13 districts of Andhra Pradesh each with its geographical extent. Anantapur is the largest district with 19.1 thousand sq.km followed by Kurnool with an area of 17.7 sq.km. Srikakulam is the smallest district with 5.8 thousand sq.km out of 13 districts in Andhra Pradesh.

## RESULTS AND DISCUSSION

### Inter Decadal Variations (1991-2020)

**The mean seasonal rainfall distribution and anomalies:** Fig. 2(i)(a) depicts the mean rainfall during the climatology 1991-2020 while 2(i)(b-d) shows the mean rainfall during the first decade (1991-2000), the middle decade (2001-2010), and the last decade (2011-2020) respectively. Similarly, 2(ii)(a-d) displays mean rainy days (days with rainfall of 2.5 mm or more); 2(iii)(a-d) moderate rainy days (days with 15.5 mm or more rainfall) and 2(iv)(a-d) heavy rainfall (days with rainfall 64.5 mm or more). There are few district-wise very heavy and extremely heavy rainfall days or episodes to perform the analysis.

Fig. 2(i) (a) shows the mean seasonal rainfall in the districts of Andhra Pradesh during the climatological period 1991-2020. A gradual decrease in rainfall as one moves from north to south/southwest is evident in the state. The north coastal districts of Andhra Pradesh, namely, Srikakulam, Vizianagaram, Visakhapatnam, East and West Godavari districts, and South Coastal district Krishna show a conspicuously higher rainfall range of 600-800 mm with mountainous regions in western parts of these districts having received even higher rainfall of 800 mm or more. Eastern stretches of Guntur recorded 500-600 mm rainfall while the western parts of Guntur, central parts of Kurnool, and a smaller southern portion of Chittoor received 400-500 mm. The rainfall received in the rest of the south coastal districts Prakasam and Nellore, the remaining parts of Rayalaseema districts ranged between 300-400 mm with the lowest rainfall of about 300-50 mm recorded in western parts of Anantapur and northern parts of Nellore. In Fig. 2(i)- the (b), (c), and (d) panels display the decadal anomalies with respect to climatological normal rainfall. The figures show distinct positive and negative anomalies of mean decadal rainfall in the first decade (1991-2000), the middle decade (2001-2010), and the last decade (2011-2020) with respect to the long-period normal mean rainfall climatology. It clearly shows that the rainfall anomalies in the first decade are quite high in the southwestern and southern parts of Andhra Pradesh comprising Prakasam and Nellore followed by large stretches of Kurnool, southern parts of Anantapur, northern pockets of Chittoor, and discrete eastern areas of Kadapa districts. Only parts of Godavari districts have positive anomalies while the rest of the state has negative anomalies in the mean decadal rainfall. In the middle decade, parts of northern coastal districts Viz., Srikakulam, Vizianagaram, Visakhapatnam, and East & West Godavari, Guntur, Prakasam, Kurnool, Anantapur, and many parts of Kadapa recorded demarcated positive mean decadal rainfall anomalies. There is a precariously large deficit in the districts of Krishna, Nellore, and Chittoor during the middle decade. During the recent decade 2011-2020, conspicuously, parts of the coastal districts-namely, West Godavari, Krishna, Guntur, and southern parts of Chittoor recorded large positive anomalies of 50-100 mm or more mean decadal rainfall. Interestingly, major areas of Anantapur, Nellore, some parts of Kadapa, Srikakulam, Vizianagaram, Visakhapatnam, and East Godavari have positive anomalies up to 50 mm mean decadal rainfall. The remaining parts of the state have no negative anomalies. Thus, the mean rainfall regimes have exhibited distinctive decadal differences.

**Mean rainy days:** The mean rainy days (days with 2.5 mm or more rainfall as shown in Fig. 2(ii(a)) show a gradual decrease in the mean number of rainy days from the north to the southern districts of the state. The northern coastal districts have received a greater number of mean rainy days (30 days to 38; and above in mountainous areas of the northern districts) than the southern coastal districts and Rayalaseema (18 to 24 days) with eastern fringes of Kurnool and western parts of Prakasam district receiving a shade better with 24 to 28 days of rainfall during 122 days. There is a conspicuous increase in the number of rainy days during the latest decade 2011-2020. Smaller fragments of East and West Godavari, Guntur received 6 to 10 days of positive anomalies in the mean number of rainy days while larger stretches of Prakasam, Nellore, Kurnool, East Godavari, Visakhapatnam, and parts of the remaining districts also showed positive anomaly of 2 to 4 while smaller fringes of other districts have smaller negative anomalies up to 2 days of mean rainy days during the decade 2011-2020.

**Mean moderate rainfall days:** The mean Moderate rainfall days (15.5 mm or more) are shown in Fig. 2(iii(a). Mean moderate rainfall days of 12 to 16 are observed over

coastal districts from Srikakulam to Krishna districts with hilly areas recording 16 to 20 days. There are three clear stratified zones with a gradual decrease from north to south in respect of mean moderate rainfall 12-16 days, 10-12 days, and 8-10 days as observed in the Guntur district. Major portions of Kurnool and Chittoor recorded 8-10 days while the remaining southern coastal districts and Rayalaseema districts recorded 6-8 days with some pockets of Nellore and Anantapur getting only 4-8 days of mean moderate rainfall days during the climatological period 1991-2020. During the decade 2011-2020, all the districts recorded positive anomalies in the number of moderate rainfall days except Kurnool, Prakasam, some parts of Kadapa and Nellore, smaller stretches of Chittoor, Visakhapatnam and East & west Godavari districts. The districts of Vizianagaram, West Godavari, Krishna, and Guntur recorded positive anomalies for up to 4 days during the decade.

**Mean heavy rainfall days:** The mean heavy rainfall days (64.5 mm or more) during the period 1991-2020 are shown in Fig. 2 iv(a). Only the hilly areas of east Godavari recorded mean heavy rainfall days of 1.8 to 2 days. West Godavari, major parts of Krishna, and a few parts of East Godavari, Visakhapatnam, Vizianagaram, and Srikakulam reported mean heavy rainfall days ranging from 0.8 to 1.6. Rest parts of the state outside Rayalaseema districts, Prakasam and Nellore recorded 0.6 to .08 mean heavy rainfall days. It is seen that Rayalaseema districts, Prakasam, and Nellore recorded only 0.2 to 0.4 mean heavy rainfall days during the period 1991-2020. During the decade 2011-2020, most parts of Rayalaseema districts, Prakasam, and Nellore recorded negative anomalies of -0.5 to -1.0 days of mean heavy rainfall days. Major parts of Vizianagaram, Visakhapatnam, East Godavari, and smaller portions of other districts recorded positive anomalies of 0.5 days of mean heavy rainfall days. The mountainous areas of Visakhapatnam and Vizianagaram recorded mean heavy rainfall days of 0.5 to 1.0 during 2011-2020. It is thus observed that a large inter-decadal variation is recorded with no clear areal bias, with a gradual increase in the mean rainfall distribution and anomalies, rainfall intensities, and anomalies from 1991 to 2020.

## Analysing Rainfall Trends During the Recent Decade (2011-2020)

District level analysis as per the IMD criteria for the rainy days to extreme weather rainy days (2.5mm to 204.4mm) is observed to be increasing in the recent decade.

**The trend in mean rainfall for the period 2011-2021 for the monsoon season:** Table 1 depicts the monthly mean rainfall in mm and the coefficient of variance for the study period in Andhra Pradesh. From the analysis, it is evident that September month contributes the maximum rain (28.5%), followed closely by August (27.5%), July (26.3%), and June (17.7%).Fig. 3 shows rainfall for each month in the monsoon season. The trend lines for each month and season are also

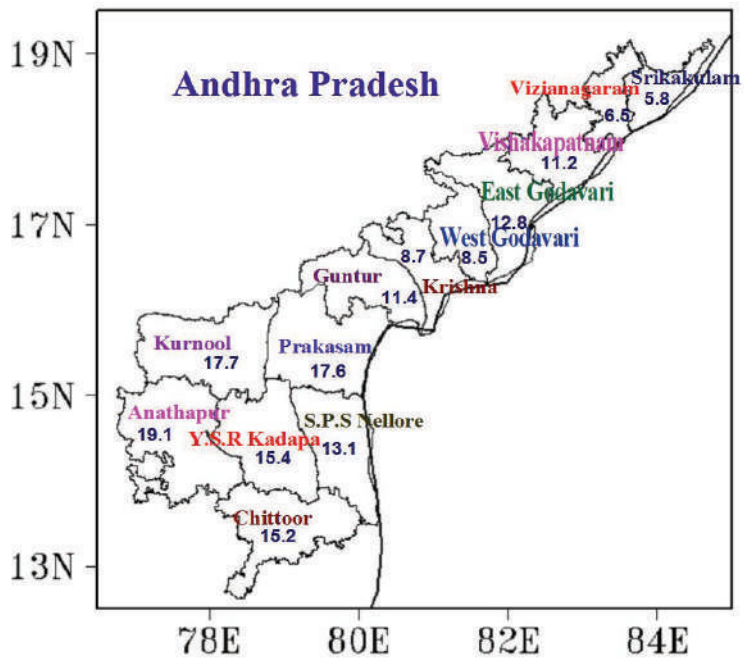


Fig. 1: The district-wise geographical area (shown in bold numbers in thousands of sq.km) of the state of Andhra Pradesh (as per the information published by the Directorate of Economics & Statistics, Vijayawada).

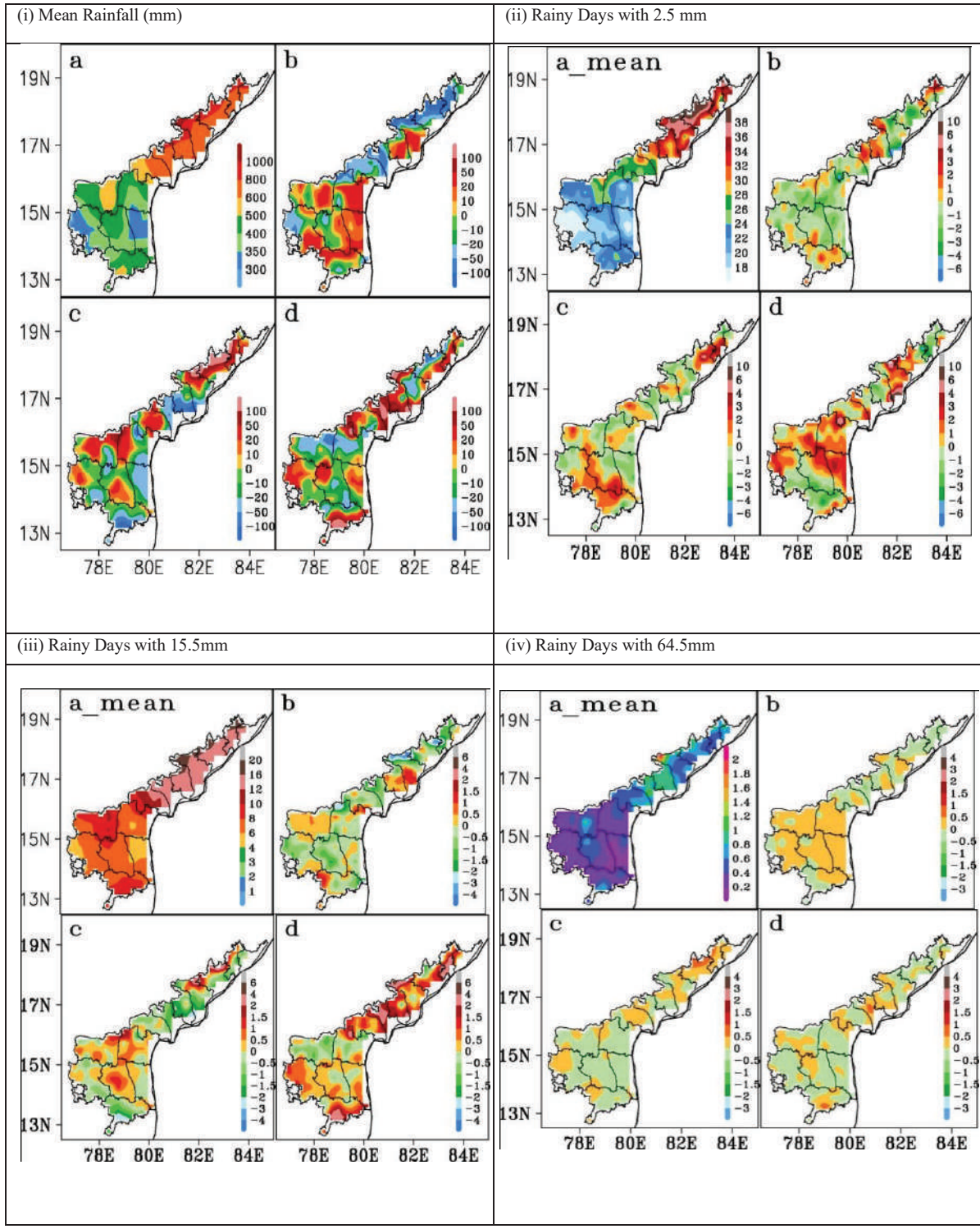


Fig. 2: The Rainfall( mm) distribution (i) (a) climatology [1991-2020],(b) first decade (1991-2000), (c) Middle decade (2001-2010) and (d) last decade (2011-2020), and the rainfall intensities with (ii) rainy days (above 2.5mm), (iii) rainy days (above 15.5mm) and (iv) rainy days (above 64.5mm) (a) mean rainy days 1991-2020 (b) differences (first decade) (1991-2000), (c) differences middle decade (2001-2010) and (d) differences last decade(2011-2020).

Table 1: Mean rainfall in mm and coefficient of variance in % (month-wise) for the study period.

| | June | July | August | September |
|---|---|---|---|---|
| Mean | 100.8196 | 149.6492 | 156.9372 | 162.6249 |
| CV | 57.35074 | 49.35901 | 48.93465 | 49.16178 |

displayed. Monthly and seasonal rainfall exhibited an upward trend; however, they are statistically not significant for June, July, and August.

The trend is upward and moderately significant during September and the entire monsoon season. During the last decade, the highest rainfall by month varied. It is June 2015 (594.4 mm). For July, it was in the year 2018(644.6 mm) while august received the maximum in the year 2020(885.4 mm) and 768.8 mm of rainfall was received in September 2013. The highest rainfall recorded for June, July, and August was in East Godavari and it was in September for Anantapur.

**The trend in district-wise rainfall:** Table 2 represents the mean rainfall and coefficient of variance (district/month-wise) for the study period. Coastal districts viz. East Godavari, West Godavari, Srikakulam, Visakhapatnam, Vizianagaram, and Krishna received mean rainfall in the range of 124-136 mm in June,148-260 mm in July, 180-244 mm in August, and 145-238 mm in September, while the districts of Rayalaseema region viz. Anantapur, Chittoor, Kadapa, and Kurnool received mean rainfall of around 67-80 mm in June, 69-122 mm in July, 73-125mm in August, and 125-143 mm in September. West Godavari received the highest mean rainfall, 207.8 mm, during the monsoon season, while Anantapur received the lowest (83.5mm).

Fig. 4 depicts mean rainfall trends for June to September. During June, Anantapur, Chittoor, and Kurnool districts registered an increasing trend in mean rainfall days at a 5% significant level, while the rest of the districts show no significant trends. There is no significant trend in Andhra Pradesh during July except in East Godavari, which exhibited an increasing trend (at a 5% significance level). Only East Godavari and Guntur showed an increasing trend at a 5 % significant level in August. However, in September, the districts of West Godavari, Chittoor, Kadapa, and Kurnool showed an increasing trend at a 5% significant level.

Fig. 5 depicts the trend in the average frequency of rainy days during the study period. In June, the average frequency of rainy days is high (3-14 days) in Krishna, Guntur, West Godavari, Visakhapatnam, Vizianagaram, and Kadapa. Anantapur, Chittoor, Nellore, and Srikakulam districts recorded rainy days of around 2-8 days. In July and August, the average frequency of rainy days in the range of 6-20 was recorded in East Godavari, West Godavari, Krishna, Srikakulam, Visakhapatnam, and Vizianagaram. The lowest frequency range is observed in Anantapur in June, July and August. On September 7-17, rainy days were recorded in East Godavari, Srikakulam, West Godavari, Vizianagaram, and Visakhapatnam. However, in Guntur, Nellore, and Prakasam, the range is between 1-14 days. For the entire

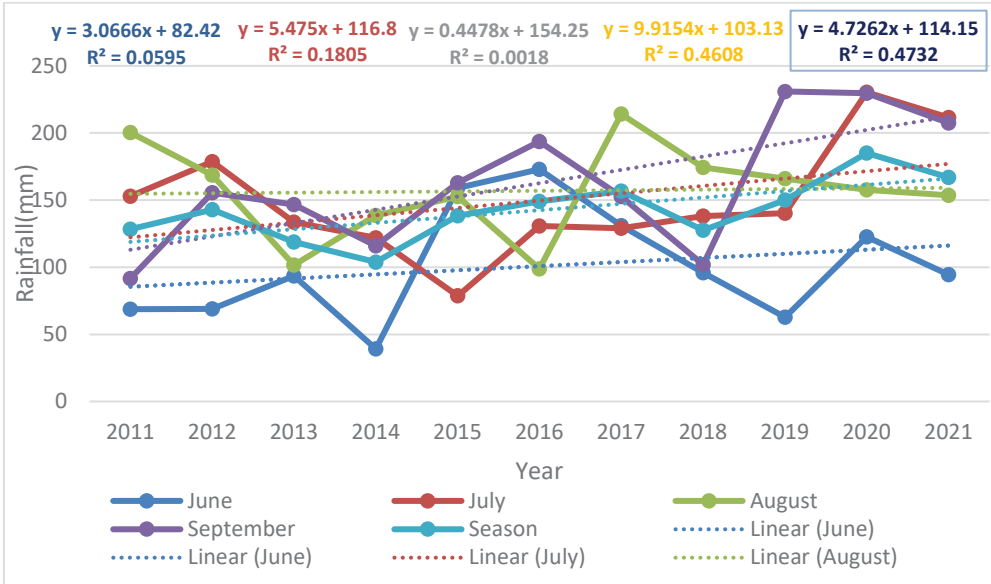


Fig. 3: Trends in rainfall for the monsoon season.

Table 2: Mean rainfall and coefficient of variance (district/month-wise) for the study period.

| | June | | July | | August | | September | |
|---|---|---|---|---|---|---|---|---|
| | Mean | CV | Mean | CV | Mean | CV | Mean | CV |
| East Godavari | 127.9 | 58 | 226.4 | 54 | 204.9 | 58 | 185.9 | 45 |
| Guntur | 112.0 | 51 | 154.3 | 40 | 171.0 | 44 | 163.7 | 50 |
| Krishna | 130.6 | 68 | 203.9 | 60 | 188.7 | 55 | 145.0 | 59 |
| Nellore | 55.0 | 76 | 87.6 | 48 | 103.3 | 45 | 97.0 | 53 |
| Prakasam | 58.9 | 69 | 97.9 | 45 | 101.2 | 56 | 115.1 | 54 |
| Srikakulam | 123.6 | 47 | 196.7 | 40 | 202.4 | 41 | 222.5 | 40 |
| Visakhapatnam | 133.6 | 52 | 148.2 | 54 | 180.4 | 45 | 213.9 | 48 |
| Vizianagaram | 135.7 | 50 | 170.2 | 36 | 212.1 | 30 | 237.8 | 35 |
| West Godavari | 134.0 | 47 | 259.9 | 37 | 243.8 | 42 | 193.4 | 44 |
| Anantapur | 67.4 | 60 | 69.3 | 62 | 72.5 | 59 | 124.8 | 54 |
| Chittoor | 80.4 | 57 | 122.2 | 59 | 125.2 | 55 | 135.9 | 53 |
| Kadapa | 71.4 | 49 | 94.2 | 55 | 119.4 | 50 | 136.3 | 50 |
| Kurnool | 80.2 | 63 | 114.5 | 54 | 115.3 | 56 | 142.8 | 55 |

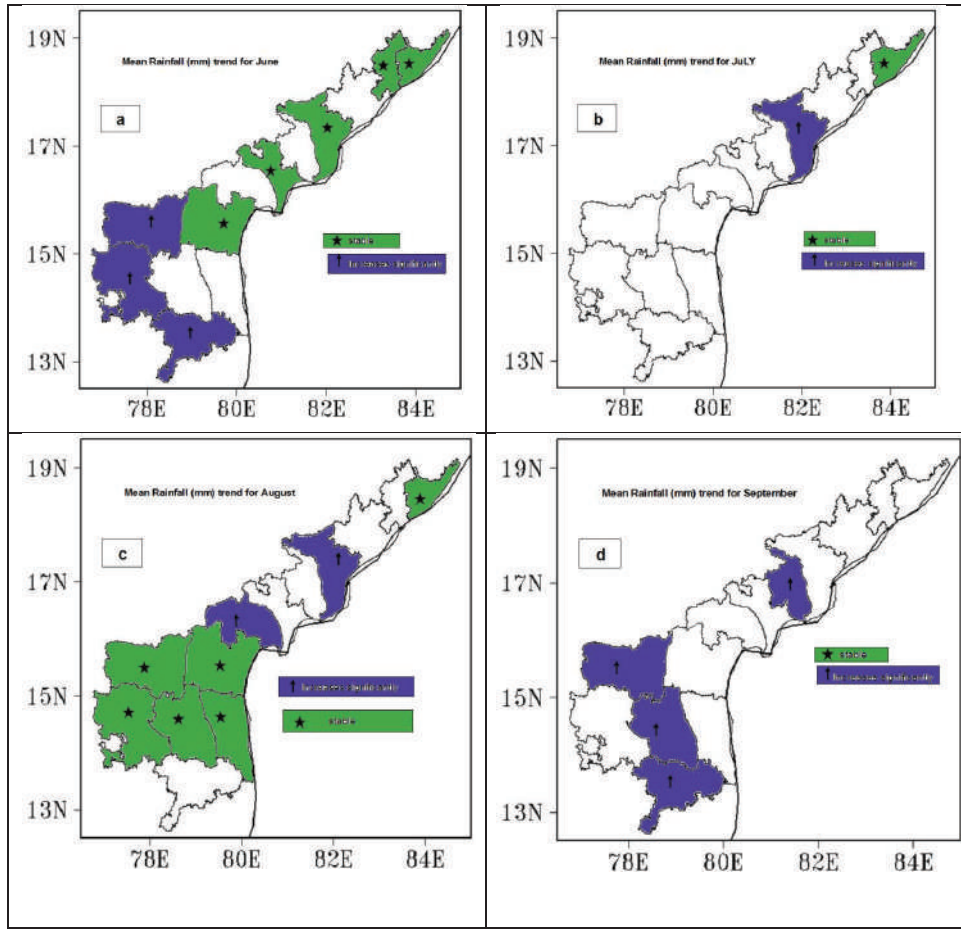


Fig. 4: Mean rainfall trend during the monsoon season.

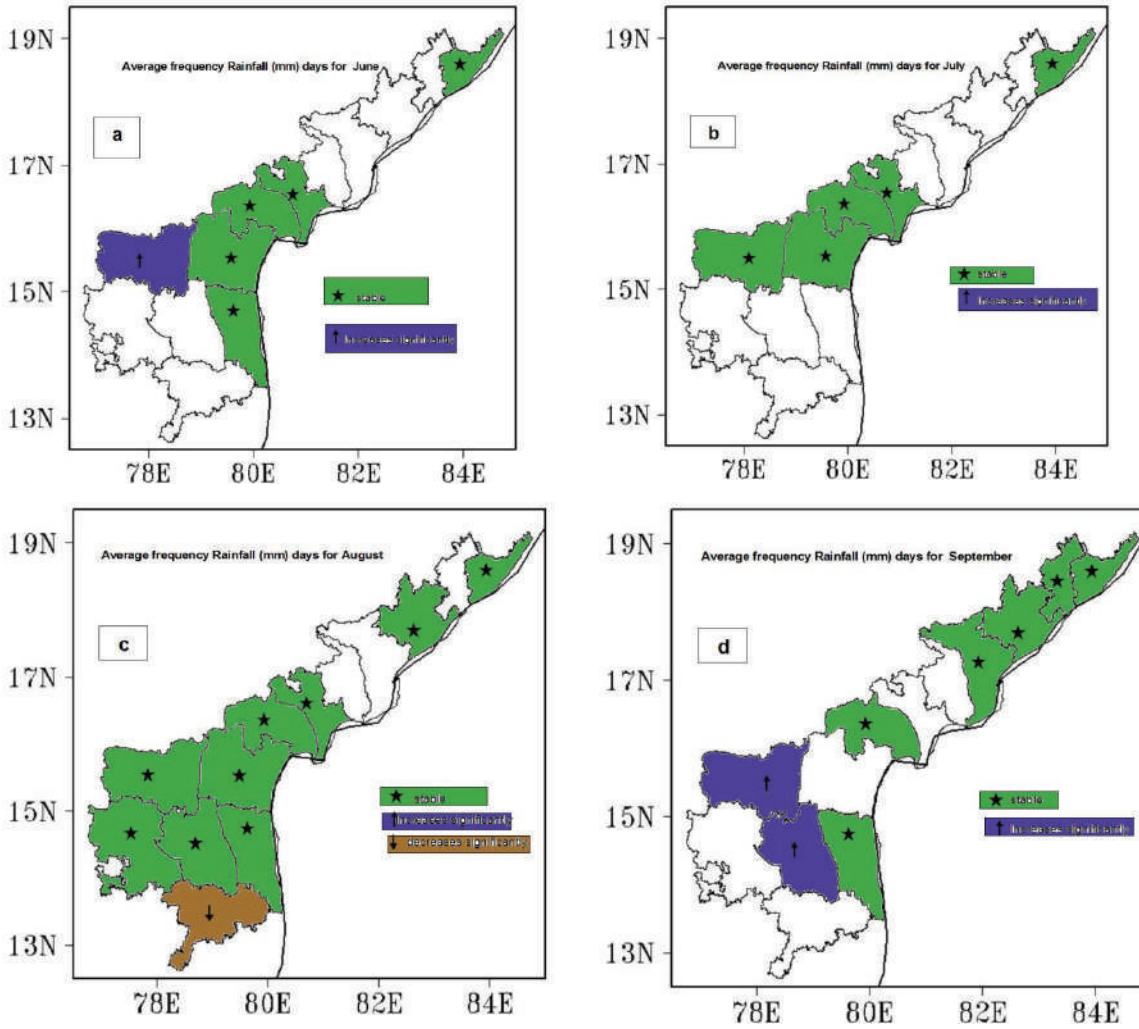


Fig. 5: Trend in an average frequency of rainfall days for the study period.

monsoon season, Guntur and Srikakulam indicated a stable trend in the average frequency of rainy days. There is a decreasing trend in Chittoor for August. Kadapa showed a significantly increasing trend for September while Kurnool witnessed the same in June and September-all significant at a 5% level.

The State's northern districts, West Godavari, Vizianagaram, Srikakulam, Krishna, and Districts of Rayalaseema region Anantapur, Kadapa, and Kurnool recorded average heavy rainfall days (2.27-6.90) for the entire monsoon season. While the central districts of Nellore and Prakasam received in the range of 0.63 to 2.81 days. Except in June, Guntur and Chittoor also recorded a more significant number of heavy rainfall days in the range of 2.36 to 5.27 days.

A statistically significant trend in heavy rainfall days at a 5% significant level is found in Anantapur and Kurnool in June, Vizianagaram in July, East Godavari in July, and August and September in Kadapa (Fig. 6). An increasing trend in the average frequency of heavy rainy days is observed in Kadapa in June, West Godavari and Chittoor in July, Guntur in August, and Nellore, Prakasam, and Kurnool in September month with varied significant levels. Only one district (Kurnool) in the state exhibited a decreasing trend in August. One northern district of the state, East Godavari, and districts of Rayalaseema region Kurnool, Kadapa, and Chittoor showed an increasing trend compared to other districts of the state. There is no trend in the central districts except Guntur in August and Prakasam in September.

The average frequency of very heavy rainfall days (Fig. 7) for the monsoon season indicates that the northern districts, West Godavari, East Godavari, and Krishna, recorded a greater number of 0.27 to1.27 heavy rainfall days than the

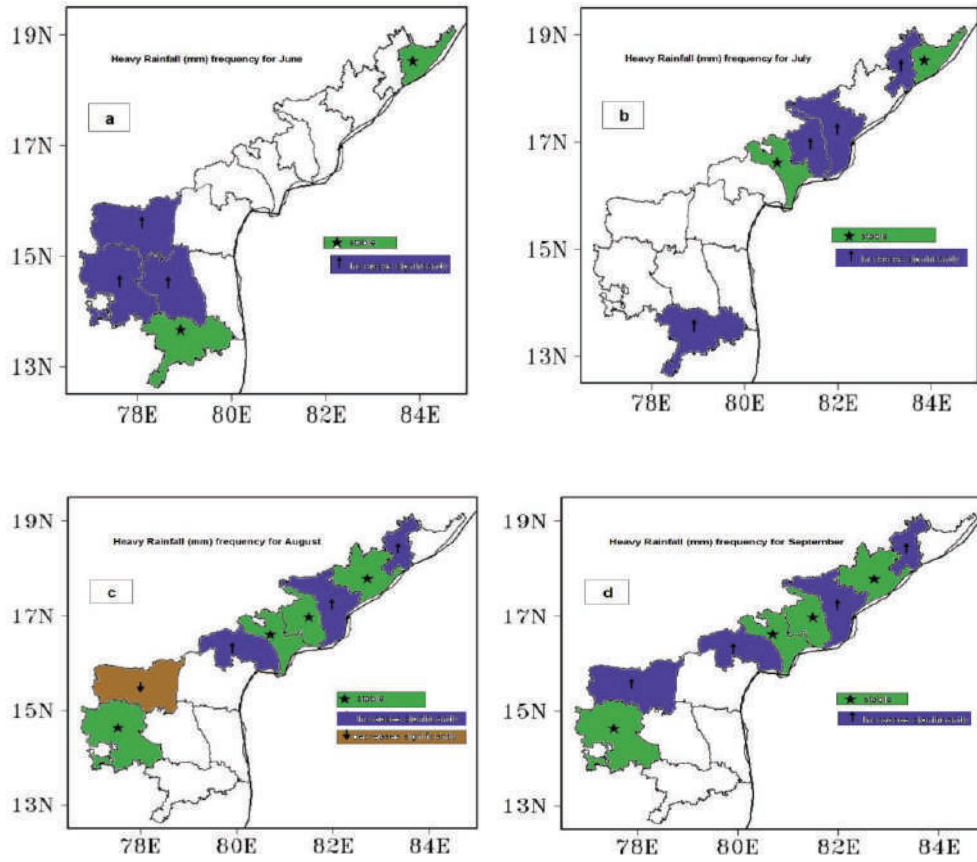


Fig. 6: Trend in an average frequency of heavy rainfall days.

central and southern parts of the state. However, Kurnool recorded the highest average number of very high rainfall days (1.72) in September for the entire study period.

There is no significant trend in very high rainfall days in the entire state most of the time. In August, Guntur recorded a decreasing trend. In September, an increasing trend in northern districts such as Krishna, Srikakulam, and West Godavari was observed at a 5% significant level.

The state's northern districts recorded extremely heavy rainfall days in the study period. West Godavari recorded extremely heavy rainfall events in June (1), July (1), and August (3). East Godavari (1 day) and Kadapa (1 day) were recorded in August, while Vizianagaram (4), Visakhapatnam (3), and Guntur (2) recorded the same in September.

## Pearson Correlation Between Crop Yield and Rainfall

Table 3 presents Pearson's correlation coefficients between crop yields and rainfall during the season in the districts of Andhra Pradesh. It can be easily noticed that rainfall is strongly and positively correlated with three major crop

Table 3: Pearson correlation matrix for mean rainfall and crop yield (district/crop-wise).

| **District** | Crop | | | |
|---|---|---|---|---|
| | Rice | Groundnut | Maize | Bajra |
| East Godavari | 0.27 | 0.77 | 0.29 | -0.09 |
| Guntur | 0.33 | 0.6 | 0.66 | -0.18 |
| Krishna | 0.26 | 0.09 | 0.25 | ND |
| Nellore | 0.21 | 0.03 | -0.02 | 0.1 |
| Prakasam | 0.068 | 0.17 | 0.33 | 0.62 |
| Srikakulam | 0.42 | -0.67 | 0.67 | 0.2 |
| Visakhapatnam | 0.57 | 0.55 | 0.19 | 0.55 |
| Vizianagaram | 0.69 | -0.11 | 0.61 | 0.72 |
| West Godavari | 0.3 | 0.62 | 0.46 | ND |
| Anantapur | 0.16 | 0.78 | 0.34 | 0.64 |
| Chittoor | 0.17 | 0.67 | 0.58 | 0.12 |
| Kadapa | -0.56 | 0.62 | 0.6 | 0.13 |
| Kurnool | 0.3 | -0.02 | 0.68 | 0.8 |

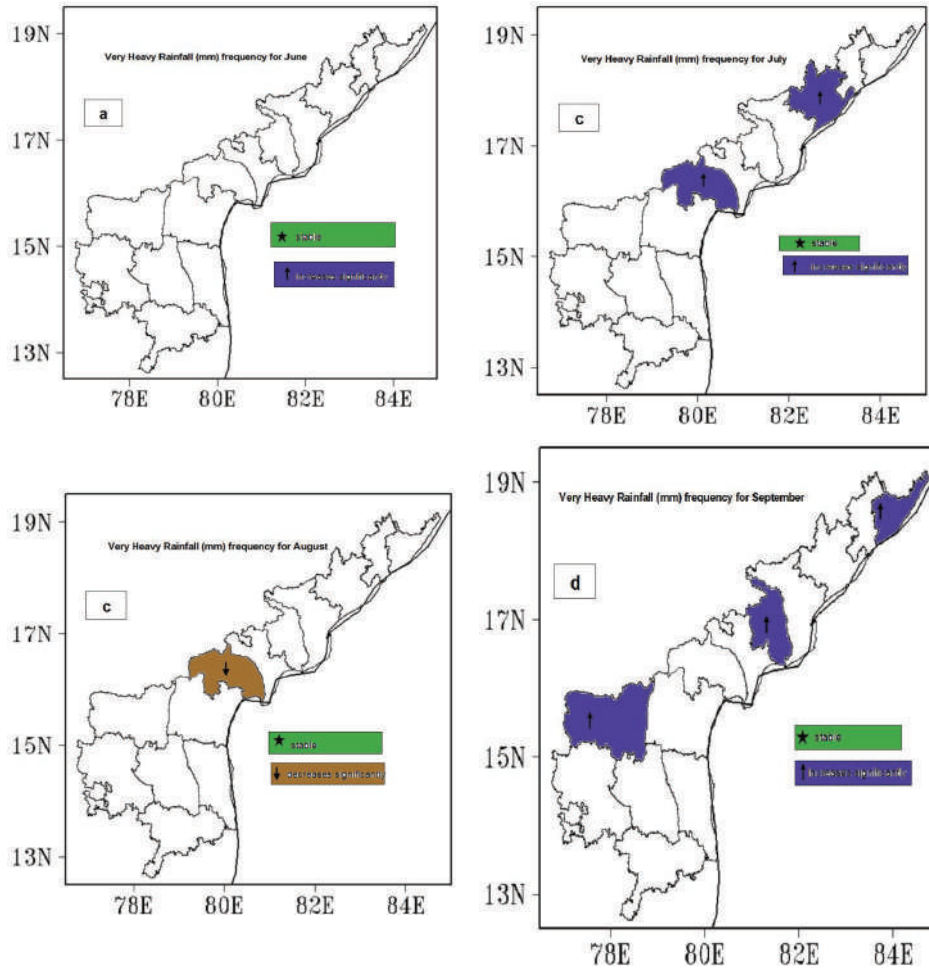


Fig. 7: Trend in the average frequency of very heavy rainfall days.

yields: rice, maize, bajra (R > 0.61), and rice, groundnut, and bajra (R > 0.55) in the districts of Vizianagaram and Visakhapatnam respectively. R > 0.58 is also found between groundnut, maize, and rainfall in Chittoor and Kadapa and with groundnut and bajra in Anantapur. A strong positive correlation of rainfall with groundnut and bajra yields is observed for Anantapur (R = 0.78), Guntur (R = 0.78), and Kurnool (0.8). Negative correlations also exist between crop yields and rainfall. Among the districts, the rainfall has less impact on the four crop yields in Krishna and Nellore while a strong impact is observed with three crop yields in Visakhapatnam and Vizianagaram.

## CONCLUSIONS

The study brought significant features of rainfall patterns during the present decade for the state of Andhra Pradesh. The study helps in regional planning and management of water resources and farming operations.

i) September month contributes to the highest monsoon rainfall (28.5%), followed closely by August (27.5%), July (26.3%), and June (17.7%). Monthly and seasonal rainfall exhibited an upward trend. The trend is upward and moderately significant during September and the entire monsoon season. East Godavari received the highest rainfall in June, July, and August and Anantapur received the same in September.

ii) Increasing propensity of rainfall in September is quite apparent during the recent decade 2011-2020. The contribution of September rainfall is more than any other month (June to August) of Southwest Monsoon. The excess rainfall and longer wet period of September will adversely affect the standing crops. Hence, it needs to be examined whether there is an imminent need to change crop calendars for certain important crops. However, other factors such as temperature and precipitation may

also influence crop yields, and these factors are not considered in this study.

iii) West Godavari received the highest mean rainfall, 207.8mm, during the monsoon season, and exhibited an increasing trend in September. Kurnool and Chittoor districts registered an increasing trend in mean rainfall days at a 5% significance level in June and September.

iv) The average frequency of rainy days varied between 6 and 20 in the entire monsoon season except in June. Guntur and Srikakulam indicated a stable trend in the average frequency of rainy days for the monsoon season.

v) The state's northern districts, West Godavari, Vizianagaram, Srikakulam, Krishna, and Districts of Rayalaseema region Anantapur, Kadapa, and Kurnool recorded average heavy rainfall days (2.27-6.90) for the entire monsoon season. East Godavari, Kurnool, Kadapa, and Chittoor showed an increasing trend in average heavy rainfall days compared to other districts of the state. There is no trend in the central districts except Guntur in August and Prakasam in September.

vi) The average frequency of very heavy rainfall days for the monsoon season indicates that the northern districts received higher heavy rainfall days than the central and southern parts of the state. However, Kurnool recorded the highest average number of very high rainfall days (1.72) in September for the entire study period. There is no significant trend in very high rainfall days in the entire state for most of the time

vii) Among the districts, the rainfall has less impact on the crop yields in Krishna and Nellore while a strong impact is observed with three crop yields in Visakhapatnam and Vizianagaram districts.

## ACKNOWLEDGEMENT

The authors profusely thank the IMD and the APS. DAC, MoAFW, Government of India. The authors also acknowledge the usage of rainfall data from their data sources. Thanks, are also due to anonymous reviewers for their valuable suggestions for revamping and reforming the content of the paper.

## REFERENCES

Aruna Jyothy, S., Srinivasa Murthy, D. and Mallikarjuna, P. 2021. Climate change impacts on seasonal rainfall trends in the regions of Andhra Pradesh and Telangana states, India. J. Inst. Eng. India Ser. A., 102: 673-685, https://doi.org/10.1007/s40030-021-00545-w

Baig, M., Shahfahad, W.N., Mohd, A., Aijaz, A.S. and Rahman, A. 2022. Spatio-temporal analysis of precipitation pattern and trend using standardized precipitation index and Mann–Kendall test in coastal Andhra Pradesh. Model. Earth Syst. Environ., 8:2733-2752.

Dash, S.K., Kulkarni, M.A., Mohanty, U.C. and Prasad, K. 2009. Changes in the characteristics of rain events in India. J. Geophys. Res., 114:1-12.

Goswami, B.N., Venugopal, V., Sengupta, D., Madhusoodanan, M.S. and Xavier, P.K. 2006. Increasing trend of extreme rain events over India in a warming environment. Science, 314:1442-1445.

Guhathakurta, P. and Rajeevan, M. 2006. Trends in the rainfall pattern over India. Natl. Clim. Centre Rep., 2:1-25.

Krishna Kumar, K., Rupa Kumar, K., Ashrit, R.G., Deshpande, N.R. and Hansen, J.W. 2004. Climate impacts on Indian agriculture. Int. J. Climatol., 24: 1375-1393.

Mallick, K., Mukherjee, J., Bal, S.K., Bhalla, S.S. and Hundal, S.S. 2007. Real time rice yield forecasting over central Punjab region using crop weather regression model. J. Agrometeorol., 9: 158-166.

Mukherjee, J., Bal, S.K. and Bhalla, S.S. 2005. Temporal climatic variations in sub-mountain region of Punjab. Indian J. Ecol., 32: 36-38.

Rajwade, Y., Waghaye, A., Randhe, R. and Kumari, N. 2018. Trend analysis and change point detection of rainfall of Andhra Pradesh and Telangana. J. Agrometeorol., 20(2): 160-163.

Rao, V.U.M., Bapuji Rao, B., Subbarao, A.V.M., Manikandan, N. and Venkateswarlu, B. 2011. Assessment of rainfall trends at micro and macro level in Andhra Pradesh. J. Agrometeorol., 13(2): 80-85.

Ray, K., Arora, K. and Srivastav, A. K. 2019. Weather extremes and agriculture. Int. Arch. Photogramm. Remote Sens. Spatial Inform. Sci., 6: 493-497.

Vijay, K., Sharad, K.J. and Yatveer, S. 2010. Analysis of long-term rainfall trends in India. Hydrol. Sci. J., 4)55): 484-496.

Nature Environment and Pollution Technology
An International Quarterly Scientific Journal

p-ISSN: 0972-6268
(Print copies up to 2016)
e-ISSN: 2395-3454

Vol. 22 | No. 1 | pp. 109-118 | 2023

Original Research Paper

https://doi.org/10.46488/NEPT.2023.v22i01.009

Open Access Journal

# Retention Behaviour of Heavy Metals from Industrial Sludge Amended with Admixtures to Use Them as Liners for Landfill Facilities

**S. S. S. Saranya*†, S. N. Maya Naik* and Shankara****
*Department of Civil Engineering, BMS College of Engineering, Bengaluru, India
**Department of Civil Engineering, Amrita School of Engineering, Bengaluru, India
†Corresponding author: S. S. S. Saranya; saranyasagiri8@gmail.com

**Nat. Env. & Poll. Tech.**
**Website: www.neptjournal.com**

*Received:* 28-03-2022
*Revised:* 13-05-2022
*Accepted:* 16-05-2022

**Key Words:**
Heavy metals
Industrial sludge
Leaching test
Lime and Solidification

## ABSTRACT

The solidification of contaminants within the soil/waste has proved to be a versatile technique to de-contaminate them and make them usable for several applications. In this method, the development of binder provisions leads to the conversion of the environmentally unstable condition of waste materials into a nearly stable material. Further, these materials pose a minimum threat that can be absorbed into the environment. Normally lime/cement and other pozzolanic materials are used as binder materials. In this work, it is proposed to use the efficiency of binding fly ash to improve the unconfined compressive strength (UCC) of soils, particularly during the curing period. This is because improvement in strength is a reflection of the improvement of bonding soil particles. Fly ash as the main source material, in addition to a minor proportion of cement and lime, is used to determine the strength. UCC test results revealed that as the percentage of fly ash increases there is an increase in compressive strength. It is also observed that with an increase in lime content and an increase in cement content, the UCC strength also increases. The strength in cement-stabilized compacted specimens is more compared to lime-stabilized mixtures. To confirm that the improvement in strength is related to the solidification of contaminated metals, particularly for soils containing copper and chromium, the stabilized mixture is tested for the leaching of these metals. Leaching tests were conducted on various stabilized mixtures at different curing periods. The leachate was examined for metal ion concentration using Atomic Absorption Spectrophotometer. The leaching behavior of heavy metals from different proportions of soil matrix revealed that with an increase in lime or cement percentage, a decrease in leachability is observed. It is found that the leaching of heavy metals from cement-stabilized soils was lower than in lime mixture combinations. However, minimum strength improves the solidification and retention of heavy metals effectively.

## INTRODUCTION

Urbanization/industrialization and the economy of a country are always interconnected. Industrial operations are linked to environmental pollution. Therefore, various types of waste generated in the industry require treatment for their disposal facilities. A treatment facility concentrates/separates all the wastes and generates sludges and solid wastes. These end products at treatment facilities, are either hazardous or non-hazardous but consist of organic and/or inorganic substances (Voglar & Lestan 2011). Developed/industrialized countries export their wastes to developing countries due to their strict environmental regulations that make waste management in developed countries expensive compared to exporting wastes to developing countries where environmental regulations are lax and waste disposal is safe. Disposal and re-processing of these wastes have resulted in various contamination issues in soils in developing countries (Moon & Dermatas 2006). The impact of hazardous wastes on human wellness and strict policies for disposing of hazardous waste on land is leading to the development of scientific management of hazardous waste facilities like sanitary landfill areas, S/S techniques, etc. Methods to dispose of industrial waste have their limitations based on the properties of wastes, policies, the cost involved, and technology. The S/S technology has given relief in many directions from all the limitations of industrial waste treatment disposals and their complexities. Heavy metals like nickel, arsenic, copper, chromium, cadmium, zinc, and mercury are extremely toxic even at low concentrations or beyond the pollution control board's limits (Minocha et al. 2003, Wentz 2005).

Previous works on solidification/stabilization (S/S) processes have clearly shown that the technique applies to most metallic waste streams. This technique involves blending the waste along a binder material to enrich the

**ORCID details of the authors:**

**S. S. S. Saranya**
https://orcid.org/0000-0003-4919-366X

physical properties of the waste and immobilize contaminants that are a threat to humans and the environment (Sivapullaiah & Arif 2010, Malviya & Chaudhary 2006).

The solidification/stabilization technique involves physical and chemical actions to produce environmentally stable substances with enhanced pollutant holding capacity. Wastes containing inorganic contaminants normally require pre-treatment before disposing of in a sanitary landfill (Voglar & Lestan 2011, Shankara et al. 2012). The solidification/stabilization technique is being used all over the world to arrest the harmful contaminants that are present in various waste streams particularly industrial sludge by amending with fly ash, lime, and cement (Shankara et al. 2015, 2014a, 2014b). The challenging part of S/S technology is to quantify the reduction of negative environmental impacts in the real world after the treatment, proper disposal, reuse options, and so on. It is documented that the S/S technology is useful to treat sludge, solid waste contaminated sites, and other waste streams containing harmful heavy metals and metalloids. The in-situ steps are the mixing of binders and other materials directly with said waste streams/contaminated soils to obtain solid material that has transformed into low leachability characteristics compared to the original state (Venkata Ramaiah et al. 2014). The focus of the present work is to explore the practicability and efficacy of fly ash, soil, and other binders in stabilizing the toxic sludge collected from the Federal mogul industry. Unconfined compressive strength (UCC) tests were conducted for stabilizing the sludge and to obtain a minimum compressive strength required for disposal at a landfill site. Leaching tests were carried out to assess the leaching potential of metal ions from the sludge and the resulting leachates were analyzed for various heavy metal ions.

## MATERIALS AND METHODS

In this paper an effort has been made to provide important insights on the compressive strength of the stabilized mixes and retention behavior of copper and chromium ions that are present in industrial sludge and the same has been evaluated using additives such as fly ash, lime, and cement blended with soil. The leaching tests were performed on stabilized mixtures at different curing periods for various combinations of additives and sludge.

### Sludge

The sludge used in the present study was collected from the Federal-Mogul industry, situated in Yelahanka, Bangalore, with the generous consent of the Karnataka State Pollution Control Board. The toxic sludge obtained was so rich in chromium ions that it was considered in the category of hazardous waste and needs special care during the stabilization/solidification process so that it can convert the unstable condition of heavy metal ions into a stabilized state of ions within the stabilized soil matrix. Further, the stabilized industrial sludge can be disposed of in scientifically designed sanitary landfills. The collected sludge was characterized for $p^H$, moisture content, and concentration of heavy metal ions at the Bangalore test house. Table 1 shows the results of the characterization of the sludge.

Table 1: Properties of industrial sludge.

| S. No | Parameter | Unit | Value |
|---|---|---|---|
| 1. | pH | - | 2.7 |
| 2. | Moisture content | [%] | 9.5 |
| 3. | Chromium | [mg.kg$^{-1}$] | 90.5 |
| 4. | Nickel | [mg.kg$^{-1}$] | 7.3 |
| 5. | Copper | [mg.kg$^{-1}$] | 24.2 |
| 6. | Aluminum | [mg.kg$^{-1}$] | 82.9 |

Source results obtained from Bangalore Test House, Bangalore

### Fly Ash

Fly ash is a by-product of coal-fired power stations. Fly ash

Table 2: Physical properties of fly ash (Venkata Ramaiah et al. 2014).

| S. No. | Physical Property | Value |
|---|---|---|
| 1. | Specific gravity G | 2.0 |
| 2. | Liquid Limit (LL) [%] | 35.0 |
| 3. | Plastic Limit(PL) [%] | -- |
| 4. | Plasticity Index(PI) [%] | -- |
| 5. | Shrinkage Limit (SL) [%] | 18.5 |
| | Compaction Characteristics | |
| 1. | Maximum dry density (MDD) [KN.m$^{-3}$] | 11.7 |
| 2. | Optimum moisture content (OMC) [%] | 25.0 |
| | Grain size distribution | |
| 1. | Gravel [%] | 00.0 |
| 2. | Sand [%] | 58.0 |
| 3. | Silt and clay [%] | 42.0 |

Table 3: Chemical composition of fly ash.

| S. No. | Constituents | Percentage [%] |
|---|---|---|
| 1. | $SiO_2$ | 61.1 |
| 2. | $Al_2O_3$ | 28.0 |
| 3. | $TiO_2$ | 1.3 |
| 4. | $Fe_2O_3$ | 4.2 |
| 5 | MgO | 0.8 |
| 6. | CaO | 1.7 |
| 7. | $K_2O$ | 0.2 |
| 8. | $Na_2O$ | 0.2 |
| 9. | L.O.I | 1.4 |

Table 4: Properties of black cotton soil.

| S. No. | Property | | Value |
|---|---|---|---|
| 1. | Specific gravity G | | 2.7 |
| 2. | Grain size Analysis | Clay (C) [%] | 54.2 |
| | | Silt (M) [%] | 16.1 |
| | | Sand (S) [%] | 26.7 |
| | | Gravel (G) [%] | 3.3 |
| 3. | Consistency limits | Liquid limit (LL) [%] | 49.1 |
| | | Plastic limit (PL) [%] | 18.4 |
| | | Plasticity index(PI) [%] | 21.3 |
| | | Shrinkage limit (SL) [%] | 8.9 |
| 4. | Compaction characteristics (Proctor's) | Optimum moisture content (OMC) [%] | 22.0 |
| | | Maximum dry density (MDD) $g.cm^{3-}$ | 2.1 |

used in the present research work is collected from Raichur Thermal Power Station (RTPS), in Karnataka, India. The fly ash used was classified as class "F" category and was grey in color. The physical properties and chemical composition of fly ash are given in Tables 2 and 3.

## Soil

The black cotton soil (BCS) used was collected from Harihara in Karnataka state. The (BCS) is preferred as it contains more silt and clay which conveys plasticity properties in the process of stabilization. The topsoil was removed to a depth of 0.5m before the soil samples were taken by the undisturbed sampling method. Before pulverizing, the soil sample was oven-dried for 24 h to obtain soil particles that could pass through a sieve with a 4.75 mm aperture. The compaction characteristics and physical properties of the BCS are given in Table 4.

## Cement and Lime

The cement and lime used in the present study were procured from local distributors in Bangalore, Karnataka.

## Preparation of Sample and Mix Proportions

The sludge, fly ash and soil were oven-dried for 24 h at 105°C and sieved using 4.75 mm to avoid the coarser materials. Different proportions were prepared by mixing all the ingredients as shown in Table 4a. A total of 20 mixes were prepared with one control set of mixes in each series.

The series of mixes are labeled indicating Fly ash: F, Soil: S, Sludge: SL, Lime: L, and Cement: C. For example,

Table 4a: Mix proportions.

| S. No. | Specimen | Fly ash | Soil | Sludge | Lime | Cement |
|---|---|---|---|---|---|---|
| | | % | % | % | % | % |
| 1. | 10F90S | 10 | 90 | - | - | - |
| 2. | 10F85S5SL | 10 | 85 | 5 | - | - |
| 3. | 10F80S10SL | 10 | 80 | 10 | - | - |
| 4. | 10F75S15SL | 10 | 75 | 15 | - | - |
| 5. | 10F70S20SL | 10 | 70 | 20 | - | - |
| 6. | 20F80S | 20 | 80 | - | - | - |
| 7. | 20F75S5SL | 20 | 75 | 5 | - | - |
| 8. | 20F70S10SL | 20 | 70 | 10 | - | - |
| 9. | 20F65S15SL | 20 | 65 | 15 | - | - |
| 10. | 20F60S20SL | 20 | 60 | 20 | - | - |
| 11. | 30F40S30SL | 30 | 40 | 30 | - | - |
| 12. | 30F36S30SL4L | 30 | 36 | 30 | 4 | - |
| 13. | 30F32S30SL8L | 30 | 32 | 30 | 8 | - |
| 14. | 30F28S30SL12L | 30 | 28 | 30 | 12 | - |
| 15. | 30F24S30SL16L | 30 | 24 | 30 | 16 | - |
| 16. | 30F40S30SL | 30 | 40 | 30 | - | - |
| 17. | 30F36S30SL4C | 30 | 36 | 30 | - | 4 |
| 18. | 30F32S30SL8C | 30 | 32 | 30 | - | 8 |
| 19. | 30F28S30SL12C | 30 | 28 | 30 | - | 12 |
| 20. | 30F24S30SL16C | 30 | 24 | 30 | - | 16 |

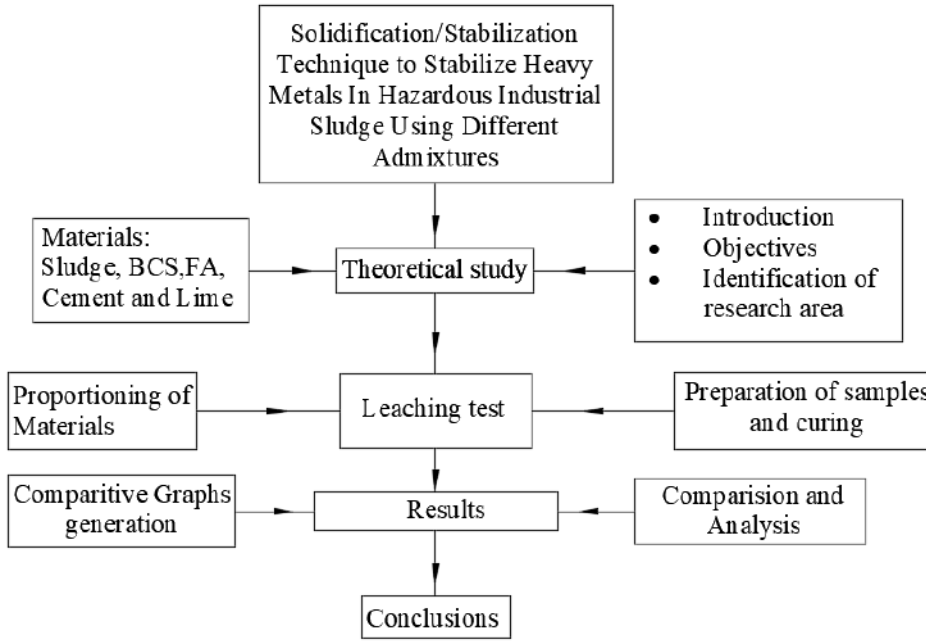


Fig. 1: Methodology used in the study.

30F36S40SL4C indicates a mixture of 30% fly ash, 36% soil, 40% sludge, and 4% cement.

Each combination of the series was compacted in a split mold and prepared cylindrical specimens (7.6 mm and diameter of 3.8mm) and cured for 1, 7, 14, and 28 days. The specimens are stored in sealed sample bags and just after the predetermined curing periods, the unconfined compressive strength was determined. The tested specimens are powdered and passed through a 4.75 mm sieve and the leaching test was conducted using the ASTM D3987-85 procedure. The leachate obtained after the test was analyzed for concentrations of the ions using an Atomic Absorption Spectrophotometer (AAS). The methodology followed in this study has been adopted and presented in the form of a flow diagram presented in Fig. 1.

## RESULTS AND DISCUSSION

After completing the experimental work, the results obtained are tabulated concerning specified series, and the values are used to generate graphs. UCC test was conducted on different proportions of black cotton soil, sludge, and fly ash with and without the addition of lime in a small percentage, and the strength parameter is investigated. Among various recommendations for the minimum compressive strength required for solid waste disposal at landfill sites, 0.3 MPa is one according to the Resource Conservation and Recovery Act (RCRA). The efficiency and practicability of the containment of the heavy metal ions in the S/S method are measured by the leaching test of stabilized mixtures. There are various leaching-related documents available in this area, but it is very difficult to get the complex leaching behavior that involves surface complexation reactions.

### Unconfined Compressive Strength of Fly Ash, Soil and Sludge Mixtures with Lime and Cement as Additives

**Unconfined compressive strength of soil and sludge mixtures with 10% fly ash:** Unconfined compressive strength tests were conducted on mixtures with 10% fly ash and varying proportions of soil and sludge. Sample "10F90S" is a blank (control) without the addition of sludge whereas for other samples the percentage of sludge increased from 5 to 20% and the respective strength of the specimens at 1, 7, 14, and 28 days of curing are presented in Table 5.

Fig. 2 shows the trend of UCC concerning varying days of curing. It is observed that the highest compressive strength is obtained for the control sample (10F90S) whereas the

Table 5: Unconfined compressive strength of soil and sludge mixtures with 10% fly ash.

| Series of mixes | UCC strength in kPa | | | |
|---|---|---|---|---|
| | 1-Day | 7-Day | 14-Day | 28-Day |
| 10F90S | 184 | 211 | 242 | 255 |
| 10F85S5SL | 176 | 202 | 230 | 247 |
| 10F80S10SL | 163 | 190 | 222 | 235 |
| 10F75S15SL | 151 | 176 | 201 | 219 |
| 10F70S20SL | 134 | 160 | 179 | 192 |

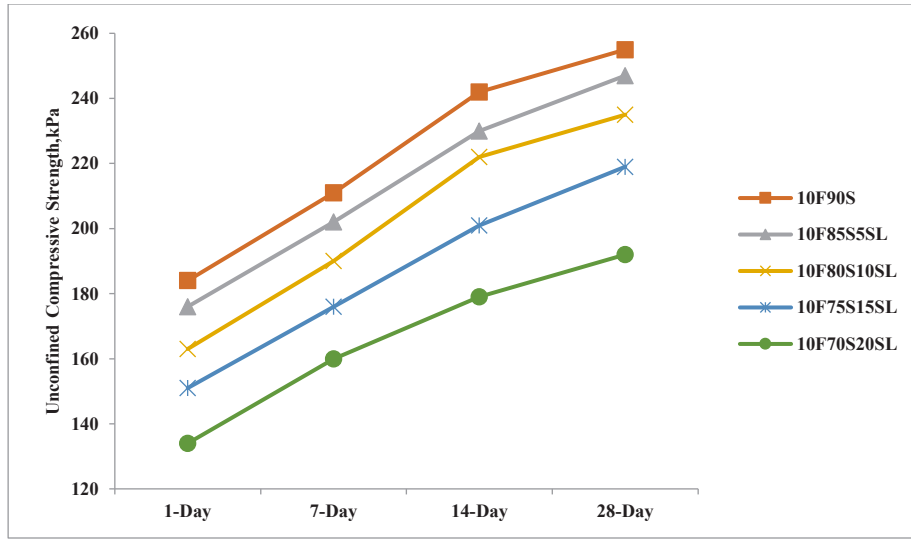


Fig. 2: Unconfined compressive strength of soil and sludge mixtures with 10% fly ash.

Table 6: Unconfined compressive strength of soil and sludge mixtures with 20% fly ash.

| Series of mixes | UCC strength in kPa | | | |
|---|---|---|---|---|
| | 1-Day | 7-Day | 14-Day | 28-Day |
| 20F80S | 252 | 277 | 305 | 318 |
| 20F75S5SL | 238 | 268 | 297 | 308 |
| 20F70S10SL | 219 | 247 | 272 | 286 |
| 20F65S15SL | 199 | 219 | 240 | 258 |
| 20F60S20SL | 194 | 211 | 232 | 243 |

addition of 5,10,15 and 20% of sludge by weight resulted in a decrease in UCC strength. Reduced compressive strength with an increase in sludge percentage can be due to the changes in pore fluid viscosity and the effect of enhanced lubrication by an excessive amount of moisture present in the sludge. Also, the decrease in strength can be due to the physio-chemical effects caused by the dielectric constant.

**Unconfined compressive strength of soil and sludge mixtures with 20% fly ash:** UCC strength test results for a set of series with 20% fly ash and varying proportions of soil and sludge are shown in Table 6. Sample "20F80S" is a blank (control) without the addition of sludge, whereas for other samples the percentage of sludge increased from 5 to 20% by weight. From Fig. 3, plotted between UCC strength and the curing period, it is noticed that the compressive strength decreases with an increase in the percentage of sludge.

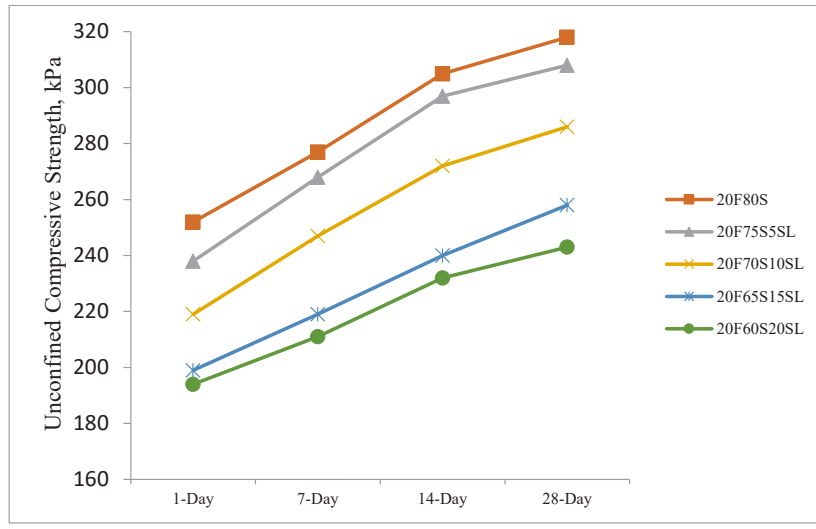


Fig. 3: Unconfined compressive strength of soil and sludge mixtures with 20% fly ash.

Table 7: Unconfined compressive strength of soil, sludge mixtures with 30% fly ash and varying percentage of lime.

| Series of mixes | UCC strength in kPa | | | |
|---|---|---|---|---|
| | 1-Day | 7-Day | 14-Day | 28-Day |
| 30F40S30SL | 202 | 228 | 250 | 265 |
| 30F36S30SL4L | 218 | 243 | 271 | 284 |
| 30F32S30SL8L | 236 | 258 | 284 | 299 |
| 30F28S30SL12L | 262 | 281 | 310 | 320 |
| 30F24S30SL16L | 274 | 295 | 321 | 336 |

Table 8: Unconfined compressive strength of soil, sludge mixtures with 30% fly ash, and varying percentage of cement.

| Series of mixes | UCC strength in kPa | | | |
|---|---|---|---|---|
| | 1-Day | 7-Day | 14-Day | 28-Day |
| 30F40S30SL | 203 | 229 | 251 | 265 |
| 30F36S30SL4C | 225 | 238 | 269 | 288 |
| 30F32S30SL8C | 245 | 262 | 294 | 325 |
| 30F28S30SL12C | 277 | 288 | 315 | 348 |
| 30F24S30SL16C | 290 | 304 | 337 | 375 |

**Unconfined compressive strength of soil, sludge mixtures with 30% fly ash, and varying percentage of lime:** UCC strength test results for the soil, sludge mixtures with 30% fly ash, and varying percentages of lime are shown in Table 7. Sample "30F40S30SL" is a blank (control) sample without the addition of lime, whereas for other samples the percentage addition of lime increases from 4 to 16% by weight. From Fig. 4, plotted between the unconfined compressive strength with respect to 1, 7, 14, and 28 days of curing, it is noticed that with an increase in lime percentage, the pozzolanic compounds are formed that bind the soil particles and results in an increase in compressive strength.

**Unconfined compressive strength of soil, sludge mixtures with 30% fly ash, and varying percentage of cement:** UCC strength test was carried out for the soil, sludge mixtures with 30% fly ash, and varying percentage of cement. Sample "30F40S30SL" is a blank (control) sample without the addition of cement, whereas for other samples the percentage addition of cement increases from 4 to 16% by weight and the respective compressive strengths at 1, 7, 14, and 28 days are shown in Table 8. From Fig. 5 plotted between UCC strength and the curing period, it is observed that the compressive strength increases with an increase in the cement percentage from 4 to 16, which results in the formation of pozzolanic compounds that bind the soil particles and result in strength increment.

## Leaching of Chromium in Soil, Sludge Mixtures with 30% Fly Ash, and Varying Percentage of Lime

The soil, sludge mixtures with 30% fly ash and varying percentage of lime starts with a control specimen of a mixture of 40% of BCS, 30% of fly ash, and 30% of industrial sludge. The other four specimens represent the percentage of lime increased from 4 to 16% as given in Table 4.

It can be seen from Fig. 6 that as the percentage of lime and the curing period increases the leaching of chromium

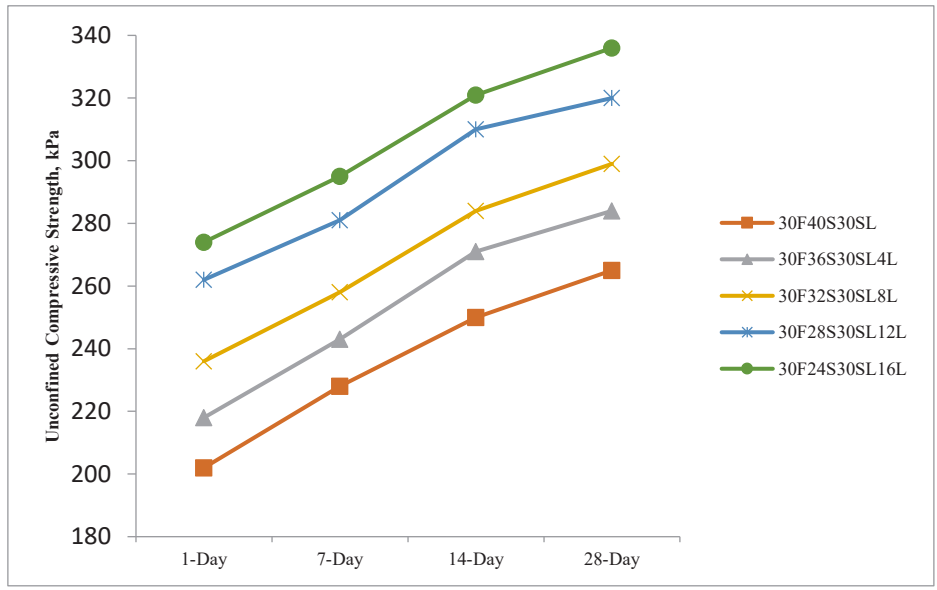


Fig. 4: Unconfined compressive strength of soil, sludge mixtures with 30% fly ash, and varying percentage of lime.

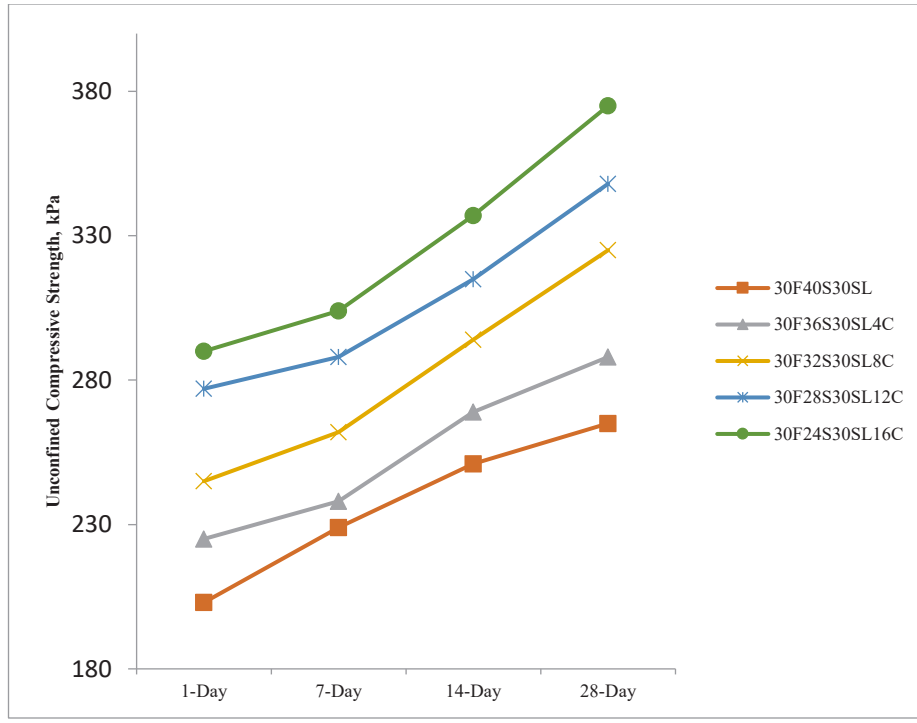


Fig. 5: Unconfined compressive strength of soil, sludge mixtures with 30% fly ash, and varying percentage of cement.

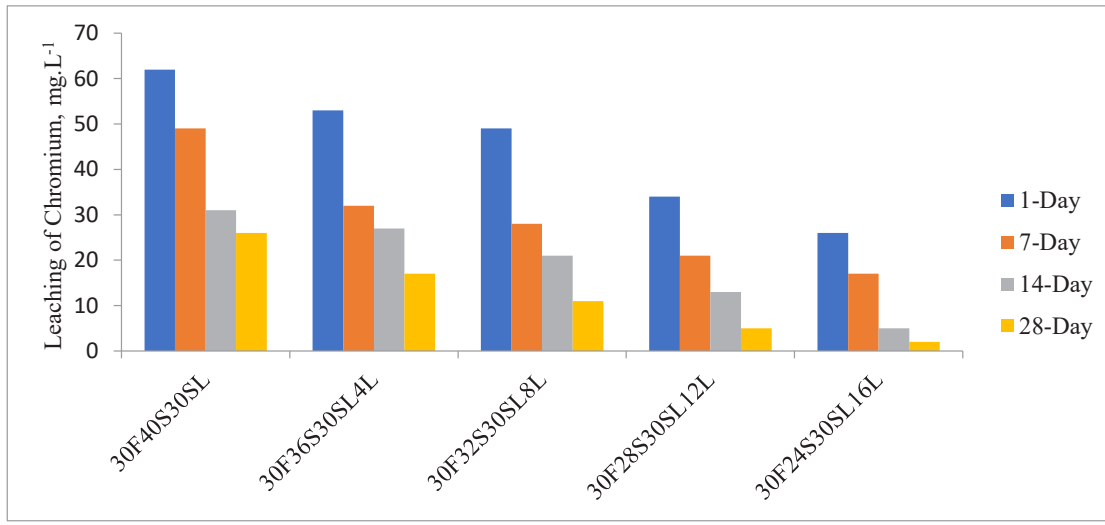


Fig. 6: Leaching of chromium in soil, sludge mixtures with 30% fly ash, and varying percentage of lime.

decreases. This retention behavior may be due to the formation of chromium hydroxide precipitate caused due to the increased lime content in the mixture and adsorption onto fly ash and BCS. The surface complexation and precipitation reactions are the reason behind the leaching behavior. It can also be seen that specimen 30F28S30SL12L gained the minimum leaching requirement of 5 mg.$L^{-1}$ at the curing of 28 days and the same is achieved by 30F24S30SL16L at 14 days of curing itself.

### Leaching of Chromium in Soil, Sludge Mixtures with 30% Fly Ash, and Varying Percentages of Cement

The soil, sludge mixtures with 30% fly ash and varying percentage of cement starts with a control specimen of mixtures of 40% of BCS, 30% of Fly ash, and 30% of industrial sludge. And other four specimens represent the percentage of cement increased from 4 to 16% as given

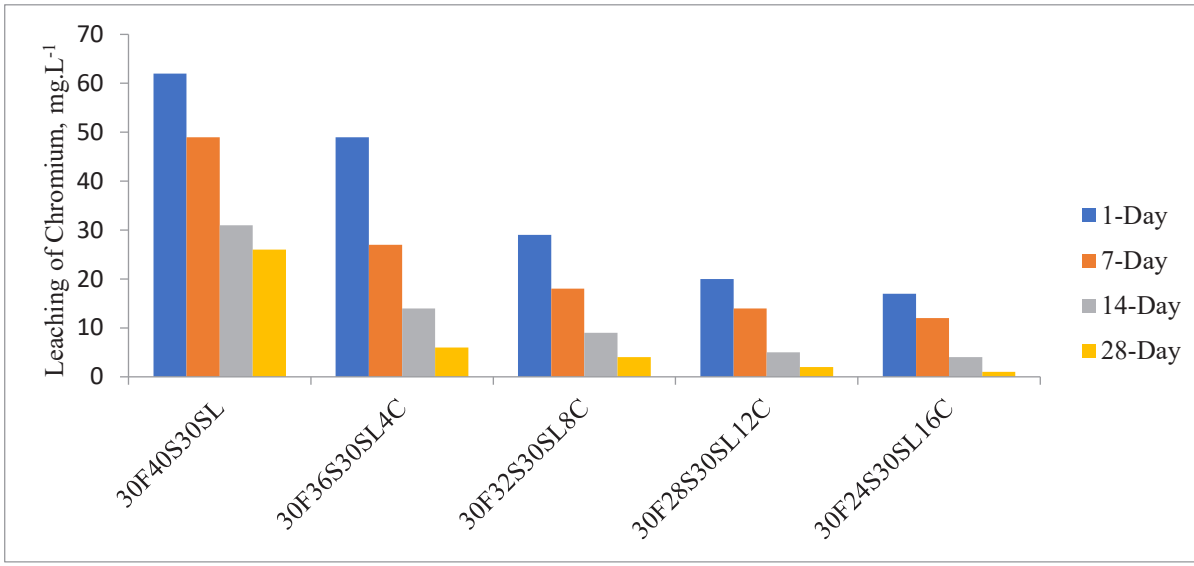


Fig. 7: Leaching of chromium in soil, sludge mixtures with 30% fly ash, and varying percentage of cement.

in Table 4. The leaching behavior of chromium against different curing periods has been presented in Fig. 7. It can be seen in the graph that as the percentage of cement and curing period increases the leaching of chromium decreases. This retention behavior may be due to the formation of hydroxide precipitate caused due to increase in cement content in the mixture and adsorption onto fly ash and BCS. The surface complexation and precipitation reactions are the reason behind the leaching behavior. It can also be seen that specimen 30F28S30SL12C established the minimum leaching requirement of 5 mg.$L^{-1}$ at the curing of 28 days and the same is achieved by 30F24S30SL16C at 14 days of curing itself.

This reduction in the leachability of chromium with an increase in the percentage of cement is observed because of hydrolysis and a series of chemical complexes developed over the time of curing.

### Leaching of Copper in Soil, Sludge Mixtures with 30% Fly Ash, and Varying Percentages of Lime

The soil and sludge mixtures with 30% fly ash and varying percentages of lime start with a control specimen of mixtures of 40% of BCS, 30% of fly ash, and 30% of industrial sludge. And other four specimens represent an increase in lime percentage from 4 to 16%. It can be noticed that

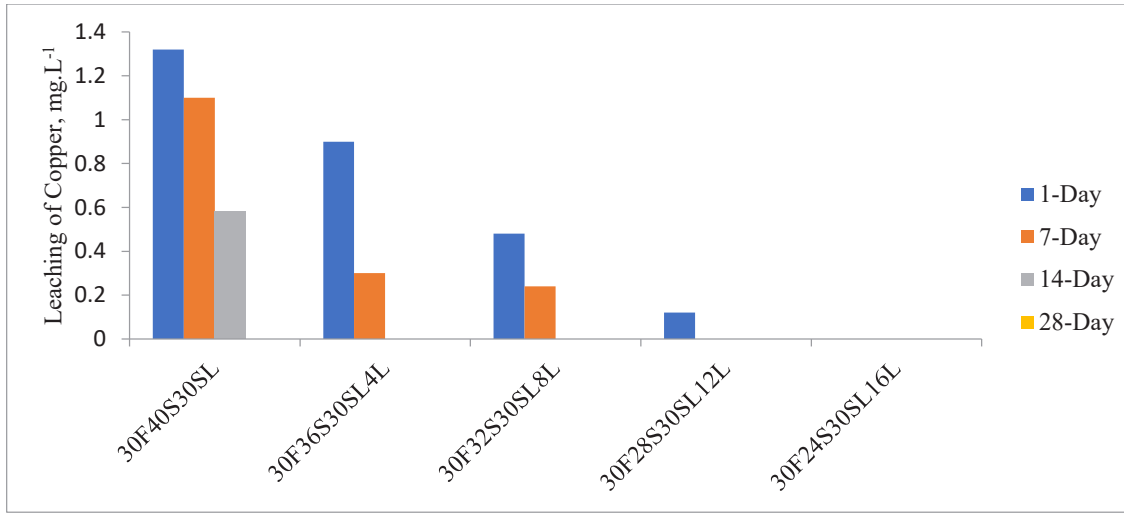


Fig. 8: Leaching of copper in soil, sludge mixtures with 30% fly ash, and varying percentage of lime.

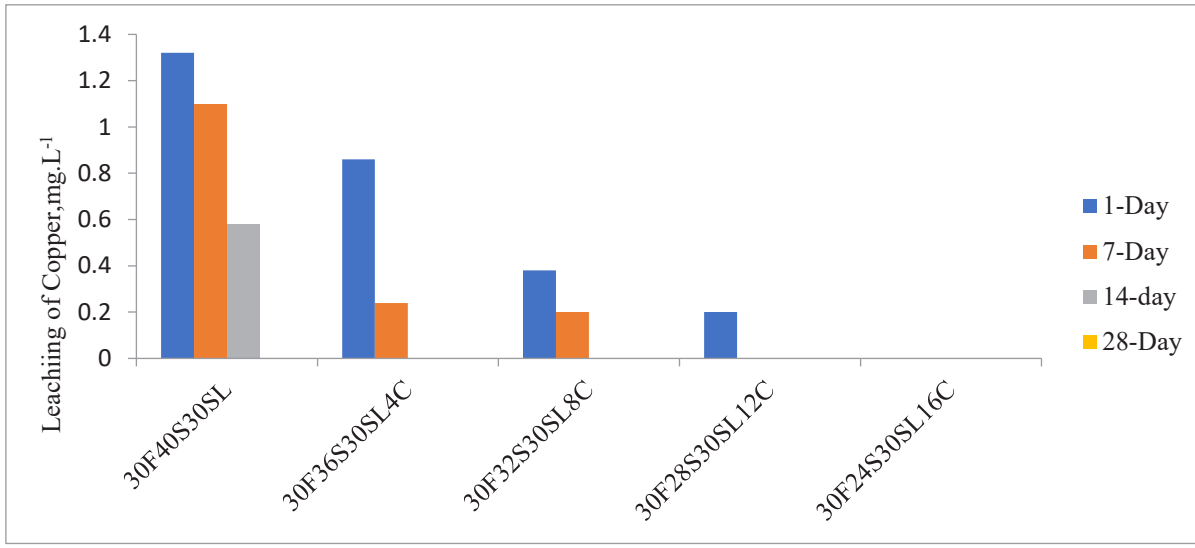


Fig. 9: Leaching of copper in soil, sludge mixtures with 30% fly ash and varying percentage of cement.

as the percentage of lime increases, a slight decrease in the leachability of copper is observed. The leaching behavior of chromium against the different curing periods has been presented in Fig. 8. It can be seen from the graph that as the percentage of lime and the curing period increases, the leaching of copper decreases. This retention behavior may be due to the precipitation of metal ions at higher $p^H$ that prevails due to the increased lime content in the mixture and adsorption onto fly ash and BCS. The surface complexation and precipitation reactions are the reason behind the leaching behavior.

### Leaching of Copper in soil, Sludge Mixtures with 30% Fly Ash, and Varying Percentage of Cement

The soil, sludge mixtures with 30% fly ash and varying percentage of cement starts with a control specimen of mixtures of 40% of BCS, 30% of fly ash, and 30% of industrial sludge. And other four specimens represent the percentage of cement increased from 4 to 16%. The combination of mixtures with an increase in cement from 4 to 16% has shown that the leaching of copper reduced drastically with an increased curing period. This may be because of the precipitation and a series of chemical complexes formed throughout curing time as depicted in Fig. 9. The stabilization process by the addition of cement is very effective at fixing copper ions and other ions. The 16% cement addition caused 100% efficiency to stop the leaching of copper as seen in the graph. It can also be noted from the graph that about 12% cement content in the matrix is enough to bring down the leaching of copper below 1 $mg.L^{-1}$.

### Comparison Between Leaching of Chromium and Copper at 28 Days Curing Period

From a comparative study on the leaching of chromium and copper in the soil, sludge and fly ash mixtures in addition to lime or cement at the curing of 28 days, it is noticed that the leaching decreases with an increase in lime or cement percentage (Table 9 and 10). The retention capacity is more in cement-stabilized mixtures when compared to lime-stabilized mixtures. Also, it is noticed that in both lime and cement stabilized mixtures 100% retention of copper is noticed at curing of 28 days.

Table 9: Leaching of chromium and copper in the soil, sludge, and fly ash mixtures with lime.

| Soil, sludge, and fly ash mixtures with lime | Leaching of chromium [$mg.L^{-1}$] | Leaching of copper [$mg.L^{-1}$] |
|---|---|---|
| 30F40S30SL | 26 | 0 |
| 30F36S30SL4L | 17 | 0 |
| 30F32S30SL8L | 11 | 0 |
| 30F28S30SL12L | 5 | 0 |
| 30F24S30SL16L | 2 | 0 |

Table 10: Leaching of chromium and copper in the soil, sludge and fly ash mixtures with cement.

| Soil, sludge, and fly ash mixtures with cement | Leaching of chromium [$mg.L^{-1}$] | Leaching of copper [$mg.L^{-1}$] |
|---|---|---|
| 30F40S30SL | 26 | 0 |
| 30F36S30SL4C | 6 | 0 |
| 30F32S30SL8C | 4 | 0 |
| 30F28S30SL12C | 2 | 0 |
| 30F24S30SL16C | 1 | 0 |

## CONCLUSIONS

Based on the results attained the UCC strength of the soil and sludge mixtures with 10% and 20% fly ash decreases with an increase in sludge content and the strength increases with an increase in fly ash percentage. The compounds formed due to pozzolanic reaction with the addition of fly ash, lime, and cement bind the soil particles increasing the strength of the soil. Also, an increase in $p^H$ increases the availability of reactive silica in soil which will react with the lime present and enhances the formation of pozzolanic compounds which increases the strength. Finally, it is noticed that the compressive strength of cement-stabilized mixtures was higher when compared to lime-stabilized mixtures and also attained a minimum compressive strength required for safe disposal at a landfill site. The leaching of chromium and copper ions from the leachate was observed from soil and sludge mixtures containing 30% fly ash with lime and cement as additives. In this work, the practicability and efficacy of the fly ash (FA), cement, lime, and soil in the treatment process of industrial sludge which is rich in heavy metal contamination for different proportions have been evaluated. The binders are also proved to be most adaptable to arrest the heavy metal ions and other pollutants present in the contaminated sludge. To check the leaching efficiency, the control mixture was maintained for both lime and cement combinations separately. According to leaching test results of mixtures with soil, sludge, and 30% fly ash in addition to lime and cement, the leaching of the heavy metals from different proportions of soil matrix revealed that with the increase in the lime or cement percentage, the leachability of the heavy metal ions decreases. With the addition of 4% lime at 28 days of curing, the leaching of chromium is 17 $mg.L^{-1}$ whereas the leaching of copper is 0 $mg.L^{-1}$ with the same mixture. With a 4% addition of cement at 28 days of curing, leaching of chromium was $mg.L^{-1,}$ and 0 $mg.L^{-1}$ of copper is observed for the same. The highest chromium retention is noticed in a series of 16% lime or 16% cement whereas the leaching of Copper is below 1 $mg.L^{-1}$ with an addition of 4% cement at 1 day. The relative precipitation of metal ions depends on the solubility product of metal hydroxide. The lower the solubility of the product, the higher the precipitation. It is also found that the leaching of heavy metals from cement-stabilized mixtures was much lower than in lime mixture combinations.

## REFERENCES

Malviya, R. and Chaudhary, R. 2006. Factors affecting hazardous waste solidification/stabilization: A review. J. Hazard. Mater., 22: 267-276.

Minocha, A.K., Jain, N. and Verma, C.L. 2003. Effect of inorganic materials on the solidification of heavy metal sludge. Cement Concr. Res., 33(10):1695-1701.

Moon, D.K. and Dermatas, D.2006. Arsenic and lead release from fly ash s/s soils under modified semi-dynamic leaching conditions. J. Hazard. Mater., 16(4): 388-394.

Shankara, S., Naik, M. and Puvvadi, S. 2014a. Modelling of the Cu and Fe transport in sand-bentonite and sand-fly ash mixtures. Int. J. Earth Sci. Eng., 7: 325-330.

Shankara, S., Naik, M. and Sivapullaiah, P.V. 2012. Studies on the use of sand-bentonite and sand-fly ash mixtures as prospective liner materials to retain iron and copper in aqueous solutions. Environ. Manag. Sustain. Develop., 16: 151-162.

Shankara, S., Naik, M. and Sivapullaiah, P.V. 2014b. Permeability of sand-bentonite and sand-fly ash mixtures. Asian J. Water Environ. Pollut., 11: 19-26.

Shankara, S., Prakash, N. and Sivapullaiah, P.V. 2015. Removal efficiencies of iron from different soils during different processes of electro-kinetic extraction. Poll. Res., 3: 97-105.

Sivapullaiah, P.V. and Arif Ali, M. 2010. Leachability of trace elements from two stabilized low lime Indian fly ashes. Environ. Earth Sci., 61: 1735-1744.

Venkata Ramaiah, G., Krishnaiah, S. and Naik, M. 2014. Leachate characterization and assessment of groundwater pollution near MSW dumpsite of Mavallipura, Bangalore. Int. J. Eng. Appl., 4: 267-271.

Voglar, E. And Lestan, M.N. 2011. Efficiency modelling of solidification/ stabilization of multi-metal contaminated industrial soil using cement and additives. J. Hazard. Mater., 192: 111-1136.

Wentz, R. 2005. Hazardous Waste Management. McGraw-Hill Book Company, New York.

Nature Environment and Pollution Technology
An International Quarterly Scientific Journal

p-ISSN: 0972-6268
(Print copies up to 2016)
e-ISSN: 2395-3454

Vol. 22 | No. 1 | pp. 119-127 | 2023

Original Research Paper

https://doi.org/10.46488/NEPT.2023.v22i01.010

Open Access Journal

# Spatial and Temporal Changes and Driving Factors of Desertification Around Qinghai Lake, China

**Q. G. Liu†**
College of Tourism and Geography, Hefei University, Hefei 230601, China
†Corresponding authors: Q. G. Liu; qgliuhf@163.com

**Nat. Env. & Poll. Tech.**
**Website: www.neptjournal.com**

*Received:* 16-03-2022
*Revised:* 18-04-2022
*Accepted:* 07-05-2022

**Key Words:**
Qinghai lake
Desertification
Temporal and spatial changes
Driving factors
Remote sensing analysis

## ABSTRACT

The area around Qinghai Lake is one of the most serious desertification areas on the Qinghai-Tibet Plateau. In this paper, combined with field investigation and indoor analysis, the classification and grading system of desertification around Qinghai Lake was established. On this basis, through remote sensing data processing and parameter inversion, the desertification monitoring index model was established. Based on the analysis of Landsat-5/TM remote sensing data from 1990 to 2020, the dynamic change characteristics of desertification land around Qinghai Lake in recent 30 years were obtained. The results show that the desertification area around Qinghai Lake was 1,359.62 km$^2$, of which the light desertification land was the main one. The desertification spread in a belt around Qinghai Lake, concentrated in Ketu sandy area in the east, Ganzi River sandy area in the northeast, Bird Island sandy area in the northwest, and Langmashe sandy area in the southeast. From 1990 to 2000, the annual expansion rate of desertification around Qinghai Lake was 2.68%, the desertification spread rapidly, and light desertification land was the main part of desertification expansion. From 2000 to 2010, the annual expansion rate of desertification was only 0.83%, but severe desertification land and moderate desertification land developed more rapidly than in the previous period. From 2010 to 2020, the annual expansion rate of desertification was 2.66%, and the desertification was spreading rapidly, mainly with moderate desertification land and light desertification land. In the process of desertification land transfer around Qinghai Lake, the transfer of desertification land and non-desertification land was the main, accompanied by the mutual transformation of different levels of desertification land. The process of desertification around Qinghai Lake was essentially the result of natural and human factors. The special geographical location, climate changes, rodent damage, and human factors around Qinghai Lake were the main causes of desertification.

## INTRODUCTION

Qinghai Lake is the biggest inland saline lake in China. With the unique climatic, hydrology, and soil environment of the Qinghai-Tibet Plateau, the Qinghai Lake Basin is a sensitive area of global change and a typical economically fragile area (Ding et al. 2018). In the past 30 years, due to the arid and windy climate, unreasonable reclamation, overgrazing, woodcutting, and others, the original vegetation cover around Qinghai Lake was destroyed, leading to the bare soil, which made the wind-sand activities increasingly serious and the desertification area rapidly expanded (Han 2000). With the rapid expansion of desertification, the functions of Qinghai Lake in enriching the biodiversity, regulating the climate, water conservation, and maintaining the ecological balance of the Qinghai-Tibet Plateau have been greatly weakened (Sun et al. 2008).

The area around Qinghai Lake has become the focus of academia, the public, and government departments. The study of desertification around Qinghai Lake began in the early 1960s (Zheng et al. 1985). Since the 1980s, many scholars have comprehensively studied the aeolian sand accumulation on the eastern shore of Qinghai Lake, the causes, current situations, harm degree, and control measures of desertification around the lake by means of wide area investigation, positioning observation, and experiment (He et al. 1993). Since the 1990s, remote sensing technology has been applied to study the ecological environment, grassland resources, lake changes, lake separation, land use, and desertification around Qinghai Lake (Jan et al. 2006).

Based on RS image processing technology and Landsat-5/TM remote sensing data, this paper analyzed the spatial and temporal evolution processes of desertification around Qinghai Lake in the past 30 years. The temporal and spatial changes and driving factors of desertification were explored in order to grasp the development trends of desertification and to provide a scientific and theoretical basis for the restoration of desertification and the ecological environment around Qinghai Lake.

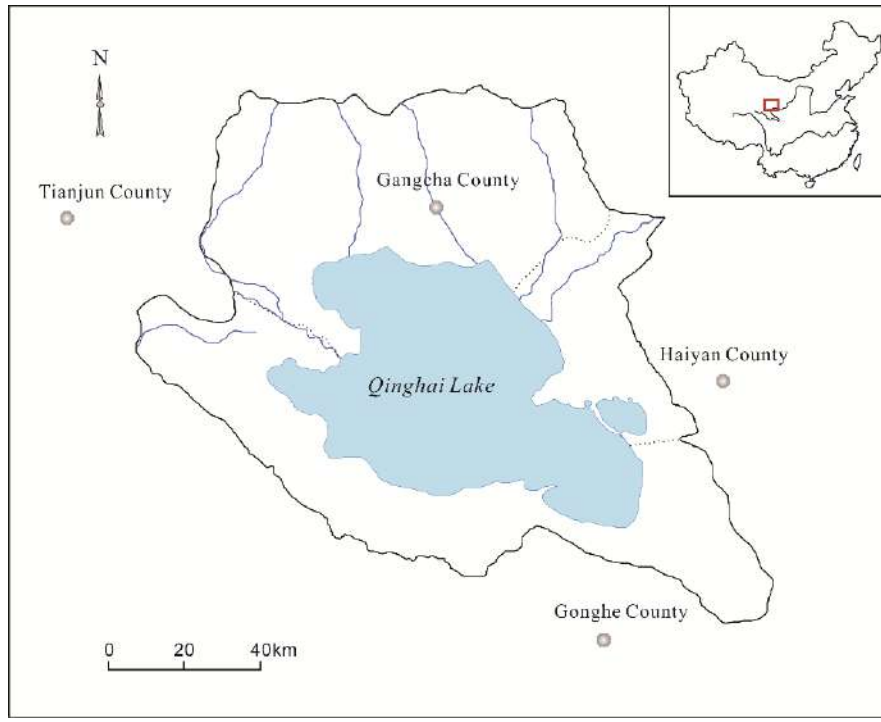


Fig. 1: Geographic location of study area in China.

## STUDY AREA

The area around Qinghai Lake is located in the northeastern edge of the Qinghai-Tibet Plateau, and the geographic coordinates are between 36°28′-38°25′ N and 97°53′-101°13′ E. It is about 120 km from north to south and 160 km from east to west, including Qinghai Lake, with a total area of 14,271.9 $km^2$ (Fig. 1). The administrative areas include some townships of Haiyan County and Gangcha County in Haibei Tibetan Autonomous Prefecture and some townships of Gonghe County in Hainan Tibetan Autonomous Prefecture. The area is adjacent to Qinghai Nan Mountain in the south, Riyue Mountain in the east, Amuniniku Mountain in the west, and Datong Mountain in the north. The terrain is inclined from northwest to southeast with an average altitude of 3,900 m, forming an independent and closed intermountain inland basin.

The study area belongs to the typical plateau semi-arid alpine climate, which is warm and cool in summer and autumn, and cold in winter and spring. The annual mean temperature is between -1.5°C and 7.0°C. The annual mean precipitation is 300-400 mm, of which the precipitation from May to September accounts for about 90% of the total, and the annual mean evaporation is about 1,440 mm. The main soil types are alpine frost desert soil, alpine meadow soil, alpine grassland soil, gray cinnamon soil, chernozem, chestnut soil, swamp soil, aeolian sand soil, etc. The vegetation types mainly include temperate grassland, desert semi-shrub, alpine shrub, and alpine meadow. The land use types are cultivated land, woodland, marshland, gravel land, bare land, sandy land, waters, beach and bedrock, etc.

## MATERIALS AND METHODS

### Desertification Land Classification

The classification of desertification land is an objective reflection of the degree of degradation. In this paper, based on the existing standards and methods for the division of desertification (Li et al. 2001), through field investigation and laboratory analysis, and then combined with the changes of vegetation, soil, and other factors, the desertification lands around Qinghai Lake were divided into light desertification land (LDL), moderate desertification land (MDL), severe desertification land (SDL), and extremely desertification land (EDL).

**LDL:** The area of quicksand is under 5%, and there is almost no wind-sand flow. The vegetation coverage is over 30%, mainly distributed in fixed coppice sandbags and sporadic grassland. Most of the surface remains in the state of native grassland. There is a small amount of wind erosion and wind deposition, and the surface appears spot-like quicksand, which is equivalent to fixed sand.

**MDL:** The area of quicksand is 5%-25%, and the wind-sand flow is not obvious. Semi-fixed sand and semi-naked gravel are distributed in the patch. The vegetation coverage is 20%-30%, and there are some sporadic sand dunes. Grassland has been significantly degraded, and the important constructive species of native vegetation have taken a secondary position, while the sandy vegetation has become the main species. Flaked quicksand and coppice dunes have appeared in large numbers, which is equivalent to semi-fixed sand.

**SDL:** The area of quicksand is 25%-50%, the wind-sand flow and the quicksand texture are obvious, with irregular patch distribution, and the sand dunes are clearly visible. The vegetation coverage is 10%-20%, and there are coppices in the topsoil. The native vegetation no longer exists, sandy grass coppices are the dominant species, and the wind erosion and wind landform are obvious.

**EDL:** The area of quicksand is over 50%, and a large area of sandland is continuously distributed. Sand dunes, dune ridges, and other landforms are obvious. The vegetation coverage is under 10%. The original surface form has been destroyed and replaced by quicksand.

## Data Sources and Processing

In this paper, eight Landsat-5/TM images in 1990, 2000, 2010, and 2020 were selected as the data source, with orbit numbers 133/34 and 133/35, respectively. In order to reduce the impact of seasonal phase and cloud cover on monitoring, remote sensing images with less than 10% cloud cover in summer and autumn were selected as far as possible, and the receiving time is shown in Table 1. In addition, the temperature, precipitation, evaporation, and other meteorological data of monitoring sites around Qinghai Lake from 1960 to 2020 were obtained. The 1:50,000 topographic map, land use map, vegetation map, and DEM data with 90m resolution around Qinghai Lake were obtained. The observation data of animal husbandry ecology and economic statistical data in Haiyan County, Gangcha County, and Gonghe County were also obtained.

We used ENVI 5.0 software to preprocess the remote sensing images, such as radiometric calibration, FLAASH atmospheric correction, and image cutting and mosaic. For geometric correction, the 1: 50,000 topographic map was taken as a reference, the control points were selected from the topographic map, and the quadratic polynomial resampling method was selected to correct them. The correction accuracy was controlled within 0.5 pixels, and the ground resolution was controlled within 30m×30m. Then, with the support of ARC/INFO software, the data were extracted by the human-computer interaction interpretation method, referring to the soil, vegetation, meteorological, and others around Qinghai Lake.

## Desertification Difference Index Model

In this paper, the normalized vegetation index (NDVI) reflecting vegetation coverage was used to indicate the degree of desertification, because it was generally considered a good indicator of desertification. Landsat TM reflectance data in infrared and near-infrared bands after radiometric and geometric correction were used to calculate NDVI. As for the inversion of surface albedo, the inversion model (1) of Landsat TM data established by Liang (2000) was used to estimate the surface albedo in the study area.

$$\text{albedo} = 0.356\rho_{TM1} + 0.130\rho_{TM3} + 0.373\rho_{TM4} + 0.085\rho_{TM5} + 0.072\rho_{TM7} - 0.0018 \quad \ldots(1)$$

Based on the Albedo-NDVI feature space, the desertification monitoring index model was established in the study area, and multi-temporal desertification index images were obtained by this model. The detailed process can be seen in the reference (Zeng et al. 2006). The expression of the desertification monitoring difference index model is:

$$DDI = 1.3437NDVI - \text{albedo} \quad \ldots(2)$$

**Monitoring information extraction:** According to the data obtained from two field surveys in 2019 and 2020, combined with the map data of vegetation type, soil type, and land use type of the study area, through the means of visual interpretation, the typical sample areas of different desertification types were selected and determined from the Landsat TM images obtained in 2020. With the support of image processing software, the connection between the map of the sample area and the image of the desertification difference index was established to determine the position of the typical sample area on the image of the desertification difference index. The DDI values of different desertification types were calculated, and the monitoring indicators of different desertification types were finally determined. Based on the desertification monitoring indicators as shown in Table 2, the spatial distribution characteristics of desertification in four phases of 1990, 2000, 2010, and 2020 were obtained.

Based on a change-monitoring tool in ENVI 5.0 software, the raster data of desertification distribution in the study period were counted, and the transfer matrix of desertification was obtained. Subsequently, the transfer quantity and direction of desertification around Qinghai Lake in recent 30 years were analyzed, and the spatio-temporal evolution processes of desertification were restored.

Table 1: Remote sensing images of Landsat-5 in the study area.

| Track No. | Receive time (year - month - day) | | | |
|---|---|---|---|---|
| 133/34 | 1990-08-12 | 2000-08-23 | 2010-08-15 | 2020-08-21 |
| 133/35 | 1990-08-12 | 2000-08-23 | 2010-08-15 | 2020-08-21 |

Table 2: Desertification detecting indicator around Qinghai Lake.

| Desertification type | LDL | MDL | SDL | EDL |
|---|---|---|---|---|
| DDI value | 51-63 | 43-50 | 34-42 | 23-33 |

## RESULTS AND ANALYSIS

### Spatial Changes of Desertification

After the development and evolution of nearly 30 years, the desertification situation around Qinghai Lake had been quite serious. In 2020, the desertification area reached 1,359.62 $km^2$, accounting for 9.53% of the total area. Among them, EDL, SDL, MDL, and LDL accounted for 18.17%, 14.89%, 23.27%, and 43.66% of the total desertification area, respectively. The desertification lands spread around

Table 3: Changes in desertification area in each county around Qinghai Lake.

| year | Haiyan County | | Gangcha County | | Gonghe County | |
|---|---|---|---|---|---|---|
| | Area ($km^2$) | Proportion (%) | Area ($km^2$) | Proportion (%) | Area ($km^2$) | Proportion (%) |
| 1990 | 442.88 | 59.98 | 98.09 | 13.28 | 197.37 | 26.73 |
| 2000 | 632.25 | 65.72 | 109.66 | 11.40 | 220.18 | 22.89 |
| 2010 | 665.76 | 63.69 | 127.14 | 12.16 | 252.40 | 24.15 |
| 2020 | 757.51 | 55.71 | 306.38 | 22.53 | 295.73 | 21.75 |

Table 4: Changes in desertification area and degrees around Qinghai Lake.

| Desertification type | 1990 | | 2000 | | 2010 | | 2020 | |
|---|---|---|---|---|---|---|---|---|
| | Area ($km^2$) | Proportion (%) | Area ($km^2$) | Proportion (%) | Area ($km^2$) | Proportion (%) | Area ($km^2$) | Proportion (%) |
| EDL | 249.73 | 33.82 | 249.73 | 25.96 | 246.59 | 23.59 | 247.06 | 18.17 |
| SDL | 183.89 | 24.91 | 191.58 | 19.91 | 205.43 | 19.65 | 202.51 | 14.89 |
| MDL | 210.65 | 28.53 | 221.18 | 22.99 | 237.54 | 22.72 | 316.42 | 23.27 |
| LDL | 94.08 | 12.74 | 299.60 | 31.14 | 355.75 | 34.03 | 593.63 | 43.66 |
| Total | 738.34 | 100.00 | 962.09 | 100.00 | 1,045.30 | 100.00 | 1,359.62 | 100.00 |

Table 5: Transfer matrix among different desertification types and non-desertification around Qinghai Lake (%).

| Period | Land type | EDL | SDL | MDL | LDL | Non-desertification |
|---|---|---|---|---|---|---|
| 1990-2000 | EDL | 100 | 0 | 0 | 0 | 0 |
| | SDL | 0 | 92.29 | 1.75 | 1.44 | 4.52 |
| | MDL | 0 | 4.54 | 92.87 | 0.63 | 1.96 |
| | LDL | 0 | 0 | 0 | 100 | 0 |
| | non-desertification | 0 | 0.05 | 0.15 | 1.55 | 98.25 |
| 2000-2010 | EDL | 98.32 | 0 | 1.68 | 0 | 0 |
| | SDL | 0 | 94.74 | 1.53 | 0.25 | 3.48 |
| | MDL | 0.07 | 4.73 | 89.12 | 3.52 | 2.56 |
| | LDL | 0 | 0 | 0.85 | 97.72 | 1.43 |
| | non-desertification | 0.01 | 0.05 | 0.15 | 0.54 | 99.25 |
| 2010-2020 | EDL | 99.84 | 0 | 0 | 0 | 0.16 |
| | SDL | 0.29 | 89.37 | 1.38 | 8.07 | 0.89 |
| | MDL | 0 | 1.91 | 53.82 | 20.65 | 23.62 |
| | LDL | 0.08 | 0.24 | 30.38 | 54.23 | 15.07 |
| | non-desertification | 0 | 0.12 | 0.57 | 2.53 | 96.78 |

Qinghai Lake in the belt mostly concentrated distribution. Among them, the large areas were the Ketu sandy area in the east of the lake, the Ganzi River sandy area in the northeast of the lake, the Bird Island sandy area in the northwest of the lake, and the Langmashe sandy area in the southeast of the lake. EDL was concentrated in the Ketu sandy area. SDL was mainly distributed in Ganzi River sandy area and Bird Island sandy area. MDL was mainly distributed in the northern pass area of the Ketu sandy area and the lakeside area of Sand Island. SDL had the largest distribution area and was the main type of desertification land in the Ganzi River sandy area, Bird Island sandy area, and Langmashe sandy area.

From the perspective of the administrative division, the main body of desertification was mainly distributed in Haiyan County. In 2020, Haiyan County, Gangcha County, and Gonghe County accounted for 55.71%, 22.53%, and 21.75% of the total desertification area, respectively. From 1990 to 2020, the desertification area in the three counties showed a continuous upward trend, but the increase ranges were slightly different in different years, resulting in obvious changes in the proportion of desertification area of the three counties in the total desertification area of the study area (Table 3). In general, the proportion of desertification areas in Haiyan County and Gonghe County in the total desertification area decreased slightly, but the proportion of desertification areas in Gangcha County in the total desertification area increased significantly.

**Changes in Desertification Area**

The spatial and temporal evolution processes of desertification around Qinghai Lake in recent 30 years were restored by using desertification images in four periods (Table 4). The desertification area around Qinghai Lake in 1990, 2000, 2010, and 2020, was 738.34 $km^2$, 962.09 $km^2$, 1,045.30 $km^2$, and 1,359.62 $km^2$, accounting for 5.17%, 6.74%, 7.32%, and 9.53% of the total area, respectively.

From 1990 to 2000, the desertification area around Qinghai Lake increased by 223.75 $km^2$, with an annual mean expansion rate of 2.68%. For different desertification types, except that the area of EDL was nearly basically, the area of SDL, MDL, and LDL showed different degrees of growth, with growth of 7.69 $km^2$, 10.53 $km^2$, and 202.52 $km^2$, respectively. During this period, desertification expanded rapidly, LDL was the main body of desertification expansion, and the degree of desertification increased year by year.

From 2000 to 2010, the desertification area around Qinghai Lake increased by 83.21 $km^2$, and the annual mean expansion rate was only 0.83%, which was significantly slower than that in the previous period. EDL was reversed, the area decreased by 3.14 $km^2$, but the areas of SDL, MDL, and LDL increased by 13.85 $km^2$, 16.36 $km^2$, and 55.15 $km^2$, respectively. During this period, the expansion rate of desertification slowed down, and the area of LDL decreased significantly, but the area of SDL and MDL developed rapidly compared with the previous period.

From 2010 to 2020, the desertification area around Qinghai Lake expanded to 314.32 $km^2$, with an annual mean expansion rate of 2.66%, which was significantly faster than the previous period. The area of SDL decreased by 2.91 $km^2$, while the area of EDL, MDL, and LDL increased by 0.47 $km^2$, 78.88 $km^2$, and 237.89 $km^2$, respectively. During this period, desertification was still expanding rapidly, MDL and LDL were the main bodies of desertification expansion, and the degree of desertification was increasing year by year.

**Desertification Type Transfer**

From 1990 to 2000, EDL did not change to other desertification types, 1.75% of SDL significantly reversed to MDL, 1.44% of SDL significantly reversed to LDL, and 4.54% of MDL developed into SDL (Table 5). During this period, the development speed of MDL was greater than the reverse speed of SDL, and desertification showed an expansion trend.

From 2000 to 2010, 1.68% of EDL significantly reversed to MDL, 1.53% of SDL significantly reversed to MDL, 0.07% of MDL developed to EDL, 4.73% of MDL developed to SDL, and 0.85% of LDL developed to MDL (Table 5). During this period, the development speed of desertification was obvious.

From 2010 to 2020, the area of EDL did not change, 0.29% of SDL developed to EDL, 1.38% significantly reversed to MDL, 1.91% of MDL developed to SDL, 30.38% of LDL developed to MDL, and 0.24% of LDL developed to SDL (Table 5). During this period, the development speed of desertification was higher than in the previous period.

**Desertification Land and Non-Desertification Land Transfer**

From 1990 to 2000, 4.52% of SDL and 1.96% of MDL reversed to non-desertification land, with the reverse area of 12.44 $km^2$; 1.75% of non-desertification land developed into desertification land, and the transfer area was 236.19 $km^2$. During this period, the development speed of desertification was much faster than the reverse speed.

From 2000 to 2010, 3.48% of SDL, 2.56% of MDL, and 1.43% of LDL reversed to non-desertification land, with the reverse area of 16.61 $km^2$; 0.75% of non-desertification land developed into desertification land, and the transfer area was

99.82 km$^2$. During this period, the development speed of desertification decreased compared with the previous period.

From 2010 to 2020, 23.62% of MDL, 15.07% of LDL, and 0.89% of SDL reversed to non-desertification land, with the reverse area of 111.94 km$^2$; 3.22% of non-desertification land developed into desertification land, and the reverse area was 426.26 km$^2$. During this period, desertification developed rapidly.

## DRIVING FACTORS OF DESERTIFICATION

### Natural Factors

The natural factors including drought, wind, and sandy soil were important factors to promote the temporal and spatial changes of desertification around Qinghai Lake.

According to the inter-annual variation curve of climate elements around Qinghai Lake in recent 60 years, we can see that the annual mean temperature increased significantly, and the annual mean precipitation increased slowly. Fig. 2 shows the annual mean temperature around Qinghai Lake has shown a rising trend in the past 60 years, the annual mean temperature was about 1.9°C, and the inter-annual trend rate was 0.30°C/10a. Since 1961, the annual mean temperature had increased year by year, but the increasing trend was obvious from 2011 to 2020. From 2011 to 2020, the annual mean temperature increased by 1.19°C, with an annual mean increase of 0.12°C. The annual mean temperature of the decade was 0.93°C higher than that of the previous 50 years, and the increase was significantly higher than that in the 1960s, 1970s, 1980s, and 1990s. In Fig. 3, the annual mean precipitation in the study area fluctuated and increased in the past 60 years, the annual mean precipitation was about 340 mm, and the inter-annual trend rate was 9.26 mm/10a. In the past 60 years, the annual precipitation exceeded 500 mm in 1967 and 1989 respectively. From 2011 to 2020, the annual mean precipitation increased significantly. The annual mean precipitation of the decade was 22.46 mm

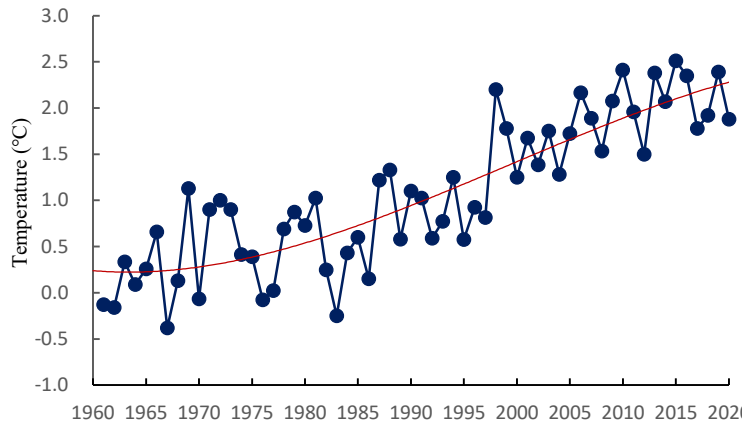


Fig. 2: Changes in annual mean temperature from 1961 to 2020.

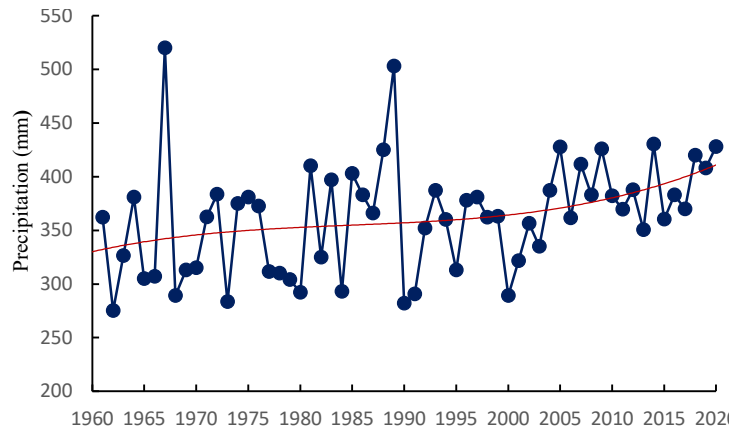


Fig. 3: Changes in annual mean precipitation from 1961 to 2020.

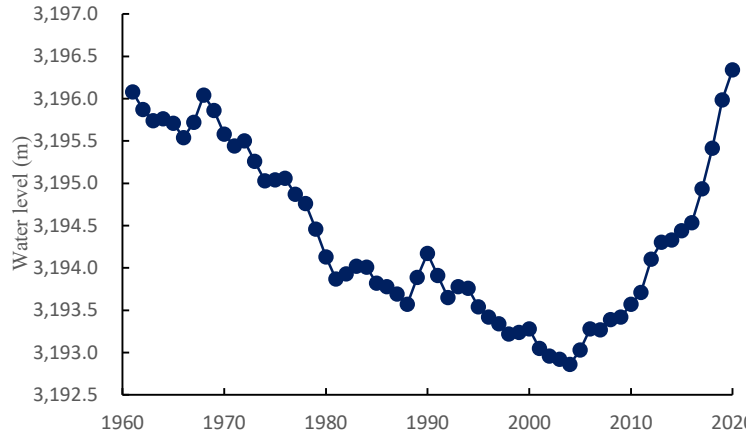


Fig. 4: Changes in the annual mean water level of Qinghai Lake from 1961 to 2020.

higher than that of the previous 50 years, and the increase was significantly higher than that in the 1960s, 1970s, and 1990s.

As for seasonal climate changes, the temperature was low in spring, but the wind speed was the largest, and the precipitation was less, so desertification was most likely to occur. The main soil types in the study area were light chestnut soil, chestnut soil, aeolian sandy soil, swamp soil, etc., the sand content of these soil types was about more than 80%, and the ability to resist wind erosion was weak. The surface vegetation was sparse and the coverage was low, which made the sandy surface in a bare or semi-bare state. All these factors combined aggravate the degree of desertification around Qinghai Lake.

**Water Level Changes in Qinghai Lake**

River water and precipitation were the main supply source of Qinghai Lake. There were 70 rivers of different sizes flowing into Qinghai Lake. In recent years, the flow of these rivers continued to decrease, with frequent seasonal interruptions. The annual mean total supply of Qinghai Lake was 3.457 billion $m^3$, and the annual mean evaporation was 3.93 billion $m^3$. The evaporation was larger than the supply, and the annual mean loss of water was 473 million $m^3$.

The water level changes of Qinghai Lake from 1961 to 2020 are shown in Fig. 4. The water level of Qinghai Lake decreased year by year from 1961 to 2004. Although there were fluctuations, the decreasing trend was obvious, and the decreasing rate was 0.76 m/10a. The water level continued to decrease from 3,196.08 m in 1961 to 3,192.86 m in 2004. Many scholars have studied the reasons for the decline of the water level, believing that the warm and dry climate is the main reason for the decline of the water level of Qinghai Lake.

With the decrease of the water level and the retreat of the lake surface, the lake-bottom sediments in some shallow water areas along the lakeside belt exposed from the water surface, becoming the main material source of desertification. Under the action of wind, land desertification was accelerated. As the water level of Qinghai Lake had been declining for a long time, the ecosystem of the whole basin had been continuously degraded, and the expansion of land desertification had been accelerated under the action of wind.

However, the water level turned into a rising period since 2005, with a rising rate of 2.01 m/10a, and the water level reached 3,196.34 m in 2020. Some scholars believe that the most important factors for the rise of the water level were climate changes, combined with the factors such as returning farmland to grassland, grassland closure, and ecological restoration, which had significantly enhanced the water conservation capacity around Qinghai Lake.

**Rodent and Locust Damage**

The rodent damage around Qinghai Lake was mainly caused by *Eospalax fontanierii* and *Ochotona curzoniae*. In severe areas, there were 75-165 rodents and more than 2,250-2,700 rodent holes per hectare. The average daily consumption of *Eospalax fontanierii* was about 264g of fresh grass, and that of *Ochotona curzoniae* was about 66g of fresh grass. The annual mean loss of fresh grass per hectare of grassland was up to 2,200-4,900 kg. Locust was another major damage to the grasslands in the study area. There were nearly 10 common locust species, such as *Altichorthippus fallax, Chorthippus dubius*, *Bryodema luctuosum*, and *Angaracris rhodopa*, among which *Chorthippus Fieber* and *Myrmeleotettix* were the most widely distributed and the most abundant. In severe areas, the density of locusts could reach

more than 300/$m^2$, and the annual mean loss of fresh grass per hectare of grassland was more than 1,500kg.

The grassland ecosystem around Qinghai Lake was frequently affected by rodent and locust damage. The rodent holes and "black soil beaches" on the natural grasslands became the breakthrough of wind erosion, which accelerated soil desertification and created conditions for grassland degradation and desert expansion. According to statistics, only in Gangcha County on the northern shore of the lake, the area of grassland degradation reached $5.794 \times 10^5$ $hm^2$, including $7.3 \times 10^4$ $hm^2$ of "black soil beaches".

**Overloading and overgrazing:** The local economy around Qinghai Lake was dominated by agriculture and animal husbandry, and the output value of animal husbandry accounted for about 70% of the total agricultural output value. The number of livestock had been increasing since 1949, especially from 1949-1969 and 2004-2013. Due to overloading and overgrazing, the grasslands could not recuperate and gradually degenerated. According to the survey, the total amount of livestock in Gangcha County in 2020 was equivalent to $126.25 \times 10^4$ sheep units, but the theoretical livestock carrying capacity of grassland in this county was only $106.97 \times 10^4$ sheep units, overloaded by $19.28 \times 10^4$ sheep units, and the degree of overloading reached 18.02%.

With the increase of livestock, grassland coverage and productivity decreased, which accelerated the process of desertification. According to vegetation monitoring data, the forage yield around Qinghai Lake decreased by 3.05-4.64 kg/a, and the height of grassland vegetation decreased by 0.75-1.28cm/a. The proportion of excellent forages represented by *gramineous* forages in the biological community decreased by 1%-3%, and the forage yield decreased, resulting in the reduction of the livestock carrying capacity of grassland. Vegetation was insufficient to cover the sandy surface, which led to the further development of grassland desertification.

### Over Cultivation and Random Digging

In the 1950s and 1960s, the grasslands around Qinghai Lake began to be blindly reclaimed. Most of the reclaimed lands were extensive management. With the decline of land fertility, farmers often abandoned these lands because their income was lower than expenditure. According to statistics, a total of 15,800 $hm^2$ of grasslands were reclaimed from 1990 to 2000, of which 2,000 $hm^2$ were returned to grasslands from 2010 to 2020, and the rest were in the barren state. Affected by severe wind erosion and desertification, some barren lands transformed into the sandy landscape, and completely lost their original ecological functions.

Due to the lack of fuel in the area around Qinghai Lake, local residents went to the fixed sandy lands to cut down shrubs such as *Salix cheilophila*, *Salix cupularis*, and *Caragana jubata*, resulting in serious damage to the vegetation. The phenomenon of arbitrarily digging traditional Chinese medicinal materials was also very serious. *Gentiana macrophylla* in beach land and piedmont plain, *Notopterygium incisum* and *Astragalus mongholicus* in the steep slope, *Ephedra geradiana* in arid grassland were dug wantonly, resulting in small pits and mounds everywhere on the grasslands. With the decrease in vegetation coverage, the land lost its natural protective barrier, and the sand was blown up by the wind, exacerbating the further development of soil erosion and desertification.

## DISCUSSION AND CONCLUSIONS

The results show that the desertification around Qinghai Lake was quite serious. In terms of spatial distribution, the desertification lands spread around Qinghai Lake in a belt shape, which is concentrated in the Ketu sandy area in the east of the lake, Ganzi River sandy area in the northeast of the lake, Bird Island sandy area in the northwest of the lake, and Langmashe sandy area in the southeast of the lake. In terms of administrative division, the desertification lands were mainly distributed in Haiyan County, while the area of Gangcha County and Gonghe County was relatively small.

The desertification area around Qinghai Lake expanded rapidly, increasing by 621.28 $km^2$ in 30 years, with an annual mean expansion rate of 2.06%. From 1990 to 2000, the annual mean expansion rate of desertification was 2.68%, and LDL was the main body of desertification expansion. From 2000 to 2010, the annual mean expansion rate of desertification was only 0.83%, but SDL and MDL developed rapidly compared with the previous period. From 2010 to 2020, the annual mean expansion rate of desertification was 2.66%, and the desertification still spread rapidly, mainly MDL and LDL. In the process of desertification land transfer around Qinghai Lake, the desertification land and non-desertification land were mainly transferred, accompanied by the mutual transfer between different levels of desertification land.

In fact, the spatial and temporal evolution processes of desertification around Qinghai Lake were the result of natural and human factors. Due to the unique natural environment around Qinghai Lake, such as drought climate, windy, sandy surface, sparse vegetation, and decline of water, there was a slow natural desertification process. Rodent damage, locust damage, and unreasonable human activities destroyed the surface ecosystem, accelerated surface erosion, and artificially exacerbated the process of desertification.

## ACKNOWLEDGMENT

This research was financially supported by the Project of the Anhui Education Department (No. SK2018A0603). The work was facilitated by the Qinghai Department of Lands, Environment and Resources.

## REFERENCES

Ding, Z., Lu, R. and Liu, C. 2018. Temporal change characteristics of climatic and its relationships with atmospheric circulation patterns in Qinghai Lake Basin. Advances in Earth Science, 33(3): 281-292.

Han, Y. 2000. Harmfulness of Qinghai Lake environment deterioration and corresponding control measures. Soil and Water Conservation in China, 8: 20-21+45.

He, D., Zhao, H. and Zhang, D. 1993. Characteristics of sandy land and trend of aeolian desertification in Qinghai Lake Basin. Scientia Geographica Sinica, 13(4): 383-388.

Jan, J., Li, H. and Dai, X. 2006. Remote sensing geo-analysis of land desertification in Qinghai Lake Area. Journal of Geo-Information Science, 8(2): 116-119.

Li, S., Dong Y. and Dong, G. 2001. Desertification Problem and Sustainable Development in Qinghai-Tibet Plateau. China Tibetology Press, pp. 37-45.

Liang, S. 2000. Narrowband to broadband conversions of land surface albedo I: Algorithms. Remote Sensing of Environment, 76: 213-238.

Sun, Y., Li, X. and Tang, J. 2008. Climate changes and its hydrological effects in Qinghai Lake Basin. Resources Science, 30(3): 354-362.

Zeng, Y., Xiang, N. and Feng, Z. 2006. Albedo-NDVI space and remote sensing synthesis index models for desertification detection. Scientia Geographica Sinica, 26(1): 75-81.

Zheng, D., Yang, Q. and Liu, Y. 1985. Study on the geological characteristics of Qinghai-Tibet Plateau in China. Science Press, pp. 19.

Nature Environment and Pollution Technology
An International Quarterly Scientific Journal

p-ISSN: 0972-6268
(Print copies up to 2016)
e-ISSN: 2395-3454

Vol. 22 | No. 1 | pp. 129-138 | 2023

Original Research Paper

https://doi.org/10.46488/NEPT.2023.v22i01.011

Open Access Journal

# Heavy Metal Removal from Contaminated Soil Using Soil Washing Techniques

**G. Resmi*†, Santosh G. Thampi** and S. Chandrakaran****
*Department of Civil Engineering, N.S.S. College of Engineering, Palakkad, Kerala, India
**Department of Civil Engineering, National Institute of Technology, Calicut, Kerala, India
†Corresponding author: G. Resmi; resmivinod@gmail.com

**Nat. Env. & Poll. Tech.**
**Website: www.neptjournal.com**

*Received:* 13-04-2022
*Revised:* 17-06-2022
*Accepted:* 30-06-2022

**Key Words:**
Soil washing
Lead removal
Heavy metal contamination
Chelating agents

## ABSTRACT

Heavy metals are discharged into the soil around us from various anthropogenic sources and also by the use of fertilizers, pesticides, pharmaceuticals, etc. In most cases, industrialization can be pointed to as the reason behind soil pollution. Contamination of soil leads to large-scale environmental degradation and health impacts. Many investigators have studied techniques for removing heavy metals from soil. Soil washing is an emerging area that can be implemented for this purpose. Studies were carried out in the controlled conditions of a laboratory environment to determine the suitability of soil-washing techniques for removing lead from polluted land. The results showing the influence of various parameters in soil washing, such as duration of washing, molar strength of the solution used, the weight ratio of soil to wash solution, etc., are presented in this paper. Batch studies were conducted to investigate the performance of chelating agents such as $Na_2EDTA$, HCl, $HNO_3$ and $CaCl_2$ with regard to the removal of lead from artificially contaminated locally available soil. Based on the batch studies, it is observed that the strength of the washing solution, the proportion of soil and solution, the period of agitation, etc. influence the removal of contaminants. Based on the studies, it is concluded that, while recommending soil washing using chelating agents for remediating lead-contaminated soils, it is essential to identify the influencing parameters and determine the optimum conditions so that higher removal can be achieved without any adverse effect.

## INTRODUCTION

Contamination of land by the discharge of heavy metals is a matter of concern all around the world. Even in trace amounts, they give rise to land degradation and health impacts. Heavy metals are naturally occurring elements. But they are also generated by various anthropogenic activities like the production and use of fertilizers, pesticides, pharmaceuticals, etc. Activities such as the release of pharmaceutical waste, industrial waste, e-waste, batteries, pesticides, etc., are considered the main source of such pollution in urban and agricultural land (Chibuike & Obiora 2014). There are chances that these metals remain in the soil for a longer period and later lead to problems such as bioaccumulation. Extraction of these metals from polluted soils is usually carried out by using acids or selected solutions that develop complexes with them. Soil washing techniques were widely experimented with to remove heavy metals from soil. Techniques for removing a few metals namely, lead and zinc from contaminated soil by washing methods were reported by Wang et al. (2015). Some efforts have been made to investigate the capability of ethylene diamine tetra acetic acid (EDTA) for sorbed metal extraction (Yang & Lin 1998 and Peters 1999). Some researchers have already investigated the use of acids like hydrochloric acid (HCl), nitric acid ($HNO_3$), and sulphuric acid ($H_2SO_4$) for removing heavy metals from soil (Peters 1999, Moutsatsou et al. 2006, Semer & Reddy 1995, Sun et al. 2001). For the extraction of these from the soil, extensive research has been conducted using organic acids as chelating agents (Wei et al. 2018). Few researchers have studied the application of potassium salts of EDTA ($K_2H_2EDTA$), calcium chloride ($CaCl_2$), and potassium hydroxide (KOH) for soil washing to remove lead (Samani et al. 1998).

The results of the studies carried out to investigate the effectiveness of soil washing technique and the influence of some parameters like molar strength of the washing solution, duration of washing, the weight ratio of soil to wash solution, etc. are presented in this article. Batch studies were conducted to investigate the performance of chelating agents such as $Na_2EDTA$, HCl, $HNO_3$, and $CaCl_2$ with regard to removing lead from polluted soil.

## MATERIALS AND METHODS

### Soil Used in the Study

The study was conducted at the NITC campus, Calicut District, Kerala, and soil samples were collected from the campus itself. Representative disturbed samples were

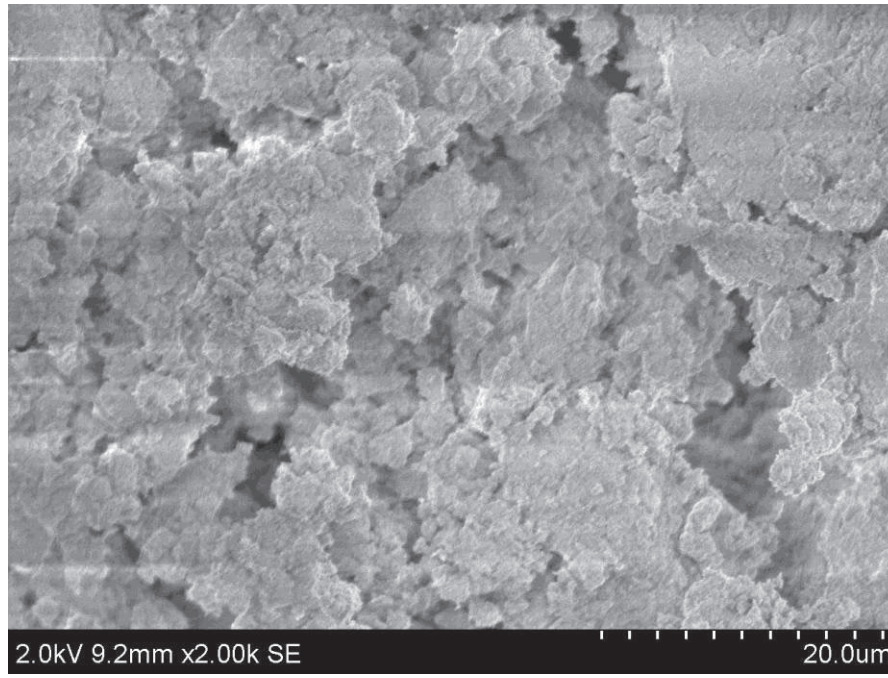


Fig. 1: SEM image of the soil used in the study.

obtained from shallow pits and carefully transported to the laboratory in such a way as to avoid any moisture loss. The soil was mixed thoroughly, kept in polyethylene bags, and stored in containers for the duration of the study. The SEM image of the dry soil sample is shown in Fig. 1.

**Artificial Contamination**

Sample preparation was carried out in a laboratory environment. For this purpose soil was soaked with a synthetic solution containing lead. In the study, lead nitrate (Pb $(NO_3)_2$) salt of analytical grade was selected. The soil was mixed with lead nitrate solution with a lead concentration of 2000 ppm. The synthetic lead solution was taken in containers, and soil samples were soaked in these. It was left without disturbance for 90 days for enhancement of sorption. The soil samples after sorption were then collected from the solution. Then it is properly dried, powdered, and passed through a 2 mm IS sieve. Later they are kept in polyethylene bags for the entire study period. The adsorbed amount of lead was observed to be 19.8 $mg.g^{-1}$.

Four washing reagents were selected for the investigation such as EDTA, $CaCl_2$, $HNO_3$, and HCl. 1M concentration of EDTA solution was prepared by dissolving 374.22 g of $Na_2EDTA.2H_2O$ in 1L of distilled water. Disodium salt of EDTA was used as it is said to have certain advantages when compared to other salts of EDTA (Raghavan et al. 1989, Moutsatsou et al. 2006, Demont et al. 2018). It is reported that the use of $Na_2EDTA$ as a solvent for removing metals has shown some merits: (a) pH of the solution turns basic and leads to metal retention (b) $Na_2EDTA$ does not degrade faster in groundwater and (c) $Na_2EDTA$ has got a greater affinity to form complexes (Abumaizar & Smith 1999, Moutsatsou et al. 2006). 1M $CaCl_2$ was prepared by dissolving 110.98g anhydrous $CaCl_2$ in 1litre of distilled water. Similarly, 1M $HNO_3$ was prepared by mixing 64ml conc. $HNO_3$ and 943ml distilled water. 1M HCl was prepared by mixing 83ml conc. HCl and 920ml distilled water.

**Batch Studies**

Studies were conducted in batch mode to find out the effectiveness of soil-washing agents under selected conditions. The optimum duration of shaking and the desirable pH were also determined by conducting batch studies. The dried soil sample was taken in 250 mL polypropylene bottles and the washing solution was added to these bottles maintaining the desired ratio of soil weight to liquid volume (S: L). For conducting preliminary studies, this ratio was fixed as 1:1, similar to the value 1:1.5 as reported by Makino et al. (2007), and later this was varied upto 1:5. The same range of solid to liquid ratio was adopted with all other solutions used in this study.

The molar concentration of the EDTA solution used was varied from 0.01 to 0.05 M, the molar concentration of $CaCl_2$ solution was varied from 0.2 to 1 M and the molar

concentration of HCl and $HNO_3$ solutions were varied from 0.01 to 1 M. Less concentrated EDTA solution was used to achieve economy in usage. However, as the effectiveness was high compared to other solutions, a solution with low molarity was sufficient for the studies conducted. In an earlier study, a small liquid-to-solid ratio was selected by Andrade et al. (2007) to reduce the amount of washing solution and chemicals, as usage of a large amount of liquid may lead to problems regarding the management of the wastewater generated. In this study, the molarity of EDTA is very less compared to that reported by Andrade et al. (2007), and hence economy is achieved. The soil–solution mixture was shaken at 150 rpm for a period of 24 h at room temperature and centrifuged for 10 min at 3000 rpm. Approximately 10 mL of the supernatant liquid was passed using filter paper of 0.45 microns in size. The strength of the lead in the residue after filtration was checked with the help of an ion meter having an ion-selective electrode for determining lead. There was an assumption behind the process that the mass of lead observed in the filtrates was the actual representation of lead released from the soil mixed with contaminants. The quantity of lead obtained in the filtrate was divided by the initial mass of lead present in each sample before the washing process. This value indicated the overall efficiency of the soil washing technique.

## RESULTS AND DISCUSSION

Results obtained from the batch studies are discussed below.

### Effect of Soil-to-Liquid Ratio

For studying the effect of solid-to-liquid ratio on the percentage removal of lead from the soil, experiments were conducted at five different ratios - 1:1, 1:2, 1:3, 1:4, and 1:5 (Makino et al. 2007) and for five different molar concentrations of EDTA - 0.01, 0.02, 0.03, 0.04 and 0.05 M. The percentage removal of lead was observed to be as high as 98.9% when the solid-to-liquid ratio was 1:5, and the molar concentration was 0.05 M. The least value (75.1%) was obtained when the solid-to-liquid ratio was 1:1 and the concentration was 0.01 M. The results are presented in Fig. 2.

It was observed that when the solid-to-liquid ratio was 1:5, the removal rate was higher than that with a ratio of 1:1. The same trend was observed for all concentrations tested. The results show that the effectiveness of soil washing using EDTA improves as the volume of washing solution is increased. However, this is not advisable from the viewpoint of the economy of the process. Hence a washing agent that can achieve comparable results with low volume is desirable. The removal achieved corresponding to the 1:2 ratio was

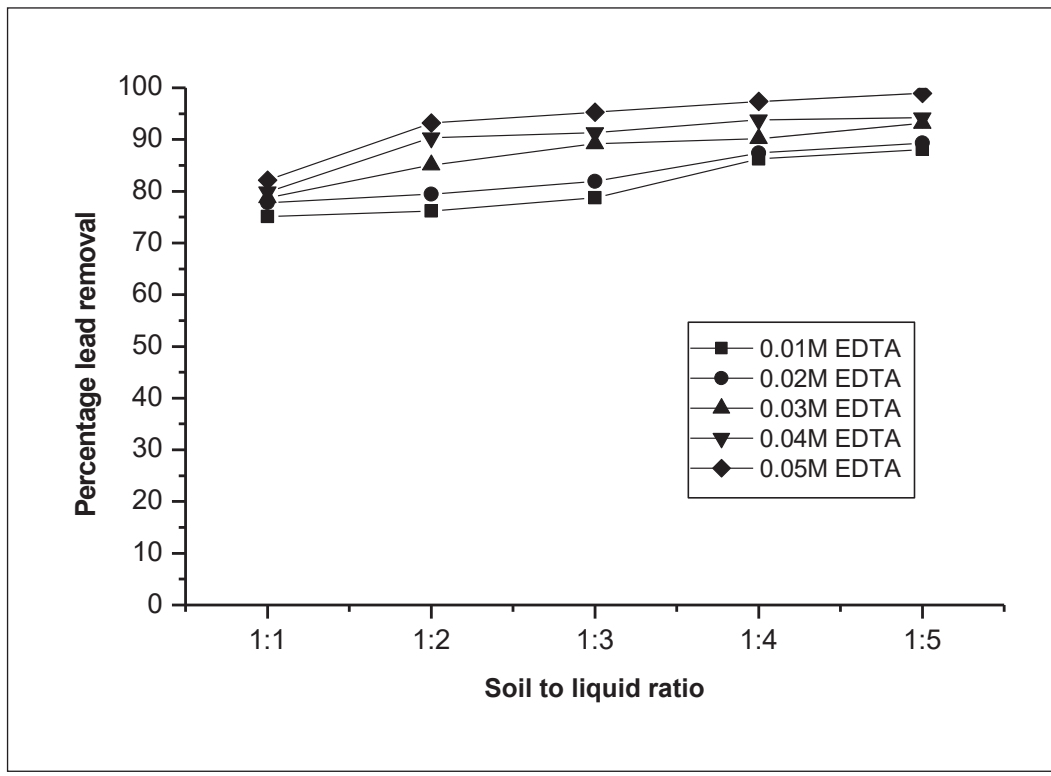


Fig. 2: Effect of soil to EDTA ratio on percentage lead removal.

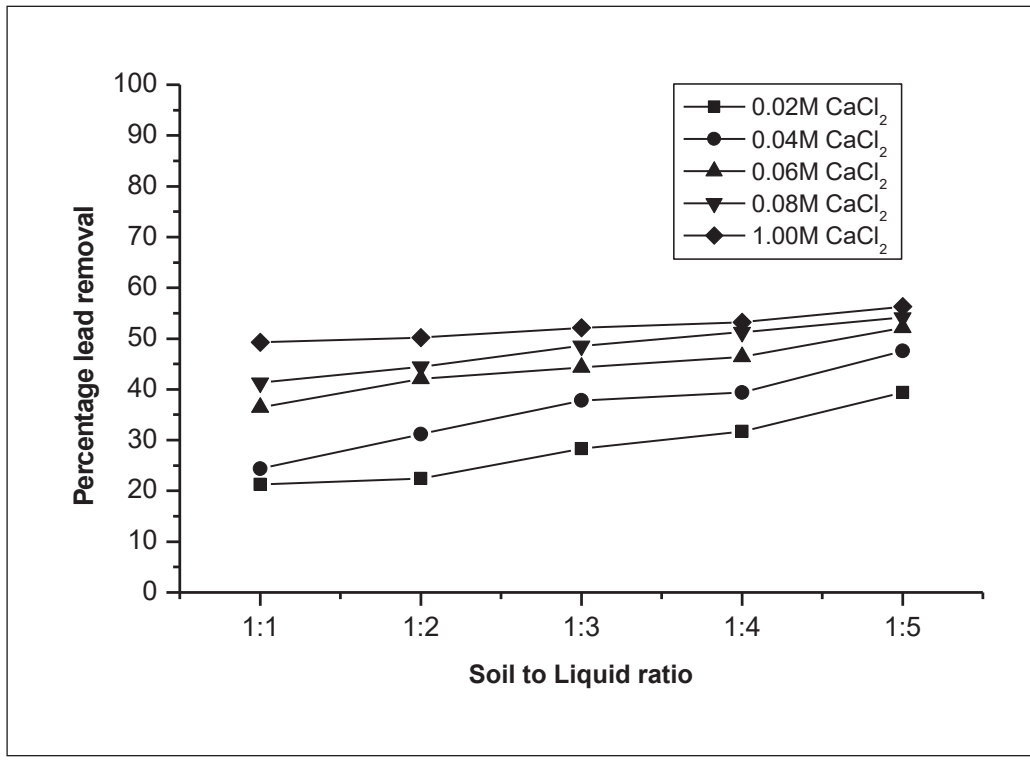


Fig. 3: Effect of soil to $CaCl_2$ ratio on percentage lead removal.

reasonably good (more than 90% removal is achieved). Hence for further studies with EDTA, this was fixed at a ratio of 1:2.

The effect of solid-to-liquid ratio on lead removal using $CaCl_2$ was also investigated at five different ratios - 1:1, 1:2, 1:3, 1:4, and 1:5. The soil-liquid mixture was kept for shaking at 150 rpm and the percentage of lead removal was computed and expressed in the graph (Fig. 3). The percentage lead removal was not as high as that achieved with EDTA (varying from 21.3% to 56.3%). In the majority of the cases investigated, the efficiency of metal removal was lower than 60%. The highest percentage of removal was observed at a proportion of 1:5, and this was selected for further studies.

The influence of solid-to-liquid ratio on lead removal with $HNO_3$ was studied by conducting tests at five different ratios as in the previous two cases, and the results are presented in Fig. 4. Similar to the previous case when the ratio of solid to liquid was 1:1, lead removal increased as the concentration of $HNO_3$ increased. Some fluctuation was observed in the range of ratios 1:2 and 1:4. At solid-to-liquid ratios 1:4 and 1:5, it was seen that there was a decrease in the percentage removal of lead at higher concentrations of $HNO_3$. The maximum percentage removal of lead (82.1%) was achieved when the solid-to-liquid ratio was 1: 3. Hence this ratio was used for further studies with $HNO_3$.

Results of experiments performed with HCl for removing lead are presented in Fig. 5. It was observed that as the proportion of liquid was increased, there was a good improvement in lead removal. At higher molar concentrations the removal was high. The maximum percentage removal (79.8%) was observed at a ratio of 1:5 and a molar concentration of 1.0 M. The rest of the batch studies using HCl were done at this solid-to-liquid ratio and molar concentration.

**Effect of Contact Period on Lead Removal Efficiency**

The influence of contact period on percentage lead removal was evaluated using EDTA, $CaCl_2$, $HNO_3$ and HCl as the washing agents. Each of the washing agents was mixed with contaminated soil and shaken for 12 h at 150 rpm. The solution concentrations were changed and the experiments were repeated. The results are presented in Fig. 6 to Fig. 9. In all the cases, rapid removal was observed in the initial stages. Thereafter, it increased gradually, and a steady state was attained after a while. This corresponds to the point of equilibrium and the contact period required for reaching

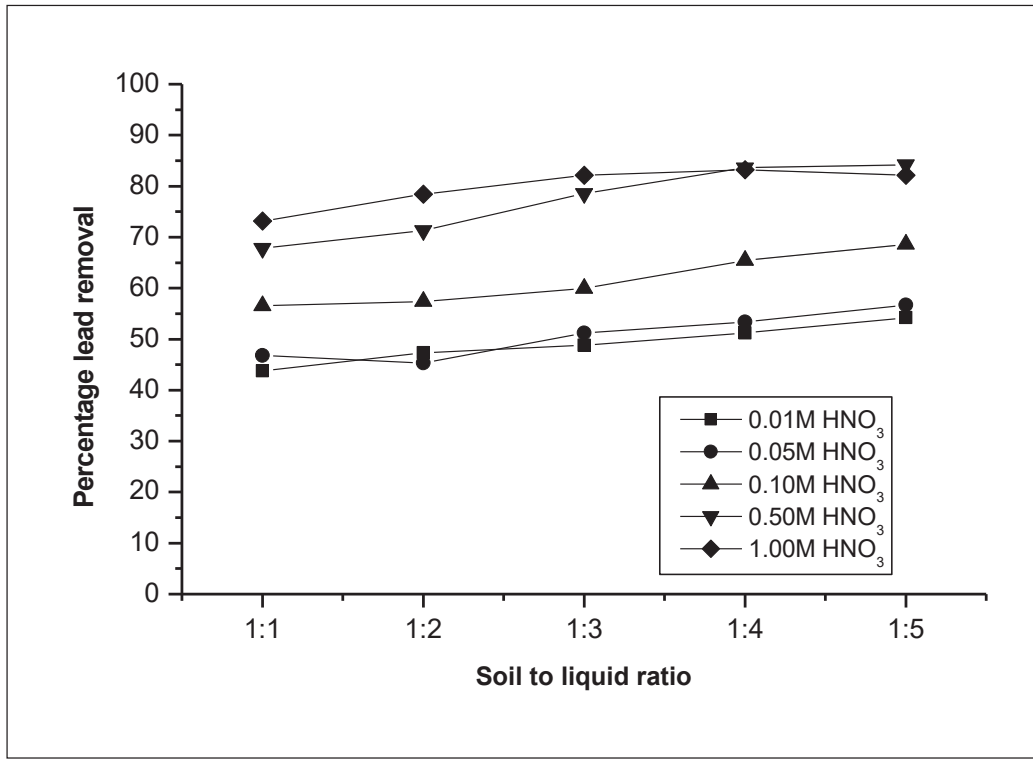


Fig. 4: Effect of soil to $HNO_3$ ratio on percentage lead removal.

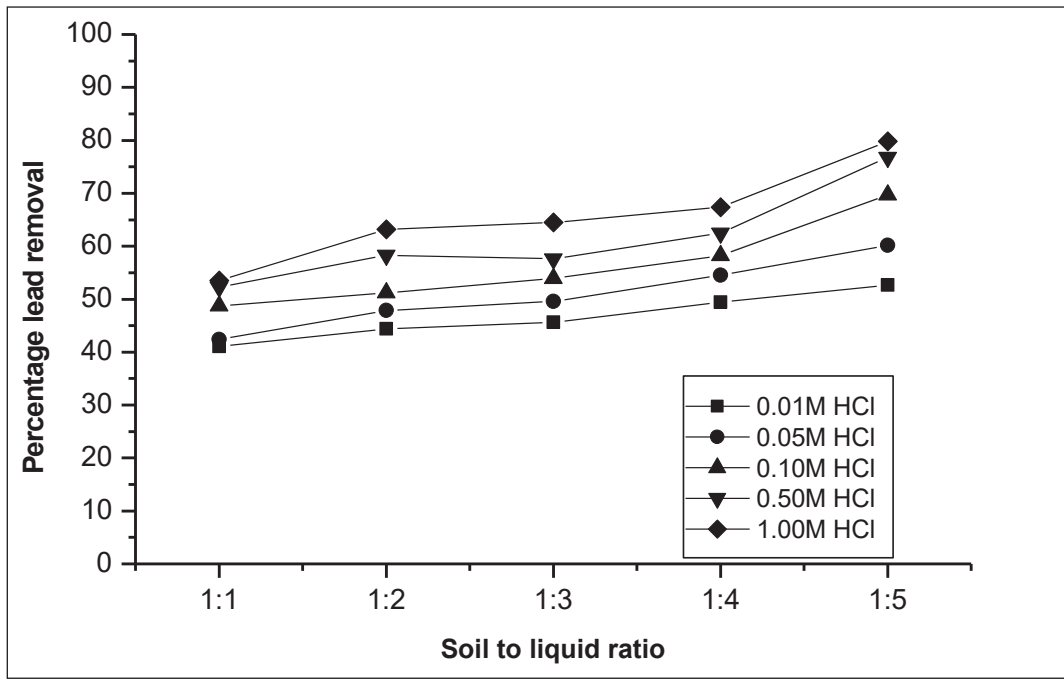


Fig. 5: Effect of soil to HCl solution ratio on percentage lead removal.

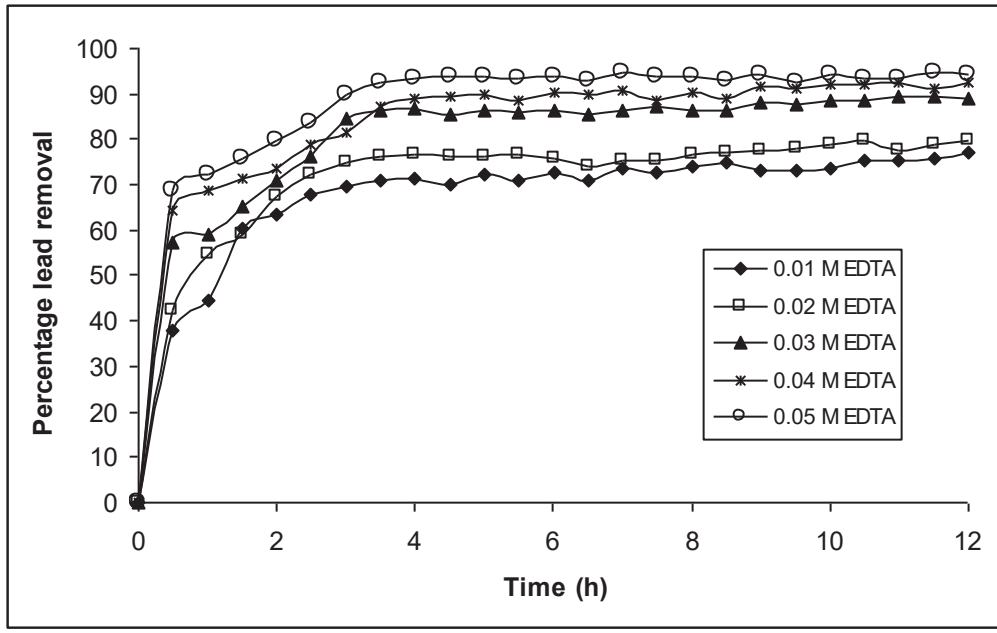


Fig. 6: Effect of contact time on percentage removal of lead using EDTA.

the equilibrium stage in each case was used for conducting other batch studies.

A close observation of Fig. 6 shows that the equilibrium period with EDTA is approximately 3.5 h, the corresponding percentage being 72.8%, 75.8%, 86.3%, 90.3% and 93.9% with 0.01 M, 0.02 M, 0.03 M, 0.04 M and 0.05 M EDTA, respectively. Moutsatsou et al. (2006) observed that 0.1 M $Na_2EDTA$ was the most effective when the mixing period was less than 1 h. They achieved a removal efficiency of 42% for the lead when the initial contamination level was as high as 64,195 $mg.kg^{-1}$ (soil to liquid ratio = 1:33, shaking speed = 150 rpm).

When $CaCl_2$ was used as the chelating agent, the equilibrium period was about 6 h (Fig. 7). Rapid increase in percentage removal was observed in the first 6 h, and thereafter increase in percentage removal was only nominal

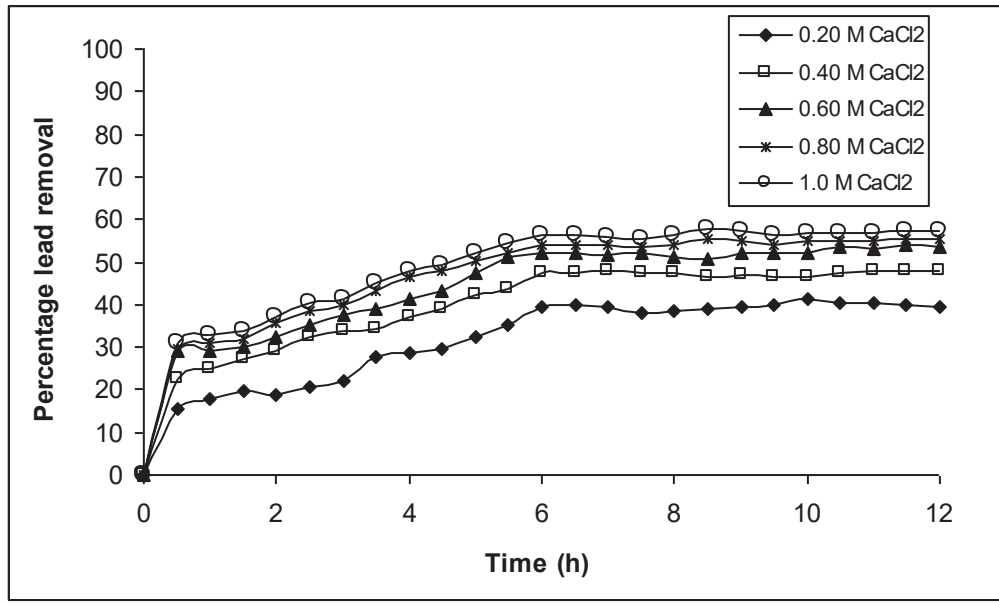


Fig. 7: Effect of contact time on percentage removal of lead using $CaCl_2$.

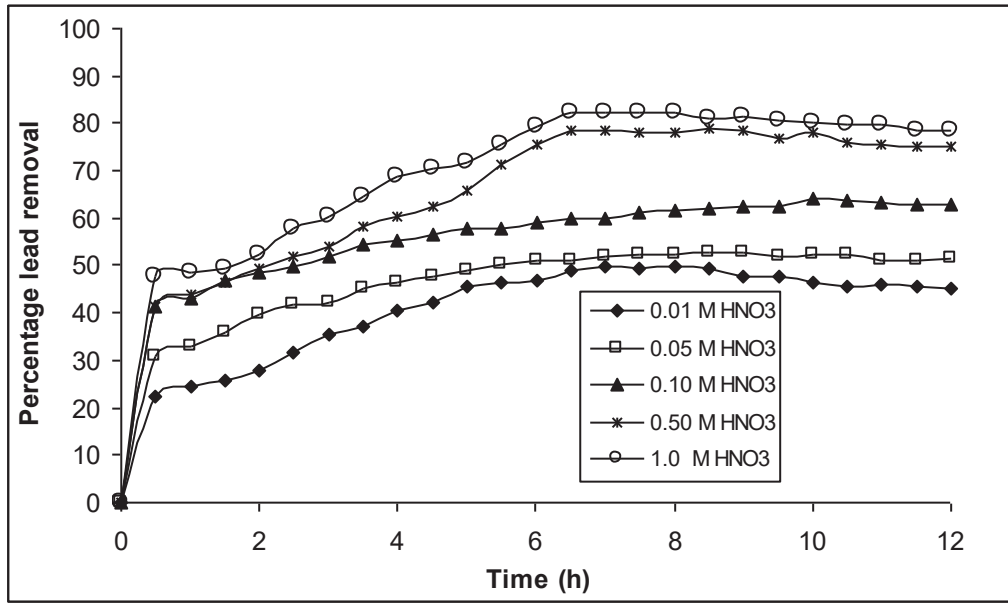


Fig. 8: Effect of contact time on percentage removal of lead using $HNO_3$.

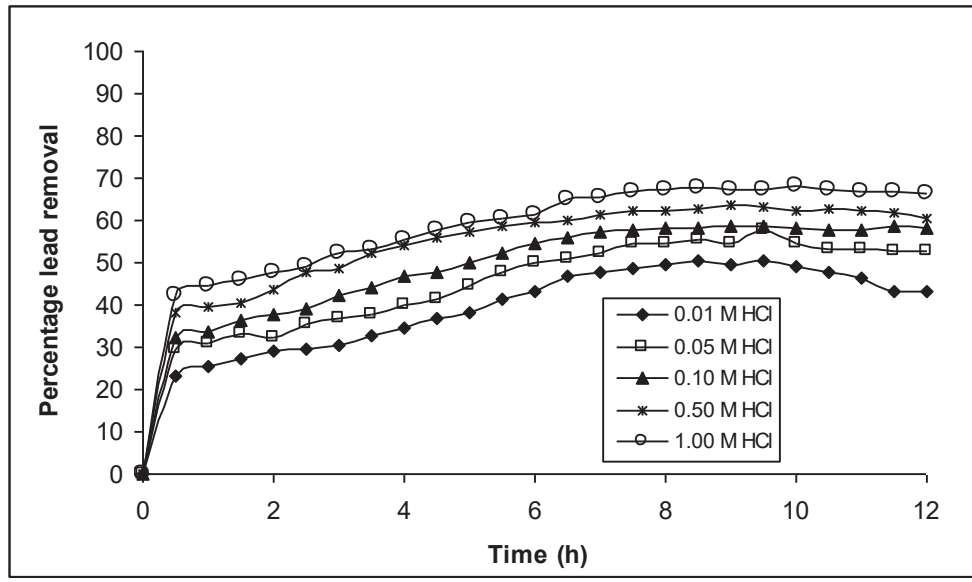


Fig. 9: Effect of contact time on percentage removal of lead using HCl.

at all concentrations. The percentage removal was 39.4%, 47.6%, 52.1%, 54.1%, and 56.3% with HCl concentrations of 0.2 M, 0.4 M, 0.6 M, 0.8 M, and 1M, respectively. Makino et al. (2007) reported that the suitability of a chemical as a chelating agent increases as the contact period to reach equilibrium is reduced. Hence EDTA is a better chelant compared to $CaCl_2$.

When $HNO_3$ was used as the chelant, a steady state was reached at around 6.5 h, and this was taken as the equilibrium period (Fig. 8). The removal percentages were 48.8%, 51.2%, 59.9%, 78.6%, and 82.1% at 0.01 M, 0.05 M, 0.1 M, 0.5 M and 1.0 M concentrations of $HNO_3$, respectively. The batch studies with HCl exhibited a similar trend. The equilibrium time was 8 h (Fig. 9).

Strong acids extract only a very small portion of metal content from contaminated soil. In the current study, EDTA-based chelating agents performed better than $HNO_3$ and HCl. Similar observations were reported by Moutsatsou et al.

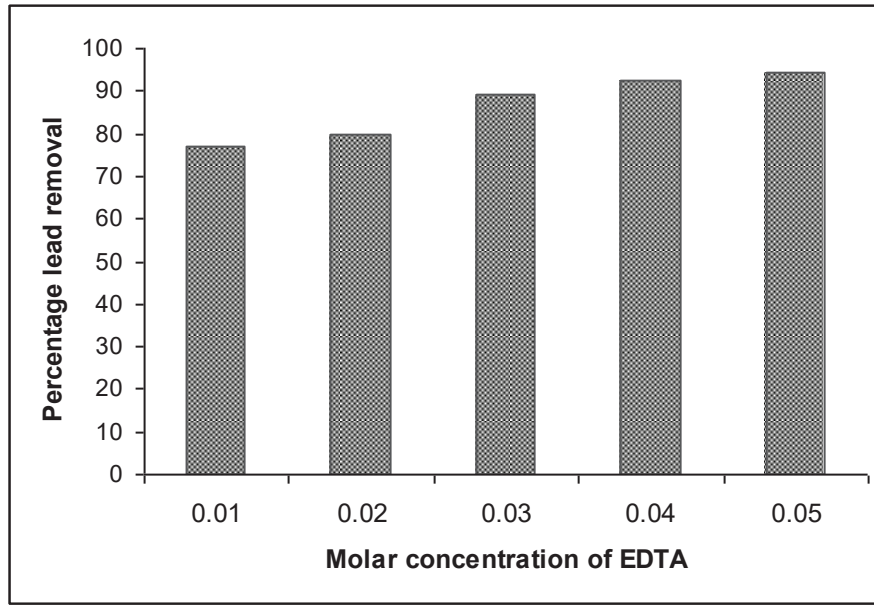


Fig. 10: Effect of the molar concentration of EDTA on the removal of lead.

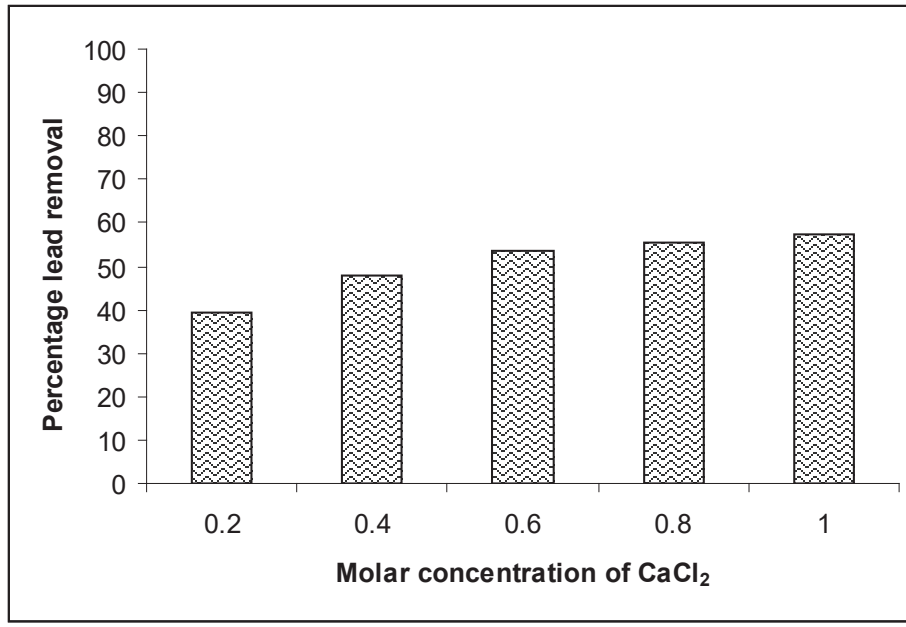


Fig. 11: Effect of the molar concentration of $CaCl_2$ on the removal of lead.

(2006) based on their investigations. $HNO_3$ exhibited high extraction capacities which may be occurring as a result of its strong oxidizing nature which results in the development of insoluble metal compounds.

**Effect of Molar Concentration**

There will be a high rate of recovery of metal when there is the presence of reagents that lead to the conversion of adsorbed metal ions into anion-dominated complexes. The ability of these agents to immobilize lead and other metals from soil matrix has been reported. EDTA is considered an effective agent which can extract some of the selected metals from soil (Finzgar & Lestan 2007). EDTA addition in small concentration could offer few advantages. Sometimes it leads to less clogging of the soil which normally occurs while washing with high strength of EDTA (Li & Shuman 1996).

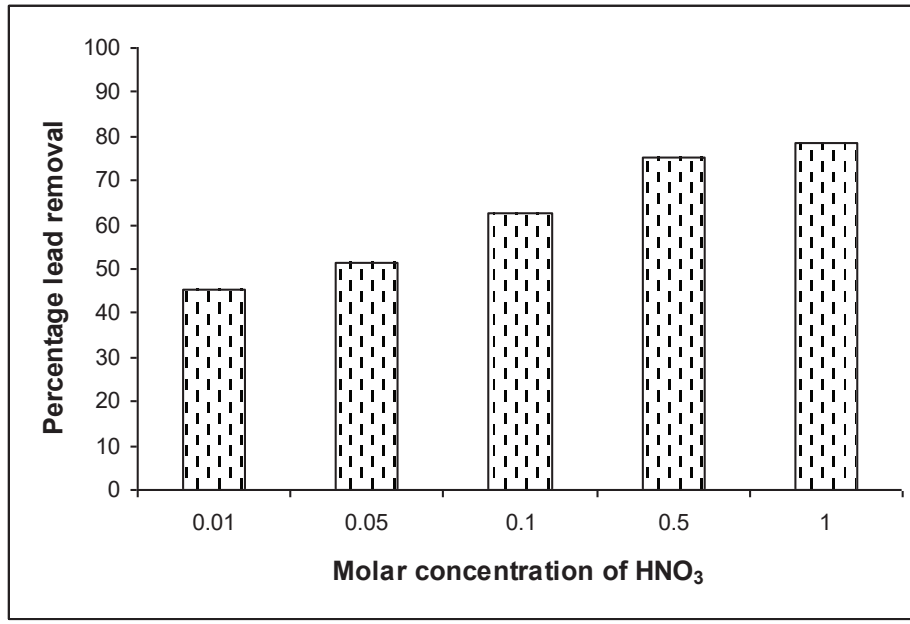


Fig. 12: Effect of the molar concentration of $HNO_3$ on the removal of lead.

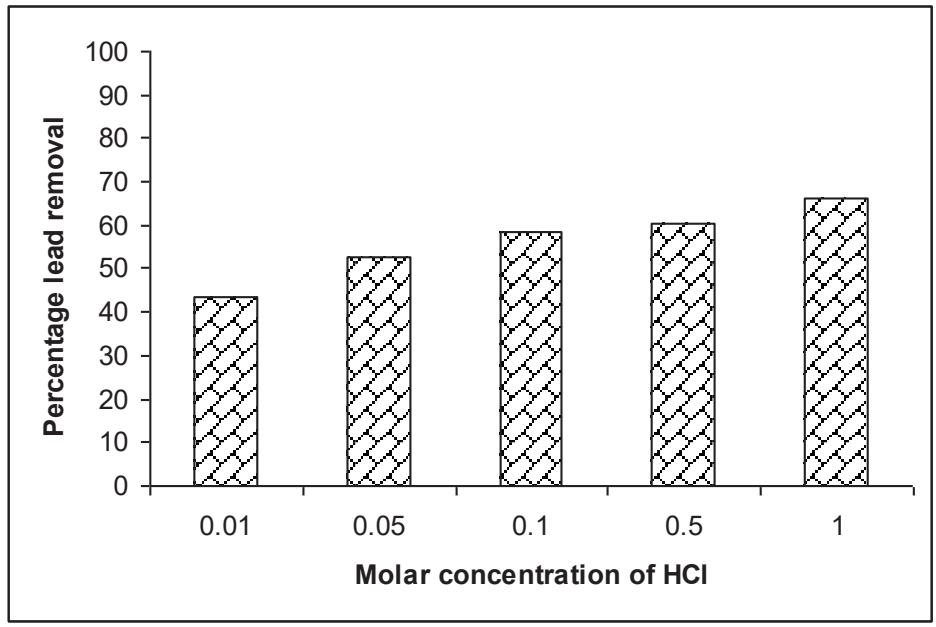


Fig. 13: Effect of the molar concentration of HCl on the removal of lead.

Elliott & Brown (1989) conducted a study using chelating agents such as EDTA and they observed that acids form strong water-soluble complexes.

The present study proved the molar concentration of the chelating chemicals influences contaminant removal considerably. This is evident from the results presented in Fig. 10 to Fig. 13. Increasing the chelant concentration resulted in higher lead solubilization. Using all chemicals, it was observed that the maximum percentage of lead removal was obtained at the maximum concentration of chemicals used for soil washing. With EDTA, the removal was maximum at 0.05 M concentration, and the corresponding percentage removal is 94.3%. The percentage removal was 77.1% at 0.01 M concentration.

With $CaCl_2$, the removal efficiency was maximum at 1.0 M concentration (57.5%). At lower concentrations (0.20 M), the percentage removal was only 39.4%. When $HNO_3$ was used, the percentage removal achieved was 45.3% and 78.3% at 0.01 M and 1.0 M concentrations, respectively. Similarly, with HCl, the percentage of lead removal was 66.4% at 1 M concentration and 43.4% at 0.01 M concentration. These results indicate that when a solution with a higher molar concentration of a finite amount was used, the atomic mass that came in contact with the contaminants was more, and hence, there was a higher opportunity to attach the contaminant with the chelant. As a result, the amount of contaminant removed from the soil mass increased.

## CONCLUSION

The study has proved the effectiveness of chelating agents, Disodium EDTA ($Na_2EDTA$), calcium chloride ($CaCl_2$), nitric acid ($HNO_3$), and hydrochloric acid (HCl) in removing lead from soils. Based on the batch studies, it is observed that the strength of the liquid used for washing, the proportion of soil and solution, the solution pH, the period of agitation, etc., influence the removal of contaminants. For each soil-liquid system, a particular molar concentration of the chelant yielded better lead removal. The agitation period, which gave maximum removal, was unique for each system. While low pH enhanced the removal by EDTA and acids (nitric acid and hydrochloric acid), $CaCl_2$ showed better performance at moderately high pH. But sometimes acid percolation through soil may lead to extremely low pH conditions which necessitate further treatment. Also, there are chances of the production of toxic substances during soil washing. Results of column experiments show that the removal rate is very much affected by the flow rate and the bed depth. It is concluded that, while recommending soil washing using chelating agents for remediating lead-contaminated soils, it is essential to identify the influencing parameters and determine the optimum conditions so that higher removal can be achieved without any adverse effect.

## ACKNOWLEDGEMENT

Authors express their deep sense of gratitude to the Kerala State Council for Science, Technology, and Environment, Thiruvananthapuram, Government of Kerala, for the financial support provided for the conduct of research. The National Institute of Technology Calicut's laboratory facilities, which were made available to carry out the experiments, is gratefully acknowledged.

## REFERENCES

Abumaizar, R.J. and Smith, E.H. 1999. Heavy metal contaminants removal by soil washing. J. Hazard Mater., 70: 71-86.

Andrade, M.D., Parser, S.O. and Hendershot, W.H. 2007. Optimizing the molarity of a EDTA washing solution for saturated soil remediation of trace metal contaminated sites., Environ. Pollut., 147: 781-790.

Chibuike, G.U. and Obiora, S.C. 2014. Heavy metal polluted soils: Effect on plants and bioremediation methods. Appl. Environ. Soil Sci., 1: 1-12

Elliott, H.A. and Brown, G.A. 1989. Comparative evolution of NTA and EDTA for extractive decontamination of Pb-polluted sites. Water Air Soil Pollut., 45: 361-369.

Finzgar, N. and Lestan, D. 2007. Multi-step leaching of Pb and Zn contaminated soils with EDTA. Chemosphere, 66: 824-832.

Makino, T., Kamiya, T., Takano, H., Itou. T., Sekiya, N., Sasaki, K., Maejima, Y. and Sugahara, K. 2007. Remediation of cadmium-contaminated paddy soils by washing with calcium chloride: Verification of on-site washing. Environ. Pollut., 147: 112-119.

Moutsatsou, A., Gregou, M., Matsas, D. and Protonotarios V. 2006. Washing as a remediation technology applicable in soils heavily polluted by mining-metallurgical activities. Chemosphere, 63: 1632-1640

Peters, R.W. 1999. Chelant extraction of heavy metals from contaminated soils. J. Hazard. Mater., 66: 151-210.

Raghavan, R., Coles, E. and Dietz D. 1989. Cleaning Excavated Soil Using Extraction Agents. A State-of-the-Art Review. US EPA Risk Reduction Engineering Laboratory, Office of Research and Development, Cincinnati, Ohio, USA.

Samani, Z., Hu, S., Hanson, A.T. and Heil, D.M. 1998. Remediation of lead contaminated soil by column extraction with EDTA: II modeling. Water Air Soil Pollut., 102: 221-238.

Semer, R. and Reddy, R.K. 1995. Evaluation of soil washing process to remove mixed contaminants from a sandy loam. J. Hazard Mater., 45: 45-57.

Sun, B., Zhao, J.F., Lombi, E. and McGrath, P.S. 2001. Leaching of heavy metals from contaminated soil using $Na_2EDTA$. Environ. Pollut., 113: 111-120.

Wang, J.M., Jiang, J.G., Li, D., Li, T.R., Li, K.M. and Tian, S.C. 2015. Removal of Pb and Zn from contaminated soil by different washing methods: the influence of reagents and ultrasound. Environ. Sci. Pollut. Res., 22: 20084-20091.

Wei, M., Chen, J. and Wang, Q. 2018. Remediation of sandy soil contaminated by heavy metals with $Na_2EDTA$ washing enhanced with organic reducing agents: element distribution and spectroscopic analysis. Europ. J. Soil Sci., 69(4): 719-731.

Yang, G.C. and Lin, S.L. 1998. Removal of lead from a silt loam soil by electrokinetic remediation. J. Hazard. Mater., 58: 285-299.

Nature Environment and Pollution Technology
An International Quarterly Scientific Journal

p-ISSN: 0972-6268
(Print copies up to 2016)
e-ISSN: 2395-3454

Vol. 22 | No. 1 | pp. 139-148 | 2023

Original Research Paper

https://doi.org/10.46488/NEPT.2023.v22i01.012

Open Access Journal

# An Integrated GIS-AHP Approach for Municipal Solid Waste Landfill Siting in Srikakulam District, Andhra Pradesh

**Penki Ramu*†, Basina Sai Santosh* and Praveen S.****
*Department of Civil Engineering, GMR Institute of Technology, Rajam, Andhra Pradesh, India
**Head of Products, ECOSTP Technologies Private Limited, Bengaluru, 562125, India
†Corresponding author: Penki Ramu; ramu.p@gmrit.edu.in

**Nat. Env. & Poll. Tech.**
**Website: www.neptjournal.com**

*Received:* 27-05-2022
*Revised:* 04-07-2022
*Accepted:* 19-07-2022

**Key Words:**
Municipal solid waste
Landfill
Geographic information system
Analytic hierarchy process
Site suitability map

## ABSTRACT

The availability of land for proper waste disposal is one of the most important and emerging potential challenges in most big cities. Although some attempts are being made to minimize and recover garbage, landfill disposal continues to be the dominant method of waste disposal. An improper landfill site can negatively impact the environment, the economy, and the environment. Thus, it should be carefully chosen, taking into consideration both rules and standards from other sources. To examine all aspects of this study, an integration of the "Geographic Information System (GIS)" and the "Analytic Hierarchy Process (AHP)" was incorporated for land-fill site selection. Various parameters were examined to make decisions about landfill site selection. These parameters included slope, elevation, soil texture, LULC, surface water, groundwater table, road network, historical areas, and residential areas. An analytic-hierarchy process was used to determine the relative importance of each parameter, and a final site suitability map was created. With an equal interval classification method, the final index model was categorized into four categories, which included "unsuitable", "less suitable", "moderately suitable" and "suitable". As a result, 30.28% of the study area was less suitable, 28.49% was moderately suitable, 12.39% was suitable, and 28.84% of the study area was unsuitable for landfilling.

## INTRODUCTION

The current environmental concerns have stimulated the interest of institutions, industries, and the general public in two critical concepts: sustainability and circular economy (Ingrassia et al. 2020, 2019). A circular economy-based production would allow us to meet current needs without compromising the ability of future generations to meet their own needs by optimizing resources, energy consumption, wastes, and emissions through protracted design, maintenance, and 5R(repair, reuse, remanufacturing, refurbishing, and recycling). This is in contrast to linear economies based on a "make-use-dispose" model of resource consumption (Ingrassia et al. 2020, Penki & Rout 2021, Silva de Souza Lima Cano et al. 2022). Many of them believe that sustainability is associated with environmentalism, but it is based on three pillars: economy, social, and environmental sustainability.

**ORCID details of the authors:**

**Penki Ramu**:
https://orcid.org/0000-0001-7551-9630

Solid waste management (SWM) has attracted new attention due to the urgent requirement to adhere to the circular economy (CE) principles and improve waste management rather than disposing of waste in landfills or dumping it in the environment (Silva de Souza Lima Cano et al. 2022). As a means of achieving CE, it is necessary to devise strategies for recovering and preserving the waste generated at all stages of both the production and consumption value chains, whether it is man-made materials, natural resources, or manufactured materials, components, and goods (Geneletti 2010, Ingrassia et al. 2020). This refers to the recovery of resources from the garbage. The recovery of resources from garbage is not an easy task. It is dependent on the different compositions of solid waste and the various collections and management schemes used across the world (Kamdar et al. 2019, Nas et al. 2010, Penki & Rout, 2021). On the other hand, recovering resources from garbage is a difficult process; garbage must be disposed of efficiently and scientifically while safeguarding health and the environment. Perhaps, the construction of landfill sites for multiple purposes provides a clear perspective for resource recovery and contributes value in the real world. However, getting this done by a manual

survey is a very big task that involves much manpower and time. So, within this approach, the application of RS and GIS is attracting significant interest in environmental considerations for sustainable municipal solid waste(MSW) site selection (Balew et al. 2022, Ingrassia et al. 2019, Şener et al. 2010).

Land-fill site selection is a significant and complicated phase that is influenced by various factors and laws. Further research is needed to consider numerous morphological, economic, and environmental elements that to provide the optimal location with the lowest socioeconomic and environmental costs (Al-Anbari et al. 2014, Barakat et al. 2017). A wide range of analyses have been conducted on urban landfill sites throughout the major regions of the world, and many criteria, such as morphological, economic, and environmental, have been employed to choose sites (Al-Anbari et al. 2014, Barakat et al. 2017, Sumathi et al. 2008). Environmental considerations are crucial, knowing that the landfill might have an impact on the bio-physical environment and the biological system of the neighboring areas (Barakat et al. 2017, Eskandari et al. 2016, Pasalari et al. 2019, Torabi-Kaveh et al. 2016). Land-fill Siting Suitability assessment is complex because of the multiple and various (morphological, economical, and environmental) criteria since it is difficult to integrate them and give them weights(Barakat et al. 2017). GIS-based multicriteria evaluation (MCE) is therefore an ideal tool for such analyses since it can handle a huge amount of spatial data from diverse sources (Barakat et al. 2017, Rahmat et al. 2017, Wang et al. 2009). Since GIS can handle enormous amounts of geographical data from diverse sources, GIS-based multicriteria evaluation (MCE) is an appropriate tool for such evaluations (Ahire et al. 2022, Al-Anbari et al. 2014, Barakat et al. 2017, Bosompem et al. 2016, Feo & Gisi 2014, Ravinder & Ramu 2020, Sumathi et al. 2008). GIS-based multicriteria suitability assessment is one of the most successful assessment strategies for generating models for garbage landfill sites because of their capacity to handle a vast level of spatial data from a range of sources (Barakat et al. 2017, Kamdar et al. 2019, Pasalari et al. 2019, Rao & Babu 2018, Silva de Souza Lima Cano et al. 2022). One of the challenges in the MCE process is evaluating the weight of selected criteria that have unequally influenced land suitability (Barakat et al. 2017). While there are numerous ways to determine the weighting of these factors, the analytical hierarchy process (AHP) has typically been used strategy (Bahrani et al. 2016, Barakat et al. 2017, Donevska et al. 2011, Geneletti 2010, Moeinaddini et al. 2010, Nas et al. 2010, Penki et al. 2022a, 2022b, Rahmat et al. 2017, Ramu 2020, Şener et al. 2010, Sumathi et al. 2008, Torabi-Kaveh et al. 2016, Wang et al. 2009).

To develop appropriate land-fill sites for the Srikakulam district, the present research used AHP and GIS techniques to develop a final suitability map. The spatial analysis was

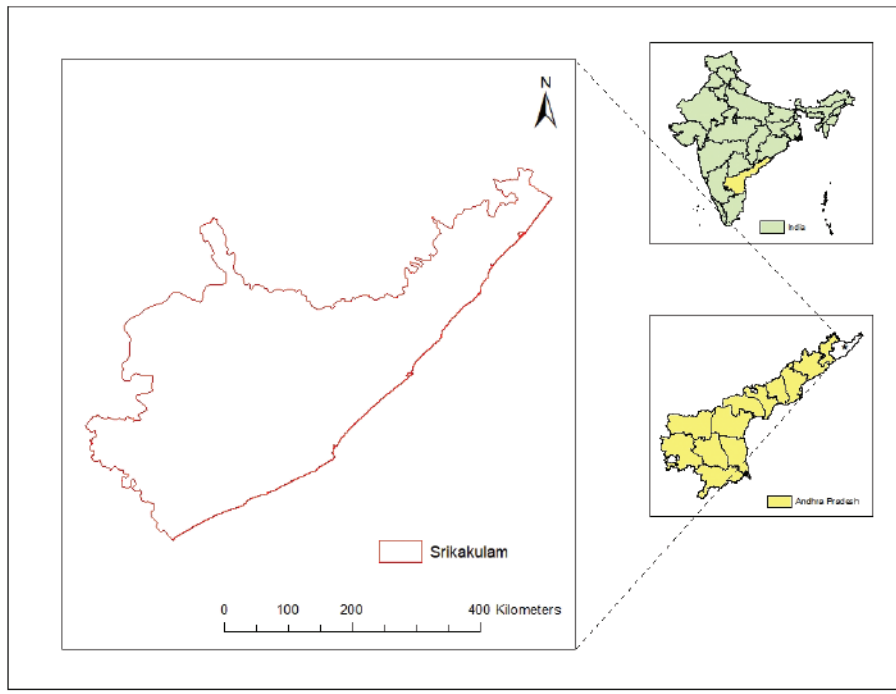


Fig. 1: Study area map.

conducted using AHP methods within a GIS environment, using quantifiable data.

## STUDY AREA

Srikakulam District is the extreme Northern District of Andhra Pradesh within the geographic coordinates of 18° 20' and 19° 10' of Northern latitude and 83° 50' and 84° 50' of Eastern longitude. It has a total area of 5,837 sq km with a total population of 2,703,114. The key features of Srikakulam are it has about 1865 revenue villages, a coast-line of 193 km, and a rail network of 128 km. Urbanization in conjunction with lifestyle change contributes to higher waste generation (Fig. 1). As per CPCB, only 68% of the MSW generated in the country is collected of which, 28% is treated by the municipal authorities. The research area is mostly surrounded by residential areas, agricultural areas, scrublands, and quarry sites. The generation of solid waste is expected to rise as a product of fast urbanization, migration of people, and an improvement in people's standard of life. This requires proper waste treatment and disposal; otherwise, unsanitary scenarios arise. However, new landfill sites are required to meet future requirements and to dispose of the waste scientifically. As a result, the study for this research focuses on GIS and AHP for landfill location selection.

## MATERIALS AND METHODS

The first stage in solid waste disposal by landfill is to pick the relevant site. The selection of a landfill site involves consideration of various morphological, environmental, and socio-economic cost aspects, as well as obeying governmental regulations. The landfill location for Srikakulam is being identified by employing GIS and AHP in the present research. To begin, the criteria for selecting the landfill are divided into three categories: morphological, environmental, and socio-economical characteristics (Fig. 2). Morphological factors such as slope, elevation, and soil texture are taken into account for evaluating appropriateness. Similarly, under the environmental criteria, land use, land cover, surface water, and groundwater table are taken into account. From the socio-economic viewpoint, the distance of various sites from roadways, the distance of various historical landmarks, and the distance from residential areas are all taken into account for evaluating suitability. A thematic map is created using GIS for each criterion. The AHP approach is used to compute rankings for each criterion. The produced thematic maps are reclassified using the previously acquired rankings for overlay analysis. The overlay analysis is used to produce the Land Suitability Index (LSI) for the study area. The research region is divided into four groups based on the acquired LSI values: unsuitable, less suitable, moderately suitable, and suitable.

### Data-Collection

The purpose of this research was to identify viable areas for "Municipal Solid Waste(MSW) disposal". The most recent data was acquired from multiple web portals. The elevation and slope maps were generated using SRTM-Dem, which was acquired from USGS Earth Explorer. The FAO/UNESCO Soil Map of the World is used to acquire data on soil texture. The LULC map was created using Landsat-8 imagery. The Global surface water explorer provided the surface water. The data for the groundwater table was

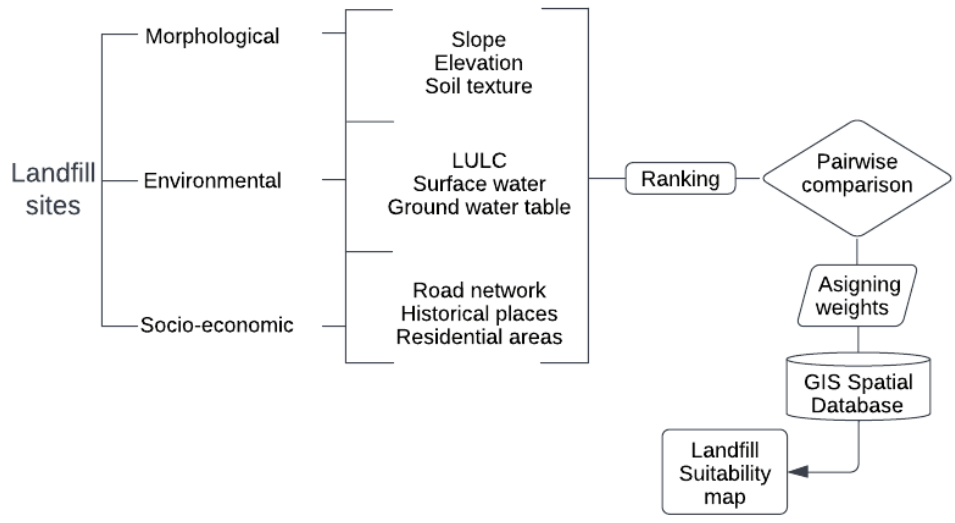


Fig. 2: Flowchart of the methodology.

collected from the India WRIS. The road network data was retrieved from Diva-Gis, and the locations of historical sites and residential areas were determined by hand.

### Morphological Perspective

#### Slope and Elevation

Slope and elevation are the two most important criteria to consider while constructing a landfill site. Highly sloping terrain demands costly operating processes that are not cost-effective making it the least desired option. In addition, very elevated places are not suggestible. Land slopes ranging from 0° to 10° have been proposed as suitable for landfill site building As a result, locations with slopes larger than 15° were deemed inappropriate, but those with only a small slope of less than 5° were deemed quite acceptable. Similarly, elevations over 120 m were deemed undesirable, but elevations below 40 m were deemed quite acceptable in this study. Using data from the USGS earth explorer, a DEM (digital elevation model) of the research region was created. ArcGIS software was used to create the slope and elevation maps.

#### Soil-Texture

"Soil" has a considerable impact on the quantity of groundwater that penetrates the earth and, as a consequence, on the number of contaminants that are capable of flowing into the unsaturated zone (Kamdar et al. 2019). Clay and silt are made up of smaller particles that can reduce the permeability of the soil and limit contaminant penetration. Sand and sandy loam are among the most permeable soils and are thus inappropriate for landfills, However, clay and clay loam are among the least permeable soil types, while sandy clay is acceptable. The water permeability and high porosity of sandy soil can cause landfill sites to impact water quality, which can lead to landfill sites releasing contaminants into the water. Thus, a soil texture map was generated for the research region using the FAO/UNESCO global soil map, and three soil type layers were discovered, with loam, sandy clay loam, and sandy loam graded as very-appropriate, moderately-suitable, and not-suitable, respectively.

### Environmental Perspective

#### LULC

Land usage depicts how humans interact with the land and the natural environment. Forest, agricultural, residential, industrial, military, and archaeological regions, water bodies, and bare and wet terrain are all examples of land-use types. However, distinct barren, vegetated, and agricultural lands are the best places for landfill construction. This criterion's goal is to conserve highly productive or undeveloped areas while still ensuring minimal capital costs. Thus, forests and residential areas were deemed unsuitable for dump sites, and historical regions were also deemed undesirable. Industrial areas, which play an essential part in the growth of an area, were graded as moderately-sensible, whereas barren, vegetated, and agricultural lands were considered extremely suitable. Finally, the most highly desirable locations designated for landfill sites in this study were barren lands.

#### Surface Water

Landfills emit toxic gases and effluent. As a result, landfills must not be built near bodies of water such as streams, lakes, ponds, & rivers. According to the Central Pollution Control Board (CPCB) Central Public Health & Environmental Engineering Organisation (CPHEEO), Govt of India, for wetlands and any other water body, a buffer zone of 300 m is recommended. Therefore, a buffer zone of 300 m was validated for all surface waters, and any area with a buffer zone of fewer than 300 m from surface water was deemed unsuitable, while buffer zones of 300 m to 600 m and 600 m to 900 m, respectively, were deemed moderately-suitable, and buffer zones greater than 900 m were deemed highly-suitable.

#### Groundwater Table

According to the CPHEEO and CPCB, a landfill site should be located in an area with a suitably low groundwater level, while sites with an immense groundwater intensity require a specific layout. In this work, the depth of the groundwater table was determined using an inverse distance weighting (IDW) interpolation technique to water level data. Groundwater depths of "0-1.5 m", "1.5-3 m", and "3-4.5 m" were found to be inappropriate, moderately suitable, and extremely suitable, respectively. Depths of more than 4.5 m were confirmed to be appropriate.

### Socio-Economic Perspective

#### Road Network

Another key economic consideration that influences dump site location selection is the distance from roadways. Since landfills are expensive to transport, they shouldn't be positioned too far away from roads; as their distance from roads increases, their suitability ranking decreases (Kamdar et al. 2019). As a result, a permanent road connecting the waste site to the active road network is required. For minor operations, the roadway ought to be 5m wide, and for bigger dumps, it must be 6 to 8 m wide. Furthermore, garbage trucks should not obstruct traffic movement. In this study, a distance of greater than 1000 m from a road network is

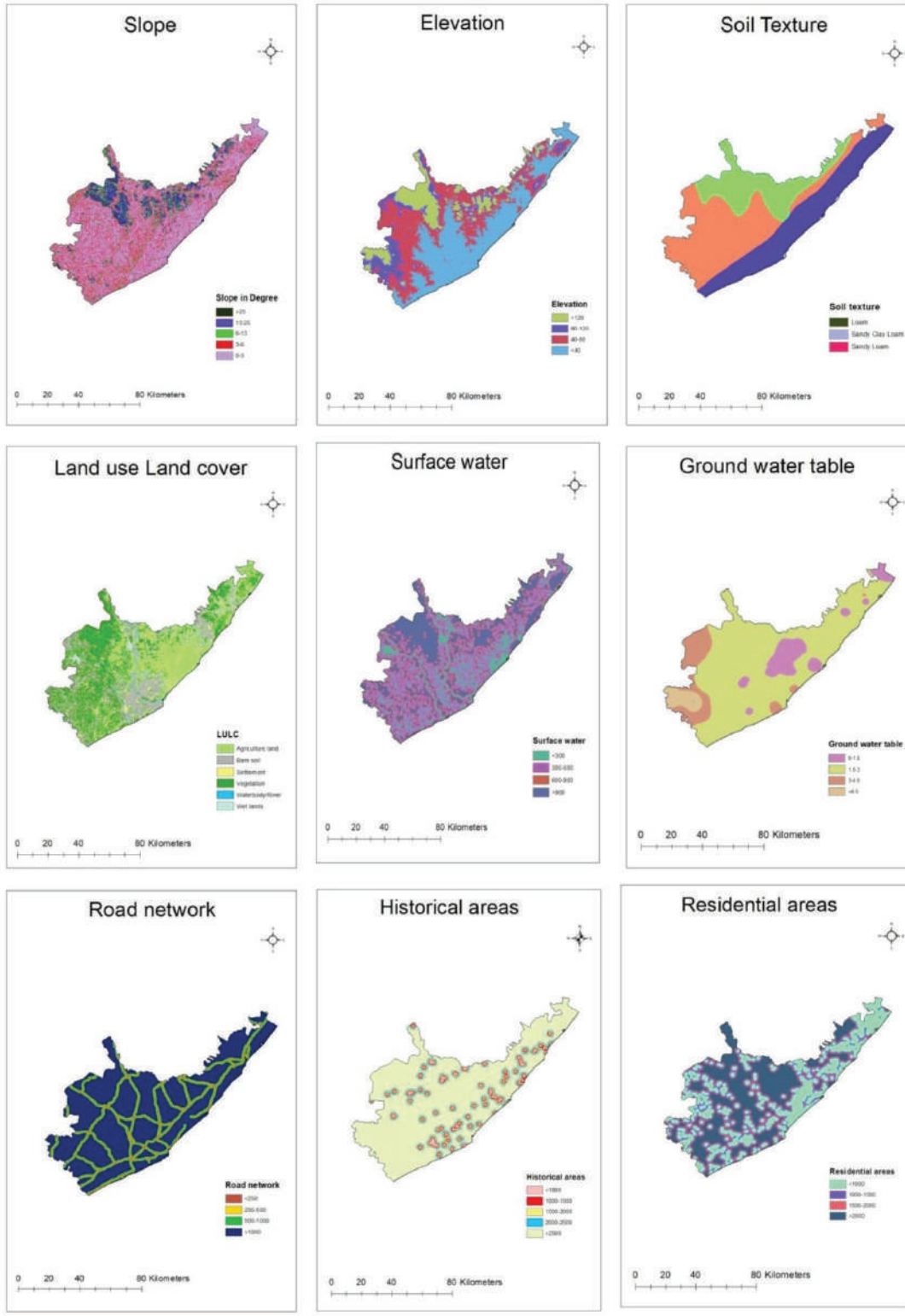


Fig. 3: Maps illustrating the suitability of evaluated criteria for Municipal solid waste landfill siting.

deemed extremely suitable for vehicles, while distances of lesser than 250 m are deemed unsuitable by the Department of Highways.

**Historical Places**

Temples, parks, restaurants, hotels, theatres, commercial malls, and waterfalls are among the historical landmarks in the studied region. According to the CPHEEO and CPCB, construction of landfill sites within 1000 m of historical sites is forbidden. As a result, based on GIS software data, a buffer zone of 1000 m was established near "historical sites." In this study, a buffer zone of less than 1000 m was deemed undesirable, whereas one of more than 2500 m was deemed extremely appropriate.

**Residential Areas**

According to the "Not In My Backyard (NIMBY)" phenomenon, this criterion is extremely essential and is the primary feature accountable for minimizing the count of appropriate sites for landfills. The vicinity of a landfill to a household area addresses a series of environmental issues, including pricing, future urban growth, and human health. As a result, in this research, a 1000-meter buffer zone was established surrounding residential areas to evade community objection. A buffer zone of below 1000 m and more than 2000 m was deemed undesirable and extremely suitable, respectively.

**AHP Application**

The AHP approach and the GIS tool were used to analyze the morphological, environmental, and socioeconomic considerations because they were unlike in nature, described in diverse units, and partly or entirely inconsistent (Kamdar et al. 2019). Weights have been assigned to several criteria through AHP. Each decisive factor was given a 'Weight' based on the author's knowledge of the local circumstances, including the local MSWM scenario (Kamdar et al. 2019). The AHP technique was used up to produce the weight for the main "criteria and sub-criteria". AHP is a widely accepted decision-making technique for evaluating data for the valuation of acceptable land-fill sites using a GIS application. The AHP method is carried out in three main phases. The first stage is to analyze the decision-making process into a hierarchical structure, as shown in Fig. 2. A 'pair-wise comparison' is used to calculate weights for the different criteria in the following step of AHP. A criterion's weight is calculated by rating its importance and compatibility. Expert judgment is used to complete the assessment of the pair-wise comparisons. A 1-9 point scale developed by Kamdar et al. (2019) and Saaty (1990) can be used to compare various criteria, as presented in Table 1. Based on expert opinion and AHP pairwise comparisons, Table 3 illustrates the final weights employed for land-fill site selection in the research region using the 'AHP approach'(Kamdar et al. 2019). The very last step is to check the consistency ratio. Eq. (1) represents the mathematical form for calculating CR.

Table 1: Saaty's 1-9 scale for AHP (Penki et al. 2022, Saaty 1990).

| Conceptual-Scale | Intensity of Importance | Inverse |
|---|---|---|
| Extremely-importance | 9 | 1/9 |
| Very strong to extremely-importance | 8 | 1/8 |
| Very strongly importance | 7 | 1/7 |
| Strongly to very strongly importance | 6 | 1/6 |
| Strongly importance | 5 | 1/5 |
| Moderately to strongly the importance | 4 | 1/4 |
| Moderately importance | 3 | 1/3 |
| Equally to moderate importance | 2 | 1/2 |
| Equally importance | 1 | 1 |

$$CR = CI/RI \quad \ldots(1)$$

Where, CI is the consistency index and RI is the random index or mean consistency index, depending on the size of the matrix. Eq. (2) describes the mathematical formulation for calculating the CI.

$$CI = (\lambda_{max} - n)/n - 1 \quad \ldots(2)$$

Where n is the matrix size (n x n) and $\lambda_{max}$ is the principal eigenvalue. Table 2 shows the RI values used for various matrix sizes.

In general, the CR should be less than 0.10 (i.e., 10%), to ensure the matrix's consistency, while a CR greater than 0.10 implies inconsistency in the expert's judgments, requiring re-evaluation. The ArcGIS 10.3 tool was utilized in this study to integrate the various map layers and their weights. To put the various data layers into a single spatial resolution, a base map of 931m was utilized for the overall data collection. Following that, the several maps with various weights are overlaid using the raster calculator tool in GIS. Using the following mathematical Eq. (3), the weights of the individual criteria were added to obtain the landfill suitability index.

$$LSI = \sum_{i=1}^{n} w_i * r_i \quad \ldots(3)$$

Table 2: Random index (RI)(Penki et al. 2022).

| n | 1 | 2 | 3 | 4 | 5 | 6 | 7 | 8 | 9 | 10 | 11 | 12 |
|---|---|---|---|---|---|---|---|---|---|---|---|---|
| RI | 0.00 | 0.00 | 0.58 | 0.90 | 1.12 | 1.24 | 1.32 | 1.41 | 1.45 | 1.49 | 1.51 | 1.54 |

Table 3: Suitability ranking of factors.

| Main criteria | Param | Sub-Class | Risk Vulnerability | Rank | Parameter weight | Sub-Class weight [%] |
|---|---|---|---|---|---|---|
| Morphological perspective | Slope | 0-3 | Highly-suitable | 1 | 0.079 | 49 |
| | | 3-6 | Suitable | 2 | | 27 |
| | | 6-13 | Moderately-suitable | 3 | | 14 |
| | | 13-25 | Less-suitable | 4 | | 8 |
| | | > 25 | Un-suitable | 5 | | 2 |
| | Elevation | < 40 | Suitable | 1 | 0.081 | 66 |
| | | 40-80 | Moderately-suitable | 2 | | 18 |
| | | 80-20 | Less-suitable | 3 | | 10 |
| | | > 120 | Un-suitable | 4 | | 6 |
| | Soil Texture | Loam | Highly-suitable | 1 | 0.065 | 55 |
| | | Sandy clay loam | Suitable | 2 | | 24 |
| | | Sandy loam | Moderately-suitable | 3 | | 21 |
| Environmental perspective | LULC | Waterbody/River | Un-suitable | 6 | 0.051 | 3 |
| | | Vegetation | Suitable | 2 | | 25 |
| | | Settlement | Less-suitable | 4 | | 7 |
| | | Agriculture land | Moderately-suitable | 3 | | 13 |
| | | Bare soil | Highly-suitable | 1 | | 48 |
| | | Wetlands | Un-suitable | 5 | | 4 |
| | Surface water | < 300 | Un-suitable | 4 | 0.217 | 7 |
| | | 300-600 | Moderately-suitable | 3 | | 16 |
| | | 600-900 | Suitable | 2 | | 25 |
| | | > 900 | Highly-suitable | 1 | | 52 |
| | Ground water table | 0-1.5 | Un-suitable | 4 | 0.199 | 6 |
| | | 1.5-3 | Less-suitable | 3 | | 14 |
| | | 3-4.5 | Moderately-suitable | 2 | | 22 |
| | | > 4.5 | Highly-suitable | 1 | | 58 |
| Socio-economic perspective | Road network | < 250 | Un-suitable | 4 | 0.044 | 6 |
| | | 250-500 | Less-suitable | 3 | | 14 |
| | | 500-1000 | Moderately-suitable | 2 | | 27 |
| | | > 1000 | Highly-suitable | 1 | | 53 |
| | Historical Areas | < 1000 | Un-suitable | 5 | 0.043 | 4 |
| | | 1000-1500 | Very less-suitable | 4 | | 6 |
| | | 1500-2000 | Less-suitable | 3 | | 12 |
| | | 2000-2500 | Moderately-suitable | 2 | | 22 |
| | | > 2500 | Highly-suitable | 1 | | 56 |
| | Residential areas | < 1000 | Un-suitable | 4 | 0.221 | 5 |
| | | 1000-1500 | Less-suitable | 3 | | 10 |
| | | 1500-2000 | Moderately-suitable | 2 | | 24 |
| | | > 2000 | Highly-suitable | 1 | | 61 |

Table 4: Areal extent of suitability index.

| S. No. | suitability classes | Range | Area In Hectare | % Area |
|---|---|---|---|---|
| 1. | Un-Suitable | 9.61-22.87 | 180925.7559 | 28.84 |
| 2. | Less-Suitable | 22.87-29.75 | 190001.9383 | 30.28 |
| 3. | Moderately-Suitable | 29.75-36.8 | 178736.7104 | 28.49 |
| 4. | Suitable | 36.8-52.4 | 77681.9563 | 12.39 |

Where $r_i$ is the rating of criterion i, n is the number of param, and $w_i$ is the weight of criterion i.

## RESULTS AND DISCUSSION

This study resulted in the development of suitability maps (Fig. 2) for the different criteria considered. The final map displays the areas that are unsuitable, less suitable, moderately suitable, and suitable. Fig. 4 and Table 4 display the suitable index map as well as its areal extent, respectively. A 'suitability index map' of the research region was generated by combining all of the weighted criteria in an overlay analysis. A total land area of 627346.3609 hectares, reflecting 28.84%, was categorized as unsuitable, 30.28% as less suitable, 28.49% as moderately suitable, and 12.39% as suitable. The land-fill site assortment in the study area was based on a combination of morphological, environmental, and socioeconomic factors, as well as GIS and MCE methodologies.

As previously mentioned, the data was gathered from various sources and in various formats (such as raster and shapefile), but they were ultimately converted into raster format by executing of GIS tool. However, it should be noted

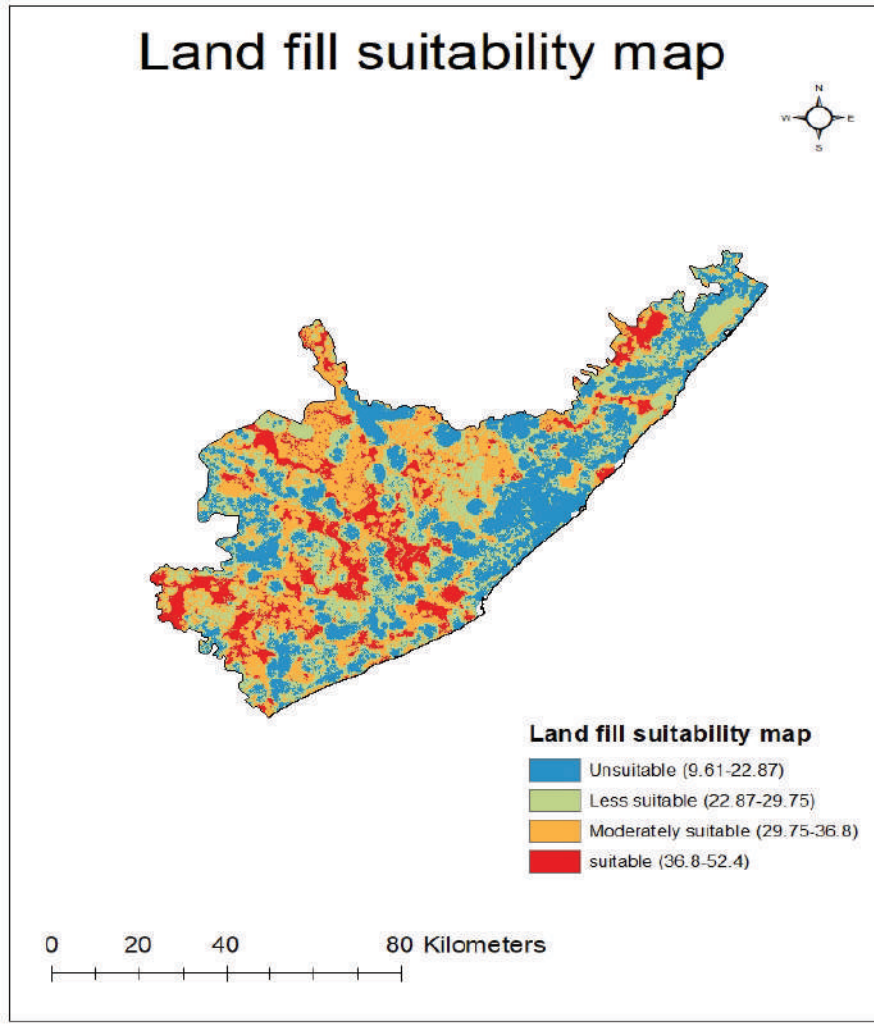


Fig. 4: Final landfill suitability map.

that all files must have the same cell size and coordinate system after conversion to raster format.

On the final map, there are some values that denote areas that are unsuitable, less suitable, moderately suitable, and suitable; these values were taken using the AHP as a core. Greater impact areas receive more weight in the AHP process, and lesser impact areas receive less weight. As a result, areas with high values on the final map are best suited for landfill disposal.

It's worth noting that the approach has worked well and produced accurate results for landfill site selection that was in line with field observations. Additionally, before making a final decision on the best site, it is recommended that they be further evaluated according to other local criteria and field investigations since some of these criteria must be explored in landfills, as described by the requirements of the landfill environmental impact assessment regulation. Finally, the applied technique employed in the study may be used as a reference for establishing the best site selection choice for MSW dumps, as well as a framework for future research in other disciplines.

## CONCLUSIONS

A landfill site selection is complex and challenging that demands a high level of complex tasks that requires a substantial balance between morphological, environmental, and socioeconomic considerations. The ideal location for dump sites in the Srikakulam district was investigated using an MCDM approach that was used in a GIS platform. It is advised that the findings of the study be compared to those acquired from field investigations to select the most acceptable landfill-building sites. Additional studies, such as thorough geological and geotechnical investigations, public acceptability surveys, a waste inventory, and the evaluation of building appropriateness, should be conducted in selected locations.

In the case of landfills, implementing landfill site taxes would put together a more expensive waste management preference, which would reduce waste dumped into landfills. A landfill tax would encourage households to recycle more of their waste as the municipality would use a unit-based pricing system to charge households for the high costs of landfills. Further, the landfill tax policies would encourage waste prevention and recycling so that landfilling would become more financially attractive as well as encourage waste-to-value technology.

Insofar as this study's approach is scientific, its outcomes are likely to be an efficient tool for decision-makers, planners, and stakeholders. This is because they can decide where to site landfills in the future. Furthermore, this strategy can assist decision-makers in solving waste management problems by completing decision analysis functions for landfill dumping. Also, the strategy used in this study could be easily applicable to other regions of the world where landfill siting is a major issue.

## REFERENCES

Ahire, V., Behera, D.K., Saxena, M.R., Patil, S., Endait, M. and Poduri, H. 2022. Potential landfill site suitability study for environmental sustainability using GIS-based multi-criteria techniques for Nashik. Environ. Earth Sci., 81: 178. https://doi.org/10.1007/s12665-022-10295-y

Al-Anbari, M., Al-Ansari, N. and Kareem, H. 2014. GIS and multicriteria decision analysis for landfill site selection in Al-Hashimyah Qadaa. Nat. Sci., 06: 282-304. https://doi.org/10.4236/ns.2014.65032

Bahrani, S., Ebadi, T., Ehsani, H., Yousefi, H. and Maknoon, R. 2016. Modeling landfill site selection by multi-criteria decision making and fuzzy functions in GIS, case study: Shabestar, Iran. Environ. Earth Sci., 75: 337. https://doi.org/10.1007/s12665-015-5146-4

Balew, A., Alemu, M., Leul, Y. and Feye, T. 2022. Suitable landfill site selection using GIS-based multi-criteria decision analysis and evaluation in Robe town, Ethiopia. Geo. J., 87: 895-920. https://doi.org/10.1007/s10708-020-10284-3

Barakat, A., Hilali, A., Baghdadi, M.E. and Touhami, F. 2017. Landfill site selection with GIS-based multi-criteria evaluation technique. A case study in Béni Mellal-Khouribga Region, Morocco. Environ. Earth Sci., 76: 413. https://doi.org/10.1007/s12665-017-6757-8

Bosompem, C., Stemn, E. and Fei-Baffoe, B. 2016. Multi-criteria GIS-based siting of transfer station for municipal solid waste: The case of Kumasi Metropolitan Area, Ghana. Waste Manag. Res., 34: 1054-1063. https://doi.org/10.1177/0734242X16658363

Donevska, K., Gorsevski, P., Jovanovski, M. and Peshevski, I. 2011. Regional non-hazardous landfill site selection by integrating fuzzy logic, AHP, and geographic information systems. Environ. Earth Sci., 67: 1485. https://doi.org/10.1007/s12665-011-1485-y

Eskandari, M., Homaee, M. and Falamaki, A. 2016. Landfill site selection for municipal solid wastes in mountainous areas with landslide susceptibility. Environ. Sci. Pollut. Res. Int., 23: 12423-12434. https://doi.org/10.1007/s11356-016-6459-x

Feo, G.D. and Gisi, S.D. 2014. Using MCDA and GIS for hazardous waste landfill siting considering land scarcity for waste disposal. Waste Manag., 34: 2225-2238. https://doi.org/10.1016/j.wasman.2014.05.028

Geneletti, D. 2010. Combining stakeholder analysis and spatial multicriteria evaluation to select and rank inert landfill sites. Waste Manag., 30: 328-337. https://doi.org/10.1016/j.wasman.2009.09.039

Ingrassia, L.P., Lu, X., Ferrotti, G. and Canestrari, F. 2019. Chemical and rheological investigation on the short- and long-term aging properties of bio-binders for road pavements. Constr. Build. Mater., 217: 518-529. https://doi.org/10.1016/j.conbuildmat.2019.05.103

Ingrassia, L.P., Lu, X., Ferrotti, G., Conti, C. and Canestrari, F. 2020. Investigating the "circular propensity" of road bio-binders: Effectiveness in hot recycling of reclaimed asphalt and recyclability potential. J. Clean. Prod., 255: 120193.

Kamdar, I., Ali, S., Bennui, A., Techato, K. and Jutidamrongphan, W. 2019. Municipal solid waste landfill siting using an integrated GIS-AHP approach: A case study from Songkhla, Thailand. Resour. Conserv. Recycl., 149: 220-235. https://doi.org/10.1016/j.resconrec.2019.05.027.

Moeinaddini, M., Khorasani, N., Danehkar, A., Darvishsefat, A.A. and Zienalyan, M. 2010. Siting MSW landfill using weighted linear combination and analytical hierarchy process (AHP) methodology in GIS environment (case study: Karaj). Waste Manag., 30: 912-920. https://doi.org/10.1016/j.wasman.2010.01.015

Nas, B., Cay, T., Iscan, F. and Berktay, A. 2010. Selection of MSW landfill site for Konya, Turkey using GIS and multi-criteria evaluation. Environ. Monit. Assess., 160: 491-500. https://doi.org/10.1007/s10661-008-0713-8

Pasalari, H., Nodehi, R.N., Mahvi, A.H., Yaghmaeian, K. and Charrahi, Z. 2019. Landfill site selection using a hybrid system of AHP-Fuzzy in GIS environment: A case study in Shiraz city, Iran. MethodsX, 6: 1454-1466. https://doi.org/10.1016/j.mex.2019.06.009

Penki, R. and Rout, S.K. 2021. Next-generation bitumen: a review on challenges and recent developments in bio-bitumen preparation and usage. Biomass Conv. Bioref., 11: 80. https://doi.org/10.1007/s13399-021-01803-4

Penki, R., Basina, S.S. and Tanniru, S.R. 2022a. Application of geographical information system-based analytical hierarchy process modeling for flood susceptibility mapping of Krishna District in Andhra Pradesh. Biomass Conv. Bioref., 16: 71. https://doi.org/10.21203/rs.3.rs-1399020/v1

Penki, R., Srinivasa Rao, T., Vinod Naik, G. and Aparna, R. 2022b. Identification of parking sites in the Kukatpally region using GIS and AHP. Adv. Constr. Mater. Sustain. Environ., 111: 447-456.

Rahmat, Z.G., Niri, M.V., Alavi, N., Goudarzi, G., Babaei, A.A., Baboli, Z. and Hosseinzadeh, M. 2017. Landfill site selection using GIS and AHP: A case study: Behbahan, Iran. KSCE J. Civ. Eng., 21: 111-118. https://doi.org/10.1007/s12205-016-0296-9.

Ramu, P. 2020. Fuzzy AHP, RS & GIS based hybrid approach for airport site selection: Kothagudem district. Int. J. Adv. Sci. Technol., 29: 1645-1653.

Rao, T.S. and Babu, I.N. 2018. MSW landfill site selection for Hyderabad city using GIS and AHP. J. Rem. Sens. GIS, 9: 15-25. https://doi.org/10.37591/.v9i1.81

Ravinder, R. and Ramu, P. 2020. Flood risk assessment using remote sensing and GIS for Anigunta watershed, Telangana. Int. J. Sci. Technol. Res., 9: 10.

Saaty, T.L. 1990. How to make a decision: The analytic hierarchy process. Europ. J. Oper. Res., 48: 9-26. https://doi.org/10.1016/0377-2217(90)90057-I

Şener, Ş., Şener, E., Nas, B. and Karagüzel, R. 2010. Combining AHP with GIS for landfill site selection: A case study in the Lake Beyşehir catchment area (Konya, Turkey). Waste Manag., 30: 2037-2046. https://doi.org/10.1016/j.wasman.2010.05.024

Silva de Souza Lima Cano, N., Iacovidou, E. and Rutkowski, E.W. 2022. Typology of municipal solid waste recycling value chains: A global perspective. J. Clean. Prod., 336: 130386. https://doi.org/10.1016/j.jclepro.2022.130386

Sumathi, V.R., Natesan, U. and Sarkar, C. 2008. GIS-based approach for optimized siting of municipal solid waste landfill. Waste Manag., 28: 2146-2160. https://doi.org/10.1016/j.wasman.2007.09.032

Torabi-Kaveh, M., Babazadeh, R., Mohammadi, S. and Zaresefat, M. 2016. Landfill site selection using combination of GIS and fuzzy AHP, a case study: Iranshahr, Iran. Waste Manag. Res., 34: 438-448. https://doi.org/10.1177/0734242X16633777.

Wang, G., Qin, L., Li, G. and Chen, L. 2009. Landfill site selection using spatial information technologies and AHP: A case study in Beijing, China. J. Environ. Manag., 90: 2414-2421. https://doi.org/10.1016/j.jenvman.2008.12.008.

Nature Environment and Pollution Technology
An International Quarterly Scientific Journal

p-ISSN: 0972-6268
(Print copies up to 2016)
e-ISSN: 2395-3454

Vol. 22 | No. 1 | pp. 149-157 | 2023

Original Research Paper

https://doi.org/10.46488/NEPT.2023.v22i01.013

Open Access Journal

# Experimental Study on Heat Recovery of Air Dryer from Waste Heat Energy of Condensing Unit from VCRS Air Conditioner

**S. N. Yaakop*(**), M. H. F. Md Fauadi*† and A. A. Muhammad Damanhuri*****

*Faculty of Manufacturing Engineering, Universiti Teknikal Malaysia Melaka, 76100 Melaka, Malaysia
**Kolej Komuniti Kota Marudu, Jaya Industrial Centre, 89108 Kota Marudu, Sabah, Malaysia
***Faculty of Mechanical and Manufacturing Engineering Technology, Universiti Teknikal Malaysia Melaka, 76100 Melaka, Malaysia
†Corresponding author: M.H.F. Md Fauadi; hafidz@utem.edu.my

**Nat. Env. & Poll. Tech.**
**Website: www.neptjournal.com**

*Received:* 20-07-2022
*Revised:* 12-09-2022
*Accepted:* 15-09-2022

**Key Words:**
HVAC system
Heat recovery unit
Air conditioning
Air dryer

## ABSTRACT

Heating, Ventilating, and Air Conditioning (HVAC) is a system to condition indoor air by cooling or heating to achieve thermal comfort for a human being. The HVAC system operates based on the refrigeration cycle, where heat is dissipated from the condensing unit in the warm air arrangement. This represents an ironic foundation of heat that might be recovered for further schemes or applications. In this paper, experimental work was developed to validate the proposed heat recovery system using heated air released from the condenser unit of the HVAC system as a source for the air dryer for the drying rack. Four different output parameters are to be observed in this research: the dry-bulb temperature of the air exit from the condenser unit, the dry-bulb temperature of the air inflowing the dryer, and the drying time and the relative humidity of the air leaving the dryer. These experimental works were conducted using a domestic application of a 1.0 hp air conditioning (AC) system with R-22 refrigerant gas and based on the following factors: The three-variant mass of wet clothes, the three-stage of mechanical fan speed for releasing warm air from the condenser, and the effect of variable ambient or surrounding air dry-bulb temperature were studied. A physical prototype of the dryer was constructed for proof-of-concept purposes. The experimental output was then analyzed to obtain precision and accurate data. To determine the system behavior, a refrigeration cycle analysis was conducted. It has been shown that an AC system of 1.0 hp can cover wet clothes drying of weights 1950 g, 4255 g, and 6350 g at 55, 80, and 110 min with a constant air velocity of 0.34 $m^{-3}.s^{-1}$ in an ambient temperature of 33°C. The significant contribution of this research is the proposed heat-recovery-based air dryer system with the capability to increase the Coefficient of Performance (COP) of the AC unit from 2.36 to 2.70. Hence, the energy-saving was received using the heat-recovered-based air dryer instead of a commercial electric air dryer system that uses high power consumption from their heater element.

## INTRODUCTION

Nowadays, free energy sources are wasted due to inefficient technological ability. This includes heat energy waste from electrical appliances, which consume ambient temperature rise, especially in the city area. In 2016, the Paris Agreement stated that the temperature of pre-industrial levels rises to 2°C, which required further actions to edge the temperature rise not more than 1.5°C (Analytics 2016). To decrease the temperature and increase any system operation, waste heat generated from the system must be recycled for useful applications. For example, waste heat can be recouped from multiple sources, including the automotive system (internal combustion engine) (Song et al. 2020), industrial system (boiler) (Kim et al. 2020), and residential system (split type AC). For instance, in an internal combustion engine widely used in rail transport, vehicle, marine, and decentralized power generation, the fuel energy in an internal combustion engine is transformed into sound mechanical work output is only 30% to 40%. The rest is a waste of heat energy (Badescu et al. 2017). It is critical to minimize the waste produced to ensure sustainable processes can be achieved. Several waste heat recovery methods have been explored to optimize energy consumption proficiency. Thakar et al. (2018) highlighted that exhaust vapors from a diesel machine can be recovered. Apart from that, the special heat exchanger design placement adjacent to the inlet and outlet vessel of the engine to facilitate the unused energy from the exhaust can be used to warm up the air passed to the engine. In China, ordinary gas-fired boilers were traditionally used to

substitute coal-fired boilers due to their fairly low emissions and opportune fuel delivery system (Hou et al. 2018).

Meanwhile, Suntivarakorn & Treedet (2016) researched the enhancement of boiler effectiveness using heat recovery for 9 tons.hr$^{-1}$ fire tube boilers, which belonged to an engineering facility in Thailand. The experimental result shows that fuel moisture content can be reduced by 3%, and the boiler efficiency increases by 0.41% when applying the heat recovery to parch the fuel and put on it to warm up the air before inflowing the burning compartment. A previous study determined that the HVAC system contributes to the major peak energy consumption for residential, commercial, and industrial buildings (Wang et al. 2020, Wei 2019). Fig. 1 illustrates the energy consumption breakdown for a building based on typical services, and AC shows the highest energy consumption with 34%.

Most research is conducted to uncover heat waste in an AC system derived from the second law of thermodynamics. Borri et al. (2017) did a simulation of absorption chiller integration to recover waste heat from the compression stage of the liquefaction sequence and used that heat to drive the absorption sequence. The results show a decrease in specific consumption of about 10% (537 kWh.t$^{-1}$ to 478 kWh.t$^{-1}$) and a rise in energy efficiency of approximately 11.5%. Recently, many researchers investigated the drying process through waste heat recovery, especially using an AC system (Kane et al. 2016, Husainy 2017, Nelwan et al. 2018). In the frame of this paper, a new recovery technology system for air dryers is suggested. The idea relies on recovering the heated air from the condenser unit of an AC system to supply an air dryer. Four different output parameters to be considered in this research are the dry-bulb temperature of the air exit from the condenser unit, the dry-bulb temperature of the air inflowing the dryer, the drying time, and the relative humidity of the air leaving the dryer. To validate the code, experimental works were conducted using a domestic application of a 1.0 hp AC system with R-22 refrigerant gas. Experimental shown based on the following factors: 1) the three-variant mass of a wet object, 2) the three-stage of the mechanical fan speed for releasing warm air from the condenser, and 3) the effect of variable ambient or surrounding air dry-bulb temperature. As far as the review is concerned, no prior study focuses on investigating the use of air dryers based on heat recovery from an HVAC system taking into account ambient temperature, the mass of the wet object, and airflow rate capacity. Therefore, the findings of this study may systematically reveal the interaction of essential variables in increasing the performance of the heat-recovered-based air dryer. This paper was organized as follows, starting with Section 2 illustrates the fundamental of the vapor compression cycle system. Section 3 describes the past studies of air dryers from AC units. Section 4 defines the new proposed air dryer system. Section 5 describes the procedure for setting up the experimental works. Section 6 describes three parametric study's critical parameters with the results and discussion. The final section illustrates the conclusion of this paper.

## Vapor Compression Cycle System

In an HVAC system, the AC operates using a vapor compression cycle consisting of four basic components (Shaban et al. 2020): compressor, condenser, expansion valve, and evaporator, as shown in Fig. 2.

First, process the compression of refrigerant gas through the compressor and leave it as high-pressure and high-temperature gas. In the second stage, the refrigerant

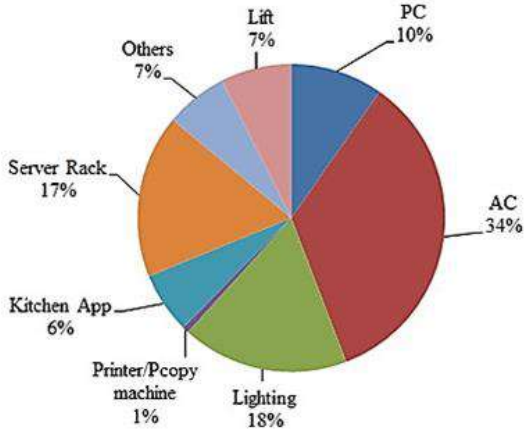


Fig. 1: The typical energy consumption breakdown of a building (Aus Govt - Department of Industry 2013).

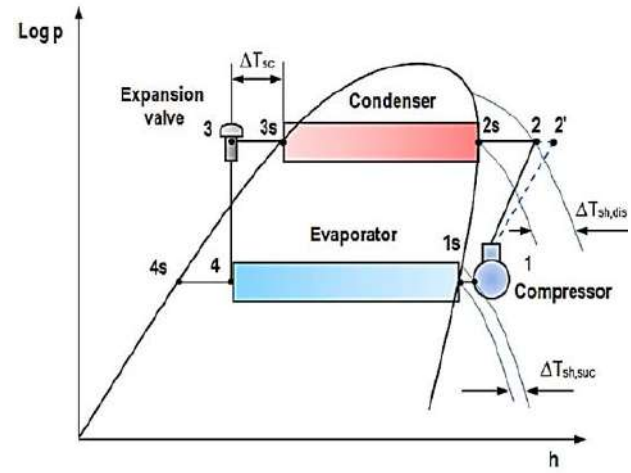


Fig. 2: P-h diagram for Vapor Compression Refrigeration System (VCRS) (Kocyigit et al. 2014).

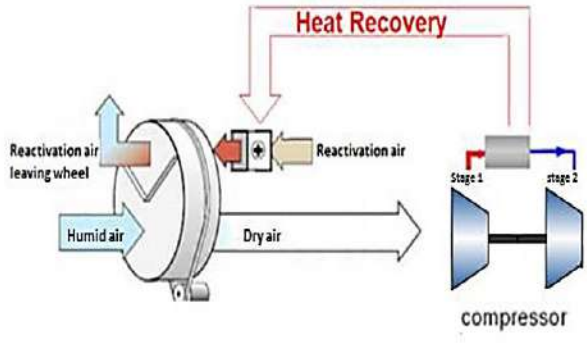


Fig. 3: Heat recovery for drying ambient air (Goodarzia et al. 2017).

gas passes through the condenser unit, which uses an air-cooled or water-cooled heat exchanger to dissipate the heat. During this process, the hot refrigerant gas is cooled by a condenser and becomes a warm liquid form. In the third stage, the warm refrigerant was regulated in an expansion valve or capillary tube to become a low-pressure and low-temperature refrigerant. Lastly, the refrigerant gas flowed into the evaporator, absorbing heat in the specified area. This stage will be affected by the increasing temperature of the refrigerant gas (Wang 2001). Finally, the refrigerant gas returns to the compressor, and the cycle is repeated in the operational mode of the AC system.

**Past Studies of Air Dryers from the AC Unit**

In a VCRS, the condensing unit rejects heat from a refrigerant in the condensing process. It produces a lot of waste heat, about 1.15 to 1.25 times the cooling effect on the evaporator side (Bhatia 2012). This percentage is more significant due to the heat of compression added into the system. The real proportion that arises is subject to the discharge and suction temperatures. High discharge and/or low suction temperature will increase the percentage. In recent years, there has been a growing amount of literature on discovering energy-efficient and industrial technology using heat recovery from the condensing unit. This is widely reported and extensively explored in the previous literature conducted to produce a recovery heat dryer system. Energy-saving for residential or industrial applications is the main issue recently focused on by researchers. Due to that issue, some researchers perform investigation and experimental work to recover waste heat from any resources to be integrated with an application to reduce energy consumption (Ramadan et al. 2017). Every residential or industrial may use AC for thermal comfort and to ensure indoor air quality (Wu et al. 2020). Some of the users may use the AC system for their cleanroom area. Waste heat generated from the compressor of AC can be recycled in many ways, including drying. Goodarzia et al. (2017) studied the effectiveness of drying the ambient air with the coupled air from the compressor and solid desiccant wheel. The first stage of the air compressor recovered to reactivate the desiccant wheel and remove the moisture in ambient air, as shown in Fig. 3.

Other than drying the ambient air, another study is about the drying characteristics and the heat pump's performance for the clothes drying process (Goodarzia et al. 2017). They construct a small-scale prototype using the necessary heat pump components and accessories of a 1-meter cube drying chamber of 1400 mm x 1000mm x 1080mm. The heat pump capacity in this model is 800 watts with an R-22 refrigerant set-up. The clothes are moistened and initially dried via the conventional spinner for about 3 min. Three samples of clothes are taken in this experiment. The first sample clothes weight when dry is 1.96 kg and when wet is 3.00 kg, the second sample clothes weight when dry is 3.42 kg and when wet is 5.25 kg, and the last sample clothes weight when dry is 4.15 kg and when wet is 6.38kg. The initial weights to be dried will be taken based on weight after passing through the spinner.

The results in Fig. 4 show that the clothes for sample 3.0 kg will be dried in 65 min, sample 5.25 kg will be dried in 102 min, and sample 6.38 kg will be dried in 121 min. The summary of the graph proves that the highest temperature inside the drying chamber, the faster the clothes are dried. The recent literature review shows no methods exist for replacing the air dryer chamber with an open space concept. The minimum space required for the air dryer chamber in the previous study is a 1-meter cube, not including the other fittings and accessories, which is not suitable if this technology is provided for residential usage. In this research, experimental works were conducted to study the effectiveness of replacing the air dryer chamber with an open space chamber concept. If future works to use the waste heat recovery technology of VCRS are applicable, much saving of energy consumption can be done; hence the performance of the VCRS also be improved.

**Proposed New Air Dryer System**

This research presents an improved air dryer application technology to recover the waste heat from the condenser unit from the AC system. The initial stage is to identify the critical elements involved in the waste heat recovery process for the air dryer system. The critical elements were selected based on the previous results conducted by other researchers. To gain useful results for the proposed system, critical elements are the main factors that contribute to system performance and efficiency. The parameters required to find the drying time of the proposed system are shown in Fig. 5. Meanwhile,

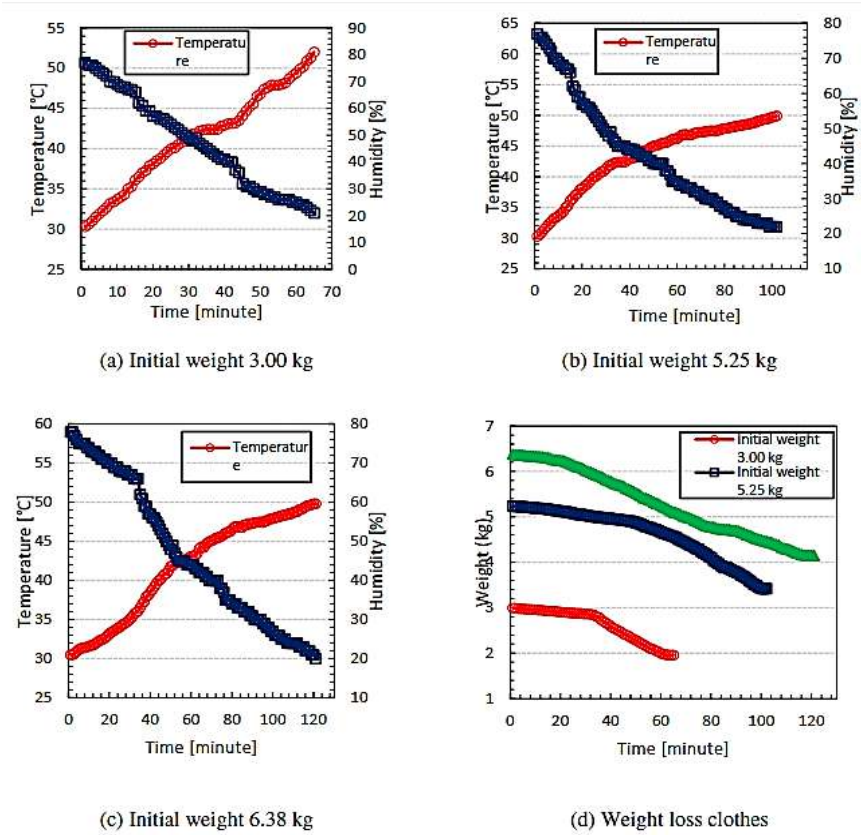


Fig. 4: Typical temperatures and weight loss of the clothes dried in the drying chamber (Goodarzia et al. 2017).

the schematic of the proposed air dryer system is shown in Fig. 6. The ambient air will pass through the condensing unit and become the hot air temperature, which is then used in the air dryer system to dry and return to the surrounding area.

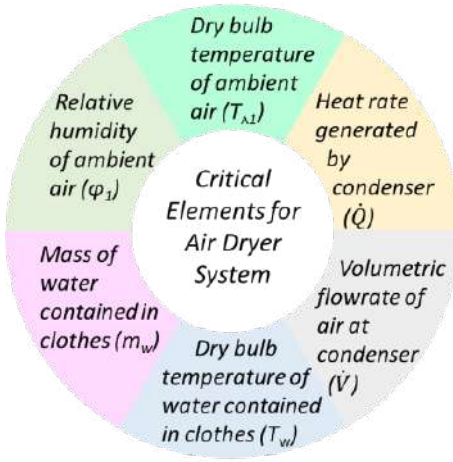


Fig. 5: Critical elements for air dryer system.

## MATERIALS AND METHODS

Fig. 7 depicts a research flowchart on developing a new proposed air dryer to identify product performance. The first step involves several phases to determine the standard performance condition. Correspondingly, it is necessary to consider the preliminary design for this project to give users the best product. It is an excellent way to detect functionality and discover better ways and combinations of the achieved functionality. The next stage is to choose several design alternatives for the best choices of products. Examples of requirements are dryer size, AC type, and size. After all, criteria have been determined; fabrication is done to produce the product. Subsequently, testing this product operationally is done to find the coefficient of performance of this product. Note that this process must meet the criteria of this project to ensure that this product has a suitable performance to benefit users in terms of energy saving. This process goes to the preceding stages if it fails to meet its requirements. The final step is to collect data and analyze the performance of the new proposed air dryer system.

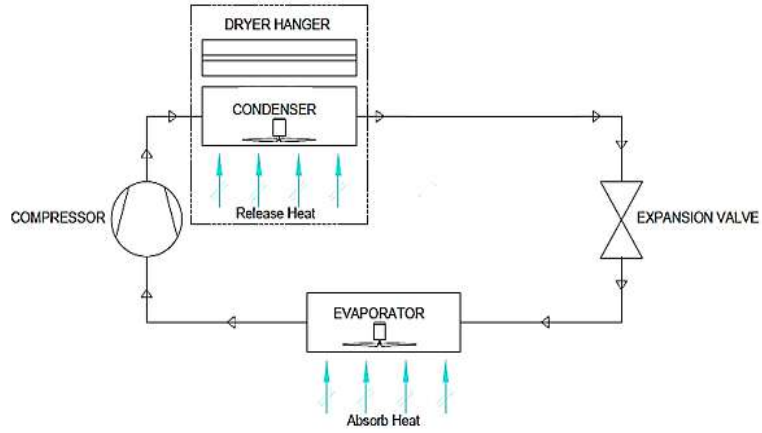


Fig. 6: The proposed schematic of the air dryer system.

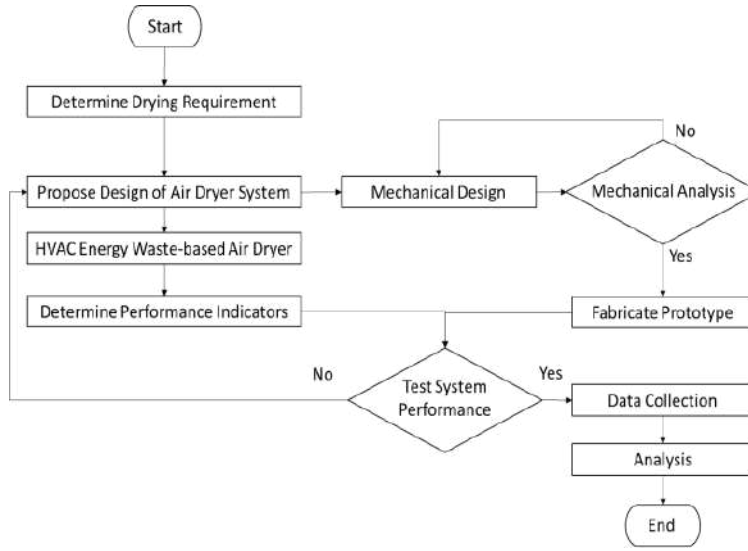


Fig. 7: Flowchart of the research procedure.

The fabrication process must follow the schematic design of the product as selected during the design stage. This experiment was conducted using a 1.0 hp AC system with R-22 refrigerant gas. The domestic user commonly uses the AC capacity of 1.0hp due to this capacity at the house, and easy to study the effectiveness of the proposed system compared to the commercial system. The specification of the AC system is shown in Table 1.

The proposed air dryer system was constructed based on five main components: a drying clothes hanger rack, condenser, capillary tube, evaporator, and compressor. The air dryer design constructs with axes to hold the clothes. Two temperature sensors are placed on the drying hanger (upstream and downstream of the clothes) to measure the dry-bulb temperature of condensing air passed through the clothes. The dry-bulb temperature detected by the temperature sensor placed before clothes are equivalent to the dry-bulb temperature of the air released from the condenser unit. To identify the mass of the wet clothes, an EBalance 1501 electronic digital scale weight balance with an accuracy of 0.01 decimal places is placed at the drying hanger axes. Apart from that, the mechanical fan from the 860W fan motor has three speeds low (0.14 $m^3.s^{-1}$), medium (0.24 $m^3.s^{-1}$), and high (0.34 $m^3.s^{-1}$), which will be placed at the upper hanger to blow hot air from the condenser coil to pass through wet clothes. Clothes will be hanging on the axes with the staggered configuration.

Table 1: Technical specification of the selected AC system.

| Item | Specification |
|---|---|
| Brand | MEC |
| Refrigerant type | R-22 |
| Nominal cooling capacity [Btu.hr$^{-1}$. kW$^{-1}$] | 10,000/2.93 |
| Nominal running current for cooling [A] | 4.38 |
| Power source [V.Ph$^{-1}$.Hz$^{-1}$] | 220 – 240/1/50 |
| Indoor air flowrate, Low/Medium/High (cfm) | 225/282/342 |
| Condenser tube material | Copper |
| Condenser tube diameter [mm] | 7.00 |
| Condenser fin material | Aluminium |
| Condenser fin face area [m$^2$] | 0.29 |
| Compressor-rated running current [A] | 3.99 |
| Condenser fan motor power [Watt] | 860 |
| Custom condenser air flowrate, Low / Medium / High [m$^3$.s-$^1$] | 0.14 / 0.24 / 0.34 |

## RESULTS AND DISCUSSION

### Parametric Study

This research aims to formulate the time required for drying based on the following factors: The three-variant mass of wet clothes, three stages of a mechanical fan speed for releasing hot air from the primary condenser, and the effect of variable ambient or surrounding air dry-bulb temperature. Table 2 shows the critical research factors with the scenarios in this research.

This parametric study aims to study the behavior of the air dryer system in various conditions.

Knowing that each of the 1hp of domestic AC systems can be delivered, the evaporator capacity is about 9,600 Btu.h$^{-1}$, the condenser air volumetric flow rate is around 0.34 m$^3$.s$^{-1}$, and the recovered hot air temperature is 33°C for outdoor air temperature. The relative humidity is 25°C and 50%, respectively. The size of this AC is being used in this experiment because of the major utilization by domestic and commercial users in Malaysia.

### Effect of Cloth Weight

The first factor is to study residential application, which is the most effective drying time depending on the number of people per house. Currently, the number of people in a house varies depending on the size, type of house, and social and geographical regions. Therefore, the number of people was interpreted as the various weight of clothes. Each of the sample weights of cloth included the 100g weight of the hanger to hold the cloth in a staggered method. The details of the configuration weight of clothes are presented in Table 3.

The statistical data for drying time was increased with the weight of clothes since the mass of water to be evaporated increased. Based on Fig. 8, the drying time was increased from 55 min for 1 person to 110 min for 3 persons. When the hot air from the condenser was fully recovered to dry the clothes, the condensing temperature came out is about 70°C. The significant effect of this recovery of condenser air can be observed at the evaporator unit, where the evaporating temperature can drop to 4°C, which raises the cooling capacity created by the AC. The evaporating temperature can achieve at 4°C because the heat at the condenser coil has been fully extracted to the recovery air dryer application. Moreover, when the heat rejection at the condenser site increases, the cooling capacity and heat absorption at the evaporator side will also increase. It can be concluded that the proposed air dryer system can replace a commercial electric air dryer if the 1 hp AC system operates for at least

Table 2: Key research factors for experimental works.

| Research Factor | Description | Scenario |
|---|---|---|
| Mass of the wet clothes | There are three samples for wet clothes mass which are 1950 g, 4255 g, and 6350 g | The system runs with high airflow capacity and is tested at 33°C of ambient temperature. |
| Airflow rate capacity | Variable airflow capacity (low, medium, high) with 860watt fan motor | System ran with the mass of 6350g of clothes and tested at 33°C of ambient temperature. |
| Ambient Temperature | Variable dry bulb temperature, which is 27°C, 30°C, and 33°C | System running with the mass of 6350g of clothes and high airflow capacity |

Table 3: The total mass of wet and dry weight for six samples in the function of the number of people.

| Sample | Number of people | Description | Dry weight [g] | Wet weight [g] | Water weight [g] | Weight loss [%] |
|---|---|---|---|---|---|---|
| 1 | 1 | 1 T-shirt, 1 pant, 1 towel | 1150 | 1950 | 800 | 41.0 |
| 2 | 2 | 2 T-shirts, 1 pant, 1 skirt, 2 towels | 2450 | 4255 | 1805 | 42.4 |
| 3 | 3 | 3 T-shirt, 2 pants, 1 skirt, 3 towels | 3600 | 6350 | 2750 | 43.3 |

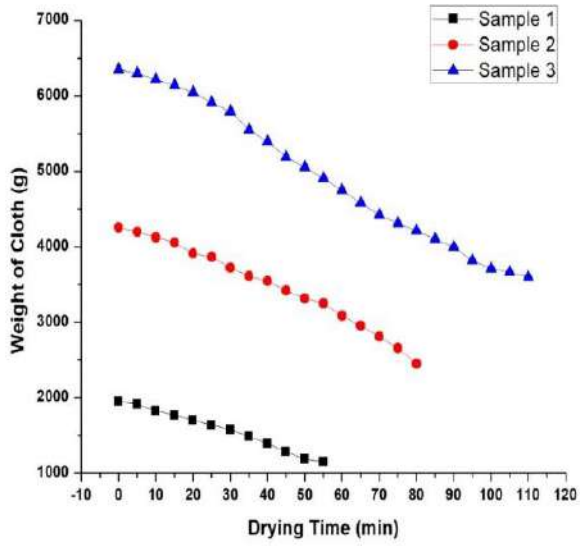


Fig. 8: Effect of cloth weight on drying time.

2 hours to serve 3 persons in each house. Other than that, the side effect of the cooling process of the AC system can be improved.

### Effect of Air Flowrate

In domestic AC systems, there are two types of AC systems: non-inverter and inverter. If the proposed new air dryer system was combined with an inverter AC unit, the drying time might differ from the results in Table 1. This happened due to the speed of the condenser fan motor for the inverter AC unit running based on the cooling load cater on the evaporator side. Therefore, when the cooling load decreases in a conditioned room, the condensing unit's air flow rate might decrease and vice versa. Hence, the second parameter in this experiment is to study the effect of drying time when the air flowrate of the condensing system is low (0.14 $m^3.s^{-1}$), medium (0.24 $m^3.s^{-1}$), and high (0.34 $m^3.s^{-1}$). For these cases, the weight of the cloth is fixed to sample 3 in Table 3, and the ambient temperature is 33°C.

Based on the data shown in Fig. 9, the drying time varies with the airflow rate of the condenser unit. The drying time increases when the air flow rate is low at 0.14 $m^3.s^{-1}$. While the air flow rate increases, the drying time becomes faster. From this situation, it was clearly shown that the proposed air dryer system might be convenient to use with the inverter AC system because the gap in drying time for low and high airflow rates of the condenser unit is not big. It still can dry the cloth for 3 persons if the AC system operates for at least 3.5 hours.

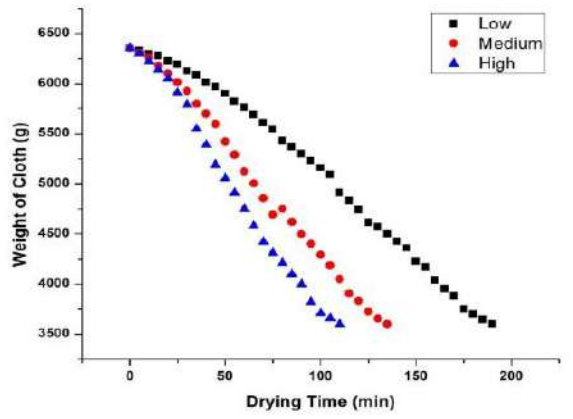


Fig. 9: Graph of effect on airflow rate to drying time.

### Effect of Air Flowrate

The climate conditions can change the ambient or surrounding temperature significantly. Thus, it also depends on the geographical zone. When the ambient air change, it might affect the subcooling temperature at condensing unit. To study the consequences of ambient temperature on the performance of the proposed air dryer system, the experimental work was set up with three sample data. The first sample is the set-up system operated within 27°C surrounding temperature, the second within 30°C, and the third within 33°C. For these cases, the weight of the cloth is fixed to sample 3 in Table 2, and the airflow rate of the condenser side is 0.34 $m^3.s^{-1}$.

Fig. 10 shows the drying time results versus the recovered condensing air temperature. It can be shown that the ambient air temperature increment will fasten the time needed to dry the clothes. This is because the evaporation rate depends on the ambient temperature of the air. Besides that, the evaporation process can lower the drying time when the air

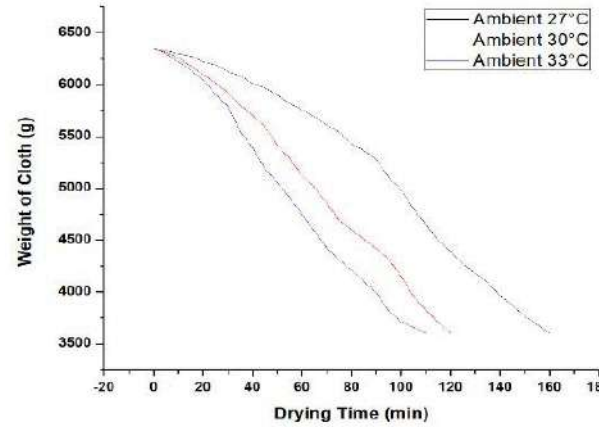


Fig. 10: Effect of ambient Temperature and weight of cloth on drying time.

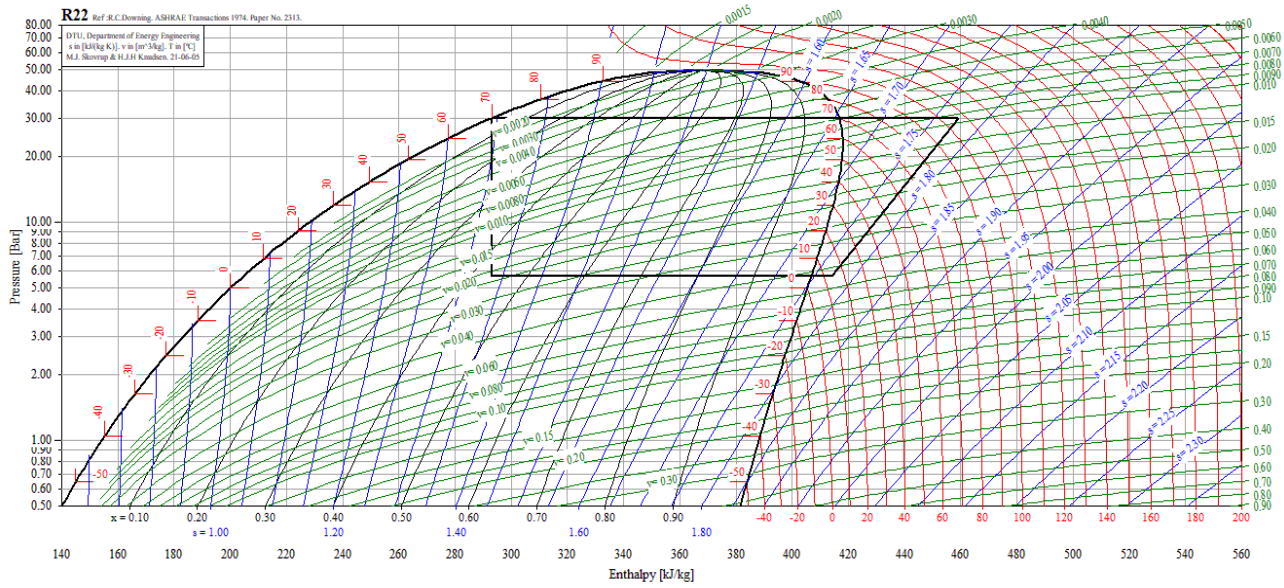


Fig. 11: p-h diagram of the proposed air dryer system.

Table 4: Performance test data generated from Coolpack 1.49.

| Parameter | Test data |
|---|---|
| Evaporator Heat [kJ.kg$^{-1}$] | 121.134 |
| Condenser Heat [kJ.kg$^{-1}$] | 165.957 |
| Condensing temperature [°C] | 70.00 |
| Enthalpy h1 [kJ.kg$^{-1}$] | 414.16 |
| Enthalpy h2 [kJ.kg$^{-1}$] | 458.98 |
| Enthalpy h3 [kJ.kg$^{-1}$] | 293.02 |
| Enthalpy h4 [kJ.kg$^{-1}$] | 293.02 |

temperature increases. The drying time for a 3-person cloth is 160 min when the ambient air temperature is 27°C. Note that the drying time decreases to 110 min for a recovered ambient air temperature of 33°C.

### Air Dryer Performance

To clarify the performance of the proposed air dryer system, the data collected was simulated in Coolpack 1.49 version software which can generate an accurate and precise p-h diagram of the system operation. A 1.0hp AC system powers the proposed air dryer system with a specific refrigerant of R-22, Chlorodifluoromethane, which will be phased out by 2030 for developed countries and 2040 for developing countries according to the Montreal Protocol (Abdur et al. 2020). The performance test was conducted with the best air dryer-operated data in the previous experiment. The 3-person weight of cloth, condenser airflow rate at 0.34 m$^3$.s$^{-1}$, and the recovered ambient temperature at 33°C. While conducting this performance test, the evaporating temperature is 4°C with a superheat value of 10°K. At the condenser site, the heat rejection from the condensing unit is 70°C which consumes the whole condenser heat source of 165.957 kJ.kg$^{-1}$. The p-h diagram representing the behavior of the proposed air dryer system is illustrated in Fig. 11. The Coefficient of Performance (COP) for the AC system was increased from 2.36 to 2.70, respectively. The performance test data is shown in Table 4, and the COP value was derived from the p-h diagram, which can extract the enthalpy data at each point as per Equation 1 (Nurhadi et al. 2021).

$$COP = \frac{h_1 - h_4}{h_2 - h_1}. \quad ...(1)$$

## CONCLUSION

To encounter the challenges of speedily growing cooling load demand by users, it is vital to enhance the performance and the efficiency of a VCRS and to reduce the power consumption produced by the speedy surge of cooling load demand. To enhance the performance and efficiency of the VCRS, waste heat from the condensing unit of VCRS must be recycled for other applications, such as the proposed air dryer system. As a result, all experiments have proven that the waste heat energy from the VCRS can be recovered significantly for an air dryer system and can raise the Coefficient Of Performance (COP) of the VCRS from 2.36 to 2.70 concurrently. The AC system of 1.0hp can cover the drying of wet clothes of weights 1950 g, 4255 g, and 6350 g at 55, 80, and 110 min with a constant air velocity of 0.34 m$^3$.s$^{-1}$ in an ambient temperature of 33°C. For future research, it

was recommended to study the effectiveness of the proposed recovery air dryer unit with commercial or industrial AC systems such as chiller and refrigeration systems. As the current industry of the AC system was tried very hard to reduce power consumption and, at the same time to increase the COP of the system, this proposed system might be useful for them to uncover the waste of free energy.

## ACKNOWLEDGEMENTS

The authors would like to thank Universiti Teknikal Malaysia Melaka for enabling the research to be carried out.

## REFERENCES

Abdur Razzaq, M.E., Ahamed, J.U. and Hossain, M.A.M. 2020. Energy and exergy savings of an air conditioner using blends of R22 / R600a with TiO2 / MO nano-lubricant to retrofit R22/ R600a. Int. J. Automot. Mech. Eng., 17(4): 8283-8297. (doi: 10.15282/ijame.17.4.2020.06.0626).

Analytics, C. 2016. Implications of the Paris Agreement for coal use in the power sector. Climate Analytics, Berlin.

Badescu, V., Aboaltabooq, M.H.K., Pop, H., Apostol, V., Prisecaru, M. and Prisecaru, T. 2017. Design and operational procedures for ORC-based systems coupled with internal combustion engines driving electrical generators at full and partial load. Energy Convers. Manag., 139: 206-221. (doi: 10.1016/j.enconman.2017.02.046).

Bhatia, A. 2012. Heat rejection options in HVAC systems credit : 4 PDH. PDH Online, 877: 6014.

Borri, E., Tafone, A., Comodi, G. and Romagnoli, A. 2017. Improving liquefaction process of microgrid scale liquid air energy storage (LAES) through waste heat recovery (WHR) and absorption chiller. Energy Proced., 143: 699-704. (doi: 10.1016/j.egypro.2017.12.749).

El Hage, H., Ramadan, M., Jaber, H. and Khaled, M. 2019. Environmental Effects A short review on the techniques of waste heat recovery from domestic applications. Energy Sour. Part A Recover. Util. Environ. Eff., 20: 1-16, (2019), (doi: 10.1080/15567036.2019.1623940).

Goodarzia, G., Dehghani, S., Akbarzadeh, A. and Date, A. 2017. Energy saving opportunities in air drying process in high-pressure compressors. Energy Proced., 110: 428-433, (doi: 10.1016/j.egypro.2017.03.164).

Hou, J., Che, D., Liu, Y. and Jiang, Q. 2018. A new system of absorption heat pump vs. boiler for recovering heat and water vapor in flue gas," Energy Proced., 152: 1266-1271. (doi: 10.1016/j.egypro.2018.09.180).

Husainy, A., Suganawar, M., Patil, M. and Sannake, M. 2017. Review of waste heat recovery from household refrigerator. J. Research., 03(08): 6-8.

Kane, S., Mishra, A. and Dutta, A. 2020. Preface: International Conference on Recent Trends in Physics. J. Phys. Conf. Ser., 755(1): 011001. (doi: 10.1088/1742-6596/755/1/011001).

Kim, D.H., Park, T. and Lee, C.E. 2020. Heat recovery boilers with water spray: Part : Parametric analysis and optimization of design specifications. Therm. Sci. Eng. Prog., 19: 100643, (2020), (doi: 10.1016/j.tsep.2020.100643).

Kocyigit, N., Bulgurcu, H. and Lin, C.X. 2014. Fault diagnosis of a vapor compression refrigeration system with hermetic reciprocating compressor based on the p-h diagram. Energy Econ., 45: 44-54. (doi: 10.1016/j.ijrefrig.2014.05.027).

Nelwan, L., Wulandani, D., Subrata, I., Tri, L., Djafar, M. and Damawidjaya. 2018. Simulation on absorption heat pump system to generate drying air. Proced. AESAP., 06(22): 85-94.

Nurhadi, L., Listiyono, M., Maskuri, B. and Prasetyo, R. 2021. The effect of variation of extra fan condenser and engine speed to COP of mobile air conditioners. IOP Conf. Ser. Mater. Sci. Eng., 1073: 012077. (doi: 10.1088/1757-899x/1073/1/012077).

Ramadan, M., Ali, S., Bazzi, H. and Khaled, M. 2017. New hybrid system combining TEG, condenser hot air, and exhaust airflow of all-air HVAC systems. Case Stud. Therm. Eng., 10: 154-160. (doi: 10.1016/j.csite.2017.05.007).

Shaban, N., Nasser, I., Asfar, J., Al-Qawabah, S. and Olimat, A. 2020. Thermodynamic and economic analysis of a refrigerator display cabinet equipped with a DC compressor and electronic expansion valve. Int. J. Heat. Tech., 38(2): 432-438. (doi: 10.18280/ijht.380219).

Song, J., Li, X., Wang, K. and Markides, C.N. 2020. Parametric optimisation of a combined supercritical CO2 (S-CO2) cycle and organic Rankine cycle (ORC) system for internal combustion engine (ICE) waste-heat recovery. Energy Convers. Manag., 218:. 112999. (doi: 10.1016/j.enconman.2020.112999).

Suntivarakorn, R. and Treedet, W. 2016. Improvement of boiler's efficiency using heat recovery and automatic combustion control system. Energy Proced., 100: 193-197. (doi: 10.1016/j.egypro.2016.10.164).

Thakar, R., Bhosle, S. and Lahane, S. 2018. Design of heat exchanger for waste heat recovery from exhaust gas of diesel engine. Proc. Manuf., 20: 372-376. (doi: 10.1016/j.promfg.2018.02.054).

Wang, C., Pattawi, K. and Lee, H. Energy saving impact of occupancy-driven thermostat for residential building. Energy Build., 211: 1791. (doi: 10.1016/j.enbuild.2020.109791).

Wang, S.K. 2001. Air Conditioning Systems: System Classification, Selection, and Individual Systems.

Wei, W. 2019. Energy & buildings energy consumption, indoor thermal comfort and air quality in a commercial office with retrofitted heat, ventilation, and air conditioning ( HVAC ) system. Energy Build., 201: 202-215. (doi: 10.1016/j.enbuild.2019.06.029).

Wu, H., Skye, M and Domanski, P.A. 2020. Selecting HVAC systems to achieve comfortable and cost-effective residential net-zero energy 0buildings. Appl. Energy, 212: 577-591. (doi: 10.1016/j.apenergy.2017.12.046).

Nature Environment and Pollution Technology
An International Quarterly Scientific Journal

p-ISSN: 0972-6268
(Print copies up to 2016)
e-ISSN: 2395-3454

Vol. 22 | No. 1 | pp. 159-168 | 2023

Original Research Paper

https://doi.org/10.46488/NEPT.2023.v22i01.014

Open Access Journal

# Optimization of Biodiesel Parameters Using Response Surface Methodology and Production of Biodiesel

**Y. K. Singh***

*Department of Biotechnology, Delhi Technological University, New Delhi-110042, India
†Corresponding authors: Y. K. Singh; ykumars@yahoo.com

**Nat. Env. & Poll. Tech.**
**Website: www.neptjournal.com**

*Received:* 31-05-2022
*Revised:* 20-07-2022
*Accepted:* 22-07-2022

**Key Words:**
Biodiesel
Response surface methodology
CCD
Methanol/oil ratio
KOH catalyst

## ABSTRACT

The requirement for a renewable and environmentally gracious alternative resource of energy has grown in recent years as a result of increased knowledge of the negative impacts of petroleum-based fuels on the environment and the regular rise in crude oil prices. Biodiesel has been proven to be the ideal replacement for diesel because of its unique qualities, such as a huge decrease in greenhouse gas emissions, nonparticulate matter pollutants, non-sulfur emissions, less toxicity, and degradability. This article examines the pre-treatment stage, the physiological and chemical features of WCO, transesterification, esterification, and the manufacturing of biofuel from waste-cooked oil using several techniques and catalyst types. The elements that influence the stated process parameters are investigated, with a particular focus on the methanol to oil ratio (molar ratio), time of reaction, the temperature of the reaction, catalyst percentage, and yield of biodiesel. After the production of biodiesel, we can optimize the process parameters, for example, methanol to oil ratio, the temperature of the reaction, duration of reaction, and catalyst percentage, and also optimize the yield of biofuel generation with the CCD design of the Response surface methodology (RSM) algorithm using Design Expert software.

## INTRODUCTION

Waste cooking oil refers to the production of oil from different frying activities, such as oil used in restaurants for frying purposes. Two categories of second-hand cooking are formed and used: primary and secondary-hand cooking oils. Primarily used cooking oil prefers to squander oil from clean vegetable oils and is usually generated by restaurants and shops. While second- or secondary-used cooking oil is waste oil derived from first- or primary-used cooking oil, it is typically generated by street vendors. These days, the oil is generally just thrown away, lacking any treatment. Then it will infect the whole environment when we just pay no attention to it. One single alternative to treating this second or secondary-used cooking oil is by conversion into biodiesel. That substitute will not only have environmental advantages but also be economical (Kawentar & Budiman 2013, Uddin et al. 2013). In today's world, power/energy is a crucial dynamic component for socioeconomic advancement. It has an impact on all aspects of human endeavors, for example, crop production, education, and transportation, amongst others. Petro-linked fuels are the most common type of fuel used in the transportation industry in practically all developed countries. Though climate change and rising pumping costs have shifted research focus to sustainable energy resources (Samuel et al. 2013, Phan & Phan 2008). The search for green energy sources is a topical subject that is gaining widespread communal and political attention owing to its abridged greenhouse gas emissions, biodegradability, sustainability, and spirited nature in comparison to fossil fuels and food supplies. Transesterification produces biodiesel from vegetable oil (waste cooking oil). According to the American Society for Testing and Materials (ASTM), biodiesel is distinct as a single alkyl ester of a lengthy chain of fatty acids resulting from sustainable feedstocks. The main disadvantage is the cost, which is significantly greater than that of oil-derivative diesel. The increased price of virgin or fresh oils, which might account for up to 75% of the overall built-up price, has resulted in biodiesel manufacturing prices being around 1.5 times more than petro-diesel. Waste cooking oils are 2 to 3 times less expensive than new virgin oils.

As a result, the total built-up price of biodiesel can be considerably reduced (Samuel et al. 2013). Though there are several successful reports on biodiesel generation from used cooking oil, it is not highly explored owing to

**ORCID details of the authors:**

**Y. K. Singh**
https://orcid.org/0000-0002-6225-495X

the difficulty in transesterification as a result of high free fatty acid constituents. In recent work, we report the direct-scale manufacture of biofuel from waste cooking oil with a free fatty acid (FFA) content in the range of 4 to 5%. The generation is achieved in a single stage without any preceding acid treatment. That's why the utilization of used oil for fatty acid methyl ester (FAME) production or formation is highly suggested (Unni et al. 2013).

## REACTIONS OF WASTE OIL AND BIODIESEL

### Transesterification

As indicated in Fig. 1, the triglyceride constituent of oil combines with the methanol in the presence of sodium hydroxide or another catalyst to produce esters and glycerol. In common, when using vegetable oil and animal fat as an initial material, there are three types of transesterification systems: homogeneous, heterogeneous, and enzymatic, depending on the catalyst used. Because methanol is more efficient, UVO is usually reacted with alcohol. Ethyl alcohol is used for animal fats, but ethyl alcohol and isopropyl alcohol can be used as well. Transesterification is supposed to be influenced by a variety of factors, such as temperature for reaction, pressure, time of reaction, agitation rate, type of alcohol (whether ethanol or methanol is used) and molar ratio, kind and concentrations of catalysts used, and dampness and FFA concentration in the feedstock oil (Sarno & Iuliano 2019, Rizwanul Fattah et al. 2020). The physical and chemical qualities of the feedstock oil determine the best values for these parameters to achieve higher conversion. Today, the majority of biodiesel is made from edible vegetable oils that have been transesterified using a homogenous alkali catalyst. Homogeneous catalysts, which might be liquid or gaseous, are soluble during the process. Acidic and alkaline are the two types of them. For esterification, acidic catalysts such as $H_2SO_4$ are commonly employed, while transesterification uses alkaline catalysts, for example, NaOH and KOH (Sarno & Iuliano 2019). Homogeneous catalysts have the following advantages: (i) the ability to catalyze reactions at lower reaction temperatures and air pressures; (ii) the ability to achieve a higher level of conversion in a shorter period of time; and (iii) availability and cost. This method produces a high-quality artifact with a quick turnaround time. Only refined vegetable oil with a low level of 0.5 wt. percent or less is permitted. Free fatty acid or an acid value of not greater than 1 mg $KOH.g^{-1}$ can be used effectively with an alkaline homogeneous catalyst. Furthermore, after the reaction is completed, the separation of these catalysts necessitates washing biodiesel through water, which may result in the slaughter of fatty acid alkyl (methyl or ethyl) esters, energy utilization, and the generation of huge amounts of dissipated water. As a catalyst is not easy to recover and catalyst can induce reactor deterioration, this raises the overall cost of biodiesel production. To avoid soap generation (due to alkaline catalyst use) and low product yields, the triglyceride and alcohol (methanol or ethanol) must be anhydrous, and the raw material must have a low free fatty acid (FFA) concentration (Sarno & Iuliano 2019, Rizwanul Fattah et al. 2020).

### Esterification

Because FFAs can cause deposits and engine damage, most biodiesel requirements have a maximum FFA level. As illustrated in Fig. 2, esterification can be utilized to switch free fatty acids to biodiesel while also reducing FFAs. Fatty acids interact using alcohol in the absence of a catalyst to form fatty acid alkyl (methyl or ethyl) ester in this reaction (Biodiesel). The goal of the esterification process is to

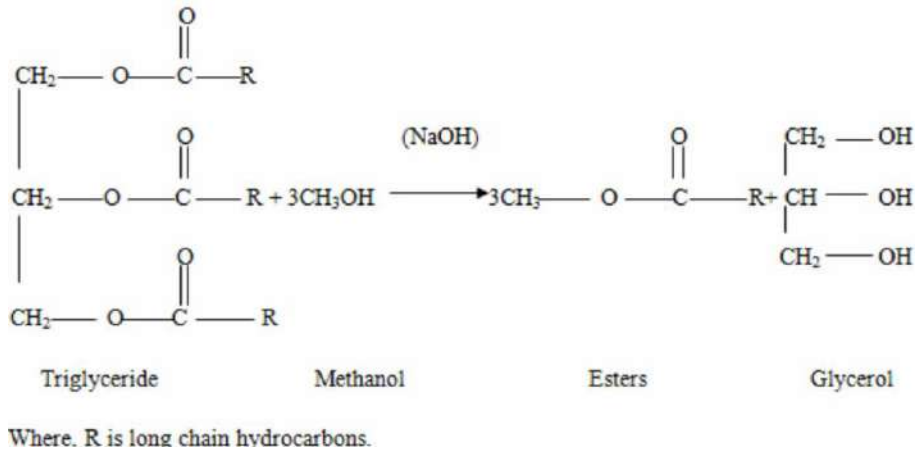


Fig. 1: A schematic illustration of the transesterification reaction (Sarno & Iuliano 2019).

reduce WCO's acidity. As conventional acid catalysts in the esterification process, sulphuric acid ($H_2SO_4$), hydrochloric acid (HCl), butyl-methyl imidazolium hydrogen sulfate ($BMIMHSO_4$), and sulfonic acid are commonly used (Sarno & Iuliano 2019, Ghiaci et al. 2011). Titration of oil through ethanol and diethyl ether (1:1) alongside potassium hydroxide (KOH) via phenolphthalein as a marker determines the acid values of the oil. The acid value is equal to $56.1*CV.m^{-1}$, where V represents the quantity of KOH (mL), C represents the concentration of potassium hydroxide (KOH) in M, and m represents the heaviness of the oil sample in g. For official techniques, AOCS Cd 3d-63 and ASTMD-664 were followed in this titration. The catalyst is chosen based on acidity. The feedstock can be transesterified without any pretreatment if the FFA content is less than 1%. According to research findings, maximum conversion is achieved at 2% v/v $H_2SO_4$. Because the reaction is reversible, equilibrium is the greatest stumbling block to its completion. The FFA can be reduced by reducing water by preheating in an oven. The Alcohol to Methanol Ratio, the catalyst and its amount used, and the process temperature are the primary factors determining the esterification reaction (Sarno & Iuliano 2019, Ghiaci et al. 2011).

## MATERIALS AND METHODS

If the free fatty acid content in oil exceeds 5% of the feedstock, then a pretreatment process is required before reacting with the alkaline base catalyst (Ribeiro et al. 2011).

### Materials

The WCO used in the making of biodiesel was collected from the local street shops and FFA was measured with two different oil samples collected from different shops (0.7% and 0.2%). For example, methanol with 99% purity, potassium hydroxide (KOH) with 90% purity, and for some quality checks for oil and biodiesel, phenol red indicator LR grade, isopropyl alcohol with 99% purity, bromophenol blue, hydrochloric acid 0.01N LR grade for soap content, and 1% phenolphthalein indicator were used for excess catalyst in the process. Alcohol (methanol) is used for the transesterification process, and the KOH base catalyst is used as the base catalyst (Table 1).

### Synthesis of Methyl Esters

The synthesis or production of biodiesel initially requires pretreatment if the FFA content is high. First, the oil is heated

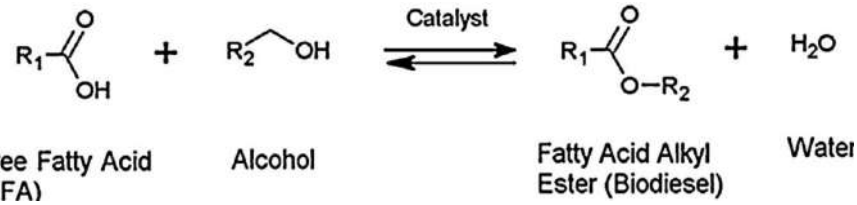


Fig. 2: Schematic illustration of the esterification reaction (Sarno & Iuliano 2019).


Fig. 3a: Shows two layers of upper layer of biodiesel and the bottom layer of glycerol.

Fig. 3b: Shows biodiesel after washing.

Table 1: Quality analysis of oil and biodiesel.

| Quality parameters | Analysis result |
|---|---|
| Acid value of oil | 9mg.$KOH^{-1}$.$g^{-1}$ |
| Free fatty acid content in oil | 4.5% |
| Soap content(ppm) | 285ppm |

to a temperature of 100°C to eliminate any moisture content available in the oil, then the heated oil is cooled down. Again, heat the oil to a different temperature range, from 40 to 75°C, the process temperatures are given in the process Table 4. After heated oil reaches the desired temperature, KOH (normally 0.3 to 1 percent of oil according to FFA content of oil, the catalyst % is taken) with methanol is mixed (ratio of methanol to oil is calculated as per desired data given in Table 4) and added to the process for transesterification reaction with continuous stirring of the process mixture at a desired temperature. The stirring was also continuous for about 45 min to 120 min (all data in Table 4 show the minimum range and maximum range of different parameters). Thereafter, two layers were produced; the upper layer is of biodiesel, and the lower layer is of glycerol, as shown in Fig. 3a and 3b. Then, the mixture was allowed 24 h to properly settle so that all the biodiesel was properly separated from the glycerol. After 24 h, the glycerol was separated from the biodiesel and further processing was done (washing and testing). Washing of biodiesel is done through hot water with 3 to 5 washes with water and then drying of the biodiesel with heating at a temperature of above 100°C for 1 h.

**Analysis of Process (Biodiesel)**

After the synthesis of biodiesel and before washing, the quality check for biodiesel is done. By using the 3/27 methanol test (Heisner 2020), you can check whether the oil is properly reacted or not. In this test, 3mL of prepared biodiesel was taken and added to 27 mL of methanol, then mixed vigorously in the vial for 5 to 10 seconds. If there is any oil or unreacted oil or fall seen at the bottom of the vial, it means the oil is not properly reacted. If there is no fall seen at the bottom, it means the oil is properly reacted. The 3/27 methanol test was performed both before and after washing the biodiesel (see Fig. 4a and 4b).

**Excess Catalyst in Biodiesel**

The high level of catalyst content in biodiesel leads to the problem of soap formation and increases the soap ppm level in biodiesel. By eliminating or removing excess catalyst (KOH) in prepared biodiesel, take 100 mL of isopropyl alcohol into a 250 mL beaker and then add about 12 mL of biodiesel. Mix properly. Add 5 drops of 1% phenolpthalein indicator to the beaker. If the solution in the beaker stays clear, it means there is no extra catalyst in the biodiesel. If the solution turns magenta after the addition of the indicator, it means there is some extra catalyst present in the biodiesel. The biodiesel requires some treatment to neutralize it, so take 0.01 N HCL and put the HCL drop-wise in the beaker slowly until the solution color changes from magenta to clear solution. After the excess catalyst removal process, the next step is the soap content test for the biodiesel.

**Soap Content Test for Biodiesel**

The high level of soap content in biodiesel results in the clogging of filters and engines of automobiles. The soap

Fig. 4a: Conversion complete (no fall seen).

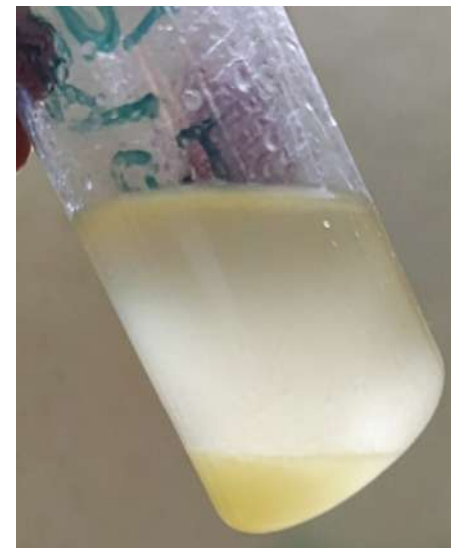

Fig. 4b: Incomplete conversion (fall seen).

Table 2: Analyzing the quality of biodiesel based on the soap content chart.

| Soap Content | Fuel Quality |
|---|---|
| at or below 41 ppm (NaOH) or 66 ppm (KOH) | Within ASTM standards |
| Above ASTM Standards but Below 200 ppm | Should not pose any threat to a fuel filter or engine |
| 200-300 ppm | maximum soap content which should be allowed in fuel |
| 300-400 ppm | May clog fuel filters, not recommended, wash more |
| 400-500 ppm | High soap content, not recommended, wash more |
| Above 500 ppm | Can possibly leave ash in your engine and cause long-term damage, not recommended, wash more |

content of fuels should be according to the ASTM standard as shown in Table 2. The testing of soap content for biodiesel requires 0.01 N HCL, bromophenol blue, and isopropyl alcohol. Take 100 mL of isopropyl alcohol into a 250 mL beaker, then add about 12 mL of biodiesel into the beaker and mix them. Add 15 to 20 drops of bromophenol blue into the beaker until the solution turns a dark blue color. After that, titrate the solution with 0.01 N HCL. Note that the mL of HCL is required to change the color of the solution from a dark blue color to a yellowish color. Soap content should be checked before and after washing and drying. In the case of the KOH catalyst, the 320 value factor is taken, and in the case of the NaOH catalyst, the 304 value factor is used. The ppm is calculated by multiplying the catalyst factor by the amount of HCL required to get the PPM of the biodiesel sample.

## RESULTS AND DISCUSSION

### Experimental Design and Parameters Optimization

Box-Behnken design (BBD) and central composite design are the two major experimental designs utilized for response surface optimization (CCD). In this study, we used design expert software to apply the CCD design of the response surface methodology. In the response surface approach, two essential models are typically used, namely the first-degree and second-degree models (Kumar Ghosh & Mittal 2021). When the response can be well explained by a linear function of independent variables, a first-degree model is used. However, when the system has curvature, a second-degree model is used, and a high-degree polynomial is used. In all of these models, there is a correlation between independent variables like time of reaction, temperature, molar ratio, catalyst weight percent, and the resulting variable (yield percent). Table 3 shows the practical amounts and ranges of several independent variables used in the production of biodiesel. In this work, 30 experimental runs were done and consisted of 16 factorial, 8 axial, and 6 center points. The 2nd-degree model is applied in this article, which suggests 30 runs. We already discussed how this system shows curvature.

Experimental design for the production of biodiesel: the coded values of different independent variables are specified in Table 4. The methanol to oil (molar ratio) and catalyst percent are represented by the coded variables $x_1$ and $x_2$. The $x_3$ and $x_4$ denote the temperature of the reaction and time, respectively (Kumar Ghosh & Mittal 2021).

Quadratic equation Eq. (1) states the performance of the system. For multiple regression data analysis, a statistical program was utilized. Calculating the regression equation and studying the response of 3D surface plots and contour plots provides the optimum value of selected variables.

$$Y = \beta_0 + \sum_j^k{}_{=1} \beta_j x_j + \sum^k{}_{i=1} \beta_{jj} x_j^2 + \sum\sum^k{}_{i<j} \beta_{ij} x_i x_j + \varepsilon \ldots(1)$$

Whereas Y denotes the biodiesel yield percentage, and *xi*, and *xj* represent actual independent variables in the appearance of encoding; $\beta_0$, $\beta_j$, $\beta_{jj}$, *and* $\beta_{ij}$ expressed as intercept,linear,quadratic, and interaction constant coefficients also ε denotes a random error.

### Regression Equation for Yield of Biodiesel

The essential parameters that affect the resultant (biodiesel yield) are; the molar ratio (methanol to oil ratio (*x1*)), catalyst percentage (*x2*), the temperature of reaction (*x3*), time of reaction (*x4*) (Kumar Ghosh & Mittal 2021). Experimental

Table 3: Levels of independent variables for the experimental design.

| Factor | Name | Units | Minimum | Maximum | Mean |
|---|---|---|---|---|---|
| A | Methanol/oil ratio ($x_1$) | $Mol.mol^{-1}$ | 1.0000 | 13.00 | 7.00 |
| B | KOH catalyst ($x_2$) | % | -0.0500 | 1.75 | 0.8500 |
| C | Temperature ($x_3$) | °C | 42.50 | 72.50 | 57.50 |
| D | Time ($x_4$) | Min | 7.50 | 157.50 | 82.50 |

Table 4: CCD design for biodiesel production.

| Runs | Independent variables | | | | Points | Yield |
|---|---|---|---|---|---|---|
| | ($x_1$) | ($x_2$) | ($x_3$) | ($x_4$) | | |
| 1 | 7 | 0.85 | 72.5 | 82.5 | Axial | 98.4 |
| 2 | 4 | 0.4 | 65 | 120 | Factorial | 70.6 |
| 3 | 10 | 0.4 | 50 | 120 | Factorial | 96.8 |
| 4 | 7 | 0.85 | 57.5 | 82.5 | Center | 86.8 |
| 5 | 4 | 0.4 | 50 | 45 | Factorial | 32.6 |
| 6 | 7 | 0.85 | 57.5 | 82.5 | Center | 86.2 |
| 7 | 7 | 0.85 | 57.5 | 82.5 | Center | 98.7 |
| 8 | 7 | 0.85 | 57.5 | 82.5 | Center | 98.7 |
| 9 | 10 | 1.3 | 65 | 120 | Factorial | 80 |
| 10 | 4 | 1.3 | 65 | 45 | Factorial | 84.2 |
| 11 | 4 | 0.4 | 65 | 45 | Factorial | 38.7 |
| 12 | 4 | 1.3 | 50 | 45 | Factorial | 82.2 |
| 13 | 10 | 0.4 | 50 | 45 | Factorial | 82 |
| 14 | 4 | 1.3 | 65 | 120 | Factorial | 92.5 |
| 15 | 7 | 0.85 | 57.5 | 82.5 | Center | 98.7 |
| 16 | 7 | 0.85 | 57.5 | 157.5 | Axial | 98.5 |
| 17 | 10 | 0.4 | 65 | 120 | Factorial | 94.8 |
| 18 | 7 | 1.75 | 57.5 | 82.5 | Axial | 78 |
| 19 | 1 | 0.85 | 57.5 | 82.5 | Axial | 38.9 |
| 20 | 7 | 0.85 | 57.5 | 82.5 | Center | 98.7 |
| 21 | 4 | 0.4 | 50 | 120 | Factorial | 85.7 |
| 22 | 10 | 1.3 | 65 | 45 | Factorial | 92.3 |
| 23 | 4 | 1.3 | 50 | 120 | Factorial | 90.6 |
| 24 | 10 | 1.3 | 50 | 120 | Factorial | 86.5 |
| 25 | 7 | 0.05 | 57.5 | 82.5 | Axial | 41.3 |
| 26 | 7 | 0.85 | 42.5 | 82.5 | Axial | 95.2 |
| 27 | 10 | 1.3 | 50 | 45 | Factorial | 94.6 |
| 28 | 13 | 0.85 | 57.5 | 82.5 | Axial | 88.8 |
| 29 | 7 | 0.85 | 57.5 | 7.5 | Axial | 60.1 |
| 30 | 10 | 0.4 | 65 | 45 | Factorial | 92.3 |

runs are carried out to find the coordination between different parameters. The observed verdicts of the whole factorial central CCD were compared to the polynomial Eq. (1) using multiple regression analysis in Table 4. The equation of multiple regression for the yield of biodiesel formation as a function of many variables is shown in Eq. (2).

$$Y = -1.73211 + 1.47311x_1 + 10.17824x_2 - 0.145439x_3 + 0.107262x_4 - 0.045366x_1^2 - 2.26447x_2^2 + 0.001667x_3^2 - 0.000111x_4^2 - 0.391099x_1x_2 + 0.000304x_1x_3 - 0.003777x_1x_4 - 0.006894x_2x_3 - 0.025322x_2x_4 - 0.000504x_3x_4 \quad \ldots(2)$$

The sign attached to the coefficient predicts the impact of the regression coefficients on the result or response. A negative sign indicates a combative effect, while a positive sign indicates a coadjuvant result. $x_1, x_2, x_3, x_4$ are four linear factors, and the interaction of $x_1x_4$ The coadjuvant effect is represented by the remaining quadratic intercepts. $x_1^2$, $x_2^2$, $x_3^2$, $x_4^2$ and relations of $x_1x_2$, $x_1x_3$, $x_1x_4$, $x_2x_3$, $x_2x_4$, $x_3x_4$ predicts the combative effect. Confirmation of adequacy of the model is determined by the use of analysis of variance (ANOVA) (Kumar Ghosh & Mittal 2021) given in Table 5. Coefficient of determination $R^2$ is utilized to test whether the model is fit or not, the $R^2$ is calculated as 0.9363, suggesting that previously model states or explain 93.63% of the response variability, the transesterification experiment factors exhibited a total variation of 93.63($R^2$) and adj.$R^2$

Table 5: ANOVA analysis of variance for a yield of biodiesel.

| Source | Sum of Squares | df | Mean Square | F-value | p-value | |
|---|---|---|---|---|---|---|
| Model | 41.41 | 14 | 2.96 | 15.75 | < 0.0001 | significant |
| A-Methanol/oil ratio | 9.65 | 1 | 9.65 | 51.39 | < 0.0001 | |
| B-KOH catalyst | 5.94 | 1 | 5.94 | 31.62 | < 0.0001 | |
| C-Temperature | 0.0011 | 1 | 0.0011 | 0.0060 | 0.9391 | |
| D-Time | 4.85 | 1 | 4.85 | 25.83 | 0.0001 | |
| AB | 4.46 | 1 | 4.46 | 23.75 | 0.0002 | |
| AC | 0.0007 | 1 | 0.0007 | 0.0040 | 0.9505 | |
| AD | 2.89 | 1 | 2.89 | 15.38 | 0.0014 | |
| BC | 0.0087 | 1 | 0.0087 | 0.0461 | 0.8329 | |
| BD | 2.92 | 1 | 2.92 | 15.55 | 0.0013 | |
| CD | 0.3215 | 1 | 0.3215 | 1.71 | 0.2105 | |
| $A^2$ | 4.57 | 1 | 4.57 | 24.34 | 0.0002 | |
| $B^2$ | 5.77 | 1 | 5.77 | 30.71 | < 0.0001 | |
| $C^2$ | 0.2411 | 1 | 0.2411 | 1.28 | 0.2750 | |
| $D^2$ | 0.6692 | 1 | 0.6692 | 3.56 | 0.0786 | |
| Residual | 2.82 | 15 | 0.1878 | | | |
| Lack of Fit | 2.28 | 10 | 0.2281 | 2.12 | 0.2099 | not significant |
| Pure Error | 0.5369 | 5 | 0.1074 | | | |
| Cor Total | 44.23 | 29 | | | | |

"$R^2$ = 93.63% and adj.$R^2$ = 87.68%

of 87.68%. This states to facilitate the model has the best association and makes an accurate prediction. In an analysis of variance, (ANOVA) of Table 5 shows the probability of p-value is not greater than 0.0001 which means the model is significant (Anbessa & Karthikeyan 2019).

## Analysis of the Impact of Transesterification Parameters

Graphically, contour and 3D surface plots show the effects of transesterification parameters on the result (biodiesel yield).

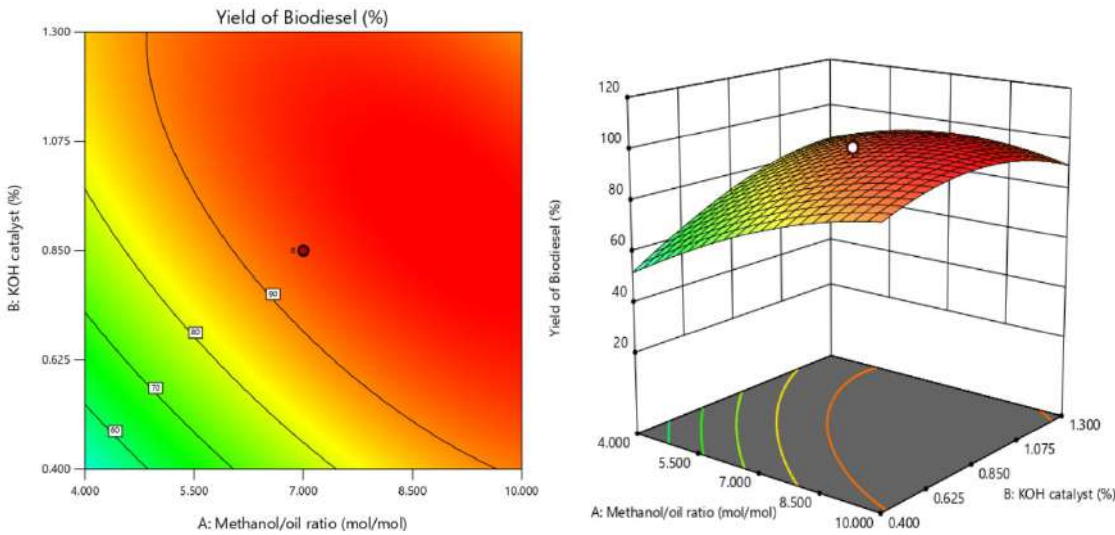


Fig. 5: (a) Represents a Contour plot and (b)shows a 3D surface plot showing the interaction of methanol/oil ratio and catalyst wt%.

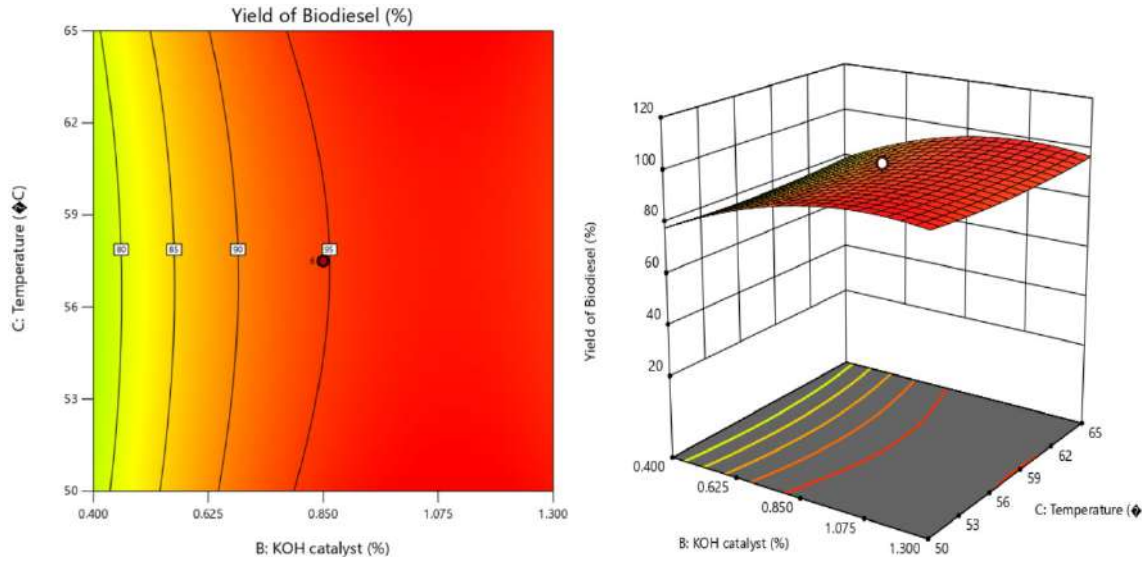


Fig. 6: (a) Represents contour plot (b) 3D surface plot shows the interaction of catalyst % and temperature.

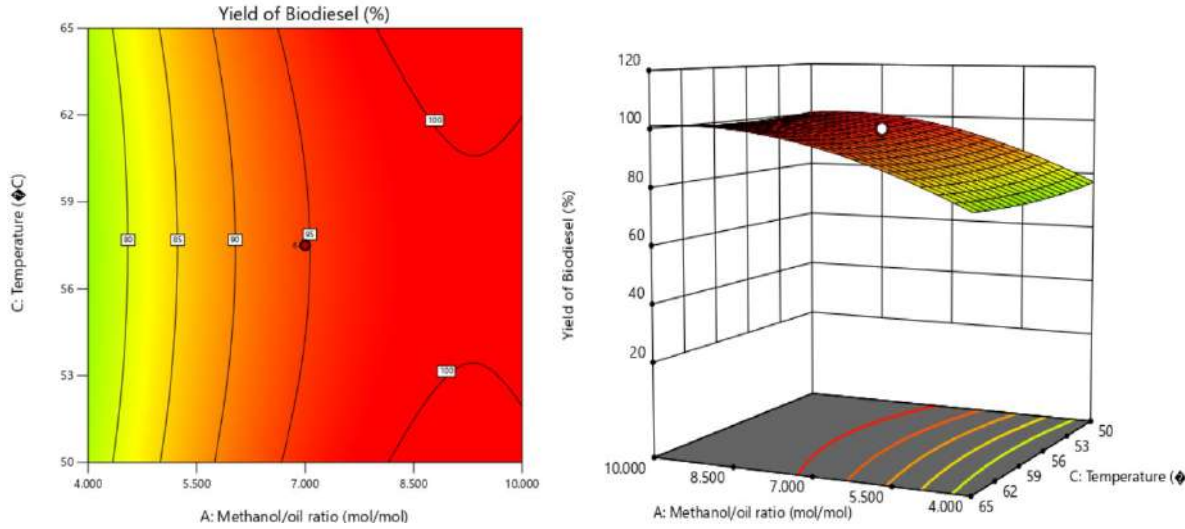


Fig. 7: (a) Represents contour plot (b) Shows 3D surface plot andrelations of methanol/oil ratio and temperature.

Fig. 5(a) depicts the relationship between the methanol/oil ratio and the catalyst percent, as well as the effect on yield. According to Fig. 5(b) of the 3D surface plot, as the molar ratio (methanol/oil ratio) increases, so does the yield of biodiesel, which ranges from 4:1 to 10:1. the optimal methanol/oil ratio is determined by optimization. The best optimum ratio that was achieved is a 10:1 methanol/oil ratio, and this gives a yield of 98.84% for biodiesel. By observing the data, it is found that increasing the methanol/oil ratio with catalyst gives an increment in biodiesel yield due to the higher number of active sites. However, too much catalyst percent results in excess emulsion (Hazmi et al. 2021). maximum yield is obtained at optimized conditions of methanol/oil ratio (10:1) and catalyst 1.3%, which gives 98.84 yields.

Likely, Fig. 6(a) and (b) indicate the effects of interactive factors such as KOH catalyst percentage and temperature of reaction on the resultant response. Fig. 7(a) and (b) show the response of correlated factors to the methanol/oil ratio and temperature of the reaction. A 3D surface plot represents the increase in yield of biodiesel as temperature increments from 50°C to 65°C. This increase in yield is because the speed of transesterification ranges increases as the temperature increments due to the enhancement of a

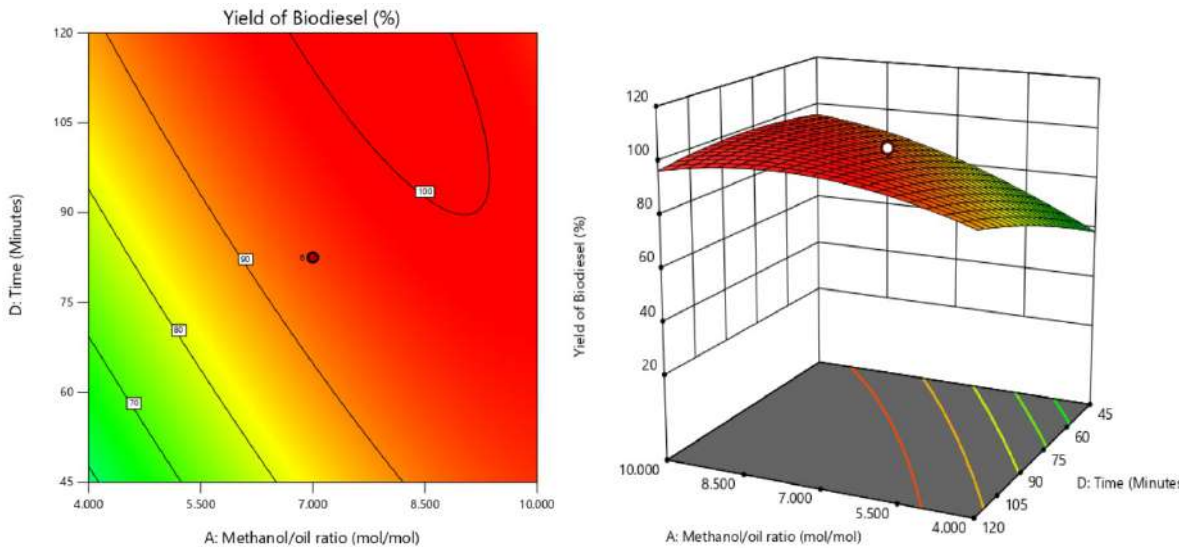


Fig. 8: (a) Represents contour plot (b) Shows 3D surface plot and relations of methanol/oil ratioand reaction time.

Table 6: Optimized result of the process.

| Transesterification parameters | Optimum values |
|---|---|
| Yield of biodiesel | 98.84% |
| Methanol/oil ratio | 10:1 |
| Catalyst% | 1.3% |
| temperature | 65°C |
| time | 45 min |

homogenous mixture (miscibility) when methanol and oil are mixed at high temperatures (Kumar Ghosh & Mittal 2021). The optimum temperature for the best yield is 65°C, which is optimized through RSM optimization with 1.3% catalyst loading for a higher yield.

Fig. 8(a) and (b) represent the interaction of molar ratio (methanol to oil ratio) and reaction time and its effect on the resultant (yield) of biodiesel. Higher ratios of methanol to oil lead to a more rapid conversion of biodiesel. Also, the time of reaction for the process depends on the nature of the catalyst (acid or base catalyst). Typically, the catalyst requires less significant time (1–2 h) for the conversion of biodiesel from oil. As the yield of biodiesel increases with reaction time, excess time of the reaction can lead to deteriorated yield and more glycerol production (Kumar Ghosh & Mittal 2021). After optimization, the optimum reaction time was 45 min for high conversion.

The optimized values are calculated from the regression equations. The different transesterification parameters are summarized. After studying the contour plot and 3D surface plots, we get optimum values for the highest yields of biodiesel production. The maximal yield of biodiesel is calculated to be 98.84% and was predicted using design expert software as the methanol/oil ratio =10:1 catalyst =1.3%, temperature =65°C, and time =45 min. We can conclude from the analysis of all contours and surfaced plots that the maximum yield of biodiesel obtained was 98.84%. The optimized results are given in Table 6.

## CONCLUSION

The conversion of biodiesel from triglycerides is based on important parameters and the response surface methodology. The optimized results are obtained by solving the regression equation by using the CCD of the response surface methodology. The response surface methodology is a suitable method to optimize the best or highest level of yield. Thirty experimental runs were carried out for analysis using CCD-based RSM. Studying contours and 3D surface plots were utilized to find optimum results. Whereas we get 98.84% of the yield achieved at methanol/oil ratio (10:1), catalyst percentage (1.3%), temperature (65°C), and time (45 min). This study represents a better yield of biodiesel production and a long-term solution for environmental benefits.

## REFERENCES

Anbessa, T.T. and Karthikeyan, S. 2019. Optimization and mathematical modeling of biodiesel production using homogenous catalyst from waste cooking oil. Int. J. Eng. Adv. Technol., 9(1): 1733-1739. https://doi.org/10.35940/ijeat.F9005.109119

Ghiaci, M., Aghabarari, B. and Gil, A. 2011. Production of biodiesel by esterification of natural fatty acids over modified organoclay catalysts. Fuel, 90(11): 3382-3389. https://doi.org/10.1016/j.fuel.2011.04.008

Hazmi, B., Rashid, U., Ibrahim, M.L., Nehdi, I.A., Azam, M. and Al-Resayes, S.I. 2021. Synthesis and characterization of bifunctional magnetic nano-catalyst from rice husk for production of biodiesel.

Environ. Technol. Innov., 21: 101296. https://doi.org/10.1016/j.eti.2020.101296

Heisner, B. 2020. Utilizing the 3 / 27 conversion test to measure the effects of temperature on the base-catalyzed transesterification of waste vegetable oils into fatty acid methyl esters. J. Autom. Technol., 15: 3-14.

Kawentar, W.A. and Budiman, A. 2013. Synthesis of biodiesel from second-used cooking oil. Energy Procedi., 32: 190-199. https://doi.org/10.1016/j.egypro.2013.05.025

Kumar Ghosh, U. and Mittal, V. 2021. Application of response surface methodology for optimization of biodiesel production from microalgae through nano catalytic transesteriication process. Fuel Process. Technol., 92(3): 407-413. https://doi.org/10.21203/rs.3.rs-771200/v1

Phan, A.N. and Phan, T.M. 2008. Biodiesel production from waste cooking oils. Fuel, 87(17-18): 3490-3496. https://doi.org/10.1016/j.fuel.2008.07.008

Ribeiro, A., Castro, F. and Carvalho, J. 2011. Influence of free fatty acid content in biodiesel production on non-edible oils. International Conference Waste Sol. Treat. Oppor., 12: 141.

Rizwanul Fattah, I.M., Ong, H.C., Mahlia, T.M.I., Mofijur, M., Silitonga, A.S., Ashrafur Rahman, S.M. and Ahmad, A. 2020. State of the art of catalysts for biodiesel production. Front. Energy Res., 8: 1-17. https://doi.org/10.3389/fenrg.2020.00101

Samuel, O.D., Waheed, M.A., Bolaji, B.O. and Dario, O.U. 2013. Production of biodiesel from Nigerian restaurant waste cooking oil using blender. Int. J. Renew. Energy Res., 3(4): 976-979. https://doi.org/10.20508/ijrer.35021

Sarno, M. and Iuliano, M. 2019. Biodiesel production from waste cooking oil. Green Process. Synth., 8(1): 828-836. https://doi.org/10.1515/gps-2019-0053

Uddin, M.R., Ferdous, K., Uddin, M.R., Khan, M. and Islam, M.A. 2013. Synthesis of biodiesel from waste cooking oil. Chem. Eng. Sci., 1(2): 22-26. https://doi.org/10.12691/ces-1-2-2

Unni, K.S., Yaakob, Z., Pudukudy, M., Mohammed, M. and Narayanan, B.N. 2013. Single step production of biodiesel from used cooking oil. Proceedings of 2013 International Renewable and Sustainable Energy Conference, IRSEC 2013, 461-464. https://doi.org/10.1109/IRSEC.2013.6529712

Nature Environment and Pollution Technology
An International Quarterly Scientific Journal

p-ISSN: 0972-6268
(Print copies up to 2016)
e-ISSN: 2395-3454

Vol. 22 | No. 1 | pp. 169-177 | 2023

Original Research Paper

https://doi.org/10.46488/NEPT.2023.v22i01.015

Open Access Journal

# Exemplarity of the State for the Energy Efficiency of Buildings Institutional - Case of Morocco

**Y. Kasseh†, A. Touzani and S. EL Majaty**
Mohammedia School of Engineers-Avenue Ibn Sina B.P 765, Agdal Rabat 10090, Morocco
†Corresponding author: Y. Kasseh; Youssefkasseh.emi@gmail.com

**Nat. Env. & Poll. Tech.**
**Website: www.neptjournal.com**

*Received:* 19-07-2022
*Revised:* 06-10-2022
*Accepted:* 16-10-2022

**Key Words:**
Energy
Energy efficiency
Buildings institutional
Administration exemplarity pact

## ABSTRACT

Engaged for many years in a strategy to control climate change, Morocco is committed to leverage on sustainable development as a new development model and as a true project for society. This commitment resulted in implementing several reforms targeting the consolidation of a developed economy, improving social conditions, and accelerating positive environmental changes. The public administration developed the Administration Exemplarity Pact (AEP) as a concrete action to lead by example in implementing the National Strategy for Sustainable Development. Developed in accordance with the main stake of the National Strategy of Sustainable Development, its goal is to promote sustainable development governance in our country through several strategic focus areas. This document presents the experience of a Moroccan administration that has implemented the guidelines described in the AEP. The approach and results are detailed and could be used as an example for other Moroccan companies. The first step of the methodology consists of a diagnostic phase to establish the current situation. The second step is related to the strategy to define the approach's main orientations and the action plan. These key steps allow us to identify areas of improvement and build a roadmap adapted to the current context and constraints. One of the best practices for this approach is to define the main orientations to act by positive contagion on the ecosystem. In conclusion, the AEP axes deployed in a dynamic improvement logic give convincing results. By acting with partners (subcontractors and suppliers), the Moroccan administration can act on the whole value chain and induce an essential change in the Moroccan economic fabric.

## INTRODUCTION

After the Club of Rome warning in 1975 (Idowu et al. 2013), it is mandatory today to manage natural resources well. Since the oil shocks of 1973 to 1979, developed countries have realized that their financial sustainability was based on the intensive use of limited natural resources. Nevertheless, one important aspect has been neglected, i.e. the environment (Ahmad et al. 2022).

The Sustainable Development Goals (SDGs) were defined as the seventeen goals established by the United Nations member states. They are assembled in the 2030 Agenda (Idowu et al. 2013). The Organization of the United Nations adopted this agenda in September 2015 after two years of negotiations, including governments and civil society. It defines targets to be achieved by 2030. The implementation of the SDGs within a State requires the active commitment of governments and all stakeholders, such as companies, communities, associations, and researchers.

Morocco has minimal energy resources and imports more than 95% of its need (Bouyghrissi et al. 2021). In this context, the Moroccan government gives primary importance to the energy sector as the main driver of economic development and social progress. Several strategic actions have been developed (Choukri et al. 2017):

- The Constitution of Morocco recognizes sustainable development as a right for all citizens to achieve better democratic governance.
- A national charter for the environment and sustainable development was deployed.

**ORCID details of the authors:**

**Y. Kasseh**
https://orcid.org/0000-0001-7776-5034
**A. Touzani**
https://orcid.org/0000-0002-5987-455X
**S. EL Majaty**
https://orcid.org/0000-0002-4408-4969

- Law No. 99-12 was adopted and required the government to develop and implement a national strategy for sustainable development.
- Morocco is committed to international environmental and sustainable development conventions (The Kingdom of Morocco Ministry of Energy Transition and Sustainable Development 2017).

The adoption of the National Strategy for Sustainable Development by the Council of Ministers under the presidency of His Majesty King Mohammed VI (Kingdom of Morocco Ministry of Energy Transition and Sustainable Development 2017) was a crucial step in the process of consecrating sustainable development at the national level.

The first axis of this strategy aims to make the exemplarity of the administration a lever for implementing sustainable development. Thus, the public administration has developed the Administration Exemplarity Pact (AEP) as a concrete action to set an example for implementing the National Strategy of Sustainable Development (Kingdom of Morocco Ministry of Energy Transition and Sustainable Development 2019b).

This paper presents the experience of a Moroccan administration that implemented the guidelines described in the AEP. The approach and results are detailed and could be used as an example for other Moroccan companies.

## EXEMPLARITY OF THE ADMINISTRATION - THE CASE OF MOROCCO

In the frame of the Administration Exemplarity Pact (AEP), the public administration has the challenge of leading by example in the implementation of national sustainable development strategies (The Kingdom of Morocco Ministry of Energy Transition and Sustainable Development 2019b).

Adopted by the National Committee for Sustainable Development in February 2019, the Administration Exemplarity Pact (AEP) reflects the commitment of the Moroccan administration to sustainable development.

For the effective implementation of the AEP, a circular from the Head of Government has been sent to all public administrations concerned.

Since its launch, the deployment of the AEP has aimed to encourage and promote best practices of sustainable development among all economic and social stakeholders at the national level. The main objectives of the Administration Exemplarity Pact (Kingdom of Morocco Ministry of Energy Transition and Sustainable Development 2019a) can be summarized in 6 items, as described in Fig. 1:

To support the ministerial departments in the process of preparing their Exemplarity Pact, the Environment Department within the Ministry of Energy, Mines, and the Environment has carried out several actions. These actions include:

- The development and dissemination of a methodological guide on the Exemplarity of the Administration,
- Orientation sheets by the domain (water, waste, mobility, energy efficiency),
- and standardized terms of reference on environmental auditing in public buildings (Kingdom of Morocco Ministry of Energy Transition and Sustainable Development 2019a).

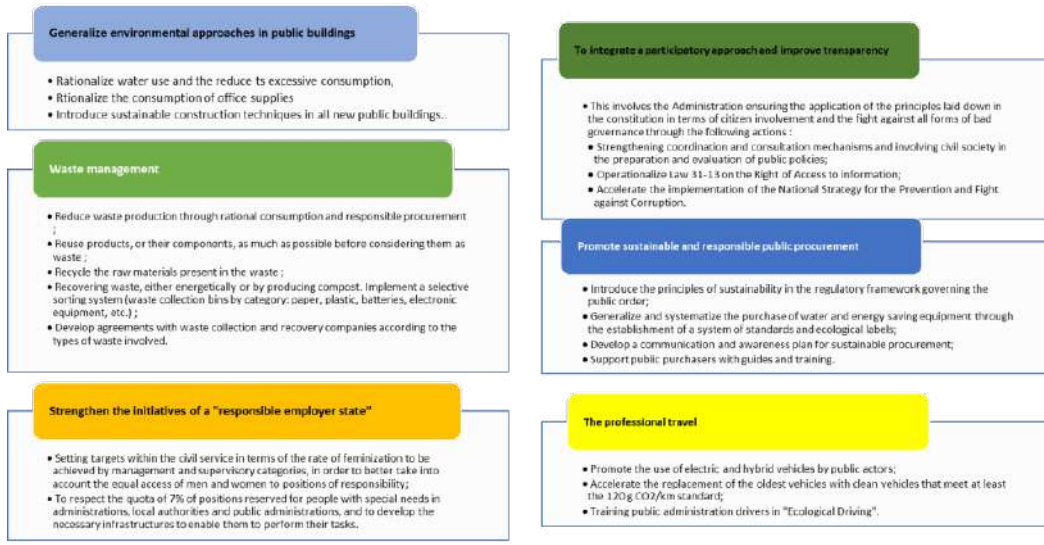


Fig. 1: AEP objectives.

In addition, technical assistance has been made available to ministerial departments within the framework of international cooperation to accelerate the pace of implementation and generalize these measures to public entities and local authorities.

The exemplarity of the administration concerns several domains: energy (mainly electricity), water, waste, public procurement, mobility, and Office consumables.

## MATERIALS AND METHODS

The Moroccan authorities are convinced that the state, in the broadest sense, and the public administration in particular, have a decisive role to play in the process of the Kingdom's energy transition (Kingdom of Morocco Ministry of Energy Transition and Sustainable Development 2017). The AEP is a disposition by the Moroccan government to encourage the exemplarity of administrations in terms of sustainable development.

The purpose of this study is to present the methodology and results of a Moroccan administration that has implemented the AEP guidelines. This study aims to provide a methodology for implementing PEA tested in a public administration in Morocco. The article focuses on two components of this study: the results of the diagnosis and the actions implemented.

The study also demonstrates the need to involve stakeholders as early as possible in the process to ensure the wide dissemination of these principles.

This study could be extended to other administrations and companies to address the challenges of climate change, economic development, and energy security.

To carry out this mission, a methodology in 3 steps was developed. As explained in Fig. 2, an initial phase related to the diagnosis and inventory of the equipment, analysis, and treatment of the preliminary data by carrying out field visits and working meetings with the concerned. The second phase is devoted to the realization of the field audit and synthesizing it to propose improvement tracks. The third phase was devoted to studying the technical and economic feasibility of the recommendations and implementing an action plan. This was an essential phase of the mission, which allowed the definition of the strategy and monitoring framework (analysis of operational objectives, monitoring indicators, etc.) and the definition of an action plan.

According to the AEP requirements, the audit (Boharb et al. 2016) covered: energy, water, waste, and paper use. During these audits, the following elements were analyzed: Energy contracts, use of renewable energy, lighting, office equipment, heating/ventilation/air conditioning, kitchen equipment, and hot water. The water consumption, the quantities of water discharged, the characteristics of the installed facilities, and the wastewater collection were examined for the water audit. It was also a question of evaluating the quantity of waste produced and making a point on the use of paper.

## RESULTS AND DISCUSSION

### Results of Diagnosis

At the current stage of diagnosis, it was essential to analyze the data to understand the energy situation at the site. It

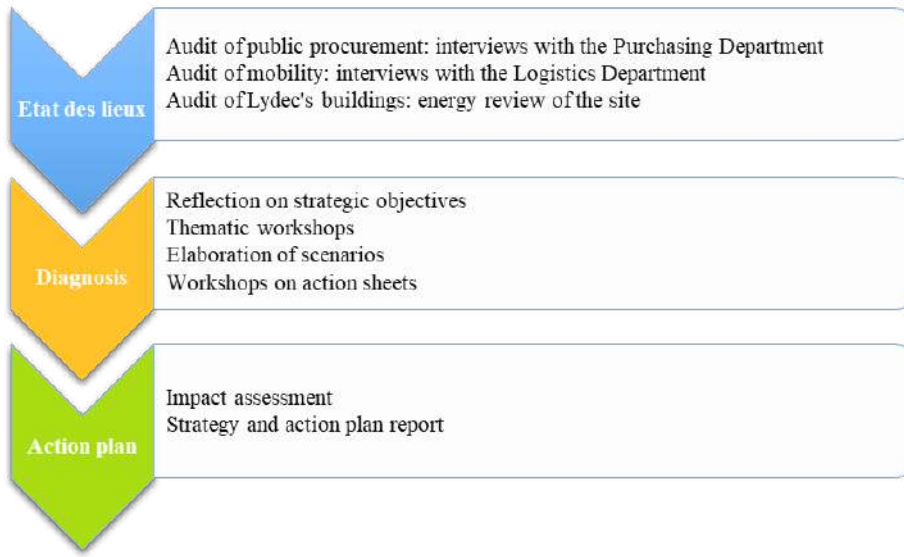


Fig. 2: The methodology of the study.

is often useful to graph the consumption data to visualize the changes in consumption. Establishing relationships between energy consumption and influencing factors provides a clear understanding of what is happening at the site.

## Electricity Consumption

Electricity consumption varied from 2,090,678 kWh in 2018 to 1,766,671 kWh in 2019 and 1,526,111 in 2020, a change of -15% and -14%, respectively (Fig. 3).

## Water Consumption

Water consumption varied from 4,950 $m^{-3}$ in 2018 to 2,207 $m^3$ in 2019 and 2,080 $m^3$ in 2020, i.e., a change of -55% and -6%, respectively (Fig. 4).

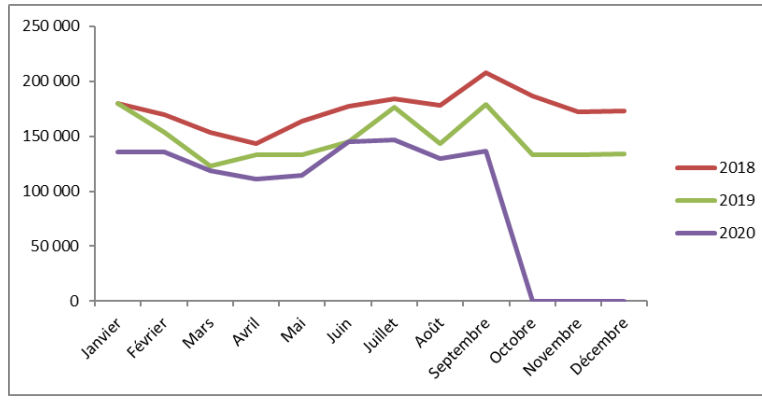


Fig. 3: Evolution of electricity consumption 2018, 2019, 2020.

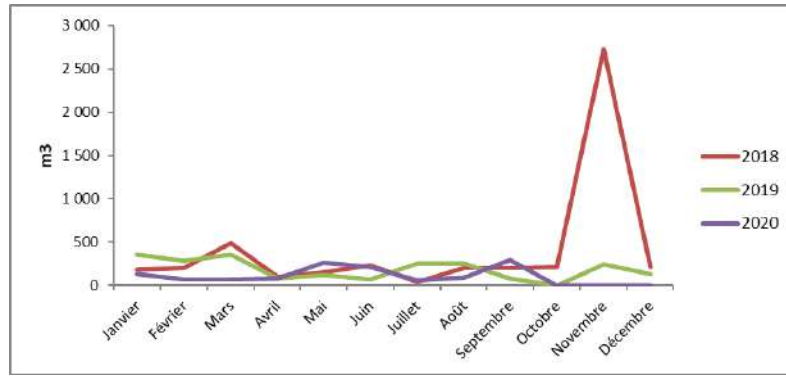


Fig. 4: Evolution of water consumption, 2018, 2019, 2020.

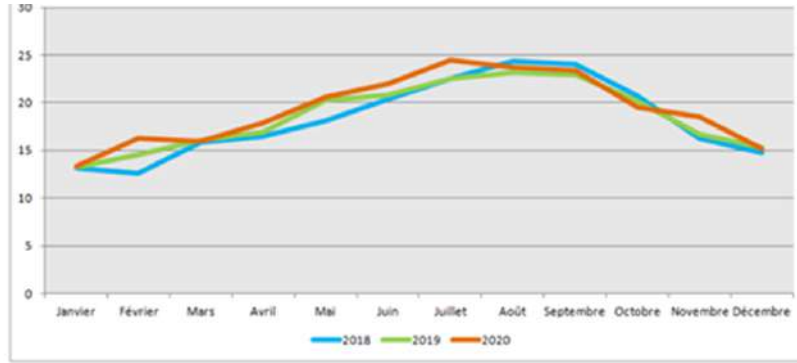


Fig. 5: Average temperatures in Casablanca (2018, 2019 and 2020). (Source: www.infoclimat.fr)

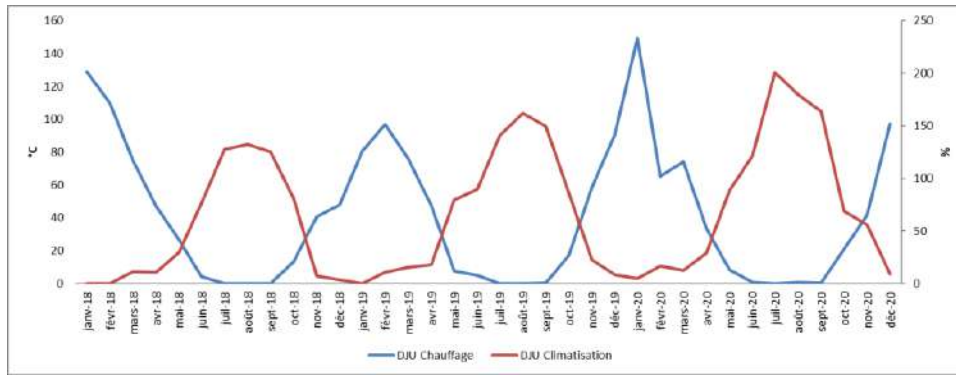


Fig. 6: Degree days in Casablanca (2018, 2019, 2020). (Source: www.infoclimat.fr)

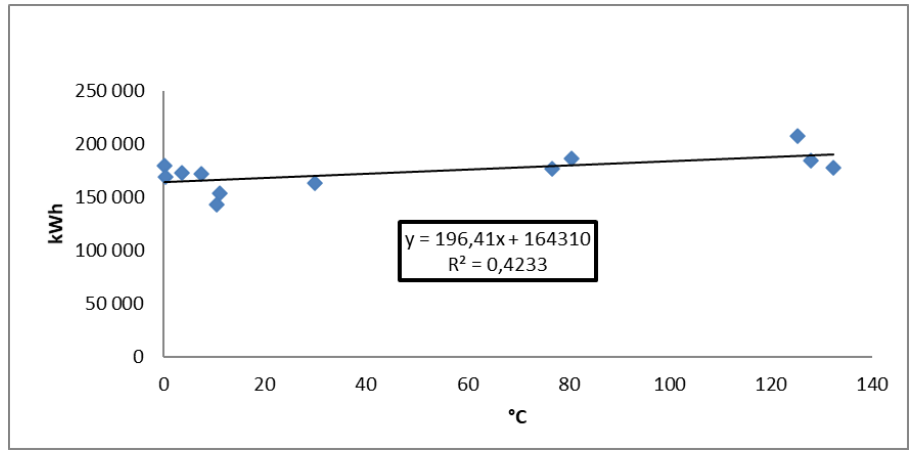


Fig. 7: Electricity consumption VS DJU Air conditioning.

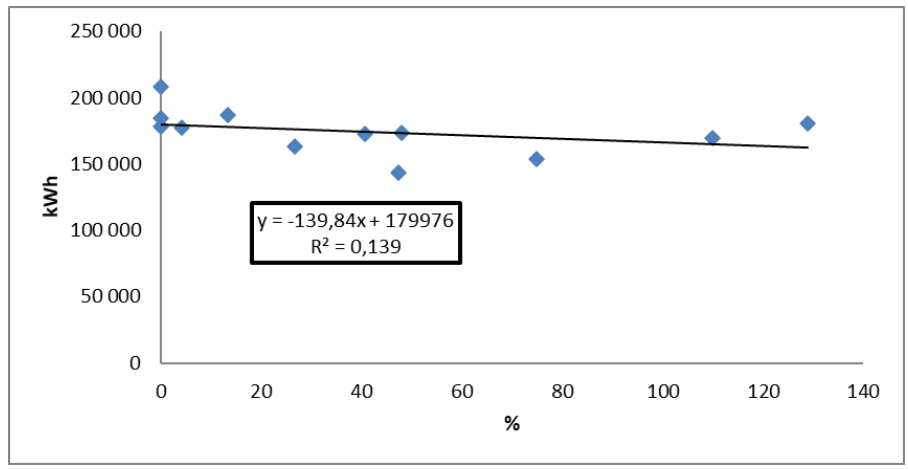


Fig. 8: Electricity consumption VS DJU heating.

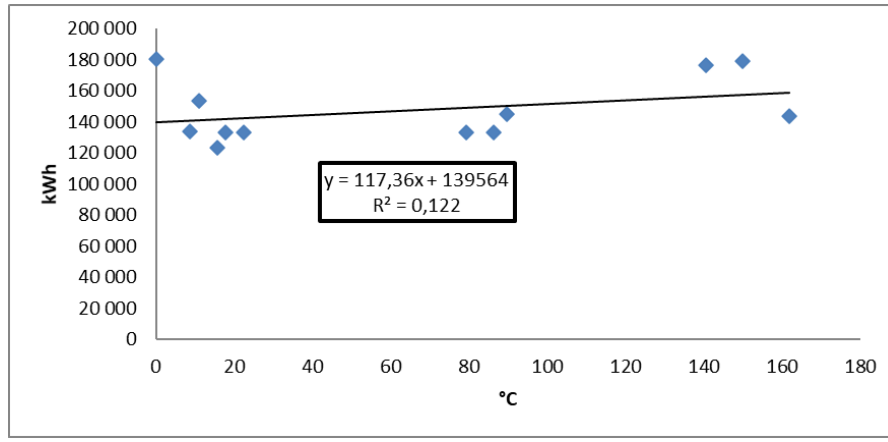


Fig. 9: Electricity consumption VS DJU air conditioning.

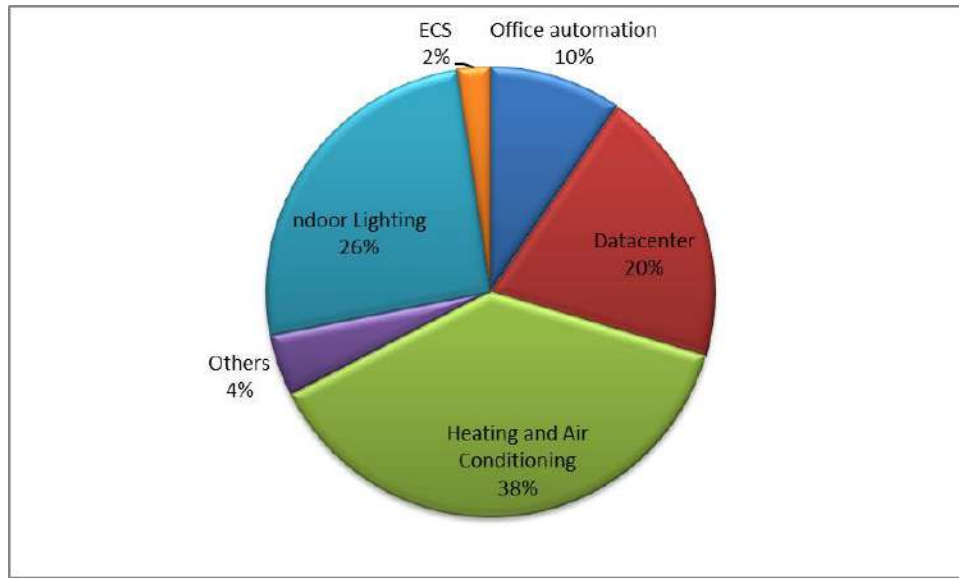


Fig. 10: Significant uses.

## The Climate of Casablanca

The climate of the city of Casablanca is temperate, influenced by the Atlantic. The average temperatures do not vary much. The temperature profiles of the years 2018, 2019, and 2020 seem to be close (Fig. 5).

On the other hand, the heating and cooling degree days show that 2020 was warmer than 2019 and 2018 (Fig. 6).

## Consumption Ratios

The variation of consumption in a building can be influenced by its surface, the number of occupants, and the climate when the building has an air conditioning system. In our case, we do not have information on the number of occupants and the surface. Therefore, we will be satisfied to do the exercise with the meteorological data of Casablanca.

## Electricity Consumption Ratio

A linear regression analysis of the available data showed a possible correlation with the air-conditioning degree days (Fig. 7, Fig. 8, Fig. 9). The correlation coefficients obtained for 2018, 2019, and 2020 are, respectively, $R^2 = 0.84$ and 0.78 and 0.74. And the respective residual consumptions are 147 MWh, 117 MWh, and 104 MWh.

## Significant Energy Uses

The selection of significant uses is made for any use whose share of consumption exceeds 10%. Hence the significant

uses for the company are air conditioning, lighting, the Datacenter, and office automation (Fig. 10).

**Mobility Audit**

The reduction of greenhouse gas emissions has become a critical global objective. Recent scientific studies estimating the socio-economic costs of the effects of global warming reinforce concerns about environmental and energy constraints and emphasize the nature and modalities of the policies to be put in place (Fouillé et al. 2012). Transport is now the leading sector in terms of greenhouse gas emissions and carbon dioxide emissions (Jia et al. 2009). The mobility audit carried out for the company in question highlighted the numerous measures already implemented for the management of its truck fleet, which has led to a reduction in fuel consumption in recent years. Optimizing the fleet and experimenting with new modes of transport through pilot projects (electric cars, electric mopeds, etc.) is an asset for finding solutions to reduce the environmental impact of mobility.

**Recommendations**

Various studies have shown that it is possible to reduce electricity costs without significantly reducing energy consumption when time-of-use electricity rates are applicable (Hu et al. 2020). These strategies typically require little or no capital outlay and use optimized control strategies to prioritize electrical energy use outside the more expensive periods of the day through time-shifting.

In general, it is claimed that buildings consume energy, even if the "building" is responsible for very low energy consumption during its operational life but much more during the design, construction, and deconstruction phases. Indeed, most of the energy is consumed by the occupants. However, they do not have direct contact with the energy carriers (fuel, gas, electricity), and more precisely, with the equipment and goods that provide them with services; therefore, the users do not feel directly responsible for the energy consumption, which is consumed by the equipment and, more generally, by the buildings. It is interesting to note that energy consumption is measured in kW h.m-$^{2}$ year and not in kW h.person-year$^{-1}$ (Delgoshaei et al. 2017).

Thus, actions related to user behavior have also been implemented to ensure compliance with good energy use practices, including turning on lighting only when necessary, turning off lighting when leaving the premises, using air conditioning only when necessary, appropriate adjustment of the air conditioning temperature (winter/summer), closing doors and windows when using air conditioning, limiting the use of table water in plastic bottles and favoring tap water. The choice of low-consumption equipment is an important axis of the action plan.

The optimization of water consumption through the use of drip systems and programming of watering time (avoid watering in full sun), as well as the choice of plants with low water demand.

Other recommendations have been implemented to improve the building's electrical energy performance: the generalization of the replacement of light points by LED lighting, the generalization of the choice of equipment with low power consumption, automatic control of lighting by presence detector, especially for sanitary facilities, adjustment of the automatic control of exterior lighting, and realization of programmed cut-off of lighting taking into account the working hours and functions of each room.

The following areas for improvement have been identified: Improve the management of document archiving, generalization of the digital archiving of documents, implementation of a charter for the use of paper in the offices with the aim of Optimize pagination, use of appropriate fonts, preventing on-screen correction, minimizing the number of printouts, using electronic forms instead of paper forms, using double-sided functionality whenever possible, reuse paper waste, generalization of the monitoring of paper consumption by site and by function.

In conclusion, the energy-water-waste-paper audit of administrative buildings also highlighted many actions already underway in buildings, including the deployment of low-energy LED lighting and the replacement of air conditioners with equipment that emits less greenhouse gas, the development of renewable energy production and the monitoring of electricity and water consumption. The deployment of digital technology to reduce paper consumption is also recommended.

**Analysis of Public Procurement**

Responsible public procurement can be understood as a new concept of public purchasing (El Asri et al. 2022), which could affirm the role of public actors in sustainable development.

This initiative also aims to professionalize the "purchasing" function by developing skills and improving decision-making tools (Gayot 2019). Therefore, the combination of efficiency and sustainable development objectives is at the heart of the new governance of purchasing (Cantillon 2010).

The analysis carried out as part of this study shows that a corporate social responsibility policy is already

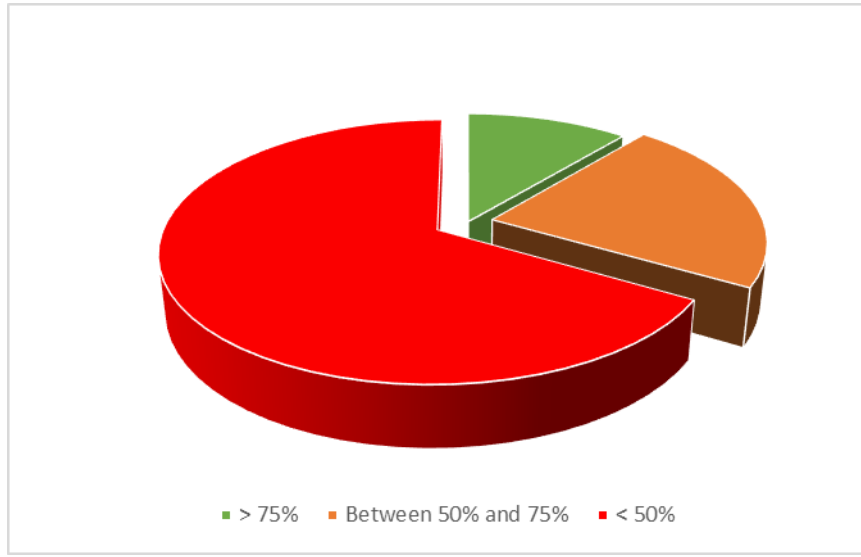


Fig. 11: Audit companies results.

in place for responsible purchasing management. The framework documents governing supplier contracts refer to environmental protection, and almost all contracts include clauses on services' social or environmental impacts.

To go further, an audit of the most significant subcontractors was carried out to evaluate their performance in terms of respect for the environment. The audit was carried out based on a grid integrating objective criteria linked to respect for the environment.

As shown in Fig. 11, only 2 companies have a high level of global maturity. This study shows that public administrations have an important role in supporting and engaging subcontractors in energy efficiency initiatives. Beyond the contractual obligations, a work of accompaniment of these companies must be carried out.

So it is very important to involve stakeholders as early as possible in the process to ensure wide dissemination of these principles.

## CONCLUSION

In this paper, a common framework has been developed for the evaluation of an energy management system. The PEA is based on provides a framework for improving the energy performance of organizations. This document offers a methodological framework for deploying the principles of the AEP.

A Moroccan administration operating in the Casablanca area was chosen as a case study. In particular, its buildings were used to assess energy performance and serve as an illustrative application to demonstrate the general validity of the method.

The application of all the steps of the method revealed to the energy manager the necessary actions to be implemented. In addition, monitoring and controlling performance proved to be a fundamental step in gaining efficiency.

In conclusion, the PEA axes deployed in a dynamic improvement logic give convincing results. By acting with partners (subcontractors and suppliers), the Moroccan administration can act on the whole value chain and induce an essential change in the Moroccan economic fabric.

This commitment has enabled several ministries to make real savings in terms of resources. For example, some departments have reduced their water consumption by 50% and produced 22% of their electricity needs from renewable energy. While others have been able to achieve 32% of their fleet of clean vehicles and achieve a rate of 1 waste of about 35% (Diao 2021).

## REFERENCES

Ahmad, M., Ahmed, Z., Yang, X., Hussain, N. and Sinha, A. 2022. Financial development and environmental degradation: Do human capital and institutional quality make a difference? Gond. Res., 105: 299-310. https://doi.org/10.1016/j.gr.2021.09.012

Boharb, A., Allouhi, A., Saidur, R., Kousksou, T., Jamil, A., Mourad, Y. and Benbassou, A. 2016. Auditing and analysis of energy consumption of an industrial site in Morocco. Energy, 101: 332-342. https://doi.org/10.1016/j.energy.2016.02.035

Bouyghrissi, S., Berjaoui, A. and Khanniba, M. 2021. The nexus between renewable energy consumption and economic growth in Morocco. Environ. Sci. Pollut. Res., 28(5): 5693-5703. https://doi.org/10.1007/s11356-020-10773-5

Cantillon, G. 2010. Sustainable public procurement: A tool at the service of the regulatory state. French J. Pub. Admin., 134(2): 335. https://doi.org/10.3917/rfap.134.0335

Choukri, K., Naddami, A. and Hayani, S. 2017. Renewable energy in emergent countries: Lessons from energy transition in Morocco. Energy Sustain. Society, 7(1): 25. https://doi.org/10.1186/s13705-017-0131-2

Delgoshaei, P., Heidarinejad, M., Xu, K., Wentz, J. R., Delgoshaei, P. and Srebric, J. 2017. Impacts of building operational schedules and occupants on the lighting energy consumption patterns of an office space. Build. Simul., 10(4): 447-458. https://doi.org/10.1007/s12273-016-0345-9

Diao, M. 2021. Exemplary Administration Pact: Some Ministries Stand Out. . https://fnh.ma/article/developpement-durable/pacte-de-l-exemplarite-de-l-administration-certains-ministeres-sortent-du-lot

El Asri, N., Nouira, Y., Maaroufi, I., Marfak, A., Saleh, N. and Mharzi, M. 2022. The policy of energy management in public buildings procurements through the study of the process of delegated project management: Case of Morocco. Energy Pol., 165: 112944. https://doi.org/10.1016/j.enpol.2022.112944

Fouillé, L., Broc, J.S., Bourges, B., Bougnol, J. and Mestayer, P. 2012. The place of traffic models in recent modeling of the environmental impacts of transport. Importance of explaining methods and assumptions. Transp. Saf. Res., 20(03-04): 191-200. https://doi.org/10.1007/s13547-012-0037-5

Gayot, O. 2019. From the social responsibility of organizations to responsible public purchasing: between constraints and performance: Study day report. Sustain. Dev. Terr., 10(1): 1366. https://doi.org/10.4000/developpementdurable.13666

Hu, S., Yan, D., Azar, E. and Guo, F. 2020. A systematic review of occupant behavior in building energy policy. Build. Environ., 175: 106807. https://doi.org/10.1016/j.buildenv.2020.106807

Idowu, S.O., Capaldi, N., Zu, L. and Gupta, A.D. (Eds.). 2013. Encyclopedia of Corporate Social Responsibility. Springer Berlin Heidelberg, Berlin. https://doi.org/10.1007/978-3-642-28036-8

Jia, S., Peng, H., Liu, S. and Zhang, X. 2009. Review of transportation and energy consumption-related research. J. Transp. Syst. Eng. Inf. Technol., 9(3): 6-16. https://doi.org/10.1016/S1570-6672(08)60061-6

Kingdom of Morocco Ministry of Energy Transition and Sustainable Development. 2017. National Sustainable Development Strategy, 2030. Morocco Government, Morroco

Kingdom of Morocco Ministry of Energy Transition and Sustainable Development. 2019a. Methodological Guide for the exemplarity of the administration in matters of Sustainable Development. Morocco Government, Morroco

Kingdom of Morocco Ministry of Energy Transition and Sustainable Development. 2019b. Pact of Exemplarity of the Administration. Morocco Government, Morroco

Nature Environment and Pollution Technology
An International Quarterly Scientific Journal

p-ISSN: 0972-6268
(Print copies up to 2016)
e-ISSN: 2395-3454

Vol. 22 | No. 1 | pp. 179-187 | 2023

Original Research Paper

https://doi.org/10.46488/NEPT.2023.v22i01.016

Open Access Journal

# Efficiency of *Paecilomyces variotii* in Bioremoval of Reactive Black Dye from Tannery Effluent

**Priya Chokkalingam†*, Mahi Anamalagundam*, Chaithanya Lahari*, Shreya Singh*, G. Mohan Kumar** and Rajeswary Hari***

*Department of Biotechnology, Dr. M.G.R. Educational and Research Institute, Madhuravoyal, Chennai, Tamilnadu, India
**Faculty of Physiotherapy, Dr. M.G.R. Educational and Research Institute, Chennai, Tamilnadu, India
†Corresponding author: Priya Chokkalingam; priyamohan.2984@gmail.com

**Nat. Env. & Poll. Tech.**
**Website: www.neptjournal.com**

*Received:* 29-06-2022
*Revised:* 24-08-2022
*Accepted:* 05-09-2022

**Key Words:**
Reactive black dye
*Paecilomyces variotii*
Decolorization
Tannery effluent
Water pollution

## ABSTRACT

The present work investigates the efficiency of *Paecilomyces variotii* upon degrading Reactive Black dye which has been termed a recalcitrant variety of synthetic dye. In this research, initially a predominant fungal species, *Paecilomyces variotii* was isolated from the tannery effluent sample. The study was carried out by assessing the ability of fungi to decolorize the dye under various parameters like pH (5,7 and 9), Temperature (7°C, 30°C, and 45°C), Dye concentration (200, 300, and 400 mg/L) for different incubation or exposure time interval (3, 5 and 7 days). From the experimental study, it was found that *Paecilomyces variotii* showed a maximum percentage of dye decolorization at 7°C at pH 9 with 75%, at 30°C at pH 7 with 85%, at 45°C at pH 5 with 82% and a maximum period of incubation with 7 days in 200 $mg.L^{-1}$ concentration. This result conveys that the strength of *Paecilomyces variotii* in decolorizing the synthetic dye is effective at a moderate temperature with neutral pH for maximum exposure time. So *Paecilomyces variotii* could be a good candidate of choice for the biodegradation of various synthetic dyes when manipulated wisely. Also, the result sparks a positive attribute toward decreasing industrial wastewater pollution.

## INTRODUCTION

These days, water has become an essential resource for humans and other species in the world for existence and survival (Wang et al. 2020). Wastewater from various factories and industries poses a great threat to water quality. Especially, tannery and textile effluent release a wide range of hazardous compounds containing heavy metals and synthetic dyes into nearby water systems which impart deleterious effects on surrounding flora and fauna. Every year, about $7 \times 10^7$ tons of synthetic dyes are produced worldwide, which have been used by various industries like textile, tannery, food, cosmetics, etc. (Chandanshive et at. 2020). These dyes are highly reactive, chemically stable, and resistant to the degradation process (Martínez-Huitle & Brillas 2015). Among the dye used in tannery and textile industries, Reactive Black 5 (RB5) accounts for 50% of the azo and becoming a recalcitrant to natural aquifers (Nabil et al. 2014). Leather industries make use of these azo dyes in large proportion because of their strong binding ability towards the collagen in respective pH ranges. But the fate of unbounded dyes present in untreated effluents greatly spoils nearby water streams (Rocha et al.2017). Normally, industrial effluents correspond to high levels of BOD, COD, pH, and color which is lethal to all forms of life associated with water. Among other pollutants, color is one of the vivid signs of pollution caused by various synthetic dyes that a water body can receive (Nigam et al. 1996). The carcinogenic effect of these dyes poses a big threat to living organisms also the intensity of different dyes interferes with the photosynthetic activity of water flora that indirectly affects the food chain (Weisburger 2002). Everything considered, the deleterious sequel of dye on the ecosystem, discarding and subsequent decolorizing of the dyes should be the prime concern (John et al. 2020).

Several physico-chemical methods such as electrolysis, adsorption, ion exchange, ultrafiltration chemical oxidation, ozonation, electrochemical degradation, etc., have been employed for dye decolorization as well as the degradation process (Jagadeesan et al. 2013). Anyway, all these procedures retain a few intrinsic factors such as expensiveness, formation of harmful by-products, and exhaustive energy requirements (Aravindhan et al. 2007). The biological way of removing the dyes from wastewater through bioaccumulation and biodegradation has been proven to be more effective against the above conventional procedures since it is economical and environmentally friendly also the treatment process

can be carried out on site itself with very less or no by-products (Jagadeesan et al. 2013). So, recently scientists are significantly addressing the issue of effluent treatment through biological methods (Vijayaraghavan et al. 2008). Among the biological methods, microbial degradation of dyes is proven to be one of the prime methods, since most of the bacterial, fungal, and algae species present in the contaminated area were recorded as effective in dye decolorization and degradation. It was observed that during the decolorization process by fungi and algae, dye adsorption plays a major part (Slama et al. 2021). Scientific studies have stated that microbes possessing genes that code for various enzymes like laccase, peroxidase, and azoreductase cleave the aromatic ring present in dyes for its effective degradation (Chen et al. 2003, Babu et al. 2015). Fungi species such as *Cladosporium, Chaetomium globosum, Fusarium solani, Alternaria,* and *Aspergillus niger* secrete manganese peroxidase, lignin peroxidase, and laccase enzymes extracellularly having the ability to degrade various complex synthetic dyes (El-Gendi et al. 2021). In this study, predominant fungi present in the tannery effluent were isolated and their efficiency in decolorizing the reactive black B dye was analyzed under various parameters like different pH, Temperature, time, and concentration of dye.

## MATERIALS AND METHODS

### Media and Chemicals

Fungal growth media, namely potato dextrose agar (PDA), potato dextrose broth (PDB), and Czepak's dox broth were purchased from HiMedia. Reactive Black 5 (RB5) (Fig. 1) dye was procured from Sigma Aldrich (Bangalore).

### Collection of Tannery Effluent Sample and Its

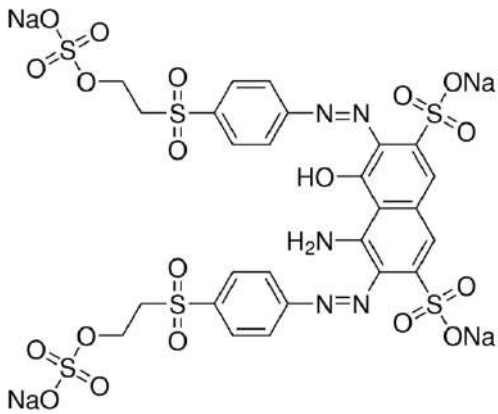


Fig.1: Chemical structure of Reactive Black 5 azo Dye.

### Physico-Chemical Property Analysis

The tannery effluent was collected in a sterile sample container tube from the leather industry located in Nagalkeni, Chennai (Lat Long (12.961140, 80.135430) GPS Coordinates (12°57□40.104□-N80°8□7.548□ E) and taken to the laboratory for further analysis. The physicochemical parameters of the effluent such as color, odor, pH, Electrical conductivity (EC), Total dissolved solids (TDS), Total suspended solids (TSS), BOD, COD, Copper, Chromium, Chloride, and sodium were analyzed following the standard approved by CPCB (1995) (Table 1).

### Fungal Isolation from Tannery Effluent Sample and Culture Conditions

From the tannery effluent sample, the predominant fungal species were identified by serial dilution technique followed by inoculation in potato dextrose agar (PDA) by pour plate technique subsequently incubation was done at 37°C for 3-4 days. After the incubation period, the colonies were identified based on morphological, microscopic observations, and cultural characteristics and identified up to the species level (Gilmann 1971, Subramanian 1971, Ellis 1971, Udaya Prakash 2004). A fungal species was selected based on its prevalence and dominance and used to evaluate its efficiency in the bioremoval of reactive black dye. Initially, the efficiency of dye decolorizing property of predominant fungal species was determined by cultivating in Czepak's dox broth containing Reactive Black dye (100 $mg.L^{-1}$). After 3 days of incubation, the culture sample was read using UV-spectrophotometer at 470 nm (Khatid et al. 2008). The fungal species which showed maximum efficiency was selected for further studies. To improve its dye decolorizing efficacy, the process was studied under various parameters

Table 1. Analysis of physicochemical parameters of untreated tannery effluent.

| S. No. | Parameters | Observations | Reference value (CPCB-195) |
|---|---|---|---|
| 1 | Color | Blackish | Colorless |
| 2 | Odor | Disagreeable odor | Odorless |
| 3 | pH | 8.5 | 5.5-9.0 |
| 4 | EC | 12013 $\mu s.cm^{-1}$ | 400 $\mu s.cm^{-1}$ |
| 5 | TDS | 3021 $mg.L^{-1}$ | 2100 $mg.L^{-1}$ |
| 6 | TSS | 151 $mg.L^{-1}$ | 100 $mg.L^{-1}$ |
| 7 | BOD | 829 $mg.L^{-1}$ | 30 $mg.L^{-1}$ |
| 8 | COD | 1131 $mg.L^{-1}$ | 250 $mg.L^{-1}$ |
| 9 | Chromium | 4.6 $mg.L^{-1}$ | 2 $mg.L^{-1}$ |
| 10 | Copper | 5 $mg.L^{-1}$ | 3 $mg.L^{-1}$ |

like pH, temperature, time, and concentration of dye sample.

### Optimization of Conditions

#### *Effect of Dye Concentration*

The commercially available dye was taken in three different concentrations such as 200 mg.$L^{-1}$, 300 mg.$L^{-1}$, and 400 mg.$L^{-1}$in separate flasks containing czepak's dox broth. One milliliter of the fungal inoculum was added to each bottle aseptically and incubated for 3 days at 37°C. The absorbance was measured and calculated periodically to evaluate the effect of concentration and percentage of decolorization.

#### *Effect of pH*

The pH of the medium with different dye concentrations (200 mg.$L^{-1}$, 300 mg.$L^{-1}$, and 400 mg.$L^{-1}$) was maintained at 5, 7, and 9 individually. The pH was adjusted using 0.1 M hydrogen chloride (HCL) and 0.1 N Sodium hydroxide (NaOH) before inoculation of fungi. It was followed by incubation for 3-4 days at 37°C. The absorbance was measured and calculated periodically to evaluate the effect of concentration and percentage of decolorization. Based on the absorbance, the percentage of dye decolorization at various pH was calculated.

#### *Effect of Temperature*

The temperature was maintained at 7°C, 30°C, and 45°C for different dye concentrations i.e., 200 mg.$L^{-1}$, 300 mg.$L^{-1}$, and 400 mg.$L^{-1}$, and various pH levels (5, 7, and 9). The temperature is maintained by keeping flasks in the refrigerator setting the temperature at 7°C, room temperature at 30°C, and moderately high temperature at 45°C by incubating them at respective temperatures in incubators. After the incubation period, the absorbance was recorded and calculated.

#### *Effect of Time*

The Czepak's dox broth amended with different concentrations of the dye at different pH was studied for the removal of dye when inoculated with fungal isolate. The absorbance of the solutions was measured at different periods, viz., 72, 120, and 168 h. All the above experiments were performed in triplicates to maintain the reliability of the procedures.

### Percentage of Decolorization

For analyzing the decolorizing efficacy of isolated fungal species, after incubation of respective parameters, the sample was centrifuged at 3,000 rpm for 30 min. Using a supernatant solution absorbance was measured through a UV spectrophotometer. A sample with the same experimental condition but without fungi was taken as a control.

The percentage of decolorization was calculated using the formula:

$$\% \text{ removal} = \frac{(\text{Control absorbance} - \text{Test absorbance})}{\text{Control absorbance}} \times 100$$

Where, control is the absorbance of the initial dye solution and it is constant which is equal to 0% decolorization. Test absorbance is studied after the experimental parameter. Decolorization percentage refers to the percentage mean of decolorization percentage of three replicas.

### Statistical Analysis

All the data from dye decolorization assays were tested for statistical significance by comparing the mean of different test conditions using One-way ANOVA with the Dunnett Multiple Comparisons Test. The data were considered significant if $p < 0.05$, and highly significant if $p < 0.001$.

## RESULTS AND DISCUSSION

### Diversity of Fungi from Leather Effluent

On serial dilution of the contaminated tannery effluent followed by the pour plate method, after incubation different colonies of fungi were observed. The predominant colonies were subcultured in PDA and identified. A total of 23 different colonies were recorded among which *Paecilomyces variotii* alone dominated with more than 50% of fungal species. This

Fig. 2: Organisms isolated from tannery effluents.

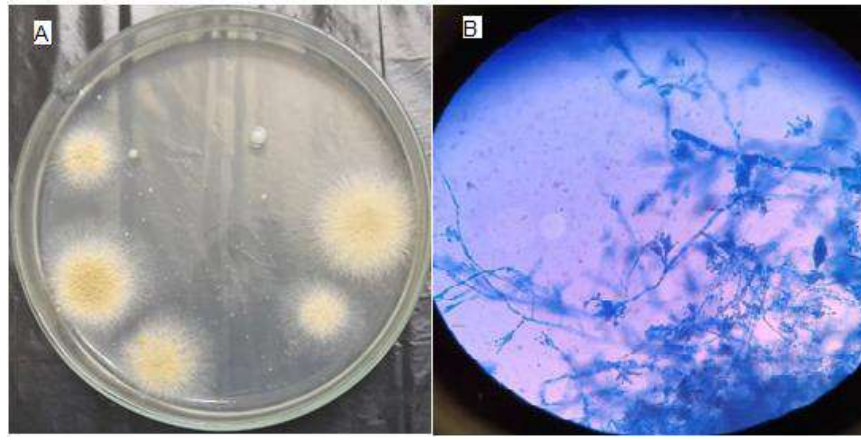


Fig. 3: A-Plate containing a pure culture of *Paecilomyces variotii* and B-Microscopic observation of *Paecilomyces variotii.*

was followed by *Aspergillus flavus, Penicillium* sp., and a non-sporulating colony. Fig. 2 shows the fungal colonies with varied morphologies. Fig. 3 reveals the *Paecilomyces variotii* culture growth in SDA and its microscopic structure when viewed at 40X magnification through the microscope.

**Removal of Reactive Dye Black at the Temperature of 7°C**

For culture conditions at 7°C in 200 mg.L$^{-1}$ concentration in pH 5, there is a 35%, 42%, and 50% dye decolorization rate that happened in 200 mg.L$^{-1}$ concentration for 3$^{rd}$, 5$^{th,}$ and 7$^{th}$ day of incubation consequently. For conditions at pH 7, there are is33%, 46%, and 55% decolorization rates that happened on the 3$^{rd}$, 5$^{th,}$ and 7$^{th}$ day of incubation respectively. While maintained at pH 9, there is 55%, 68%, and 75% decolorization rates occurred on the 3$^{rd}$, 5$^{th,}$ and 7$^{th}$ day of incubation respectively. The efficiency of *Paecilomyces variotii* dye degradation was compared between three different concentrations and at three different pH conditions for different time intervals. Among these conditions, *Paecilomyces variotii* maintained at 7°C, exhibits its maximum efficiency in alkaline pH of 9 exposed for 7 days in a dye concentration of 200 mg.L$^{-1}$ with 75% dye decolorization rate (Fig. 4). This proves that at low

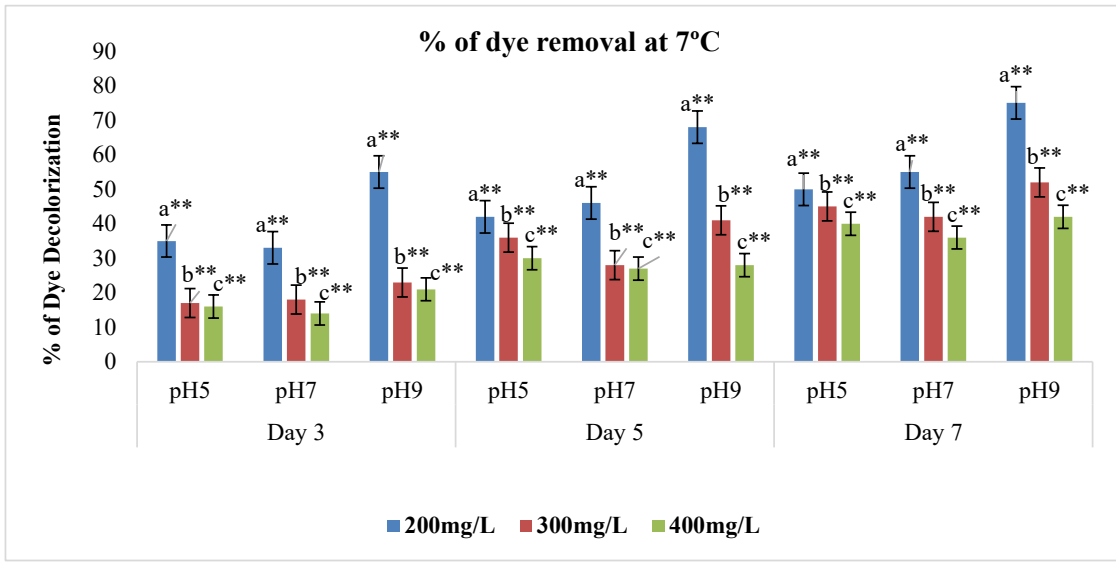


Fig. 4: Values are expressed in mean ± SD (n = 3), statistically significant test for comparison was done by ANOVA followed by Dunnet's 't-test. Comparison of dye decolorization % between a – Control vs dye concentration at 200 mg.L$^{-1}$ in different pH ranges and time intervals, b – Control vs dye concentration at 300 mg.L$^{-1}$ in different pH ranges and time intervals, c - Control vs dye concentration at 400 mg.L$^{-1}$ in different pH range and time intervals, *p < 0.05, **p < 0.01 and ns – Non-Significant.

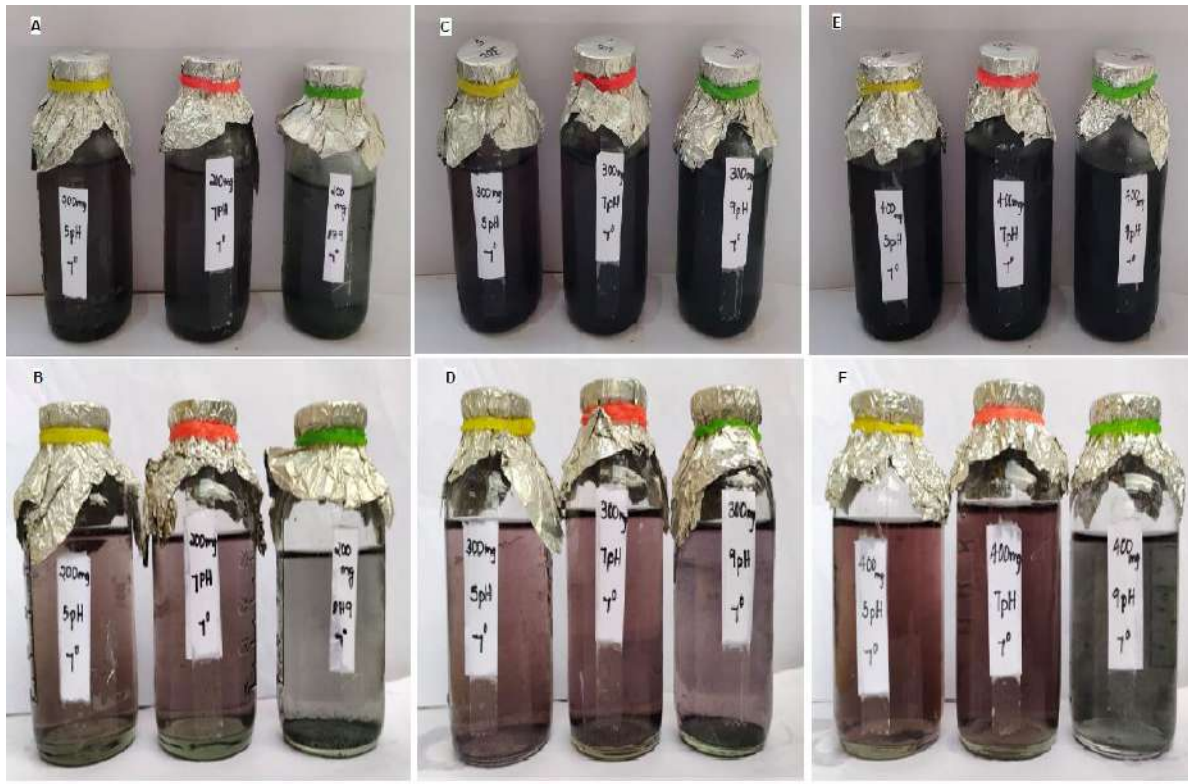


Fig. 5: photograph of dye with concentration 200 mg.L$^{-1}$ at 7$^{o}$C before (A) and after processing at pH 5, 7, and 9 (B). Photograph of dye with concentration 300 mg/L at 7$^{o}$C before (C) and after processing at pH 5, 7, and 9 (D). Photograph of dye with concentration 400 mg.L$^{-1}$ at 7$^{o}$C before (E) and after processing at pH 5, 7 and 9 (F).

temperatures the enzymes needed for dye degradation works at alkaline pH. The demand for fungi demand in the dye-degrading process can be achieved greater by accelerating their metabolism through various factors. Fungi usually secrets intracellular and extracellular enzymes which enhance their metabolism in treating dye effluents (Rania et al. 2022). Fig. 5 shows the vivid difference in color change by the action of *P. variotii* grown at different concentrations, times, and pH by keeping the temperature constant at 7$^{o}$C.

**Removal of Reactive Dye Black at the Temperature of 30°C**

Keeping the temperature of 30$^{o}$C at constant, the dye bio-removal efficacy of *Paecilomyces variotii* was studied at various pH ranges (5, 7 and 9). Also, it was done at different day intervals of the 3$^{rd}$, 5$^{th,}$ and 7$^{th}$ day with increasing concentrations of 200, 300, and 400 mg.L$^{-1}$. During 30$^{o}$C, the function of *Paecilomyces variotii* becomes less effective at pH5 with 20%, 38%, and 55% of dye color reduction with 200mg/L concentration on the 3$^{rd}$, 5$^{th,}$ and 7$^{th}$ day of incubation respectively. But in pH7, it shows maximum efficiency with 50%, 62%, and 85% on the 3$^{rd}$, 5$^{th,}$ and 7$^{th}$ day of incubation respectively. Also at pH 9 for the same culture conditions, it gives tough with 48%, 60%, and 80 % of dye decolorization from the above results (Fig. 6). It is clear that in moderate temperature the enzymes become active at neutral pH of 7 exhibiting its maximum efficiency in dye degradation with increased period of incubation (Radha et al. 2005). It is found that at low concentrations of dye, the degradation process is faster which corresponds to other studies also where 80% decolorization occurred with 75 mg.L$^{-1}$ concentration (Puentes-Cárdenas et al. 2012). Also in another study decolorization was recorded at 97% with an RB5 concentration of 1 mg L-1 after 150 min of treatment (Chong et al. 2014). Fig. 7 shows the vivid difference of color change by the action of *P. variotii* grown at different concentrations, times, and pH by keeping the temperature constant at 30$^{o}$C. From the above experimental condition, it is stated that *P. variotii* showed a maximum of 85% dye decolorization effect when compared with other prevailed conditions.

**Removal of Reactive Dye Black at the Temperature of 45°C**

The bio-removal efficacy of *Paecilomyces variotii* was

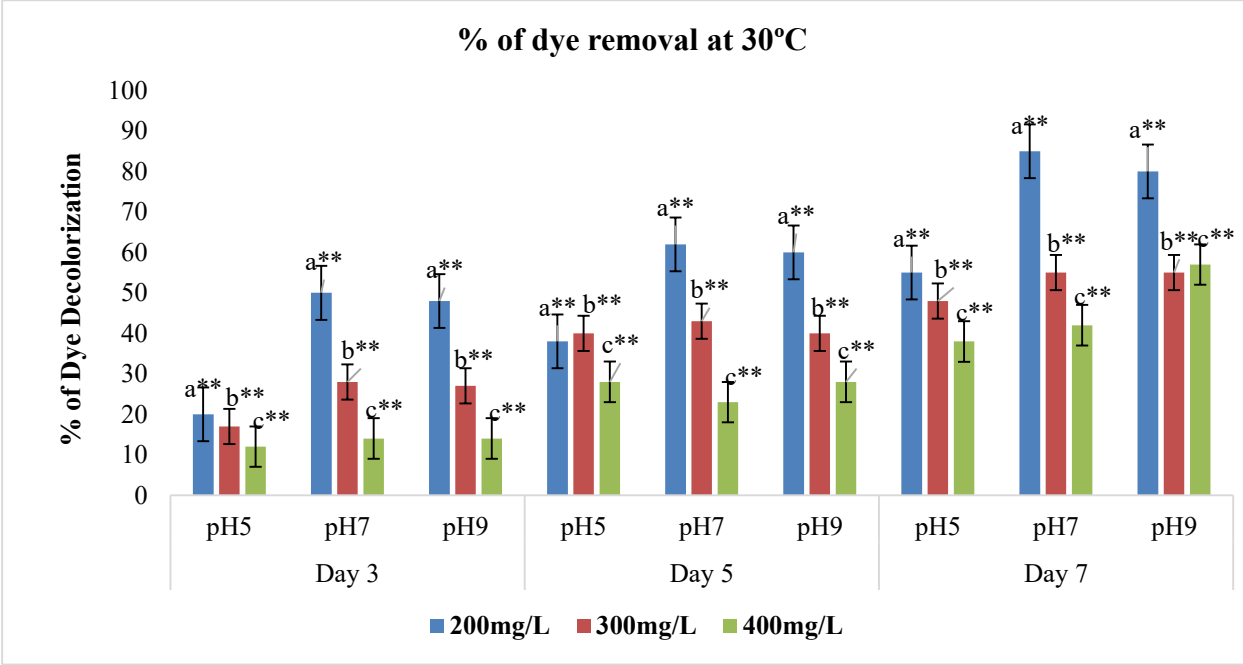


Fig. 6: Values are expressed in mean±SD (n=3), statistically significant test for comparison was done by ANOVA followed by Dunnet's 't-test. Comparison of dye decolorization % between a – Control vs dye concentration at 200 mg.$L^{-1}$ in different pH ranges and time intervals, b – Control vs dye concentration at 300mg.$L^{-1}$ in different pH range and time intervals, c - Control vs dye concentration at 400 mg.$L^{-1}$ in different pH range and time intervals, *p < 0.05, **p < 0.01 and ns – Non-Significant.


Fig. 7: Photograph of dye with concentration 200 mg.$L^{-1}$ at 30°C before (A) and after processing at pH 5, 7, and 9 (B). Photograph of dye with concentration 300 mg.$L^{-1}$ at 30°C before (C) and after processing at pH 5, 7, and 9 (D). Photograph of dye with concentration 400 mg.$L^{-1}$ at 30°C before (E) and after processing at pH 5, 7 and 9 (F).

studied at various pH ranges (5, 7, and 9). Also, it was done at different day intervals of the 3rd, 5th, and 7th day with increasing concentrations of 200, 300, and 400 mg.L$^{-1}$ by maintaining the temperature at 45°C. In experimental conditions at 45°C, pH 5 for 200 mg.L$^{-1}$ concentration, the dye degradation efficiency of *Paecilomyces variotii* was recorded at 55%, 60%, and 82% during the 3rd, 5th, and 7th days of incubation respectively. For the condition availed at 45°C and pH 7 for 200 mg.L$^{-1}$ concentration the efficiency of *Paecilomyces variotii* in dye degradation was found to be 38%, 52% and 71% during the 3rd, 5th and 7th days of incubation respectively. With the conditions at 45°C and pH 9 for 200 mg.L$^{-1}$ concentration, the dye decolorization effect was found to be 20%, 38%, and 55% during the 3rd, 5th and 7th days of incubation respectively (Fig. 8). The results from above experimental conditions revealed that when the fungi allowed to grow in increased temperature, the enzymes become active at acidic pH (9). Here at pH 5, the *Paecilomyces variotii* showed maximum efficiency with 82% dye decolorization property. Fig. 9 shows the vivid difference of color change by the action of *P. variotii* grown at different concentrations, time, and pH by keeping the temperature constant at 45°C. There is a significant decline rate in decolorization efficiency at 7°C. This finding correlates with the other research studies where it is found that low temperatures could significantly inhibit dye decolorization. Comparatively, in this study, *P. variotii* still showed a potential decolorizing capability at higher temperatures like 30°C and 45°C, suggesting its valuable potential in the bioremediation of azo dyes.

Presently scientists have turned towards bioremediation using fungal communities due to their applicability of high biomass rather than employing bacterial species (Rani et al. 2014). Researchers have proposed that the filamentous nature of fungi aids in greater uptake and conversion of pollutants to other metabolites with lesser or no environmental impact. Recent research studies already proved the effectiveness of various fungal species in the biodegradation of volatile organic compounds. Also when compared to bacterial species, fungi can be handled effectively in extreme conditions due to their resistive nature (Kennes & Veiga 2001, 2004). The fungi, *P. variotii has* already been studied for their competence in the biodegradation of hydrocarbons in soils polluted with petroleum products (Nrior & Jirigwa 2017). The result from the above study also conveys that *P. variotii* will be a good candidate for bio removal of reactive dyes in a moderate temperature range (30-35°C) and at moderate pH of 7. So the bio removal of dye could be made possible

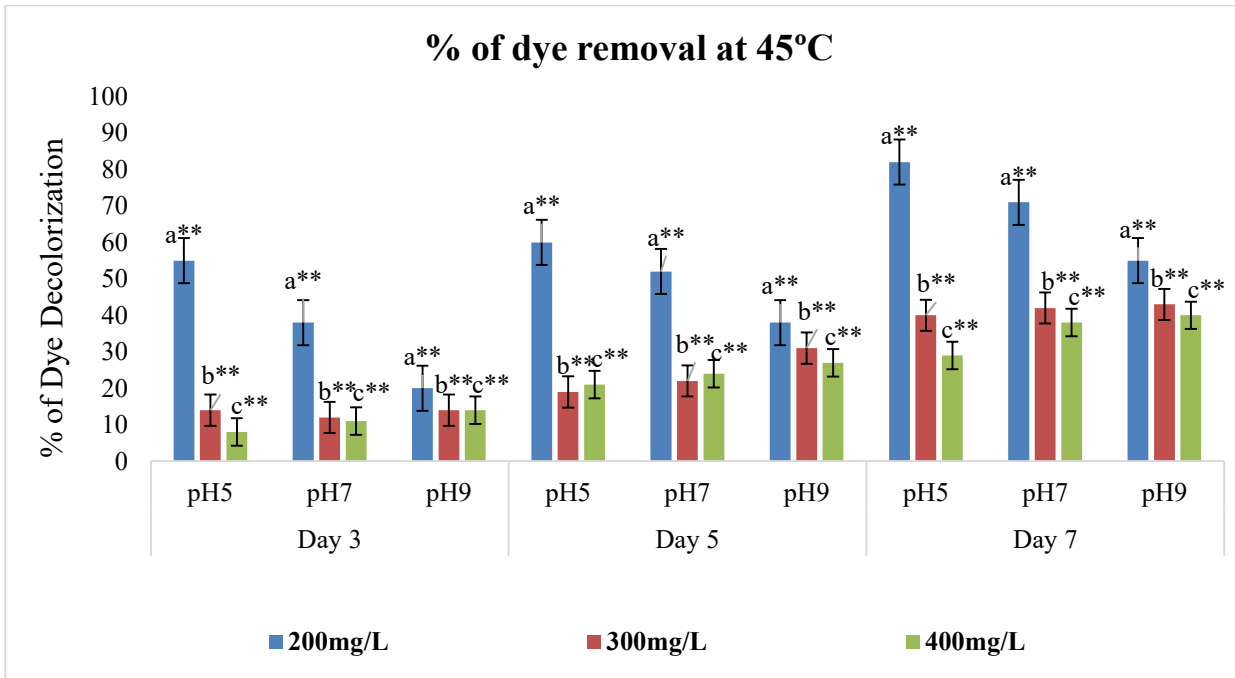


Fig. 8: Values are expressed in mean±SD (n=3), statistically significant test for comparison was done by ANOVA followed by Dunnet's 't-test. Comparison of dye decolorization % between a - Control vs dye concentration at 200 mg.L$^{-1}$ in different pH ranges and time intervals, b - Control vs dye concentration at 300 mg.L$^{-1}$ in different pH ranges and time intervals, c - Control vs dye concentration at 400 mg.L$^{-1}$ in different pH range and time intervals, *p < 0.05, **p < 0.01 and ns – Non-Significant.


Fig. 9: Photograph of dye with concentration 200 mg.L$^{-1}$ at 45°C before (A) and after processing at pH 5, 7 and 9 (B). Photograph of dye with concentration 300 mg.L$^{-1}$ at 45°C before (C) and after processing at pH 5, 7 and 9 (D). Photograph of dye with concentration 400 mg.L$^{-1}$ at 45°C before (E) and after processing at pH 5, 7 and 9 (F).

even at normal temperatures for the effect result. Even when it is grown at a slightly high temperature of 45°C, the fungi works well at acidic pH of 5 with an 82 % decolorization effect. When it is studied at a very low temperature of 7°C, it is showing 75% effectiveness in reducing the dye color to an alkaline pH of 9. It was studied that decolorization and biosorption of dyes take place by forming complexes, making precipitation, and finally reserving them in the interior walls of mycelia. The higher dye absorption capability of fungi relates to their augmented cell-to-surface ratio while in contact with pollutants in the environment (Yeddou-Mezenner 2010, Fu & Viraraghavan 2002). When planned accordingly *P. variotii* not only severs to reduce the color even it will also act as a good choice for bioaugmentation of dye by removing the contaminant from the polluted site.

## CONCLUSION

In this research work, the efficacy of *P. variotii* in dye decolorization was studied at various parameters like pH (5,7 and 9), Temperature (7°C, 30°C, and 45°C), Dye concentration (200, 300, and 400 mg.L$^{-1}$) and Time (3, 5 and 7 days). Fruitful results were attained with a maximum percentage of dye decolorization at 30°C, pH 7, and when the fungi is grown for 7 days. This productive nature of fungi in the case of bioremediation of dyes could efficiently be increased by altering their metabolism when grown in different carbon sources. Since Extracellular Fungal enzymes play a critical role in dye decolorization, the enzyme secretion could be highly influenced by growing them in different carbon sources to achieve, a higher percentage of dye decolorization. The usage of living sources or biological products creates very less impact on the environment in the case of bioremediation processes. The cost-effective and environmentally friendly attributes of the above kind create a best-preferred approach for bioremediation. Furtherly, the competent fungal strains can be genetically improved and more than one fungal strain can be co-cultured for aiming effective results in dye biodegradation in adverse environmental conditions.

## REFERENCES

Aravindhan, R., Rao, J.R. and Nair, B.U. 2007. Removal of basic yellow dye from aqueous solution by sorption on green alga *Caulerpa scalpelliformis*. J. Hazard. Mater., 142(1): 68-76.

Babu, S.S., Mohandass, C., Vijayaraj, A. and Dhale, M.A. 2015. Detoxification and color removal of Congo red by a novel *Dietzia* sp. (DTS26): A microcosm approach. Ecotoxicol. Environ. Saf.,114: 52-60.

Chandanshive, V., Kadam, S., Rane, N., Jeon, B.H., Jadhav, J. and Govindwar, S. 2020. In situ textile wastewater treatment in high-rate transpiration system furrows planted with aquatic macrophytes and floating phytobeds. Chemosphere, 252: 126513.

Chen, K.C., Wu, J.Y., Huang, C.C., Liang, Y.M. and Hwang, S.C.J. 2003. Decolorization of azo dye using PVA-immobilized microorganisms. J. Biotechnol.,101: 241-252.

Chong, M.N., Cho, Y.J., Poh, P.E. and Jin, B. 2015. Evaluation of Titanium dioxide photocatalytic technology for the treatment of reactive Black 5 dye in synthetic and real greywater effluents. J. Clean. Prod., 89: 196-202.

El-Gendi, H., Saleh, A.K., Badierah, R., Redwan, E.M., El-Maradny, Y.A. and El-Fakharany, E.M. 2021. A comprehensive insight into fungal enzymes: structure, classification, and their role in mankind's challenges. J. Fungi, 8(1): 23.

Ellis, M.B. 1971. Dematiaceous Hyphomycetes. 1st Edn., Commonwealth Mycological Institute, Kew, Surrey, UK, p. 608.

Fu, Y. and Viraraghavan, T. 2002. Removal of Congo red from an aqueous solution by fungus *Aspergillus niger*. Adv. Environ. Res., 7: 239-247.

Gilman, J.C. 1971. A Manual of Soil Fungi. Second Edition. Iowa State College Press, Ames, Iowa, p. 450.

Vijayaraghavan, J., Sardhar, B. and Josephraj, J. 2013. A review of efficacious methods to decolorize reactive azo dye. J. Urban Environ. Eng., 7(1): 30-47.

John, J., Ramadoss, D., Kaveripakam, R., Hemalatha, M., Peter, D., Dharani, G. and Kumar, A. 2020. Bio-decolorization of synthetic dyes by a halophilic bacterium*Salinivibrio sp*. Front. Microbiol., 21: 616-626.

Kennes, C. and Veiga, M.C. 2001. Bioreactors for Waste Gas Treatment. Kluwer, Dordrecht

Kennes, C. and Veiga, M.C. 2004. Fungal biocatalysts in the biofiltration of VOC-polluted air. J. Biotechnol., 113: 305-319

Khatid, A., Arshad, M. and Crowley, D.E. 2008. Accelerated decolonization of structurally different azo dyes by newly isolated bacterial strains. Appl. Microbiol., 78: 361-369.

Martínez-Huitle, C.A. and Brillas, E. 2015. Decontamination of wastewaters containing synthetic organic dyes by electrochemical methods: A updated review. Appl. Catal. B Environ., 166-167, 603-643.

Nabil, G.M., El-Mallah, N.M. and Mahmoud, M.E. 2014. Enhanced decolorization of reactive black 5 dye by active carbon sorbent-immobilized-cationic surfactant (AC-CS). J. Ind. Eng. Chem., 20: 994-1002.

Nigam, P., Banat, I .M., Singh, D. and Marchant, R. 1996. Microbial process for the decolonization of textile effluent containing azo, diazo, and reactive dyes. Process Biochem., 31: 435-442.

Nrior, R.R. and Jirigwa, C.C. 2017. Comparative bioremediation potential of *Mucor racemosus* and *Paecilomyces variotii* on crude oil spill site in Gio Tai, Ogoni land. J. Environ. Sci. Toxicol. Food Technol., 61: 2319-402.

Puentes-Cárdenas, J., Florido-Cuellar, A., Cardona-Bedoya, J., Bohorquez-Echeverry, P., Campos-Pinilla, C. and Guitiérrez-Romero, V. 2012. Simultaneous decolorization and detoxification of black reactive 5 using $TiO^2$ deposited over borosilicate glass. Univ. Sci., 17: 53-63.

Radha, K., Regupati, I., Arunagiri, A. and Murugesan, T. 2005. Decolourization studies of synthetic dyes using *Phanerochaete chrysosporium* and their kinetics. Process Biochem., 40: 3337-3345.

Rani, B., Kumar, V., Singh, J., Bisht, S., Teotia, P., Sharma, S. and Kela, R. 2014. Bioremediation of dyes by fungi isolated from contaminated dye effluent sites for bio-usability. Braz. J. Microbiol., 45(3): 1055-1063.

Rania, A., Sameh S., Ali., F., Kamal, M., Okasha, Y., Mahmoud, A.G., Tamer, E., Haixin, J., Yinyi, F. and Jianzhong, S. 2022. A critical review on the treatment of dye-containing wastewater: Ecotoxicological and health concerns of textile dyes and possible remediation approaches for environmental safety. Ecotoxicol. Environ. Saf., 231: 113-120

Rocha, O.P., Cesila, C.A., Christovam, E.M., Barros, S.B., Zanoni, M.V.B. and de Oliveira, D.P. 2017. Ecotoxicological risk assessment of the "Acid Black 210" dye. Toxicology, 376: 113-119.

Slama, H.B., Chenari Bouket, A., Pourhassan, Z., Alenezi, F.N., Silini, A., Cherif-Silini, H., Oszako, T., Luptakova, L., Golinska, P. and Belbahri, L. 2021. Diversity of synthetic dyes from textile industries, discharge impacts, and treatment methods. Appl. Sci., 11: 6255.

Subramanian, C.V., 1971. Hyphomycetes An Account of Indian Species Except for Cercosporae. ICAR, New Delhi, pp. 1-930.

Udaya Prakash, N.K., 2004. Indoor molds: Isolation and identification. Col. Wings, 11: 99.

Vijayaraghavan, K. and Yun, Y.S. 2008. Biosorption of C.I. Reactive Black 5 from aqueous solution using acid–treated biomass of brown seaweed *Laminaria* sp. Dyes and Pigm., 76(7): 726-732.

Wang, X., Deng, B., Yu, L., Cui, E., Xiang, Z. and Lu, W. 2020. Degradation of azo dyes Congo red by MnBi alloy powders: Performance, kinetics, and mechanism. Mater. Chem. Phys., 251: 123096

Weisburger, J.H. 2002. Comments on the history and importance of aromatic and heterocyclic amines in public health. Mutat. Res., 506/507: 9-20.

Yeddou-Mezenner, N. 2010. Kinetics and mechanism of dye biosorption onto an untreated antibiotic waste. Desalination, 262: 251-259.

Nature Environment and Pollution Technology
An International Quarterly Scientific Journal

p-ISSN: 0972-6268
(Print copies up to 2016)
e-ISSN: 2395-3454

Vol. 22 | No. 1 | pp. 189-197 | 2023

Original Research Paper

https://doi.org/10.46488/NEPT.2023.v22i01.017

Open Access Journal

# Economic Valuation and Benefit Transfer of Restoring the Teesta Riverine Ecosystem

**Pravesh Tamang**
Department of Economics, Presidency University, 86/1, College Street, Kolkata 700073, West Bengal, India
†Corresponding author: Pravesh Tamang; pravesh.econ@presiuniv.ac.in

**Nat. Env. & Poll. Tech.**
**Website: www.neptjournal.com**

*Received:* 25-05-2022
*Revised:* 27-06-2022
*Accepted:* 30-06-2022

**Key Words:**
Economic valuation
Teesta river
Contingent valuation
Benefit transfer

## ABSTRACT

This study seeks to understand the socio-economic and ecological impacts of the hydroelectric power projectsalong the upper basin of the river Teesta in Sikkim. This study estimates the non-market benefits of restoring the Teesta riverine ecosystem and evaluates the transferability of welfare estimates. This study is a first of its kind undertaken in the Teesta basin which uses a unique dataset of 830 households obtained from the affected regions of the river basin. During the study, nine villages adjacent to the river Teesta, dams, and powerhouses were identified and surveyed. Double bounded dichotomous choice questions were used to elicit willingness to pay (WTP). Both the logistic and normal distribution models were fitted and the results were mostly similar. The median WTP was INR 373.00 and the variables that described the rating on dams, ownership of property, monthly expenditure of the household, informal employment status, and satisfaction about the state of the river Teesta were among the significant variables in the model. The benefit function value transfer estimated was INR 232.00 with the percentage transfer error (PTE) of 61.9%.

## INTRODUCTION

The rivers of the Earth not only play an important role in shaping the physical landscape of the planet but also have an impact on the well-being of billions of people living around the world. Rivers provide ecosystem goods like fish, drinking water, wildlife, etc., and services such as boating and swimming. Free-flowing rivers add to the aesthetic values and recreation, leading to an increase in property values for those living near them (Lewis et al. 2008). In addition, free-flowing rivers also help dilute wastewater discharges helping maintain water quality. Rivers also provide habitat for endangered and threatened species (Richardson & Loomis 2009, Mathieus et al. 2010).

However, the ability of the rivers to provide such ecosystem goods and services is reduced when anthropogenic activities are performed beyond a sustainable threshold level. For instance, river-damming creates a threat to many native species of fish due to the reduction in the fish passage. Extensive anthropogenic interventions have resulted in the loss of biodiversity in recent decades in India. In particular, development works such as the construction of roads, dams, and urban spaces have been carried out in the Himalayan region of India, which has created a negative impact on the Himalayan biodiversity (Gaur 1999, Kanwal & Joshi 2010).

The river Teesta is a major river in the Himalayan region that originates from the glaciers of Sikkim in the north at an elevation of 8,250 m. The entire state of Sikkim covers the upper basin of the river Teesta. The Teesta River joins the river Rangeet at Teesta Bazar (in West Bengal) and then flows through the Darjeeling district in West Bengal before joining the river Brahmaputra in Bangladesh. The Sikkim Himalaya, with its rugged topography, ongoing seismic activity, and heavy rainfall, is subjected to intense landslide activities.

India has an estimated total hydroelectric power potential of 84 GW. Of this, Sikkim's potential share is 2.9% or about 4.29 GW. The Central Electricity Authority of India prepared a preliminary feasibility report in 2004 on the establishment of 162 new hydroelectric schemes with a total potential of over 50,000 MW. In this scheme, Sikkim has ten projects with an installed capacity of 1,469 MW (CEA 2015). The total hydroelectricity potential in Sikkim stands at 5,325 MW spread across different stages of implementation (EDPS 2020). Currently, 15 projects are under different stages of construction, and according to the Draft National Electricity Plan 2018, all the projects shall be completed by 2022.

However, in recent times, there has been a disappearance of springs/streams leading to a decrease in water shortages in different parts of Sikkim. Also, dams have blocked the natural river water and reduced downstream river levels.

The use of dynamites in road construction and underground tunneling by hydropower projects have caused cracks in aquifers resulting in water loss. Traffic congestion, accidents, and deaths are other issues faced by the local people living near the project sites. While cultural intrusion also forms a major issue levied by the local people upon migration, there also seems to be a change in the agricultural productivity in the project sites. Thus, there is an intense need to evaluate the restoration benefits of the Teesta Riverine Ecosystem for long-term sustainability and a wide range of flora and fauna protection. Such benefits could be accrued not only to wildlife but also could be utilized for achieving long-term inclusive growth.

Understanding public support for ecosystem restoration is critical to its successful implementation because the sustainability of sound resource management is rooted in stakeholders' support (Alam 2013). The contingent valuation method (CVM) is one of the important tools widely used in the restoration literature. Alam (2013) used CVM to estimate the WTP for restoring the Buriganga river in Bangladesh. It was found that there existed a significant relationship between participants' willingness to participate in the ecosystem restoration and their socio-demographic characteristics and their perceptual characteristics. A variety of factors, including demographic and socioeconomic variables such as gender, age, race, number of people living in the household, level of education, size of the household, respondent's status within the household, individual and household income, and bid values, are likely to influence public preferences (Pate & Loomis 1997, Bandara & Tisdell 2004, Haile & Slangen 2009, Mohammed 2009, Nallathiga & Paravasthu 2010).

Other variables include residence proximity to the resources in question and frequency of uses/visits to the resources (del Saz Salazar & García Menéndez 2007, Weber & Stewart 2009), residence location (Zhongmin et al. 2003), awareness of the current state of the services (Weber & Stewart 2009), and membership in environmental organizations or NGOs (Haile & Slangen 2009). The attractiveness of the resource, degree of trust, environmental priorities, prior awareness of pollution/degradation, prospective danger, and existing level of protection are all proven to be influential determinants of WTP (Haile & Slangen 2009).

The Contingent Valuation method (CVM) is a major source of economic values for benefit transfer-based policy analysis (Johnston & Wainger 2015). According to Carson (2011), the CVM has been mostly used since 2007 and is hence the most cited method in the valuation literature. However, considering the amount of time and resources required in CVM surveys, the benefits transfer approach was developed so that the findings from one site (the study site) can be applied to another site (the policy site). Benefit transfer has been used in different policy contexts since the 1950s. Two influential CVM-benefit transfer studies done by (Luken et al. 1992) and (Desvousges et al. 1992) motivated the development of benefit transfer as a distinct field of research. Both the studies employed unit value transfer which is applying the WTP estimate obtained in the study site directly to the policy site. However, Loomis (1992) introduced the benefit function transfer in which an empirical model developed in a study site can be used to estimate the benefits at the policy site. Generally, the results from a benefit function transfer are better than the ones from a unit value transfer (Johnston & Rosenberger 2010). Boyle & Bergstrom (1992) were the first to propose the convergent validity test i.e. the percentage transfer error, which is very commonly used in contemporary research.

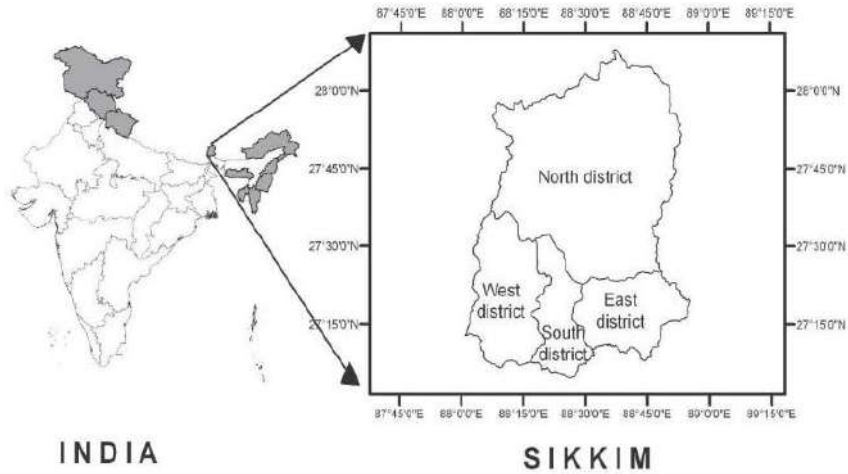


Fig. 1: Map of Sikkim.

Downing & Ozuna (1996) use the CVM-benefit transfer method to estimate the benefits of marine recreational fishing in Texas bay and find a few equal coefficients. Also, another study by Kirchhoff et al. (1997), find that the transfer of the benefit estimates obtained from Arizona and New Mexico studies resulted in the rejection of the convergent validity test in 55 to 90% of the benefit function transfer. Kaul et al. (2013) remark that benefits function transfer outperforms the unit value transfer and the CVM performs equally to other methods.

Over the last three decades, the use and challenges of benefit transfer have grown along with the concerns of validity and accuracy (Johnston & Wainger 2015). Newer developments in the fields of understanding, application, and limitations have come up while the objective of the benefit transfer has remained the same. The benefit transfer is used not only for WTP estimates but also for other welfare estimates, and newer methods and understanding of the factors that influence transfer accuracy have evolved.

This study is the first of its kind that looks into the restoration of ecosystem services and benefits transfer in the upper basin of the Teesta River. This study also uses a unique dataset of 830 households obtained from a primary survey in the affected areas of the river basin. This paper tries to (a) analyze the effects of hydropower projects in the upper basin of the Teesta River on various issues such as natural ecosystems, culture, livelihoods, and river water quality, (b) estimate the willingness to pay (WTP) for restoration of the riverine ecosystem and evaluate the transferability of welfare estimates.

## MATERIALS AND METHODS

### The Study Area

The survey was implemented in the different villages and small towns near the river Teesta, the Teesta Stage V dam, and the Teesta Stage V powerhouse. More specifically, the Teesta Stage V in Sirwani and the Dikchu dam in Dikchu were prominent destinations. More precisely the places of survey and the sample size are outlined in Table 1. The villages were chosen considering their proximity to the river Teesta as well as the dams so that the impact becomes prominent (Fig. 2).

### Questionnaire and Sampling

Purposive sampling was used to select the villages based on the geographic location and proximity to the river Teesta, the Teesta Stage V dam, and the Teesta Stage V powerhouse. After the villages were selected, sample households in each village were selected randomly. A pre-testing of the questionnaire was done in all the villages outlined in Table 1. In each village, 5 households were surveyed amounting to a total of 45 households for pre-testing the questionnaire. In the pre-test questionnaire an open-ended Willingness-to-Pay (WTP) question regarding the hypothetical river

Table 1: Survey villages with sample size.

| Village | Bardang | Dikchu | Majitar | Makha | Mamring | Manglay | Rangpo | Singtam | Sirwani |
|---|---|---|---|---|---|---|---|---|---|
| Sample | 82 | 198 | 92 | 48 | 72 | 122 | 42 | 132 | 42 |

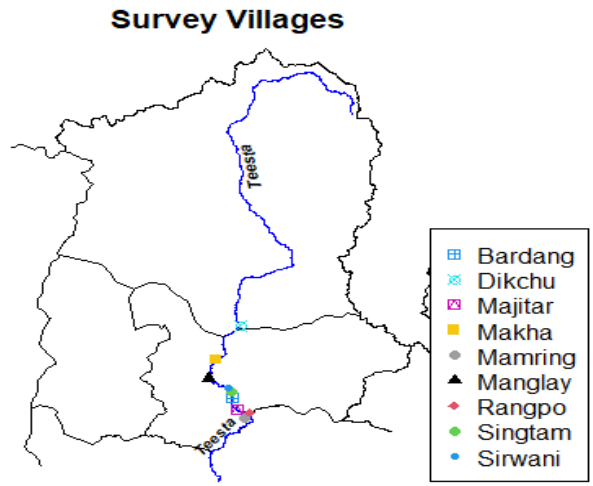


Fig. 2: Map showing the survey sites.

Table 2: Bid values for the main survey.

| Bids | Initial.bid | High.bid | Low.bid |
|---|---|---|---|
| Bid 1 | 100 | 200 | 50 |
| Bid 2 | 250 | 500 | 125 |
| Bid 3 | 500 | 1,000 | 250 |

restoration project was asked. A follow-up question was also asked to understand the specific reason for the contribution.

Similarly, for those who answered *No* to the open-ended WTP question, a similar follow-up question to understand the specific reason for not contributing was asked.

For the main survey, double-bounded dichotomous choice (DBDC) willingness-to-pay (WTP) questions were asked. The rationale behind using the DBDC format was the improvement in statistical efficiency that it provides in contingent valuation studies (Jeanty et al. 2007). In the DBDC format, the respondents were asked if they were willing to pay the initial bids, and the 'yes/no' answers were followed by the corresponding 'high/low' bids as specified in Table 2. All three bids (Bid 1, Bid 2, and Bid 3) were randomly presented to the households.

The questionnaire was carefully designed after considering the different aspects of the river Teesta including its ecological, economic, and other socio-cultural values. The questionnaire was conceptually focused on assessing information on the socio-economic profile of the households, water availability and consumption behavior, impact of the hydroelectric projects on the agricultural lands (if they own) and the livelihood of the people, perception of impact on water and wild habitat, environment, culture, and the river itself, identifying the ecosystem services or functions that could be associated with the river, and finally asking the willingness-to-pay questions on restoring the river Teesta. The question on WTP was a double-bounded dichotomous choice (DBDC) type. The bid values used in the main survey, detailed in Table 2, were obtained from the estimates of the pre-testing survey.

**Contingent Valuation**

A survey-based methodology that can be used for eliciting the values that people place on different kinds of goods and services is the Contingent Valuation (CV) method (Boyle 2003). In the CV method, there are different formats like the bidding games and open-ended questions. These two formats were widely used in the early years of CV. In the bidding game, the willingness-to-pay WTP is elicited by an auction, and in the open-ended format a direct question like "How much are you willing to pay?" is asked. During the 1980s, two other formats emerged - the Single Bound Dichotomous Choice (SBDC) and the double-bound dichotomous choice (DBDC) (Boyle & Bishop 2012). The main drawback of the open-ended format is that the respondent may not be familiar with the price of the good or service in question. So in the SBDC format a question like *"Will you be willing to pay Rs. X ?"* makes it easier for the respondent to answer the WTP question. The SBDC format is easier from the perspective of the respondent, but it is "statistically less efficient and requires the large sample to attain a given level of precision" (Hanemann et al. 1991). The double-bounded dichotomous choice (DBDC) format improves th e efficiency of the SBDC.

In the DBDC format, a question is asked after an SBDC format question like *"Will you be willing to pay Rs X?"*, and if the respondent answers Yes, then a follow-up question with double the bid value is asked like *"If yes, will you be willing-to-pay Rs 2X ?"*. Similarly, if the respondent answers No, then a follow-up question with half the bid value is asked as *"If No, will you be willing-to-pay Rs. 0.5X ?"*. This DBDC method is asymptotically more efficient than the SBDC method(Hanemann et al. 1991).

Following Hanemann et al. (1991) the parametric DBDC model can be summarised as follows. Let the first bid be $t_n$ and the second bid be $t_n^U$ if respondent n answers "yes" to the first question, and $t_n^L$ otherwise. Further, let respondent n's maximum WTP be denoted by $y_n^*$.

The probability that the respondent n answers "yes" to the first and the second questions is given by $P^{yy}(t_n, t_n^U) = \Pr(t_n \le y_n^*, t_n^U \le y_n^*) = \Pr(t_n^U \le y_n^*) = 1 - F(t_n^U)$

Similarly, the probability that respondent n answers "no" to the first and the second questions is equal to $P^{nn}(t_n, t_n^L) = \Pr(y_n^* \le t_n, y_n^* \le t_n^L) = \Pr(y_n^* \le t_n^L) = 1 - F(t_n^L)$

The probability that respondent n answers "yes" to the first question and "no" to the second question, or "no" to the first and "yes" to the second is given, respectively, by $P^{yn}(t_n, t_n^U) = \Pr(t_n \le y_n^*, y_n^* < t_n^U) = \Pr(t_n^U \le y_n^* < t_n^U) = F(t_n^U) - F(t_n)$

and, $P^{ny}(t_n, t_n^L) = \Pr(y_n^* \le t_n, y_n^* \ge t_n^L) = \Pr(t_n^L \le y_n^* < t_n) = F(t_n) - F(t_n^L)$

Therefore, for a given sample of N independent observations, the log-likelihood function can be written as;

$$\ln L = \sum_{N-1}^{N} [d_n^{yy} \ln\{P^{yy}(t_n, t_n^U\} + d_n^{nn} \ln\{P^{nn}(t_n, t_n^L)\} + d_n^{yn} \ln\{P^{yn}(t_n, t_n^U\} + d_n^{ny} \ln\{P^{ny}(t_n, t_n^L)\}]$$

where $d_n^{yy}$, $d_n^{nn}$, $d_n^{yn}$, and $d_n^{ny}$ are binary-valued indicator variables. For example, $d_n^{yy}$ is equal to 1 if the respondent answers "yes" to the first bid $t_n$ and second bid $t_n^U$, and 0 otherwise.

**Benefit Transfer**

Benefit transfer can be defined as using the research results from an existing primary study at one or more policy or study sites to predict welfare estimates (Rolfe et al. 2015). But certain criteria must be met to conduct a benefit transfer study estimate. According to Boyle & Bishop (2012), benefits transfer is valid only when source and target or policy sites, population, and welfare measures are identical. Bennett (2006) also points out that the biophysical conditions, the scale of environmental change, and the socio-economic characteristics of the population in the source site must be similar to those of the target or policy site.

The economic theory and methods of benefit transfer applied to most market and non-market goods are also the same as ecosystem services (Champ et al. 2017, Freeman et al. 2014). However, some sources of error can diminish the accuracy of the results in benefit transfer. Two types of errors can occur – the measurement error and the generalization error. Measurement errors are caused by the errors in primary or source studies which are used for transfer and get transferred to policy sites (Rosenberger & Stanley 2006). The second type of error which is the generalization error is caused by a lack of similarity between study and policy contexts.

Usually, two types of benefit transfers can be calculated – unit value transfers and benefits function value transfers. Unit value transfers include a single number or a set of numbers from pre-existing primary studies. The transferred quantities can include a single unadjusted value, a value adjusted according to the attributes of the policy context, a mean or a median value of the study site, or a range of estimates from prior studies (Johnston & Wainger 2015). Benefit function transfers are based on the benefit function derived from a primary study or a set of studies and used to calculate a welfare estimate, such as the WTP, calibrated to the characteristics of the policy site (Loomis 1992, Rosenberger & Stanley 2006). There are two requirements for a benefit function transfer. The first one is a parametric function and the second is a set of variables for the policy site.

Following Johnston & Wainger (2015), a single-site benefit function transfer can be illustrated as

$$\widehat{y_{js}} = g(x_{js}, \widehat{\beta_{js}})$$

where $j$ is the survey site, $s$ is the population at the survey site $j$, $\widehat{y_{js}}$, is a predicted welfare estimate, $x_{js}$ is a vector of variables, and $\widehat{\beta_{js}}$ is a vector of estimated parameters. A simple linear benefit function would be

$$\widehat{y_{js}} = \widehat{\beta_{js0}} + \sum_{k=1}^{K} \widehat{\beta_{jsk}}\, x_{jsk} + \widehat{\epsilon_{js}}$$

where $K$ is the number of non-intercept variables in the model and $\widehat{\epsilon_{js}}$ is the residual.

For a single-study benefit function transfer all the information would be gathered from a single primary study Johnston & Wainger (2015). Normally all the information for $x_{js}$ for policy sites are not available. For this we can split $x_{js}$ into $x_{js} = [x_{js}^1, x_{js}^2]$, where $x_{js}^1$, where are the variables for which policy site data are available, $x_{js}^2$ and are the variables for which policy site data are not available. If we are considering a benefit function transfer to a similar site $i$ with population $r$, then the parallel value for $x_{js}^1$ shall be $x_{ir}^1$ and the associated benefit transfer estimate shall be given by

$$\hat{y}_{ir}^{BT} = g([x_{ir}^1 x_{js}^2], \hat{\beta}_{js})$$

The parameterized function $g(.)$ is used to calculate the benefit transfer estimate by substituting the updated values of those variables for which policy site information is available $x_{ir}^1$. For variables with no updated policy site information, the original values from the study site are used $x_{js}^2$ (Johnston & Wainger 2015).

The reliability of empirical accuracy of a benefit transfer is measured by the magnitude of transfer error and is quantified with convergent validity tests. Convergent validity is a measure of benefit transfer accuracy in which transfer error is calculated based on the difference between a transferred value estimate and an alternative value estimate for the same site. For unit value (UV) transfers and benefits function value (BFV) transfers, the percentage transfer error (PTE) is

$$PTE_{UV} = ((WTP_s - WTP_p)/WTP_p) \times 100$$

where $WTP_S$ is the transfer value estimate of the study site and $WTP_P$ is the transfer value estimate of the policy site. The average value of percentage transfer error is 36% and the range lies between 20% to 125% (Barton 2002, Kaul et al. 2013). According to Kaul et al. (2013), the benefit function value transfer tends to outperform unit value transfer in the benefit transfer literature.

## RESULTS AND DISCUSSION

**Willingness to Pay**

Table 3 describes the different variables used in the DBDC model. The variable *r1* describes the response to the initial bid of the DBDC question on WTP. If the respondent answers

'yes', the value 1 is registered and a higher bid option is placed before the respondent. If the respondent answers 'no' then the value 0 is registered and a lower bid option is placed. The follow-up bid with a higher value and a lower value is captured by the variable *r2*. Again, in this case, too, a 'yes' answer gets a 1 and a 'no' gets 0. The median and standard deviation for *r1* and *r2* are 1, 0, and 0.43, 0.45 respectively.

The other variable coded *age* describes the age of the respondent in years. The median age of the respondents was 41 with a standard deviation of 41.87. The variable *religious* describes whether the households practice any religious activities near the river. This question was asked because people who practice Hinduism and some tribal religions perform many rituals related to the river. This came up when we talked with some of the local people, as in focus-group interviews, during our pre-testing of the questionnaire.

The most common rituals associated with the river include – funerals along the river bank, Chat puja, Sansari puja, and Makar Sankranti. The median number of members in a household (members) is 4, and the median rating of the respondents on whether hydroelectric projects are important is 3 which is a pretty high rating. Most of the households do not own any agricultural land near the river ownership. The median value of this variable *ownership* is 2 which indicates 'do not own any agricultural land near the river Teesta'.

The median monthly expenditure of the household *exp* is INR 8,000.00. Also, a significant number of respondents or family members were working in informal businesses, shops, food sellers in the market, working in a private company, as casual workers, or were unemployed indicated by the variable employ. The variable *satisfied* captures the idea that whether the respondent is satisfied with the current state and condition of the river Teesta. A majority of respondents (median value of satisfied = 2 meaning 'not satisfied') in the sample are not satisfied with the condition of the river. Finally, the variables *bd1* and *bd2* are the initial and the follow-up bid values for the double-bounded dichotomous choice questions.

We can see from the logistic distribution regression output in Table 4 that the variable rating is significant and negatively related to WTP. The implication is that if the importance of hydroelectric projects (HEP) is rated high by the households then the WTP for restoration would decline. This would mean that the households who rate the HEPs high are attaching more value to employment and other economic benefits rather than the restoration benefits of the river Teesta.

The other significant variable is the *ownership*. The implication is that if a household owns any agricultural land near the river then the household shall be willing to pay for the restoration of the river. The reason for such a decision would be the *flood prevention benefit* that the household sees from river restoration. Even the households who have rented the land for irrigation, the variable *ownershipRented*, are willing to pay for river restoration because of the same *flood prevention benefit* that these households would get and thus not lose the land which is a major source of their income.

The variable *log.exp* which is the log of the expenditure is also significant and positive implying that households with higher monthly expenditures are willing to pay for the restoration of the river. The other variable that has turned out to be significant is the *employ.other* variable. This variable describes the category of employment among the household members who are in informal business, works in a shop, sells food in the market, works in a private compa-

Table 3: Description of variables used in the model (N = 830).

| Variables | Description | Median | sd |
|---|---|---|---|
| r1 | response to initial bid (1 = Yes, 0 = No) | 1 | 0.43 |
| r2 | response to follow-up bid (1 = Yes, 0 = No) | 0 | 0.45 |
| age | age of the respondent (in years) | 41 | 41.87 |
| religious | whether the household practices any religious activities in the river Teesta | 2 | 0.35 |
| members | number of members in the household | 4 | 2.03 |
| rating | how important are the HEPs to the area and the river Teesta? (rating on the scale of 0 to 5. 0 = HEPs are not important at all, 5 = HEPs are a must. | 3 | 1.32 |
| ownership | whether the household owns any agricultural land near the river? | 2 | 0.65 |
| exp | monthly expenditure of the household (Rs/month) | 8000 | 9,670.93 |
| employ | employment status of the head (government employee, farmer, others | 3 | 0.55 |
| satisfied | Whether satisfied with the state and conditions of the river Teesta? | 2 | 0.42 |
| bd1 | initial bid value | 250 | 161.07 |
| bd2 | follow-up bid value | 500 | 335.23 |

Table 4: DBDC Logistic distribution output.

| | Estimate | Std. Error | z value | Pr(>\|z\|) | |
|---|---|---|---|---|---|
| (Intercept) | 0.769527 | 1.071887 | 0.7179 | 0.472808 | |
| log.age. | 0.032537 | 0.15272 | 0.213 | 0.83129 | |
| religiousYes | -0.21059 | 0.186607 | -1.1285 | 0.259109 | |
| log.members. | 0.013905 | 0.164878 | 0.0843 | 0.932788 | |
| Rating | -0.15153 | 0.050635 | -2.9925 | 0.002767 | ** |
| ownershipOwned | 0.418503 | 0.207769 | 2.0143 | 0.043981 | * |
| ownershipRented | 0.485399 | 0.218181 | 2.2248 | 0.026098 | * |
| log.exp. | 0.147915 | 0.084772 | 1.7448 | 0.081012 | . |
| employGovt..employee | -0.12047 | 0.368587 | -0.3268 | 0.743795 | |
| employOther | -0.57704 | 0.266647 | -2.1641 | 0.030459 | * |
| satisfiedNot.satisfied | 0.300565 | 0.152049 | 1.9768 | 0.048068 | * |
| BID | -0.00484 | 0.000181 | -26.6946 | < 2.2e-16 | *** |

Signif. Codes: 0 '***' 0.001 '**' 0.01 '*' 0.05 '.' 0.1 ' ' 1
Distribution: logistic
Number of Obs.: 830
Log-likelihood: -1226.101465
LR statistic: 74.291 on 1e+01 DF, p-value: 0.000
AIC: 2476.202931 , BIC: 2532.522815

Table 5: 95% Confidence interval of the DBDC logistic model.

| | Estimate | LB | UB |
|---|---|---|---|
| Mean | 405.32 | 382.12 | 428.91 |
| truncated Mean | 395.45 | 373.75 | 417.13 |
| adjusted truncated Mean | 414.73 | 389.17 | 441.16 |
| Median | 373.67 | 346.57 | 399.46 |

ny, is a casual worker, or is unemployed. This category is negatively related to WTP for river restoration compared to the other categories (farmers and government employees). Since this category does not have any direct economic dependence on the river as opposed to the farmers (possibly those having landed near the river), it could be a reason for the negative and significant relation seen in the regression result.

Also, the variable *satisfied* describes whether the respondent was satisfied with the present state and condition of the river Teesta. The regression result shows that the variable is significant and positively related to the WTP. This means that the respondents who were not satisfied with the current state and condition of the river Teesta are willing to pay for the restoration of the river.

Next, we look at the median WTP estimates in Table 5 using the Krinsky-Robb (Krinsky & Robb 1986) procedure. The median WTP is INR 373.27. The 95% confidence interval for the median WTP estimate is INR 346.41 to INR 373.267. In Fig. 3, the median WTP estimate has

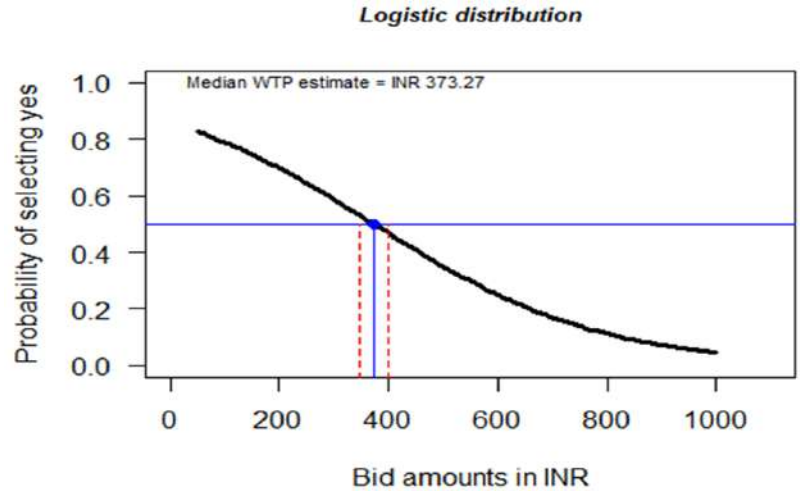


Fig. 3: DBDC logistic distribution.

Table 6: Benefit transfer estimate.

| Variables | Coefficient | Mean | Product |
|---|---|---|---|
| Const | 0.76952676 | 1.0000000 | 0.76952676 |
| Age | 0.03253655 | 44.8843373 | 1.46038149 |
| religious | -0.21058544 | 0.8530120 | -0.17963192 |
| members | 0.01390538 | 4.7365854 | 0.06586404 |
| Rating | -0.15152592 | 2.4793187 | -0.37568105 |
| ownership | 0.41850305 | 2.2092457 | 0.92457609 |
| ownership | 0.48539882 | 2.2092457 | 1.07236528 |
| exp (INR/1000) | 0.14791446 | 11.0648458 | 1.63665070 |
| satisfied | 0.30056500 | 0.2481928 | 0.07459806 |
| D | | | 5.44864945 |

been plotted along with the 95% confidence interval obtained using the Krinsky-Robb (Krinsky & Robb 1986) procedure.

### The Benefit Transfer Estimate

Following Johnston & Wainger (2015) key variables were selected from the regression model, and their coefficients and their corresponding mean values have been calculated as in Table 6. The product of the coefficient values and their means are calculated.

The sum of these products is labeled as *D* whose value is 5.4486494 as shown in Table 6. This value represents the predicted natural log of WTP for the restoration of the river Teesta. In the final step, a standard formula is used to transform this predicted natural log to the desired WTP estimate (Johnston & Wainger 2015).

$$WTP = e^{D}$$

where *e* is the exponential operator and *D* is the sum of the products of the means and coefficients. Using this formula the value of *WTP* is INR 232.44 which represents per household willingness to pay for the restoration of the river Teesta. This estimate can be transferred to approximate ecosystem service value for the illustrated policy change, in the absence of the original study results.

The percentage transfer error (PTE) is calculated using the formula (Brouwer et al. 2016):

$$PTE = [(WTP_{source} - WTP_{policy})/WTP_{policy}] \times 100$$

The weighted mean transfer error of the CVM studies in Kaul et al. (2013) is 36% with a range of 20% (Barton 2002) to 125%. In this study, the percentage transfer error is 61.98%. This value is the benefit function value transfer which is regarded better in the benefit transfer literature (Barton 2002).

## CONCLUSION

This study seeks to understand the socio-economic and ecological impacts of the hydroelectric power projects along the upper basin of the river Teesta in Sikkim. Double-bounded dichotomous choice questions were used to elicit willingness to pay (WTP) for the restoration of the Teesta riverine ecosystem. The median WTP was INR 373.00 and the variables that described the rating on dams, ownership of property, monthly expenditure of the household, informal employment status, and satisfaction about the state of the river Teesta were among the significant variables in the model. One important issue that can be understood is that people having property or fam lands near the river have been more affected by the dams and they are more interested in the river restoration project as compared to those who derive livelihood in the dam sites as informal or private employees (the variables *ownership* and *employ*). Those who have expressed their dissatisfaction over the state of the river seem to be more interested in the restoration project and are willing to pay.

The benefit function value transfer estimated is INR 232.44 which represents per household willingness to pay for the restoration of the river Teesta. This estimate can be transferred to approximate ecosystem service value for the illustrated policy change, in the absence of the original study results.

## ACKNOWLEDGMENT

The study was funded by Impactful Policy Research in Social Science – Indian Council for Social Science Research (IMPRESS-ICSSR), Government of India.

## REFERENCES

Alam, K. 2013. Factors affecting public participation in river ecosystem restoration: Using the contingent valuation method. J. Develop. Areas, 47(1): 71-89.

Bandara, R. and Tisdell, C. 2004. The net benefit of saving the Asian elephant: A policy and contingent valuation study. Ecol. Econ., 48(1): 56-63.

Barton, D.N. 2002. The transferability of benefit transfer: Contingent valuation of water quality improvements in Costa Rica. Ecol. Econ., 42(1-2): 111-121.

Bennett, J. 2006. Choice Modelling and the Transfer of Environmental Values. Edward Elgar, Cheltenham, UK, pp. 1-9.

Boyle, K.J. 2003. Contingent Valuation in Practice. In P. Champ, K. Boyle, and T. Brown (eds), A Primer on Nonmarket Valuation, Springer, Cham, pp. 111-169.

Boyle, K.J. and Bergstrom, J.C. 1992. Benefit transfer studies: Myths, pragmatism, and idealism. Water Resour. Res., 28(3): 61.

Boyle, K.J. and Bishop, R.C., 1988. Welfare measurements using contingent valuation: A comparison of techniques. American Journal of Agricultural Economics, 70(1): 20-28.

Carson, R. 2011. Contingent Valuation: A Comprehensive Bibliography and History. Edward Elgar, Northampton, M. A.

CEA. 2015. Status of 50,000 MW Hydro Electric Initiative. https://cea.nic.in/wp-content/uploads/hpi/2021/01/Status%20of%2050000.pdf

Champ, P.A., Boyle, K.J. and Brown, T.C. 2017. The Economics of Non-Market Goods and Resources: A Primer on Nonmarket Valuation. Second Edition. Springer, Cham.

del Saz Salazar, S. and García Menéndez, L. 2007. Estimating the non-market benefits of an urban park: Does proximity matter? Land Use Policy, 24(1): 631.

Desvousges, W.H., Naughton, M.C. and Parsons, G.R. 1992. Benefit transfer: Conceptual problems in estimating water quality benefits using existing studies. Water Resour. Res., 28(3): 675-683.

Downing, M. and Ozuna, T. 1996. Testing the reliability of the benefit function transfer approach. J. Environ. Econ. Manag., 30(3): 71-89

EDPS. 2020. Status of Ongoing and/or Completed Schemes. Energy and Power Department Sikkim. Available at: https://power.sikkim.gov.in/status-of-ongoing-andor-completed-schemes (Accessed December 26, 2020).

Freeman, A.M., Herriges, J.A. and Kling, C.L. 2014. The Measurement of Environmental and Resource Values. Third edition. RFF Press, Routledge, New York.

Gaur, R. 1999. Flora of the District Garhwal, Northwest Himalaya (with Ethnobotanical Notes). Transmedia, Srinagar, UP.

Haile, D.T. and Slangen, L. 2009. Estimating the willingness to pay for the benefit of AES using the contingent valuation method. J. Nat. Resour. Policy Res., 1(2): 545.

Hanemann, W.M., Loomis, J. and Kanninen, B.J. 1991. Statistical efficiency of double bounded dichotomous choice contingent valuation. Am. J. Agric. Econ., 73: 1255-1263.

Jeanty, P., Habb, T. and Hitzhusen, F. 2007. Willingness to Pay for biodiesel in Diesel Engines: A Stochastic Double Bounded Contingent Valuation Survey. Research in Agricultural and Applied Economics, Ohio, pp. 1-37

Johnston, R.J. and Rosenberger, R.S. 2010. Methods, trends, and controversies in contemporary benefit transfer. J. Econ. Surveys, 24(3): 69.

Johnston, R.J. and Wainger, L.A. 2015. Benefit transfer for ecosystem service valuation: An introduction to theory and methods. In: R. J. Johnston, J. Rolfe, R. S. Rosenberger and R. Brouwer (eds) Benefit Transfer of Environmental and Resource Values. pp. 273-237, Springer, Dordrecht.

Kanwal, K. and Joshi, H. 2010. Floral diversity assessment in four forest types of Garhwal Himalaya, Uttarakhand. Vegetos Int. J. Plant Res., 23(2): 76-85.

Kaul, S., Boyle, K.J., Kuminoff, N. V., Parmeter, C.F. and Pope, J.C. 2013. What can we learn from benefit transfer errors? Evidence from 20 years of research on convergent validity. J. Environ. Econ. Manag., 66(1): 41-50

Kirchhoff, S., Colby, B.G. and LaFrance, J.T. 1997. Evaluating the performance of benefit transfer: An empirical inquiry. J. Environ. Econ. Manag., 33(1): 141.

Krinsky, I. and Robb, A. 1986. On approximating the statistical properties of elasticities. The Rev. Econ. Stat., 68: 715-719.

Lewis, L.Y., Bohlen, C. and Wilson, S. 2008. Dams, dam removal, and river restoration: A hedonic property value analysis. Contemp. Econ. Policy, 26(2): 175-186.

Loomis, J.B. 1992. The evolution of a more rigorous approach to benefit transfer: Benefit function transfer. Water Resources Research, 28(3): 701-705.

Luken, R.A., Johnson, F.R. and Kibler, V. 1992. Benefits and costs of pulp and paper effluent controls under the clean water act. Water Resour. Res., 28(3): 89.

Mathieus, G., Suplee, M. and Blend, J. 2010. Final Report to the Environmental Quality Council on Progress Toward Numeric Nutrient Standards for Montana's Surface Water. https://leg.mt.gov/content/Committees/Interim/2009_2010/Environmental_Quality_Council/Meeting_Documents/July/deq-nutrient-report-2010.pdf

Mohammed, E.Y. 2009. Measuring the benefits of river quality improvement using the contingent valuation method: The case of the ping river, Chiang Mai, Thailand. J. Environ. Assess. Policy Manag., 11(3): 64-77.

Nallathiga, R. and Paravasthu, R. 2010. Economic value of conserving river water quality: Results from a contingent valuation survey in Yamuna river basin, India. Water Policy, 12(2): 54.

Pate, J. and Loomis, J. 1997. The effect of distance on willingness to pay values: A case study of wetlands and salmon in California. Ecol. Econ., 20(3): 14-28.

Richardson, L. and Loomis, J. 2009. The total economic value of threatened, endangered and rare species: An updated meta-analysis. Ecol. Econ., 68(5): 1535-1548.

Rolfe, J., Johnston, R.J., Rosenberger, R.S. and Brouwer, R. 2015. Introduction: Benefit Transfer of Environmental and Resource Values. Springer, Cham.

Rosenberger, R.S. and Stanley, T.D. 2006. Measurement, generalization, and publication: Sources of error in benefit transfers and their management. Ecol. Econ., 60(2): 541-552.

Weber, M.A. and Stewart, S. 2009. Public values for river restoration options on the Middle Rio Grande. Restor. Ecol., 17(6): 762-771.

Zhongmin, X., Guodong, C., Zhiqiang, Z., Zhiyong, S. and Loomis, J. 2003. Applying contingent valuation in China to measure the total economic value of restoring ecosystem services in Ejina region. Ecol. Econ., 44(2-3): 345-358.

Nature Environment and Pollution Technology
An International Quarterly Scientific Journal

p-ISSN: 0972-6268
(Print copies up to 2016)
e-ISSN: 2395-3454

Vol. 22 | No. 1 | pp. 199-210 | 2023

Original Research Paper

https://doi.org/10.46488/NEPT.2023.v22i01.018

Open Access Journal

# Assessment and Prediction of Air Quality Level Using ARIMA Model: A Case Study of Surat City, Gujarat State, India

**H. N. Mahendra*†, S. Mallikarjunaswamy*, D. Mahesh Kumar*, Shilpi Kumari*, Shubhali Kashyap*, Sapna Fulwani* and Aishee Chatterjee***

*Department of Electronics and Communication Engineering, JSS Academy of Technical Education, Bengaluru-560060, Karnataka, India

†Corresponding author: H. N. Mahendra; mahendrahn@jssateb.ac.in

**Nat. Env. & Poll. Tech.**
**Website: www.neptjournal.com**

*Received:* 26-07-2022
*Revised:* 06-10-2022
*Accepted:* 17-10-2022

**Key Words:**
Air quality
ARIMA model
Monitoring of air
Prediction system

## ABSTRACT

Air quality has recently been a huge concern as it directly affects people's lives. An air quality level assessment and prediction system is essential to keep track of air quality. Therefore, developing an efficient air quality assessment and prediction system has become one of the most important concerns. In the present work air quality level of Surat city, India is assessed and predicted for the period from 2020 to 2023 using the Autoregressive integrated moving average (ARIMA) model. Experimental results show that the ARIMA model outperforms the other models. According to the findings, the maximum quantity of $SO_2$ and $NO_2$ present in the air in 2020 is 37 mm and 18 mm, respectively, with a maximum of 27 mm and 31 mm in 2021. Thus, we can observe that even though $SO_2$ has reduced a bit, the amount of $NO_2$ has increased, thus degrading the quality of air.

## INTRODUCTION

Today, many industrial and daily activities have produced significant air pollution, particularly in emerging metropolises like China and India. Exposure to outdoor air pollution can have adverse health effects that can prove to be complicated results of pollutant compositions and concentrations (Badas et al. 2019). Ozone ($O_3$), nitrogen oxide, volatile organic compounds, metals, particulate matter, and metals are among the significant causes of air pollutants in cities (Arsov et al. 2020, Bhalgat et al. 2019). Increased air pollutants (such as $SO_2$, $O_3$, and PM) have been linked to higher death and morbidity rates. The urban environment's air quality (PM2.5 concentrations) has severely harmed people's work and lives in major cities (Al-Awadi 2018). The major sources of outdoor pollution are automobiles, factories, and industries, while smoke, toxins, and pollutants in the home cause indoor air pollution. Primary pollutants and secondary pollutants are the two categories of pollutants that cause air pollution (Baran et al. 2018). Primary pollutants are distinguishable from secondary pollutants as primary pollutants are straight discharged into the air from the source. Secondary pollutants, on the other hand, cause concentrations to rise when they react with primary pollutants or other air particles.

Several toxins are responsible for air pollution, but PM2.5 is the most notable, according to the author and their research (Angelin et al. 2019). The concentrations of PM2.5 can be calculated using logistic regression and autoregression (Zhu et al. 2018; Qingping et al. 2014). Various writers removed the day-by-day predictions of pollution levels by predicting hourly data using algorithms (Kumar & Pande 2022, Cosma & Simha 2018, Samal et al. 2019). The first stage is rating the air quality of an urban setting to actively collect sample air particles in every area of the city. In most nations, the current technique of assessment of air quality is via static air pollution monitoring stations (Li & He 2017, Santos et al. 2020). These reference stations can give very high precise readings from a small count of well-chosen areas that should reflect a variety of distinct environments (Amado & Dela Cruz 2018). Air pollution affects humans and plants negatively (Marjovi et al. 2015, San José et al. 2019). It causes ailments that are not life-threatening, such as throat and nasal discomfort (Daisey et al. 2003). Headaches can progress to more serious illnesses such as lung cancer, respiratory problems, brain disease, renal disease, shortness

**ORCID details of the authors:**

**H. N. Mahendra**
https://orcid.org/0000-0003-3854-5500

of breath, and even death. Some masks defend us from rising air pollution, and numerous laws regulate air pollution (Jain & Mandowara 2019, Savita et al. 2018). It is also very important to raise public awareness about the dangers created by air pollution (David et al. 2019). The air quality should be evaluated very accurately, and an air quality prediction system is essential to take the appropriate action to minimize air pollution (Chang et al. 2020).

There are a variety of traditional techniques for measuring it, but the results are not always exact, and it requires a big amount of mathematical computation (Ferrari et al. 2017, Huang et al. 2018). Machine learning is a form of artificial intelligence that requires many mathematical operations (Gaganjot et al. 2018, Zhu et al. 2018). Artificial intelligence, known as machine learning, plays a key role in air quality assessment and prediction (Kumar et al. 2021, Pasupuleti et al. 2020). Machine learning algorithms are being used in several studies to measure the Air Quality Index (Nandini & Fathima 2019, Kostandina & Dimoski 2018, Madan et al. 2020). The first step in reducing air pollution is correctly assessing the air quality level. Machine learning methods are essential for measuring the air quality level (Xiang et al. 2016). In the present study, several algorithms are compared to several conditions in various sectors.

The motivation for doing this study was primarily an interest in focusing on the impact of air quality on human health. Also, people's lifestyles have become heavily interested in information about air quality. Real-time air quality assessment of data is obtained using current air quality monitoring devices, stations, and satellite meteorological data. However, this is insufficient, and it is essential to calculate the expected air pollution trend. Therefore, in the present study, the "Autoregressive integrated moving average (ARIMA) model" is used to assess and predict the air quality of the study area.

## RELATED STUDIES

Huang et al. (2018) developed an algorithm to determine the air exchange condition of the car, which extract the pollutant concentration from the state that the concentration trend converges when we open the window, and eventually, the measured convergence. The measured values are specified as equivalent environmental air quality levels. The algorithm gives fast results, but prediction accuracy is low.

Xiang et al. (2016) presented a predictive method for the quality of air that depends on "Spatiotemporal deep learning (STDL)" that essentially considers spatial and temporal correlations. When comparing it with the existing air quality prediction model, this model simultaneously predicts air quality for all centers and shows adequate stability. Still, the prediction accuracy is too low and requires more computation time.

Qingping et al. (2014) developed a hybrid "Empirical mode decomposition general regression neural network (EEMDGRNN) model," which depends on preprocessing of data and analysis for 1-day prediction of PM2.5 concentrations. It gives accurate results but with tremendous time complexity.

Cosma & Simha (2019) presented an intelligent control method that depends on a Support Vector Machine (SVM) classifier (using a human-centric HVAC control system) in their study. Skin temperature is the only input given to the method and has shown good predictive power in acknowledging fixed heat needs. Although one skin temperature is used to predict 80% of heat demand accurately, it does not apply to time-series data analysis and has poor accuracy.

Zhu et al. (2018) formalized 24-hour forecasting as multi-task learning (MTL) by proposing in a study an improved model for predicting hourly air pollution concentrations based on previous meteorological data. It is based on standard regression models (linear or nonlinear) in machine learning. This helps speed up the learning process on big data, but with less accuracy.

Bhalgat et al. (2019) presented an integrated model to predict air pollution levels using artificial neural networks and kriging in their study. This model uses a linear regression protocol and a multilayer perceptron (ANN) to predict the next day. AR and ARIMA models successfully predict $SO_2$ values, but more studies are needed to predict PM2.5 and calculate AQI.

Chang et al. (2020) proposed a mixed model and framework to enhance reliability in predicting air pollution compared to traditional methods. This approach integrates various predictive models to educate the ensemble, together with the Pearson correlation coefficient to evaluate the dependence of different models on each other. For physical integration of this model, demonstrate predicted air pollution of 1 to 9 hours. The results suggested that the proposed mixed model exceeds one conventional method that teaches the machine in terms of MAE and RMSER. Still, it is difficult to determine the concentration of pollutants.

Pandey et al. (2018) use a wide range of classifiers like neural networks, Bayesian networks, SVMs, and decision trees in their research to determine PM1.0 levels along with UFP levels. Set traffic data and environment variables. The forecast is reasonably accurate for the PM1.0 level but has data limitations. Mahendra et al (2022) have use the SVM to analyse the performance in remote sensing image classification. In another study, Mahendra et al (2019) have

analyse supervised classification in remote sensing image classification.

The comparative analysis of different air quality prediction models is shown in Table 1. The comparative study shows that the ARIMA model performs better than other machine learning algorithms.

## OBJECTIVES OF THE STUDY

This study aims to assess and predict the air quality of Surat city for the years 2020 to 2023. The main objectives of this study are:

1. To assess pollutant concentrations of the study area by utilizing historical air quality and meteorological data.
2. To predict and forecast pollutant concentrations based on the assessment study of current and previous pollutant concentrations.

## MATERIALS AND METHODS

### Study Area and Data Set

The study area considered in this work is Surat city, located in Gujarat state, India. Gujarat is a region on the west coast of India with a shoreline of about 1,600 miles, a maximum of that on the Kathiawar peninsula. The capital of Gujarat is Gandhinagar, with a population of about 60.4 million. Surat is one of the most populated cities in Gujarat, with a population of 7,784,276. Surat city has a latitude of 21.1702° and a longitude of 72.8311°.

With its large population, Surat city's air quality is paramount. Air quality directly affects the occurrence of diseases and lowers the quality of life. Proper decision-making at the right time depends on measuring and analyzing air parameters, creating the need for real-time improved air quality monitoring. The use of multi-parameter air quality monitoring systems makes it possible to perform a detailed analysis of the level of significant pollution and its sources. Monitoring systems are integral to many smart city projects to monitor air quality and control the concentration of key pollutants in urban areas.

In the present work, three years of air quality data in 2020, 2021, and 2022 of the study area of Surat city is collected from Gujarat's Environmental Protection Administration (EPA) to build multiple speculative models. Air quality monitoring parameters such as $NO_2$, $SO_2$, PM2.5, PM10, CO, and $O_3$ are obtained from the data. The collected parameters are used to assess the present and predict future air quality of the study area.

The methodology followed in the present work is divided into four distinct phases. They are Data collection, Assessment, Prediction, and Forecast.

### Identification

The first stage is initiated by identifying the various contents of the pollutants present in the air. Then, we assemble the previous data set by giving input to the system. It is followed by comparing the latest data to the assembled previous data set.

Table 1: Comparative analysis of air quality prediction model.

| Ref. | Prediction Model | Prediction Performance | Pollutants | Study Areas |
|---|---|---|---|---|
| Korunoski et al. (2019) | Internet of the things-based algorithm. | Accuracy: 92.4% | $CO_2$, PM2.5, TVOC | Skopj, Methodius |
| Xiang et al. (2016) | STDL Model | Accuracy: 82.66% | PM2.5 | China |
| Qingping et al. (2014) | Hybrid EEMD-GRNN Model | (Calculated using formula) | $SO_2$, $NO_2$, PM10, PM2.5, CO, $O_3$ | Republic of Macedonia |
| Cosma and Simha (2018) | The method based on SVM Classifier | Accuracy: 80.9% | - | General |
| Zhu et al. (2018) | Standard regression models (linear or nonlinear) | - | $SO_2$, PM2.5, $O_3$ | Chicago area |
| Chang et al. (2020) | Model using ANN and Kriging | - | $SO_2$ | Mumbai, India |
| Pandey et al. (2018) | Hybrid model (LSTM, SVR, GBT, LSTM2) | High accuracy compared to the traditional method | CO, NO, $NO_2$, $O_3$, PM10, PM2.5, $SO_2$ | EPA of Taiwan |
| Kostandina and Dimoski (2018) | Classifiers (Neural Network, Bayesian Network, SVM, and Decision Trees) | - | PM1.0 | Hangzhou, China |
| Kumar et al. (2021) | ARIMA model | High accuracy compared to machine learning algorithms | CO, NO, $NO_2$, $O_3$, PM10, PM2.5, $SO_2$ | Assam, India |

### Assessment

In the second phase, the concentration of pollutants is estimated by prevailing air standard monitoring devices, stations, and satellite weather specifics for 2020, 2021, and 2022. It can issue information about real-time air status monitoring.

### Prediction

By using existing historical air data for weather conditions, prediction is carried out with the help of machine learning for the year 2023. The ARIMA model helps in the processing of high-dimensional large-scale data. We implement the de-exploration of multidimensional time-space using a sliding window mechanism. With access to the concentration of contaminants, we evaluate their impact on health and vegetation.

### Forecast

Finally, in the last phase, we forecast estimated pollutants concentration for the year 2020, 2021, and 2022 and predicted pollutants concentration for the year 2023. The methodology followed in the present work is shown in Fig. 1.

### ARIMA Model

Box and Jenkins introduced the ARIMA model, which can be termed a time series forecast model, in the early 1970s (Stellwagen & Tashman 2013)). The present value of a time series is linearly characterized by its primary importance in an ARMA model. The ARIMA model incorporates the concept of integration and is an extension of the Autoregressive Move Average. The values are forecasted using the previous stage data by an auto-regression model. Equation (1) describes a satisfactorily central principle that may lead to correct predictions of a chain of problems (1).

$$Y_{hat} = b_0 + b_1 * X_I \quad \ldots(1)$$

The value of $X_I$ is an input for prediction, while the values b0 and b1 are model coefficients.

This approach can be used for time series when lag variables are included in past observations. Equation (2) describes the regression model's expression.

$$X_{(T+1)} = b_0 + b_1 * X_{(T-1)} * b2 + X_{(T-2)} \quad \ldots(2)$$

Based on the results of the previous two phases, the value of the (T+1) can be calculated (T-1 and T-2). Autoregressions are regression models that utilize the same input variable throughout the forecasting process.

## RESULTS AND DISCUSSION

In the present work, MATLAB 9.6 R2019a has been used to assess and predict the air quality level from the data set of the study area. Table 1 shows the air quality index value

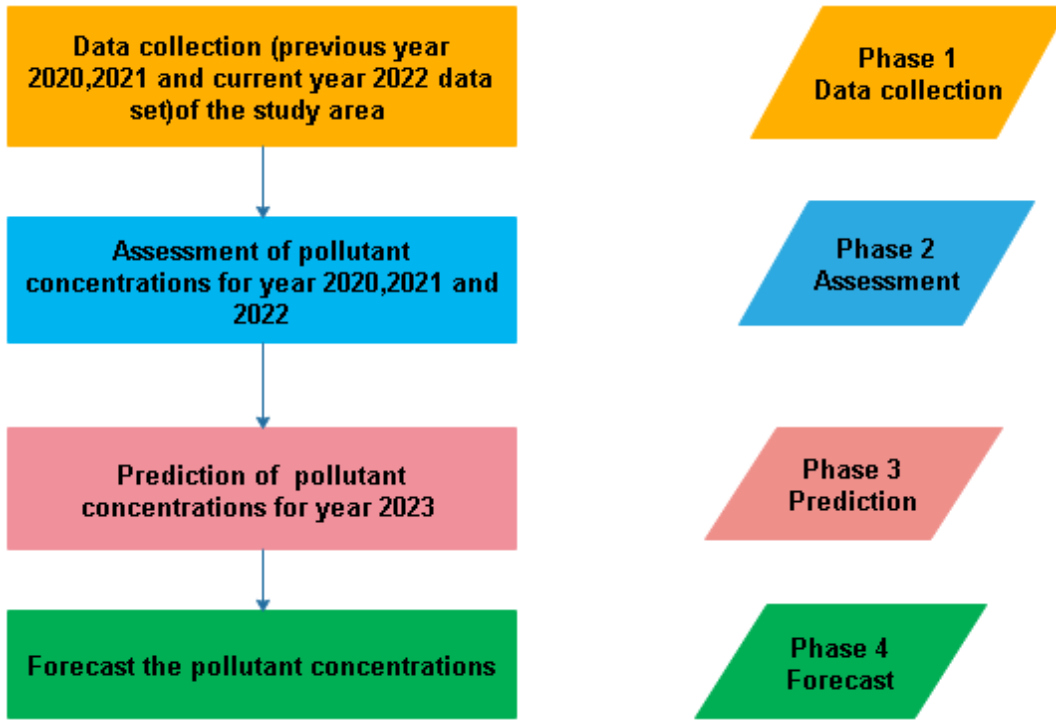


Fig. 1: Methodology followed in the present work.

(AQI). An AQI value of 50-0 indicates the air quality is good, and there is a limited possibility of affecting the environment and human health. Levels between 50-100 are acceptable, but if values exceed 100, they can be harmful to human health. If the value is between 151-200, people might experience more severe health effects. If the value ranges from 201 to 300, it is very unhealthy for the environment. On the other hand, an AQI value of 300 or higher indicates precarious air quality that is likely to harm the environment and public health. Table 2 shows the air quality index value of the different categories.

**Air Quality Level Assessment**

Table 3 shows the pollutant concentrations assessment for the year 2020. The results show that in 2020, the minimum amount of nitrogen and Sulfur dioxide in the air was 12 mm and 6 mm. The maximum amount of nitrogen and Sulphur dioxide in the air is 37 mm and 18 mm. Nitrogen dioxide and Sulphur dioxide mean values are 20.22 and 13.03, respectively.

Table 4 shows the pollutant concentrations assessment for the year 2021. The results show that in the year 2021, the minimum amount of Nitrogen dioxide and Sulphur dioxide present in the air are 15mm and 6mm, and the maximum amount of Nitrogen dioxide and Sulphur dioxide present in the air are 27mm and 31mm, the mean value of nitrogen dioxide and Sulphur dioxide are 20.36 and 13.57.

Table 5 shows the pollutant concentrations assessment for the year 2022. The results show that in the year 2022, the minimum amount of Nitrogen dioxide and Sulphur dioxide present in the air are 18 mm and 12 mm, and the maximum amount of Nitrogen dioxide and Sulphur dioxide present in the air is 29 mm and 22 mm, the mean value of nitrogen dioxide and sulphur dioxide are 21.14 and 14.61.

Fig. 2 shows the minimum values of the pollutants $SO_2$, $NO_2$, PM10, PM2.5, CO, and $O_3$, in the years 2020, 2021, and 2022 respectively. The results show that the concentration of most pollutants was minimal in 2020 and then gradually increased.

Fig. 3: Shows the maximum values of the pollutants $SO_2$, $NO_2$, PM10, PM2.5, CO, and $O_3$, in the years 2020, 2021, and 2022 respectively. The results show that the concentration of PM2.5 is the maximum in the year 2022,

Table 2: Air Quality Index value.

| Air Quality Index Category | Air Quality Index Value | Description Of Air Quality |
|---|---|---|
| Good | 0-50 | Minimal Impact |
| Moderately Polluted | 51-100 | Acceptable quality of air |
| Unhealthy for responsive groups | 101-150 | Members of responsive groups may undergo health issues. |
| Harmful | 151-200 | Common people may experience health effects, while sensitive people might experience more serious health effects |
| Injurious | 201-300 | Health Alert |
| Hazardous | >300 | Health warning of emergency conditions |

Table 3: Pollutant concentrations assessment for the year 2020.

| | $SO_2$ [m] | $NO_2$ [mm] | PM10 [mm] | PM 2.5 [mm] | CO [mm] | $O_3$ [mm] |
|---|---|---|---|---|---|---|
| Min | 6 | 12 | 53 | 43 | 6 | 53 |
| Max | 18 | 37 | 179 | 9 | 18 | 179 |
| Mean | 13.03 | 20.22 | 85.47 | 28.78 | 12.81 | 85.39 |

Table 4: Pollutant concentrations assessment for the year 2021.

| | $SO_2$ [mm] | $NO_2$ [mm] | PM10 [mm] | PM 2.5 [mm] | CO [mm] | $O_3$ [mm] |
|---|---|---|---|---|---|---|
| Min | 6 | 15 | 63 | 12 | 11 | 63 |
| Max | 31 | 27 | 180 | 48 | 31 | 180 |
| Mean | 13.57 | 20.36 | 87.88 | 30.88 | 13.96 | 88.38 |

Table 5: Pollutant concentrations assessment for the year 2022.

| | $SO_2$ [mm] | $NO_2$ [mm] | PM10 [mm] | PM 2.5 [mm] | CO [mm] | $O_3$ [mm] |
|---|---|---|---|---|---|---|
| Min | 12 | 18 | 66 | 13 | 15 | 58 |
| Max | 22 | 29 | 133 | 133 | 15 | 133 |
| Mean | 14.61 | 21.14 | 89.17 | 31.46 | 15 | 88.40 |

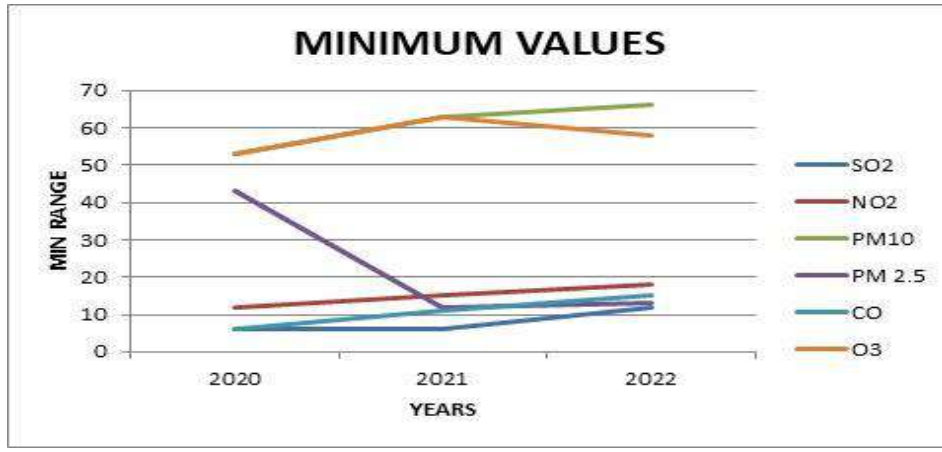


Fig. 2: Minimum values of the pollutants.

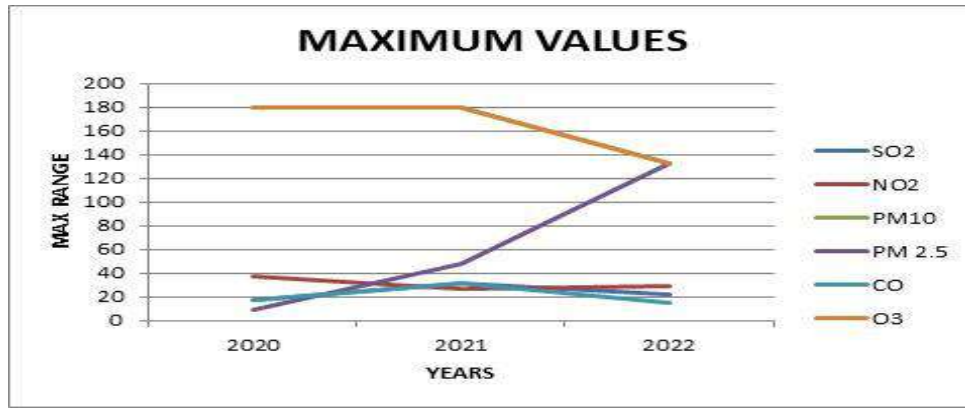


Fig. 3: Maximum values of the major pollutants.

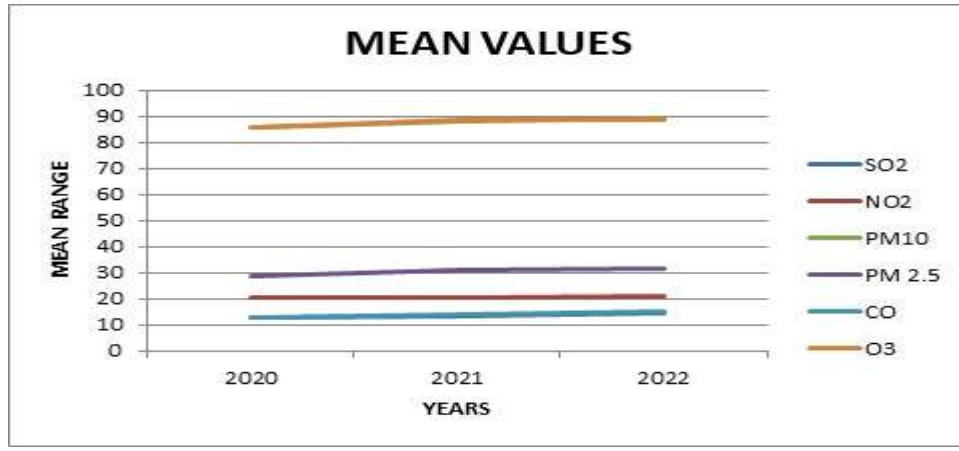


Fig. 4: Calculated mean values.

which means it is increasing day by day. The corresponding calculated mean value for the 3 years is shown in Fig. 4.

### Air Quality Level Prediction

The air quality monitoring parameters detected are $SO_2$ (Sulphur Dioxide in mm), $NO_2$ (Nitric Dioxide in mm), PM10 (Particulate Matter 10-micrometer in mm), PM2.5 (Particulate Matter 2.5-micrometer in mm), CO, and $O_3$, which are also used to predict future air quality data. All the above six parameters contain 574 datasets (January 2020-until April 2023). The observed and prediction of all six parameters, i.e., $SO_2$, $NO_2$, PM10, PM2.5, CO, and $O_3$, are shown in Figs. 5, 6, 7, 8, 9, and 10, respectively.

The prediction of Sulphur dioxide ($SO_2$) levels is shown in Fig. 5. The values of $SO_2$ are observed from January 2020 to January 2022. By using the ARIMA model, it is forecasted up to August 2023. $SO_2$ is composed of Sulphur and oxygen and has a strong odor. It is a colorless, reactive air pollutant and contributes to air pollution. Hence, it can be harmful to human, animal, and plant lives. The main sources of Sulphur dioxide emissions are fossil fuel combustion and natural volcanic activity. Due to the COVID-19 pandemic prevention, commercial ships and incineration activities were

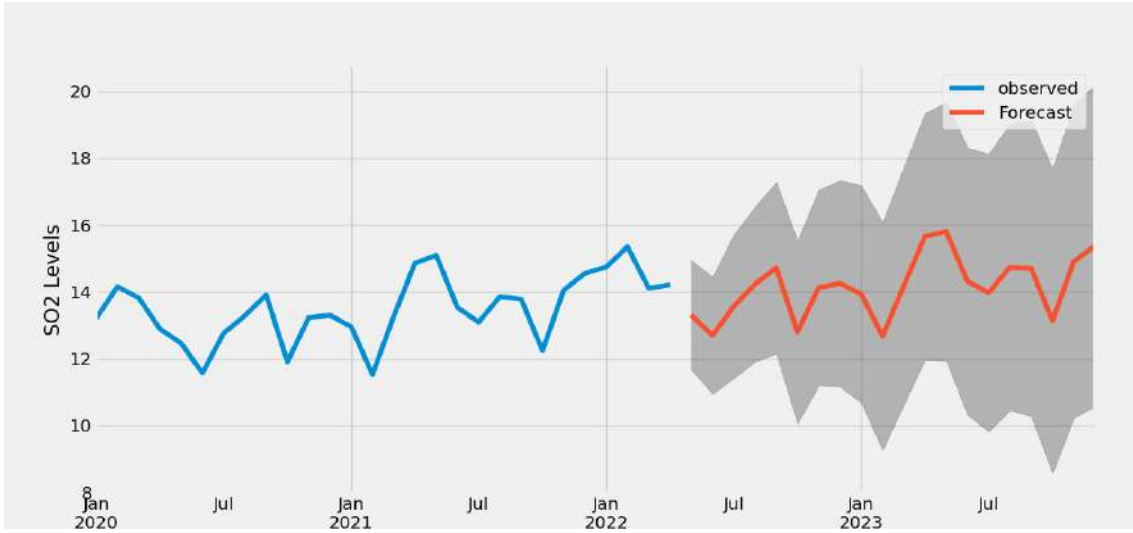


Fig. 5: Prediction of $SO_2$ levels.

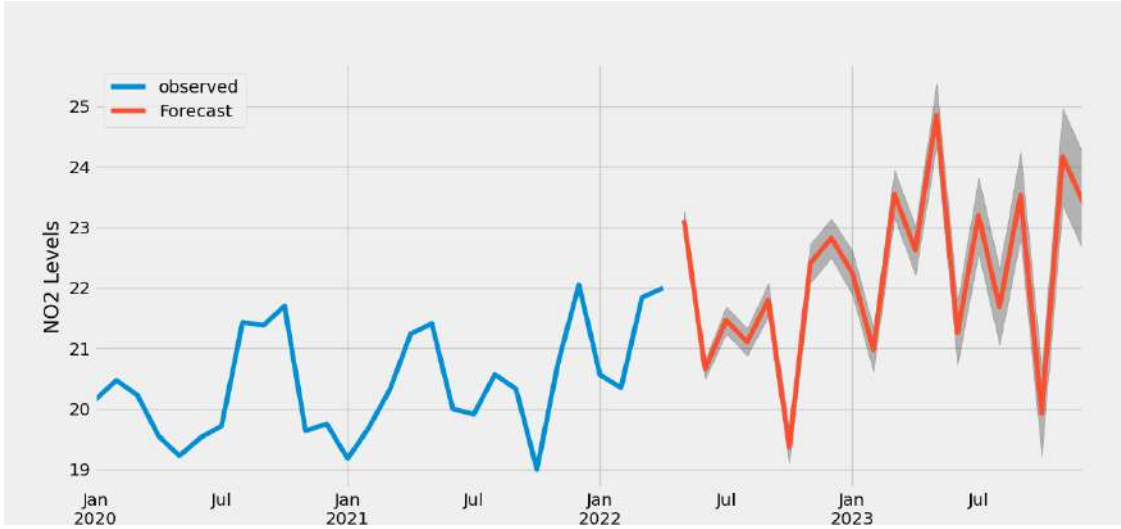


Fig. 6: Prediction of $NO_2$ levels.

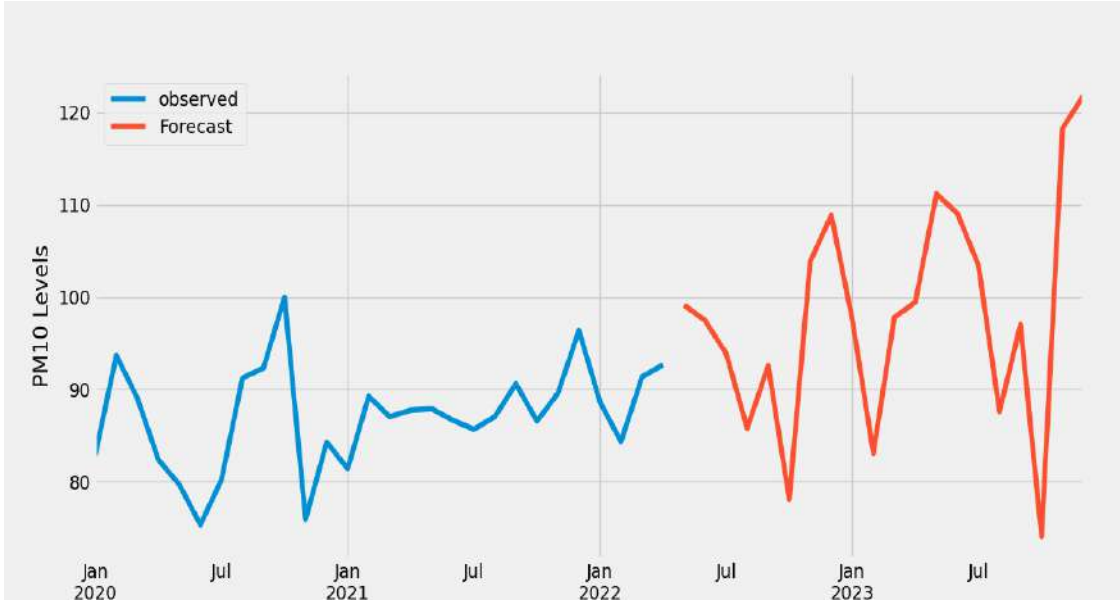


Fig. 7: Prediction of PM10 levels.

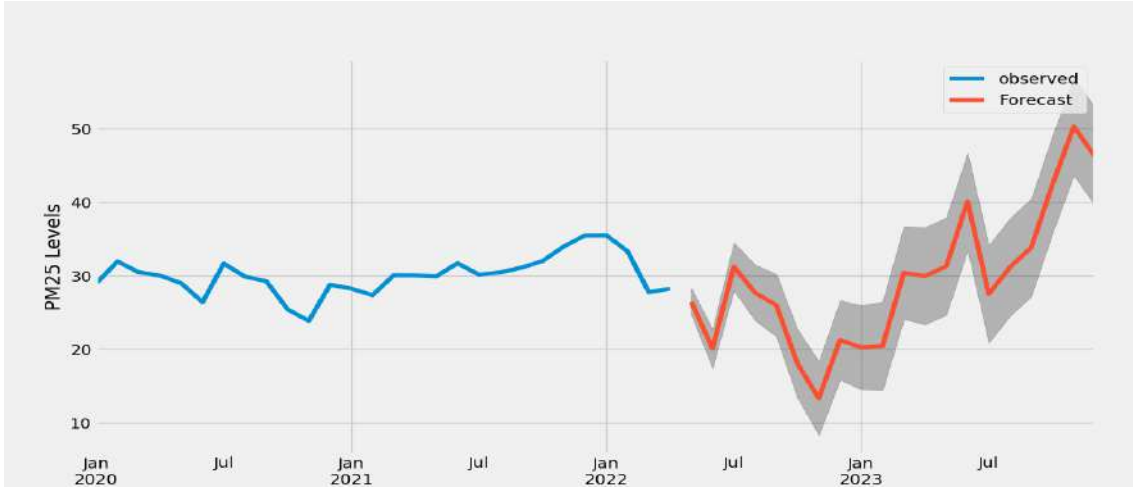


Fig. 8: Prediction of PM2.5 levels.

closed, which decreased the $SO_2$ emissions in the year 2020. In the short-term period, there was a downfall in the values of $SO_2$ emissions, but in the long-term period, an improvement in its values is inevitable. Hence, it is important to consider measures to reduce $SO_2$ levels in the environment.

The prediction of nitrogen dioxide ($NO_2$) levels is shown in Fig. 6. The values of $NO_2$ are observed from the duration of January 2020 to January 2022. By using the ARIMA model, it is forecasted up to August 2023. $NO_2$ is composed of nitrogen and oxygen and arises from high-temperature combustion processes of fossil fuels, like vehicle exhaust and transportation. During the year 2020 (January to July), there was a significant decrease in the values of $NO_2$ concentrations. The COVID-19 protective measures to terminate commercial activities helped in a limitation in $NO_2$ emissions from production and automobile exhaust.

The prediction of PM10 levels is shown in Fig. 7. The values of PM10 are observed from the duration of January 2020 to January 2022. By using the ARIMA model, it is forecasted up to August 2023. PM10s are very small particles with a diameter of 10 microns or less, found in dust and smoke. The pattern of PM10 primarily results from roadway

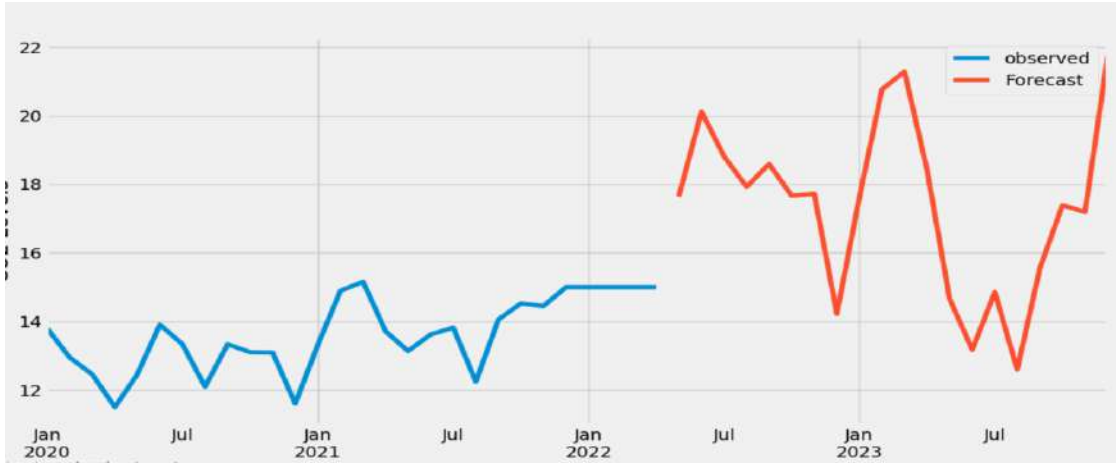


Fig. 9: Prediction of CO levels.

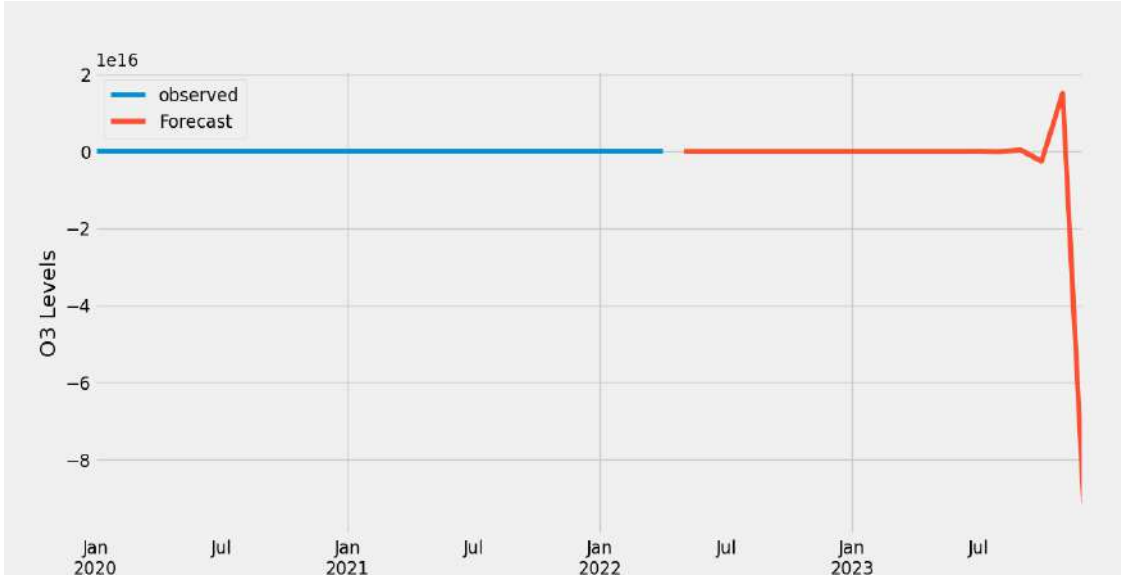


Fig. 10: Prediction of $O_3$ levels.

traffic, architecture activities, and dust entertainment. Variations in PM10 concentrations can be observed during the period 2020-2021. The consequences of reduced city pollution had a limited effect on PM10 concentrations.

The prediction of PM2.5 levels is shown in Fig. 8. The values of PM2.5 are observed from the duration of January 2020 to January 2022. By using the ARIMA model, it is forecasted up to August 2023. PM2.5 is an air pollutant with a size of 2.5 microns or smaller. Fine particulate matter (PM2.5) is a pollutant in the atmosphere that threatens people's health when its levels are high in the atmosphere. The observed PM2.5 levels were constant for the period 2020 to 2022. The predicted PM2.5 levels indicate an increase in its values for the year 2023.

The prediction of carbon monoxide (CO) levels is shown in Fig. 9. CO values are observed from January 2020 to January 2022. By using the ARIMA model, it is forecasted up to August 2023. Carbon monoxide is a clear, odorless gas that is a common air pollutant. The main sources of CO in the environment are automobiles and industrial emissions. The significant change in the observed and predicted values of CO can be noticed in Fig. 9.

The Ozone ($O_3$) level prediction is shown in Fig. 10. The values of $O_3$ are observed from January 2020 to

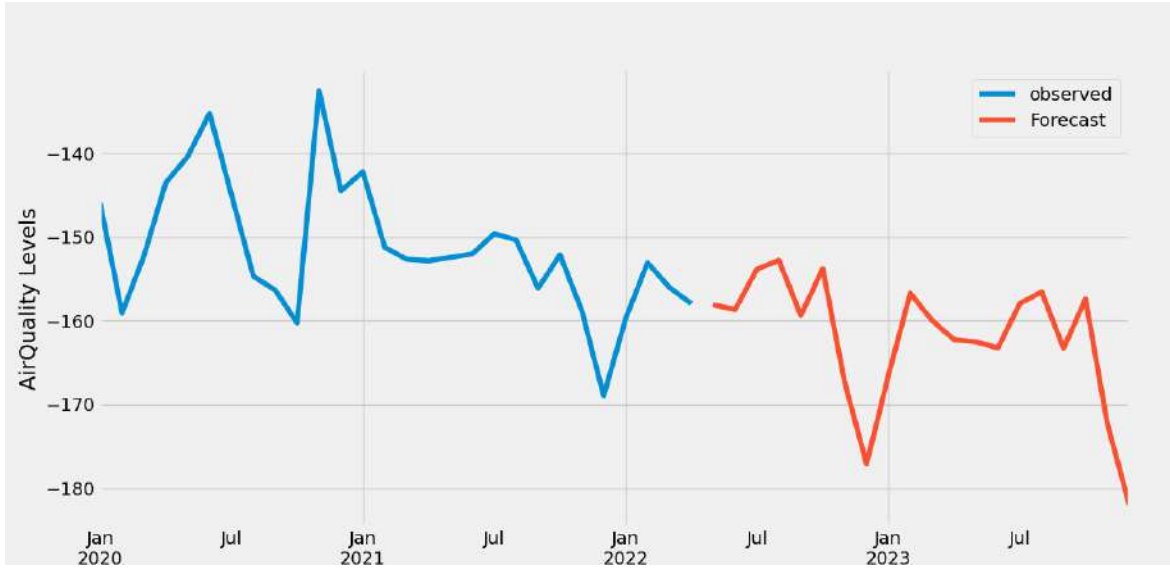


Fig. 11: Prediction of air quality levels.

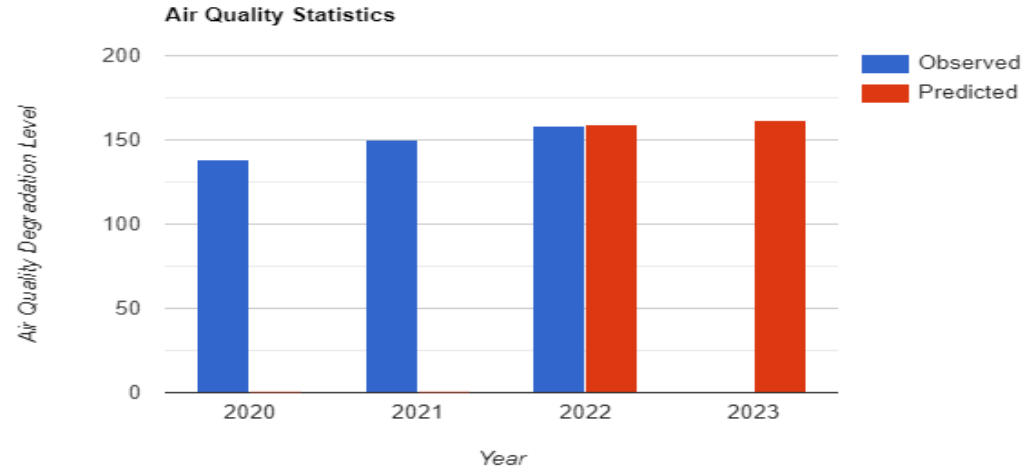


Fig. 12: Statistical representation of air quality level from 2020 to 2023.

January 2022. By using the ARIMA model, it is forecasted up to August 2023. $O_3$ gas is present in two layers of the atmosphere. High up in the atmosphere, $O_3$ forms a layer that protects and shields the Earth from harmful ultraviolet rays. The values of $O_3$ are expected to be uniform till July 2023, but they can be reduced strictly after July 2023.

The prediction of air quality levels is shown in Fig. 11. The blue color curve in the graph represents the observed values of air quality levels, while the red color curve represents the forecasted values. The dataset is observed from the duration of January 2020 to January 2022. The ARIMA model forecasts air quality levels up to August 2023. As we can see in the observed curve in 2020, quality improved linearly from January to July 2020. Again, air quality started degrading from July 2020 to December 2020. The sudden improvement and degradation in the year 2020 were due to the lift of the lockdown during the COVID-19 pandemic. In the year 2021, the quality of air started degrading exponentially. This was the year after the lockdown.

The cause of change in air quality in the year 2021 were conveyance (36.0 %), production (33.0%), and wind-blown dust (21.0%). The major cause of the degradation in air quality levels was the expansion of industries. Total estimated emissions for the year 2021, PM2.5, were almost

6,500 tons from the road, rail, aviation, and shipping transportation modes. Add to this the residential emissions, industrial emissions, dust, and open burning pollutants, emissions from diesel generators, and emissions from brick kilns, and the annual figure rises to a substantial 61,000 tons. Other pollutants measured included PM10, Sulphur dioxide ($SO_2$), nitric oxide (NOx), and carbon monoxide (CO). As we can see from the red curve in the predicted data graph, the air quality is degrading. The major contributors are industries and vehicles. The leading growth of urbanization and industrialization are making cities like Ahmedabad, Surat, Vadodara, and Rajkot the primary target for air pollution. According to reports, Surat has more than 2000 industries contributing to air pollution as of May 2012. The report states that the number of vehicles has doubled in the past 10 years.

The statistical representation of the air quality level is displayed in Fig. 12. The blue-colored histogram indicates the observed values, and the red-colored histogram shows the predicted values for the years 2022 and 2023. The accuracy of the predicted values can be observed from the bar graph. The observed values of degrading air quality levels were: 135 in July 2020 and 150 in July 2021,155 in July 2022. The predicted values of degrading air quality levels were 162 in July 2022 and 165 in July 2023.

The approach presented in our work has the advantage of following date columns and not exhibiting data fluctuation during the event. It is capable of overcoming unpredictability in data and generating effective results. The large data fluctuations if the data is collected around festivals such as Diwali, a major cause of increasing pollution due to big fireworks displays. It was also observed that the large data fluctuations and not following the date column in sequence might lead to incorrect results.

## CONCLUSION

In this present study, we predict and forecast the air quality level using the ARIMA model. The various baseline models fail to forecast air quality due to frequent fluctuations in the dataset. This model enables us to deeply mine and explore the time-series data concept. The experiment results show that in the year 2020, the minimum amount of Nitrogen dioxide and Sulphur dioxide present in the air were 12 mm and 6 mm, and the maximum amount of Nitrogen dioxide and Sulphur dioxide present in the air was 37 mm and 18 mm. The mean value of Nitrogen dioxide and Sulphur dioxide are 20.22 and 13.03. Also, the predicted air quality level for the year 2023, the minimum amount of Nitrogen dioxide and Sulphur dioxide present in the air would be 18 mm and 12 mm, and the maximum amount of Nitrogen dioxide and Sulphur dioxide present in the air would be 29 mm and 22 mm. The mean value of Nitrogen dioxide and Sulphur dioxide would be 21.14 and 14.61, respectively. The predicted values from the system are highly accurate for analyzing time-series data. Hence, it can effectively turn on automatic air quality forecasting in the future.

## ACKNOWLEDGEMENT

We would like to thank the JSS Academy of Technical Education Bengaluru, Visvesvaraya Technological University, Belagavi, and Vision Group on Science and Technology (VGST) Karnataka for all the support and encouragement provided by them to take up this research work.

## REFERENCES

Al-Awadi, L.J. 2018. Assessment of indoor levels of volatile organic compounds and carbon dioxide in schools in Kuwait. J. Air Waste Manag. Assoc., 68(1): 54-72.

Amado, T.M. and Dela Cruz, J.C. 2018. Development of Machine Learning- based Predictive Models for Air Quality Monitoring and Characterization, TENCON IEEE Region Conference, 16-19 Nov 2020, Osaka, Japan, IEEE, NY, pp. 0668-0672.

Angelin, J. and Sasi Kumar, A. 2019. PM2.5 prediction using machine learning hybrid model for smart health. Int. J. Eng, Adv. Technol., 9(1): 6500-6504.

Arsov, M., Zdravevski, E., Lameski, P., Corizzo, R., Koteli, N., Mitreski, K. and Trajkovik, V. 2020. Short-term air pollution forecasting based on environmental factors and deep learning models. IEEE Conference on Computer Science and Information Systems, pp. 15-22.

Badas, M.G., Salvadori, L., Garau, M., Querzoli, G. and Ferrari, S. 2019. Urban areas parameterization for CFD simulation and cities air quality analysis, Int. J. Environ. Pollut., 66(1/2/3): 5-18.

Baran, B. 2019. Prediction of Air Quality Index by Extreme Learning Machines. 2019 International Conference on Artificial Intelligence and Data Processing (IDAP), Malatya, Turkey, Piscataway, IEEE, pp. 123-139.

Bhalgat, P., Bhoite, S. and Pitare, S. 2019. Air quality prediction using machine learning algorithms. Int. J. Comp. Appl. Technol. Res., 8(9): 367-390.

Chang, Y.S., Abimannan, S., Chiao, H.T., Lin, C.Y. and Huang, Y.P. 2020. An ensemble learning-based hybrid model and framework for air pollution forecasting. Environ. Sci. Pollut. Res., 27(30): 38155-38168.

Cosma, A. and Simha, R. 2018. Machine learning method for real-time non-invasive prediction of individual thermal preference in transient conditions. Build. Environ. 148: 372-383.

Daisey, J.M., Angell, W.J. and Apte, M.G. 2003. Indoor air quality, ventilation, and health symptoms in schools: An analysis of existing information. Indoor Air, 13(1): 53-64.

David, C., Amy, S., Daniel, C., Jo, D., Rod, J., Ian, L., Olalekan, A.M., Popoola, K. and Martin, S. 2019. Urban emission inventory optimisation using sensor data, an urban air quality model, and inversion techniques. Int. J. Environ, Pollut., 66(4): 252-266.

Ferrari, S., Badas, M.G., Garau, M., Querzoli, G. and Seoni, A. 2017. The air quality in narrow two-dimensional urban canyons with pitched and flat roof buildings. Int. J. Environ. Pollut., 62(1): 347-368.

Gaganjot, K.K., Jerry, Z., Gao, S.C., Shengqiang, L. and Gang, X. 2018. Air quality prediction: Big data and machine learning approaches. Int. J. Environ. Sci. Dev., 9(1): 8-16.

Huang, J., Duan, N., Ji, P., Ma, C., Hu, F., Ding, Y. and Yu, Y. 2018. A crowdsource-based sensing system for monitoring fine-grained air quality in urban environments. IEEE IoT J., 6(2): 142.

Jain, S. and Mandowara, V. 2019. Study on particulate matter pollution in Jaipur city. Int. J. Appl. Eng. Res., 14(3): 637-645.

Korunoski, M., Risteska, S., Biljana, M. and Trivodaliev, K. 2019. Internet of Things Solution for Intelligent Air Pollution Prediction and Visualization. IEEE EUROCON 2019 - 18th International Conference on Smart Technologies, 8-11 July, 2019, Novi Sad, Serbia, IEEE, NY, pp. 1-6.

Kostandina, V. and Dimoski, A. 2018. Air quality index prediction using simple machine learning algorithm., Int. J. Emerg, Trends Technol. Comp. Sci., 7(1): 25-30.

Kumar, K. and Pande, B.P. 2022. Air pollution prediction with machine learning: A case study of Indian Cities. Int. J. Environ. Sci. Technol., 51: 28-32

Kumar, T.S., Das, H.S., Choudhary, U., Dutta, P.E., Guha, D. and Laskar, Y. 2021. Analysis and Prediction of Air Pollution in Assam Using ARIMA/SARIMA and Machine Learning. In Muthukumar, P., Sarkar, D.K., De, D.and De, C.K. (eds), Innovations in Sustainable Energy and Technology, Springer, Cham, pp. 317-330.

Li, Y. and He, J. 2017. Design of an intelligent indoor air quality monitoring and purification device. IEEE Information Technology and Mechatronics Engineering Conference (ITOEC), 3-5 October 2017, Chongqing, China, IEEE, NY, pp. 1147 -1150.

Madan, T., Sagar, S. and Virmani, D. 2020. Air quality prediction using machine learning algorithms: A review. International Conference on Advances in Computing, Communication Control and Networking (ICACCCN), 18-19 December 2020, Greater Noida, India, IEEE, NY, pp. 140-145.

Mahendra, H.N. and Mallikarjunaswamy, S. 2022. An efficient classification of hyperspectral remotely sensed data using support vector machine, International Journal of Electronics and Telecommunications, 68(3): 609-617.

Mahendra, H. N., Mallikarjunaswamy, S., Rekha, V., Puspalatha, V. and Sharmila, N. 2019. Performance analysis of different classifier for remote sensing application. International Journal of Engineering and Advanced Technology, 9: 2249-8958. DOI: 10.35940/ijeat.A1879.109119.

Marjovi, A., Arfire, M. and Martinoli, A. 2015. High-Resolution Air Pollution Maps in Urban Environments Using Mobile Sensor Networks, International Conference on Distributed Computing in Sensor Systems, 10-12 June 2015, Fortaleza, Brazil, IEEE, NY, pp. 11-20.

Mudholkar, A., Akash, S., Ajay, C. and Gowramma, G.S. 2019. Air pollution data analysis using the ARIMA model. In Wang, J., Reddy, G.R., Prasad, K.V. and Reddy, V.S. (eds), Soft Computing and Signal Processing Proceedings, Springer, Cham, pp. 74-78.

Nandini, K. and Fathima, G. 2019. Urban air quality analysis and prediction using machine learning. International Conference on Advanced Technologies in Intelligent Control, Environment, Computing & Communication Engineering (ICATIECE), 19-20 March 2019, Bengaluru, IEEE, NY, pp. 98-102.

Pandey, G., Zhang, B. and Jian, L. 2018. Predicting submicron air pollution indicators: a machine learning approach. Environ. Sci. Process. Impacts, 15(5): 996-1005.

Pasupuleti, V.R., Uhasri, P., Kalyan, S. and Reddy, H.K. 2020. Air Quality Prediction of Data Log by Machine Learning. International Conference on Advanced Computing and Communication Systems (ICACCS), 6-7 March 2020, IEEE, NY, pp. 1395-1399.

Qingping, Z., Haiyan, J., Jianzhou, W. and Jianling, Z. 2014. A hybrid model for PM2.5 forecasting based on ensemble empirical mode decomposition and a general regression neural network. Sci. Total Environ., 496(1): 264-274.

Samal, K.K., Babu, K.S., Das, S.K., and Acharaya, A. 2019. Time Series-Based Air Pollution Forecasting using SARIMA and Prophet Model. Proceedings of the International Conference on Information Technology and Computer Communications, 16-18, 2019, Singapore, IEEE, NY, pp. 124-129.

San José, R., Pérez, J.L., Pérez, L. and Barras, R.M.G. 2019. Global climate-driven effects on urban air pollution simulations using very high spatial resolution. Int. J. Environ. Pollut., 66(1): 143-161.

Santos, J.A., Jiménez, M. and Espinosa, F. 2020. Effect of event-based sensing on IoT node power efficiency: Case study: Air quality monitoring in smart cities. IEEE Access, 7: 132577-132586.

Savita, V.M., Mohurle, R.P. and Manisha, P. 2018. A study of fuzzy clustering concept for measuring air pollution index. Int. J. Adv. Sci. Res., 3(1): 43-45.

Singh, T., Narasimhan, T.L. and Lakshminarayanan, C.S. 2020. Deep Air: Air quality prediction using deep neural network. TENCON IEEE Region Conference (TENCON), 16-19 Nov 2020, 124-129.

Stellwagen, E. and Tashman, L. 2013. ARIMA: The models of box and Jenkins. Int. J. Appl. Forecast, 16: 28-33.

Xiang, L., Peng, L., Hu, Y., Shao, J. and Chi T. 2016. Deep learning architecture for air quality predictions. Environ. Sci. Pollut. Res. Int., 23(22): 22408-22417.

Zhu, C., Cai, T., Yang, C. and Zhou, X. 2018. A machine learning approach for air quality prediction: model regularization and optimization. Big Data Cognit. Comp., 2(1): 5-10.

Zhu, D., Changjie, C., Tianbao, Y. and Xun, Z. 2018. A machine learning approach for air quality prediction: Model regularization and optimization. Big Data Cognit. Comput, 11: 1-5

Nature Environment and Pollution Technology
An International Quarterly Scientific Journal

p-ISSN: 0972-6268
(Print copies up to 2016)
e-ISSN: 2395-3454

Vol. 22 | No. 1 | pp. 211-219 | 2023

Original Research Paper

https://doi.org/10.46488/NEPT.2023.v22i01.019

Open Access Journal

# Evapotranspiration Over the Indian Region: Implications of Climate Change and Land Use/Land Cover Change

**Garima Singh and Sudhir Kumar Singh†**
K. Banerjee Center of Atmospheric and Ocean Studies, University of Allahabad, Prayagraj, 211002, India
†Corresponding author: Sudhir Kumar Singh; sudhirinjnu@gmail.com

**Nat. Env. & Poll. Tech.**
**Website: www.neptjournal.com**

*Received:* 23-07-2022
*Revised:* 06-10-2022
*Accepted:* 17-10-2022

**Key Words:**
Land use/Land cover
Precipitation
Temperature
Canopy interception
Evapotranspiration
Normalized Difference
Vegetation Index

## ABSTRACT

Evapotranspiration (ET) plays a significant role in climatic studies, directly influencing the hydrological cycle, energy balance equation, and surface vegetation. ET comprises three components: bare soil or ground evaporation, evaporation, and transpiration, in which vegetation removes water influenced by food grain production. In turn, soil moisture availability depends on precipitation characteristics over land, surface net radiation, and wind speed are the major climatic factors that together determine the magnitude of ET. This controls moisture availability in the lower troposphere, hence atmospheric stability, chances of cloud formation, and precipitation. Though the study of evapotranspiration is important for determining agricultural water consumption and analyzing drought situations, there is a lot of uncertainty in its accurate estimation. Land use/Land cover changes (LULCC) occurring throughout the Indian subcontinent have been found to affect the characteristics of low to moderate rainfall events and surface temperature extremes (Halder et al. 2016). A global warming scenario will change the hydrological cycle, and the impact of anthropogenic factors has also necessitated the need to understand the mechanisms that control changes in ET over India. In this study, we want to analyze the relationship between transpiration and the Normalized Difference Vegetation Index (NDVI) and investigate the relationship between canopy interception with respect to NDVI all over the Indian region. Attempts have been made to assess the impact of changes in climate and LULC on ET and its three components over the Indian region from 1981 till the present time. The monsoon season increases precipitation, and soil evaporation is found to increase at first, along with an increase in NDVI followed by canopy evaporation and transpiration. It is noted that changes in precipitation and LULCC across the Indian subcontinent have contributed significantly to changes in ET in different seasons. As variability in surface net radiation also plays an important role in controlling changes in total ET, it is being investigated.

## INTRODUCTION

Global climate, as well as that over the Indian region, has been changing since the last century due to natural and anthropogenic factors, per the IPCC Fifth Assessment Report (IPCC) AR5 (Stocker et al. 2013). Significant global warming has resulted in rapid intensification of the hydrological cycle with adverse impacts on ecosystems and agricultural and water resources worldwide. In a regional context, modeling studies suggest that unprecedented changes have occurred, varying in terms and trend of average daily value and extreme (Both the maximum and the minimum) surface air temperature and heavy and very heavy precipitation (Halder et al. 2016). Cloudiness and associated changes in the incoming shortwave radiation, atmospheric humidity, aerosols, heat and cloud waves, and droughts (Rohini et al. 2016, Rajeevan & Nayak, 2017) over the Indian land parts in the last few decades. Understanding the mechanism inherent in such changes over India, particularly in terms of precipitation, soil moisture, runoff, evapotranspiration, and surface temperature, contributes to an accurate evaluation of the state of the surface weather in the area present Anthropocene and estimating better and improved model projections of the future climate under different radiative forcing (Stocker et al. 2013) scenarios.

A combination of evaporation and transpiration is known as evapotranspiration, evaporation is a process in which water moves from the liquid state to back into the atmospheric water vapor, and transpiration is a process in which loss of water vapor through open leaf stomata. Under sunny, warm weather, the amount of water lost through evaporation is higher than in cool, cloudy weather. Solar radiation absorbs the solar radiation, and heat radiated by the earth increases the temperature of the air. ET increases with the temperature, and molecular water gains more energy, move faster, and escapes

more quickly. Solar radiation (Warmer water evaporates faster as the air temperature is increased by solar energy in addition to heating the air, the sun also causes the rate of evaporation to increase due to the warmth) and wind draws in drier air, which improves the evaporation rate (since humid air is blown away by the wind). ET decreases with increasing humidity (because the air already has high moisture content as a result, excess moisture will not be able to accumulate). An ET rate is typically measured in millimeters (mm) per unit of time, and it expresses the amount of water lost per unit of time from a cropped surface over several time frames, such as an hour, a day, a month, a decade, or even a growing season.

The need to attain self-sustainability in food grain production led to the Indian green revolution in the 20th century. However, large-scale increases in agricultural practices and irrigation activity resulted in declination in surface and groundwater in northern India (Rodell et al. 2009). Such activities also altered the surface temperature variability on the northern Indian subcontinent (Roy et al. 2007). On the other hand, studies also show that rapid deforestation and an increase in crop cover fraction over the Indian region has resulted in surface temperature changes on a daily and extreme basis and rainfall distribution and intensity (Halder et al. 2016).

Changes in near-surface and low to mid-tropospheric atmospheric variables can occur through changing fluxes near the surface and state variables such as soil moisture. Net surface net radiation (NRAD) is a component of the hydrological cycle broken down into sensible, latent heat fluxes by soil moisture. Changes in the different components of the hydrologic cycle mentioned before are linked thermodynamically and dynamically (Seneviratne et al. 2012). Spatiotemporal and vertical changing circumstances in the distribution of clouds and aerosols bring about alterations in the net surface radiation (NRAD) that contributes significantly to determining the surface fluxes of moisture and heat. Therefore, to understand long-term variability in ET and its effect on the surface climate throughout India in a changing climate scenario and anthropogenic land use/ land cover (LULC) change, there is a need for a detailed investigation of all the components.

So far, very few studies have investigated the characteristics and causes of changes in global ET or that over India. One of the factors for that is the lack of accurate data and high uncertainty in the estimation of ET. Land use/ Land cover changes (LULCC) occurring throughout India in the form of conversion of forest cover into agriculture or bare land have been found to affect the characteristics of low to moderate rainfall events and surface temperature extremes (Halder et al. 2016). Furthermore, under a global warming scenario, the hydrological cycle would change. The impact of various anthropogenic factors has also necessitated an urge to understand the factors that control ET characteristics in India. Goroshi et al. (2017) analyzed the spatial seasonal trend of ET all over India from 1983-2006. For the forest region, they observed decreasing trend of ET. An analysis of the seasonal trend shows a declining trend during summer monsoons and post-monsoons, and the northeast monsoon and premonsoon period, the trend has been increasing. Goroshi et al. (2017) calculate the correlation between ET and some climatic factors (soil moisture, precipitation, temperature, and insolation). They found a positive correlation in ET related to rainfall and soil moisture in arid semi-arid regions. An inverse correlation is also seen between ET and temperature in the dry areas of western India. Chattopadhyay and Hulme (1996) analyzed the pan evaporation and potential evapotranspiration, India's time series for various stations, and seasonal analysis for all over India in both short term (15 years) and long term (32 years). They find a diminished trend in pan evaporation and potential evapotranspiration all over India. Lin et al. (2018) analyzed the spatiotemporal trend of global vegetation and its connection with some anthropogenic forces (GHG) and the influences of ENSO, AO, and AMO on vegetation with the help of NDVI. This analysis showed an increasing trend Throughout Europe and other land areas. In high northern latitudes, NDVI is influenced by temperature. Still, in dry and semi-arid regions, it's influenced by water, and East and southern Asia, as well as the Amazon, is influenced by radiation. Previous studies analyzed Climate change as a local driver of vegetation change. The climate is determined by precipitation, radiation, and temperature. Temperature dominates in arid and semi-arid zones; Tropical rainforests are the only areas where radiations are the limiting factor. This study aimed to examine the long-term mean and inter-annual variation of vegetation cover and ET components over the Indian region and their relationship.

## Study Area

India is located in the tropics 6°-38°N; 68°-98°E. Its vegetation and ecosystems are known for their diversity and climatic variability. The climate of India is divided into four seasons. The southwest monsoon season lasts from June to September, the post-monsoon season lasts from October to November, the winter season lasts from December to February, and the pre-monsoon season lasts from March to May. The southwest monsoon season brings warm and humid weather. The country receives 80% of its annual rainfall during this time. This is a cold and dry period during the northeast monsoon; however, significant amounts of rain recorded in the southeast of the country are primarily dry and moderately

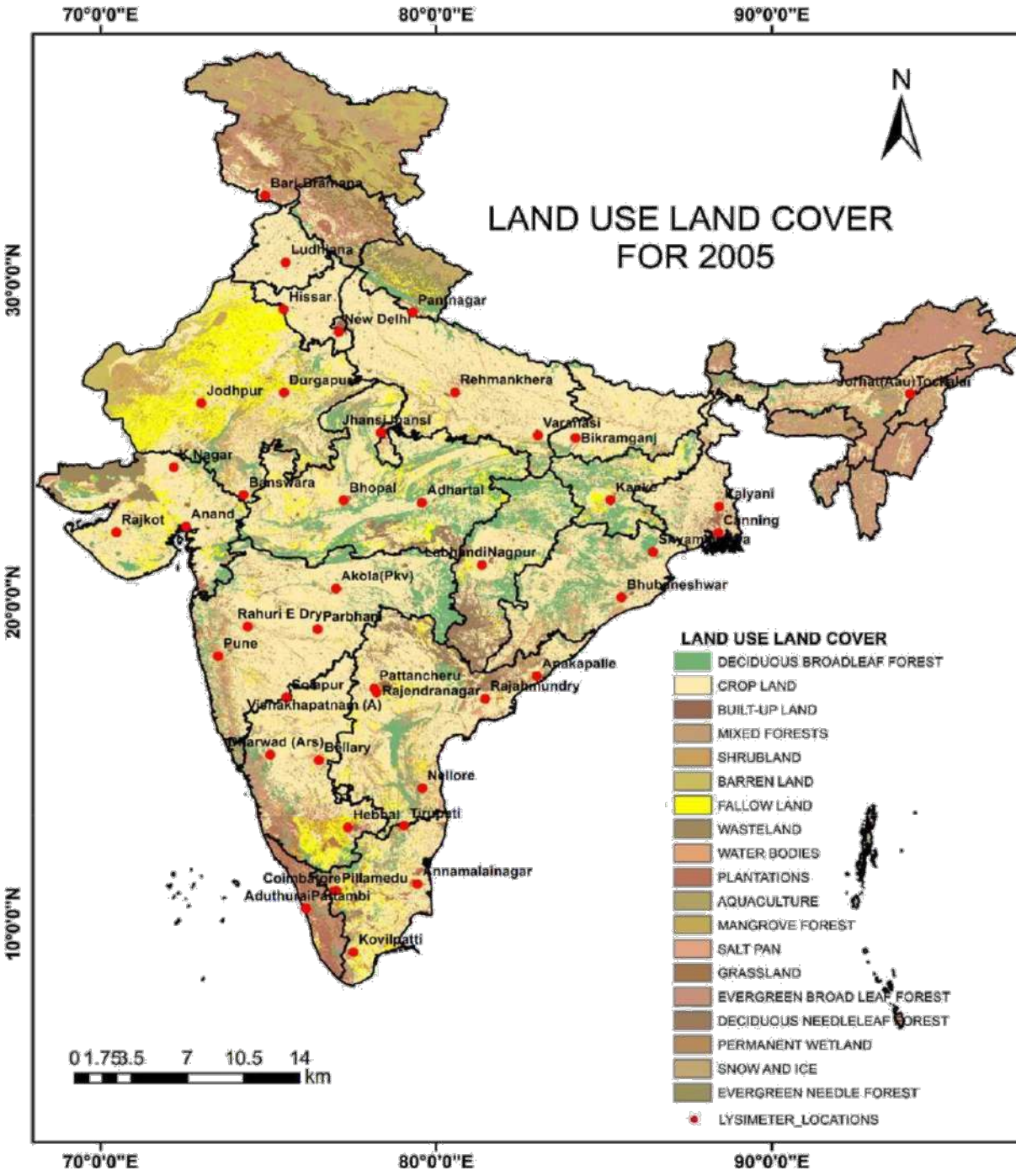


Fig. 1: Land use land cover types derived for 2005 (Roy et al. 2015, Meiyappan et al. 2016). Lysimeter sites in India are indicated in red circles.

warm during the two inter-monsoonal periods. A typical annual temperature varies by latitude, with humid regions experiencing 25°C and arid regions experiencing 45°C. Throughout the country, the latitudinal zonation of vegetation is caused by climate variability. The country's most common vegetation types are broadleaf forests, mixed forest types, grasslands, short woods and meadows, and desert steppe cover the deserts and semi-desert regions (Fig. 1).

The country is divided into 29 states and seven union territories. As of 2021, there are 748 districts within states and territories. In terms of population, There are 1.38 billion people in India, among the world's second-largest population. Agriculture provides the primary source of income for over 70% of rural households.

## MATERIALS AND METHODS

In the absence of in-situ ET observations, we have used meteorological observation-driven global reanalysis data on ET for this study.

### Normalized Difference Vegetation Index (NDVI)

The NDVI estimates the amount of light absorbed by vegetation over the land's surface. NASA Goddard Space Flight Center provides future NDVI updates and this NDVI log. This www provides NDVI data in various spatial and temporal resolutions. The data version of the current www page is the monthly average data for 1-degree longitude and latitude.

We calculated net CDF for this data and calculated the mean and the standard deviation for (the 1981-2001 AVHRR) from the NASA platform (http://research.jisao.Washington.edu) and the Moderate Resolution Imaging Spectroradiometer (MODIS, 2002-2015). Definitions of NDVI: A ratio between the reflected solar energy an incident leaf receives in the red spectrum band through the chlorophyll and the reflected solar energy reflected through the spongy mesophyll the plant emits near-infrared light. It is calculated as:

$$NDVI = NIR\text{-}RED/NIR+RED$$

The measurement of crop production has been based on an integrated series of NDVI during the growing season and how these affect the overall health and growth of the plant, water stress, and photosynthetic activity.

### GLDAS 2.0

Monthly evapotranspiration and its components (transpiration, bare soil evaporation, and canopy evaporation) data (1981-2010; at 0.25 x 0.25 resolution) from the NASA Global Land Data Assimilation System. Princeton's meteorological forcing inputs are entirely used in Version 2.0 (Goroshi et al. 2017); Trend analysis of evapotranspiration over India: Observed from long-term satellite measurements). We are using these data sets to study evapotranspiration and its components. (https://disc.gsfc.nasa.gov/uui/datasets/GLDAS_NOAH025_M_V2.0/)

### GPCP 2.2

From January 1979 to the present, the Global Precipitation Climatology Project (GPCP) version 2 monthly precipitation analysis is available at 2.5° latitude * 2.5° longitude resolution. We calculated NetCDF for this data, mean, standard deviation, and long-term changes, including the trend of seasonal precipitation ($mm.day^{-1}$) over India for 1981-2015. At NASA Goddard Space Flight Center's Mesoscale Atmospheric Processes Laboratory - Atmosphere, the GPCP combined precipitation data were calculated as part of the GEWEX program.

GrADS (Grid Analysis and Display System), Earth science data can easily be accessed, manipulated, and visualized with GrADS. GrADS has 2 data models to handle gridded and station data. GRADS uses a five-dimensional data environment with four conventional dimensions (longitude, latitude, vertical altitude, and time) and one optional fifth dimension for grids, which is typically not used but could be used for ensemble applications. The GrDAS is open-source software, and FORTRAN programming has been used to perform different analyses. Long-term means characteristics and interannual variability of the climate, vegetation, and ET data have been analyzed. Correlation and regression analysis were performed to understand how climate and anthropogenic variables relate to evapotranspiration.

## RESULTS AND DISCUSSION

The boreal summer monsoon season, comprising of the month approximately 80% of India's annual precipitation, occurs from June to September. (Fig. 2) Mean and long-term changes, including the trend of seasonal precipitation in $mm.day^{-1}$ over India). The southwest monsoon season begins in June and ends in September. For the Indian Subcontinent, the southwest monsoon is a major rainy season. The summer monsoon period is when the southwest monsoon holds off over the country. This is the time when nearly 80% of the Indian rainfall occurs. Maximum rainfall during the season reaches the western ghats, parts of central and eastern India, the foothills of the Himalayas, and the northeastern region. The southwest monsoon arrives by the end of May over the southern tip of the peninsula. During the beginning of the monsoon season, there is an explosive increase in rainfall. As the storm progresses inland, By mid-July, it has covered the whole country. By the beginning of September, it starts to pull away from the extreme northwest, gradually moving southward. Because of its location on the eastern (eastward) side of the western ghats, Tamil Nadu is considered a rain shadow region. It rains most often over the southernmost part of the state.

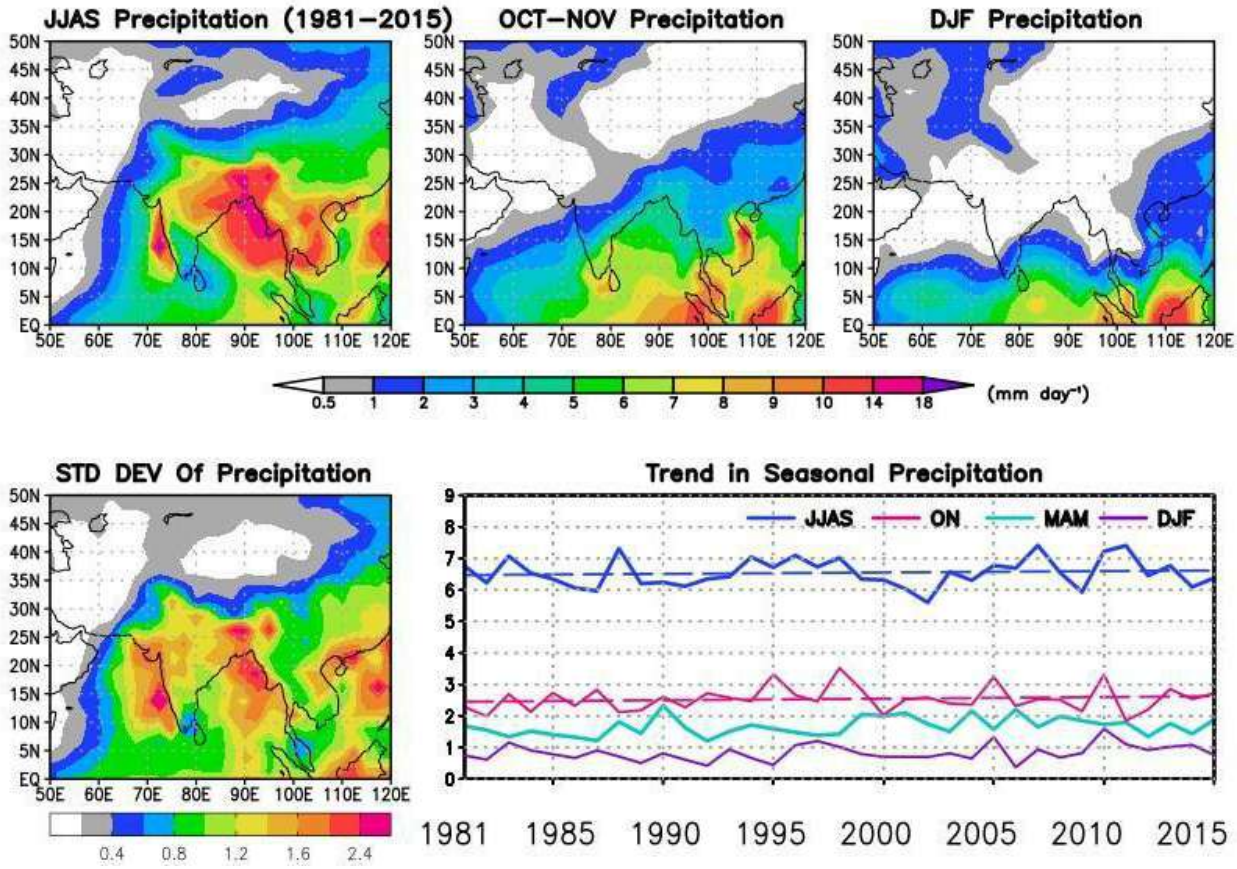


Fig. 2: (Top) Mean, (bottom) interannual standard deviation and long–term changes, including the trend of seasonal precipitation (mm.day$^{-1}$) over India.

Fig. 3 shows an analysis of the mean seasonal distribution of ET over three seasons - southwest summer monsoon season (June to September), Post monsoon season (October to November), and northeast monsoon (December to February) for the study period 1981-2015. During different seasons, different spatial patterns can be observed in India. The average ET during the southwest summer monsoon was 1.8 mm.day$^{-1}$ but ranged from 1 to 3.2 mm.day$^{-1}$ in more than a third of the pixels in the country. ET was more significant than 1 mm.day$^{-1}$. During JJAS, the highest amounts of ET were seen when crops (Indo - Gangetic plains, eastern peninsula) and forests prospered, topsoil moisture was adequate, and the weather was ideal. The magnitude of the ET further grew during the autumn or mid-fall season (October-November) and reached its maximum level in all parts of the country. ET was more than 1.6 mm.day$^{-1}$ in more than 80% of pixels, an average of 2.2 mm.day$^{-1}$. In addition to this high ET, most deciduous vegetation had peak growth during this time; soil moisture was adequate, and the weather was congenial. The ET varied between 0-3.4 mm.day$^{-1}$ during DJF, with an average of 1.2 mm.day$^{-1}$. This season, more than 30% of pixels showed ET<1 mm.day$^{-1}$. A deciduous forest experiencing leaf fall, low crop production, dry weather, and little rain during the northeast winter monsoon are the primary causes of the low magnitude of the season. However, ET was high (1-1.6 mm.day$^{-1}$) in the Indo-Gangetic plains and Tamil Nadu compared with other agricultural areas in the country. It was caused mainly by the peak growth stages of winter crops.

Fig. 4 shows the inter-seasonal variations and trends in ET over India during three seasons (JJAS, ON, DJF) over 30 years (1981-2010). ET increases during the northeast winter monsoon season. Meanwhile, a decreasing trend was observed during the summer southwest monsoon and the fall post-monsoon. ET was higher during the northeastern winter monsoon during the past decade due to improved management of cropping in India's arid and semi-arid regions through irrigation and crop intensity. Due to higher aerosol loads and cloudiness, there has been an increase in solar dimming over major parts of India, and southwest monsoon and post-monsoon activity have decreased over the past years (Padmakumari & Goswami 2010).

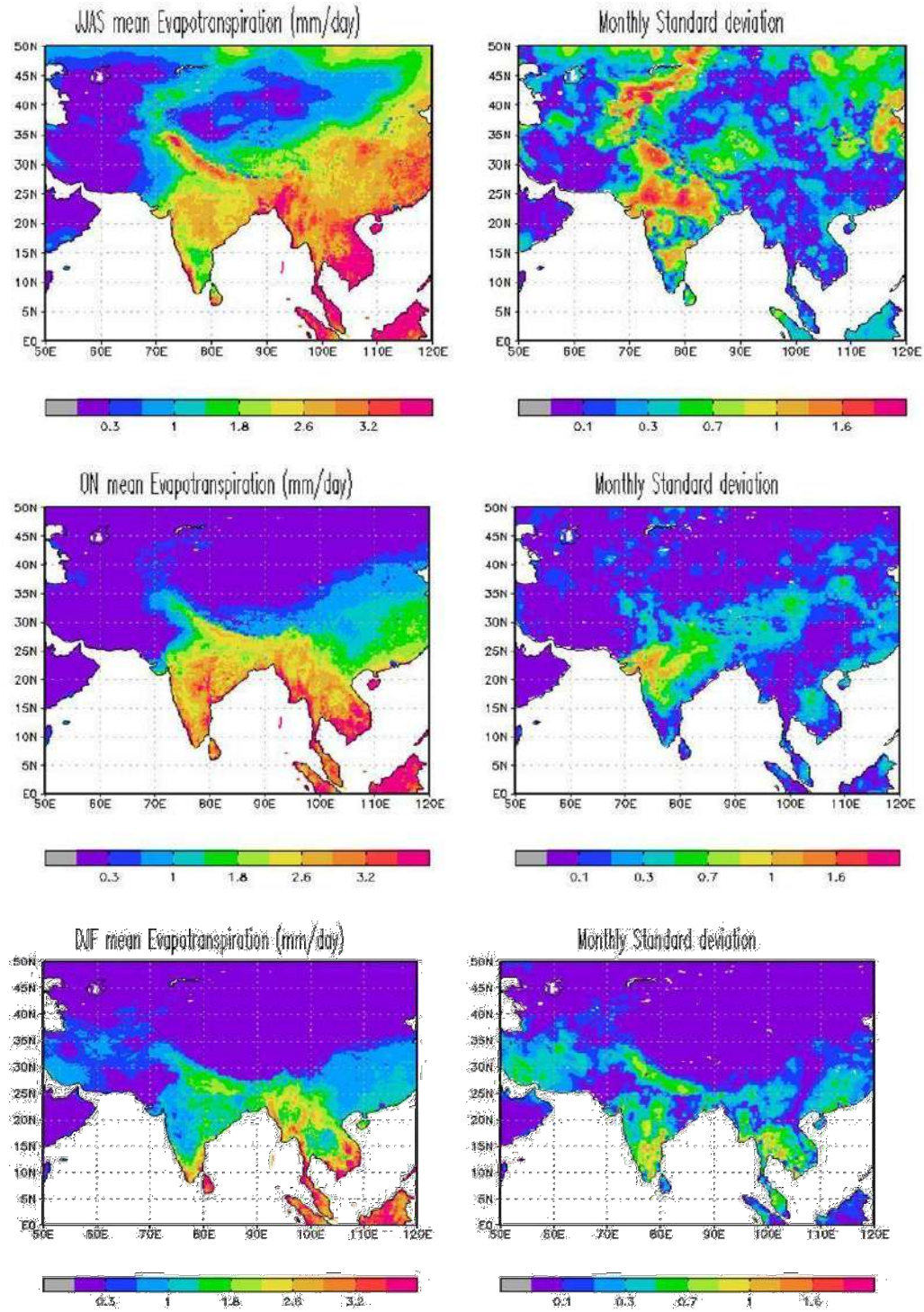


Fig. 3: (Left) Mean and (right) interannual standard deviation of monsoon (June- September), post-monsoon (October – November), and winter season (December-February) evapotranspiration (mm.day$^{-1}$) over India.

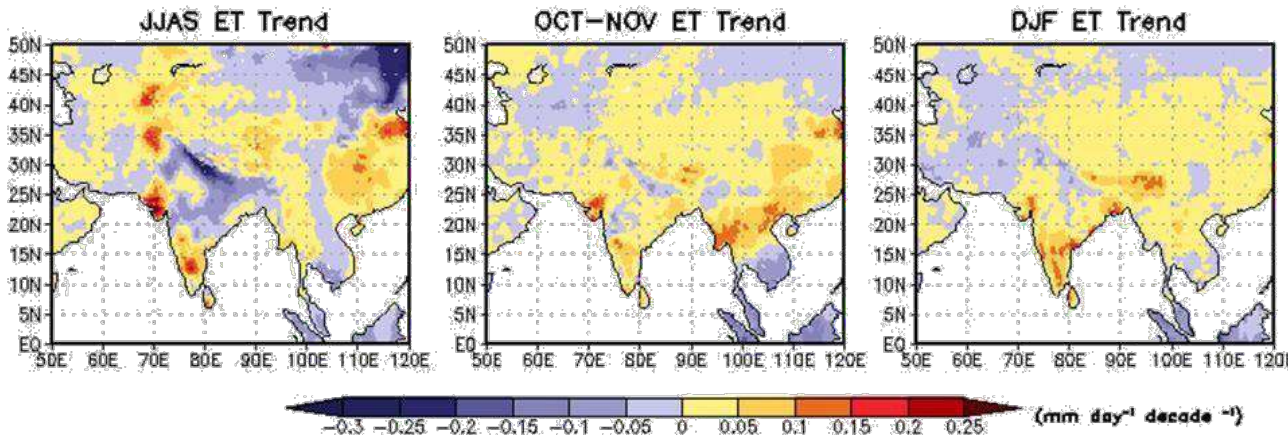


Fig. 4: Trend (1981-2010) in total evapotranspiration (ET, mm.day$^{-1}$decade) over India.

For the summer season, the NDVI chart showed less than 0.3 in most places and more than 0.3 in the northeast. However, the northwest and western ghats had a low vegetation index, around 0.15, compared to other areas of the country. Fig. 5 shows the vegetation cover has recovered over many parts of the country (southwest monsoon), varying from 0.1 (northwest part) to a maximum of 0.5 (northeast part). The vegetation pattern changes from hot weather to the southwest monsoon season. The two branches of the monsoon trough merge in the region for more rainfall across India, resulting in fairly widespread vegetation conducive to better harvesting. The eastern ghats and eastern parts of the Deccan plateau have NDVI values of 0.4, possibly attributed to the southwest monsoon currents along the Arabian sea and the Bay of Bengal. It is a slower process that the monsoon withdraws from northwest India and leaves the rest of the country by the end of November. By October, the northeast winds cause the northeast monsoon to develop over the peninsula's southern half. Monsoon retreat usually follows the withdrawal of the southwest monsoon. Thus the impact of retreat season on vegetation cover can be seen in the western ghats as NDVI increases above 0.4, whereas at the time of southwest monsoon season, it is below 0.4. Tamil Nadu and Kerala receive rain during this season (Fig. 2), leading to good vegetation in some western ghats. In general, NDVI data showed a positive trend in the country. India's northeastern region of India, namely the Assam region and surrounding area climate, is always wet and humid, and the vegetation index is always the highest (NDVI > 0.6). In parts of India, the NDVI has gradually decreased by winter (DJF). Parts of the western ghats and the Gangetic plains are experiencing reduced vegetation (NDVI < 0.3). The northwest part of the country is covered in deserts and semi-arid regions with a vegetation index of under 0.2. In parts of the Gangetic plains, there is low vegetation (NDVI<0.3); in the northeast, the NDVI is highest over the country and is more than 0.6.

The spatial pattern of NDVI and ET during the monsoon season also appears to follow that of rainfall, which is quite expected. However, ET's components, bare soil evaporation, transpiration, and canopy evaporation, follow different spatial patterns in different months. Interestingly, there is much difference in the spatial pattern of interannual variability of the monthly parameters over the Indian region. It can be inferred that vegetation characteristics (e.g., NDVI) and other climatic factors, such as precipitation and air temperature, also determine the variability of monthly ET over the Indian region. This has been further quantified based on correlation and regression analyses.

On the contrary, precipitation received during the pre-monsoon season (March through May) is relatively low except during severe thunderstorm events (Nor'westers) occurring over the eastern region. Monthly and seasonal temperatures are the highest during this season. As a result, the evaporative demand of the atmosphere is very high. The relative impact of the three components on total ET is characteristically different than that observed during the summer monsoon. The relative contribution of soil evaporation to ET is stronger in northern Indian states, whereas agriculture is mainly supported by irrigation activity. Though the sources of NDVI datasets before and after the year 2000 are different, one can notice significant changes not only in the spatial distribution of NDVI but also in precipitation and temperature. Our analysis has revealed interesting facets of the relationship between climatic variables and NDVI with ET during the decades before and after 2000.

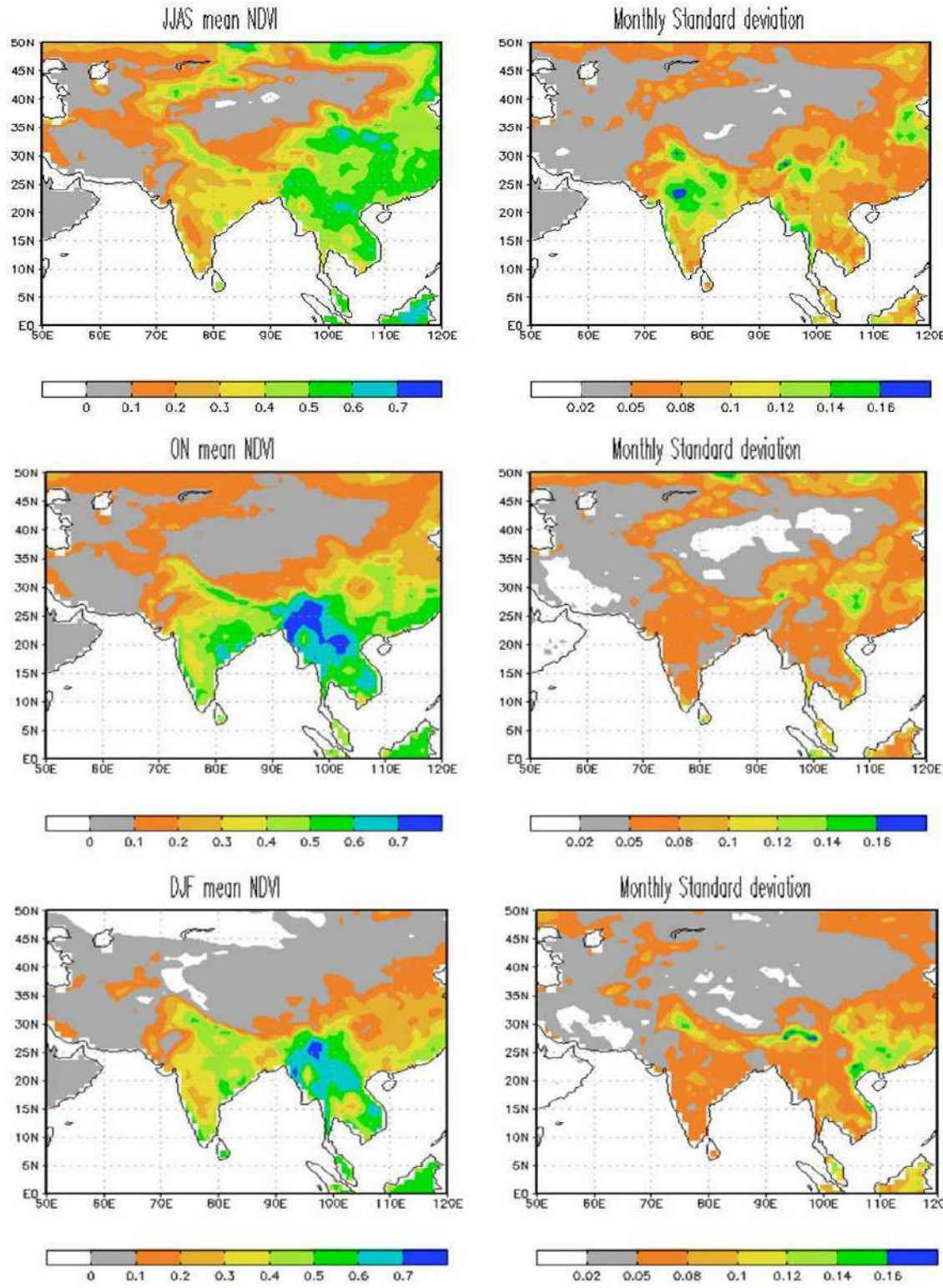


Fig. 5: (Left) Mean and (right) inter-annual standard deviation of the monsoon season (June-September), the post-monsoon season (October-November), and the winter season (December-February) NDVI over India.

## CONCLUSION

A study has been conducted to investigate the impact of climate change and LULC on ET and its three components (evaporation, transpiration, and canopy interception) over the Indian region from 1981 till the present time. It is noted that there is a distinct difference in the characteristics of vegetation and climate and three components of ET and their relationship during the premonsoon seasons, as brought out by detailed statistical analysis and tests of significance. The monsoon season increases precipitation, and canopy evaporation increases along with NDVI, followed later by transpiration variability in surface net radiation, controlled by cloud cover, aerosols, and surface albedo changes, which also play an important role in controlling total ET. At the same time, ground evaporation is strongly correlated with precipitation. In this analysis, we find out 1. With increased precipitation during the monsoon season, soil evaporation is found to increase at first, along with an increase in NDVI, followed by canopy evaporation and transpiration. 2. It is noted that changes in precipitation and LULCC over the Indian region have contributed significantly to the changes in ET in different seasons. 3. As variability in surface net radiation also plays an important role in controlling changes in total ET, it is being investigated.

Another is suggested that further detailed study on the daily time scale with in-situ and remote sensing data can bring more interesting insight regarding these processes. An attempt is further made to demonstrate the impact of climatic changes and ET on food grain production over the Indian region.

## ACKNOWLEDGMENT

The authors thank the Hon'ble Vice-Chancellor, University of Allahabad, and the Coordinator, K. Banerjee Centre of Atmospheric and Ocean Studies, for their encouragement and for providing all the facilities for conducting this study.

## REFERENCES

Chattopadhyay, N. and Hulme, M. 1997. Evaporation and potential evapotranspiration in India under conditions of recent and future climate change. Agric. Forest Meteorol., 87: 55-73

Goroshi, S., Pradhan, R., Singh, R. and Singh, K.K. 2017. Trend analysis of evapotranspiration over India: Observed from long-term satellite measurements. J. Earth Syst. Sci., 126: 113. https://doi.org/10.1007/s12040-017-0891-2.

Halder, S., Saha, S.K., Dirmeyer, P.A., Chase, T.N. and Goswami, B.N. 2016, Investigating the impact of land-use land-cover change in Indian summer monsoon daily rainfall and temperature during 1951-2005 using a regional climate model. Hydrol. Earth Syst. Sci., 205: 1765-1784. doi: 10.5194/hess-20-17652016

Lin, Z., Aiguo, D. and Bo, D. 2018. Changes in global vegetation activity and its driving factors during 19822013; Agricultural and Forest Meteorology, 249: 198-209

Padmakumari, B. and Goswami, B.N. 2010 Seminal role of clouds on solar dimming over the Indian monsoon region; Geophys. Res. Lett., 37.

Rajeevan, M.N. and Nayak, S. (eds). 2017. Observed Climate Variability and Change Over the Indian Region. Springer, Singapore, pp.305. doi: 10.1007/978-981-10-2531-0

Rodell, M., Velicogna, I. and Famiglietti, J.S. 2009. Satellite-based estimates of groundwater depletion in India. Nature, 460: 999-1003.

Rohini, P., Rajeevan, M.N. and Srivastava, A.K. 2016. On the variability and increasing trends of heat waves over India. Sci. Rep., 6: 26153. doi: 10.1038/srep26153

Roy, S.S., Mahmood, R., Niyogi, D., Lei, M., Foster, S.A., Hubbard, K.G., Douglas, E.M. and Pielke, R.A. 2007. Impacts of the agricultural green revolution induced land use changes on air temperature in India. J. Geophys. Res., 112: 21108. doi:10.1029/2007JD008834

Roy, S.S., Roy, A., Joshi, P.K., Kale, M.P., Srivastava, V.K., Srivastava, S.K., Dwivedi, R.S., Joshi, C., Behera, M.D. and Meiyappan, P. 2015. Development of decadal (1985–1995–2005) land use and land cover database for India. Remote Sens., 7: 2401-2430.

Seneviratne, S., Nicholls, N., Easterling, D. and Goodess, C.M. 2012. Changes in Climate Extremes and Their Impacts on the Natural Physical Environment: An Overview of the IPCC SREX Report. In Field, V., Barros, T.F., Stocker, D., Qin, D.J., Dokken, K.L., Ebi, M.D., Mastrandrea, K.J., Mach, G.K., Plattner, S.K., Allen, M., Tignor, M. and Midgley, P.M. (eds.), Managing the Risks of Extreme Events and Disasters to Advance Climate Change Adaptation (SREX), Cambridge University Press, Cambridge, pp. 12566-12572.

Stocker, T.F., Qin, D., Plattner, G.K., Tignor, M., Allen, S.K., Boschung, J., Nauels, A., Xia, Y., Bex, V. and Midgley, P.M. (eds.). 2013. The Physical Science Basis: Contribution of Working Group I to the Fifth Assessment Report of the Intergovernmental Panel on Climate Change. Cambridge University Press, Cambridge, New York, p. 533.

Nature Environment and Pollution Technology
An International Quarterly Scientific Journal

p-ISSN: 0972-6268
(Print copies up to 2016)
e-ISSN: 2395-3454

Vol. 22 | No. 1 | pp. 221-228 | 2023

Original Research Paper

https://doi.org/10.46488/NEPT.2023.v22i01.020

Open Access Journal

# Forecasting Particulate Matter Emissions Using Time Series Models

**S. Suresh†, M. R. Sindhumol, M. Ramadurai, D. Kalvinithi and M. Sangeetha**
Department of Statistics, University of Madras, Chepauk, Chennai-600005, Tamil Nadu, India
†Corresponding author: S. Suresh; sureshstat22@gmail.com

**Nat. Env. & Poll. Tech.**
**Website: www.neptjournal.com**

*Received:* 25-05-2022
*Revised:* 17-07-2022
*Accepted:* 19-07-2022

**Key Words:**
Particulate matter
$PM_{2.5}$
Forecast
ARIMA
LSTM
Prophet

## ABSTRACT

Environmental pollution is a serious concern nowadays with its disastrous impact on living organisms. In several types of pollution, Air pollution takes on a crucial role by directly affecting the respiratory system and causing fatal diseases in humans. Air pollution is a mixture of gaseous and particulate matter interweaved by different sources and emanating into the atmosphere. In particular, particle pollutants are critical in growing air pollution in India's main cities. Forecasting the particulate matter could mitigate the complications caused by it. The employment of a model to predict future values based on previously observed values is known as time series forecasting. In this paper, the $PM_{2.5}$ pollutant emission data recorded at the Kodungaiyur region of Chennai city were forecasted using three-time series models. The standard ARIMA model is compared with the deep learning-based LSTM model and Facebook's developed Prophet algorithm. This comparison helps to identify an appropriate forecasting model for $PM_{2.5}$ pollutant emission. The Root Mean Squared Error (RMSE) acquired from experimental findings is used to compare model performances.

## INTRODUCTION

Air is an inhalable elixir and without it, life is out of the question. The contamination of air affects living beings significantly termed as air pollution. The combination of Gaseous and Particle elements are the primary sources of air pollution. Particulate matters are substances with a diameter of fewer than 10 microns that are categorized as highly prioritized pollutants. Particulate Matters generated from interconnected sources such as protracted road constructions, infrastructural activities, big dumpsites, and those particles from automobile exhaust have been a major cause of pollution in cities in recent years. Substantially, particulate matter is a complex mixture of metals, nitrates, sulfates, dust, water, and tire rubber. Domingo & Rovira (2020) mention sulfur dioxide, particulate matter, and oxides of nitrogen have an immediate and profound effect on human health. These pollutants can be directly emitted from different sources and have different chemical compositions. Chen et al. (2019) discussed Fugitive road dust (FRD) particles which are discharged from vehicular traffic, combustion of gasoline, oil, diesel fuel, and wood produce most of the particulate matter pollution found in outdoor air. Lo et al. (2016) and Fang et al. (2019) brought up the association between daily exposure to particulate matter and respiratory mortality. Buoli et al. (2018) stated that the actual risk of detrimental effects depends on one's state of health. But on the contrary, Sivarethinamohan et al. (2020) argued that polluted air can cause critical problems in healthy people, including respiratory irritation or breathing difficulties during exercise or outdoor activities. Therefore, it is inevitable to combat air pollution.

The research conducted by Pavlos et al. (2005) suggests that setting up continuous monitoring stations at excess pollution-emitting areas would help to restrain air pollution. The Monitoring stations give the air pollution data recorded at different time stamps which are known as time series data. The Methods for studying time series data to extract useful statistics and other aspects of the data are referred to as time series analysis. The Time series analysis carried out by Bai et al. (2018) overviewed different forecasting models to predict the future values of air pollution. The forecasting also gives insights to track the pattern which helps us to appropriate

**ORCID details of the authors:**

**S. Suresh**
https://orcid.org/0000-0003-1894-8548
**D. Kalvinithi**
https://orcid.org/0000-0003-2928-5057
**M. Sangeetha**
https://orcid.org/0000-0003-0450-5287
**M. Ramadurai**
https://orcid.org/0000-0001-7067-8827

actions against the worsened environment. Several methods were experimented with in a wide range of studies to identify suitable forecasting models to predict air pollution. Gourav et al. (2020) utilized the monitoring stations data obtained from one of the highly polluted capital cities, Delhi, and forecasted it using the ARIMA model to make recurrent decisions makings. Jai Shankar et al. (2010) discussed the model selection for a given problem using the ARIMA process which can be supported by diagnostic checking and error analysis. Abhilash et al. (2018) and Claudio et al. (2018) also used the ARIMA model to forecast air pollution. The state-of-art deep learning technique is also used to forecast pollutant emissions by considering it as sequential data. Chang et al. (2020) Liu et al. (2020) and Alghieth et al. (2021) took existing pollutant data as sequential data and forecasted it using the Long Short Term Memory model, a type of Recurrent Neural Network. Shen et al. (2020) and Topping et al. (2020) conducted experiments on the non–linear pollutant data using the viable prophet algorithm works on the Generalized additive regressive model. Siami-Namini et al. (2018) and Peter et al. (2019) compared ARIMA and LSTM models in their research works. The ARIMA model and Prophet algorithm were also compared in the experiments conducted by Samal Krishnan et al. (2019) and Ziyuan (2019). The findings of Nath et al. (2021) reflect that the statistical models outperform the deep learning methods.

In the event of health vulnerability due to $PM_{2.5}$ at Kodungaiyur in recent times, as evidence found and discussed by Krishnan et al. (2020), the major dumpsite of Chennai city is considered as the study area. Owing to numerous small-scale industries, the locality also holds commuters from outside the area on a daily basis which causes more traffic congestion. Nadeem et al. (2020) argued how the poorest quality of air in a single locality affects an entire city. These pieces of literature show, the Kodungaiyur region has a substandard environment to breathe due to its highest exposure to particulate matter of diameter less than 2.5 microns. Moreover, it is complex to understand which forecasting method predicts the future $PM_{2.5}$ with high accuracy. Thus, the ARIMA model, Prophet algorithm, and LSTM model were adopted in this study for forecasting $PM_{2.5}$ emissions. This work aims at forecasting $PM_{2.5}$ emissions using a suitable model. The performance of the models was estimated using root mean squared error.

In this article, three established forecasting methods models were applied to the time series data of $PM_{2.5}$ emissions and the results were compared. This experimentation shows, the standard ARIMA model of order (3,1,1) gives the best fit for predicting the observations with a low error rate when compared to other models taken for study. Using the ARIMA model, the future values of 6 months are forecasted and the comparative results were shown.

This paper is organized as follows: The second section of the paper describes the data utilized. The third section has three sub-sections that explain the methods adopted in this study. The fourth section put forth the outcomes of the experimental results carried out on three different methods. The final and concluding section discusses the recommendation of a suitable model for air pollutant forecasting in a given locality and highlights several causes that led to worsening air quality which can be treated carefully in the near future.

## MATERIALS AND METHODS

Kodungaiyur is an industrial neighborhood located in the northern part of Chennai city. Day-wise data on $PM_{2.5}$ for the Kodungaiyur area was collected from Tamil Nadu Pollution Control Board for the period from 1st January 2019 to 31st December 2022. The data contain the variables date and $PM_{2.5}$ with 1096 observations.

### Forecasting Methods

The study employs three forecasting methods, the ARIMA model, Recurrent Neural Network's Long Short Term Memory algorithm, and Facebook's Prophet algorithm.

### ARIMA Model

The Autoregressive Integrated Moving Average is a model of regression type where the predictors contain lags of the dependent variable and/or forecast errors. The linear equation for the ARIMA model is as follows

$$y_t = C + \emptyset_1 y_{t-1} + \emptyset_2 y_{t-2} + \cdots + \emptyset_p y_{t-p} + \varepsilon_t \quad \ldots(1)$$

$$y_t = C + \varepsilon_t - \theta_1 \varepsilon_{t-1} - \theta_2 \varepsilon_{t-2} - \cdots - \theta_q \varepsilon_{t-q} \quad \ldots(2)$$

$$y_t = C + \emptyset_1 y_{t-1} + \emptyset_2 y_{t-2} + \cdots + \emptyset_p y_{t-p} + \varepsilon_t - \theta_1 \varepsilon_{t-1} - \theta_2 \varepsilon_{t-2} - \cdots - \theta_q \varepsilon_{t-q} \quad \ldots(3)$$

whereare $\emptyset_1, \emptyset_2, \ldots \emptyset_p, \theta_1, \theta_2, \ldots, \theta_q$ AR and MA coefficients respectively and C is the intercept.

Equation (1) is for a $p^{th}$ order autoregressive (AR) model, equation (2) is a $q^{th}$ order moving average (MA) model, and equation (3) is the equation for an ARIMA (p, d, q) model.

Several combinations of AR(p), I(d), and MA(q) were applied to the obtained time series data and finally, the model with comparatively low AIC value is considered for forecasting.

**Prophet Model**

The Prophet model relies on Generalised Additive Regression Model which is highly suited for non–linear repressors. The Prophet is a decomposable time series model with four main components,

- The trend of a piecewise linear or logistic growth curve is represented in equation (4). Prophet detects changes in trends automatically by selecting change points from the data.
- A yearly seasonal component represented by a Fourier series represented in equation (5)
- Dummy variables are used to create a weekly seasonal component.
- A list of important holidays submitted by users is given in equation (6)

$$g(t) = \frac{C_t}{1+exp(-k+a(t)^T\delta)(t-(m+a(t)^T\gamma)))} \quad \ldots(4)$$

$$s(t) = \sum_{n=1}^{n}\left( a_n cos\left(\frac{2\pi nt}{P}\right) + b_n sin\left(\frac{2\pi nt}{P}\right)\right) \ldots(5)$$

$$h(t) = Z(t)k \quad \ldots(6)$$

The combined equation turns out to be,

$$y(t) = g(t) + s(t) + h(t) + \epsilon_t \quad \ldots(7)$$

where $\epsilon_t$ in equation (7) is the error term.

**LSTM Model**

A long short-term memory is a type of recurrent neural network. The output of the previous step is used as input in the current step in RNN. Long-term dependency is the issue of RNN addressed, in which the RNN is unable to predict words stored in long-term memory but can make more accurate predictions based on current data. RNN does not provide an efficient performance as the gap length rises. By default, the LSTM can keep the information for a long time. It is used for time-series data processing, prediction, and classification. The LSTM features (Fig. 1) a chain structure with four neural networks and various memory blocks known as cells.

The cells store information, whereas the gates manipulate memory. The model has three gates.

(a) **Forget Gate:** The forget gate deletes information that is no longer useful in the cell state. Two inputs, $x_t$ (at-the-time input) and $h_{t-1}$ (previous cell output) are fed into the gate and multiplied with weight matrices before bias is added. The result is fed into an activation function, which produces a binary output. If the output for a specific cell state is 0, the information is lost; if the output is 1, the information is saved for future use.

(b) **Input Gate:** The input gate is responsible for adding useful information to the cell state. First, the information is regulated using the sigmoid function, and the values to be remembered are filtered using the $h_{t-1}$ and $x_t$ inputs, similar to the forget gate. The tanh function is then used to generate a vector with values ranging from -1 to +1 that contains all of the possible values from $h_{t-1}$ and $x_t$. Finally, the vector and regulated values are multiplied to obtain useful information.

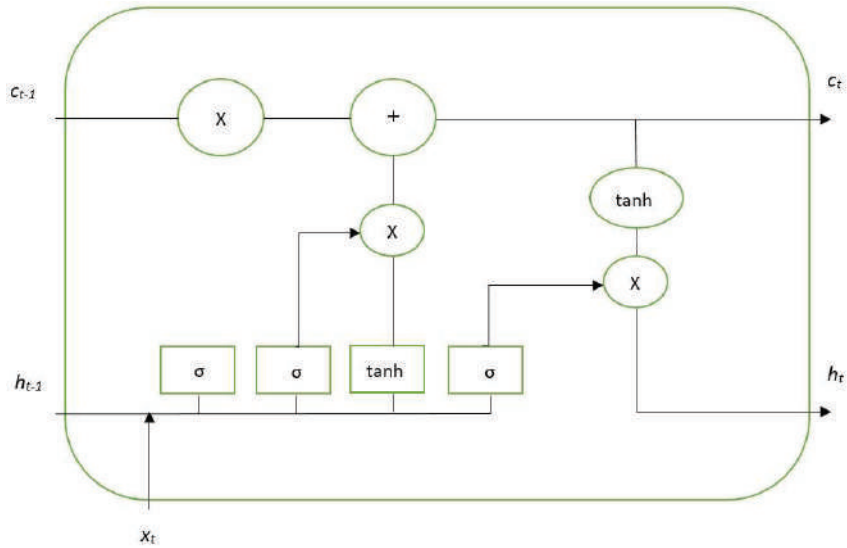


Fig. 1 Structure of an LSTM Cell.

(c) **Output Gate:** The output gate is in charge of extracting useful information from the current cell state and presenting it as output. To begin, a vector is created by applying the tanh function to the cell. The information is then regulated using the sigmoid function and filtered by the values to be remembered using $h_{t-1}$ and $x_t$ inputs. Finally, the vector values and the regulated values are multiplied and sent as output and input to the next cell.

The three methods are implemented and their empirical out-turns are stated in the following section.

## RESULTS AND DISCUSSION

In the experimental phase, several combinations of parameters attributed to each time series model were evaluated. The parameter estimation for individual methods gives the best models and is implemented to predict the observations.

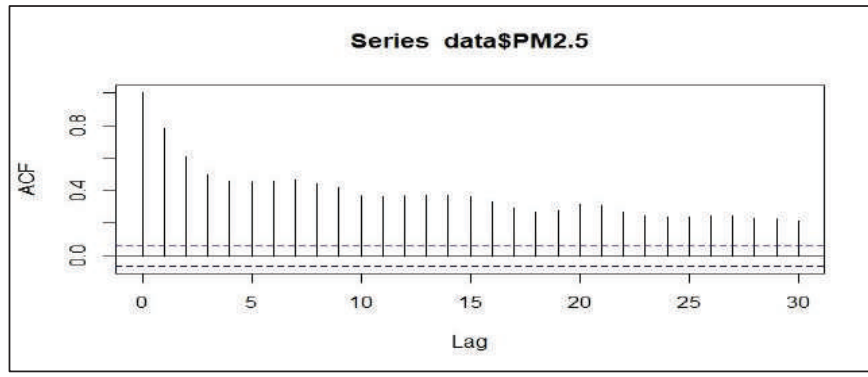


Fig. 2: ACF correlogram for $PM_{2.5}$ emission data.

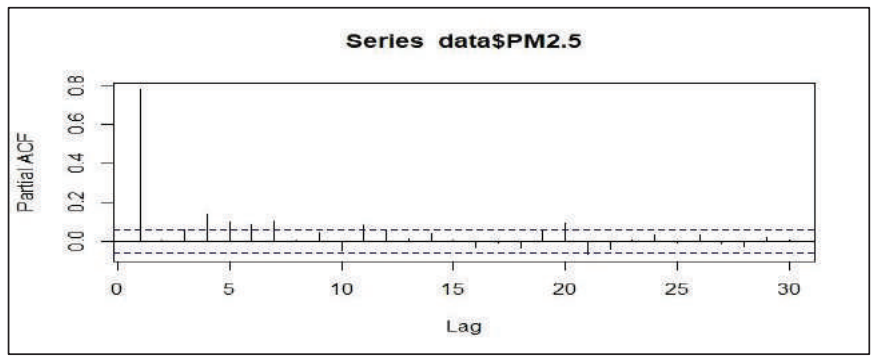


Fig. 3: PACF correlogram for $PM_{2.5}$ emission data.

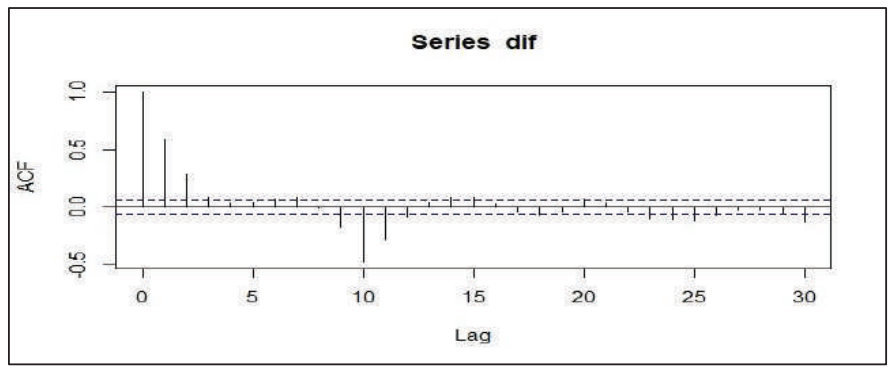


Fig. 4: ACF Correlogram for first differenced $PM_{2.5}$ emission data.

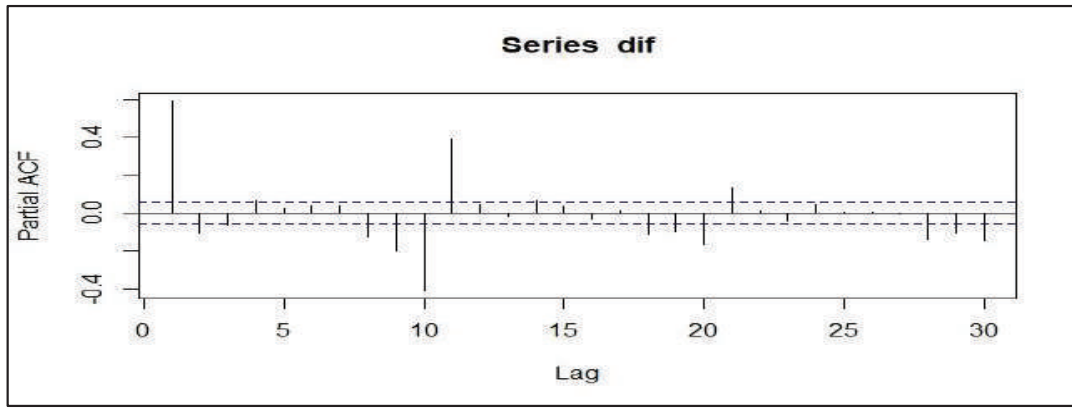


Fig. 5: PACF Correlogram for first differenced $PM_{2.5}$ emission data.

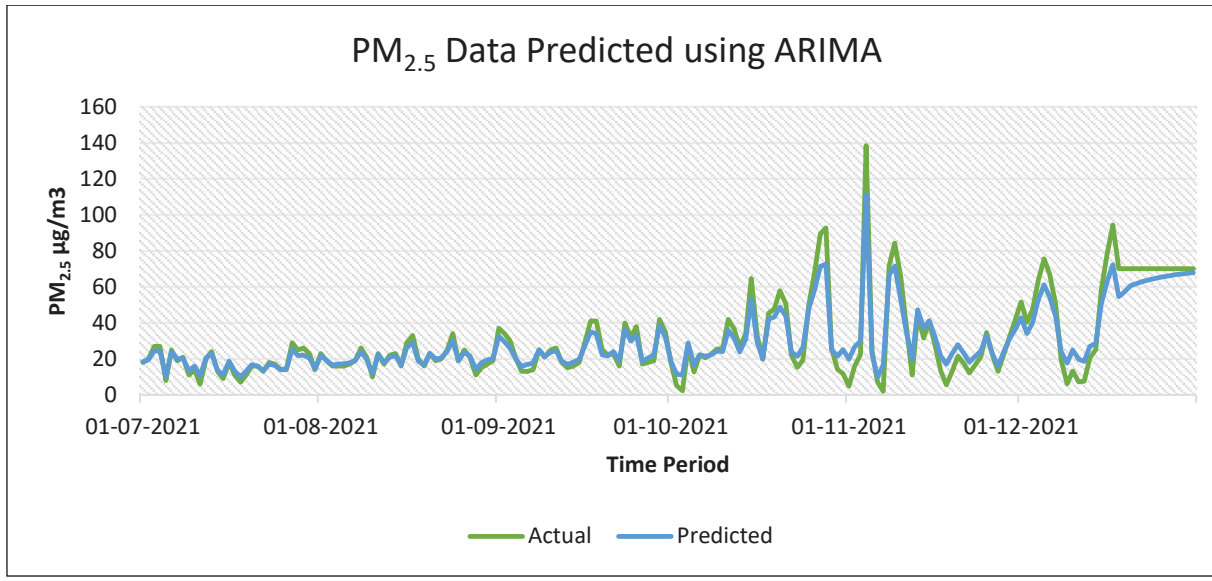


Fig. 6: $PM_{2.5}$ pollutant data predicted using ARIMA (3,1,1).

Based on the residual difference between the observed and predicted value, the error value for each model is calculated. Later, the $PM_{2.5}$ data is forecasted for 6 months (from 01-01-2022 to 30-06-2022). The identified models were stated in this section.

**Fitted ARIMA Model**

ACF and PACF Correlograms were plotted to identify the best ARIMA model for forecasting. The ACF plot gives the order of Moving Average (MA) and the PACF gives the order of Auto-Regressive (AR). In addition to that, the model is also tested for low Akaike's Information Criteria (AIC). The parameters *p, d, q,* and corresponding optimum AIC value give the tentative ARIMA model.

Fig. 2 and Fig. 3 show the ACF and PACF Correlograms plotted for $PM_{2.5}$ emission data, which indicates the non – stationarity of data. Hence the first differences in the data are taken for analysis.

Fig. 4 and Fig. 5 show the ACF and PACF plots for different $PM_{2.5}$ emission data. Fig. 4 indicates the MA (1) order. Fig. 5 shows that there are significant spikes at lags 1, 10, and 11 in the PACF indicating the order of AR to be 3. Therefore, for the obtained data, the model ARIMA (3,1,1) is performed for predicting the observations.

**Fitted Prophet Model**

The Prophet algorithm accounts for the change points, which influence the trend of the time series

data. The trend of the fitted values becomes flexible when the value for the range of the change point gets increased. The fitted Prophet model is displayed below.

```
# Initializing the Model
model=Prophet(interval_width=0.95, yearly_seasonality=True, weekly_sea
sonality=True, changepoint_prior_scale=2, changepoint_range = 0.8)
```

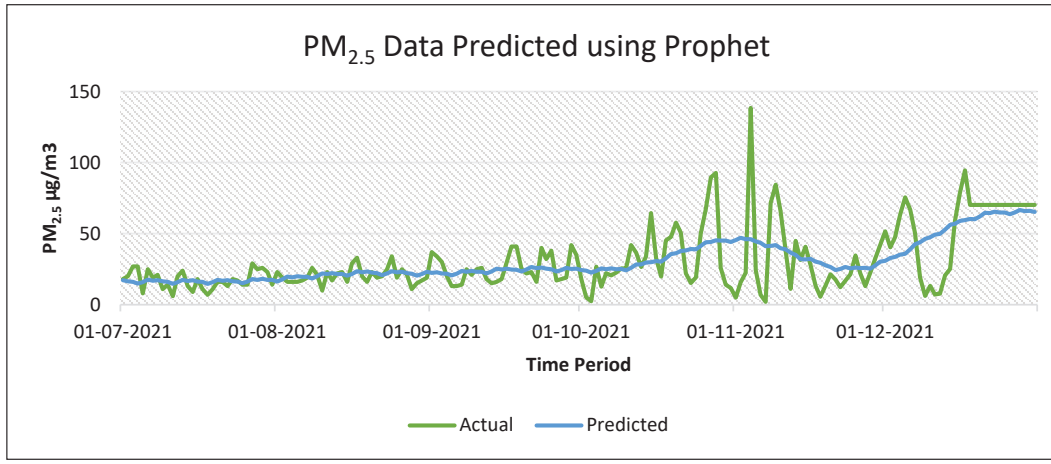


Fig. 7: $PM_{2.5}$ pollutant data predicted using Prophet model.

**Fitted LSTM Model**

The LSTM model is built on multiple layers comprised of two LSTM layers, one Dropout layer, and one Dense layer. The LSTM layers are counted under input layers and the Dense layer is termed the output layer. The role of the Dropout layer is to make the trivial input values as 0's. This Sequential model is used for predicting the observations present in $PM_{2.5}$ Pollutant data.

Based on the analysis, the actual values are compared with the predicted values of each model and the error rates were determined. Fig. 6, Fig. 7, and Fig. 8 show the line graph of $PM_{2.5}$ pollutant data observations and their predictions made by respective models which are plotted against time period. In this study, the estimated Root Mean Squared Error is used to obtain the error rates of fitted models which are shown in Table 1.

From Table 1, it can be inferred that ARIMA is found to be the best predicting model which has a low RMSE on comparing with the other models. Therefore, the ARIMA (3,1,1) model is used for forecasting the future values.

```
Model: "sequential"
_________________________________________________________________
 Layer (type)                 Output Shape              Param #
=================================================================
lstm (LSTM)                  (None, 7, 64)             16896

 lstm_1 (LSTM)                (None, 32)                12416

 dropout (Dropout)            (None, 32)                0

 dense (Dense)                (None, 1)                 33

=================================================================
```

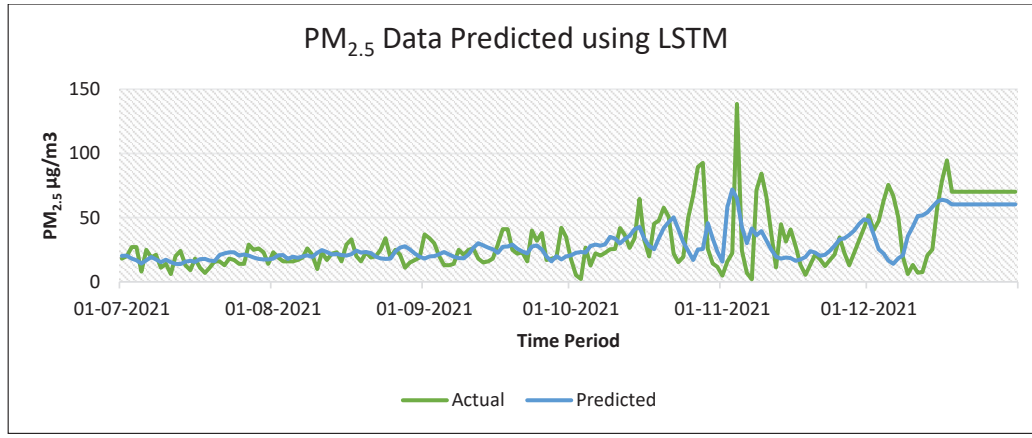


Fig. 8: $PM_{2.5}$ pollutant data predicted using LSTM model.

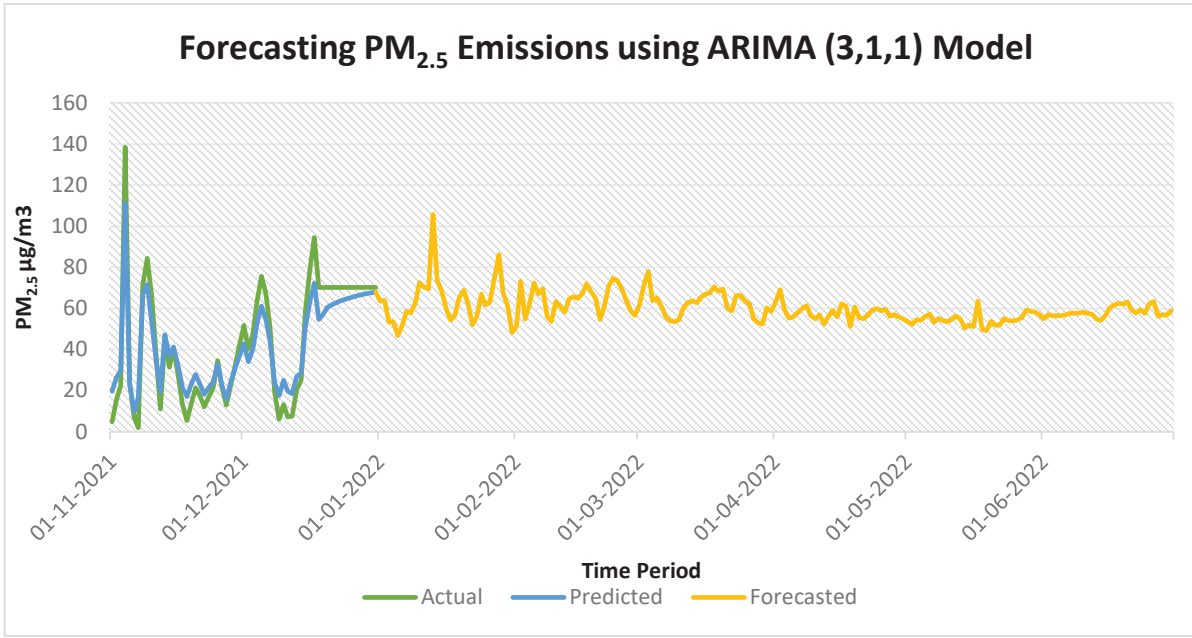


Fig. 9: $PM_{2.5}$ pollutant emissions forecasted using ARIMA(3,1,1) for 6 months.

Table 1: Error rates of the models implemented.

| MODELS | ARIMA | PROPHET | LSTM |
|---|---|---|---|
| RMSE | 4.33 | 11.17 | 12.45 |

Fig. 9 shows using ARIMA (3,1,1) model the $PM_{2.5}$ pollutant data is forecasted for future values from 01-01-2022 to 30-06-2022.

## CONCLUSION

The ARIMA model of order (3,1,1) turns out to be the well-suited model to predict the data with low error rates compared to the other models implemented. Using the suitable model, the forecast of $PM_{2.5}$ is computed shown in Fig 9. The forecast shows the month of January witnessed high emissions of $PM_{2.5}$ over 100 $\mu g.m^{-3}$ due to the Pongal festival. Fig 9 depicts that, the $PM_{2.5}$ emissions at

Kodungaiyur for the first six months of 2022 average around 60 $\mu g.m^{-3}$ which is the 24 h average of $PM_{2.5}$ as prescribed by CPCB. This forecast also manifests the scenario that the sources of air pollution are not only industrial and vehicular emissions but also the particulate matter emitted from unpaved roads, construction sites, and several indoor activities such as domestic burning and natural specks of dust. The performance of every forecasting model highly relies on the data used. For the recorded $PM_{2.5}$ emissions from the Kodungaiyur region, the ARIMA model is viable to use, which will assist policymakers in mitigating air pollution problems caused by particulate matter.

Further, as an extensive study, this research can be focused on the computation of the magnitude of the sources of particulate matter and their contribution to air pollution.

## ACKNOWLEDGEMENT

This research work is funded by Rashtriya Uchchatar Shiksha Abhiyan (RUSA2.0), Ministry of Human Resource Development, Government of India.

## REFERENCES

Abhilash, M.S.K., Thakur, A., Gupta, D. and Sreevidya, B. 2018. Time series analysis of air pollution in Bengaluru using ARIMA model. Amb. Commun. Comp. Sys. Adv. Intell. Sys. Com., 71: 696.

Alghieth, M., Alawaji, R., Saleh, S.H. and Alharbi, S. 2021. Air pollution forecasting using deep learning, Int. J. Online Biomed. Eng., 17(14): 50-64.

Bai, L., Wang, J., Xuejiao, M. and Lu, H. 2018. Air pollution forecasts: An overview. Int. J. of Env. Res. and Pub. Health, 15(4): 780.

Buoli, M., Grassi, S., Caldiroli, A., Carnevali, G.S., Mucci, M., Lodice, S., Cantone, L., Pergoli, L. and Bollati. V. 2018. Is there a link between air pollution and mental disorders? Environ. Int., 118: 154-168.

Chang, Y.S., Chiao, H., Abimannan, S., Huang, Y. and Tsai, Y. 2020. An LSTM-based aggregated model for air pollution forecasting. Atmos. Poll. Res., 11(8): 1451-1463.

Chen, S., Zhang, X., Lin, J., Huang, J., Zhao, D., Yuan, T., Huang, K., Kuo, Y, Jhia, Z., Zang, Z., Qiu, Y. and Xie, L. 2019. Fugitive road dust $pm_{2.5}$ emissions and their potential health impacts. Environ. Sci. Technol., 53(14): 8455-8465.

Claudio, G., Griselda, C.J., Breton, R.M.C. and Tepedion, C. ARIMA models application to air pollution data in Monterrey, Mexico. AIP Conf. Proceed., 82(1): 020041.

Domingo, J.L. and Rovira, J. 2020. Effects of air pollutants on the transmission and severity of respiratory viral infections. Environ. Res., 16: 187.

Fang, X., Fang, B., Wang, C., Xia, T., Boottai, M., Fang, F. and Cao, Y. 2019. Comparison of frequentist and Bayesian generalized additive models for assessing the association between daily exposure to fine particles and respiratory mortality: A simulation study. Int. J. Env. Res. Pub. Health, 16(5): 746.

Gourav, R., Jusleen, N., Preeti, J. and Rachna, J. 2020. Forecasting air quality of Delhi using ARIMA model. Adv. Data Sci., Sec. Appl., 612: 315-325.

Jai Sankar, T., Prabakaran, R., Senthamarai Kannan, K. and Suresh, S. 2010. Stochastic modelling for cattle production forecasting. J. Modern. Math. Stat., 4: 53-57.

Krishnan, M.A., Jawahar, K., Perumal, V., Devraj, T., Thanarasu, A., Kubendran, K. and Sreenivasan, S. 2020. Effects of ambient air pollution on respiratory and eye illness in population living in Kodungaiyur, Chennai. Atmos. Env., 203: -171.

Liu, D., Lee, S., Huang, Y. and Chien‐Ju, C. 2020. Air pollution forecasting based on attention‐based LSTM neural network and ensemble learning. Exp. Sys., 37(8): 444.

Lo, W.C., Shie, R.H., Chan, C.C. and Lin, H.H .2017. Burden of disease attributable to ambient fine particulate matter exposure in Taiwan. J. Formos. Med. Assoc., 111: 4516.

Nadeem, I., Ilyas, A. and Uduman, P.S. 2020. Forecasting ambient air quality of Chennai city in India. Geo. Env. Sust., 13(3): 12-21.

Nath, P., Saha, P. and Middya, A.I. 2021. Long-term time-series pollution forecast using statistical and deep learning methods. Neural Comput. Appl., 33: 12551-12570.

Pavlos, S.K, Jerett, M., Morrison, J.B. and Beckerman, B. 2005. Establishing an air pollution monitoring network for intra-urban population exposure assessment: A location-allocation approach. Atmos. Env., 39(13): 2399-2409.

Peter, T., Yamak, L., Yujian, M. and Pius, K.G. 2019. A Comparison between ARIMA, LSTM, and GRU for Time Series Forecasting. Association for Computing Machines, New York, NY, USA, pp. 49-55.

Shen, J., Valagolam, D. and Mccalla, S. 2020. Prophet forecasting model: A machine learning approach to predict the concentration of air pollutants ($PM_{2.5}$, $PM_{10}$, $O_3$, $NO_2$, $SO_2$, CO) in Seoul, South Korea. Peer J., 8: 11-21.

Siami-Namini, S., Tavakoli, N. and Siami-Namini, A. 2018. A Comparison of ARIMA and LSTM in Forecasting Time Series. Proceedings - 17th IEEE International Conference on Machine Learning and Applications, ICMLA 2018, December 17-20, 2018, Orlando, Florida, IEEE, Piscataway, NJ, USA, pp. 1394-1401,

Sivarethinamohan, R., Sujatha, S., Priya, S. and Sankaran, M. 2020. Impact of air pollution in health and socio-economic aspects: Review on future approach. Mater. Today Proceed., 16: 45-66.

Topping, D., Watts, D., Coe, H., Evans, J., Bannan, T.J., Lowe, D., Jay, C. and Taylor, J.W. 2020. Evaluating the use of Facebook's Prophet model v0.6 in forecasting concentrations of $NO_2$ at single sites across the UK and in response to the COVID-19 lockdown in Manchester, England. J. Geosci. Mod. Dev., 56: 919-930.

Ziyuan, Y. 2019. Air pollutants prediction in Shenzhen based on ARIMA and prophet method. E3S Web Conf., 13: 56.

Nature Environment and Pollution Technology
An International Quarterly Scientific Journal

p-ISSN: 0972-6268
(Print copies up to 2016)
e-ISSN: 2395-3454

Vol. 22 | No. 1 | pp. 229-236 | 2023

Original Research Paper

https://doi.org/10.46488/NEPT.2023.v22i01.021

Open Access Journal

# Susceptibility Evaluation of Debris Flow Disaster in Plateau Hydropower Cascade Development Reservoir Area

**Feng Yang*(**), Xudong Hu*(**)†, Zhenyao Xia*(**), Lei Cui*** and Qi Yang******

*Key Laboratory of Geological Hazards on Three Gorges Reservoir Area, Ministry of Education, China Three Gorges University, Yichang 443002, China

**College of Civil Engineering & Architecture, China Three Gorges University, Yichang, 443002, China

***China Renewable Engineering Institute, Beijing 100049, China

****Gui Yang Engineering Corporation Limited, Guiyang 550081, Guizhou, China

†Corresponding author: Xudong Hu; hxd@ctgu.edu.cn

**Nat. Env. & Poll. Tech.**
**Website: www.neptjournal.com**

*Received:* 26-03-2022
*Revised:* 04-05-2022
*Accepted:* 07-05-2022

**Key Words:**
Rumei hydropower station
Debris flow
Binary logistic regression model
Susceptibility

## ABSTRACT

The Rumei Hydropower Station is a typical cascade hydropower development project in a plateau area. The dam site is located in an area with complex topography, lithology, and geological structure. Geological disasters are developed in the area, mainly debris flow. Thus, taking the dam site and the surrounding areas as key evaluation objects, the engineering geological characteristics, geological environment characteristics, and the susceptibility and risk of geological disasters that may be caused are predicted and evaluated. The main methods used in this assessment are the binary logistic regression model and expert evaluation. The results show that the susceptibility to geological disasters is small and medium. The results of this study could provide a scientific basis for the rationality of the general layout and site selection of the project construction in the plateau water elevator level development reservoir area.

## INTRODUCTION

Debris flow is one of the most common geological disasters in mountainous areas. Determinants of debris flow are abundant sources, sufficient hydrodynamics, and favorable topography. The Rumei Hydropower Station is located southeast of the strong uplift area of the Qinghai-Tibet Plateau. The geographical structure in the region is active and affected by topography, geological structure, seismic activity, and human activities. The terrain is undulating, and the spatial distribution of rainfall is extremely uneven, Geological disasters (collapses, landslides and debris flows) are often prone to occur (Cui et al. 2020, Li et al. 2021b). This poses a threat to the safety of the Rumei Hydropower Station, camp, access roads, and diversion tunnels, which is not conducive to the transformation of local resource advantages into economic advantages and the promotion of the economic and social development of Tibet. Therefore, exploring the susceptibility of debris flow disasters in the reservoir area of plateau hydropower cascade development is of great significance because it can provide certain theoretical support and reference for the rationality of the general layout and site selection of reservoir engineering construction and disaster risk assessment.

The development process of debris flow is affected by many factors such as topography, lithology, hydrology and meteorology, rainfall conditions, vegetation, and human activities (Guo et al. 2021, Xiong et al. 2021, Yang et al. 2021), and a very obvious regional development difference can be observed. The total area of hills, plateaus, and mountains in China accounts for two-thirds of the land area. The geological conditions are complex, and geological disasters such as landslides, collapses, and debris flows are frequent. Debris flow has the characteristics of a sudden outbreak, rapid flow, and serious damage, often causing a large number of casualties and property losses (Xiong et al. 2021). The work on the risk assessment of debris flow is deepening, and many scientific researchers have made great achievements. For example, most researchers use certainty factor rate and the logistic regression model (Liu et al. 2021), logistic regression and frequency ratio models (Achour et

**ORCID details of the authors:**

**Feng Yang**
https://orcid.org/0000-0001-5772-9255

al. 2018), information value and logistic regression coupled model, power-law thresholds and logistic regression models (Nikolopoulos et al. 2018), borderline-SMOTE method (Li et al. 2021a), numerical simulation (Hu et al. 2019), TRIGRS and flow-R coupled models (Nie et al. 2022), GIS (Sung et al. 2020), PCA-GRNN model (Wang et al. 2020), RS-GIS (Zhang et al. 2012), Grey correlation analysis method (Wu et al. 2017), etc. to evaluate the risk of debris flow. This combined method is used to evaluate the susceptibility to debris flow and quantitatively evaluate the risk of debris flow under different rainfall intensities. The most widely used methods are the binary logistic regression model and the analytic hierarchy process. The AHP and GIS technology process different factors into raster, and then obtain the risk assessment of debris flow under the effects of different factors. However, the disadvantage of this method is that the selection of factors is highly subjective, and it has a high demand for data, causing differences in the evaluation results obtained by the same evaluation factors in the same region. Therefore, the evaluation results of the susceptibility to geological disasters may have different results. In factor selection, the binary logistic regression method can determine factors and weights through objective methods, which compensate for the shortcomings of AHP. The expert evaluation method is to interpret the data obtained from remote sensing interpretation and on-site investigation based on expert experience and evaluate and analyze the results of the investigation to reduce misjudgment.

Based on the advantages and disadvantages of the above methods, this paper adopts binary logistic regression combined with the expert judgment method to evaluate debris-flow susceptibility to reduce misjudgments, thereby improving the accuracy of the debris-flow susceptibility assessment. Thereby, provides certain theoretical support and reference for the susceptibility evaluation of debris flow disasters and the disaster prevention and mitigation of debris flow and further provides a certain scientific basis and reference for the rationality of the general layout and site selection of construction projects in the reservoir area of plateau hydropower cascade development.

## ENVIRONMENTAL BACKGROUND OF THE RESEARCH AREA

### Geomorphic Environment

The assessment area is located in the south-eastern part of the strong uplift area of the Qinghai-Tibet Plateau, where the geomorphological forces are intertwined and complex, resulting in many types of landforms, large morphological changes, and complex geomorphic combinations. The area has the following types of landforms: (1) modern seasonal ice and snow effects and freezing weathering landforms in the ridge area with an altitude of more than 4000 m, (2) ice edge of the alpine shrub-meadow belt above the forest line at an altitude of 3800 m geomorphology, (3) quaternary residual geomorphology above 2500 m above sea level, (4) slope disaster geomorphology and (5) dry-hot valley geomorphology. The above-mentioned main landforms are grouped into three basic types: alpine, sloping, and valley landforms, as well as active mountain geological hazard landforms. There are four large debris flow basins within 5 km upstream and downstream of the dam site.

### Geological Structure

The assessment area is located in the south-eastern part of the strong uplift area of the Qinghai-Tibet Plateau. The plateau is bounded by the main boundary faults and adjacent to the surrounding ancient block depression belts. The two areas have a huge height difference, and the areas have strong tectonic movement, seismic activity, geothermal activity, and Cenozoic magmatism. The characteristics of neotectonic movements are mainly large-scale integral and intermittent uplifting, and the inheritance, regeneration, and difference of faults and fault-block activities are obvious. The larger grade II structural plane (Fz01) near the dam site is 0.2 km, mainly in the structural plane of grade IV and V. The larger grade II structural plane (Fz01) near the dam site is 0.2 km, mainly in the structural plane of grade IV and V. Structural fissures are relatively developed, mostly steeply dipping fissures. After investigation, three groups of slope rock mass were identified: (1) N50ºE, NW75º, (2) N56ºW, SW80º, and (3) N80ºE, SE73º. The fissures are mostly straight and rough, and the spacing is generally 0.3 m to 3 m. The rock masses on both sides of the fissure are mostly altered and brown. The dacite and rhyolite in the reservoir area have gentle bedding joints, mostly N57°W, NE25°, but with poor continuity, mostly in the form of general joints.

### Hydrometeorology

The closest weather station to the camp in the Rumei Hydropower Station is the Mangkang Weather Station. The straight-line distance between the two places is 48km, and its elevation is 3870 m. According to the 30-year meteorological data from the Mangkang Meteorological Station from 1981 to 2010, the rainfall in this area is mostly concentrated from June to September, accounting for about 85% of the annual rainfall, and the inter-annual variation is small. The average relative humidity for many years is 61.1%, the average annual rainfall for many years is 575.4 mm, the maximum daily rainfall is 55 mm, and the number of precipitation days $\geq$30.0 mm is mainly concentrated from July to September. The Rumei Hydropower Station is

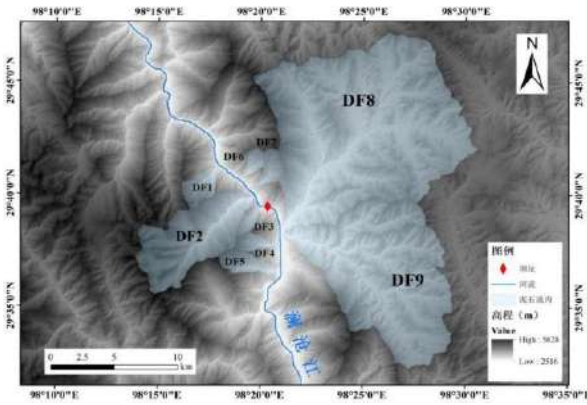


Fig. 1: Spatial distribution of debris flow geological hazards in the assessment area.

located in the Lancang River Valley. The high altitude of the basin is surrounded by mountains, making it conducive to the development of vertical air movement and condensation of water vapor. The rainy season in this area is dominated by bursts of precipitation, and there is more rain at night. The annual average rainfall days are 114.4 days, the annual average evaporation for many years is 1632 mm (20 cm evaporation dish), the annual average wind speed is 1.15 $m.s^{-1}$, the maximum regular wind speed is 11 $m.s^{-1}$, the most wind direction for many years is south, the annual sunshine is 2686h and the monthly average temperature is 2.77–25.9 Celsius. There are about 110 frost-free days throughout the year.

## CHARACTERISTICS AND DISTRIBUTION OF DEBRIS FLOW DISASTER

A total of nine debris flow geological disasters were investigated in the dam site and the surrounding area of Rumei Hydropower Station, distributed mainly along both sides of the Lancang River. According to "specification of geological investigation for debris flow stabilization", debris flows are classified according to the scale of the outbreak. They were divided into two large, two medium, and five small. The debris flow line density in the evaluation area reached 1.25 km/strip (Fig. 1 and Table 1).

Rongsong debris flow gully is located upstream of the dam site, distributed on the right bank of Lancang River, about 1.3 km from the dam site (Fig. 2a). The elevation of the highest point of the basin is 5376 m, the elevation of the lowest point is 2680 m and the elevation difference is 2696 m. The basin area is 40.5 $km^2$. The length of the main gully is 8.6 km, and the average longitudinal slope is 173.5‰ (Fig. 2b). The No. 2 debris flow gully is located 400 m upstream of the dam site and is distributed in the right bank of Lancang River, about 400 m away from the dam site (Fig. 2c). The highest point elevation of the basin is 4826 m, the lowest point elevation is 2656 m, the elevation difference is 2170 m, the basin area is 2.1 $km^2$ and the main gully is 1.62 km long. The Zhuka No. 1 debris flow gully is located downstream of the dam site and distributed on the right bank of the Lancang River, about 3.8 km from the dam site (Fig. 2e). The elevation of the highest point of the

Table 1: Statistical table of the basic situation of geological disasters that threaten construction projects.

| Name | Site | Longitude | Latitude | Volume ($10^4m^3$) | Scale | Susceptibility assessment | | Risk |
|---|---|---|---|---|---|---|---|---|
| | | | | | | Present situation | Trend | |
| DF1 | No.1 debris flow gully 5 km upstream of the dam site | 98° 18'1.35" | 29° 41'17.70" | 1.5 | small | mild | medium | small |
| DF2 | Rongsong debris flow gully | 98° 19'44.7" | 29° 39'57.26" | 18.5 | medium | medium | medium | small |
| DF3 | No. 2 debris flow gully 400 m upstream of the dam site | 98° 19'59.2" | 29° 39'29.07" | 1.8 | small | mild | medium | small |
| DF4 | Zhuka No. 1 debris flow gully | 98° 21'2.94" | 29° 37'41.94" | 13.2 | medium | medium | medium | medium |
| DF5 | No.1 debris flow gully 5 km downstream of the dam site | 98° 20'54.1" | 29° 36'34.72" | 1.7 | small | mild | mild | small |
| DF6 | No. 3 debris flow gully 3 km upstream of the dam site | 98° 19'1.38" | 29° 40'42.74" | 1.3 | small | mild | medium | small |
| DF7 | No. 4 debris flow gully 1.7 km upstream of the dam site | 98° 19'34.7" | 29° 40'9.29" | 1.5 | small | mild | mild | small |
| DF8 | Rongqu debris flow gully | 98° 21'3.02" | 29° 38'29.51" | 47.8 | large | medium | medium | medium |
| DF9 | Duiba debris flow gully | 98° 21'5.18" | 29° 38'10.89" | 36.5 | large | medium | medium | medium |

Note: DF1, DF2, DF3, DF6 and DF7 pose a threat to the Rumei Hydropower Station. DF4 and DF5 pose a threat to Hydropower Station camp. DF8 and DF9 pose a threat to the left bank entry highway.

Fig. 2: (a) and (b) are the Rongsong debris flow gully channel form and Rongsong debris flow gully upstream left bank view, respectively. (c) shows the remote view of the left bank downstream of the No. 2 debris flow gully mouth at 400 m upstream of the dam site. (d) is the gully mouth of Duiba debris flow gully and the bedrock on both sides. (e) and (f) are the remote views of the old debris flow accumulation fan in Zhuka No. 1 gully and the natural 'drainage groove' on the old debris flow accumulation fan in Zhuka No. 1 gully, respectively. (g) and (h) are the panorama of the main channel of the Rongqu debris flow gully and the accumulation thickness of the main channel of the Rongqu debris flow gully, respectively.

basin is 4830 m, the elevation of the lowest point is 2639 m and the elevation difference is 2191 m (Fig. 2f). The basin area is 3.6 km$^2$. The length of the main gully is 2.6 km, and the average longitudinal slope is 334.3‰. The Rongqu debris flow gully is located downstream of the dam site and distributed on the left bank of the Lancang River, about 2.4 km away from the dam site. The maximum elevation is 4700 m, the minimum elevation is 2637 m, the elevation difference is 2063 m, the basin area is 181.2 km$^2$, the main gully length is 16.2 km and the average longitudinal slope is 89.9‰. Duiba debris flow gully is located downstream of the dam site and is distributed on the left bank of Lancang River, about 3.0 km away from the dam site (Fig. 2d). The highest point elevation of the basin is 4752 m, the lowest point elevation is 2630 m, the height difference is 2122 m, the basin area is 108.4 km$^2$, the main gully length is 11.4 km and the average longitudinal slope is 31.5‰.

## EVALUATION OF SUSCEPTIBILITY

The comprehensive evaluation of the susceptibility of debris flow gully is based on the survey results of the current situation of debris flow, as well as according to the comprehensive index reflecting the susceptibility of debris flow gully in the 'Specifications of geological investigation for debris flow stabilization' (DZ/T0220-2006). In this work, the stability of the nine potential geological hazard points of debris flow caused by the proposed construction of the Rumei hydropower station in the plateau hydropower cascade development reservoir area is identified qualitatively, and the hazard level is determined according to the hazard of each disaster point to the proposed construction project. The hazard level is determined according to the hazards of each disaster point to the proposed project. Among the nine debris flow geological disaster sites, 0 disaster sites are at high risk, 3 sites are medium risk and 6 sites are at low risk. The risk of geological disasters is small and medium. These disaster spots pose a threat to the safety of Rumei Hydropower Station, camps, access roads, and water diversion tunnels to varying degrees. Hence, the prevention and control of these debris flow geological disasters cannot be ignored in engineering construction.

### Binary Logistic Regression Model

The logistic regression model is the earliest discrete choice model. It is widely used in sociology, economics, geography, geology, and other fields. The model is a multivariate statistical analysis method formed based on linear regression combined with logistic function. It is suitable for studying the relationship between the results of binary classification and its influencing factors. The influencing factors of geological disasters in the region are independent variables. Through logistic regression model analysis, the weights of independent variables can be obtained and we can understand that these factors are the main factors causing geological disasters, and at the same time, according to the weights of the influencing factors, the probability of disaster occurrence can be predicted. The predicted result value is between 0 and 1. Because the logistic regression model is fast to solve, easy to apply, and has unique advantages in the free distribution of data, it has been widely used in geological disaster susceptibility evaluation and mapping. Its function is the following formula:

$$p = 1/[1 + e^{-(\alpha+\beta_1 X_1+\cdots+\beta_i X_i)}] \quad \ldots(1)$$

Where $\alpha$ is the constant term, $P$ is the probability of disaster occurrence, $\beta$ is the regression coefficient and $i$ is the number of types of evaluation factors. Taking the natural logarithm on both sides of Equation (1), we get the following:

$$Ln[P/(1-P)] = \alpha + \beta_1 x_1 + \beta_2 x_2 + \cdots + \beta_i x_i = \alpha + \beta x \quad \ldots(2)$$

The independent variable of the logistic regression model, that is, the unit of the evaluation factor is different. Before establishing a logistic regression model, the secondary division values of each evaluation factor must be normalized into standardized values. In this paper, the ratio of the disaster area in each evaluation factor to the total disaster area is divided by the ratio of the area of each grading factor to the total area as the index value, and the index values are standardized. The calculation formula is as follows:

$$x_{ij} = Z_{ij} / S_{ij} \quad \ldots(3)$$

$$X_{ij} = x_{ij} \Big/ \sum_{j=1}^{m} x_{ij} \quad \ldots(4)$$

where $Z_{ij}$ is the proportion of the disaster area in the secondary classification of each factor to the total disaster area, $S_{ij}$ is the ratio of the secondary classification area of each factor to the total area, i is the serial number of each evaluation factor (i = 1,2...6,7), j is the secondary classification number of each evaluation factor (j = 1,2...,m), $x_{ij}$ is the initial calculated metric value and $X_{ij}$ is the standardized value of the secondary classification of each factor.

### Selection and Grading of Susceptibility Evaluation Factors

The evaluation unit is the smallest and indivisible space used for geological hazard evaluation and can have a regular or irregular shape. In practical applications, an appropriate evaluation unit can be selected according to research needs. In this paper, the grid unit is used as the evaluation unit for the susceptibility evaluation of geological disasters. For the

convenience of calculation, the grid size of the study area is taken as 30 m.

There are three main types of geological disasters in hydropower stations: landslides, collapses, and debris flows. The accuracy of susceptibility zoning depends on the selected evaluation factors. Therefore, an in-depth understanding of the contribution of each influencing factor to regional disasters and the cumulative effect between factors could improve the susceptibility evaluation and zoning accuracy of geological hazards. Therefore, investigating geological disasters, the stability of the disaster-prone environment, the risk of disaster-causing factors, and the vulnerability of disaster-affected bodies in the study area is necessary. After analysis, six factors including daily rainfall, slope gradient, aspect, elevation, slope curvature, and stratum lithology are selected as the evaluation factors of geological disaster susceptibility in hydropower stations. The classification indices for each factor are shown in Table 2.

The analysis of interpreting the spatial distribution law of debris flow geological disasters is performed through the spatial statistical analysis function of GIS. First, the raster layer of each factor is prepared, and each factor is divided into grades (for example, divide the daily rainfall into <10, 10-25, 25-50, 50-100, 100-250 and >250). Then, through GIS spatial analysis, the relative occurrence probability of disasters in each factor classification is calculated and normalized. The higher the numerical value of a factor classification, the stronger the positive correlation between it and the probability of disaster occurrence. This paper selects six factors (Table 2) among the three types of factors and calculates the density of geological hazards in each factor classification and the area occupied by each factor in the total study area through the spatial statistical analysis function of GIS. The results are then normalized. Each evaluation factor is classified according to the grading index, and the relationship between each evaluation factor and geological hazards is studied statistically to evaluate the spatial correlation and importance of each factor classification and the distribution of geological hazards.

## Evaluation Results of Geological Hazard Susceptibility

The distribution map of the probability value of disaster susceptibility is obtained using the ArcGIS spatial grid overlay function according to the obtained regression coefficients of each factor combined with formula (1). Through the natural discontinuity method, it is divided into

Table 2: Index classification of geological disaster susceptibility evaluation factors in the water-level development reservoir area in the plateau area.

| First level factor | Secondary evaluation factor | series | Index grading |
|---|---|---|---|
| Rainfall factor | daily rainfall | 6 | <10, 10-25, 25-50, 50-100, 100-250 and >250 |
| Topographic factor | Slope (°) | 7 | <10, 10-20, 20-30, 30-40, 40-50, 50-60 and >60 |
| | Slope direction | 9 | flat, north, northeast, east, southeast, south, southwest, west and northwest |
| | Elevation (m) | 10 | <2200, 2200-2400, 2400-2600 and 2600-2800, 2800-3000, 3000-3200, 3200-3400, and 3400-3600, 3600-3800 and >3800 |
| | curvature | 3 | <-0.5, -0.5-0.5 and >0.5 |
| Geological factors | stratigraphic lithology | 6 | Quaternary, Triassic, Permian, Carboniferous Permian, Carboniferous, Devonian |

Table 3: Risk prediction table of engineering construction exacerbating existing geological disasters

| Name | Site | Disaster types | Volume ($m^3$) | Scale | Susceptibility/P |
|---|---|---|---|---|---|
| DF1 | No.1 debris flow gully 5 km upstream of the dam site | debris flow | 15000 | small | Medium /0.43 |
| DF2 | Rongsong debris flow gully | debris flow | 185000 | medium | Medium /0.56 |
| DF3 | No. 2 debris flow gully 400 m upstream of the dam site | debris flow | 18000 | small | Medium /0.45 |
| DF4 | Zhuka No. 1 debris flow gully | debris flow | 132000 | medium | Medium /0.61 |
| DF5 | No.1 debris flow gully 5 km downstream of the dam site | debris flow | 17000 | small | Mild /0.25 |
| DF6 | No. 3 debris flow gully 3 km upstream of the dam site | debris flow | 13000 | small | Medium/0.33 |
| DF7 | No. 4 debris flow gully 1.7 km upstream of the dam site | debris flow | 15000 | small | Mild/0.19 |
| DF8 | Rongqu debris flow gully | debris flow | 478000 | large | Medium/0.68 |
| DF9 | Duiba debris flow gully | debris flow | 365000 | large | Medium/0.64 |

Note: DF1, DF2, DF3, DF6 and DF7 pose a threat to the Rumei Hydropower Station. DF4 and DF5 pose a threat to the hydropower station camp. DF8 and DF9 pose a threat to the left bank entry highway.

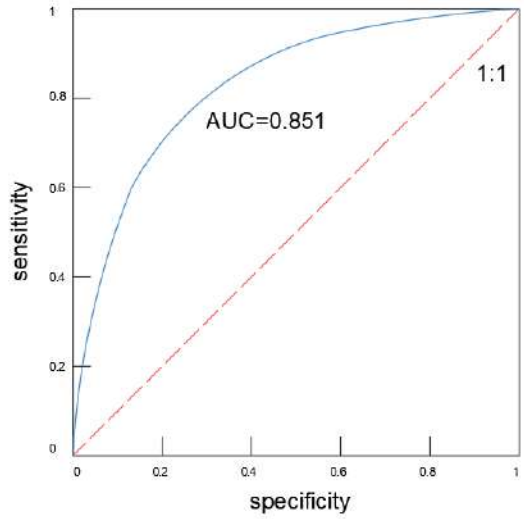


Fig. 3: ROC curve for evaluating the susceptibility to geological hazards in hydropower development zones.

five areas from small to large: low, low, medium, high, and relatively high-prone areas. Table 3 shows the degree of debris-flow susceptibility of the Rumei hydropower station based on the logistic regression model.

### Verification of Geological Hazard Evaluation Results

The accuracy of geological disaster susceptibility evaluation results is related directly to the reliability of the model and affects economic development and social progress directly or indirectly. Therefore, it is very necessary to test the accuracy of the susceptibility rating results. The classification performance of different susceptibility evaluation models can be compared accurately by checking the accuracy of geological disaster susceptibility evaluation results so that the best susceptibility evaluation model suitable for a certain area can be selected. The ROC curve and success rate curve are the most commonly used methods to test the performance of the geological hazard susceptibility evaluation model. The accuracy of the model can also be evaluated by using the ROC curve (Wu et al. 2019). Taking the proportion of units without disasters that are predicted correctly as the abscissa and the proportion of units with disasters being predicted correctly as the ordinate, a curve is drawn. The closer the curve is to the upper left corner, the higher the accuracy of the model classification as shown in Fig. 3.

The Area Under Curve (AUC) value is defined as the area below the ROC curve to the abscissa, and the value ranges from 0.5 to 1. The higher the AUC value, the higher the model accuracy. The evaluation model AUC = 0.851, which means it has good accuracy.

## CONCLUSION

(1) The area of assessment area is about 2.03 $km^{2.}$ The types of geological disasters are mainly medium-sized debris flows, and the susceptibility to debris flows is mainly moderate. The hazard to the Rumei Hydropower Station is small, while the hazard to the hydropower station camp and the left access road is medium.

(2) The risk of engineering construction causing and exacerbating geological disasters is small. However, there is still a possibility that geological disasters could be caused or aggravated in the excavation and filling of local engineering slopes, excavation and soil dumping in engineering construction and in the construction and use of construction camps and access roads.

(3) According to the evaluation results of this paper, for Zhuka No.1, Rongqu and Daba debris flow basins, disaster prevention and mitigation measures, such as source fixation and construction of sand dams can be taken, and the construction camp is relatively far from the slope toe area.

(4) Overall, the advantages of this method are the application of a binary logistic regression model for debris flow susceptibility evaluation, which is combined with the expert evaluation method. Experts can reduce the misjudgment of evaluation results by explaining the data obtained from remote sensing interpretation and field investigation and evaluating and analyzing the survey results. Finally, the accuracy of the model can be evaluated using the ROC curve to determine whether the model had good accuracy. The shortcomings of this paper are as follows. In the selection of geological hazard susceptibility evaluation factors, only three main influencing factors, namely rainfall, topography, and geology are considered, and relatively minor evaluation factors, such as distance from fault and fault line density in the region are not considered. However, these shortcomings have little influence on the evaluation results. In the future, when selecting the evaluation factors of geological disaster susceptibility, these secondary evaluation factors can be considered to increase the accuracy of the model, and the evaluation results are closer to the actual situation, which provides a more reliable scientific basis and theoretical support for disaster prevention and mitigation of geological disasters.

## ACKNOWLEDGEMENTS

This work has been supported by CRSRI Open Research Program (Program SN: CKWV2021888/KY), the Key Laboratory of Mountain Hazards and Earth Surface

Processes, Chinese Academy of Sciences (Grant No. KLMHESP-20-02), the National Natural Science Foundation of China (Grant No. 42001002), and the Power China Science and Technology Projects (Grant No. DJ-ZDXM-2016-04). All the DEM data are available through the ASF Data Research at the following URL: https://search.asf.alaska.edu/.

## REFERENCES

Achour, Y., Garcia, S. and Cavaleiro, V. 2018. GIS-based spatial prediction of debris flows using logistic regression and frequency ratio models for Zezere River basin and its surrounding area, Northwest Covilha, Portugal. J. Arabian Journal of Geosciences, 11(18): 550.

Cui, Z., Wang, J., Cui, C. and Pan, G. 2020. Evaluation of the susceptibility of debris flow in Badan Gully of Dongxiang County of Gansu based on. J. The Chinese Journal of Geological Hazard and Control, 31(1): 44-50.

Guo, X., Chen, X., Song, G., Zhuang, J. and Fan, J. 2021. Debris flows in the Lushan earthquake area: formation characteristics, rainfall conditions, and evolutionary tendency. J. Natural Hazards, 106(3): 2663-2687.

Hu, X., Hu, K., Tang, J., You, Y. and Wu, C. 2019. Assessment of debris-flow potential dangers in the Jiuzhaigou Valley following the August 8, 2017, Jiuzhaigou earthquake, western China. J. Engineering Geology, 256: 57-66.

Hu, X., Hu, K., Zhang, X., Wei, L. and Tang, J. 2019. Quantitative assessment of the impact of earthquake-induced geohazards on natural landscapes in Jiuzhaigou Valley. J. Journal of Mountain Science, 16(2): 441-452.

Li, Y., Chen, J., Tan, C., Li, Y., Gu, F., Zhang, Y. and Mehmood, Q. 2021a. Application of the borderline-SMOTE method in susceptibility assessments of debris flows in Pinggu District, Beijing, China. J. Natural Hazards, 105(3): 2499-2522.

Li, Z., Chen, J., Tan, C., Zhou, X., Li, Y. and Han, M. 2021b. Debris flow susceptibility assessment based on topo-hydrological factors at different unit scales: a case study of Mentougou district, Beijing. J. Environmental Earth Sciences, 80(9): 365.

Liu, F., Cui, C., Wang, J., Cao, Y. and Li, W. 2021. Hazard assessment of debris flow based on the certainty factor rate and the logistic regression mode. J. Journal of Safety and Environment, 21(4): 1693-1073.

Nie, Y., Li, X. and Xu, R. 2022. Dynamic hazard assessment of debris flow based on TRIGRS and flow-R coupled models. J. Stochastic Environmental Research and Risk Assessment, 36(1): 97-114.

Nikolopoulos, E., Destro, E., Bhuiyan, M., Borga, M. and Anagnostou, E. 2018. Evaluation of predictive models for post-fire debris flow occurrence in the western United States. J. Natural Hazards and Earth System Sciences, 18(9): 2331-2343.

Sung, C. and Liaw, S. 2020. A GIS-based approach for assessing social vulnerability to flood and debris flow hazards. J. International Journal of Disaster Risk Reduction, 46: 101531.

Wang, X., Sun, Y., Li, S. and Meng, F. 2020. Hazard assessment of debris flows based on a PCA-GRNN model: a case study in Liaoning Province, China. J. Arabian Journal of Geosciences, 13(4): 151.

Wu, S., Chen, J., Xu, C., Zhou, W., Yao, L., Yue, W. and Cui, Z. 2019. Susceptibility assessments and validations of debris-flow events in meizoseismal areas: Case study in China's Longxi river watershed. J. Natural Hazards Review, 21(1): 05019005.

Wu, W., Zhang, S., Zhang, G. and Tao, S. 2017. Debris flow risk assessment based on crey correlation analysis method a case study of YinPoHe debris flow in Lushui county. J. Journal of Geological Hazards and Environment Preservation, 28(3): 30-32.

Xiong, J., Tang, C., Chen, M., Zhang, X., Shi, Q. and Gong, L. 2021. Activity characteristics and enlightenment of the debris flow triggered by the rainstorm on 20 August 2019 in Wenchuan County, China. J. Bulletin of Engineering Geology and the Environment, 80(2): 873-888.

Yang, F., Fan, X., Subramanian, S., Dou, X., Xiong, J., Xia, B., Yu, Z. and Xu, P. 2021. Catastrophic debris flows triggered by the 20 August 2019 rainfall, a decade since the Wenchuan earthquake, China. J. Landslides, 18(9): 3197-3212.

Yu, M., Xing, H. and Hu, S. 2021. Debris flow susceptibility assessment based on information value and logistic regression coupled model : case of Shimian County, Sichuan Province. J. Yangtze River, 52(12): 107-114.

Zhang, H., Fan, J., Hu, K., Guo, F., Liu, F. and Chen, Y. 2012. Distribution of collapse and landslide clast deposit in debris flow basin with RS-GIS after Wenchuan earthquake. J. Journal of Mountain Science, 30(1): 78-86.

Nature Environment and Pollution Technology
An International Quarterly Scientific Journal

p-ISSN: 0972-6268
(Print copies up to 2016)
e-ISSN: 2395-3454

Vol. 22 | No. 1 | pp. 237-244 | 2023

Original Research Paper

https://doi.org/10.46488/NEPT.2023.v22i01.022

Open Access Journal

# Utilization of Waste Glass for Enhancement of Chemical Properties of Concrete

**Jagriti Gupta*†, A. S. Jethoo* and Nandeshwar Lata****
*Department of Civil Engineering, Malaviya National Institute of Technology, Jaipur 302017, India
**Department of Civil Engineering, Poornima University, Jaipur 303905, India
†Corresponding author: Jagriti Gupta; 2019rce9055@mnit.ac.in

**Nat. Env. & Poll. Tech.**
**Website: www.neptjournal.com**

*Received:* 13-05-2022
*Revised:* 18-07-2022
*Accepted:* 20-07-2022

**Key Words:**
C-S-H gel
Chemical properties
Concrete
Beverage glass

## ABSTRACT

The world is facing a huge problem of waste generation; among these, solid waste in the form of glass has become a prime concern for the environment. The composition of the glass is silica-based, and its utilization in the preparation of concrete can be an efficient step in the direction of sustainable development by reducing the cement content. The formation of secondary calcium silicate hydrates (C-S-H) could take place due to the pozzolanic reaction of the fine ground glass with the cement. TGA techniques were used in this research to investigate the chemical properties of the waste glass, and later, these were compared with the properties of the cement. By keeping a constant w/b ratio for all the replacement levels from 0% to 35%, the evaluation of the workability and compressive strength were done. The evaluation showed that workability increased with an increase in the content of the waste glass. With 7 and 28 days cured samples, the strength and chemical investigation were conducted on the samples prepared with the same mix design. Constant Dose of superplasticizer used by weight of cement for mixes as 0.8%. Compared with the control sample, The level of replacement of waste glass to cement as 30% has depicted the augmentation in the compressive strength. Thus, the use of waste glass was found to be cost-effective and an environment-friendly solution for the sustainable development of concrete.

## INTRODUCTION

In developed nations like the USA, EU, and China, the estimated average production of waste glass worldwide in the year 2005 was approximately 130 Mt (Gupta et al. 2020, Rashad et al. 2015). Open land dumping practice is mostly adopted for the disposal of waste glass and this leads to environmental and surrounding pollution along with negative economic impacts. Amenable and feasible management of the available resources with environment-friendly considerations is the sustainable practice of construction (Rashad 2014). Cement is the vital key ingredient for preparing concrete; the production of cement involves many processes which cause the emission of greenhouse gases. The substitution to cement with supplementary cementitious materials (SCMs) in concrete preparation may appear as an environment-friendly solution (Taha et al. 2009). Dissimilar to the above-discussed materials, waste glass is less likely to be used in studies as SCM besides being more feasible, due to its least commercial achievements (Matos & Sousa-Coutinho 2012, Gupta et al. 2021, 2020). Rashed et al. (2014) and Taha et al. (2009) utilized the waste glass in substitution of the natural aggregates. Besides the concern of the alkali-silica reaction, the long-duration enhancement has been depicted in various studies against chloride ingress. Sublimate ASR due to the chemical compound like alkalis and sulfates tend to produce more alkalis in the mix and this phenomenon creates peril to the concrete life span. Matos & Sousa-Coutinho (2012) and Rashed (2014) depicted that efflorescence created from lime can be minimized along with ASR suppression by employing the benign pozzolana function.

Recent research has represented the feasibility of waste glass in the production of brick and ceramics (Afshinania et al. 2016). Pozzolans, fineness, and pore solution along with the chemical composition of waste glass have efficacy on the properties of the concrete (Omran & Tagnit-Hamou 2016, Bisht et al. 2020, Nahi et al. 2020, Carsana et al. 2014 ). Shayan & Xu (2006) depicted in their study that waste glass particle sizes less than 300 lm show pozzolanic behavior, even at lesser cement content, the particle size lesser than 100 lm presents pozzolanic properties at 90 days of curing. Nassar and Soroushian in the year 2011 represented enhanced compressive strength by incorporating waste glass replacement as 15 to 20% to the main binder cement.

The United States disposed of waste glass to almost 9.3 million metric tons in the year of 1994 and almost eighty percent of it was only container glass (Tanwar et al. 2021). The substitution of aggregates with glass waste has been tried for a long duration, though it depicted the formation

of cracks in the concrete (Ballester et al. 2007, Farinha et al. 2011, Idir et al. 2011). Whereas, finely ground waste glass has been used as a substitution for cement in a few studies only for concrete preparation (Choi et. al 2017). Few efforts have been made in recent duration for the preparation of Portland cement by incorporation of the waste glass, this waste is utilized by considering in form of raw siliceous material (Du & Tan 2017). The flash setting depicted by the cement due to the high alkali content, when waste glass is incorporated, the chemical compound found to be formed is $2CaSO_4 \cdot K_2SO_4$ (Ling & Poon 2013). In concrete as well as in mortar the substitution of waste glass for cement is found to be the emphatic solution for the utilization of waste and minimizing the recycling efforts (Somani & Gaur 2020, Bisht & Ramana 2018). The chemical reaction between the pore solution of alkaline and the silica-containing forms of metastable which have their presence in various types of aggregates leads to the Alkali–silica reaction (ASR), and this reaction is found to have detrimental effects on the concrete (Matos & Sousa-Coutinho 2012). Decomposition of the silica due to the attack of alkali produces the ASR gel when the waste glass is substituted in place of the aggregates, and this phenomenon leads to the formation of cracks in concrete (Saccani & Bignozzi 2010). Perhaps, the glass powder in the form of fine grinding powder will prevent the expansion of the ASR when utilized as the supplementary cementitious material (Byars et al. 2019). This phenomenon can be understood by the fact that the particle size of glass has much impact on the expansion of the ASR, and it was depicted in the experimental studies (Gupta et al. 2020, Schwarz et al. 2008). Also, it has been reported that waste glass having a size of particle finer than 75 μm were tend to propagate the issue of ASR (Ling & Poon 2011). On other hand, particle sizes ranging from 1.18mm - 2.36 mm are more likely to rise the issue of ASR (Bisht et al. 2019). Furthermore, a particle size having size of less than 0.30 mm does not cause the ASR, but when the size of the particle of waste glass rises above 0.60 mm, it starts to present the issue of the ASR (Siad et al. 2018). How it be, the critical particle size of the waste glass can mitigate the ASR side effects is still a matter of technical argument (Gupta et al. 2021).

## MATERIALS AND METHODS

### Cement

The standards of IS 8112-2003 were followed for the sample preparation with the use of OPC 43 grade. Also, as per the standards of 10262:2009, the mix design was prepared by keeping the w/c ratio at 0.45 and the water incorporated in the preparation was having a pH of 6.5 (Fig. 1). However, to maintain the standard workability of the

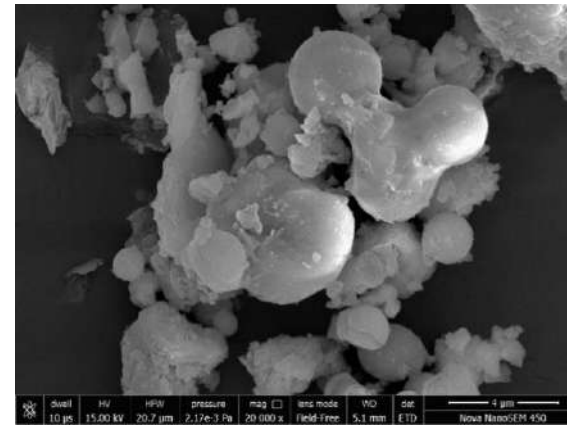

Fig. 1: Higher magnification image of cement particles.

mixes, superplasticizers were used (SP-431) and the amount kept by cement weight was 0.8%.

### Aggregates

i. **Coarse-** The specific gravity of the aggregates used was 2.66. The aggregates were ranging from 10-20 mm in this work.

ii. **Fine**- Banas River and Rajasthan sand were used in this work. The specific gravity of the aggregates used was 2.62. the percentage finer was observed as 99.4. The aggregates were ranging from 4.75 mm to 150 mm.

iii. The NaOH solution was prepared by utilizing $Na_2O$, which was procured from Jaipur. 1.0 $mol.L^{-1}$ chemical reagent was used in this work.

### Beverage Glass (BG)

The size of the BG was identified before the addition of cement, and the size was lesser than 75 microns. The specific gravity was also tested for this and the value was found as

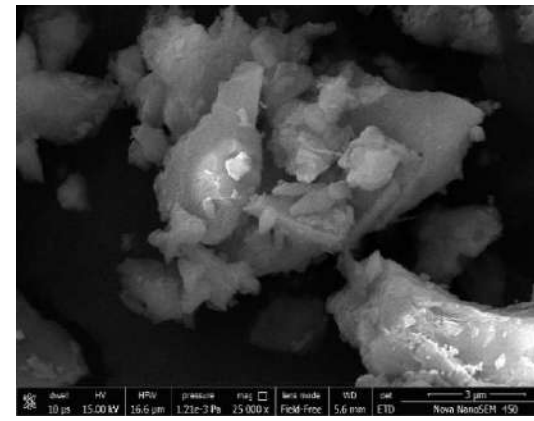

Fig. 2: Higher magnification of glass particles.

Table 1: Concrete preparing ingredients properties.

| Material | Specific Gravity | Color | pH |
|---|---|---|---|
| Fine Aggregate | 2.62 | Light brown | - |
| Coarse Aggregate | 2.66 | Greyish white | - |
| Waste Glass (WG) | 2.55 | Dark grey | - |
| Water | - | Colorless | 7-6.5 |

2.55 (Fig. 2 & Fig. 3). SEM image of glass shows its irregular shape and sharp edges which helps to provide better binding.

## Mix Proportioning

For this experiment, M30 grade concrete with a fixed w/c ratio of 0.45 is used, in accordance with BIS 10262:2009. To achieve the desired workability, 0.8% by weight of cement is used as an additive. As shown in Table 2 below, PWG is substituted for cement at intervals of 5% from level 5 to level 40%.

## Test Methods

**ASR Expansion**: The standards of the ASTM C1567 were followed for the conduction of the experiments on materials. The cement mortar bars were prepared for the testing and the dimension of the specimen was as 25 mm × 25 mm × 285 mm. After a day, the prepared and demolded sample was then cured for 24 h in the water bath by keeping

Table 2: Replacement percentage with cement.

| Mix designation | Binder ($kg.m^{-3}$) | | |
|---|---|---|---|
| | Cement | % of WG | WG |
| M | 385.00 | 0 | 0 |
| BG1 | 365.75 | 5 | 19.25 |
| BG2 | 346.50 | 10 | 38.5 |
| BG3 | 327.25 | 15 | 57.75 |
| BG4 | 308.00 | 20 | 77 |
| BG5 | 288.75 | 25 | 96.25 |
| BG6 | 269.50 | 30 | 115.50 |
| BG7 | 250.25 | 35 | 134.75 |

a constant temperature of the water bath at 80°C. The water used in the water bath was distilled water. The DEMEC-type strain gauges were used for the measurements of the length variation of the sample. The initial length was recorded as L0. The sample marked with the initial points was then cured in the solution of NaOH. In the continuations the sample was cured in a curing tub at a fixed temperature of 80 °C, the curing tub contains the solution of the 1.0 mol/L NaOH. The afterward length measurements of the sample were denoted as Lt. and the time for the measurements was kept as 3, 7, 14, 28, and 35 days. By considering all these values of length variations the ASR expansion for the samples was determined by utilizing the following equation-1.

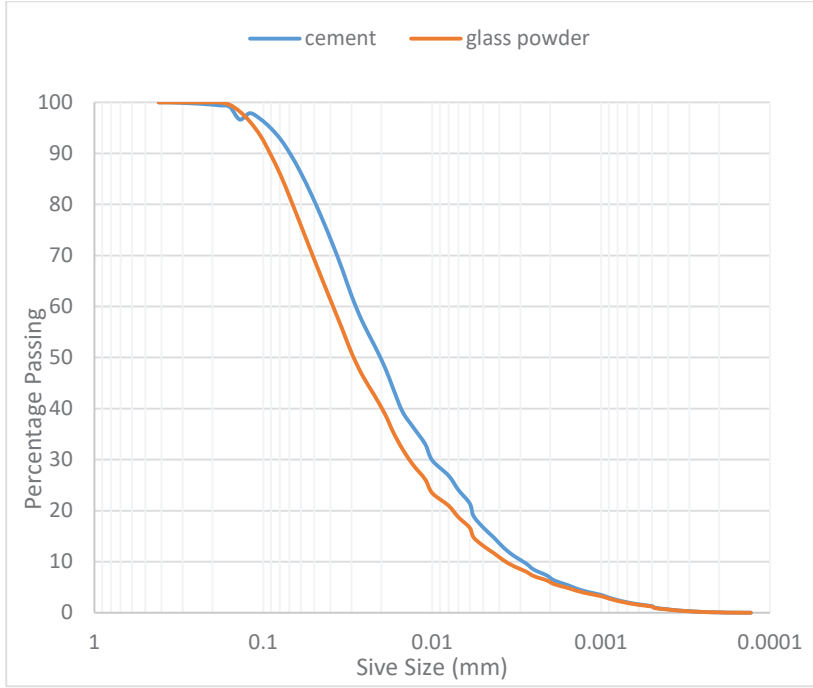


Fig. 3: Gradation curve of BG and OPC.

The average of three samples was considered for the final result.

$$P_t = \frac{L_t - L_o}{L_o} \times 100\ \%$$

Here:

L0: Initial length of the sample (mm).

Lt: Final length at a time interval of T days (mm).

Pt: ASR expansion of sample (%).

In measurements of L0 and Lt the copper head length was not considered.

**Concrete Mix Proportion:** As per the standards of IS 10262: 2009, the trial mix was prepared. The preparation is so done to achieve 100-125 of the slump value along with the 30 MPa target strength. The dose of the glass powder substitution to the cement varied ranging from 0% to 35%. Table 3 below represents the proportion of the mixes.

Table 3: Mix proportions for control mix.

| Material | Weight [kg.m$^{-3}$] | Slump [mm] |
|---|---|---|
| Cement OPC | 385 | 100 |
| Coarse aggregate (20 mm) | 645.81 | |
| Coarse aggregate (10 mm) | 424.05 | |
| Fine aggregate | 780.80 | |
| Water | 173 | |
| Admixture | 3.08 | |

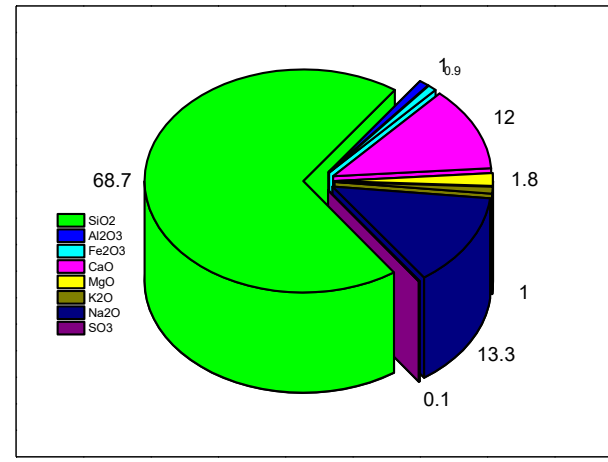


Fig. 4: Chemical composition of beverage glass.

## RESULTS AND DISCUSSION

### Chemical Composition of Beverage Waste Glass Powder and OPC

The EDX technique was used to investigate the composition of the chemical ingredients of the samples of glass powder. Table 4 represents the comparison of investigated findings with the other pozzolanic materials. The specimen of the waste glass depicts the standard content of the pozzolana, as per the IS 1727: 1967. The minimum required content of the ($SiO_2$+$Al_2O_3$+ $Fe_2O_3$) should be 70 %. The moisture content in BG samples was found lesser than the standard of acceptability and the respective values are 4%, 10%, and 3%. Also, the findings depict that the moisture content along with the LoI and $SO_3$ are nearly absent. Under the considerable limits of standards, the presence of NiO, CuO, BaO, PbO, $Cr_2O_3$, $ZrO_2$ $TiO_2$, and $As_2O_3$ was found in samples of the glass. Additionally, it has been noted that their presence is less than 0.5%. Thus, the beverage glass powder is expected to depict the pozzolanic nature in a cementitious system.

### Chemical Reaction to Enhance the C-S-H Gel

**OPC**: It achieves strength with the help of the chemical reaction of water with the cement since it is hydraulic cement (Fig. 5). The vital strength-gaining factor of OPC is calcium silicate hydrate (or C-S-H), and it is considered to be the primary hydration product. This whole phenomenon is named hydration. The main compounds of the cement are depicted in Table 5.

Table 4: Chemical composition depicted by EDX technique for waste glass samples, OPC, and other reference pozzolanas.

| Compound | Bevrage glass | OPC | Waste glass (Nassar & Soroushian (2012) | Slag | Silica fume | Fly ash |
|---|---|---|---|---|---|---|
| $SiO_2$ | 68.7 | 22.8 | 68 | 35 | 90.9 | 59.2 |
| $Al_2O_3$ | 1.0 | 5.9 | 7 | 12 | 1.1 | 25.6 |
| $Fe_2O_3$ | 0.9 | 3.5 | <1 | 1 | 1.5 | 2.9 |
| CaO | 12.0 | 63.0 | 11 | 40 | 0.7 | 1.1 |
| MgO | 1.8 | 1.5 | <1 | – | 0.8 | 0.3 |
| $K_2O$ | 1.0 | 1.0 | <1 | - | - | 0.9 |
| $Na_2O$ | 13.3 | 0.1 | 12 | 0.3 | - | 0.2 |
| $SO_3$ | 0.1 | 2.0 | – | 9.0 | 0.4 | 0.3 |
| LOI | - | 1.5 | – | 1.0 | 3.0 | 1.4 |

Table 5: Cement compound.

| Chemical Formula | Composition | Weight [%] |
|---|---|---|
| $CaSO_4.2H_2O$ | Gypsum | 5 |
| $Ca_4Al_2Fe_2O_{10}$ or 4CaO. $Al_2O_3.Fe_2O_3$ | Tetra-calcium alumi-no-ferrite | 10 |
| $Ca_3Al_2O_6$ or $3CaO.Al_2O_3$ | Tri-calcium aluminate | 10 |
| $Ca_2SiO_4$ or $2CaO.SiO_2$ | Di-calcium silicate | 25 |
| $Ca_3SiO_5$ or $3CaO.SiO_2$ | Tri-calcium silicate | 50 |

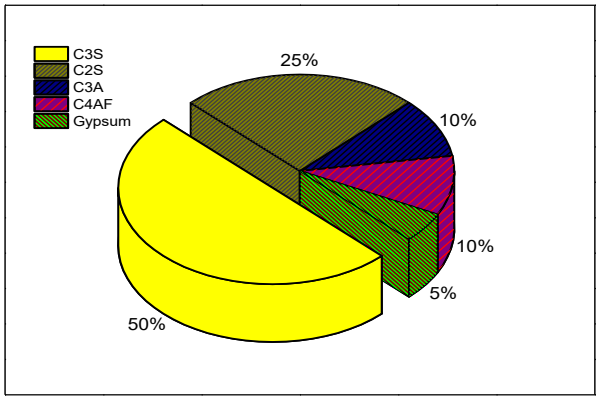


Fig. 5: Chemical compounds of cement.

The ettringite formation takes place during the complex hydration process. Some compound formed may depict shapes that looks like rod or needles and are in the form of amorphous solids. The complex reactions are presented below.

$$2\,Ca_3SiO_5 + 7\,H_2O \rightarrow 3\,CaO.2SiO_2.4H_2O + 3\,Ca(OH)_2 + 173.6\,kJ$$

$$2\,Ca_2SiO_4 + 5\,H_2O \rightarrow 3\,CaO.2SiO_2.4H_2O + Ca(OH)_2 + 58.6\,kJ$$

$$C_3A + 3\,CSH_2 + 26H \rightarrow C_6AS_3H_{32}, D\,H = 207\,cal/g$$

$$2C_3A + 3\,C_6AS_3H_{32} + 22H \rightarrow 3C_4ASH_{18}$$

$$C_3AF + 3\,CSH_2 + 3H \rightarrow C_6(A,F)S_3H_{32} + (A,F)H_3 + CH$$

$$C_4AF + C_6(A,F)S_3H_{32} + 2CH + 23H \rightarrow 3C_4(A,F)\,SH_{18} + (A,F)H_3$$

**Rates of hydration:** The dicalcium silicate has the least hydration rate compared to tetra calcium ferrite, also tricalcium silicate and tricalcium aluminate have more rate of hydration than both above respectively.

Air bubbles are trapped in the 5-6% voids that make up the cement paste after it has been created. Ettringite is also available in paste in amounts ranging from 15-20%. The amounts of CSH and calcium hydroxide in the paste are 50–60% and 20–25%, respectively.

The change in microstructure to enhance the strengthening process of the concrete can be achieved by reducing the w/c ratio, whereas the reaction for hydration can be compensated by the utilization of the superplasticizers. Hence this has been adopted on a large scale for concrete preparation (Jani & Hogland 2014). The reaction of hydration is a rapid process and to inhibit this process, the superplasticizers are used to provide more time for self-assembling along with the firm structure of the products borne during the process of cement hydration (Lu et al. 2017a). This phenomenon helps in the enhancement of mechanical strength (Lu et al. 2017b). The composition of the calcium silicate hydrate takes place during the hydration process, along with this, just after the CSH formation, the composition of the calcium hydroxide takes place. This is also termed Portlandite and is considered to be the product of the secondary reaction. While reacting with the $CO_2$, the portlandite changes to the compound named calcium carbonate. In the presence of adequate content of calcium hydroxide, this carbonation phenomenon provides the compact structure formation of the porous matrix.

**Beverage glass:** The degree of reaction during a time period is termed the pozzolanic activity of glass. This can also be identified as the $Ca^{2+}$ or calcium hydroxide ($Ca(OH)_2$) - the rate of the reaction with the pozzolan along with the water. The main determining factors that influence the pozzolan's reaction rate are its active phase content, distinct surface area, and chemical composition. The factors that have an impact on the external control of pozzolanic reaction include reaction temperature, water content, mix proportioning, and hydration product expansion. Pozzolan reactions are frequently impacted by the mix design blend, w/b ratio, and pozzolan substitution ratio. When water is available, it is discovered that the pozzolan confines the calcium hydroxides. As a result, pozzolanic materials are evaluated by the chemical measurement of the reactivity of the pozzolans. By examining calcium hydroxide intake over time, an assessment can be made. When the w/b ratio is higher, the Titrimety method can be used to measure it, as well as the spectroscopic method. When the w/b ratio is lower, however, the X-ray powder diffraction method was traditionally used. In this study, selective dissolutions, X-ray powder diffraction, or scanning electron microscopy image analysis methods are used for the examination. In this study selective dissolutions, X-ray powder diffraction, or scanning electron microscopy image analysis methods are used for the investigation. It was also shown that ASR will be higher if the size increases beyond the limit to obtain the pozzolanic reactivity particle size indicated by the strength activity index in the limits of 45-75 m. The glass powder particles with a size range of 45 to 75 m were tested to address this issue.

$$SiO_2 + Al_2O_3 + Fe_2O_3 \geq 70\ wt.\%$$

$$Aluminate\ (Al(OH)_4^-)\ and\ calcium\ hydroxide\ (Ca(OH)_2)\ with\ Water\ H_2O$$

$$Al(OH)_4^- + Ca(OH)_2 \rightarrow C_4AH_{13}, C_3AH_6$$

$$(Calcium\ Aluminate\ hydrates)$$

$$Portlandite\ (Ca(OH)_2)\ and\ Silicic\ acid\ (H_4SiO_4\ or\ Si(OH)_4)$$

$$\underset{(CH)}{Ca(OH)_2} + \underset{(SH)}{H_4SiO_4} \rightarrow \underset{(C-S-H)}{CaH_2SiO_4 . 2H_2O}$$

$$(Calcium\ Silicate\ Hydrate)$$

## ASR Expansion

The cement mortar bars were prepared for testing and the dimension of the specimen was as 25 mm×25 mm×285 mm. The water used in the water bath for samples was distilled water. The comparison of control and BG mixes ASR expansion is shown in Fig. 6. According to Siad et al. (2018), the use of glass in mortar in place of sand is the primary cause of ASR expansion. All BG mortar bar mixtures demonstrated alkali-silica reaction expansion below the permitted limit specified by the code. The ASR expansion value was lower compared to the control mortar mix, according to BG. Similar to this, no ASR expansion was detected for glass particles smaller than 1 mm, according to the literature review. The size of the glass particle has a significant impact on the alkali-silica reaction. When compared to the control mix, which had an ASR expansion of 0.027% at 7 days and 0.068 at 28 days, it was shown that the GP mix reduced this expansion.

## Compressive Strength

This test was performed to analyze the early age strength development along with the late ages for the mixes prepared with the utilization of ground glass. The control mix properties were compared with the mixes prepared with the ground glass up to 40 % replacement level. Fig. 7 shows the results of the compressive strength test for various mixes. All the samples have presented higher values of compressive strength than compared to the control sample, whereas the mix having substitution levels of 35 % and 40% are reported with a decrement in the strength than the control sample when tested at a duration of 28 days curing. The optimum results for the strength were obtained at a substitution of 30% tested for 28 days of curing. Also, the sample depicted the same trend when tested at a duration of 180 days. Whereas, a sample of mortar with a substitution level of 25% has shown the greatest strength out of all mixes. Statical insignificance was observed in the samples reported with increment in strength at 90 and 180 days of water curing when compared with the control sample. Since, the sample tested on 365 days depicted higher strength with a 25% substitution of the glass waste compared to the sample tested on 90 days of curing, which is higher by 8% compared with the control sample.

## Flexural and Split Tensile Strength

The prism and cylinder samples were tested for the investigation of flexural and splitting strength (Fig. 8). The standards of the BIS 516: 1959 were followed for the flexural strength testing of the samples. The results of the investigation are 5.60, 5.75, 5.96, 6.20, 6.85, 6.95, 7.15, 6.10, and 5.15 $N.mm^{-2}$ for mixes from G0 to G8 respectively. The graphical representation in Fig.8 shows that the optimum results were achieved at a 30% powder glass substitution level with the cement. The standards of the BIS 5816:1999 were adopted for the investigation of the split tensile strength. The investigation shows that the same phenomena followed in the case of the split tensile test. The result of the investigation is as 4.40,4.62, 4.95, 5.25, 5.48, 5.90, 6.01, 5.05, and 4.96 $N/mm^2$ for mixes from G0 to G8 respectively.

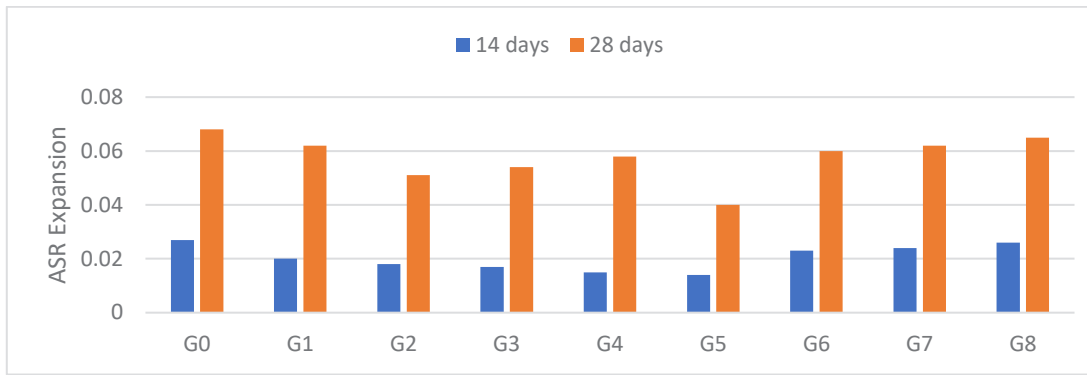


Fig. 6: ASR expansion for mixes.

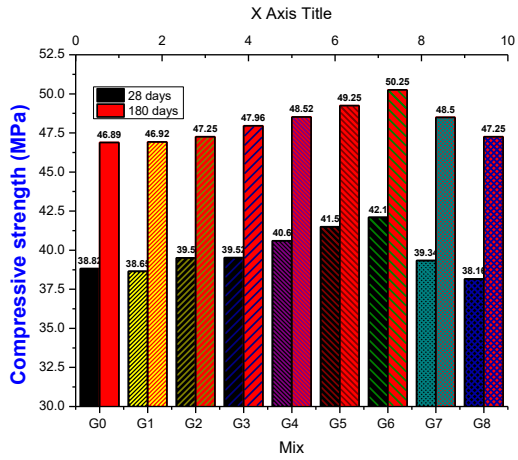


Fig. 7: Compressive strength for mixes.

## Abrasion Resistance

The friction is applied on the faces of the concrete due to the skidding along with another exposure, then the wear and tear take place. IS 1237 (2012) recommendations were followed to determine the abrasion resistance. The abrasion resistance of the samples is shown in Fig. 9. The observation represents that up to the substitution level of 30% of BG, the resistance was found to be in increasing order, whereas, the substitution above this value decreases the abrasion resistance of the samples. This phenomenon provides the samples prepared with higher waste glass content with lower abrasion resistance. Despite the 20% replacement level the compression resistance goes on decreasing and this phenomenon alters the glass powder concrete volume.

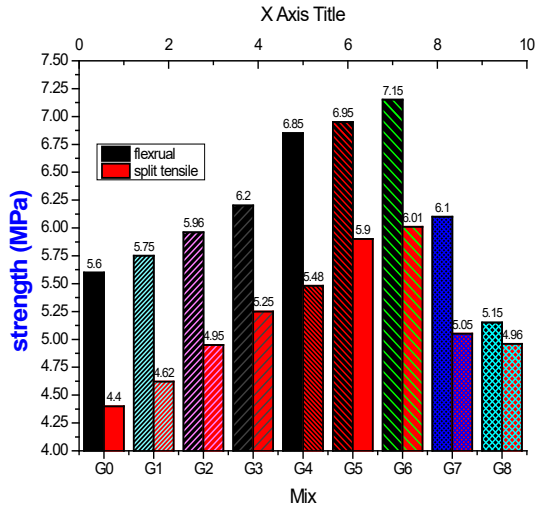


Fig. 8: Flexural and split tensile strength for a mix.

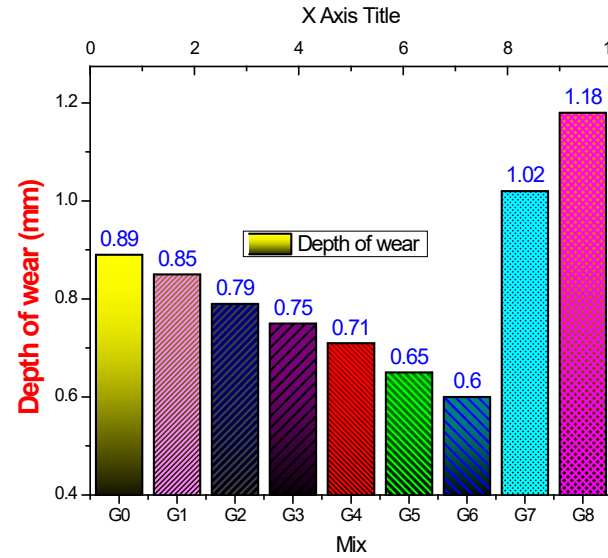


Fig. 9: Depth of wear (mm) for mixes.

## Environmental and Economic Considerations

To obtain sustainable construction techniques, the utilization of waste products tends to be more practice in the construction industry. Almost 0.9 tons of $CO_2$ along with $NO_X$ and $SO_X$ in moderate amounts are released into the environment in the production of 1-ton cement (Khan et al. 2014). Theoretically, a 1-ton number of natural resources can be protected while performing recycling for the same amount of waste glass. The nature of the glass is considered to be non-biodegradable and the disposal practices adopted for this are mostly land-fill techniques, thus its incorporation in the construction industry will save a lot of useful land along with more benefits to the environment. Optimum quantity utilization of the waste glass enhances the concrete properties this also proves to be beneficial for the environment by reducing the waste load in the atmosphere (Patzias 1987). The experimental study depicted that 20% substitution to the cement of the waste glass proves to be beneficial for concrete mixes. At the study place, waste glass procurement was done for 3 rup.kg$^{-1}$, and after processing waste glass, the cost reached 3.5 rup.kg. Whereas, the cost of the cement bag is 450 rup. kg$^{-1}$., which contains a cement weight of 50 kg. So, a 7 to 14% price decrement can be achieved by utilization of 15 to 25% of the waste glass.

## CONCLUSIONS

1. Beverage glass's physical, mechanical, and chemical characteristics fulfill the limits of Class F and Class C pozzolanic materials according to ASTM C 618.

2. ASR expansion shows that smaller particles of waste glass improve the resistance against alkali-silica reactions.
3. Compressive strength results indicated that waste glass increased up to 30% replacement with OPC increased the strength. The increment variation was 8.44% at 28 days and 7.14% at 180 days as compared to the control, but after that decrement in strength due to an increase in the finer voids in waste glass mixes.
4. Flexural strength and split strength show similar behavior as compressive due to its pozzolanic behavior. The variation in strength was achieved as 17.44% at 28 days for flexural and 7.57% at 28 days for spilled tensile but further increasing waste glass tensile strength was decreasing.
5. The economical consideration depicted that 25% substitution to the cement of the waste glass proves to be beneficial for concrete mixes. 7 to 14% price of concrete decreased by utilization of 15- 25% of waste glass.

## REFERENCES


Afshinnia, K. and Rangaraju, P.R. 2016. Impact of combined use of ground glass powder and crushed glass aggregate on selected properties of Portland cement concrete. Constr. Build. Mater., 117: 263-272.

Ballester, P., Mármol, I., Morales, J. and Sánchez, L. 2007. Use of limestone obtained from waste of the mussel cannery industry for the production of mortars. Cem. Concr. Comp., 37(4): 559-564.

Bisht, K. and Ramana, P.V. 2018. Sustainable production of concrete containing discarded beverage glass as fine aggregate. Constr. Build. Mater., 177: 116-124.

Bisht, K., Kabeer, K.S.A. and Ramana, P.V. 2020. Gainful utilization of waste glass for production of sulphuric acid resistance concrete. Constr. Build Mater., 235: 117486.

Bisht, K., Siddique, S. and Ramana, P.V. 2019. Employing atomic force microscopy technique and X-ray diffraction analysis to examine nanostructure and phase of glass concrete. Europ. J. Environ. Civil Eng., 51: 1-19.

Byars, E.A., Morales-Hernandez, B. and HuiYing, Z 2004 Waste glass as concrete aggregate and pozzolan: laboratory and industrial projects Concr. Soc., 38(1): 41-46.

Carsana, M., Frassoni, M. and Bertolini, L. 2014. Comparison of ground waste glass with other supplementary cementitious materials. Cem. Concr. Comp., 45: 39-45.

Choi, S.Y., Choi, Y.S. and Yang, E.I. 2017. Effects of heavy weight waste glass recycled as fine aggregate on the mechanical properties of mortar specimens. Ann. Nucl. Energy, 99: 372-382.

Du, H. and Tan, K.H. 2017. Properties of high volume glass powder concrete. Cem. Concr. Comp., 75: 22-29.

Farinha, C., De Brito, J. and Veiga, R. 2015. Incorporation of fine sanitary ware aggregates in coating mortars. Constr. Build. Mater., 83: 194-206.

Gupta, J., Jethoo, A.S. and Lata, N. 2020. Assessment of mechanical properties by using powder waste glass with cement in concrete mix. IOP Conf. Ser. Mater. Sci. Eng., 872: 012122.

Gupta, J., Jethoo, A.S. and Ramana, P.V. 2021. Magnetize mechanical strength effect on concrete due to diverse water. Mater. Today Proceed., 44: 4867-4872.

Idir, R., Cyr, M. and Tagnit-Hamou, A. 2011. Pozzolanic properties of fine and coarse color-mixed glass cullet. Cem. Concr. Comp., 33(1): 19-29.

Jani, Y. and Hogland, W. 2014. Waste glass in the production of cement and concrete–A review. J. Environ. Chem. Eng., 2(3): 1767-1775.

Khan, S.U., Nuruddin, M.F., Ayub, T. and Shafiq, N. 2014. Effects of different mineral admixtures on the properties of fresh concrete. Sci. World, 11: 56-63

Ling, T.C. and Poon, C.S. 2011. Utilization of recycled glass derived from cathode ray tube glass as fine aggregate in cement mortar. J. Hazard. Mater., 192(2): 451-456.

Ling, T.C. and Poon, C.S. 2013. Effects of particle size of treated CRT funnel glass on properties of cement mortar. Mater. Struct., 1)46): 25-34.

Lu, J.X., Duan, Z.H. and Poon, C.S. 2017b. Fresh properties of cement pastes or mortars incorporating waste glass powder and cullet. Constr. Build. Mater., 131: 793-799.

Lu, J.X., Zhan, B.J., Duan, Z.H. and Poon, C.S. 2017a. Using glass powder to improve the durability of architectural mortar prepared with glass aggregates. Mater. Des., 135: 102-111.

Matos, A.M. and Sousa-Coutinho, J. 2012. Durability of mortar using waste glass powder as cement replacement. Constr. Buil. Mater., 36: 205-215.

Nahi, S., Leklou, N., Khelidj, A., Oudjit, M.N. and Zenati, A. 2020. Properties of cement pastes and mortars containing recycled green glass powder. Constr. Build. Mater., 262: 120875.

Omran, A. and Tagnit-Hamou, A. 2016. Performance of glass-powder concrete in field applications. Constr. Build Mater., 109: 84-95.

Patzias, T. 1987. evaluation of sulfate resistance of hydraulic-cement mortars by the ASTM C 1012 test method. Spec. Pub., 100: 2103-2120.

Rashad, A. 2015. Brief on high-volume class F fly ash as cement replacement: A guide for civil engineer. Int. J. Sustain. Built. Environ., 4: 278-306

Rashed, A. 2014. Recycled waste glass as fine aggregate replacement in cementitious materials based on Portland cement. Constr. Build. Mater., 72: 340-357

Saccani, A. and Bignozzi, M.C. 2010. ASR expansion behavior of recycled glass fine aggregates in concrete. Cem. Concr. Res., 40: 531-536

Schwarz, N., Cam, H. and Neithalath, N. 2008. Influence of a fine glass powder on the durability characteristics of concrete and its comparison to fly ash. Cem. Concr. Comp., 6(30): 486-496.

Shayan, A. and Xu, A. 2006. Performance of glass powder as a pozzolanic material in concrete: A field trial on concrete slabs. Cem. Concr. Res., 3(36): 457-468.

Siad, H., Lachemi, M., Sahmaran, M., Mesbah, H.A. and Hossain, K.M.A. 2018. Use of recycled glass powder to improve the performance properties of high volume fly ash-engineered cementitious composites. Constr. Build. Mater., 163: 53-62.

Somani, P. and Gaur, A. 2020. Evaluation and reduction of temperature stresses in concrete pavement by using phase changing material. Mater. Today Proceed., 32: 856-864.

Taha, G.N. 2009. Utilizing waste recycled glass as sand/cement replacement in concrete. J. Mater. Civ. Eng., 21: 709-721

Tanwar, V., Bisht, K., Kabeer, K.S.A. and Ramana, P.V. 2021. Experimental investigation of mechanical properties and resistance to acid and sulphate attack of GGBS based concrete mixes with beverage glass waste as fine aggregate. J. Build. Eng., 41: 102372.

Nature Environment and Pollution Technology
An International Quarterly Scientific Journal

p-ISSN: 0972-6268
(Print copies up to 2016)
e-ISSN: 2395-3454

Vol. 22 | No. 1 | pp. 245-252 | 2023

Original Research Paper

https://doi.org/10.46488/NEPT.2023.v22i01.023

Open Access Journal

# Analysis of Water Quality of Hatirjheel Lake, Dhaka, Bangladesh

**A. B. M. Kamal Pasha, Syed Omayer Mustafa, S. M. Mahmudur Rahman†, Muhammad Abdullah, Md. Azharul Haque Chowdhury and Mahfuza Parveen**

Department of Environmental Science and Disaster Management (ESDM), Daffodil International University (DIU), Daffodil Smart City, Birulia, Savar, Dhaka, 1216, Bangladesh

†Corresponding author: S. M. Mahmudur Rahman; mahmudur.esdm0017.r@diu.edu.bd

**Nat. Env. & Poll. Tech.**
**Website: www.neptjournal.com**

*Received:* 09-04-2022
*Revised:* 28-05-2022
*Accepted:* 29-05-2022

**Key Words:**
Hatirjheel lake
Water quality parameters
Dissolved oxygen
Aquatic ecosystem

## ABSTRACT

The study assessed the status of water quality parameters for an urban water body (Hatirjheel Lake) in Dhaka, the Capital city of Bangladesh. Nine different water samples were collected from nine points of the lake during the dry season in January 2021. Water quality parameters such as pH, electrical conductivity (EC), total dissolved solids (TDS), total suspended solids (TSS), total alkalinity, total acidity, total hardness, $Ca^{2+}$ hardness, free $CO_2$, and dissolved oxygen (DO) were determined for the samples. The status of the parameters is pH (6.51-7.05), EC (510-600 $\mu S.cm^{-1}$), TDS (450-590 ppm), TSS (0.0-0.034 $mg.L^{-1}$), total alkalinity (80-392 $mg.L^{-1}$), total acidity (224-500 $mg.L^{-1}$), total hardness (348-452 $mg.L^{-1}$), $Ca^{2+}$ hardness (74-162 $mg.L^{-1}$), free $CO_2$ (730-1170 $mg.L^{-1}$), DO (2.7-5.5 $mg.L^{-1}$). However, the DO value at some points of the lake is too less (2.7 $mg.L^{-1}$ and 3.7 $mg.L^{-1}$) than the standard value (> 5-6 $mg.L^{-1}$) of ECR, DoE, which might not be healthy for any water body and aquatic ecosystem. Other water quality parameters are within the permissible limit of WHO and ECR, DoE.

## INTRODUCTION

Water is the most essential aspect of all-natural resources and is necessary for all living organisms to keep functioning. The regional and seasonal availability of water, as well as the quality of surface and groundwater, have a major impact on Bangladesh's environment, economic growth, and development. Water bodies are an essential component of a smart city. As Dhaka has grown into a megacity over the last few decades, the importance of green areas, wetlands, different water bodies, and uncluttered spaces is clearly understood. The city's waterbody is approximately 10-15% of its total terrestrial area (Miah et al. 2017). In the center of Dhaka, Hatirjheel lake plays a significant role in the city's drainage system. It was previously linked to the Banani, Dhanmondi, and Gulshan Lakes, as well as the Begun Bari Khal at the Rampura Bridge (Tariquzzaman et al. 2016). The lake, which covers 302 acres in the Tejgaon, Moghbazar, and Rampura regions, has played an important role as the area's only drainage system (Miah et al. 2017). It performs critical hydrologic functions such as source and sinks for the storm of the wide area of Dhaka. The storm sewers that discharge into Hatirjheel are built to carry stormwater. As a result, the Hatirjheel-Begunbari Khal system is the largest and most significant drainage system in Dhaka (Hossain et al. 2020) where approximately one-third of the city's stormwater is drained through this lake (Tehsin 2020).

Within the Dhaka Metropolitan Area (DMP), Haitrjheel is a prominent depression and the lake has long been in demand by city dwellers seeking physical and spiritual sustenance. Intense urban growth, combined with human intervention, has resulted in water quality depletion (bad odor, turbid water, inappropriate for use), as well as siltation and contamination from residential, industrial, and agricultural waste (Chowdhury & Chowdhury 2018). Different forms of urban waste are trapped and excessive waste water is deteriorating the quality of the lake ecosystem. As a result, it creates a great impact on biodiversity. Habitats for the species are deteriorating as well at the lake. Birds, fishes, aquatic plants, and other species have disappeared from the

**ORCID details of the authors:**

**A. B. M. Kamal Pasha**
https://orcid.org/0000-0002-6144-2537
**S. M. Mahmudur Rahman**
https://orcid.org/0000-0003-1992-8864
**Muhammad Abdullah**
https://orcid.org/0000-0001-6129-9622
**Md. Azharul Haque Chowdhury**
https://orcid.org/0000-0002-6383-4964
**Mahfuza Parveen**
https://orcid.org/0000-0002-1491-0481

lake where solid wastes are creating a problematic situation. In the lake bed, a dense layer of solid waste sediments is forming. As a result, plants that grow in a lake's bed that provide food for fish and other living organisms are no longer viable. The reverse scenario, on the other hand, is still being pursued. Excess nitrogen and phosphorous from waste will accumulate in lake water, and consequently, rooted aquatic plants and algae can invade quickly. Further, the algal bloom can cause navigation problems in lake water, as well as other environmental issues (Tariquzzaman et al. 2016).

Bangladesh, luckily, has sufficient freshwater reserves due to its geographic location. However, in Dhaka city, due to overcrowding, ignorance, and a lack of legal compliance, the overall quality of almost all of the waterbodies deteriorated (Parvin et al. 2019). The Hatirjheel Lake has been reduced to a drain and it is no longer pleasing to the eye. In contrast to the surrounding landscapes and the environment, this lake often spread excessive bad odor, and form a type of color that is not pleasant to the eyes. In this consequence, finding the present condition of water pollution and evaluating the water quality of this lake is very necessary. Thus, the present study was conducted to evaluate the water quality of Hatirjheel Lake by using the physicochemical properties of water.

## MATERIALS AND METHODS

### Study Area

Hatirjheel Lake (23°44′58.47″ N and 90°23′48.35″ W) is an urban recreational zone with a combination of integrated transportation facilities in the center of Dhaka city, with a length of 4.1 km and a surface area of 0.79 $km^2$ (Google earth). It is 2.6 meters deep on average. The lake is 460 meters wide at its widest point (Tariquzzaman et al. 2016). The lake is surrounded by the north, south, east and west by Gulshan-Banani, Maghbazar-

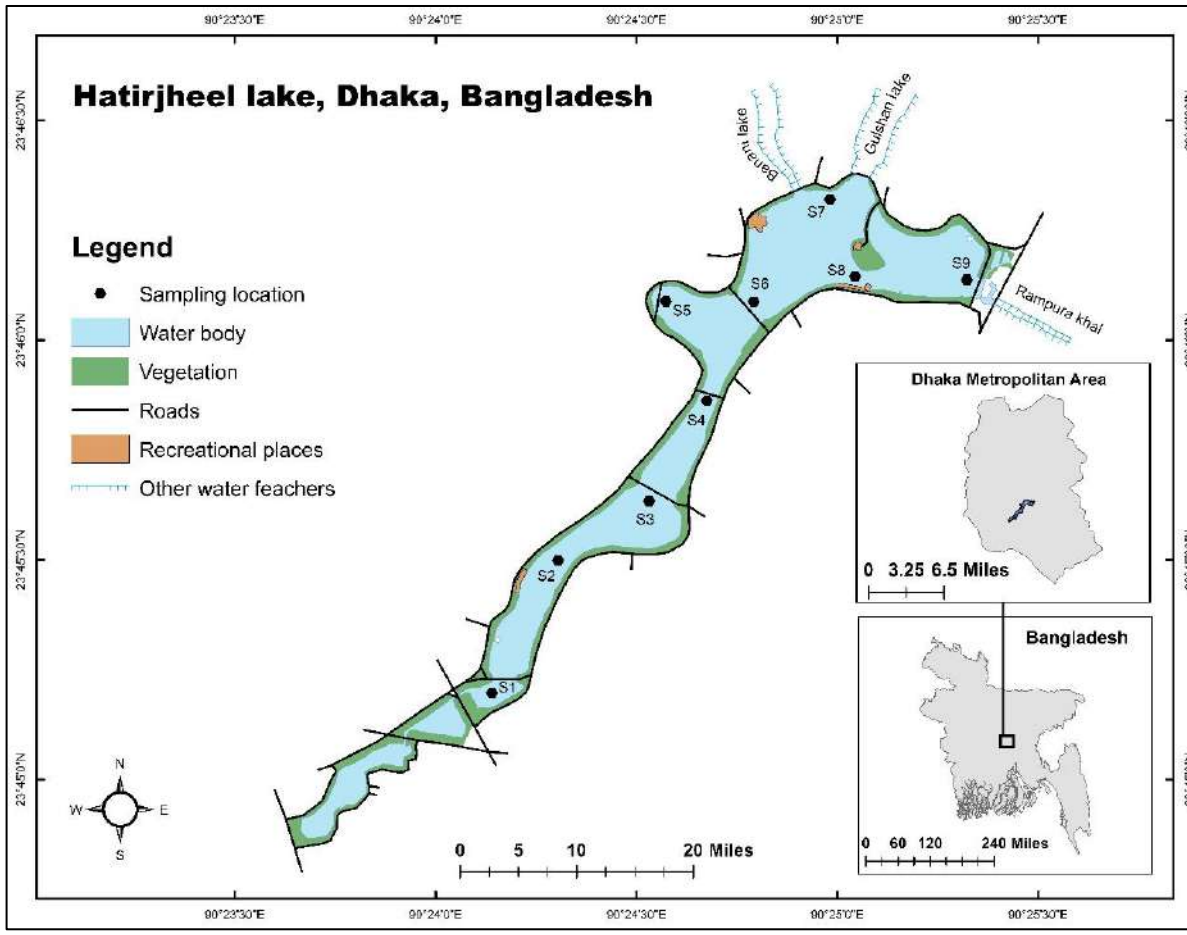


Fig. 1: Study area and the sampling locations.

Banglamotor, Rampura-Badda, and Tejgaon industrial areas respectively.

### Sampling and Sampling Locations

Nine (09) different water samples (surface water) were collected into 250 ml sample collection bottles (HDPE) from nine (09) different locations of this lake during the dry season on 16th January 2021 (Fig. 1). Before the collection of water samples, the bottles were cleaned and washed with detergent solution, and then rinsed with deionized water and dried. After completion of the sample collection, bottles were closed instantly and labeled distinctly (Rezwan et al. 2022). Finally, the samples were immediately transported to the laboratory for water quality parameter measurements and analysis.

### Sample Analysis and Instrumental Techniques

This study was carried out to explore the state of water and its quality throughout Hatirjheel Lake, after bringing the samples to the laboratory. To do that, the physical and chemical properties of the lake water were analyzed. The pH and Total Dissolved Solids (TDS) were determined by the *HANNA* pH/EC/TDS/Temperature Meter (HI9814), whereas. The electrical conductivity (EC) and temperature were measured by *HANNA* Pocket Conductivity Meter (HI-98303), DiST®4 EC Tester, and Dissolved Oxygen (DO) by Lutron 5509 Dissolved Oxygen Meter. The samples were diluted every time before each lab test to get the value within the existing range of the equipment. Acidity was analyzed through the titrimetric method using a standard solution of 0.02N NaOH solution, whereas, the alkalinity was measured through the same titrimetric method by titrating water samples against 0.02N HCl solution. Total Hardness and Calcium hardness were analyzed through a titration process by using a standard solution of 0.01N EDTA. The concentration of Free $CO_2$ was determined by the titrimetric method using 0.05N NaOH standard solution.

### Statistical Analysis

All experimental results are presented as the mean ± S.D. (n = 3). The mean difference was evaluated at the significant level of 0.01 and 0.05. Pearson's correlation was calculated among the water quality parameters. IBM SPSS (Version 23) and Microsoft Excel (Version 2016) were used to analyze the collected data. Bar charts and tabular forms were used to present the findings of this study.

## RESULTS AND DISCUSSION

The status of the physio-chemical properties of nine water samples in this study are given in Fig. 2. Among the water quality parameters, pH is a significant one (Hasan et al. 2009). The pH status of the samples ranges from 6.51-7.05 (Table 1). The study identified the highest pH value in sample 1 (S1) whereas the lowest pH value was in sample 7 (S7) (Fig. 2 A), which demonstrates that the water quality of S7 was quite acidic. The study found the presence of battery industries effluent and effluent from the restaurants around the area of S7 that indicated a lower pH value at the site compared to all other samples. A smiler study reported that Hatirjheel Lake water poses a mean value of pH 7.18 (Islam et al. 2015).

Electrical conductivity (EC) is an essential water quality parameter that indicates the water capacity for conducting the electrical current (Pasha et al. 2022). The status of EC throughout the lake ranges between 510-600 $\mu S.cm^{-1}$ (Table 1). The study recorded the highest EC value in samples 1 and 2 (S1 and S2) respectively, and the lowest in sample 8 (S8) (Fig. 2 B). The concentration of EC has exceeded the permissible limits in the lake (WHO 2003). Another study shows that the EC value of the same season was found about 709.3 $\mu S.cm^{-1}$ (Islam et al. 2015). They have also found that, during the post-monsoon season, the EC was lower, than that of the pre-monsoon season. Total dissolved solids (TDS) are the number of solids that exists in a water sample (Uddin et al. 2016). The concentration of TDS in the lake ranges between 450-590 ppm (Table 1). The study found the highest TDS value in sample 1 (S1) and the lowest in sample 8 (S8) (Fig. 2 C). The study identified the dumping of household wastes and discharge of household effluents in the area that indicated a higher TDS value at the sampling site among all other sampling sites. The standard limit of TDS is 1000 ppm (ECR 1997, Gorchev & Ozolins 2004). The concentration of TSS in the lake ranges between 0-0.034 $mg.L^{-1}$ (Table 1) whereas the standard value of TSS is 10 $mg.L^{-1}$ (ECR 1997) and 150 $mg.L^{-1}$ (Gorchev & Ozolins 2004). The study found the highest TSS value in sample 8 (S8) and the lowest in sample 2 (S2) (Fig. 2 D). The filtration process has been used through the Buchner Funnel in the TSS determination.

The titrimetric method has been used in the acidity, alkalinity, hardness, and free carbon dioxide determination (Pasha et al. 2022, Rezwan et al. 2022). Water has the capability to neutralize bases, which is considered acidity (Pasha et al. 2022). The concentration of Total acidity of the lake ranges between 224-500 $mg.L^{-1}$ (Table 1). The analysis shows that the highest value of acidity was found in sample 1 (S1) and the lowest in sample 7 (S7) (Fig. 2 E). Due to the existence of weak acid and a higher amount of base water can be highly alkaline, generally (Islam & Majumder 2020). The concentration of Total Alkalinity of the lake ranges between

Table 1: Level of different water quality parameters of Hatirjheel lake.

| Parameters | Minimum | Maximum | Mean | SD | ECR 1997 | WHO 1984 |
|---|---|---|---|---|---|---|
| pH | 6.51 | 7.05 | 6.80 | 0.18 | 6.5-8.5 | 6.5-8.5 |
| EC (µS/cm) | 510 | 600 | 558.89 | 30.18 | 500-700 | 150 |
| TDS (ppm) | 450 | 590 | 488.89 | 41.67 | 1000 | 1000 |
| TSS (ppm) | 0.00 | 0.04 | 0.02 | 0.01 | 10 | 150 |
| Acidity (mg/L) | 224 | 500 | 385.78 | 75.79 | - | - |
| Alkalinity (mg/L) | 80 | 392 | 248 | 126.68 | 200-500 | 200 |
| Total hardness (mg/L) | 348 | 452 | 392 | 35.72 | 200-500 | 500 |
| $Ca^{2+}$ hardness (mg/L) | 74 | 162 | 122.44 | 25.59 | - | 500 |
| Free $CO_2$ (mg/L) | 730.40 | 1170.40 | 906.36 | 162.34 | - | - |
| DO (mg/L) | 2.70 | 5.50 | 4.42 | 0.94 | > 5-6 | - |

* SD = Standard deviation

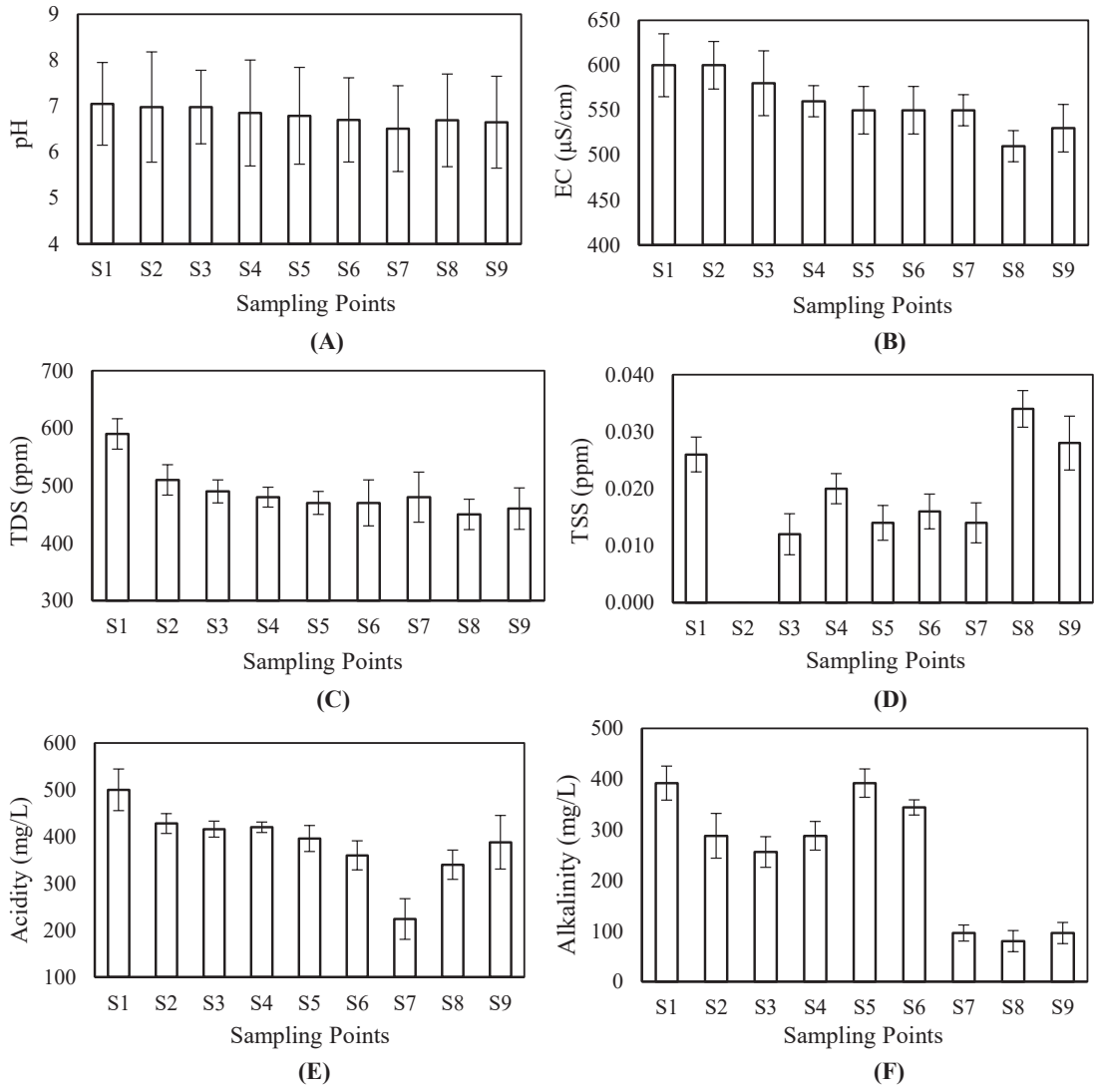

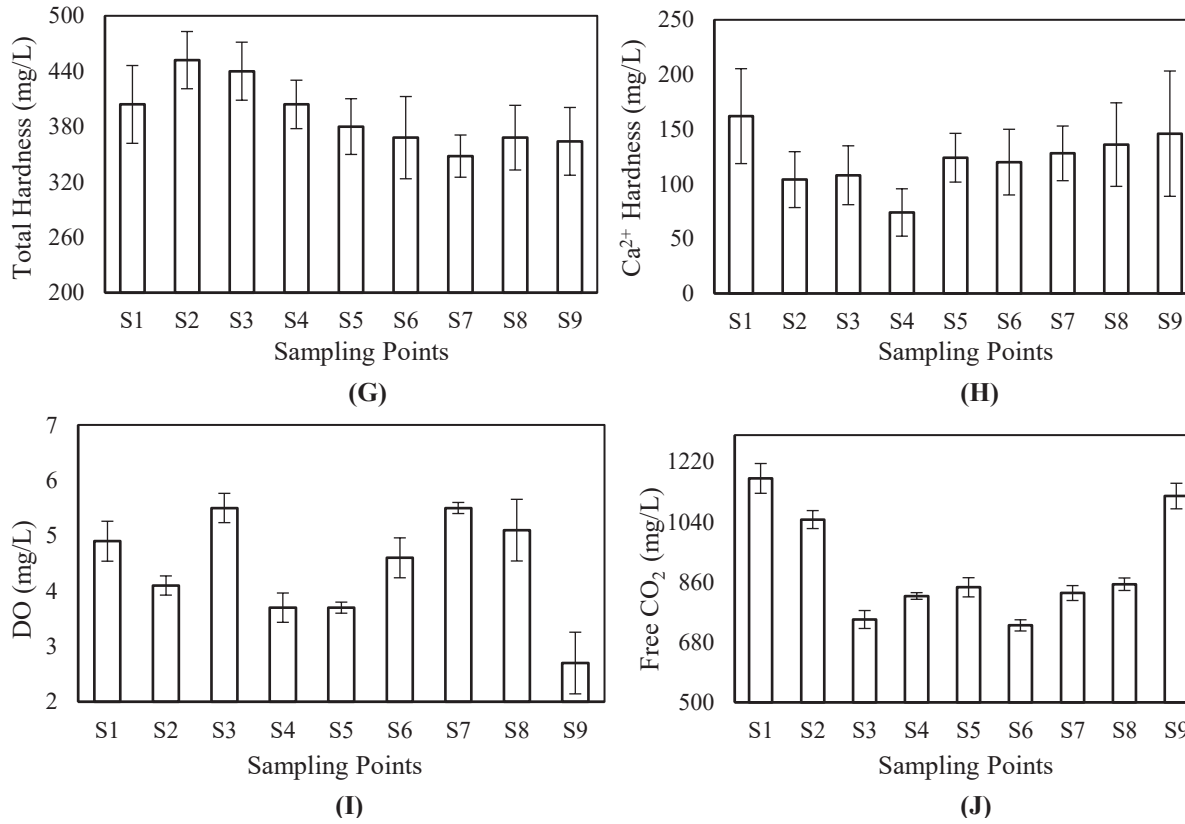


Fig. 2: Status of water quality in the Hatirjheel lake, (A) pH; (B) Electrical conductivity (EC); (C) Total dissolved solids (TDS); (D) Total suspended solids (TSS); (E) Total acidity; (F) Total alkalinity; (G) Total hardness; (H) $Ca^{2+}$ Hardness; (I) Dissolved oxygen (DO); (J) Free carbon dioxide.

Table 2: Cross-correlation matrix between the water quality parameters.

| WQP | pH | EC | TDS | TSS | Acidity | Alkalinity | TH | $Ca^{2+}$ H | Free $CO_2$ | DO |
|---|---|---|---|---|---|---|---|---|---|---|
| pH | 1 | | | | | | | | | |
| EC | **0.802 | 1 | | | | | | | | |
| TDS | *0.702 | **0.814 | 1 | | | | | | | |
| TSS | -0.280 | -0.621 | -0.106 | 1 | | | | | | |
| Acidity | **0.893 | 0.593 | 0.618 | -0.002 | 1 | | | | | |
| Alkalinity | 0.664 | 0.641 | 0.539 | -0.381 | 0.659 | 1 | | | | |
| TH | **0.879 | *0.774 | 0.440 | -0.567 | 0.665 | 0.440 | 1 | | | |
| $Ca^{2+}$ H | -0.132 | -0.142 | 0.326 | 0.515 | 0.017 | -0.147 | -0.423 | 1 | | |
| Free $CO_2$ | 0.316 | 0.319 | 0.581 | 0.193 | 0.487 | 0.011 | 0.146 | 0.558 | 1 | |
| DO | 0.059 | 0.176 | 0.232 | -0.084 | -0.301 | -0.070 | 0.068 | 0.089 | -0.405 | 1 |

Legend: ** = Significant at 0.01 level; * = Significant at 0.05 level

WQP = Water Quality Parameters; TH = Total Hardness; $Ca^{2+}$ H = $Ca^{2+}$ Hardness;

80-392 $mg.L^{-1}$ (Table 1), where the standard value is 200-500 $mg.L^{-1}$ (ECR 1997, WHO 2003). The highest alkalinity was found in samples 1 and 5 (S1 and S5) and the lowest in sample 8 (S8) (Fig. 2 F). The study observed the mixing of sewage effluents with the water body around the sampling site of S1 and S5. The effluents from the households contained several chemical compounds that contributed to the higher alkalinity in the S1 and S5 sampling area compared to all other samples.

Hardness in water is the presence of minerals (calcium and magnesium) in the water. Hard water contains dissolved minerals in a significant amount, and soft water contains minerals dissolved in fewer amounts (Takahashi & Imaizumi

1988). The value of the total hardness of the lake is found between 348-452 mg.L$^{-1}$ (Table 1). The highest total hardness was found in sample 2 (S2) and the lowest in sample 7 (S7) (Fig. 2 G). The standard concentration of Total Hardness is 200-500 mg.L$^{-1}$ (ECR 1997, WHO 2003). All nine (09) water samples were evaluated to detect the $Ca^{2+}$ hardness. The value of $Ca^{2+}$ Hardness of the lake is ranged between 74-162 mg.L$^{-1}$ (Table 1) and the standard limit of $Ca^{2+}$ Hardness is 500 mg.L$^{-1}$ (Gorchev & Ozolins 2004, WHO 2003)a basic human right and a com- ponent of effective

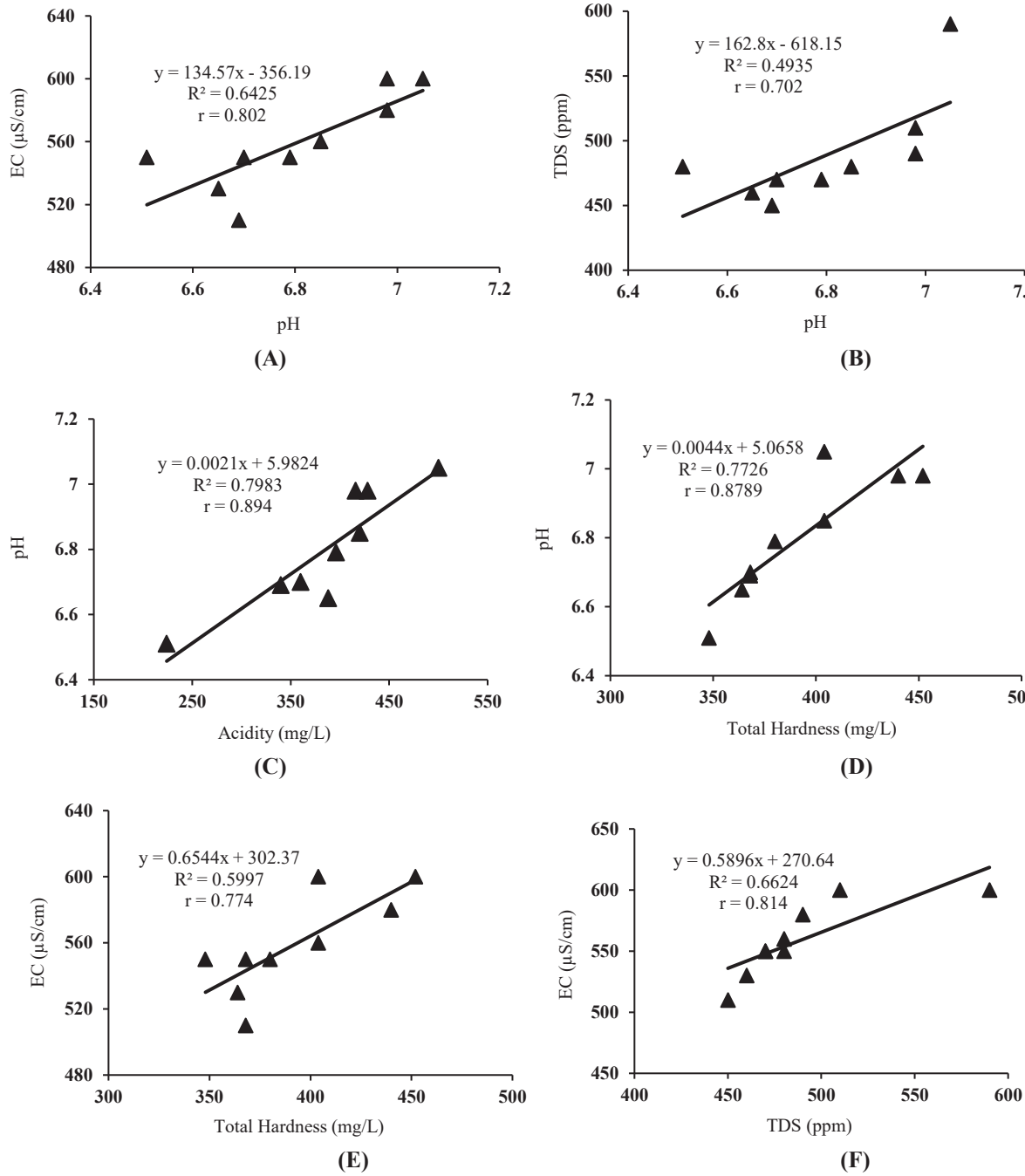


Fig. 3: Correlation between, (A) pH and EC; (B) pH and TDS; (C) pH and Acidity; (D) pH and Total Hardness; (E) EC and Total Hardness; (F) EC and TDS.

policy for health protection. The importance of water, sanitation and hygiene for health and development has been reflected in the outcomes of a series of international policy forums. These have included health-oriented conferences such as the International Conference on Primary Health Care, held in Alma-Ata, Kazakhstan (former Soviet Union. The highest total hardness was found in sample 1 (S1) and the lowest in sample 4 (S4) (Fig. 2 G). Fig. 2 (J) shows that the concentration of Free $CO_2$ in the lake is found between 730-1170 $mg.L^{-1}$. The highest free $CO_2$ was found in sample 1 (S1) and the lowest in sample 6 (S6) (Fig. 2 J). As an indicator of the appropriate water quality, dissolved oxygen (DO) is a vital parameter (Pasha et al. 2022). The concentration of DO in the water of Hatirjheel Lake is ranged between 2.7-5.5 $mg.L^{-1}$. In the present study, the highest DO was found in samples 3 and 7 (S3 and S7), and the lowest in sample 9 (S9) (Fig. 2 I). According to the Environmental Conservation Rules by the Department of Environment, Government of Bangladesh, the DO value should have to be 5 $mg.L^{-1}$ for a healthy aquatic ecosystem and the survival of the aquatic species (Uddin et al. 2016, ECR 1997). The study found that the value of dissolved oxygen was significantly lower in all other samples except samples 3, 7, and 8. It indicates that the concentration of DO is not sufficient in the lake water.

The cross-correlation matrix here is showing the correlation between the water quality parameters in Table 2. The relationship between pH and EC represents that the value of pH is increasing with the increase of EC. It is a positive relationship, where r = 0.802 (strong positive relationship) (Fig. 3 A). The relationship between pH and TDS of the sample waters represented that the value of pH is increasing with the increase of TDS. It is also a positive relationship, where the r = 0.702 (moderate positive relationship) (Fig. 3 B). The relationship between pH and Acidity represents that the value of pH is increasing with the increase in total hardness. It is a positive relationship, where r = 0.894 (strong positive relationship) (Fig. 3 C). The relationship between pH and Total Hardness of the sample waters represented that the value of pH is increasing with the increase of Total Hardness. It is also a positive relationship, where the r = 0.879 (strong positive relationship) (Fig. 3 D). The relationship between EC and Total Hardness represents that the value of EC is increasing with the increase in total hardness. It is a positive relationship as well, where r = 0.774 (moderate positive relationship) (Fig. 3 E). The relationship between EC and TDS of the sample waters represented that the value of EC is increasing with the increase of TDS. It is also a positive relationship, where the r = 0.814 (strong positive relationship) (Fig. 3 F).

## CONCLUSIONS

The status of the determined water quality parameters (pH, EC, TDS, TSS, alkalinity, acidity, hardness, $Ca^{2+}$ hardness, Free $CO_2$) of the Hatirjheel Lake is quite good in terms of the surrounding environment, as the responsible authorities working continuously to improve the water quality of the lake from 2014. However, the water quality is not good enough for the purpose of human use. Though, the DO value at some point of the lake is too less (2.7 $mg.L^{-1}$ at S9, 3.7 $mg.L^{-1}$ at S4 and S5) than the standard value (>5-6 $mg.L^{-1}$), and the mean DO value of the lake is only 4.4 $mg.L^{-1}$. So, still, there is scope to work on the biological water quality, turbidity of the water body, etc. to ensure the healthy ecosystem of the lake.

## ACKNOWLEDGMENTS

The authors are grateful and give thanks for this work being supported by the faculty and officials of the Department of Environmental Science and Disaster Management (ESDM), Daffodil International University (DIU).

## REFERENCES

Chowdhury, S. and Chowdhury, R. 2018. Assessment of water quality of Hatirjheel and Gulshan lakes. International Journal of Innovative Research in Science, Engineering, and Technology, 7(7): 8374-81.

ECR 1997. The Environment Conservation Rules. Ministry of Environment and Forest, Government of the People's Republic of Bangladesh, pp. 179-227.

Gorchev, H.G. and Ozolins, G. (ed.) 2004. Guidelines for Drinking-Water Quality, 3rd Edition. WHO 1:564.

Hasan, I. Rajia, S. Kabir, K.A. and Latifa, G.A. 2009. Comparative study on the water quality parameters in two rural and urban rivers emphasizing on the pollution level. Glob. J. Environ. Res., 3(3): 218-222.

Hossain, M.I. Ansari, M.N.A. and Saika, U. 2020. Lake base urban recreation in Dhaka metropolitan area: Hatirjheel lake as a potential case. International Journal of Research Granthalaya, 5(12): 266-74.

Islam, M.S. and Majumder, S.M.M.H. 2020. Alkalinity and hardness of natural waters in Chittagong City of Bangladesh. Int. J. Sci. Bus., 4(1): 137-150.

Islam, M.S. Rehnuma, M. Tithi, S.S. Kabir, M.H. and Sarkar, L. 2015. Investigation of water quality parameters from Ramna, Crescent and Hatirjheel lakes in Dhaka city. Journal of Environmental Science and Natural Resources, 8(1): 1-5.

Miah, M.B. Majumder, A.K. and Latifa, G.A. 2017. Evaluation of microbial quality of the surface water of Hatirjheel in Dhaka city. Stamford Journal of Microbiology, 6(1): 30-33.

Parvin, M. Muzahed, M. and Majumder, A.K. 2019. A comparative study on the selected parameters of water quality of Dhanmondi, Ramna and Hatirjheel lakes in Dhaka city. Journal of the Asiatic Society of Bangladesh, Science, 45(2): 261-65.

Pasha, A.B.M.K. Abdillahi, M. M. Rahman, S.M.M. Mozumder, S. Chowdhury, A.H. Fuente, J.A.D. and Parveen, M. 2022. Studies on physicochemical properties of Buriganga river water and the vegetation coverage of surrounding area, Dhaka, Bangladesh. Sci. Int. (Lahore), 34(2): 73-78.

Rezwan, S.M. Chowdhury, M.A.H. and Rahman, S.M.M. 2022. Assessment of ecosystem services, plant diversity pattern, and water quality of an urban water body in Dhaka, Bangladesh. In: Abdalla, H. Rodrigues, H. Gahlot, V. Salah Uddin, M. and Fukuda, T. (eds) Resilient and Responsible Smart Cities. Advances in Science, Technology & Innovation. Springer, Cham.

Tariquzzaman, S.M. Nishu, S. Saeed, T.F. and Reday, R.A. 2016. Water quality and EIA of simple Hatirjheel lake. In: Proceedings of the 3rd International Conference on Civil Engineering for Sustainable Development, (February), pp. 978–84.

Takahashi, Y. and Imaizumi, Y. 1988. Hardness in drinking water. Eisei Kagaku, 34(5): 475-579.

Tehsin, S. 2020. Ecosystem Services of Hatirjheel Lake of Dhaka, Bangladesh. (Unpublished).

Uddin, M.G. Moniruzzaman, M. Hoque, M.A.A. Hasan, M.A. and Khan, M. 2016. Seasonal variation of physicochemical properties of water in the Buriganga River, Bangladesh. World Appl. Sci. J., 34(1): 24-34.

WHO 2003. Guidelines for the Safe Recreational Water Environment. Vol. 1, Coastal and Fresh Waters. World Health Organization.

Nature Environment and Pollution Technology
An International Quarterly Scientific Journal

p-ISSN: 0972-6268
(Print copies up to 2016)
e-ISSN: 2395-3454

Vol. 22 | No. 1 | pp. 253-259 | 2023

Original Research Paper

https://doi.org/10.46488/NEPT.2023.v22i01.024

Open Access Journal

# Bioinspired Trichogenic Silver Nanoparticles and Their Antifungal Activity Against Plant Pathogenic Fungi *Sclerotinia sclerotiorum* MTCC 8785

**V. Guleria and J. Saxena†**

Department of Biotechnology, University Institute of Biotechnology, Chandigarh University, S.A.S Nagar, Punjab, India

†Corresponding author: J. Saxena; jina.saxena@gmail.com

**Nat. Env. & Poll. Tech.**
**Website: www.neptjournal.com**

*Received:* 10-06-2022
*Revised:* 04-08-2022
*Accepted:* 10-08-2022

**Key Words:**
Trichoderma
Enzyme stimulation
AgNPs
Antifungal
Sclerotinia

## ABSTRACT

There is a pressing need for new nanomaterials for multipurpose functions. The biological synthesis of nanoparticles is environment-friendly, least toxic, and cost-effective. An experiment was designed to use extracellular amylases in the cell-free filtrate (CFF) for the biosynthesis of silver nanoparticles (AgNPs) from the *Trichoderma harzianum* MTCC 801 strain. Potato dextrose broth (PDB) as general-purpose growth media and amylase production media (APM) as enzyme-specific production media have been used for sub-merged fungal cultivation and nanoparticle synthesis. AgNPs synthesized in the CFF of PDB were compared with AgNPs synthesized from the CFF using APM. The cell-free filtrate obtained upon enzyme stimulation has contributed to the reduction and capping process of nanosilver. The synthesized AgNPs showed a spectral peak at 420 nm, a characteristic feature of AgNPs. The particles were monodispersed, 50 nm in size, and spherical in shape as well as have shown an antifungal effect (100% inhibition) against *Sclerotinia sclerotiorum* MTCC8785. This is the first report to synthesize trichogenic AgNPs using extracellular amylases against the phytopathogen *Sclerotinia* strain.

## INTRODUCTION

The field of nanobiotechnology has gained massive attraction over the last few decades, curating the applications of nanomaterials into diverse fields of daily importance. Nanomaterials fall into the size range of 1-100 nm and exhibit remarkable surface, physical, chemical, and biological properties (Ahamed et al. 2010). There is a lot of attraction among researchers for biogenic AgNPs as it is a new-age nano alternative and is employed as a modern tool in agriculture, medicine, and industry. The biological route is the bottom-up approach with preferences over physical and chemical routes for nanoparticle synthesis. This approach offers advantages like less waste generation, low energy consumption, and simple and cost-effective steps (Vigneshwaran et al. 2007). All microbes and herbal extracts can be utilized for such type of blend as they served as a source for bio reductants and bio stabilizers (Siddiqi et al. 2018).

Fungi are easy to handle and culture in laboratories. Moreover, they are the excellent secretor of extracellular enzymes, metabolites, and other proteins. Due to these potent reasons, several fungi have prospected for the synthesis of metal nanoparticles (Duhan & Gahlawat 2014). Fungal enzymes and proteins are involved in the reducing and capping process of metal ions into a metal zero-oxidation state. Fungal proteins provide a better range to control the shape, size, and stability of nanoparticles (Saxena et al. 2017).

Enzymes can serve as a set of structurally assorted tools in bionanotechnology and play crucial roles in the self and dynamic assembly of nanostructures. The enzymes are available commercially, however, the pure form is very costly. Extraction of microbial enzymes offers cost-effective procedures and ease of handling. Microbes like bacteria and fungi have enzymes with specific amino acids, and chemical groups catalyzing biochemical and biological processes. The putative mechanism for nanoparticle synthesis involves the interaction of reducing thiol groups from cysteine with silver ions to form Ag-S bonds and complete bioreduction (Mishra & Sardar 2010, Thapa et al. 2017).

Phytopathogens are emerging threats to commercially important crops and harm the economy of developing countries the most. Over the last decade, *T. harzianum,* which is a mycoparasitic fungus has been used as a strong biocontrol agent against many plants' pathogenic fungi. *Trichoderma* strains release several hydrolytic enzymes upon the growth of fungal hyphae and degrade the cell wall of pathogenic fungi. The enzymes are amylases, Proteases, and chitinases which are also associated with the

mycoparasitic nature of Trichoderma strains. The promising role of *T. harzianum* as a biocontrol agent along with its simple handling opens avenues for its extensive use in the field of bionanotechnology to develop value-added products. Fungi that belong to the genus *Trichoderma* sp also secrete nitrate reductases, which are equipped for the synthesis and stability of nanoparticle cores (Guilger-Casagrande et al. 2019).

*S. sclerotiorum* is a very harmful plant pathogenic fungi that cause sclerotium disease on crop plants resulting in tremendous global economic losses. *S. sclerotiorum* exhibit a wide host range covering 278 genera in 75 families of plants. The most common disease is Sclerotinia stem rot (SSR) or white mold along with crown rot, drop, cottony rot, and blossom blight (Carpenter et al. 2021). Multicellular melanized sclerotia are the hardest structure known from these fungi that can live for many years in heterogeneous conditions. The pathogenesis initiates from the ascospores after the germination of these hardened black structures. The emergence of high-level resistance in sclerotinia strains against benzimidazole and carbendazim is alarming and has been difficult to control so it is imperative to find new alternatives against this pathogen to check for any sudden outbreak. Applications of fungicides could be possible solutions but may cause severe environmental hazards. Researchers have reported the effect of AgNPs from the Penicillium strain against *S. sclerotiorum* however there is a pressing need to explore more and develop a new breed of stable AgNPs with better bioefficacy (Saxena et al. 2017, Tomah et al. 2020).

## MATERIALS AND METHODS

### Fungal Growth Conditions

*T. harzianum* MTCC 801 and *S. sclerotiorum* MTCC 8785 were acquired from Microbial Type Culture Collection (MTCC), Chandigarh, India. Both the fungal strains were grown on potato dextrose agar (PDA) at 28ºC for 96 h and routinely maintained on PDA slants.

### Extracellular Synthesis of Biogenic AgNPs

The mycelium of *T. harzianum* MTCC 801 was inoculated in PDB as well as APM (containing 1 % soluble starch as inducer) and kept at 28°C for 120 h. After incubation, mycelia were collected by washing with autoclaved distilled water to get rid of media components and transferred to autoclaved distilled water followed by incubation for 48 hrs at 28°C. The cell-free filtrate procured after filtration of mycelia was exposed to 1 mM silver nitrate ($AgNO_3$) and incubated at room temperature in the dark for 3-5 days. A CFF without $AgNO_3$ was used as a negative control (Guilger-Casagrande et al. 2019).

### Extracellular Amylase Production Using *T. harzianum* MTCC 801

*T. harzianum* MTCC 801 was cultured on PDA containing starch 1% (w/v) as a sole source of carbon. After incubation for three days, the plates were exposed to Iodine-KI solution and the clear zone of hydrolysis surrounding the colony was observed (Molla et al. 2022).

### Characterization of AgNPs

#### Morphological Valuation

The color change of the incubated solution was recorded which further suggested the synthesis of AgNPs.

#### UV-Visible Spectroscopy Analysis

The synthesized AgNPs using PDB and amylase production media were scanned in scales between 300-800 nm at 0.1 nm resolution using a UV-Vis spectrophotometer.

#### Transmission Electron Microscope (TEM) Analysis

To assess the proportions of synthesized AgNPs using PDB and APM, TEM analysis was done. A small amount of AgNPs solution was loaded on copper grids in TEM and images were captured followed by the analysis of AgNPs (Alves & Murray 2022).

#### Purification of AgNPs

AgNPs from the solution were separated during centrifugation at 9000-10,000 for 5 min at 4°C. Dark brown pellets obtained were splashed with distilled water, dried, and used for further experimental assays.

#### Antifungal Assay

To demonstrate the antifungal activity of synthesized AgNPs using PDB and amylase production media, PDA plates were prepared using different concentrations of AgNPs (25, 50, and 100 $\mu g.mL^{-1}$). Point inoculation of *S. sclerotiorum* MTCC 8785 was done onto each plate and incubated at 28°C for 7 days. The growth of fungal mycelium over the plate was recorded and compared with the control. Plate prepared using antifungal fluconazole (100 $\mu g.mL^{-1}$) and inoculated with $10^5$ spores of *S. sclerotiorum* MTCC 8785 was used as a positive control (Essghaier et al. 2022).

## RESULTS AND DISCUSSION

### Morphological and Microscopic Characterization of *T. harzianum* MTCC 801

In this present investigation, fungal strains were routinely sub-cultured and characterized morphologically (Fig 1A). Colonies of *T. harzianum* MTCC 801 were fast-growing, initially white and gradually developing yellowish-green

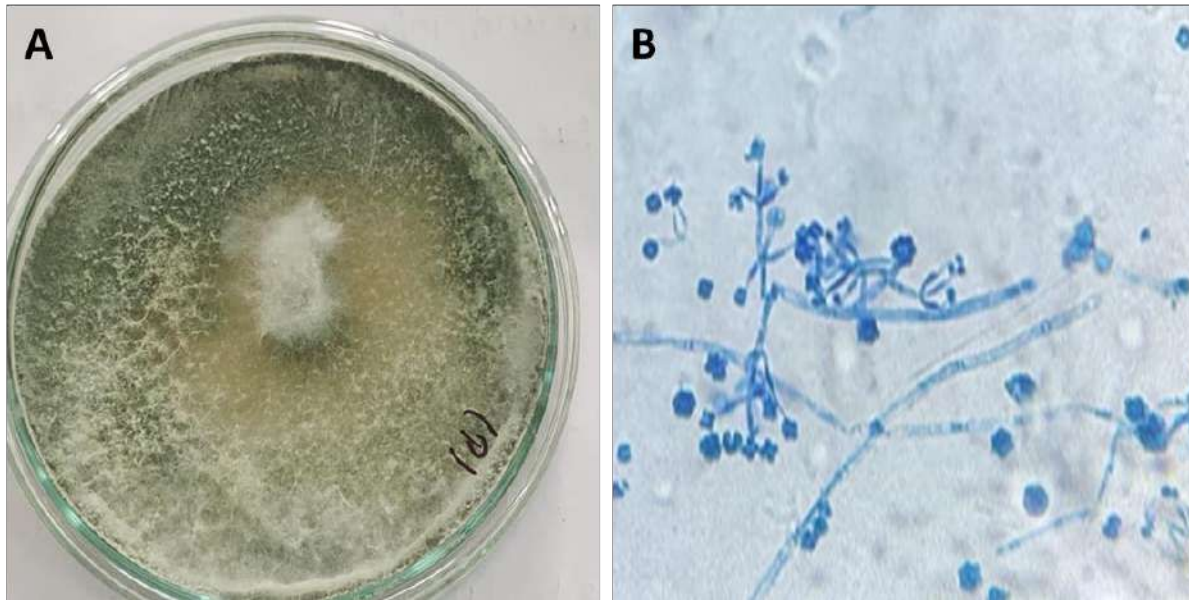


Fig. 1: Fungal characterization. (A) Plate morphology of *T. harzianum* MTCC 801 after 7 days of growth on PDA. (B) Microscopic features of the fungal strain at 40 X.

to deep green tufts, in small zones or with concentric rings on the media surface. Microscopically the fungi exhibit conidiophores which are irregularly branched and bear flask-shaped phialides. Conidia are green and born on conidial tips clustered together. (Fig. 1B).

**Synthesis of AgNPs**

At the first step for synthesis of Trichogenic AgNP, the fungal (1X105 spores.mL$^{-1}$) strain was inoculated and cultivated separately in 100 mL PDB and Amylase production media for 3-5 days at 28$^{o}$C, 120 rpm under submerged batch cultivation. The growth of fungi can be observed as a round ball of biomass which is characteristic of submerged cultivation (Fig. 2A and 2C). Through filtration,

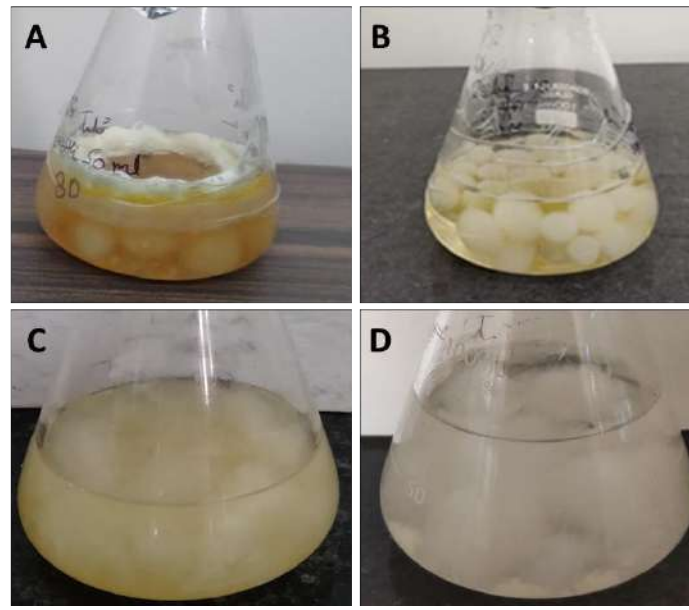


Fig. 2: (A) Subculture of *T. harzianum* MTCC 801 using PDB at 28$^{o}$C, (B) Fungal biomass in deionized distilled water for harvesting extracellular proteins, (C) Subculture of fungal strain using amylase production media (with starch as inducer) at 28$^{o}$C, (D) Fungal biomass in deionized distilled water for harvesting extracellular proteins (amylases).

media components were then removed, and the biomass (10 gm, fresh wet weight) after washing was transferred to 50 mL distilled water, which was kept under the same conditions for three days (Fig. 2B and 2D). In cell-free filtrate, fully, grown biomass secretes extracellular enzymes by reverse osmosis, which are agents for bioreduction and capping during the synthesis process. Amylase production media (APM) was used because amylase-mediated bioreduction is well documented (Mishra & Sardar 2010). Moreover, starch is used as an inducer in APM, which stimulates the strain to secrete more extracellular amylase under controlled conditions. In this paper, we have for the first time utilized extracellular amylases from the *Trichoderma* strain for nanoparticle synthesis. Moreover, microbes secrete nitrate reductase enzymes in the extracellular milieu which reduces the $Ag^+$ to AgNPs (Das et al. 2014). Further, Guilger-Casagrande et al. (2019) reported that *Trichoderma harzianum* utilizes nitrate reductase for the reduction of $Ag^+$ to AgNPs (Guilger-Casagrande et al. 2019).

### Amylase Assay

Colonies of *T. harzianum* MTCC 801 were assessed for amylase production using starch hydrolysis assay. The fungus grown with inducer starch agar media is capable of growing by producing extracellular amylases. The amylolytic activity was monitored by the qualitative KI-iodine halo zone assay. *T. harzianum* MTCC 801 showed a clear zone of hydrolysis (Fig. 3).

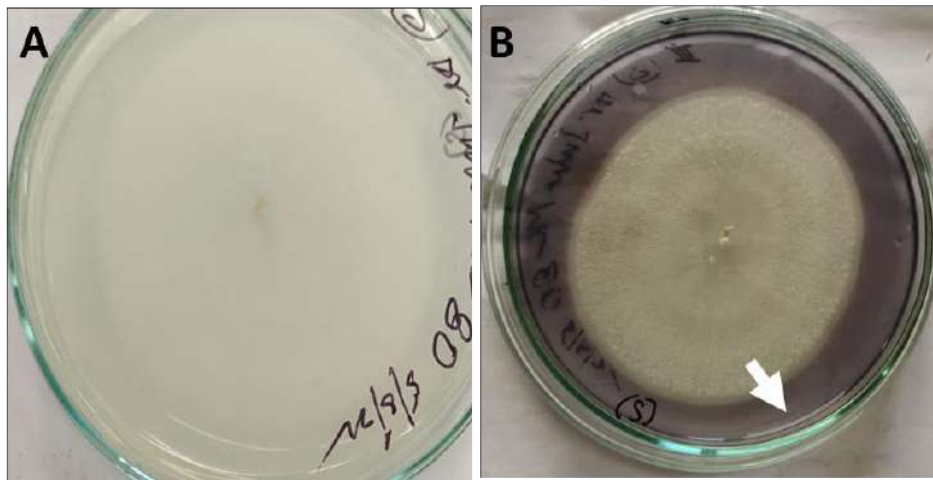


Fig. 3: Primary (Starch Hydrolysis Plate assay) screening of *T. harzianum* MTCC 801 for extracellular amylase production. (A) Growth of fungal strain on Starch agar before adding KI-$I_2$ solution. (B) Clear areas (marked with red arrow) show positive detection of fungal strain for starch hydrolysis as shown by an arrow.

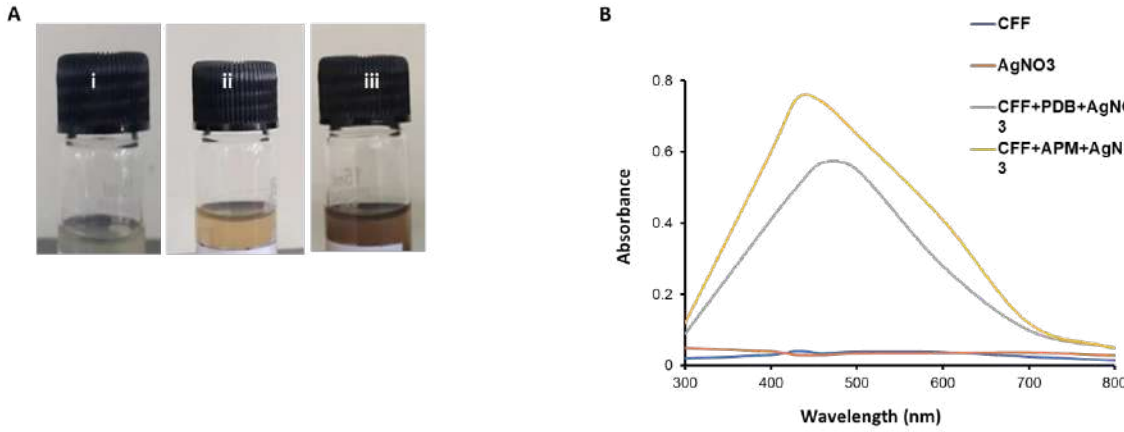


Fig. 4: AgNPs synthesis. (A) Change in color in cell-free filtrate harvested (i) without $AgNO_3$, (ii) using biomass grown in PDB, and (iii) using biomass grown in APM. (B) UV–Vis spectral peak of AgNPs.

## Characterization of AgNPs

**UV-VIS Spectrophotometer:** Fungal biomass in CFF was removed by filtration and challenged by metal stress with $AgNO_3$ at 1 mM concentration under dark conditions. The color changed gradually to reddish-brown from yellow in CFF indicating the synthesis of AgNPs (Fig. 4A). The sharp color change was observed on the fifth day of exposure to metal ions with reductants under dark conditions at room temperature. However, the color change was dark brown in CFF-APM as compared to CFF-PDB which was further confirmed with a UV-Vis spectra scan (Fig. 4B). The color changes differently in both the cell filtrates because of the difference in enzymes present in CFF (Pandey et al. 2018). Also, the silver metal ion upon reduction in presence of these enzymes shows characteristic surface plasmon resonance (Fig. 4B). The synthesis was confirmed and compared initially by UV-Vis spectroscopy, indicating the peculiar peaks for nanosilver exhibit intense absorption at 422 nm. The oscillation waves of electrons of AgNPs are in resonance with the light waves, giving rise to a unique surface plasmon resonance (SPR) absorption band (400-440 nm), which is also the origin of the observed color (Zhang et al. 2016). The sharp peak in CFF-APM indicates monodispersed particles and a size scale in nanometers. The band in CFF-APM was intense when compared to CFF-PDB, clearly correlating that the intense color change in CFF-APM was due to amylases. Fungal amylase has -SH groups that bind, reduce and stabilize AgNPs (Khan et al. 2013). Our data is in agreement with Saxena et al. (2016), who synthesized AgNPs using cell-free filtrate of *S. sclerotiorum* MTCC 8785 grown in PDB media.

Table 1: Antifungal activity of AgNPs.

| Treatment | Inhibition rate (%) |
|---|---|
| AgNPs [25 $\mu g.mL^{-1}$] | 45 |
| AgNPs [50 $\mu g.mL^{-1}$] | 75 |
| AgNPs [100 $\mu g.mL^{-1}$] | 90 |
| Flucanazole [100 $\mu g.mL^{-1}$] | 100 |

**TEM analysis:** TEM analysis revealed that particles synthesized using PDB (Fig. 5A) and APM (Fig. 5B) are spherical at 50 nm in size. APM-mediated synthesized AgNPs were monodispersed in nature whereas PDB mediated are polydisperse. This could be because of the difference in enzymes present in CFF (Pandey et al. 2018).

## Antifungal Assay

The antifungal activity was evaluated using radial growth inhibition assay in the presence and absence of different concentrations of AgNPs (25, 50, and 100 $\mu g.mL^{-1}$) on the growth of *S. sclerotiorum* MTCC 8785. Inhibition in the fungal growth was observed in a concentration-dependent manner with the maximum at 100 $\mu g.mL^{-1}$ concentration of AgNPs (Fig. 6A-D; Table 1). Plates devoid of AgNPs showed fully grown fungus (Fig. 6E). Fluconazole (100 $\mu g.mL^{-1}$) was used as a positive, hence no growth was observed for fungus in the presence of Fluconazole (100 $\mu g.mL^{-1}$) (Fig. 6F). AgNPs are known to disintegrate the membrane-bound respiratory enzymes, hence retards the growth of fungi (Saxena et al. 2014).

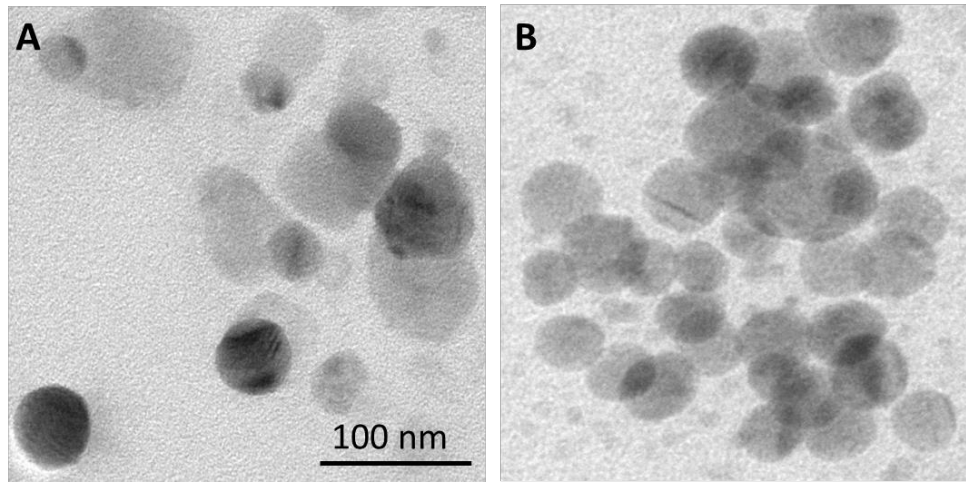


Fig. 5: TEM micrograph of AgNPs synthesized in (A) PDB and APM (B) using CFF of *T. harzianum* MTCC 801.

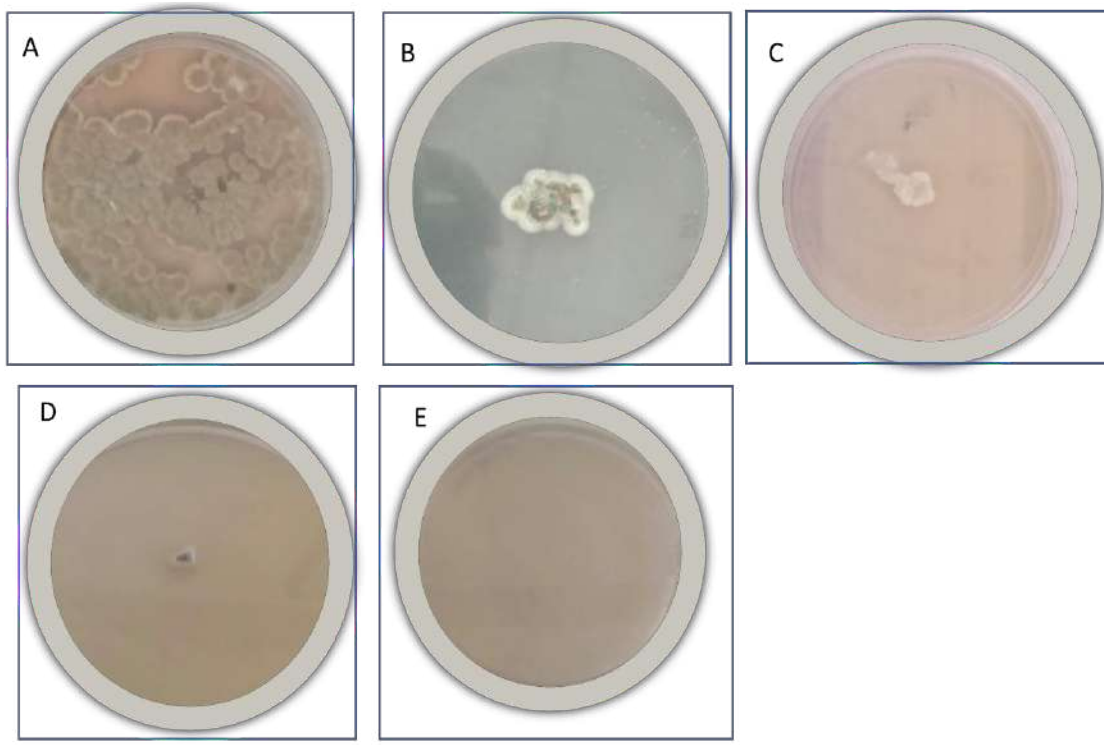


Fig. 6: Antifungal activity of AgNPs synthesized with enzyme stimulation from *T. harzianum* MTCC 801. Inhibition effect of AgNPs at (B) 25 µg.mL$^{-1}$, (C) 50 µg.mL$^{-1}$, and (D) 100 µg.mL$^{-1}$against phytopathogenic fungi *S. sclerotiorum* MTCC 8785. Fungal growth in the (E) presence of Fluconazole and (A) absence of AgNPs.

## CONCLUSION

This work establishes a simple and bio-friendly procedure to synthesize AgNPs from cell-free filtrates of *T. harzianum* MTCC 801. We have used amylase-mediated AgNP synthesis which is beneficial for nanoparticle stability and bioefficacy. The secreted amylases in CFF-APM are directly utilized for synthesis instead of using amylases purified through cumbersome steps of downstream processing. The process offers a one-step method for producing stable nanoparticles. This bioinspired enzyme-mediated synthesis can be further explored for optimization models and industrial-scale production of AgNPs as new antifungal agents.

## ACKNOWLEDGEMENT

We are indebted to Chandigarh University for supporting and providing the necessary infrastructure for the completion of this work.

## REFERENCES

Ahamed, M., AlSalhi, M.S. and Siddiqui, M.K.J. 2010. Silver nanoparticle applications and human health. Clin. Chim. Acta, 411(23-24): 1841-1848.

Alves, M.F. and Murray, P.G. 2022. Biological synthesis of monodisperse uniform-size silver nanoparticles (AgNPs) by fungal cell-free extracts at elevated temperature and pH. J. Fungi, 8(5): 439.

Carpenter, K.A., Sisson, A.J., Kandel, Y.R., Ortiz, V., Chilvers, M.I., Smith, D.L. and Mueller, D.S. 2021. Effects of mowing, seeding rate, and foliar fungicide on soybean sclerotinia stem rot and yield. Plant Health Prog., 22(2): 129-135.

Das, V.L., Thomas, R., Varghese, R.T., Soniya, E.V., Mathew, J. and Radhakrishnan, E.K. 2014. Extracellular synthesis of silver nanoparticles by the Bacillus strain CS 11 isolated from industrialized area. Biotech., 4(2): 121-126.

Duhan, J.S. and Gahlawat, S.K. 2014. Biogenesis of nanoparticles: A review. Afr. J. Biotechnol., 13(28): 616.

Essghaier, B., Smiri, M., Sehimi, H., Ben Jalloul, A., Zid, M.F. and Sadfi Zouaoui, N. 2022. Antifungal potential of two synthetic vanadium (IV) oxalate compounds to control blue mold of oranges and apples under storage conditions. J. Food Process Preserv., 111: e16860.

Guilger-Casagrande, M., Germano-Costa, T., Pasquoto-Stigliani, T., Fraceto, L.F. and Lima, R.D. 2019. Biosynthesis of silver nanoparticles employing Trichoderma harzianum with enzymatic stimulation for the control of Sclerotinia sclerotiorum. Sci. Rep., 9(1): 1-9.

Khan, Z., Singh, T., Hussain, J.I., Obaid, A.Y., Al-Thabaiti, S.A. and El-Mossalamy, E.H. 2013. Starch-directed green synthesis, characterization and morphology of silver nanoparticles. Coll. Surf. B, 102:578-584.

Mishra, A. and Sardar, M. 2012. Alpha-amylase mediated synthesis of silver nanoparticles. Sci. Adv. Mater., 4(1): 143-146.

Molla, A.H., Islam, M.J., Mosharaf, M.K., Sultana, S., Talukder, M. and Miah, M. 2022. Extracellular enzymes production and non-

phytopathogenic potential fungi isolation for the purpose of solid waste management of safe food production. Waste Biomass Valoriz., 13(1): 369-381.

Pandey, A., Shankar, S. and Arora, N.K. 2018. Amylase-assisted green synthesis of silver nanocubes for antibacterial applications. Bioinspired. Biomim. Nanobiomater., 8(3): 161-170.

Saxena, J., Sharma, M.M., Gupta, S. and Singh, A. 2014. Emerging role of fungi in nanoparticle synthesis and their applications. World J. Pharm. Sci., 3(9): 1586-1613.

Saxena, J., Sharma, P.K., Sharma, M.M. and Singh, A. 2016. Process optimization for green synthesis of silver nanoparticles by Sclerotinia sclerotiorum MTCC 8785 and evaluation of its antibacterial properties. Springer Plus, 5(1): 1-10.

Saxena, J., Sharma, P. and Singh, A. 2017. Biomimetic synthesis of AgNPs from Penicillium chrysogenum strain FGCC/BLS1 by optimising physico-cultural conditions and assessment of their antimicrobial potential. IET Nanobiotechnol., 11(5): 576-583.

Siddiqi, K.S., Husen, A. and Rao, R.A. 2018. A review on biosynthesis of silver nanoparticles and their biocidal properties. J. Nanobiotechnol., 16(1): 1-28.

Thapa, R., Bhagat, C., Shrestha, P., Awal, S. and Dudhagara, P. 2017. Enzyme-mediated formulation of stable elliptical silver nanoparticles tested against clinical pathogens and MDR bacteria and development of antimicrobial surgical thread. Anna. Clin. Microbiol., 16(1): 1-10.

Tomah, A.A., Alamer, I.S.A., Li, B. and Zhang, J.Z. 2020. Mycosynthesis of silver nanoparticles using screened trichoderma isolates and their antifungal activity against Sclerotinia sclerotiorum. Nanomaterials, 10(10):1955.

Vigneshwaran, N., Ashtaputre, N.M., Varadarajan, P.V., Nachane, R.P., Paralikar, K.M. and Balasubramanya, R.H. 2007. Biological synthesis of silver nanoparticles using the fungus Aspergillus flavus. Mater. Lett., 61(6): 1413-1418.

Zhang, X.F., Liu, Z.G., Shen, W. and Gurunathan, S. 2016. Silver nanoparticles: Synthesis, characterization, properties, applications, and therapeutic approaches. Int. J. Mol. Sci., 17(9): 1534.

Nature Environment and Pollution Technology
An International Quarterly Scientific Journal

p-ISSN: 0972-6268
(Print copies up to 2016)
e-ISSN: 2395-3454

Vol. 22 | No. 1 | pp. 261-268 | 2023

Original Research Paper

https://doi.org/10.46488/NEPT.2023.v22i01.025

Open Access Journal

# Utilization of *Enterobacter cloacae* WW1 Biomass for Biosorption of Lead(II) from Aqueous Solution

**S. Thongkrua† and A. Kasuya**
School of Energy and Environment, University of Phayao, Phayao, Thailand
†Corresponding author: S. Thongkrua; suchanya_9@yahoo.com

**Nat. Env. & Poll. Tech.**
**Website: www.neptjournal.com**

*Received:* 27-06-2022
*Revised:* 01-08-2022
*Accepted:* 03-08-2022

**Key Words:**
*Enterobacter cloacae*
Bioremediation
Lead-resistant bacteria
Heavy metal

## ABSTRACT

The present study evaluated lead biosorption by *Enterobacter cloacae* WW1 isolated from tannery wastewaters under different initial $Pb^{2+}$ concentrations, biomass concentrations, and contact times. The results showed that at an initial $Pb^{2+}$ concentration of 80 $mg.L^{-1}$, the optimal conditions for living cells were a biomass concentration of 7 $g.L^{-1}$ and a contact time of 120 min. For non-living cells, biomass was a biomass concentration of 4 $g.L^{-1}$ and contact time of 45 min, which provided removal efficiencies of 92.03 ± 0.10% and 99.51 ± 0.01%, respectively. The maximum biosorption capacity obtained for non-living cells using an initial $Pb^{2+}$ concentration of 640 $mg.L^{-1}$ was 76.65 ± 0.05 $mg.g^{-1}$. The equilibrium data followed the Langmuir and Freundlich models for living cells, and the data for non-living cell biosorbents fit the Langmuir model. The biosorption kinetics for living and non-living cells fit well with a pseudo-second-order kinetic equation. SEM-EDX analysis clearly showed the morphology and presence of $Pb^{2+}$ particles on non-living cell surfaces after biosorption. In addition, the results revealed that functional groups such as hydroxyl, amino, carboxyl, amide, and phosphate groups on the bacterial cell surface detected by FTIR were associated with the binding of $Pb^{2+}$ ions. The results indicated that *E. cloacae* WW1, a lead-resistant bacterium, can be used as an alternative biosorbent for lead removal from wastewater.

## INTRODUCTION

Lead pollution poses major environmental concerns. The significant sources of lead waste are industries such as battery manufacturing, refining, metal plating, smelting, and painting. Lead in the $Pb^{2+}$ state, and its associated hydroxyl compounds are stable, and these are the most prominent forms of lead in nature (Sevak et al. 2021). Discharging Pb-contaminated wastewater into aquatic bodies without treatment can cause many significant environmental problems for aquatic ecosystems and human health (Elgarahy et al. 2021).

Biosorption using a biosorbent based on bacterial biomass to remove heavy metals from wastewater is considered a promising alternative technology owing to the process's high efficacy, low cost, and eco-friendly nature. Lead biosorption by Pb-tolerant bacteria has been studied. These bacteria include gram-positive bacteria, such as *Bacillus badius*, *Bacillus pumilus*, *Lactobacillus brevis*, *Microbacterium oxydans*, *Rhodococcus* sp. and *Lactobacillus acidophilus* (Vishan et al. 2017, Sahoo & Goli 2018, Dai et al. 2019, Afraz et al. 2020), as well as gram-negative bacteria, such as *Klebsiella pneumoniae*, *Staphylococcus* sp., *Pseudomonas* sp. (Li et al. 2017, Aslam et al. 2020, Zhang & Huang 2020, Canaza et al. 2021). Zhang and Huang (2020) reported that the $Pb^{2+}$ biosorption rate using *Shinella zoogloeoides* PQ7 increased from 27.48% to 97.99% when the biomass dosage changed from 0.5 $g.L^{-1}$ to 4.0 $g.L^{-1}$. Canaza et al. (2021) studied $Pb^{2+}$ biosorption by dead biomass of *Pseudomonas monteilii* MA-4. Maximum removal was 250 ppm of Pb(II) within the first 30 min at the biomass of 1 $g.L^{-1}$ and pH of 4. The equilibrium data followed Langmuir and Freundlich isotherm, with $q_{max}$ and $K_f$ values of 166.67 $mg.g^{-1}$ and 11.09, respectively. *Enterobacter cloacae*, lead-resistant bacteria, are gram-negative, rod-shaped, and facultatively anaerobic bacteria (Bhar et al. 2021). Gram-negative bacteria are surrounded by an outer lipid membrane containing lipopolysaccharide and a thin peptidoglycan layer (Thomas et al. 2010). Various functional groups on the bacterial cell wall are known to be involved in heavy metal biosorption (Mitra et al. 2021).

The lead biosorption process depends on many factors, such as the capacity characteristics of the biosorbent, the properties of lead, and environmental conditions. This study aims to investigate $Pb^{2+}$ biosorption by living and non-living *E. cloacae* WW1 biomass isolated from tannery wastewater at varying initial $Pb^{2+}$ concentrations at different biomass concentrations and contact times. Biosorption isotherms and kinetics are also determined.

## MATERIALS AND METHODS

### Preparation of Bacterial Biomass

*E. cloacae* WW1, a local lead-tolerant bacterium, was isolated from tannery wastewater in Thailand (Kasuya 2017). *E. cloacae* WW1 was grown in a nutrient broth medium containing 5.0 g beef extract, 2.5 g peptone, 0.1 g potassium nitrate, 2.5 g sodium chloride, and 1 L distilled water and was cultivated in a shaking incubator at 150 rpm and 30°C for 24 h. Bacterial suspensions containing both living and non-living cells obtained by autoclaving at 121°C and 15 Ibs for 30 min were harvested by centrifugation at 8,000 rpm for 20 min. The biomass was rinsed with sterilized distilled water three times and dried at 80°C before the experiment.

### Biosorption Experiments

The effects of different initial $Pb^{2+}$ concentrations (40, 80, 160, 320, and 640 $mg.L^{-1}$), biomass concentrations (1, 4, 7, 10, and 13 $g.L^{-1}$), and contact times (5, 10, 15, 20, 25, 30, 45, 60, 120, 240, 360 and 480 min) on the removal efficiency and biosorption capacity of $Pb^{2+}$ were investigated. All experiments were conducted at the laboratory scale with a batch process and were performed in triplicate. A stock solution of $Pb^{2+}$ was prepared using lead(II)acetate $(CH_3COO)_2Pb.Pb(OH)_2$ (Ajax Finechem, Australia). The biomass of living and non-living cells was resuspended in a 150 ml $Pb^{2+}$ solution at an initial pH of 5 and shaken at 120 rpm at room temperature. Then, the suspension was centrifuged at 8,000 rpm for 20 min. The residual $Pb^{2+}$ concentration in the supernatant was analyzed by atomic absorption spectrophotometry (Shimadzu, AA-6880). The surface characteristics of non-living cells before and after biosorption were detected by scanning electron microscopy and energy dispersive x-ray spectroscopy (SEM/EDX), performed with a JEOL JSM-5910LV instrument. In addition, Fourier transforms infrared spectroscopy (FTIR) was also carried out to determine the functional groups presented in non-living cells using a Thermo Scientific spectrometer (model: Nicolet iS5). Discs were prepared by mixing dry samples with a KBr mass ratio of 1:99 (W/W) in an agate mortar and then pressing the sample pellets under a pressure of 7-8 $tons.cm^{-2}$. The FTIR spectra were recorded between 4,000 and 400 $cm^{-1}$ (Bai et al. 2014). The removal efficiency and biosorption capacity of $Pb^{2+}$ were deduced using Eqs. (1) and (2), respectively:

$$Removal\ efficiency\ (\%) = \frac{C_0 - C_t}{C_0} \times 100 \quad \ldots(1)$$

$$q_e = \frac{C_0 - C_e}{M} \times V \quad \ldots(2)$$

Where $C_0$ ($mg.L^{-1}$) and $C_t$ ($mg.L^{-1}$) are the initial and final $Pb^{2+}$ concentrations, respectively, $q_e$ ($mg.g^{-1}$) and $C_e$ ($mg.L^{-1}$) represent the biosorption capacity and the residual $Pb^{2+}$ concentration at equilibrium, respectively and V (L) and M (g) are the volume of the suspension and the dry biomass in the suspension, respectively (Dai et al. 2019, Canaza et al. 2021).

The biosorption isotherms of $Pb^{2+}$ were analyzed by Langmuir and Freundlich isotherms, which are described in linear forms by Eqs. (3) and (4), respectively:

$$\frac{C_e}{q_e} = \frac{1}{K_L q_m} + \frac{C_e}{q_m} \quad \ldots(3)$$

$$lnq_e = lnK_F + \frac{1}{n} lnC_e \quad \ldots(4)$$

Where $q_m$ ($mg.g^{-1}$) is the maximum specific uptake and $K_L$ represents the Langmuir constant, which relates to the affinity of the binding sites. $K_F$ is defined as the adsorption capacity for Freundlich isotherm, while the adsorption intensity is represented by n (Fathollahi et al. 2021).

The biosorption kinetics of $Pb^{2+}$ were studied using three models, a pseudo-first-order kinetic model, a pseudo-second-order kinetic model, and an intraparticle diffusion model, which can be expressed in linear form as Eqs. (5), (6), and (7), respectively:

$$log(q_e - q_t) = logq_{ecal} - \frac{k_1}{2.303} t \quad \ldots(5)$$

$$\frac{t}{q_t} = \frac{1}{k2^2 qecal^2} + \frac{1}{q_e} t \quad \ldots(6)$$

$$q_t = k_i t^{1/2} + C \quad \ldots(7)$$

where $q_t$ ($mg.g^{-1}$) represents the biosorption capacity at any time t (min), $k_1$ ($min^{-1}$), $k_2$ ($g.mg^{-1}.min^{-1}$), and $k_i$ ($mg.g^{-1}.min^{-1/2}$) are the rate constants for the pseudo-first-order kinetic model, pseudo-second-order kinetic model, and intraparticle diffusion model, respectively, and C ($mg.g^{-1}$) is the constant of diffusion boundary layer thickness (Fathollahi et al. 2021).

## RESULTS AND DISCUSSION

### Effect of Initial $Pb^{2+}$ Concentration

Fig. 1(a) shows the effect of the initial $Pb^{2+}$ concentration on $Pb^{2+}$ biosorption utilizing *E. cloacae* WW1 with an equilibrium time of 120 min for living cells and 45 min for non-living cells and a biomass concentration of 7 $g.L^{-1}$. For initial $Pb^{2+}$ concentrations from 40 to 640 $mg.L^{-1}$, the extent of $Pb^{2+}$ removal efficiency and biosorption capacity of non-living cells were greater than those of living cells. Since dead bacterial biomass is less sensitive to the toxicity of $Pb^{2+}$, biosorption may not be inhibited by its presence. The maximum percent removal by living and non-living cells was 92.14 ± 0.05% and 98.54 ± 0.03%, respectively.

The results demonstrated that the removal efficiencies of both biomasses were inhibited at high $Pb^{2+}$ concentrations. Various functional groups, such as carboxyl, amino, hydroxyl, carbonyl, and phosphate groups, are located on the cell walls of bacteria involved in $Pb^{2+}$ biosorption. Some of these groups carry negative changes and bind with $Pb^{2+}$ ions (Tiquia-Arashiro 2018, Mitra et al. 2021). The binding sites on the cell surface became saturated as the initial $Pb^{2+}$ concentration increased. In addition, toxic effects on living cells increase with increasing $Pb^{2+}$ concentrations (Rahman & Singh 2014). The same behavior for $Pb^{2+}$ biosorption (Zhang & Huang 2020) and other heavy metal biosorption (Rahman & Singh 2014) has been reported in previous studies.

On the other hand, the highest biosorption capacities for living and non-living biosorbents achieved at an initial $Pb^{2+}$ concentration of 640 $mg.L^{-1}$ were 59.59 ± 0.01 $mg.g^{-1}$ and 76.65 ± 0.05 $mg.g^{-1}$, respectively. The biosorption capacities of both biosorbents increase with increasing initial $Pb^{2+}$ concentration (Dai et al. 2019). The initial $Pb^{2+}$ concentration regulates the biosorption capacity of $Pb^{2+}$ on the cell surface. This is due to increased free $Pb^{2+}$ ions competing for the available binding sites at greater $Pb^{2+}$ concentrations (Li et al. 2017, Dai et al. 2019, Zhang & Huang 2020).

**Effect of Biomass Concentration**

A $Pb^{2+}$ biosorption study under different biomass concentrations from 1 to 13 $g.L^{-1}$ was performed in a $Pb^{2+}$ solution of 80 $mg.L^{-1}$, as presented in Fig. 1(b). The results indicated that the $Pb^{2+}$ removal efficiency increased when the biomass concentration increased from 1 to 7 $g.L^{-1}$ for living cells and from 1 to 4 $g.L^{-1}$ for non-living cells. The maximum removal efficiency of living and non-living cells was 92.03 ±0.10% and 97.51±0.01%, respectively. Bacterial surface properties, such as the charge and orientation of the $Pb^{2+}$ binding functional groups on the cell surface, can influence $Pb^{2+}$ biosorption. At higher biosorbent dosages, high surface areas provided large contact areas or a more significant number of binding sites interacting with $Pb^{2+}$ in an aqueous solution (Sethuraman & Balasubramanian 2010). A relevant observation for $Pb^{2+}$ biosorption was presented by Hu et al. (2020) and Zhang and Huang (2020). Moreover, at a high biomass dosage, the removal efficiency was affected by the overlap or aggregation of biosorption sites, resulting in a reduction in the total biosorbent surface available for $Pb^{2+}$ ion binding (Dai et al. 2019, Zhang & Huang 2020). The maximum biosorption capacities of living and non-living cells were achieved at the lowest biomass concentrations of 60.05 ± 0.06 $mg.g^{-1}$ and 64.05 ± 0.06 $mg.g^{-1}$, respectively. These results clearly indicated that the $Pb^{2+}$ biosorption capacity of living and non-living cells decreased with increasing biosorbent concentrations (Sethuraman & Balasubramanian 2010, Li et al. 2017, Dai et al. 2019, Hu et al. 2020, Zhang & Huang 2020). At a high biosorbent dosage, the available $Pb^{2+}$ ions insufficiently covered the binding sites on the biosorbent surface, resulting in a low $Pb^{2+}$ biosorption capacity (Sethuraman & Balasubramanian 2010, Zhang & Huang 2020).

**Effect of Contact Time**

The influence of contact time (5-480 min) on $Pb^{2+}$ biosorption was studied using a biomass dosage of 7 $g.L^{-1}$ for living cells and 4 $g.L^{-1}$ for non-living cells, as demonstrated in Fig. 1(c). The result showed that the $Pb^{2+}$ elimination percentage for all biomasses increased rapidly in the early stages and then slowed until equilibrium was reached at 120 min for living cells and 45 min for non-living cells due to complexation and binding site saturation on the biosorbent surface (Huang et al. 2013, Li et al. 2017, Zhang & Huang 2020). At equilibrium, the biosorption efficiency and biosorption capacity of living cells were 92.03 ± 0.10% and 10.52 ± 0.01 $mg.g^{-1}$, respectively, and those of non-living cells were 99.51 ± 0.01% and 19.90 ± 0.00 $mg.g^{-1}$, respectively. A similar observation for $Pb^{2+}$ biosorption was reported at an optimal time of 90 min for *Shinella zoogloeoides* PQ7 (Zhang & Huang 2020) and 30 min for *Pseudomonas monteilii* MA-4 (Canaza et al. 2021).

**Biosorption Isotherms**

The biosorption isotherms of $Pb^{2+}$ on *E. cloacae* WW1 were predicted using Langmuir and Freundlich isotherms. The Langmuir and Freundlich equations are shown in Figs. 2(a) and 2(b), respectively. Table 1 shows the isotherm parameters for $Pb^{2+}$ biosorption. For living cells biosorbents, both the Langmuir and Freundlich models fit well with $R^2$ values greater than 0.98, which indicates that $Pb^{2+}$ biosorption is a complex surface binding process (Muñoz et al. 2015, Li et al. 2017, Zhang & Huang 2020). For the Freundlich isotherm, an n value > 1 illustrated that $Pb^{2+}$ biosorption was favorable under optimum conditions (Fathollahi et al. 2021).

In contrast, for non-living cells, the experimental data appeared to fit the Langmuir model with an $R^2$ of 0.9711. This implied that the biosorption of $Pb^{2+}$ occurred at specific homogeneous sites on the biomass surface with monolayer biosorption. Similar results for $Pb^{2+}$ removal from aqueous solutions using *Pseudomonas* sp. I3 was reported by Li et al. (2017). In addition, the value of $R_L$ indicated the shape of the Langmuir isotherm and the nature of the biosorption process, which are expressed in Eq. (8):

$$R_L = \frac{1}{1 + K_L C_0} \quad \ldots(8)$$

The $R_L$ values of living and non-living cells fell within the range of $0 < R_L < 1$, which satisfied the favorable biosorption condition (Yahya et al. 2012). The predicted maximum biosorption capacity ($q_m$) and $K_L$ for non-living cells were higher than those of living cells. This finding revealed that the non-living biomass was more efficient at adsorbing $Pb^{2+}$ than the living biomass (Huang et al. 2013).

## Biosorption Kinetics

The kinetics of $Pb^{2+}$ biosorption onto the living cells and non-living cells of *E. cloacae* WW1 were studied by modeling the data with pseudo-first-order kinetic, pseudo-second-order kinetic, and intraparticle diffusion equations as shown in Fig. 3(a), Fig. 3(b) and Fig. 3(c), respectively. Table 2 presents the kinetics parameters for $Pb^{2+}$ biosorption under the optimum conditions. The pseudo-second-order kinetic model for living and non-living cells had the highest linear correlation coefficients ($R^2$) of 0.9975 and 0.9998, respectively. The results gave the best fit for the experimental data of all biosorbents. The experimental $q_e$ values were closer to the $q_{ecal}$ values in the pseudo-second-order kinetic model (Zhang & Huang 2020). Furthermore, the rate constant

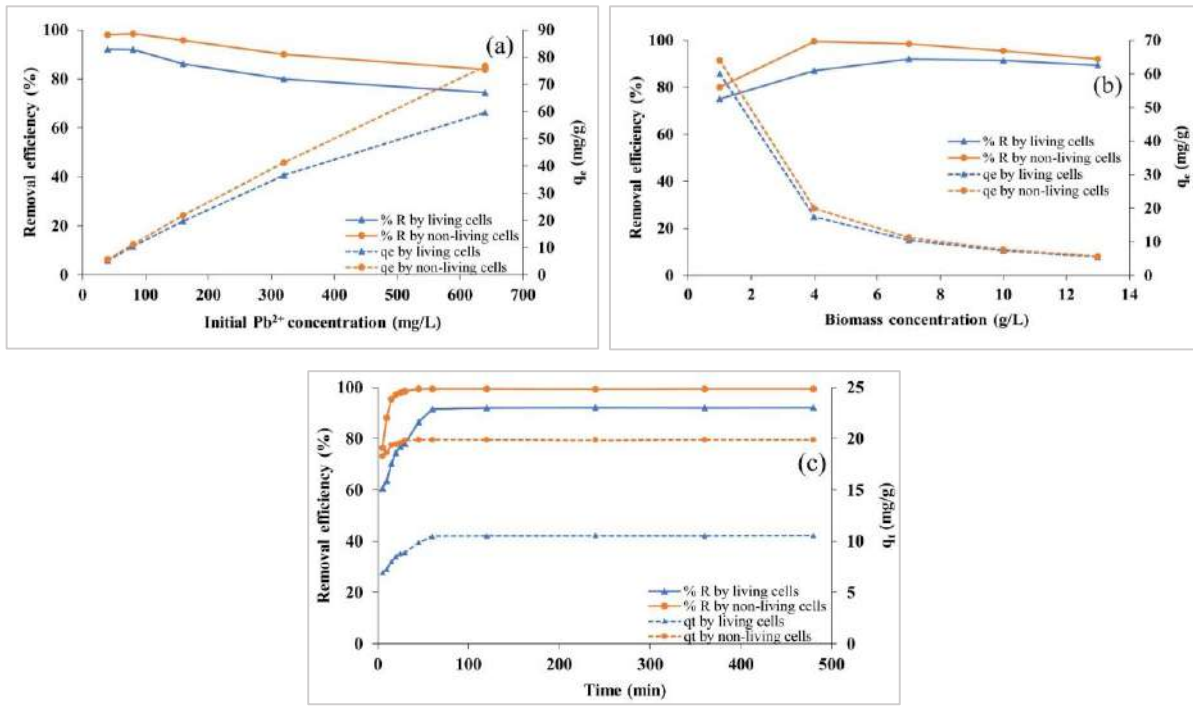


Fig. 1: The effect of the initial $Pb^{2+}$ concentration (a), biomass concentration (b), and contact time (c) on $Pb^{2+}$ biosorption.

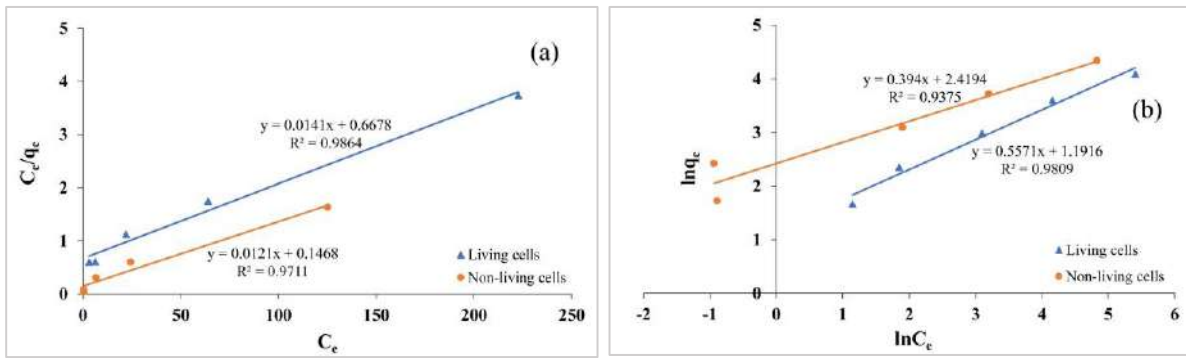


Fig. 2: Langmuir (a) and Freundlich (b) isotherm for $Pb^{2+}$ biosorption.

Table 1: Isotherm parameters for $Pb^{2+}$ biosorption.

| Biosorbents | Langmuir isotherm | | | | Freundlich isotherm | | |
|---|---|---|---|---|---|---|---|
| | $q_m$ [mg.g$^{-1}$] | $k_L$ [L.mg$^{-1}$] | $R_L$ | $R^2$ | n | $k_F$ | $R^2$ |
| Living cells | 70.92 | 0.02 | 0.07 | 0.9864 | 1.80 | 3.29 | 0.9809 |
| Non-living cells | 82.64 | 0.08 | 0.02 | 0.9711 | 2.54 | 11.24 | 0.9375 |

of k illustrated that the $Pb^{2+}$ biosorption of non-living cells was faster than that of living cells (Huang et al. 2013). In addition, it was also observed that the intraparticle plot did not pass through the origin, which indicated that intraparticle diffusion is not the sole process involved in biosorption. The results revealed that $Pb^{2+}$ biosorption was a chemisorption process involving $Pb^{2+}$ binding to the cell surface (Muñoz et al. 2015, Zhang & Huang 2020). According to a relevant study, $Pb^{2+}$ biosorption kinetics were found to fit well with pseudo-second-order kinetic models for gram-negative bacteria (Muñoz et al. 2015, Li et al. 2017, Zhang & Huang 2020) and gram-positive bacteria such as *Bacillus* spp. (Vishan et al. 2017, Cai et al. 2018, Mohapatra et al. 2019).

## SEM and EDX Analysis

The morphological characterization and EDX spectra of non-living cells of *E. cloacae* WW1 before and after $Pb^{2+}$ biosorption (80 mg.L$^{-1}$) are shown in Fig. 4. Fig. 4(a) illustrates that before biosorption, the non-living cells biosorbents were rod-shaped with clear boundaries (Song et al. 2017, Zhang et al. 2019, Dash et al. 2021). The EDX spectra shown in Fig. 4(c) recorded signals for carbon, nitrogen, oxygen, and phosphorus as present in the polysaccharides and proteins of biomass and did not show a $Pb^{2+}$ signal (Ghosh et al. 2022). The presence of lower amounts of oxygen and a high amount of carbon indicate that the non-living cells were more effective biosorbents for metal removal from aqueous solutions (Biswas et al. 2019). After biosorption, the $Pb^{2+}$ particles adhered to the cell surface after 45 min, as depicted in Fig. 4(b). Similarly, selenium (Se) aggregates onto the cell surface of *E. cloacae* Z0206 (Song et al. 2017), and the surface of *E. cloacae* RSN3 becomes rough after arsenic (As) uptake (Dash et al. 2021). Furthermore, the EDX spectra shown in Fig. 4(d) revealed that $Pb^{2+}$ accumulated on the surface of non-living cells (Muñoz et al. 2015, Hasan et al. 2016, Jalilvand et al. 2020).

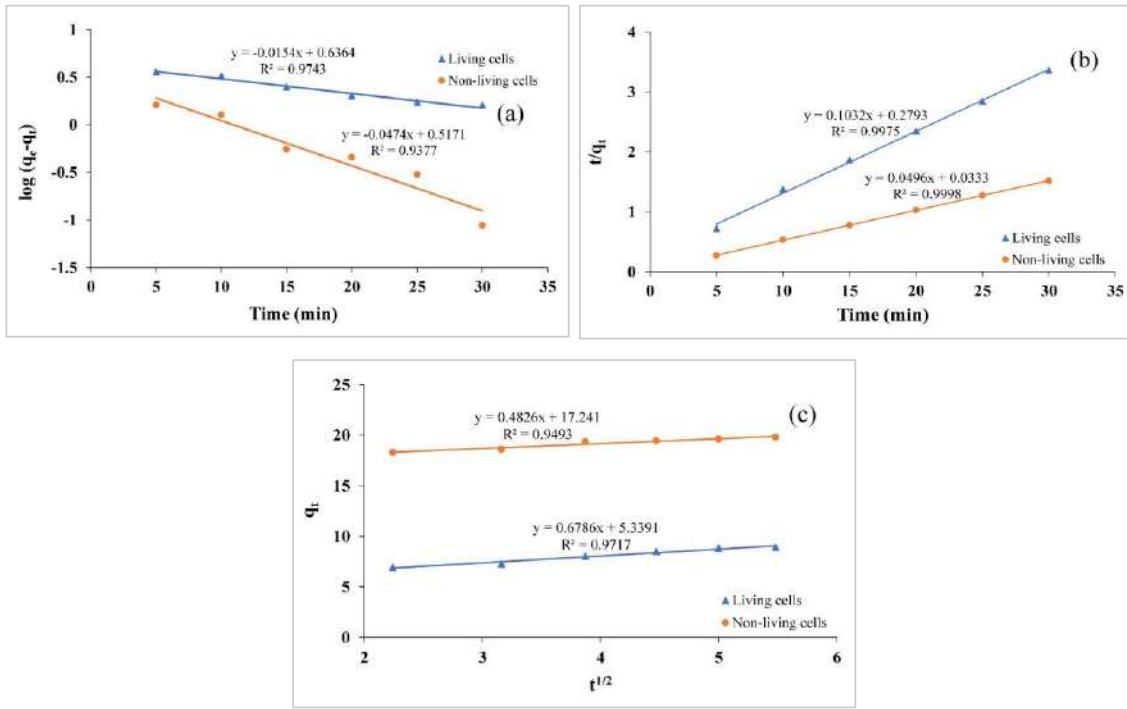


Fig. 3: Pseudo-first-order kinetic (a), Pseudo-second-order kinetic (b), and Intraparticle diffusion (c) model for $Pb^{2+}$ biosorption.

Table 2: Kinetic model parameters for $Pb^{2+}$ biosorption.

| Biosorbents | Pseudo-first-order kinetic model | | | Pseudo-second-order kinetic model | | | Intraparticle diffusion model | | |
|---|---|---|---|---|---|---|---|---|---|
| | $q_{ecal}$ [$mg.g^{-1}$] | $k_1$ [$min^{-1}$] | $R^2$ | $q_{ecal}$ [$mg.g^{-1}$] | $k_2$ [$g.mg^{-1}.min^{-1}$] | $R^2$ | $k_i$ [$mg.g^{-1}.min^{-1/2}$] | C [$mg.g^{-1}$] | $R^2$ |
| Living cells | 4.33 | 0.04 | 0.9743 | 9.69 | 0.20 | 0.9975 | 0.68 | 5.34 | 0.9717 |
| Non-living cells | 3.29 | 0.11 | 0.9377 | 20.16 | 0.27 | 0.9998 | 0.48 | 17.24 | 0.9493 |

## FTIR Analysis

FTIR analysis of non-living *E.cloacae* WW1 cells before and after $Pb^{2+}$ biosorption was carried out to confirm the presence of functional groups on the cell surface responsible for the biosorption process (Fig. 5). Fig. 5(a) shows the FTIR spectrum for $Pb^{2+}$ preadsorption. The broad peak in the range of 3367.59-3484.74 $cm^{-1}$ was assigned to the stretching of O-H groups in polysaccharides (Ghosh et al. 2022). The transmission spectrum at approximately 3350.71 $cm^{-1}$ was attributed to proteins' amino groups (N-H). Another peak ranging from 2913.43-2962.13 $cm^{-1}$ indicated C-H bonds in alkyl groups in proteins and carbohydrates of the cell wall (Suriya et al. 2013, Bai et al. 2014, Ghosh et al. 2022). A sharp peak at 1652.70 $cm^{-1}$ represented the stretching vibrations of carboxyl groups (C=O) (Hasan et al. 2016,

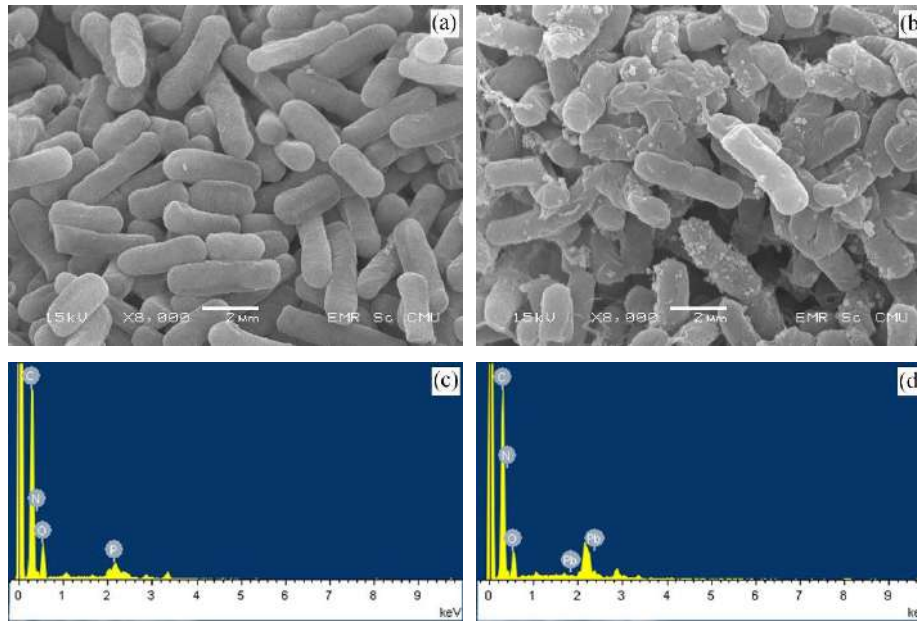


Fig. 4: SEM micrographs and EDX spectra of non-living cells of *E. cloacae* WW1 before biosorption (a and c) and after biosorption (b and d).

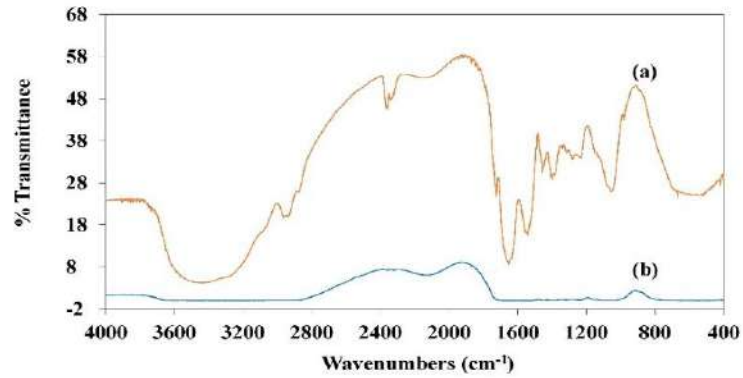


Fig. 5: FTIR spectra of the non-living cells of *E. cloacae* WW1 before biosorption (a) and after biosorption (b).

Ghosh et al. 2022). The bands approximately 1645.46 and 1573.15 $cm^{-1}$ corresponded to amide I and amide II, respectively (Suriya et al. 2013, Bai et al. 2014). The peak observed approximately 1055.35 $cm^{-1}$ denoted phosphate groups (Muñoz et al. 2015, Zhang & Huang 2020). The hydroxyl, amino, carboxyl, amide, and phosphate groups presented on the cell surface participate in the binding of $Pb^{2+}$ ions (Tiquia-Arashiro 2018). After the biosorbent was exposed to $Pb^{2+}$, several functional group spectra were shifted and decreased in band intensity, such as the phosphate groups in polysaccharides (1040.89 $cm^{-1}$) (Fig. 5(b)). The results revealed that functional groups on the bacterial cell surface were associated with $Pb^{2+}$ biosorption (Muñoz et al. 2015, Zhang & Huang 2020). Similar results were observed for cadmium (Ghosh et al. 2022) and copper biosorption (Suriya et al. 2013) using *E. cloacae*.

## CONCLUSION

*E. cloacae* WW1 isolated from tannery wastewaters was used to explore $Pb^{2+}$ biosorption at varying initial $Pb^{2+}$ concentrations, biomass concentrations, and contact times. The $Pb^{2+}$ removal efficiency and biosorption capacity of non-living cells were higher than those of living cells. Because dead bacterial biomass is insensitive to lead toxicity, its biosorption is independent of metabolism. The maximum percent removal obtained from non-living cells was 99.51±0.01% under an initial $Pb^{2+}$ concentration of 80 $mg.L^{-1}$, a biomass concentration of 4 $g.L^{-1,}$ and a contact time of 45 min. Furthermore, non-living cells also showed the highest biosorption capacity of 76.65±0.05 $mg.g^{-1}$ at an initial $Pb^{2+}$ concentration of 640 $mg.L^{-1}$. The biosorption isotherm and kinetic data for non-living cells were consistent with the Langmuir model and a pseudo-second-order kinetic model, respectively. This indicated that $Pb^{2+}$ biosorption occurred at specific homogeneous sites on the biomass surface with monolayer biosorption and consisted of a chemisorption process involving $Pb^{2+}$ binding to the cell surface. The lead-tolerant bacterial strain *E. cloacae* WW1 can be utilized for the biosorption of lead-contaminated waters because of several advantages, such as its rapid and high-efficiency processes, low potential cost, and eco-friendliness.

## ACKNOWLEDGEMENT

The authors are grateful to the School of Energy and Environment and the School of Science, University of Phayao, for laboratory equipment support.

## REFERENCES

Afraz, V., Younesi, H., Bolandi, M. and Hadiani, M.R. 2020. Optimization of lead and cadmium biosorption by *Lactobacillus acidophilus* using response surface methodology. Biocatal. Agric. Biotechnol., 29: 1-7.

Aslam, F., Yasmin, A. and Sohail, S. 2020. Bioaccumulation of lead, chromium, and nickel by bacteria from three different genera isolated from industrial effluent. Int. Microbiol., 23: 253–261.

Bai, J., Yang, X., Du, R., Chen, Y., Wang, S. and Qiu, R. 2014. Biosorption mechanism involved in immobilization of soil Pb by *Bacillus subtilis* DBM in a multi-metal-contaminated soil. J. Environ. Sci., 26: 2056-2064.

Bhar, S., Edelmann, M.J. and Jones, M.K. 2021. Characterization and proteomic analysis of outer membrane vesicles from a commensal microbe, *Enterobacter cloacae*. J. Proteomics, 231: 103994.

Biswas, R., Vivekanand, V., Saha, A., Ghosh, A. and Sarkar, A. 2019. Arsenite oxidation by a facultative chemolithotrophic *Delftia* spp. Bas29 for its potential application in groundwater arsenic bioremediation. Int. Biodeterior. Biodegrad., 136: 55-62.

Cai, Y., Li, X., Liu, D., Xu, C., Ai, Y., Sun, X., Zhang, M., Gao, Y., Zhang, Y., Yang, T., Wang, J., Wang, L., Li, X. and Yu, H. 2018. A novel Pb-resistant *Bacillus subtilis* bacterium isolate for co-biosorption of hazardous Sb(III) and Pb(II): thermodynamics and application strategy. Int. J. Environ. Res. Pub. Health, 15(4): 1-18.

Canaza, A., Pozo, L., Ferrufino-Guardia, E. and Vargas, V. A. 2021. Biosorption of lead(II) ions by dead bacterial biomass isolated from mine water. Rev. Boliv. Quím., 38(3): 119-125.

Dai, Q.H., Bian, X.Y., Li, R., Jiang, C.B., Ge, J. M., Li, B. L. and Ou, J. 2019. Biosorption of lead(II) from aqueous solution by lactic acid bacteria. Water Sci. Technol., 79(4): 627-634.

Dash, B., Sahu, N., Singh, A. K., Gupta, S. B. and Soni, R. 2021. Arsenic efflux in *Enterobacter cloacae RSN3* isolated from arsenic-rich soil. Folia Microbiol., 66: 189-196.

Elgarahy, A.M., Elwakeel, K.Z., Mohammad, S.H. and Elshoubaky, G.A. 2021. A critical review of biosorption of dyes, heavy metals and metalloids from wastewater as an efficient and green process. Clean. Eng. Technol., 4: 1-15.

Fathollahi, A., Coupe, S.J., El-Sheikh, A.H. and Nnadi, E.O. 2021. Cu(II) biosorption by living biofilms: isotherm, chemical, physical and biological evaluation. J. Environ. Manage., 282: 1-13.

Ghosh, A., Pramanik, K., Bhattacharya, S., Mondal, S., Ghosh, S.K. and Maiti, T.K. 2022. A potent cadmium bioaccumulating *Enterobacter cloacae* strain displays phytobeneficial property in Cd-exposed rice seedlings. Curr. Res. Microb. Sci., 3: 1-14.

Hasan, H.A., Abdullah, S.R.S., Kofli, T. and Yeoh, S. J. 2016. Interaction of environmental factors on simultaneous biosorption of lead and manganese ions by locally isolated *Bacillus cereus*. J. Ind. Eng. Chem., 37: 295-305.

Hu, X., Cao, J., Yang, H., Li, D., Qiao, Y., Zhao, J., Zhang, Z. and Huang, L. 2020. $Pb^{2+}$ biosorption from aqueous solutions by live and dead biosorbents of the hydrocarbon-degrading strain *Rhodococcus* sp. HX-2. PLOS ONE, 15(1): 1-24.

Huang, F., Dang, Z., Guo, C.-L., Lu, G.-N., Gu, R. R., Liu, H.J. and Zhang, H. 2013. Biosorption of Cd (II) by live and dead cells of *Bacillus cereus* RC-1 isolated from cadmium-contaminated soil. Coll. Surf. B Biointerf., 107: 11-18.

Jalilvand, N., Akhgar, A., Alikhani, H.A., Rahmani, H.A. and Rejali, F. 2020. Removal of heavy metals zinc, lead, and cadmium by biomineralization of urease-producing bacteria isolated from Iranian mine calcareous soil. J. Soil Sci. Plant Nutr., 20: 206-219.

Kasuya, A. 2017. Treatment of Lead in Synthetic Wastewater by Biosorption. Thesis, University of Phayao, Thailand.

Li, D., Xu, X., Yu, H. and Han, X. 2017. Characterization of $Pb^{2+}$ biosorption by psychrotrophic strain *Pseudomonas* sp. I3 isolated from permafrost soil of Mohe wetland in Northeast China. J. Environ. Manage., 196(1): 8-15.

Mitra, A., Chatterjee, S., Kataki, S., Rastogi, R.P. and Gupta, D.K. 2021. Bacterial tolerance strategies against lead toxicity and their relevance in bioremediation application. Environ. Sci. Pollut. Res., 28: 14271–14284.

Mohapatra, R.K., Parhi, P.K., Pandey, S., Bindhani, B.K., Thatoi, H. and Panda, C.R. 2019. Active and passive biosorption of Pb(II) using live and dead biomass of marine bacterium *Bacillus xiamenensis* PbRPSD202: kinetics and isotherm studies. J. Environ. Manage., 247: 121-134.

Muñoz, A.J., Espínola, F., Moya, M. and Ruiz, E. 2015. Biosorption of Pb(II) ions by *Klebsiella* sp. 3S1 isolated from a wastewater treatment plant: kinetics and mechanisms studies. Biomed. Res. Int., 2015: 1-12.

Rahman, Z. and Singh, V.P. 2014. Cr (VI) reduction by *Enterobacter* sp. DU17 isolated from the tannery waste dump site and characterization of the bacterium and the Cr (VI) reductase. Int. Biodeterior. Biodegradation, 91: 97-103.

Sahoo, S. and Goli, D. 2018. Bioremediation of lead by a halophilic bacteria *Bacillus pumilus* isolated from the mangrove regions of Karnataka. Int. J. Sci. Res., 9(1): 1337-1343.

Sethuraman, P. and Balasubramanian, N. 2010. Removal of Cr(VI) from aqueous solution using *Bacillus subtilis*, *Pseudomonas aeruginosa* and *Enterobacter cloacae*. Int. J. Eng. Sci. Technol., 2(6): 1811-1825.

Sevak, P.I., Pushkar, B.K. and Kapadne, P.N. 2021. Lead pollution and bacterial bioremediation: A review. Environ. Chem. Lett., 19: 4463-4488.

Song, D., Li, X., Cheng, Y., Xiao, X., Lu, Z., Wang, Y. and Wang, F. 2017. Aerobic biogenesis of selenium nanoparticles by *Enterobacter cloacae* Z0206 as a consequence of fumarate reductase mediated selenite reduction. Sci. Rep., 7: 1-10.

Suriya, J., Bharathiraja, S. and Rajasekaran, R. 2013. Biosorption of heavy metals by biomass of *Enterobacter cloacae* isolated from metal-polluted soils. Int. J. ChemTech. Res., 5(3): 1329-1338.

Thomas, J.S., Kahne, D. and Walker, S. 2010. The bacterial cell envelope: Cold spring harb. Perspect. Biol., 2(5): 1-16.

Tiquia-Arashiro, S.M. 2018. Lead absorption mechanisms in bacteria as strategies for lead bioremediation. Appl. Microbiol. Biotechnol., 102: 5437-5444.

Vishan, I., Laha, A. and Kalamdhad, A. 2017. Biosorption of Pb(II) by *Bacillus badius* AK strain originating from rotary drum compost of water hyacinth. Water Sci. Technol., 75(5-6): 1071-1083.

Yahya, S.K., Zakaria, Z.A., Samin, J., Raj, A.S.S. and Ahmad, W.A. 2012. Isotherm kinetics of Cr(III) removal by non-viable cells of *Acinetobacter haemolyticus*. Coll. Surf. B Biointerf., 94: 362-368.

Zhang, W. and Huang, Y. 2020. The synthesis of PbS NPs and biosorption of Pb(II) by *Shinella zoogloeoides* PQ7 in aqueous conditions. Water, 12(7): 1-14.

Zhang, Y., Wang, X., Li, X., Dong, L., Hu, X., Nie, T., Lu, Y., Lu, X., Pang, J., Li, G., Yang, X., Li, C. and You, X. 2019. Synergistic effect of colistin combined with PFK-158 against colistin-resistant *Enterobacteriaceae*. Antimicrob. Agents Chemother., 63(7): 1-10.

Nature Environment and Pollution Technology
An International Quarterly Scientific Journal

p-ISSN: 0972-6268
(Print copies up to 2016)
e-ISSN: 2395-3454

Vol. 22 | No. 1 | pp. 269-276 | 2023

Original Research Paper

https://doi.org/10.46488/NEPT.2023.v22i01.026

Open Access Journal

# Improved Large-Scale Ocean Wave Dynamics Remote Monitoring Based on Big Data Analytics and Reanalyzed Remote Sensing

**Subhrangshu Adhikary*† and Saikat Banerjee****

*Department of Computer Science and Engineering, Dr. B.C. Roy Engineering College, Durgapur-713206, India

**Department of Remote Sensing, WINGBOTICS, Baghajatin, Kolkata-700086, West Bengal, India

†Corresponding author: Subhrangshu Adhikary; subhrangshu.adhikary@spiraldevs.com

**Nat. Env. & Poll. Tech.**
**Website: www.neptjournal.com**

*Received:* 15-06-2022
*Revised:* 04-08-2022
*Accepted:* 10-08-2022

**Key Words:**
Big data analytics
Renewable energy
Ocean energy
Wave energy
Remote sensing

## ABSTRACT

Oceans and large water bodies have the potential to generate a large amount of green and renewable energy by harvesting the ocean surface properties like wind waves and tidal waves using Wave Energy Converter (WEC) devices. Although the oceans have this potential, very little ocean energy is harvested because of improper planning and implementation challenges. Besides this, monitoring ocean waves is of immense importance as several ocean-related calamities could be prevented. Also, the ocean serves as the maritime transportation route. Therefore, a need exists for remote and continuous monitoring of ocean waves and preparing strategies for different situations. Remote sensing technology could be utilized for a large scale low-cost opportunity for monitoring entire ocean bodies and extracting several important ocean surface features like wave height, wave time period, and drift velocities that can be used to estimate the ideal locations for power generation and find locations for turbulent waters so that maritime transportation hazards could be prevented. To process this large volume of data, Big Data Analytics techniques have been used to distribute the workload to worker nodes, facilitating a fast calculation of the reanalyzed remote sensing data. The experiment was conducted on Indian Coastline. The findings from the experiment show that a total of 1.86 GWh energy can be harvested from the ocean waves of the Indian Coastline, and locations of turbulent waters can be predicted in real-time to optimize maritime transportation routes.

## INTRODUCTION

All renewable energy sources from the ocean are referred to as "ocean energy." Wave, tidal, and ocean thermal energy are the three basic categories of ocean energy. The development of all marine renewable resources is still in its initial stages (Melikoglu 2018).

The energy contained within ocean waves is converted into electricity and used to generate wave energy as renewable energy (Khatri & Wang 2020). Various wave energy systems are being developed and tested to transform wave energy into electricity. The potential energy provided by the height difference between high and low tides is harvested by tidal range technology. Technologies that capture the kinetic energy of currents moving in and out of tidal zones are known as tidal streams or current technologies (such as seashores or coastal regions) (Wang et al. 2018).

Ocean surface observation is a necessary part of studying environmental and hydrological aspects with respect to marine renewable energy sources. Recent improvements in satellite-based optical remote sensing have booted up a new age in the field of surface water sensing (Shen et al. 2018). The phenomena also observe the current state and challenges of the ocean geothermal field, including problems with spatiotemporal scale, integration with spaceborne hydrological data, elevation data, cloud, and vegetation obscuration, and the increasing need to map and examine surface water physics on a global scale. Sensor resolutions have always been contradictory in the past. To address this inconsistency, techniques such as pixel unmixing and reconstruction, and spatiotemporal fusion, have been developed. Ocean surface water dynamics are now being predicted using remote sensing techniques and

**ORCID details of the authors:**

**Subhrangshu Adhikary**
https://orcid.org/0000-0003-1779-3070
**Saikat Banerjee**
https://orcid.org/0000-0003-0610-7266

in-situ oceanographic data. Recent research has also shown that oceanographic surface physics may be predicted simply using optical remote sensing pictures, which provides useful information for hydrological studies in unmeasured areas. Cloud and vegetation obscuration has been a problem for optical sensors. Combining synthetic aperture radar data with other data is an efficient way to overcome this issue (Liang et al. 2019). Cloud/terrain shadows were also removed using digital elevation model data. The advancement of big data and cloud computing techniques has made it easier to meet the growing need for high-resolution monitoring of global and regional marine dynamics (Guillou et al. 2020).

With the growing amount of remote sensing ocean surface data, the processing capacity needs to be improved, giving rise to Big Data Analytics techniques. This replaces the requirement for developing more powerful computers by integrating multiple low-powered devices connected via the Internet to efficiently distribute the workload among them. The field of marine science is fast moving into the digital era (Amaro & Pina 2017). Escalating the opportunity and efficiency of ocean observations, as well as automated sampling and smart sensors integrated phenomenon, has resulted in rapid growth in the dataset size. Big data techniques help reduce the time requirement and cost of processing these large-scale data. This opens up new possibilities for studying and understanding the ocean through more complicated and multidisciplinary studies and inventive methods of marine resource management (Lytra et al. 2017).

This article discusses the usage of big data on reanalyzed remote sensing statistics to estimate the electricity generation capacity of the Indian Coastline. Further, the article discusses the optimal locations for harvesting electricity from ocean waves and their power generation capacities.

## RELATED WORKS

In the areas of physical, biological, coastal, and satellite oceanography, remote sensing has a wide range of applications. The acquisition of oceanographic data, monitoring of coastal and oceanic dynamics, and analysis of numerous processes employing space and airborne sensors are all part of oceanographic research (Adhikary et al. 2021). Remote sensing enables large-scale monitoring of oceanographic properties at regular intervals with minimal cost. This can be utilized to detect the direction of waves, height, speed, time period, and many more ocean surface properties with reliable accuracy. This method can also observe the water viscosity and physical and chemical features. Deep learning and machine learning on remote sensing have been widely used for forecasting and predicting different properties and phenomena related to ocean surface properties. Deep learning-based image segmentation techniques on remote sensing data have been used to detect coastlines and seashores. Autonomous detection of multiple objects on the sea has also been widely implemented with this technique (Tiwari et al. 2021). The technique has further been used for automatic ocean eddy detection. The coastal risk has been estimated using remote sensing and GIS techniques. Heat captured by oceans and their global impact has been estimated with this approach.

The large volume of oceanographic data has been widely studied with different significant data approaches. IoT frameworks consisting of self-powered sensors have been implemented for ocean surface feature extraction, and big data on these have fetched reliable results much faster than the traditional method (Man et al. 2020, Vo et al. 2021). The Big Data Ocean project has studied several tactics for offshore grid-based optimization techniques leveraging wave energy and has been optimized by big data analytics techniques (Khare et al. 2020). Remote sensing techniques can be utilized to detect the temperatures of ocean bodies. Likewise, large-scale integration of this technique with the application of big data have been used to simulate ocean surface temperature for planning foreign trade through sea route. The technique has been further used for forecasting several maritime parameters based on satellites, buoy, GPS, drone and other components to build early warning systems for ocean-based natural calamities (Román-Rivera & Ellis 2019).

### Limitations of the State of the Art and Motivation for the Experiment

The oceans around the world have a large potential for energy generation. Estimation of the potential reserves of energy is crucial to prepare strategies to extract electricity from ocean waves. Several approaches have been performed to estimate both the theoretical and practical limits of energy production (Hernández-Fontes et al. 2020). However, most of them have lesser accuracy as most were based on in-situ observations and other approximation techniques (Srisuwan et al. 2020). Table 1 summarizes all recent works and the limitations this article has attempted to solve. These limitations motivated us to use reanalyzed remote sensing technology and observe the entire coastline at regular intervals, estimate the energy production capacity purely based on the ocean waves, and find strategic locations of high turbulence.

## MATERIALS AND METHODS

The mechanism to estimate the oceanic power generation capacity of the Indian coastline has been summarized in Fig. 1 and discussed further in the following text.

Table 1: Limitations of previously conducted related studies.

| Sources | Objective | Methods | Findings | Limitations |
|---|---|---|---|---|
| (Thirugnana et al. 2021) | Estimation of Ocean Thermal Energy | Temperature, Salinity, Dissolved Oxygen, and Water Mass Profiling | Strategic locations for energy harvesting are depicted | In-situ observations have limited scalability |
| (Wahiduzzaman & Yeasmin2020) | Potential energy estimation for tropical cyclones | Remote sensing and geographically weighted regression | Correlations have been found between tropical cyclones and convective available potential energy | It cannot be used as a renewable energy source |
| (Hoang & Baraille 2020) | Energy estimation of ocean currents | Neural network with adaptive filtering | The possibility of oceanic current energy estimation with the method was confirmed | Simulated environment |
| (Nguyen & Tona 2018) | Wave excitation force estimation | Kalman filtering approach | Up to 94% accuracy | In-Situ experiment with limited scalability |
| (Chen et al. 2021) | Estimation of oceanic current fields using a decentralized sensor network | Kalman filtering and Monte Carlo Simulation | The model works well with fast-varying dynamics | In-Situ observations have limited scalability |
| (Bergamasco et al. 2021) | Real-time estimation of oceanic current energy | Point cloud estimation | 10x faster processing compared to the State of the Art | Limited mobility of the setup makes it difficult for large-scale monitoring |
| (Choi et al. 2020) | Real-time wave height estimation from 2D and 3D images | CNN and ConvLSTM | 84% classification accuracy | Camera-based monitoring limits large-scale monitoring |

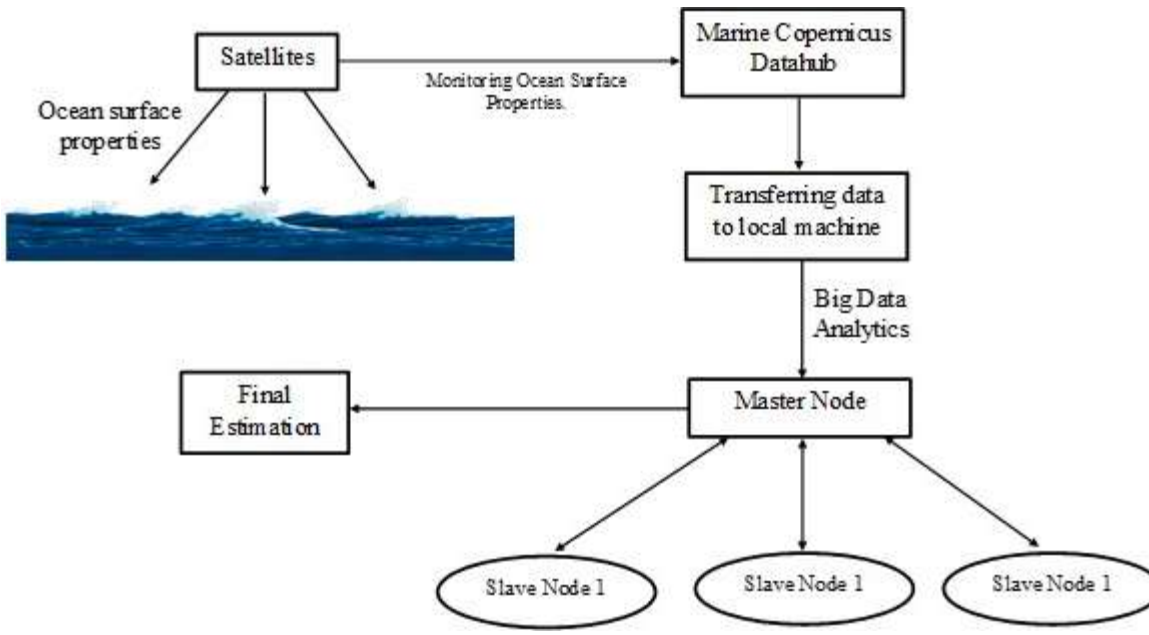


Fig. 1: The workflow diagram for the proposed mechanism to estimate oceanic power generation capacities.

## Study Location and Data Availability

The experiment has been conducted on Global Ocean Waves Analysis and Forecast statistics published by the Marine Copernicus program. Remote sensing data have been processed by the agency to track several important ocean surface features (Dalphinet et al. 2020). The study location was selected as Indian Coastline is significantly long and shares three geographically important water bodies: The Bay of Bengal, the Indian Ocean, and the Arabian Sea. The coordinates of the study location include 6º to 24º N and 67º E to 98º E. The date ranges were from 8$^{th}$ August 2021 to

8th November 2021, where 8 snapshots for each day were recorded. Each degree latitude and longitude were divided into 12 equal parts whose readings were recorded in the data. The dataset contained ocean surface features including Spectral significant wind wave height, Mean secondary swell wave direction, Mean wave direction (Mdir), Mean primary swell wave direction, Spectral moments (-1,0) wave period (Tm-10), Wave principal direction at spectral peak, Wave period at spectral peak/peak period (Tp), Spectral moments (0,2) wave period (Tm02), Spectral significant primary swell wave height, Mean wind wave direction, Spectral moments (0,1) secondary swell wave period, Stokes drift U, Spectral moments (0,1) primary swell wave period, Stokes drift V, Spectral significant wave height (Hm0), Spectral moments (0,1) wind wave period and finally Spectral significant secondary swell wave height. Table 2 contains the features along with their descriptions.

### Big Data Analytics-Based Processing of Reanalyzed Remote Sensing Data

The large volume of data associated with the study is considerably challenging to process with general-purpose

Table 2: Wave features and their short description.

| Features | Description |
|---|---|
| Spectral significant wind wave height | The average height of the highest one-third of all waves measured |
| Mean secondary swell wave direction | Mean direction of waves in the second swell partition |
| Mean wave direction (Mdir) | Mean direction toward which the waves and wind are propagating |
| Mean primary swell wave direction | Direction from which the primary swell is coming |
| Spectral moments (-1,0) wave period (Tm-10) | Turbulence energy spectra in the wavevector and frequency domain between subsequent waves |
| Wave principal direction at spectral peak | The direction of the peak of the wave spectrum |
| Wave period at spectral peak/peak period (Tp) | The time difference between the two peaks |
| Spectral moments (0,2) wave period (Tm02) | The spectral moment of the wave at 2nd order |
| Spectral significant primary swell wave height | Height of the primary swell wave for the wave spectrum |
| Mean wind wave direction | The direction of the wind blowing at the ocean/sea surface |
| Spectral moments (0,1) secondary swell wave period | Spectral moment of 1st order for secondary swell waves |
| Stokes drift U | The difference in endpoints of waves after a predefined amount of time |
| Spectral moments (0,1) primary swell wave period | The spectral moment at 1st order for the primary swell wave |
| Stokes drift V | Vertical stokes drift |
| Spectral significant wave height (Hm0) | Wave height of the spectral field |
| Spectral moments (0,1) wind wave period | 1st order spectral moment for a wind wave |
| Spectral significant secondary swell wave height | Wave height of the secondary spectral wave |

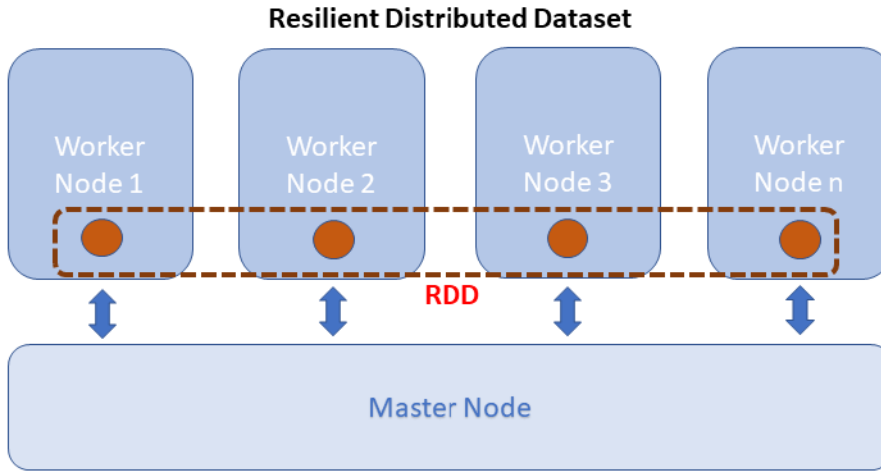


Fig. 2: Architecture of Resilient Distributed Datasets (RDD).

computers. Therefore big data analytics techniques have been implemented to distribute the workload across multiple server nodes (Qian et al. 2021). The system is controlled by a master node which splits the entire task into smaller chunks which are then processed by slave nodes and finally synchronized by the master node. The entire reanalyzed remote sensing dataset has been converted into a time series for each location pixel, and this time series has been stored with Resilient Distributed Datasets (RDD) method, which splits the entire dataset into multiple server nodes maintaining the sequence, speed, and fault tolerance (Athira & Thomas 2018). RDDs are immutable and, therefore, cannot be modified by other RDDs can be created from modifying an existing RDD. The architecture of RDD has been shown in Fig. 2. RDDs are not directly loaded into the memory for execution. First, a set of data is created to map all the functions to be executed in each row of the dataset. Therefore, because of this mapping, the immutability of RDDs can be exploited for faster and lightweight execution.

After this, multiple worker nodes are initiated for the execution by distributing the workload by the master node. Following this, each row is then separately processed by the assigned worker node fetching a limited row at a time only when necessary. This reduces the requirement for unnecessary ram usage and enables the processing of a very large volume of data efficiently without lagging. The data within the RDDs are replicated into copies spread across multiple worker nodes to make them resilient. This way, no data are lost even if there are issues with a few worker nodes, as the replicas can be processed if necessary. Following this, Map-Reduce-based operations have been performed to map each point in the RDD and create a new reduced RDD with applied conditions to get the final result. Reduce is performed to combine multiple rows of an RDD based on different conditions, and the resulting output creates another RDD. By this method, a total of 12942771x22 elements have been processed. The data are then visualized based on a different time to check for the variation of the ocean waves at different points of the day and seasonal variation. Following this, the ocean wave properties are further calculated to estimate the energy generation capacity, as discussed later. The map reduction process has been implemented to combine multiple rows of the primary RDD according to the equation conditions. The work has been conducted on 3 virtual private servers of 4GB RAM, and 2 CPU cores where one node was used as master and two other nodes were used as worker nodes.

## RESULTS AND DISCUSSION

The experimental results show that Indian Coastline potentially has a large reserve of energy production capacity based on mechanical properties like waves and tides, which can be utilized to extract electricity. Fig. 3 shows the ocean surface properties of the Indian Coastline that helps in estimating the energy generation capacities. The study reveals that the spectral significant wind wave height is maximum at the conjunction between the Bay of Bengal and the Indian Ocean. The wave heights in these areas rise above 0.8 m, which can be effectively utilized for energy production. The wave directions from the figure show the direction of waves' movement where the waves travel according to the wind movements. The waves mostly travel from the southeast and far south of the Indian subcontinent and mix with the Bay of Bengal. Further, the spectral moment wave time periods reveal that the waves at the Indian Ocean at the base of the Bay of Bengal are much longer than the waters of the Bay of Bengal. This indicates a steady near-laminar flow of water waves in this region. However, the wave time periods near the Bay of Bengal and the Arabian Sea are much shorter, more vigorous, and more turbulent. This observation indicates that both the wave height and time period of the wave are higher near the conjunction between the Indian Ocean and the Bay of Bengal, making it the ideal location for energy harvesting. The steadier flow in these regions would ensure ease of electricity generation. Similarly, the method can be utilized to find locations of high turbulence in real-time where maritime transportation could be hazardous. Therefore, routes of lower turbulence could be used for safer transportation.

The energy generation capacity has been measured by conditionally combining multiple ocean surface properties. Theoretically, any wave with kinetic energy can be harvested to produce energy in this method, but practically waves should be large enough to feasibly harvest the energy. Firstly, discussing the theoretical limits, any wave with a height greater than zero has been considered. This leaves us with 10005015x22 elements to filter from. The drift velocity of the wave for horizontal ($\xi_x$) and vertical ($\xi_z$) components of Lagrangian position ($\xi$) and amplitude $a$ and wave number $k$ is given by,

$$u_S = u_{x(\xi,t)} - u_{x(x,t)}$$
$$= [u_{x(x,t)} + (\xi_x - x)\frac{\partial u_x(x,t)}{\partial x} + (\xi_z - z)\frac{\partial u_x(x,t)}{\partial z} + \cdots] - u_x(x,t) \quad ...(1)$$
$$\approx (\xi_x - x)\frac{\partial^2 \xi_x}{\partial x \partial t} + (\xi_z - z)\frac{\partial^2 \xi_x}{\partial z \partial t}$$
$$= \left[-ae^{\{kz\}}\sin(kx - \omega t)\right]\left[-\omega kae^{\{kz\}}\sin(kx - \omega t)\right] + \left[ae^{\{kz\}}\cos(kx - \omega t)\right]\left[\omega kae^{\{kz\}}\cos(kx - \omega t\right]$$
$$= \omega k a^2 e^{\{2kz\}}[\sin^2(kx - \omega t) + \cos^2(kx - \omega t)$$
$$= \omega k a^2 e^{\{2kz\}} \quad ...(2)$$

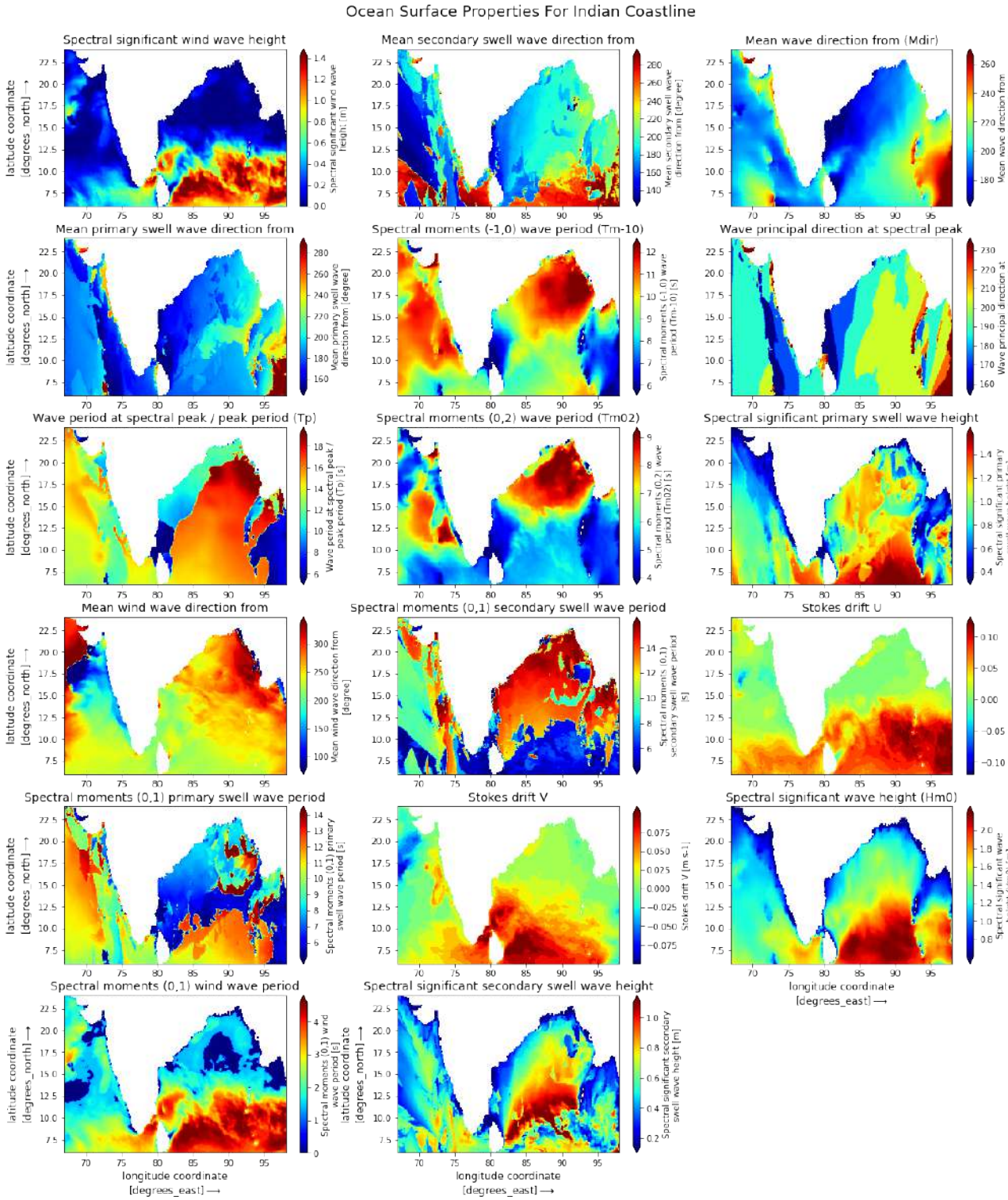


Fig. 3: Visualization of different ocean surface properties for the Indian coastline. The x-axis represents longitude, the y-axis represents latitude, and the color bar represents the magnitude of the points.

Followed by this, for wavelength L, height H, and time period T, the energy per unit area is calculated by,

$$E = \frac{\rho g H^2}{8} \quad ...(3)$$

Therefore from eqn. and eqn 3, we have the wave energy transmission rate or wave power defined by,

$$P = \frac{\rho g H^2 c}{16}\left(1 + \frac{2kh}{\sin(h\,2kh)}\right) = Ec_g \quad ...(4)$$

Where group celerity is given by,

$$c_g = \frac{c}{2}\left(1 + \frac{2kh}{\sin(h\,2kh)}\right) \quad ...(5)$$

The wave heights multiplied by the horizontal width of the waves, the drift velocity, and the wave's time period give us the waves' total volume, and multiplying that with water density gives us the total mass of the ocean waves, which is found to be 67 MT. With the usage of the big data distributed computing framework, the calculation was performed within 632 s as computed by 2 worker nodes and one master node of specification as described in an earlier section. Considering the drift velocity for waves of each location, the total power of the waves according to eqn. 4 has been estimated to be 1.86 GigaWatts (GWh). Although this is a theoretical limit, the energy could be logically harvested at a large scale if the ocean wave heights are over 1m. This condition leaves us with 1021415x22 elements, and repeating the calculation, we find 1.35 GWh power capacity in an ideal scenario. Considering 90% efficiency, 1.21 GWh could be effectively harvested. Following this, the waves could be harvested cost-effectively in case the waves are very large. Considering 2 m wave heights, 80233x22 elements of the dataset have been tested, resulting in 0.19 GWh power generation capacities with practically efficiency rates, 0.17 GWh could be harvested.

### Comparison With the State-of-the-Art Methods

The proposed ocean wave monitoring and power estimation model is better in multiple aspects than the state of the Art methods. The work conducted by Thirugnana et al. (2021), Nguyen & Tona (2018), and Chen et al. (2021) were in-situ observations. These works were conducted locally at the study location; therefore, they are immobile models making it difficult for large-scale monitoring. However, the proposed model uses remote sensing satellite technologies, enabling large-scale, low-cost remote, and continuous monitoring. Wahiduzzaman & Yeasmin (2020) showed an interesting model for the power estimation of tropical cyclones. Still, this energy cannot be harvested with state-of-the-art technology, but electricity can be harvested from ocean waves using WEC machines which have been the basis of the proposed work. Hoang & Baraille (2020) conducted the experiment for energy estimation of ocean currents using a simulated environment. Still, the proposed method uses large-scale data from real environments, making it more robust in the long run. Finally, Bergamasco et al. (2021) and Choi et al. (2020) used 2D and 3D images of the waves and estimated their power. This model has limited usage for large-scale continuous monitoring as this would require a large number of cameras at different locations, and a good amount of computational complexity is required for synchronizing all footage. But the proposed method doesn't require much cost and complexity as only one satellite combined with a cloud server can deploy the model.

## CONCLUSION

Oceans worldwide are potential sources of harvesting large amounts of renewable and green energy. Steady growth has been made to utilize this resource; however, a large amount of energy could be harvested from this abundant resource. Therefore, proper resource planning is required to use this large amount of resources. Remote sensing techniques could be utilized for remote regular monitoring of the ocean surface properties, and with the help of Big Data Analytics techniques, the processing could be accelerated. The paper presents a method to use reanalyzed remote sensing data with big data analytics techniques to estimate the total potential reserved energy generation capacity of the Indian Coastline using ocean and sea waves. The presented method is more precise than previously estimated results, mostly in-situ observations and approximations.

The experiment revealed that the conjunction area between the Indian Ocean and the Bay of Bengal shows promising areas to harvest the ocean wave energy. The theoretical limit for power generation capacity by ocean waves of the Indian Coastline was found to be 1.86 GWh. However, practically the waves should be large enough to be harvested, and therefore 1.35 GWh could be practically generated. Considering only the most promising areas for power harvesting, 0.19 GWh could be produced, ensuring lower implementation costs. The method can be used to find optimal maritime transportation routes based on the turbulence of the oceanic waters. The model could be used to set up proper strategies to implement WEC machines, ensuring maximum efficiency. Further, the model could be improved by increasing the resolution and considering other techniques to produce electricity from ocean waves.

## REFERENCES


Adhikary, S., Chaturvedi, S.K., Banerjee, S. and Basu, S. 2021. Dependence of Physiochemical Features on Marine Chlorophyll Analysis with Learning Techniques. In Siddiqui, N.A., Bahukhandi, K.D., Tauseef, S.M. and Koranga, N. (eds), Advances in Environment Engineering and Management, Springer, Cham, pp. 361-373.

Amaro, N. and Pina, J.M. 2017. Big data in power systems leveraging grid optimization and wave energy integration. 2017 International Conference on Engineering, Technology, and Innovation (ICE/ITMC), 27-29 June 2017, Madeira Island, Portugal, Piscataway, NJ, USA, pp. 1046-1054. https://doi.org/10.1109/ICE.2017.8279997

Athira, V. and Thomas, J. 2018. An approach of {RDD} optimization in big data analytics. IOP Conf. Ser. Mater. Sci. Eng., 396: 12022. https://doi.org/10.1088/1757-899x/396/1/012022

Bergamasco, F., Benetazzo, A., Yoo, J., Torsello, A., Barbariol, F., Jeong, J.Y., Shim, J.S. and Cavaleri, L. 2021. Toward real-time optical estimation of ocean waves' space-time fields. Comp. Geosci., 147: 104666. https://doi.org/https://doi.org/10.1016/j.cageo.2020.104666

Chen, H., Chen, H., Zhang, Y. and Xu, W. 2021. Decentralized estimation of ocean current field using underwater acoustic sensor networks. J. Acous. Soc. Am., 149(5): 3106-3121. https://doi.org/10.1121/10.0004795

Choi, H., Park, M., Son, G., Jeong, J., Park, J., Mo, K. and Kang, P. 2020. Real-time significant wave height estimation from raw ocean images based on 2D and 3D deep neural networks. Ocean Eng., 201: 107129. https://doi.org/https://doi.org/10.1016/j.oceaneng.2020.107129

Dalphinet, L., Aouf, S.L.C. and Fernandez, E. 2020. G-Product User Manual for Global Ocean Waves Analysis and Forecasting Product GLOBAL_ANALYSIS_FORECAST_WAV_001_027. Version 1. 1.1.

Guillou, N., Lavidas, G. and Chapalain, G. 2020. Wave energy resource assessment for exploitation: Review. J. Marine Sci. Eng., 8(9): 705. https://doi.org/10.3390/jmse8090705

Hernández-Fontes, J.V, Martínez, M.L., Wojtarowski, A., González-Mendoza, J.L., Landgrave, R. and Silva, R. 2020. Is ocean energy an alternative in developing regions? A case study in Michoacan, Mexico. J. Clean Prod., 266: 121984. https://doi.org/https://doi.org/10.1016/j.jclepro.2020.121984

Hoang, H.S. and Baraille, R. 2020. Neutral Network Adaptive Filter with Application to Ocean Current Energy Estimation. In Harrou, F. and Sun, Y. (eds), Advanced Statistical Modeling, Forecasting, and Fault Detection in Renewable Energy Systems, Intech Open, London, pp. 33.

Khare, V., Nema, S. and Baredar, P. 2020. Ocean Energy Modeling and Simulation with Big Data: Computational Intelligence for System Optimization and Grid Integration. Butterworth-Heinemann, Oxford, UK.

Khatri, P. and Wang, X. 2020. Comprehensive review of a linear electrical generator for ocean wave energy conversion. IET Renew. Power Gen., 14(6): 949-958.

Liang, S., Wang, D., He, T. and Yu, Y. 2019. Remote sensing of earth's energy budget: Synthesis and review. Int. J. Digit. Earth, 12(7): 737-780. https://doi.org/10.1080/17538947.2019.1597189

Lytra, I., Vidal, M.E., Orlandi, F. and Attard, J. 2017. A big data architecture for managing oceans of data and maritime applications. 2017 International Conference on Engineering, Technology and Innovation (ICE/ITMC), 27-29 June 2017, Madeira Island, Portugal, Piscataway, NJ, USA, pp. 1216-1226. https://doi.org/10.1109/ICE.2017.8280019

Man, Y., Sturm, T., Lundh, M. and MacKinnon, S.N. 2020. From ethnographic research to big data analytics: A case of maritime energy-efficiency optimization. applied sciences, 10(6): 2134. https://doi.org/10.3390/app10062134

Melikoglu, M. 2018. Current status and future of ocean energy sources: A global review. Ocean Eng., 148, 563-573. https://doi.org/https://doi.org/10.1016/j.oceaneng.2017.11.045

Nguyen, H.N. and Tona, P. 2018. Wave Excitation Force Estimation for Wave Energy Converters of the Point-Absorber Type. IEEE Transactions on Control Systems Technology, 26(6): 2173-2181. https://doi.org/10.1109/TCST.2017.2747508

Qian, C., Huang, B., Yang, X. and Chen, G. 2021. Data science for oceanography: From small data to big data. Big Earth Data, 11: 1-15. https://doi.org/10.1080/20964471.2021.1902080

Román-Rivera, M. A. and Ellis, J. T. 2019. A synthetic review of remote sensing applications to detect nearshore bars. Mar. Geol., 408: 144-153. https://doi.org/https://doi.org/10.1016/j.margeo.2018.12.003

Shen, H., Perrie, W., Hu, Y. and He, Y. 2018. Remote sensing of waves propagating in the marginal ice zone by SAR. J. Geophys. Res. Oceans, 123(1): 189-200. https://doi.org/https://doi.org/10.1002/2017JC013148

Srisuwan, C., Rattanamanee, P. and Rattanapitikon, W. 2020. Analytical formula for estimation of surface wave power with application in the coastal ocean of Thailand. Ocean Eng., 204: 107273. https://doi.org/https://doi.org/10.1016/j.oceaneng.2020.107273

Thirugnana, S., Jaafar, A.B., Yasunaga, T., Nakaoka, T., Ikegami, Y. and Su, S. 2021. Estimation of ocean thermal energy conversion resources in the east of Malaysia. J. Mar. Sci. Eng., 9(1): 22. https://doi.org/10.3390/jmse9010022

Tiwari, S.P., Chaturvedi, S.K., Adhikary, S., Banerjee, S. and Basu, S. 2021. Automatized Marine Vessel Monitoring from Sentinel-1 Data Using Convolution Neural Network. 2021 IEEE International Geoscience and Remote Sensing Symposium IGARSS, 11-16 July, Brussels, Piscataway, NJ, USA, pp. 1311-1314. https://doi.org/10.1109/IGARSS47720.2021.9555149

Vo, D.T., Nguyen, X.P., Nguyen, T.D., Hidayat, R., Huynh, T.T. and Nguyen, D.T. 2021. A review on the Internet of thing (IoT) technologies in controlling ocean environment. Energy Sour. Part A Recov. Utiliz. Environ. Effects, 14: 1-19. https://doi.org/10.1080/15567036.2021.1960932

Wahiduzzaman, M. and Yeasmin, A. 2020. A kernel density estimation approach of North Indian Ocean tropical cyclone formation and the association with convective available potential energy and equivalent potential temperature. Meteorol. Atmos. Phys., 132(5): 603-612.

Wang, L., Isberg, J. and Tedeschi, E. 2018. Review of control strategies for wave energy conversion systems and their validation: the wave-to-wire approach. Renew. Sustain. Energy Rev., 81: 366-379. https://doi.org/https://doi.org/10.1016/j.rser.2017.06.074

Nature Environment and Pollution Technology
An International Quarterly Scientific Journal

p-ISSN: 0972-6268
(Print copies up to 2016)
e-ISSN: 2395-3454

Vol. 22 | No. 1 | pp. 277-283 | 2023

Original Research Paper

https://doi.org/10.46488/NEPT.2023.v22i01.027

Open Access Journal

# Turbidity Reduction and Eco-friendly Sludge Disposal in Water Treatment Plants

**Roop Singh Sinsinwar*† and Munna Verma****
*Department of Civil Engineering, Bhagwant University, Ajmer-305023, India
**Department of Mechanical Engineering, Bhagwant University, Ajmer-305023, India
†Corresponding authors: Roop Singh Sinsinwar; rsroopsingh81@gmail.com

**Nat. Env. & Poll. Tech.**
**Website: www.neptjournal.com**

*Received:* 06-08-2022
*Revised:* 10-10-2022
*Accepted:* 18-10-2022

**Key Words:**
Water treatment plant
Sludge
Coagulation
Flocculation
Nephelometric turbidity unit

## ABSTRACT

Plankton and other microscopic colloids are tiny particles that are suspended in water and cause turbidity, which causes the water to seem murky or opaque. These particles are too unstable and light to settle or be naturally eliminated. These details contribute to water turbidity and pose some stability. During the process of purifying raw water, all water treatment Plants (WTPs) produce waste/residue known as water treatment sludge (WTS). The majority of the sludge's chemical components include silica, alumina, ferric oxide, lime, and many heavy metals. The surface water treatment technique included coagulation, flocculation, sedimentation, and filtration to remove colloidal and suspended particles from raw water. The sludge obtained from the WTP located at Kekri (Rajasthan), India is being investigated for its physical and chemical properties. About 60% of the sand contained in the sludge is found in the 155-60 grain size range. Additionally, nutrient reduction of soil due to contamination and runoff can be minimized or rounded out by wastewater treatment or the removal of heavy metals from water solutions. To develop water-safe and appealing sludge management solutions, the efficiency of aluminum sulfate and poly aluminum chloride was assessed at different coagulant doses in the study. To make water safe and appealing for human consumption, numerous purification procedures are employed from a variety of sources. Sludge bricks are acceptable to high temperatures in the furnace and have better compressive strength than clay bricks.

## INTRODUCTION

Water is the other term of life, and it is unquestionably the most important natural resource. The availability of clean and safe water is a key problem in many undeveloped and developing countries. Each year, diarrhea brought on by tainted water, claims the lives of more than 6 million people. In developing nations, importing chemicals for water treatment is expensive. (Ghebremichael 2004, Gomes 2005). In water treatment facilities, a flocculation treatment procedure, in which colloidal in water are destabilized so that they may coalesce and be physically removed, can reduce turbidity efficiently. To achieve consistently high coagulation effectiveness, conventional coagulants used in large-scale water treatment rely on water pH and accurate dosages such as aluminum sulfate, ferric sulfate, and ferric chloride salts. Sludge that is clotted with the use of metal salts includes leftover metals that must be carefully disposed of to avoid polluting the environment. Safe and appealing water may be made using a variety of techniques. Method selection is based on factors such as raw water quality and seasonal variations in turbidity, both of which are problematic when dealing with surface water (Connachie et al. 1999). Traditional coagulation factors have many drawbacks that restrict their utility in household water treatment. Poly aluminum chloride is one of the most common coagulants for water and wastewater treatment. Polyaluminium chloride contains about 70% Al, with an aluminum concentration of 0.35 Mol.$L^{-1}$ (Deng et al. 2015). Coagulation flocculation therapy may be broken down into two distinct steps, each of which must be followed sequentially. Destabilization of colloidal suspensions and solutions is the initial step in this process, known as coagulation, and its primary goal is the overthrow of stability-promoting factors. The so-called coagulant is used in this process, which involves the use of a suitable chemical. The inducement of destabilized particles to come together, establish contact, and therefore form huge agglomerates, is referred to as flocculation in the second subprocess. Gravity-settling coagulation normally completes in a relatively short time (approximately 10s), whereas flocculation happens usually for 20-45 minutes. It is a widespread practice, notably in Greece, the intensification of particle aggregation (Bratby 2006).

Coagulation, flocculation, sedimentation, filtration, and disinfection are often used in the treatment of drinking water. When it comes to liquid-solid separation, the coagulation and flocculation processes are vital (Yokselen & Gregory 2004,

Sudhob et al. 2015). Mostly, optimizing the coagulation/flocculation and subsequent filtration and solid-liquid separation processes may remove all organic and suspended matter to a level below water quality limits, allowing for efficient use of sewage and sludge in soil (Khan & Thiem 2008, Fotoki & Oguntowokan 2012).

Almost 11.80 billion cubic meters of water would be needed in 2050, according to the Indian government's planning commission. In a typical water treatment facility, sludge is generated at a rate of 1.0 million tons per year (Bourgeois et al. 2004). India's waste-to-energy plants (WTPs) generate enormous amounts of waste each day. Due to a lack of sludge management practices, the majority of WTPs in India release their filters' backwash water and sludge into nearby drains, polluting the water supply with colloidal and suspended contaminants found in the sludge. Wet sludge typically has a moisture level exceeding 80 WTZ percent (WHO 2011).

Discharging the water treatment sludge into the environment is not a viable alternative, thus it is necessary to develop a more eco-friendly, sustainable, and cost-effective solution. Other nations' WTS studies have shown parallels between the physio-chemical features of the sludge from the 132 MLD and 142 MLD treatment plants in Kekri, Rajasthan. These characteristics allow WTS to be used effectively in the brick-making process (Chiang et al. 2009, Huage et al. 2005). With these properties, WTS may be used to make bricks and cementitious materials, and light aggregate in a constructive way (Chiang et. al. 2009, Hong et al. 2013). Cation recovery and reuse in wastewater treatment plants as a coagulant to absorb phosphorus, hydrogen sulfurate, and boron fluorides percolate glyphosate and arsenate, lead, and selenium buffer is another feasible solution to the sludge discharge problem (Eliott & Dempser 1999). The technology will be explored to lessen the burden of safe sludge disposal while also optimizing expenses.

## MATERIALS AND METHODS

For turbidity reduction from the surface (Raw) water, alum [$Al_2$ $(SO_4)_2$] and poly aluminum chloride are used in the coagulation-flocculation process in the water treatment plants of Kekri (Rajasthan). The source of surface water was the Bisalpur Dam in Deoli Tehsil of Tonk District (Rajasthan) India. Water from the Bisalpur dam is pumped to the Thadoli Intermediate Boosting Station, then raw water is pumped through the main pipeline rising from Thadoli to Kekri, receiving at the inlet point of water treatment plants at Kekri of 142 MLD and 132 MLD capacity. A Jar testing was conducted for finding the optimum dose of poly aluminum chloride, having good water solubility and for wider pH range of surface water. The optimal PAC doses are needed to produce adequate coagulant in the pH range of 6.5-7.5. Coagulant alum is often used to coagulate drinking water in traditional water treatment systems and also used with lime to neutralize the acidic nature of water, but it has many drawbacks, including the creation of significant amounts of waste materials and is also restricted for the coagulation process in the pH range of just 6.5-8. Compared to alum application, poly aluminum chloride application delivers superior quality treated water when carried out according to the prescribed process conditions. When applied in the right concentration, poly aluminum chloride enhances the coagulation process in traditional water treatment and lowers the pH of the finished water. During the first interview with the Kekri water treatment plant's management, the mixing speed and duration, and the maximum contact time utilized in regular Jar testing (Fig. 1) were learned.


Fig. 1: Flocculator model for Jar Testing.

### Raw Water Sampling and Preparation

Raw water as received at the inlet of 142 MLD and 132 MLD water treatment facility at Kekri was sent for the Jar testing as shown in Fig. 1 and subsequent analysis was done to estimate the optimum dosage of poly aluminum chloride of medium basicity necessary for coagulation-flocculation in a conventional type water treatment plant. Further, the samples were taken in clean and sealed containers.

### Jar Testing

The impact of pH fluctuations on coagulation was studied by conducting a series of Jar flocculation experiments at predetermined pH levels. For flocculation, the jars were first mixed quickly to ensure rapid coagulant mixing, and then slowly to ensure proper flocculation. These two different mixing rates make up a mixing speed pair. The flocculation model of jar testing consists of six jars each of 1-liter capacity. Five jars out of six were used for the testing. The flocculation jars were filled with raw water and 5 consecutive doses of PAC were administered to each jar to sustain concentrations of 20 $mg.L^{-1}$, 25 $mg.L^{-1}$, 30 $mg.L^{-1}$, 35 $mg.L^{-1}$ and 40 $mg.L^{-1}$ respectively at an increasing concentration of 5 $mg.L^{-1}$ of PAC. The speed of the stirrers in the individual jars was 180 rpm for 5 minutes, then 10 minutes of gentle stirring. When the allotted time for mixing was over, the samples were allowed to stand for 15 minutes. A total of three samples of contaminated water from each Jar of supernatants have been taken with the help of a syringe and a meter. The experiment was done five times in total to assure high accuracy, and the average water quality parameter values were computed. The turbidity reduction was studied from March 2021 to June 18th, 2021 as shown in Table 1.

### Sludge Testing

To remove the colloidal and suspended impurities from the sludge produced during the clarification and flocculation process in the clarifiers of Bisalpur dam surface water, poly aluminum chloride (PAC) of medium basicity is used as a coagulant. Sludge in beds of drying WTP employs percolated drying bed water for further treatment, and samples that have been dehydrated are sent to the lab for physical and chemical examination.

The physical characteristics of the sludge samples, including pH and moisture content, were assessed in line with the Indian Standard. In addition, to determine the volatile matter, ash concentration, and ignition loss, the sample was heated in a muffle furnace as shown in Fig. 2.

Further, sieve analysis and hydrometer analysis have been used to examine the grain size distribution of the dried sludge sample. The energy dispersive x-ray technique and Florence (ED-XRF) technique were used to examine the

Table 1: Turbidity of raw water in water treatment plants Kekri at dose 30 $mg.L^{-1}$.

| Date | 142 MLD water treatment plant | | | | | 132 MLD water treatment plant | | | | |
|---|---|---|---|---|---|---|---|---|---|---|
| | Raw water Turbidity | Clarifier flocculator turbidity | Filter bed out let turbidity | CWR water turbidity | % Re-moval of turbidity | Raw water Turbidity | Clarifier flocculator turbidity | Filter bed out let turbidity | CWR water turbidity | % removal of turbidity |
| 03/03/2021 | 4.97 | 2.68 | 1.77 | 1.10 | 79.87 | 4.92 | 4.70 | 2.05 | 1.79 | 61.91 |
| 10/03/2021 | 5.12 | 2.45 | 1.29 | 1.09 | 78.71 | 5.60 | 4.85 | 2.17 | 1.82 | 69.75 |
| 17/03/2021 | 5.26 | 2.68 | 1.32 | 1.18 | 77.56 | 4.86 | 4.45 | 2.20 | 1.66 | 66.59 |
| 24/03/2021 | 5.30 | 2.21 | 1.38 | 1.19 | 77.54 | 4.49 | 4.02 | 2.05 | 1.66 | 72.42 |
| 31/03/2021 | 4.80 | 2.96 | 1.23 | 1.20 | 75.00 | 5.18 | 4.46 | 1.43 | 1.23 | 72.42 |
| 07/04/2021 | 4.86 | 2.84 | 1.51 | 1.36 | 70.81 | 5.37 | 4.24 | 1.65 | 1.45 | 72.99 |
| 14/04/2021 | 5.75 | 2.29 | 1.16 | 1.09 | 81.04 | 5.30 | 4.99 | 2.49 | 1.47 | 72.26 |
| 21/04/2021 | 6.27 | 3.57 | 1.69 | 1.57 | 74.69 | 6.22 | 4.12 | 3.10 | 1.50 | 75.56 |
| 28/04/2021 | 6.13 | 2.98 | 1.56 | 1.42 | 76.83 | 5.67 | 4.11 | 3.08 | 1.51 | 73.36 |
| 06/05/2021 | 6.27 | 2.98 | 1.87 | 1.70 | 72.88 | 6.25 | 3.95 | 1.78 | 1.73 | 72.25 |
| 13/05/2021 | 5.20 | 2.51 | 1.61 | 1.52 | 70.69 | 5.05 | 3.85 | 1.70 | 1.50 | 70.29 |
| 20/05/2021 | 5.53 | 2.85 | 1.69 | 1.35 | 75.58 | 4.92 | 4.12 | 1.54 | 1.46 | 69.70 |
| 27/05/2021 | 7.67 | 3.35 | 2.04 | 1.95 | 74.57 | 7.10 | 5.50 | 2.31 | 2.22 | 70.14 |
| 04/06/2021 | 7.92 | 3.27 | 2.10 | 1.52 | 80.80 | 8.45 | 5.54 | 2.30 | 2.13 | 74.79 |
| 11/06/2021 | 7.25 | 3.47 | 2.20 | 2.13 | 70.62 | 7.10 | 5.10 | 2.15 | 2.05 | 71.12 |
| 18/06/2021 | 6.62 | 2.76 | 1.85 | 1.69 | 74.47 | 6.57 | 5.31 | 2.10 | 1.96 | 70.16 |

Fig. 2: Muffle furnace.

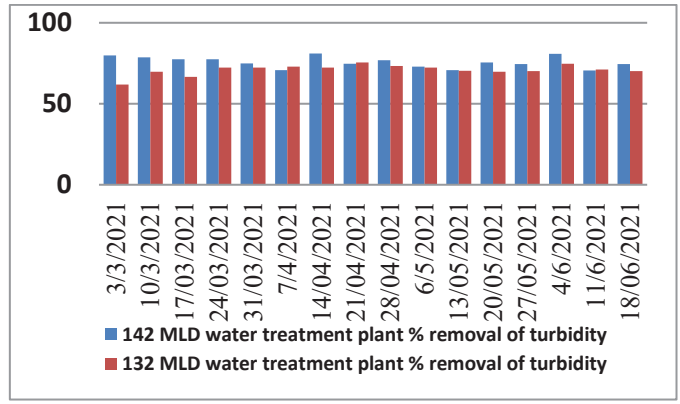


Fig. 3: Comparative bar chart of turbidity removal % of 142 and 132 MLD WTP.

principal chemical components of dry sludge, while trace elements are identified by using the wavelength X-Ray Florence (WD XRF) technique.

## RESULTS AND DISCUSSION

The turbidity removal percentage at 142 MLD and 132 MLD WTP has been analyzed as shown in Fig. 3. The best dose of PAC is found to be 30 ppm ($mg.L^{-1}$) to lower the quantity of turbidity in raw water at Kekri (Rajasthan) treatment facilities for the jar testing that conducted from 3rd March to 18th June 2021. The turbidity in clear water was measured only weekly for the samples of both the water treatment plants. The removal of turbidity of 142 MLD and 132 MLD was measured and it was found to be a maximum of 81.04% on 14/04/2021 and 75.56% on 21/04/2021 of turbidity removal rate respectively from both the water treatment plant. The turbidity removal average capacity in 142 MLD and 132 MLD at Kekri was found to be 75.32% and 70.08% respectively. The trend of turbidity removal efficiency of 142 MLD filter plant is more than that of 132 MLD water treatment plant. The trend of the turbidity reduction potential of the 142 MLD water treatment plant is 1.0 NTU and it fulfills the Indian standard code 10500-2012 of the acceptable limit of 1.00 NTU. Whereas, the turbidity reduction potential of 132 MLD water treatments is more than 1.0 NTU. However, it is more than the acceptable limit but less than 5.0 NTU, the permissible limit of turbidity as per the Indian Standard. Both the water treatment plant was found to be satisfactory in turbidity reduction within the permissible limits, i.e., the range below 5.0 NTU.

### Sludge Disposal

Turbidity and coagulant-added sludge found during the water treatment are collected as sludge samples by the process of conduction tests at water treatment plants, in Kekri. Acidity (pH 6.82), moisture content, and volatile matter (volatile

matter level of 2.65%) were identified in the sludge. The ash level found in sludge is 84.55%, which indicates its inorganic nature whereas the loss of ignition is found to be 8.39%. The physical characteristics of the sludge are given in Table 2.

In this present work, the sludge obtained from the WTP is used for making bricks. In the process of brick fabrication, the quantity of Portland cement grade 43 was mixed in the ratio of 1:6, 1:5, 1:4, and 1:3 with dry sludge, and the standard size of brick was constructed. The bricks made from cement and sludge are then kept in submerged water for 7 days and cured with water for 21 days. In the laboratory, the compressive strength of bricks was tested by a universal testing machine. Bricks constructed of sludge and cement were shown to have a stronger compressive strength than that made from clay soil. The chemical composition of the sludge contains silica dioxide ($SiO_2$)-52.74%, aluminum oxide ($Al_2O_3$)-14.61%, ferric oxide ($Fe_2O_3$)-5.13%, calcium oxide (CaO)-5.02% and potassium oxide ($K_2O$)-3.41%. Silicon dioxide ($SiO_2$) possesses the same set of properties as silica. It can be translucent to gray, crystalline, unscented, or an amorphous solid. Its melting point is 1713°C, while its boiling point is 3265°C. The density was found to be 2.64 $g.cm^{-3}$ and it is soluble in acid as well as in water. Silicon is a hard, dark gray solid with a metallic sheen and has an octahedral crystalline structure. Aluminum oxide ($Al_2O_3$) is an insert, tasteless, white amorphous substance that is extensively used in industrial ceramics. Ferric oxide ($Fe_2O_3$) comes from the electrodes used in an electric conductivity (EC) system. Calcium oxide (CaO), also known as lime or more especially quick lime; is a white or grayish whole solid, widely used for desulfurization. Spray-dried sludge is added to the clay at a rate of 20% of the dry weight of the clay. The compressive strength was increased from 9.0 to 10.2 MPa by lowering the drying time by 20% and by adding 20% of the dried sludge to the mixture.

### Effects of Waste Sludges on Compressive Strength

The compressive strength of the bricks has a significant role in deciding their utility. Typically, porosity affects compressive strength. It was discovered that the compressive strength of the bricks rapidly decreased as the amount of water treatment sludge in the mixture increased. Additionally, it was found that the compressive strength of the bricks made from different four ratios increased as the curing days increased. The specimen showed a compressive strength of 7.5 MPa and 9.3 MPa on the $7^{th}$ and $28^{th}$ days respectively after the addition of 5% of sand in the mixture with the replacement of 5% of the sludge. This was done using a mixture of cement and sand in a ratio of 1:4. However, when the sludge concentration went up, the bricks' compressive strength decreased. For instance, for control mortar and bricks containing 3, 5, 7, 10, 15, 20, and 40% of waste treatment sludge, the strength developed for the mixtures was 7.5, 8.0, 5.43, 4.63, 4.13, 2.56, and 0.47 MPa respectively. After 28 days, brick combinations with the same water-to-cement ratio had strengths of 9.67, 10.37, 5.7, 4.77, 4.77, 4.30, 2.57, 1.63,

Table 2: Physical characteristics of the sludge.

| Date | PAC dose in WTP ($mg.L^{-1}$) | Moisture (%) | Volatile matter (%) | Ash content (%) | Loss of ignition (%) |
|---|---|---|---|---|---|
| 03/03/2021 | 30 | 0.85 | 2.66 | 84.66 | 8.26 |
| 10/03/2021 | 30 | 0.84 | 2.65 | 84.64 | 8.39 |
| 17/03/2021 | 30 | 0.91 | 2.65 | 84.50 | 8.40 |
| 24/03/2021 | 30 | 0.90 | 2.65 | 84.55 | 8.30 |
| 31/03/2021 | 30 | 0.90 | 2.65 | 84.44 | 8.41 |
| 07/04/2021 | 30 | 0.90 | 2.65 | 84.55 | 8.46 |
| 14/04/2021 | 30 | 0.87 | 2.65 | 84.55 | 8.47 |
| 21/04/2021 | 30 | 0.86 | 2.67 | 84.55 | 8.39 |
| 28/04/2021 | 30 | 0.85 | 2.64 | 84.55 | 8.39 |
| 06/05/2021 | 30 | 0.85 | 2.65 | 84.55 | 8.39 |
| 13/05/2021 | 30 | 0.86 | 2.64 | 84.55 | 8.39 |
| 20/05/2021 | 30 | 0.89 | 2.64 | 84.55 | 8.39 |
| 27/05/2021 | 30 | 0.89 | 2.64 | 84.55 | 8.41 |
| 04/06/2021 | 30 | 0.90 | 2.65 | 84.55 | 8.35 |
| 11/06/2021 | 30 | 0.86 | 2.64 | 84.55 | 8.35 |
| 18/06/2021 | 30 | 0.85 | 2.64 | 84.55 | 8.39 |
| Average | | | 2.65 | 84.55 | 8.39 |

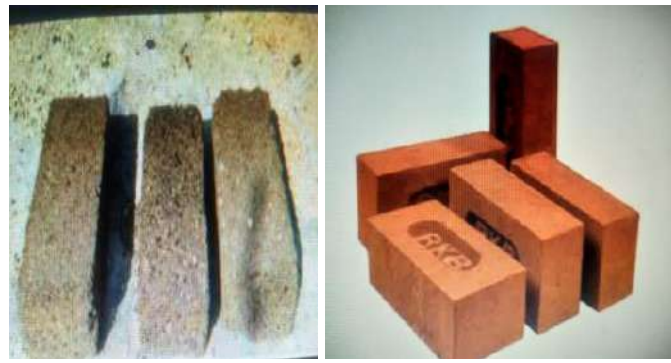

Fig. 4: Photograph of Sludge Bricks and Red Colour Bricks.

and 0.6 MPa. Here, the final compressive strength of the brick was taken as the arithmetical mean of the compressive strength of 5 bricks. Compressive strength is taken as ($C_O$ = $P/A$) . Here, P is an applied axial load on the brick at the uniform rate of 140 kg.cm$^{-2}$ per minute. A water adsorption test has been carried out for sludge bricks as per I S Code 1077-1970 and it was found to be 9.04% which is less than the prescribed limit of 25%. Adsorption percentage is given by the formula as, $W = \frac{(W_2 - W_1)}{W_1} \times 100$ %. Where, $W_1$ is dry weight and $W_2$ is the weight after immersion in water for 24 hours. In another formation, sludge bricks have been made with the mortar in a ratio of 1:4, and 5-part of sludge are mixed and then the compressive strength was measured. It was found to be 10.37 N/mm$^2$. Water absorption of these bricks was found to be 8.10%, which is well below the permissible limit of 25% as per the I S Code 1077-1970 and the brick efflorescence was found to be nil. Further, these bricks were found better in performance as compared with the red color bricks as shown in Fig. 4. The compressive strength of the red color bricks or building bricks lies within 3.5 MPa which is less as compared with the sludge bricks and the water absorption capacity of these red color bricks is up to 20% which is higher than that of the sludge bricks. Therefore, the sludge bricks have better performance than the red color bricks in a wide range of applications.

A sludge brick has high corrosion endurance, and high-temperature stability and its coefficient of thermal expansion at 25-1000°C are found to be 8.210$^{-6}$/°C. It also provides insulation in different types of applications.

## CONCLUSIONS

By using the available coagulant poly aluminum chloride (PAC), significant improvement in the reduction of turbidity and coliform has been observed in the raw water of Bisalpur dam. The maximum turbidity reduction was found in the highly turbid water after dosing poly aluminum chloride (PAC). It has been observed that highly turbid water having 5.97 & 7.92 NTU reduced to 1.09 & 1.52 NTU respectively in 142 MLD water treatment plants and turbid water having 5.18 & 4.92 NTU reduced to 1.23 & 1.46 NTU respectively in 132 MLD water treatment plant. The maximum turbidity removal reduction of up to 81.04% was found in 142 MLD WTP on 14$^{th}$ April 2021 and up to 75.56% was found in 132 MLD WTP on 21st April 2021. Therefore, 142 MLD WTP has good turbidity removal in comparison to 132 MLD WTP.

Water treatment sludge produced at Kekri, India WTP is composed of 55% fine sand, 26% silt, and 19% clay. Sustainable growth necessitates the creation of effective sludge management services. An environmentally friendly method of disposing of construction and building sludge might be recycling. The government may make money by using sludge in the construction business and benefit from its positive environmental effects. Every part of sludge may be recycled by the formation of bricks for the construction of buildings and furnaces also. Sludge bricks had better compressive strength than the clay and soil red bricks and were also found light in weight. Bricks were successfully produced in this research work from the sludges of water treatment plants. Utilizing the sludge as brick formation reduced the adverse impact on the environmental pollution caused by the sludge. Sludge bricks are acceptable to high temperatures in a furnace and have better compressive strength than clay and soil bricks.

## ACKNOWLEDGEMENT

The authors gratefully acknowledge the support provided by the Public Health Engineering Department, Kekri, and Bhagwant University, Ajmer (Rajasthan) India.

## REFERENCES

Bourgeois, S.C., Walsh, M.E. and Gagnon, G.A., 2004. Treatment of drinking water residuals, comparing sedimentation and dissolved air flotation performance with optimal cation ratio. Water Res., 38: 1173-1182.

Bratby, J. 2006. Coagulants in Coagulation and Flocculation in Water and Waste Water Treatment. Second, ed, IWA Publishing London, pp. 50-58.

Chiang, K.Y., Chou, P.J., Hna, C.R., Chein, K.L. and Chesseman, C. 2009. Ggat weight brick manufactured from WTS and rise husks. J. Hazard Mater, 171: 76-82.

Connachie, G.L., Fulkard, G.K., Matawali, M.A. and Sutherland, J.P. 1999. Field trials of appropriate hydraulic flocculation process. Water Research, 33(6): 1425-1434.

Deng, F., Wang, X., He, D., Hu, J., Gong, C., Ye, U.S., Xie, X. and Xue, Z. 2015. Microporous polymer electrolyte based on PVDF/PEO star polymer blends for lithium ion batteries. Journal of Membrane Science, 491: 82-89.

Eliott, H.A. and Dempser, B.A. 1999. Agronomic effects of land application of WTS. J. Am Water. Works Assoc., 83(4): 126-131.

Fotoki, O.S. and Oguntowokan, A.O. 2012. Effect of coagulant treatment on the metal composition of raw water. Water SA, 28: 293-297.

Ghebremichael, K.A., 2004. Morgina seed and pumicis natural after native materials for drinking water treatment, KTH land and water resources engineering. Website: https://fr.ircwash.org

Gomes, D.J. 2005. Waterborne, illness; a real disaster in Bangladesh. In: Proceeding of the Japan – Bangladesh Joint International conference on Microbiology Education & the Prospect of Japanese Collaboration in Education and Research, pp. 32-51.

Hong, G.X, Hao. J.R. and Liu, Y. 2013. Application of WTS in the manufacturing of light weight aggregate. Construction Building Material, 43: 174-183.

Huage, C.P., Pand J.R.S. and Liu, Y.R. 2005. Mixing water treatment resident with excavation waste soil in brick and artificial aggregate making. J. Env. Eng., 131: 272-277.

Khan, Z. and Thiem, L.T. 2008. Optimizing coagulation process for a low turbidity, low temperature water, electron, J. Environ. Agric. Food Chem., **7**: 2599-2610.

Sudhob, R., Islam M.S., Sazawa, K., Okazki, T., Hata, N., Taguchi, S. and Kuramitz, H. 2015. Removal of dissolved humic acid from water by coagulation method using poly aluminum chloride (PAC) with calcium carbonate as neutralizer and coagulant aid. J. Environ. Chem. Eng., 3: 770-774.

World Health Organization (WHO) 2011. Guideline for drinking water quality. World Health Organization Geneva.

Yokselen, M.A. and Gregory, J. 2004.The effect of rapid mixing on the break up and reformation offices. J. Chem. Technol. Biotechnol., 79: 782-788.

Nature Environment and Pollution Technology
An International Quarterly Scientific Journal

p-ISSN: 0972-6268
(Print copies up to 2016)
e-ISSN: 2395-3454

Vol. 22 | No. 1 | pp. 285-291 | 2023

Original Research Paper

https://doi.org/10.46488/NEPT.2023.v22i01.028

Open Access Journal

# Research on the Law of Stress of Polychlorinated Naphthalenes (PCNs) on the Physiological Ecology of Bluegrass (*Poa annua* L.)

**Chen Laiyi, Song Yundi, Li Yue, Jiang Lei, Wang Yi, Wang Song and Hou Wei†**
College of Environment, Liaoning University, Shenyang, 110036, China
†Corresponding author: Hou Wei; houwsd@163.com

**Nat. Env. & Poll. Tech.**
**Website: www.neptjournal.com**

*Received:* 17-05-2022
*Revised:* 04-07-2022
*Accepted:* 08-07-2022

**Key Words:**
CN-1
CN-75
Stress
*Poa annua* L.
Physiological indexes
Biochemical indexes

## ABSTRACT

This paper takes *Poa annua* L. as the research object and studies the law of physiological and ecological stress of 1-Chloronaphthalene (CN-1) and Octachloronaphthalene (CN-75) by using various physiological and biochemical indexes of *Poa annua* L. cultivated with soil under the stress of CN-1 and CN-75 of different concentrations. According to the research, the chlorophyll *a* and *b* first increase and then decrease with the increase of the concentration of CN-1, and continue to decrease with the increase of CN-75; Soluble sugar and soluble protein in plants decrease first and then increase with the increase of CN-1, and continue to decrease with the increase of CN-75; MDA in plants increases first and then decreases with the increase of the concentration of CN-1 and CN-75. The proline content in plants also increases first and then decreases with the increase of concentration of CN-1 and CN-75. Based on the research, it can be seen that the tolerance of the plant to CN-75 is not good as to CN-1.

## INTRODUCTION

PCNs are kinds of persistent organic pollutant with physical and chemical properties similar to dioxin organic matter (Liu et al. 2013) and are featured by semi-volatility, higher concentration in the air, remote transmission, relative good heat resistance, insulation, and thermal insulation properties. It cannot be oxidized and decomposed under natural conditions easily and will have persistent influences on the environment. It has low solubility in water, but the lipophilicity is better than that of the general organic matter. Industrial production generates most of the total amount of PCNs, and processes such as household waste treatment, chemicals, metal smelting, and electronics production will produce many PCNs (Hu et al. 2012).

PCNs in the environment can't be degraded easily, and are certainly enriched and bio-accumulated in organisms. People have detected PCNs in the atmosphere, water, soil and organisms, and PCNs have been a global environmental pollutant. Although PCNs are similar to other polychlorostyrene bicyclic hydrogen compounds (such as polychlorinated dibenzo-p-dioxins, polychlorinated dibenzofurans, and polychlorinated biphenyls) in structure and properties, PCNs have not been studied so deeply as those pollutants (Shi et al. 2014). PCNs and PCBs are certainly harmful to human, animal and plant health, and PCNs are more hazardous than PCBs (Park et al. 2010).

### Plant Stress

Plants can absorb volatile organic compounds (VOCs) from the soil in high concentrations. Plant roots can not only absorb PCNs in water and soil solutions but also transfer some compounds to the above-ground parts, affecting the growth of plants.

The environment harmful to plants is called adversity, also called stress. The reveal of plant adaptability or physiological mechanism under the stress of PCNs by studying the physiological response of plants to PCNs stress can help to study the effects and stress mechanism of PCNs on organisms, and enhance the stress resistance of organisms to PCNs or protect organisms from harm, creating favorable conditions for the growth of organisms (Ma et al. 2009). At present, there are few comprehensive and systematical studies on the effects of PCNs to plant physiology and biochemistry, and on physiological and biochemical indexes with outstanding responses to plant stress (Xu & Wang 2006).

### Research Status at Home and Abroad

There is less data on PCNs concentration in the atmosphere throughout the country. At current, most of the literature in China only studies the distribution, pollution sources and degradation of PCNs, and there are few studies on its absorption, accumulation, movement, and transformation in environmental media.

Different species of plants respond differently to naphthalene. For example, Liu et al. (2002) found that naphthalene with different concentrations (1.2-1.6 mg.$L^{-1}$) significantly reduced the respiration intensity and chlorophyll content of five plants, showing a negative relation with naphthalene content; In terms of the peroxidase (POX) activity, water hyacinth and groundnut were positively correlated with the concentration of naphthalene, while duckweed, purple duckweed, and fine leaf *Polygonum chinensis* showed a trend of first increasing and then decreasing with the concentration of naphthalene increasing. Du et al. (2006) studied the effects of 1,2,4-trichlorobenzene on rice seed germination and seedling growth and found that the plant height and root length of rice seedlings were inhibited, and showed a certain concentration-effect and time-effect relationship. Yufang et al. (2002) found that 1,2,4-trichlorobenzene can significantly inhibit root elongation of three higher plants of wheat, cabbage and tomato. In general, bioconcentration is enhanced with the increase of the number of chlorine atoms.

## MATERIALS AND METHODS

### Selection of *Poa annua* L.

Belonging to Gramineae, *Poa annua* L. is mainly distributed in temperate and cold regions and is rare in the tropics. China has about 100 species, mainly distributed in northern China, and they are the important components of grassland and meadow vegetation. With features such as good palatability, strong regeneration ability, rich nutrition, long green period, and good trampling resistance, it is a forage resource with great development and utilization prospects in northern China; At the same time, as the excellent cool-season lawn plant, it is widely used in various lawn establishment and is a valuable plant germplasm resource (Xie 2001).

The *Poa annua* L. is taken as the research object to treat leaves with CN-1 and CN-75 at different concentrations and to study the content changes of photosynthetic pigments, soluble sugars, soluble proteins, MDA, and proline of plants under the stress of PCNs.

In the experiment, the spectrophotometer is used to measure the absorbance at different wavelengths, and to calculate the content indirectly, and the comparison of the content of the above matters in a certain amount of organisms under normal conditions and adversity stress can help to understand changes in physiological and biochemical indexes of *Poa annua* L.

### Planting of *Poa annua* L.

*Poa annua* L. is cultivated in brown soil. According to the plastic flowerpot's specification, the length of the basin is 20 cm, and the depth of the basin is 15 cm. Put soils of the same amount in flowerpots, and split water over them after soil compaction. Select full *Poa annua* L. seeds of the same size, and sow 250 seeds per pot. Cover the surface with fine sand, and place them on an indoor windowsill. Water them regularly after seed germination. Perform a stress simulation experiment when the *Poa annua* L. seedlings' length grows to more than 10 cm.

Select the leaves with similar size and the same growth status, then spray with a spray pot containing different concentrations of PCNs 1, 3 and 5 days before the experiments to make bluegrass grow under the stress of PCNs. The control of CN-1 is ethanol mixed with water, while the blank control of CN-75 is hypochloronaphthalene mixed with water. The concentration of the experimental group solution is CN-1 and CN-75 (10 mg.$L^{-1}$, 20 mg.$L^{-1}$, 50 mg.$L^{-1}$, 100 mg.$L^{-1}$, 200 mg.$L^{-1}$), CN-75 (10 mg.$L^{-1}$, 20 mg.$L^{-1}$, 50 mg.$L^{-1}$, 100 mg.$L^{-1}$, 200 mg.$L^{-1}$). Three parallel repeated samples are set for each treatment group and control group for the planting. Use quantitative leaves cut into pieces for pretreatment measurement and analysis.

### Measurement Methods of Each Index

The photosynthetic pigments are measured by the spectrophotometric method, and the content of photosynthetic pigments can be calculated based on the absorption of visible light at a specific wavelength. This method can measure out the contents of chlorophyll a, chlorophyll b, and carotenoids without separation; The soluble sugars are measured by the anthrone mensuration, and under the action of concentrated sulfuric acid, sugars can be dehydrated to form furfural or methyl furfural which then can be reacted with anthrone to form blue-green furfural derivates. Within a certain range, the intensity of the color is directly proportional to the sugar content, which can be used for the quantitative determination of sugars. The soluble proteins are measured by the coomassie brilliant blue G-250 method which uses the principle of protein-dye combination to quantitatively determine the concentration of microproteins. The MDA is measured with the stable red product after heating the proline and ninhydrin reagent under acidic conditions, and its content is positively correlated with the color depth. There is a maximum absorption peak at 515 nm, which can be measured with a spectrophotometer.

### Analysis Method

Each treatment is repeated 3 times. SPSS19.0 statistical software is used for statistical analysis of experimental data,

and the figures were finished with Origin software 8.0. The statistical software is used to conduct "one-way ANOVA" of the mean of each data, and complete the difference analysis among numeric values; $p < 0.05$ indicates a significant difference; $p < 0.01$ indicates an extreme difference. Different lowercase letters in the figure indicate the significant difference between the values, and the same letters indicate no significant difference between them.

## RESULTS

### Photosynthetic Pigments Content

Photosynthetic pigments include chlorophyll a, chlorophyll b, carotenoids and lutein. The change of photosynthetic pigment content in plants with the change of PCNs concentration is shown in Figs. 1-4. Different lowercase letters indicate the significant difference among different concentrations, and the same letters indicate no significant difference between them.

As shown in the figures, the content of chlorophyll *a*, chlorophyll *b*, and carotenoids in *Poa annua* L. increase correspondingly with the increase of the concentration of CN-1 while the concentration of CN-1 is lower than 50 $mg.L^{-1}$. When the concentration of CN-1 is 50 $mg.L^{-1}$, the content of chlorophyll a and b in *Poa annua* L. reach the maximum, increasing by 123.7% and 129.8% respectively compared with the control. When reaching the peak, the content of chlorophyll in plants decreases with the increase of the concentration of CN-1.

The content of chlorophyll a and b decreases with the increase of the concentration of CN-75. With the increase of the concentration of CN-75, the content of carotenoids decreases first and then increases, reaching the minimum when the concentration of CN-75 is 20 $mg.L^{-1}$.

### Soluble Sugars Content

The content of soluble reducing sugars in *Poa annua* L. under the stress of different concentrations is studied, and changes of soluble reducing sugars in plants with changes in PCNs concentration are shown in Fig. 5. There is no significant difference ($P > 0.05$) between the two groups with CN-1 of 0 $mg.L^{-1}$ and CN-1 of 200 $mg.L^{-1}$, CN-1 of 20 $mg.L^{-1}$ and

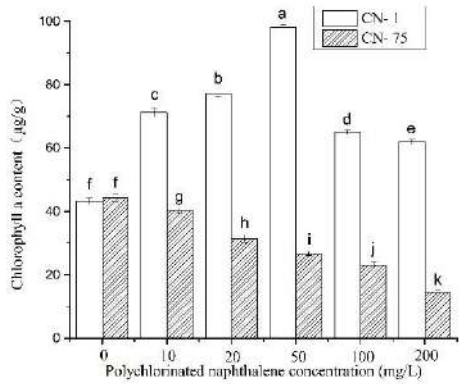


Fig. 1: Chlorophyll a content with changes in PCNs concentration.

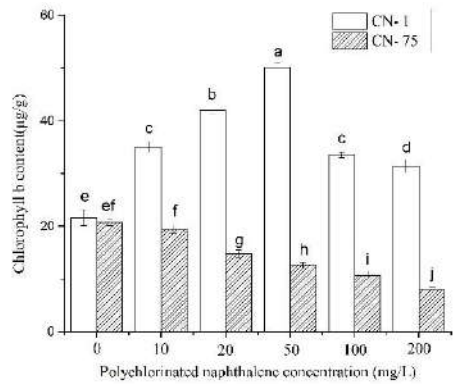


Fig. 2: Chlorophyll b content with changes.

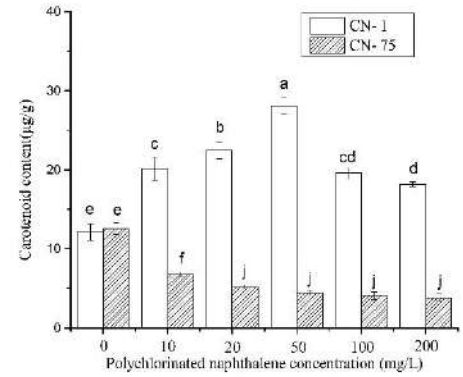


Fig. 3: Carotenoids content with changes in PCNs concentration.

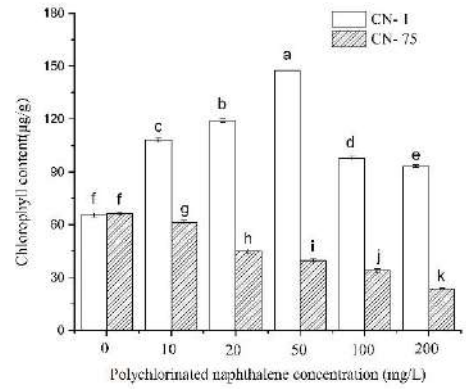


Fig. 4: Total chlorophyll content with changes.

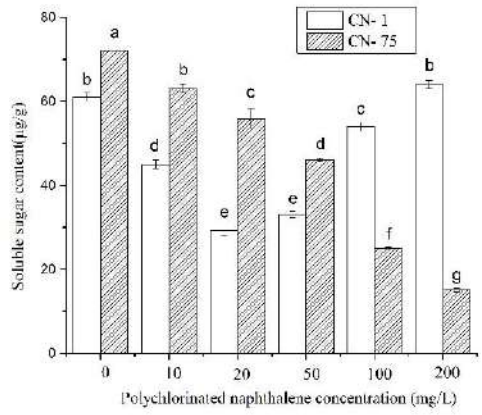


Fig. 5: Soluble sugar content with changes in PCNs concentration.

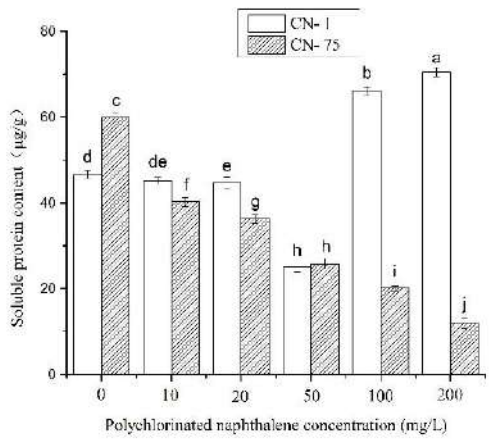


Fig. 6: Soluble protein content with changes.

CN-1 of 50 mg.L$^{-1}$, CN-1 of 0 mg.L$^{-1}$ and CN-75 of 10 mg.L$^{-1}$, CN-1 of 10 mg.L$^{-1}$ and CN-75 of 50 mg.L$^{-1}$, CN-1 of 100 mg.L$^{-1}$ and CN-75 of 20 mg.L$^{-1}$, and there are significant differences in the soluble sugar content corresponding to concentrations of other indexes.

The content of soluble sugars in *Poa annua* L. decreases first and then increases with the concentration of CN-1 increasing. When the concentration is 20 mg.L$^{-1}$, the content of soluble sugars in *Poa annua* L. reaches the minimum, decreasing by 51.2% compared with the control group. Then, the content of soluble sugars in plants increases with the increase of concentration of CN-1. When the concentration of CN-1 is 200 mg.L$^{-1}$, the content of soluble sugars in plants is 6.1% higher than that in the control group.

The content of soluble sugars in *Poa annua* L decreases with the continuous increase of the concentration of CN-75. Compared with the concentration of the previous group, when the concentration of CN-75 increases accordingly, the contents of soluble sugars decrease by 12.5%, 5.3%, 24%, 44.5%, and 38.1%.

## Soluble Proteins Content

The changes of soluble proteins in plants with changes in PCNs concentration are shown in Fig. 6. According to the variance analysis by SPSS software, there is no significant difference ($P > 0.05$) between the two groups with CN-1 of 10 mg.L$^{-1}$ and CN-75 of 0 mg.L$^{-1}$, and there are significant differences in the soluble protein content corresponding to concentrations of other indexes.

The content of soluble proteins in plants decreases first with the increase in the concentration of CN-1. When the concentration of it reaches a certain level, the content of soluble proteins in plants increases accordingly. When the concentration of it reaches 50 mg.L$^{-1}$, the content of soluble proteins in *Poa annua* L. reaches the minimum, decreasing by 46% compared with the control group. When the concentration of it reaches 200 mg.L$^{-1}$, the content of soluble proteins reaches the maximum, increasing by 50% compared with the control group.

The content of soluble proteins decreases with the continuous increase of the concentration of CN-75 d. When the concentration of CN-75 increases accordingly, the contents of soluble proteins decrease by 32.8%, 12.3%, 26.7%, 22.0%, and 40.8%, compared with the concentration of the previous group.

## MDA Content

The changes in the content of MDA in plants with changes in PCNs concentration are shown in Fig. 7. The content of MDA in plants increases then decreases with the increase of concentration of CN-1. When its concentration reaches a certain level, the content of MDA in plants reaches the maximum. When its concentration is 50 mg.L$^{-1}$, the content of MDA in *Poa annua* L. reaches the maximum, increasing by 289.8 % compared with the blank control group. With a continuous increase of concentration of CN-1, the content of soluble proteins decreases, but still increases compared with the blank control group.

In a normal growth environment, the content of MDA in *Poa annua* L. is only 0.03 μmol.g$^{-1}$. When the concentrations of CN-75 are 10 mg.L$^{-1}$ and 20 mg.L$^{-1}$, the contents of MDA are 0.05 μmol.g$^{-1}$ and 0.10 μmol.g$^{-1}$, respectively, showing a slight increase compared with those under normal growth conditions; When the concentration of CN-75 is 100 mg.L$^{-1}$, the content of MDA increases sharply to 0.40 μmol.g$^{-1}$. Then with a further increase in its concentration, the content of MDA decreases sharply.

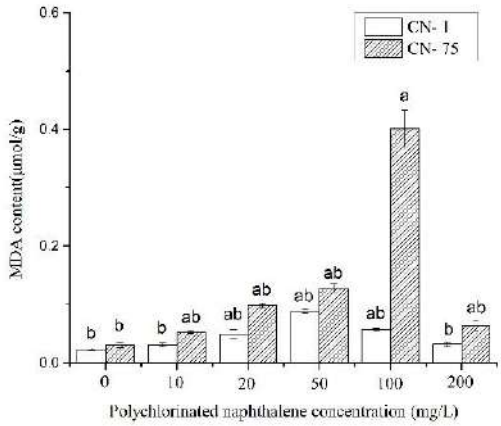


Fig. 7: MDA content with changes in PCNs concentration.

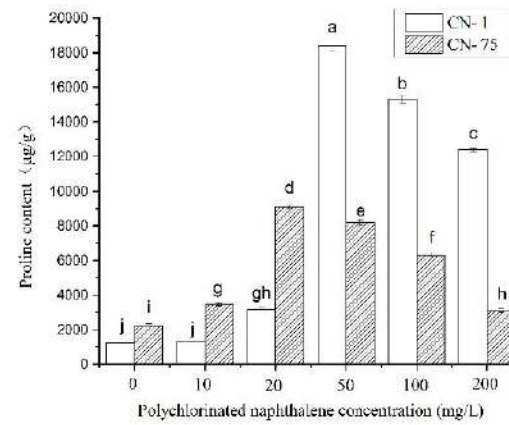


Fig. 8: Proline content with changes.

### Proline Content

The changes in the content of proline in plants with changes in PCNs concentration are shown in Fig. 8. Among them, there is no significant difference ($P > 0.05$) among the CN-1 of 0 mg.L$^{-1}$ and CN-1 of 10 mg.L$^{-1}$, and there are significant differences in proline content corresponding to concentrations of other indexes.

With the increase of the concentration of CN-1, the proline content in *Poa annua* L. leaves increases first and then decreases. When its content is 50 mg.L$^{-1}$, the proline content increases 22 times compared with the control group. At this time, the proline content in plants reaches the maximum, and the cell structure might have changed to work abnormally. When its content is 200 mg.L$^{-1}$, the corresponding proline content increases by nearly 10 times compared with the control group.

With the increase of the concentration of CN-75, the proline content in *Poa annua* L. leaves increases first and then decreases. When the concentration of CN-75 is 20 mg.L$^{-1}$, the proline content increases sharply compared with that under low concentration stress. After CN-75 content reaches 50 mg.L$^{-1}$, the proline content decreases.

## DISCUSSION

(1) With the increase of the concentration of CN-1, the content of chlorophyll in *Poa annua* L. plants increases correspondingly. When it reaches the growth peak, the content of chlorophyll in plants will decrease with the increase of the concentration of CN-1. The above shows that CN-1 can be taken as the nutrient for the growth of *Poa annua* L. but the increased concentration is harmful to *Poa annua* L., affecting its photosynthesis. The results of this experiment showed that the content of chlorophyll a and b in *Poa annua* L. leaves increased first and then decreased with the increase of the concentration of CN-1, which is consistent with the research of Li et al. (2018) that salt stress causes the increase in the chlorophyll content in spathiphyllum with the increase of alt stress concentration.

With the increase of the concentration of CN-75, the chlorophyll in *Poa annua* L. leaves is degraded and the content decreased in case the leaves are severely damaged. While the carotenoid content starts to increase and leaves become withered and yellow. This trend is consistent with the results of the effects of naphthalene stress on the mangrove plant, *Kandelia candel*, studied by Lu et al. (2008). The PAHs concentration reaching a certain level will harm the plants and decrease the contents of chlorophyll *a*, chlorophyll *b* and total chlorophyll in plant leaves.

(2) With the increase of the concentration of CN-1, the normal metabolic activities of the cells in the plant are disturbed, causing weakened stress resistance of the cells, and decreased soluble sugar content in the plant. The concentration value of CN-1 increasing to a certain degree may stimulate plant cells badly and cause cell mutation, thus increasing the soluble sugar content in the plant.

With the continuous increase of concentration of CN-75, the soluble sugar content in *Poa annua* L. gradually decreases, indicating that the sugar in *Poa annua* L. decreases under the effect of CN-75. At the early stage of stress, due to water deficit in the plant, the amylolysis of leaves is enhanced and photosynthetic product output is slowed, causing sugar accumulation; with further strengthening of stress, water deficit is exacerbated, and the chloroplast thylakoid structure is destroyed.

At the same time, stoma opening and closing, and the photosynthetic rate of leaves are inhibited, which makes photosynthesis weakened and photosynthetic products reduced. Thus, the accumulation of soluble sugars in the leaves tends to slow down or stop. This is consistent with changes in soluble sugar and soluble protein in maize leaves under Pb (lead) stress studied by Zheng et al. (2006).

(3) With the increase of the concentration of CN-1, the content of soluble proteins in plants decreases first and then increases. Other studies have shown that the content of soluble proteins in plants growing under stress conditions will changes certainly, and based on this, the corresponding structural functions of plant cells will change, thus further influencing the regulation of plant cells (Wei 2010). Jiao et al. (2019) studied the oil-contaminated reed seedlings and found that the content of soluble proteins in the reed seedlings did not increase but was lower than that of the control group, which was consistent with the experimental study of the effect of CN-1 with a low concentration on *Poa annua* L. but was opposite to the effect of CN-1 with a high concentration on *Poa annua* L.

With the increase of concentration of CN-75, the content of soluble proteins decreases. Strong pollution stress will destroy the cell's biofilm severely and will have irreversible effects on the growth of plants. Excessive stress will inhibit the normal growth of the plant. Restrictions on plant growth and death cause a reduction in the content of the matter. The results are consistent with the changes of soluble sugars and soluble proteins in maize leaves under Pb (lead) stress studied by Zheng et al. (2006).

(4) With the increase of the concentration of CN-1, the content of MDA in plants first increases and then decreases. Chen et al. (2013) studied that the MDA content in *Bidens pilosa* leaves, under the stress of heavy metal Cd, increases first and then decreases with the increase of Cd stress concentration, which is consistent with this paper.

The MDA content in *Poa annua* L. increases first with the increase of concentration of CN-75. It increases sharply and then decreases with the concentration of CN-75 reaching 50 $mg.L^{-1}$. This indicates that CN-75 with low concentration will certainly damage the cell membrane of *Poa annua* L. but will not affect all life activities of the cells. The plant itself has resistance and repair functions to stress. In case the concentration of CN-75 is too high and the stress is huge, the cell membrane in the plant will be damaged to a large extent causing function failure of the membrane, and finally, the plant may die. This can be evidenced by the death of *Poa annua* L. in this experiment.

(5) The proline content in *Poa annua* L. leaves increases first and then decreases with the increase of concentration of CN-1. In the beginning, proline content in plants continues to increase. The higher the concentration of CN-1, the higher the proline content in plants. When the CN-1 content is 50 $mg.L^{-1}$, the proline content increases 22 times compared with that of the control group. At this time, the cell structure of the plant may have changed to work abnormally. CN-1 is harmful to the normal growth of *Poa annua* L., so to alleviate the toxic effects of CN-1, the plant will produce a large amount of proline so as to enhance the adjustment inside and outside the cell membrane. Therefore, CN-1 has strong toxic effects on the growth of plants. The changing trend of proline content in this experiment is the same as the changing trend of proline content in spathiphyllum leaves under salt stress studied by the scholar, Li et al (2018).

The proline content in *Poa annua* L. leaves increases first and then decreases with the increase of concentration of CN-75, which is consistent with the results of the effects of NaCl stress on the growth of mulberry seedlings studied by Dong et al. (2017). When the concentration of CN-75 is 20 $mg.L^{-1}$, the proline content increases sharply compared with that under the stress of low concentration, which shows that the cell structure and function of *Poa annua* L. are severely damaged under the stress of high concentration. The proline content decreases when the concentration of CN-75 reaches 50 $mg.L^{-1}$, which is related to the death of *Poa annua* L. under the stress of CN-75 of 50 $mg.L^{-1}$.

## CONCLUSIONS

In conclusion, chlorophyll *a* and *b* in plants increase first and then decrease with the increase of CN-1. But the stress of CN-75 on plants is stronger, and the chlorophyll a and b in plants continue to decrease with the increase of CN-75. The carotenoid content in plants increases first and then decreases with the increase of concentration of CN-1, and it decreases first and then increases with the increase of concentration of CN-75. Soluble sugar and soluble protein in plants decrease first and then increase with the increase of concentration of CN-1, and continue to decrease with the increase of concentration of CN-75. This may be because CN-75 is more toxic to plants making cells lose water rapidly, and the biofilm is damaged, which is irreversible to organisms; the MDA content in plants increases first and then decreases with the increase of concentration of CN-1. When the content

of it reaches 50 mg.$L^{-1}$, the MDA content in plants reaches the maximum. The MDA content in plants increases first and then decreases with the increase of concentration of CN-75. But when its content reaches 50 mg.$L^{-1}$, the MDA content increases sharply. This may be because CN-75 of low concentration damages the cell membrane certainly, but the plant has the resistance and repair functions to stress. Too high CN-75 concentration will damage the cell membrane badly, and cause membrane function failures, finally causing the death of plants. The proline content in plants increases first and then decreases with the increase of concentration of CN-1 and CN-75. The difference is that CN-1 reaches its maximum at 50 mg.$L^{-1}$, while CN-75 starts decreasing when reaching its maximum at 20 mg.$L^{-1}$. Based on the above, it can be seen that the tolerance of plants to CN-75 is not good as to CN-1.

## ACKNOWLEDGEMENTS

This research has been financed by the National Natural Science Foundation of China (31600311) and (31972522), the National Key Research and Development Project of China (2018YFC1801200), Major Science and Technology Project of Liaoning Province (2019JH1/10300001).

## REFERENCES

Chen, J. 2013. Study on the response and remediation potential of *Bidens Pilosa* L. to Cd and Pb stress. Chongqing, Southwest University.

Dong, Y., Sun, J., Zhao, D., Du, J., Wang, Z. and Chen, C. 2017. Effects of NaC1 stress on seed germination and seedling growth of two mulberry species. Northern Sericulture, 38(02): 16-19.

Du, Q., Jia, X. and Yuan, B. 2006. Toxic effects of 1, 2, 4-trichlorobenzene on rice seed germination and seedling growth. The Journal of Applied Ecology, 17(11): 2185-2188.

Hu, J., Zheng, M., Liu, W., Li, C., Nie, Z., Liu, G., Zhang, B., Xiao, K. and Gao, L. 2013. Characterization of polychlorinated naphthalenes in stack gas emissions from waste incinerators. Environmental Science and Pollution Research, 20(5): 2905-2911.

Jiao, D., Cao, R., Jiang, Q. and Yan, Q. 2019. Effects of oil pollution on growth and physiological characteristics of *Phragmites australis* seedlings. Jiangsu Agricultural Sciences, 47(07): 239-242.

Li, L., Zhang, H., Ye, J., Hao, L., Zhang, Y. and Zheng, Y. 2018. Effects of salt stress on physiological parameters and chlorophyll content of *Cynostoma sativa*. Northern Horticulture, (15): 103-108.

Liu, J., Lin, F. and Wang, Y. 2002. Study on the ability of aquatic plants to purify naphthalene wastewater. Shanghai Environmental Science, 21(07): 412-415.

Liu, Y., Liu, G., Zheng, M. and Gao, L. 2013. Research on the origin and environmental pollution characteristics of polychloronaphthalenes. Science in China: Chemistry, 43(03): 279-290.

Lu, Z., Zheng, W. and Ma, L. 2008. Effects of naphthalene and pyrene stress on membrane permeability and antioxidant enzyme activity of mangrove eggplant seedlings. Journal of Xiamen University Natural Science, 5: 757-760.

Ma, L., Sheng, L., He, C. and Fan, J. 2009. Effect of naphthalene on growth and physiology of Oryza sativa cv. Matsumae and the residues of Nap. Journal of Agro-Environment Science, 28(10): 1997-2004.

Park, H., Kang, J.H., Baek, S.Y. and Chang, Y.S., 2010. Relative importance of polychlorinated naphthalenes compared to dioxins, and polychlorinated biphenyls in human serum from Korea: contribution to TEQs and potential sources. Environmental Pollution, 158(5): 1420-1427.

Shi, L. 2014. Photoconversion of 2-Chloronaphthalene in Water and Soil. Jilin University.

Wei, X. 2010. Effects of heavy metal lead stress on wheat seed germination and seedling physiological and biochemical characteristics. Northwest Normal University, Gansu.

Xie, K. 2001. Genetic diversity and phylogeny of 10 wild Poa plants. Gansu Agricultural University, Gansu.

Xu, H. and Wang, X. 2006. Stress on Plant Growth and Development and Its Research Methods. Proceedings of the seventh Youth Symposium of the Chinese Society of Horticulture. China Agriculture Publishers Inc., pp. 901-907.

Yufang, S., Qixing, Z., Huaxia, X., Liping, R., Xueying, S. and Ping, G. 2002. Eco-toxicological effects of phenanthrene, pyrene and 1, 2, 4-trichlorobenzene in soils on the inhibition of root elongation of higher plants. Acta Ecologica Sinica, 22(11): 1945-1950.

Nature Environment and Pollution Technology
An International Quarterly Scientific Journal

p-ISSN: 0972-6268
(Print copies up to 2016)
e-ISSN: 2395-3454

Vol. 22 | No. 1 | pp. 293-301 | 2023

Review Research Paper

https://doi.org/10.46488/NEPT.2023.v22i01.029

Open Access Journal

# The Influence of Geographical Factors on Polyploidy in Angiosperms with Cartographic Evidence from the Northwestern Himalayas: A Review

**Anupreet Singh Tiwana*, Siva PrathapThummalakunta**, Saurabh Gupta***, Vijay Singh**** and Ramesh Chand Kataria*****†**

*Department of Geography, Mata Gujri College (Autonomous), Fatehgarh Sahib-140406, Punjab, India
**Department of Earth Science, YogiVemana University, Kadapa-516005, Andhra Pradesh, India
***Department of Microbiology, Mata Gujri College (Autonomous), Fatehgarh Sahib-140406, Punjab, India
****Department of Botany, Mata Gujri College (Autonomous), Fatehgarh Sahib-140406, Punjab, India
*****Department of Zoology, Govt. Degree College, Bassa-175029, Dist. Mandi, Himachal Pradesh, India
†Corresponding author: Ramesh Chand Kataria; professorkataria@gmail.com

**Nat. Env. & Poll. Tech.**
**Website: www.neptjournal.com**

*Received: 31-01-2022*
*Revised: 30-04-2022*
*Accepted: 02-05-2022*

**Key Words:**
Polyploidy
Geographical factors
Spatial distribution
Habitat correlation

## ABSTRACT

The review paper comprised the impact of geographical and environmental factors on polyploidy and vice versa. The review covers different effects of geographical factors, like spatial isolation, altitude, and local climate on polyploidy, and the behavior of polyploid(s) in abiotic factors, such as temperature and light with a few examples of northwest Himalayas. The paper concludes that polyploid plants behave differently in environmental conditions, as polyploids are more prominent in higher altitudes, colder environments, and nutrient-rich soil than diploid progenitors, but have a mixed distribution in different geographical conditions. Further, polyploidy is more common among perennials than annuals, while niche differentiation depends more on the local environment. The virtual case study results from North and North Western India have been shown with the help of ArcGIS online software. The scrutiny of spatial distribution on maps highlights the fact that polyploidy is still a complex research puzzle with interesting perspectives.

## INTRODUCTION

Polyploidy or whole genome duplication (WGD), a naturally occurring phenomenon in plants (rare in animals), involves more than two whole sets of chromosomes and is considered a key determinant in studying plant evolution. This inducible phenomenon results in multiple gene copies, which led to genome plasticity and adaption by the neo-fictionalization of genes (Cheng et al. 2018). Polyploidy can arise naturally in many ways, either by chromosome doubling in meristematic cells during mitosis or by the fusion of unreduced gametes in meiosis (Lewis 1980, Levin 2002, Ramsey & Ramsey 2014). In nature, polyploids are of three types: autopolyploids, allopolyploids, and segmental allopolyploids (Stebbins 1947). The effect of chromosomal duplications on phenotypes has attracted the attention of researchers since the beginning of the 20$^{th}$ century (Stebbins 1947) and is well known as the "gigas effect," i.e., enlargement of cellular size in both flora and fauna (Stebbins 1971, Knight & Beaulieu 2008). It is evident in plants that polyploidy modifies physiological features like transpiration, photosynthesis, and growth rates (Otto & Whitton 2000, Levin 2003, Maherali et al. 2009, Pacey et al. 2020, Van De Peer et al. 2021), which further improves its ecological tolerance (Levin 2002). Polyploids also have increased reproductive efficiency, are known to have more flowers per inflorescence, and reduce the barrier of self-incompatibility (Robertson et al. 2010). The polyploids are often thought to be ecologically better adapted and show gigas effect over diploid progenitors (Stebbins 1971). Such effects might be a result of increasing genome size (DNA), which relatively increases the level of gene and protein expression, and also increases the cell size, reduces cell division, and delays the onset of flowering and reproductive growth (Stebbins 1971). Hence, the insight of all the above characters and the molecular studies of over a decade show that polyploids are better adapted than their diploid ancestors (Otto & Whitton 2000, Comai 2005), and may help in species diversification in the harsh ecological environment (Otto 2007), where polyploid species evolve much faster or in a different direction compared to the diploids (Otto &Whitton 2000). The current review emphasizes the impact of abiotic factors, such as soil, temperature, light, and other geographical factors on polyploidy. The detailed review has been presented for the entire globe with special

reference to the studies conducted by different scholars in northwest India (Table 1).

## INCIDENCE OF GEOGRAPHICAL FACTORS OF POLYPLOIDY

### Geographical Isolation

The spatial distribution of sexual asexual taxa is termed "Geographical parthenogenesis". Later on, many authors discussed the broader geographical distribution of asexual(s). It is a belief that polyploidy enhances the adaptability of apomictic plants in higher elevations (Bierzychudek 1985) or extreme range of niches (Vrijenhoek 1984), but, very little is known about the vegetative performance and reproductive fitness of plants in severe alpine conditions (Ladinig et al. 2013). Parapatric distribution of the *Centaurea phrygia* (2x and 4x) was reported in Central Europe (Koutecký 2012), and of these, diploids are prominently distributed all over Central and North Europe, while tetraploids are confined to Western Carpathians. Similar observations were also observed in the *Centaurea* sect. Jacea, where a diploid/tetraploid paring, leads to a low incidence of triploid(s) in both natural/experimental populations (Hardy et al. 2000, 2001, Koutecký et al. 2011). Triploids have reported being sterile or nearly so, in the population of the *Centaurea* sect. Jacea (Hardy et al. 2000, 2001). The distribution of cytotypes (parapatric) depends upon two mechanisms: minority cytotype exclusions or habitat differentiation (Hardy et al. 2000). The study on habitat requirement in cytotype(s) has been documented in both natural and laboratory conditions (Van Dijk et al. 1992). However, the distribution of polyploidy is not directly related to geographical isolation, as there are few reports of sympatric speciation, viz. *Aster thomosonii* and *Elsholtzia cilliata* (Fig. 1, Table 1).

### Altitude Variation

It is believed that polyploidy predominance increases with an increase in altitude and are adapted more to cold temperature than diploid ancestor (Hagerup1932). Löve and Löve (1957) observed similar results in the higher altitudes of Eurasia and Arctic regions, where 85.9 percent polyploids were recorded compared to lower altitude flora (37%), and a similar view was supported by many scholars (de Wet 1980, Soltis & Soltis 1999, Brochmann et al. 2004). However, the theory of better resilience of polyploids was firmly rejected by many scholars (Bowden 1940, Gustafsson 1948). It is generally

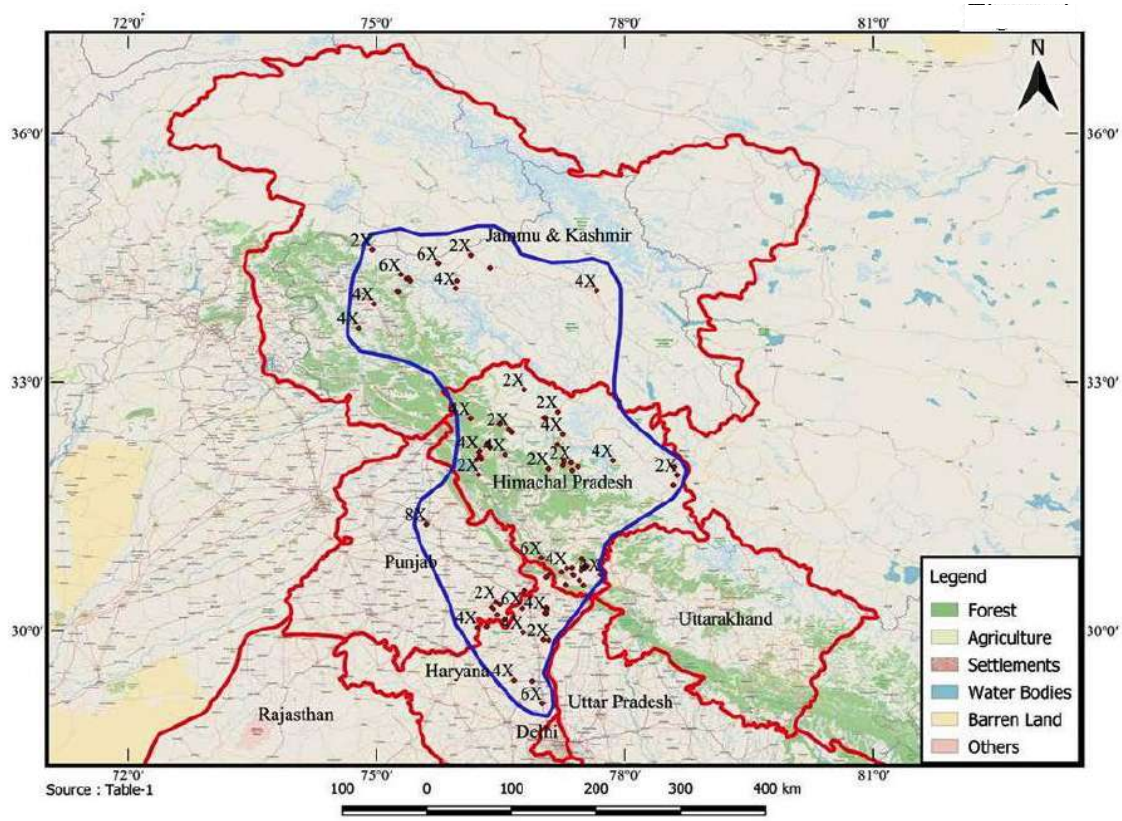


Fig. 1: Incidence of polyploidy and land use pattern in North and North Western India.

Table 1: List of Intraspecific cytotypes reported in Northwest Himalayas.

| S. No. | Name of Taxon | Diploids | | Polyploids | | | | References |
|---|---|---|---|---|---|---|---|---|
| | | 2x | 3x | 4x | 6x | 8x | | |
| 1. | *Agrimonia eupatoria* L. (x=7) | Dharmshala, (H.P) (PID: 102001) Kangra, (H.P) (PID: 102002) Timbi, Sirmaur (PID: 102003) | | Palampur (H.P.) (PID: 104002) Kangra (H.P.) (PID: 104003) ChurDhar, Simraur (PID: 104004) Aharbal, Kashmir (PID: 104006) | Sonmarg; Kashmir (PID: 106001) | | | Kumar et al. (2011a) |
| 2. | *Ajuga parviflora* Benth. (x=16) | Sangrah, Sirmaur (PID:102005 ) | | Haripurdhar, Sirmaur (PID: 104021) | | | | Singh et al. (2018b) |
| 3. | *Alchemilla vulgaris* L. (x=17) | Aru, Kashmir (PID: 102004) | | | | | Thajwas, Kashmir (PID: 112001) | Jeelani et al. (2012) |
| 4. | *Argimon emexicana* L. (x=7) | Dehra, Kangra (H.P.) (PID: 102006) | | Kalaamb, Sirmaur(H.P.) (PID: 104022) | | | | Jeelani et al. (2014) |
| 5. | *Artemisia martima* L. (x=9) | Manali (H.P.) (PID: 102007 ) | | | | | | Gupta et al. (2014a) |
| 6. | *Artemisia scoparia*Waldst. ex Kit. (x=9) | Manikaran Sahib (PID: 102008) | | Baru Sahib, Sirmaur (PID: 104007) | | | | Gupta et al. (2014a) |
| 7. | *Aster thomsonii* L. (x=9) | Shilai, Sirmaur (PID: 102009) | | Churdhar, Sirmaur (PID: 104008) | | | | Gupta and Singh 2015 |
| 8. | *Brachyactis pubescens* (DC.) Aitch. & C.B.Clarke (x=9) | Drass, Leh and Ladhakh (PID: 102010) | | Schnag, Leh and Ladhakh (PID: 104009) | | | | Tantray et al. (2018) |
| 9. | *Cenchrusciliaris*L. (x=12) | | | Mullana, Ambala (PID: 204001) | Jabli, Shivaliks | | | Dhaliwal et al. (2018a) |
| 10. | *Cynodon dactylon* (L.) Pers. (x=9) | Barara, Ambala (PID: 202001) | | Pinjaur, Panchkula (PID: 204002) | | | | Dhaliwal et al. (2018b) |
| 11. | *Dicanthium annulatum* (Forssk.) Stapf (x=10) | Indri, Karnal (PID: 202002) | | Lalru, Ambala (PID: 204003) | | | | Gupta et al. (2017b) |
| 12. | *Digitaria ciliaris* (Retz.) Koel. (x=9) | | | Barara, Ambala (PID: 204004) | Mohri, Ambala (PID: 206002) | Mirpur, Rewari (PID: 206002) | | Gupta et al. (2017a) |
| 13. | *Elsholtzia ciliate* Benth. (x=8) | Thajwas, Kashmir (PID: 102011) | | Thajwas, Kashmir (PID: 104010) | | | | Malik et al. (2012) |
| 14. | *Geranium pratense* L. (x=14) | Mulbekh (PID: 102012) | | Drass (PID: 104011) | | | | Khan et al. (2020) |

| S. No. | Name of Taxon | Diploids | | Polyploids | | | References |
|---|---|---|---|---|---|---|---|
| | | 2x | 3x | 4x | 6x | 8x | |
| 15. | *Hemarthria compressa* (L.f.) R. Br (x=) | 18 Sriganganagar (PID: ) | | 36 Indri, Karnal (PID: 204005) | | | Gupta et al. (2017b) |
| 16. | *Hieracium umbellatum* (x=5, 9) | Jispa, Spiti (H.P.), (PID: 102014) | | | Keylong, Lahaul (H.P.), (PID: 106002) | | Gupta et al. (2014b) |
| 17. | *Imperata cylindrica* (L.) P. Beauv. (x=10) | Mullana, Ambala (PID: 202004) | | Morni, Panchkula (PID: 204006) | | | Gupta et al. (2017b) |
| 18. | *Inula grandiflora* (x=8) | Nerang, Kullu (PID: 102013) | | Malana, Kullu (PID: 104012) | | | Himshikha et al. (2017), Gupta et al. (2017a) |
| 19. | *Panicum antidotale* Retz (x=9) | Cheeka, Kithal (PID: 202005) | | Safidon, Jind (PID: 204007) | | | Bir and Sahni (1985) |
| 20. | *Papaver dubium* L. (x=7) | NahanSirmaur (H.P.) (PID: 102015) | | Ratnipora, Pulwama (PID: 104013) | | | Kumar et al. 2013 |
| 21. | *Pennisetum purpureum* (x=7) | | | Khaniara, Kangra (PID: 104014) | Loharari, Kangra (PID: 106003) | | Kaur et al. (2014) |
| 22. | *Physochlain apraealta* (Decne.) Miers. (x=21) | Nako Lake (PID: 102016) | | Panikhar Village (PID: 104015) | | | Singhal et al. (2017) |
| 23. | *Plantago depressa* Willd. (x=6) | Nahan, Sirmaur (PID: 102017) | | Sangrah, Sirmaur (PID: 104016) | Chapdhar, Sirmaur (PID: 106004) | | Gupta et al. (2017c) |
| 24. | *Primula denticulata* Sm. (x=11) | Sanko, Ladhakh (PID: 102018) | | Dundi village,Kullu (PID: 104017) | | | Singhal et al. (2018) |
| 25. | *Ranunculus hirtellus* Royle (x=8) | GauriKund, Chamba (PID: 102019) Manimahesh hills, Chamba (PID: 102019) | | Rohtang Pass, Kullu, (PID: 104018) Keylong, Lahaul-Spiti (PID: 104019) | | | Kumar andSinghal (2011) |
| 26. | *Rorippa palustris* (x=7) | Suru Valley (PID: 102021) | | | Drass Valley (PID: 106005) | | Khan et al. (2019) |
| 27. | *Saccharum bengahlense* (x=10) | Patiala (PID: 202006) | | Patiala (PID: 204008) | Patiala (PID: 206001) | | Bir et al. (1992) |
| 28. | *Saxifraga diversifolia* (x=4, 5) | Thajwas, Kashmir (PID: 102022) | | Barabhnagal, Kangra (PID: 104020) | | | Kumar et al. (2011b) |
| 29. | *Scirpus roylei* (Nees) R.Parker(x=11) | Patiala (PID: 202007) | | | | Jalandhar (PID: 208001) | Dhaliwal et al. (2018b) |
| 30. | *Setaria glauca* (L.) P. Beauv.(x=9) | | | Barara, Ambala, (PID: 204012) | | Lalru, Ambala (PID: 208002) | Gupta et al. (2018) |
| 31. | *Setaria verticillata* (L.) P. Beauv. (x=9) | Mirpur, Rewari (PID: 202011) | | | Ganaur, Sonipat (PID: 206003) | | Bir and Sahni (1985) Gupta et al. (2018b) |

| S. No. | Name of Taxon | Diploids | | Polyploids | | | References |
|---|---|---|---|---|---|---|---|
| | | 2x | 3x | 4x | 6x | 8x | |
| 32. | *Sibbaldia micropetala* (x=7) | Churdhar, Sirmaur (PID: 102023) | | Shilai, Simaur (PID: 104023) | | | Kumar et al. (2012) |
| 33. | *Siegesbeckia orientalis* L. (x=15) | Sangrah, Sirmaur (PID: 102026 ) | | Chapdhar, Sirmaur (PID: 104025) | | | Singh et al. (2018a) |
| 34. | *Silene vulgaris* (Moench) Garcke (x=12) | Udaipur, Lahaul-Spiti (PID: 1020244) Dhancho, Chamba (PID: 102025) | | Malana Village, Kullu (PID: 104024) | | | Gupta et al. (2018a) |
| 35. | *Sium latijugam* C. B. Clarke' (x=12) | Gurez, (PID: 102027) | | Aru, (PID: 104026) | | | Jeelani et al. (2012) |
| 36. | *Spergularia diandra* (Guss.) Heldr. &Sart. (x=9) | Pooh, Kinnaur (PID: 102028) | | Chango, Kinnaur (PID: 104027) | | | Kaur & Singhal (2011) |
| 37. | *Sporobolus diander* (Retz.) P. Beauv.(x=9) | Sanauli, Panipat (PID: 202008) | | KUK, Kurukshetra (PID: 204009) | | | Dhaliwal et al. (2018b) |
| 38. | *Sporobolus helvolus* (Trin.) T. Durand and Schinz. (x=9) | Lalru, Ambala (PID: 202009) | | Ferozpur | | | Dhaliwal et al. (2018b) |
| 39. | *Sporobolus marginatus* Hochst. ex A. Rich (x=9) | Sadhu Vela, Punjab (PID: 202010) | | NIS, Patiala (PID: 204011) | | | Dhaliwal et al. (2018b) |
| 40. | *Strobilanthes alatus* Nees. (x=8) | Haripurdhar, Sirmaur (PID: 102029) | | Chapdhar, Sirmaur (PID: 104028) | | | Singh et al. (2016) |
| 41. | *Taraxa cumofficinale* (x=8) | Jari, Kullu (PID: 102030) | Malana, Kullu (PID: 103001) | Nerang, Kullu (PID: 104029) | | | Gupta et al. (2017a) |
| 42. | *Thalictrum foliolosum* (x=7) | Sali, Kangra, H.P. (PID: 102032) | | ChottaBhangal, Kangra, H.P. (PID: 104030) | Jabli, Shivaliks (PID: 106006) | | Rani et al. (2014) |
| 43. | *Tordyliopsis brunonis* DC. (x=11) | BhaironGhat (PID: 102033) | Manimahesh (PID: 103002) | | | | Kumar et al. (2014) |
| 44. | *Tragopogon dubius* Scop. (x=7) | Keylong, (H.P) (PID: 102034) | | Lossar, Spiti (H.P.) (PID: 104031) | | | Gupta et al. (2014b) |
| 45. | *Urochloa panicoides* (x=8) | Sadhubella, Patiala (PID: 202012) | | Bahadurgarh, Patiala (PID: 204013) | Mohri, Ambala, (PID: 206004) | | Bir et al. (1988) |
| 46. | *Valeriana jatamansi* (x=8) | Salooni, Chamba (PID: 102035) | | Tisa, Chamba (PID: 104001) | | Kullu (PID: 108001) | Rani et al. (2015) |
| 47. | *Verbena officinalis* L (x=7). | Sangrah, Sirmaur (PID: 102036) | | | | Sangrah, Sirmaur (PID: 108002) | Singh (2017) |

*PID- , x-basic chromosome number

believed that plants reproducing asexually frequently grow on higher altitudes and latitudes than their sexual relatives (Bierzychudek 1985, Hörandl et al. 2008) and most of these are polyploids. Fig. 2 indicates that the spatial patterns of polyploidy have no direct relation with altitude in the reviewed sites of the northwestern Himalayas.

**Polyploidy and Temperature**

Cytogeographical studies reveal polyploids replace diploid ancestors along with ecological gradients since polyploids generally prefer drier habitats (Watanabe 1986, Maherali et al. 2009) and extensively exposed habitats (Watanabe 1986, Lumaret et al. 1987). However, Fukuda (1967) reported the opposite of this, where diploid species of *Achlys* are dominant over tetraploids. As an earlier view, polyploidy is higher in plants of cold temperatures (Hieter & Griffith 1999). It is believed that cold stress alters the microtubule formation, which obstructs cytokinesis and ultimately, forms unreduced gametes (Ramsey & Schemske 1998, Bomblies et al. 2015), which is a potent cause of sexual polyploidization (De Storme et al. 2012). This view is experimentally supported by Otto and Whitton (2000) that the frequency of unreduced gametes can be increased with cold temperature treatments. However, in northern latitudes, the high ploidy level in the species is due to the dominant perennial life forms and is not related to the lower temperature adaptability (Soltis et al. 2004). The more frequency of polyploids at high altitudes, the more ecological adaptation and efficiency than diploid ancestors (Vamosi & Dickinson 2006). It is evident that in higher altitudinal ranges, most plant species adapt to perennial life forms, and annuals are mostly dominant in lower altitudes. In the end, the perennial polyploids are more adaptive to a colder temperature than diploid progenitor and annuals cohorts, which has been also observed in the northwest Himalayas.

**Polyploidy and Habit Correlations**

According to de Wet (1980), the origin and ecological adaptation of polyploids depend upon habit, habitat, and breeding system, which makes the relationship between polyploidy and habit more critical. Polyploidy usually occurs in perennial herbs than annuals and woody species (Stebbins 1950, 1971). Perennial life form, despite lack of immediate fitness, provides a better chance for autopolyploids and allopolyploids to conquer the sterility problems that arise due to chromosome pairing and interaction between new cytoplasmic genomes (Hilu 1993). Generally, polyploids have the advantage of additional alleles that increase biochemical and genic flexibility, and heterozygosity, which provides a broader range of habitat adaptability in harsh

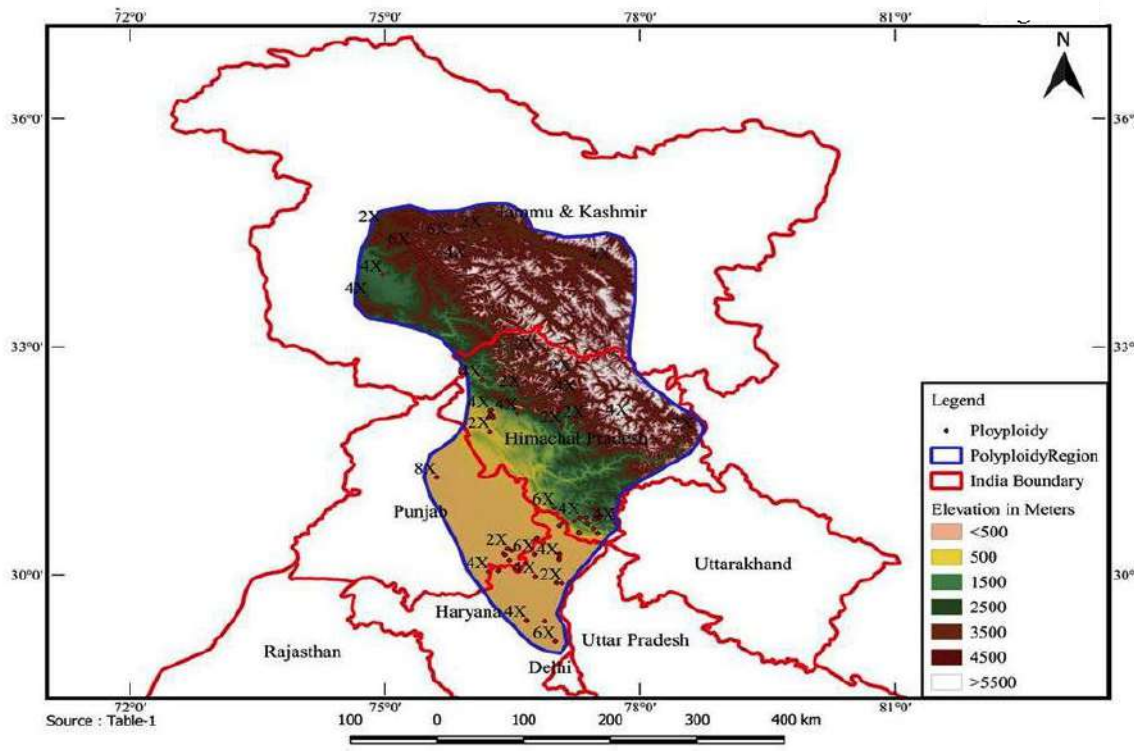


Fig. 2: Altitude variation and predominance of polyploidy in North and North Western India.

and unstable climates over diploid progenitors (Stebbins 1985, Matzke et al. 1999). However, all the polyploids are not only perennials, numerous annuals polyploids are equally successful. The broad-scale comparative studies also highlight that polyploidy is similarly widespread in annuals and perennials with diverse life histories and ecological characters (Vamosi & Dickinson 2006). Otto & Whitton (2000) reported polyploidy index (PI) in ferns (41.7%), monocots (31.7%), and dicots (17.7%), meaning that almost half of the new haploid chromosomes are the result of polyploidization in ferns and so forth. Nevertheless, within dicots, herbaceous dicots have more PI (26.3%) compared to woody (-2.2%), which means a positive correlation is found in herbaceous dicots, while it is missing in the latter (Otto & Whitton 2000). The low polyploidy rate in woody angiosperms and gymnosperms may be due to the constraining cell size of vascular cambium, and ecological/historical factors like a reduced rate of new habitat emergence (Stebbins 1971). Further, chromosome conditions of the phanerogams correspond to life forms as annuals generally show low base numbers and keep to the diploid or other lower polyploidy, while perennials, attain high base numbers and ploidy level (Gustafsson 1948). As per previous studies, in Pakistan only, two different views are reported for polyploidy and perenniality, polyploidy is rich in perennials in the first view (Baquar 1976), while it is more in annuals (Khatoon & Ali 2006) in another view. While in Polish flora, perennials and woody plants generally had higher chromosome numbers and polyploid frequencies than annuals and biennials (Góralski et al. 2014). However, due to some antagonistic reports (Vamosi & Dickinson 2006), no direct conclusion can be drawn for the correlation between polyploidy and herbaceous growth habit. Although, there is a shift from annual habit to perennial in the case of polyploids (Sano et al. 1980), which might be due to increased cell size that provides an advantage of superior longevity and slower metabolism (Garbutt & Bazzaz 1983). The evolutionary analysis of 1751 angiosperms species for polyploidy, clonality, and life history, reveals a significant relationship between polyploidy and perenniality (Van Drunen & Husband 2018a, b).

Polyploidy is among the critical determinants in studying plant evolution and results in genome plasticity and adaption by neo-fictionalization of genes. The current study predicts that environmental factors do not have any direct relation to the geographical/environmental allocation of cytotypes, but can promote chance colonization. Polyploid plants behave differently in other environmental conditions, as polyploids are more prominent in higher altitudes, and colder environments, and have a mixed distribution in different geographical conditions.

## REFERENCES


Baquar, S.R. 1976. Polyploidy in the flora of Pakistan in relation to latitude, life form, and taxonomic groups. Taxonomy, 25: 627.

Bierzychudek, P. 1985. Patterns in plant parthenogenesis. Experientia, 41: 1255-1264.

Bir, S.S. and Sahni, M. 1985. Cytological investigation on some grasses from Punjab plains, North India. Proc. Indian Natn. Sci. Acad. B, 51: 609-626.

Bir, S.S., Sahni, M. and Singh, C.P. 1988. Cytology of Genus *Sporobolus* R. Br. from North India (Punjab Plain). Cytologia, 53: 53-57.

Bomblies, K., Higgins, J.D. and Yant, L. 2015. Meiosis evolves: Adaptation to external and internal environments. New Phytol., 208: 306-323.

Bowden, W.B. 1940. Diploidy, polyploidy, and winter hardiness relationships in the flowering plants. Am. J. Bot., 27: 357-371.

Brochmann, C., Brysting, A.K., Alsos, I.G., Borgen, L., Grundt, H.H., Scheen, A.C. and Elven, R. 2004. Polyploidy in arctic plants. Biol. J. Linn. Soc. Lond., 82: 521-536.

Cheng, F., Wu, J., Cai, X., Liang, J.L., Freeling, M. and Wang, X.W. 2018. Gene retention, fractionation and subgenome deference in polyploid plants. Nature Plants, 4: 258-268.

Comai, L. 2005. The advantages and disadvantages of being polyploid. Nat. Rev. Genet., 6: 836-846.

De Storme, N., Copenhaver, G.P. and Geelen, D. 2012. Production of diploid male gametes in Arabidopsis by cold-induced destabilization of post-meiotic radial microtubule arrays. Plant Physiol., 160: 1808-1826.

de Wet, J.M.J. 1980. Origin of Polyploids. In Lewis, W.H. (ed.) Polyploidy: Biological relevance. Plenum Press, New York, USA, pp. 3-16.

Dhaliwal, A., Dhaliwal, R.S., Kaur, N. and Gupta, R.C. 2018a. Cytomorphological study in Genus *Cenchrus* L.: An important medicinal plant from North India (Family: Poaceae). Cytologia, 83: 45-52.

Dhaliwal, A., Kaur, N. and Gupta, R.C. 2018b. Cytology of some grasses from Haryana and Shiwalik Hills. Cytologia, 83: 23-30.

Fukuda, I. 1967. The biosystematics of *Achlys*. Taxon, 16: 308-316.

Garbutt, K. and Bazzaz, F.A. 1984. The effects of elevated CO2 on plants. III. Flower, fruit and seed production and abortion. New Phytol., 98: 433-446.

Góralski, G., Bal, M., Gacek, P., Orzechowski, T.M. and Kosecka-Wierzejska, A. 2014. Chromosome numbers and polyploidy in life forms of Asteraceae, Poaceae and Rosaceae in Polish flora. ABC Ser. Bot., 56:7-15.

Gupta, H., Gupta, R.C., Kumar, R. and Singhal, V.K. 2017a. A profile of chromosome counts, male meiosis, and pollen fertility in 45 species of Asteraceae from Parvati Valley in Kullu district, Himachal Pradesh. Caryologia,70: 128-140.

Gupta, H., Kumar, R., Gupta, R.C. and Singhal, V.K. 2018a. New chromosome counts and evolutionary tendencies in some dicots analyzed from Parvati Valley, Kullu district, Himachal Pradesh. Caryologia,71: 238-262.

Gupta, R.C. and Singh, V. 2015. Cytogenetic Variation among Populations of *Aster thomsonii* C. B. Clarke from District Sirmaur, Himachal Pradesh (India). Cytologia80:81-87.

Gupta, R.C., Dhaliwal, A. and Kaur, N. 2018b. Cytological study in some members of tribe Paniceae (Poaceae) from Haryana and Adjoining Shiwalik Hills. Cytologia, 83: 73-79.

Gupta, R.C., Goyal, H. and Singh, V. 2014a. Cytology of the genus *Artemisia* (Anthemidae, Asteraceae) in the Western Himalayas. Biologia, 69: 1134-1141.

Gupta, R.C., Goyal, H., Singh, V. and Goel, R.K. 2014b. Meiotic studies in some species of tribe Cichorieae (Asteraceae) from Western Himalayas. Scientific World J.2014: 1-9.

Gupta, R.C., Gupta, A. and Kaur, N. 2017b. Meiotic studies in some members of tribe Andropogoneae (Poaceae) from semi desert area of north India. Cytologia, 82: 105-113.

Gupta, R.C., Singh, V., Bala, S., Malik, R.A., Sharma, V. and Kaur K. 2017c. Cytomorphological variations and new reports of B-chromosomes in the genus *Plantago* (Plantaginaceae) from the Northwest Himalaya. Flora, 234: 69-76.

Gustafsson, A. 1948. Polyploidy, life-form and vegetative reproduction. Hereditas, 34: 1-25.

Hagerup, O. 1932. Über polyploidie in Beziehung zu Klima, Ökologie und Phylogenie: Chromosomenzahlen aus Timbuktu. Hereditas, 16(102): 19-40.

Hardy, O.J., de Loose, M., Vekemans, X. and Meerts, P. 2001.Allozyme segregation and inter-cytotype mating barriers in the polyploid complex *Centaureajacea*. Heredity, 87: 136-145.

Hardy, O.J., Vanderhoeven, S.O.N.I.A., De Loose, M. and Meerts, P. 2000. Ecological, morphological and allozymic differentiation between diploid and tetraploid knapweeds (*Centaurea jacea*) from a contact zone in the Belgian Ardennes. The New Phytologist, 146(2): 281-290.

Hieter, P. and Griffiths, T. 1999. Polyploidy-more is more or less. Science, 285: 210-211.

Hilu, K.W. 1993. Polyploidy and the evolution of domesticated plants. Am. J. Bot., 80: 1494-1499.

Himshikha, Gupta, R.C., Kumar, R. and Singhal, V.K. 2017. Cytomixis and intraspecific polyploidy (2x, 4x) in *Inula grandiflora* Willd. from Malana Valley, Kullu District, Himachal Pradesh. Cytologia, 82: 273-278.

Hörandl, E., Cosendai, A.C., Temsch, E. 2008. Understanding the geographic distributions of apomictic plants: A case for a pluralistic approach. Plant Ecol. Divers., 1: 309-320.

Jeelani, S.M., Kumari, S. and Gupta, R.C. 2012. Meiotic studies in some selected angiosperms from the Kashmir Himalayas. J. Syst. Evol., 50: 244-257.

Jeelani, S.M., Kumari, S., Gupta, R.C. and Siddique, M.A.A. 2014. Detailed cytomorphological investigations through male meiosis of polypetalous plants from the Kashmir Himalaya. Plant. Syst. Evol., 300: 1175-1198.

Kaur, D. and Singhal, V.K. 2012. Phenomenon of cytomixis and intraspecific polyploidy (2x, 4x) in *Spergularia diandra* (Guss.) Heldr. & Sart. in the cold Desert Regions of Kinnaur district (Himachal Pradesh). Cytologia, 77: 163-171.

Kaur, H., Mubarik, N., Kumari, S. and Gupta RC. 2014. Meiotic studies in some species of *Pennisetum* Pers. (Poaceae) from the Western Himalayas. Cytologia, 79: 247-259.

Khan, N.A., Singhal, V.K., Tantray, Y.R. and Gupta, R.C. 2019. Report of intraspecific polyploidy (2x, 6x) in *Rorippa palustris*, Brassicaceae from cold deserts of Ladakh division (J & K), India. Cytologia, 84: 207-210.

Khan, N.A., Singhal, V.K., Tantray, Y.R., Kumar, R. and Gupta, R.C. 2020. A case of intraspecific euploidy (2x, 4x) and secondary chromosomal associations in wild accessions of *Geranium pratense* L. from cold deserts of Ladakh (India). Nucleus (India), 63: 143-149.

Khatoon, S. and Ali, S.I. 2006. Chromosome numbers and polyploidy in the legumes of Pakistan. Pak. J. Bot., 38: 935-945.

Knight, C.A. and Beaulieu, J.M. 2008. Genome size scaling through phenotype space. Ann Bot., 101: 759-766.

Koutecký, P. 2012. A diploid drop in the tetraploid ocean: hybridization and long-term survival of a singular population of *Centaureaweldeniana* Rchb. (Asteraceae): A taxon new to Austria. Plant Syst. Evol., 298: 1349-1360.

Koutecký, P., Bad' urová, T., Štech, M., Košnar, J. and Karásek, J. 2011. Hybridization between diploid *Centaureapseudophrygia* and tetraploid *C. jacea* (Asteraceae): The role of mixed pollination, unreduced gametes, and mentor effects. Biol. J. Linn. Soc., 104: 93-106.

Kumar, P. and Singhal, V.K. 2011. Male meiosis, morphometric analysis and distribution pattern of 2× and 4× cytotypes of *Ranunculus hirtellus* Royle, 1834 (Ranunculaceae) from the cold regions of northwest Himalayas (India). Comp. Cytogen., 5: 143-161.

Kumar, P., Rana, P.K. and Singhal, V.K. 2014. Male meiosis, morphometric analysis and natural propagation in the 2× and 3× cytotypes of *Tordyliopsis brunonis* (Apiaceae) from northwest Himalayas (India). Plant Syst. Evol., 300: 1477-1486.

Kumar, S., Jeelani, S.M., Rani, S., Gupta, R.C. and Kumari, S. 2011b. Cytomorphological studies of genus *Saxifraga* L. from Western Himalaya. Nucleus, 54: 77-83.

Kumar, S., Jeelani, S.M., Rani, S., Gupta, R.C. and Kumari, S. 2013. Cytology of five species of subfamily Papaveroideae from the Western Himalayas. Protoplasma, 250: 307-316.

Kumar, S., Jeelani, S.M., Rani, S., Kumari, S. and Gupta, R.C. 2011a. Exploration of intraspecific cytomorphological diversity in *Agrimonia eupatoria* L. (Rosaceae) from Western Himalayas, India. Cytologia, 76: 81-88.

Kumar, S., Kumari, S. and Gupta, R.C. 2012. Cytological investigations of some polypetalous plants from District Sirmaur of Himachal Pradesh in the Western Himalayas, India. Chrom. Bot., 7: 87-96.

Ladinig, U., Hacker, J., Neuner, G. and Wagner, J. 2013. How endangered is the sexual reproduction of high-mountain plants by summer frosts? Frost resistance, frequency of frost events, and risk assessment. Oecologia,171: 743-760.

Levin, D.A. (ed). 2002. The Role of Chromosome Change in Plant Evolution. Oxford University Press, New York, USA, pp. 241.

Levin, D.A. 2003. The ecological transition in speciation. New Phytol., 161: 91-96.

Lewis, W.H. (ed). 1980. Polyploidy: Biological Relevance. Plenum Press, New York, USA, pp. 595.

Löve, A. and Löve, D. 1957. Arctic Polyploidy. Proc. Gen. Soc. Canada. 2: 23-27.

Lumaret, R., Guillerm, J.L., Delay, J., AitLhajLoutfifi, A., Izco, J. and Jay, M. 1987. Polyploidy and habitat differentiation in *Dactylis glomerata* L. from Galicia (Spain). Oecologia, 73: 436-446.

Maherali, H., Walden, A.E. and Husband, B.C. 2009. Genome duplication and the evolution of physiological responses to water stress. New Phytol., 184: 721-731.

Malik, R.A., Gupta, R.C. and Kumari, S. 2012. Cytogenetic diversity of *Elsholtziaciliata* Benth. (Lamiaceae) from Kashmir Himalaya. ABC Ser. Bot., 54: 76-83.

Matzke, M.A., MittelstenScheid, O. and Matzke, A.J. 1999. Rapid structural and epigenetic changes in polyploid and aneuploid genomes. BioEssays, 21: 761-767.

Otto, S.P. 2007. The evolutionary consequences of polyploidy. Cell, 131: 452-462.

Otto, S.P. and Whitton, J. 2000. Polyploidy: Incidence and evolution. Annu. Rev. Gen., 34: 401-437.

Pacey, E.K., Maherali, H. and Husband, B.C. 2020. The influence of experimentally induced polyploidy on the relationships between endopolyploidy and plant function in Arabidopsis thaliana. Ecol. Evol., 10: 198-216.

Ramsey, J. and Ramsey, T.S. 2014. Ecological studies of polyploidy in the 100 years following its discovery. Phil. Trans. R. Soc. B, 369: 20130352.

Ramsey, J. and Schemske, D.W. 1998. Pathways, mechanisms, and rates of polyploid formation in flowering plants. Annu. Rev. Ecol. Syst., 29: 467-501.

Ramsey, J. and Schemske, D.W. 2002. Neopolyploidy in flowering plants. Annu. Rev. Ecol. Syst., 33: 589-639.

Rani, S., Kumari, S., Gupta, R.C. and Chahota, R.K. 2014. Cytological studies of Angiosperms (174 species) from District Kangra, Himachal Pradesh (India). Plant Syst. Evol., 300: 851-862.

Rani, S., Sharma, T.R., Kapila, R. and Chahota, R.K. 2015. Identification of new cytotypes of *Valeriana jatamansi* Jones, 1970 (Valerianaceae) from north-western Himalayan region of India. Comp. Cytogen., 9: 499-512.

Robertson, K., Goldberg, E.E. and Igic, B. 2010. Comparative evidence for the correlated evolution of polyploidy and self-compatibility in Solanaceae. Evolution, 65: 139-155.

Sano, Y., Morishima, H. and Oka, H.I. 1980. Intermediate perennial-annual populations of *Oryzaperennis* found in Thailand and their evolutionary significance. Bot. Mag., 93: 291-305.

Singh, V. 2017. Evaluation of Cytomoprhological Diversity in Gamopetale from District Sirmaur (H.P.). Ph.D. thesis, Punjabi University, Patiala

Singh, V., Gupta, R.C. and Kaur, K. 2016. IAPT/IOPB chromosome data 21. Taxonomy, 65: 676

Singh, V., Gupta, R.C., Chauhan, H.S., Kaur, L., Kaur, K. and Sharma, M. 2018a. Male meiotic studies in intraspecific polyploids of four species of subclass Gamopetalae from district Sirmaur (H.P.). Agriways, 6: 61-68.

Singh, V., Gupta, R.C., Sharma, K., Sharma, V., Sharma, M. and Kaur, K. 2018b. Male meiotic studies in 29 species of Lamiaceae from Sirmaur District of Himachal Pradesh, India. Cytologia, 83: 235-243.

Singhal, V.K., Tantray, Y.R., Kaur, D. and Gupta, R.C. 2017. First report of intraspecific polyploidy (2x, 4x) in *Physochlaina praealta* (Decne.) Miers. (Family: Solanaceae). Cytologia, 82: 245-250.

Singhal, V.K., Tantray, Y.R., Kaur, M., Rana, P.K. and Gupta, R.C. 2018. Intraspecific euploidy (2x, 4x) in *Primula denticulata* Sm. from North West Himalayas in India. Cytologia, 83: 31-35.

Soltis, D.E. and Soltis, P.S. 1999. Isozyme evidence for ancient polyploidy in primitive angiosperms. Syst. Bot., 15: 328-337.

Soltis, D.E., Soltis, P.S. and Tate, J.A. 2004. Advances in the study of polyploidy since plant speciation. New Phytol., 161: 173-191.

Stebbins, G.L. (ed) 1971. Chromosome Evolution in Higher Plants. Edward, Arnold, London, pp. 216.

Stebbins, G.L. (ed). 1950. Variation and evolution in plants, Columbia University Press, New York, USA, pp. 643.

Stebbins, G.L. 1947. Types of polyploids: Their classification and significance. Ad. Genet., 1: 403-429.

Stebbins, G.L. 1985. Polyploidy, hybridization, and the invasion of new habitats. Ann Mo Bot. Gard., 72: 824-832.

Tantray, Y.R., Singhal, V.K., Kaur, M. and Gupta, R.C. 2018. Cytomorphological comparison in natural intraspecific cytotypes (2x, 4x) in *Brachyactis pubescens* from Northwest Himalayas, India. Cytologia, 83: 245-249.

Vamosi, J.C. and Dickinson, T.A. 2006. Polyploidy and diversification: A phylogenetic investigation in Rosaceae. Int. J. Plant. Sci., 167: 349-358.

Van de Peer, Y., Ashman, T.L., Soltis, P.S. and Soltis, D.E., 2021. Polyploidy: An evolutionary and ecological force in stressful times. Plant Cell, 26-11 :33.

Van Dijk, P., Hartog, M. and Van Delden, W. 1992. Single cytotype areas in autopolyploid *Plantago media* L. Biol. J. Linn. Soc., 46: 315-331.

Van Drunen, W.E. and Husband, B.C. 2018a. Whole genome duplication decreases clonal stolon production and genet size in the wild strawberry *Fragaria vesca*. Am. J. Bot., 105: 1712-1724.

Van Drunen, W.E. and Husband, B.C. 2018b. Immediate vs. evolutionary consequences of polyploidy on clonal reproduction in an autopolyploid plant. Ann. Bot., 122: 195-205.

Vrijenhoek, R.C. 1984. Ecological differentiation among clones: The frozen niche variation model. In: Woermann, K. and Loeschcke, V. (eds), Population Biology and Evolution. Springer, Berlin, pp. 217-23.

Watanabe, K. 1986. The cytogeography of the genus *Eupatorium* (Compositae): A review. Plant Species. Biol., 1: 99-116.

Nature Environment and Pollution Technology
An International Quarterly Scientific Journal

p-ISSN: 0972-6268
(Print copies up to 2016)
e-ISSN: 2395-3454

Vol. 22 | No. 1 | pp. 303-309 | 2023

Original Research Paper

https://doi.org/10.46488/NEPT.2023.v22i01.030

Open Access Journal

# Study of Some Stability Parameters in the Atmosphere of Oil Al-Dura Refinery, Southeast Baghdad

**Farant H. S. Lagenean*, Salwa S. Naif* and Monim H. Al-Jiboori*†**

*Atmospheric Sciences Department, College of Science, Mustansiriyah University, Baghdad, Iraq

†Corresponding author: Monim H. Al-Jiboori; mhaljiboori@gmail.com

**Nat. Env. & Poll. Tech.**
**Website: www.neptjournal.com**

*Received:* 09-06-2022
*Revised:* 15-07-2022
*Accepted:* 18-07-2022

**Key Words:**
Atmospheric stability
Al-Dura refinery
Bulk Richardson number
Gradient Richardson number
Monin-Obukhov length

## ABSTRACT

Wind and temperature measurements at an oil refinery site located southeast of Baghdad city at two levels, 15 and 30 m, are presented. Three schemes are used to determine different stability classifications: Monin-Obukhov length, gradient, and bulk Richardson numbers. Meanwhile, vertical changes in air temperature and wind shear are also computed. There were lapse rate and inversion cases during the nights and days while favorable wind shear was dominant. The variation of stability in each scheme is large, covering the entire range of stability for a given class. The results of stability schemes are compared to each other. The results show that the schemes based on gradient and bulk Richardson numbers reasonably compare them.

## INTRODUCTION

The study of atmospheric stability classification is required to quantify the dispersion capability of ambient atmosphere in the air quality models for concentration prediction. Also, it is of prime concern for estimating the heat and momentum fluxes in the surface boundary layer (Anto et al. 1980, Al-Jiboori et al. 2001). This study, in terms of its degree and intensity, has the most important role in the transport and behavior of air pollutants (Lazaridis 2011). Furthermore, it represents a primary parameter in the expressions describing wind speed and temperature profiles (Al-Jiboori 2010, Newman & Klein 2014, Rodrigo et al. 2015). It can be defined as the atmospheric tendency to reduce or intensify the vigor of vertical motion or to suppress or augment existing turbulence (Seinfeld & Pandis 1998). Therefore it is related to vertical changes in air temperature and wind speed. In general, there are three states of atmospheric stability at low altitudes (i.e., less than 100 m): unstable, neutral, and stable.

There were different methods to determine the stability and instability with varying degrees of complexity. There are more than seven classification schemes, such as Pasqill-Gifford-Turner, the horizontal wind direction standard deviation, temperature gradient, gradient Richardson number, bulk Richardson number, Monin-Obukhov (M-O) length, and wind speed ratio. Most of these methods are based on the relative importance of convective and mechanical production in atmospheric motions. The difference between such methods is due to the use of various parameters for this production. Atmospheric stability is divided into seven categories starting from A to G, designated as: A (highly unstable or convective), B (moderately unstable), C (slightly unstable), D (neutral), E moderately stable, and F (extremely stable). Stability G is added to represent low wind night stable conditions as in urban areas (Mohan and Siddiqui, 1998). In this paper, these stability parameters will be determined, and their results will be compared through the frequency percentage.

## MATERIALS AND METHODS

### Atmospheric Stability Schemes

In micrometeorology, six schemes are commonly used to determine the degree of stability or instability. These schemes are Pasquill-Gifford-Turner based on wind speed at 10 m and solar insolation/cloud cover, temperature gradient based on temperature measurements at least two levels, wind speed ratio based on the wind at also two levels, wind direction fluctuation relating with a calculation of standard deviation of horizontal wind direction, gradient Richardson number, bulk Richardson number, and M-O length. For more detail, the description for each scheme can be found in (Golder

1972, Zoumakis 1992, Zoumakis & Kelessis 1993, Mohan & Siddiqui 1998).

Because the wind ratio and the wind direction schemes are directly associated with mechanically generated turbulence as well as temperature gradient scheme is associated more with thermally generated turbulence, their results could not be identified with other results derived from other schemes (Mohan & Siddiqui 1998), which may be attributed to the fact these do not involve ratio scheme of the mechanical-to-convective turbulence. In addition, the Pasquill-Gifford-Turner method requires estimation for parameters such as solar insolation during daytime and an assessment of cloud cover during nighttime. Thus, it cannot be applied in this research. The following subsection describes the methods used in this work to define stability.

**Gradient Richardson Number (Ri)**

This parameter is the most widely used indicator of atmospheric stability; a nondimensional parameter representing the relative importance of buoyancy and shear in producing turbulence (Kaimal & Finnigan 1994) is

$$\mathrm{Ri} = \frac{\mathrm{g}}{\bar{\mathrm{T}}} \frac{\partial\bar{\theta}/\partial \mathrm{z}}{\left(\partial\bar{\mathrm{u}}/\partial \mathrm{z}\right)^2} \quad \ldots(1)$$

where Θ and u are potential temperature and wind speed at the height z above the ground level, respectively, $\bar{T}$ The mean temperature for the layer and g is the acceleration due to gravity. In this equation $g\,(\partial\bar{\theta}/\partial z)\bar{T}$ is an indicator of convection and $(\partial\bar{u}/\partial z)^2$ is the pointer of mechanical turbulence due to shear force. Ri is positive for stable, negative for unstable, and 0.25 for neutral stratification.

**Bulk Richardson number (Rb)**

This inductor is a nondimensional stability ratio that uses temperature at two levels but requires wind speed at only one level. It is defined as (Golder 1972):

$$\mathrm{Rb} = \frac{(g/\bar{\theta})\,(\partial\bar{\theta}/\partial z)}{u^2}\,\bar{z}^2 \quad \ldots(2)$$

where $\bar{z}$ Is usually taken to be the geometric mean height $[(z_1{*}z_2)^{1/2}]$.

**M-O Stability Parameter $(\bar{z}/L)$**

The last key stability parameter is the ratio of $\bar{z}$ to the M-O length (L) (Kaimal and Finnigan, 1994),

$$\frac{\bar{z}}{L} = -\frac{\left(\frac{g}{\bar{\theta}}\right)\left(\overline{w'\theta'}\right)_o}{\frac{u_*^3}{kz}} = \frac{kzg}{\bar{\theta}}\frac{\theta_*}{u_*^2} \quad \ldots(3)$$

where k is the von Kármán constant (=0.4), $\theta_*$ is the scaling temperature and $u_*$ is the friction velocity, and $\overline{(w'\theta')}_o$ the mean surface heat flux. In the present paper, the parameters $u_*$ and $\theta_*$ are calculated by the following equations (Ashrafi & Hoshyaripour 2010):

$$\mathrm{u}_* = \mathrm{k}\,\Delta\mathrm{u}_\mathrm{z}\left[\ln\frac{\mathrm{z}_2}{\mathrm{z}_1} - \Psi_\mathrm{m}\left(\frac{\bar{\mathrm{z}}}{\mathrm{L}}\right)\right]^{-1} \quad \ldots(4)$$

$$\theta_* = \mathrm{k}\,\Delta\theta_\mathrm{z}\left[\ln\frac{\mathrm{z}_2}{\mathrm{z}_1} - \Psi_\mathrm{h}\left(\frac{\bar{\mathrm{z}}}{\mathrm{L}}\right) + \Psi_\mathrm{h}\left(\frac{\bar{\mathrm{z}}}{\mathrm{L}}\right)\right]^{-1} \quad \ldots(5)$$

The universal function $\psi_h$ under unstable conditions is given by

$$\Psi_\mathrm{m} = 2\ln\left(\frac{1+\mathrm{x}}{2}\right) + \ln\left(\frac{1+\mathrm{x}^2}{2}\right) - 2\tan^{-1}(\mathrm{x}) + \frac{\pi}{2} \quad \ldots(6)$$

with $x = (1 - 16 * \bar{z}/L)^{1/4}$ and for stable conditions is

$$\Psi_\mathrm{m} = -5 * \frac{\bar{\mathrm{z}}}{\mathrm{L}} \quad \ldots(7)$$

In Eq. (5), the function $\psi_h$ for stable conditions is given by

$$\Psi_\mathrm{h} = 2\ln\left(\frac{1+\mathrm{y}}{2}\right) \quad \ldots(8)$$

with $y = (1 - 16 * z/L)^{1/2}$, and lastly, for stable conditions

$$\Psi_\mathrm{h} = \Psi_\mathrm{m} = -5 * \frac{\bar{\mathrm{z}}}{\mathrm{L}} \quad \ldots(9)$$

For the estimation of $\bar{z}/L$ by use of Eq. (3), $u_*$ and $\theta_*$ have to be determined from Eqs. (4) and (5) by starting with $\bar{z}/L = 0$ (i.e. $\Psi_h = \Psi_m = 0$). First estimates of $u_*$ and $\theta_*$ are then computed, which used to calculate $\bar{z}/L$ by Eq. (3). Subsequently, the new value of $\bar{z}/L$ is substituted in Eqs. (4) and (5) to obtain improved estimates for $u_*$ and $\theta_*$. These steps are repeated for five iteration times to achieve more accuracy for $\bar{z}/L$. The practical advantage of using (4) and (5) is that the large magnitudes of roughness length become unimportant. The limits used to specify stability classes in this study are presented in Table 1.

**The Experiment Site and Dataset**

Experimental slow response data, including wind speed and air temperature, were used in the presented paper. This experiment occurred at an oil refinery site located in Al-Dura municipality (see Fig. 1), southeast of Baghdad city (33.1° N, 44.2° E, and 40 m above mean sea level). This particular site was chosen because the atmosphere in this site is always pollutant, and it can be considered as a pollution-producing site where in addition to the refinery, a sizable electric power plant is located in the northeast, about 1.5 km distance (Shubbar et al. 2018, Anad et al. 2022). This pollution has several effects on environmental sectors, human health, and local climate behavior (Halos et al. 2017).

For the purpose of the present study, two slow-response meteorological instruments, such as three cup anemometer

Table 1: $\bar{z}/L$, Ri, and Rb limits for stability classification employed in this study.

| Type of stability | Symbol | $\bar{z}/L$ interval (Businger 1973) | Ri interval | Rb interval |
|---|---|---|---|---|
| Extremely unstable | A | $-2.25 < \bar{z}/L < -\infty$ | $-1.3 \leq Ri < -\infty$ | $Rb < -0.91$ |
| Moderately unstable | B | $-0.11 \leq \bar{z}/L \leq -2.25$ | $-0.073 \leq Ri < -1.3$ | $-0.91 \leq Rb < -0.051$ |
| Slightly unstable | C | $-0.00023 \leq \bar{z}/L \leq -0.11$ | $-0.00017 \leq Ri < -0.073$ | $-0.051 \leq Rb \leq -0.00012$ |
| Neutral | D | $\lvert\bar{z}/L\rvert < 0.00023$ | $\lvert Ri\rvert < 0.00017$ | $\lvert Rb\rvert \leq 0.00012$ |
| Slightly stable | E | $0.23 > \bar{z}/L > 0.00023$ | $0.096 \geq Ri > 0.00017$ | $0.0672 \geq Rb > 0.00012$ |
| Moderately stable | F | $2.25 > \bar{z}/L > 0.22$ | $0.19 \geq Ri > 0.096$ | $0.133 \geq Rb > 0.0672$ |
| Extremely stable | G | $\infty \geq \bar{z}/L > 2.25$ | $\infty \geq Ri > 0.19$ | $Rb > 0.13$ |

with a vane in one body (Demo-6 type of Chinese origin) and a thermometer, were used. Before running these instruments, the calibration was made with standard instruments used in meteorological offices. The results show that all observations do not appear to have significant differences. The first set is mounted on a tower of 3 m which place on the mid-point of the roof of the water tank (27 m high), so the first height of the instrument location is 30 m, see Fig. 2, which also shows the areas surrounding the experiment site with different directions. About 50 m distance from the first site, the second set was set up on a tower of 15 m.

The observational data: wind speed, its direction, and air temperature measured at two heights were recorded at the same time every 30 seconds for 20 min. It means that the one run length has 40 records of each above parameter. The recording period was 20 days starting from 10 to 20 April 2018, except for two days (18 and 28 days) when the weather was very bad. Every day, the observing runs were taken at different times, from midnight to evening. Briefly, during the whole observing period for both heights, the wind came northwest direction, mostly prevailing. Mean values for air temperature ( $\bar{T}$ ) and wind speed ( $\bar{u}$ ) at two levels with their number runs according to the observing times are presented in Table 2.

In general, at both heights, $\bar{T}$ It has maximum values of 33.6 and 32.2°C, respectively, at noon, while minimum values of 22.4 and 22.1 in the early morning. From $\bar{u}$ Values reported in Table 2, it can be shown that wind speeds at 15 m levels generally are less than those at 30 m levels along all daily times, with a slightly increasing at noon time.

Fig. 1: Photograph of oil Al-Dura refinery.

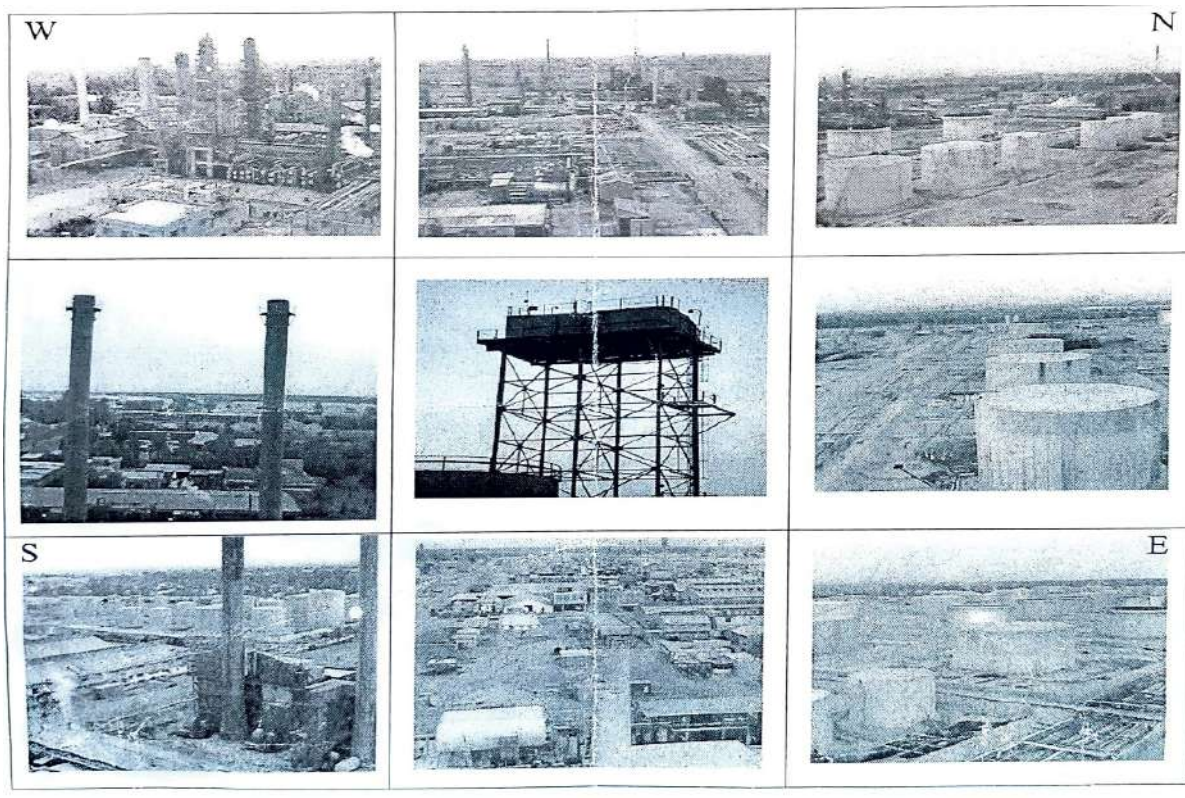


Fig. 2: Photographs of areas surrounding the site in different directions. The middle photograph shows the location of the measurement instruments.

Table 2: Observing times, number of runs, and mean wind and temperature during this study.

| Time | Observing times | No. of runs | $\bar{T}$ (°C) | | $\Delta\ \bar{T}$ (°C) | $\Delta\bar{T}/\Delta z$ (°C/m) | $\bar{u}$ (m.s$^{-1}$) | | $\Delta\ \bar{u}$ (m.s$^{-1}$) | $\Delta\bar{u}/\Delta z$ s$^{-1}$ |
|---|---|---|---|---|---|---|---|---|---|---|
| | | | 15 (m) | 30 (m) | | | 15 (m) | 30 (m) | | |
| | 1:00-1:20 am | 19 | 25.1 | 25.4 | 0.3 | 0.02 | 1.3 | 4.1 | 2.8 | 0.19 |
| Night | 1:30-1:50 am | 19 | 24.9 | 25.1 | 0.2 | 0.01 | 1.5 | 4.1 | 2.6 | 0.17 |
| | 2:00-2:20 am | 19 | 24.5 | 24.7 | 0.2 | 0.01 | 1.2 | 3.5 | 2.3 | 0.15 |
| | 2:30-2:50 am | 19 | 24.1 | 24.5 | 0.4 | 0.03 | 1.6 | 3.4 | 1.8 | 0.12 |
| Early | 6:00-6:20 am | 17 | 22.4 | 22.1 | -0.3 | -0.02 | 1.4 | 3.6 | 2.2 | 0.15 |
| morning | 7:00-7:20 am | 17 | 23.6 | 23.3 | -0.3 | -0.02 | 1.5 | 3.6 | 2.1 | 0.14 |
| | 10:00-10:20 am | 19 | 29.8 | 28.6 | -1.2 | -0.08 | 2.1 | 4.6 | 2.5 | 0.17 |
| Noon | 11:00-11:20 am | 19 | 30.7 | 29.5 | -1.2 | -0.08 | 2.3 | 5.0 | 2.7 | 0.18 |
| | 2:00-2:20 pm | 19 | 33.1 | 32.1 | -1.0 | -0.07 | 1.8 | 4.0 | 2.2 | 0.15 |
| | 3:00-3:20 pm | 19 | 33.6 | 32.2 | -1.4 | -0.09 | 1.9 | 4.2 | 2.3 | 0.15 |
| | 5:00-5:20 pm | 19 | 32.6 | 31.5 | -1.1 | -0.07 | 2.2 | 4.1 | 1.9 | 0.13 |
| Afternoon | 5:30-5:50 pm | 19 | 31.9 | 31.1 | -0.8 | -0.05 | 2.1 | 3.9 | 1.8 | 0.12 |
| | 6:00-6:20 pm | 19 | 31.4 | 30.8 | -0.6 | -0.04 | 1.7 | 3.6 | 1.9 | 0.13 |
| | 6:30-6:50 pm | 19 | 30.8 | 30.3 | -0.5 | -0.03 | 1.4 | 3.3 | 1.6 | 0.11 |
| Evening | 9:00-9:20 pm | 19 | 27.6 | 28.4 | 0.8 | 0.05 | 1.6 | 3.8 | 2.2 | 0.15 |
| | 10:00-10:20 pm | 19 | 27.0 | 27.5 | 0.5 | 0.03 | 1.5 | 3.8 | 2.3 | 0.15 |

## RESULTS AND DISCUSSION

### Air Temperature Gradient and Wind Shear

Mean vertical temperature gradient $(\Delta\bar{T}/\Delta z)$ between two heights, 15 and 30 m, was calculated for all observing times, and their results are reported in Table 2. From these results, atmospheric lapse rate, i.e., the temperature naturally decreases with elevation, and temperature inversion, i.e., temperature increases with elevation instead of decreasing (Al-Ghrybawi & Al-Jiboori 2020), can be calculated. These quantities play a vital role in determining air stability types and hence, controlling the dispersion of air pollutants (Al-Ghrybawi & Al-Jiboori 2019). Mean lapse rates were dominated at times of the early morning, noon and afternoon, while temperature inversion was at night and evening. The largest lapse rate was found at noon with an average value of -0.08 °C/m and was weak in the early morning and afternoon. In the same way, mean values of temperature inversion in the evening (0.04°C/m) are higher at night (-0.02°C/m).

Wind shear changes wind speed and direction over a short distance (Federal Aviation Administration 2008). It is most often associated with strong temperature inversions. In the last column of Table 2, the mean vertical wind difference (wind shear) through two heights has positive values at all times studied in this paper, which range from 0.11 to 0.19 $s^{-1,}$ and no indication is found.

### Diurnal Analysis of Stability

The atmospheric stability has been assessed using gradient Richardson number, bulk Richardson number, and M-O length. The kinds of stability classification using these methods have been determined using the intervals given in Table 1. For detail analysis, the percentage frequency of occurrence of the stability classes for all observation runs at five different times (namely, night, early morning, noon, afternoon, and evening) as well as at two main times of day (i.e., nighttime and daytime) are presented in Figs. 3 and 4, respectively. Generally, results from Ri and Rb schemes are primarily closed, especially in classes B and C.

During the nighttime, frequencies for stability classes from E to G are larger than others, while during the noon and afternoon times (see Fig. 3c and 3d), frequencies for classes

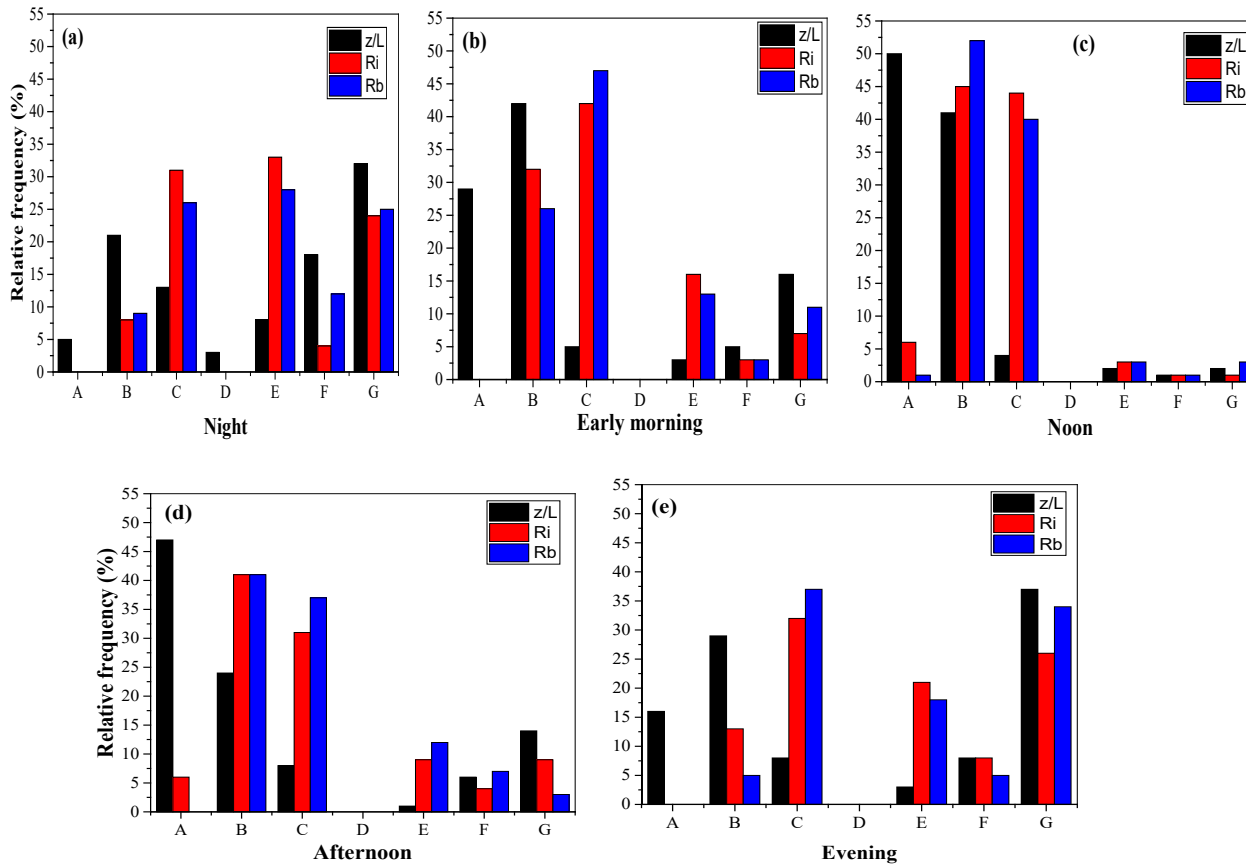


Fig. 3: Percentage of frequencies of occurrence of stability classes using $\bar{z}/L$, Ri and Rb for times (a), (b), (c), (d), and (e).

B and C are the largest. Class B is the most frequent in the early morning, and in the evening, there is a large variation in the frequency distribution.

Now results for stability classes calculated in the presented paper at five times above are unified into two primary times of the whole day, i.e., nighttime (night and evening) and daytime (early morning, noon, and afternoon), as shown in Figs. 4a and 4b, respectively.

Hourly evaluation of results reveals that instability increases from sunrise to local noon and decreases from noon to sunset, while variation in stability is vice versa. During the daytime, most frequencies in classes B and C obtaining from Ri and Rb schemes, while class A derived from $\bar{z}/L$, is the largest. In contrast, at nighttime, most frequencies are of class G, derived from $\bar{z}/L$, scheme and of classes F and G obtained from Ri and Rb.

Fig. 5 shows the comparison among the results obtained from three classification schemes by calculating the percentage of relative frequencies of occurrences of the stability classes for each stability class. Generally, all schemes show a wide variation of stability between in- and stability. The stability classes show a good agreement for the results obtained from schemes Ri and Rb. As shown in this figure, instability cases are frequent, especially for B- and C-class, while stability cases are less. As expected, neutral class D has no results, just only a few frequencies for z/L, because it is rare in the real atmosphere (Arya 2001, Al-Jiboori 2010). Class B, D, F, and G frequencies are often closed. Still, they have significant differences in classes A and C, especially M-O length, as illustrated in Fig. 5. This difference is expected because the application of the M-O scheme needs exact information such as those measured by fast-response instruments.

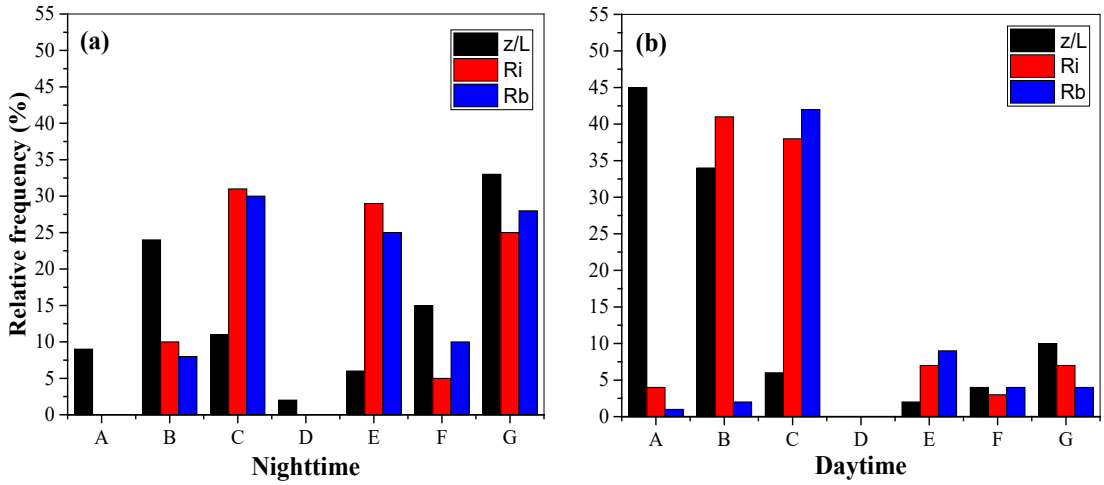


Fig. 4: Percentage of relative frequencies of occurrence of stability classes derived from $\bar{z}/L$, Ri and Rb for two times (a) nighttime and (b) daytime.

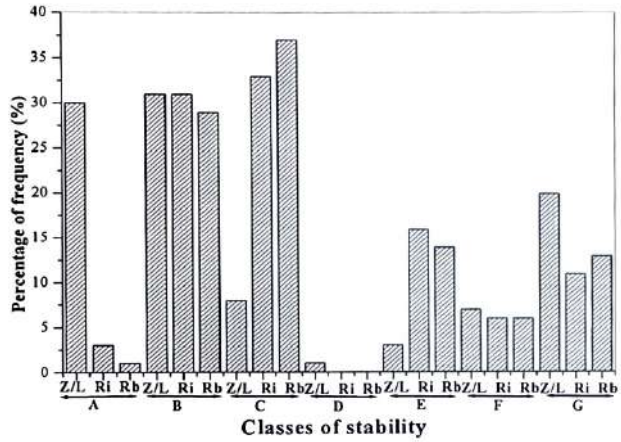


Fig. 5: Percentage of availability of atmospheric stability classes obtained by $\bar{z}/L$, Ri and Rb schemes.

## CONCLUSIONS

Based on the observational measurements of wind speed and air temperature at two levels, 15 and 30 m, which came from the field experiment at the Dura refinery, southeast of Baghdad, atmospheric stability has been estimated from three different schemes. Stability classes and their frequency of occurrence were obtained. Results showed that the majority of stable to very stable atmospheric conditions and periods of temperature inversions occur in the evening and night. During the day, between 6 am and 7 pm, atmospheric stability tends to be most unstable, with a few neutral conditions and even fewer stable or inversion conditions.

The relevance of instability during the day and stability at night was obtained from the schemes: z/L, Ri, and Rb with relative frequencies of 85%, 83%, and 83% and 54%, 60%, and 63%, respectively. During the day, instability increases from sunrise to local noon and decreases from noon to sunset, while variation in stability is vice versa.

## ACKNOWLEDGMENT

The authors of the present work express their deepest appreciation to Mustansiriyah University (www.uomustansiriyah.edu.iq) for their support during the work.

## REFERENCES

Al-Ghrybawi, A.R. and Al-Jiboori, M.H. 2019. Study of surface heat inversions characteristics around Baghdad station. Sci. Rev. Eng. Environ. Sci., 28(4): 610-618. doi:10.22630/PNIKS.2019.28.4.55

Al-Ghrybawi, S.R. and Al-Jiboori, M.H. 2020. Study of Intensity and thickness of surface heat inversion for Baghdad. J. Phys. Conf. Ser.,9: 1660. doi:10.1088/1742-6596/1660/1/012072

Al-Jiboori, M.H. 2010. Determining neutral and unstable wind profiles over Baghdad city. Iraqi J. Sci., 51(2): 343-350.

Al-Jiboori, M.H., Yumao, X. and Yongfu, Q. 2001. Effects of different terrain on velocity standard deviations. Atmos. Sci. Lett., 11: 1-7. doi:10.1006/asle.2001.0038

Anad, A.M., Hassoon, A.F. and Al-Jiboori, M.H. 2022. Assessment of air pollution around Durra refinery (Baghdad) from emission NO2 gas at April Month. Bagh. Sci. J., 19: 515-522. doi:http://ds.doi.org: 10.21123/bsj.2022.19.3.0515

Anto, A.F., Hasse, L. and Murty, C.S. 1980. Stability parameters and their inter-relationships at the Naviface. Mahasagar Bull. Natl. Instit. Oceanogr., 13(4): 295-301.

Arya, S.P. 2001. Introduction to Micrometeorology. Second edition. Academic Press, San Diego, USA.

Ashrafi, K. and Hoshyaripour, A. 2010. A model to determine atmospheric stability and correction with CO concentration. Int. J. Environ. Sci. Eng., 2: 83-88.

Businger, J.A. 1973. Turbulent Transfer in the Atmospheric Surface Layer. American Meteorology Society, CA.

Federal Aviation Administration. 2008. Wind Shear. Retrieved from http://FAASafety.gov

Golder, D. 1972. Relation among stability parameters in the surface layer. Bound. Layer Meteorol., 13: 47-58.

Halos, S.H., Al-Taai, U.T. and Al-Jiboori, M.H. 2017. Impact of dust events on aerosol optical properties over Iraq. Arab. J. Gesci., 10: 263. doi:10.1007/s12517-017-3020-2

Kaimal, J.C. and Finnigan, J.T. 1994. Atmospheric Boundary Layer Flows: Their Structure and Measurement. Oxford University Press, Oxford, UK

Lazaridis, M. 2011. First Principles of Meteorology Air Pollution. Springer, Cham. doi:10.1007/978-94-007-0162-5

Mohan, M. and Siddiqui, T.A. 1998. Analysis of various schemes for the estimation of atmospheric classification. Atmos. Environ., 32: 3775-3781.

Newman, J.F. and Klein, P.M. 2014. The impacts of atmospheric stability on the accuracy of wind speed extrapolation methods. Resources, 3: 81-105. doi:10.3390/resources.3010081

Rodrigo, J.S., Cantero, E., Garcia, B., Borbon, F., Irigoyen, U., Lozano, S., Fernandes, P.M. and Chavez, R.A. 2015. Atmospheric stability assessment for the characterisation of offshore conditions. J. Phys. Conf. Ser., 625: 1-11. doi:1.1088/1742-6596/625/1/012044

Seinfeld, J.H. and Pandis, S.N. 1998. Atmospheric Chemistry and Physics: From Air Pollution to Climate Change (Vol. 51). John Wiley & Sons. Inc., NJ.

Shubbar, R.S., Suadi, A.J. and Al-Jiboori, M.H. 2018. Study the concentration of SO2 emitted from Daura refinery by using a screen view model. Al-Mustansiriyah J. Sci., 29(3): 7-15. doi:http://doi.org/10.23851/mjs.v29i3.616

Zoumakis, N.M. 1992. On the relationship between the gradient and bulk Richardson number for the atmospheric boundary layer. Nuovo cimento, C15: 111-116.

Zoumakis, N.M. and Kelessis, A.G. 1993. On the theoretical relationship between the Monin-Obukhov stability parameter and the bulk Richardson number. Nuovo cimento, 16C, pp. 1-6.

Nature Environment and Pollution Technology
An International Quarterly Scientific Journal

p-ISSN: 0972-6268
(Print copies up to 2016)
e-ISSN: 2395-3454

Vol. 22 | No. 1 | pp. 311-317 | 2023

Original Research Paper

https://doi.org/10.46488/NEPT.2023.v22i01.031

Open Access Journal

# A Coupled Study on Carbon Emission Assessment and Emission Reduction Coupling of Tourism Activities in Beautiful Countryside Taking Zhahan Village, Qiongzhong County, Hainan as an Example

**Liping Zhu*, Yadong Zhou**† and Qing Li*****

*Hainan College of Vocation and Technique, Haikou 570216, China
**Hainan Vocational College of Political Science and Law, Haikou 571900, China
***Hainan Academy of Agricultural Reclamation Group Co. Ltd., Haikou 570311, China
†Corresponding author: Yadong Zhou; hcvtzyd@163.com

**Nat. Env. & Poll. Tech.**
**Website: www.neptjournal.com**

*Received:* 15-06-2022
*Revised:* 20-07-2022
*Accepted:* 21-07-2022

**Key Words:**
Rural revitalization
Tourism activities
Carbon emission
Energy resources
Carbon neutrality

## ABSTRACT

Taking Zhahan village in Qiongzhong County, Hainan, as an example, and based on its 160,000 tourist arrivals in 2019 and taking into account the real circumstances of Hainan, this research composes the emission models of carbon emissions from tourism transportation, tourism accommodation, tourism catering, other tourism activities and pollutants in this village. The outcomes indicate that Zhahan village's tourism catering consumes the most energy and emits the most carbon, accounting for 53.95% of all carbon emissions. Furthermore, the emission of tourism accommodation is the second, occupying 24.13%. Then, its tourism waste emission is the third, constituting 13.61%. In addition, its annual sewage discharge from tourism activities amounts to 15,144 t. This article promoted 1MW photovoltaic and 10 square solar hot water in the entire village, scientifically developing the evaluation system of rural tourism carbon emission, and making a low carbon brand of emission reduction coupling. The research and operation can be replicated and extended to enable the harmonious development of tourism development and organic unity of energy resource utilization.

## INTRODUCTION

Zhahan Village in Hongmao Town, Qiongzhong Li and Miao Autonomous County, Hainan Province, is located in the high mountain basin between Limu Mountain and Yinggeling. Its altitude is 800 meters above sea level, making it one of the villages with the most elevated terrain in Hainan. The village is surrounded by natural forest reserves to the east, west, and north, totaling 104,000 mu. The climate in the reserve area is mild, with plentiful rainfall and streams winding. The village is hidden in the clouds, with the advantages of the original scenery incomparable to modern cities. Meanwhile, its average year-round temperature is 22, which is lower than Hainan's 26°C; therefore, it has the reputation of being the "heavenly Zhahan" (Zeng & Wu 2018), which is a holiday, tourism, leisure, and summer resort desired by urbanites. Among the 108 families in the village, 65% are Hmong villagers, and 35% are Li villagers (Hainan Lakeview Life 2018). Due to the high altitude of the entire village, the inconvenient access roads, and the treacherous terrain, the development of Zhahan village is disconnected from the socio-economic growth of China. The per capita annual income of the village residents in 2009 was 946 RMB, a typical poor village in Qiongzhong County.

Since the extraordinary natural environment and the continuous promotion of the national poverty alleviation policy, the Miao and Li compatriots started to see hope for the future. In 2013, Zhahan village was honored as the "most beautiful Chinese countryside" in constructing beautiful countryside, so it became well-known inside and outside the province within one night. Since 2013, tourists from all over the world have been visiting Zhahan village for tourism, holiday, and adventure, thus making the per capita annual income of Zhahan village residents approach more than 18,000 yuan in 2020 and achieving the progress of the village out of poverty (China Youth Daily 2021). On the contrary, while all tourism activities bring villagers a wealthy life, carbon emissions are also growing, and environmental problems are becoming more prominent. Since 2018, Hainan has introduced the construction of the free trade port around the Regulations of Hainan Province on the Prevention and Control of Atmospheric Pollution, Emission Standards

**ORCID details of the authors:**

**Yadong Zhou**
https://orcid.org/0000-0003-1532-641X

for Pollutants in Betel Nut Processing Industry in Hainan Province (DB46/455-2018), Compensation Implementation Plan for Horizontal Ecological Protection in Upstream and Downstream Watersheds in Hainan Province (Trial) and other regulations, but there is a shortage of environmental protection laws and regulations concerning the construction of new rural areas. Based on incomplete statistics, the village has seen an immediate increase in the daily domestic waste produced since 2018, forcing environmental issues to become increasingly obvious. The continuous promotion of rural revitalization guarantees the harmonious unification and sustainable development of rural tourism, and the environment turns into an important topic. Accordingly, this study takes the dimension of tourism as the entry point, investigates the overall structure of Zhahan village in terms of energy consumption via data collection and research in the village for one year, further launches each emission model, and puts forward recommendations for the harmonious development of energy resource utilization and tourism opening positioning.

## CARBON EMISSION MODEL CONSTRUCTION OF RURAL REVITALIZATION TOURISM

### Carbon Emission Model Construction of Transportation

The carbon emission of the transportation of the village tour is currently mostly accounted for by the total consumption of petroleum, gas, and electricity of the annual tourism transportation and the coefficient of each energy unit emission. Normally, the tourists to the village come to this province from a radius of 5 km, while tourists from other provinces only account for less than 5%. Because of the village's high altitude, there is only one access road into the village, and the roads in the village are simple; hence, most local tourist transportation is largely self-driving. In the meantime, vehicles usually do not need to drive again after entering the village and stopping at the accommodation, so the transportation means and driving range are comparatively single. The literature utilizes the IPCC carbon emission estimation method and the top-down and bottom-up calculation methods of transport energy consumption (Peihua & Pu 2011, Chunlin 2018). The exact parameters through actual parameters to build its evaluation formula are as below:

$$C_{ct} = \sum_{i=1}^{n} P_t \times N_i \times D_i \times 2 \quad \ldots(1)$$

In the formula, $C_{ct}$ is the carbon emission of passenger transportation, kg; $P_t$ is the carbon emission factor (kg.km$^{-1}$) of the village road type of transportation to Zhahan village, and the empirical value is 0.133 kg.km$^{-1}$. *N*i is the number of passengers who pick to travel by car; $D_i$ is the distance traveled by car.

### Carbon Emission Model Construction of Tourist Accommodation

The structure of the guesthouse in Zhahan village is identical. The carbon emissions of tourist accommodations are concentrated in the lighting, ventilation, air conditioning, and hot water supply of basic accommodation facilities, mainly indirect carbon emissions based on electricity consumption. Integrate the advantages and disadvantages of the top-down method and bottom-up method for carbon emission accounting of the accommodation industry by Hongxia et al. (2017) and the literature of Yanyan et al. (2020) to compose the formula.

$$C_{ht} = B \times T \times P \times 0.936 \times H \quad \ldots(2)$$

In the formula is the carbon emission from the accommodation, kg. *B* is the total number of guesthouses; *T* is the occupancy rate of guesthouses; *P* is the weighted electricity consumption per guesthouse, kWh; 0.936 is the amount of $CO_2$ emitted by standard coal to make 1kWh of electricity, kg; *H* is the proportion of coal-fired power generation in Hainan. Based on the Hainan Provincial Bureau of Statistics announced in March 2021, the province's clean energy generation occupied 41.8% of all industrial power generation above the scale in 2020, (Ecological Civilization Construction 2021), hence 58.2% is chosen here.

### Carbon Emission Model Construction of Tourism Catering

The carbon emission of tourism catering is primarily the carbon emission generated by the consumption of energy resources such as natural gas, gas, and firewood applied in meals, non-staple food, and services offered by the village for tourists. It is estimated that the tourism catering will be moderately more complicated, and the real condition of 7 restaurants of a certain scale in Zhahan village will be calculated, combined with the energy consumption of ingredients consumed by individual tourists dining, as well as the cooking and environmental consumption of natural gas and electricity, as presented by Huang Heping. Most of the tourists visit Zhahan village to taste the local food. Zhahan village's meat consumption is largely based on the village's chickens, ducks, geese, pork, and lamb. Its aquatic products are dominated by local fish and shrimp from streams and lakes and special wild vegetables. According to the General Office of the State Council issued in 2014, the Notice of the General Office of the State Council on Issuing the Outline of the Program for Food and Nutrition Development in China (2014-2020) sets food consumption targets, integrated with

the IPCC (Intergovernmental Panel on Climate Change) Guidelines for GHG inventories generated by different foods (Jianhong et al. 2011). The evaluation models are built by:

$$C_{ft} = N \times D \times \sum(\alpha_i \times \delta_i) + \sum(\beta_i \times 0.936 \times H) + \sum (\varepsilon_i \times 2.117) \quad \ldots(3)$$

In the formula, is the catering carbon emission kg; *N* is the total number of tourists; *D* is the average number of tourist days. Under the statistics of Zhahan village, the average annual tourist stay is 1.17 days; is the average daily consumption of *i* food consumption per tourist, kg; is the emission of *i* food per kg, kg; is the average daily electricity consumption of a restaurant, kWh; is the average daily gas consumption of a restaurant, kg. 2.117 is the $CO_2$ emission from 1kg of natural gas combustion, kg.

### Carbon Emission Model Construction of Other Tourism Activities

Carbon emissions from other rural tourism activities largely comprise rural entertainment, leisure, shopping for agricultural products, and Zhahan village making full use of the village's superior air and environmental resources. In order to attract tourists and widen the tourism industry, they dig out the rural characteristics of tourism, execute a children's recreation ground, designated route adventure, rock climbing, fishing, and other recreational activities. In addition, it endeavors walking picking and high-end ornamental planting under traditional agriculture. The carbon emissions of other rural tourism activities are counted in terms of the total number of people in each activity with the related activities involved in electricity, water, and environmental carbon emission systems. On the basis of the carbon emission study by Wang Kai et al. on scenic spots, the following formula is adopted to calculate the carbon emission based on the actual situation in Hainan.

$$C_{lt} = \sum_{l=1}^{n} N_l \times \delta_l \quad \ldots(4)$$

In the formula, is the total amount of carbon emissions when tourists engage in other activities, kg; is the number of tourists participating in l other activities; is the $CO_2$ emission coefficient of joining in l activities; n is the number of types of tourist attractions or tourist activities.

### Emission Model Construction of Tourism Waste

**Emission construction of tourism solid waste:** Tourism waste contains solid waste, sewage, manure, soot, $SO_2$, NOx, etc. Integrate with the fact that solids comprise organic household waste such as food waste and paper generated by food and shelter and inorganic waste such as plastic and metal packaging discarded during recreation, (Yingmiaol et al. 2012). As well as, after a study to determine the daily per capita waste generation data of 3.5 kg/person-day, which is 2.5 kg for food waste and 1 kg for park waste (Peng et al. 2008) for reference. Solid waste in rural tourism contains the product of the total amount of a certain waste generated per day and the emissions generated per unit mass of that waste. The evaluation models are built by:

$$C_{gt} = N \times D \times \sum_{i=1}^{n} (G_i \times \delta_i) \quad \ldots(5)$$

In the formula, is the amount of $CO_2$ emitted from tourism solid waste, is the daily per capita production of *i* kinds of waste, kg/day; is the amount of $CO_2$ made by 1kg of *i* kinds of waste stored, kg.

**Emission construction of tourism liquid waste:** The discharge of liquid waste in rural tourism is largely the sewage discharge generated by tourists' accommodation and dining, and the total nitrogen (TN), total phosphorus (TP), chemical oxygen demand (COD), and biochemical oxygen demand (BOD) required to treat the sewage.

$$S_{yt} = (N_z + N_c + N_q) \times \delta_i \quad \ldots(6)$$

In the formula, is the weighted total number of accommodations, person; is the per capita water discharge of accommodation travelers, dining travelers, and other tourists, t/person; is the weighted total number of dining tourists, person; is the weighted total number of other travelers, person; is the total water consumption, t. Integrate with the literature tourism accommodation activities per capita NOX, total phosphorus, chemical oxygen demand, and biochemical oxygen demand are taken as 0.004kg/d, 0.00066kg/d, 0.03759kg/d, 0.00872kg/d, respectively (Meifeng & Jianchao 2012).

## ANALYSIS OF THE PERCENTAGE OF EACH TOURISM SEGMENT

### Fundamental Data

Rural tourism in Zhahan village was initiated in 2012, using the original ecological circumstances and the features of minority resources located in the "ecological environment + folk culture" of rural leisure tourism. Therefore, the first step is to accomplish full ecological tourism to alleviate poverty. Since 2012, Zhahan village has increased from 5 thatched guesthouses built by the village community to several individual guesthouses in 2020, with an average of 1 to 2 spare rooms per family. As a result, under normal conditions, the total number of guesthouses on holidays has around 50 to 60 rooms, with other forms of accommodation through combining cycling, camping, boat-shaped tent houses, and

village buses, which have turned into a tourist fashion in the village.

Based on field survey statistics, the tourism receiving capacity of Zhahan village before the pandemic in 2019 was approximately 130,000 people/times, the total tourism income was more than 10 million, and the annual average occupancy rate of the guesthouse was 58%. As the living standard of people enhances and the connotation construction of rural revitalization deepens, the leisure methods, tourism methods, and tourism activities of rural tourism have been diversified and refined in the past few years, and carbon emissions, energy resource utilization, and consumption have also been diversified and exponentially expanded (Ruiying et al. 2018) influenced by the pandemic, tourism in the village was favored by the province's residents in the first half of 2021, welcoming more than 80,000 visitors of all types. In accordance with the village statistics, merely sightseeing tours and buying agricultural products accounted for 32.2%, cycling, camping, etc., accounted for 28%, accommodation, and leisure tourism accounted for 32%, and others accounted for 7.8%.

## Data Outcome

The annual carbon emission calculations of rural tourism transportation are given in Table 1. The tourist number to the village, except for those who are biking and camping, tourist number by car accounts for 72% of the total tourists. With an average of 4 people per car, there are 28,800 household cars and 115,200 tourists, the annual traffic emissions. Based on the current national six standards for NOx emissions in China, 60 mg/Km for domestic cars, and a 9.5 km length village road, Qiongzhong G224 National Road, from the village entrance to the village cottage.

Table 2 shows the annual carbon emission calculation for rural tourism guesthouses. Combined with Hainan's exceptional climate conditions for weighted estimates, and calculated by utilizing a one horsepower air conditioner 18 h a day in the guesthouse, 60-80L electric water heater 2kW 3 h a day, 70W TV 10 h a day, 100W light 12 h a day, and 100 to 113 guesthouse rooms.

The calculations in Table 3 show that there are 160,000 tourists throughout the year, of which 32.2% are tourists who only sightsee and buy agricultural products, and this group of tourists considers consuming one meal. Biking and camping tourists accounted for 28%, and this part of travelers considered consuming two meals. Tourists for accommodation and leisure tourism accounted for 32%; this part of travelers consider having three meals. Other accounted for 7.8%, considering this part of travelers does

Table 1: Annual carbon emission calculation of rural tourism transportation.

| Transportation | $P_t$ /kg/km | Number of vehicles/unit | $N_t$/person-times | $D_t$/km | $C_{ct}$/kg | $C_{tn}$/kg |
|---|---|---|---|---|---|---|
| Car | 0.133 | 28800 | 115200 | 9.5 | 72777 | 32.8 |

Table 2: Annual carbon emission calculation for rural tourism guesthouses.

| $B$/room | $T$/% | $P$/kWh*room | $H$/% | γ/ kg | $C_{ht}$/kg |
|---|---|---|---|---|---|
| 113 | 58 | 24 | 58.2 | 0.936 | 312758 |

Table 3: Annual carbon emissions calculation for rural tourism's food consumption (Heping et al. 2019, Enter Renaissance Forum 2014, Mengrong et al. 2021).

| Food Category | Per capita Kg/m3 | Emission factor for primary processing/kg | Emission factor for reprocessing/kg | $\Sigma\delta_i$/Kg | $N \times D \times \Sigma(a \times \delta)$/Kg | $C_{fc}$/Kg |
|---|---|---|---|---|---|---|
| Rice, pasta | 0.037 | 0.82 | 0.89 | 0.06 | 646213 | 699308.88 |
| Soybeans | 0.036 | 0.26 | 0.06 | 0.01 | | |
| Pork | 0.08 | 4.25 | 1.11 | 0.38 | | |
| Beef and lamb | 0.11 | 26.14 | 1.11 | 3.00 | | |
| Chicken, duck and goose | 0.13 | 4.25 | 1.11 | 0.70 | | |
| Shrimp | 0.10 | 1.88 | 0.28 | 0.22 | | |
| Fish | 0.11 | 1.88 | 0.28 | 0.24 | | |
| Eggs | 0.25 | 1.14 | 0.70 | 0.46 | | |
| Vegetables | 0.44 | 0.26 | 0.06 | 0.14 | | |
| Vegetable oil | 0.08 | 0.26 | | 0.02 | | |
| Fruits | 0.16 | 0.89 | | 0.20 | | |
| Firewood | 0.65 | 1.87 | | 1.22 | | |
| Natural gas | 0.20 | 2.117 | | 0.42 | *6701.62* | |
| Electricity | 0.5 | 0.936 | | 0.468 | *40655.16* | |

not have meals in the village. Weighted calculation of 83,306 people, an average of 33 people per day per family dining, divided into 17 people each for lunch and dinner (the proportion of rural tourism consumption of breakfast is not high, here, do not do the calculation). With a daily dining time of 3 hours per meal, if 2 to 3 horsepower for air conditioners, rice cookers, cooking, etc., are adopted during meals, the daily electricity consumption for every meal is 14-17 kWh. The villagers of Zhahan village keep cooking with firewood, and more than 80% of the travelers also like to have wood-fired meals. However, firewood's volatile organic compound emission is also quite significant, approaching 115 Kg apart from the carbon emission.

According to Table 4, rural tourism activities comprise sightseeing tours (32.2% of the total annual number of people), adventure activities (28% of the total annual number of people), and other activities (number of people in accommodation + number of people in other activities, 39.8% of the total annual number of people).

Table 5 reveals that among the footprint of tourism activities in Zhahan Village, tourism catering is the most prominent activity in the village in terms of $CO_2$ emissions, accounting for 53.95% of total emissions. Emissions from ingredients account for most of these emissions, largely through electricity, gas, or firewood. Tourist accommodation contributes 24.13%, direct or indirect emissions of waste account for 13.61% of total emissions, and carbon emissions from transportation account for only 5.61%.

According to Table 6, the wastewater discharge of rural tourism accommodation activities is 88.68 $L.d^{-1}$. Due to the overall hotness of the Hainan region, the water consumption of accommodation visitors is higher than the national level, and the average water consumption is 120 $L.d^{-1}$. The per capita sewage discharge in catering activities is 40.95 $L.d^{-1}$ (Hong et al. 2015), estimated here as two meals; the sewage discharge from tourist toilets is 7.54 $L.d^{-1}$ (Ling-yu et al. 2009), which is taken twice. The waste COD is the amount of oxygen used for five days.

Table 4: Annual carbon emissions calculation of other rural tourism activities.

| Number of sightseeing people to total number of tourists (%) | Number of adventure people to total number of tourists (%) | Number of people in accommodation + other as a percentage of the total number of tourists (%) | $CO_2$ emission factor for sightseeing (%) | $CO_2$ emission factor for adventure (%) | $CO_2$ emission factor for accommodation + others (%) | $C_{lc}$ (kg) |
|---|---|---|---|---|---|---|
| 32.2 | 28 | 39.8 | 0.417 | 0.057 | 0.172 | 34990.4 |

Table 5: Annual carbon emissions calculation of rural tourism's solid waste.

| Total number of garbage generators | Total mass of annual garbage [kg] | Emission factor of transported garbage [$kg.t^{-1}$] | Mass of food waste [kg] | Emission factor of food waste/[kg] | The total amount of park waste [kg] | The emission factor of park waste / [kg=] | $C_{lc}$ [kg] |
|---|---|---|---|---|---|---|---|
| 111840 | 391440 | 5.11t | 279600 | 0.44 | 111840 | 0.46 | 176470 |

Table 6: Wastewater waste discharge of rural tourism.

| $N_z$ | $O_z$(t) | $N_c$ | $O_c$(t) | $N_q$ | $O_q$(t) | $C_{yl}$(t) | TN(t) | TP(t) | $COD_5$(t) | BOD(t) |
|---|---|---|---|---|---|---|---|---|---|---|
| 63680 | 0.120 | 83306 | 0.041 | 44800 | 0.015 | 15144 | 56.3 | 9.3 | 2650 | 122.7 |

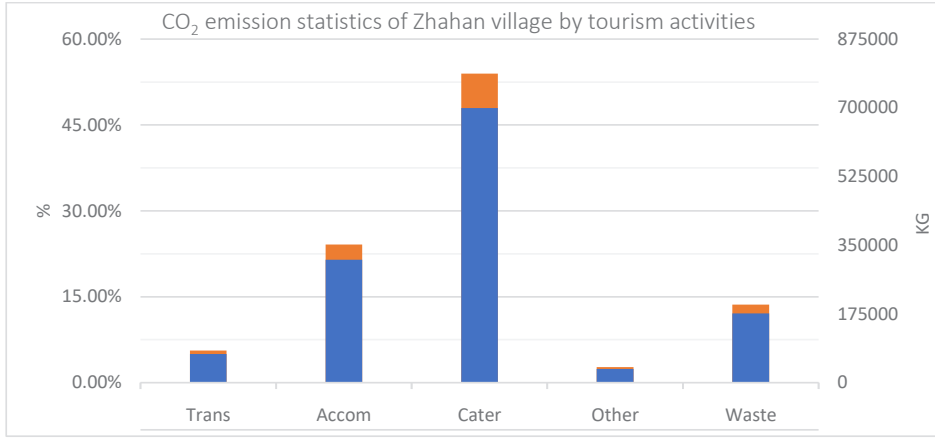


Fig. 1: Comparison of $CO_2$ emissions from tourism activities in Zhahan Village.

## RESULT ANALYSIS OF TOURISM EMISSIONS

### Comparison of $CO_2$ Emissions from Tourism Activities

Through the above precise assessment of tourism activity footprint emissions, Zhahan village emits 1296.3 t of $CO_2$ from tourism waste for transportation, accommodation, catering, and other activities in a year. The comparison of specific tourism activities is depicted in Fig. 1.

Fig. 1 reveals that among the footprint of tourism activities in Zhahan Village, tourism catering is the most prominent activity in the village regarding $CO_2$ emissions, accounting for 53.95% of total emissions. Emissions from ingredients account for most of these emissions, mainly through electricity, gas, or firewood. Tourist accommodation contributes 24.13%, direct or indirect emissions of waste account for 13.61% of total emissions, and carbon emissions from transportation account for only 5.61%.

### Emissions of Nitrogen Oxides and Sewage

Zhahan village welcomes more than 160,000 visitors a year, and the amount of sewage discharged by it amounts to 15,144t. Since a considerable amount of water is discharged, the chemical and biochemical oxygen demand for treating these water resources amount to 2650t and 122.7t. The amount of nitrogen oxides emitted by tourist vehicles is not high, only 32.8kg per year, but nitrogen oxide emitted directly or indirectly by waste is as high as 75.3t.

### Emission Reduction Coupling

With the accelerated development of tourism resources in Zhahan Village, carbon emission is also growing proportionally to overall carbon emission. To determine the issue of high carbon emission of rural tourism in Zhahan village, to preserve the reputation of "heavenly Zhahan" to the maximum extent, and to accomplish the simultaneous development of clear water, lush mountains, tourism, and wealth, it is required to present the planning of energy resource utilization and harmonious development via comprehensive energy analysis of tourism. For this reason, Zhahan village must have a sense of advance in rural revitalization and do well in advance to arrange for neutralization and zero-carbon emission.

They are encouraging the whole village and setting up a 1MW photovoltaic power station and solar water heater. The villagers of each household take out 40 square meters of the roof, and the village collective vacates 2,000 square meters of the public part to plan and construct 1MW solar photovoltaic power station. In this way, the annual power generation capacity is 286,150,000 KWH (Yadong et al. 2020), and $CO_2$ emission reduction is 1434 t, which benefits the villagers on average by about 10,000 yuan, further enhances the quality of rural revitalization and decreases the quality of the entire $CO_2$ emission of tourism activities for a year.

Supervise residents and guesthouses to install solar water heaters. According to the analysis of actual solar water heater energy-saving measurements made by Li Chenyu et al. (2009), the average installation of 10 square solar water heaters per household can generate a 60°C hot water output of approximately 700 L.(Chenyu et al. 2018). In this case, the annual power saving is about 5230 kWh, the annual $CO_2$ emission reduction is 4865 kg, and the annual $CO_2$ emission reduction is 150 t for 30 guesthouses on average.

Scientific planning of rural tourism activities. Launch a parking plant for fuel tour buses and private cars at the village entrance, and organize electric buses to pick up and drop off people to guarantee that the exhaust fumes do not enter the village. Install several electric vehicles charging piles utilizing the village's self-generated electricity to fulfill the village's electric vehicle charging needs. Arrange the gradual transformation of village infrastructure to energy-saving and emission-reducing standards, adapting national characteristics and contemporary atmosphere to low-carbon, energy-saving, and environmental protection. Motivate and direct the restaurant industry to change the concept of applying coal and firewood, and choose more natural gas and electricity to lower the direct impact on the air quality of tourist sites.

Unify action and create a low-carbon brand. Zhahan village is small in area and late in development, and expects to develop tourism development and economy harmoniously through making “carbon neutral” tourism, education theme brand, and demonstration education base. Propose low-carbon evaluation to estimate the village team, villagers, and tourists in an all-around way and encourage rural tourism’s institutionalized and low-carbon development.

## CONCLUSION

Zhahan village is a pearl in the high mountain basin of central Hainan and a direct beneficiary of the construction of China's beautiful countryside and the implementation of comprehensive rural revitalization. Its use of natural resources to raise rural tourism and special agricultural products has enabled the villagers to move from poverty to prosperity. Still, tourism carbon emission is an essential issue that village tourism must encounter.

According to 160,000 tourists in Zhahan village in a year, the carbon emission model created for each link of tourism, the carbon emission of tourism vehicles, tourism accommodation, tourism catering, and other activities in the village is estimated to be 1296.3 t, and the carbon

emission of tourism solid waste is 176 t. The huge sewage discharge in tourism liquid waste is 15144t; tourism catering carbon emission contributes the most significant proportion, which must attract the attention of associated departments.

To accomplish zero carbon emission, every resident of Zhahan village must work together to "create zero carbon emission, and clear water and lush mountains, which are sustainable wealth," and propose to construct "carbon neutral" and create tourism and education theme brands. Subsequently, the entire village will stimulate the solar photovoltaic 1MW power station and the installation of 10 square meters of solar water heaters in guesthouses, which can directly achieve 1,584 tons of emission reduction, thus directly carbon neutralizing the enormous $CO_2$ emissions brought on by the electricity used for accommodation and catering in the village.

A three-dimensional parity system for village cadres, villagers, and tourism is proposed to encourage the institutionalization of rural tourism. It can be replicated and radiated in the province and even in the whole Chinese rural revitalization.

## REFERENCES


Chenyu, L., Haitao, J. and Jian, W. 2018. Comparative analysis of energy-saving between solar water heating system and photovoltaic system. Residential Technology, 38(08): 55-57. doi:10.13626/j.cnki.hs.2018.08.012

China Youth Daily 2021. Qiongzhong Zhahan Village: The Former Poor Village Transformed into “The Most Beautiful Countryside in China “. Retrieved from https://baijiahao.baidu.com/s?id=1705690069544766143&wfr=spider&for=pc.

Chunlin, L. 2018. An empirical study on carbon emission estimation and carbon compensation in rural tourism development taking SongKou village as an example. (Master), Fujian Agriculture and Forestry University, Available from CNKI.

Ecological Civilization Construction 2021. 2020 Clean Energy Power Generation in Hainan’s Industries Above the Size of 8.4% Year-on-year Growth Coal-fired Power Generation Accounted for a Record Low. Retrieved from https://www.sohu.com/a/453310877_99911373

Enter Renaissance Forum 2014. China Sets a Food Consumption Target of 29 kg of Meat Per Capita by 2020 Retrieved from http://news.cntv.cn/2014/02/11/ARTI1392063908521653.shtml

Hainan Lakeview Life 2018. Research Report on the Development of Leisure Agriculture in Zhahan Village, Qiongzhong County. Retrieved from https://zhuanlan.zhihu.com/p/46933501. 2018-10-16

Heping, H., Zhipeng, W. and Yiyao, S. 2019. Carbon footprint and eco-efficiency of rural tourism destination under the background of rural revitalization: A case study of Huangling scenic spot in Wuyuan of Jiangxi Province. Research of Agricultural Modernization, 40(04): pp.683-691.

Hong, Z., Guo-lin, H., Zhen-fang, H., Ye-lin, F. and Wei, T. 2015. Environmental effect of tourism waste in ancient town:case study of Zhouzhuang, Jinxi, Qiandeng. SCIENTIA GEOGRAPHICA SINICA, 35(11): 1419-1428. doi:10.13249/j.cnki.sgs.2015.11.010

Hongxia, Z., Qin, S. and Yuguo, T. 2017. Research progress in energy saving and carbon emission reduction research of the tourist accommodation industry. Progress in Geography, 36(06): 774-783.

Jianhong, X., Aifen, Y. and Min, W. 2011. Carbon footprint evaluation in tours: a case study of Zhoushan Islands. Tourism Science, 25(04): 58-66. doi:10.16323/j.cnki.lykx.2011.04.007

Ling-yu, L., Yan-li, Y. and Pei-dong, Z. 2009. Estimation of $CO_2$ emissions from rural biomass consumption in China. Renewable Energy, 27(02): 91-95. doi:10.13941/j.cnki.21-1469/tk.2009.02.019

Meifeng, Z. and Jianchao, X. 2012. Emissions from the tourism industry and patterns of environmental disturbance in the Liupan mountain eco-tourism area. Resources Science, 34(12): 2418-2426.

Mengrong, Z., Sha, C. and Sumei, L. 2021. A life-cycle-based case study of greenhouse gas emissions and emission reduction from food consumption in Beijing-style restaurants. Advances in Climate Change Research, 17(02): 140-150.

Peihua, S. and Pu, W. 2011. A rough estimation of energy consumption and $CO_2$ emission in tourism sector of China. Journal of Geography, 66(02): 235-243.

Peng, L., Gui-Hua, Y., Biao, Z. and Yi-Qun, Z. 2008. GHG emission-based eco-efficiency study on tourism itinerary products in Shangri-La,Yunnan Province,China. ACTA ECOLOGICA SINICA, (05): 2207-2219.

Ruiying, Z., Jianchao, X., Xinge, W., Zhu, L. and Xianhong, L. 2018. Correlation analysis of economic diversification, peasants’ happiness and their influencing factors in rural tourism area: a case study of Yesanpo tourism destination, China. Power Technology, 34(11): 172-176+236.

Yadong, Z., Shijun, Z., Qiong, L., Jie, Z. and Huijun, C. 2020. Test evaluation and correction of an off-grid photovoltaic system for offshore ice-making vessels. Power Technology, 44(03): 425-428.

Yanyan, S. 2020. Estimation of $CO_2$ emission and its effect decomposition in tourism sector of Shanghai City. Geographical Research and Development, 39(01): 122-126. doi:10.3969/j.issn.1003-2363.2020.01.022

Yingmiaol, J., Yanju, L., Hua, B., Yu, H., Zhizhong, Z. and Peng, W. 2012. Visitor’s carbon footprint of a three-day tour in Hainan. Journal of Hainan Normal University (Natural Science), 25(01): 99-103.

Zeng, L.M. and Wu, Z.W. 2018. Research on the tourism model of poverty alleviation in Hainan-Taking Qiongzhong County Zhahan village as an example. Vacation Tourism, (12): 7-9.

Nature Environment and Pollution Technology
An International Quarterly Scientific Journal

p-ISSN: 0972-6268
(Print copies up to 2016)
e-ISSN: 2395-3454

Vol. 22 | No. 1 | pp. 319-325 | 2023

Original Research Paper

https://doi.org/10.46488/NEPT.2023.v22i01.032

Open Access Journal

# Effect of Geographic Altitude on Carbon Stock in two Physiographic Units of the Reserved Forest of the Universidad Nacional Agraria de la Selva

**M. Reategui***, **D. Reategui****, **E. Morales***(****)†, **R. Reategui***** and **C. Aguirre******

*Escuela Profesional de Ingeniería Ambiental, Universidad Nacional Intercultural de la Selva Central Juan Santos Atahualpa, Av. Perú 612, Pampa del Carmen, Chanchamayo, Perú

**Laboratorio Central de Investigación, Universidad Nacional Agraria de la Selva, Carretera central km 1.2, Tingo María, Perú

***Facultad de Ciencias Naturales y Aplicadas, Universidad Nacional Intercultural Fabiola Salazar Leguía de Bagua (UNIFSLB), Bagua 01721, Perú

****Instituto de Ciencias de Datos, Universidad Nacional de Jaén, Cajamarca, Perú

*****Facultad de Ingeniería, Universidad Nacional Amazónica de Madre de Dios, Av. Jorge Chávez N°1160 - Ciudad Universitaria 2do. Piso Biblioteca Central, Madre de Dios, Perú

******Facultad de Recursos Naturales Renovables, Universidad Nacional Agraria de la Selva, Carretera central km 1.2, Tingo María, Perú

†Corresponding author: E. Morales; emorales@unibagua.edu.pe

**Nat. Env. & Poll. Tech.**
**Website: www.neptjournal.com**

*Received:* 23-07-2022
*Revised:* 12-09-2022
*Accepted:* 15-09-2022

**Key Words:**
Geographic altitude
Above-ground biomass
Carbon stocks
Reserved forest

## ABSTRACT

The objective of the research was to evaluate the effect of geographic altitude on the carbon stock in two physiographic units of the Reserved Forest of the Universidad Nacional Agraria de la Selva, Tingo Maria-Huanuco. The methodology used was the field manual for the remeasurement and establishment of plots of the Amazon Forest Inventory Network (RAINFOR), for which 2 hectares were permanently established (one hectare in low and high hills) in which the diameter (greater than or equal to 10 cm) and the height of the trees were measured. Finally, the density of the wood was obtained from previous studies. The pantropical model formula was used to estimate the carbon stock. The results show that geographic altitude significantly affects carbon stock ($p < 0.05$) in low and high-hill forests, concluding that this may be due to differences in meteorological variables such as precipitation, temperature, and humidity.

## INTRODUCTION

Forests around the world sequester important carbon stocks, which are responsible for carbon fluxes between the land and the atmosphere through photosynthesis and respiration (Jandl 2001, Tipper 1998). Approximately 80% of the total carbon in all terrestrial vegetation is stored in tropical forests (Clark 2007, Gitay et al. 2002, Phillips & Gentry 1994) and is located in stems, branches, leaves, roots, and organic matter (Leith & Whithacker 1975, Raev et al. 1997).

The International Panel on Climate Change - IPCC (1996) estimated in its second assessment report that 60 and 87 gigatons (Gt) of carbon could be conserved or sequestered in forests by 2050 (Yáñez 2004).

Global warming is a priority that today afflicts various countries of the world, which is also reflected in the geographical altitude modifying the temperature, precipitation, humidity, etc., of tropical forests (Pilco 2020).

Peruvian forests are an important carbon reserve at the global level and occupy more than half of the national territory (56.9%), with the Amazon being the region with the largest forest area in the country (94%) (WWF 2021).

**ORCID details of the authors:**

**M. Reategui**
https://orcid.org/0000-0002-5417-6509
**D. Reategui**
https://orcid.org/0000-0001-6689-2345
**E. Morales**
https://orcid.org/0000-0002-8623-3192
**R. Reategui**
https://orcid.org/0000-0003-1532-991X
**C. Aguirre**
https://orcid.org/0000-0003-0683-8675

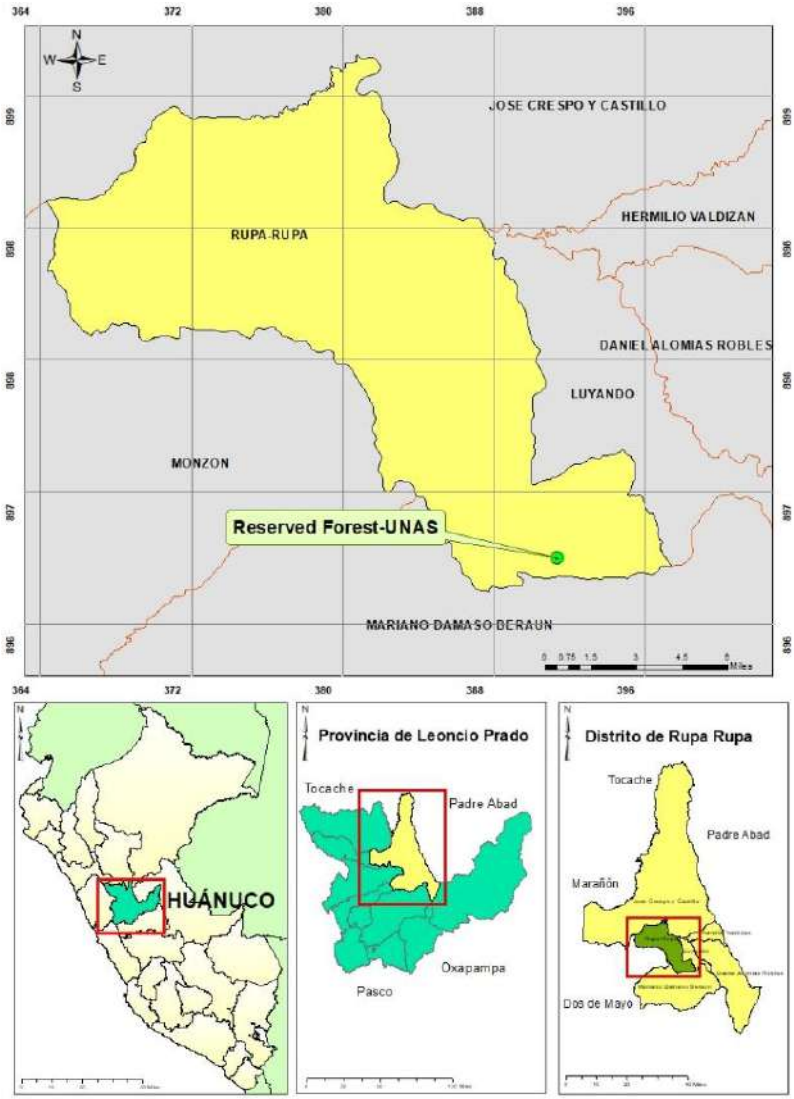


Fig. 1: Map of the location of the Reserved Forest of the Universidad Nacional Agraria de la Selva.

In research carried out between 1983 and 2007 with field data and forest flora inventories, the concentrations of stored carbon were calculated to be between 2.782 and 13.241 megatonnes (Mt) of carbon (Gibbs et al. 2007). On the other hand, in the study of aboveground carbon stored in the Peruvian Amazon, it was reported that the forests with the highest carbon content are located in the lowland and sub-mountain regions of the Amazon (Asner et al. 2014)

Based on the above, the objective of this study was to evaluate the effect of geographic altitude on the carbon stock in two physiographic units of the Reserved Forest of the Universidad Nacional Agraria de la Selva.

## MATERIALS AND METHODS

### Scope of Study

The geographical area was the Reserved Forest of the Universidad Nacional Agraria de la Selva, with an area of 217.22 ha and a perimeter of 6 935.36 m; whose UTM coordinate is 391359 East - 8970535 North Fig. 1, with 667 to 1092 masl (Puerta 2007), in the Department of Huánuco, Province of Leoncio Prado, District of Rupa Rupa, where two physiographic units were identified, low hill and high hill.

### Location and Demarcation of Permanent Plots

The low hill is located at 391084 East, 8970688 North,

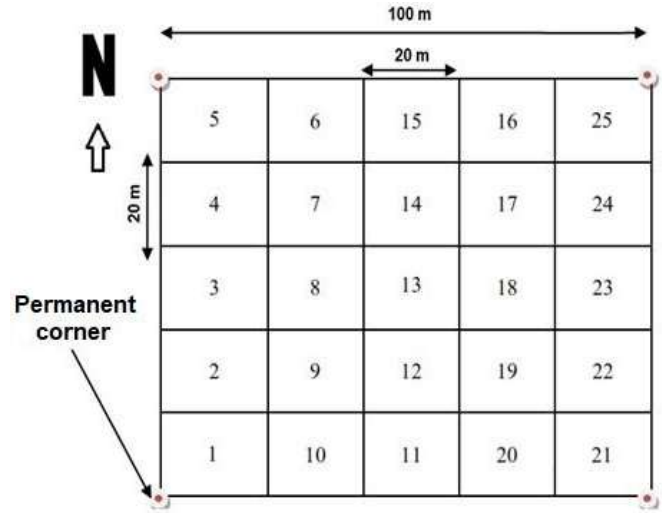


Fig. 2: Subdivision of plots into the low hill and high hill.

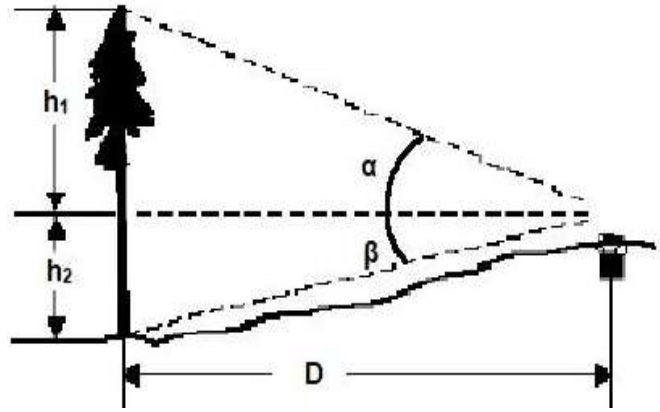


Fig. 3: Tree height measurement in low and high hills; source: Romero (2014).

and 750 meters above sea level, while the high hill is located at 391540 East, 8970335 North, and 900 meters above sea level. For each hill, the area under study was one hectare, where it was divided into 25 subplots of 20 x 20 m Fig. 2.

**Data Collection**

To determine the sample, all trees more significant than 10 cm in diameter at breast height were counted, and the same number of trees was selected for both hills. In this sense, the sample consisted of 512 trees for 1024 trees. The diameter of the trees was measured with a diametric tape. The wood density was obtained from the database of Soto (2016), and the height of the trees was measured using a winch and clinometer Fig. 3, then the height was calculated using the following formula:

$$Ht = D * [\tan(\alpha) + \tan(_{\beta})]$$

Where: Ht = Height of the tree; $\alpha$ = Angle towards the tip of the crown; $\beta$ = Angle towards the base of the tree; D = Distance (15 - 20 m).

**Estimation of the Stock of Aboveground Biomass Stored Per Tree ($AG_{Best}$)**

Using the variables of diameter (D), height (H), and wood-specific density (p), we proceeded to replace the allometric equation for tropical trees, where it obtained a better fit (Chave et al. 2014):

$$AGB_{est} = 0{,}0673 * (pD^2H)^{0{,}976}$$

Where:

p = Wood density ($g.cm^{-3}$); D = Tree diameter (cm); H = Tree height (cm).

The results obtained were expressed in weight units in grams (g) and were therefore converted to tons (t).

Table 1: Sum of measurement variables in low and high hill forests.

| Measurement variables | Low hill (trees) | High hill (trees) |
|---|---|---|
| Density of wood [g.cm$^{-3}$] | 290.669 | 304.175 |
| Tree diameter [cm)] | 10 560.29 | 12 806.05 |
| Tree height [cm] | 849 997.50 | 1 122 254.15 |

### Estimated Biomass Stock Total Stored Area ($AGB_{total}$)

To calculate the total aboveground biomass stored per hectare, all values obtained per tree were summed (Chave et al. 2014):

$$AGB_{total} = \sum_{i}^{n} AGBest/ A$$

Where:

$AGB_{total}$ = Aerial biomass stored per tree (t); A = Plot area (ha)

### Data Analysis

For the normality of the data, the Kolmogorov-Smirnov test was applied, resulting in the distribution not being expected. We proceeded to apply a nonparametric test in function by means of a nonparametric test (Mann-Whitney U) to identify significant differences between data from the plots. The software used was SPSS version 26 (SilvaParra 2018).

## RESULTS

### Carbon Stock

Table 2: Sum of measurement variables in low and high hill forests.

| | | Carbon stock- Lower Hill |
|---|---|---|
| N | | 512 |
| Normal parameters[a,b] | Media | 13049.34 |
| | Deviation | 18097.21 |
| Maximum external differences | Absolute | .255 |
| | Positive | .224 |
| | Negative | -.255 |
| Test statistic | | .255 |
| Asymptotic sign (bilateral) | | .000[c] |

a. The test distribution is normal.
b. Calculated from data
c. Lilliefors significance correction

Table 1 shows the sum of wood densities, diameters, and heights of trees in low and high-hill forests.

Fig. 4 shows that the highest amount of carbon stored is in the high hill forest with 17.07 t/ha, while the lowest value of carbon stored is in the low hill.

### Inferential Analysis

**Normality:** Table 2 shows that $p = 0.00 < p = 0.05$; therefore, the data in low-hill forests do not have a normal distribution. Of the 512 trees, the mean carbon stock was 13049.34 with a standard deviation of 18097.21.

Table 3, which $p = 0.00 < p = 0.05$ therefore, the data

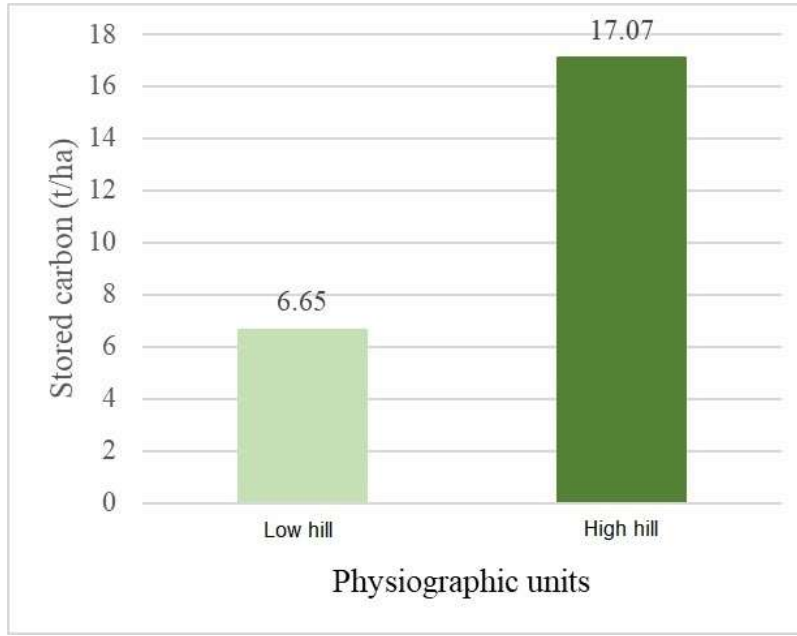


Fig. 4: Carbon stock stored in low and high-hill forests.

Table 3: Kolmogorov-Smirnov normality test for carbon stock in tall hill forest.

| | | Carbon Stock-High Choline |
|---|---|---|
| N | | 512 |
| Normal parameters[a,b] | Media | 33338.99 |
| | Deviation | 80611.43 |
| Maximum external differences | Absolute | .344 |
| | Positive | .287 |
| | Negative | -.344 |
| Test statistic | | .344 |
| Asymptotic sign (bilateral) | | .000[c] |

a. The test distribution is normal.
b. Calculated from data.
c. Lilliefors significance correction.

Table 4: Average rank and the sum of ranks in carbon stock in low and high-hill forests.

| | Altitude | N | Average range | Sum of ranks |
|---|---|---|---|---|
| Carbon Stock | Low hill | 512 | 462.41 | 259877 |
| | High hill | 512 | 619.92 | 317398 |
| Total | | 1074 | | |

in high hill forests do not have a normal distribution. The mean was 33338.99, with a standard deviation of 80611.43.

**Effect of geographic altitude on carbon stock in low and high hill forests:** Table 4, the $p = 0.00 < p = 0.05$; therefore, the geographic altitude in two physiographic units (low and high hill) affects the carbon stock of the Reserved Forests of the Universidad Nacional Agraria de la Selva.

Table 5 shows the carbon stock statistics for the low and high hills with an asymptotic significance of 0.00, which confirms that the carbon stock is a function of the number of trees and altitude.

## DISCUSSION

The carbon stored is related to the tree's species, density, diameter, and height (Cámara-Cabrales et al. 2013). Also, different researchers mention that the carbon content stored varies according to the forest species (Gayoso & Guerra 2005, Martin & Thomas 2011). For this reason, these variables were contemplated for the estimation of carbon.

Table 5: Mann-Whitney U test between carbon stock in low and high-hill forests.

| | Carbon Stock |
|---|---|
| Mann-Whitney U | 101674 |
| Asymptotic sig. | 0.00 |

Esparza & Martínez (2018) found a greater amount of carbon stored in trees with a diameter greater than 31.5 cm. In the same context, Santamaria et al. (2014) and Berenguer et al. (2014) found greater carbon stored in intermediate diameters of 10 - 20 cm and greater than 20 cm. This coincides that the high hill forest's total diameter was 12 806.05 cm compared to the low hill forest's 10 560.29 cm. The high hill forest's carbon stock was also higher at 17.07 $t.ha^{-1}$. As indicated by Sione et al. (2019) and Naji et al. (2013), the larger the diameter of the tree, the greater the amount of carbon stored. This is because the larger the diameter, the greater the availability of water and nutrients for optimal development.

Similarly, trees with greater height have a greater amount of stored carbon (Quiceno et al. 2016). This is reflected in the sum of the heights in high hill forests with 11 222 54.15 cm and stored carbon of 17.07 $t.ha^{-1}$, unlike the low hill forest (936 351.50 cm), which was 6.65 $t.ha^{-1}$. As mentioned by Mendoza-Hernández (2015) and Granado-Victorino et al. (2017), the growth rate in height and diameter of trees is related to the increase in aerial biomass.

On the other hand, the high content of carbon stored in the high-hill forest may be because it has a greater basal area than the low-hill forest. As indicated by Jadan et al. (2017) and Cueva et al. (2019), the geographic altitude increases the density and basal area in the forest. As a result, the aerial biomass increases. Additionally, the difference in carbon stocks among forest species is related to tree diameter, age, wood density, and forest type, among others (Chave et al. 2006, Brown 1997).

Rojas et al. (2019) stated that carbon sequestration in ecosystems is related to the wood's floristic composition, age, and density. On the other hand, Paredes (2018) indicated that the greater the volume and density of wood, the greater the amount of carbon stored in the parts of the trees. The mentioned is related to the sum of the density of wood (304.175 $g.cm^{-3}$) in high hill forests, where it was found greater carbon stored.

The organic carbon in the soil has a proportional relationship with the carbon stored, Leuschner et al. (2013), Mogollón et al. (2015), Echeverria (2017), and Huamán-Carrión et al. (2021) indicated that as the geographical altitude rises, the organic carbon in the soil will increase. This is because there is an increase in precipitation (Díaz 2017) which is essential for developing a forest.

The high-hill forest has had a higher carbon stock, which could be due to its greater abundance and dominance than the low-hill forest (Camones 2014). The results obtained

coincide with Sosa (2016), where he obtained a higher carbon stock in high hill forest with 142.50 $t.ha^{-1}$ and lower stock in low hill forest with 127.62 $t.ha^{-1}$.

Finally, it is necessary to determine the amount of biomass that exists in the tree species, since from these it is possible to calculate the carbon concentration of a forest and thus contribute to the management of natural resources towards sustainable development (Avendaño et al. 2007).

## CONCLUSION

Geographical altitude has an effect on the carbon stock in low and high hills, since the Mann-Whitney U test gave a value of $p = 0.00 < p = 0.05$, which could be due to differences in meteorological variables such as precipitation, temperature, humidity, added to this, the different species that inhabit different areas influencing the density of wood, diameter and height of the tree.

## REFERENCES


Asner, G., Knapp, D., Martin, R., Tupayachi, R., Anderson, C., Mascaro, J. Sinca, F., Chadwick, K., Sousan, S., Higgins, M., Farfan, W., Silman, M., Llactayo, W. and Neyra, A. 2014. The High-Resolution Carbon Geography of Perú. Minuteman Press, Berkeley, CA. 64 p.

Avendaño, H., Acosta, M., Carrillo, A. and Etchevers, B. 2007. Estimation of biomass and carbon in Abies religiosa (HB K) Schl. using allometric equations. Wood Forest, 19(2): 73-86.

Berenguer, E., Ferreira, J., Gardner, T., Aragão, L., De Camargo, P., Cerri, C., Durigan, M., Oliveira, R., Vieira, I. and Barlow, J. 2014. A large-scale field assessment of carbon stocks in human-modified tropical forests. Glob. Change Biol., 20: 3713-3726. https://doi.org/10.1111/gcb.12627

Brown, S. 1997. Estimating Biomass Change of Tropical Forests: A Primer. Forestry Working Paper No. 134. Food and Agricultural Organization, FAO, Rome.

Cámara-Cabrales, L., Arias-Montero, C., Martínez-Sánchez, J. and Castillo-Acosta, O. 2013. Carbon stored in the medium-sized forest of *Quercus oleoides* and plantations of *Eucalyptus urophylla* and *Gmelina arborea* in Huimanguillo, Tabasco. Curr. Knowl. Carbon Cycl. Interact. Mex., 15: 249-256. https://www.researchgate.net/publication/300026552

Camones, J. 2014. Carbon Stock in the Vegetal Component in Different Strata of the Reserved Forest of the Universidad Nacional Agraria de la Selva. Undergraduate Thesis. Institutional Repository. Universidad Nacional Agraria de la Selva.

Chave, J., Muller-Landau, H.C., Baker, T.R., Easdale, T.A., Steege, H.T. and Webb, C.O. 2006. Regional and phylogenetic variation of wood density across 2456 neotropical tree species. Ecol. Appl., 16: 2356-2367. https://doi.org/10.1890/1051-0761(2006)016[2356:RAPVOW]2.0.CO;2

Chave, J., Réjou-Méchain, M., Búrquez, A., Chidumayo, E., Colgan, M, Delitti, W., Duque, A., Eid, T., Fearnside, P., Goodman, R., Henry, M., Martínez-Yrízar, A., Mugasha, W., Muller-Landau, H., Mencuccini, M., Nelson, B., Ngomanda, A., Nogueira, E., Ortiz-Malavassi, E., Pélissier, R., Ploton, P., Ryan, C., Saldarriaga, J. and Vieilledent, G. 2014. Improved allometric models to estimate the aboveground biomass of tropical trees. Glob. Change Biol., 20: 3177-3190. https://doi.org/10.1111/gcb.12629

Clark, D. 2007. Detecting tropical forests responses to global climatic and atmospheric change: Current challenges and a way forward. Biotropica, 39(1): 4-19.

Cueva, E., Lozano, D. and Yaguana, C. 2019. Effect of the altitudinal gradient on the floristic composition, structure, and tree biomass of the Andean dry forest, Loja, Ecuador. Bosque, 40(3): 365-378. https://doi.org/10.4067/S0717-92002019000300365

Díaz, S. 2017. Estimation of stored aerial carbon and its relationship with environmental factors in three Central American forested landscapes. Master's Thesis. Institutional Repository. Tropical Agricultural Research and Higher Education Center (CATIE), Costa Rica.

Echeverria, M. 2017. Determination of the carbon stock in the Igualata-Ecuador páramo. Ph.D. Thesis. Digital Theses Repository. National University of San Marcos, Peru.

Esparza, L. and Martínez, E. 2018. Diversity and carbon stored in the permanent forest area of Álvaro Obregón, Calakmul, Campech. Mex. J. Forest Sci., 9(45): 152-186. https://doi.org/10.29298/rmcf.v9i45.141

Gayoso, J. and Guerra, J. 2005. Carbon content in the aerial biomass of native forests in Chile. Bosque, 26(2): 33-38.

Gibbs, H., Brown, S., Niles, J. and Foley, J. 2007. Monitoring and estimating tropical forest carbon stocks: making REDD a reality. Environ. Res. Lett., 2: 1-13.

Gitay, H., Suárez, A., Watson, R. and Dokken, J. 2002. Climate Change and Biodiversity. Australian National University, Ministry of Science, Technology, and Environment (Cuba), University Corporation for Atmospheric Research and World Bank, Geneva (Switzerland). p. 85.

Granado-Victorino, L., Sánchez-González, A., Martínez-Cabrera, D. and Octavio-Aguilar, P. 2017. Tree structure and composition of three successional stages of sub-evergreen forest in the municipality of Huautla, Hidalgo, Mexico. Mex. Mag. Biodiv., 88: 122-135. https://doi.org/10.1016/j.rmb.2017.01.024

Huamán-Carrión, M., Espinoza-Montes, F., Barrial-Lujan, A. and Ponce-Atencio, Y. 2021. Influence of altitude and soil characteristics on the organic carbon storage capacity of high Andean natural pastures. Agric. Sci., 12(1): 83-90. https://doi.org/10.17268/sci.agropecu.2021.010

Intergovernmental Panel of Climate Change (IPCC). 1996. Report of the Twelfth Session of the Inter-governmental Panel of Climate Change. Reference manual and workbook of the IPCC 1996 revised guidelines for national greenhouse gas inventories. IPCC, Mexico

Jadan, O., Toledo, C., Tepán, B., Cedillo, H., Peralta, Á., Zea, P., Castro, P. and Vaca, C. 2017. Forest communities in high Andean secondary forests (Azuay, Ecuador).. Bosque, 38(1): 141-154. http://doi.org/10.4067/S0717-92002017000100015

Jandl, R. 2001. Measurement of trends in soil carbon storage over time. International Symposium on Measurement and Monitoring of Carbon Sequestration in Forest Ecosystems. Valdivia, Chile.

Leith, H. and Whithacker, R. 1975. Primary Productivity of the Biosphere. Springer-Verlag, New York-USA.

Leuschner, C., Zach, A., Moser, G., Homeier, J., Graefe, S., Hertel, D., Wittich, B., Soethe, N., Lost, S., Röderstein, M., Horna, V. and Wolf, K. 2013. The Carbon Balance of Tropical Mountain Forests Along an Altitudinal Transect. In: Bendix J. (ed), Ecosystem Services, Biodiversity and Environmental Change in a Tropical Mountain Ecosystem of South Ecuador. Springer, Berlin, Heidelberg, pp. 66-115. https://doi.org/10.1007/978-3-642-38137-9_10

Martin, A. and Thomas, S. 2011. A reassessment of carbon content in tropical trees. Plos One, 6(8): e23533. https://doi.org/10.1371/journal.pone.0023533

Mendoza-Hernández, M. 2015. Diameter increase of five tree species with timber potential of the mountain cloud forest in central Veracruz. Doctorate Thesis, Universidad Veracruzana, México.

Mogollón, J., Rivas, W., Martínez, A., Campos, Y. and Márquez, E. 2015. Soil organic carbon in an altitudinal gradient in the Paraguaná Peninsula, Venezuela. Multiciencias, 15(3): 271-280.

Naji, H., Sahri, M., Nobuchi, T. and Bakar, E. 2013. The effect of growth

rate on wood density and anatomical characteristics of Rubberwood (Hevea brasiliensis Muell. Arg.) in two different clonal trails. J. Nat. Prod. Plant Resour., 1(2): 71-80.

Paredes, W. 2018. Structure and Carbon Stock of the Aerial Biomass of A Low Terrace And Low Hill Forest of the Mazán River Basin, Loreto 2018. Undergraduate thesis, Digital File. National University of the Peruvian Amazon, Peru.

Phillips, O. and Gentry A. 1994. Increasing turnover through time in tropical forest. Science, 263: 954-958.

Pilco, L. 2020. The role of Peru's proposals and commitments to the Paris Agreement for the protection of the Amazonian tropical forest in relations with the Kingdom of Norway. Undergraduate Thesis. Institutional Repository. Technological University of Peru, Peru.

Puerta, R. 2007. Digital elevation model of the reserved forest of the Universidad Nacional Agraria de la Selva. Thesis Master of Science in Agroecology Mention Environmental Management. Universidad Nacional Agraria de la Selva, Tingo María, Peru. p. 70

Quiceno, N., Tangarife G. and Álvarez, R. 2016. Estimation of biomass content, carbon sequestration and environmental services, in an area of primary forest in the Piapoco Chigüiro-Chátare indigenous reservation of Barrancominas, Department of Guainía. (Colombia). Luna Azul, 43: 171-202. https://doi.org/10.17151/luaz.2016.43.9

Raev, I., Asan, Ü. and Grozev, O. 1997. Accumulation of $CO_2$ in the above-ground biomass of the forests In Bulgaria and Turkey in the recent decades. Proceed. World Forest. Cong., 1: 131-138.

Rojas, E.P., Silva-Agudelo, E.D., Guillén-Motta, A.Y., Motta-Delgado, P.A. and Herrera-Valencia, W. 2019. Carbon stored in the arboreal stratum of livestock and natural systems of the municipality of Albania, Caquetá, Colombia. Cien. Agric., 16(3): 35-46. https://doi.org/10.19053/01228420.v16.n3.2019.9515

Romero, H. 2004. Methods to Estimate the Height of Trees. https://asignatura.us.es/abotcam/temas/eaa5.jpg

Santamaria, S., Lindner, A. and Ligia, E. 2014. Aboveground biomass and carbon stock of a medium-stature semi-evergreen tropical forest in the Intensive Carbon Monitoring Site of Calakmul-Campeche, Mexico. Thesis of Master. Institute of International Forestry and Forest Products.

Silva-Parra, A. 2018. Modeling soil carbon stocks and carbon dioxide emissions (GHG) in production systems of Plain Altillanura. Meta Colombia, 22(2): 158-171

Sione, S., Andrade-Castañeda, H., Ledesma, S.L.J., Rosenberger, L., Oszust, J. and Wilson, M. 2019. Aerial biomass allometric models for Prosopis Affinis Spreng. in native Espinal forests of Argentina. Rev. Brasil. de Eng. Agríc. Amb., 23(6): 467-473.

Sosa, J. 2016. Economic Valuation of $CO_2$ Sequestration in Three Types of Forests in the District of Alto Nanay, Loreto-Peru-2014. Undergraduate Thesis. Digital Institutional Repository. National University of the Peruvian Amazon, Peru

Soto, L. 2016. Aerial Biomass and Floristic Composition in Two Permanent Measurement Plots (PPM) in the Reserved Forest of the Universidad Nacional Agraria de la Selva. Unpublished Undergraduate Thesis. Universidad Nacional Agraria de la Selva, Tingo María, Peru

Tipper, R. 1998. Update on carbon offsets. Tropical Forest Update, 8(1): 2-5.

World Wildlife Fund (WWF) 2021. Forests and Indigenous Affairs. https://www.wwf.org.pe/nuestro_trabajo/bosques

Yáñez, A. 2004. Carbon sequestration in forests: a tool for environmental management? Gaceta Ecol., 11: 5-18.

Nature Environment and Pollution Technology
An International Quarterly Scientific Journal

p-ISSN: 0972-6268
(Print copies up to 2016)
e-ISSN: 2395-3454

Vol. 22 | No. 1 | pp. 327-338 | 2023

Original Research Paper

https://doi.org/10.46488/NEPT.2023.v22i01.033

Open Access Journal

# Evaluation of the Energy Factor and Equivalent $CO_2$ Gas Emission by Utilization of Industrial By-products in Concrete for Environmental Protection

**B. Saravanan*†, R. Divahar**, S. P. Sangeetha** and M. Bhuvaneshwari*****

*Department of Civil Engineering, Vinayaka Missions Research Foundation, Salem, Tamilnadu, India
**Department of Civil Engineering, Aarupadai Veedu Institute of Technology, Chennai, India
***Department of Civil Engineering, SRM Institute of Science and Technology, Kattankulathur, India
†Corresponding author: B. Saravanan; saravanan.civil@avit.ac.in; sprsaro600@gmail.com

**Nat. Env. & Poll. Tech.**
**Website: www.neptjournal.com**

*Received:* 07-07-2022
*Revised:* 22-08-2022
*Accepted:* 07-09-2022

**Key Words:**
Global warming
Pozzolanic reaction
Red mud
Silica fume
Environmental issues
Binary blended cementitious system
Ternary blended cementitious system

## ABSTRACT

Climate change and global warming are two of the world's most pressing environmental issues. With $CO_2$ being one of the most significant greenhouse gases released into the atmosphere, and cement and concrete manufacturing accounting for roughly 10% of worldwide $CO_2$ emissions, the construction sector must employ an environmentally sustainable substance as a substitute for cement. The $CO_2$ emissions, energy factor, and strength qualities of concrete were investigated. Those negative reaction of conventional cementitious substances is reduced by the development of binary and ternary cementitious systems. In this study, two mineral admixtures obtained from industrial waste substances, red mud (RM) and silica fume (SF), had been used as the alternatives for cement and fine aggregate was fully replaced by manufactured sand (M-sand). An experimental examination of the compressive strength, water absorption, density of concrete, equivalent $CO_2$ emission, and energy factor for environmental benefits with the comparison of RM on SF-based eco-friendly concrete mix of $M_{30}$ grade was used. A binary and ternary blended cementitious system with RM and SM was created with twelve various mix proportions, varying from 0-20% by 5% increases. From the binary blended cementitious system (BBS), based on the observed mechanical characteristic of concrete it was found that the optimum level of RM was 15% and SF was 10 % by the volume of cement. Similarly, for the ternary blended cementitious system (TBS), the level of 10% RM and 10% SF in the cement mixture provides a much higher improvement in compression strength compared to the alternative trials. The negative sign implies that replacing cement with RM and SF reduces energy consumption (-1.91% to -6.97%) and $CO_2$ emissions (-4.52% to -16.16%). The use of mineral admixtures such as RM and SM in supplementary cementitious materials results in a significant outcome and potential impact on the production of sustainable concrete that addresses environmental issues.

## INTRODUCTION

A developing country like India requires enormous development of large infrastructural facilities which requires concreting for the infrastructural developments such as bridges, roads, and buildings. Concrete is a heterogeneous construction material formed by mixing cement and aggregates in the right amount of water to create a composite composition, that hardens with time. Consumption of concrete across the globe crosses 5.5 billion tonnes a year. The two main ingredients in concrete are cement and fine aggregates. Usually, a mix ratio is set at 15 to 20% of water, 60 to 75% aggregates, and 10 to 15% of cement. (Metilda et al. 2015, Venu Malagavelli et al. 2018). To lessen the $CO_2$ emissions brought on by the manufacture of portland cement and the significant demand for river sand. For sustainable construction, alternative materials must be found and used in concrete instead of fine aggregate and cement.

The cement industries are working on a sustainable approach to production to address environmental issues. Cost and energy-intensive aspects are issues in the manufacture of Portland cement. However, the main issue nowadays is that large amounts of greenhouse gases are produced, which have a negative impact on the environment. Several methods, substitutions, and supplements were used to lessen the use of portland cement (Kothai & Malathy 2015, Ushaa et al. 2015).

Additionally, within the forthcoming decade, as the construction intensity is at a very high level, the traditional fine aggregate, which was more suited to concrete, is anticipated to lose favor due to cost. As this anticipation of the proposed scarcity and unavailability of the natural fine

aggregate (sand) is highly expected, M-sand could be the best alternative in the case that it satisfies the basic requirements to adapt to the concrete such as workability and strength (Verma et al. 2015, Mane et al. 2019, Nataraja et al. 2014).

Cement replaced partially with different percentages of Red mud, fly ash, Silica fume, GGBS, and metakaolin in the experimental concrete mix resulted in significant cost savings and the elimination of greenhouse gas emissions. (Anantha Lakshmi et al. 2016, Tanu & Sujatha 2022, Satyendra et al. 2015, Azad et al. 2021).

Red mud (RM) is a solid waste from bauxite ore processing with caustic soda to produce alumina ($Al_2O_3$). It increases the initial cement strength and sulfate attack resistance. Amorphous silicon dioxide and necessary fineness generate silica fume (SF), also known as micro silica, a highly reactive pozzolanic substance. SF is produced during the melting process used to produce silicon and ferrosilicon. M-sand is created by breaking down rock deposits into fine aggregate; it often has an angular form and size, a rougher surface, and a high concentration of microfine. In this investigation, binary and ternary cementitious systems were used to determine the performance of concrete, including silica fume and red mud substituted completely for fine aggregate in favor of M-Sand in the binary and ternary blends with regular portland cement.

Red mud was substituted for cement in concrete in various amounts during experiments, and it was found that 12.5% substitution provided the best compressive, flexural, and tensile strength. The findings show that red mud recycling can be employed in large-scale construction to reduce the financial and environmental costs associated with the production and use of conventional cement (Nenadovic et al. 2017, Shetty et al. 2014, Venkatesh et al. 2019). The workability was reduced while adding red mud which was rectified with the use of a super plasticizer (Al Menhosh et al. 2018, Ribeiro et al. 2012).

The compressive strength of the mix is significantly altered when cement containing a variable amount of silica fume is substituted. The required guarantee for employing silica fume to consistently replace cementitious pozzolanic components in concrete is provided by the larger improvements in average strength with 10% silica fume (Sobolev 2004, Wild et al. 1995, Behnood & Ziari 2008, Mazloom et al. 2004, Wong & Razak 2005). They concluded that, at room temperature, silica fume-containing concrete was significantly stronger than OPC concrete (Koksal et al. 2008, Bentur & Goldman 1989, Almusallam et al. 2004, Babu & Babu 2003). Similarly to this, the impact of silica fume on concrete's tensile strength at 28 days of age was examined (Hooton 1999, Bhanja & Sengupta 2005, Tanyildizi & Coskun 2008). They concluded that the silica fume-based concrete mixes will improve the tensile strength at the split. As a result, the environmental problems caused by the manufacturing and use of conventional cement will be resolved by this alternative cementitious material (Vivek et al. 2014).

Due to the rapid increase in construction activity and the need for construction materials, natural river sand has become scarce. As a result, a suitable substitute material that satisfies the necessary physical and mechanical requirements is needed. High tensile strength, high compressive strength, and high stiffness are characteristics of concrete that have had M-sand partially replaced; as a result, the concrete has a higher elastic modulus and less ductility (Weiguo et al. 2016, 2017 & 2018).

The objective of this research is to evaluate the mechanical properties of concrete and identify the optimum replacement % of silica fume and red mud with partially replacement cement and fully replacement M-sand with fine aggregate in concrete added with silica fume and red mud by its density of concrete, compressive strength, water absorption, equivalent $CO_2$ emission and energy factor for environmental benefits.

## MATERIALS AND METHODS

### Binder

The binder in concrete utilized for casting the requisite grade was OPC (53 grade). It confirms the specifications of IS: 12269 (1987), and its properties are given in Table 1.

### Coarse Aggregate (CA)

Locally available Coarse aggregate used in the study of 20 mm size as per IS 383:1970. Some preliminary tests were done and their properties are described in Table 2.

Table 1: Physical properties of cement (53 grade).

| Characteristics | Experimental Values |
|---|---|
| Soundness | 1.2 mm |
| Specific gravity | 3.15 |
| Initial setting time | 50 min |
| Final setting time | 320 min |
| Consistency | 32% |
| Compressive strength (MPa) | 31.2 at 28 days |

Table 2: Physical properties of CA.

| Physical properties | Experimental Values |
|---|---|
| Surface Texture | Smooth |
| Specific gravity | 2.8 |
| Water absorption | 3.5% |
| Fineness modulus | 6.67 |
| Impact Value | 14.2 |

Table 3: Physical properties of M-sand.

| Physical properties | Experimental Values |
|---|---|
| Size, micron | 0.1 |
| Surface area, $m^2.kg^{-1}$ | 20,000 |
| Specific gravity | 2.2 |
| Bulk density, $kg.m^{-1}$ | 576 |

## Water

Potable tap water was used to prepare and harden the concrete.

## Manufactured Sand

As an alternative fine aggregate material, localized M Sand was used, which was tested for gradation and fineness according to IS: 383-1970 and the properties listed in Table 3.

## Super Plasticizer

CONPLAST SP 430 was used as a water-reducing agent to achieve the necessary workability based on a new generation of modified sulfonated naphthalene polymers.

## Red Mud

Red mud is a byproduct of the process used to make aluminum from its ore. The color of the resulting mud is determined by the original ore's makeup, or by the combination of minerals and bauxite. Fig. 1 shows the sample of mineral admixtures.

## Silica Fume

The particle structure of the silica fume is very fine spheres and the chemical contents are high amorphous

(a) Red mud (b) Silica fume

Fig. 1: Sample of mineral admixtures.

Table 4: Chemical and physical composition of Red mud.

| Chemical Composition (%) | | Physical Possessions | Outcomes |
|---|---|---|---|
| $SiO_2$ | 3-50 | Partial Size Distribution (in micrometer) | |
| $Na_2O$ | 4-4.5 | D10 | 1.641 |
| $Al_2O_3$ | 10-20 | D50 | 14.41 |
| $Fe_2O_3$ | 30-60 | D90 | 62.458 |
| $TiO_2$ | 2.5-.3.5 | Specific Gravity($g.cm^{-3}$) | 2.51 |
| LOl | 11-15 | Fineness ($cm^2.gm^{-1}$) | 1000-3000 |
| CaO | 1.5-2.5 | pH | 10.5-12.5 |

Table 5: Chemical and physical composition of silica fume.

| Chemical Composition (%) | | Physical Possessions | Outcomes |
|---|---|---|---|
| $SiO_2$ | 92.1 | | |
| MgO | 0.3 | Particle Size (typical) | <1µm |
| $Al_2O_3$ | 0.5 | Specific Surface Area ($cm^2.gm^{-1}$) | 2.22<br>13000-30000 $m^2.kg^{-1}$ |
| $Fe_2O_3$ | 1.4 | Bulk Density ($kg.m^{-3}$)<br>Specific Gravity | 450<br>2.22 |
| $SO_3$ | - | | |
| LOl | 2.8 | | |
| CaO | 0.5 | | |
| $Na_2O$ | 0.3 | | |
| $K_2O$ | 0.7 | | |

silicon dioxide. Small amounts of oxides of alkali metals, magnesium, and iron are also found. The physicochemical composition of red mud and silica fume is given in Table 4 and Table 5.

## Experimental Investigation

### *Mix Proportioning*

An M30 grade mix of concrete (1:1.765: 3.14) that complies with IS 10262:2009 codal provision was created. Based on different trial mixes with changing percentages of 0.25%, 0.5 %, 0.75 %, and 1 % of chemical admixture by the weight of cementitious material, the optimum dose of chemical admixture to be utilized in concrete is found.

### *Mix Preparation*

The OPC, Red Mud, Silica fume, Coarse aggregate, and M-sand, are mixed with the designed proportion with power mixers thoroughly for 30 seconds in dry condition. Water cement ratio (0.4) and superplasticizer (1%) are added in portions in accordance with the design mix after the dry materials have been combined to create the concrete mixes. Tables 6 and 7 show the binary and ternary blended systems of mineral admixtures respectively.

### *Casting and Curing of Moulds*

With the prepared concrete mix, 108 binary and ternary cementitious concrete specimens were cast in the size of standard concrete cubes, cylinders, and prisms in accordance with IS456:2000. The concrete specimens are dried in the curing tank at a constant temperature of 27°C for various lengths of time, including 7, 14, and 28 days. The casting, curing, and testing of specimens are shown in Fig. 2.

Table 6: Percentage of Red Mud (RM) and Silica Fume (SF) in BBS for kg for 1-$m^3$ concrete

| Mix ID | Factors | | M-Sand | CA | Water | Cement | Workability [mm] |
|---|---|---|---|---|---|---|---|
| | RM [%] | SF [%] | [kg.$m^{-3}$] | [kg.$m^{-3}$] | [kg.$m^{-3}$] | [kg.$m^{-3}$] | |
| RM0SF0 | 0 | 0 | 695 | 1254 | 157.6 | 435.00 | 85 |
| RM5SF0 | 5 | 0 | 695 | 1254 | 157.6 | 413.25 | 78 |
| RM10SF0 | 10 | 0 | 695 | 1254 | 157.6 | 391.50 | 76 |
| RM15SF0 | 15 | 0 | 695 | 1254 | 157.6 | 369.75 | 76 |
| RM20SF0 | 20 | 0 | 695 | 1254 | 157.6 | 348.00 | 74 |
| RM0SF5 | 0 | 5 | 695 | 1254 | 157.6 | 413.25 | 80 |
| RM0SF10 | 0 | 10 | 695 | 1254 | 157.6 | 391.50 | 78 |
| RM0SF15 | 0 | 15 | 695 | 1254 | 157.6 | 369.75 | 75 |
| RM0SF20 | 0 | 20 | 695 | 1254 | 157.6 | 348.00 | 72 |

Table 7: Percentage of Red Mud (RM) and Silica Fume (SF) in TBS kg for 1-$m^3$ concrete.

| Mix ID | Factors | | M-Sand | CA | Water | Cement | Workability (mm) |
|---|---|---|---|---|---|---|---|
| | RM [%] | SF [%] | [kg.$m^{-3}$] | [kg.$m^{-3}$] | [kg.$m^{-3}$] | [kg.$m^{-3}$] | |
| RM5SF15 | 5 | 15 | 695 | 1254 | 157.6 | 391.50 | 80 |
| RM10SF10 | 10 | 10 | 695 | 1254 | 157.6 | 348.00 | 76 |
| RM15SF5 | 15 | 5 | 695 | 1254 | 157.6 | 304.50 | 72 |

Fig. 2: Casting, curing, and testing of concrete specimen.

## RESULTS AND DISCUSSION

### Workability

In the context of concrete technology, "workability" refers to the characteristics of concrete that make it simple to lay, compact, and finish concrete. The slump cone test measures the workability of fresh concrete. Table 6 and Table 7 represent the slump characteristics of various combinations of concrete mixes.

### Compressive Strength

The average compression strength of concrete cubes tested after 7, 14, and 28 days of curing is shown in Tables 8 and 9.

The compressive strength test results of the BBS with red mud and silica fume replacement are presented in Fig. 3.

At 28 days after being compressed, concrete in a BBS with 5%, 10%, 15%, and 20% red mud replacement (RM5SF0, RM10SF0, RM15SF0, and RM20SF0, respectively) had compressive strengths that were 1%, 7%, 10%, and 3% higher than those of the control mix (RM0SF0). Similarly, specimens with silica fume demonstrated a 2% lower compressive strength than the control mix during a 28-day compression test of concrete with 5% silica fume substitution (RM0SF5) than the control mix (RM0SF0). However, 10%, 15%, and 20% silica fume substitution (RM0SF10, RM0SF15, and RM0SF20) produced compressive strengths that were 7%, 1%, and 0.5% greater than the control mix (RM0SF0), respectively.

In TBS, at 28 days of compression testing of concrete with 5% RM and 15% SF, 10% of both RM & SF, 15% RM and 5% SF replacement (RM5SF15, RM10SF10 & RM15SF5) gave 4%, 15% and 9% higher compressive strength than the control mix (RM0SF0). The compressive strength test findings for red mud and silica fume in the TBS are shown in Table 9 and Fig. 4.

Table 8: Compressive strength of BBS.

| Mix ID | Average Compressive Strength [Mpa] | | | Compressive strength variation as a percentage when compared to the control mix after 28 days |
|---|---|---|---|---|
| | $7^{th}$ | $14^{th}$ | $28^{th}$ | |
| | Days | | | |
| RM0SF0 | 21.98 | 27.22 | 32.80 | - |
| RM5SF0 | 22.14 | 27.43 | 33.05 | 1% |
| RM10SF0 | 23.42 | 29.01 | 34.95 | 7% |
| RM15SF0 | 24.16 | 29.93 | 36.06 | 10% |
| RM20SF0 | 22.55 | 27.93 | 33.65 | 3% |
| RM0SF5 | 21.47 | 26.6 | 32.05 | -2% |
| RM0SF10 | 23.42 | 29.01 | 34.95 | 7% |
| RM0SF15 | 22.15 | 27.44 | 33.06 | 1% |
| RM0SF20 | 21.88 | 27.10 | 32.65 | 0.5% |

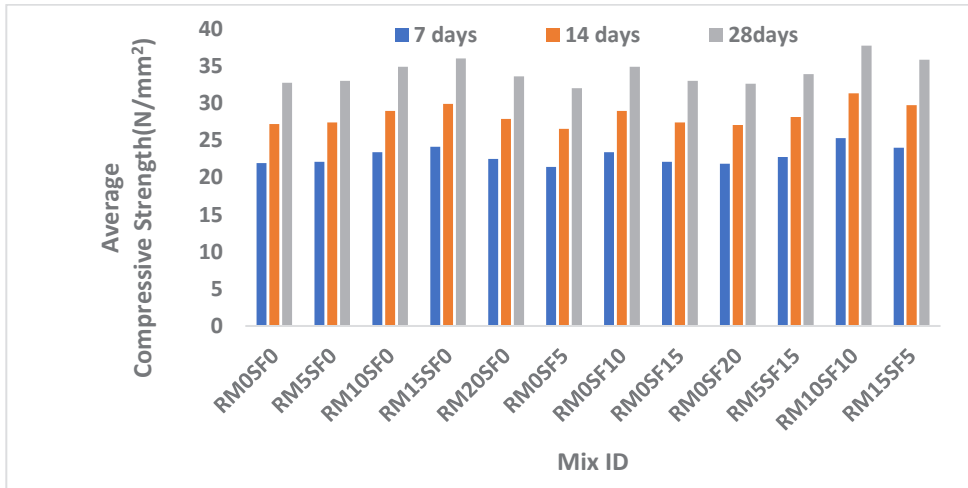


Fig. 3: Compressive strength comparison with BBS.

The mixtures with 15% red mud and 10% silica fume replacement have the highest compressive strengths (RM15SF0 & RM0SF10). Red mud speeds up the pozzolanic reaction between cementitious ingredients because of its high alkalinity (pH > 12) character (cement and red mud). The strength of the concrete was seen to decrease after the replacement of 10% silica fume and 15% red mud, but it was not lower than usual concrete mixtures. The concrete compressive strength decreased at a red mud replacement level of 20% due to insufficient cement hydration caused by the greater red mud and silica fume concentration. Metilda et al. (2015) provided a similar defense; red dirt has a large specific surface area in the concrete mix that absorbs more water, resulting in a lack of water for adequate cement hydration.

**Water Absorption (WA)**

Due to its porosity, concrete absorbs water, and the amount of water absorption is directly inversely proportional to the volume of pore space. Water absorption tests are carried out in line with IS 1124-1974, a standard test technique for water absorption, to get the parameter. A concrete test sample with dimensions of 150x150x150 mm and a replacement percentage of pozzolanic red mud and silica fume materials ranging from 0% to 20% were selected for testing and weighed before submersion in water. After that, the test sample spends 24 hours submerged in distilled water. After a predetermined age of curing for 7, 14, and 28 days, a water absorption test was performed. The specimen's weight before immersion is recorded as W1, and its weight following water immersion is recorded as W2. The percentage of water absorption $W_A$ is calculated by Equation (1).

$$\mathbf{WA(\%)} = \frac{(\boldsymbol{W2} - \boldsymbol{W1})}{\boldsymbol{W1}} \times \mathbf{100} \quad \ldots(1)$$

Where WA is the percentage of water absorption and W1 and W2 are the sample's initial weights before and after a 24-hour immersion, respectively.

At 7 days, concrete with 5%, 10%, 15%, and 20% replacement of red mud (RM5SF0, RM10SF0, RM15SF0, and RM20SF0, respectively) had water absorption that was 3.8%, 3.5%, 3%, and 2.5% higher than the control mix (RM0SF0). Similar to this, concrete with 5%, 10%, 15%, and 20% substitution of red mud (RM5SF0, RM10SF0, RM15SF0, and RM20SF0, respectively) over 28 days

Table 9: Compressive strength of TBS.

| Mix ID | Average Compressive Strength [MPa] | | | Compressive strength variation as a percentage when compared to the control mix after 28 days |
|---|---|---|---|---|
| | 7th | 14th | 28th | |
| | Days | | | |
| RM0SF0 | 21.98 | 27.22 | 32.80 | - |
| RM5SF15 | 22.77 | 28.20 | 33.98 | 4% |
| RM10SF10 | 25.33 | 31.37 | 37.80 | 15% |
| RM15SF5 | 24.05 | 29.80 | 35.90 | 9% |

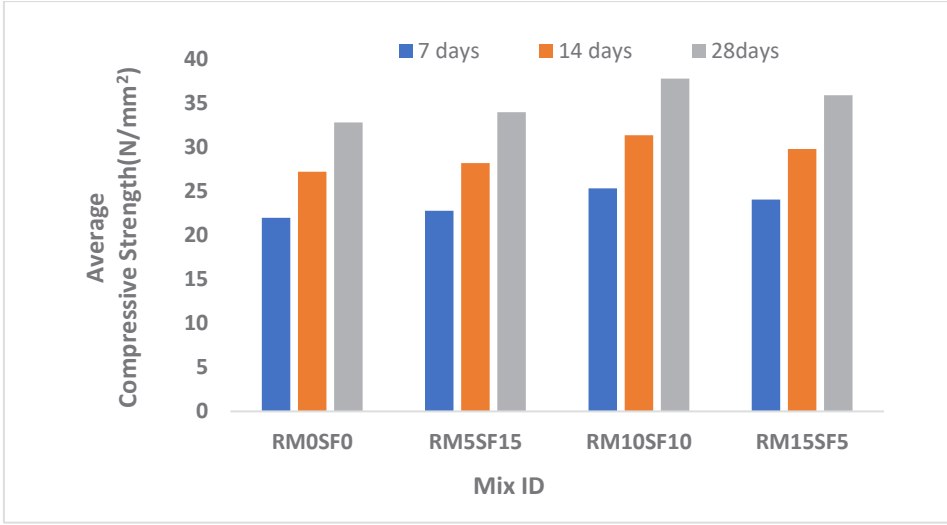


Fig. 4: Compressive strength comparison with TBS.

showed water absorption that was 3.6%, 2.5%, 2.6%, and 2.0% higher than the control mix (RM0SF0). Additionally, concrete 5%, 10%, 15%, and 20 % replacement of silica fume (RM0SF5, RM0SF10, RM0SF15, and RM0SF20) at 7 days had water absorption that was, correspondingly, 3.7%, 3.1%, 2.7%, and 2.3% higher than the control mix (RM0SF0). Similar to this, concrete with replacements of 5%, 10%, 15%, and 20% of silica fume (RM0SF5, RM0SF10, RM0SF15, and RM0SF20) over 28 days showed water absorption that was 3.2%, 2.9%, 2.5%, and 2.0% higher than the control mix (RM0SF0), respectively.

In a TBS, at 7 days concrete with 5% RM and 15% SF, 10% of both RM & SF, 15% RM, and 5% SF replacement (RM5SF15, RM10SF10, & RM15SF5), respectively, had water absorption that was 2.4%, 3.2%, and 3.0% higher than the control mix (RM0SF0). In a similar, concrete with 5% RM and 15% SF, 10% of both RM & SF, 15% RM, and 5% SF replacement (RM5SF15, RM10SF10, & RM15SF5), showed increased water absorption than the control mix by 2.2%, 3.0%, and 2.8% after 28 days (RM0SF0). The binary and ternary blend binder system shown in Tables 10 and 11 and Figs. 5 and 6 was replaced by the water absorption test findings for red mud and silica fume in the binary and ternary blended cementitious system.

The findings show that the values for water absorption decrease as curing age and replacement level increase. Red mud also increases pozzolanic activity later in life; this reduces connections between pores. Red mud's fineness (average particle size: 14 m), which seals all pores and microcracks in the concrete, is another factor that lowers water absorption. Due to its huge specific surface area, red mud and silica fume can reduce the amount of water that concrete absorbs. Nenadovic et al. (2017) provided a similar explanation, stating that the larger Ca $(OH)_2$ crystals were fractured into several smaller crystals and less orientated during the hydration process of red mud-based cement, which minimizes pore

Table 10: Water absorption of BBS.

| Mix ID | The initial weight of the sample before immersion, W1 [kg] | Weight of the sample after 24 hours immersion, W2 [kg] | | | Percentage of water absorption, $W_A$ [%] | | |
|---|---|---|---|---|---|---|---|
| | | $7^{th}$ | $14^{th}$ | $28^{th}$ | $7^{th}$ | $14^{th}$ | $28^{th}$ |
| | | Days | | | Days | | |
| RM0SF0 | 8.950 | 9.00 | 8.98 | 8.94 | 6.2 | 5.7 | 5.2 |
| RM5SF0 | 8.624 | 8.95 | 8.94 | 8.93 | 3.8 | 3.7 | 3.6 |
| RM10SF0 | 8.509 | 8.83 | 8.82 | 8.81 | 3.5 | 3.0 | 2.5 |
| RM15SF0 | 8.412 | 8.66 | 8.65 | 8.63 | 3.0 | 2.8 | 2.6 |
| RM20SF0 | 7.963 | 8.16 | 8.14 | 8.12 | 2.5 | 2.25 | 2.0 |
| RM0SF5 | 8.524 | 8.87 | 8.86 | 8.84 | 3.7 | 3.4 | 3.2 |
| RM0SF10 | 8.420 | 8.68 | 8.67 | 8.66 | 3.1 | 3.0 | 2.9 |
| RM0SF15 | 8.135 | 8.35 | 8.34 | 8.33 | 2.7 | 2.6 | 2.5 |
| RM0SF20 | 7.863 | 8.04 | 8.03 | 8.01 | 2.3 | 2.15 | 2.0 |

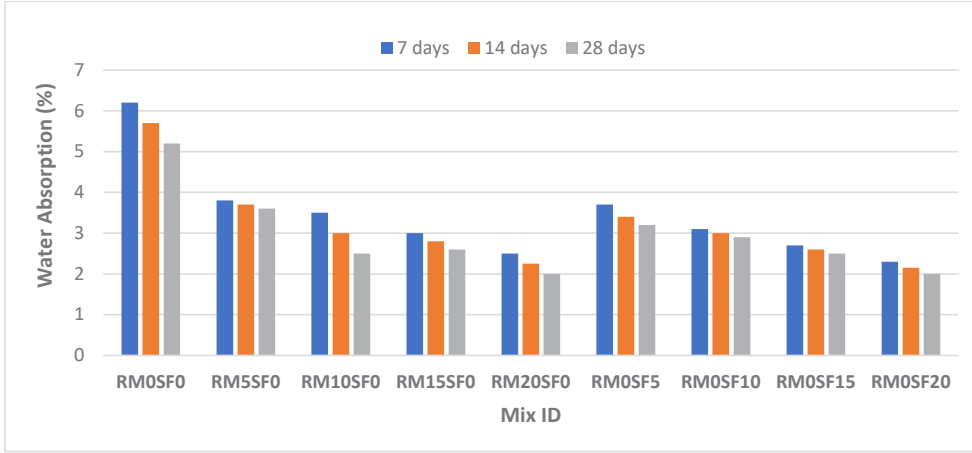


Fig. 5: Water absorption comparison with BBS.

Table 11: Water absorption of TBS.

| Mix ID | The initial weight of the sample before immersion, W1 [kg] | Weight of the sample after 24 hours immersion, W2 [kg] | | | Percentage of water absorption, $W_A$ [%] | | |
|---|---|---|---|---|---|---|---|
| | | $7^{th}$ | $14^{th}$ | $28^{th}$ | $7^{th}$ | $14^{th}$ | $28^{th}$ |
| | | Days | | | Days | | |
| RM0SF0 | 8.95 | 9.0 | 8.98 | 8.94 | 6.2 | 5.7 | 5.2 |
| RM5SF15 | 8.10 | 8.29 | 8.28 | 8.27 | 2.4 | 2.3 | 2.2 |
| RM10SF10 | 7.98 | 8.23 | 8.22 | 8.21 | 3.2 | 3.1 | 3.0 |
| RM15SF5 | 7.85 | 8.08 | 8.07 | 8.06 | 3.0 | 2.9 | 2.8 |

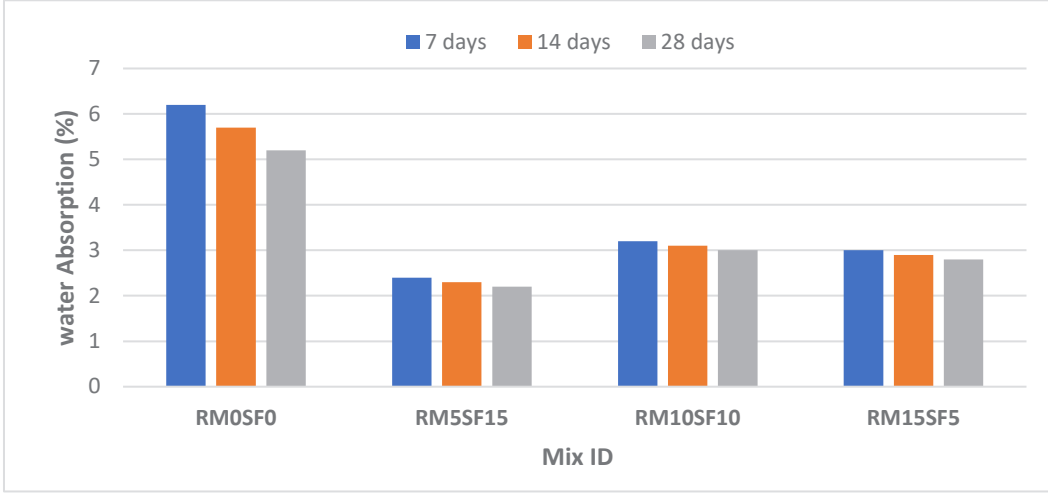


Fig. 6: Water absorption comparison with TBS.

connections and water absorption. Due to the impact of the pozzolanic and micro filler, the water absorption values of the concrete mixtures replaced with silica fume decreased as the amount of silica replacement increased.

## Density of Concrete

Concrete density is a measurement of its weight. Based on its determined value of density, concrete is classified as either lightweight or regular weight. Getting the parameter is necessary. A concrete specimen of the M30 grade with dimensions of 150x150x150 mm and silica fume materials substitution percentage ranging from 0% to 20% was selected for testing. The specimen was weighed before being submerged in water to represent weight. The density is then calculated taking into account the concrete specimen's volume. Equation (2) is used to determine the density of concrete.

$$\rho = \frac{Mass\ of\ Concrete\ Specimen}{Volume\ of\ Concrete\ Specimen}\ [kg/m3] \qquad \ldots(2)$$

The control mix (RM0SF0) in a BBS reached a maximum density of 2651.85 $kg.m^{-3}$. Red mud and silica fume were used in place of cement, which reduced density. Fresh concrete densities decreased for 5%, 10%, 15%, and 20% red mud replacement (RM5SF0, RM10SF0, RM15SF0, and RM20SF0) mixes compared to control concrete by 3.61%, 4.9%, 5.98%, and 11%, respectively. For 5%, 10%, 15%, and 20% of silica fume replacement (RM0SF5, RM0SF10, RM0SF15, and RM0SF20) mixes were found to be 4.73%, 5.89%, 9.08%, and 12.12% respectively. Similarly, in TBS, the density of concrete with 5% RM and 15% SF, 10% of both RM & SF, 15% RM and 5% SF replacement (RM5SF15, RM10SF10 & RM15SF5) mixes was found to be 9.47%, 10.8%, and 12.26%, respectively. Because density depends on specific gravity, there has been a drop in density. The control mix has the highest density because cement has higher specific gravity than red mud and silica fume. The binary and ternary blend binder system depicted in Tables 12 and 13 and Figs. 7 and 8 were replaced by the concrete density test findings for red mud and silica fume in the binary and ternary blended cementitious system.

## Equivalent $CO_2$ Gas Emission and Energy Factor

Compared to cement production, RM and SF production emits less $CO_2$ into the atmosphere. The $CO_2$ emissions

Table 12: Mass, volume and density of BBS.

| Mix ID | Mass of Concrete Specimens [kg] | The volume of Concrete Specimen [$m^3$] | The density of Concrete [$kg.m^{-3}$] |
|---|---|---|---|
| RM0SF0 | 8.95 | 0.003375 | 2651.85 |
| RM5SF0 | 8.624 | 0.003375 | 2555.25 |
| RM10SF0 | 8.509 | 0.003375 | 2521.18 |
| RM15SF0 | 8.412 | 0.003375 | 2492.44 |
| RM20SF0 | 7.963 | 0.003375 | 2359.40 |
| RM0SF5 | 8.524 | 0.003375 | 2525.62 |
| RM0SF10 | 8.42 | 0.003375 | 2494.81 |
| RM0SF15 | 8.135 | 0.003375 | 2410.36 |
| RM0SF20 | 7.863 | 0.003375 | 2329.77 |

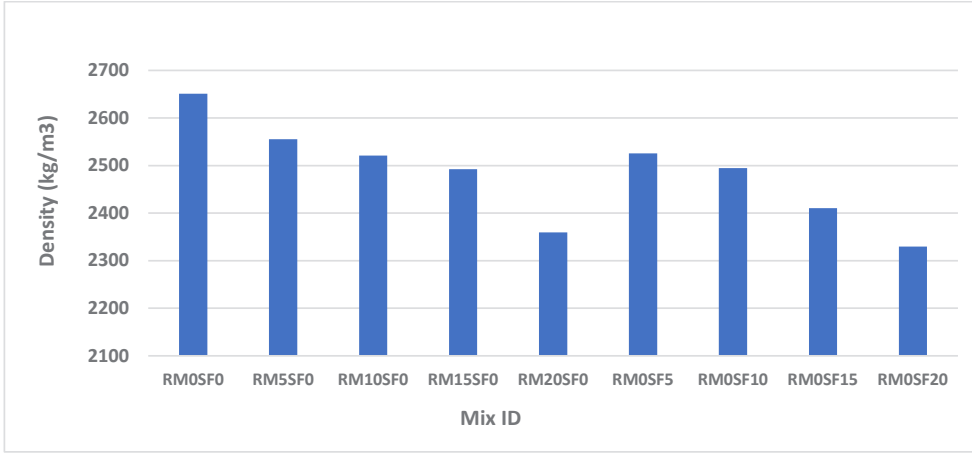


Fig. 7: Density of concrete comparison with BBS.

Table 13: Mass, volume and density of TBS.

| Mix ID | Mass of Concrete Specimens [kg] | Volume of Concrete Specimen [$m^3$] | Density of Concrete [$kg.m^{-3}$] |
|---|---|---|---|
| RM0SF0 | 8.95 | 0.003375 | 2651.84 |
| RM5SF15 | 8.10 | 0.003375 | 2399.99 |
| RM10SF10 | 7.98 | 0.003375 | 2364.44 |
| RM15SF5 | 7.85 | 0.003375 | 2325.92 |

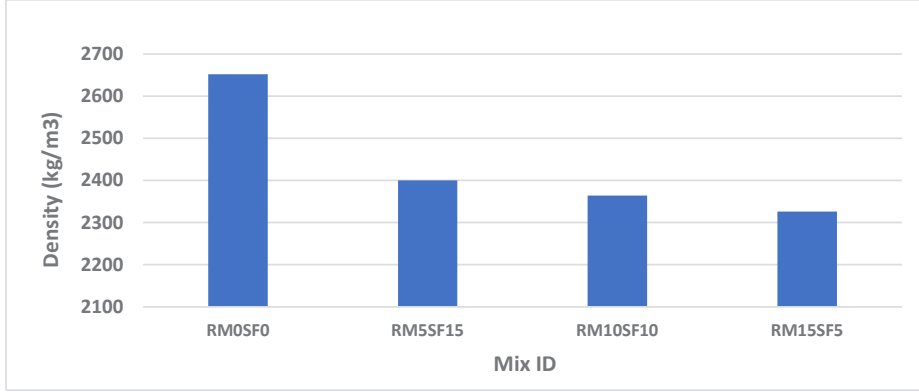


Fig. 8: Density of concrete comparison with TBS.

from the manufacturing of RM and SF (100 kg of $CO_2$ for every ton of RM produced and 14 kg of $CO_2$ for every ton of SF produced) are caused by the extraction of raw materials and the kiln, not by a chemical reaction (dehydroxylation). However, the decarboxylation of calcium carbonate during cement manufacturing results in the release of $CO_2$ (1 ton of cement produced equals 521.5 kg of $CO_2$; 1 ton of cement produced equals 478.5 kg of $CO_2$; Additionally, RM and SF demand less thermal energy during manufacture than cement (1 ton of RM produced needs 1.70 GJ) and SF (1 ton of RM produced needs 0.24 GJ) than the cement (1 ton of cement produced needs 4.65 GJ) (Kelechi et al. 2022, Cassagnabere et al. 2010).

Without taking into account the transportation of raw materials, carbon dioxide ($CO_2$) emission is calculated based on chemical reactions and energy consumption to manufacture 1 ton of cement and RM with SF, calculated as reported by Cassagnabere et al. (2010).

The emission of $CO_2$ and Energy saved were calculated as follows in Equations (3) & (4):

$$\textbf{Energy saved (\%)} = \frac{Ei - Eo}{Eo} \times 100 \quad \ldots(3)$$

Where,

$E_o$ = Consumption of energy in control mix (RM0SF0)

$E_i$ = Consumption of energy in binary and ternary cementitious systems.

$$\textbf{CO}_2\textbf{ Emission (\%)} = \frac{Ci - Co}{Co} \times 100 \quad \ldots(4)$$

Where,

$C_o$ = Emission of $CO_2$ by control mix (RM0SF0)

$C_i$ = Emission of $CO_2$ by binary and ternary cementitious systems.

The emission of $CO_2$ and Energy saved was calculated for all binary and ternary cementitious systems and control mix using Equations 3 & 4. Fig. 9 presents the values of energy consumption and $CO_2$ release into the atmosphere. The environmental balance for the binders (cement + RM + SF) based on the $CO_2$ emission and energy requirement is also presented in Table 14.

The negative sign implies that replacing cement with RM and SF reduces energy consumption (-1.91% to -6.97%) and $CO_2$ emissions (-4.52% to -16.16%). The result shows that the maximum replacement of RM with SF provides a positive environmental effect and saves raw materials consumption.

## CONCLUSION

The results of an experimental investigation using red mud and a silica fume mineral additive to create binary and ternary blended cementitious systems. According to a study on compressive strength, the ideal proportion of red mud and silica fume in cement was 15% by volume and 10%. Similar results were found for the ternary blended system, where the replacement of 10% red mud and 10% silica fume combination produced the maximum compressive strength in comparison to all other combinations,

- The Compressive strength parameters showed that RM15SF0 and RM15SF5 give 10% and 9% higher than the control mix (RM0SF0) respectively. Red mud

Table 14: Environmental balance of binary and ternary cementitious systems based on the emission of $CO_2$ and energy saved for $1m^3$ of concrete.

| Mix ID | Energy (GJ) | | | | $CO_2$ Emission ([g] | | | | | | | Environmental benefit regarding | |
|---|---|---|---|---|---|---|---|---|---|---|---|---|---|
| | | | | | Extraction & Kiln | | | Chemical reaction | | | Total | Energy [%] | $CO_2$ emission [%] |
| | OPC | RM | SF | Total | OPC | RM | SF | OPC | RM | SF | | | |
| RM0SF0 | 2.34 | 0.00 | - | 2.34 | 239.3 | 0 | 0 | 260.8 | 0 | 0 | 500.10 | | |
| RM5SF0 | 2.22 | 0.43 | - | 2.65 | 227.3 | 2.5 | - | 247.7 | 0 | 0 | 477.50 | -1.91 | -4.52 |
| RM10SF0 | 2.11 | 0.85 | - | 2.96 | 215.3 | 5 | - | 234.7 | 0 | 0 | 455.00 | -2.82 | -9.02 |
| RM15SF0 | 1.99 | 1.28 | - | 3.27 | 203.4 | 7.5 | - | 227.5 | 0 | 0 | 438.40 | -4.32 | -12.34 |
| RM20SF0 | 1.87 | 1.70 | - | 3.57 | 191.1 | 10 | - | 220.3 | 0 | 0 | 421.43 | -7.76 | -15.73 |
| RM0SF5 | 2.22 | - | 0.060 | 2.28 | 227.3 | - | 0.35 | 247.7 | 0 | 0 | 475.35 | -1.65 | -4.95 |
| RM0SF10 | 2.11 | - | 0.119 | 2.23 | 215.3 | - | 0.7 | 234.7 | 0 | 0 | 450.70 | -2.12 | -9.88 |
| RM0SF15 | 1.99 | - | 0.179 | 2.17 | 203.4 | - | 1.05 | 227.5 | 0 | 0 | 431.95 | -2.87 | -13.63 |
| RM0SF20 | 1.87 | - | 0.238 | 2.11 | 191.1 | - | 1.4 | 220.3 | 0 | 0 | 412.83 | -4.58 | -17.45 |
| RM5SF15 | 1.87 | 0.43 | 0.179 | 2.47 | 191.1 | 2.5 | 1.05 | 220.3 | 0 | 0 | 414.98 | -5.38 | -17.02 |
| RM10SF10 | 1.87 | 0.85 | 0.119 | 2.84 | 191.1 | 5 | 0.7 | 220.3 | 0 | 0 | 417.13 | -6.17 | -16.59 |
| RM15SF5 | 1.87 | 1.28 | 0.060 | 3.20 | 191.1 | 7.5 | 0.35 | 220.3 | 0 | 0 | 419.28 | -6.97 | -16.16 |

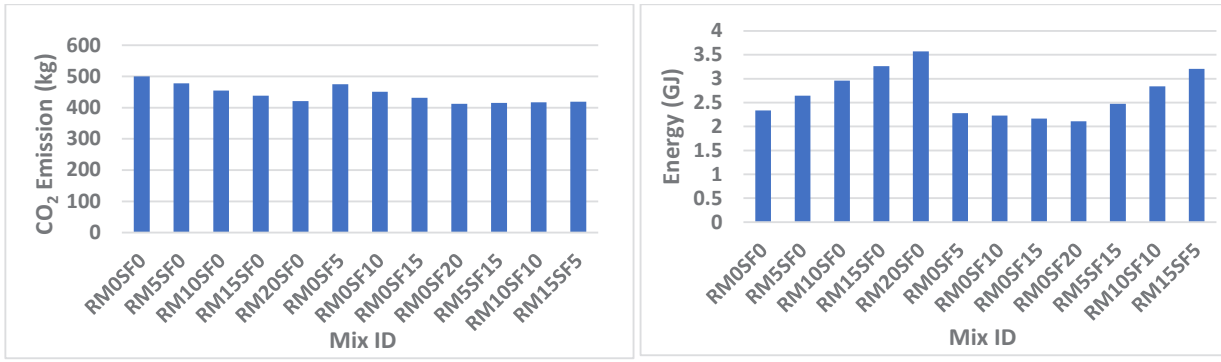


Fig. 9: Comparison of equivalent $CO_2$ emission of binary and ternary blended systems.

speeds up the pozzolanic reaction between cementitious ingredients because of its high alkalinity (pH > 12) nature.

- Due to the pozzolanic and micro filler effects, concrete specimens absorb less water. The water absorption values of concrete mixtures containing silica fume decreased as the amount of silica replacement increased.
- The concrete density revealed that the relationship between density and specific gravity is what causes the decrease in density. The control mix has the highest density because cement has higher specific gravity than red mud and silica fume.
- Equivalent $CO_2$ emission and energy factor with a negative sign indicate that RM and SF replace cement in a way that reduces both energy use (-1.91 to -6.97%) and $CO_2$ emissions (-4.52 to -16.16%). The outcome demonstrates that substituting RM with SF as much as possible has a favorable impact on the environment and reduces the use of raw materials.
- A pozzolanic substance with strong reactivity is silica fume. Due to its roughness and high content of amorphous silica content and red mud, a higher specific surface area accelerated the setting process and reduced the pozzolanic. By reducing porosity through the production of C-S-H gel, the combined effect of silica fume and red mud will obtain distinctive materials that will improve workability, strength, and higher chemical attack resistance.
- As the results found encouraging the utilization of red mud and silica fume can be applied in large-scale construction to compensate for the environmental and economical drags imposed by conventional cement production and usage. Therefore, red mud and silica fume are suggested for the creation of environmentally friendly, cost-effective, sustainable, and concrete with low $CO_2$ emissions, which will be especially useful today as the world is confronting the difficulties of global warming.

## REFERENCES

Venkatesh, C., Nerella, R. and Chand, M.S.R 2020. Experimental investigation of strength, durability, and microstructure of red-mud concrete. J. Korean Ceram. Soc., 174-167 :57.

Shetty, K.K., Nayak, G. and Vijayan, V. 2014. Effect of red mud and iron ore tailings on the strength of self-compacting concrete. Eur. Sci. J., 10(21): 168-176.

Metilda, D.L., Selvamony, C., Anandakumar, R. and Seeni, A. 2015. Investigations on the optimum possibility of replacing cement partially with red mud in concrete. Sci. Res. Essays., 10(4):137-143.

Nenadovic, S., Mucsi, G., Kljajevic, L., Mirkovic, M., Nenadovic, M., Kristaly, F. and Vukanac, I. 2017. Physicochemical, mineralogical, and radiological properties of red mud samples as secondary raw materials. Nucl. Technol. Radiat. Prot., 32(3): 261-266.

Menhosh, A,A., Wang, Y., Wang, Y. and Nelson, L.A. 2018. Long-term durability properties of concrete modified with metakaolin and polymer admixture. Constr. Build. Mater., 172: 41-51.

Ribeiro, D.V., Labrincha, J.A. and Morelli, M.R. 2012. Effect of red mud addition on the corrosion parameters of reinforced concrete evaluated by electrochemical methods. IBRACON Struct. Mater. J., 5(4): 451-467.

Tanu, H.M. and Sujatha, U. 2022. Utilization of industrial and agricultural waste materials for the development of geopolymer concrete- A review. Mater. Today: Proc., 4: 192. https://doi.org/10.1016/j.matpr.2022.04.192.

Azad, N.M., Samindi, S.M. and Samarakoon, M.K. 2021. Utilization of industrial by-product /waste to manufacture geopolymer cement/ concrete. Sustainability, 13(2): 873. https://doi.org/10.3390/su13020873.

Anantha Lakshmi, K., Anvesh Reddy, I.S. and Sai Kumar, A.V.S. 2016. Strength characteristics of concrete with partial replacement of cement with fly ash & metakaolin. Int. J. Innov. Sci. Res. Technol., 1(7): 18-22.

Satyendra, D., Rajiv, C. and Yadav, R.K. 2015. Experimental study of concrete with metakaolin as partial replacement of OPC. Int. J. Adv. Eng. Res. Sci., 2(6): 38-40.

Venu Malagavelli., Srinivas Angadi., Prasad, J.S.R. and Joshi, S. 2018. Influence of metakaolin in concrete as partial replacement of cement. Int. J. Civ. Eng. Technol., 9(7): 105-111.

Kothai, P. S. and Malathy, R. 2015. Effective utilization of wastes from steel industries in concrete. Nat. Environ. Pollut. Technol., 14(2): 419-422.

Mane, K.M., Kulkarni, D.K. and Prakash, K.B. 2019. Properties and microstructure of concrete using pozzolanic materials and manufactured sand as partial replacement of fine aggregate. SN Appl. Sci., 1: 1025.

Nataraja, M.C., Manu A.S. and Girih, G. 2014. Utilization of different types of manufactured sand as fine aggregate in cement mortar. Indian Concr J., 88(1):19-25.

Verma, K. and Pajgade, P.S. 2015. Effect of partial replacement of natural sand with crushed sand along with supplementary cementing materials (fly ash and GGBS). Int. J. Res. Eng. Technol., 4(1): 288-292.

Almusallam, A.A., Beshr, H., Maslehuddin, M. and Al-Amoudi, O.S.B. 2004. Effect of silica fume on the mechanical properties of low-quality coarse aggregate concrete. Cem. Concr. Comp., 26(7): 891-900.

Babu, K.G. and Babu, D.S. 2003. Behaviour of lightweight expanded polystyrene concrete containing silica fume. Cem. Concr. Comp. Res., 33(5): 755-762.

Behnood, A. and Ziari, H. 2008. Effects of silica fume addition and water-to-cement ratio on the properties of high-strength concrete after exposure to high temperatures. Cem. Concr. Comp., 30(2): 106-112.

Bentur, A. and Goldman, A. 1989. Curing effects, strength, and physical properties of high strength silica fume concrete. J. Mater. Civil Eng., 1(1): 46-58.

Bhanja, S. and Sengupta, B. 2005. Influence of silica fume on the tensile strength of concrete. Cem. Concr. Comp. Res., 35(4): 743-747.

Hooton, R.D. 1993. Influence of silica fume replacement of cement on physical properties and resistance to sulfate attack freezing and thawing, and alkali-silica reactivity. ACI Mater. J., 90(2): 143-52.

Koksal, F., Altun, F., Yigit, I. and Sahin, Y. 2008. Combined effect of silica fume and steel fiber on the mechanical properties of high-strength concretes. Constr. Build. Mater., 22(8): 1874-1880.

Mazloom, M., Ramezanianpour, A.A. and Brooks, J.J. 2004. Effect of silica fume on mechanical properties of high-strength concrete. Cem. Concr. Comp., 26(4): 347-357.

Sobolev, K. 2004. The development of a new method for the proportioning of high-performance concrete mixtures. Cem. Concr. Comp., 26(7): 901-907.

Tanyildizi, H. and Coskun, A. 2008. Performance of lightweight concrete with silica fume after high temperature. Constr. Build. Mater., 22(10): 2124-2129.

Wild, S., Sabir, B.B. and Khatib, J.M.1995. Factors influencing strength development of concrete containing silica fume. Cem. Concr. Res., 25(7): 1567-1580.

Wong, H.S. and Razak, H.A. 2005. Efficiency of calcined kaolin and silica fume as a cement replacement material for strength performance. Cem. Concr. Comp. Res., 35(4): 696-702.

Needhidasan, S., Ramesh, B. and Prabu, S.J.R. 2020. Experimental study on use of E-waste plastics as coarse aggregate in concrete with manufactured sand, Mater. Today Proc., 22(3): 715-721.

Weiguo, S., Yi, L., Zhongwen, W., Lianghong, C., Dingle, W., Yujie, W. and Xiaoli, J. 2018. Influence of manufactured sand's characteristics on its concrete performance. Constr. Build. Mater., 172: 574-583.

Weiguo, S., Zhenguo, Y., Lianghong, C., Liu, C., Yi, L., Hui, Y., Zili, L. and Jian, Bai. 2016. Characterization of manufactured sand: Particle shape, surface texture, and behavior in concrete, Constr. Build. Mater., 114: 595-601.

Weiguo, S., Yi, L., Lianghong, C., Xujia, H., Zhenguo, Y., Congcong, Zhou., Pengtao, H. and Zili, Lu. 2017. Mixing design and microstructure of ultra-high strength concrete with manufactured sand, Constr. Build. Mater., 143: 312-321.

Ushaa, T.G., Anuradha, R. and Venkatasubramani, G.S. 2015. Reduction of greenhouse gases emission in self compacting geopolymer concrete using sustainable construction materials. Nat. Environ. Pollut. Technol., 14(2): 451-454.

Vivek, S., Kumar., A. and Agarwal, S. K. 2014. Comparative Hydration Behavior of Metakaolin-Microfine System. J. Eng. Comp. Appl. Sci., 3(4): 60-65.

Cassagnabere, F., Mouret, M., Escadeillas, G., Broilliard, P and Bertrand, A. 2010. Metakaolin a solution for the precast industry to limit the clinker content in concrete: Mechanical aspects. Constr. Build. Mater., 24(7): 1109-1118.

Kelechi, S.E., Adamu, M., Mohammed, A., Obianyo, I.I., Ibrahim, Y.E. and Alanazi, H. 2022. Equivalent $CO_2$ Emission and cost analysis of green self-compacting rubberized concrete. Sustainability., 14: 137.

Nature Environment and Pollution Technology
An International Quarterly Scientific Journal

p-ISSN: 0972-6268
(Print copies up to 2016)
e-ISSN: 2395-3454

Vol. 22 | No. 1 | pp. 339-353 | 2023

Original Research Paper

https://doi.org/10.46488/NEPT.2023.v22i01.034

Open Access Journal

# Vulnerability of Mangroves to Changing Coastal Regulation Zone: A Case Study of Mandovi and Zuari Rivers of Goa

**T. V. Deshpande*† and P. Kerkar****

*Department of Geography, Rosary College of Commerce and Arts, Navelim, Goa

**Department of Geography, Government College of Arts, Science and Commerce, Khandola, Marcela, Goa

†Corresponding author: T. V. Deshpande tanvi@rosarycollege.org

**Nat. Env. & Poll. Tech.**
**Website: www.neptjournal.com**

*Received:* 21-07-2022
*Revised:* 11-10-2022
*Accepted:* 17-10-2022

**Key Words:**
Coastal Regulation Zone
Mangroves
Land use land cover
Geographic information system

## ABSTRACT

Goa is a coastal State located on the west coast of India, known for its pristine sandy beaches and environment. Ministry of Environment and Forest implemented Coastal Regulation Zone Notification in 1991 for monitoring the coastal zones for unplanned developmental activities but has been just for name-sake purposes (Mascarenhas 1999, Agarwal 2019). The regulation has been changed in recent years thereby making the coastal and the riverine ecosystem more vulnerable to human interference. In the name of development, various hap-hazardous, unplanned activities have taken place which is degrading the coastal and riverine environment, especially mangroves. This paper studies the vulnerability of mangroves to the changing regulations with respect to 1991 and the 2018 CRZ notifications considering the land use land cover changes in the regulated zones of Mandovi and Zuari rivers. Spatial analysis techniques and software such as Arc GIS 10.3, and ERDAS IMAGINE 2014 have been used for analysis and results. The findings from the study can be effectively implemented in monitoring the regulated zones and protecting mangroves efficiently.

## INTRODUCTION

### Coastal Regulation Zone

The Ministry of Environment and Forest issued the Coastal Zone Regulation notification under the Environment Protection Act of 1986. The main purpose of issuing the notification was to regulate, minimize and protect the sensitive coastal environment from unplanned human interference (Mascarenhas 1999). The Government of India declared the coastal stretches of seas, bays, estuaries, creeks, rivers, and backwaters as CRZ. These areas are influenced by tidal action (on the landward side) up to 500 meters from the High Tide Line (Ministry of Environment and Forests 1991).

India adopted formal Coastal Regulation Zone legislation in the year 1991 which was the first specialized step to control the unsustainable activities around the coastal zones (Agarwal 2019). It identified the necessity to protect the interests of millions of people along the coastal areas of India while ensuring their overall development and protecting fragile coastal ecology (Agarwal 2019).

**ORCID details of the authors:**

**T. V. Deshpande**
https://orcid.org/0000-0003-2237-6968
**P. Kerkar**
https://orcid.org/0000-0002-0405-0131

However, the Coastal Regulation Zone notifications were further modified and revised in the years 2011 and 2018. As per the 2011 CRZ Notification, the coastal areas from High Tide Line to 500 meters on the landward side and the land area between High Tide Line to 100 meters along the tidal-influenced water bodies that are connected to the sea are declared as protected under Coastal Regulation Zone (CRZ Notification 2011).

As per the recent implementation of the CRZ Notification of 2018, the CRZ shall apply to the land area between High Tide Line to 50 meters of the coast or the width of the creek, influenced by tidal action (CRZ Notification 2018). With the new CRZ Notification of 2018, the coastal areas will be heavily impacted by numerous unsustainable developmental activities that will lead to tragedy and imbalance in the ecological system if due care is not taken (Dhargalkar & Kavlekar 2019).

### Mangroves

Mangroves are salt-tolerant plants commonly found in tropical and sub-tropical regions located in intertidal zones

either as narrow strips or as extensive patches (Ajai et al. 2013). Kathiresan & Rajendran (2005), stated mangroves are the only forest situated at the convergence zone of land and sea. The mangrove ecosystem plays a very important role in terms of ecology and economy (Kamboj & Das 2019).

India is among the 17 mega biodiversity countries in the world, well known for its terrestrial, coastal, and marine biodiversity (Saravanan et al. 2013). India is home to a diversity of coastal and marine ecosystems including mangrove forests (DasGupta & Shaw 2013a). Mangroves are found along the 7516.6 kilometers of coastline of India including the islands (Sahu et al. 2015). India has the fourth largest mangrove area in the world occupying 0.14% of the country's land area (Sahu et al. 2015, Saddhe et al. 2016, Basha 2018).

The mangrove cover in Goa is approximately 0.5% of the total mangrove cover of India (Mesta et al. 2014). As per the recent data published by the India State of Forest Report (2021), Goa has a mangrove cover of 27 $km^2$. Mangroves are found along the estuaries of Terekhol, Chapora, Mandovi, Zuari, Sal, Talpona, Galgibag, and Cumbarjua canal (Singh et al. 2004).

### Land Use Land Cover (LULC)

Land use land cover conversion refers to the process of transformation of land cover to land use and change in land uses from one type to another in periodical time due to natural or anthropogenic activities (Kaliraj et al. 2017). Butt et al. (2015), stated that it is essential to study change analysis for a better understanding of the relationship between human activities and natural phenomena. Land use land cover change detection has become a significant necessity for developing efficient strategies for managing natural resources monitoring environmental changes and planning policy in various coastal areas (Muttitanon & Tripathi 2005, Kaul & Ingle 2012, Islam et al. 2016). Monitoring the land use land cover change along the Coastal Regulation Zone (CRZ) areas is essential for understanding the existing status of ecologically sensitive areas to protect the ecosystems from damaging activities (Shaji et al. 2017).

Remote sensing and Geographic Information System (GIS) provide efficient tools for ecosystem and socio-economic management (Haque & Basak 2017). Misra & Balaji (2015), stated that these tools provide unique opportunities for building information sources and support in decision-making activities for various coastal zone applications. Remote sensing data is a very useful source of information as it provides up-to-date and complete coverage of any area and is proven useful in assessing and monitoring land use land cover changes (Muttitanon & Tripathi 2005). To manage and protect the coastal environment from further exploitation, land use land cover changes must be studied.

The present study is carried out to understand the vulnerability of mangroves to changing CRZ limits. The objective of the paper is to study the changes in land use land cover along the Zuari and Mandovi rivers (including Cumbarjua Canal) using remote sensing data and geospatial techniques.

## STUDY AREA

Goa, a coastal State on the Western Coast of India lies between 1455°' N to 1545°' N and 7440°' E to 7410°' E (Nagi et al. 2014). Numerous estuaries in Goa, namely Terekhol, Chapora, Mandovi, Zuari, Sal, Talpona, and Galgibag support mangroves. Mandovi estuary has luxuriant mangrove growth in its 68 kilometers length estuarine channel. Cumbarjua Canal is 15 kilometers long and joins Mandovi and Zuari estuaries and is commonly called as "Mandovi-Zuari-Cumbarjua estuarine complex" (Nagi et al. 2014). Most of the mangroves in Goa are fringing mangroves bordering the estuaries and creeks (Jagtap et al. 2001, Mesta et al. 2014).

The major mangrove formations are along the Mandovi, Zuari, and Cumbarjua estuaries comprising almost 80% of the total mangrove cover in Goa (Mesta et al. 2014). There are 16 true mangrove species in Goa belonging to 11 genera and 7 families. Amongst all these estuaries, Mandovi River has the most number of mangrove species in Goa (Ragavan et al. 2016). *Avicennia*, *Sonneratia* and *Rhizophora* species dominate the Mandovi-Zuari-Cumbarjua estuarine complex (Ajai et al. 2013). Fig. 1 represents a map of the study area.

## MATERIALS AND METHODS

In the current study, both primary and secondary data were utilized. The primary data includes ground-truthing through field visits. However, a major part of the study is based on secondary data sources which include satellite imageries of different periods. For analysis, geospatial software such as ArcGIS 10.3 and ERDAS IMAGINE 2014 software were used.

LANDSAT satellite images are used to classify and map the land use land cover changes within the CRZ using geospatial techniques. LANDSAT 4-5 TM and LANDSAT 8 OLI images of the years 1991 and 2018 of 30 m resolution each and Survey of India (SOI) topographic maps of 1:50,000 scale are used to derive necessary data for analysis. Both the rivers including Cumbarjua Canal are demarcated up to the tidal influence using the toposheets as shown in Fig.

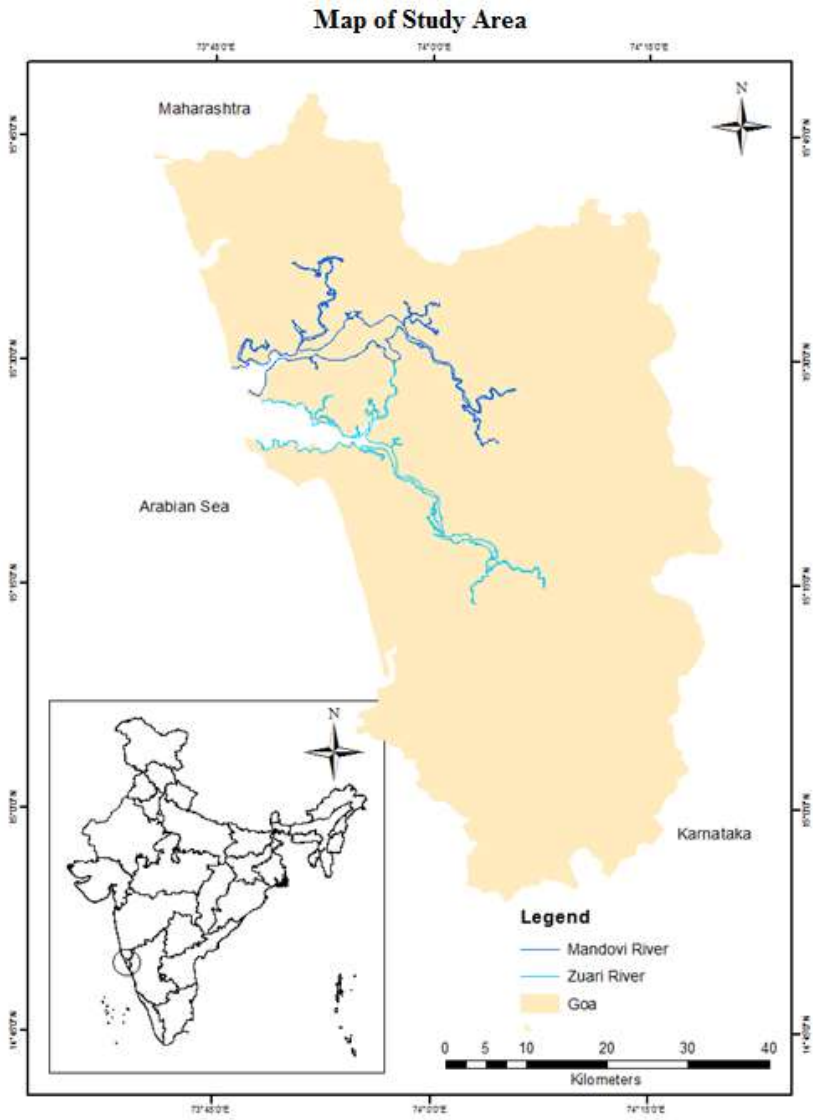


Fig. 1: Map of the study area.

Table 1: Data source and data derived.

| Sr. no. | Data | Source | Data derived |
|---|---|---|---|
| 1. | Survey of India (SOI) toposheets of 1:50,000 scale (48 E/14, 48 E/15, 48 I/2, 48 I/3) | Survey of India | High Tide Line (HTL) |
| 2. | LANDSAT 8OLI images (19/01/2018) LANDSAT 4-5 TM images (10/02/1991) 30 meters spatial resolution each | United States Geological Survey (USGS) website | Land use land cover (LULC) |
| 3. | GPS Survey Google Earth | Field Visit | Ground Truthing |

1. Cloud-free LANDSAT images are downloaded from the United States Geological Survey (USGS) website. The satellite images corresponding to low tide conditions were preferred to get maximum exposure to the land features and to yield accurate results. Table 1 displays the data used and derived for the analysis.

The pre-processing of the images (atmospheric and radiometric corrections), layer stacking, and mosaic were carried out using the image processing software ERDAS IMAGINE 2014. Stacking of Green, Red, and Near Infra-Red (NIR) generated False Colour Composite (FCC) images for both satellite data. ArcGIS 10.3 software was used for geo-referencing and projecting the Survey of India toposheets (WGS84 UTM Zone 43 N). Survey of India (SOI) toposheets were used for reference and for the generation of foundation data i.e. to demarcate the high tide line. The high tide line was demarcated up to the tidal influx in the rivers.

Upon demarcation of the high tide line, the Buffer Analysis tool was used to extract 100 meters and 50 meters zone along the HTL of Zuari and Mandovi rivers including the Cumbarjua Canal which connects rivers Mandovi and Zuari. The extracted zones of 100 meters and 50 meters for the years 1991 and 2018 were used for studying land use land cover changes and the vulnerability of mangroves to the changing CRZ Regulation. The satellite images of 1991 and 2018 were specifically chosen, as the CRZ notifications were implemented and amended during the same time frame.

The land use land cover classes were categorized into 5 classes namely, vegetation, mangroves, built-up, water, and barren lands. The classes were demarcated using the onscreen digitization method. Mangrove patches were verified and identified from other land use using high-resolution images on the Google Earth platform. Field visits and ground truthing have added more details in discriminating mangroves from other vegetation. Later, change detection of LULC classes for 100 meters zone between the period 1991 and 2018 was performed in ArcGIS 10.3 software. Graphs and charts were prepared using MS Excel.

## RESULTS AND DISCUSSION

According to Berlanga-Robles and Ruiz-Luna (2011), land use land cover changes are responsible for 35-50% loss of coastal wetlands. Anthropogenic activities harm the natural environment through the dynamic change of land use land cover (Daba & You 2022). Increasing human interference in the form of infrastructure development, pollution, and over-exploitation of resources along the regulated zones has increased the vulnerability of ecosystems. Moreover, the natural problems of cyclones, tidal surges, and rise in sea level are also threatening the sensitive ecosystems. To combat the problems related to the development and regulate human activities, regulated zones were implemented. But the integrity of the government's intentions for coastal protection is doubtful as meager executive action to address such a big issue shows gross negligence. Legislation has failed to implement and monitor the regulation (Agarwal 2019).

In Goa, most of the mangroves are located in the estuarine regions. Mandovi-Zuari-Cumbarjua estuarine complex has a dense area under mangroves. Zuari and Mandovi, the twin rivers are the lifelines of the Goans and their economy. Hence, the mangroves are vulnerable due to various anthropogenic activities taking place in these rivers and along their bank which includes settlement, bridge construction, widening of roads, agriculture, aquaculture, salt extraction, tourism, etc. Over the last two decades, vast mangrove areas along the Goan rivers are being reclaimed for developmental purposes such as settlements, industrial establishment, road extension, construction of bridges, harbors, and jetties, dredging and discharge of sediments, dumping of garbage, pollution, etc. which has resulted in severe damage to the fragile ecosystem (Dhargalkar & Kavlekar 2019).

Through the study of land use land cover change within the 100 meters and 50 meters CRZ, it was found that tremendous changes have occurred within the regulated zones along the Mandovi and Zuari rivers including Cumbarjua Canal. Moreover, in 2018 the changes in the CRZ notification which reduced the CRZ from 100 meters to 50 meters along the creeks and estuaries are likely to enhance changes in the land use pattern.

Table 2: LULC changes within the 50 meters and 100 meters CRZ Zone of the Zuari and Mandovi Rivers (including Cumbarjua Canal) (1991 and 2018).

| Land use / Year | Zuari River (Area in km$^2$) | | | Overall Loss (Area in km$^2$) | Mandovi River (Area in km$^2$) | | | Overall Loss (Area in km$^2$) |
|---|---|---|---|---|---|---|---|---|
| | 1991 (100 meters) | 2018 (100 meters) | 2018 (50 meters) | 2018-1991 (100 meters) | 1991 (100 meters) | 2018 (100 meters) | 2018 (50 meters) | 2018-1991 (100 meters) |
| Barren land | 3.17 | 4.30 | 1.16 | 1.13 | 6.79 | 3.84 | 1.23 | -2.95 |
| Built-up | 1.17 | 1.65 | 0.89 | 0.48 | 1.44 | 2.35 | 1.08 | 0.91 |
| Mangroves | 6.66 | 5.50 | 3.90 | -1.16 | 6.70 | 6.40 | 4.65 | -0.3 |
| Vegetation | 6.12 | 6.21 | 2.56 | 0.09 | 8.55 | 11.06 | 4.62 | 2.51 |
| Water | 4.07 | 3.53 | 2.29 | -0.54 | 3.59 | 3.42 | 2.17 | -0.17 |
| Total | 21.19 | 21.19 | 10.80 | - | 27.07 | 27.07 | 13.75 | - |

Source: Image Classification

As inferred in Table 2, changes are observed in the land use land cover pattern along the high tide zones of Mandovi and Zuari rivers over 27 years (1991-2018), most of the changes are the result of human interference. In the year 1991, the area under barren land, built-up, mangroves, vegetation, and water in Zuari river was 3.17 $km^2$, 1.17 $km^2$, 6.66 $km^2$, 6.12 $km^2$, and 4.07 $km^2$ respectively. Whereas, in the year 2018, the area under barren land, built-up, mangroves,

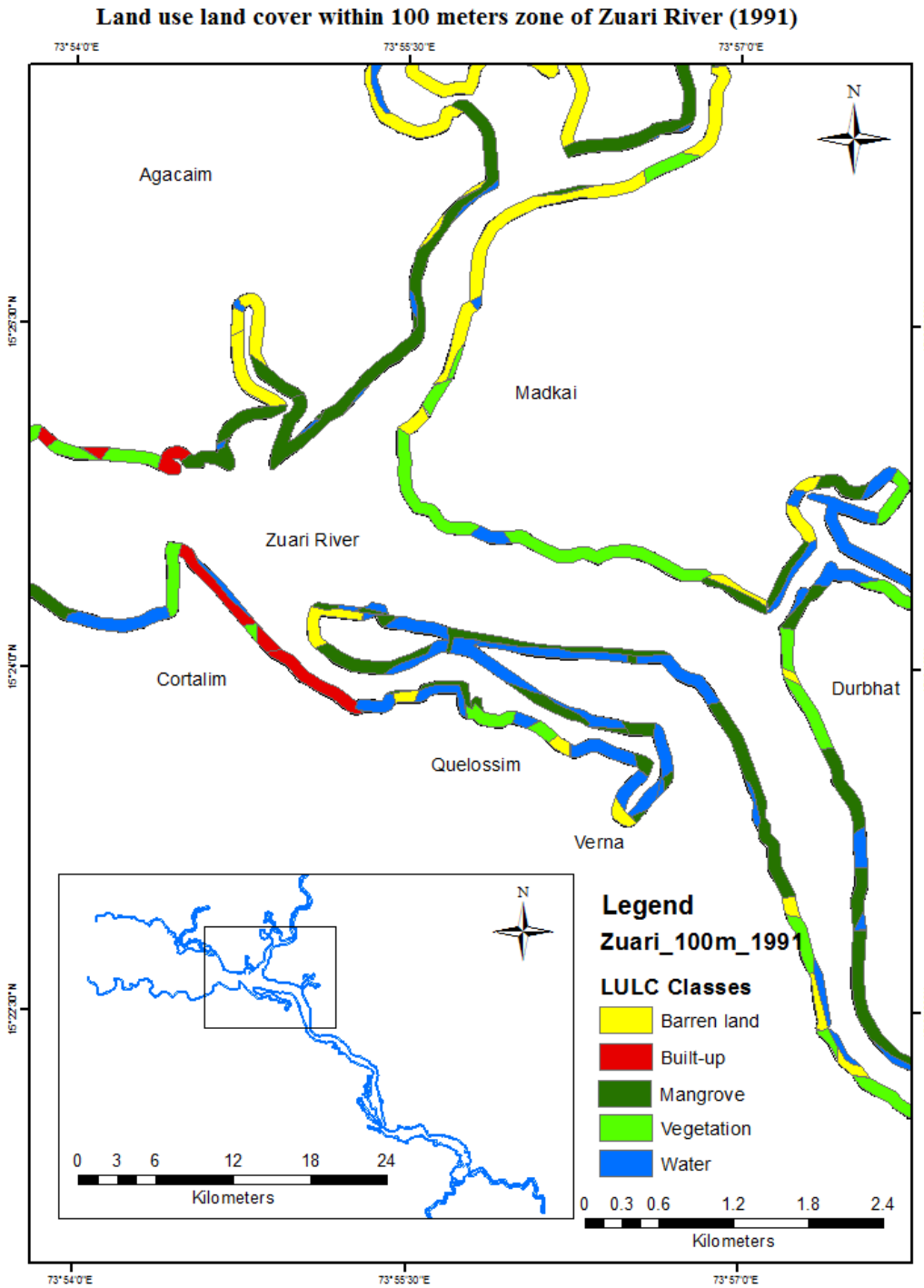


Fig. 2: LULC changes within 100 meters zone of Zuari River (1991).

vegetation, and water in Zuari river was 4.30 km$^2$, 1.65 km$^2$, 5.50 km$^2$, 6.21 km$^2$, and 3.53 km$^2$ respectively. In the case of the Zuari river, over 27 years, the area under barren land, built-up, and vegetation has increased by 1.13 km$^2$, 0.48 km$^2$, and 0.09 km$^2$ respectively. On the other hand, areas under mangroves and water have decreased by 1.16 km$^2$ and 0.54 km$^2$ respectively. Figs. 2, 3, 4, and 8 represent LULC changes within 100 meters and 50 meters zones of the Zuari river. Fig. 10 depicts the conversion of the LULC classes in the Zuari river from 1991 to 2018.

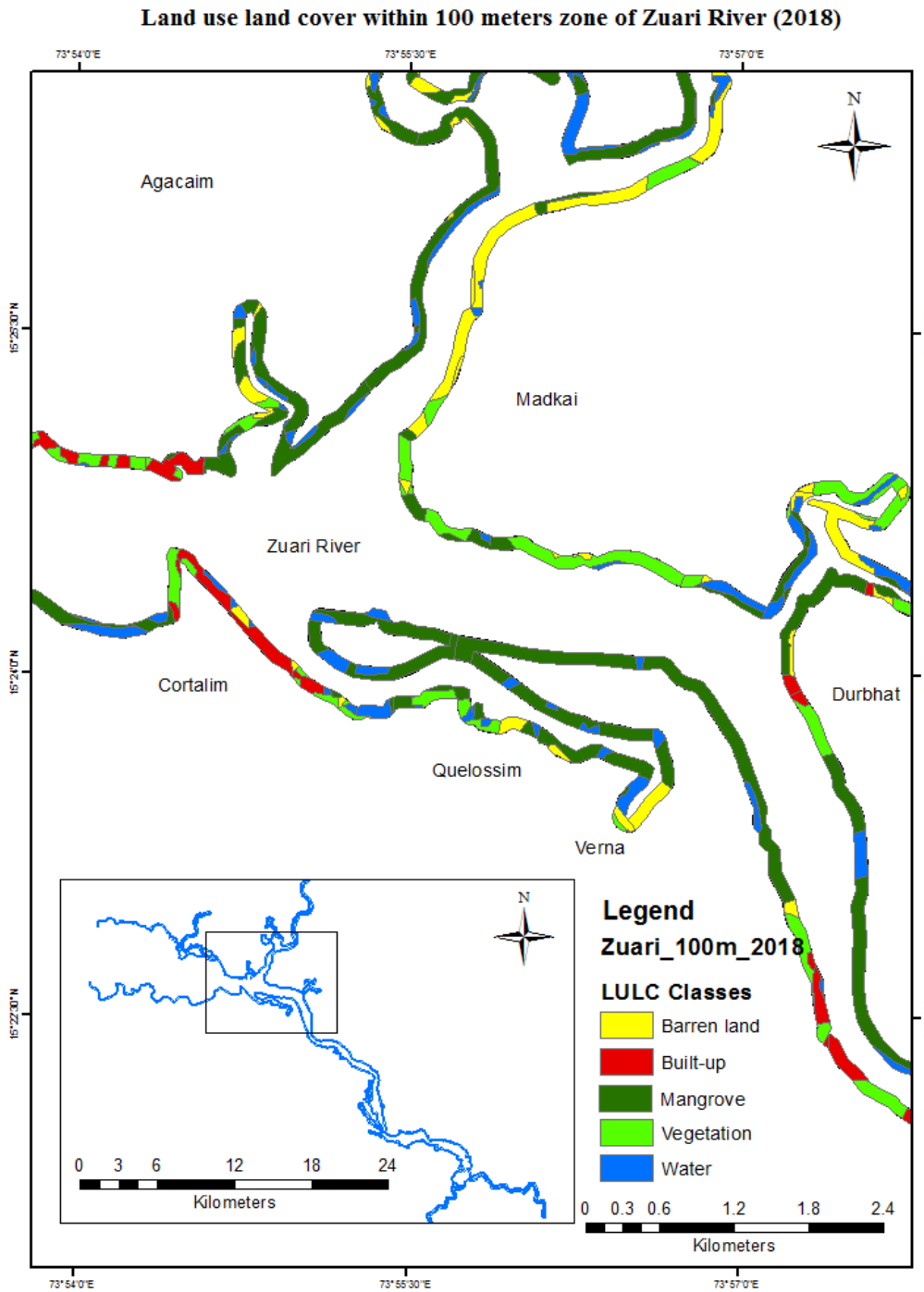


Fig. 3: LULC changes within 100 meters zone of Zuari River (2018).

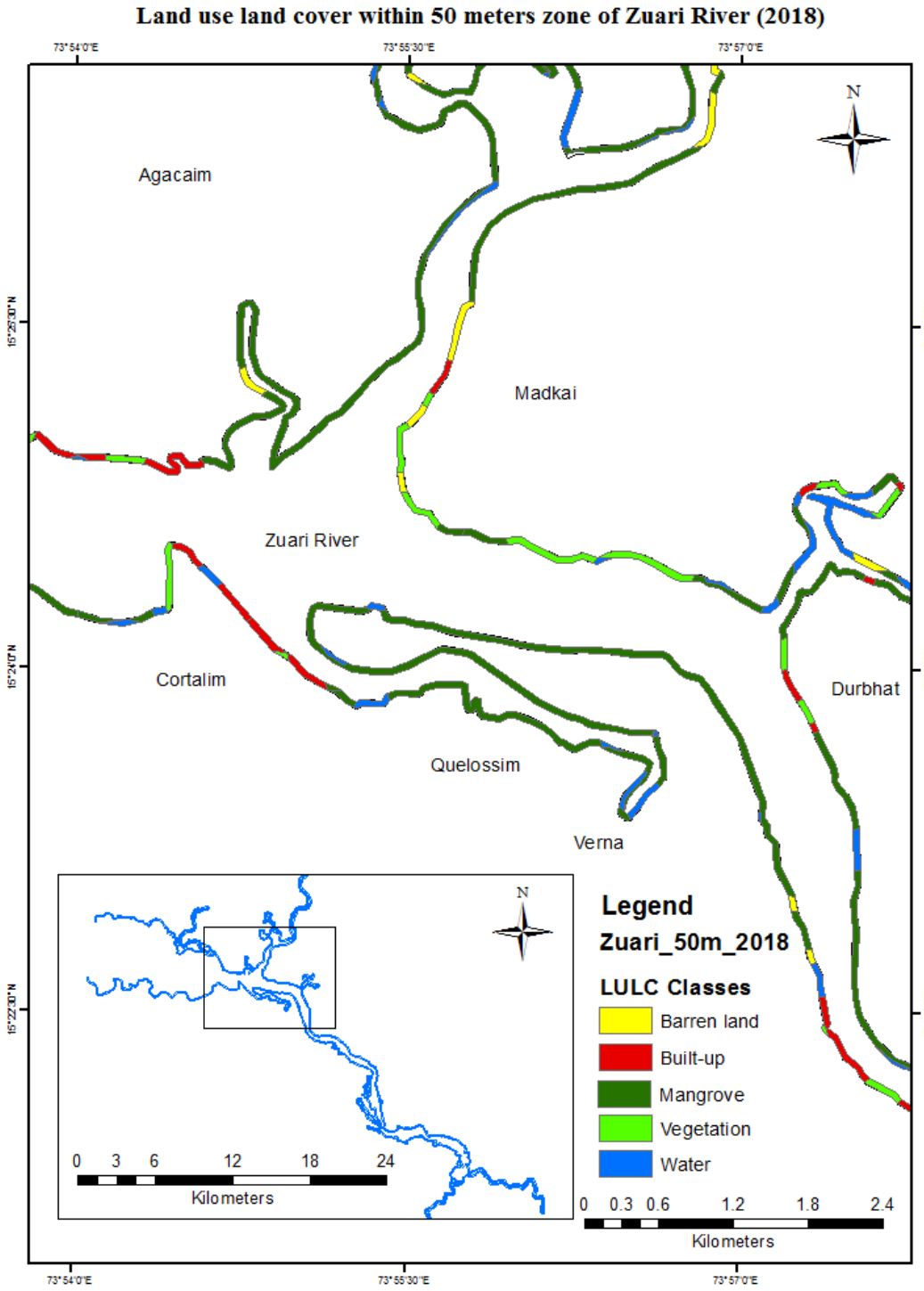


Fig. 4: LULC changes within 50 meters zone of Zuari River (2018).

Similarly, in the year 1991, the area under barren land, built-up, mangroves, vegetation, and water in Mandovi river was 6.79 $km^2$, 1.44 $km^2$, 6.70 $km^2$, 8.55 $km^2$, and 3.59 $km^2$ respectively. Whereas, in the year 2018, the area under barren land, built-up, mangroves, vegetation, and water in Zuari river was 3.84 $km^2$, 2.35 $km^2$, 6.40 $km^2$, 11.06 $km^2$, and 3.42

km$^2$ respectively. In the case of the Mandovi river, over 27 years, the area under built-up and vegetation have increased by 0.91 km$^2$ and 2.51 km$^2$ respectively. But, the area under barren land, mangroves, and water is found to have decreased by 2.95 km$^2$, 0.3 km$^2$, and 0.17 km$^2$ respectively. Figs. 5, 6, 7 and 9 represent LULC changes within 100 m and 50 m zones of Mandovi river. Fig. 11 depicts the conversion of the LULC classes in the Mandovi river from 1991 to 2018. Figs. 12 and 13 are glimpses of mangroves in the Zuari and Mandovi rivers.

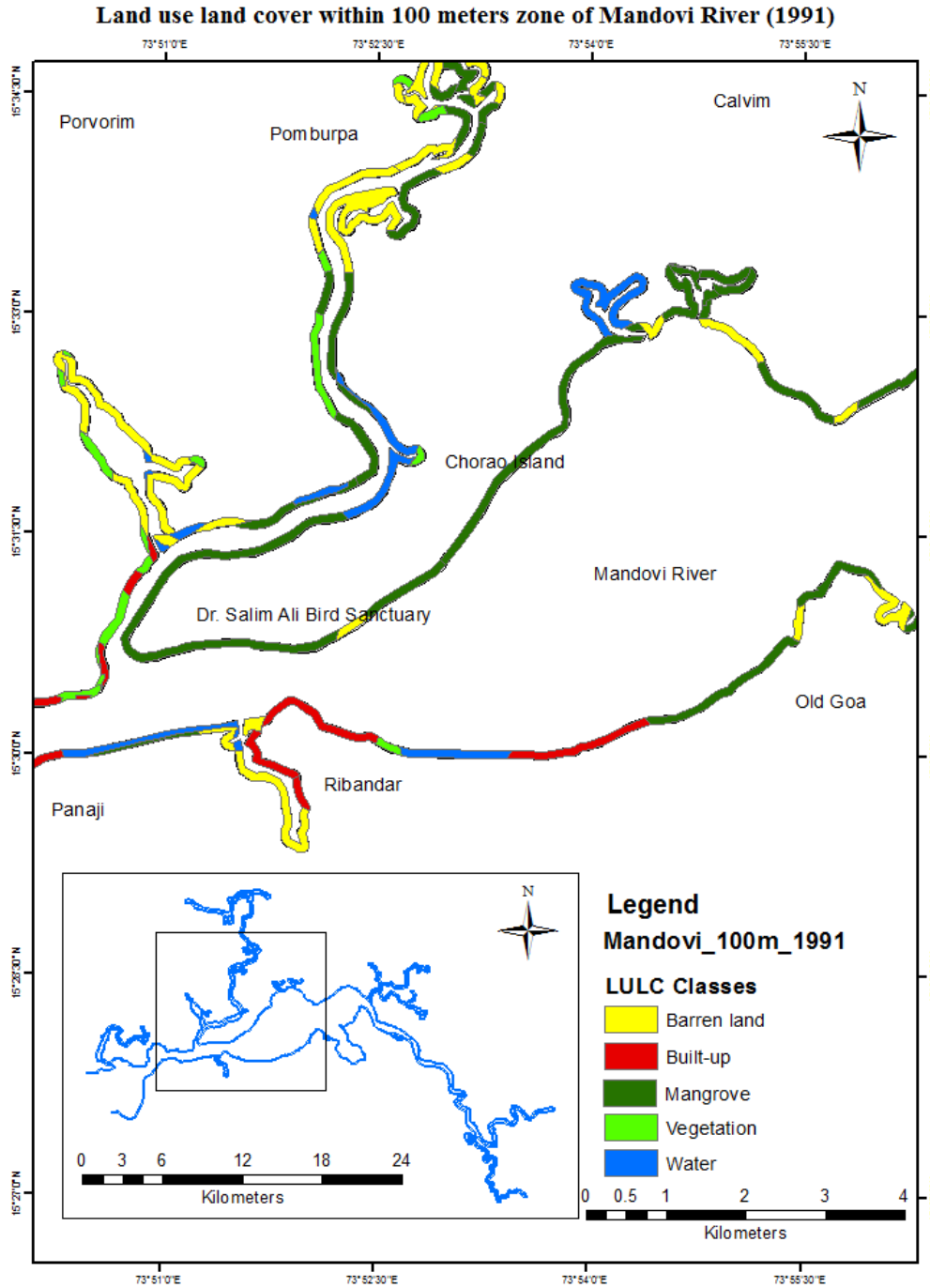


Fig. 5: LULC Changes within 100 meters zone of Mandovi River (1991).

As per the CRZ Notification of 2018, the regulated zone was reduced to 50 m from HTL. With the reduction in the CRZ demarcation, human interference is likely to increase leading to more hap-hazardous and unplanned development within the zone, thereby making mangroves vulnerable to degradation. From the findings, it was observed that a major portion of the mangrove is present within 50 m of the high tide line. Upon reducing the CRZ limit to 50 m, depletion

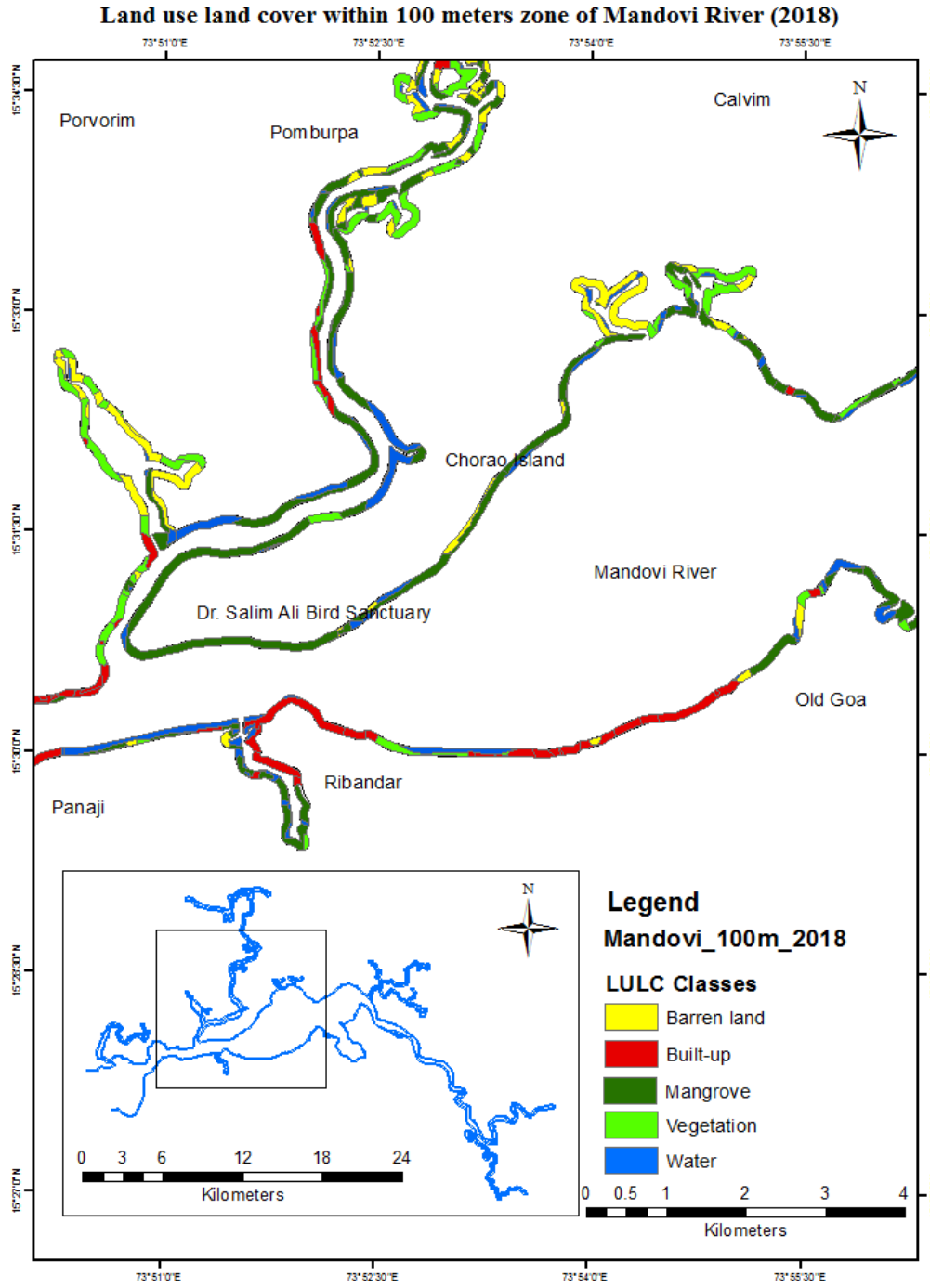


Fig. 6: LULC changes within 100 meters zone of Mandovi River (2018).

of mangroves will occur definitely, and the mangrove ecosystem will almost cease which we cannot afford to lose. The proportion of mangrove cover is 3.90 $km^2$ and 4.65 $km^2$ respectively within the 50 m zone of the Zuari and Mandovi rivers. The mangroves are vulnerable to changing land use patterns likely to arise with the implementation of a 50 m regulation zone. Agarwal (2019) stated that inefficient and inadequate monitoring of the demarcated CRZ coupled with increasing human interference is placing the mangroves at immense threat and overall the absence of monitoring the regulation by the government poses additional threats.

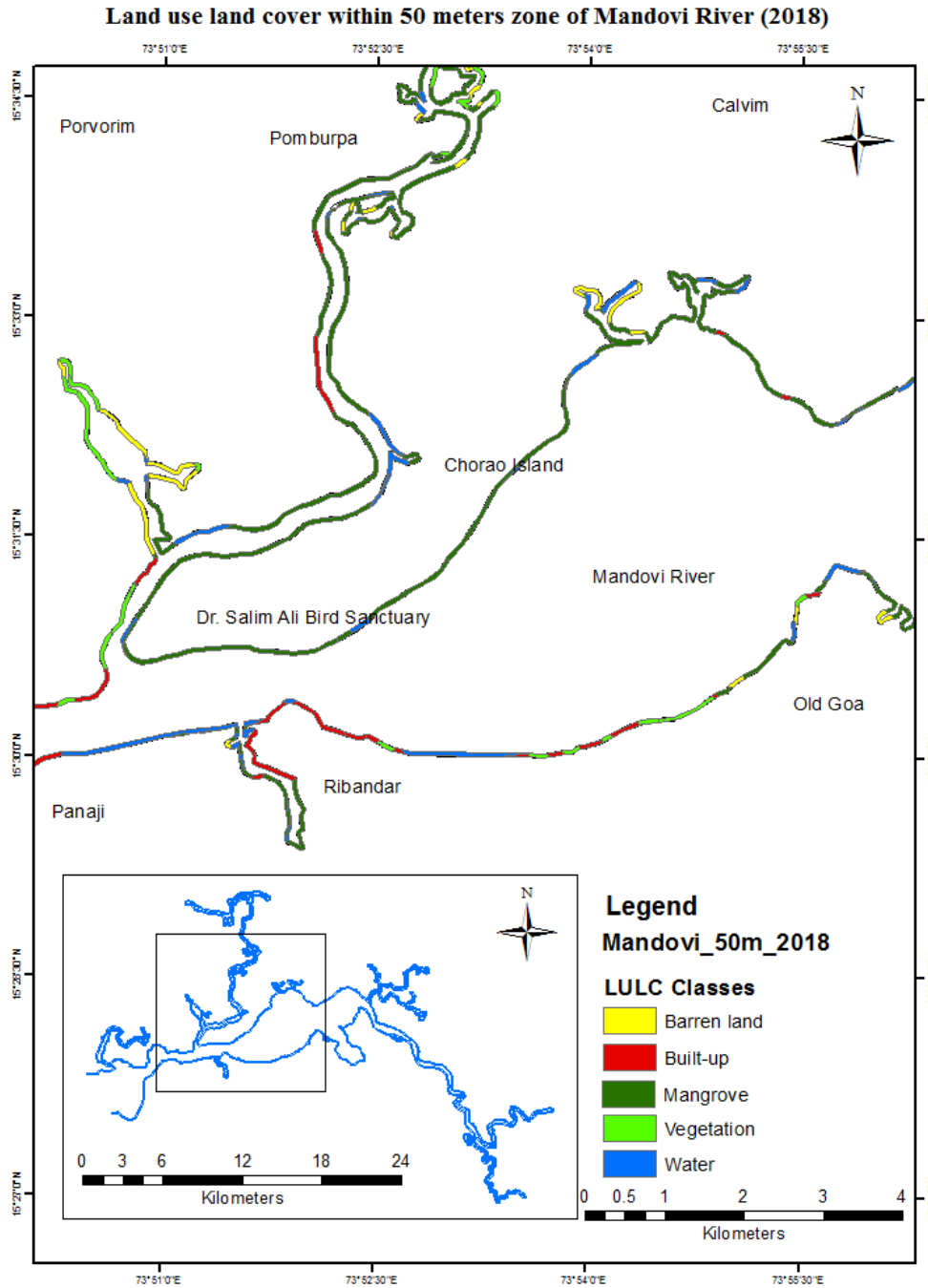


Fig. 7: LULC changes within 50 meters zone of Mandovi River (2018).

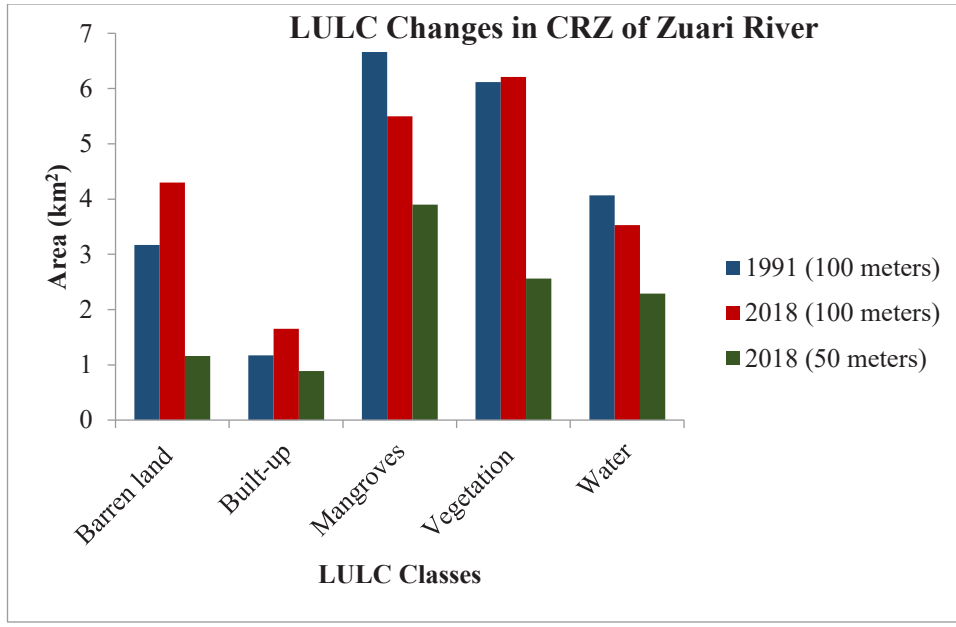


Fig. 8: LULC changes in 100 meters and 50 meters zones of Zuari River.

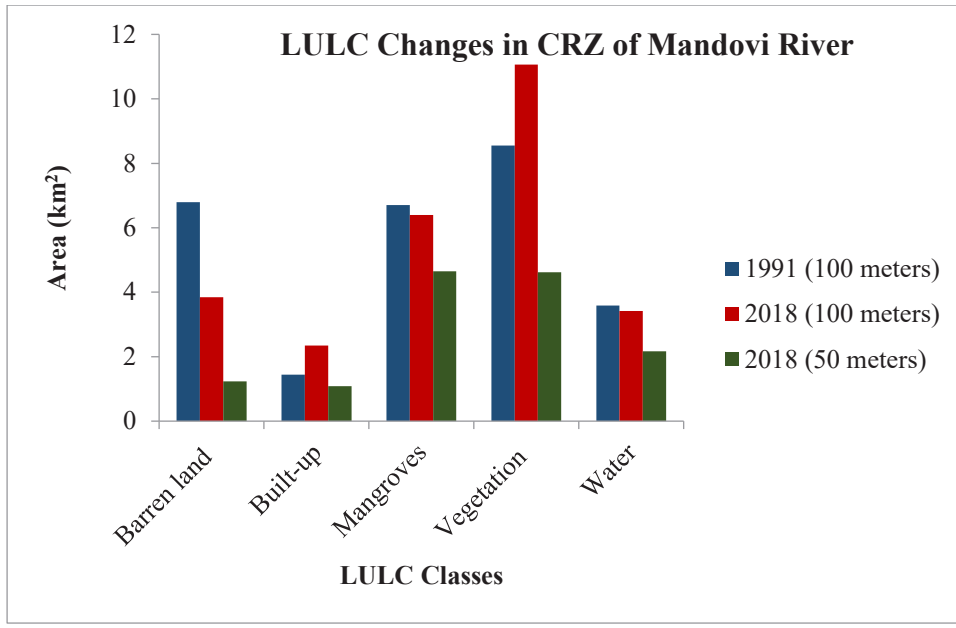


Fig. 9: LULC changes in 100 meters and 50 meters zones of Mandovi River.

Recent developmental activities including settlements, construction of bridges, road widening, and land reclamation constitute major negative changes in the HTL zone of both the rivers. Moreover, agriculture and aquaculture, plantations, and salt extraction activities are dominating the areas formerly covered by mangrove vegetation. Several of the activities mentioned here cause direct or indirect damage to the environment such as habitat fragmentation, the natural loss of available resources, and the addition of pollutants thereby affecting the water quality, etc. This indicates the vulnerability of mangroves to the changing land use pattern. Despite the formulation of regulation, coastal and estuarine areas are under threat from unplanned and hap-hazardous human activities.

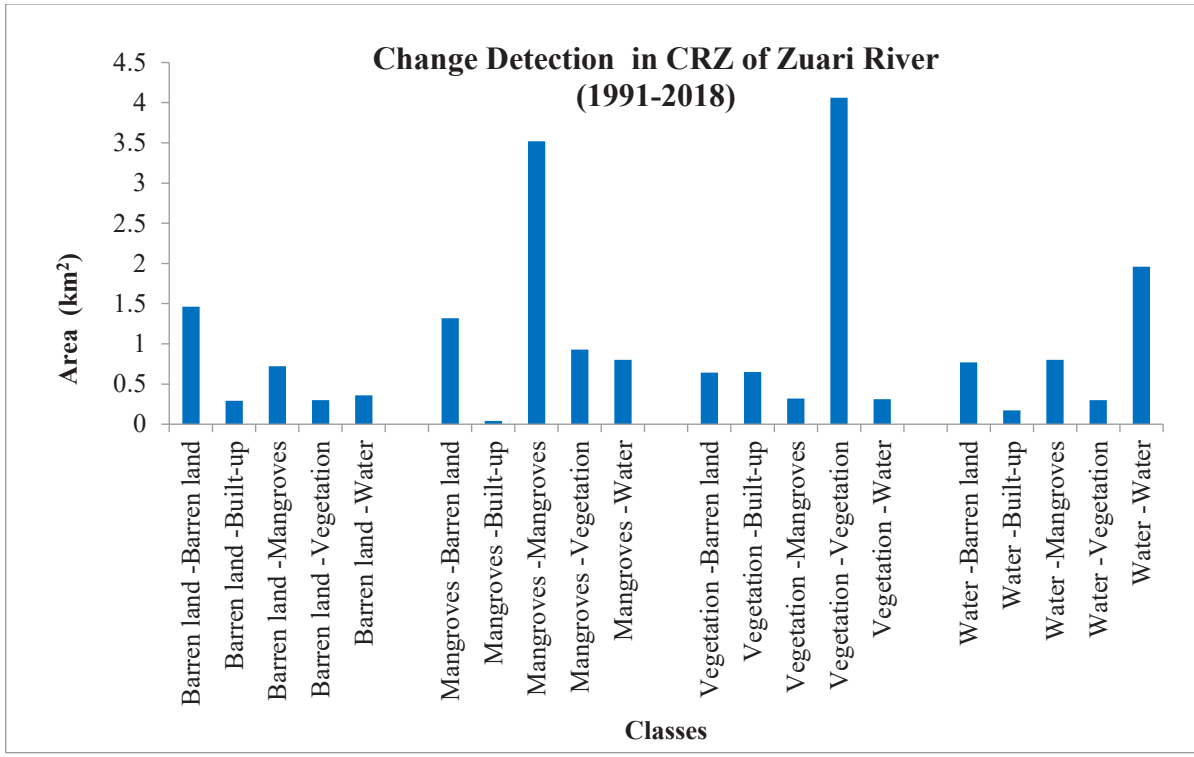


Fig. 10: Change detection in 100 meters zone of Zuari River (1991-2018).

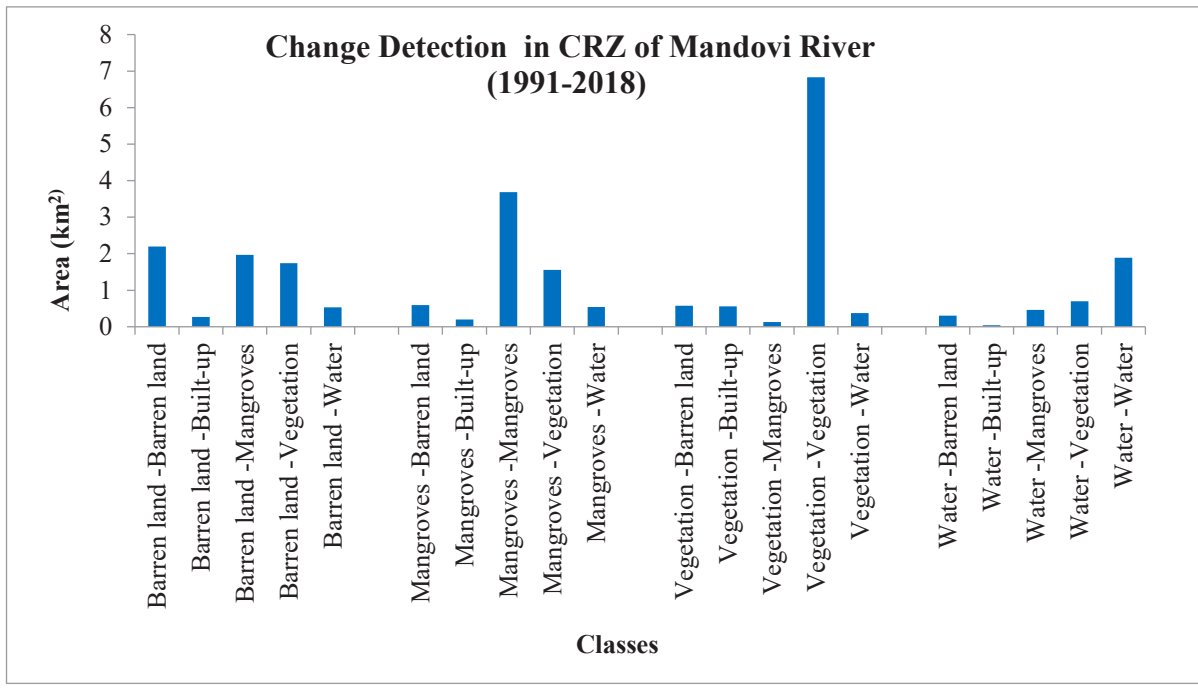


Fig. 11: Change detection in 100 meters zone of Mandovi River (1991-2018).

Fig. 12: Mangroves in Zuari river. (Source: Field visit)

Fig. 13: Mangroves in Mandovi river. (Source: Field visit)

## CONCLUSION

From the above study it was found that, over 27 years, the land use land cover pattern in CRZ of Mandovi and Zuari rivers has undergone changes which can be attributed to the interference of human activities followed by a lack of implementation and monitoring of rules and regulations and as well as natural factors. Over 27 years, there has been an increase in the area of some land use classes in the Zuari river such as barren land, built-up, and vegetation by 1.13 $km^2$, 0.48 $km^{2,}$ and 0.09 $km^{2,}$ and a decrease in mangroves and water class by 1.16 $km^2$ and 0.54 $km^2$. In Mandovi river, an increase in the area has been observed for built-up and vegetation by 0.91 $km^2$ and 2.51 $km^2$, whereas the area under barren land, mangroves, and water has decreased by 2.95 $km^2$, 0.3 $km^2$ and 0.17 $km^2$.

Increasing anthropogenic interference in the regulated zone is making mangroves more vulnerable to degradation. Mangroves are the most important ecosystem and yet the most fragile. Regardless of their importance, the mangrove ecosystem remains threatened. Threatened by rising sea levels, storm surges, and human interventions (Pramanik 2014, DasGupta & Shaw 2013b). Its role in maintaining biodiversity, reducing the impact of natural disasters, and providing a source of livelihood is often ignored due to a lack of awareness (Avatar et al. 2021).

Uncontrolled and hap-hazardous development needs to be replaced by sustainable development. Government individually or in association with NGOs or Private partners should undertake the rejuvenation of areas under mangroves. This herculean task requires proper surveys, documentation, and mapping. Organizing plantation drives and encouraging people's participation could go a long way in saving the fragile ecosystem for posterity. There is a need for special implementation for the regulation of the riverine ecosystem i.e. River Regulation Zone (RRZ) to monitor human interference along the river banks. This regulation needs to be propounded and should be implemented at the earliest for preventing further damage to the mangrove ecosystems. Moreover, sustainable tourism can be promoted in mangrove areas to create awareness about the mangrove ecosystem amongst the people and generate a source of livelihood amongst the locals.

## REFERENCES

Agarwal, A. 2019. Climate change and coastal zone regulation: dilution of coastal protection, an analysis of CRZ notification, 2018. IOSR Journal of Environmental Science, Toxicology and Food Technology, 13(8): 49-56.

Ajai, Bahuguna, A., Chauhan, H., Sen Sarma, K., Bhattacharya, S., Ashutosh, S., Pandey, C., Thangaradjou, T., Gnanppazham, L., Selvam, V. and Nayak, S. 2013. Mangrove inventory of India at community level. The National Academy of Sciences, 36(1).

Avtar, R., Navia, M. and Fujii, M. 2021. Impacts of changes in mangrove ecosystems in the Ba and Rewa deltas, Fiji using multi-temporal Landsat data and social survey. Coastal Engineering Journal, 63(3): 386-407.

Basha, C. 2018. An overview on global mangroves distribution. Indian Journal of Geo Marine Sciences, 47(04): 766-772.

Berlanga-Robles, C. and Ruiz-Luna, A. 2011. Integrating remote sensing techniques, geographical information systems (GIS), and stochastic models for monitoring land use and land cover (LULC) changes in the northern coastal region of Nayarit, Mexico.GIScience & Remote Sensing, 48(2): 245-263.

Butt, A., Shabbir, R., Ahmad, S. and Aziz, N. 2015. Land use change mapping and analysis using Remote Sensing and GIS: A case study of Simly watershed, Islamabad, Pakistan. The Egyptian Journal of Remote Sensing and Space Sciences, 18: 251-259.

Coastal Regulation Zone (CRZ) Notification 2011. (2011, January 06). Retrieved March 01, 2022, from Coastal Regulation Zone (CRZ) Notification 2011: http://www.indiaenvironmentportal.org.in/files/CRZ-Notification-2011.pdf

Daba, M. and You, S. 2022. Quantitatively assessing the future land-use/land-cover changes and their driving factors in the upper stream of the Awash river based on the CA–Markov model and their implications for water resources management. Sustainability, 14 (3).

DasGupta, R. and Shaw, R. 2013a. Changing perspectives of mangrove management in India: an analytical overview. Ocean & Coastal Management, 80: 107-118.

DasGupta, R. and Shaw, R. 2013b. Cumulative impacts of human interventions and climate change on mangrove ecosystems of South and Southeast Asia: An Overview. Journal of Ecosystems.

Dhargalkar, V. and Kavlekar, D. 2019. CRZ notification 2018 - disastrous to ecosystem functioning. International Journal of Ecology and Ecosolution, 6(1): 10-15.

Draft-Crz-Notification-20181.pdf - Government Of Goa. (2018, April 18). Retrieved March 01, 2022, from DRAFT-CRZ-NOTIFICATION-20181.pdf - Government Of Goa: https://www.goa.gov.in/wp-content/uploads/2018/05/DRAFT-CRZ-NOTIFICATION-20181.pdf

Haque, I. and Basak, R. 2017. Land cover change detection using GIS and remote sensing techniques: A spatio-temporal study on TanguarHaor, Sunamganj, Bangladesh. The Egyptian Journal of Remote Sensing and Space Sciences, 20(2): 251-263.

India State of Forest Report 2021 - Forest Survey of India. Dehradun: Forest Survey of India (Ministry of Environment Forest and Climate Change).

Islam, R., Miah, G. and Inoue, Y. 2016. Analysis of land use and land cover changes in the coastal area of Bangladesh using LANDSAT imagery. Land Degradation & Development, 27(4): 899-909.

Jagtap, T., Naik, S. and Nagle, V. 2001. Assessment of coastal wetland resources of central west coast, India, using LANDSAT data. Journal of the Indian Society of Remote Sensing, 29(3): 143-150.

Kaliraj, S., Chandrasekar, N., Ramachandran, K., Srinivas, Y. and Saravanan, S. 2017. Coastal land use and land cover change and transformations of Kanyakumari coast, India using remote sensing and GIS. The Egyptian Journal of Remote Sensing and Space Sciences, 20(2): 169-185.

Kamboj, R. and Das, L. 2019. The dynamics of mangrove cover in India. Indian Forester, 145(7): 607-613.

Kathiresan, K. and Rajendran, N. 2005. Mangrove ecosystems of the Indian Ocean region. Journal of Marine Sciences, 34(1): 104-113.

Kaul, H. and Ingle, S. 2012. Land use land cover classification and change detection using high resolution temporal satellite data. Journal of Environment, 1(4): 146-152.

Mascarenhas, A. 1999. The coastal regulation zone of Goa: oceanographic,

environmental and societal perspectives. Current Science, 77(12): 1598-1605.

Mesta, P., Setturu, B.,Chandran, S.,Rajan, K. and Ramachandra, T. 2014. Inventorying, mapping and monitoring of mangroves towards sustainable management of west coast, India. Journal of Geophysics & Remote Sensing, 3(3).

Ministry of Environment and Forests - PARIVESH. (1991, February 19). Retrieved March 01, 2022, from Ministry of Environment & Forests - PARIVESH: https://parivesh.nic.in/writereaddata/ENV/crz75.PDF

Misra, A. and Balaji, R. 2015. A study on the shoreline changes and land-use/land-cover along the South Gujarat coastline. Procedia Engineering, 116: 381-389.

Muttitanon, W. and Tripathi, N. 2005. Land use/land cover changes in the coastal zone of Ban Don Bay, Thailand using LANDSAT 5 TM data. International Journal of Remote Sensing, 26(11): 2311-2323.

Nagi, H., Rodrigues, R., Mani Murali, R. and Jagtap, T. 2014. Using remote sensing and GIS techniques for detecting land cover changes of mangrove habitats in Goa, India. Faculty of Science Bulletin, 26: 21-33.

Pramanik, M. K. 2014. Assessment the impact of sea level rise on mangrove dynamics of Ganges Delta in India using remote sensing and GIS. Journal of Environment and Earth Science, 4(21): 117-127.

Ragavan, P., Saxena, A., Jayaraj, R., Mohan, P., Ravichandran, K., Saravanan, S. and Vijayaraghavan, A. 2016. A review of the mangrove floristics of India. Taiwania, 61(3): 224-242.

Saddhe, A., Jamdade, R. and Kumar, K. 2016. Assessment of mangroves from Goa, west coast India using DNA barcode. Springer Plus, 5.

Sahu, S., Suresh, H., Murthy, I. and Ravindranath, N. 2015. Mangrove area assessment in India: implications of loss of mangroves. Journal of Earth Science and Climate Change, 6 (5).

Saravanan, K., Chowdhury, B. and Sivakumar, K. 2013. Important coastal and marine biodiversity areas on east coast of India. ENVIS Bulletin: Wildlife & Protected Areas, 15: 292-298.

Shaji, J., Sajith, S., Joseph, J. and Ramachandran, K. 2017. LULC change along central Kerala coast and perception on implementation of CRZ Notification. National Conference on Geospatial Technology.

Singh, I., Singh, S., Kushwaha, S., Ashutosh, S. and Singh, R. 2004. Assessment and monitoring of estuarine mangrove forests of Goa using satellite remote sensing. Journal of the Indian Society of Remote Sensing, 32(2): 167-174.

Nature Environment and Pollution Technology
An International Quarterly Scientific Journal

p-ISSN: 0972-6268
(Print copies up to 2016)
e-ISSN: 2395-3454

Vol. 22 | No. 1 | pp. 355-368 | 2023

Original Research Paper

https://doi.org/10.46488/NEPT.2023.v22i01.035

Open Access Journal

# Characterization of Wastewater and Evaluation of Recycling Technologies Using Analytical Hierarchical Process for a University Community

**O. J. Oyebode *†[ID] and O. Waterway***
*Civil and Environmental Engineering Department, Afe Babalola University, Ado-Ekiti, Ekiti State, Nigeria
†Corresponding author: O. J. Oyebode; oyebodedare@yahoo.com

**Nat. Env. & Poll. Tech.**
**Website: www.neptjournal.com**

*Received:* 15-09-2022
*Revised:* 18-10-2022
*Accepted:* 19-10-2022

**Key Words:**
Recycling technologies
Analytical hierarchical process
Wastewater
Greywater

## ABSTRACT

Characterization and treatment of greywater are major environmental issues in most nations of the world. The research aims to characterize and evaluate recycling technologies using an analytical hierarchical process for Afe Babalola University Ado-Ekiti (ABUAD) community. A survey was conducted around ABUAD to determine the number of functioning boreholes and active water systems in the area, the total population of students was derived from the total head count of each room and student in each hostel, and a population projection for the next 3 years was conducted to determine the rate at which the student body will grow in terms of future water demands, and daily water volume and questionnaires were used to collect data. Before developing the small-scale model of the greywater filter system (consisting of activated carbon, shaft sand, pebbles, cotton fiber, and gravel), water grey samples were gathered from several ABUAD locations to evaluate the pollution level of each greywater source. A total of 88 students (43 males and 45 females) replied to the survey, revealing their high need for clean water and their dissatisfaction with the water supply in their respective hostels. The water quality tests conducted in the various locations of ABUAD reveal high levels of total dissolved solids (TDS) and turbidity, particularly in the girl's hostels, and the water was discovered to be predominantly alkaline. After passing a sample of greywater through the small-scale greywater filtering device, it was determined to be effective, since it produced clear, reusable water and a greywater filtration system in ABUAD will yield favorable outcomes.

## INTRODUCTION

Greywater is any effluent generated in homes or offices from streams or outlet pipes that is free of feces. Greywater, by definition, is wastewater from showers, baths, basins, and washing machines. Greywater treatment is simpler and less expensive than municipal wastewater treatment, which has sparked a lot of interest and a lot of focus on its use and recycling methods. Greywater re-use and reuse are commonly used in restroom flushing, washing, and other non-potable applications. Water shortages caused by poor rainfall or high demand, as well as environmental and economic drivers, are all recycling reasons. It's also true that recycling is an emotional issue that grows in proportion to the public's proximity to the recycling application. Water pollution is caused by the influx of foreign material that can degrade a body of water's water quality, endangering human life and health in the process. One particular point source of water pollution is industrial effluents (Mathurin et al. 2022; Awomeso et al. 2010). Industrial effluents that include harmful substances can harm both people and animals and deteriorate the quality of the water (WHO 2008).

As a result, public perception difficulties can often exceed technical issues as impediments to adoption, resulting in the cancellation of otherwise viable economic reuse programs. Water recycling in the urban setting is one of the four generic water recycling strategies available for water resource management and use that is likely the least well-developed. Utilizing recycled greywater lessens the pressure on the water supply system and the sewage treatment process. It also reduces the quantity of downstream wastewater infrastructure required (collection, treatment, and disposal). One of the most prevalent applications of reusable greywater is the lowering of sewage effluent into surface water, which is environmentally advantageous. This research concentrates on greywater water quality metrics such as BOD, COD, turbidity, heavy metals, salinity, conductivity

**[ID] ORCID details of the authors:**

**O. J. Oyebode**
https://orcid.org/0000-0003-2792-146X

in $mg.L^{-1}$, pH, and microbiological content values, as well as a decentralized viable treatment process to bring these parameters to the appropriate quality to meet the reusable water quality requirements.

## PAST STUDIES

Water is composed of the chemical components hydrogen and oxygen, and water exists in gaseous, liquid, and solid states (Fernández et al. 2022). It is one of the most abundant and indispensable. At room temperature, it is a tasteless, odorless liquid with the ability to dissolve a wide variety of other compounds. Water's versatility as a solvent is essential for the survival of all living things. It is necessary for all known forms of life despite lacking caloric or biological ingredients. Surface water and subterranean water are the two primary sources of water. Water is one of the most essential elements for human survival among those that are necessary for the survival of humans, animals, and plants. Man can survive for days without food, but not without water. It is believed that life began in the aqueous solutions of the world's oceans, and biological activities such as blood and digestive juices are dependent on aqueous solutions. Water exists on planets and moons outside and within the solar system. Small amounts of water appear colorless, but a slight absorption of light at red wavelengths imparts a blue hue to the substance. Although water molecules ($H_2O$) have a simple structure, the physical and chemical properties of the compound are exceedingly complicated and not typical of most substances on Earth. Water occurs as a liquid on the Earth's surface under normal conditions, making it invaluable for transportation, leisure, and as a habitat for a variety of plants and animals. The ability of water to readily transform into a vapor (gas) enables it to be transported from the oceans to inland places, where it condenses and nourishes plant and animal life like rain. The majority of the water on the Earth's surface is found in the oceans (97.25 percent) and polar ice caps and glaciers (2.05 percent), with the remaining distributed among freshwater lakes, rivers, and groundwater. As the global population and demand for freshwater rise, water filtration, and recycling are becoming increasingly important. Surprisingly, industrial water purity standards are frequently greater than those for human use. For example, the water used in high-pressure boilers must be at least 99.999998 percent pure. Because it includes significant levels of dissolved salts, seawater must be desalinated for most uses, including human consumption.

To reuse greywater for toilet flushing, bathing, cleaning, and washing, the primary objective of this study is to analyze various treatment methods, characterize them, and develop a water recycling process. Because flushing, bathing, cleaning and washing account for 25-35 percent of total household freshwater usage, reusing wastewater for toilet flushing, bathing, cleaning, and washing can save up to 25%-35% of total household freshwater demand. Petroleum hydrocarbon pollution is one of the most serious problems affecting the globe today since it is one of the most hazardous pollutants in aquatic and land habitats (Imron et al. 2019, Khalid et al. 2021). Oil spills, whether they are caused naturally or artificially, can contaminate the oceans with petroleum compounds. Natural spills include those caused by volcanic eruptions and natural leaks from underwater reservoirs. Synthetic spills include those caused by a variety of processes, such as oil extraction and transportation spills, oil loading operations, and transportation accidents. The poor management of medical waste and environmental pollution are two key issues that emerging nations must address to improve public health, natural ecosystems, and the environment (Oyebode & Otoko, 2022, Andarge 2019). The absence of water treatment technologies has led to substantial pollution in emerging and rapidly developing countries. Increasing aquatic pollution puts aquatic life in jeopardy and encourages water scarcity (Dey et al. 2021, Tse-Lun et al. 2021). One of the most economical and environmentally responsible wastewater treatment techniques to be developed in recent years is adsorption. Academic interest has been drawn to several adsorbent materials because of their effectiveness in removing ammonium ions from wastewater (Chopin et al. 2012, Neori et al. 1998). Local geology, land use/management techniques, climate, and human activities can all have an impact on groundwater quality (Ogarekpe et al. 2023, Oyebode 2022a). In transdisciplinary educational research, biomedical engineering (BME) is becoming more important because of technological advancements, a lack of equipment, difficulties in medical practice, and better healthcare-related causes. The question of whether the building materials used are of high quality and whether the design techniques utilized are of high standards has always been essential to sustainability (Oyebodeb 2022). To reduce agricultural non-point-source pollution, numerous technologies have been created (ANPSP). Instead of treating an entire region with numerous pollution sources as a control unit, the majority, however, simply reduce pollution from a single source. To safeguard the environment and promote agricultural sustainability, a regional pollutant reduction system for regulating ANPSP might be constructed by combining technology and the reuse of treated wastewater (TWR) and nutrients (NR) (Sun et al. 2019).

One of the most urgent problems at hand is the possible impact that poor water quality could have on soil, plants, and people. On the other hand, untreated water has a diverse microbial population and can include dangerous species in

it. When human or animal excrement enters greywater from washing hands, clothes, or produce, as well as surface water sources, pathogens, which are microscopic organisms that can cause illness or disease, are frequently linked to these sources. A bathroom leak, washing vegetables, or washing hands and contaminated clothing can all introduce people to harmful germs found in greywater (Rose et al. 1991, Birks et al. 2004, Jefferson et al. 2004). Many operations that use freshwater produce wastewater (Tchobanoglous 2003). Typically, these procedures flush or wash away waste materials and nutrients that have been introduced to the water supply. Wastewater needs to be cleaned of pollutants to produce effluent that can be recycled. Effluent can be recycled or used again in the water cycle (Nathanson 2020). Nigeria's population is growing as a result of urban techno-economic growth, changing production and consumption patterns, and increased waste generation. Due to their detrimental effects on the environment and public health, colored pollutants in wastewater must be eliminated before discharge. The quality of groundwater is a deeply held issue for people since it is crucial to preserving water resources and is directly tied to human welfare (Oyebode 2019). Environmental deterioration has existed ever since man first began to live in cities. In the early nomadic hunting societies, the tribe group would move on when their present location's food supply ran out and the area around their camp became polluted or unclean (Oyebode 2018). Wastewater has a wide variety of connotations that might mean different things to different people. Wastewater treatment's main objective is normally to enable the disposal of industrial and human effluents without harming public health or creating an unacceptable risk to the environment (Aderomose & Oyebode 2022).

## NEEDS AND IMPORTANCE OF WATER CONSERVATION

Water is a necessity for every life on Earth, including our own. Many human activities rely on the usage of water. These include food preparation (drinking), cleaning (washing), and energy production (producing). Even though 70% of Earth's surface is covered with water, just a little quantity of it may be used for drinking and cooking. Water that has been exposed to salt is unsafe for human consumption in 97% of the world's water. Only 1% of the world's freshwater is fit for human use, making up only 3% of total water. Glaciers and ice caps cover the remaining 2% of the planet's surface. 70% of the water supply is polluted in some way or another. We can only use the water that is available to us at this time. It may seem like a small amount of water, but with an ever-growing population and dwindling water supplies, there is a growing concern that there will one day be insufficient water sources to meet even the most basic demands of the people. Since it is unsuitable for human consumption or industrial use, even for power generation, extremely salty seawater cannot be used. Because of the high salt content, using this water in factories and power plants can lead to salt buildup on machinery, which can be extremely hazardous and even cause major industrial disasters. Seawater does not provide any benefit to humans as a result. Because freshwater supplies are limited and just 3% of the planet's total water supply is available to us, it is only logical that we must protect and conserve our water if we are to continue to exist as a species. There will be no water left in the world if this does not occur.

Source: (Gutiérrez-Ramírez et al. 2018)

## BASIC GREYWATER GUIDELINES

Greywater is different from fresh water and requires different guidelines for it to be reused.

i. The storage of greywater is not recommended (more than 24 hours). During storage, the nutrients in greywater begin to degrade and produce an unpleasant stench.

ii. Reduce your exposure to greywater. A disease may enter the water if an infected individual excreted in the water, thus your system should be set up so that water is absorbed into the ground rather than accessible to humans or animals.

iii. Understanding how well water drains into the soil (or the earth's percolation rate) will aid in the right design of a greywater treatment system. A mosquito breeding ground, as well as a site where people can come into touch with greywater, can be found in a greywater pool.

iv. Avoid pumps and filters that require regular maintenance and keep your system as basic as possible. Simple systems last longer, consume less energy, and cost less to maintain.

v. Make switching between the greywater and sewer/septic systems easier by installing a 3-way valve.

vi. Match the amount of greywater to the amount of irrigation water your plants need.

## MATERIALS AND METHODS

The methodology adopted includes a survey of borehole functionality in ABUAD. The total population of students was derived from the total head count of each room and student in each hostel, a population projection for the next 20 years was conducted to determine the rate at which the student body will grow in terms of future water demands, and daily water volume and questionnaires were used to collect data. People, businesses, community groups, or even individuals can provide water through a network of pipes via

a pumping system. For communities to function correctly, they must have access to clean water.

**Uses of Water in a University Environment**

1. Personal Hygiene
2. Sanitary
3. Lab Work
4. Industrial Functions

**Procedures for Determination of Data**

- Obtaining the number of pumps

  The authors went around the different structures and areas in ABUAD, counting the pumps to obtain the number of functioning pumps on the ABAUD campus. In doing that they also looked out for signs that indicated the functionality of each.
- Obtaining population data

Table 1: Interpretation of functionality of water systems in ABUAD.

| S/N | Location | Number of Boreholes | Status |
|---|---|---|---|
| 1. | New guesthouse | 1 | Yet to be connected |
| 2. | Front of college 1 | 1 | Dormant |
| 3. | Back in college 1 | 1 | Dormant |
| 4. | Left-back of college 1 | 1 | Dormant |
| 5. | Right-back of college 1 | 3 | Dormant |
| 6. | Back of college 2 | 2 | Functioning |
| 7. | The back of the boys hostel | 2 | Regulated |
| 8. | Sport complex | 1 | Yet to be connected |
| 9. | Towards the second adjacent | 1 | Regulated |
| 10. | The left side towards the anatomy building | 1 | Yet to be connected |
| 11. | Abuad female hostel | 3 | Very Good |
| 12. | Back of Abuad female hostel | 1 | Regulated |
| 13. | Back of Abuad female hostel (behind A and D wing | 1 | Functioning |
| 14. | Central hall of residence | 2 | Dormant |
| 15. | Beside Alfa Balgore hall | 2 | Dormant |
| 16. | Ventures Local kitchen (cafeteria 1) | 2 | Dormant |
| 17. | Front of kitchen | 2 | Pumping to capacity |
| 18. | Beside Water plant | 2 | Pumping to capacity |
| 19. | In front of the laundry | 2 | Pumping to capacity but not satisfying the users |
| 20. | Back of the water plant | 1 | Pumping to capacity but not connected |
| 21. | Old Abuad quarters (front of block C) | 2 | Pumping to capacity |
| 22. | Front of block f | 1 | Working to capacity |
| 23. | Back of block I | 2 | It is regulated because of its low yield, also low recharging strength |
| 24. | Front of block | 1 | Defective |
| 25. | White Rock | 1 | Very Good |
| 26. | Inside ABUAD teaching hospital | 2 | Good |
| 27. | ABUAD medical hostel 1 | 1 | Working to capacity |
| 28. | ABUAD medical hostel 2 | 1 | Working to capacity |
| 29. | Beside Caf 1 | 1 | Yet to be connected |
| 30. | Behind Captain Cook | 2 | Pumping to capacity |
| 31. | Behind NFH1 | 1 | Pumping to capacity but not satisfying the users |
| 32. | Behind PTCF | 1 | Pumping to capacity |
| Total | | 48 | |

Table 2: Population data:

| Name of hostel | 4 bedded rooms | 2 bedded rooms | 1 bedded room |
|---|---|---|---|
| Hostel 1 | 128 | 184 | 16 |
| Hostel 2 | 128 | 184 | 16 |
| 4 man deluxe | 48 | | |
| 2 man deluxe | | 160 | 24 |
| Freshers' Hostel | 192 | 8 | |
| Med. Hostel | | 112 | |
| Total Rooms | 496 | 648 | 56 |
| Total Students | 1984 | 1296 | 56 |
| **Total Boys** | **3336** | | |
| Name of hostel | 4 bedded rooms | 2 bedded rooms | 1 bedded room |
| Abuad Hostel | 425 | 2 | 17 |
| Wema Hostel | 400 | 5 | 4 |
| NFH 1 | 96 | 260 | 13 |
| NFH 2 | 96 | 14 | |
| Med. Hostel | | 112 | |
| Total Rooms | 1017 | 393 | 34 |
| Total Students | 4068 | 786 | 34 |
| **Total Girls** | **4888** | | |
| **Grand Total (students):** | **8224** | | |

Source: (Field Study, 2022)

To obtain the number of students on campus, the authors went to all hostels and determined their capacity by counting the number of rooms and multiplying by the room capacity. They also obtained population data for previous years from the school registry.

- Daily water volume

  Using the data provided from obtaining the student population, they calculated the total volume of water used in each hostel by multiplying the value by the average volume of water used daily by an ABUAD student

- Population projection data

  The authors projected the future population of ABUAD using the different population forecasting formulas

- Obtaining survey data

  They created a google form containing questions to gather data on the student's interactions with ABAUD water supply facilities and how they perceive the current situation of water supply on campus. Table 1 indicates the functionality of water systems in ABUAD while Table 2 presented information on population data.

## Water Consumption

The population of students is 8500 (Wikipedia)

Assumed Consumption per head = 141litres

Total Consumption (water needed) = 1,198,500 litres/day

Breakdown:

- Bathing twice (2) a day at 20 liters = 40 liters
- Flushing of toilets twice (2) per day at 20 liters = 40 liters
- Washing (laundry) at 20 liters (3 buckets) = 60 liters
- Brushing twice (2) a day 0.5 liters = 1.0 liter

Total 141 liters

Water Demands in the hostel = (8500*141) litres

= 1,198,500 liters/day

$$\text{Average water consumed hourly} = \frac{1,198,500 \, litres/day}{24 \, hrs}$$

= 49,938 liters/hr.

## Water Savings

The population of students is 8500 (Wikipedia)

Assumed Consumption per head = 141 liters

Total Consumption = 1,198,500 litres/day

So, if the consumption of water was saved.

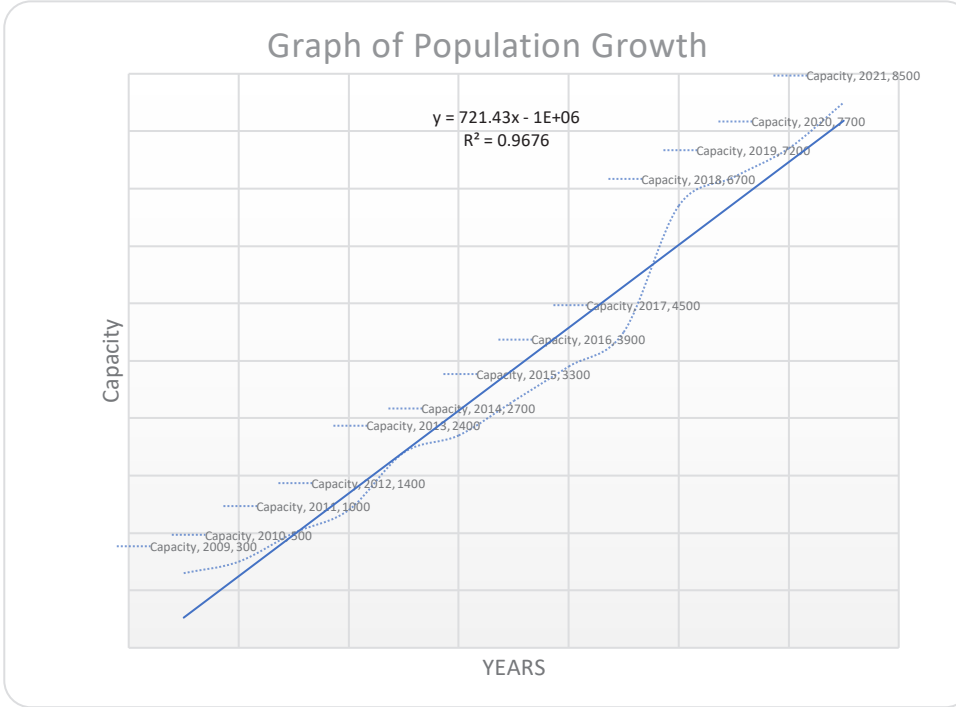


Fig. 1: Population growth between 2010 to 2022.

- Bathing = 40 liters
- Flushing = 20 liters
- Washing = 40 liters

Total 100 liters

100 litres × 8500 people = 850000 liters/day

If Greywater recycling is implemented, 50% of the water used in the ABUAD hostels would save up to 425000 litres/day. Fig. 1 presented the population growth between 2010 to 2022.

So, the volume of freshwater that would be needed to be supplied to the hostel would be Freshwater = total consumption – Recycled water

=1,198,500 – 425000

= 773,500 liters/day

Table 3 presented information on the capacity.

Table 3: Capacity forecast.

| Years | Capacity |
|---|---|
| 2009 | 300 |
| 2010 | 500 |
| 2011 | 1000 |
| 2012 | 1400 |
| 2013 | 2400 |
| 2014 | 2700 |
| 2015 | 3300 |
| 2016 | 3900 |
| 2017 | 4500 |
| 2018 | 6700 |
| 2019 | 7200 |
| 2020 | 7700 |
| 2021 | 8500 |

Methods for predicting future population growth use both current and historical demographic data. The value of a particular area's current and historical populations can be found in local census records. Population Growth data from 2009-2021:

Total population = 8500

Forecasting for 3 years, that means in 2023, the population will be estimated to be based on the Exponential Increase Method;

$$P_0 = P_n \times e^{k(t_2 - t_1)}$$

$$P_{2023} = 8500 \times e^{0.1(2023-2021)}$$

= 10,382 students (for the year 2023)

Water Consumed in 2023 = 10,382 student × 141 litres = 1,463,862 litres/day

Water saved with greywater system = 50% = 731,931 litres/day saved

As the population grows the water demand also increases over time to prevent water stress within ABUAD, a greywater filtration system should be implemented within the residential areas.

**Design of the Greywater Filtration System**

Greywater would enter the tank via 762 mm (30 inches) PVC piping from the structure. Scum accumulates on the surface of each tank as greywater runs through it, while solids or heavier particles fall at the bottom. The greywater is then filtered using a greywater filtering system that includes;

1. The gravel and pebbles filter out larger sediments.
2. The sand filters out the fine impurities.
3. The Activated carbon removes contaminants and impurities by absorption through the pores of the activated carbon.

Note: - Water from the filter is still unsafe to drink unless it is purified further for human consumption. Significant suspended particles, biochemical oxygen demand (BOD), turbidity, chemical oxygen demand (COD), and other water parameters are predicted to be reduced at the tank's final exit.

**Calculations for Male Hostels Only**

For Male Hostels, total population is 3336 boys

Water Consumption for Boys

= 141 liters/day (as previously calculated) * 3336 boys

= 470,376 liters/day

Therefore, the water consumption will be approximated to 500,000 litres/day for design safety.

If 1 $m^3$ = 1000 litres

Then 500,000 liters = 500 $m^3$ (Capacity of Sedimentation Tank)

500 $m^3$ (3.05 m × 14.63 m)

Height × Diameter

Area of tank

= 3.05 m × 14.63 m

= 44.6215 $m^2$

**Water Pipe Sizing**

Diameter of pipe = 30 inches

Diameter = 0.762 m

Volume Flow rate =?

Flowrate = Area × Velocity

$$\text{Area (A)} = \frac{\pi}{4}D^2$$

$$\text{A} = \frac{3.14}{4}(0.762)^2$$

A = 0.4558 $m^2$

**Velocity**

Average Velocity = Length of pipe × Time Taken to flow

= 1.8228 m × 2.4 sec

= 4.4 m/s

For 30 inches pipe, an average velocity will be 4.4 m/s

Now; - Flowrate= Area × Velocity

Q = 0.4558 × 4.4

Q = 2.0 m/s

Q = 2.0 × 3600

Q = 7220 $m^3$/h

**For Sedimentation Tank**

Capacity of tank = 500 $m^2$ (3.05 m × 14.63 m)

The volume of tank = 44.6215 $m^2$

$$\text{Detention period} = \frac{Volume\ of\ tank}{Rate\ of\ Flow}$$

$$= \frac{44.6215}{\left(\frac{500*10^3}{24}*10^{-3}\right)}$$

= 2.14 h

$$\text{Average flow velocity} = \frac{length}{Detenton\ time}$$

$$= \frac{3.05m}{2.14hrs} = \frac{305cm}{(2.14*60)} = 2.375 \text{ cm/min} = 1.425 \text{ m/h}$$

Flowrate = Area × Velocity

Q = VA

$$\text{A} = 2\pi r(r+h)$$

$$= 2 \times 3.14 \times \left(\frac{14.63}{2}\right) \times \left[\left(\frac{14.63}{2}\right) + 3.05\right]$$

A = 476.4 m

Q = 1.425 m/h × 476.4

= 678.87 $m^2$/h = 0.188575 $m^2$/s

**Sand Filter and Carbon filter**

Following the septic tank, a sand filter and carbon filter will

be used to reduce BOD, COD, TSS, and fecal coliform. Sand filter medium supplemented by gravel and activated carbon would be utilized in a 500 $m^3$ tank.

The surface area required for the filters will be calculated using a greywater flow rate of 7220 $m^3$/hr. and a sand media filtration rate of 15 $m^3/m^2$.hr. The surface area = 476.4 $m^2$

Filtration Velocity =

$$\frac{Flow\ rate\ from\ the\ pipe}{Surface\ Area} = \frac{7220m^3/h}{476.4m^2} = 15.16\ m^3/m^2/h$$

Since this tank's area is larger than the required filtration area it should be sufficient for use.

Like the septic tank system, the sand filer would be placed in a trench with backfilled gravel and activated carbon at a depth of 3/4 the height of the tank.

### Disinfection Tank

The disinfection tank will contain chlorine, which will be used to disinfect the water after it has been filtered. This will ensure that the water is not contaminated. Therefore, the chlorine dosage for the water will be 130 mg/L if the desired chlorine residual is 60 mg/L

Chlorine demand, mg/L = Chlorine dose, mg/L - Chlorine residual, mg/L

= 130 mg/L – 60 mg/L = 70 mg/L

### Storage Tank

The sand, carbon, and gravel filter-treated greywater will be stored in the storage tank. A 500 $m^3$ storage tank would be used since the capacity is the nearest size that is available locally. The efficacy of the filter calculated above was tested using a small-scale model, which was then used to filter the wastewater. All water that has come into touch with rubbish contained in a landfill is considered landfill leachate. Continuous confined animal operations, such as milk and egg production, necessitate agricultural wastewater treatment. With mechanical treatment devices that are equivalent to those used in industrial waste disposal, it can be done as long as the property is easily accessible, seasonal use circumstances such as breeding or harvesting may necessitate lower operational expenditures. Anaerobic lagoons are frequently used to store animal slurries before they are sprayed or dripped onto grassland. Occasionally, manmade wetlands are used to dispose of animal feces. Fig. 1 presented leachate sewage treatment flow chart. Fig. 2 presented the membrane Bioreactor design, while Fig. 3 presented a hydrological map of Nigeria showing the major inland waters.

Membrane bioreactors join microfiltration (MF) or ultrafiltration (UF) with a biological process, such as a suspended growth bioreactor, for wastewater treatment (WWT). The membranes act as a filter, removing particles that form during the biological process and producing a clean, pathogen-free product. Fig. 3 presented a typical Membrane Bioreactor design.

The hydrological map of Nigeria depicts the country's most important inland waterways. Fig. 4 presented the hydrological map of Nigeria.

## RESULTS AND DISCUSSION

A questionnaire was prepared to measure the daily water usage in the ABUAD Community's male and female hostels and to determine whether the water supply in ABUAD is enough. It comprises everything that must be assessed to determine the study's viability.

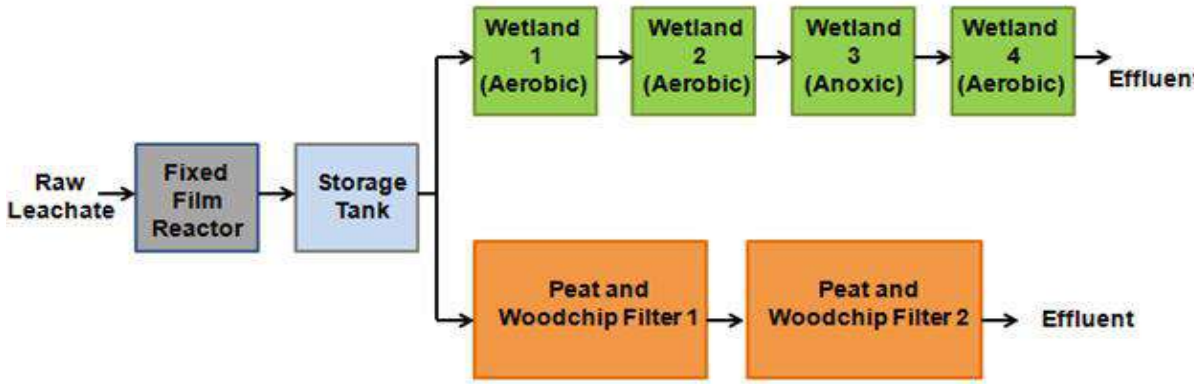


Source: (Lugowski et al. 2014)

Fig. 2: Leachate sewage treatment flow chart.

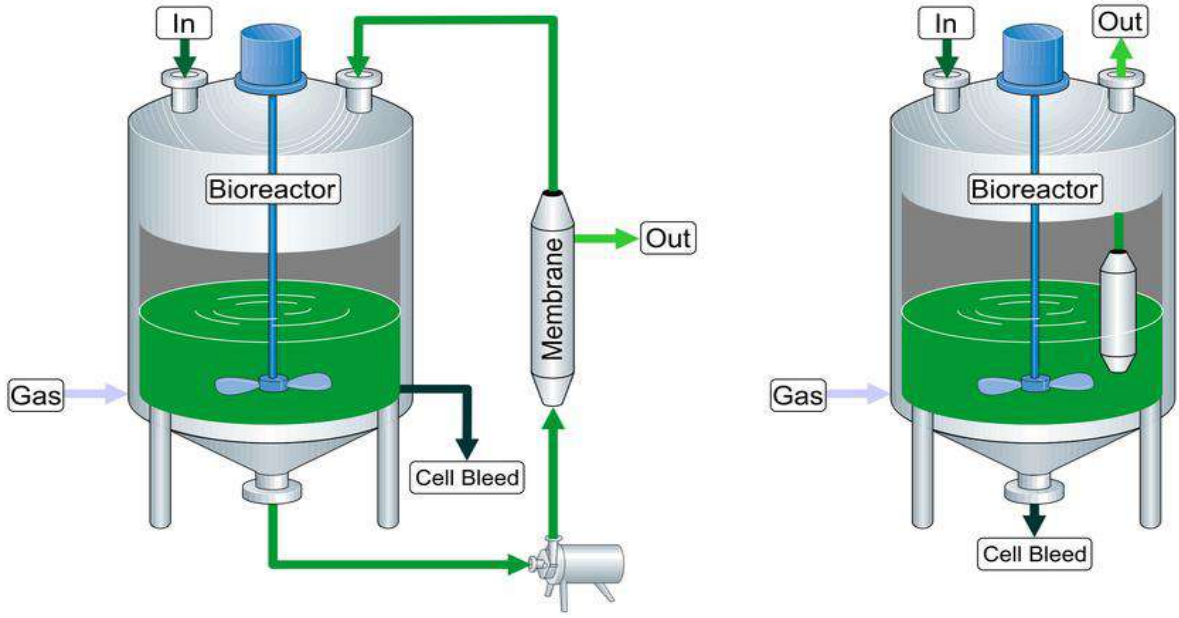


Source: (Sárvári Horváth 2016)

Fig. 3: Membrane bioreactor design.

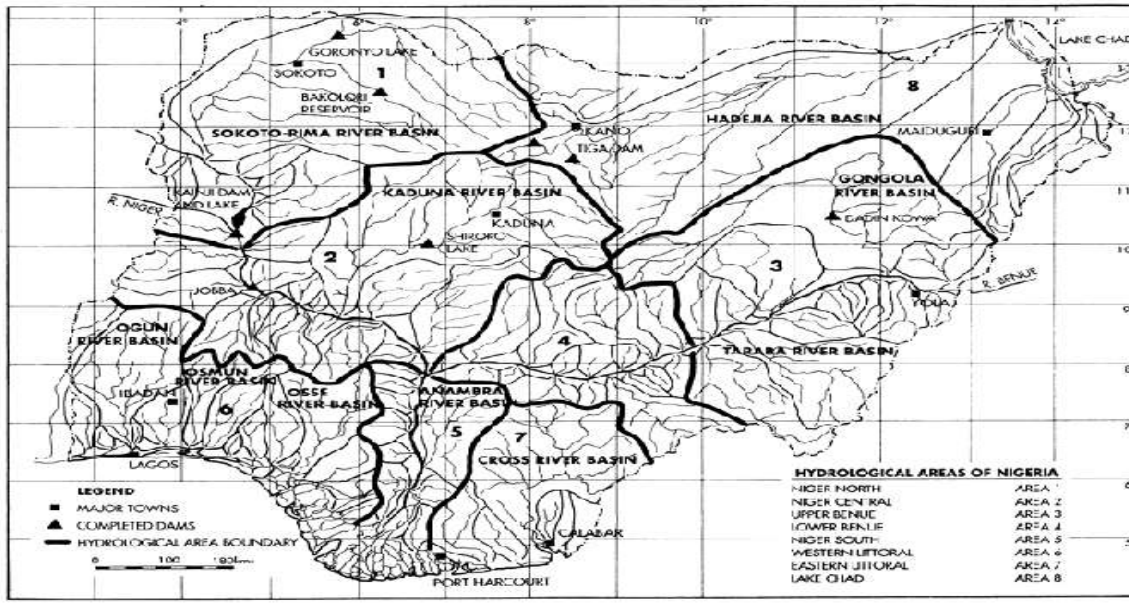


Source: (Oladimeji 2018)

Fig. 4: Hydrological map of Nigeria showing the major inland waters.

Fig. 6 presented information on the daily use of water in the hostel while Fig. 7 presented a statistical analysis of various use of water in the hostel.

The above survey results reflect the numerous responses received from both male and female students in their hostels, demonstrating their various water usage and satisfaction

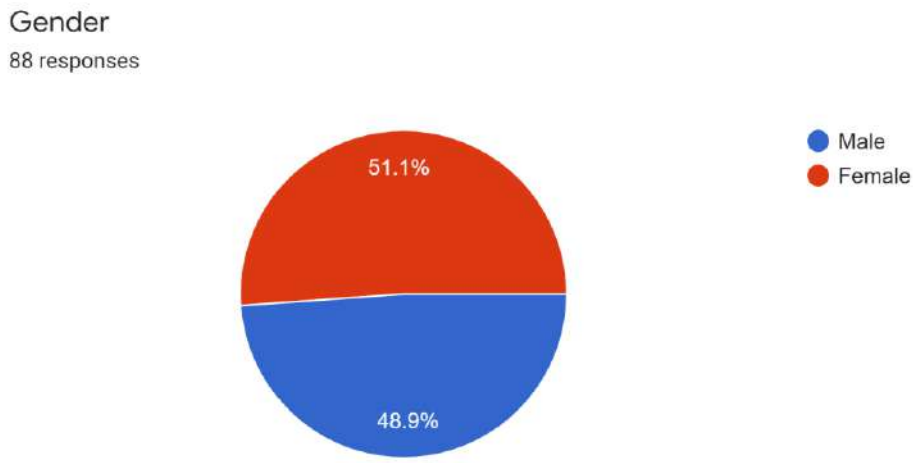


Fig. 5: Results from Google Form Questionnaire.

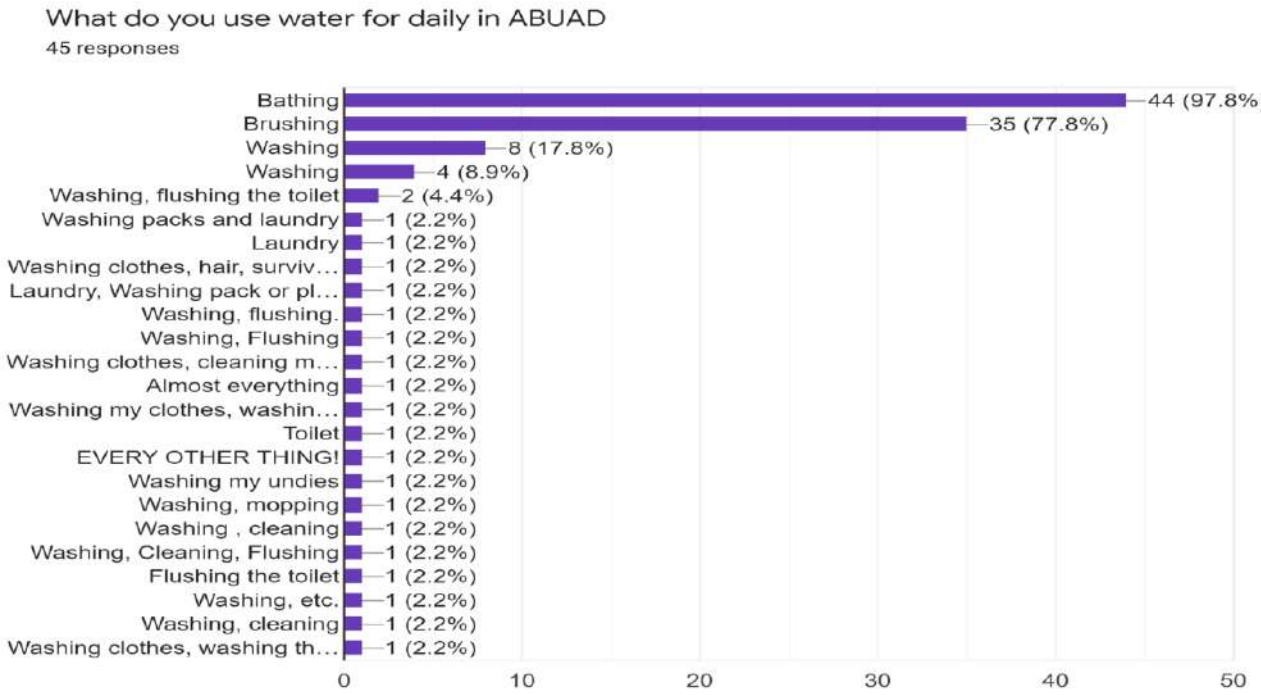


Fig. 6: Daily use of water in the hostel.

levels with the water supply. The results of the survey reflect their discontent with the water supply in their hostel, as shown in the survey form above, which received 88 replies (43 responses from boys and 45 responses from ladies).

**Results for the Water Quality test done before and after Filtration**

Table 4 presents the results of the water quality test carried out before treatment.

The water qualities in Table 5 demonstrate the various qualities and metrics of wastewater collected from several locations in ABUAD. Table 5 presented heavy Metals present in the greywater sample and Table 6 presents the results of the water quality test carried out after treatment and their comparison to the required water quality standard. It also presented the water qualities of the sample collected after they have been passed through the filtration system and their comparison to NDW standards.

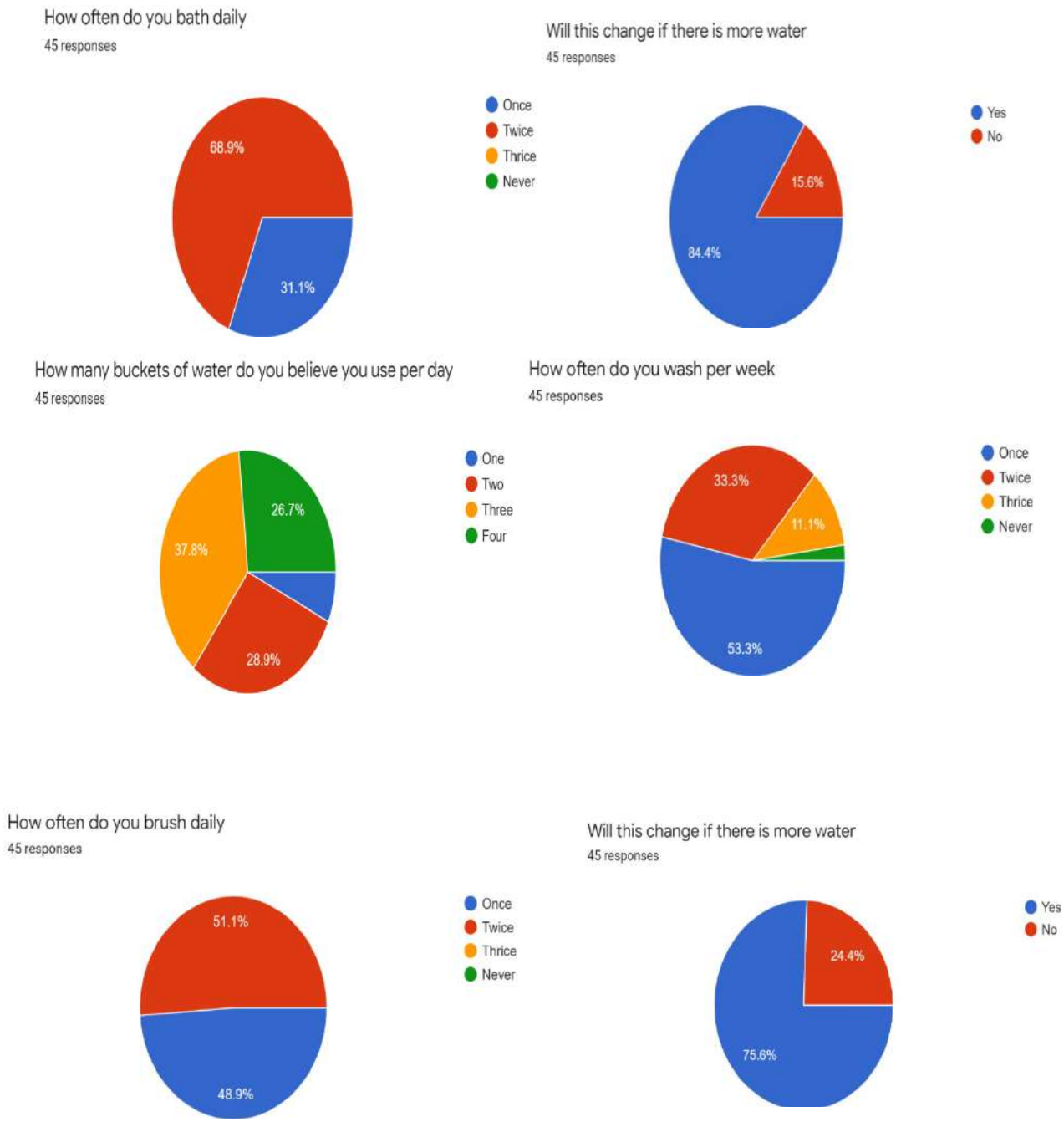


Fig. 7: Statistical analysis of various use of water in the hostel.

Results and values for the calculations are presented in Table 7.

## CONCLUSIONS

Although a greywater system can provide an alternative source of water and so reduce demand for main water supplies, it does not reduce overall water consumption; rather, it recycles water that has already been consumed. Residential non-profit water recycling for washing and toilet flushing has been demonstrated to significantly reduce the amount of potable water used. The system has been demonstrated to be a technically viable water delivery solution, especially in long-established institutions such as ABUAD. The

Table 4: Results of the water quality test carried out before treatment.

| S/N | TEST | Unit | Boys Hostel 2 | Laundry | Cafeteria | Girls Hostel 1 | Boys Hostel 2 |
|---|---|---|---|---|---|---|---|
| 1. | Ph | TCU | 8.4 | 10.94 | 7.3 | 8.5 | 10.2 |
| 2. | Total dissolved solids (TDS) | mg/L | 9.63 | 12.71 | 1424 | 1232 | 681 |
| 3. | Turbidity | NTU | 516 | 854 | 88.7 | 697 | 270 |
| 4. | Calcium Hardness | mg/L | 184 | 180 | 194 | 189 | 174 |
| 5. | Conductivity | µs/cm | 19.28 | 25.4 | 12.87 | 12.46 | 13.79 |
| 6. | Dissolved Oxygen | mg/L | 5.68 | 4.22 | 5.87 | 5.88 | 5.71 |
| 7. | Biochemical Oxygen Demand (COD) | mg/L | 30 | 22 | 48 | 46 | 41 |
| 8. | Chemical Oxygen Demand (COD) | mg/L | 96 | 113 | 164 | 128 | 124 |

Table 5: Heavy metals present in the greywater sample.

| | | Sample #1 | | Sample #2 | |
|---|---|---|---|---|---|
| S/N | Metals | Absorbance | Concentration (mg/L) | Absorbance | Concentration |
| 1. | Pb | 0.035 | 1.570 | 0.052 | 9.667 |
| 2. | Cd | 0.140 | 1.950 | 0.167 | 2.360 |
| 3. | As | 0.004 | 0.036 | 0.013 | 0.199 |
| 4. | Cr | 0.160 | 3.260 | 0.102 | 2.044 |
| 5. | Mn | 0.206 | 2.270 | 0.174 | 2.476 |
| 6. | Fe | 0.145 | 2.618 | 0.156 | 2.817 |
| 7. | Cu | 0.230 | 3.245 | 0.476 | 6.774 |
| 8. | Zn | 0.107 | 1.361 | 0.239 | 3.137 |

Table 6: Results for the water quality test carried out after treatment and their comparison to the required water quality standard.

| S/N | TEST | Unit | Boys Hostel 2 | Laundry | Cafeteria | Girls Hostel 1 | Boys Hostel 2 | Nigeria Drinking Water Standard |
|---|---|---|---|---|---|---|---|---|
| 1. | pH | TCU | 7.43 | 7.31 | 7.46 | 8.11 | 7.61 | 6.5-8.5 |
| 2. | (TDS) | mg/L | 360 | 288 | 12.2 | 10 | 234 | 500 |
| 3. | Turbidity | NTU | 4.68 | 4.35 | 5.68 | 4.85 | 4.42 | 5 |
| 4. | Calcium Hardness | mg/L | 85 | 85 | 123 | 136 | 112 | 150 |
| 5. | Conductivity | µs/cm | 178 | 182 | 184 | 188 | 174 | 1000 |
| 6. | Dissolved Oxygen | mg/L | 3.86 | 3.65 | 3.78 | 3.64 | 3.52 | 6.5-8 |
| 7. | Biochemical Oxygen Demand (BOD) | mg/L | 2.57 | 3.6 | 3.9 | 3.96 | 2.87 | 1 |
| 8. | Chemical Oxygen Demand (COD) | mg/L | 16.5 | 16.8 | 27 | 22 | 17.8 | - |

Table 7: Results for population forecast and water demand.

| | |
|---|---|
| Total current population of ABUAD 2021 | 8500 people |
| Future Design period | 3 years |
| Total Population in 2023 | 10,382 students |
| Water Consumption per student | 141 liters |
| Water Demand in the hostel daily | 1,198,500 liters/day |
| Water Recycled (50%) | 425,000 liters/day |
| Freshwater Saved | 773,500 liters/day |

fundamental objective of this research is to investigate the viability of implementing greywater recycling systems in ABUAD residential areas, characterize wastewater in the ABUAD community, and evaluate recycling technologies using Analytical Hierarchy methodologies. The amount of water that was calculated to be saved daily with the use of a greywater recycling system was demonstrated to be effective if it was implemented in ABUAD residential area. There are numerous options for water treatment, recovery, and reuse. For best efficiency, many low-tech greywater recycling solutions can be combined. As a result, you can't compare

treatment methods because the treatment method we choose is determined by the rate of pollution of recycled wastewater. Each recycling method has its own characteristics.

## RECOMMENDATIONS

Since recycling wastewater has been shown to offer financial benefits and reduce the quantity of freshwater consumption, these practices ought to be made more widespread shortly. There is not enough knowledge among the general people. As a result, it is recommended that the importance of recycling wastewater is brought to the attention of more people, as well as that awareness be raised. It is possible to explain the significance of wastewater, as well as support the dependability and high quality of reclaimed water. Demonstration projects need to receive more focus, and members of the general public should be invited to see urban water reuse facilities. A facility for recycling greywater should be designed or built at ABUAD so that it may be used to facilitate the reuse of greywater, which in turn will help save freshwater and improve the quality of the environment. Communities and educational institutions should implement a greywater recycling system within their residential areas in other to save costs and increase the shelf life of the environment. Storage of greywater should not be kept for more than 24 hours in other for it not to develop a foul odor. When recycling greywater it should always undergo biological treatment to prevent microorganisms like bacteria, fungi, worms, etc., so it may be consumable for humans.

## ACKNOWLEDGMENT

We acknowledge Aare Afe Babalola and the entire management of ABUAD for their support for quality research and special drive towards excellent education in Africa geared towards the achievement of sustainable development goals.

## REFERENCES

Aderomose, K.S. and Oyebode, O.J. 2022. Effective Wastewater Management for Health and Sustainable Environment in Afe Babalola University (ABUAD).

Andarge, N. A. 2019. Assessment of greywater treatment methods for reuse in Addis Ababa condominiums-a case of summit condominium. Addis Ababa Science and Technology University

Awomeso, J.A, Taiwo, A.M, Gbadebo, A.M. and Adenowo, J.A. 2010. Studies on the pollution of a waterbody by textile industry effluents in Lagos, Nigeria. J. Appl. Sci. Environ. Sanit., 5(4): 353-359.

Birks, R., Colbourne, J., Hills, S., and Hobson, R. 2004. Microbiological water quality in a large in-building, water recycling facility. Water Sci. Technol., 50(2): 165-172.

Chopin, T., Buschmann, A.H., Troell, M., Kautsky, N., Neori, A. and Yarish C. 2011. Integrating seaweeds into marine aquaculture systems: A key toward sustainability. J. Phycol., 37: 975-986.

Dey, S., Haripavan, N., Basha, S.R. and Babu, G .V. 2021. Removal of ammonia and nitrates from contaminated water by using solid waste bio-adsorbents. Curr. Res. Chem. Biol., 1: 100005.

Fernández, C. H. Z., Téllez, C. A. L., Orea, Y. F., and Barbosa, E. M. 2022. Total angular momentum of water molecule and magnetic field interaction. arXiv preprint arXiv:2210.01867.

Gutiérrez-Ramírez, R., Fernández-Luqueño, F., Medina-Pérez, G., Pérez-Hernández, H., López-Valdez, F., Vázquez-Núñez, E., Loera-Serna, S., Salas-Herrera, G., Zavala-Cortés, A. and Inchauregi, V.U. 2018. Agronanobiotechnologies to Improve the Water Quality in Irrigation Systems. In: López-Valdez, F. and Fernández-Luqueño, F. (eds), Agricultural Nanobiotechnology: Modern Agriculture for a Sustainable Future, Springer International Publishing, Cham, pp. 141-157.

Jefferson, B., Palmer, A., Jeffrey, P., Stuetz, R. and Judd, S. 2004. Greywater characterization and its impact on the selection and operation of technologies for urban reuse. Water Sci. Technol., 50(2): 157-164.

Imron, M.F., Kurniawan, S.B. and Titah, H.S. 2019. Potential of bacteria isolated from diesel-contaminated seawater in diesel biodegradation. Environ. Technol. Innov., 14: 100368.

Khalid, F.E., Lim, Z.S., Sabri, S., Gomez-Fuentes, C., Zulkharnain, A. and Ahmad, S.A. 2021. Bioremediation of diesel contaminated marine water by bacteria: A review and bibliometric analysis. Journal of Marine Science and Engineering, 9(2): 155.

Lugowski, A., Arabi, S., Millar, D. and Wilsey, S. 2014. Biological treatment of landfill leachate: overview and case examples. In: Global Waste Management Symposium, pp. 13-1.

Mathurin, Z.G., Kisito, T.P., Francois, N. and Fogue, M. 2022. Risk assessment of chemical pollution of industrial effluents from a soap production plant. Nat. Environ. Pollut. Technol., 21(3): 65-73

Nathanson, J.A. 2020. Wastewater Treatment. https://www.britannica.com/technology/wastewater-treatment. (Accessed 3 March 2022).

Neori A., Ragg, N.I.C. and Shpigel, M. 1998. The integrated culture of seaweed, abalone, fish, and clams in modular intensive land-based systems: II: Performance and nitrogen partitioning within an abalone (Haliotis tuberculata) and macroalgae culture system. Aquacult. Eng., 17: 215-239.

Ogarekpe, N. M., Nnaji, C. C., Oyebode, O. J., Ekpenyong, M. G., Ofem, O. I., Tenebe, I. T., and Asitok, A. D. 2023. Groundwater quality index and potential human health risk assessment of heavy metals in water: a case study of Calabar metropolis, Nigeria. Environmental Nanotechnology, Monitoring and Management, 100780.

Oladimeji, Y. 2018. Assessment of Trend of Artisanal Fish Production in Nigeria Vis-a-Vis Implications on Economic Growth. Department of Fisheries, Faculty of Agriculture, University of Maiduguri, Nigeria.

Oyebode, O.J. 2019. Strategic approach for controlling soil and groundwater contamination in urban and rural areas of Nigeria. Arid Zone J. Eng. Technol. Environ., 15(4): 973-984.

Oyebode, O. J. 2022a. Biomedical engineering education: equipment, prospect and challenges for environmental healthcare in Nigeria. In: Advanced Manufacturing in Biological, Petroleum, and Nanotechnology Processing: Application Tools for Design, Operation, Cost Management, and Environmental Remediation, pp. 157-163. Cham: Springer International Publishing.

Oyebode, O. J. 2022b. Design of water retaining structures and application of environmental engineering for sustainable environment. In: Advanced Manufacturing in Biological, Petroleum, and Nanotechnology Processing: Application Tools for Design, Operation, Cost Management, and Environmental Remediation, pp. 287-299. Cham: Springer International Publishing.

Oyebode, O. J. and Otoko, J. A. 2022. Medical waste management and design of a low-cost incinerator for reduction of environmental pollution in a multi-system hospital. Nature Environment and Pollution Technology, 21(4).

Rose, J.B., Sun, G-S., Gerba, C.P. and Sinclair, N.A. 1991. Microbial quality and persistence of enteric pathogens in greywater from various household sources. Water Research, 25(1): 37-42.

Sárvári, H., Ilona, T., Meisam, K. and Kumar, R. 2016. Recent updates on biogas production: A review. Biofuel Res. J., 3: 394-402. 10.18331/BRJ2016.3.2.4.

Sun, X., Hu, Z., Li, M., Liu, L., Xie, Z., Li, S. and Liu, F. 2019. Optimization of pollutant reduction system for controlling agricultural non-point-source pollution based on grey relational analysis combined with analytic hierarchy process. Journal of Environmental Management, 243: 370-380.

Tchobanoglous, Burton, F.L. and Stensel, D.H. 2003. Wastewater Engineering: Treatment and Reuse. Fourth Edition. Metcalf & Eddy Inc., Wakefield, MA, USA.

Tse-Lun, C., Li-Heng, C., Yupo, J.L., Chang-Ping, Y., Hwong-Wen, M. and Pen-Chi, C. 2021. Advanced ammonia nitrogen removal and recovery technology using electrokinetic and stripping process towards a sustainable nitrogen cycle: A review. J. Clean. Prod., 309: 127369.

WHO 2008. Guidelines of World Health Organization for Drinking-Water Quality. Geneva, Switzerland.

Yusuff, A. S., Thompson-Yusuff, K. A., Adeniyi, O. D. and Olutoye, M.A. 2022. Siliceous termite hill supported ZnO-TiO2 as a solar light responsive photocatalyst: synthesis, characterization, and performance in the degradation of methylene blue dye. Surf. Interf., 786: 102360.

Nature Environment and Pollution Technology
An International Quarterly Scientific Journal

p-ISSN: 0972-6268
(Print copies up to 2016)
e-ISSN: 2395-3454

Vol. 22 | No. 1 | pp. 369-382 | 2023

Original Research Paper

https://doi.org/10.46488/NEPT.2023.v22i01.036

Open Access Journal

# Groundwater Quality Assessment in Korba Coalfield Region, India: An Integrated Approach of GIS and Heavy Metal Pollution Index (HPI) Model

**Vijayendra Pratap Dheeraj*†, C. S. Singh*, Nawal Kishore* and Ashwani Kumar Sonkar***

*Department of Mining Engineering, Indian Institute of Technology (Banaras Hindu University), Varanasi-221005, India

†Corresponding author: Vijayendra Pratap Dheeraj; vijayendrapdheeraj.rs.min19@itbhu.ac.in

**Nat. Env. & Poll. Tech.**
**Website: www.neptjournal.com**

*Received:* 15-08-2022
*Revised:* 01-10-2022
*Accepted:* 04-10-2022

**Key Words:**
Water quality
Heavy metal pollution index
GIS
Correlation matrix
Cluster analysis
KCF region

## ABSTRACT

The goal of this study was to examine the water quality for drinking and domestic purposes in the Korba coalfield region of Chhattisgarh, India. The Korba Coalfield region has seen the collection of fifteen groundwater samples from different places. The content of eight metals was determined using ICP-MS instruments: aluminum (Al), barium (Ba), cadmium (Cd), iron (Fe), magnesium (Mn), lead (Pb), nickel (Ni), and zinc (Zn). Spatial distribution maps were produced using GIS software to make it simple to understand the groundwater's quality. The groundwater samples were collected during the pre-monsoon season and the amount of Al, Ba, Cd, Fe, Mn, Pb, Ni, and Zn exceeded the ideal drinking water standards in a few sites. The elevated metal concentrations in the study region's groundwater could be hazardous to the quality of water. The HPI value based on mean concentration was calculated to be 21.64, which is significantly lower than the reference pollutant index score of 100. The HPI calculation revealed that 73.33% of groundwater samples had low HPI values, 6.67% had medium HPI values, and the remaining 20% had high HPI values. The correlation between heavy metals and HPI was calculated; HPI is positively correlated with Fe ($r > 0.9471$), Pb ($r > 0.9666$), and Zn ($r > 0.9634$), indicating that these elements contribute significantly more to heavy metal concentration in the various samples examined than the other selected elements. The box plot seems to be a graphical representation of the outcomes of the different parameter concentrations which show the mean, maximum, and minimum metal values. The cluster analysis was performed and it was classified into two clusters. Cluster-1 comprises 14 members (93.33%) of the water samples examined and is distinguished by relatively low Ba (<700 $\mu g.L^{-1}$), pH, TDS, Al, Fe, Cd, Mn, Pb, and Zn concentrations. Cluster-II is made up of 1 member (6.67%), which is primarily made up of groundwater samples (GW-10) taken in the KCF region, India. High values of HPI are found in the eastern portion of Chhattisgarh's KCF region, reflecting the spatial distribution of metals. Heavy metal leaching from open-pit mining and transit routes was observed to have contaminated groundwater in the eastern section of the research region.

## INTRODUCTION

Water is very essential for all living things for sustaining on earth, therefore, its quality and quantity examination are important at a certain time interval. Sharp changes have been found in demands for potable water due to surface water scarcity and the vast increase in population in many regions around the world. Two vital methods HPI and GIS were used to map the distribution of metals in groundwater in the KCF Region. People in India mostly use groundwater for household and drinking uses, therefore water contamination from mining is a big problem in this area (Tiwari et al. 2017). Chemical contamination in the surrounding area is only increasing as a result of the mining process, disposal of overburdens, and coal washing, which also impacts the quality and quantity of surface and groundwater (Singh et al. 2008, Ahmed et al. 2022)

The quality of groundwater is degraded due to untreated waste discharge and groundwater resource overexploitation. In India, approx 21% of communicable diseases in humans are occurring only because of contaminated water (Brandon & Hommann 1995, Dheeraj et al. 2022). The HPI assesses the total impact of individual pollutants on water quality (Giri & Singh 2014). Many of the researchers have done their studies on topics related to mining and its impacts on surface and groundwater with reference to heavy metals for different coal mines (Singh 1988; Tiwary & Dhar 1994; Prasad & Bose 2001; Giri et al. 2010; Tiwari et al. 2017). However, only a few studies are available on mines, especially on surface and groundwater regarding heavy metals in India (Senapaty & Behera 2012, Mahato et al. 2014, Tiwari et al. 2017, Singh et al. 2017).

Heavy metal concentration is induced in groundwater through many sources that may be natural or anthropogenic

(Adaikpoh et al. 2006, Vishwakarma et al. 2020). In most native habitats, the metal content is extremely low which is almost generated from weathering of geological formations and minerals (Karbassi et al. 2008). The solid waste generated from municipal can share some amounts of metals into groundwater through medicines and household pesticides, body care products, plastics, and paints and inks (Bardos 2004). According to (Lee et al. 2007, Adams et al. 2008, Lohani et al. 2008), non-biodegradable metal contamination is extremely important due to its potential toxicity for both humans and human body systems, such as the nervous system and internal organs, which can be damaged rapidly. In this study, the main aim was to evaluate the groundwater suitability for drinking uses around the mining area of KCF through the HPI model.

## STUDY REGION

The Korba Coalfield region is situated in the Korba district of Chhattisgarh which lies between 22° 15' N 22° 30' N latitude and longitude of 82° 15' to 82° 55' E as given in Fig. 1. This selected region of KCF is extended around 226.57 km$^2$ in Chhattisgarh state and lies in the Toposheet number F44K11 as per Survey of India (SOI). The non-coking coal is produced by these KCF coal mines.

These coal mines are located in the basin of the Hasdev River, a tributary of the Mahanandi River. The three mega-operated opencast mines such as Gevra OC, Dipka OC, and Kushmunda OC come under the Korba mine. KCF region is characterized by tropical climates having very hot about 45°C in May- June month and low about 2-4°C from December to January month. The average annual rainfall is around 1287 mm in the monsoon season (June - September) accounting for more than 85% of the total.

### Geology and Hydrogeology

The geology of the research region is defined by the Gondwana Super Group's Barakar Formation, which lies directly above the Precambrian schist (Raja Rao 1983). The formations in this area have an overall dip of 5° to 8° to the south and are trending E-W. Many transverse faults that run NE-SW, NW-SE, and EW and have different throw magnitudes further distinguish the area differently. Among these, the E-W trending fault with a southerly throw in the northern half of the study region is significant because it is in juxtaposition with the Upper and Lower Barakar formations. This fault divides the Upper Barakar Formation from the Lower Barakar and it likely disappears or has a negligible throw near the Hasdeo River (CMPDIL 2014). The majority

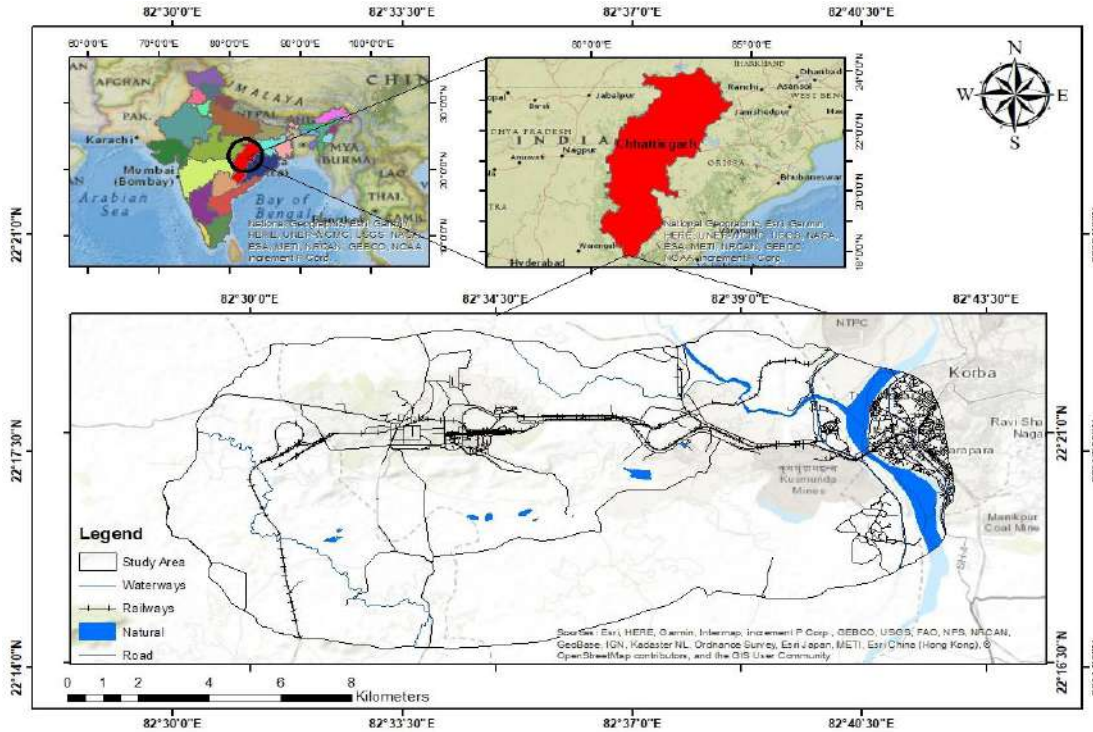


Fig. 1: Study area map.

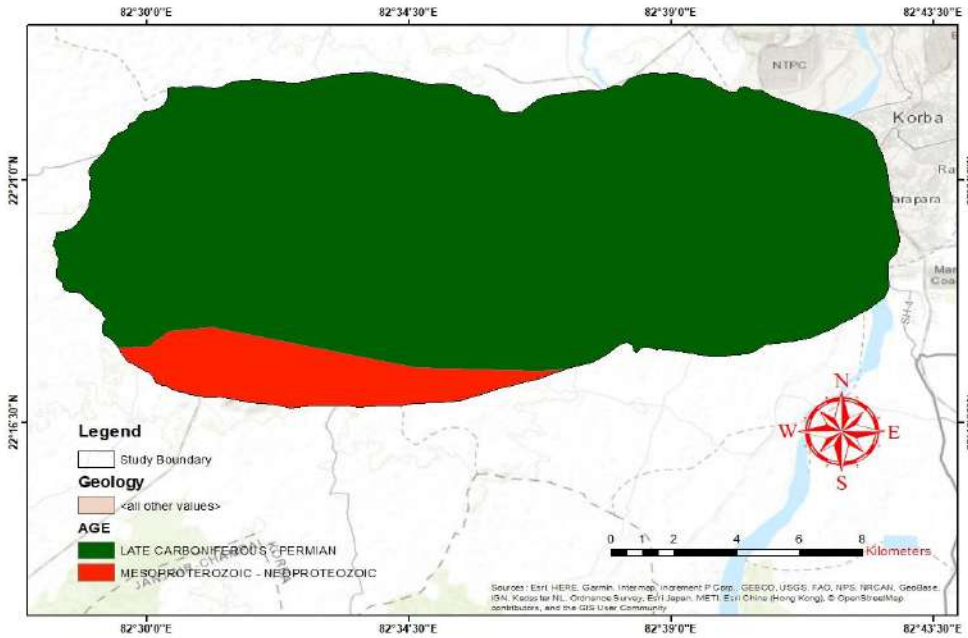


Fig. 2: Geology of the study area.

of the examined region is covered hydrogeological by the Upper Barakar Formation, which is composed of arkosic sandstone with a range of grain sizes, carbonaceous shale beds, and thick coal seams. The superficial deposit, which is composed mostly of alluvium & sandstone and is located above the active coal seams, acts as an unconfined aquifer. The lower formations, on the other hand, are semi-confined or confined aquifers because they are made mainly of compact sandstone with secondary porosity (CGWB 2012). Apart from it, the geology and geomorphology of this area are shown in Fig. 2 & 3 (GSI 2019).

## MATERIAL AND METHODS

### Sampling and Water Assessment

During the pre-monsoon season (March 2022), a total of (n=15) groundwater samples from the KCF region were collected in narrow-mouth polyethylene bottles with a capacity of 100 mL for this investigation. The pH concentration of groundwater samples was determined which ranged from 6.3 to 7.8 with the multiparameter instrument. This instrument was calibrated with pH 4.0 & 7.0 buffer solution. It was found that the water samples were near neutral to alkaline in nature in pre-monsoon season. Before experiments, all samples got filtered through a 0.22 m syringe filter by changing the pH value using a nitric acid solution (Radojevic et al. 1999). The TDS concentration was determined, ranging between 97 an d 715 mg.$L^{-1}$ with a multiparameter instrument after calibration. To ensure reliability, the proper quality assurance process and safety measures were required, and each sample was easily handled to prevent contamination. All the used glassware was appropriately cleaned and ultrapure water from Milli-Q was utilized throughout the studies (Tiwari et al. 2017).A total of eight important elements (Al, Ba, Cd, Fe, Mn, Pb, Ni and Zn) were considered through ICP-MS (inductively coupled plasma-mass spectroscopy). To determine the ICP-confirmation MS's status, a calibration blank, and an independent calibration verification standard have been analyzed for every 10 samples. Most of the time, with comparable accuracy, the precision improved to better than 5% RSD.

### HPI Specification

A model of grading called the Heavy Metal Pollution Index (HPI) enables the composite impact of individual metal on the overall quality of water (Sheykhi et al. 2012). To estimate of HPI, the unit weight (Wi) and recommended standard value (Si) of the appropriate elements were taken into consideration and these are inversely proportional to each other. The unit weight ranging from 0 to 1 has been assigned for heavy metals (Reddy 1995). The critical value of HPI is 100 according to (Prasad & Bose 2001). In this study area, the three types of HPI were taken into account. Correspondingly low HPI<15, Medium HPI 15-30, and High HPI>30 (Edet & Offiong 2002). There are several steps for calculating HPI with the following equation as per Venkata Mohan et al. (1996).

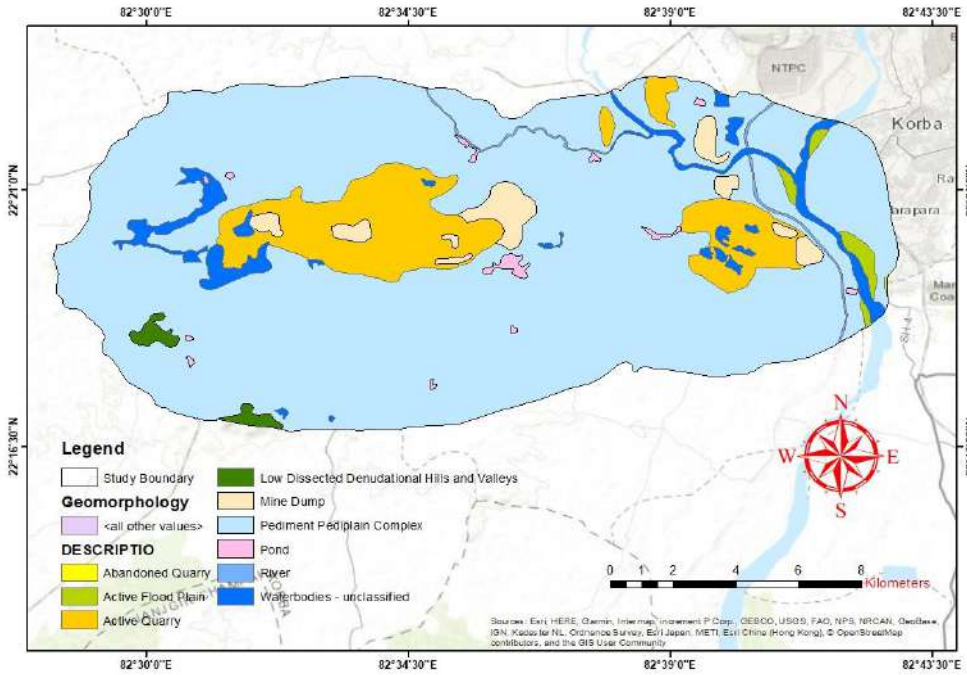


Fig. 3: Geomorphological map of the study area.

$$HPI = \frac{\sum_{i=1}^{n} WiQi}{\sum_{i=1}^{n} Wi} \quad ...(1)$$

Where n – Number of parameters

$W_i$ – unit weightage

$Q_i$ – Sub-index of $i^{th}$ parameter calculated by Equation 2.

$$Qi = \sum_{i=1}^{n} \frac{(Mi - Ii)}{(Si - Ii)} \times 100 \quad ...(2)$$

Where Sign (-) – represents a numerical difference of two value, not used for algebraic importance

$M_i$ – Monitored concentration

$I_i$ – Ideal value

$S_i$ – Standard value for the $i^{th}$ parameter ($\mu g.L^{-1}$).

Each pollutant concentration was converted into HPI when the HPI result was calculated. A higher HPI value can be harmful to one's health.

### Spatial Distribution Map

The HPI is a rating mechanism based on empirical data that determines the total influence of individual metals on water quality. The grading system gives a general sense of a rating that can be anywhere between 0 and 1, based on how significant each parameter is to the overall quality. The Toposheet number of this study area was geo-referenced with projection UTM Datum WGS-84 & Zone-45N on ArcGIS 10.8 software. The study area map was digitized on ArcGIS software. The spatial distribution of different elements was prepared with the spatial analyst tool in ArcGIS 10.8. The two different tools used to prepare the spatial distribution map with contour lines are IDW (Inverse distance weighted) interpolation and the contour option in ArcGIS software. With the help of these two modules in ArcGIS, it has drowned the spatial distribution maps for (pH, TDS), (Al, Fe, Pb, Zn, Cd), (Ba, Mn, Ni) and calculated HPI for the study area as shown in Fig. 4 and 7 respectively.

## RESULTS AND DISCUSSION

### Groundwater contamination

The concentration of contaminant has been determined and statistics have been listed in Table 1. The average value of all eight metals (Al, Fe, Pb, Zn, Cd, Ba, Mn, Ni) were 28.82, 658.29, 9.78, 1078, 0.09, 242.37, 111.59 & 24.86 $\mu g.L^{-1}$ in pre-monsoon season (March 2022). Only one element Cd was not exceeded its desirable limit as specified by WHO (2006) & BIS 2012 (IS 10500) at all selected sites (GW-1, 2, 3, 4, 5, 6, 7, 8, 9, 10, 11, 12, 13, 14 & 15).

In a previous study around KCF (Singh et al. 2017), it has been reported that the few metal concentration of

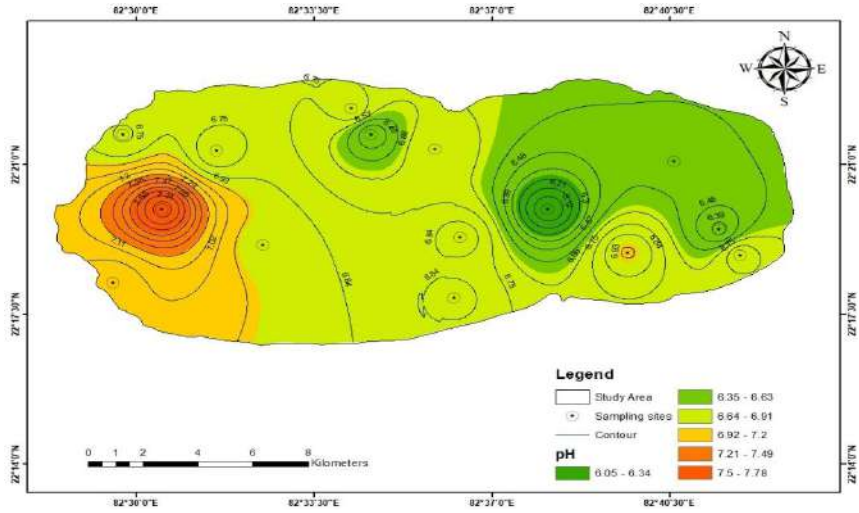
Legend
Study Area
Sampling sites
Contour
pH
6.05 - 6.34
6.35 - 6.63
6.64 - 6.91
6.92 - 7.2
7.21 - 7.49
7.5 - 7.78
Kilometers

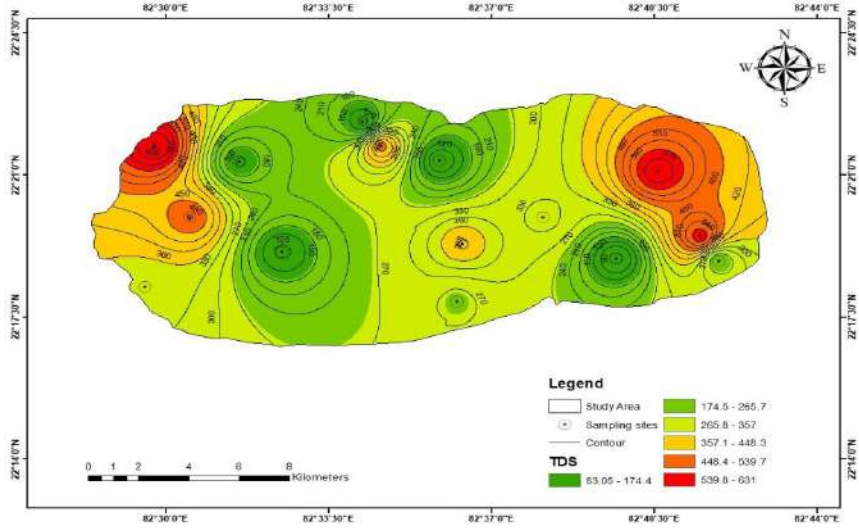
Legend
Study Area
Sampling sites
Contour
TDS
53.05 - 174.4
174.5 - 265.7
265.8 - 357
357.1 - 448.3
448.4 - 539.7
539.8 - 631
Kilometers

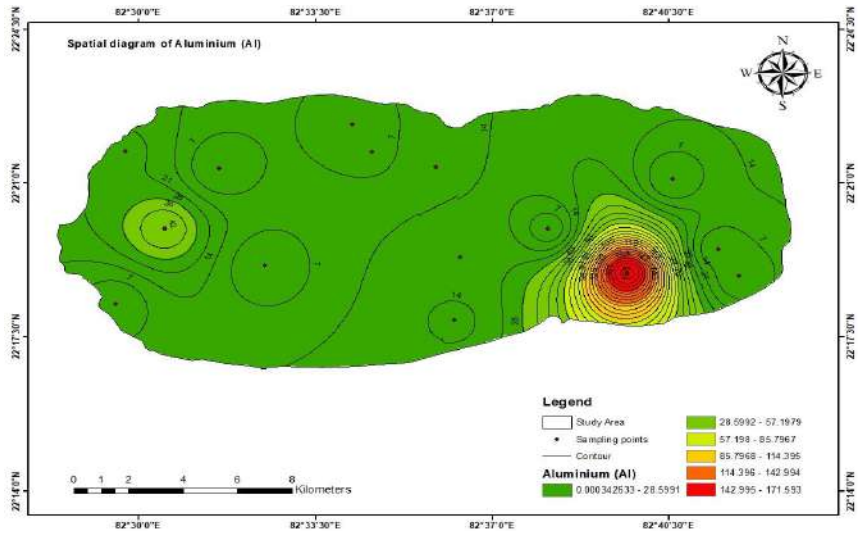
Spatial diagram of Aluminium (Al)
Legend
Study Area
Sampling points
Contour
Aluminium (Al)
0.000342633 - 28.5991
28.5992 - 57.1979
57.198 - 85.7967
85.7968 - 114.395
114.396 - 142.994
142.995 - 171.593
Kilometers

Fig. cont....

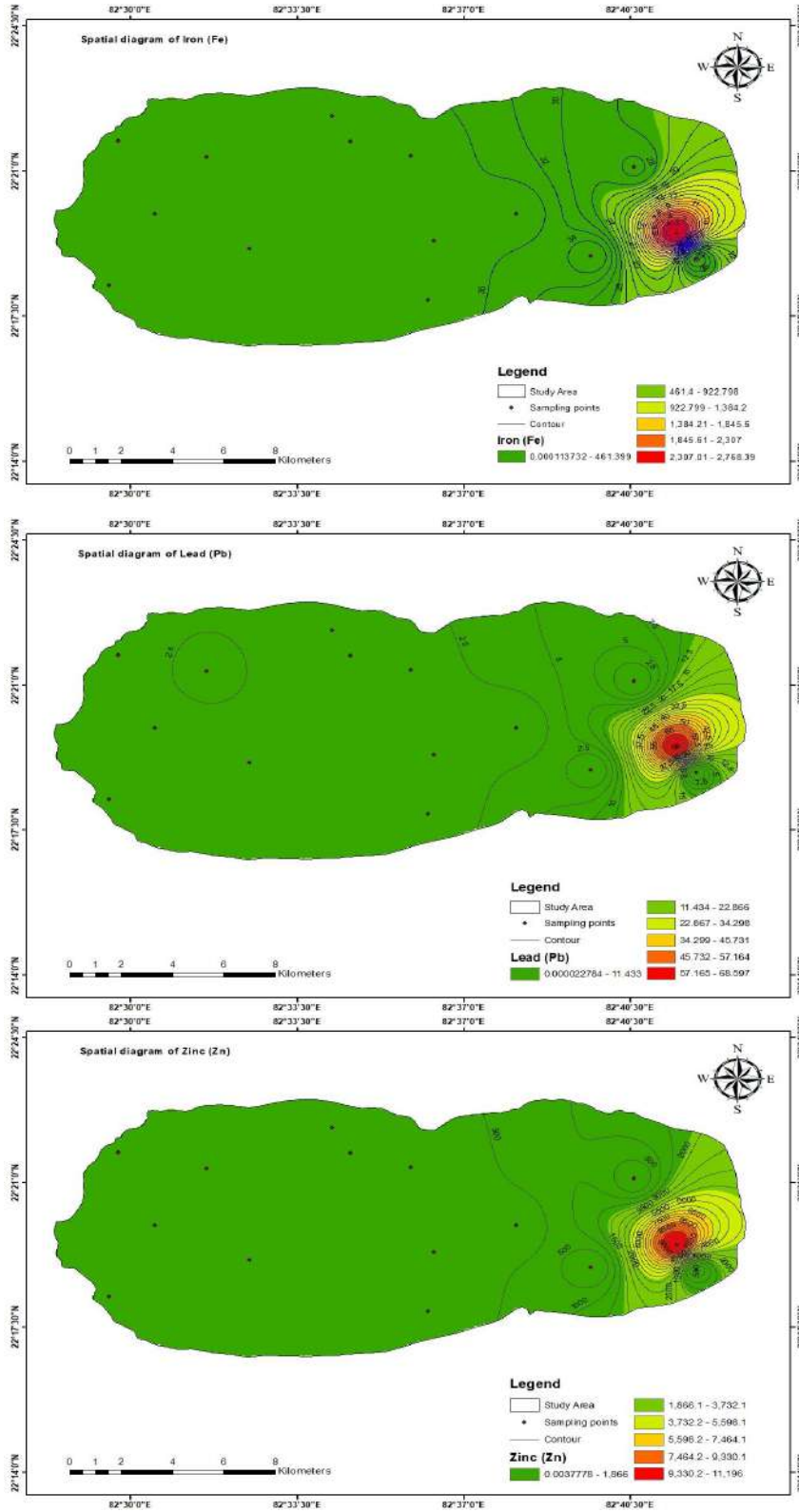
Spatial diagram of Iron (Fe)
Legend
Study Area
Sampling points
Contour
Iron (Fe)
0.000113732 - 461.399
461.4 - 922.798
922.799 - 1,384.2
1,384.21 - 1,845.6
1,845.61 - 2,307
2,307.01 - 2,768.39
Kilometers
Spatial diagram of Lead (Pb)
Legend
Study Area
Sampling points
Contour
Lead (Pb)
0.000022784 - 11.433
11.434 - 22.866
22.867 - 34.298
34.299 - 45.731
45.732 - 57.164
57.165 - 68.597
Kilometers
Spatial diagram of Zinc (Zn)
Legend
Study Area
Sampling points
Contour
Zinc (Zn)
0.0037778 - 1,866
1,866.1 - 3,732.1
3,732.2 - 5,598.1
5,598.2 - 7,464.1
7,464.2 - 9,330.1
9,330.2 - 11,196
Kilometers

Fig. cont....

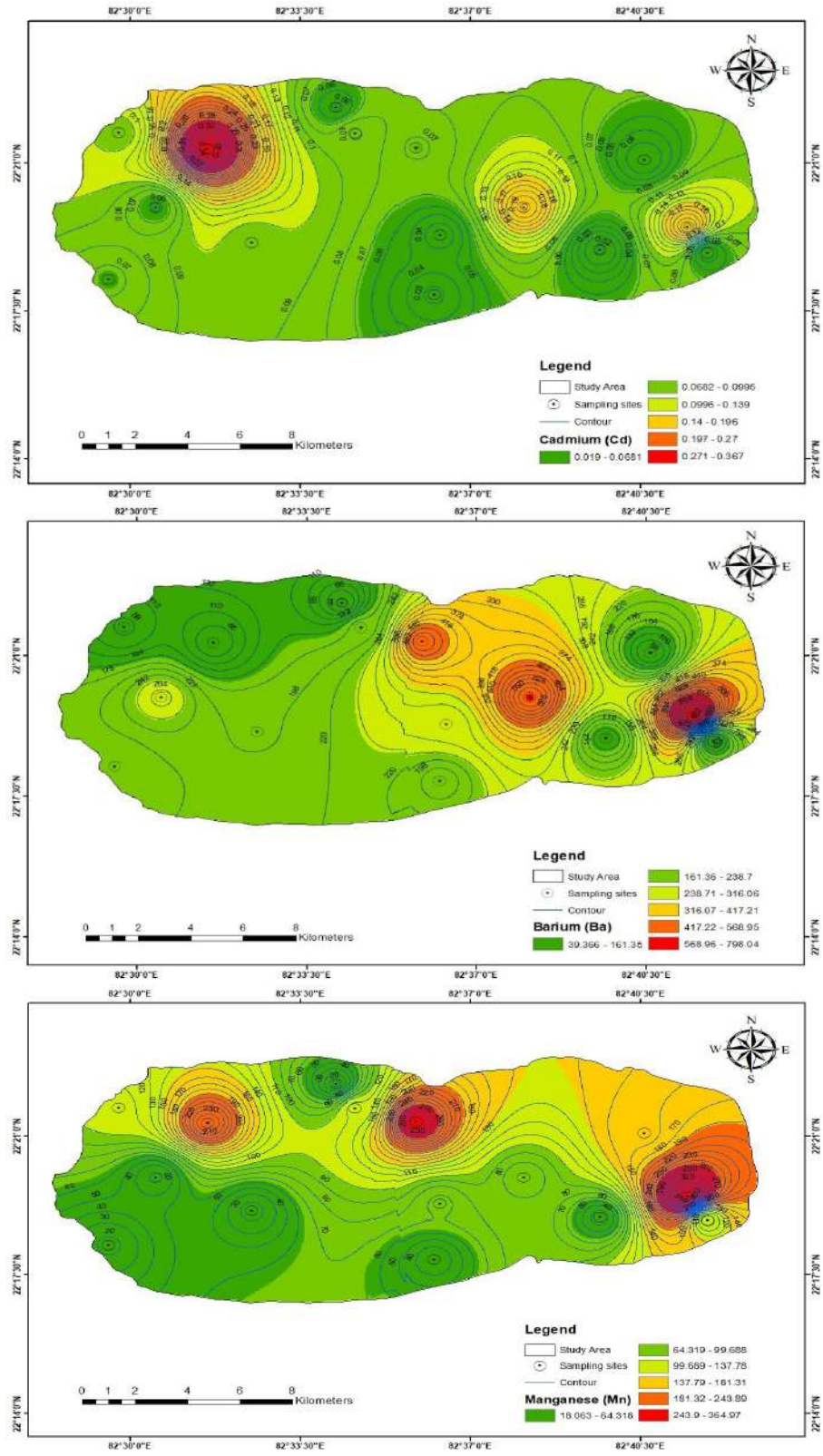
82°30'0"E
82°33'30"E
82°37'0"E
82°40'30"E
22°21'0"N
22°17'30"N
22°14'0"N
N
W
E
S
0 1 2 4 6 8
Kilometers
Legend
Study Area
Sampling sites
Contour
Cadmium (Cd)
0.019 - 0.0681
0.0682 - 0.0996
0.0996 - 0.139
0.14 - 0.196
0.197 - 0.27
0.271 - 0.367
Legend
Study Area
Sampling sites
Contour
Barium (Ba)
39.366 - 161.35
161.36 - 238.7
238.71 - 316.06
316.07 - 417.21
417.22 - 568.95
568.96 - 798.04
Legend
Study Area
Sampling sites
Contour
Manganese (Mn)
18.063 - 64.318
64.319 - 99.688
99.689 - 137.78
137.79 - 181.31
181.32 - 243.89
243.9 - 364.97

Fig. cont....

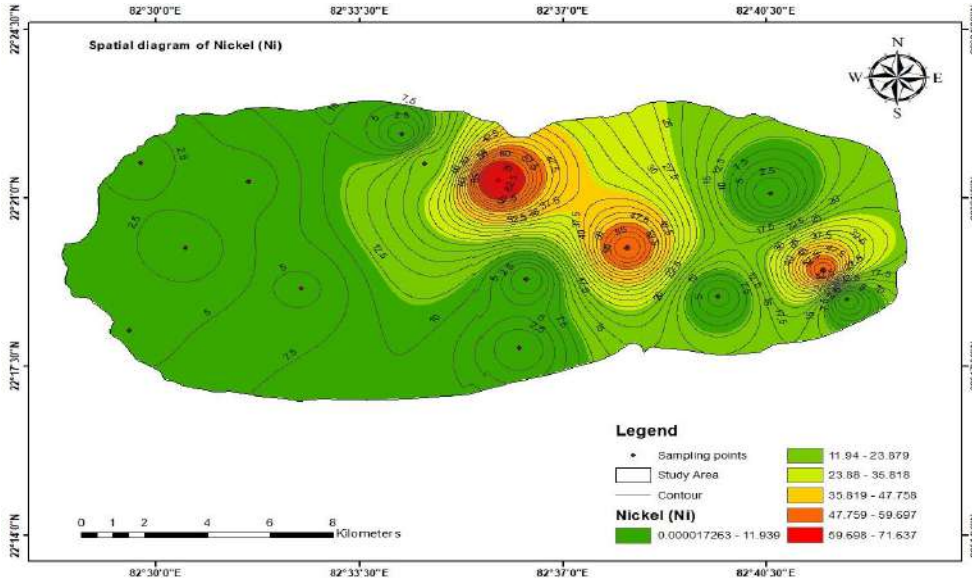


Fig. 4: Spatial distribution maps for pH, TDS, aluminum, iron, lead, zinc, cadmium, barium, manganese, and nickel respectively in the KCF region.

Table 1: Summary of dissolved metals compared with standard values specified by WHO (2006) and BIS (2012) (IS 10500) for drinking (unit: $\mu g.L^{-1}$) except pH & TDS.

| Metals | Mean | Min | Max | Std. Dev. | WHO (2006) | BIS (2012) (IS 10500) | | Percent Exceeded desirable limit | Percent Exceeded per. limit |
|---|---|---|---|---|---|---|---|---|---|
| | | | | | | Requirement | Permissible limit | | |
| pH | 6.77 | 6.05 | 7.78 | 0.38 | 7.0-8.5 | 6.5-8.5 | NR* | Nil | Nil |
| TDS | 323.4 | 83 | 631 | 190.64 | 500-2000 | 500 | 2000 | 20% | Nil |
| Al | 28.83 | 1.03 | 171.62 | 43.78 | 100-200 | 30 | 200 | 13.33% | Nil |
| Ba | 242.37 | 39.36 | 798.4 | 214.97 | 300 | 700 | NR* | 20% | Nil |
| Cd | 0.09 | 0.02 | 0.37 | 0.09 | 3 | 3 | NR* | Nil | Nil |
| Fe | 658.29 | 69.85 | 2769.6 | 709.29 | 300 | 300 | NR* | Nil | 6.67% |
| Mn | 111.59 | 18.06 | 365.1 | 107.58 | 100 | 100 | NR* | 40% | 6.67% |
| Pb | 9.78 | 0.09 | 68.63 | 17.58 | 10 | 10 | NR* | 6.67% | Nil |
| Ni | 24.86 | 1.13 | 71.65 | 24.96 | 20 | 20 | NR* | 26.67% | Nil |
| Zn | 1078 | 13.01 | 11201.2 | 2880.55 | 4000 | 5000 | 15000 | 6.67% | Nil |

NR*- No relaxation

such as Ba, Fe, Ni, Mn and Al exceeded their desirable limit in groundwater samples caused by mining and related activities such as leaching from overburden, dump materials & waste effluents from the coal mine. The concentration range of metals with mean value is expressed in $\mu g.L^{-1}$ is listed in Table 1. Origin 9 pro software was used to prepare the map for mean, maximum, and minimum values of metal presented by box-whisker plots are shown in Fig. 5. In case of three metal concentrations such as Al, Mn and Ni have exceeded their desirable limit at several locations as specified by BIS 2012 (IS 10500) and rest elements (Fe, Pb, Zn, Cd & Ba), also exceeded the desirable limit only at few locations.

The Mn concentration ranged between 18.06 to 365.09 $\mu g.L^{-1}$ with its mean value of 111.59 $\mu g.L^{-1}$, 46.67% of samples exceeded the desirable limit of 100 $\mu g.L^{-1}$ as per WHO (2006) & BIS 2012 (IS 10500) and only one sample (GW-10) exceeded the maximum permissible limit of 300 $\mu g.L^{-1}$ as per given by BIS 2012 (IS 10500).

The Ni concentration ranged between 1.3 $\mu g.L^{-1}$ to 71.65 $\mu g.L^{-1}$ with an average of 24.84 $\mu g.L^{-1}$. About 26.67%

(4 samples) of total groundwater samples exceeded its desirable limit as given by WHO (2006) & BIS 2012 (IS 10500). The rest of the four elements concentrations such as of Ba, Zn, Fe and Pb were determined of which 93.37% of groundwater were not exceeded the acceptable limit as specified by WHO (2006) & BIS 2012 (IS 10500) for drinking purposes and only 6.67% of all four elements concentration exceeded their desirable limits as per given by BIS (2012). The only one element i.e., Cd concentration was not exceeded its desirable limit and acceptable limit as per WHO (2006) & BIS 2012 (IS 10500) standards. 100% of groundwater samples lay within acceptable limits as given by WHO (2006) & BIS 2012 (IS 10500) in the pre-monsoon season.

**Statistical Correlation of the Groundwater Quality Parameters**

According to the correlation matrix between metal content and estimated HPI, Ni and pH have a strong negative correlation ($r > -0.538$). However, a strong positive correlation between Pb and Fe ($r > 0.99$), Zn and Fe ($r > 0.995$) and Zn and Pb ($r > 0.998$) were established. While HPI is positively correlated with Fe ($r > 0.947$), Pb ($r > 0.967$), and Zn ($r > 0.963$) as listed in Table 2.

This high level of correlation indicates that Fe, Pb, and Zn loading has made a significant contribution to heavy metal concentration in various samples examined more than the other selected elements, and they were also responsible for the high level of HPI obtained for different sites in the study area, asserting that Fe, Pb, and Zn pollution in groundwater.

**Hierarchical Cluster Analysis (HCA)**

Cluster analysis is a set of multivariate approaches for identifying real data clusters or stations. Water sample classification and the development of geochemical models have both been done with the help of the effective geochemical data analysis technique known as HCA (Meng & Maynard 2001; Singh et al. 2005, 2016). After normalizing the data set to Z-scale, Ward's linkage approach (Ward 1963) was used to perform HCA on the heavy metal parameters of 15 groundwater samples using PAST 4.03 software as shown in Fig. 6. The dendrogram is split into different groups, each of which has several sub-groups and singletons. It might, however, be divided into two major clusters for the purposes of interpretation. Cluster-I is made up of 14 members, with the majority of the groundwater samples (GW- 1, 2, 3, 4, 5, 6, 7, 8, 9, 11, 12, 13, 14 and 15) coming from the KCF region of Chhattisgarh, India. This group comprises 93.33 % of the water samples examined and is distinguished by relatively low Ba ($<700\ \mu g.L^{-1}$), pH, TDS, Al, Fe, Cd, Mn, Pb, and Zn concentrations. Cluster-II is made up of 1 member, which is primarily made up of groundwater samples (GW-10) taken in the KCF region. The variable dendrogram reveals two major clusters. This category accounts for 6.67 % of all tested samples and is characterized by greater Ba ($>700\ \mu g.L^{-1}$), TDS, Fe, Mn, Pb, and Zn concentrations. The higher concentrations in sample (GW-10) indicate that water quality has been influenced by mining and anthropogenic factors. Cluster-I consists of 10 metals such as pH, TDS, Al, Ba, Cd, Fe, Mn, Pb, and Ni. Cluster-II contains only Zn, which behaves differently than the other dissolved elements in groundwater.

**Heavy Metal Pollution Index**

The concentration of heavy metals such as Al, Ba, Cd, Mn, Ni, Zn, Fe, and Pb was taken into account for the calculation of HPI of groundwater samples collected at the KCF mine. The HPI value was determined and ranges from 1.06 to 177.99 with a mean value of 21.52 (see Table 3). The

Table 2: Correlation matrix between heavy metals and calculated HPI of groundwater sample in KCF region, Chhattisgarh, India.

| | pH | TDS | Al | Ba | Cd | Fe | Mn | Pb | Ni | Zn | HPI |
|---|---|---|---|---|---|---|---|---|---|---|---|
| pH | 1.000 | | | | | | | | | | |
| TDS | -0.113 | 1.000 | | | | | | | | | |
| Al | 0.313 | -0.252 | 1.000 | | | | | | | | |
| Ba | -0.368 | 0.198 | -0.140 | 1.000 | | | | | | | |
| Cd | -0.388 | -0.040 | -0.296 | 0.261 | 1.000 | | | | | | |
| Fe | -0.313 | 0.372 | -0.145 | 0.684 | 0.266 | 1.000 | | | | | |
| Mn | -0.429 | 0.176 | -0.254 | 0.558 | 0.524 | 0.660 | 1.000 | | | | |
| Pb | -0.283 | 0.315 | -0.132 | 0.715 | 0.339 | 0.990 | 0.682 | 1.000 | | | |
| Ni | -0.538 | -0.025 | -0.164 | 0.853 | 0.296 | 0.427 | 0.636 | 0.456 | 1.000 | | |
| Zn | -0.302 | 0.341 | -0.128 | 0.721 | 0.299 | 0.995 | 0.658 | 0.998 | 0.458 | 1.000 | |
| HPI | -0.400 | 0.248 | -0.166 | 0.838 | 0.400 | 0.947 | 0.759 | 0.967 | 0.665 | 0.963 | 1.000 |

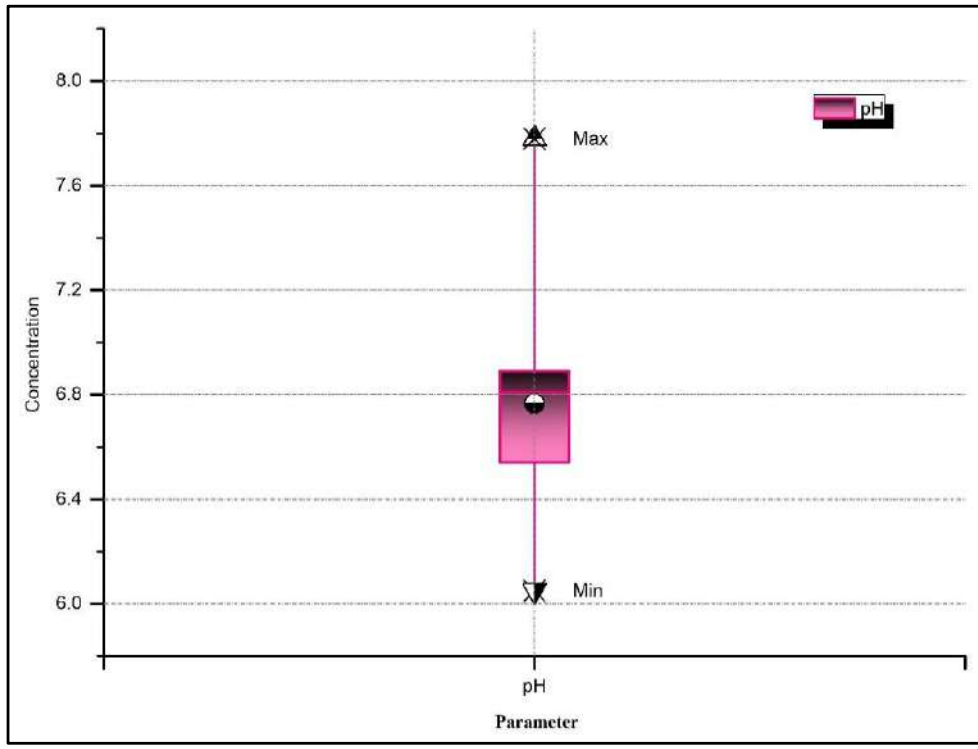
8.0
7.6
7.2
6.8
6.4
6.0
Concentration
pH
Max
Min
pH
Parameter

(a) pH

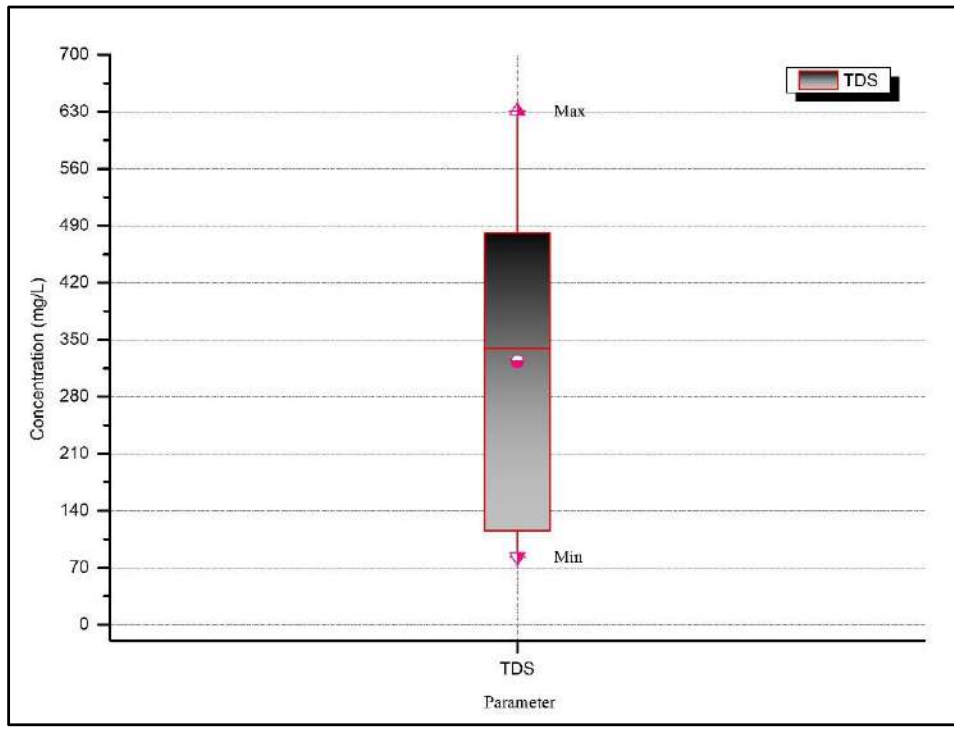
700
630
560
490
420
350
280
210
140
70
0
Concentration (mg/L)
TDS
Max
Min
TDS
Parameter

(b)TDS

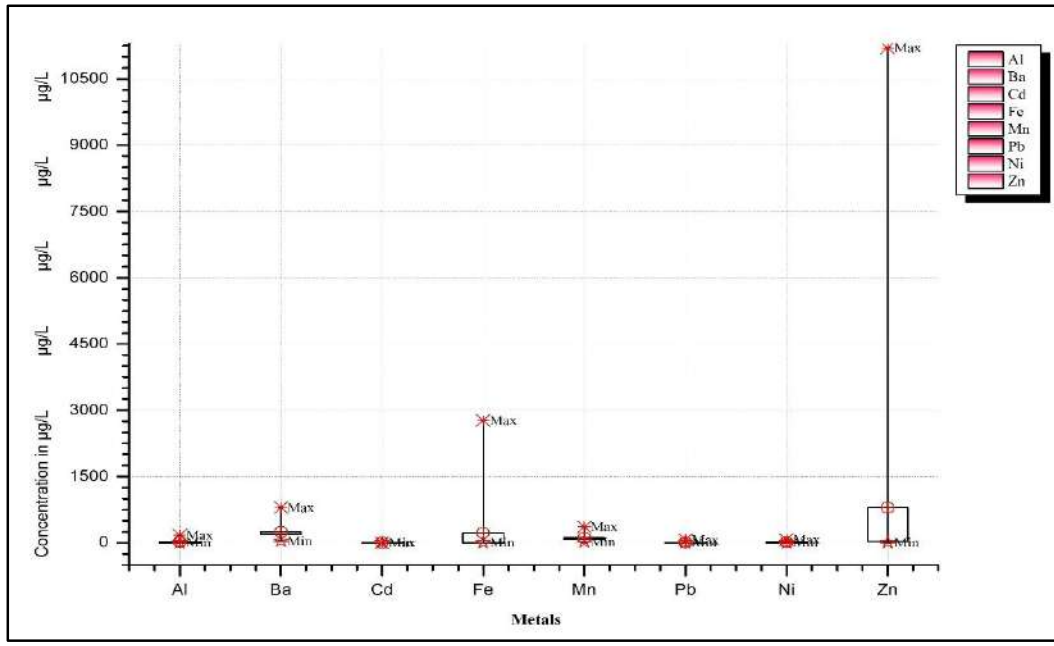


Fig. 5: Box-whisker plots for (a) pH, (b) TDS (unit in mg.L$^{-1}$), and (c) heavy metals (unit in µg.L$^{-1}$).

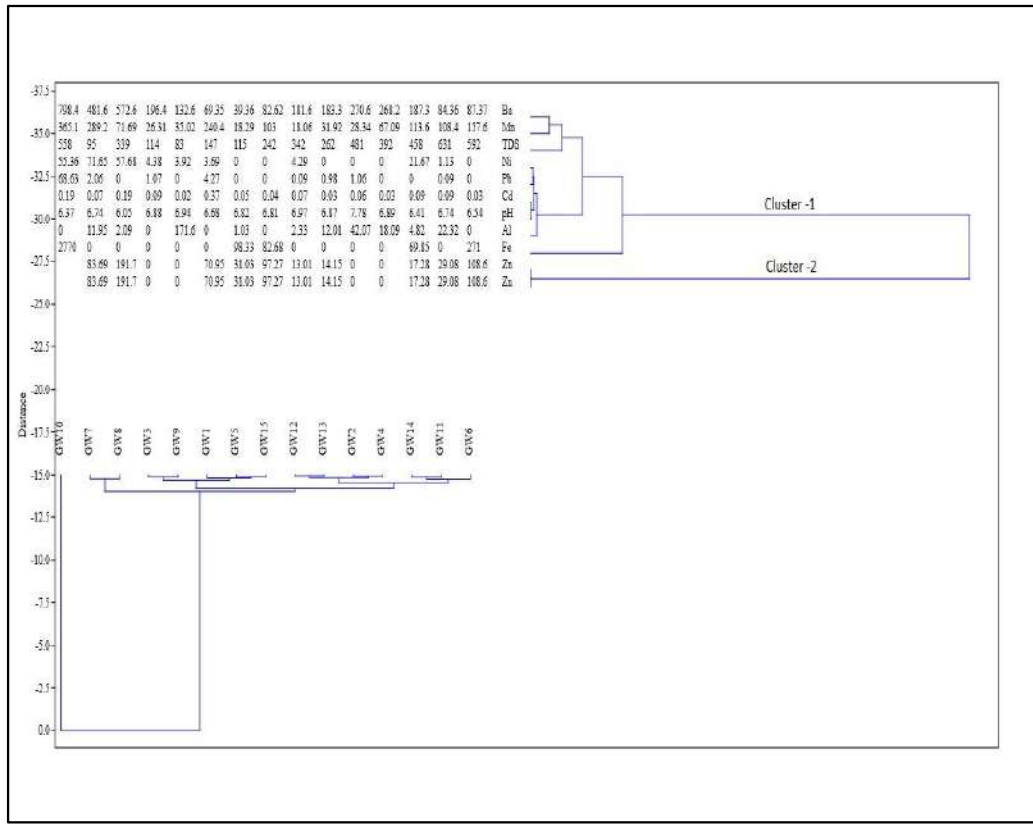


Fig. 6: Dendrogram map showing clustering metals variables and sampling sites.

Table 3: The calculated HPI value of the KCF region.

| S No. | Sampling code | HPI values | Class |
|---|---|---|---|
| 1. | GW-1 | 19.35 | Medium |
| 2. | GW-2 | 3.89 | Low |
| 3. | GW-3 | 6.91 | Low |
| 4. | GW-4 | 1.06 | Low |
| 5. | GW-5 | 1.79 | Low |
| 6. | GW-6 | 1.71 | Low |
| 7. | GW-7 | 42.69 | High |
| 8. | GW-8 | 33.82 | High |
| 9. | GW-9 | 3.52 | Low |
| 10. | GW-10 | 177.99 | High |
| 11. | GW-11 | 2.91 | Low |
| 12. | GW-12 | 4.36 | Low |
| 13. | GW-13 | 8.02 | Low |
| 14. | GW-14 | 13.38 | Low |
| 15. | GW-15 | 1.35 | Low |

calculated HPI was higher at three sites (GW-6, 7 & 10) in pre-monsoon (March 2022). The calculated HPI value for the study area (14 sites) comes within the critical pollution index of 100 and only one site (GW-10) HPI value exceeded the critical pollution index value.

With HPI calculation, it was found the result that 73.33% of groundwater samples have low HPI values, 6.67% of water samples had medium HPI, and the rest 20% lay in high HPI values. In the case of a high calculated HPI value, it was associated with open-cast mining with transportation routes only. The spatial distribution diagram of HPI drowns is shown in Fig 7. The groundwater of the eastern side of the selected study area has had high HPI value and some area of the KCF region was likely affected with high HPI values and the rest area were having low HPI value.

## CONCLUSIONS

Based on pH concentration, the groundwater samples were close to being neutral to alkaline in nature. The groundwater is safe based on TDS concentration for drinking in the KCF region. The concentration of dissolved different elements like Al, Ba, Cd, Mn, Ni, Zn, Fe and Pb exceeded their desirable limits at a few locations only but their HPI values have laid within the critical pollution index value of 100 in the pre-monsoon season, KCF region Chhattisgarh. HPI has a positive correlation with Fe ($r > 0.9471$), Pb ($r > 0.9666$), and Zn ($r > 0.9634$), indicating that Fe, Pb, and Zn have contributed significantly to heavy metal concentrations in groundwater. A cluster analysis was also performed, and it was divided into two clusters. Cluster-1 contains 14 water samples (93.33 %) and is distinguished by low Ba

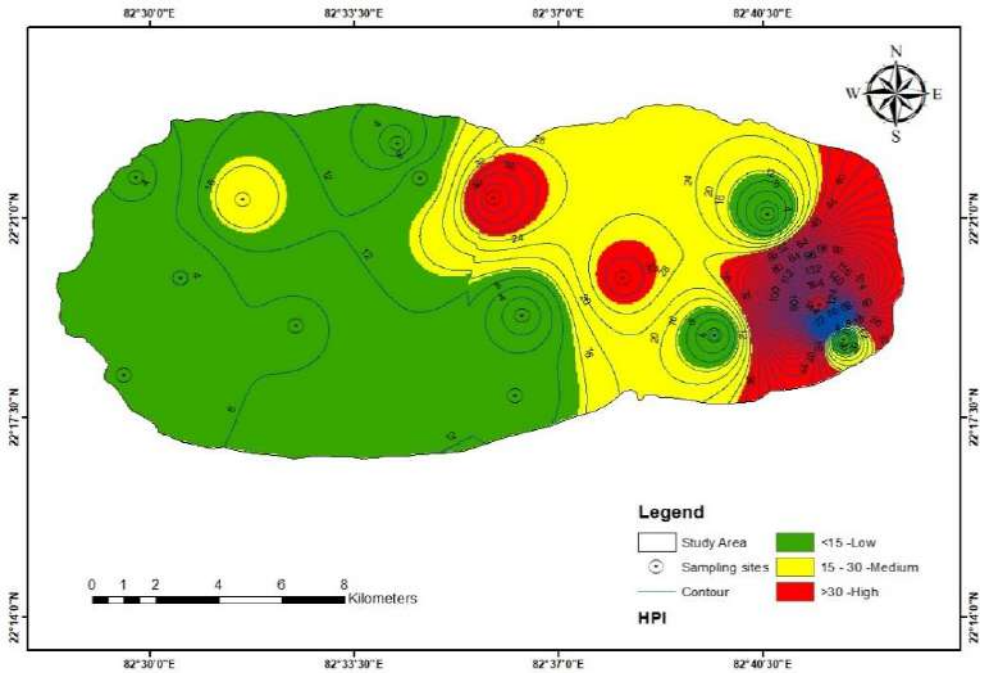


Fig. 7: Spatial distribution maps for HPI in the study region.

(700 μg.$L^{-1}$), pH, TDS, Al, Fe, Cd, Mn, Pb, Ni, and Zn concentrations. Cluster-II has one member (6.67 %), which is primarily made up of groundwater samples (GW-10) collected in the KCF region. An empirical evaluation system called the HPI is used to assess how particular metals generally affect the quality of water. With HPI calculation, it was found that 73.33% of groundwater samples have low HPI values, 6.67% of water samples had medium HPI, and the rest 20% lay in high HPI values. In the case of a high calculated HPI value, it was associated with open-cast mining with transportation routes only. The spatial distribution of HPI reflects that of metals, with high values of HPI in the eastern part of KCF region. It was discovered that the groundwater in the eastern part of the study area was most likely contaminated by heavy metal leaching from open-pit mining and transit routes. It was determined that the drinking water in the KCF region is of good quality in terms of heavy metals. Given the significant growth in socioeconomic activity in the study area, continuous monitoring of groundwater quality for heavy metals is deemed required.

## ACKNOWLEDGEMENT

The authors are grateful to the Central Instrument Facility (CIF) and the Indian Institute of Technology (Banaras Hindu University) for providing lab space and funds for the metals analysis in this study.

## REFERENCES

Adaikpoh, E., G. Nwajei and J. Ogala. 2006. Heavy metals concentrations in coal and sediments from River Ekulu in Enugu, Coal City of Nigeria. J. Appl. Sci. Environ. Manag., 9(3). doi: 10.4314/jasem.v9i3.17343.

Adams, R.H., F.J. Guzmán Osorio and J. Zavala Cruz. 2008. Water repellency in oil contaminated sandy and clayey soils. Int. J. Environ. Sci. Technol., 5(4): 445-454. doi: 10.1007/BF03326040

Ahmed, S.I., A.K. Sonkar, N. Kishore and D. Jhariya. 2022. Evaluation of groundwater quality in Jampali coal mine, Raigarh, Chhattisgarh, India. Environ. Qual. Manag., 31(3): 9-17. doi: 10.1002/TQEM.21767

Bardos, P. 2004. Composting of mechanically segregated fractions of municipal solid waste – a review. SITA Environ. Trust, 30: 143.

BIS 2012 (Bureau of Indian Standards) IS: 10500 Indian Standard for Drinking Water-Specification. Second Revision, New Delhi.

Brandon, C., and K. Hommann. 1995. The cost of inaction: valuing the economy-wide cost of environmental degration in India. Asia Environ. Div. World bank 7, Oct. memo.

Central GroundWater Board (CGWB), NCCR (2012) Aquifer systems of Chhattisgarh. Central Ground Water Board, North Central Chhattisgarh Region, Ministry of Water Resources, Government of India, New Delhi.

Dheeraj, V.P., A.K. Sonkar and C.S. Singh. 2022. Evaluation of groundwater quality using water quality index (WQI) in Ambedkar Nagar City, Uttar Pradesh, India. Lect. Notes Civ. Eng., 172: 429-441. doi: 10.1007/978-981-16-4396-5_38.

Edet, A.E. and O.E. Offiong. 2002. Evaluation of water quality pollution indices for heavy metal contamination monitoring. A study case from Akpabuyo-Odukpani area, Lower Cross River Basin (southeastern Nigeria). GeoJournal, 57(4): 295-304. doi: 10.1023/B:GEJO.0000007250.92458.DE

Giri, S. and A.K. Singh. 2014. Assessment of surface water quality using heavy metal pollution index in Subarnarekha River, India. Water Qual. Expo. Heal., 5(4): 173-182. doi: 10.1007/s12403-013-0106-2

Giri, S., G. Singh, S.K. Gupta, V.N. Jha and R.M. Tripathi. 2010. An evaluation of metal contamination in surface and groundwater around a proposed uranium mining site, Jharkhand, India. Mine Water Environ., 29(3): 225-234. doi: 10.1007/S10230-010-0107-3

Karbassi, A.R., S.M. Monavari, G.R. Nabi Bidhendi, J. Nouri and K. Nematpour. 2008. Metal pollution assessment of sediment and water in the Shur River. Springer, 147(1-3): 107-116. doi: 10.1007/s10661-007-0102-8

Lee, C.S.L., X.D. Li, G. Zhang, J. Li, A.J. Ding, et al. 2007. Heavy metals and Pb isotopic composition of aerosols in urban and suburban areas of Hong Kong and Guangzhou, South China-Evidence of the long-range transport of air contaminants. Atmos. Environ., 41(2): 432-447. doi: 10.1016/j.atmosenv.2006.07.035

Lohani, M.B., A. Singh, D.C. Rupainwar and D.N. Dhar. 2008. Seasonal variations of heavy metal contamination in river Gomti of Lucknow city region. Environ. Monit. Assess., 147(1-3): 253-263. doi: 10.1007/S10661-007-0117-1

Mahato, M.K., P.K. Singh, and A.K. Tiwari. 2014. Evaluation of metals in mine water and assessment of heavy metal pollution index of east bokaro coalfield area, Jharkhand, India. Int. J. Earth Sci. Eng., 7(4): 1611-1618.

Meng, S.X. and J.B. Maynard. 2001. Use of statistical analysis to formulate conceptual models of geochemical behavior: Water chemical data from the Botucatu aquifer in São Paulo state, Brazil. J. Hydrol., 250(1-4): 78-97. doi: 10.1016/S0022-1694(01)00423-1

Prasad, B. and J.M. Bose. 2001. Evaluation of the heavy metal pollution index for surface and spring water near a limestone mining area of the lower himalayas. Environ. Geol., 41(1-2): 183-188. doi: 10.1007/S002540100380

Radojevic, M., V. Bashkin and V. Bashkin. 1999. Practical environmental analysis. Royal Soc of Chemistry, London.

Raja Rao, C.S. 1983. Coal resources of Madhya Pradesh, Jammu and Kashmir. Coalfields of India. Bull. Geol. Surv. India, Ser. A, (45): 1-204.

Reddy, S. 1995. Encyclopaedia of environmental pollution and control. Env. Media, Karlia 1: 342.

Senapaty, A. and P. Behera. 2012. Concentration and distribution of trace elements in different seams of the talcher coalfield, Odisha. Int. J. Earth Sci. Eng., 5(1): 80-87.

Sheykhi, V., F.M.-W. quality, exposure and health, and undefined 2012. 2012. Geochemical characterization of Kor River water quality, fars province, Southwest Iran. Springer, 4(1): 25-38. doi: 10.1007/s12403-012-0063-1

Singh, G. 1988. Impact of coal mining on mine water quality. Int. J. Mine Water, 7(3): 49-59. doi: 10.1007/BF02504598

Singh, K.P., A. Malik, V.K. Singh, D. Mohan and S. Sinha. 2005. Chemometric analysis of groundwater quality data of alluvial aquifer of Gangetic plain, North India. Anal. Chim. Acta, 550(1-2): 82-91. doi: 10.1016/j.aca.2005.06.056

Singh, A.K., G.C. Mondal, S. Kumar, T.B. Singh, B.K. Tewary, et al. 2008. Major ion chemistry, weathering processes and water quality assessment in upper catchment of Damodar River basin, India. Environ. Geol., 54(4): 745-758. doi: 10.1007/S00254-007-0860-1

Singh, A.K., N.P. Varma and G.C. Mondal. 2016. Hydrogeochemical investigation and quality assessment of mine water resources in the Korba coalfield, India. Arab. J. Geosci., 9(4). doi: 10.1007/S12517-015-2298-1

Singh, R., A.S. Venkatesh, T.H. Syed, A.G.S. Reddy, M. Kumar, et al. 2017. Assessment of potentially toxic trace elements contamination in groundwater resources of the coal mining area of the Korba Coalfield, Central India. Environ. Earth Sci., 76(16). doi: 10.1007/S12665-017-6899-8

Tiwari, A.K., P.K. Singh and M.K. Mahato. 2017. Assessment of metal contamination in the mine water of the west Bokaro Coalfield, India. Mine Water Environ., 36(4): 532-541. doi: 10.1007/s10230-017-0440-x

Tiwary, R.K. and B.B. Dhar. 1994. Environmental pollution from coal mining activities in Damodar River Basin, India. Mine Water Environ., 13: 10.

Venkata Mohan, S., P. Nithila and S. Jayarama Reddy. 1996. Estimation of heavy metals in drinking water and development of heavy metal pollution index. J. Environ. Sci. Heal. - Part A Toxic/Hazardous Subst. Environ. Eng., 31(2): 283-289. doi: 10.1080/10934529609376357

Vishwakarma, A.K., T. Behera, R. Rai, A.K. Sonkar, A.P. Singh, et al. 2020. Impact assessment of coal mining induced subsidence on native soil of South Eastern Coal Fields: India. Geomech. Geophys. Geo-Energy Geo-Resources, 6(1). doi: 10.1007/S40948-020-00156-Y

Ward, J.H. 1963. Hierarchical grouping to optimize an objective function. J. Am. Stat. Assoc., 58(301): 236-244. doi: 10.1080/01621459.1963.10500845

WHO 2006. Guidelines for Drinking-Water Quality. 3rd edit, World Health Organization, Geneva.

Nature Environment and Pollution Technology
An International Quarterly Scientific Journal

p-ISSN: 0972-6268
(Print copies up to 2016)
e-ISSN: 2395-3454

Vol. 22 | No. 1 | pp. 383-396 | 2023

Original Research Paper

https://doi.org/10.46488/NEPT.2023.v22i01.037

Open Access Journal

# Research on Ecological Land Expansion: A Case Study of Haixing County of China

**L. He*(**), Z. Du*, J. B. Tian* and Y. H. Chen*(**)†**

*College of Land Resources, Hebei Agricultural University, Baoding, Hebei, 071000, China

**Cangzhou Field Research Station, Hebei-Land Use of Circum Bohai Sea for the Ministry of Land and Resources, Cangzhou, Hebei, 061000, China

†Corresponding author: Yaheng Chen; chenyaheng@hebau.edu.cn

**Nat. Env. & Poll. Tech.**
**Website: www.neptjournal.com**

*Received:* 19-01-2022
*Revised:* 09-03-2022
*Accepted:* 06-04-2022

**Key Words:**
Ecological land
Ecological security
Food security
Construction land expansion
Land use
Haixing county

## ABSTRACT

As China's natural resource governance has turned to high-quality management, establishing reasonable and ecological land-use patterns is an effective means of promoting natural resource utilization and improving the quality of the ecological environment. Therefore, this study used ecological land as the expansion source to construct an ecological land-use pattern with the minimum cumulative resistance model in Haixing County, China, based on regional food security, ecological security, and construction land expansion patterns. This work also involved designing ecological corridors, radiation channels, strategic nodes, and other ecological components. The results demonstrate that (1) the ecological land source is 7976.93 $hm^2$, accounting for 9.19% of the total area. It is mainly distributed in the southeast of the county, mainly in the river system and woodland; (2) the food security situation of Haixing County can be divided into four zones, most of which are agricultural adjustment areas, indicating that the ecological security of cultivated land in this area needs to be improved; (3) the ecological security level of Haixing County is divided into four areas, and the ideal safety zone accounts for the smallest area, indicating that the regional ecological situation is very unstable; (4) construction land expansion zone is divided into four parts. A suitable construction zone occupies the largest area and is mainly distributed around the current construction land; (5) the expansion of the ecological land-use pattern of Haixing County includes four zones, 15 ecological corridors, 12 radiation channels, and 35 strategic nodes, which is conducive to optimal land allocation from an ecological security perspective. This paper puts forward some suggestions for ecological protection and intensive urban development.

## INTRODUCTION

Since the 21st century, China's land-use patterns have undergone complex and drastic changes, including the gradual expansion of construction land and the reduction of natural land. Such changes significantly affect the natural and social development systems and cause serious ecological and environmental problems (Zheng et al. 2019). The land is the basic carrier of natural ecosystems and human activities, and its structure and pattern reflect the influence of external factors such as nature, society, and the economy (Lambin & Meyfroidt 2011). As a land-use type with important ecological value, ecological land plays an important role in maintaining regional land ecological security and guaranteeing natural ecosystem services and functions, which can effectively promote the sustainable development of a society (Fu 2019).

Changes in ecological land have been seen as one of the most significant driving factors for changes in ecological processes and ecosystem services (Liang et al. 2021). Scholars recognize that ecological land is the basic carrier for maintaining regional land ecological security and ensuring ecological material flow and energy exchange (Wang et al. 2019). The study of ecological land started with greenway design. The emergence of urban parks and nature reserves in the United States is based on the initial concept of greenway design, which has been gradually popularized and applied after extensive research (Jongman & Pungetti 2005). The Greenway movement in Singapore has developed gradually, and its experience and model have been constantly promoted (Tan 2006). After extensive research, ecological land use has gradually been promoted and applied by international scholars (Fath et al. 2017, Green et al. 2016). Ecological land use has been planned based on qualitative and quantitative analyses, gradually into data calculation, static structure optimization, dynamic simulation state, and trend analysis of rapid development. The research methods are mainly related to ecological suitability/sensitivity,

landscape pattern index, scenario analysis, and index systems (Huck et al. 2011, Chaudhary et al. 2019, Macmillan et al. 2007, Ojea et al. 2016). The research topics mainly include biodiversity assessment, ecological conservation and restoration, coupling analysis of human-natural systems (Gergely & Leah 2019, Schröter et al. 2020), and ecological security pattern (Tang et al. 2020).

Chinese scholars have discussed the connotation and classification of ecological land from many fields and perspectives; however, no consensus has yet been reached. Scholars have studied ecological issues from different perspectives, and further clarified the conceptual scope of ecological land, and the role of ecological land in maintaining biodiversity, improving ecological environment quality, adjusting climate, and improving human-land relationships (Yu et al. 2009, Zhang et al. 2017, Liu et al. 2021). Methods of ecological value (Cao et al. 2020), reverse recursion (Long et al. 2015), and construction of the land-use pattern and ecological security pattern (Zhou et al. 2020) are used to identify the spatial extent of ecological land and provide a basis for its further. The matter element analysis method, entropy weight method (Yu et al. 2012), and ecological footprint method (Xiu et al. 2020) are used to construct a land ecological security evaluation index system. The theory of "patch-corridor-matrix" and the model of cumulative minimum resistance is used to identify ecological strategic nodes and ecological corridors, and the ecological security pattern has been widely constructed in China in recent years to optimize land-use pattern (Liu et al. 2020, Yu et al. 2021).

To meet the need for ecological land use and sustainable human development at the county scale, this study researched the expansion of ecological land in Haixing County, which is a coastal county. It is relatively backward in economic development. Its economic development is bound to expand on construction land, and this could pose risks to food security and ecological security. How to realize ecological security construction at the county level while protecting cultivated land and developing the economy is a problem that Haixing County must face and solve. This study took the quality of cultivated land, the level of ecological security, and the expansion trend of construction land as the premises for realizing the optimal allocation of ecological land, then researched the ecological land expansion. The results provide accurate planning and layout scheme for food security, economic development, and ecological protection in Haixing County and the similar areas.

## DATA AND METHODS

### Study Area

Haixing County is located in Hebei province, at the junction of Hebei and Shandong; to the east is in the proximity of the Bohai Sea (Fig. 1), and experiences a warm temperate sub-humid continental monsoon climate.

The county covers a total area of 86825.84 $hm^2$, including 197 administrative villages, among which ecological land covers a total area of 26776.83 $hm^2$, mainly woodland, grassland, garden land, water area, wetland, and unused land (Table 1).

### Data Sources

There are two types of data sources: File data and remote sensing data. The file data were mainly obtained from the

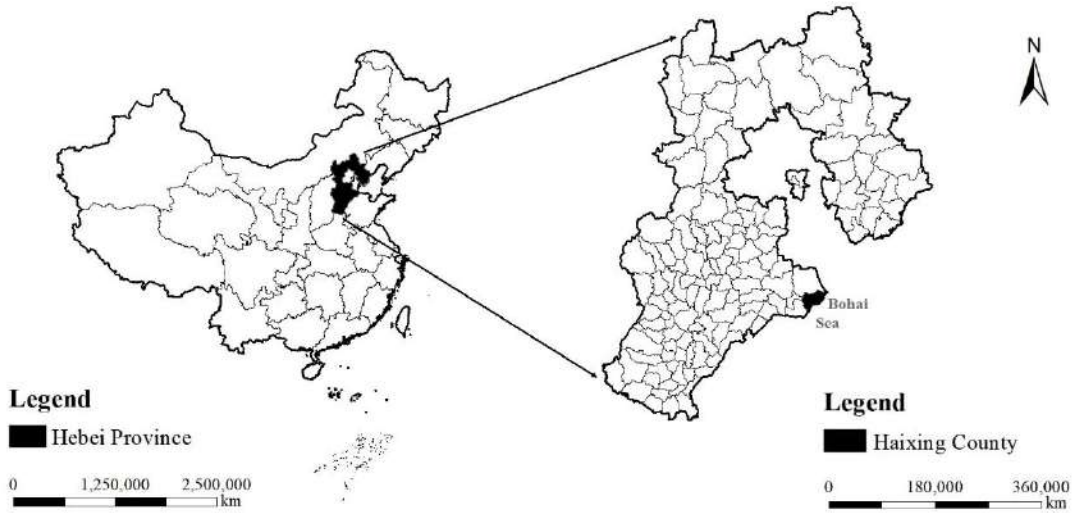


Fig. 1: Location of Haixing County.

Table 1: Classification of ecological land in Haixing County.

| Ecological land type | Area ($hm^2$) | Proportion (%) |
|---|---|---|
| Water area | 4609.48 | 17.21 |
| Wetland | 2453.91 | 9.16 |
| Woodland | 1412.04 | 5.27 |
| Garden land | 900.64 | 3.36 |
| Grassland | 1609.73 | 6.01 |
| Unused land | 15791.02 | 58.97 |

Note: Although there are no wetlands (which are not at the same level as other ecological land) in the 73 secondary categories of land-use classification in 2017, wetlands play a primary role in maintaining regional ecological environment stability, and they are treated as separate categories here and regarded as ecological land.

Haixing County Natural Resources and Planning Bureau, including the land-use database of Haixing County in 2017, grading results of cultivated land quality in 2018, the overall land-use plan of Haixing County (2013-2030), and the land survey update data of Haixing County (2017). By downloading Landsat OLI imagery and DEM data with 30 m spatial resolution from the USGS and using ArcGIS10.2's spatial analysis and processing function, the index status of Haixing County was obtained. The impact distances of roads, residential locations, and geological disasters were obtained by distance analysis of the current situation of roads, residential areas, and ponds extracted from the geographical map. Vegetation coverage was extracted from remote sensing images and the slope was extracted from digital elevation model data. Other data, such as habitat quality and landscape diversity, were obtained through relevant mathematical models. The research unit was a 30 × 30 m grid unit.

### Evaluation Method of Ecological Land Expansion Constraint Factor

The expansion of ecological land will inevitably occupy other types of land. Whether to allow the expansion of ecological land to occupy cultivated land and construction land, and whether to ensure ecological security in the expansion process, need to be demonstrated from food security, ecological security, and the expansion of construction land.

### Food Security Zoning Method

**Global spatial autocorrelation analysis:** Using ArcGIS10.2 and GeoDa software, the Global Moran's I index was run to verify the spatial similarity of the quality grading index of all cultivated land polygons. The Global Moran's I value was between [-1, 1]. A value > 0, indicates that the space is positively correlated, and the research objects are spatially aggregated. A value < 0 indicates that the space is negatively correlated and that the studied objects tend to be spatially discrete, and 0 means that Moran's I significance test cannot be passed, and that the studied objects are randomly distributed. Moran's I was calculated as follows:

$$I = \frac{n\sum_{i=1}^{n}\sum_{j=1}^{n} w_{ij}\left(x_i - \bar{x}\right)\left(x_j - \bar{x}\right)}{\sum_{i=1}^{n}\sum_{j=1}^{n} w_{ij}\sum_{i=1}^{n}\left(x_i - \bar{x}\right)^2} \quad \ldots(1)$$

where $I$ represents the adjacent relation between the spatial positions $i$ and $j$. $X_i$ and $X_j$ have cultivated land quality indices for units I and J, respectively. $\bar{x}$ is the average value of cultivated land quality index in the study area. When $i$ and $j$ meet the adjacent spatial relation, $w_{ij}$ is assigned as 1. When $i$ and $j$ don't meet the adjacent spatial relation, $w_{ij}$ is assigned a value of 0. $w_{ij}$ $w_{ij}$

**Local spatial autocorrelation analysis:** Local spatial autocorrelation is mainly used to analyze the spatial position of agglomeration or dispersion of cultivated land quality in this article. Local Moran's I (LISA) is taken as the statistic to measure the degree of spatial difference between the spatial unit $i$ and its adjacent units (Anselin 2010). $LISA_i$ was calculated using Eq (2).

$$LISA_i = \frac{(x_i - \bar{x})}{\sum_i (x_i - \bar{x})^2 / n} \sum_j w_{ij} (x_i - \bar{x}) \quad \ldots(2)$$

Here, $LISA_i$ is the local Moran's I of the $i$th cultivated land polygon. A positive $LISA_i$ indicates that the spatial unit is similar to the attribute value of a neighboring unit, and a negative $LISA_i$ value indicates that the attribute value of the spatial unit is different from that of a neighboring unit.

### Ecological Security Zoning Method

**Index system construction:** Based on the principles of data accessibility, operability, and comprehensiveness, this study combined the actual situation of the study area to construct an ecological security index system (Table 2).

Relevant software and models were used to obtain all indicators. For example, the Biodiversity module in the InVEST model was used to obtain the habitat quality; ArcGIS10.2 and ENVI 5.3 were used to calculate the Normalized Difference Vegetation Index (NDVI) for vegetation coverage; landscape diversity, distance from roads, and landscape fragmentation were supplied by ArcGIS10.2.

Human interference is used to describe the overall intensity of human disturbance to the land ecological environment, it was calculated as follows:

$$HAI = \sum_{i=1}^{N} A_i P_i / TA \quad \ldots(3)$$

Table 2: Ecological security zoning construction index system in Haixing County.

| Target layer | Constraint layer | Indicator layer |
|---|---|---|
| Comprehensive indicators of ecological security | Ecological stability index | Habitat quality |
| | | Vegetation coverage |
| | | Landscape diversity |
| | Ecological interference index | Human interference |
| | | Distance from road |
| | | Landscape fragmentation |

Where *HAI* represents the synthetic index of human interference; N is the number of land types. $A_i$ is the area of ecosystem type i; $P_i$ is the intensity coefficient of anthropogenic influence reflected by the $i^{th}$ ecosystem type. *TA* is the total area. This article uses Lohani list method, Leopold matrix method and Delphi method to determine the artificial influence intensity factor Pi.

### Cumulative Correction Summation Method

When the ecosystem service functions of an ecological unit are diversified, the accumulation of multiple functions can promote the maximum comprehensive effect. Therefore, this study uses the cumulative correction summation method to calculate the comprehensive ecological security index and analyze the regional ecological security level. The calculation method is as follows:

$$EL = \max(Q,V,S,H,D,C)+(Q+V+S+H+D+C-\max(Q,V,S,H,D,C))/3 \quad \ldots(4)$$

where *EL* is the ecological security composite index; *Q* is the habitat quality index; *V* is the vegetation coverage index; *S* is the landscape diversity index; *H* is the man-made influence composite index; *D* is the distance from the road index; and *C* is the landscape fragmentation index.

### Zoning Method for Construction Land Expansion

**Construction land expansion "source":** The "source" of construction land expansion, referred to as the construction source, reflects the core driving force of construction land expansion. The expansion of construction land was refined into the urbanization process of land. The administrative towns and village settlements were selected as the sources of construction land expansion.

**Expansion of resistance surfaces:** The resistance surface was constructed to analyze the limiting factors and driving factors in construction land expansion. This study selected slope, geological disaster, distance from the road, distance from the settlement, and land development cost as the main factors affecting construction land expansion, divided the classification standards, and provided different resistance values (Table 3).

**Minimum cumulative resistance model:** The minimum cumulative resistance (MCR) model was used to calculate the MCR value of construction land expansion, and the cumulative resistance value was classified according to the natural breakpoint classification to obtain the construction land expansion pattern. The MCR was calculated as follows:

$$MCR = f_{\min}\sum(D_{ij}\times R_i) \ (i=1, 2, 3...n, j= 1, 2, 3...m) \quad \ldots(5)$$

where MCR is the minimum cumulative resistance of matter, energy, and phenomenon diffusing from the source point to a certain point in space, which is related to distance and cost; *f* is a monotonically increasing unknown function that maps the relationship between MCR and the variable ($D_{ij} \times R_i$) in direct proportion; $D_{ij}$ represents the distance of a matter, energy, and phenomenon passing through unit *i* when moving from unit *i* to unit *j* in the path of motion after leaving the source; $R_i$ represents the resistance coefficient of the *i*th element to a motion.

Table 3: Resistance value and weight of factors affecting construction land expansion.

| Influencing factor | Resistance value | | | | Weight |
|---|---|---|---|---|---|
| | 10 | 20 | 50 | 100 | |
| Slope | $0^o$–$2^o$ | $2^o$–$6^o$ | $6^o$–$15^o$ | > $15^o$ | 0.0691 |
| Distance from geological disaster (m) | > 300 | 200~300 | 100~200 | 0~100 | 0.1265 |
| Distance from road (m) | 0~500 | 500~1000 | 1000~1500 | > 1500 | 0.2474 |
| Distance from settlement (m) | 0~500 | 500~1000 | 1000~1500 | > 1500 | 0.3176 |
| Land development cost | Construction land | Cultivated land, Ditches, Grassland | Woodland, Garden land | Water area, Wetland, Unused land | 0.2394 |

Note: Haixing County is a key area for flood control due to its special geographical location and climatic characteristics. The geological disaster was analyzed taking ponds facing the sea as the origin of the geological disaster buffer.

### Research on Ecological Land Expansion

**Ecological land source:** The ecological land source is the most suitable land for ecological protection, with a strong ecological function and the least expansion resistance (Yu et al. 2009). Based on the land-use database, the overall land-use plan, and relevant research theories (Costanza et al. 1997, Xie et al. 2015), the extraction of ecological land sources was mainly selected by high-value areas of ecosystem services, such as nature reserves, water areas, wetlands, and centralized contiguous woodland with an area of > 3 $hm^2$.

**Ecological land expansion model construction:** (1) First, ArcGIS10.2, spatial analyst function, and options module were used to set the scope of the work content and the size of the unit, and then the convert tool was used to convert the map into a raster data format. Second, the raster calculator tool was used to calculate the cost surface. Third, the minimum resistance surface was obtained using a cost-weighted tool to generate the expansion partition of ecological land. Finally, the zoning of food security patterns, ecological security patterns, and construction land expansion patterns were taken as the resistance factors (Table 4).

(2) The ridge lines and valley lines were extracted using the hydrologic analysis method. The low-resistance valley lines that diverged from the ecological source to all directions were radiation channels. The ecological strategy point plays a key role in the flow of ecological materials and energy. It was a significant "springboard" between two adjacent ecological land sources.

## RESULTS

### Expansion of Ecological Land Source

The ecological land source area of Haixing County was 7976.93 $hm^2$, accounting for 9.19% of the total study area. As shown in Fig. 2, the ecological land sources were mainly distributed in the southeast of the county, mainly in the river system and woodland, while other ecological sources are scattered in each town and township.

Table 4: Ecological land expansion resistance value of each factor.

| Resistance factor | Resistance value | | | |
|---|---|---|---|---|
| | 10 | 20 | 50 | 100 |
| Food security zone | Non-agricultural construction zone | Agricultural structure adjustment zone | Key promotion zone | Permanent protected zone |
| Ecological security zone | Low-security zone | Basic security zone | Medium security zone | Ideal security zone |
| Construction land expansion zone | Prohibited construction zone | Restricted construction zone | Construction buffer zone | Suitable construction zone |

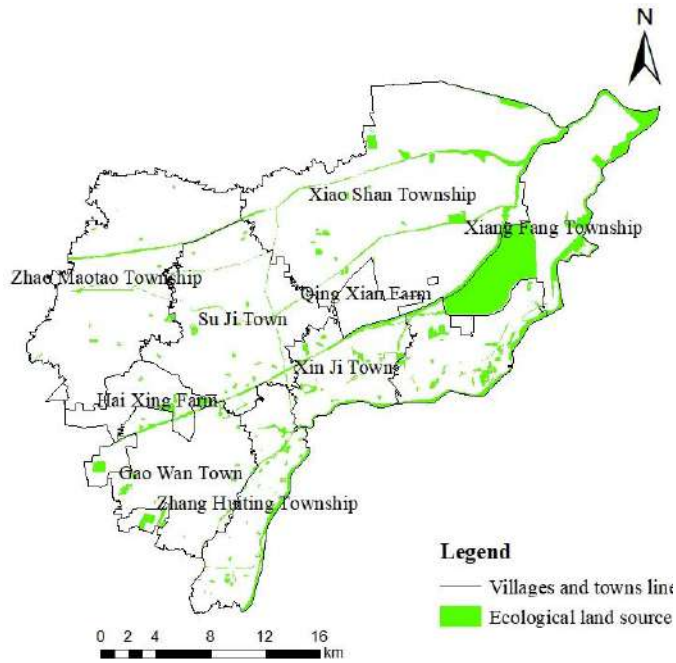


Fig. 2: Expansion of ecological land sources in Haixing County.

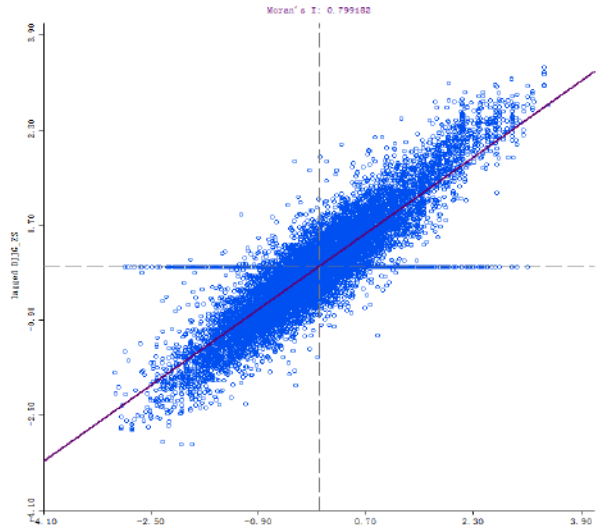


Fig. 3: Result of Moran's I.

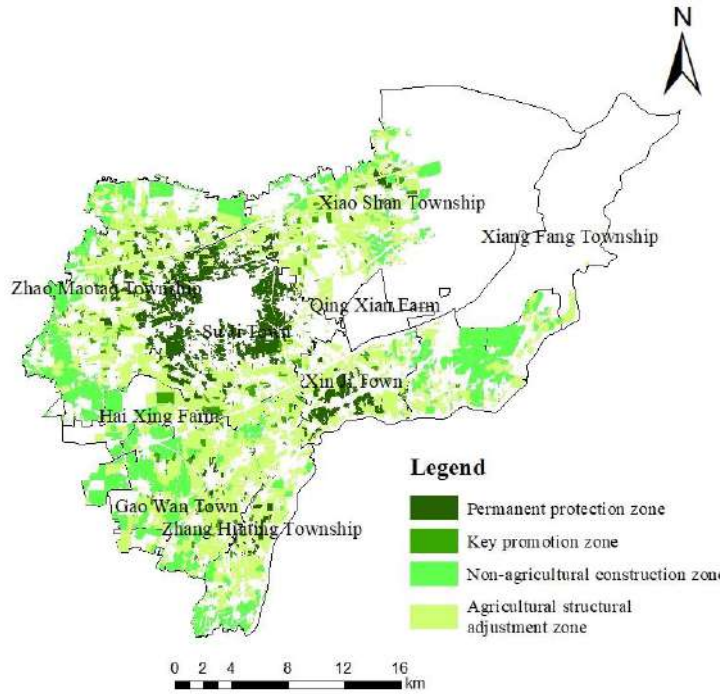


Fig. 4: Food security zone in Haixing County.

Table 5: Statistics of spatial autocorrelation types in Haixing County. HH – high value aggregation, LL – low value aggregation, HL – high low discrete distribution, LH – low high discrete distribution.

| Autocorrelation type | HH type | LL type | HL type | LH type | Non-obvious type |
|---|---|---|---|---|---|
| Number | 1889 | 2266 | 249 | 278 | 7734 |
| Proportion (%) | 15.21 | 18.25 | 2.01 | 2.24 | 62.29 |

## Food Security Assessment

With the aid of the cultivated land quality classification index, based on global spatial autocorrelation analysis and the local spatial autocorrelation type and proportion (Fig. 3, Table 5), the autocorrelation type of cultivated land quality index was analyzed.

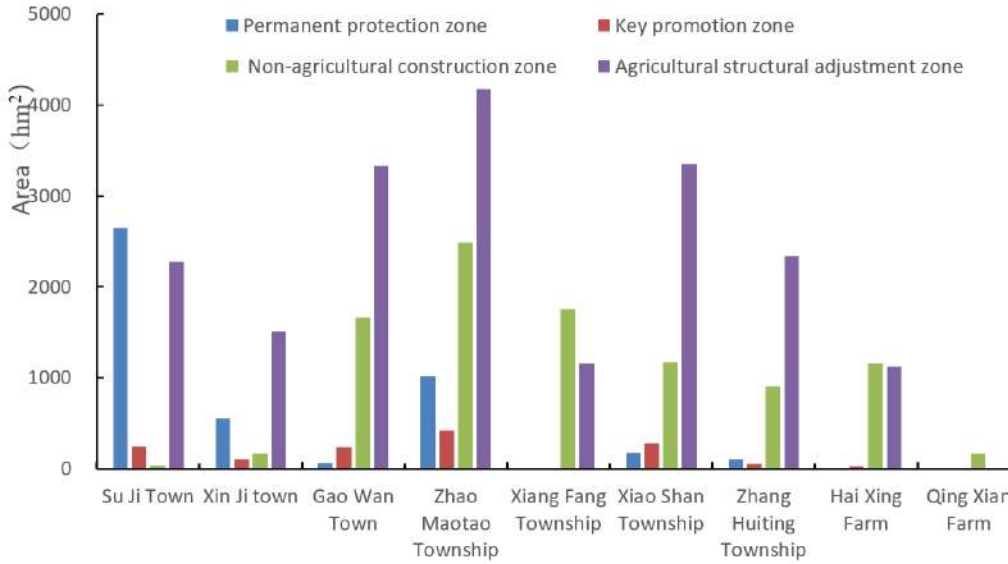


Fig. 5: Statistics on food security zone in each township in Haixing County.

Through the combination of all spatial autocorrelation types, Haixing County has developed a cultivated land protection zone to ensure food security. The HH type was classified as a permanent protection zone, the HL and LH types were classified as key promotion zone, the LL type was classified as a non-agricultural construction zone, and the non-sobvious was classified as an agricultural structural adjustment zone (Fig. 4 and Fig. 5).

(1) **Permanent protection zone:** This zone was mainly distributed in Su Ji Town. This region has better natural conditions, utilization level, and output benefits of cultivated land than the other three. Cultivated land with high quality accumulates and is distributed, and is an ideal area for the construction of high-standard basic farmland.

(2) **Key promotion zone:** This zone was mainly distributed in Zhao Maotao Township. The natural conditions and output benefits of this region were relatively good; however, the utilization and management levels of cultivated land were deficient. The utilization of cultivated land and the status of input and output can be improved through land consolidation projects.

(3) **Non-agricultural construction zone:** This zone was mainly distributed in Zhao Maotao Township and Xiang Fang Township. The natural conditions of cultivated land in this region were poor, the accessibility of roads was low, and the input-output of cultivated land was relatively poor. We can comprehensively adjust the distribution of cultivated land, garden land, woodland, and grassland based on food security and ecological land use patterns.

(4) Agricultural structural adjustment zone:

This zone was mainly distributed in Zhao Maotao Township and Gao Wan Town. The cultivated land quality had no obvious aggregation rules and a spatially random distribution. In order to improve the comprehensive quality of cultivated land, it is necessary to carry out the rotation and fallow experiments.

## Ecological Security Assessment

The ecological security pattern of Haixing County can be divided into ideal security zones ($7 < EL$), medium security zones ($5 < EL \leq 7$), basic security zones ($3 < EL \leq 5$), and low-security zones ($1 \leq EL \leq 3$). The higher the level, the better the ecological safety (Table 6, Fig. 6 and Fig. 7).

(1) **Ideal security zone:** This zone was mainly distributed in the south of Xiang Fang Township and east of Zhang Huiting Township, as well as in a large area of woodland in the southwest of the study area. This area must be strictly protected, which is the basic guarantee for maintaining regional ecological security and ecosystem stability.

**(2) Medium security zone:** This zone was distributed across all regions except the Qing Xian farm. The ecological conditions in this area were good, and the

Table 6: Ecological security zone in Haixing County.

| Ecological security zone | Ideal security zone | Medium security zone | Basic security zone | Low security zone |
|---|---|---|---|---|
| Area ($hm^2$) | 6494.57 | 28965.10 | 29885.45 | 21480.71 |
| Proportion (%) | 7.48 | 33.36 | 34.42 | 24.74 |

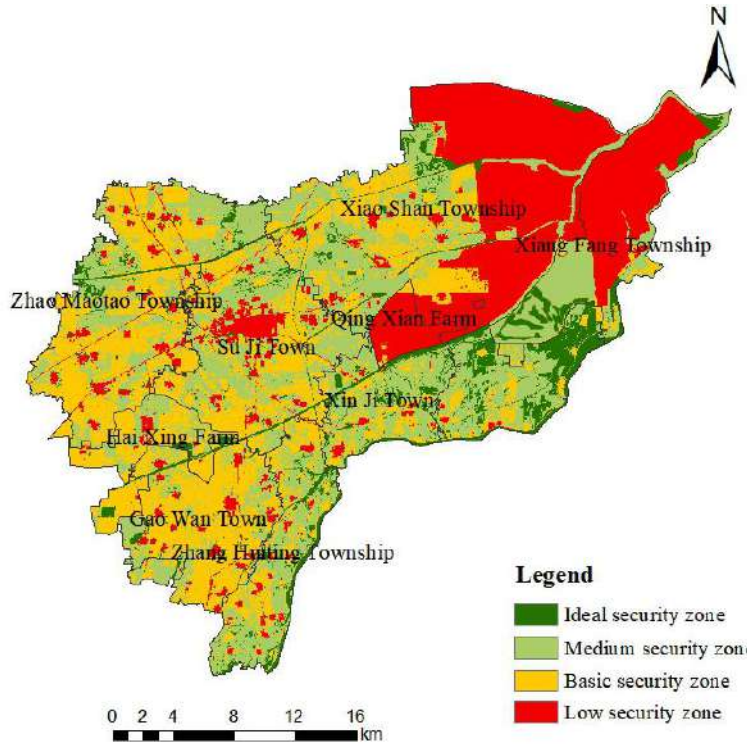


Fig. 6: Ecological security zone in Haixing County.

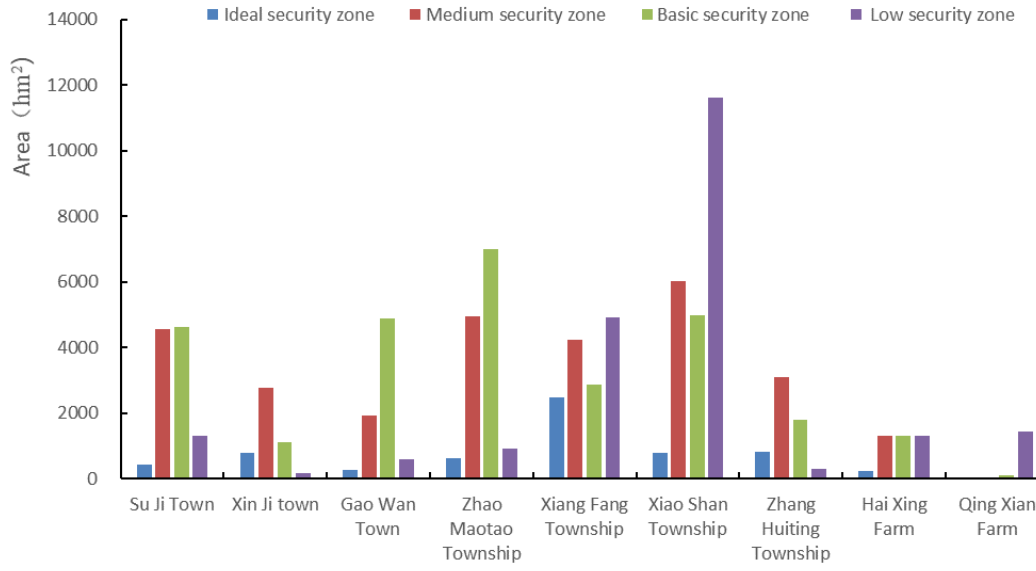


Fig. 7: Statistics on ecological security zone of each township in Haixing County.

balance of the ecosystem was maintained. The key point is to protect the ecological environment, and the development and construction activities that are harmful to the function of the ecosystem should be strictly prohibited.

(3) **Basic security zone:** This zone was a transition between medium and low security zones. This region was of great significance to the maintenance of basic ecological processes and played a buffer role in the

conflict between urban expansion and the ecological environment.

(4) **Low security zone:** This zone was mainly distributed in the northeast of the study area, with some scattered in other areas. This region is close to a human active area and is subject to a high degree of spatial stress from Haixing County's economic construction activities and urbanization process.

### Construction Land Expansion Assessment

According to the natural breakpoint method, the cumulative resistance value was graded to obtain the pattern of construction land expansion, i.e., suitable construction, construction buffer, restricted construction, and prohibited construction zones (Table 7, Fig. 8 and Fig. 9).

**(1) Suitable construction zone:** The proportion of this zone was relatively high, and this zone was mainly distributed around the current construction land, with a trend of outward expansion from the center of the county. This area can carry out construction activities and is ideal for the expansion of construction land.

**(2) Construction buffer zone:** Based on the spatial proximity effect, the construction buffer zone was mainly distributed in the peripheral areas of the suitable construction zone, which was a buffer pattern to maintain and provide the demand for urban expansion. Industrial land and ecological land can be increased appropriately through a reasonable industrial layout to realize regional economic development and improve the level of ecological security.

**(3) Restricted construction zone:** Restricted construction zone occupied the smallest area and was close to the construction buffer zone. This area had great resistance and a high cost of construction land expansion; therefore, it was generally not selected as the development area of construction land.

**(4) Construction zone:** This zone was mainly distributed in the northeastern region of the county and the surrounding areas. The resistance to construction land expansion was high, and the spatial distribution was

Table 7: Construction land expansion in Haixing County.

| Construction land expansion partition | Suitable construction zone | Construction buffer zone | Restricted construction zone | Prohibited construction zone |
|---|---|---|---|---|
| Area ($hm^2$) | 32783.62 | 17972.56 | 16952.67 | 19116.98 |
| Proportion (%) | 37.76 | 20.70 | 19.52 | 22.02 |

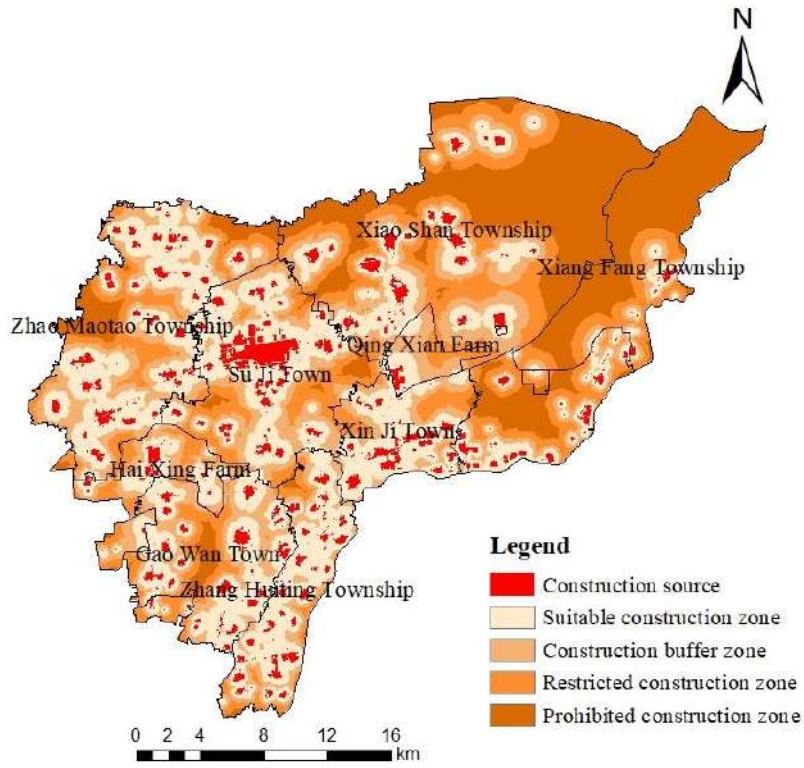


Fig. 8: Construction land expansion zone in Haixing County.

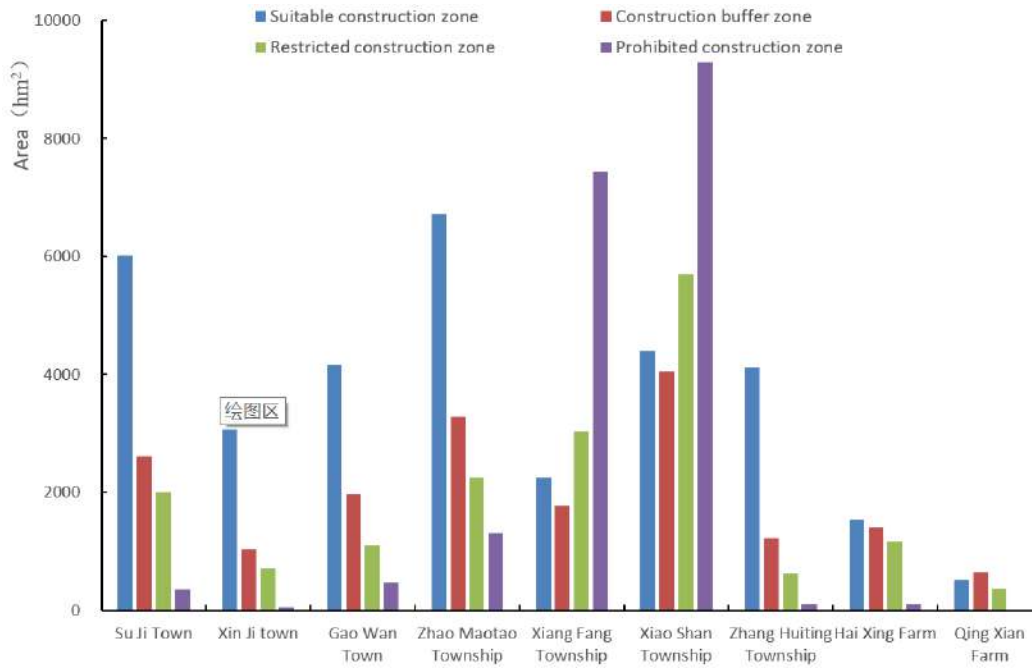


Fig. 9: Statistics on construction land expansion zone of each township in Haixing County.

a long distance from the source of urban expansion. Therefore, the development boundary of construction land should be delineated.

## Comprehensive Evaluation

The natural breakpoint method was used to divide the calculation results into four levels. Using the hydrological analysis method in ArcGIS, the minimum cumulative resistance cost path was extracted, and the spatial locations of 15 major ecological corridors, 12 radiation channels, and 35 strategic nodes were then identified (Table 8, Fig. 10, Fig. 11 and Fig. 12).

(1) **Optimal expansion zone:** This zone was mainly distributed around the ecological source, mostly concentrated in Xiao Shan and Xiang Fang townships. The ecological conflicts caused by land degradation can be effectively alleviated by increasing the amount of ecological land and the intensity of ecological governance.

Table 8: Areas and proportions of ecological land expansion zones.

| Extended type | Area ($hm^2$) | Proportion (%) |
|---|---|---|
| Optimal expansion zone | 42087.30 | 48.47 |
| Suitable expansion zone | 26305.77 | 30.30 |
| Extended adjustable zone | 13591.20 | 15.65 |
| Extended restricted zone | 4841.57 | 5.58 |

(2) **Suitable expansion zone:** This zone was adjacent to the optimal expansion zone, in the southwest and south of the county. The ecological land that should be increased was mainly distributed in a banded or scattered manner around the existing ecological land, such as by appropriately increasing the number of banded ecological land areas around the cultivated land, building shelterbelts, etc.

(3) **Extended-adjustable zone:** Extended-adjustable zone was mainly distributed in the vicinity of a residential area and had a scattered distribution. By increasing the greening of relevant areas and carrying out ecological restoration and renovation, the sustainable development of regional ecological security can be achieved in a friendly direction to drive the ecological civilization construction of the entire region.

(4) **Extended restricted zone:** Extended restricted zone was mainly distributed in areas of basic cultivated land. To ensure food security, basic cultivated land was prohibited from being used for other purposes. However, green passageways can be added around the high-quality cultivated land, so that an ecological corridor maintaining ecological mobility was maintained, which can achieve the optimal result of cultivated land protection and an increase in ecological land.

(5) **Ecological corridors, radiation channels, and strategic nodes:** The ecological expansion corridor

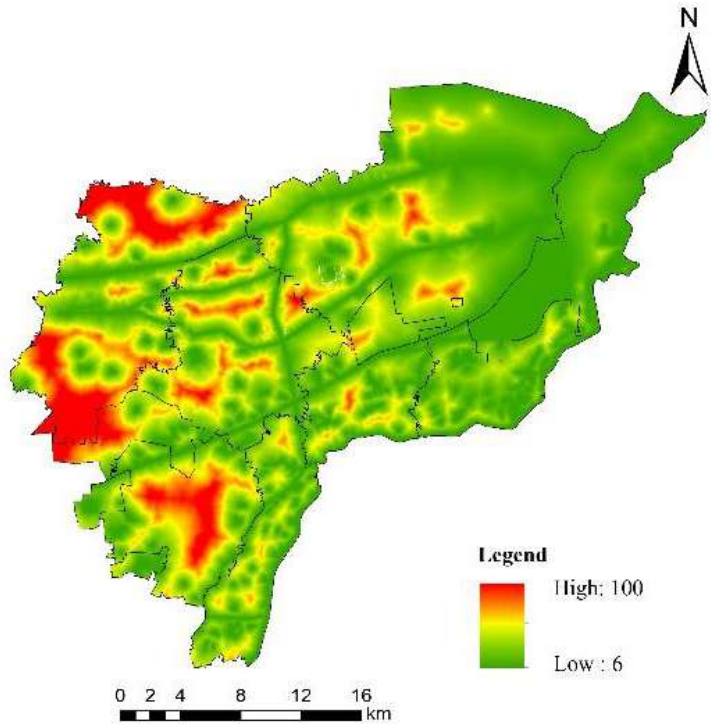


Fig. 10: The minimum comprehensive resistance surface.

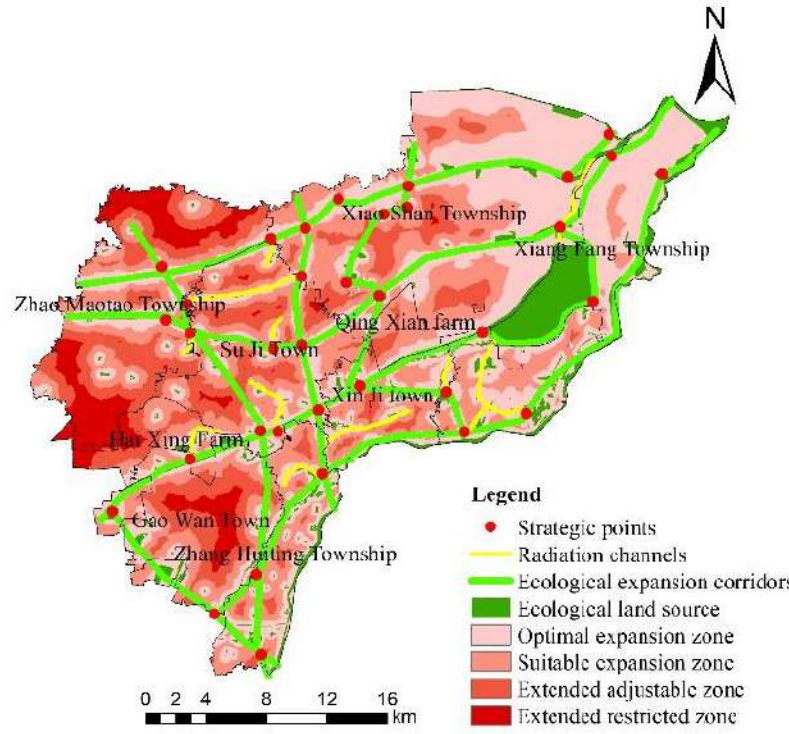


Fig. 11: Ecological land expansion pattern in Haixing County.

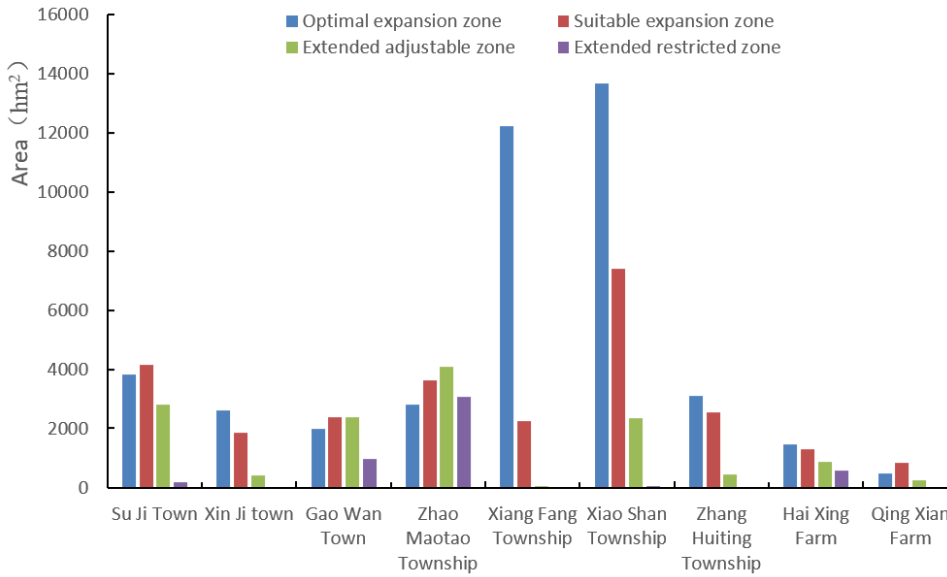


Fig. 12: Statistics on the ecological land expansion of each township in Haixing County.

was the most easily connected low-resistance channel between adjacent ecological sources (Wu et al. 2000). The radiation channel was the low-resistance valley line of radiation from an ecological source, and was a possible path for species diffusion. The strategic node was a significant "springboard" between two adjacent ecological sources. In short, ecological corridors, radiation channels, and strategic nodes cooperate to jointly promote the flow of material and energy in the ecosystem and maintain its healthy and sustainable development (Fig. 11 and Fig. 12).

## DISCUSSION

### Ecological Land Expansion

(1) The food security zone can be divided into four districts, among which the agricultural structural adjustment zone occupied the largest area, and the permanent protection zone occupied the same area as the non-agricultural construction zone. The key promotion zone occupied the smallest area and was mainly distributed in the buffer area in the central part of the county.

(2) The ecological security zone was divided into four districts, among which the ideal security zone occupied the smallest area and was mainly distributed in the northern part of the county. The medium security, basic security, and low security zones occupied the same area. The medium and basic security zones were cross-distributed in the county space, and the low security zone was mainly distributed in the northeast of the county.

(3) The expansion zone of construction land was divided into four districts, among which the proportion of suitable construction zones was relatively high. Each of the construction buffer zones restricted construction zones, and prohibited construction zones occupied approximately 20% of the study area, which can be regarded as multiple buffer zones suitable for the outward direction of the construction area.

(4) The expansion zone of ecological land consisted of four expansion areas, 15 ecological corridors, 12 radiation channels, and 35 strategic nodes. The area surrounding the ecological land source was mainly the optimal expansion zone. The suitable expansion zone was close to the optimal expansion zone, and the area that was suitable for an increase in ecological land was mainly distributed around the existing ecological land in a banded or scattered manner. In addition, the 15 ecological corridors were distributed in four horizontal and three vertical directions, promoting the flow of materials and energy in the natural ecosystem. The 12 radiation channels were the supplement of ecological corridors and the low-resistance routes of potential ecological land expansion. The 35 strategic nodes played a key role in the ecological land expansion.

### Limitations and Implications

This study had several limitations. First, we only analyzed the current land-use situation in one year, and statically analyzed the ecological land development pattern at the county scale and failed to reveal the internal mechanism between different

activities. Future research should involve identifying change processes at different scales and analyzing the internal relationships. By comprehensively considering climate, public security, and other factors, a more perfect evaluation system for land ecological-use pattern expansion will be established. The ecological land-use pattern is affected by many human factors such as land conversion cost, local ecological network, and different interest groups' demands (Liang et al. 2021). In future studies, optimization algorithms such as tradeoffs and synergies should be introduced into the expansion of land ecological use patterns, which will greatly improve the rationality of the research results.

Second, the limitations of the evaluation indices may affect the accuracy of the quantification results. For example, only six primary indices reflect ecological security pattern construction. Further studies are needed to integrate multiple evaluation indexes to obtain more accurate results.

Third, the limitations of the evaluation models may affect the accuracy of the quantification results. For example, using Analytic Hierarchy Process (AHP) to determine resistance factor weights is more objective, and the consistency of the judgment matrix is discussed. In the future, it is necessary to introduce other weight confirmation methods, such as Delphi and the fuzzy comprehensive evaluation method, and to use the highest-accuracy method.

## CONCLUSIONS

Based on the perspective of ecological land security, this study used the MCR model, etc. to research Haixing County. First, woodland, grassland, garden land, water area, wetland, and unused land were determined as ecological land. Second, the cultivated land quality, ecological security level, and expansion direction of construction land were determined, and a three-in-one pattern of food security, ecological security, and expansion of construction land was established. Finally, the MCR model was used to determine the expansion of ecological land, which is mainly composed of four extension areas, 15 ecological corridors, 12 radiation channels, and 35 strategic nodes.

Although this study had some limitations, it provides an extended framework of ecological land expansion for decision-makers to clarify the concept of constructing ecological security patterns. This research will contribute towards solving the contradiction between the expansion of construction land and the protection of cultivated land and realizing the multiple protection of food security, ecological security, and economic development. This study provides not only guidance for local governments to improve ecological environment quality and achieve the goal of promoting sustainable development, but also the essential basis for rural revitalization strategy.

## ACKNOWLEDGMENTS

This research was supported by the Social Science Foundation of Hebei Province (No. HB17GL057), and Key R & D projects of Hebei Province (20327506D).

## REFERENCES

Anselin, L. 2010. Local indicators of spatial association-LISA. Geogr. Anal., 27(2): 93-115.

Cao, Y.H., Liu. M.Y. and Zhang, Y. 2020. Spatiotemporal evolution of ecological security in the Wanjiang City Belt, China. Chin. Geogr. Sci., 30(6): 1052-1064.

Chaudhary, S., Wang, Y.K., Dixit, A.M., Khanal, N. R., Xu, P., Fu, B., Yan, K., Liu, Q., Lu, Y.F. and Li, M. 2019. Spatiotemporal degradation of abandoned farmland and associated eco-environmental risks in the high mountains of the Nepalese Himalayas, land, 9.

Costanza, R., D'Arge, R., Groot, R., Farber, S., Grasso, M., Hannon, B., Limburg, K., Naeem, S., O'Neill, R., Paruelo, J., Raskin, R., Sutton, P. and Belt, M. 1997. The value of the world's ecosystem services and natural capital. Nature, 387(1): 3–15.

Fath, B.D., Scharler, U.M., Ulanowicz, R.E. and Hannon, B. 2017. Ecological network analysis: network construction. Ecol. Model., 208(1): 49-55.

Fu, B.J. 2019. Cognition of land resource system and pattern of national ecological security. China land, 12: 9-11 (in Chinese).

Gergely, B. and Leah, M. 2019. The grid as algorithm for land use: a reappraisal of the 1811 Manhattan grid. Plan. Perspect., 34(3): 391-414.

Green, T.L., Kronenberg, J., Andersson, E., Elmqvist, T. and Gómez-Baggethun, E. 2016. Insurance value of green infrastructure in and around cities. Ecosystems, 19(6): 1051-1063.

Huck, M., Jędrzejewski, W., Borowik, T., Jędrzejewska, B., Nowak, S. and Mysłajek, R.W. 2011. Analyses of least cost paths for determining effects of habitat types on landscape permeability: wolves in Poland. Acta. Theriol., 56(1): 91-101.

Jongman, R.H.G. and Pungetti, G. 2005. Ecological Networks and Greenways: Concept, Design, Implementation. Cambridge University Press, Cambridge.

Lambin, E.F. and Meyfroidt, P. 2011. Global land use change, economic globalization, and the looming land scarcity. Proc. Natl. Acad. Sci. U. S. A., 3472-3465 :(9)108.

Liang, J., Li, S., Li, X.D., Li, X., Liu, Q., Meng, Q.F., Lin, A.Q. and Li, J.J. 2021. Trade-off analyses and optimization of water-related ecosystem services (wress) based on land use change in a typical agricultural watershed, Southern China. J. Clean. Prod., 279.

Liu, B.L., Dong, D.M., Hua, X.Y., Dong, W.H. and Li, M. 2021. Spatial distribution and ecological risk assessment of heavy metals in surface sediment of Songhua River, Northeast China. Chin. Geogr. Sci., 31(2): 223-233.

Liu, Z.Z., Wu, W., Liu, W.F. and Shen, L.B. 2020. Study on construction land reduction based on "Source-Corridor" ecological security pattern paradigm. Acta Ecol. Sin., 40(22): 8230-8238 (in Chinese).

Long, H.L., Liu, Y.Q., Li, T.T., Wang, J. and Liu, A. 2015. A primary study on ecological land use classification. Ecol. Environ. Sci., 24(1): 1-7 (in Chinese).

Macmillan, R.A., Moon, D.E. and Coupé, R.A. 2007. Automated predictive ecological mapping in a forest region of B.C. Canada, 2001–2005. Geoderma, 140(4): 353-373.

Ojea, E., Loureiro, M.L., Alló, M. and Barrio. M. 2016. Ecosystem services and Redd: estimating the benefits of non-carbon services in worldwide forests. World. Dev., 78: 246-261.

Schröter, M., Crouzat, E., Hölting, L., Massenberg, J., Rode, J., Hanisch, M., Kabisch, N., Palliwoda, J., Priess, J., Seppelt, R. and Beckmann, M. 2020. Assumptions in ecosystem service assessments: increasing transparency for conservation. Ambio.

Tan, K.W. 2006. A greenway network for Singapore. Landsc. Urban Plan., 76(1-4): 45-66.

Tang, F., Wang, L., Zhang, P. and Fu, M.C. 2020. Construction of county-level ecological security pattern based on ecological protection red line and network in China. Transactions of the Chinese Society of Agricultural Engineering (Transactions of the CSAE), 36(9): 263-272 (in Chinese).

Wang, Y. and Pan, J.H. 2019. Building ecological security patterns based on ecosystem services value reconstruction in an arid inland basin: a case study in Ganzhou district, NW China. J. Cleaner. Prod., 241.

Wu, J.G. 2000. Landscape Ecology: Pattern, Process, Scale and Hierarchy. Higher Education Press, Beijing (in Chinese).

Xie, G.D., Zhang, C.X., Zhang, L.M., Chen, W.H. and Li, S.M. 2015. Improvement of the evaluation method for ecosystem service value based on per unit area. J. Nat. Resour., 30(8): 1243-1254 (in Chinese).

Xiu, N., Ignatieva, M., Bosch, C.K. and Zhang, S.X. 2020. Applying a socioecological green network framework to Xi'an City, China. Landsc. Ecol. Eng., 16: 135-150.

Yu, C.L., Liu, D., Feng, R., Tang, Q. and Guo, C.L. 2021. Construction of ecological security pattern in Northeast China Based on MCR model. Acta Ecol. Sin., 41(1): 290-301 (in Chinese).

Yu, J., Fang, L., Cang, D.B., Zhu, L. and Bian, Z.F. 2012. Evaluation of land eco-security in Wanjiang district base on entropy weight and matter element model. Trans. Chin. Soc. Agric. Eng., 28(5): 260-266 (in Chinese).

Yu, K.J., Wang, S.S., Li, D.H. and Li, C. 2009. Beijing's ecological security pattern and urban long-term prospecting method. Acta Ecol. Sin., 29(3): 1189-1204 (in Chinese).

Zhang, G.J., Zhou, Z., Zhang, P.T., and Zhang, Y.G. 2017. Study on ecological safety monitoring practice of county cultivated land: A case study from Huanghua City, Hebei Province of China. Nat., Environ. Pollut. Technol., 16(4): 1195-1204.

Zheng, Y.N., Zhang, F.R., Xie, Z., Zhang, T.Z., Li, C. and Wang, X. 2019. Research on spatial-temporal evolution of grain production and sustainable use of cultivated land in China. World Regional Studies, 28(6): 120-131 (in Chinese).

Zhou, S.Y., Li, W., Lu, Z.Y.F. and Cheng, R.H. 2020. An ecosystem-based analysis of urban sustainability by integrating ecosystem service bundles and socio-economic-environmental conditions in China. Ecol. Indic., 117.

Nature Environment and Pollution Technology
An International Quarterly Scientific Journal

p-ISSN: 0972-6268
(Print copies up to 2016)
e-ISSN: 2395-3454

Vol. 22 | No. 1 | pp. 397-409 | 2023

Original Research Paper

https://doi.org/10.46488/NEPT.2023.v22i01.038

Open Access Journal

# Self-Healing and Thermomechanical Properties of Activated Carbon Pyrochar Derived from Municipal Mixed Plastic Waste Pyrolysis with Self-Healing Epoxy Vitrimer Composites

**Krishna Moorthy Rajendran*†, Bhawna Yadav Lamba** and Deepak Kumar***

*Centre for Alternate Energy Research and Department of Mechanical Engineering, School of Engineering, University of Petroleum and Energy Studies, Dehradun, Uttarakhand, India

**Department of Chemistry, School of Engineering, University of Petroleum and Energy Studies, Dehradun, Uttarakhand, India

†Corresponding author: Krishna Moorthy Rajendran; krishnov1992@gmail.com

**Nat. Env. & Poll. Tech.**
**Website: www.neptjournal.com**

*Received:* 21-06-2022
*Revised:* 15-08-2022
*Accepted:* 17-08-2022

**Key Words:**
Municipal mixed plastic waste
Pyrolysis
Activated carbon
Pyrochar
Vitrimer

## ABSTRACT

An ecological vitrimer is being developed using activated carbon pyrochar from municipal mixed plastic waste pyrolysis into an epoxy composite. Durable vitrimeric materials may be created by adding pyrochar to polymeric composites. Due to their ductility, reusability, and recyclability, vitrimeric materials have become popular and reliable materials. As a result, the self-healing temperature of composite vitrimers is lower via disulfide exchanges than that of virgin epoxy vitrimers. Additionally, compressive studies have been used to study self-healing capacities, and modulus variations have been used to highlight changes in the healing efficiency of the materials.

## INTRODUCTION

Plastics are made from hydrocarbon-based petroleum products. At the same time, they contain several additives that are not necessarily good for the environment, such as antioxidants, colorants, and stabilizers (Brems et al. 2012). Char is a solid substance made up of tiny particles high in carbon and contains some oxygen and hydrogen (Xu et al. 2020). These particles have a large surface area and porosity, are chemically stable, are inexpensive, and may be prepared at temperatures between 500 and 700 degrees Celsius (Ahmed & Hameed 2020). To attain the desired material properties, plastics often incorporate additives such as color pigments, reinforcing fillers, plasticizers, flame retardants, antioxidants, and UV stabilizers (around 5 percent of total weight) (Beach et al. 2013). However, there has been little research on the use of char in composite manufacturing, and none of these composites used epoxy resin (ER) as a matrix. For example, coconut shell char was used in aluminum alloy matrix composites (Murali et al. 1982, Moorthy Rajendran et al. 2020)

White et al. (2001) recently proposed one of the autonomic self-healing systems adapted to fulfill specific objectives in the realm of aeronautic applications (White et al. 2001, Krishnakumar et al. 2020). As a result, the mending mechanisms of animated bodies are imitated. High chain mobility permits multiple possible self-healing methods in soft materials with low glass transition temperatures (lower than the material's service temperature). There are substantial limitations in selecting self-healing methods for load-bearing materials with high stiffness and little chain mobility, resulting in limited chances of success. Hollow fibers and microvascular networks have lately been presented as alternatives to microencapsulated systems.(Patrick et al. 2016, White et al. 2014). Although several chemistries for vitrimer materials have been investigated, the reported materials are fairly limited in scope. Their mechanical properties are frequently not equivalent to commercial resins or conventional engineering polymers (Brutman et al. 2014).

Epoxy resins are used to make epoxy composite materials. Epoxy resins comprise a matrix and particles as a filler material (Kang et al. 2001, Verma et al. 2017, 2018). Talc, calcium carbonate, and synthetic additives like carbon black are used to make these particles (Kang et al. 2001, Verma et al. 2017, 2019, 2018). Because of its copious resources from maize and its high stiffness and thermal stability, isosorbide

was chosen as a natural building block for renewable polymers with high glass transition temperatures (Tg). The thermal reprocessing of epoxy vitrimers was helped by the relatively high thermal stability of isosorbide. Meanwhile, the dynamic disulfide bond reaction comprises several mechanisms influenced by reaction conditions. Disulfide connections broke mechanically due to external stressors, releasing thiol radicals that might swiftly exchange with other disulfide bonds, resulting in self-healing or reprocessing of crosslinked networks (Fenouillot et al. 2010, Duan et al. 2015, Martin et al. 2016, Yang et al. 2015, Black et al. 2014).

In developing bio-based vitrimers based on this technique, some bio-based compounds with multiple epoxy groups have been investigated by curing sebacic acid poxy with ozonized Kraft lignin, a bio-based vitrimer with shape memory, mending properties, and potential adhesive usage was produced. A vitrimer with similar strength and modulus to cured bisphenol A epoxy was created by curing another bio-based triepoxy (TEP) with an anhydride monomer (Zhang et al. 2018, Liu et al. 2018). Furthermore, because of the new trend in composite material manufacturing, Out of autoclave, a significant amount of study has been committed to understanding the nature of thermoplastic composite materials (Yassin & Hojjati 2017).

To further understand the impact of the inorganic filler, we used epoxy resins cured at moderate temperatures of less than 120°C in the first study. We used tertiary amines as curing catalysts to do this. Anionic polymerization occurs when Lewis bases, such as tertiary amines, are present. Due to the lengthy cure cycles required and the low heat-distortion point of the resultant resins, anionic initiator polymerization of epoxy resins has not yet received widespread commercial use. However, the most recent discoveries described in this paper provide strong potential for reducing earlier concerns and boosting the adoption of this class of catalytic curing agents in the future. Only a small amount of literature on diepoxide (or polyepoxide) resins using anionic initiators as curing agents. However, in recent years, these curative agents have become more popular among researchers working on aeronautical functional applications worldwide (Brown et al. 2002, 2004, Kessler & White 2002, Kessler et al. White et al. 2001, Krishnakumar et al. 2020). Peng et al. (2016) employed a similar process to create rGO/epoxy polymer nanocomposites with good rGO nanosheet dispersion, which they found to be quite beneficial. The GO was reduced by suspending it in an epoxy resin (triglycidyl paraaminophenol) for 5 min at 200°C, followed by curing the epoxy resin with the addition of 3,5-dimethylthio-2,4-toluenediamine and curing the epoxy resin (Peng et al. 2016).

The exchangeable link concept can also be used to create materials that are hard at room temperature yet flexible but insoluble at higher temperatures. Hydroxy groups and ester linkages are found in used epoxy-anhydride resins (Tesoro 1988). Within that work, we investigate a reliable method for creating self-healing epoxy vitrimer nanocomposites that are encouraged by graphene oxide without needing a catalyst. The capacity of the self-healing nanocomposites is attributed to disulfide exchange-based covalent adaptive network activity, in which aromatic disulfide hardeners stimulate radical-mediated exchanges to affect bond exchange in such vitrimers (Krishnakumar et al. 2020, Luzuriaga et al. 2016a, 2016b)

Altuna et al. (2016) investigated an epoxy vitrimer cured with carboxylic acids and imidazole as a catalyst to improve its performance. After 1 h of heating at 160°C, the BERs of esterification and transesterification were utilized to analyze the properties of the epoxy vitrimer's reconfigurable forms. The samples' shape fixities and shape recovery ratios were 99 percent accurate. During partial stress relaxation, the characteristics of vitrimers can be identified to a limited extent (Altuna et al. 2016).

Zako et al. devised a method for incorporating small thermoplastic adhesive particles into glass/epoxy composite laminates (50m). The epoxy resin matrix was cured at a temperature of 100-110°C. When damaged composites were heated to 120°C for 10 min on a hot plate, the thermoplastic particles implanted in them melted. The percentage of curing was documented in the subsequent three-point bend test based on the measurement of the flexural strength of the repaired specimen, and the load-displacement curve revealed that stiffness was recovered in the repaired specimen (Zako & Takano 2016).

Thermal activation is some of the most prominent approaches for developing self-healing characteristics in biological systems. As a result, raising the heat conductivities of polymers would assist in enhancing the self-healing efficiency and effect of the polymers (Yang et al. 2018, Burger et al. 2016). The self-healing properties of the synthesized nanocomposites are attributed to covalent adaptive network activity based on disulfide exchange, in which aromatic disulfide hardeners strengthen radical-mediated exchanges to conduct the link change in such vitrimers (Krishnakumar et al. 2020, Luzuriaga et al. 2016a, 2016b)

To create a low-temperature self-healing material, activated carbon pyrochar derived from municipal mixed plastic waste pyrolysis was combined with an epoxy vitrimer system to create more environmentally friendly composites. As a result, a composite vitrimer with aromatic disulfide crosslink-assisted self-healing has been developed. Various

aromatic disulfide concentrations are also used to improve the chemical and mechanical properties of epoxy vitrimer composites. The thermomechanical and self-healing properties of plastic pyrochar-derived activated carbon epoxy vitrimer composites have yet to be thoroughly explored. The issues highlighted in this paper have been dealt with succinctly.

## MATERIALS AND METHODS

### Materials

A lab-scale pyrolysis setup was developed @ UPES. Fig. 1 presents an illustration of the manufacturing flow process that converts waste plastic into an alternative fuel with activated carbon char.

Two components of the epoxy resins were acquired from Sigma-Aldrich: 2- Aminophenyl disulfide (AFD) (248.37 $g.mol^{-1}$)/diethylenetriamine (DETA) (103.17 $g.mol^{-1}$) and bisphenol A diglicidyl ether (BADGE) (340.41 $g.mol^{-1}$). This paper describes the preparation of the activated carbon (AC) pyrochar produced from municipal mixed plastic waste pyrolysis (Krishnakumar et al. 2021).

### Calculation for Epoxy and Amine Hardener Ratio

Parts by weight of amine to be used with 100 parts by weight of BADGE resin (phr)

$$= \left( \frac{\text{amine hardener molecular weight} / \text{number of hydrogens per molecule}}{\text{BADGE equivalent weight}} \right) \times 100\%$$

BADGE resin has an equivalent weight of 176 g/mole (as stated by the manufacturer), and active hydrogen in 2-AFD is four.=> $\left(\frac{248/4}{176}\right) \times 100\% = 35.6\%$

To cure 100 g of BADGE resin, 35.6 g of AFD is required.

### Preparation of Epoxy Nanocomposite

The synthesized AC (300 mg) was diffused in 20 mL ethanol and ultrasonicated for 30 min to obtain a homogeneous suspension. The AC solution was immediately added to the Bisphenol A diglicidyl ether resin and stirred vigorously until entirely dissolved (EP- x percent; x: 0,0.1,0.2,0.5,1,2), where 'x' is the amount of AC added to the epoxy resin mixture in weight percentages. The mixture was also heated to 80°C and vacuum degassed until the ethanol was completely gone. The hardener (2-aminophenyl disulfide (APD)) was then added and mixed at the same temperature for 15 min. The degassed liquid was put into a silicon mold to set the color and baked for 5 h at 150°C. Bisphenol A diglicidyl ether resin-based reference specimens were also created, with diethylenetriamine (DETA) functioning as a hardener, to study the influence of APD on self-healing in accordance with previously reported procedures. To study the activated carbon impacts, reference clean (R-epoxy) and AC-impregnated epoxy (R-Epoxy-1 percent) nanocomposites were constructed (Hummers & Richard 1958, Nia et al. 2014, Rana et al. 2016, Park et al. 2019, Krishnakumar et al. 2020).

### Material Characterization Methods

The D8 ADVANCE ECO-Bruker was used to conduct

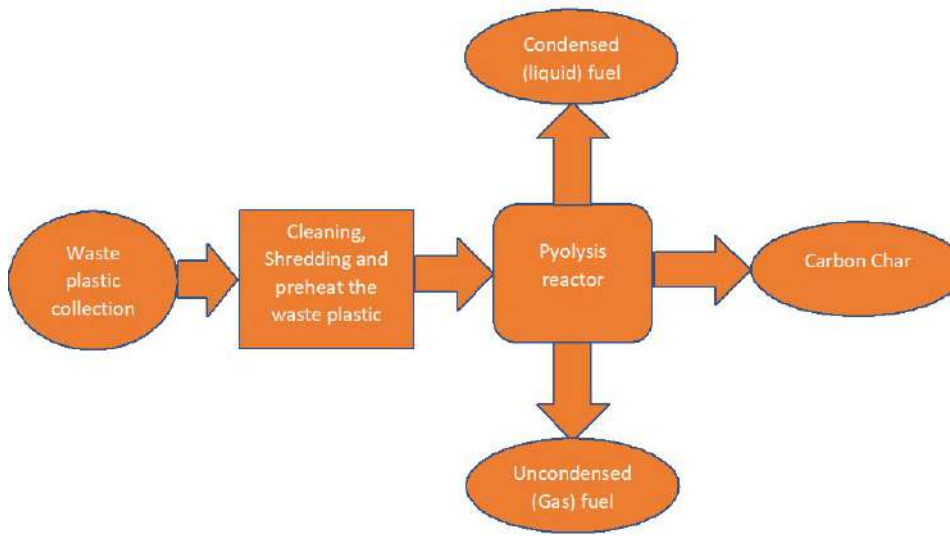


Fig. 1: Schematic flow process diagram of domestic plastic waste to alternate fuel.

an X-Ray Diffraction spectroscopy analysis to detect the activated carbon. Epoxy's activated carbon was studied using the spectroscopic UV-Visimeter (LAMDA 35, Perkin Elmer). The curing process was studied by FT-IR spectra analysis (Frontier FT-IR/FIR, Perkin Elmer). The effects of activated carbon dispersion in the epoxy matrix were investigated using an HR-TEM, JEM 2100F, from JEOL. The glass transition temperature was determined using differential scanning calorimetry (DSC) tests and TA-Q400em dimensional change studies. At temperatures ranging from 30 to 220 degrees Celsius, Perkin Elmer differential scanning calorimetry (DSC-7) was used with a nitrogen purge gas flow rate of 19.8 mL per minute and a pressure of 3 bars. Three-point bending tests were performed on rectangular specimens (15×5×0.5 mm) in the TA-Q400em to evaluate their mechanical properties. All mechanical characteristics tests were carried out at temperatures ranging from 40 to 120 degrees Celsius, with heating rates of 10 degrees Celsius per minute, a nitrogen purge gas flow of 50 ml per minute, and a force of 0.02 Newton. To straighten the specimen in the stress relaxation experiment, a preloaded force of $1\times10^{-3}$ N was applied. After determining the temperature and strain, testing consisted of applying 1% strain at the proper temperature and measuring the relaxation modulus with respect to time. Stress-strain experiments were conducted in strain ramp mode with a force of 0.02 N, and the strain was measured at an isothermal temperature of 40°C.

## RESULTS AND DISCUSSION

### Material Characterization

Activated carbon in an epoxy vitrimer composite was detected using ultraviolet spectroscopy (UV). The material was characterized by a fine-grinded matrix efficiently diffused in ethanol using ultrasonication. The absorbance peak revealed the presence of activated carbon in the epoxy composite at 237 nm. In Fig. 2a, the obtained UV data for epoxy-activated carbon and epoxy-AC composites were plotted together.

The x-ray diffraction spectroscopy (XRD) analysis of the activated carbon synthesized from pyrochar (Fig. 2b) shows that the peak at 27.23°C marks their formation. The lack of distinct peaks indicated the amorphous nature because of the hexagonal shape resembling a graphite flake peak found at 27.23°C. AC might be considered assemblages of imperfect graphene.

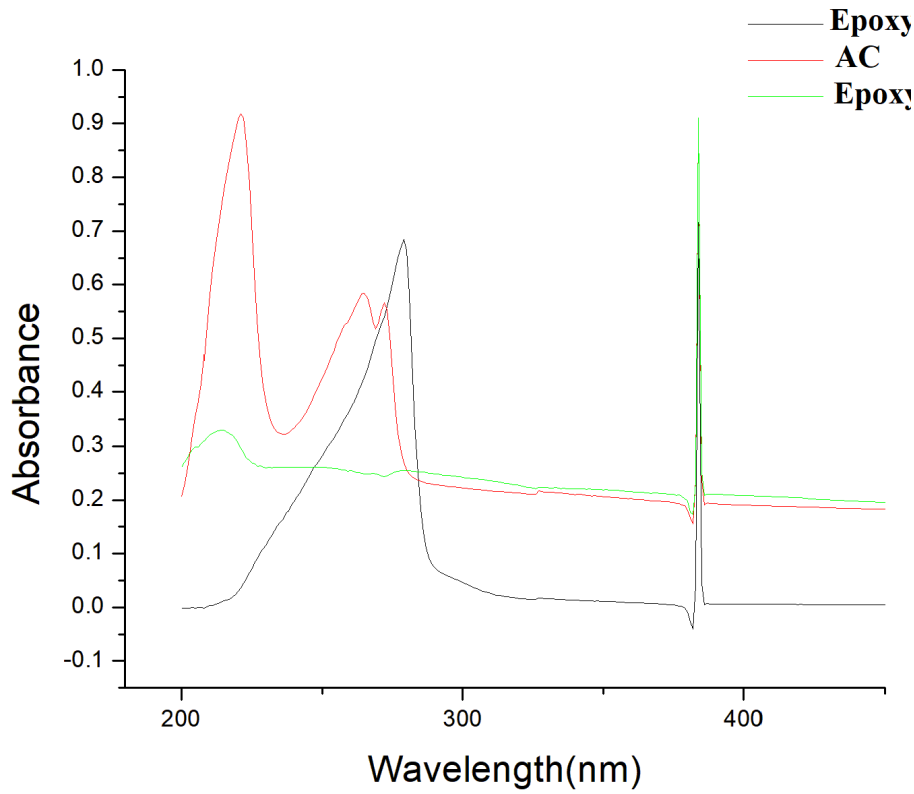


Fig. 2a: UV spectrum for epoxy, activated carbon, and epoxy-activated carbon composite.

The curing and uncuring of epoxy vitrimer composites were determined using FT-IR analysis. The disappearance of the oxirane rings of the oxirane ring (917 $cm^{-1}$) was noticed, which indicated that the epoxy had completed its curing process (Fig. 2c). The curing of the epoxy was monitored using FT-IR analysis at intervals of 1 h. It was discovered that the curing process was complete after 5 h of observation.

SEM analysis shows that carbon pyrochar is generated from municipal mixed plastic waste pyrolysis and activated carbon surface, in which the chemically activated carbon reveals pores on its surface (Fig. 2d, 2e). Because of their modest volume, these pores allow activated carbon to increase the surface area for chemical reactions.

**Mechanical and Thermo-Mechanical Properties**

A thermomechanical analyzer was used to determine the Tg and dynamic mechanical performance of activated carbon-epoxy vitrimer composites. The thermal characteristics of pristine epoxy composites have been investigated. The TA Q-400em is effective in finding Tg from temperature-influenced aspect variations.

Tg values for virgin epoxy vitrimer and activated carbon-epoxy vitrimer composites with different quantities of activated carbon filler are shown in Table 1. Among the studied epoxy samples, EP-1 had the lowest Tg.

Furthermore, the lack of reactivity between epoxy and activated carbon improves chain mobility, allowing for more free space between the filler and matrix. As a result, chains near the interface easily flow into the free volume, boosting mobility and lowering Tg (Grady 2012). The free volume space between matrix and nanofillers (Sun et al. 2004) may have reduced Tg for all composites, enhancing chain mobility and achieving low-temperature self-healing characteristics. However, adding 1 wt% activated carbon filler increases Tg somewhat, perhaps owing to the amalgamation of activated carbon in the epoxy matrix (Landel & Nielsen 1994, Krishnakumar et al. 2020).

The lower Tg aids low-temperature self-healing and shape memory. As a result, more study was conducted on composites containing up to 1% activated carbon in the matrix. A dynamic three-point bending test was used to investigate the effects of activated carbon filler on the

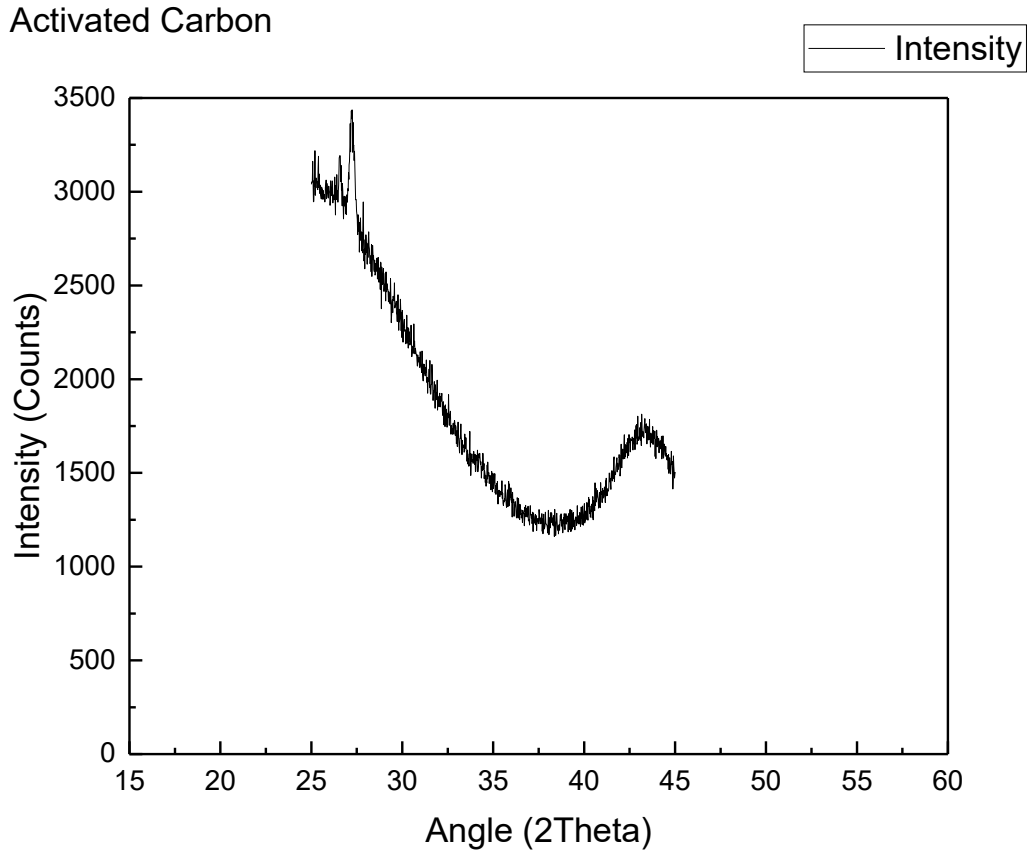


Fig. 2b: XRD spectrum for activated carbon.

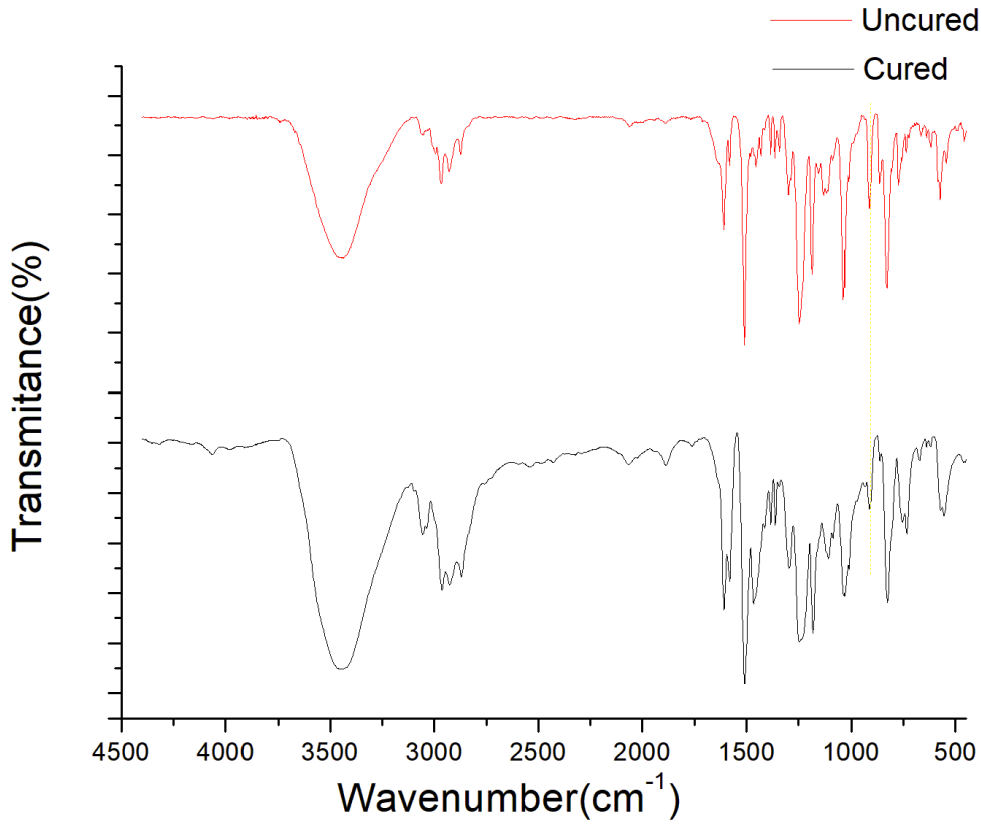


Fig. 2c: UV spectrum for cured and uncured epoxy composite.

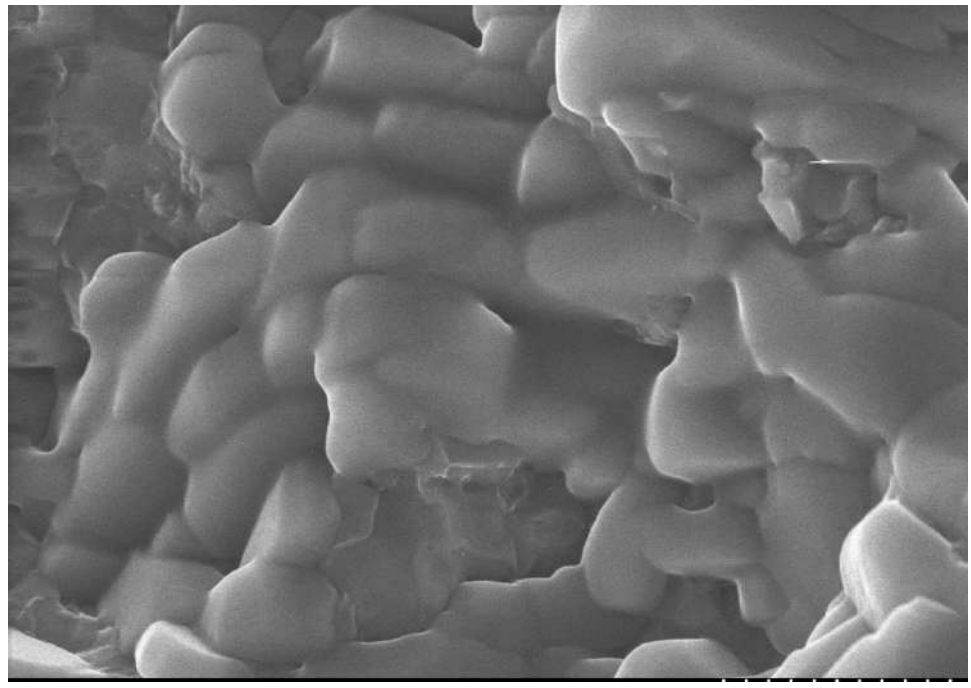

Fig. 2d: SEM images for pyrochar carbon.

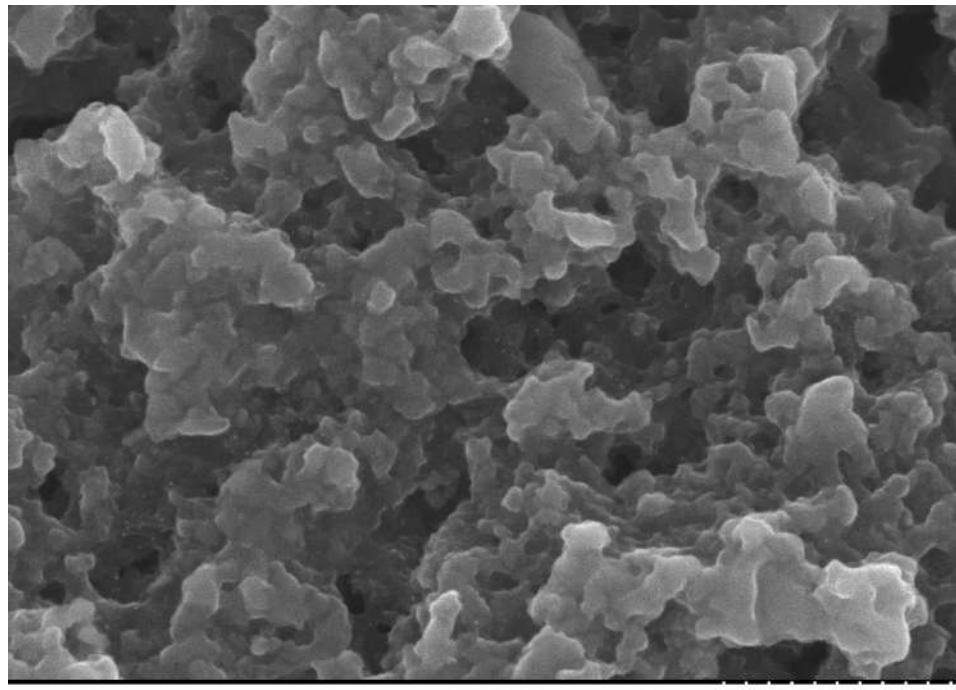

Fig. 2e: SEM images for activated carbon.

mechanical behavior of epoxy vitrimer. Table 2 shows the changes in mechanical parameters of vitrimer epoxy when utilizing cured pristine and activated carbon epoxy. The viscoelasticity of pristine epoxy vitrimer and activated carbon-epoxy vitrimer composites was investigated at different temperatures (Fig. 3a and 3b). The storage (E') and loss (E) modulus of the epoxy vitrimer material were addressed. In the high activated carbon sample, the storage modulus (52.2 GPa) (EP-1%). Fig. 3a shows a steady rise in storage modulus with nanofiller, and Table 2 shows the achieved values.

The wavy structure of activated carbon may aid in achieving effective intercalate interlocking with polymer matrix, thereby increasing modulus. The loss modulus (E) (Fig. 3b) also shows the material's viscoelasticity (E'>E). The shoulder peak (Fig. 3a) represents the rubbery area of the vitrimer materials following Tg. The glass transition temperature (Tg) of the epoxy vitrimer was decreased by adding 1% activated carbon to EP-1. With the addition of fillers, Tg decreases, resulting in a low-temperature rubbery zone in vitrimeric composites (Landel & Nielsen 1994)

Table 1: The glass transition temperature of epoxy composites.

| Material | $T_g$ (TMA) ($^oC$) |
|---|---|
| EP-pristine | 83 |
| EP-0.1% | 62 |
| EP-0.2% | 58 |
| EP-0.5% | 56 |
| EP-1% | 53 |

As a result, the solid-to-rubbery phase shift temperature completely depended on material viscoelasticity (storage and loss modulus) (Guadagno et al. 2011).

The stress-strain relationship of developed vitrimer composites was determined using three-point bending tests at 40°C. According to Fig. 3c, EP-1 % has greater flexural strength than EP-Pristine, and EP-1 % has higher flexural strengths than EP-pristine samples (Table 2). Combining activated carbon with epoxy composites gains stiffness and bending resistance while reducing strain-at-break (Bortz et al. 2012). Using activated carbon fillers enhanced the flexural modulus from 0–9.4% to 0–9.4%.

The pure epoxy sample has a lower flexural modulus than EP-P and EP-1%. Fig. 3b shows the nanofiller-based variation in flexural strength and modulus. The flexural values (strength and strain at break) of conventional and vitrimer epoxy networks are listed in Table 2 (Ebnesajjad & Arthur 2015).T

## Dynamic Properties

**Stress relaxation:** By performing stress relaxation analysis on the epoxy composites, which is designed to determine the relaxation modulus of malleable materials, it has been

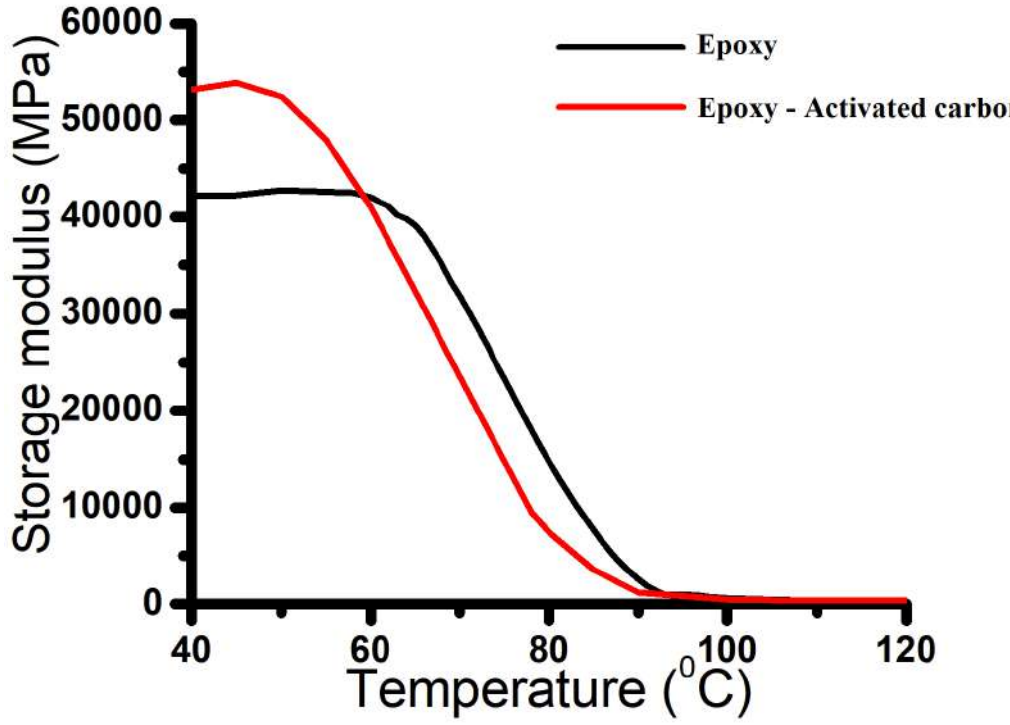


Fig. 3a: Storage modulus for epoxy vitrimer.

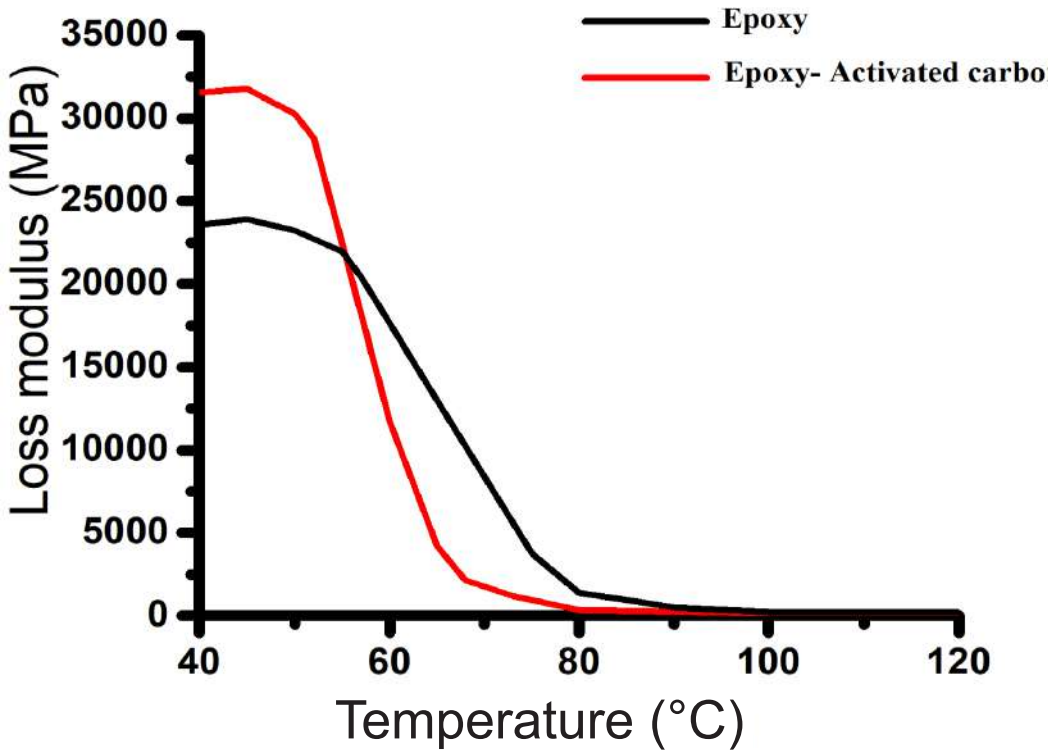


Fig. 3b: Loss modulus for epoxy vitrimer.

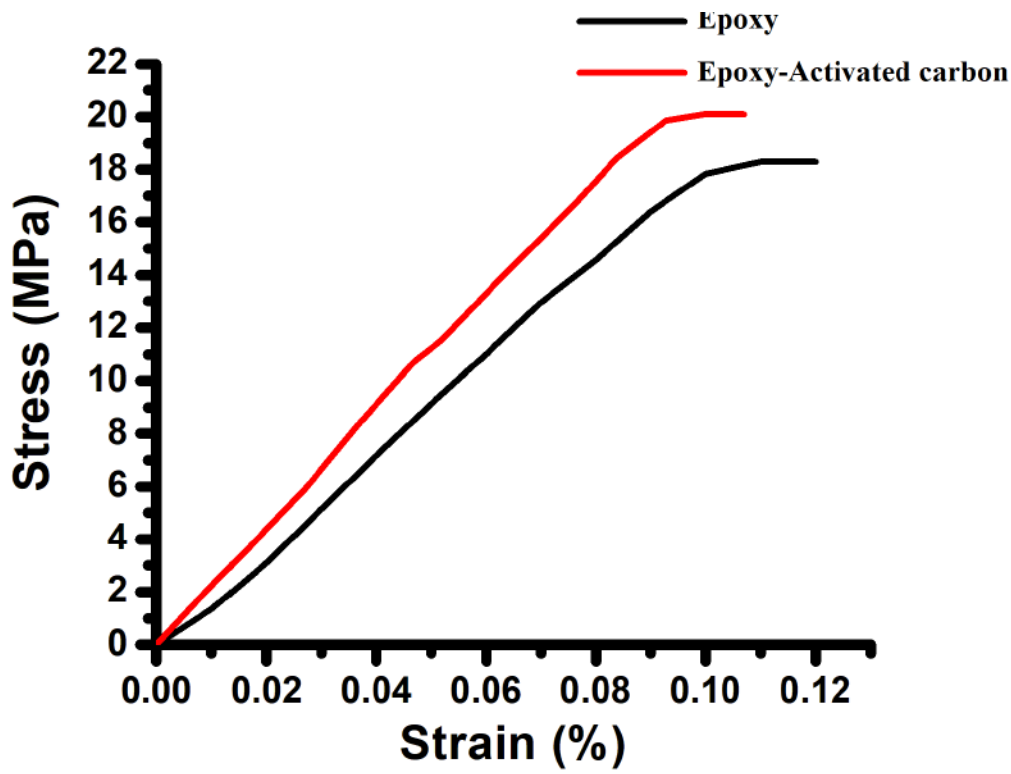


Fig. 3c: Stress-strain curve for epoxy vitrimer.

verified that they exhibit vitrimer behavior (Ogden & Guan 2018). In this study, an EP-pristine stress relaxation investigation was carried out, and the resulting time-dependent relaxation modulus was plotted in accordance with the data received from their temperature measurements. The high relaxation rates reported in the material suggest a fast disulfide exchange in the substance. Because of the relationship between temperature and relaxation time, a shorter relaxation period corresponds to a quicker disulfide exchange rate. The temperatures of 60°C, 70°C, and 80°C used in the experiments resulted in relaxation durations of 112.8 s, 40.8 s, and 34 s, respectively. The obtained findings indicate a quick exchange response after Tg and that the imposed tension is rapidly relaxed. By using an Arrhenius equation (1), the acquired data were displayed, which allowed for the calculation of a low activation energy (Ea = 59/KJ.mol$^{-1}$) (Jousseaume et al. 2002).

$$\tau^* = \tau_0 \exp (E_a/RT) \quad \ldots(1)$$

According to some theories, this is due to activated carbon, which has lower epoxy vitrimer crosslinking density and increased viscosity. However, it was discovered that the development of free volume between the filler and the matrix was the most important factor in the diminution of the glass transition temperature (Sun et al. 2004). Generally, when viscosity exceeds $10^{12}$ Pa.s, it is necessary to consider the temperature of the material topology transition shift (Dyre 2006). Using Maxwell's and Arrhenius' equations, the projected topological freezing transition temperature (Tv) was calculated to be 19°C due to this typical study.

**Self-healing:** A temperature value of 75°C was used to study the produced samples' self-healing behavior. The findings indicate that the samples had considerable self-healing effects. It is anticipated that a lower temperature self-healing will be associated, which will be beneficial in lowering the Tg, where the S-S bonds will be able to reorganize more quickly at the lower Tg. As a result of the inclusion of the filler, the self-healing capability has been enhanced, which is beneficial in accelerating and constraining the flow constraints for the disulfide groups. For the sample, EP-1 %, a low-temperature self-healing (75°C for 5 min) was achieved, which was beneficial in lowering the Tg. A razor

Table 2: Mechanical properties of epoxy AC nanocomposites.

| Epoxy material | Storage modulus [GPa] | Flexural strength [MPa] | Flexural strain% | Flexural modulus [GPa] |
|---|---|---|---|---|
| EP-P | 39.9 | 19.4 | 0.05 | 32.5 |
| EP-1% | 53.5 | 19.2 | 0.11 | 15.7 |

blade was used to split the test specimen in half, and the parts were instantly assembled at 75°C for 5 min with the use of a tweezer to assess their bond strength (Olowojoba et al. 2017). The effectiveness of the healed samples was determined using flexural testing, and the stress-strain correlations of the healed samples were presented in Fig. 4a for two different healed samples.

No changes in flexural strength were seen after healing. However, the flexural modulus was significantly reduced due to the increased strain, as shown in Table 3. Specifically, this decrease establishes the upper limit for crosslinked chains and is related to the drop in crosslink density (Guadagno et al. 2018, Florea et al. 2015). After healing, EP-pristine and EP-1 percent returned 72% and 83% of their flexural modulus, respectively, and the second healing cycle demonstrated a 60% and 75% increase in flexural modulus, respectively (Fig. 4b). So, the reported values proved to be useful in determining the healing efficiency that had prevailed. It was identified that Carbon pyrochar generated from municipal mixed plastic waste pyrolysis was good in achieving effective healing.

## CONCLUSION

According to this study, activated carbon from municipal mixed plastic waste pyrolysis could be employed as a filler in an epoxy vitrimer biocomposite. The enormous surface area of activated carbon in the AC-epoxy vitrimer biocomposite allows for chain exchanges. Self-healing was observed in virgin epoxy vitrimer at 80°C for 5 min; however, when activated carbon was added, the material showed a lower self-healing temperature at 75°C for 5 min. Comparing the composite EP-1 % (which contains 1 wt % AC) to virgin epoxy vitrimers, the EP-1 % composite exhibits 17% greater flexural strength and modulus and a 16.9% increase in modulus. Vitrimer composites with 1 wt% AC (EP-1) exhibited 83 and 75 % recovery efficiency after two successive healings in flexural trials. Composite vitrimer research will be useful in the future to witness ecologically sound vitrimer composite materials for practical uses.

## ACKNOWLEDGMENTS

The authors thank the Department of Applied science, Mechanical Engineering, Centre for Alternate Energy Research, UPES, Dehradun, Uttarakhand, for their continuous help and support. The authors would also like to acknowledge Dr. Sravendra Rana (Department of chemistry, UPES), Dr. Balaji. K (Industrial & Manufacturing Engineering, FAMU- FSU college of engineering, Florida), and Mr. Charu Chandra Pant (Central Instrumentation

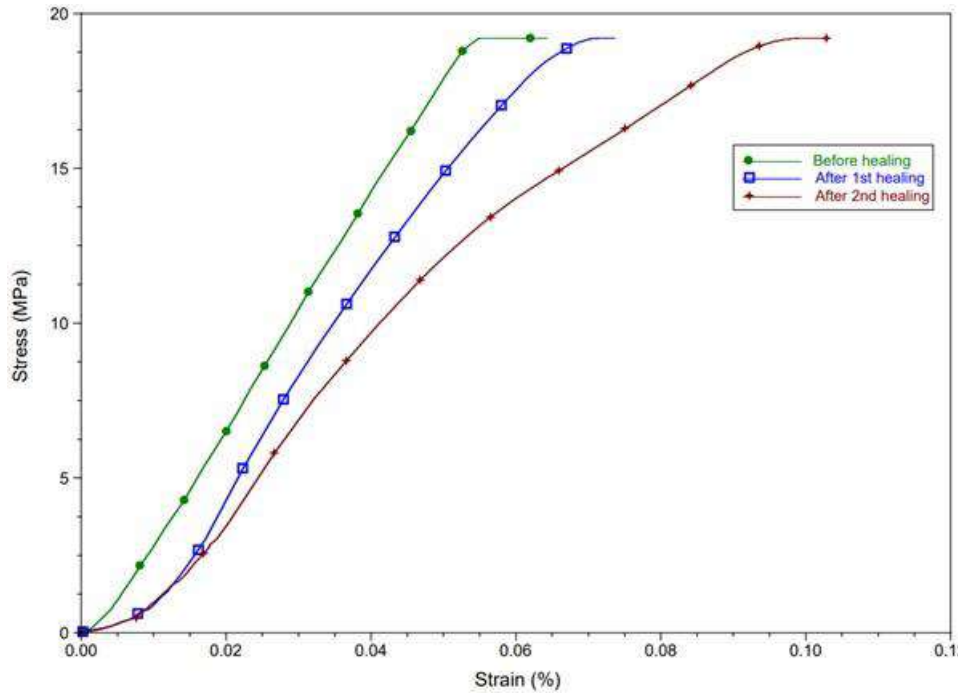


Fig. 4a: EP-pristine healing represented stress-strain curve.

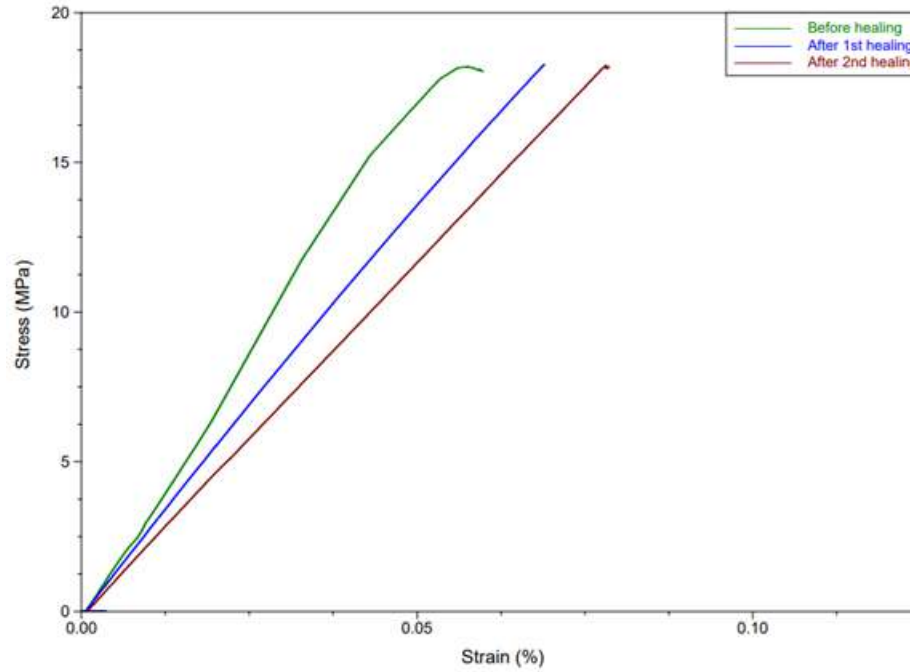


Fig. 4b: EP-1% healing represented stress-strain curve.

Table 3: Flexural modulus changes after healing.

| Sample EP-x% | Before healing [GPa] | After healing [GPa] | |
|---|---|---|---|
| | | 1st | 2nd |
| EP-pristine | 34.2 | 28.7 | 20.9 |
| EP-1 | 39.8 | 34.6 | 32.3 |

Center, UPES) for their active assistance while working with laboratory facilities.

## REFERENCES

Ahmed, M.J. and Hameed, B.H. 2020. Insight into the co-pyrolysis of different blended feedstocks to biochar for the adsorption of organic and inorganic pollutants: a review. J Clean. Prod., 265: 121762. https://doi.org/10.1016/J.JCLEPRO.2020.121762.

Altuna, F.I., Hoppe, C.E. and Williams, R.J.J. 2016. Shape memory epoxy vitrimers based on DGEBA crosslinked with dicarboxylic acids and their blends with citric acid. RSC Adv., 6(91): 88647-88655. https://doi.org/10.1039/C6RA18010H.

Beach, E.S., Weeks, B.R., Stern, R. and Anastas, P.T. 2013. Plastics additives and green chemistry. Pure Appl Chem., 85 (8): 1611-1624. https://doi.org/10.1351/PAC-CON-12-08-08.

Black, S.P., Jeremy, K., Sanders, M. and Artur, R.S. 2014. Disulfide exchange: exposing supramolecular reactivity through dynamic covalent chemistry. Chem. Soc. Rev., 43(6): 1861-1872. https://doi.org/10.1039/C3CS60326A.

Bortz, D.R., Heras, E.G. and Martin-Gullon, I. 2012. Impressive fatigue life and fracture toughness improvements in graphene oxide/epoxy composites. Macromolecules, 45: 238-245. https://doi.org/10.1021/ma201563k.

Brems, A., Jan, B. and Raf, D. 2012. Recycling and recovery of post-cet alonsumer plastic solid waste in a European context. Therm. Sci., 16(3): 669-685. https://doi.org/10.2298/TSCI120111121B.

Brown, E.N., Sottos, N.R. and White, S.R. 2002. Fracture testing of a self-healing polymer composite. Exp Mech. 42(4): 372-379. https://doi.org/10.1007/BF02412141.

Brown, E.N., White, S.R. and Sottos, N.R. 2004. Microcapsule-induced toughening in a self-healing polymer composite. J. Mater. Sci., 39(5): 1703-10. https://doi.org/10.1 023/B:JMSC.0000016173.73733.DC.

Brutman, J.P, Paula, A.D. and Marc, A.H. 2014. Polylactide vitrimers. ACS Macro Lett., 3(7): 607-610. https://doi.org/10.1021/mz500269w.

Burger, N., Laachachi, A., Ferriol, M., Lutz, M., Toniazzo, V. and Ruch, D. 2016. Review of thermal conductivity in composites: mechanisms, parameters, and theory. Prog. Polym. Sci., 61: 1-28. https://doi.org/10.1016/J.PROGPOLYMSCI.2016.05.001.

Duan, R., Qiu-Xia, H., Xue, D., De-Fu, L., Xiu-Li, W. and Yu-Zhong, W. 2015. Renewable sugar-based diols with different rigid structure: Comparable investigation on improving poly (butylene succinate) performance. ACS Sustain. Chem Eng., 4(1): 350-362. https://doi.org/10.1021/ACSSUSCHEMENG.5B01335.

Dyre, J.C. 2006. Colloquium: The glass transition and elastic models of glass-forming liquids. Rev. Mod. Phys., 78(3): 953-972 https://doi.org/10.1103/RevModPhys.78.953.

Ebnesajjad, S. and Arthur, H.L. 2015. Characteristics of Adhesive Materials. Adhesives Technology Handbook, January, 84-159. https://doi.org/10.1016/B978-0-323-35595-7.00005-X.

Fenouillot, F., Rousseau, J., Colomines, Saint-Loup and J. P. Pascault. 2010. Polymers from Renewable 1,4:3,6-Dianhydrohexitols (Isosorbide, Isomannide and Isoidide): A Review. Progress in Polymer Science (Oxford) 35 (5): 578-622. https://doi.org/10.1016/J.PROGPOLYMSCI.2009.10.001.

Florea, N.M., Lungu, A., Badica, L., Craciun, M., Enculescu, D.G., Ghita, C., Ionescu, R., Zgirian, G. and Iovu, H. 2015. Novel nanocomposites

based on epoxy resin/epoxy-functionalized polydimethylsiloxane reinforced with POSS. Compos. B. Eng., 75: 226-234. https://doi.org/10.1016/J.COMPOSITESB.2015.01.043.

Ghodke, P.K. 2021. High-quality hydrocarbon fuel production from municipal mixed plastic waste using a locally available low-cost catalyst. Fuel Commun., 8: 100022. https://doi.org/10.1016/J.JFUECO.2021.100022.

Grady, B.P. 2012. Effects of carbon nanotubes on polymer physics. J. Polym. Sci. B Polym. Phys., 50(9): 591-623. https://doi.org/10.1002/POLB.23052.

Guadagno, L., de Vivo, B., di Bartolomeo, A., Lamberti, P., Sorrentino, A. and Tucci, V. 2011. Effect of functionalization on the thermo-mechanical and electrical behavior of multi-wall carbon nanotube/epoxy composites. Carbon, 49(6): 1919–1930. https://doi.org/10.1016/J.CARBON.2011.01.017.

Guadagno, L., Vertuccio, L., Naddeo, C., Calabrese, E., Barra, G. and Raimondo, M. 2018. Development of aeronautical epoxy nanocomposites having an integrated self-healing ability. MATEC Web Conf., 233:300021. https://doi.org/10.1051/MATECCONF/201823300021.

Hummers, W.S. and Richard, E.O. 1958. Preparation of graphitic oxide. J. Am. Chem. Soc., 80(6): 1339-

Jousseaume, B., Laporte, C., Toupance,T. and Bernard, J.M. 2002. Efficient bismuth catalysts for transcarbamoylation. Tetrahedron Lett., 43(36): 6305-7. https://doi.org/10.1016/S0040-4039(02)01391-6.

Kang, S., Sung, H., Chul Rim, C., Min, P., Soonho, R. and Junkyung, K. 2001 Preparation and characterization of epoxy composites filled with functionalized nano silica particles obtained via sol–gel process. Polymer, 42(3): 879-887. https://doi.org/10.1016/S0032-3861(00)00392-X.

Kessler, M.R., Sottos, N.R. and White, S.R. 2003. Self-healing structural composite materials. Compos A Appl. Sci. Manuf., 34(8): 743-53. https://doi.org/10.1016/S1359-835X(03)00138-6.

Kessler, M.R. and White, S.R. 2002. Cure kinetics of the ring-opening metathesis polymerization of dicyclopentadiene. J. Polym. Sci. A Polym. Chem., 40(14): 2373-2383 https://doi.org/10.1002/pola.10317.

Krishnakumar, B., Debajyoti, B., Manjeet, S., Siva, R.S.V.P., Gurunadh, V.V.S.S., Shailey, S. and Vijay, P. 2021. Sugarcane bagasse-derived activated carbon- (ac-) epoxy vitrimer biocomposite: Thermomechanical and self-healing performance. Int. J. Polym. Sci., 65: 202-211. https://doi.org/10.1155/2021/5561755.

Krishnakumar, B., Siva, R.V.S.P., Wolfgang, H., Binder, C.P., Jiwon, J., Vijay, P., Sravendra, R. and Gun, Y.J. 2020. Catalyst-free self-healable Vitrimer/Graphene oxide nanocomposites. Compos B Eng., 184: 107647. https://doi.org/10.1016/j.compositesb.2019.107647.

Liu, T., Cheng, H., Shuai, Z., Xiaoning, Y., Liwei, W., Jiarui, H., Yuzhan, L., Junna, X. and Jinwen, Z. 2018. A self-healable high glass transition temperature bioepoxy material based on vitrimer chemistry. Macromolecules, 51(15): 5577-5585. https://doi.org/10.1021/ACS.MACROMOL.8B01010.

Luzuriaga, A.R., Roberto, M., Nerea, M., Alaitz, R., Germán, C., Javier, R. and Ibon, O. 2016a. Epoxy resin with exchangeable disulfide crosslinks to obtain reprocessable, repairable, and recyclable fiber-reinforced thermoset composites. Mater. Hori., 3(3): 241-47. https://doi.org/10.1039/C6MH00029K.

Luzuriaga, A.R., Jon. M.M., Fernando, R., Roberto, M., José, M.A., Germán, C. and Ibon, O. 2016b. Mechanochromism in epoxy vitrimer composites containing aromatic disulfide crosslinks. J. Mater. Chem. C., 4(26): 6220-23. https://doi.org/10.1039/C6TC02383E.

Martin, R., Rekondo, A., Ruiz, A., de Luzuriaga,m., Cabañero, H., Grande, J. and Ibon, O. 2014. The processability of a poly(urea-urethane) elastomer reversibly crosslinked with aromatic disulfide bridges. J. Mater. Chem. A, 2(16), 5710-5715. https://doi.org/10.10239/C3TA14927G.

Moorthy Rajendran, K., Venkateswarlu, C., Amit, S., Shashank, P., Jitendra, K.P. and Praveen, G. 2020. Review of catalyst materials in achieving the liquid hydrocarbon fuels from municipal mixed plastic waste (MMPW). Mater. Today Commun., 24: 100982. https://doi.org/10.1016/J.MTCOMM.2020.100982.

Murali, T.P., Prasad, S.V., Surappa, M.K., Rohatgi, P.K. and Gopinath, K. 1982. Friction and wear behaviour of aluminium alloy coconut shell char particulate composites. Wear, 80(2): 149-158. https://doi.org/10.1016/0043-1648(82)90214-9.

Nia, A.S., Sravendra, R., Diana, D., Xavier, N., Alice, B. and Wolfgang, H.B. 2014. Click chemistry promoted by graphene-supported copper nanomaterials. Chem Commun., 50(97): 15374-15377. https://doi.org/10.1039/C4CC07774A.

Ogden, W.A. and Guan, Z. 2018. Recyclable, strong, and highly malleable thermosets based on boroxine networks. J. Am. Chem. Soc., 140(20): 6217-6220. https://doi.org/10.1021/JACS.8B03257/SUPPL_FILE/JA8B03257_SI_001.PDF.

Olowojoba, G.B., Kopsidas, S., Eslava, S., Gutierrez, E.S., Kinloch, A.J. and Mattevi, C. 2017. A facile way to produce epoxy nanocomposites having excellent thermal conductivity with low contents of reduced graphene oxide. J Mater Sci., 52(12):7323-44. https://doi.org/10.1007/S10853-017-0969-X.

Taynton, P., Yu, K., Shoemaker, R.K., Jin, Y., Qi, H.J. and Zhang, W. 2014. Heat- or water-driven malleability in a highly recyclable covalent network polymer. Adv Mater., 26(23): 3938-3942. https://doi.org/10.1002/ADMA.201400317.

Park, C., Jung, J. and Yun, G.J. 2019. Thermomechanical properties of mineralized nitrogen-doped carbon nanotube/polymer nanocomposites by molecular dynamics simulations. Compos. B Eng., 161: 639-50. https://doi.org/10.1016/J.COMPOSITESB.2019.01.002.

Patrick, J.F., Maxwell, J.R., Nancy R.S., Jeffrey, S., Moore, S. and Scott, R.W. 2016. Polymers with autonomous life-cycle control. Nature, 540: 363-370. https://doi.org/10.1038/nature21002.

Peng, M., Tang, X. and Zhou, Y. 2016. Fast phase transfer of graphene oxide from water to triglycidyl para-aminophenol for epoxy composites with superior nanosheet dispersion. Polymer, 93: 1-8. https://doi.org/10.1016/J.POLYMER.2016.03.016.

Rana, S., Diana, D., Ali, S.N., Mahmood, N., Mario, B. and Wolfgang, H.B. 2016. 'Click'-triggered self-healing graphene nanocomposites. Macromol. Rapid Commun., 37(21): 1715-22. https://doi.org/10.1002/MARC.201600466.

Landel, R.F. and Nielsen, L.E. 1994. Mechanical Properties of Polymers and Composites, Second Edition. Marcel Dekker, Inc. https://www.routledge.com/Mechanical-Properties-of-Polymers-and-Composites/Landel-Nielsen/p/book/9780824789640.

Sun, Y., Zhuqing, Z., Kyoung, S.M. and Wong, C.P. 2004. Glass transition and relaxation behavior of epoxy nanocomposites. J. Polym. Sci. B Polym. Phys., 42(21): 3849-58. https://doi.org/10.1002/POLB.20251.

Tesoro, G. 1988. Epoxy resins-chemistry and technology. J. Polym. Sci. B Polym. Lett. Ed., 26(12): 509-539. https://doi.org/10.1002/POL.1988.140261212.

Verma, A., Amit, G. and Singh, V.K. 2017. Mechanical properties and microstructure of starch and sisal fiber biocomposite modified with epoxy resin. Mater. Perform. Char., 6(1): 500-520. https://doi.org/10.1520/MPC20170069.

Verma, A., Pratibha, N. and Vinay, K.S. 2019. Experimental analysis on carbon residuum transformed epoxy resin: Chicken feather fiber hybrid composite. Polym. Compos., 40(7): 2690-2699. https://doi.org/10.1002/PC.25067.

Verma, A., Pratibha, N. and Vinay, K.S. 2018. Experimental investigation of chicken feather fiber and crumb rubber reformed epoxy resin hybrid composite: Mechanical and microstructural characterization. J. Mech. Behav. Mater., 27 (3-4): 14-27. https://doi.org/10.1515/JMBM-2018-0014.

White, S.R., Moore, J.S., Sottos, N.R., Krull, B.P., Santa Cruz, W.A.

and Gergely, R.C.R. 2014. Restoration of large damage volumes in polymers. Science, 344(6184): 620-623. https://doi.org/10.1126/SCIENCE.1251135.

White, S.R., Sottos, N.R., Geubelle, P.H., Moore, J.S., Kessler, M.R., Sriram, S.R., Brown, E.N. and Viswanathan, S. 2001. Autonomic healing of polymer composites. Nature, 409(6822): 794-797. https://doi.org/10.1038/35057232.

Xu, J., Liu, J., Ling, P., Zhang, X., Xu, K. and He, L. 2020. Raman spectroscopy of biochar from the pyrolysis of three typical Chinese biomasses: A novel method for rapidly evaluating the biochar property. Energy, 202: 117644. https://doi.org/10.1016/J.ENERGY.2020.117644.

Yang, W.J., Jing, X.T., Tingting, Z., Lixing, W., En-Tang, K. and Lianhui, W. 2015. Antifouling and antibacterial hydrogel coatings with self-healing properties based on a dynamic disulfide exchange reaction. Polym. Chem., 6(39): 7027-7035. https://doi.org/10.1039/C5PY00936G.

Yang, X., Chaobo, L., Tengbo, M., Yongqiang, G., Jie, K., Junwei, G., Minjiao., C. and Jiahua, Z. 2018. A review on thermally conductive polymeric composites: classification, measurement, model and equations, mechanism and fabrication methods. Adv. Compos. Hybrid. Mater., 21(2): 207-230. https://doi.org/10.1007/S42114-018-0031-8.

Yassin, K. and Hojjati, M. 2017. Processing of thermoplastic matrix composites through automated fiber placement and tape laying methods: a review. J. Thermoplast. Comp. Mater., 31(12): 1676-1725. https://doi.org/10.1177/0892705717738305

Zako, M. and Takano,N. 2016. Intelligent material systems using epoxy particles to repair microcracks and delamination damage in GFRP. J. Intell. Mater. Syst. Struct., 10(10): 836-41. https://doi.org/10.1106/YEIH-QUDH-FC7W-4QFM.

Zhang, S., Tuan, L., Cheng, H., Liwei, W., Jiarui, H., Hang, L. and Jinwen, Z. 2018. Preparation of a lignin-based vitrimer material and its potential use for recoverable adhesives. Green Chem., 20(13): 2995-3000. https://doi.org/10.1039/C8GC01299G.

Nature Environment and Pollution Technology
An International Quarterly Scientific Journal

p-ISSN: 0972-6268
(Print copies up to 2016)
e-ISSN: 2395-3454

Vol. 22 | No. 1 | pp. 411-416 | 2023

Original Research Paper

https://doi.org/10.46488/NEPT.2023.v22i01.039

Open Access Journal

# Identification and Characterization of Aluminium Tolerant Bacteria Isolated from Soil Contaminated by Electroplating and Automobile Waste

**H. Bisht* and N. Kumar*†**

*Department of Biotechnology and Bioinformatics, NIIT University, Neemrana-301705, Rajasthan, India

†Corresponding author: N. Kumar; narayan.kumar@niituniversity.in

**Nat. Env. & Poll. Tech.**
**Website: www.neptjournal.com**

*Received:* 01-07-2022
*Revised:* 22-08-2022
*Accepted:* 05-09-2022

**Key Words:**
Bioremediation
*Cedecea davisae*
Metal tolerance
Aluminum toxicity
Antibiotic resistance

## ABSTRACT

Due to anthropogenic activities and the advancement of industries, metal contamination is growing globally. Aluminum toxicity is seriously endangering plants, animals, and humans by rapidly rising in soil and water. Even though some fungi can tolerate aluminum, researchers are interested in finding bacteria that are resistant to aluminum. The current state of knowledge on bacteria resistant to aluminum is extremely limited. In the present study, bacterial isolates from soil near a metal electroplating and automobile industry in Punjab, India, were isolated and then screened for high aluminum metal tolerance. The aluminum tolerant bacterial isolate was identified as *Cedecea davisae* M1, a member of the *Enterobacteriaceae* family, using morphological, biochemical, and 16srRNA gene sequence analyses. The spectroscopic results indicate that the strain may tolerate up to 150 ppm of aluminum. Antibiotic resistance of *Cedecea davisae* M1 was determined using disks on Luria agar plates, and the bacteria were found to be resistant to vancomycin, ampicillin, carbenicillin, and rifampicin. The findings of the study indicated that the strain might be able to remove aluminum toxicity from the environment, which needs to be further explored.

## INTRODUCTION

Over the last few decades, the population, industrialization, urbanization, and agricultural practices have all increased considerably. These industries' waste products and toxic effluents are dumped into the environment without being treated (Ashraf et al. 2019). As a result, contamination of the air, land, and water is increasing day by day around the planet. It is a real global matter of concern, as it is hazardous to plants, animals, and humans. Because inorganic pollutants such as metals, salts, and minerals cannot be destroyed like other pollutants, they are considered the most hazardous. They tend to accumulate along the food chain and try to ruin our ecosystem (Kobya et al. 2005). Aluminium metal (Al) is one of the hazardous inorganic contaminants and is identified as the third most abundant metal in the earth's crust. Due to the disposal of Al trash by construction activities, the aerospace and automobile sector, electroplating, solid rocket fuels, pharmaceuticals and cosmetics, and other packaging industries, Al toxicity in soil and water is increasing rapidly (Igbokwe et al. 2019). Excessive Al is particularly neurotoxic in animals and has been linked to a variety of bone deformities and neurodegenerative diseases in humans (Bondy 2014). Acidification of soil due to Al affects plants by limiting root growth and cell division, thus reducing cation uptake, such as $Ca^{2+}$, and decreasing stomatal opening and photosynthetic efficiency, lowering plant growth and yield (Panda et al. 2009).

To detoxify or recycle Al waste, many physiochemical procedures, such as adsorption, absorption, and chemical precipitation are used, but these methods are quite expensive and can produce even more harmful contaminants (Dada et al. 2015). As compared to traditional approaches, bioremediation is the most promising strategy for detoxifying or recycling the Al waste present in soil and water these days since it is environmentally safe, cheaper, lower maintenance, faster, and produces fewer toxic by-products (Jan et al. 2014, Purwanti et al. 2017). Microorganisms are considered the most suited and effective bioremediation agents for reducing Al toxicity and studying Al tolerance mechanisms (Haytham 2016). *Pseudomonas aeruginosa*, *Brochothrix thermosphacta*, and *Vibrio alginolyticus* have been reported to be resistant to Al exposure in acidic conditions (Kurniawan et al. 2018). Ji et al. (2016) isolated four strains of bacteria: *Chryseobacterium* sp. B1, *Brevundimonas diminuta* B3, *Hydrogenophaga* sp. B4, and *Bacillus cereus* B5 from activated sludge, which were capable of tolerating up to 20 mM concentration of Al. In another study, dead biomass of *Aspergillus oryzae* was isolated from waste sites of Al mills and biosorption of Al ions at low concentrations of 10-50 $mg.L^{-1}$ was observed (Omeike et al. 2013). Several

ectomycorrhizal fungi, including *Pisolithus tinctorius* and *Lactarius deliciosus*, emerged as promising candidate species for high Al tolerance and for understanding the role of Al immobilization and accumulation (Gu et al. 2021).

Most studies focus on the isolation and identification of Al-tolerant fungi. To our knowledge, just a few studies on Al-tolerant bacteria have been conducted. The purpose of this research is to identify Al metal-tolerant bacteria from the metal-contaminated sites to reduce Al toxicity in the environment. Our in-vitro research found a bacterial strain from soil samples that showed high metal tolerance when exposed to Al and exhibited multiple antibiotic resistance.

## MATERIALS AND METHODS

### Sample Collection

The soil sample was collected from a metal-contaminated waste disposal location near an electroplating and automobile workshop in Patiala, Punjab. Sampling was done and transferred to sterilized polyethylene bags, which were then stored at 4°C before analysis and evaluation.

### Isolation and Screening of Al-Resistant Bacteria

The soil sample was serially diluted and plated on Luria-Agar (LA) medium supplemented with a particular concentration of Al. Incubation was done at 37°C for 24-48 hrs. Aluminium chloride ($AlCl_3$) was used as a metal stock solution. Colonies were picked and streaked on another LA plate enriched with a predetermined dose of Al. To allow for comparison, control plates were made using LA medium without Al metal. Plate streaking was repeated until morphologically separate colonies were seen, resulting in the isolation of pure cultures. A bacterial isolate was chosen and stored at -80°C for future analysis.

### Identification of Bacterial Isolate: Morphological and Biochemical Tests

Various morphological and biochemical tests, such as oxidase, catalase, urease, indole, starch hydrolysis, gelatin hydrolysis, citrate utilization, and Gram staining were carried out to identify the bacterial isolate, according to Bergey's Manual of Determinative Bacteriology (Krieg & Holt 1984).

### Identification of Bacterial Isolate: 16srRNA Gene Amplification and Sequencing

The modified Rapid One-Step Extraction method (ROSE) was used to isolate genomic DNA (Steiner et al. 1995). The extracted DNA was PCR amplified using universal primers (8F: 5' AGA GTT TGA TCC TGG CTC AG 3' and 1492R: 5' CGG TTA CCT TGT TAC GAC TT 3') in a gene AMP PCR system (Applied Biosystems, California, USA) (Xiang et al. 2005). For 16srRNA gene amplification, the PCR conditions were as follows: 5 minutes at 95°C for pre-denaturation, 1 minute at 95°C for denaturation, 1 minute at 56°C for annealing, 1 minute at 72°C for extension, and 5 minutes at 72°C for the final extension. The cycle was repeated 30 times from denaturation to extension. The purified PCR product was sequenced by Amnion Biosciences, Bangalore, India. The resultant sequence was corrected with Seq-Man V 4.1 software (Swindell & Plasterer 1997) before being compared to existing sequences in the GenBank database. The 16srRNA gene sequence was compared using NCBI-BLASTN (Altschul et al. 1990). We retrieved highly comparable sequences from the NCBI GenBank database (www.ncbi.nlm.nih.gov.) and compared them using multiple sequence alignment. The sequencing result of the 16s rRNA gene of a bacterial isolate was submitted to the GenBank database (KF146959).

### Maximum Tolerance Concentration of Al-Resistant Bacteria

The maximum tolerance concentration (MTC) of the Al-resistant bacterial isolate was determined as follows: The bacteria were inoculated in LB medium with varying concentrations of filter-sterilized Al (50 ppm, 75 ppm, 100 ppm, 150 ppm, and 200 ppm), and incubated at 37°C with agitation (150 rpm). As a control, the same bacterial isolate was cultured in the LB medium without Al. The OD600 of bacterial culture was determined using a UV VIS Spectrophotometer (HITACHI U-2900) at every 12 hr interval (0 hr, 12 hrs, 24 hrs, 48 hrs, and 72 hrs).

### Antibiotic Resistance

The bacterial isolate was tested for antibiotic susceptibility against eight different antibiotics using the disk diffusion method (Bauer et al. 1966). Antibiotic disks used in this study were Streptomycin (10 mcg), Vancomycin (30 mcg), Tetracycline (30 mcg), Kanamycin (30 mcg), Ampicillin (10 mcg), Carbenicillin (100 mcg), Rifampicin (5 mcg), and Chloramphenicol (30 mcg). With the help of a sterile swab, 100 µL of overnight-grown culture was taken and spread evenly on LA plates. Disks of different antibiotics were placed on the plate and incubated at 37$^{o}$C for 24 hrs. The results were depicted according to the guidelines of the Clinical Laboratory Standard Institute (CLSI 2018). Based on the zone of inhibition, the isolated strain was classified as resistant, intermediate, or sensitive with respect to the specific antibiotic. The diameter of the zone of inhibition was measured with the help of a ruler in millimeters.

### Statistical Analysis

All the experiments were done in triplicates with the selected isolate against different concentrations of Al. The mean and standard deviation were calculated in Microsoft Excel software, version 2010.

## RESULTS AND DISCUSSION

### Identification of an Al-Tolerant Bacterial Isolate Based on Morphological, Biochemical, and Molecular Analyses

Nowadays, Al toxicity in soil and water is a major concern. It is one of the hazardous metals that has been identified as having harmful effects on plants, animals, and human health (Kochian 1995). In this study, an Al-tolerant bacterial strain was isolated after screening from metal-contaminated soil and was named M1. Identification of isolate M1 was done at genus and species level by morphological, biochemical, and 16srRNA gene sequence analyses. It was milky white in appearance, rod-shaped, motile, and Gram-negative. It showed a positive reaction to catalase while a negative reaction to oxidase, indole, and urease. It was also found that the isolate was capable of fermenting citrate. Isolate M1 was checked for starch and gelatin hydrolysis tests and found a positive reaction for starch hydrolysis rather than gelatin. It produced convex colonies when grown on a medium at 37°C. Based on the morphological and biochemical analyses, it was determined that the isolate belongs to the *Enterobacteriaceae* family as given in Table 1. Similar results of morphological and biochemical tests, such as Gram negative, rod shaped, positive citrate utilization test, and negative oxidase, urease, and indole tests for the Enterobacteriaceae family, were also observed by some researchers (Bhagat et al. 2016, Singh et al. 2018). The negative oxidase test is a key test to differentiate families of Enterobacteriaceae from Pseudomonadaceae and Pasteurellaceae. In addition to the conventional phenotypic and biochemical methods, PCR amplification of the 16srRNA gene (Fig. 1) and its sequencing is an important method for the identification of bacteria at the species level. The unknown Al-tolerant bacterial isolate M1 was identified as *Cedecea davisae* (*C. davisae*) with the highest 99.46% homology based on 16srRNA gene sequencing and BLAST homology search. The identified isolate M1 was designated as *C. davisae* strain M1. The 16srRNA gene sequence of *C. davisae* strain M1 has been deposited in the GenBank with accession number KF146959.1 (Table 2).

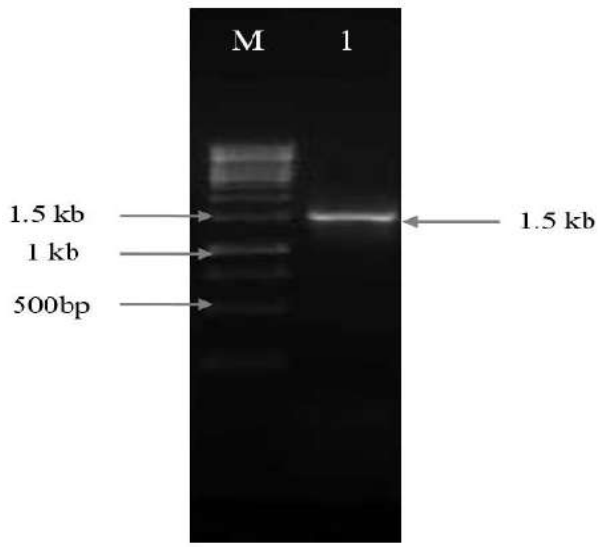


M: 1kb DNA ladder SM0312 (Thermo scientific); 1: Amplified product

Fig. 1: PCR amplification of 16srRNA gene of bacterial isolate M1.

Table 1: Morphological and biochemical characterization of Al tolerant bacterial isolate M1.

| Characteristics | Bacterial Isolate M1 |
|---|---|
| Color | Milky white |
| Shape | Rods, Convex colonies |
| Motility | Motile |
| Gram Staining | - |
| Catalase test | + |
| Indole test | - |
| Citrate utilization test | + |
| Gelatin hydrolysis test | - |
| Oxidase test | - |
| Starch hydrolysis test | + |
| Urease test | - |

+: Positive; -: Negative

Table 2: Sequence similarity analysis of the isolate M1 based on BLASTn comparison to the GenBank database.

| Isolate | BLAST identification with accession no. | Similarity | Submitted in Genbank with accession no. |
|---|---|---|---|
| M1 | *Cedecea davisae* isolate ABRL062 (MZ597848.1) | 99.46% | *Cedecea davisae* M1 (KF146959.1) |

### Maximum Tolerance Concentration Analysis

*C. davisae* M1 was examined for its maximum tolerance concentration for Al at various concentrations and time periods with the help of a UV-VIS spectrophotometer (Fig. 2). There was no research done on bacteria- *C. davisae* for Al tolerance. In our study, *C. davisae* M1 has grown in the culture media supplemented with different doses of Al (50 ppm, 75 ppm, 100 ppm, 150 ppm, and 200 ppm). We

Table 3: Antibiotic resistance profile of *C. davisae* M1.

| Antibiotics | Zone of Inhibition (mm) | Classified as | Interpretative criteria for *Enterobacteriaceae* according to CLSI Standard | | |
|---|---|---|---|---|---|
| | | | Sensitive (mm or more) | Intermediate (mm) | Resistance (mm or less) |
| Tetracycline (30 mcg) | 17 | S | 15 | 12-14 | 11 |
| Streptomycin (10 mcg) | 14 | I | 15 | 12-14 | 11 |
| Vancomycin (30 mcg) | NI | R | 17 | 15-14 | 13 |
| Kanamycin (30 mcg) | 14 | I | 18 | 14-17 | 13 |
| Ampicillin (10 mcg) | NI | R | 17 | 14-16 | 13 |
| Carbenicillin (100 mcg) | NI | R | | | |
| Rifampicin (5 mcg) | NI | R | | | |
| Chloramphenicol (30mcg) | 18 | S | 18 | 13-17 | 12 |

Diameter of disks: 6mm; NI: No inhibition; S: Sensitive; I: Intermediate; R: Resistant; mm: millimetres; mcg: microgram; CLSI: Clinical Laboratory Standard Institute; Zone of inhibition: diameter of the zone along with the disk.

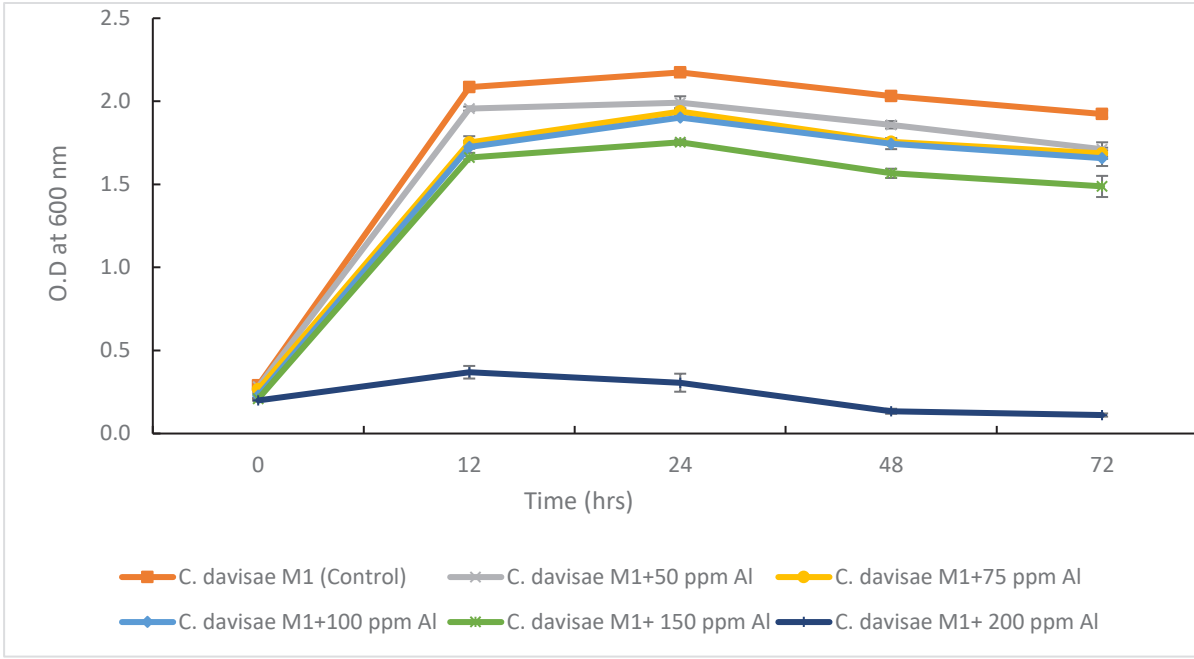


Fig. 2: The growth curve of *C. davisae* M1 in various concentrations of Al monitored for 72 hrs. The graph represents mean results from the value of triplicate cultures with error bars indicating standard deviations (n = 3). The growth was observed at up to 200 ppm Al supplemented in the culture medium.

noticed that the bacterial strain *C. davisae* M1 showed higher Al tolerance, up to 150 ppm for a period of 24 hrs. Metal ion accumulation inside the cell, metal extrusion, metal ion adsorption on the cell surface, membrane or cell wall binding, extracellular or intracellular chelation, producing extracellular compounds, or conversion into a less toxic state could all be the possible factors in the strain's tolerance to high Al concentrations (Piña & Cervantes 1996). Appanna et al. (1994) reported one of the mechanisms for metal tolerance, where an Al-tolerant strain of *Pseudomonas fluorescens* was able to accumulate and detoxify Al by producing an extracellular lipid compound that was rich in phosphorus. However, when we exposed Al to higher concentrations of 200 ppm (higher than MTC), it induced bacterial cell ruptures, resulting in a significant decrease in its biosorption capabilities (Titah et al. 2019). A higher concentration of Al also decreases the growth rate of bacteria by altering or inhibiting some enzymatic reactions (Kurniawan et al. 2018).

## Antibiotic Resistance Analysis

The *C. davisae* M1 bacteria was tested against eight

different antibiotics using the Disk-diffusion method. The bacteria were found to be highly resistant to vancomycin, ampicillin, carbenicillin, and rifampicin while being moderately resistant to kanamycin and streptomycin. However, it also showed high susceptibility to tetracycline and chloramphenicol (Table 3). There have been few reports on antibiotic resistance by *C. davisae* strains, which were published before. In a report by Kanakadandi et al. (2019), *C. davisae* has shown resistance to a variety of antibiotics. The antibiotic resistance profile of *Cedecea* sp. was also published by Grimont et al. (1981). The multidrug resistance of *C. davisae* is caused by a combination of AmpC synthesis and porin deficiency in the cell wall (Ammenouche et al. 2014). Thompson & Sharkady (2020) reported that strains of *C. neteri* harbor multiple chromosomes encoded β-lactamase genes, which help in antibiotic resistance. Some resistance nodulation-cell division (RND) multidrug efflux pumps were also identified, such as AcrB, AcrD, OqxB, and MdtBC.

Previous research has also revealed that different microorganisms have distinct metal tolerance capabilities and antibiotic resistance profiles. Metal tolerance and antibiotic resistance both have been observed in *C. davisae* in a few cases. *C. davisae* GCC 19S1 was isolated and found to be cadmium, copper, lead, iron, and zinc resistant and also showed resistance to a variety of antibiotics (Nath et al. 2020). Four bacterial isolates were isolated in Behrampur. Among these, isolate 3 showed the highest tolerance of 100 ppm to $Al_2O_3$. It also showed resistance to the antibiotic Cloxacillin and was most sensitive to gentamicin (Mohapatra et al. 2018). Therefore, we might conclude that there may be some relationship between Al tolerance and antibiotic resistance that has yet to be discovered and explored.

## CONCLUSION

The present study reported the isolation and identification of the Al- tolerant bacterial strain *C. davisae* M1 based on morphological, biochemical, and 16srRNA gene sequence analyses. It showed tolerance to Al at a concentration of up to 150 ppm. However, with a higher concentration of Al (200 ppm), the growth of bacteria was suddenly inhibited. The bacterial strain also exhibited resistance to many antibiotics, such as vancomycin, carbenicillin, rifampicin, and ampicillin, and moderate resistance to kanamycin and streptomycin. It was also susceptible to tetracycline and chloramphenicol. Different microbes show distinct metal tolerance capacities, antibiotic resistance, and metal resistance systems. Most research has focused on the bioremediation of Al by plants and fungi from contaminated soil and water, whereas limited research has been done on the removal of Al by bacteria, resulting in less study on the bacterial resistance system for Al. In future studies, *C. davisae* M1 could be exploited as a bioremediation agent to remove Al and other toxic metals from metal-contaminated soil and wastewater. In addition, it could also seem to be a good candidate for exploring bacterial resistance systems for Al.

## ACKNOWLEDGEMENT

The authors are thankful to the Department of Biotechnology and Bioinformatics, NIIT University, Neemrana, Rajasthan for the encouragement of research activity and for providing necessary laboratory facilities. Sincere thanks to Prof. Sunil Khanna also, who guided and helped in this research work.

## REFERENCES

Altschul, S.F., Gish, W., Miller, W., Myers, E.W. and Lipman, D.J. 1990. Basic local alignment search tool. J. Mol. Biol., 215(3): 403-410.

Ammenouche, N., Dupont, H. and Mammeri, H. 2014. Characterization of a novel AmpC -lactamase produced by a carbapenem-resistant *Cedecea davisae* clinical isolate. Antimicrob. Agents Chemother., 58(11): 6942-6945.

Appanna, V.D., Kepes, M. and Rochon, P. 1994. Aluminum tolerance in *Pseudomonas fluorescens* ATCC 13525: Involvement of a gelatinous lipid-rich residue. FEMS Microbiol. Lett., 119(3): 295-301.

Ashraf, S., Ali, Q., Zahir, Z.A., Ashraf, S. and Asghar, H.N. 2019. Phytoremediation: Environmentally sustainable way for reclamation of heavy metal polluted soils. Ecotoxicol. Environ. Saf., 174: 714-727.

Bauer, A.W., Kirby, W.M., Sherris, J.C. and Turck, M. 1966. Antibiotic susceptibility testing by a standardized single disk method. Am. J. Clin. Pathol., 45(4): 493-496.

Bhagat, N., Vermani, M. and Bajwa, H.S. 2016. Characterization of heavy metal (cadmium and nickel) tolerant gram-negative enteric bacteria from polluted Yamuna River, Delhi. Afr. J. Microbiol. Res., 10(5): 127-137.

Bondy, S.C. 2014. Prolonged exposure to low levels of aluminum leads to changes associated with brain aging and neurodegeneration. Toxicology, 315: 1-7.

CLSI 2018. Performance Standards for Antimicrobial Disk Susceptibility Tests, M100S, 28th Ed.

Dada, E.O., Njoku, K.I., Osuntoki, A.A. and Akinola, M.O. 2015. A review of current techniques of physico-chemical and biological remediation of heavy metals polluted soil. Ethiop. J. Environ. Stud. Manag., 8(5): 606-615.

Grimont, P.A., Grimont, F., Farmer III, J.J. and Asbury, M.A. 1981. *Cedecea davisae* gen. nov., sp. nov. and *Cedecea lapagei* sp. nov., new *Enterobacteriaceae* from clinical specimens. Int. J. Syst. Evol. Microbiol., 31(3): 317-326.

Gu, X., Jiang, Y., Wang, X., Jia, H., Li, J., Cui, Y. and He, X. 2021. Differences in aluminum tolerance and immobilization between two indigenous ectomycorrhizal fungi *Lactarius deliciosus* and *Pisolithus tinctorius* from Southwest China's forest stands. Ecotoxicol. Environ. Saf., 213: 112042.

Haytham, I.M.M. 2016. Biodegradation of used engine oil by novel strains of *Orchrobactrum anthropic* HM-1 and *Citrobacter freundii* HM-2 isolated from oil-contaminated soil. J. Biotech., 3(226): 1-13.

Igbokwe, I.O., Igwenagu, E. and Igbokwe, N.A. 2019. Aluminium toxicosis: a review of toxic actions and effects. Interdiscip. Toxicol., 12(2): 45-70.

Jan, A.T., Azam, M., Arif, A. and Haq, Q. 2014. Prospects for exploiting bacteria for bioremediation of metal pollution. Critic. Rev. Environ. Sci. Technol., 44: 519-560.

Ji, B., Chen, W., Zhu, L. and Yang, K. 2016. Isolation of aluminum-tolerant bacteria capable of nitrogen removal in activated sludge. Mar. Pollut. Bull., 106(1-2): 31-34.

Kanakadandi, V.S., Sarao, M.S. and Cunningham, J.M. 2019. A rare case of *Cedecea Davisae* bacteremia presenting as biliary sepsis. Cureus, 11(8): e5298.

Kobya, M., Demirbas, E., Senturk, E. and Ince, M. 2005. Adsorption of heavy metal ions from aqueous solutions by activated carbon prepared from apricot stone. Bioresour. Technol., 96(13): 1518-1521.

Kochian, L.V. 1995. Cellular mechanisms of aluminum toxicity and resistance in plants. Annu. Rev. Plant Biol., 46(1): 237-260.

Krieg, N.R. and Holt, J.G. (eds.) 1984. Bergey's Manual of Systematic Bacteriology. Williams & Wilkins Co., Baltimore, pp. 161-172.

Kurniawan, S.B., Purwanti, I.F. and Titah, H.S. 2018. The effect of pH and aluminium to bacteria isolated from aluminium recycling industry. J. Ecol. Eng., 19(3): 154-161.

Mohapatra, D., Mohapatro, M., Sabat, G., Padhy, R., Nayak, S.P. and Mohanty, B.K. 2018. Heavy metal ($Al_2O_3$) tolerance of soil bacteria isolated from plant rhizosphere region of *Vigna mungo* l. Res. J. Life Sci. Bioinform. Pharm. Chem. Sci., 4(4): 374-382.

Nath, S., Sinha, A., Singha, Y.S., Dey, A., Bhattacharjee, N. and Deb, B. 2020. Prevalence of antibiotic-resistant, toxic metal-tolerant and biofilm-forming bacteria in hospital surroundings. Environ. Anal. Health Toxicol., 35(3): e2020018.

Omeike, S.O., Kareem, S.O., Adewuyi, S. and Balogun, S.A. 2013. Biosorption of aluminium from solution by dead *Aspergillus oryzae* biomass isolated from aluminium mills waste site. Ife J. Sci., 15(1): 119-124.

Panda, S.K., Baluška, F. and Matsumoto, H. 2009. Aluminum stress signaling in plants. Plant Signal. Behav., 4(7): 592-597.

Piña, R.G. and Cervantes, C. 1996. Microbial interactions with aluminium. Biometals, 9(3): 311-316.

Purwanti, I.F., Kurniawan, S.B., Tangahu, B.V. and Rahayu, N.M. 2017. Bioremediation of trivalent chromium in soil using bacteria. Int. J. Appl. Eng. Res., 12(20): 9346-9350.

Singh, R.P., Mishra, S., Jha, P., Raghuvanshi, S. and Jha, P.N. 2018. Effect of inoculation of zinc-resistant bacterium *Enterobacter ludwigii* CDP-14 on growth, biochemical parameters and zinc uptake in wheat (*Triticum aestivum* L.) plant. Ecol. Eng., 116: 163-173.

Steiner, J.J., Poklemba, C.J., Fjellstrom, R.G. and Elliott, L.F. 1995. A rapid one-tube genomic DNA extraction process for PCR and RAPD analyses. Nucleic Acids Res., 23(13): 2569.

Swindell, S.R., Plasterer, T.N. 1997. SEQMAN: Contig assembly. In: Swindell, S.R. (eds.) Sequence Data Analysis Guidebook. Methods in Molecular Medicine, Springer, Totowa, NJ.

Thompson, D.K. and Sharkady, S.M. 2020. Expanding spectrum of opportunistic Cedecea infections: Current clinical status and multidrug resistance. Int. J. Infect. Dis., 100: 461-469.

Titah, H.S., Purwanti, I.F., Tangahu, B.V., Kurniawan, S.B., Imron, M.F., Abdullah, S.R.S. and Ismail, N.I. 2019. Kinetics of aluminium removal by locally isolated *Brochothrix thermosphacta* and *Vibrio alginolyticus*. J. Environ. Manage., 238: 94-200.

Xiang, S., Yao, T., An, L., Xu, B. and Wang, J. 2005. 16S rRNA sequences and differences in bacteria isolated from the Muztag Ata glacier at increasing depths. Appl. Environ. Microbiol., 71(8): 4619-4627.

Nature Environment and Pollution Technology
An International Quarterly Scientific Journal

p-ISSN: 0972-6268
(Print copies up to 2016)
e-ISSN: 2395-3454

Vol. 22 | No. 1 | pp. 417-426 | 2023

Original Research Paper

https://doi.org/10.46488/NEPT.2023.v22i01.040

Open Access Journal

# Influence of Different Particle Sizes of Sediments on the Lower Reaches of the Basin and its Significance in the Liao River Governance

**Chen Yang†**
College of Water Conservancy, Shenyang Agriculture University, Shenyang 110161, China
†Corresponding author: Chen Yang; 20209087@qq.com

**Nat. Env. & Poll. Tech.**
**Website: www.neptjournal.com**

*Received:* 19-05-2022
*Revised:* 30-06-2022
*Accepted:* 01-07-2022

**Key Words:**
Channel deposit
Sediment size
Sediment storage
Geomorphology
Liao river

## ABSTRACT

Based on the sand volume and sedimentation volume data for different particle size (PS) groups, the relationship between the annual scouring and silting amount of the Juliu River-Liujianfang section and the yearly sediment volume entering the downstream river channel was established. The critical values of sediment storage and release for the downstream river channel were obtained. It was found to decrease with an increase in the sediment particle size. The correlation coefficient between the annual scouring and silting amount of the Juliu River-Liujianfang section and the annual sediment volume entering the downstream river channel increased with the coarsening of sediment PS. It indicated that the sediment size was proportional to the sediment amount (SA) entering the river channel. As the sediment size increased, the deposition amount increased due to the variation of unit sediment amount. Based on the treatment and achievement of source areas with sediment sizes larger than 0.05 mm, it is significant to concentrate on treatment areas with sediment sizes larger than 0.10 mm.

## INTRODUCTION

The PS characteristics of sediment transport and its impact on river sedimentation are important theoretical issues. Many studies have been carried out that have played an important role in solving the siltation in the lower reaches of rivers (Schumm 1977, Walling & Kane 1984, Walling & Moorehead 1987). The sediment deposition in the lower reaches of rivers depends on the SA from the midstream and the granular composition of the sediments. Based on data statistics, Qian obtained the discharge ratio of sediments with different particle sizes. Moreover, the sedimentation laws of the Yellow River were proposed for sediments of sizes greater than 0.10 mm, 0.05-0.10 mm, 0.025-0.05 mm, and less than 0.025 mm (Ning 1980). Xu suggested that 0.455t of sediment was deposited in the lower reaches of the Yellow River for each ton of sediment from the coarse sediment areas (Xu 2008, 2007). It was also found that the sedimentation amount in the lower reaches of the Yellow River was 0.154t, almost three times as large as the delicate sediment areas. By restricting the coarse and fine discharge through Xiaolangdi Reservoir and reducing the coarse sediment into the lower reaches of the Yellow River, the siltation in the lower reaches of the Yellow River was reduced.

Similarly, it is important to solve the sediment siltation in the lower reaches of the Liao River. Our research is aimed at studying the erosion and siltation behavior of sediments of different sizes in the lower reaches of the Liao River.

### An Overview of the Research Area

The area of study is the lower reaches of the Liao River. It begins from the Juliu River and ends at Liujianfang, with a length of 119.8 km. The middle and lower reaches of the Liao River were originally flooded by the river and accumulated over a long time. Therefore, the terrain is flat, and the river channel ratio ranges from 0.14 to 0.3‰. According to the multi-year average, before the construction of Shifo Reservoir, the sediment into the downstream channel was $1316\times10^4$t per year, with only $987\times10^4$t sediment entering the sea and $329\times10^4$t sediment accumulating on the riverbed. The main siltation site is Liukou delta, below Xinmin Station, which rises at a rate of 4~8cm per year and becomes a suspended river. With regard to the entire downstream river channel, there is no tributary recirculation. Only the Liu River in the upper part of the Liao River enters. The water and sediment in the interval have little influence on the sedimentation process. Therefore, the river channel in the lower reaches of the Liao River provides an ideal place for studying the response process of the river channel deposition to input water and sediment (Fig. 1).

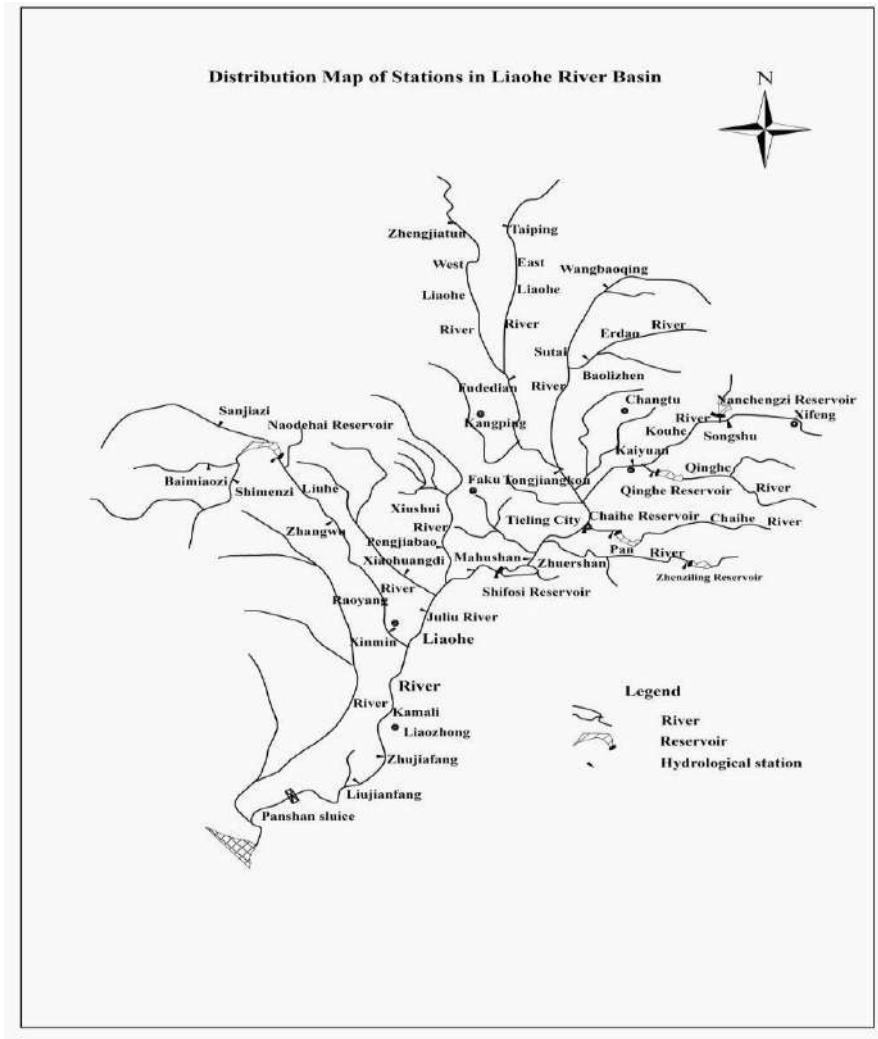


Fig. 1: The map depicting the river network and the hydrometric stations for the middle and lower reaches of the Liao River.

## MATERIALS AND METHODS

### Source of Data

The Juliu River station is the water and sediment inlet control station for the mainstream in the lower reaches of the Liaohe River. Liujianfang is the entering sea control station, and the section tributary is the Liu River. The amount of water and sediment in the sink is represented by Xinmin Station. According to the principle of sediment balance (Xu 2007, Hao et al. 2015), the amount of sedimentation-siltation in the lower reaches of the Liao River is obtained by the following equations:

$Dep$ = Input sediment amount – output sediment amount

$$= Q_{s,j} + Q_{s,x} - Q_{s,l}, \quad \ldots(1)$$

Where $Q_{s,j}$ the sediment amount is in JuLiuRiver station, Xinmin station, and Liujianfang station, respectively. The total amount of sediment scouring and silting with different particle sizes can be calculated by the input sediment amount (ISA) and output sediment amount with different PSs, namely:

$$Dep_i = \text{Input sediment amount of particle size i} - \text{Output sediment amount of particle size i} \quad \ldots(2)$$

$$= Q_{s,j,i} + Q_{s,x,i} - Q_{s,l,i}$$

Where $Q_{s,j,i}$, $Q_{s,x,i}$, $Q_{s,l,i}$ are the SA of PS $i$ for JuLiu River station, Xinmin station, and Liujianfang station, respectively. As the hydrological stations are in the lower reaches of Liao River, the PS of suspended sediment can be divided into the following six levels: (1) <0.007mm (2) 0.007mm~0.01mm; (3) 0.01mm~0.025mm; (4) 0.025mm~0.05mm (5) 0.05mm~0.10mm; (6)>0.10mm. Moreover, $i$ represents any one of these grades.

The hydrological, sediment and sediment PS data used in this paper were all obtained from the above hydrological stations. Sediment particle size data collection was limited to the year 2005 as the Shifo Reservoir was built in the middle reaches of the Liao River after that. It is also important to note that, for the downstream river sections, the construction of rubber dams and other water conservancy projects have greatly affected the natural process of river sediment transport. Therefore, the data period of this paper is from 1988 to 2005.

### Research Methodology

This paper uses statistical methods to study the effect of sediment PS on sediment deposition in the lower reaches of the Liao River. The sedimentation for the five particle sizes below JuliuRiver-Liujianfang is calculated by using the sediment-receiving amount and the suspended sediment PS data of each station: (1)>0.007mm; (2)>0.01mm; 3)>0.025mm; (4)>0.05mm; (5)>0.10mm. There were 6 groups of data obtained by adding the annual silt amount. The ISAs of the above six groups were obtained according to the PS group, i.e., the sum of SAs for the JuLiu station and the Xinmin station. The relationship between the annual sluicing amount and the ISAs of the six groups was then established. Thus, the relationship between the sediment deposition in the Liao River's lower reaches and the PS group's PS variation is discussed, and the critical points can be determined (Xu et al. 2006, Chang 2003, Yan & Zhang 2007).

## RESULTS AND DISCUSSION

### The Relationship Between the Scouring-Silting Amount and the ISA with Six Particle Size Groups

As shown in Fig. 2, the relationship between the annual scouring-silting amount of Julihe-Liujianfang and the input sediment volume of PS groups was ascertained. The regression equation's linear regression and the correlation coefficient's squared value were also ascertained. The significance of the correlation coefficient was tested, and the results showed that the correlation is significant while the significance probability is less than 0.01. The results of the statistical analyses are listed in Table 1. The linear fitting equation in each graph is shown as follows:

$$Dep = aQ_{s,input} - b, \quad \ldots(3)$$

where *Dep* is the sluicing amount, $Q_{s,\ input}$ is the ISA, and a and b are the positive constants. After differentiating two ends of the upper type, we obtain:

$$dDep/dQ_{s,input} = a. \quad \ldots(4)$$

This indicates that the coefficient a of the regression equation can represent the change in the amount of deposition caused by the change in the amount of input sediment per unit, that is, the amount of sediment per ton of sediment.

As shown in Fig. 2, each regression line has an intersection with the line of Dep=0, and the ISA corresponding to the intersection leads to zero sedimentation amount. The intersection point can be regarded as the critical point of erosion and siltation. This can be called the storage-release critical point. The corresponding ISA is the critical ISA. When the ISA is greater than the critical ISA, the river channel appears silted, with the sediment storage increasing. The river channel is scoured when the ISA is less than the critical ISA, and the sediment storage is reduced. As Dep in equation 3 becomes zero, we can obtain the ISA corresponding to the storage-release critical point of sediment:

$$Q_{s,input} = b/a. \quad \ldots(5)$$

According to the above method, the sedimentation amount per ton of sediment and the sedimentation threshold corresponding to the sediment storage release (the critical value of the input sediment without sluicing) are obtained in Table 1.

Figs. 2(a)-(f) show the results of subtracting a finer PS group from the whole sediment. A comparison can be used to ascertain how the channel responds to the gradual thinning of sediment. The following recognition can be obtained according to Fig. 2 and Table 1.

(1) The correlation coefficient between the annual scouring-silting amount of the JuLiu River-Lijianjian section and the annual amount of sediment entering the downstream channel increases with the coarsening of the sediment PS group. As the sediment size increases, the relationship between SA and river siltation increases. The correlation coefficient with sediment size is shown in Fig. 3. It can be seen that for the three sediments of whole sediment, >0.007 mm and >0.01 mm, the correlation coefficient slightly increases with the coarsening of PS at a low rate. As for three coarser-grade sediments of >0.025 mm, >0.05 mm, and >0.10 mm, this correlation coefficient rapidly increases as the PS increases. For sediments of >0.05 mm and >0.10 mm, the square of correlation coefficient R2 is 0.7898 and 0.9256. It is suggested that the coarse sediment of >0.05mm is closely related to the sedimentation of the lower reaches of the Liao River, while the coarse sediment of >0.10mm is even closely related to the sedimentation of the lower reaches of the Liao River.

(2) The sedimentation amount variation caused by the unit amount variation of input sediment increases as the PS increases (Fig. 4). As for three sediments of whole

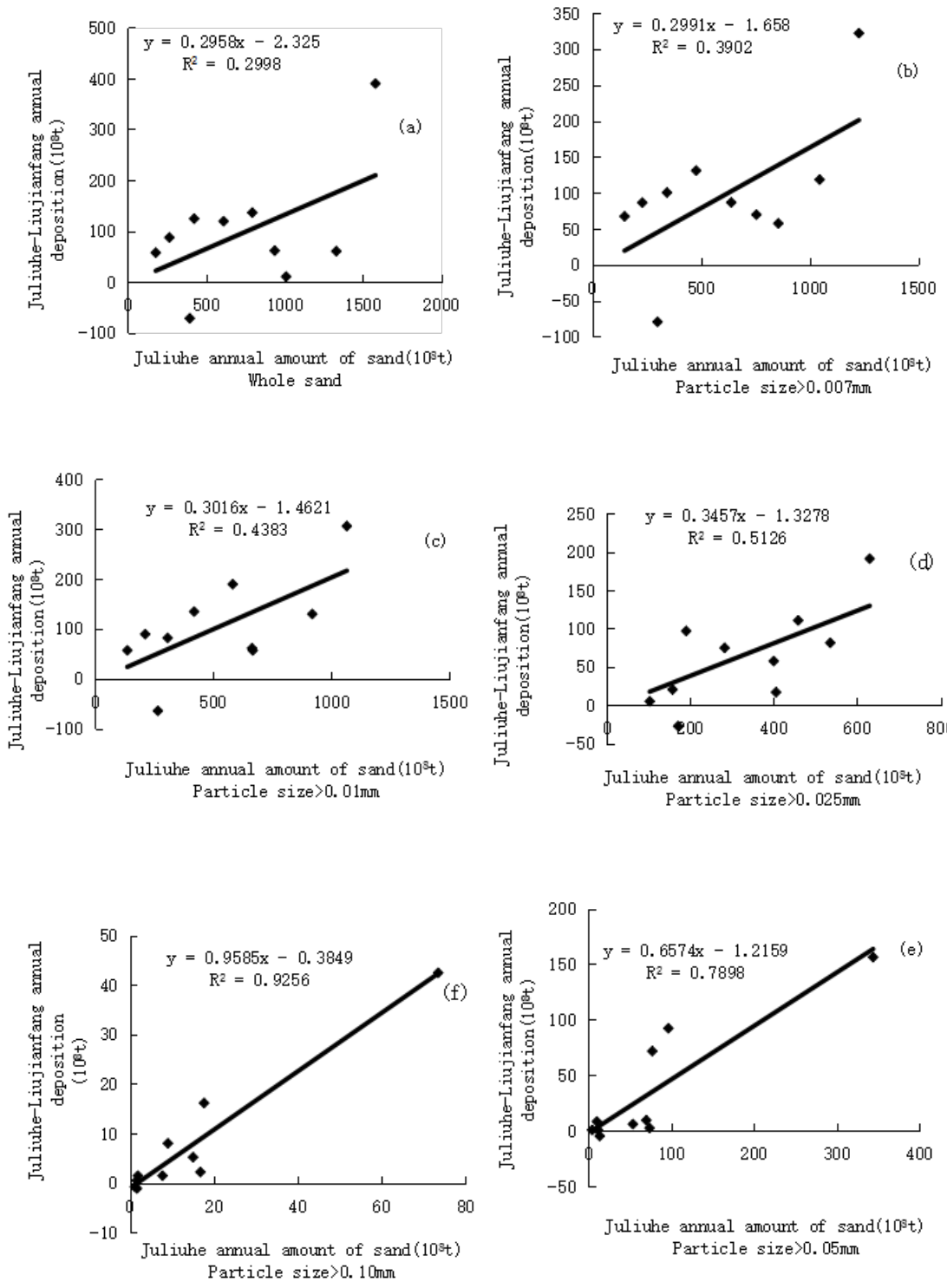


Fig. 2: The relationship between the annual deposition of JuLiu River to Liujianfang with 6 size groups and the annual sediment amount of the corresponding group. Comment: (a) whole sediment; (b) particle size > 0.007 mm; (c) particle size > 0.01 mm; (d) particle size > 0.025 mm; (e) particle size > 0.05 mm; (f) particle size > 0.10 mm.

Table 1: The relationships and the results of statistical analysis between annual deposition (y) of group size six and sediment input (x) of the corresponding group.

| Project | Regression equation | Correlation coefficient squared value R2 | Correlation coefficient squared value | Critical value of input sediment that does not rush and does not deposition | Deposition amount of per ton input sediment [t] |
|---|---|---|---|---|---|
| Suspended whole sediment | y=0.2958x-2.325 | 0.2998 | <0.01 | 7.860 | 0.2958 |
| >0.007 mm Sediment | y=0.2991x-1.658 | 0.3902 | <0.01 | 5.543 | 0.2991 |
| >0.01 mm Sediment | y=0.3016x-1.4621 | 0.4383 | <0.01 | 4.848 | 0.3016 |
| >0.025 mm Sediment | y=0.3457x-1.3278 | 0.5126 | <0.01 | 3.197 | 0.3457 |
| >0.05 mm Sediment | y=0.6574x-1.2159 | 0.7898 | <0.01 | 1.616 | 0.6574 |
| >0.1 mm Sediment | y=0.9585x-0.3849 | 0.9256 | <0.01 | 0.402 | 0.9585 |

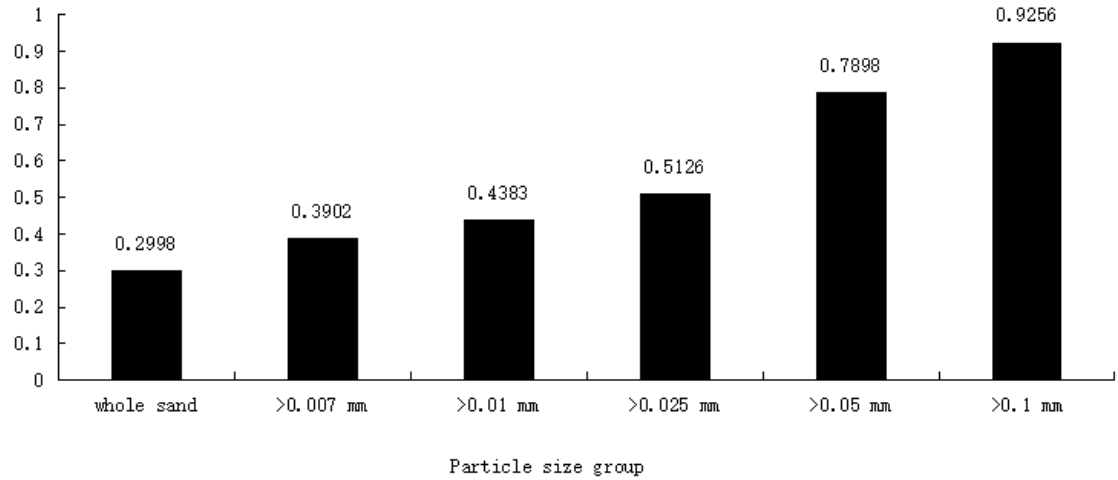


Fig. 3: The correlation coefficient changes pertaining to annual deposition and the amount of annual sediment entering the river course in the lower reaches of the Liao river following the particle size group.

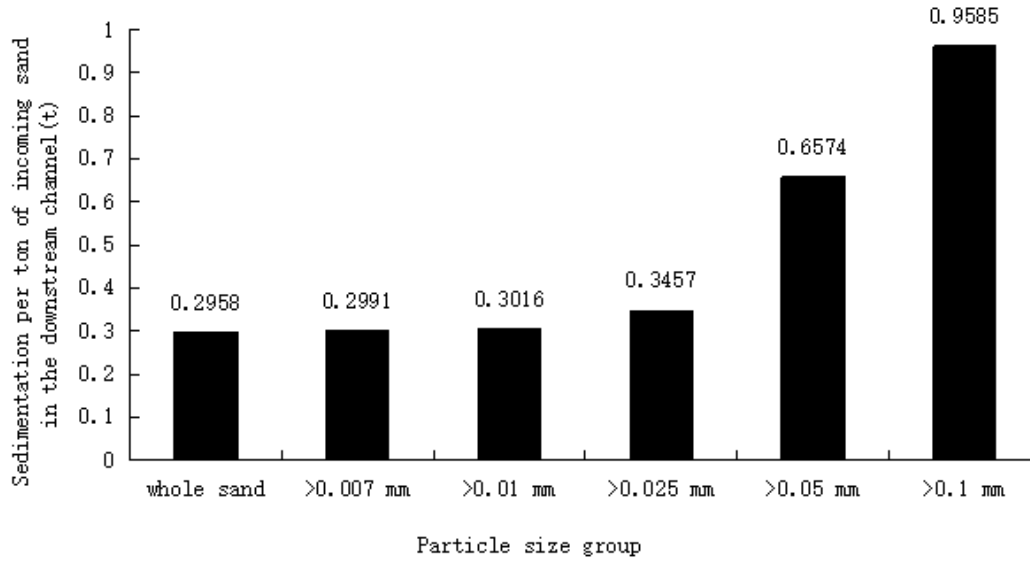


Fig. 4: The changes of the volume per ton sediment deposition of the various size groups in the river course of the lower reaches of Liao river with group size.

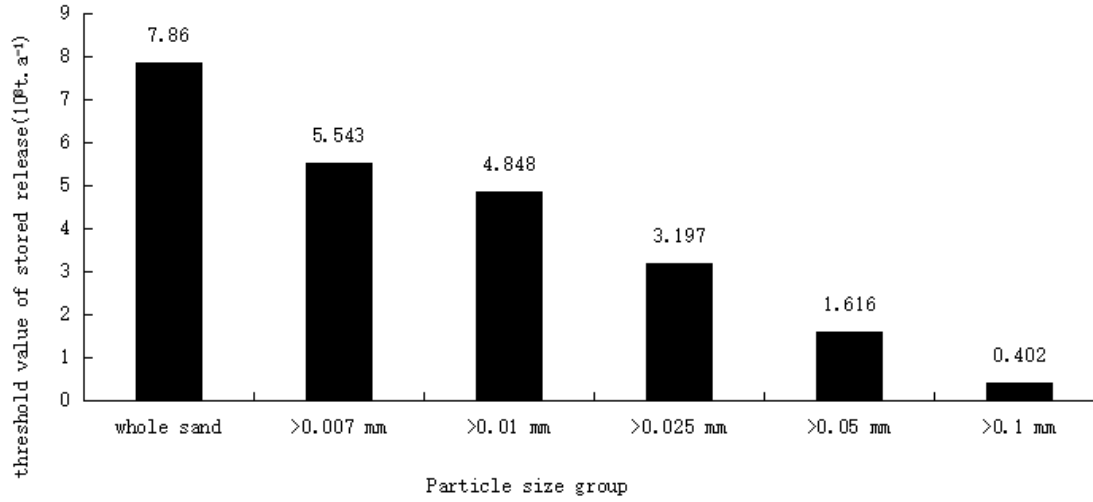


Fig. 5: The changes in the critical value of the incoming sediment from storage to release, with a sediment-size group.

sediment, >0.007mm and >0.01mm, the correlation coefficient between the amount of sedimentation and siltation is not high, so the SA is returned according to the amount of sedimentation and siltation. The SA variation caused by the unit amount variation of input sediment, estimated by the equation, is selected for reference. There is not much change in the value for the three fine PS groups, approximately 0.3 t. As for three coarser-grade sediments of >0.025mm, >0.05mm, and >0.10mm, this value rapidly increases with the PS increase, which is 0.3457t, 0.6574t, and 0.9585t, respectively. It is found that 34.57% of sediment >0.025mm, 65.74% of sediment >0.05mm, and 95.85% of sediment >0.10 mm entering the downstream channel is deposited in the channel. In the upper and middle reaches, the reduction effect of sediments greater than 0.10 mm is 1.458 times larger than 0.05mm and 2.773 times larger than 0.025mm.

The sediment transportation ability of water is closely related to the PS of sediment. Under the same hydraulic conditions, the transportation ability of water for fine sediments is stronger than for coarse sediments. Zhang (1961) associated the sediment-capturing capacity ρ with the flow velocity v, the water depth h with the sedimentation velocity ω, and obtained the following sediment-splitting capacity equation (Zhang 1961):

$$\rho = k\left(\frac{v^3}{gh\omega}\right)^m \quad \ldots(6)$$

Where g is the gravity acceleration and ω is the sinking sediment rate. As the PS increases, the sinking speed ω increases, and the sediment-capturing capacity ρ decreases. Therefore, an increase in PS can lead to the reduction of water sedimentation capacity. As the amount of sediment is constant, the river siltation can increase. It is suggested that the deposition amount variation caused by the unit amount variation of input sediment is proportional to the PS. According to the principle of sediment movement mechanics, the suspended sediment can be divided into two parts: the bed material sediment and the washed sediment. The former consumes adequate energy of water flow, which is sensitive to the intensity of water flow. The latter does not consume adequate energy for water flow, which is irritated the river and makes it insensitive to the water flow's intensity (Ning & Hui 1983). As for the lower reaches of Liao River, the sediment of >0.025mm is generally the bed material sediment, and the sediment of <0.025mm is used for wash sediment. As for three particle sizes, including the whole sediment, the sediment >0.007mm and the sediment >0.01mm, the scouring-silting amount is not high. As for the sediment >0.025mm, >0.05mm, and> 0.1mm, these three grades do not contain the coarse PS of wash sediment, and the correlation between the slag amount and the SA is significant.

(3) The critical value of sediment from the storage to the release in the downstream river is reduced as the sediment PS increases (Fig. 5). As shown in Table 1, it can be seen that the sediment in the downstream river is not silted, and the annual SA of whole sediment should be lessthan$7.860\times10^8$t.To prevent silting of sediments >0.007mm, >0.01mm, >0.025mm, >0.05mm, and >0.10mm in the downstream river channel, the annual SA should be less than $5.543\times10^8$t, $4.848\times10^8$t, $3.197\times10^8$ t, $1.616\times10^8$t, and $0.402\times10^8$t, respectively.

It can be seen that the damage to the river channel by the sediment entering the lower reaches of Liao River increases with the particle size increases. As for various particle size grades, sediments >0.10 mm are the most harmful, followed by sediment sizes >0.05 mm and >0.025 mm.

**The Relationship between the Sedimentation-Siltation Amount and the ISA, As Well As the Input Water Amount for Six Particle Size Groups**

The relationship between the sedimentation amount and the ISA for six size groups is discussed above. The sedimentation-siltation amount of sediment is not only related to the ISA but also related to the input water amount (IWA). The former is the river load, while the latter is the power for sediment transportation. The power of sediment transportation is related to the total runoff amount and depends on the runoff process. As a preliminary approximation, the annual runoff is used to express the sediment transportation power. Based on the hydrological year data of six particle sizes, the binary linear regression equation is established for the sedimentation-siltation amount $Dep_i$ from JuLiu River to Liujianfang and the ISA $Q_{s,i}$ of each particle size group as well as the IWA from the downstream river, which is shown as follows:

$$Dep_i = a + bQ_{s,i} + cQ_w \quad \ldots(7)$$

Where the subscript $i$ represents any particle size group. The established equations are listed in Table 2, and the negative correlation coefficient varies between 0.878 and 0.974, which is highly significant.

In the equation, 7 $Q_w$ is assumed to keep constant with $Q_{s,i}$ changes, and when the partial derivative of two ends is conducted, the following equation can be obtained:

$$\delta Dep_i/\delta Q_{s,i} = b \quad \ldots(8)$$

The equation means the sedimentation increment of any group with the sediment addition of $1\times10^8$t and the IWA keeping constant. Equation 7 $Q_{s,i}$ is assumed to keep constant with $Q_w$ changes, and the following equation can be obtained after the partial derivative:

$$\delta Dep_i/\delta Q_w = c \quad \ldots(9)$$

As the ISA keeps constant, the sedimentation increment of any group is calculated according to the above two equations, which is caused by the runoff of $1\times10^8$m$^3$, as given in Table 2.

Since the variable magnitudes in equation 7 differ greatly, the contribution magnitude of each variable cannot be directly determined from the magnitude of the regression coefficient. Thus, the data can be normalized, which changes between 0 and 1, and the regression is recalculated. Moreover, a linear regression equation is established with a constant term of 0, which is shown as follows:

$$Dep_i = cQ_{s,i} + dQ_w \quad \ldots(10)$$

It is assumed that the contribution rate of the two variables at the right to $Dep_i$ is proportional to the absolute values of regression coefficients $c$ $d$. Also, it is assumed that the total contribution rate is 100%, the contribution rate of $Q_{s,i}$ to $Dep_i$ is $c/(|c|+|d|)$, and the contribution rate of $Q_w$ to $Dep_i$ is $d/(|c|+|d|)$. The results are also shown in Table 2 (Hu & Guo 2004, Xu et al. 2006, Wang et al. 2006).

As shown in Table 2, after adding the input water variable, it can be seen that the complex correlation coefficient is significantly higher than the simple correlation coefficient between the sedimentation-siltation amount and the ISA, especially for the finer PS group. It can also be seen that the contribution rates of ISA and IWA to the sedimentation-siltation amount, and the sedimentation-siltation amount caused by 1t sediment as well as the $10^{10}$ m$^3$ runoff, present a regular variation with the particle size changing. As shown in Table 2 and Fig. 6, it is indicated that as the particle size increases, the contribution rate of erosion amount to sedimentation increases, and the contribution rate of IWA to sedimentation decreases. As the particle size is more significant than 0.025 mm, the variation rate of the scouring amount is significantly accelerated. The contribution rate of the SA to the sedimentation amount increases with an increase in particle size, and the transportation of coarse sediment can consume more water energy, so the siltation probability increases. The contribution rate of the input water to the siltation amount decreases with an increase in particle size. It is suggested that the variation of IWA significantly influences sedimentation and has little influence on coarse sediment erosion. As shown in Fig. 7, as the input water is constant, the amount of silt caused by increasing 1t sediment increases with an increase in the particle size. The sedimentation amount of a certain group of sediment caused by the decreasing $10^{10}$ m$^3$ runoff decreases with increased particle size. This further indicates that the sedimentation amount of coarse sediment is more sensitive to the amount change of coarse sediment, and is less sensitive to the change of input water volume. The sedimentation amount of fine sediment is less sensitive to the SA change of fine sediment, which is sensitive to the change of IWA. This is mainly because the fine silt is mainly deposited on the beach. As the deposition occurs in the floodplain, the input water mount reduces the chance of floodplain, which can significantly reduce the sedimentation of fine silt. The coarse sediment is mainly deposited in the main tank. As the flow rate is reduced, the flow rate reduction of the main tank is smaller

Table 2: Regression analysis results between the amount of sedimentation and the amount of sediment in each particle size group and the amount of water coming from the particle size group a.

| Particle size group | Regression equation<br>1. Based on raw data<br>2. Based on standardized data | $R$ | $r_s$ | $r_w$ | $A_s$/% | $A_w$/% | $B_s$/t | $B_w$/$10^8$t |
|---|---|---|---|---|---|---|---|---|
| Whole sand | 1. $Dep_i = 4.198 + 0.387Q_{S,I} - 0.0175Q_W$ | 0.936 | 0.537 | -0.562 | 49.52 | 50.48 | 0.387 | 1.75 |
| | 2. $Dep_i = 0.659Q_{S,I} - 0.717Q_W$ | | | | | | | |
| >0.007mm | 1. $Dep_{>0.007} = 1.974 + 0.302Q_{S>0.007} - 0.0098Q_W$ | 0.901 | 0.573 | -0.519 | 51.53 | 48.47 | 0.302 | 0.98 |
| | 2. $Dep_{>0.007} = 0.649Q_{S>0.007} - 0.638Q_W$ | | | | | | | |
| >0.01mm | 1. $Dep_{>0.01} = 1.793 + 0.231Q_{S>0.01} - 0.0079Q_W$ | 0.897 | 0.614 | -0.543 | 51.87 | 48.13 | 0.231 | 0.79 |
| | 2. $Dep_{>0.01} = 0.626Q_{S>0.01} - 0.542Q_W$ | | | | | | | |
| >0.025mm | 1. $Dep_{>0.025} = 1.872 + 0.351Q_{S>0.025} - 0.00536Q_W$ | 0.878 | 0.693 | -0.469 | 57.92 | 42.08 | 0.351 | 0.536 |
| | 2. $Dep_{>0.025} = 0.191Q_{S>0.025} - 0.172Q_W$ | | | | | | | |
| >0.05mm | 1. $Dep_{>0.05} = 1.002 + 0.782Q_{S>0.05} - 0.00357Q_W$ | 0.965 | 0.831 | -0.451 | 63.34 | 36.66 | 0.782 | 0.357 |
| | 2. $Dep_{>0.05} = 0.171Q_{S>0.05} - 0.197Q_W$ | | | | | | | |
| >0.10mm | 1. $Dep_{>0.1} = 0.105 + 0.941Q_{S>0.1} - 0.00137Q_W$ | 0.974 | 0.963 | -0.508 | 82.85 | 17.15 | 0.941 | 0.137 |
| | 2. $Dep_{>0.1} = 0.124Q_{S>0.1} - 0.179Q_W$ | | | | | | | |

a: *Dep* for the amount of scouring and silting ($10^8$t/a), $Q_s$ is the annual water quantity ($10^8$t.a$^{-1}$), and $Q_w$ is the annual water quantity ($10^8$m$^3$.a$^{-1}$).In the subscript, i is all sediment, >0.007 means >0.007mm particle size group, and the rest is analogous; R is the negative correlation coefficient, $r_s$ is the correlation coefficient between the amount of scouring and silting in a certain particle size group and the amount of sediment in the particle size group, and $r_w$ is the correlation coefficient between the amount of scouring and silting of a certain particle size group and the amount of input water is the contribution rate of the change of the amount of erosion and sedimentation in the input sediment, $A_w$ is the contribution rate of the change of the flushing and silting amount of the input water change; $B_s$ is the sediment of a certain group of 1t when the input water is constant. The amount of sedimentation in the sediment caused by this group, $B_{w,}$ is the amount of sedimentation of a certain group of sediment caused by the decrease of $10^{10}$ m$^3$ runoff when the input sediment is constant.

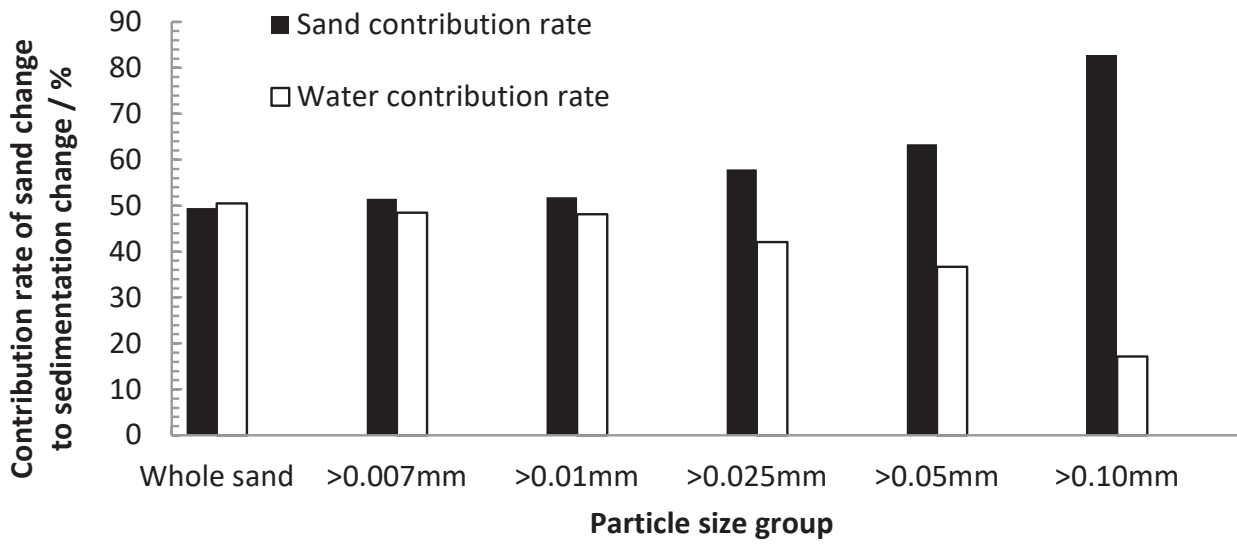


Fig. 6: Comparison of contribution rate of variation of scour and siltation in sediment and water changes in different particle size groups.

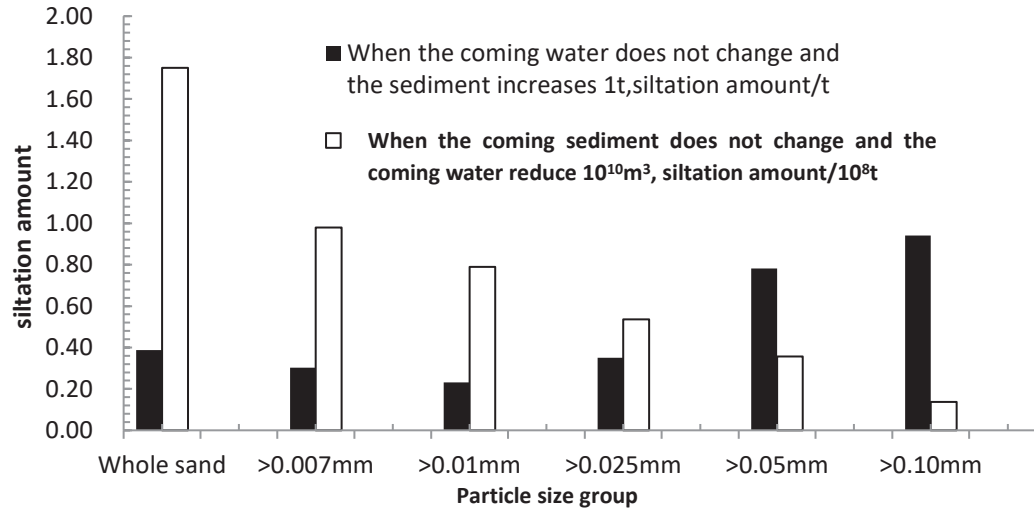


Fig. 7: Comparison of sedimentation changes in water and sediment change in different particle size groups.

than that of the beach. Therefore, the amount of reduction of coarse sediment is not large.

## CONCLUSIONS

(1) The correlation coefficient between the annual sedimentation-siltation amount of the JuLiu-Liujianfang section and the annual SA entering the downstream channel increases with an increase in the sediment particle size. As the sediment particle size increases, there is an increased correlation between the sediment and the river siltation. The threshold value of sediment from the storage to the release in the downstream river is reduced as the sediment particle size increases.

(2) The deposition amount caused by the unit amount change of input sediment increases as the particle size increases. The damage to the river channel caused by the sediment entering the lower reaches of Liao River increases with the increased sediment particle size. When the various particle size grades are taken into consideration, it is found that sediment >0.10 mm is the most harmful, followed by >0.05 mm and >0.025 mm sediments.

(3) It was found that the thicker the particle size, the greater the contribution rate of sediment to the amount of erosion and siltation. On the other hand, the contribution rate of input water to the amount of erosion and sedimentation decreased. As the IWA is constant, the amount of silt caused by each additional 1t of sediment increases with the increased particle size. As the ISA is constant, each $10^{10}$ $m^3$ of runoff is reduced. The amount of silt reduction decreases as the particle size increases.

The research results of this paper are important for the governance of the Liao River. This study shows that 34.57% of sediment >0.025 mm, 65.74% of sediment >0.05 mm is silt in the channel, and 95.85% of sediment >0.10 mm entering the downstream channel is deposited in the river. For the upper and middle reaches, the reduction effect of sediment >0.10 mm is reduced 1.458 times and 2.773 times compared with the reduction effect of sediment>0.05 mm and >0.025 mm, respectively. Based on the treatment and effectiveness of the source area with coarse sediment >0.05 mm, managing the production area of sediment >0.10 mm is of great significance.

The analysis of this paper is based on data from 1988 to 2005. The statistical relationship and critical values obtained in this paper only apply to a certain range of input water from 1988 to 2005. In this period, the maximum annual flood runoff is $20.99\times10^8$ $m^3$, the minimum annual flood runoff is $5.57\times10^8$ $m^3$, the maximum annual runoff is $29.25\times10^8$ $m^3$, and the minimum annual runoff is $7.79 \times 10^8$ $m^3$. Since 2005, the construction of Shifo Reservoir in the middle reaches of the Liao River, the construction of rubber dams and other water conservancy projects in the middle and lower reaches of the Liao River, and the implementation of river improvement engineering measures have caused some changes in the river boundary conditions. Therefore, the results of this study may not be entirely suitable for the situation after 2005. As the data after 2005 has not been collected, it cannot be further analyzed. However, this study's methodology is important and can be used for further studies.

The scouring-silting process in the lower reaches of the Liao River is affected by many factors related to the quantity, particle size composition, and change process of input

sediment, the quantity and process of input water, and the shape and variation of the Liao River. This paper has obtained a single-factor criticality, and the direction of future studies should reveal the multi-factor composite criticality, including the above factors that influence the scouring-silting process.

## REFERENCES

Chang, X. 2003. Sediment deposition distribution analysis of the Yellow River sediment transport system since 1855. Sed. Res., 2: 1-6.

Hao, M.F., Cai, J.K. and Yang, C.J. 2015. Hayu basin sediment balance analysis. J. Agric. Eng., 21: 52-55.

Hu, C.H. and Guo, Q.C. 2004. Discussion on the critical threshold of dynamic balance of mathematical model of river sediment in the lower Yellow River. Sci. China Ser. E Tech. Sci., 34: 133-1431.

Ning, Q. 1980. The Influence of the Coarse Sediment Source Area on the Scouring and Silting of the Lower Yellow River in the Middle Reaches of the Yellow River. Guanghua Publishing House, Beijing.

Ning, Q. and Hui, W.Z. 1983. Sediment Movement. Science Press, Beijing.

Schumm, S.A. 1977. The Fluvial System. John Wiley, New York, 219 p.

Walling, D.E. and Kane, P. 1984. Suspended sediment properties and their geomorphological significance. In: Butt T.P., Walling D.E., (Eds). Catchment Experiments in Huvial Geomorphology. Norwich: Geo Books Co.

Walling, D.E. and Moorehead, P.W. 1987. Spatial and temporal variation of the particle-size characteristics of fluvial sediment. Geogr. Ann., 69: 47-59.

Wang, Z.Y., Zhou, J. and Li, C.Z. 2006. Changes in water and sediment in the lower Yellow River and the evolution of the vertical and horizontal sections of the riverbed. J. Hydraul. Eng., 25: 42-45.

Xu, J.H., Gao, Y.J. and Chen H. 2006. Analysis of particle size composition of sediments in the lower reaches of the Yellow River before 1960. Sed. Res., 3: 1-5.

Xu, J.X. 2007. The coupling relationship between the water production and sediment yield system of the upper and middle reaches of the Yellow River and the downstream river channel sedimentary system. J. Geophys., 52: 421-429.

Xu, J.X. 2008. Effect of suspended sediment grain size on channel sedimentation in the lower Yellow River and some implications. Sci. China Ser. E Technol. Sci., 1: 34-46.

Yan, B.S. and Zhang, Y.F. 2007. The laws and calculation methods for the change of sediment transport in the lower Yellow River. Sed. Res., 1: 30-35.

Zhang, R.J. 1961. River Flow Mechanics. China Industrial Press, Beijing.

Nature Environment and Pollution Technology
An International Quarterly Scientific Journal

p-ISSN: 0972-6268
(Print copies up to 2016)
e-ISSN: 2395-3454

Vol. 22 | No. 1 | pp. 427-432 | 2023

Original Research Paper

https://doi.org/10.46488/NEPT.2023.v22i01.041

Open Access Journal

# Feasibility of Waste-to-Energy Plants for STT-PLN Campus Canteen

**Pawenary*, Amelia Dwita Larasati*, Suhdi** and Rulyanti Susi Wardhani**†**
*PLN Institute of Technology, Cengkareng, Jakarta 11750, Indonesia
**Universitas Bangka Belitung, Merawang, Bangka 33172, Bangka Belitung, Indonesia
†Corresponding author: Rulyanti Susi Wardhani; rulyantiwardhani67@gmail.com

**Nat. Env. & Poll. Tech.**
**Website: www.neptjournal.com**

*Received:* 06-06-2022
*Revised:* 14-07-2022
*Accepted:* 18-07-2022

**Key Words:**
Community power
Gasification
Gasifier engine
Waste-to-Energy

## ABSTRACT

The pellets of waste produced by Society Electric [*Listrik Kerakyatan* (LK) 2] at the STT-PLN have not been efficiently utilized in terms of energy. The STT-PLN canteen consists of 14 stalls with an installed electricity capacity of 1300 VA, each with 12h of use/day. This study aimed to convert LK 2 waste pellets into electrical energy to supply electricity to the STT-PLN canteen. This research method uses quantitative methods, i.e., by calculating the amount of energy produced adjusted to the needs of the canteen. Gasification technology was chosen due to its high efficiency and lower emission impacts in the waste combustion technique. Based on the analysis, the gasifier engine that complies with this requirement was TG30-1 with a maximum capacity of 25 kVA and requires a flow rate of 10 $kg.h^{-1}$ of waste pellets. The amount of waste pellets used for this plan was 120 $kg.day^{-1}$. The assessment results of this plan indicated a net present value of IDR 302,218,609.33, an internal rate of return of 25.7983%, and a PBP of 5.66 years. Based on the economic analysis, the establishment of plants for the conversion of waste to power was declared feasible to operate.

## INTRODUCTION

In Indonesia, especially in the capital city, a lot of waste is generated by the public. The DKI Jakarta Sanitation Department records 7,000 tons of waste produced every day (Komara 2018). The waste is generated from a wide variety of settlements to offices. It was estimated that waste production reaches 0.5-0.8 $kg.person^{-1}.day^{-1}$ (Supriyanti 2014). Waste classified as biomass can be used as fuel for electricity generation. In a previous study, it was observed that processing waste into waste pellets could increase the calorific value of waste fuel, i.e., 2,700-3,350 $kcal.kg^{-1}$ (Sirait 2018).

Society Electric (*Listrik Kerakyatan* (LK) 2) is an innovative development project initiated by the Technical College of State Electrical Company (*Sekolah Tinggi Teknik–Perusahaan Listrik Negara* (STT-PLN)). LK 2 can be utilized to generate income if electricity generated from waste fuel can be used for the school's canteen, i.e., it could be used to supply energy to 14 kiosks of the STT-PLN canteen. Therefore, this study discusses the economic and technical feasibility of LK for supplying energy. This study also compares how much costs can be minimized if the electricity requirements for the STT-PLN canteen are supplied from LK. In addition, this would also facilitate LK in realizing 23% achievement in the project of renewable energy utilization by 2025 (Humas EBTKE 2019).

## MATERIALS AND METHODS

Waste as fuel for a 15-kilowatt (kW) waste-to-energy (WtE) plant (*Pembangkit Listrik Tenaga Sampah* (PLTSa)) is evaluated to supply electricity to the STT-PLN canteen. The study is carried out at LK Campus 2 (STT-PLN), Jakarta, Indonesia. The STT-PLN canteen consists of 14 stalls, each with a power capacity of 1,300 VA. This plan was carried out to provide an overview using waste pellets in LK 2. The pellets are then used in specific generators to produce energy.

### Electric Power Distribution Planning

This electricity distribution starts from the generator to the miniature circuit breaker (MCB) installed in each stall. This distribution system was designed with PLTSa as the main supplier of electricity in mind, but PLN is still used PLN in case PLTSa needs to undergo any kind of equipment maintenance in the future. The power distribution system sources from PLTSa use a TR (low voltage) system because the generator output voltage is 220/380 V.

### Operation and Maintenance of Gasification PLTSa

The operation and maintenance of gasification PLTSa are based on engine operations and engine maintenance related to generation. The operational necessities of the engine are

calculated by the fuel needed by the gasifier and generator to generate the electricity needed according to its capacity. The operation of a generator requires operators or workers of LK.

### Cost Analysis

In development planning or project expansion, it was necessary to assess the cost and economic factors before reaching the stage of development/project implementation. Based on the results of the operational study, we can achieve the estimated project costs and its economic analysis. The analysis includes an evaluation of the net present value (NPV), internal rate of return (IRR), and payback period (PP).

### NPV

According to Candra (2011), NPV is the difference between the present value of incoming cash flows and the present value of cash outflows at a given time (Gallo 2015). NPV can be interpreted as Equation (1):

$$NPV = \sum_{t=0}^{n} \frac{CIFt}{(1+k)^t} - COF \quad \ldots(1)$$

Where,

$k$ : Discount rate (%),

$COF$ : Cash outflow or initial investment,

$CIFt$ : Cash inflow at the period, and

$n$ : Last period cash flow is expected

### IRR

IRR is the rate of return that results in an NPV of cash inflows equal to the NPV of cash outflows (Sari et al. 2018). IRR is expressed as a percentage (%) per period, which is usually positive (I > 0). The project is considered profitable if the IRR yield is greater than the interest rate.

### PP

PP is the length of time required to return the investment funds and can be calculated as Equation (2) (Candra 2011):

$$PPKum = Pkum + \left(\frac{|Akum|}{A\ after\ Akum}\right) \quad \ldots(2)$$

Where,

*PPKum* : Period of the last cumulative negative cash flow,

*|AKum|* : Absolute value of the last negative cumulative cash flow, and

*A after Akum* : Next cumulative cash flow after the cumulative cash flow has the last value

## RESULTS AND DISCUSSION

### LK 2 STT-PLN Waste Pellet Production

Based on the local waste management method analysis, LK 2 produces 300–400 kg of waste pellets per day. This waste

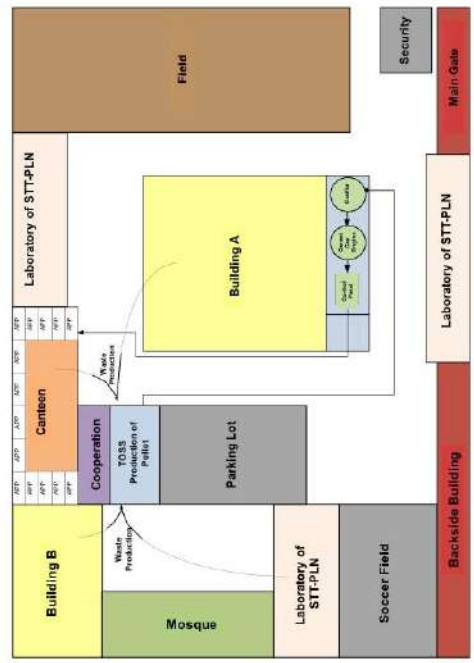


Fig. 1: Layout of PLTSa LK 2 area in the STT-PLN Campus.

pellet is sold in the range of IDR 500–600 per kg, excluding transportation costs. Meanwhile, the selling price of waste pellets in LK 2 including transportation costs is around IDR 900–1,000 per kg.

### Electricity Requirement of STT-PLN Canteen

The total capacity of the 14 stalls is as follows: 1300 VA × 14 stalls = 18200 VA = 18.2 kVA. Assuming insulation factors of cos $^{\varphi}$, 0.8, the power capacity in the canteen is 18.2 kVA × 0.8 = 14.56 kW. The canteen operates 12 h per day and 26 days per month.

### Electricity Requirement of STT-PLN Canteen

The STT-PLN canteen area is located close to LK 2, thereby reducing the electricity distribution costs. Fig. 1 shows the layout of the STT-PLN campus area and the placement of PLTSa equipment.

As shown in Fig. 1, the various locations in the school can be used to collect waste materials. When there is a shortage of material, waste can also be obtained from outside of the area. Waste is then processed in the TOSS pellet production plant and is then continued to the PLTSa.

### Single Line and Wiring Diagram

As shown in Fig. 2, a single wiring through a Three Pole Double Throw (3PDT) switch can be used. The two electricity sources, which can be used together or interchangeably, can be managed by this device. The design then uses, for 1300 VA capacity, a miniature circuit breaker (MCB 1P), due to its small 6 A rating. Therefore, the use of the device is adequate. The MCB capacity is determined using Equation (3) for source output from the generator or PLN as follows:

$$I = \frac{P}{\sqrt{3}\ x\ V\ x\ Cos\varphi} \quad \ldots(3)$$

$$I = \frac{15000\ W}{\sqrt{3}\ x\ 380\ V\ x\ 0{,}8} = 28{,}478\ A$$

$$28{,}478\ A\ x\ 120\% = 34{,}1736\ A$$

The above calculation shows that it requires a molded-case circuit breaker (MCCB) for capacity that is placed after the power source, assuming operation at the generator load of 75% (15 kW). Based on the analysis, MCCB 3P with a capacity of 40 A for the generator or PLN output can be used.

Fig. 3 shows that the circuit uses a 3 PDT switch (power source), which can be connected to Throw 1 or Throw 2.

### Cost Comparison between PLN and PLTSa Power Sources

The canteen is open from 6:00 to 18:00, not at peak load time (past peak load time), and 26 days per month. The basic electricity tariff of PLN in March 2019 was IDR 1467.28 (LWBP) (attached). This sums up to 18.2 kVA for the 14 stalls, and it decreases to 14.56 kVA due to insulating factors. The canteen load is estimated to be 70% as it is the average load used by the facility. This shows a total of IDR

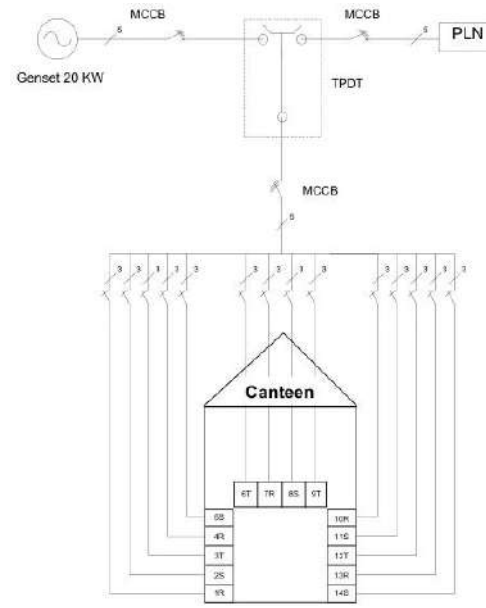


Fig. 2: PLTSa distribution diagram using direct distribution line.

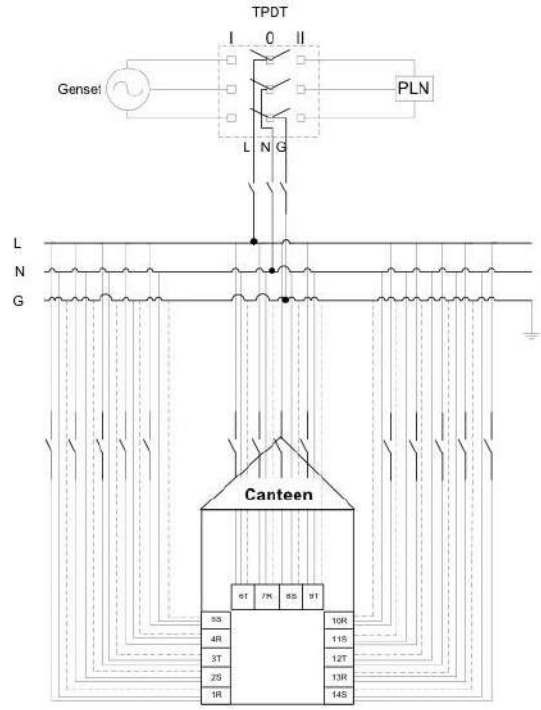


Fig. 3: Wiring diagram of PLTSa electricity distribution.

Fig. 4: Trillion gasifier (TG30-1).

179.454,213,-/day = IDR 4.665.809,5,-/month paid to the PLN.

For calculations with the tariff using the PLTSa, the production cost per kilowatt-hour is calculated from the raw material cost of IDR 500/kg, the operational cost of IDR 1.500.000/month, and supporting the cost of 10%. This gives a cost of IDR 687.17/kWh. With this production cost, the selling electricity price to the STT-PLN canteen can be set at IDR 1400/kWh with a profit of IDR 712.83/kWh. The total cost of the canteen in a month would be IDR 4.451.856,6/month, with a monthly saving of IDR 213,952,938 /month compared to PLN.

## PLTSa Operational Equipment

**Gasification technology (gasifier):** Gasification is the process of processing solid organic material into flammable gases, such as methane, carbon monoxide, and hydrogen. A 30-hp trillion gasification unit (TG30-1, shown in Fig. 4) is utilized based on the listed specifications from the study of Sirait (2018). The design uses 510-kW PLTSa using a gasifier with TG30-1 and a 33-kVA generator installed for 3 × 8 h, where it takes 10 kg of waste pellets per hour to run gasification devices and generate electricity. The canteen load is assumed to be on for 12 $h.day^{-1}$ (6:00–18:00 West


Fig. 5: Green power genset gas engine GP25NG.

Indonesia Time), and the pellets needed per day were 10 kg × 12 h.day$^{-1}$ = 120 kg. day$^{-1}$.

**Genset gas engine capacity:** The PLTSa generator utilized in the design planning is the Green Power Engine Generator type RMG3000 GP25NG (Fig. 5), which uses gas fuel. Only one set of generator sets is needed because PLN will continue to be connected as an electricity supplier to the canteen when PLTSa equipment maintenance is held or when there is an interruption. The gas generator capacity used was 25 kVA/20 kW. The generator was planned to operate at a load of 75% of the power capacity owned by the generator (15 kW). Table 1 summarizes the specifications of the generator.

### Economic Analysis

**Initial investment:** The initial investment represents all costs that must be incurred for development from the preparation stage to the operation phase of the plant. The data in Table 2 is obtained from interviews and observations in the field.

In this plan, it is assumed that land and buildings are already available, so no land acquisition or building costs are needed.

**Expenses:** This expenditure includes the cost of pellet fuel, which was assumed to be sold at the price of IDR. 500/kg (Table 3 and Table 4).

Table 1: Genset gas specification.

| Generator Engine | RMG3000 |
|---|---|
| Type | Four-cycle, water-cooled, gas engine |
| Cylinder arrangement | In-line |
| No. of cylinders | 4 |
| Bore × Stroke | 101.6 mm × 91.4 mm |
| Prime-rated power (PIDR) | 25 kVA/20 kW |
| Limited time-running power (LTP) | 27.5 kVA/22 kW |
| Rated current | 45 A |
| Rated voltage | 400 V/230 V |
| Land use type of unit | Low noise, automatic type |
| Dimension (L × B × H) | 150000 mm × 1500 mm |

## DISCUSSION

### Income

The revenue obtained is the result of electricity sales to the STT-PLN canteen. PLTSa set a price of IDR 1400/kWh. The electricity tariff determined in this study is assumed to increase by 4% every year because it refers to PLN's electricity tariff, which also goes up annually.

The generator is planned to operate at 75% (15 kW). Every year, it is estimated that there is a decrease in the electricity production performance to anticipate the addi-

Table 2: Initial investment development.

| Initial investment | | |
|---|---|---|
| No | Item | Total (IDR) |
| 1 | Mechanical and electrical equipment | 160,000,000 |
| 2 | Distribution network | 15,500,000 |
| Total | | 175,500,000 |
| Tax 10% | | 17,550,000 |
| Total + Tax | | 193,050,000 |

Table 3: Operational cost.

| Operational | | | |
|---|---|---|---|
| No | Remark | Monthly (IDR) | Yearly (IDR) |
| 1 | Fuel | 1.716.000 | 20.592.000 |
| 2 | Operational (operator, admin/overhead) | 1.500.000 | 18.000.000 |
| Expenses | | 38.592.000 | 3.216.000 |

Table 4: Operating costs with a 10% increase rate.

| The assumptions increase operational costs every 5 years (in IDR) | | | |
|---|---|---|---|
| 1st | 6$^{th}$ | 11th | 16th |
| 20,592,000 | 22,651,200 | 24,916,320 | 27,407,952 |
| 18,000,000 | 19,800,000 | 21,780,000 | 23,958,000 |
| 38,592,000 | 42,451,200 | 46,696,320 | 51,365,952 |
| 28,692,000 | 32,551,200 | 36,796,320 | 41,465,952 |

tional costs of maintaining the generator annually. The total income multiplied by the factor is around IDR 2.232 billion for 20 years.

Based on the evaluation of the feasibility of the project with a value of NPV > 0, the requirements have been met based on the calculation results. Furthermore, the IRR value obtained from calculations using the Microsoft Excel formula was 18.519%, which was higher than the initial interest rate (10%). Meanwhile, the PP calculated using Equation (2) resulted in the 4.45th year.

### Qualitative Impact Analysis

PLTSa is part of the development of renewable energy in Indonesia. Local waste management such as this study would help reduce waste transport fees including those toward a dumping site. Transport could generate more emissions and requires more manpower, which could be reduced using this method. The biological–chemical processing such as anaerobic digestion and sanitary landfills can also produce biological gas energy and the risk of accumulation of gas deposits and low energy efficiency (Woodard & Curran, Inc. 2006). Waste and sewage treatment through a modern gasification process can increase efficiency by up to 90%, reducing many environmental impacts (Sikumbang et al. 2018). Therefore, although the PP is not as fast as other businesses, the environmental impact could be better.

Analysis of the environmental impact is as follows:

1. Promote, support, and develop the use of EBT in Indonesia.
2. Payment for canteen electricity was cheaper per kWh.

## CONCLUSİONS

Based on the results of this research, the following can be concluded:

1. 120 kg of waste pellets per day was needed for the operation of the TG30-1 as a supplier of gas (fuel) for the GP3NG type GP25NG Green Power Engine, which was planned to operate at 75% of the capacity of the generator, i.e., 15 kW.
2. A three-phase MCCB with 40-A capacity was needed for the output of the generator set. Meanwhile, to distribute electricity to the canteen, the connection switch panel was designed with a 3PDT switch that functions to change the source flow from PLTSa (I) to PLN (II), if at any time there was maintenance or disruption in distribution at PLTSa.

With a selling price of IDR 1400/kWh, the profit gained by the canteen will be IDR 213,952,938/month so that it will not burden consumers. In this plan, NPV > 0 is IDR 302,218,609.33, the IRR value > interest rate (10%) is 25.7983%, and the return on investment of this PLTSa planning is 4.45 years. Therefore, this study is feasible to proceed.

## ACKNOWLEDGMENT

The authors would like to thank the PLN Institute of Technology and the University of Bangka Belitung for supporting this research activity.

## REFERENCES

Candra, K.P. 2011. Ekonomi Teknik Kuliah Ke-9 Net Present Value (NPV) dan Kriteria Investasi Lain [Engineering Economics 9th Lecture Net Present Value (NPV) and Other Investment Criteria] (Unpublished). Lecture Material for Engineering Economics.

Gallo, A. 2015. A Refresher on Net Present Value. Harvard Business Publishing, MA, USA.

Humas EBTKE. 2019. Pemerintah Harapkan Dukungan Penuh Stakeholder EBTKE untuk Akselerasi Pengembangan Energi Surya [Government Expects the Full Support of EBTKE Stakeholders for the Acceleration of Solar Energy Development]. Available at: http://ebtke.esdm.go.id/post/2019/07/12/2288/pemerintah.harapkan.dukungan.penuh.stakeholder.ebtke.untuk.akselerasi.pengembangan.energi.surya?lang=en. (Accessed 12 July 2019).

Komara, I. 2018. Setiap Hari Jakarta Hasilkan 7.000 Ton Sampah [Every Day Jakarta Generates 7,000 Tons of Waste]. Available at: https://news.detik.com/berita/d-3825854/setiap-hari-jakarta-hasilkan-7000-ton-sampah (Accessed 21 January 2018).

Sari, C.F.K., Sawaki, M.E. and Sabarofek, M.S. 2018. Pengaruh analisis investasi terhadap kelayakan penambangan batu mangan di PT. Berkat Esa Mining [The effect of investment analysis on the feasibility of manganese mining at PT. Berkat Esa Mining]. J. Sci. Tech., 4(1): 11-18.

Sikumbang, H., Cahyaningtyas, R., Indrianto and Haris, A. 2018. Simulasi pembuatan dan pemanfaatan briket pada listrik kerakyatan [Simulation of making and utilizing briquettes in community electricity]. J. Petir., 11(1): 52-59.

Sirait, M.H. 2018. Perancangan Pembakit Listrik Tenaga Sampah (PLTSa) 510 KW dengan Menerapkan Tempat Olah Sampah Setempat (TOSS) pada Setiap Desa di Kecamatan Klungkung, Bali [Design of a 510 KW Waste Power Plant (PLTSa) by Implementing Local Waste Processing Facilities (TOSS) in Every Village in Klunkung District, Bali]. Undergraduate Thesis, STT PLN, Jakarta.

Supriyanti, A. 2014. Produksi Sampah Capai 0,8 Kg Per Orang Per Hari [Waste Production Reaches 0.8 kg Per Person Per Day]. Available at: https://beta.beritasatu.com/kesra/233419-produksi-sampah-capai-08-kg-per-orang-per-hari.html (Accessed 15 December 2014).

Woodard and Curran, Inc. 2006. Solid Waste Treatment and Disposal. In: Woodard & Curran, Inc. (eds.) Industrial Waste Treatment Handbook, Second Edition, Elsevier, Cham, pp. 363-405.

Nature Environment and Pollution Technology
An International Quarterly Scientific Journal

p-ISSN: 0972-6268
(Print copies up to 2016)
e-ISSN: 2395-3454

Vol. 22 | No. 1 | pp. 433-443 | 2023

Original Research Paper

https://doi.org/10.46488/NEPT.2023.v22i01.042

Open Access Journal

# Pathogen Treatment in Single and Two-Stage Vertical Flow Wetland as a Potential Sanitation Technology for Rural India

**Prajakta Pratap Patil*, Anant Yadav*(**), Lalita Vithal Baragi* and Srikanth Mutnuri*†**
*BITS Pilani, K K Birla Goa Campus, Applied Environmental Biotechnology Laboratory, Goa 403726, India
**Bauer Nimr LLC, PO Box 1186, PC114 Al Mina, Muscat, Oman
†Corresponding author: Srikanth Mutnuri; srikanth@goa.bits-pilani.ac.in

**Nat. Env. & Poll. Tech.**
**Website: www.neptjournal.com**

*Received:* 27-06-2022
*Revised:* 22-08-2022
*Accepted:* 07-09-2022

**Key Words:**
Environmental pollution
Pathogen removal
Sanitation
Vertical flow constructed wetland
Wastewater

## ABSTRACT

Vertical flow-constructed wetlands (VFCW) are well-established, cost-effective, and sustainable options for wastewater treatment. Along with organic matter removal, wetlands are helpful in the removal of microbial pathogens. This study focuses on understanding the bacterial pathogen removal efficacy of three different design types of VFCWs and understands the best designs for the efficient removal of pathogens in a tropical climate. The three wetlands studied for removal efficiency were (a) two-stage vertical flow constructed wetland (TSVFCW), (b) Single-stage vertical flow constructed wetland (SSVFCW), and (c) single-stage saturated vertical flow constructed wetland (SSSVFCW). Results revealed that all three types of wetlands were effective in removing pathogenic bacteria. Still, TSVFCW was found to be more efficient in pathogen removal (Total Coliforms, *Shigella* spp., *Salmonella* spp., *Pseudomonas* spp., *Vibrio* spp., *Enterococcus faecalis*) 7.04 ± 0.17, 6.53 ± 0.08, 4.0 ± 0.42, 7.67 ± 0.08, 5.73 ± 0.70 and10 5.23 ± 0.96 $Log_{10}$ reductions respectively compared to SSVFCW (5.28 ± 0.18, 5.18 ± 0.09, 3.74 ± 0.74, 6.98 ± 0.01, 3.97 ±0.32, 4.74 ± 1.08 $Log_{10}$ reductions respectively) and SSSVFCW (4.48 ± 0.46, 4.83 ± 0.15, 2.74 ± 0.44, 6.71 ± 0.03, 4.31 ± 0.49, 5.03 ± 1.20 $Log_{10}$ decreases respectively). For abiotic factors (Chemical oxygen demand, total Kjeldahl nitrogen, and phosphorus) also TSVFW shows better efficiency (45 ± 8.7, 24.7±4.5 and 3.1, ± 0.2 $g.m^{-2}$, respectively) than SSVFCW (12 ± 1.3, 7.6 ± 0.4 and 1.8 ± 0.2 $g.m^{-2}$ respectively) and SSVFCW (6.3 ± 1.1, 7.7 ± 0.1 and 1.2 ± 0.1 $g.m^{-2}$ respectively). However, the removal efficiency of both single-stage wetlands was comparable.

## INTRODUCTION

India, the second most populated country in the world, has a huge water demand, mainly for drinking, agricultural and industrial uses (Goel 2006). In Class I and II cities of India, an estimated 72368 million liters per day (MLD) of sewage is generated, but the sewage treatment capacity is only available for 12197 MLD. Similarly, just 60% of industrial wastewater is treated, especially in large-scale enterprises (CPCB 2021). Also, most treated water doesn't meet the slandered for discharge, especially pathogen concentration (Kaur et al. 2012, Schellenberg et al. 2020).

Under the new government scheme of India, "Swachh Bharat Abhiyan," each household will have a toilet in all the country's rural areas (Jain et al. 2020). As these villages are situated far from the city, and the population density is low compared to cities, it will not be possible to provide and sewerage network (Chandana & Rao 2021, Yadav et al. 2018, Axelrood et al. 1996, Talekar et al. 2018, Massoud et al. 2009, Morvannou et al. 2015, Badejo et al. 2018, Singh et al. 2019). Without a suitable decentralized wastewater treatment system, sewage will end up in local rivers or fields, adversely affecting the environment.

Vertical flow-constructed wetlands (VFCW) are a well-established technology for the nutrient treatment and other contaminant removals. However, the system's pathogen removal efficacy is still being studied (Dzakpasu et al. 2015, Pang et al. 2015). The effectiveness of constructed wetlands (CW) for the treatment of microbiological pollutants depends on various physical (sedimentation, retention time of the system, temperature and pH of water), chemical (UV, oxidation, biocides), and microbiological parameters (antibiosis, predation, lytic bacteria or viruses) (Díaz et al. 2010, Agrawal 1999). One of the factors, which play an important role in the removal of pathogenic bacteria from CW, is the retention time. In Horizontal flow and other types of sub-surface or surface flow wetlands, the residence time is usually long to get optimal output. Still, in the case of VFCW, the residence time is very short, which does not provide sufficient time for the natural die-off and removal of

pathogens by other mechanisms (Franceys et al. 1992, Arias et al. 2003). The sedimentation process also plays a vital role in treating various pathogens (Gersberg et al. 1989). Several studies have found that *Salmonella*, protozoans, and virus tend to stay in sediment (Gerba & McLeod 1976, Hendrick 1971, Van Donsel & Geldreich 1971). Viruses get adsorbed on larger particles and settle at the bottom (Gersberg et al. 1987).

VFCWs' chances of sedimentation are very low due to low retention time; this can be improved by designing saturated vertical flow constructed wetlands, which will help increase residence time. This study aimed to understand the application of VFCW for pathogen treatment and the removal efficiency of different types of VFCW.

## MATERIALS AND METHODS

### Study Site and Wetland Characterisation

Three VFCWs were chosen for the study, located in different parts of the BITS Pilani KK Birla Goa Campus, Goa, India. (a) Two-stage vertical flow constructed wetland (TSVFCW), situated in the STP (sewage treatment plant) of campus, is fed with raw domestic sewage from campus. (b) Single-stage vertical flow constructed wetland (SSVFCW), located near one of the hostels. The system is fed with black water from the output of two chambered septic tanks connected to hostel toilets. (c) Single-stage saturated vertical flow wetland (SSSVFCW) is fed black water from single-chambered septic tank wastewater. Fig. 1 shows the schematics of the wetlands, and table 1 shows the characteristics of VFCWs.

### Design and Working

The beds of all three wetlands (TSVFCW, SSVFCW, and SSSVFCW) were constructed using laterite stones, plastered and leak-proof. 40 mm pipes passively aerated beds at the bottoms. For TSVFCW, the surface area of 1$^{st}$ bed was four $m^2$ and 2$^{nd}$ bed had a surface area of 1.9 $m^2$. The gravel size and depth of different gravel layers are given in Table 2. The hydraulic loading rate (HRL) for the 1$^{st}$ stage is 0.1 $m.day^{-1}$. Wastewater from the storage tank (300 $m^3$ tank, where the water from campus is stored and aerated continuously for further large-scale treatment SBR) is fed to the 1$^{st}$ stage, and from 1$^{st}$ stage, it percolates down through gravity to the 2$^{nd}$ storage tank; from this, it is provided to the 2$^{nd}$ stage. The SSVFCW has a surface area of 40 $m^2$. The HLR of the wetland was 0.036 $m.day^{-1}$ with no HRT. The black water from the hostel toilets was collected into two chambered septic tanks. From the tank, it was transferred to the wetland with the help of a submersible pump twice a day. The SSSVFCW is a single-stage saturated VFCW of 3 $m^2$ surface area. The hydraulic loading rate for the wetland was 0.067 $m^2.day^{-1}$. The wetland was fed wastewater from a single-chambered septic tank directly connected to the toilet. So, whenever the toilet is flushed, the wastewater from the septic tank flows down to the wetland through gravity. No pumping system was used for this wetland. The system has a hydraulic retention time of 24 h to develop a partial anaerobic condition at the bottom of the system.

### Water Sample Collection and Analysis of Abiotic and Biotic Parameters

The samples were collected from the inlet and outlet of SSVFCW and SSSVFCW. In the case of the TSVFCW wetland, it was collected from the inlet of the 1$^{st}$ stage, outlet 1$^{st}$ stage, and 2$^{nd}$ stage. Five liters of the sample were collected from each collection point and analyzed for abiotic

Table 1: Design characteristics of all three types of wetlands.

| Wetland Name | TSVFW | SSVFW | SSSVFW |
|---|---|---|---|
| Wetland Type | Two-stage vertical flow | Single-stage vertical flow | Single-stage saturated vertical flow |
| Age (Functional years) | 4 | 3 | 3 |
| No. of stages | 2 | 1 | 1 |
| Depth [m] | 1 | 1 | 1 |
| Saturation level [cm] | 0 | 0 | 7 |
| HRT [day] | - | - | 1 |
| Septic Tank Volume | Aerated tank of 300 $m^3$ | 6 $m^3$ | 1.5 $m^3$ |
| Vegetation type | *Canna indica* | *Canna indica* | *Canna indica* |
| Area [$m^2$] | 6 | 40 | 3 |
| Average inflow [$l.day^{-1}$] | 600 | 1500 | 200 |
| HLR [$m.day^{-1}$] | 0.1 | 0.036 | 0.067 |
| No. of batches/day | 3/day | 2/day | It depends on the no. of time toilet used |

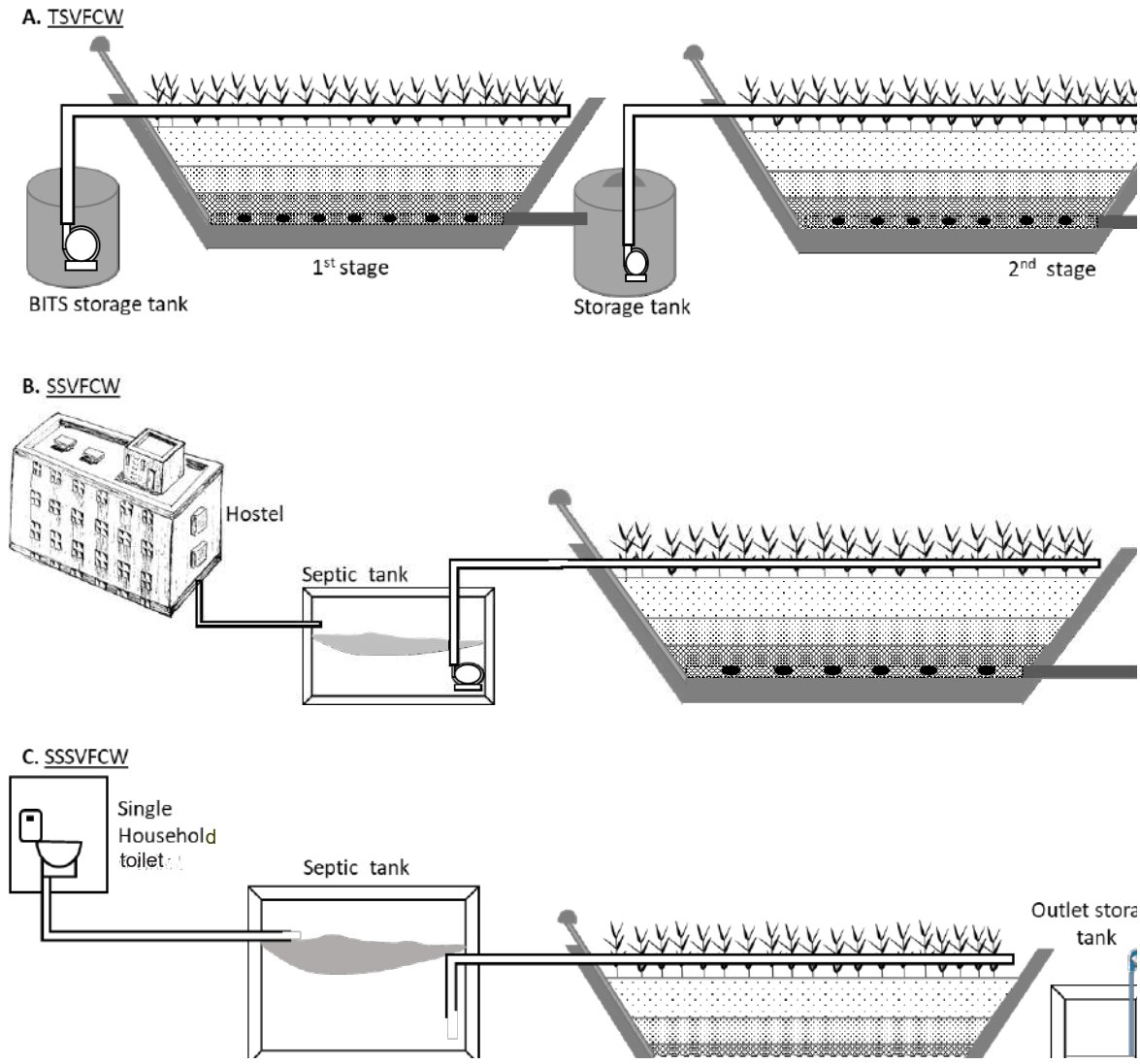


Fig. 1: Design of different wetlands (A) Two-stage vertical flow constructed wetland (TSVFCW), (B) Single-stage vertical flow constructed wetland (SSVFCW), and (C) Single-stage saturated vertical flow constructed wetland (SSSVFCW).

Table 2: Gravel size and depth of layers of all three types of wetlands.

| Layers (bottom to top) | TSVFCW | | SSVFW | SSSVFW |
|---|---|---|---|---|
| | 1st Stage | 2nd stage | | |
| 20 cm | Gravel 20-30 mm | Gravel 10-20 mm | Gravel 10-20 mm | Gravel 10-20 mm |
| 20 cm | Gravel 10-20 mm | Gravel 2-8 mm | Gravel 2-8 mm | Gravel 2-8 mm |
| 40 cm | Gravel 2-8 mm | Gravel 0-2 mm | Gravel 0-2 mm | Gravel 0-2 mm |

and biotic factors (No precipitation effect). The pathogenic bacteria from wastewater were quantified using specific (selective and differential) media. All the media plates were prepared per the manufacturer's instructions on the media bottle (HiMedia). A list of bacteria quantified (referred to as biotic factors), along with the media used and colony characters, are listed in Table 3.

Wastewater samples were serially diluted in bacteriological saline and spread-plated (0.1 mL) in replicates on respective media plates. Plates were incubated

at 28 ± 2ºC (Nutrient Agar plates) and 37 ± 2ºC (Specific media plates) for 24-48 h till the colonies were observed. After incubation, colonies were counted, and numbers were represented as CFU (Colony Forming Unit).

Parameters like pH, Chemical Oxygen Demand (COD), Total Kjeldahl Nitrogen (TKN), Ammonical Nitrogen ($NH_4$-N), Phosphorus (P) (APHA 2005), and Nitrates ($NO_3^-$), Nitrites ($NO_2^-$) (Merk analysis Kit) were considered as abiotic factors and analyzed for all the samples, pH was measured by using Oakton pH meter.

The system's size and hydraulic loading rate are different for each, making it difficult to compare all three types of wetlands. So, to make the basis equal for comparison, load reduction per meter square of each wetland was calculated for biotic and abiotic parameters.

$$\text{Load removal rate (CFU/m}^2\text{ d)} = \left(\frac{Q(Ci - Co)}{A}\right) \times 10$$

Where Q is the inflow rate ($l.d^{-1}$), Ciand Coare is the concentration in the influent and effluent, respectively ($CFU.100mL^{-1}$), and A is the area of the bed ($m^2$).

### Statistical Analysis

All data were checked for normality and homogeneity of variances. ANOVA was performed to check the variation between the abiotic and biotic parameters with respect to wetlands. Further, Pearson correlation and Principal Component analysis (PCA) were performed to assess the relationship between the abiotic and biotic parameters. All the statistical analysis was performed using SPSS software. PCA analysis was done using Primer software.

## RESULTS

### Removal Efficiency Of Different VFCW

**Two-stage vertical flow constructed wetland (TSVFCW):** TSVFCW showed significant pathogen removal efficiency. The values of biotic factors reduction are given in Table 4 (both logarithmic units and load reduction per meter square). The total coliform number significantly reduced from $1.42 \times 10^7$ $CFU.100mL^{-1}$ to $1.65 \times 10^6$ $CFU.100mL^{-1}$ after the second stage with a 7.04 $\log_{10}$ reduction (Table 4). TSVFCW showed a 4.0 $\log_{10}$ reduction of *Salmonella* spp. The number of *Salmonella* spp. in inlet water was $2.3 \times 10^4$ $CFU.100mL^{-1}$, which was reduced to $7 \times 10^3$ $CFU.100mL^{-1}$ in outlet water. *Shigella* spp. number reduced from $3.7 \times 10^6$ $CFU.100mL^{-1}$ (Inlet water) to $3 \times 10^5$ $CFU.100mL^{-1}$ (outlet water), with 6.53$\log_{10}$ reduction. Pseudomonas's inlet water concentration was $9.9 \times 10^7$ $CFU.100mL^{-1,}$ which was reduced to $8.8 \times 10^7$ $CFU.100mL^{-1}$ after the first stage and further reduced to $5.2 \times 10^7$ $CFU.100mL^{-1}$ in outlet water resulting in 7.67$\log_{10}$ reduction. *Enterococcus* spp. number reduced from $1.06x10^6$ $CFU.100mL^{-1}$ to $3.08 \times 10^5$ $CFU.100mL^{-1}$ from inlet to outlet water, with 5.23$\log_{10}$ reduction. TSWFCW showed a 5.73 $\log_{10}$ reduction for *Vibrio* spp. The number of *Vibrio* spp. reduced from $1.37 \times 10^6$ $CFU.100mL^{-1}$ to $1.65 \times 10^4$ $CFU.100mL^{-1}$ from inlet to outlet water (Table 4).

TSWFCW efficiently reduced COD from 877 $mg.L^{-1}$ to 600 $mg.L^{-1}$ after the first stage and further decreased to 427 $mg.L^{-1}$ with 45 $g.m^{-2}$ average load reduction in outlet water. Nitrogen removal in TSVFCW was found to be significantly efficient in terms of TKN and $NH_4$-N reduction. TKN values reduced from 394 $mg.L^{-1}$ to 217 $mg.L^{-1}$ after the first stage and further reduced to 147 $mg.L^{-1}$ (24.7 $g.m^{-2}$ average load reduction) in outlet water. $NH_4$-N concentration significantly decreased from 59 $mg.L^{-1}$ to 34 $mg.L^{-1}$ after the first stage and further reduced to 17 $mg.L^{-1}$ after the second stage. Thus, resulting in a 4.2 $g.m^{-2}$ average load reduction after the second stage. $NO_3^-$ as well as $NO_2^-$concentration got increased in outlet water than in inlet water. The average load reduction of phosphorous of TSVFW was 3.1 $g.m^{-2}$. The pH of the inlet water was acidic (6), which was neutralized (7) after the first stage and became acidic (6) again after passing from the second stage (Table 5 and Fig. 3).

**Single-stage vertical flow constructed wetland (SSVFCW):** Pathogen removal was observed in SSVFCW. It showed a 5.28 $\log_{10}$ reduction of total coliform from inlet water ($2.5x10^5$ $CFU.100mL^{-1}$) to outlet water ($5.37x10^4$

Table 3: Identification of different bacteria based on characteristics of colony formed on specific media.

| | Bacteria | Media Used (HiMedia) | Characteristics of the colony selected |
|---|---|---|---|
| 1. | Total Coliforms (TC) | MacConkey's Agar | Pink-red with bile precipitate |
| 2. | *Pseudomonas* spp. (Pseu) | *Pseudomonas* agar | All the colonies were counted |
| 3. | *Salmonella* spp. (Sal) | SS Agar | Colorless with black centre |
| 4 | *Shigella* spp. (Shi) | SS Agar | Colorless |
| 5. | *Vibrio* spp. (VS) | Thiosulphate-Citrate-Bile Salts (TCBS) | Yellow and bluish green |
| 6. | *Enterococcus faecalis* (EF) | *Enterococcus* Agar | Pink to dark red |

CFU.100mL$^{-1}$). *Salmonella* spp. numbers reduced to 2.5x10$^2$ CFU.100mL$^{-1}$ from initial count 1.57x10$^4$ CFU.100mL$^{-1}$ with 3.74log$_{10}$ reduction. *Shigella* spp. count of inlet water was 1.83x10$^5$ CFU.100mL$^{-1}$ which reduced to 3.15x10$^4$ CFU.100mL$^{-1}$ in outlet water with 5.18 log$_{10}$ reduction. *Pseudomonas* spp. cell numbers reduced from 1.05x10$^7$ CFU.100mL$^{-1}$ to 1.12x10$^6$ CFU.100mL$^{-1}$ after treatment showing 6.98log$_{10}$ reduction. SSVFW showed a 4.74log$_{10}$ reduction of *Enterococcus* spp. Total *Vibrio* spp. It was reduced by 3.97log$_{10}$ from the inlet (1.7x10$^4$ CFU.100mL$^{-1}$) to outlet water (5.2x10$^3$ CFU.100mL$^{-1}$) (Table 4).

SSVFCW reduced COD with 12 g.m$^{-2}$ average load reduction from inlet water (470 mg.L$^{-1}$) to outlet water (198 mg.L$^{-1}$). SSVFCW showed a reduction in TKN and $NH_4$-N concentration, whereas $NO_3^-$ and $NO_2^-$ increased. TKN of the inlet was 448 mg.L$^{-1}$ which was reduced to 222 mg.L$^{-1}$ in outlet water (7.6 g.m$^{-2}$ average load reduction). $NH_4$-N was decreased to 50 mg.L$^{-1}$ from 174 mg.L$^{-1}$ showed 4.7 g.m$^{-2}$ average load reduction. However, $NO_3^-$ and $NO_2^-$ values increased from 2 mg.L$^{-1}$ and 0.07 mg.L$^{-1}$ to 22 mg.L$^{-1}$ and 2.59 mg.L$^{-1}$ after treatment by SSVFCW. The average load reduction of phosphorous was 12 g.m$^{-2}$ from inlet water (65 mg.L$^{-1}$) to outlet water (17mg.L$^{-1}$). The pH of the inlet was neutral (7), which became acidic (5) after treatment (Table 5 and Fig. 3).

**Single-stage saturated vertical flow constructed wetland (SSSVFCW):** Similar to other wetlands, SSSVFCW also showed effective removal of pathogenic bacteria. Total coliform showed a reduction in numbers by 4.48 log$_{10}$ decrease from the inlet (9.07x10$^4$ CFU.100mL$^{-1}$) to outlet water (4.35x10$^4$ CFU.100mL$^{-1}$).

*Salmonella* spp. cell numbers reduced from 1.11 × 10$^3$ CFU.100mL$^{-1}$ to 2.50 × 10$^2$ CFU.100mL$^{-1}$ after treatment showing 2.74log$_{10}$ reduction. SSSVFCW showed a 4.83 log$_{10}$ reduction in *Shigella* spp. from the inlet (7.5 × 10$^4$ CFU.100mL$^{-1}$) to outlet water (4 × 10$^3$ CFU.100mL$^{-1}$). *Pseudomonas* spp. number reduced to 7.25 × 10$^5$ CFU.100mL$^{-1}$ in outlet water from 5.8 × 10$^6$ CFU.100mL$^{-1}$ resulting in 6.71log$_{10}$ reduction. The removal efficiency for *Enterococcus* spp. was 5.30 log$_{10}$. The CFU.100mL$^{-1}$ reduced from 9.09 × 10$^5$ to 0 number in the outlet leading to the complete removal. *Vibrio* spp. also showed a 4.3 log$_{10}$ reduction from the inlet (3.65 × 10$^4$ CFU.100mL$^{-1}$) to the outlet (1.75x10$^3$ CFU.100mL$^{-1}$) after treatment (Table 4).

SSSVFCW reduced the concentration of COD by 6.3 g.m$^{-2}$ from the inlet (190 mg.L$^{-1}$) to outlet water (108 mg.L$^{-1}$). Nitrogen removal in SSSVFCW was also observed, wherein TKN was significantly removed by 7.7 g.m$^{-2}$ average load reduction. $NH_4$-N concentration reduced to 22 mg.L$^{-1}$ from 86 mg.L$^{-1}$ with 4.5 g.m$^{-2}$ average load reduction. However, $NO_3^-$and $NO_2^-$concentrations increased after treatment by SSSVFCW as observed in other wetlands, $NO_3^-$ and $NO_2^-$ concentrations increased to 45 mg.L$^{-1}$ and 0.37 mg.L$^{-1}$ from 4 mg.L$^{-1}$ and 0.02, respectively. Phosphorous was removed efficiently with 1.2 g.m$^{-2}$ average load reduction from the inlet (25 mg.L$^{-1}$) and outlet (7 mg.L$^{-1}$). The inlet water had neutral (7) pH that became acidic (6) after treatment by wetland (Table 5 and Fig. 3).

**Removal efficiency of biotic and abiotic parameters by different VFCWs:** All wetlands removed the abiotic and biotic factors with varying degrees. In terms of pathogenic bacterial removal, all three wetlands showed pathogen reduction, but TSWFCW was found to be more efficient in removing all the pathogens studied (Table 5). However, there was not much difference in the removal of *Pseudomonas* spp. and *Enterococcus* spp. of TSVFCW, SSVFCW, and SSSVFCW.

Among the three types of wetlands, TSWFCW was found to be efficient in removing COD, TKN, and phosphorous with 45, 24.7, and 3.1 g.m$^{-2}$ average load reduction, respectively. $NH_4$-N (4.7 g.m$^{-2}$) was removed efficiently by SSVFCW compared to the TSWFCW and SSSVFCW. The pH of the outlet water of TSVFCW and SSSVFCW was 6, and of SSVFCW, it was 5.

TSVFCW was found to be efficient in removing abiotic (Table 5) and biotic factors compared to the single-stage wetlands. Still, the removal efficiencies of both the single-stage wetland were comparable.

The correlation of different water quality parameters showed a positive correlation, indicating that these parameters favor the growth of pathogenic bacteria. However, from the correlation matrix of the water quality parameters, it is evident that there is a reduction in abiotic and biotic parameters. PCA analyses revealed a significant inverse relationship between all the parameters and $NO_3^-$ and $NO_2^-$ (Fig. 4). There is a significant reduction of all the abiotic and biotic parameters however increase in $NO_3^-$ and $NO_2^-$ in all the wetlands (Table 5). All the pathogenic bacteria showed a significant positive correlation with pH, TKN, $NH_4$-N, and COD.

### Areal Removal Rates of Biotic Factors

TSVFCW had the greatest areal removal rate for all pathogens compared to other wetlands. When the first and second stages of TSVFCW are compared, the second stage (TC, Shi, Sal, Pseu, and Vibrio species: -10.1, 7.2, 9.5, 10.7, 8.9 and 9.1Log$_{10}$CFU.m$^{-2}$.d$^{-1}$ reduction respectively) has a higher removal efficiency than the first (TC, Shi, Sal, Pseu, and Vibrio specie: -10.0, 7.0, 9.4, 10.0, 7.5, and 9.0Log$_{10}$

Table 4: Pathogen concentration at inlet and outlet and removal rates for different wetlands.

| Wetland Type | | Total Coliform (TC) | *Shigella* spp. (Shi) | *Salmonella* spp.(Sal) | *Pseudomonas* spp. (Pseu) | *Vibrio* spp. (VS) | *Enterococcus faecalis* (EF) |
|---|---|---|---|---|---|---|---|
| TSVFCW (HLR 100 l.m$^{-2}$d$^{-1}$) | Influent concentration [CFU.100mL$^{-1}$] | $1.4 \times 10^7 \pm 1.2 \times 10^6$ | $3.7 \times 10^6 \pm 8.8 \times 10^4$ | $2.3 \times 10^4 \pm 4.7 \times 10^3$ | $9.9 \times 10^7 \pm 8.0 \times 10^6$ | $1.4 \times 10^6 \pm 3.1 \times 10^5$ | $1.1 \times 10^6 \pm 2.6 \times 10^5$ |
| | Effluent concentration [CFU.100mL$^{-1}$] | $2.4 \times 10^6 \pm 1.9 \times 10^5$ | $3.0 \times 10^5 \pm 5.0 \times 10^4$ | $7.0 \times 10^3 \pm 1.7 \times 10^3$ | $5.2 \times 10^7 \pm 5.9 \times 10^6$ | $1.7 \times 10^4 \pm 4.1 \times 10^3$ | $3.1 \times 10^5 \pm 7.3 \times 10^4$ |
| | $Log_{10}$ reduction [CFU.100mL$^{-1}$] | $7.04 \pm 0.17$ | $6.53 \pm 0.08$ | $4.0 \pm 0.42$ | $7.67 \pm 0.08$ | $5.73 \pm 0.70$ | $5.23 \pm 0.96$ |
| | Areal load removal rate [CFU.m$^2$.d$^{-1}$] | $1.18 \times 10^{10} \pm 5.41 \times 10^8$ | $3.40 \times 10^9 \pm 6.88 \times 10^7$ | $1.60 \times 10^7 \pm 3.0 \times 10^6$ | $4.70 \times 10^{10} \pm 1.06 \times 10^9$ | $1.35 \times 10^9 \pm 1.56 \times 10^8$ | $7.59 \times 10^8 \pm 9.26 \times 10^7$ |
| SSVFCW [HLR 37.5 l. m$^2$.d$^{-1}$] | Influent concentration [CFU.100mL$^{-1}$] | $2.60 \times 10^5 \pm 6.38 \times 10^3$ | $1.84 \times 10^5 \pm 6.88 \times 10^2$ | $1.58 \times 10^4 \pm 3.69 \times 10^3$ | $1.06 \times 10^7 \pm 2.13 \times 10^5$ | $1.70 \times 10^4 \pm 5.00 \times 10^2$ | $3.27 \times 10^5 \pm 8.07 \times 10^4$ |
| | Effluent concentration [CFU.100mL$^{-1}$] | $5.38 \times 10^4 \pm 1.34 \times 10^4$ | $3.15 \times 10^4 \pm 7.87 \times 10^3$ | $2.51 \times 10^2 \pm 6.24 \times 10^1$ | $1.12 \times 10^6 \pm 2.58 \times 10^5$ | $5.25 \times 10^3 \pm 1.31 \times 10^3$ | 0.00 |
| | $Log_{10}$ reduction [CFU.100mL$^{-1}$] | $5.28 \pm 0.18$ | $5.18 \pm 0.09$ | $3.74 \pm 0.74$ | $6.98 \pm 0.01$ | $3.97 \pm 0.32$ | $4.74 \pm 1.08$ |
| | Areal load removal rate [CFU.m$^2$.d$^{-1}$] | $7.72 \times 10^7 \pm 3.71 \times 10^6$ | $5.71 \times 10^7 \pm 1.35 \times 10^6$ | $5.81 \times 10^6 \pm 6.80 \times 10^5$ | $3.54 \times 10^9 \pm 8.44 \times 10^6$ | $4.41 \times 10^6 \pm 3.40 \times 10^5$ | $1.23 \times 10^8 \pm 1.51 \times 10^7$ |
| SSSVFCW [HLR 66.7 l. m$^2$.d$^{-1}$] | Influent concentration [CFU.100mL$^{-1}$] | $9.08 \times 10^4 \pm 2.31 \times 10^3$ | $7.50 \times 10^4 \pm 6.25 \times 10^3$ | $1.11 \times 10^3 \pm 2.25 \times 10^2$ | $5.80 \times 10^6 \pm 1.50 \times 10^5$ | $3.65 \times 10^4 \pm 8.31 \times 10^3$ | $9.09 \times 10^5 \pm 2.23 \times 10^5$ |
| | Effluent concentration [CFU.100mL$^{-1}$] | $4.35 \times 10^4 \pm 6.88 \times 10^3$ | $4.00 \times 10^3 \pm 5.00 \times 10^2$ | $2.50 \times 10^2 \pm 6.25 \times 10^1$ | $7.25 \times 10^5 \pm 8.13 \times 10^4$ | $1.75 \times 10^3 \pm 4.38 \times 10^2$ | 0.00 |
| | $Log_{10}$ reduction [CFU.100mL$^{-1}$] | $4.48 \pm 0.46$ | $4.83 \pm 0.15$ | $2.74 \pm 0.44$ | $6.71 \pm 0.03$ | $4.31 \pm 0.49$ | $5.03 \pm 1.20$ |
| | Areal load removal rate [CFU.m$^2$.d$^{-1}$] | $3.15 \times 10^7 \pm 3.06 \times 10^6$ | $4.74 \times 10^7 \pm 1.92 \times 10^6$ | $5.67 \times 10^5 \pm 1.08 \times 10^4$ | $3.39 \times 10^9 \pm 2.29 \times 10^7$ | $2.32 \times 10^7 \pm 4.71 \times 10^6$ | $6.06 \times 10^8 \pm 1.49 \times 10^8$ |

$CFU.m^{-2}.d^{-1}$ reduction respectively) (Fig. 2). Table 4 shows that SSVFCW wetland has higher removal efficacy for TC, Shi, Sal, Pseu, and Vibrio species than SSSVFCW. SSVFCW outperforms SSVFCW in terms of EF removal efficiency. Both wetland exhibit 100 percent EF removal with 0.0 $CFU.100mL^{-1}$ concentration in the outlet, indicating that both types of wetlands might have similar EF removal efficiency as the difference in removal efficiency is dependent on the inlet concentration in this case (Fig. 2).

## DISCUSSION

The present study revealed the importance of constructed wetlands in reducing pathogens in wastewater. However, the type of pathogen removal is dependent on the constructed wetland used for the treatment (Weber & Legge 2008, Wu et al. 2016) also demonstrated that *Salmonella* spp. is bacteria of great concern as well as a good representative of the reduction of other bacterial pathogens because they are typically

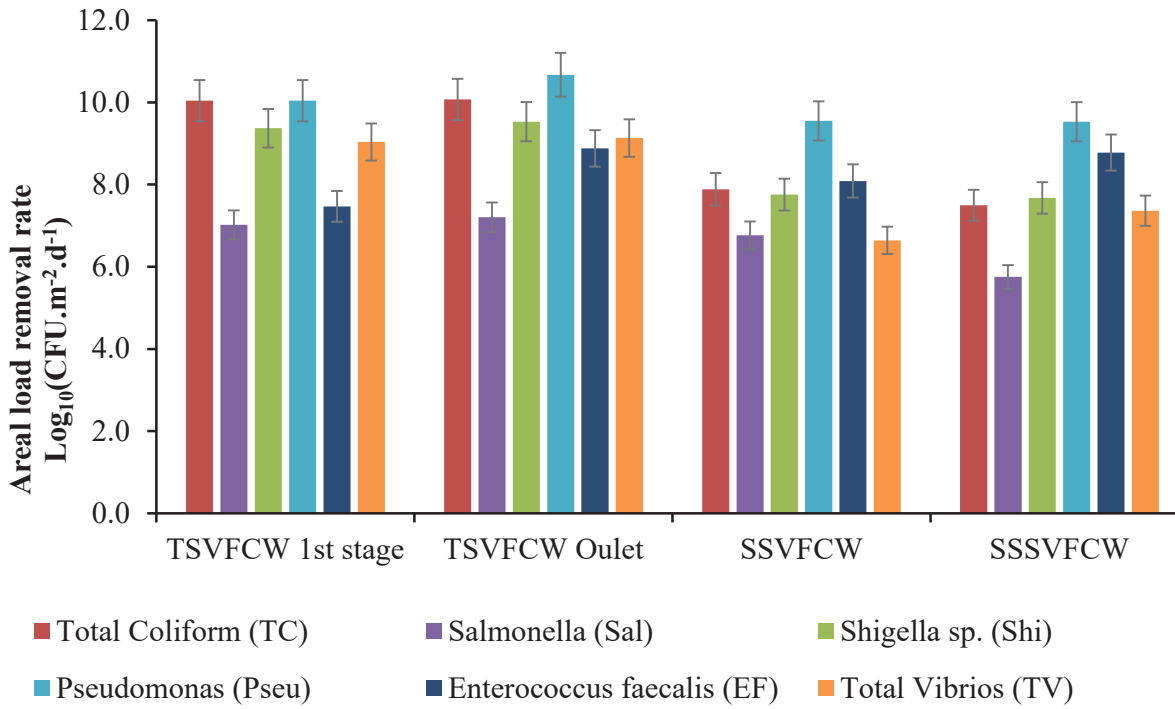


Fig. 2: Areal load reduction of Biotic parameters

Table 5: Concentration of abiotic parameters in all three types of wetlands.

| | COD [ppm] | TKN [ppm] | Nitrate [ppm] | Nitrite [ppm] | $NH_3$-N [ppm] | $PO_4$ [ppm] | pH |
|---|---|---|---|---|---|---|---|
| TSVFW | | | | | | | |
| Inlet | 877 ± 18 | 394 ± 66 | 1.23 ± 0.61 | 0.17 ± 0 | 59 ± 10 | 61 ± 3 | 6 ± 0.05 |
| 1st stage | 600 ± 64 | 217 ± 35 | 1.05 ± 0.53 | 0.17 ± 0.02 | 34 ± 7 | 42 ± 2 | 7 ± 0.11 |
| 2nd stage | 427 ± 68 | 147 ± 21 | 14 ± 0.34 | 2 ± 0.45 | 17 ± 3 | 31 ± 5 | 6 ± 0.08 |
| SSVFW | | | | | | | |
| Inlet | 470 ± 8 | 448 ± 7 | 2 ± 0.95 | 0.07 ± 0.01 | 174 ± 7 | 65 ± 0.37 | 7 ± 0.02 |
| outlet | 198 ± 20 | 222 ± 1 | 22 ± 3 | 3 ± 0.25 | 50 ± 4 | 17 ± 4 | 5 ± 0.7 |
| SSSVFW | | | | | | | |
| Inlet | 190 ± 12 | 273 ± 4 | 4 ± 2 | 0.07 ± 0.02 | 86 ± 13 | 25 ± 3 | 7 ± 0.07 |
| outlet | 108 ± 33 | 152 ± 3 | 45 ± 4 | 1.27 ± 0.37 | 22 ± 4 | 7 ± 1 | 6 ± 0.09 |

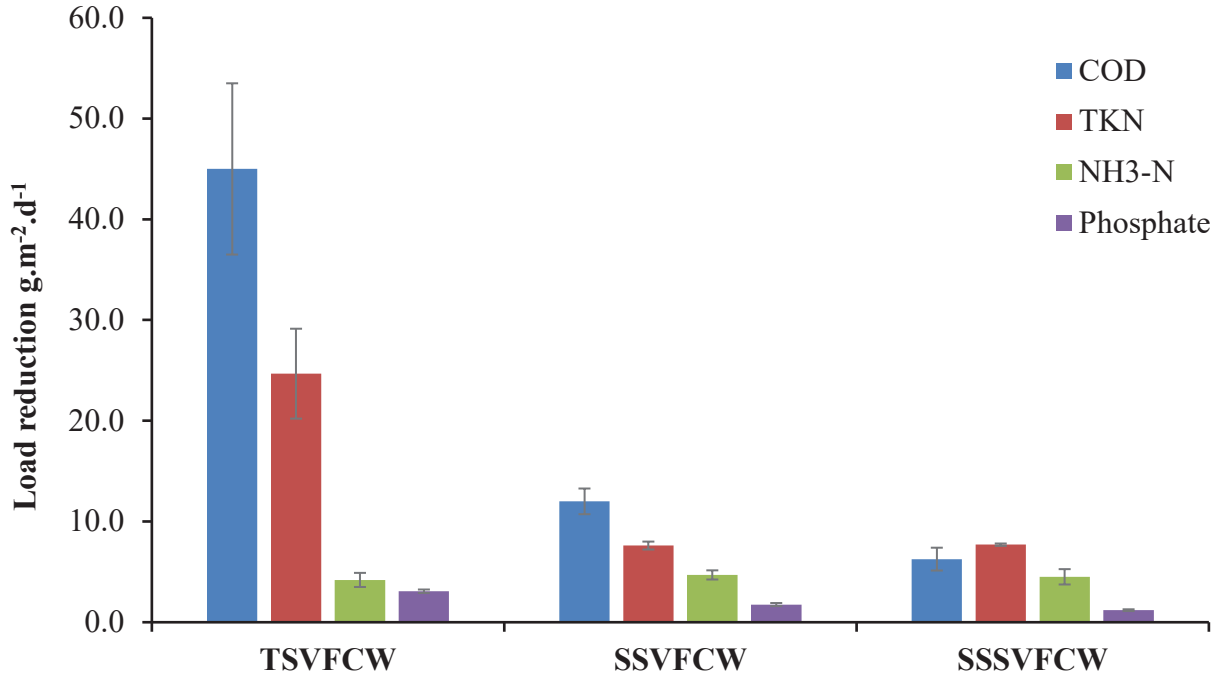


Fig. 3: Areal load reduction of abiotic parameters.

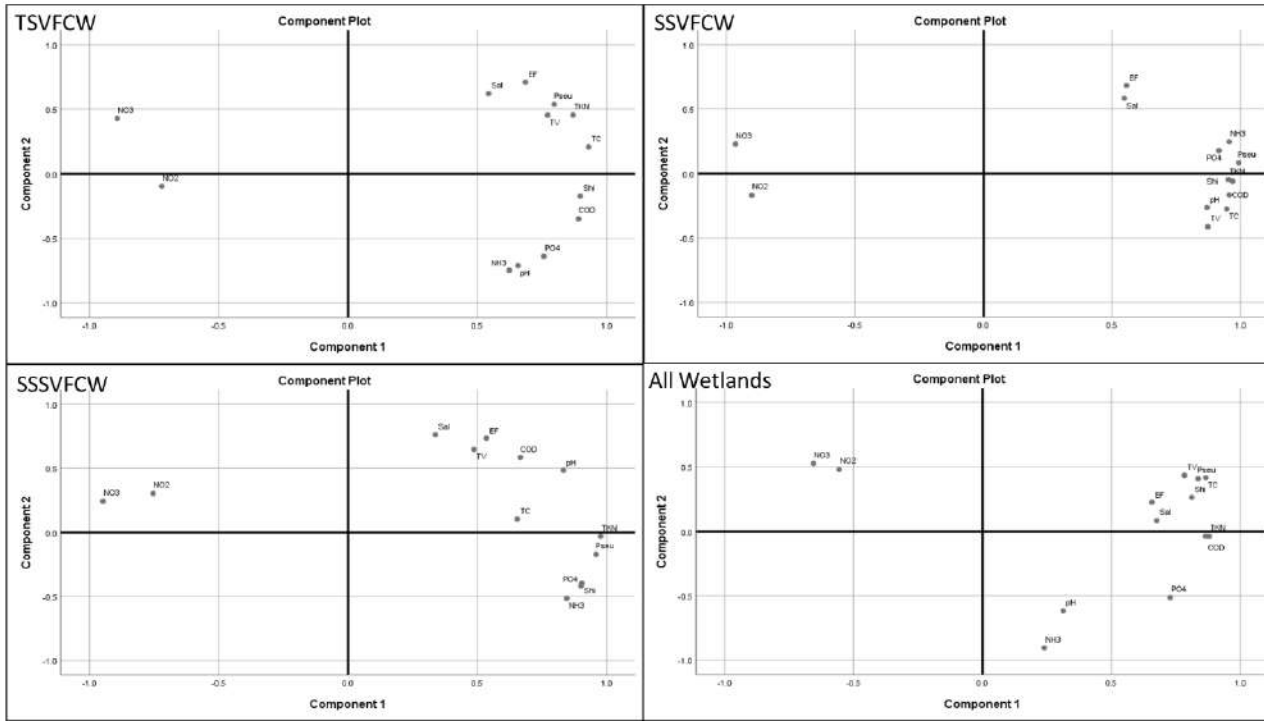


Fig. 4: Principal component analysis for all the TSVFCW, SSVFCW, SSSVFCW, and All wetlands together.

present in higher densities than other bacterial pathogens and can survive for a long time in the environment. TSVFCW significantly reduces all the pathogenic bacteria (Total Coliforms, *Shigella* spp., *Salmonella* spp., *Pseudomonas* spp., *Vibrio* spp., *Enterococcus faecalis*: -7.04 ± 0.17, 6.53 ± 0.08, 4.0 ± 0.42, 7.67 ± 0.08, 5.73 ± 0.70 and10 5.23 ± 0.96$Log_{10}$ reductions respectively) thus suggesting its highest removal efficiency from wastewater compared to other two wetlands SSVFCW (5.28 ± 0.18, 5.18 ± 0.09, 3.74 ± 0.74, 6.98 ± 0.01, 3.97 ±0.32, 4.74 ± 1.08$Log_{10}$ reductions respectively) and SSSVFCW (4.48 ± 0.46, 4.83 ± 0.15, 2.74 ± 0.44, 6.71 ± 0.03, 4.31±0.49, 5.03 ± 1.20$Log_{10}$ decreases respectively).

Pathogen removal in VFCW depends on many physical, chemical, and biological processes like filtration, adsorption, sedimentation, residence time, oxidation, predation activity, and biolytic processes. But in the case of TSVFCW and SSVFCW, the residence time is very low, which will not provide sufficient time for sedimentation and other chemical or biological processes (Alexandros. et al. 2016). According to Arias et al. (2003), the first stage of TSVFCW wetland was more efficient in the removal of fecal coliform (0.8-1.7$Log_{10}$ unit) than that of 2nd stage (0.5-1.1$Log_{10}$ unit) and suggested that the removal efficacy of the system depends on inlet concentration rather than hydraulic loading. The result shows that TSVFCW has a higher inlet concentration of pathogens than single-stage wetlands (Table 4), suggesting a higher removal rate for TSVFCW. The current study also observed that both stages of TSVFCW have the same loading rate. Even though receiving a lower inlet concentration of pathogens for 2nd stage (as it receives water after the 1st stage treatment), it still shows an equivalent removal efficiency (Fig 2). This suggests the removal efficiency also depends on the size (0-2 mm sand layer on the top for 2nd stage) of the media used in the bed (Arias et al. 2003, Pundsack et al. 2001, Wang et al. 2021). Pundsack et al. (2001) were able to reduce *Salmonella* in the order of 1-9$Log_{10}$ from winter to summer using different types of sand and peat filters, which is also comparable to the result obtained in the current study (*Salmonella*: 2.7-4$Log_{10}$ reduction). So, it can be concluded that the pathogen removal in VFCWs is mainly filtration through the media or adsorption of the pathogen to the surface of the media. After filtration or adsorption, the pathogens are neutralized by natural die-offs or other chemical and biological processes.

SSSVFCW also showed comparatively lower pathogen removal than other unsaturated wetlands (TSVFCW and SSVFCW), as unsaturated flow is likely to provide better removal conditions than saturated flow (Stevik et al. 2004). Higher the size and density, the higher the sedimentation rate. This allows the bacteria with a higher settling velocity, such as fecal coliforms, fecal *streptococci*, and helminths, to be removed more efficiently than other microorganisms (e.g., protozoa cysts) and viruses (Alexandros & Akratos 2016). Comparing all three types of wetlands (Fig. 2), it was observed that TSVFCW are more efficient in terms of pathogen removal, indicating that filtration through both stages plays a cumulative role in pathogen removal.

The overall organics (COD) removal efficiency of all three types of wetlands (TSVFCW, SSVFCW, and SSSVFCW are 45, 12, and 6.3 $g.m^{-2}.d^{-1}$ was found to be lower as compared to other reported studies by Abdelhakeem et al. (2016) which was around 60.8 $g.m^{-2}.d^{-1}$ in gravel and vermiculite media and in the study reported by Herouvim et al. (2011) which was around 217 $g.m^{-2}.d^{-1}$. Also, in the study on two experimental combined wetlands in tropical climates reported by Kantawanichkul et al. (2003), the average COD removal rate was 53.3 $g.m^{-2}.d^{-1}$ for the first system (combined). For the other two-stage system, it was 82.9 $g.m^{-2}.d^{-1}$. This may be due to the low batch frequency of the wetland (Kengne et al. 2019), which was just three times per day in the case of TSVFCW and SSVFCW. In the case of the SSSVFCW wetland, it was purging (mainly in the morning and very few times during the whole day) the water only when the toilet was in use, so per batch volume was also low. The hydraulic aspect of VFCW is significant; one important factor is the number of batches applied per day (batch frequency), which can influence the oxygen transfer rate (Molle 2014, Green et al. 1997, Abou-Elela et al. 2013). The high number of batches applied daily can reduce the volume per batch, favoring more organic removal (Kengne et al. 2019, Brix & Arias 2005).

French VFCW are designed for a higher oxygen transfer rate, which helps in the growth of nitrifying bacteria favoring the nitrification of organic nitrogen in the wastewater. In this study, the batch frequency per day was low (Table 1). So, the batch volume was significant, which favored a high oxygen transfer rate in the wetland, resulting in a high nitrification rate (Molle et al. 2006, Brix & Arias 2005), leading to high TKN and $NH_3$-N removal per $m^2$ of the area as compared to study Abdelhakeem et al. (2016) ($NH_3$-N:-1.1-2.1 $g.m^{-2}.d^{-1}$). The decrease in NO3- and NO2- after the first stage of TSVFCW indicates the development of anaerobic areas in the wetland, favoring the denitrification of available nitrates and nitrites (Table 5) (Sirivedhin & Gray 2006). The $NO_3^-$ and $NO_2^-$ concentrations increased in the outlet of SSVFCW, SSSVFCW, and after the second stage of TSVFCW, indicating better aerobic conditions in the wetland. This is also evident from PCA analysis. SSSVFCW was designed to provide an anaerobic condition at the bottom by adding

a saturated layer to enhance denitrification. Since the hydraulic loading rate was very low and water was pumped out continuously throughout the day with a peristaltic pump shown in Fig. 4 (for post-wetland treatment, which is not included in the current study). It may develop a suction at the bottom of the wetland, resulting in more air entering and helping to make the wetland aerobic (Brix & Arias 2005).

## CONCLUSION

The study points out significant pathogenic bacterial removal efficiency by VFCWs. All three types of wetlands studied effectively removed pathogenic bacteria and abiotic parameters with varying degrees despite short residence time. The study concludes with a few key points below.

1. The pathogen removal efficiency of VFCW constructed depends on the filtration media and the size of the media used.
2. The removal efficiency of VFCW depends on the inlet pathogen concentration of wastewater. Higher inlet pathogen concentration leads to a higher removal rate.
3. The study also concluded that removal efficacy depends on the number of stages used to treat wastewater. Two stages have better removal efficiency than single-stage vertical flow wetlands.
4. Unsaturated VFCW have higher removal efficacy than saturated VFCW

VFCW can be a very efficient technology for treating raw sewage in rural areas of India, as it does not require higher operating costs or any particular skill. Still, further treatment is required to ensure the safe reuse of wastewater for the complete inactivation of pathogens.

## ACKNOWLEDGMENT

The authors also greatly acknowledge the support of BITS-Pilani K.K. Birla Goa Campus for providing the facility for the work.

## DECLARATION

The authors also confirm that the analyzed data supporting the findings of this study can be obtained from the corresponding author (SM) on request.

## REFERENCES

Abdelhakeem, S.G., Aboulroos, S.A. and Kamel, M.M. 2016. Performance of a vertical subsurface flow constructed wetland under different operational conditions. J. Adv. Res., 7(5): 803-814.

Abou-Elela, S.I., Golinielli, G., Abou-Taleb, E.M. and Hellal, M.S. 2013. Municipal wastewater treatment in horizontal and vertical flows constructed wetlands. Ecol. Eng., 61: 460-468.

Agrawal, G.D., 1999. Diffuse agricultural water pollution in India. Water Sci. Technol., 39(3): 33-47.

Alexandros, S.I. and Akratos, C.S. 2016. Removal of Pathogenic Bacteria in Constructed Wetlands: Mechanisms and Efficiency. Springer, Cham, pp. 327-346.

American Public Health Association (APHA), 2005. Standard Methods for the Examination of Water and Wastewater. Twenty-First edition. American Public Health Association, Washington, DC

Arias, C.A., Cabello, A., Brix, H. and Johansen, N.H. 2003. Removal of indicator bacteria from municipal wastewater in an experimental two-stage vertical flow constructed wetland system. Water Sci. Technol., 48(5): 35-41.

Axelrood, P.E., Clarke, A.M., Radley, R. and Zemcov, S.J.V. 1996. Douglas-fir root-associated microorganisms with inhibitory activity towards fungal plant pathogens and human bacterial pathogens. Canad. J. Microbiol., 7)42): 690-700.

Badejo, A.A., Omole, D.O. and Ndambuki, J.M. 2018. Municipal wastewater management using Vetiveriazizanioides planted in vertical flow constructed wetland. Appl. Water Sci., 8(4): 1-6.

Brix, H. and Arias, C.A. 2005. The use of vertical flow constructed wetlands for on-site treatment of domestic wastewater: New Danish guidelines. Ecol. Eng., 25(5): 491-500.

Chandana, N. and Rao, B. 2021. Status of sustainable sanitation chain in rural, semi-urban, and urban regions: a case study of Maharashtra, India. J. Water Sanit. Hyg. Dev., 11(1): 112-125.

CPCB 2022. National Inventory of Sewage Treatment Plants. https://cpcb.nic.in/openpdffile.php?id (Accessed 1 March 2022).

Díaz, F.J., O'Geen, A.T. and Dahlgren, R.A. 2010. Efficacy of constructed wetlands for removal of bacterial contamination from agricultural return flows. Agric. Water Manag., 97(11): 1813-1821.

Dzakpasu, M., Scholz, M., McCarthy, V. and Jordan, S.N. 2015. Assessment of long-term phosphorus retention in an integrated constructed wetland treating domestic wastewater. Environ. Sci. Pollut. Res., 22(1): 305-313.

Franceys, R., Pickford, J. and Reed, R. 1992. A guide to the development of on-site sanitation. World Health Organization, Washington DC.

Gerba, C.P. and McLeod, J.S. 1976. Effect of sediments on the survival of Escherichia coli in marine waters. Appl. Environ. Microbiol., 32(1): 114-120.

Gersberg, R.M., Brenner, R., Lyon, S.R. and Elkins, B.V. 1987. Survival of bacteria and viruses in municipal wastewaters applied to artificial wetlands. Appl. Environ. Microbiol., 53(4): 2037.

Gersberg, R.M., Gearheart, R.A. and Ives, M. 1989. Pathogen Removal in Constructed Wetlands. Lewis Publishers, Chelsea, UK, pp. 431-445

Goel, P.K. 2006. Water Pollution: Causes, Effects, and Control. New Age International, Tamil Nadu.

Green, M.B., Griffin, P., Seabridge, J.K. and Dhobie, D. 1997. Removal of bacteria in subsurface flow wetlands. Water Sci. Technol., 35(5): 109-116.

Hendricks, C.W. 1971. Increased recovery rate of salmonellae from stream bottom sediments versus surface waters. Appl. Microbol., 21(2): 379-380.

Herouvim, E., Akratos, C.S., Tekerlekopoulou, A. and Vayenas, D.V. 2011. Treatment of olive mill wastewater in pilot-scale vertical flow constructed wetlands. Ecol. Eng., 37(6): 931-939.

Jain, A., Wagner, A., Snell-Rood, C. and Ray, I. 2020. Understanding open defecation in the age of Swachh Bharat Abhiyan: Agency, accountability, and anger in rural Bihar. Int. J. Environ. Res. Pub. Health 17(4): 1384.

Kantawanichkul, S., Somprasert, S., Aekasin, U. and Shutes, R.B.E. 2003. Treatment of agricultural wastewater in two experimental combined constructed wetland systems in a tropical climate. Water Sci. Technol., 48(5): 199-205.

Kaur, R., Wani, S.P., Singh, A.K. and Lal, K. 2012. Wastewater production,

treatment, and use in India. In National Report Presented at the 2nd Regional Workshop on Safe Use of Wastewater In Agriculture, 16-18 May 2012, New Delhi, UNW-AIS, pp. 1-13.

Kengne, E.S., Nzouebouet, W.A.L., Djumyom, G.V. and Noumsi, I.M.K. 2019. Effect of feeding frequency on the performance of Compact Vertical Flow Constructed Wetland treating faecal sludge leachate under high hydraulic load. Int. J. Biol. Chem. Sci., 13(5): 68-80.

Massoud, M.A., Tarhini, A. and Nasr, J.A. 2009. Decentralized approaches to wastewater treatment and management: Applicability in developing countries. J. Environ. Manag., 90(1): 652-659.

Molle, P. 2014. French vertical flow constructed wetlands: a need of a better understanding of the role of the deposit layer. Water Sci. Technol., 69(1): 106-112.

Molle, P., Liénard, A., Grasmick, A. and Iwema, A. 2006. Effect of reeds and feeding operations on hydraulic behaviour of vertical flow constructed wetlands under hydraulic overloads. Water Res., 3)40): 606-612.

Morvannou, A., Forquet, N., Michel, S., Troesch, S. and Molle, P. 2015. Treatment performances of French constructed wetlands: results from a database collected over the last 30 years. Water Sci. Technol., 71(9): 1333-1339.

Pang, Y., Zhang, Y., Yan, X. and Ji, G. 2015. Cold temperature effects on long-term nitrogen transformation pathway in a tidal flow constructed wetland. Environ. Sci. Technol., 49(22): 13550-13557.

Pundsack, J., Axler, R., Hicks, R., Henneck, J., Nordman, D. and McCarthy, B. 2001. Seasonal pathogen removal by alternative on□site wastewater treatment systems. Water Environ. Res., 73(2): 204-212.

Schellenberg, T., Subramanian, V., Ganeshan, G., Tompkins, D. and Pradeep, R. 2020. Wastewater discharge standards in the evolving context of urban sustainability: The case of India. Front. Environ. Sci., 8: 30.

Singh, A., Sawant, M., Kamble, S.J., Herlekar, M., Starkl, M., Aymerich, E. and Kazmi, A. 2019. Performance evaluation of a decentralized wastewater treatment system in India. Environ. Sci. Pollut. Res., 26(21): 21172-21188.

Sirivedhin, T. and Gray, K.A. 2006. Factors affecting denitrification rates in experimental wetlands: Field and laboratory studies. Ecol. Eng., 26(2): 167-181.

Stevik, T.K., Aa, K., Ausland, G. and Hanssen, J.F. 2004. Retention and removal of pathogenic bacteria in wastewater percolating through porous media: a review. Water Res., 38(6): 1355-1367.

Talekar, G.V., Sharma, P., Yadav, A., Clauwaert, P., Rabaey, K. and Mutnuri, S. 2018. Sanitation of blackwater via sequential wetland and electrochemical treatment. Clean Water, 1(1): 1-9.

Van Donsel, D.J. and Geldreich, E.E. 1971. Relationships of Salmonellae to fecal coliforms in bottom sediments. Water Res., 5(11): 1079-1087.

Wang, M., Zhu, J. and Mao, X. 2021. Removal of pathogens in onsite wastewater treatment systems: A review of design considerations and influencing factors. Water, 13(9): 1190.

Weber, K.P. and Legge, R.L. 2008. Pathogen removal in constructed wetlands. Wetlands Ecol. Conserv. Restor., 16: 1-35.

Wu, S., Carvalho, P.N., Müller, J.A., Manoj, V.R. and Dong, R. 2016. Sanitation in constructed wetlands: a review on the removal of human pathogens and fecal indicators. Sci. Total Environ., 541: 8-22.

Yadav, A., Chazarenc, F. and Mutnuri, S. 2018. Development of the "French system" vertical flow constructed wetland to treat raw domestic wastewater in India. Ecol. Eng., 113: 88-93.

Nature Environment and Pollution Technology
An International Quarterly Scientific Journal

p-ISSN: 0972-6268
(Print copies up to 2016)
e-ISSN: 2395-3454

Vol. 22 | No. 1 | pp. 445-461 | 2023

Original Research Paper

https://doi.org/10.46488/NEPT.2023.v22i01.043

Open Access Journal

# Modeling of Activated Sludge Process Using Multi-Layer Perceptron Neural Networks

**Saurabh Sahadev*(**) †, G. Madhu** and M. Roy Thomas****
*Department of Chemical Engineering, Government Engineering College, Thrissur, Kerala, India
**School of Engineering, Cochin University of Science and Technology, Kochi, Kerala, India
†Corresponding author: Saurabh Sahadev; saurabhsdev@gmail.com

**Nat. Env. & Poll. Tech.**
**Website: www.neptjournal.com**

*Received:* 14-07-2022
*Revised:* 01-10-2022
*Accepted:* 15-10-2022

**Key Words:**
Activated sludge process
Modeling
Biochemical oxygen demand
Suspended solids

## ABSTRACT

Mathematical Modeling of the activated sludge process (ASP) enhances the understanding of the process and improves the quality of the effluent released. However, as the process is complex and nonlinear, mathematical modeling of the process has been a challenge. In this study, multi-layer perceptron neural networks (MLP-ANN) are investigated to predict water quality parameters for better control of wastewater treatment plants employing an activated sludge process. The study area selected was in a central district of the southern state of India. The parameters to be investigated are biochemical oxygen demand (BOD), suspended solids (SS), and pH. The model is evaluated based on statistical parameters of correlation coefficient R and mean square error (MSE). The neural network toolbox of MATLAB 2015b is used for modeling and simulation study. It has been found that effluent biochemical oxygen demand was predicted with a maximum correlation coefficient of 0.927 and minimum mean square error of 0.0022, effluent suspended solids were predicted with a maximum correlation coefficient value of 0.947 and minimum mean square value of 0.0058, effluent pH was predicted with a maximum correlation coefficient value of 0.8299 and minimum mean square value of 0.0132.

## INTRODUCTION

India has finished at the bottom of the Environment Performance Index-2022 released by the World Bank. This means India is among those countries in the world that have the worst environmental health. Out of 180 countries that have been ranked, India is in the bottom five with a score of 18.9. The study area selected is in a central district of the southern Indian state of Kerala.

Water resources management and planning require the development of the evaluation system and processes for the maintenance of effluent water quality parameters and conforming to health and environmental standards. (Hamed et al. 2004). Treatment of wastewater using biological processes has been found very promising and the activated sludge process (ASP) is one of the most preferred processes among them. It utilizes microorganisms like bacteria to remove contaminants by digesting them. Mathematical models are required for better control of treatment plants so that treated effluent conforms to environmental standards. Also tuning of operating parameters can be studied more effectively by models and alternate control strategies can be developed on computers without the need for actual systems. (Pai et al. 2011). Simulations of models using operating parameters lead to rapid responses in the event of unforeseen changes in processes, (Nair et al. 2016); Several mechanistic models were developed and used as the mechanistic models can predict beyond the range of data, but these techniques require a large amount of data and have complex nonlinear interaction between variables, (Fu & Poch 1995). Also, several factors which affect plant performance and are part of mechanistic model representation are routinely not monitored in actual plants. (Henze et al. 1987). Also, unpredictable conditions such as toxic material release, and explosions, (Manfred et al. 2002) are difficult to model.

Artificial Intelligence (AI) approaches mimic the human ability of learning and rational problem solving for better control of complex engineering systems. Artificial neural networks (ANN) are employed to model wastewater treatment processes due to high accuracy, less time for model development, and a limited amount of data required, (Pareek et al. 2002). Artificial neural networks require no explicit knowledge of processes and parameters and develop knowledge through historical observations of input-output data. They learn by examples and with suitable design, accurate predictions are obtained. However, the

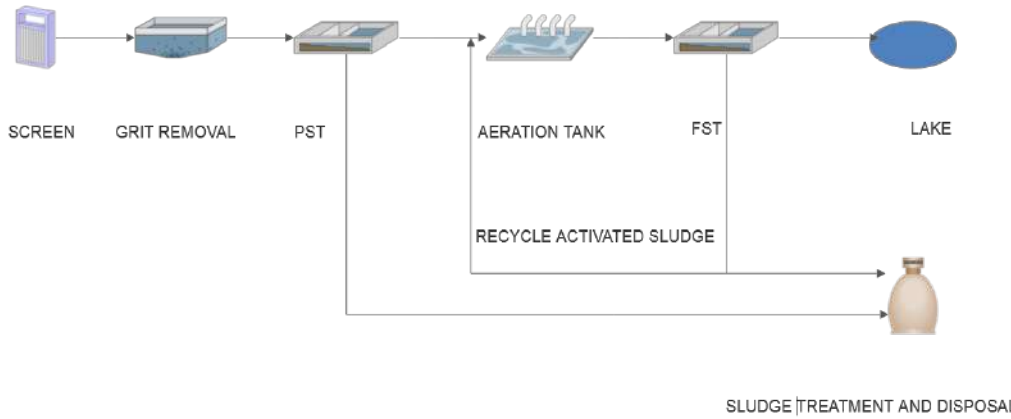


Fig. 1: Schematic of the sewage treatment plant.

limitation of the artificial neural network is that they do not compute outside the range of training data, (Vos & Rientjes 2005).

In the activated sludge process many variables are utilized to evaluate plant operation. These variables include biochemical oxygen demand (BOD), chemical oxygen demand (COD), total suspended solids (TSS), pH, etc. The literature survey done in this study area has used these variables and found that modeling sewage treatment plants using artificial neural networks is an effective tool in predicting effluent parameters.

The outcome of this research was to find the best model which represents the activated sludge process in terms of BOD, SS, and pH prediction. The data collected were fluctuating under different seasons and periods of the year. The study was conducted to model STP performance by using soft computing techniques of feed-forward multilayer perceptron artificial neural networks (FFMLP). The main aim was to find the best network structure of the artificial neural network for predicting effluent parameters.

## MATERIALS AND METHODS

### Study Area

The sewage treatment plant studied is situated in a central district of the southern state of Kerala in India. The plant which started its operation in 1970 can treat wastewater at 5 million liters per day.

As shown in Fig. 1, the plant consists of a typical STP in which influent wastewater passes through a screen, grit chamber, primary settling tank, aeration tank, and final settling tank. Secondary treatment is done in the aeration tanks after which the treated water is discharged into a nearby lake.

### Data Collection and Analytical Methods

Data were analyzed from October 2008 to January 2022 and sampled and investigated once every month when the plant received good flow. The data for the influent stream was collected at the line after the grit chamber and that of the effluent stream was collected at the effluent line after the final settling tank. The influent and effluent parameters were stipulated as per the environmental regulations in force in the sewage treatment plant. The inputs were pH, oil and grease OG, suspended solids SS, and biochemical oxygen demand BOD and the output parameters modelled in this study were pH, SS, and BOD (Hamada et al. 2018). All influent and effluent parameters were measured according to IS 3025. A total of 113 data points were used for this study.

Further data normalizing was done according to equation (1)

$$Y_{Norm} = (Y - Y_{Min})/(Y_{Max} - Y_{Min}) \quad \ldots(1)$$

Where $Y$ represents the variable studied. The statistical parameters of the variables of STP are given in Table 1 where, $Y_{max}$ = maximum value, $Y_{min}$ = minimum value, $Y_{mean}$ = mean value Sd = standard deviation and Cv = variance

### Mathematical Modeling

**Artificial neural networks (ANNs):** The development of ANNs as a computational tool similar in working to the human brain started in 1940 (Lippmann 1988). Generally, artificial neural networks consist of layers of neurons in a connected structure from which output is generated. ANNs due to their ability to represent highly non-linear systems, high learning speed, and data processing are used in pattern recognition, classification, and problem-solving. ANN is a good tool for modeling relationships between several variables based on training data.

Table 1: Statistical indices of parameters.

| | $pH_{Inf}$ | $SS_{Inf}$ | $BOD_{Inf}$ | $OG_{Inf}$ | $pH_{Eff}$ | $SS_{Eff}$ | $BOD_{Eff}$ | $OG_{Eff}$ |
|---|---|---|---|---|---|---|---|---|
| $Y_{Max}$ | 66 | 624 | 937 | 56 | 8.2 | 139 | 79 | 8.4 |
| $Y_{Min}$ | 5.1 | 16 | 42.6 | 0.8 | 5.8 | 4 | 5.6 | 0 |
| Sum | 801.06 | 14757 | 38069.8 | 1330.4 | 803.91 | 4456.8 | 2344.23 | 216.34 |
| $Y_{Mean}$ | 7.089 | 130.592 | 336.90 | 11.773 | 7.11 | 39.44071 | 20.74 | 1.91 |
| Cv | 31.79 | 7585.58 | 100565 | 85.959 | 0.24 | 2066.724 | 437.89 | 360.45 |
| Sd | 5.63 | 87.0952 | 317.12 | 9.2714 | 0.49 | 45.46124 | 20.925 | 18.98 |

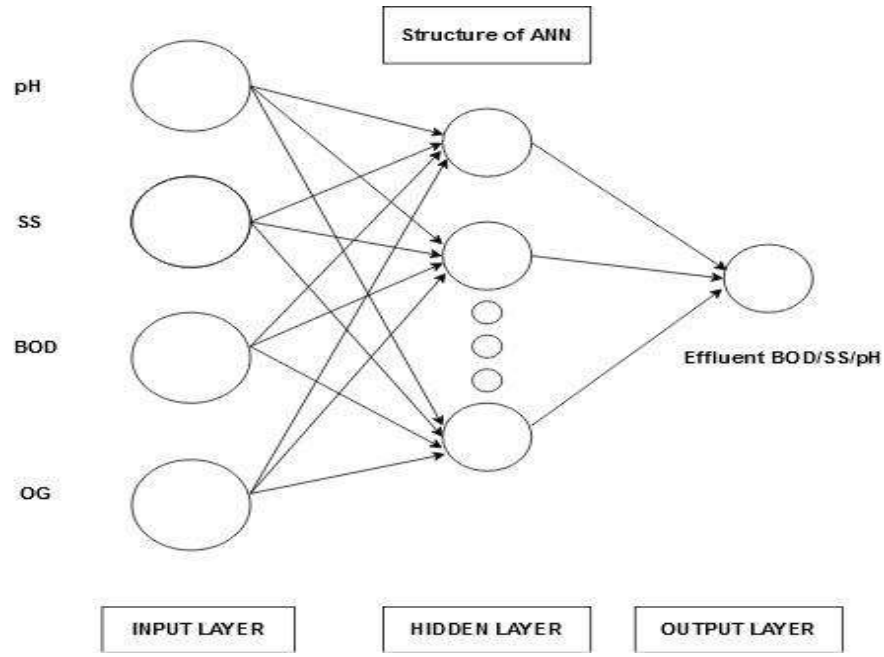


Fig. 2: Structure of ANN.

Fig. 2 shown below shows a feed-forward structure consisting of three layers of neurons. The first layer which receives the input data is called the input layer and sends these data to the second layer called the hidden layer. The hidden layer and the output layer perform the computations before producing the output.

The basic processing elements are the neurons that receive the input. The inputs are processed by activation functions to produce an output signal. Also, the connecting weights between neurons and the activation functions used to determine the output from each neuron. The mathematical expression of the neural network is given in Equation (2) below.

$$Y_i = f\left(\sum_{j=1}^{M} W_{ij} X_j + b_i\right) \quad \ldots(2)$$

Where, $Y_i$ is the predicted output, $f$ is the activation function, $W_{ij}$ is the weight assigned to each input j, $X_j$ is the input, M is the total number of inputs and $b_i$ is the bias.

For predicting the effluent parameters in the STP, a three-layer feed-forward ANN structure was developed. The number of neurons in the input layer was equal to the number of influent parameters considered for training. The number of neurons in the hidden layer was found by trial and error and the number of neurons in the output layer was one which is the effluent parameter predicted in the study. The network needs to be optimized in terms of statistical parameters and avoid overfitting. (Geman et al. 1992)

**ANN training and testing:** The available data is divided into three parts. The first part is the training set, which is used for computing the difference between predicted and actual outputs and updating the weights and biases of the network. The second part is called the validation set which is used to find out the stopping point of neural network training. The training error and validation error are found during the training and it is generally seen that both errors tend to decrease initially. But when the network starts overfitting, the

validation error starts to increase and training is stopped. The network parameters corresponding to minimum validation error are fixed and the optimum number of neurons in the hidden layer is returned. The third part of the data is called the testing data which is used to test the ability of the model to generalize to new data. Ideally, the testing error should be a minimum.

The performance of neural networks is determined by the number of hidden layers, the number of neurons in hidden layers, the transfer functions used in neurons, and the algorithms used in training. When the number of hidden layer neurons and subsequently the number of parameters in the network are less than the number of training data points over-fitting problems can be avoided.

The ANN network used the Levenberg-Marquardt back-propagation algorithm for training with one hidden layer. The backpropagation algorithm returns the error produced by neural networks to modify the connection weights and biases. The tangent hyperbolic function (Haykin 2009) Equation (3) is used in the hidden layer and the linear activation function Equation (4) is used in the output layer.

$$f(x) = \frac{2}{1+e^{-2x}} - 1 \quad \ldots(3)$$

$$f(x) = x \quad \ldots(4)$$

The performance of the model was determined by the correlation coefficient R equation (5) and mean square error (MSE) equation (6) calculated between predicted and measured data.

$$R = \frac{\left[\sum_{i=1}^{N}(Y_i - Y_{Mean})(P_i - P_{Mean})\right]}{\sqrt{\sum_{i=1}^{N}(Y_i - Y_{Mean})^2 \ \sum_{i=1}^{N}(P_i - P_{Mean})^2}} \quad \ldots(5)$$

$$MSE = \sum_{i=1}^{N} \frac{(Y_i - P_i)^2}{N} \quad \ldots(6)$$

Where, $Y_i$ and $P_i$ are the predicted and measured data, $Y_{mean}$ and $P_{mean}$ are the average values of predicted and measured data and N is the total number of data points. When the mean square error was at a minimum and the correlation coefficient was at a maximum the model was considered to be optimum.

**ANN software:** The software MATLAB 8.6 (Version–R2015b) (Math Works, Inc., USA) is used to perform neural network modeling and simulation. The ratio of 60:20:20 is used for data division, 60 per cent for training, 20 per cent for validation and 20 per cent for testing. The multilayer perceptron ANNs (MLP-ANNs) were used due to their simplicity and ease of coding.

The ANN is trained using a different combination of inputs containing up to a maximum of four inputs for each of the three output parameters used in this study. Table 2 shows the different combinations used. The data is normalized before training. To find the optimum number of hidden layer neurons, the performance of each network is evaluated by trial and error.

In the present study, the Levenberg-Marquardt (LM) back-propagation training algorithm is used as it is the fastest algorithm and converges quickly. The convergence of the network is also determined by the learning rate parameter which prevents the network from being trapped in a local minimum than the global minimum. The learning rate parameter was fixed as 0.01. Figs. 3, 4, 5 show ANN training for biochemical oxygen demand BOD, suspended solids SS and pH prediction.

## RESULTS AND DISCUSSION

### Correlation Matrix (CM)

The correlation matrix is a table showing the relationship between several variables. In Table 3, there exists a positive correlation between $BOD_{Eff}$ and $SS_{Inf}$, $BOD_{Inf}$, and $OG_{Inf}$ and a negative correlation between $BOD_{Eff}$ and $pH_{Inf.}$ This is because the decomposition of suspended solids and oil and grease at the inlet stream will demand more oxygen leading to a positive correlation between $BOD_{Eff}$ and $SS_{Inf}$, $BOD_{Inf}$ and $OG_{Inf}$ (Lelie et al. 2021) The negative correlation between $BOD_{Eff}$ and $pH_{Inf.}$ is due to the fact that when pH goes above the normal range of 6-8, organisms which decompose organic materials may not survive and $BOD_{Inf}$ will not decrease.

Table 2: Input parameter used in the study.

| Input | Input parameter combination |
|---|---|
| Input1 | $pH_{Inf}$ |
| Input2 | $SS_{Inf}$ |
| Input3 | $BOD_{Inf}$ |
| Input4 | $OG_{Inf}$ |
| Input5 | $pH_{Inf} + SS_{Inf}$ |
| Input6 | $pH_{Inf} + BOD_{Inf}$ |
| Input7 | $pH_{Inf} + OG_{Inf}$ |
| Input8 | $SS_{Inf} + BOD_{Inf}$ |
| Input9 | $SS_{Inf} + OG_{Inf}$ |
| Input10 | $BOD_{Inf} + OG_{Inf}$ |
| Input11 | $pH_{Inf} + SS_{Inf} + BOD_{Inf}$ |
| Input12 | $SS_{Inf} + BOD_{Inf} + OG_{Inf}$ |
| Input13 | $pH_{Inf} + SS_{Inf} + OG_{Inf}$ |
| Input14 | $pH_{Inf} + BD_{Inf} + OG_{Inf}$ |
| Input15 | $pH_{Inf} + SS_{Inf} BD_{Inf} + OG_{Inf}$ |

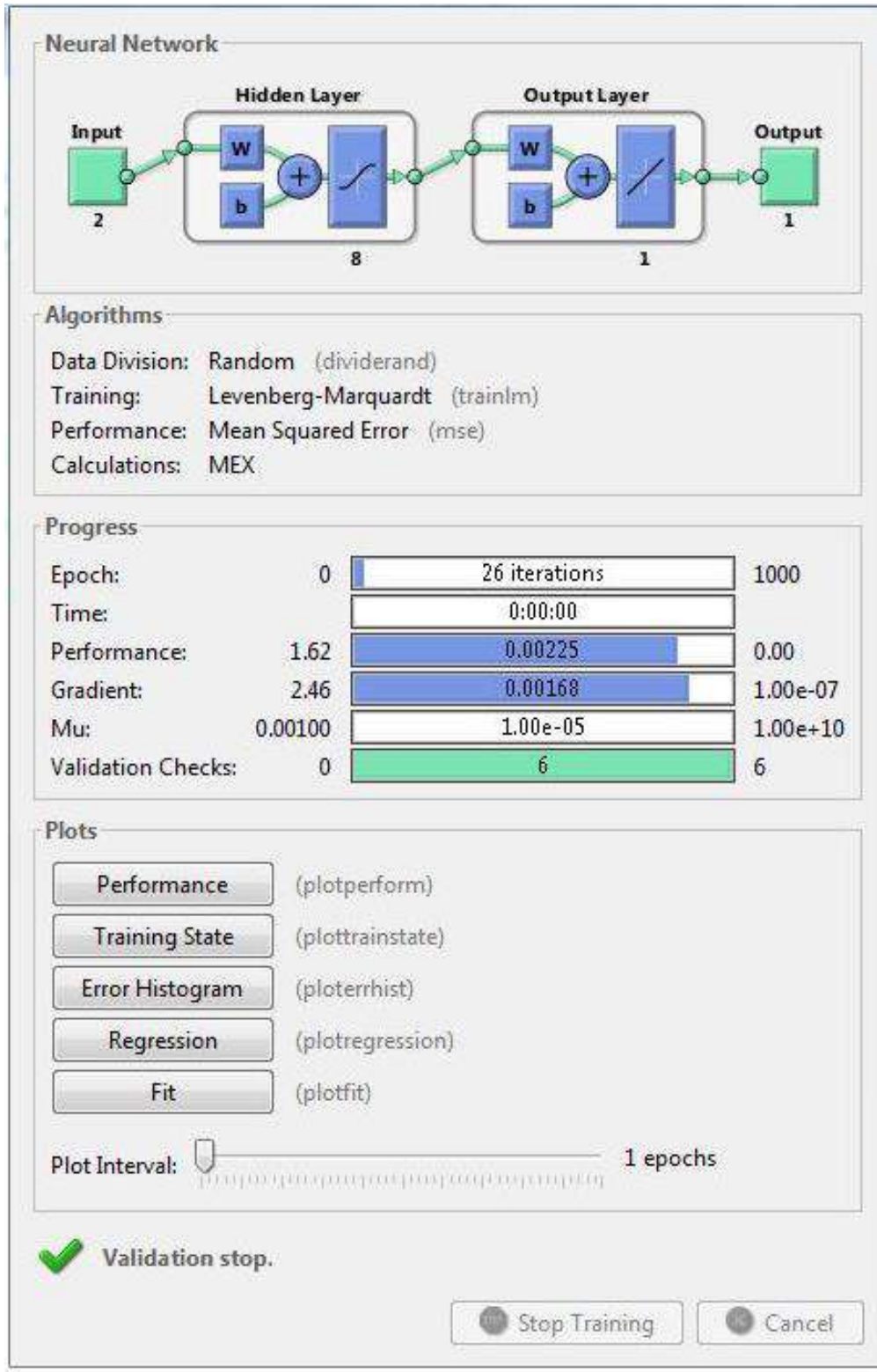


Fig. 3: ANN training for BOD prediction.

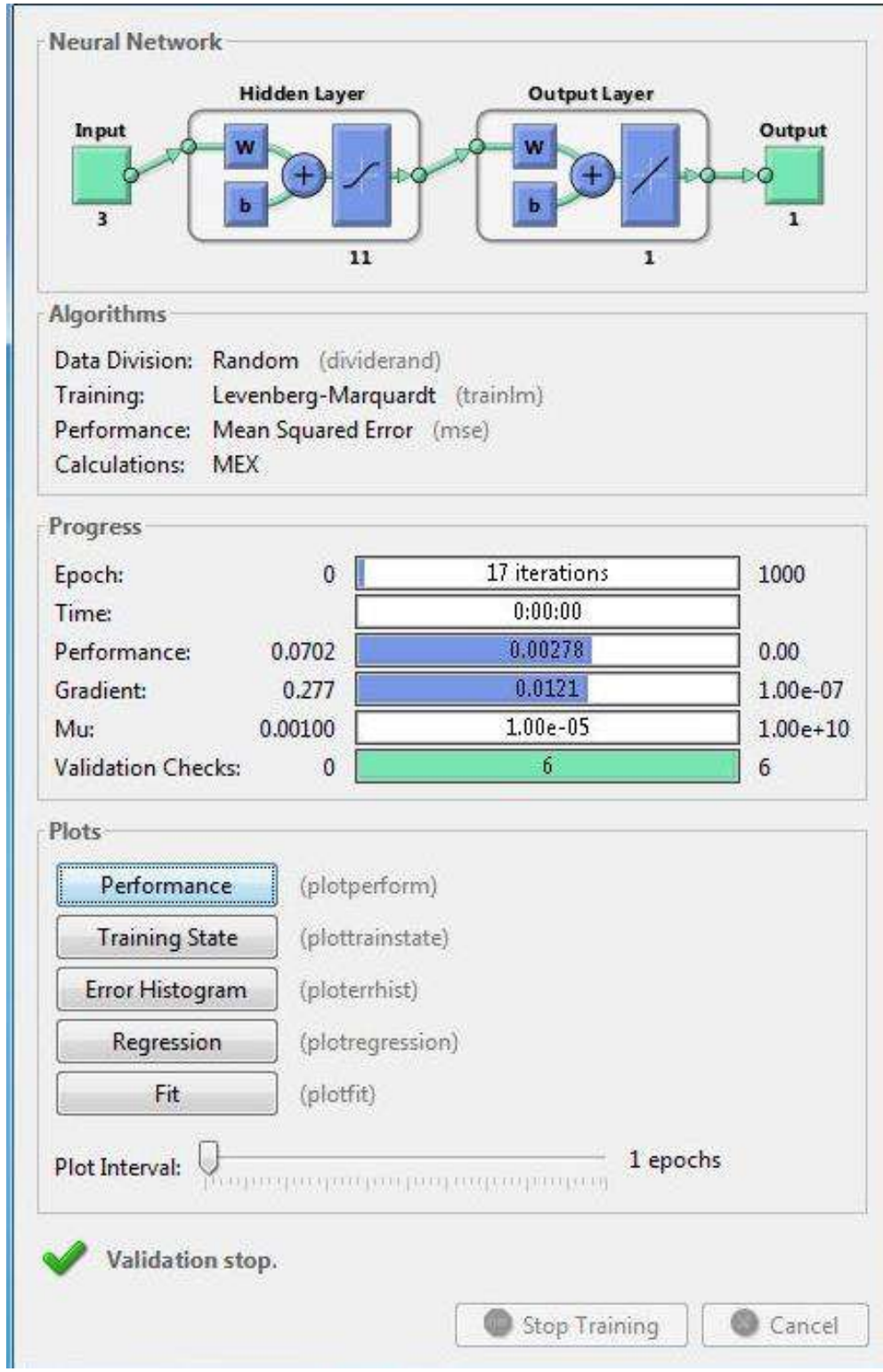


Fig. 4: ANN training for SS prediction.

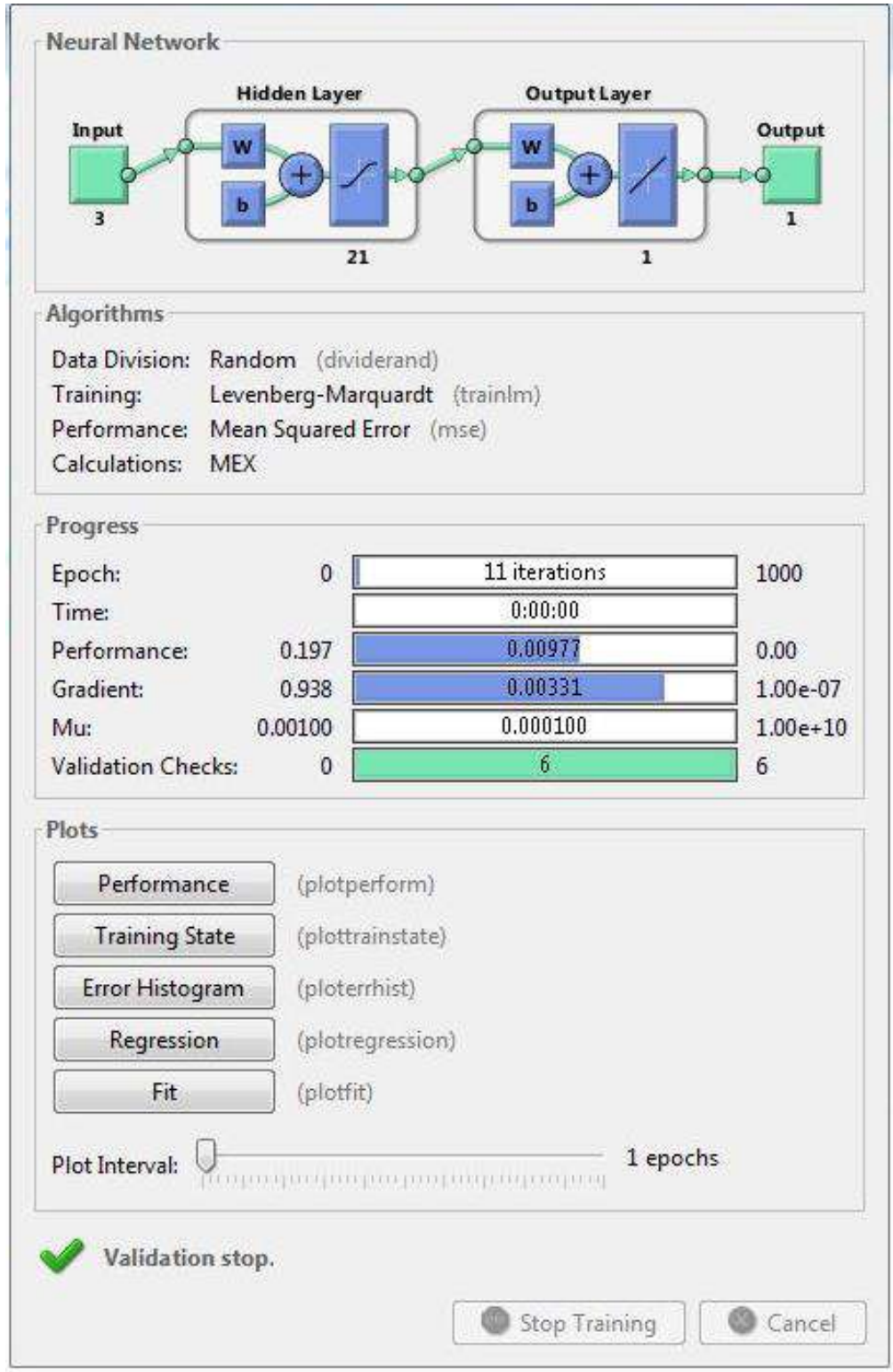


Fig. 5: ANN training for pH prediction.

Table 3: Correlation matrix.

| Parameter | $pH_{Eff}$ | $SS_{Eff}$ | $BOD_{Eff}$ | $OG_{Eff}$ |
|---|---|---|---|---|
| $pH_{Inf}$ | 0.18784 | -0.0351 | -0.1018 | -0.0016 |
| $SS_{Inf}$ | -0.0925 | 0.61159 | 0.57309 | 0.62197 |
| $BOD_{Inf}$ | -0.1848 | 0.85927 | 0.54389 | 0.52597 |
| $OG_{Inf}$ | 0.2057 | 0.29457 | 0.47785 | 0.26874 |

Similarly, there exists a positive correlation between $SS_{Eff}$ on one hand and $SS_{Inf}$ $BOD_{Inf}$ and $OG_{Inf}$ and a negative correlation between $SS_{Eff}$ and $pH_{Inf}$ respectively. The positive correlation is because oil and grease and particles contributing to biochemical oxygen demand may be themselves suspended in water. (Giokas et al. 2002) The weak negative correlation between $SS_{Eff}$ and $pH_{Inf}$ is because the acidic or basic nature of a substance doesn't influence its settling characteristics.

Parameters showing a positive correlation should be included in the modeling of $BOD_{Eff}$ and $SS_{Eff}$. The meaning of a positive correlation coefficient is that the increase of one variable causes the other variable also to increase and vice versa. While $pH_{Eff\,is}$ positively correlated to $pH_{Inf}$ and $OG_{Inf}$, it is negatively correlated to $SS_{Inf}$ and $BOD_{Inf}$.

**ANN Model Development**

The performance of networks is evaluated by finding the optimum number of neurons in the hidden layer. A trial and error procedure is adopted to find out the optimum number of neurons. The performance of the network was compared using mean square error MSE and correlation coefficient R values. When the correlation coefficient was maximum and the mean square error was minimum, a model was considered to be the best. The results of developing one input, two inputs, three inputs, and four input models' model, (Mjalli et al. 2006) for the estimation of BOD, SS, and pH in terms of R and MSE are summarized in Tables 4, 5 and 6.

It is seen that two input models of pH and biochemical oxygen demand BOD are giving a maximum correlation coefficient R values of 0.927 and minimum MSE of 0.0022 with eight hidden layer neurons for effluent BOD prediction. The optimum network structure is given in Table 4. The regression curves of training, validation, testing, and total regression are shown in Fig. 6, the best neural network for predicting BOD is shown in Fig. 7, plots of measured and predicted BOD is shown in Fig. 8, and plot of error between predicted and measured BOD is shown in Fig. 9. The developed model performs to accepted standards of model development with a correlation coefficient greater than 0.9 and low mean square values.

It is seen that three input models of pH, biochemical oxygen demand, and oil and grease are giving a maximum correlation coefficient R values of 0.947 and minimum MSE of 0.0058 with seventeen neurons in the hidden layer for effluent SS prediction. The optimum network structure is given in Table 5. The combined regression curves are presented in Fig. 10, the best neural network for predicting SS is shown in Fig. 11, plots of measured and predicted BOD is shown in Fig. 12, and plot of error between predicted and measured BOD is shown in Fig. 13. The developed model performs to accepted standards of model development with a correlation coefficient greater than 0.9 and low mean square error values.

It is seen that three input models of pH, suspended solids and biochemical oxygen demand are giving a maximum correlation coefficient R values of 0.8299 and minimum MSE of 0.0132 with twenty-one neurons in the hidden layer for effluent pH prediction. The optimum network structure is given in Table 6. The combined regression curves are presented in Fig. 14, the best neural network structure for pH prediction is shown in Fig. 15, plots of measured and predicted BOD is shown in Fig. 16, and plot of error between predicted and measured BOD is shown in Fig. 17. Prediction of pH requires the study of more input parameters affecting pH for better correlation coefficient and mean square error values.

Most of the literature survey on the application of ANNs for modeling WWTPs utilized these variables and found that the ANN-based models provide an efficient and robust tool in predicting WWTP performance. For modeling wastewater treatment plants using ANN, (Hamoda et al. 1999) found a correlation coefficient of 0.74 for BOD prediction and .72 for TSS. Mjalli et al. (2004) predicted BOD with a correlation coefficient of 0.951 and TSS with a correlation coefficient R of 0.987. Abyaneh (2014) found RMSE = 25.1 $mg.L^{-1}$ and R = 0.83 for the prediction of BOD and Nasr et al. (2012) found that the ANN can predict the plant performance with a correlation coefficient of 0.903. Hamada et al. (2018) predicted BOD with a correlation coefficient of 0.786 and TSS of 0. 765. Alsulaili (2021) showed that the ANN model developed to predict the BOD concentration performed the best among the three outputs. The top-performing ANN models yielded $R^2$ values of 0.752 and 0.631 for the prediction of the BOD and TSS concentrations, respectively. Only a study done by Mjalli et al. (2004) gives a better prediction of BOD and TSS although the number of neurons used in that study was comparatively higher.

**Sensitivity of Input Parameters**

Analysis of the sensitivity of input factors for each predicted output was carried out by keeping the number of neurons in the hidden layers constant and using the same network

Table 4: Optimized neural network structure for BOD prediction.

| Input parameter | ANN | Epoch | MSE | Train | Valn | Test | Reg | Train | Valn | Test |
|---|---|---|---|---|---|---|---|---|---|---|
| pH Inf | 1-9-1 | 13 | 0.0064 | 0.0072 | 0.0035 | 0.0054 | 0.7707 | 0.7907 | 0.5514 | 0.7204 |
| SS Inf | 1-13-1 | 10 | 0.0069 | 0.0086 | 0.0026 | 0.0031 | 0.7508 | 0.7401 | 0.8621 | 0.7513 |
| $BOD_{Inf}$ | 1-10-1 | 10 | 0.0028 | 0.0023 | 0.0024 | 0.0054 | 0.91 | 0.9367 | 0.854 | 0.8456 |
| $OG_{Inf}$ | 1-3-1 | 408 | 0.0078 | 0.0049 | 0.0254 | 0.0037 | 0.7143 | 0.7709 | 0.8024 | 0.6349 |
| pH Inf + SS Inf | 1-10-1 | 11 | 0.007 | 0.0081 | 0.0048 | 0.004 | 0.747 | 0.767 | 0.7572 | 0.6369 |
| pH Inf+ BOD Inf | 1-8-1 | 6 | 0.0022 | 0.0025 | 0.0021 | 0.0009 | 0.927 | 0.92 | 0.954 | 0.8801 |
| pH Inf + OG Inf | 1-13-1 | 9 | 0.0059 | 0.0026 | 0.0058 | 0.0209 | 0.8302 | 0.8103 | 0.9361 | 0.9119 |
| SS Inf + BOD Inf | 1-11-1 | 10 | 0.0031 | 3.60E-03 | 0.0021 | 0.0017 | 0.9057 | 0.9079 | 0.9094 | 0.9366 |
| SS Inf + OG Inf | 1-8-1 | 13 | 0.0063 | 0.0076 | 0.0053 | 0.0016 | 0.783 | 0.7444 | 0.8632 | 0.8523 |
| BOD In f+ OG Inf | 1-14-1 | 15 | 0.0036 | 0.0021 | 0.013 | 0.0008 | 0.8806 | 0.861 | 0.8748 | 0.9445 |
| pH Inf + SS Inf + BOD Inf | 1-10-1 | 8 | 0.0043 | 0.0053 | 0.002 | 0.0023 | 0.8579 | 0.8604 | 0.8911 | 0.8062 |
| SS Inf + BOD Inf + OG Inf | 1-11-1 | 25 | 0.0026 | 0.0021 | 0.003 | 0.0046 | 0.9139 | 0.932 | 0.7715 | 0.9395 |
| pH Inf + SS Inf + OG Inf | 1-9-1 | 15 | 0.0029 | 0.0029 | 0.0024 | 0.0036 | 0.9071 | 0.9072 | 0.777 | 0.9653 |
| pH Inf + BD Inf + OG Inf | 1-7-1 | 21 | 0.0027 | 0.0032 | 0.0014 | 0.0013 | 0.9111 | 0.9182 | 0.8663 | 0.7995 |
| $(pH + SS + BOD + OG)_{Inf}$ | 1-7-1 | 11 | 0.0028 | 0.0023 | 0.0013 | 0.0066 | 0.9079 | 0.9277 | 0.9205 | 0.9229 |

Table 5: Optimised neural network structure for SS prediction.

| Input parameter | ANN | Epoch | MSE | Train | Valn | Test | Reg. | Train | Valn | Test |
|---|---|---|---|---|---|---|---|---|---|---|
| pH Inf | 1-10-1 | 27 | 0.017 | 0.0168 | 0.0176 | 0.0173 | 0.8312 | 0.8241 | 0.8822 | 0.788 |
| SS Inf | 1-13-1 | 35 | 0.0181 | 0.015 | 0.022 | 0.028 | 0.821 | 0.845 | 0.833 | 0.7033 |
| $BOD_{Inf}$ | 1-16-1 | 10 | 0.0093 | 0.0082 | 0.0192 | 0.0049 | 0.9115 | 0.933 | 0.83 | 0.95 |
| $OG_{Inf}$ | 1-14-1 | 15 | 0.0203 | 0.0183 | 0.0358 | 0.014 | 0.794 | 0.806 | 0.737 | 0.827 |
| pH Inf + SS Inf | 1-10-1 | 7 | 0.0167 | 0.0151 | 0.0196 | 0.0215 | 0.8385 | 0.867 | 0.823 | 0.6889 |
| pH Inf + BOD Inf | 1-13-1 | 9 | 0.9182 | 0.9213 | 0.934 | 0.9159 | 0.0086 | 0.0075 | 0.0087 | 0.0138 |
| pH Inf + OG Inf | 1-6-1 | 25 | 0.0124 | 0.0096 | 0.0052 | 0.0324 | 0.881 | 0.8988 | 0.9539 | 0.789 |
| SS Inf + BOD Inf | 1-11-1 | 9 | 0.0109 | 0.0119 | 0.0149 | 0.0051 | 0.8988 | 0.905 | 0.877 | 0.952 |
| SS Inf + OG Inf | 1-2-1 | 29 | 0.0127 | 0.0146 | 0.0114 | 0.0048 | 0.8788 | 0.873 | 0.879 | 0.938 |
| BOD Inf + OG Inf | 1-4-1 | 18 | 0.0081 | 0.0097 | 0.0056 | 0.0031 | 0.9238 | 0.919 | 0.946 | 0.9341 |
| pH Inf + SS Inf + BOD Inf | 1-7-1 | 24 | 0.0067 | 0.0055 | 0.0126 | 0.0063 | 0.9383 | 0.946 | 0.9381 | 0.9289 |
| SS Inf + BOD Inf + OG Inf | 1-7-1 | 20 | 0.0079 | 0.0068 | 0.0114 | 0.009 | 0.9259 | 0.9251 | 0.892 | 0.8926 |
| pH Inf + SS Inf + OG Inf | 1-5-1 | 32 | 0.0082 | 0.007 | 0.0043 | 0.0178 | 0.9226 | 0.9334 | 0.9742 | 0.8307 |
| pH Inf + BD Inf + OG Inf | 1-11-1 | 17 | 0.0058 | 0.0039 | 0.0041 | 0.0161 | 0.947 | 0.959 | 0.969 | 0.9044 |
| $(pH+ SS+BOD+OG)_{Inf}$ | 1-7-1 | 6 | 0.0057 | 0.005 | 0.0072 | 0.0073 | 0.9473 | 0.957 | 0.941 | 0.863 |

Table 6: Optimized neural network structure for pH prediction.

| Input parameter | ANN | Epoch | MSE | Train | Valn | Test | Reg | Train | Valn | Test |
|---|---|---|---|---|---|---|---|---|---|---|
| pH Inf | 1-10-1 | 7 | 0.023 | 0.0223 | 0.0314 | 0.018 | 0.6719 | 0.747 | 0.3944 | 0.44 |
| SS Inf | 1-11-1 | 55 | 0.0262 | 0.0262 | 0.0364 | 0.163 | 0.617 | 0.7638 | 0.7346 | 0.6221 |
| $BOD_{Inf}$ | 1-18-1 | 7 | 0.0275 | 0.0302 | 0.0192 | 0.0234 | 0.5902 | 0.5343 | 0.7445 | 0.6644 |
| $OG_{Inf}$ | 1-15-1 | 17 | 0.0325 | 0.0325 | 0.0508 | 0.014 | 0.475 | 0.525 | 0.182 | 0.55 |
| pH Inf + SS Inf | 1-5-1 | 26 | 0.0145 | 0.0093 | 0.0204 | 0.0327 | 0.809 | 0.8664 | 0.7585 | 0.6789 |
| pH Inf + BOD Inf | 1-15-1 | 15 | 0.0151 | 0.0135 | 0.0207 | 0.0165 | 0.8023 | 0.808 | 0.8405 | 0.707 |
| pH Inf + OG Inf | 1-9-1 | 12 | 0.019 | 0.0196 | 0.0149 | 0.0201 | 0.742 | 0.742 | 0.839 | 0.543 |
| SS Inf + BOD Inf | 1-9-1 | 8 | 0.0294 | 0.0295 | 0.0412 | 0.0174 | 0.5523 | 0.4351 | 0.449 | 0.5889 |
| SS Inf + OG Inf | 1-9-1 | 8 | 0.0346 | 0.0342 | 0.0512 | 0.0199 | 0.4207 | 0.483 | 0.959 | 0.324 |
| BOD Inf + OG Inf | 1-16-1 | 18 | 0.0235 | 0.0199 | 0.034 | 0.0295 | 0.6677 | 0.7277 | 0.5119 | 0.57 |
| pH Inf + SS Inf + BOD Inf | 1-21-1 | 11 | 0.0132 | 0.0116 | 0.0182 | 0.0153 | 0.8299 | 0.872 | 0.529 | 0.7374 |
| SS Inf + BOD Inf + OG Inf | 1-27-1 | 14 | 0.0235 | 0.0196 | 0.0299 | 0.0351 | 0.67 | 0.743 | 0.467 | 0.6313 |
| pH Inf + SS Inf + OG Inf | 1-21-1 | 9 | 0.0135 | 0.12 | 0.0155 | 0.0183 | 0.8244 | 0.8687 | 0.6142 | 0.6667 |
| pH Inf + BD Inf + OG Inf | 1-22-1 | 17 | 0.0134 | 0.0085 | 0.0254 | 0.024 | 0.826 | 0.8905 | 0.5978 | 0.6796 |
| $(pH+SS+BOD+OG)_{Inf}$ | 1-14-1 | 13 | 0.0136 | 0.0075 | 0.04 | 0.0152 | 0.823 | 0.8966 | 0.3932 | 0.86 |

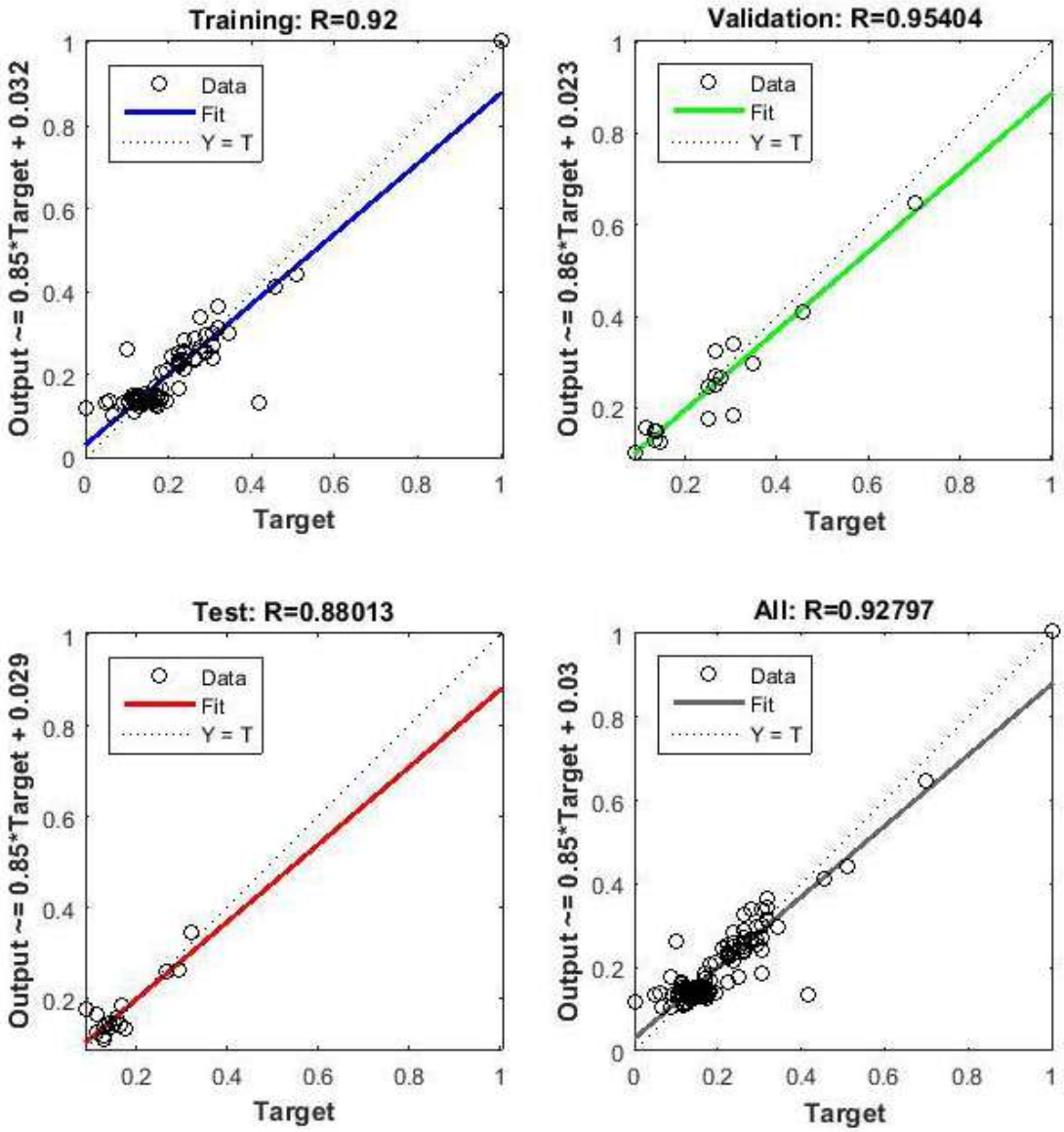


Fig. 6: Best regression curves of ANN for BOD prediction.

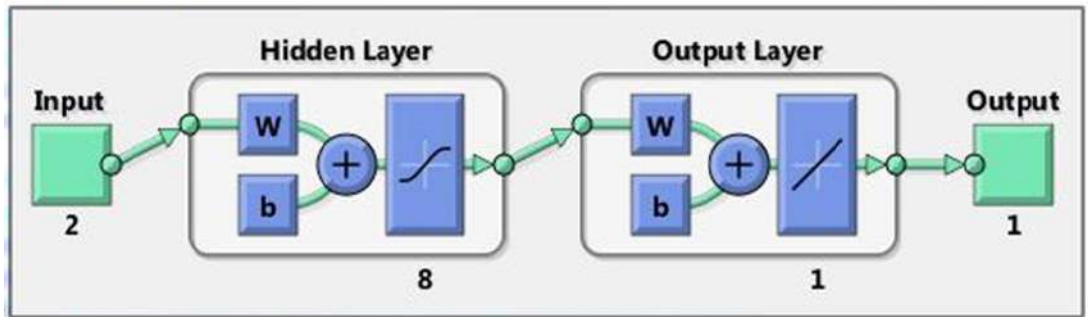


Fig. 7: Best ANN structure for BOD prediction.

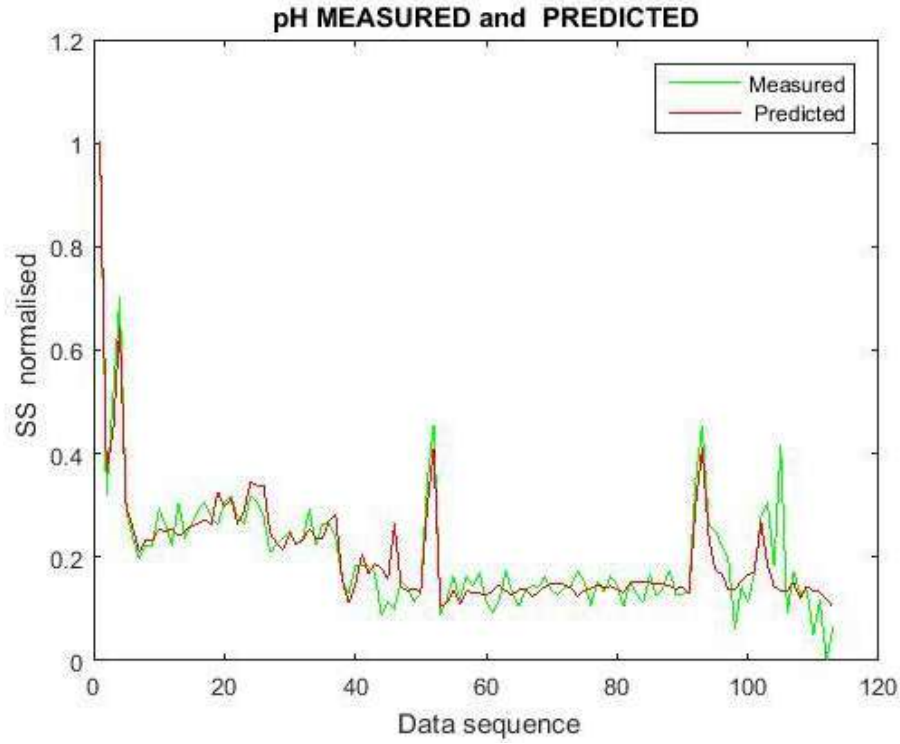


Fig. 8: Plot of measured and predicted BOD.

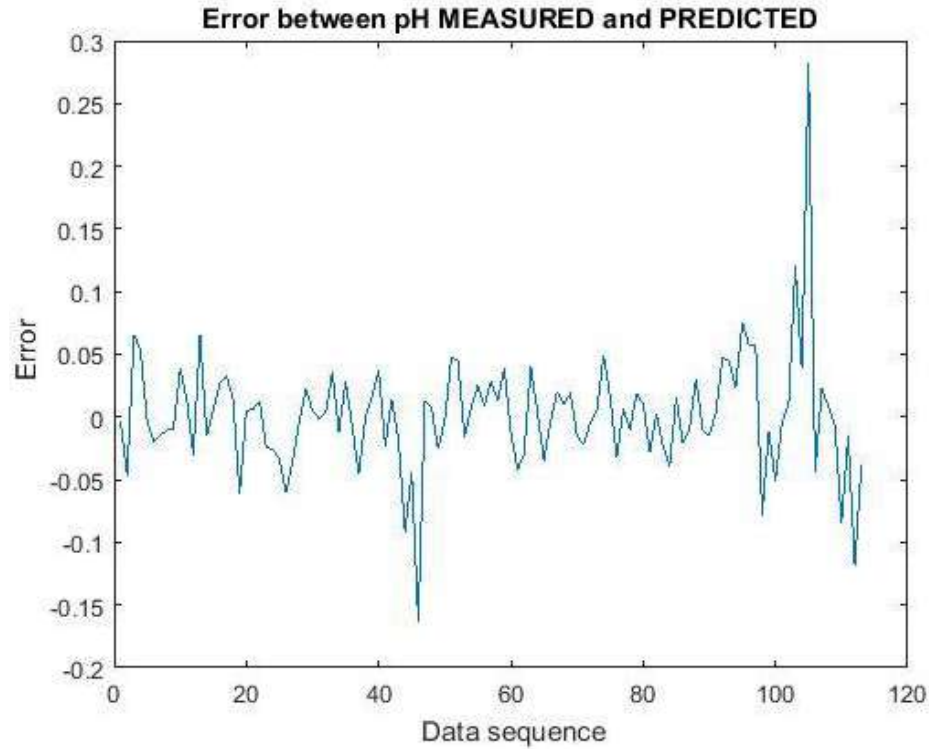


Fig. 9: Error between measured and predicted BOD.

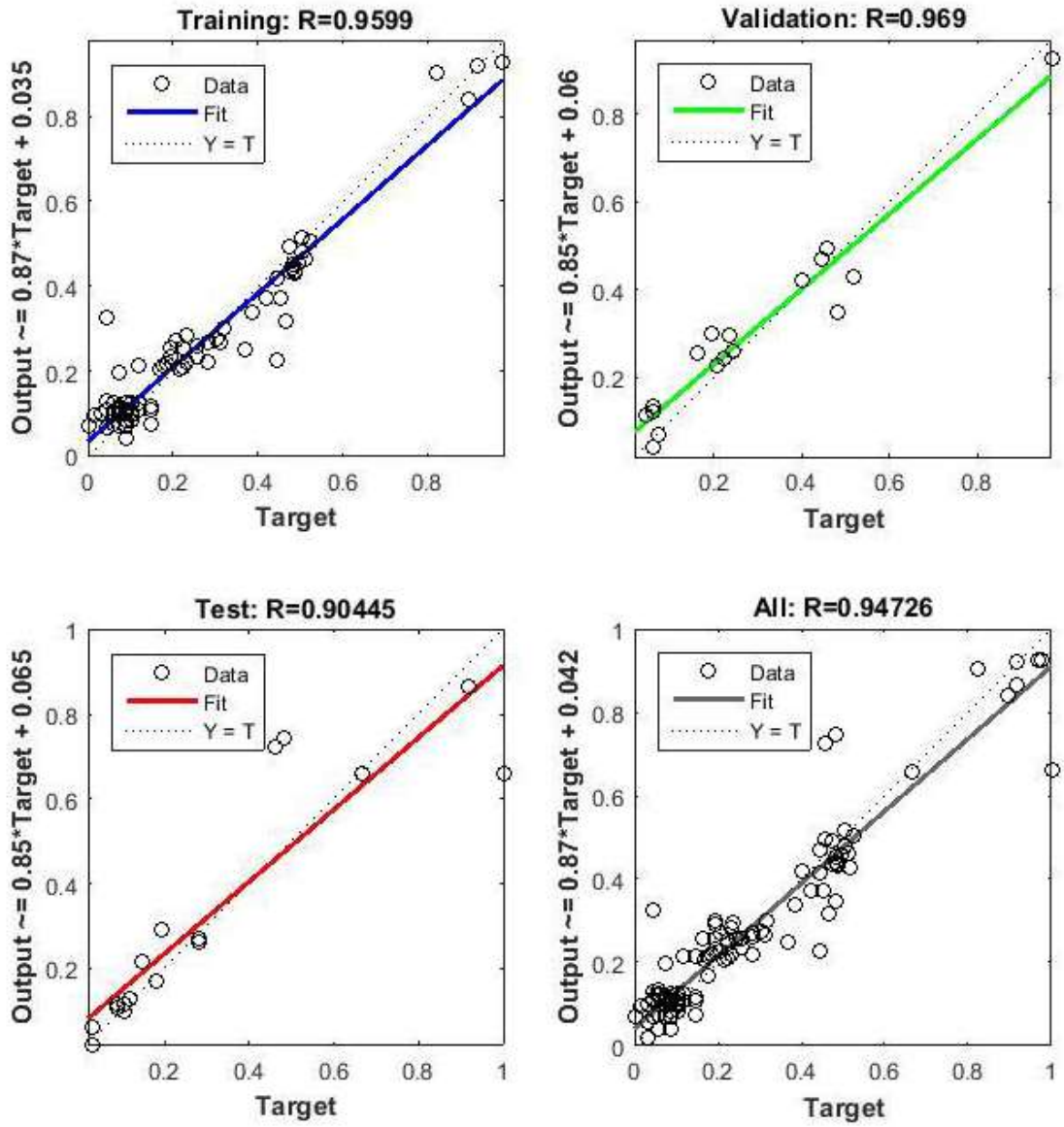


Fig. 10: Best regression curves of ANN for SS prediction.

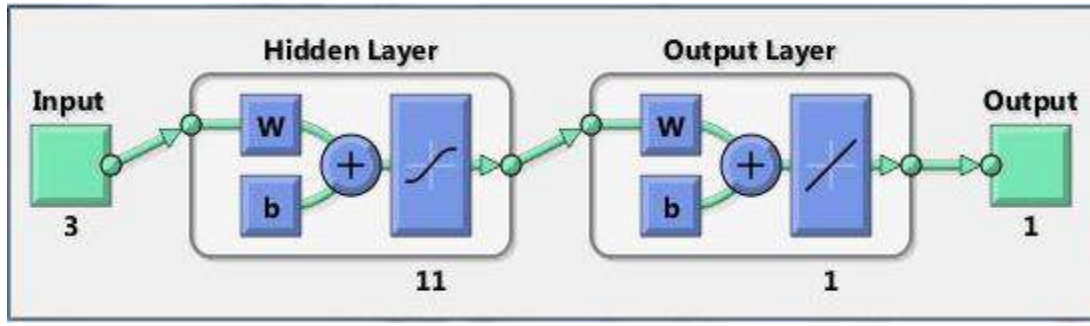


Fig. 11: Best ANN structure for SS prediction.

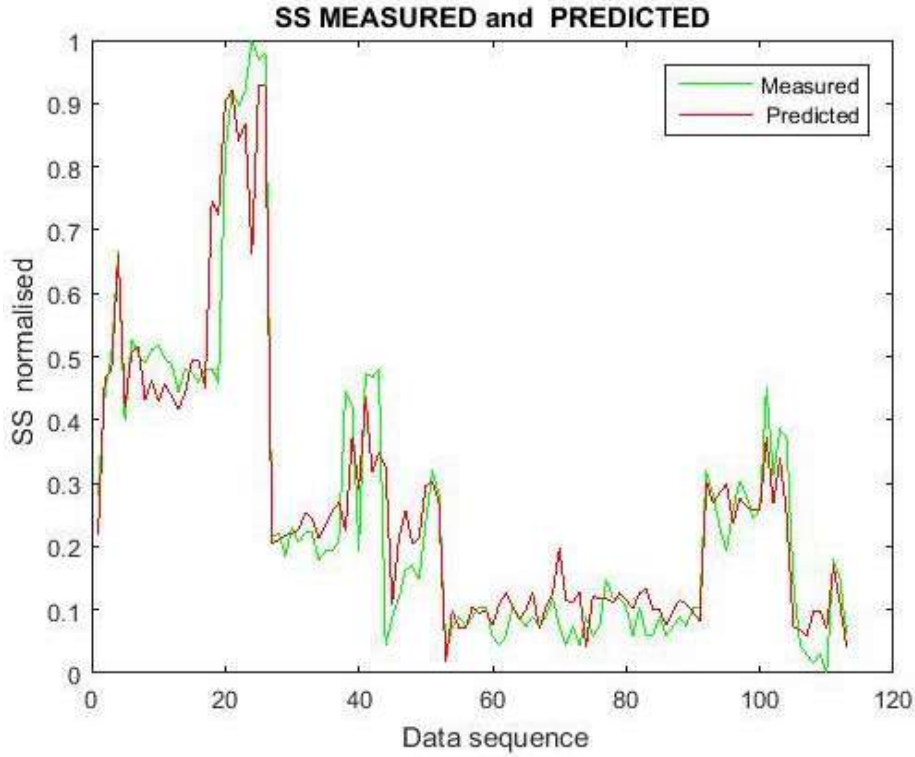


Fig. 12: Plot of measured and predicted SS.

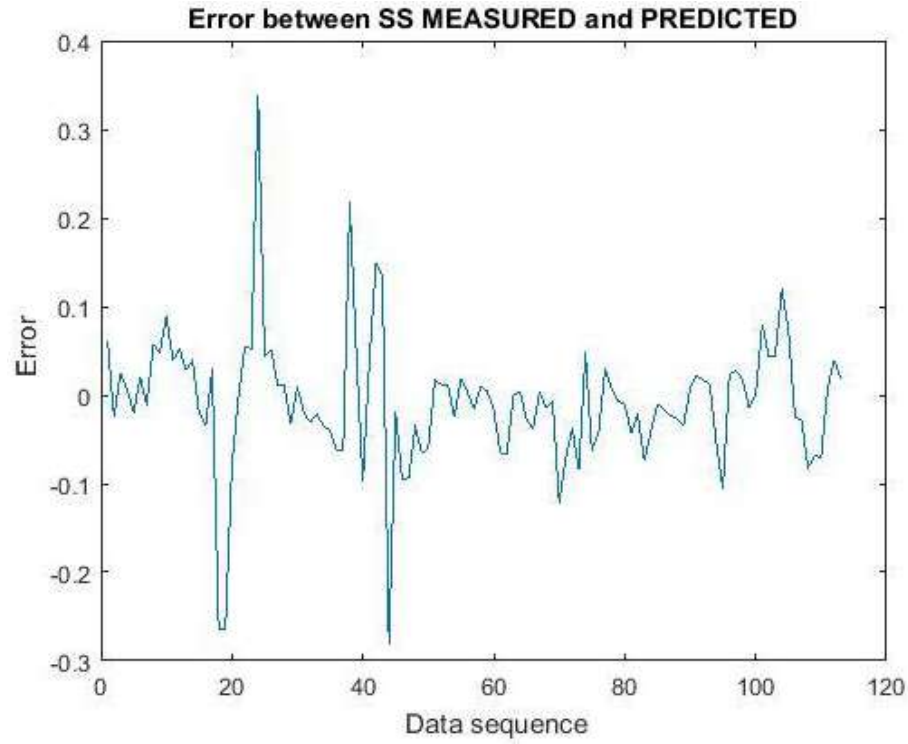


Fig. 13: Error between measured and predicted SS.

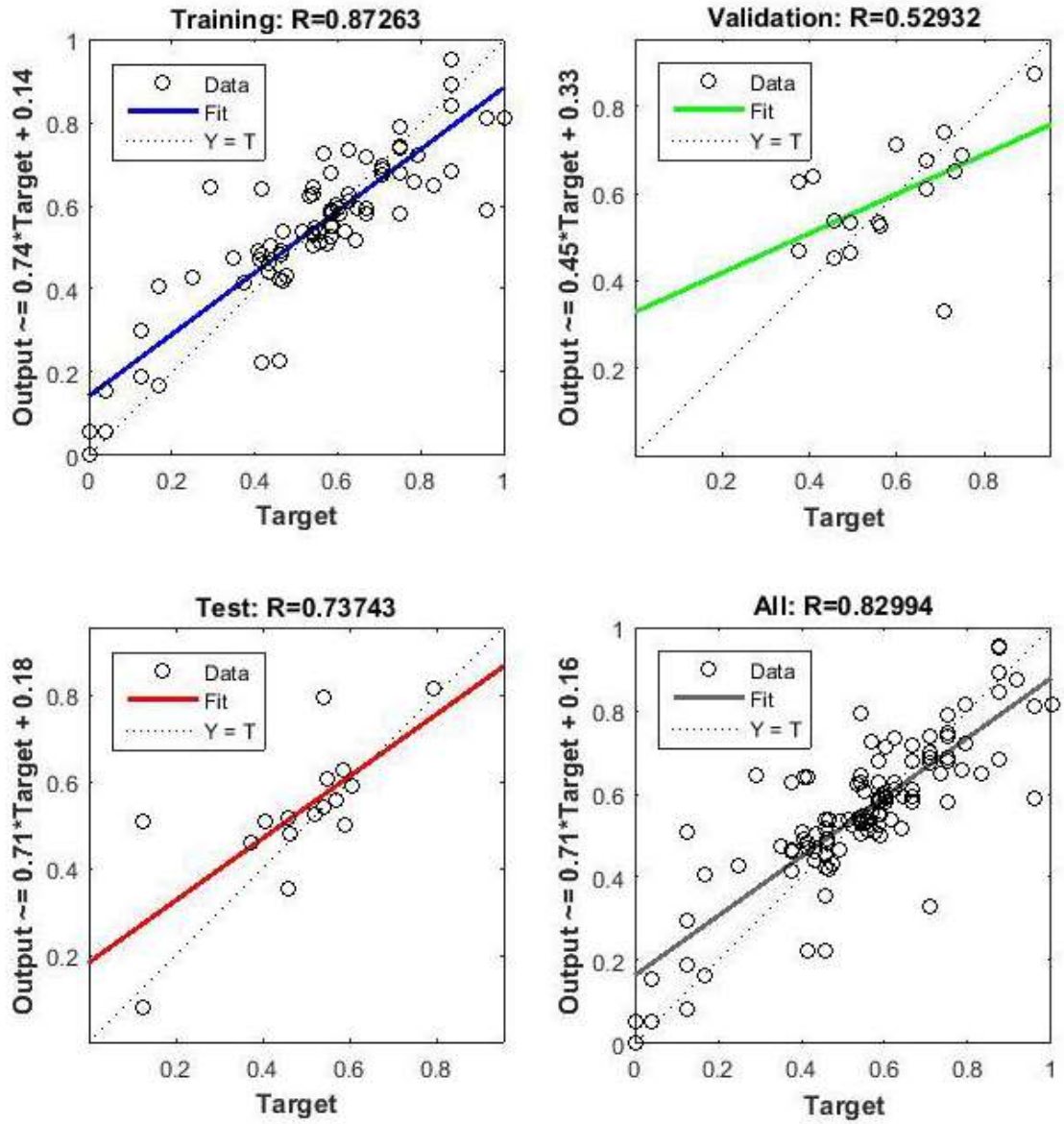


Fig. 14: Best regression curves of ANN for pH prediction.

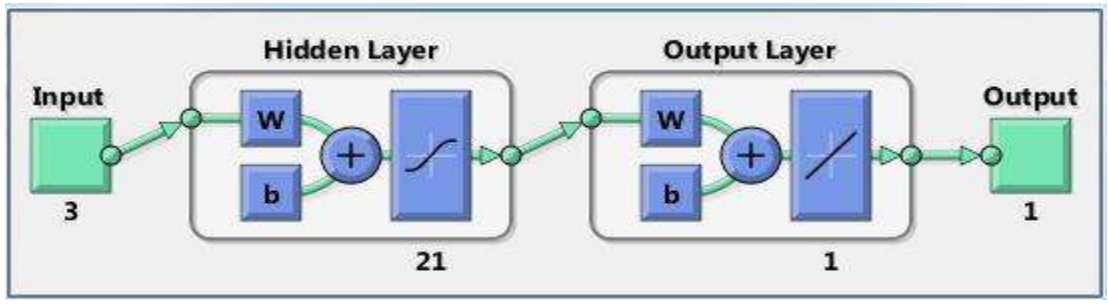


Fig. 15: Best ANN structure for pH prediction.

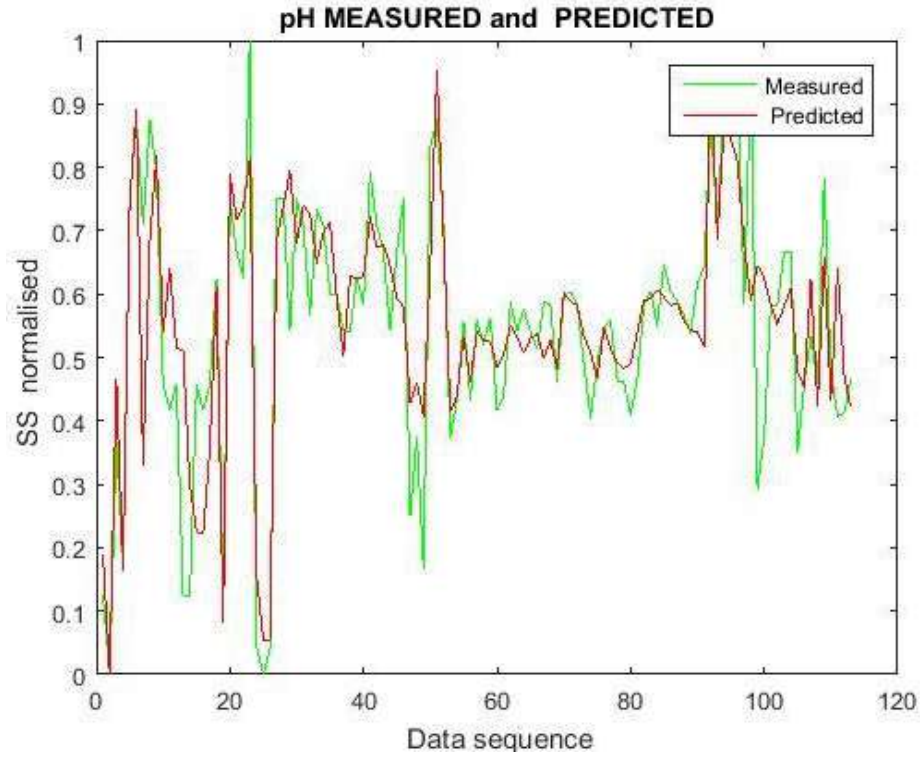


Fig. 16: Plot of measured and predicted pH.

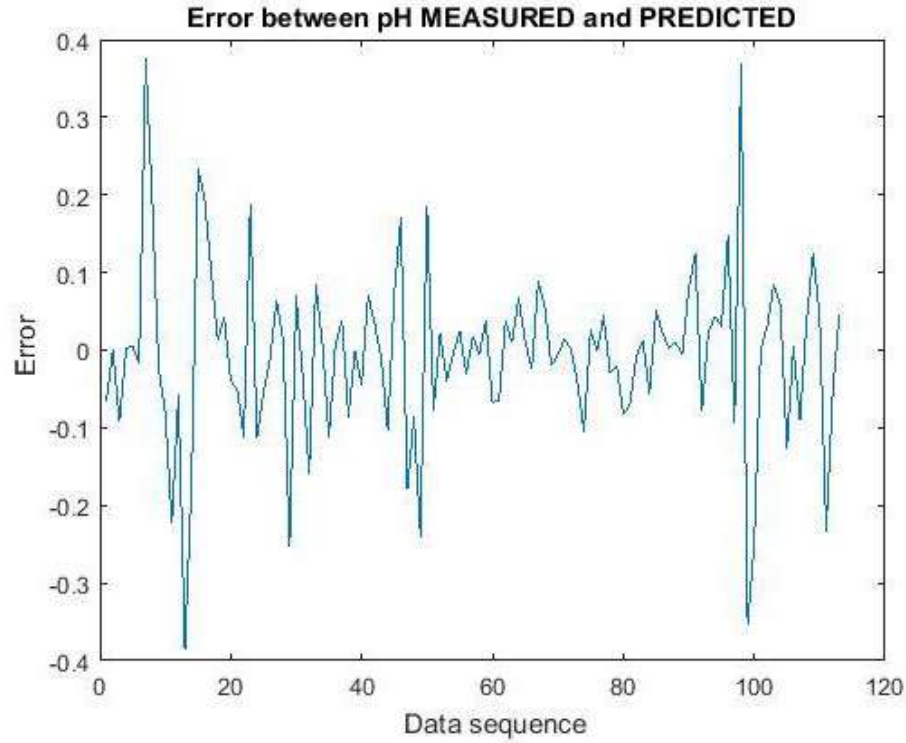


Fig. 17: Plot of error between measured and predicted pH.

parameters used in the network optimization study. For selecting the most important network input the periodic remove method was used where a particular input parameter was removed from the four different parameters and the mean square error was calculated.

The sensitivity analysis shows which input parameters are likely to have the greatest impact on the selected variables. This is done by error analysis where the individual variables are eliminated one by one from the input data. The greater the error computed after eliminating an input variable compared to the error computed with all the input variables together, the more sensitive the network becomes to the absence of this variable. The results of sensitivity analysis for biochemical oxygen demand, suspended solids and pH prediction are given in Tables 7, 8 and 9 respectively.

It has been found that for BOD prediction SS> pH >OG >BOD. It means that SS is the most sensitive parameter in BOD prediction followed by OG, pH and SS. This implies that suspended solids present in the influent stream are the biggest contributor to BOD at the outlet stream and is the most important parameter in predicting BOD (Hamada et al. 2018). For SS prediction pH >OG>SS>BOD and for pH prediction pH>SS. It means that for predicting suspended solids and pH with the least error pH at the influent stream is the most important parameter to be included in modeling.

Table 7: Sensitivity analysis for BOD prediction.

| Input parameters for BOD prediction | Mean Square error |
|---|---|
| $pH_{Inf} + SS_{Inf} + BOD_{Inf} + OG_{Inf}$ | 0.0028 |
| $pH_{Inf} + BD_{Inf} + OG_{Inf}$ | 0.0027 |
| $pH_{Inf} + SS_{Inf} + OG_{Inf}$ | 0.0023 |
| $pH_{Inf} + SS_{Inf} + BOD_{Inf}$ | 0.0024 |
| $SS_{Inf} + BOD_{Inf} + OG_{Inf}$ | 0.0025 |

Table 8: Sensitivity analysis for SS prediction.

| Input parameters for SS prediction | Mean Square error |
|---|---|
| $pH_{Inf} + SS_{Inf} + BOD_{Inf} + OG_{Inf}$ | 0.0047 |
| $pH_{Inf} + BD_{Inf} + OG_{Inf}$ | 0.0043 |
| $pH_{Inf} + SS_{Inf} + OG_{Inf}$ | 0.0029 |
| $pH_{Inf} + SS_{Inf} + BOD_{Inf}$ | 0.0061 |
| $SS_{Inf} + BOD_{Inf} + OG_{Inf}$ | 0.0142 |

Table 9: Sensitivity analysis for pH prediction.

| Input parameters for pH prediction | Mean Square error |
|---|---|
| $pH_{Inf} + SS_{Inf} + BOD_{Inf} + OG_{Inf}$ | 0.0217 |
| $pH_{Inf} + BD_{Inf} + OG_{Inf}$ | 0.0262 |
| $pH_{Inf} + SS_{Inf} + OG_{Inf}$ | 0.0193 |
| $pH_{Inf} + SS_{Inf} + BOD_{Inf}$ | 0.0171 |
| $SS_{Inf} + BOD_{Inf} + OG_{Inf}$ | 0.0341 |

## CONCLUSION

Artificial neural networks-based modeling and simulation of any sewage treatment plant is effective in predicting its performance and controlling the operation of the plant resulting in the improved treated effluent. The modeling methodologies adopted with different combinations of input variables gave good predictions between the measured and predicted values.

Effluent biochemical oxygen demand BOD was predicted with a maximum correlation coefficient value of 0.927 and minimum mean square error of 0.0022 with eight neurons in the hidden layer. Effluent-suspended solids were predicted with a maximum correlation coefficient value of 0.947 and minimum mean square value of 0.0058 with seventeen neurons in the hidden layer. Effluent pH was predicted with a maximum correlation coefficient value of 0.8299 and minimum mean square value of 0.0132 with twenty-one neurons in the hidden layer.

From the sensitivity analysis, it has been found that the most important parameter for predicting biochemical oxygen demand is suspended solids followed by pH, oil and grease, and BOD at the influent stream. The most important parameter for predicting suspended solids is pH followed by oil and grease, suspended solids, and biochemical oxygen demand. Also, the most important parameter for predicting pH is pH followed by suspended solids at the influent stream.

## REFERENCES

Abyaneh, H.Z. 2014. Evaluation of multivariate linear regression and artificial neural networks in prediction of water quality parameters. J. Environ. Health Sci. Eng., 12: 40.

Alsulaili, A. and Refaie, A. 2021. Artificial neural network modeling approach for the prediction of five-day biochemical oxygen demand and wastewater treatment plant performance. Water Supply., 21(5): 1861-1877.

Fu, C.S. and Poch, M. 1995. System identification and real-time pattern recognition by neural networks for an activated sludge process. Environ. Int., 21 (1): 57-69.

Geman, S., Bienenstock, E. and Doursat, R. 1992. Neural networks and the bias/variance dilemma. Neural Comput., 4(1): 1-58.

Giokas, D., Vlessidis, A., Angelidis, M. Tsimarakis, G. J. and Karayannis, M.2002. Systematic analysis of the operational response of activated sludge process to variable wastewater flows. A case study. Clean Technol. Environ. Policy, 4(3): 183-190.

Hamada, M. Adel Zaqoot, H. and Abu Jreiban, A. 2018. Application of artificial neural networks for the prediction of Gaza wastewater treatment plant performance - Gaza strip. J. Appl. Res. Water Wastewater., 5(1): 399-406.

Hamed, M.M. Khalafallah, M.G. and Hassanien, E.A. 2004. Prediction of wastewater treatment plant performance using artificial neural networks. Environ. Model. Softw., 19(10): 919-928.

Hamoda, M.F., Al-Gusain, I.A. and Hassan, A.H. 1999. Integrated wastewater treatment plant performance evaluation using artificial neural network. Water Sci. Technol., 40: 55-69.

Haykin, S. S. 2009. Neural Networks and Learning Machines. Prentice Hall., pp. 36-54.

Henze, M. Grady, C.P.L. Gujer, W. Marais, G.V.R. and Matsuo, T. 1987. Activated Sludge Model no 1. IWAPRC. Scientific and Technical Report No., 1.IWA Publishing.

Lelie, L. B. Bantay, A.J. and Paug, D A. 2021. Correlational analysis of the effluent from the San Carlos Biopower, Inc. Wastewater Treatment Plant. J. Eng. Technol., 9: 12-20.

Lippmann, R. P. 1988. An introduction to computing with neuralnets. In: Artificial Neural Networks. Theoretical Concepts (V. Vemuri, ed.). IEEE Computer Society Press., pp. 36-54.

Manfred, S. Butler, D. and Beck, M. B. 2002. Modelling, Simulation and Control of Urban Wastewater Systems. Springer-Verlag London Limited., pp. 27-29, 357.

Mjalli, F.S. Al-Asheh, S. and Alfadala, H.E. 2007. Use of artificial neural network black-box modeling for the prediction of wastewater treatment plants performance, J. Environ. Econ. Manag., 83(3): 329-338.

Nair, V.V. Dhar, H. Kumar, S. Thalla, A.K. Mukherjee, S. and Wong, J.W. 2016. Artificial neural network based modeling to evaluate methane yield from biogas in a laboratory-scale anaerobic bioreactor. Bioresour. Technol., 217: 90-99.

Nasr, M.S., Moustafa, M.A.E., Seif, H.A.E. and El, Kobrosy J. 2012. Application of artificial neural network (ANN) for the prediction of EL-AGAMY wastewater treatment plant performance EGYPT. Alex. Eng., J., 51: 37-4.

Pai, T.Y. Yang, P.Y. Wang, S.C. Lo, M.H. Chiang, C.F. Kuo, J.L. and Chang, Y.H. 2011. Predicting effluent from the wastewater treatment plant of industrial park based on fuzzy network and influent quality. Appl. Math. Model., 35: 3674-3684.

Pareek, V.K. Brungs, M.P. Adesina and A.A. Sharma, R. 2002. Artificial neural network modeling of a multiphase photodegradation system. J. Photochem. Photobiol., 149: 139-146.

Vos, N. J. and Rientjes, T. H. M. 2005. Constraints of artificial neural networks for rainfall-runoff modelling: trade-offs in hydrological state representation and model evaluation. Hydrol. Earth Syst. Sci., 9: 111-126.

Nature Environment and Pollution Technology
An International Quarterly Scientific Journal

p-ISSN: 0972-6268
(Print copies up to 2016)
e-ISSN: 2395-3454

Vol. 22 | No. 1 | pp. 463-470 | 2023

Original Research Paper

https://doi.org/10.46488/NEPT.2023.v22i01.044

Open Access Journal

# Sustainable Campus Policy Strategy in Estimating $CO_2$ Emissions at the Universitas Negeri Semarang, Indonesia

**Said Sunardiyo*†, P. Purwanto** and H. Hermawan*****

*Department of Electrical Engineering, Faculty of Engineering, Universitas Negeri Semarang, 50229, Indonesia
**Department of Chemical Engineering, Faculty of Engineering, Diponegoro University, Semarang, 50275, Indonesia
***Department of Electrical Engineering, Faculty of Engineering, Diponegoro University, Semarang, 50275, Indonesia
†Corresponding author: Sunardiyo Said; saidelektro@gmail.com

**Nat. Env. & Poll. Tech.**
**Website: www.neptjournal.com**

*Received:* 09-07-2022
*Revised:* 21-09-2022
*Accepted:* 29-09-2022

**Key Words:**
Campus management policies
Forecasts
Electricity consumption
BP-ANN
$CO_2$ emissions

## ABSTRACT

In the fight against global warming, various options for reducing $CO_2$ emissions are being implemented on campus. Furthermore, the management of campus sustainability at the Universitas Negeri Semarang (UNNES), Central Java, Indonesia, should be supported by accurate forecasts of electrical energy consumption. Therefore, this research aims to develop a predictive model to forecast the consumption of electrical energy in reducing $CO_2$ emissions and to determine the factors triggering the increase. The prediction model is developed using Back Propagation Neural Network Artificial (BP-ANN) architecture. Furthermore, the data on the occupancy of lecturers and education staff as well as on students was obtained from the University's staffing and student affairs bureau. Climatic data such as temperature, humidity, wind speed, the duration of irradiation, and the average intensity of solar radiation were obtained per month from the Meteorology, Climatology, and Geophysics Agency of Semarang, Central Java for the 2013-2019 period as input data. The results of the empirical analysis showed an increase in electrical energy consumption from 2020 to 2025. In March, the consumption decreased but increased from April to June and decreased in July. It then increased until November and December, and it decreased every year. The results of $CO_2$ emissions calculated by considering the emission factors from Indonesia's RUPTL-PLN in 2020-2025 showed an increase in electrical energy consumption and the ecological consequences affecting the campus area. Furthermore, the main factors causing the high consumption of electrical energy are the occupancy rate, lecturers, students, and campus employees, as well as local climate influences such as temperature, humidity, wind speed, duration of solar radiation, and intensity of solar radiation. Therefore, developing guidelines to reduce power consumption on campus should be a priority

## INTRODUCTION

Based on empirical data, several studies have shown an increase in energy demand in campus buildings (Amaral et al. 2020). This is considered unfavorable regarding the environment, especially for unsustainable resources (Ambariyanto et al. 2018). Estimating the energy efficiency of educational buildings needs to consider the composition of research-related factors (Agdas et al. 2019, Yeo & Wang 2019). Currently, the consumption of electrical energy in green campus buildings is an essential factor in the energy system. The construction sector is responsible for most global greenhouse gas emissions and all primary energy consumption (Ahmad et al. 2014, Beceric-Gerber et al. 2014, Rochester University 2015). Therefore, total electrical energy consumption needs to be estimated in planning. This is an essential factor in improving building performance, energy management and saving, fault detection and diagnosis, and optimizing smart buildings (Liu et al. 2019) stated that accurate energy forecasts help building managers prepare future budgets for their management (Amber et al. 2015).

Meanwhile, it stated that an accurate forecast of the electricity consumption of a building is a basis for energy management and shows the energy-saving potential of a building (Ding et al. 2019). The North China University Of Science and Technology, a large customer of electrical energy resources, has conducted actual measurements and simulations of consumption in energy-saving analysis for the campus (Ruijiang et al. 2017, Qiao & Liu 2020, Ghedamsi 2015). The campus is considered an area with a high level of energy use through educational activities, as well as large waste products from the activities of the

residents (Meng et al. 2007, Min & Chunga 2014, Hongwei et al. 2014). Subsequently, Universitas Negeri Semarang has different guidelines for implementing sustainable campus management, such as the Green, Clean, and Healthy (H-Bat) program integrated into UI Greenmetric. Campus arrangement and infrastructure provide an overview of tendencies toward a green environment, energy and climate change, waste, water, transportation, and education (Prihanto 2018, Rokhman & Zaenuri 2020, Wahyuningsih et al. 2020). The selection of a suitable forecast model and good results is the basis for significant future research on electrical energy forecasting on campus. Several models have been considered to select the Artificial Neural Network (ANN) model to forecast electrical energy consumption.

Artificial Neural Network (ANN) is an approach used for forecasting, considering the ability to study and recognize historical data patterns stated. That it is often applied in studying building energy systems (Sharma & Nijhawan 2015, Kalogirou 2006, Malik et al. 2016), according to Li et al. (2019), Ahmad et al. (2014), Babu et al. (2020) and Deb (2016), ANN is the most widely used artificial intelligence model in the field of building performance optimization because of its speed and high accuracy, and can also handle nonlinear relationships between variables. Furthermore, it is an information-processing system with characteristics similar to biological neural networks. It is inspired by the human brain, where neurons are interconnected in a nonlinear manner. Neurons are the processing units of artificial neural networks, and each neuron receives input, processes it, and sends the result as output (Fausett 1994). The back-propagation algorithm adjusts the weights between neurons to achieve a minimal error between the forecasted and the real output (Lee & Choi 2012, Safi & Bouromi A 2013).

Furthermore, back-propagation neural networks have advantages over other artificial types when supervised training. A neural network is said to be supervised when the expected output is known (Park & Kang 2007, Runge & Zmeureanu 2019, Siregar & Wanto2017, Fang & He 2014). Therefore, this research uses Artificial Neural Network (ANN) back-propagation (Chen & Jain 1994, Olawoyin 2016, Tarigana et al. 2017) to (1) predict the electricity consumption on campus and (2) calculate the $CO_2$ emission. Based on the researchers' study, it is important to develop a model for forecasting electrical energy consumption in reducing $CO_2$ emissions on campuses. This is because the current campus is a large user of electrical energy, and the commercial sector has many buildings and many occupancy rates. BP-ANN was chosen as a forecast model with a high accuracy level capable of short-term to long-term forecasts.

## MATERIALS AND METHODS

This research was conducted in the eastern area of the UNNES campus in Semarang, Central Java, Indonesia (Fig, 1). It included 6 administrative office buildings, lectures, and laboratories in the Faculties of Education, Economics, Social Sciences, Law, Sports Science, and Engineering. Based on reviews and research, most of which affect the consumption of electrical energy such as the density of building occupants as well as the local climate (Li & Sailor 1995, Lupato 2019, Farah & Whaley 2019, Moazami et al. 2019, Hashimoto & Ihara 2013, Ahmed et al. 2012, Obaidellah & Danaee 2019)


Fig. 1: Research location map.

Meanwhile, the staffing and student affairs office obtained data on the monthly building occupants consisting of lecturers, education staff, and students. The monthly data on temperature, humidity, wind speed, duration of irradiation, and average solar radiation intensity per month from January 2013 to December 2019 were collected from the Office of the Meteorology, Climatology, and Geophysics Agency in Semarang, Central Java, Indonesia.

## Modeling of Back Propagation Artificial Neural Network

### Data Preprocess

The monthly data on learning used as a reference was 40% of the initial ones for 2013-2019. It was adjusted to the input and output patterns determined as follows: (1) Input Pattern, BP-ANN learning input data for 72 months from 2013-2019 divided into 2 parts, namely learning patterns using 60%

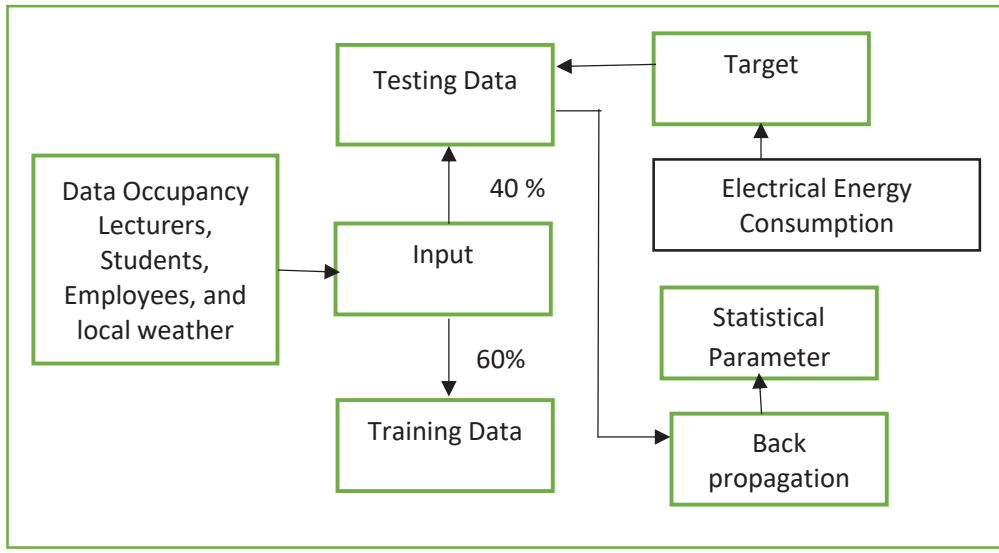


(a)

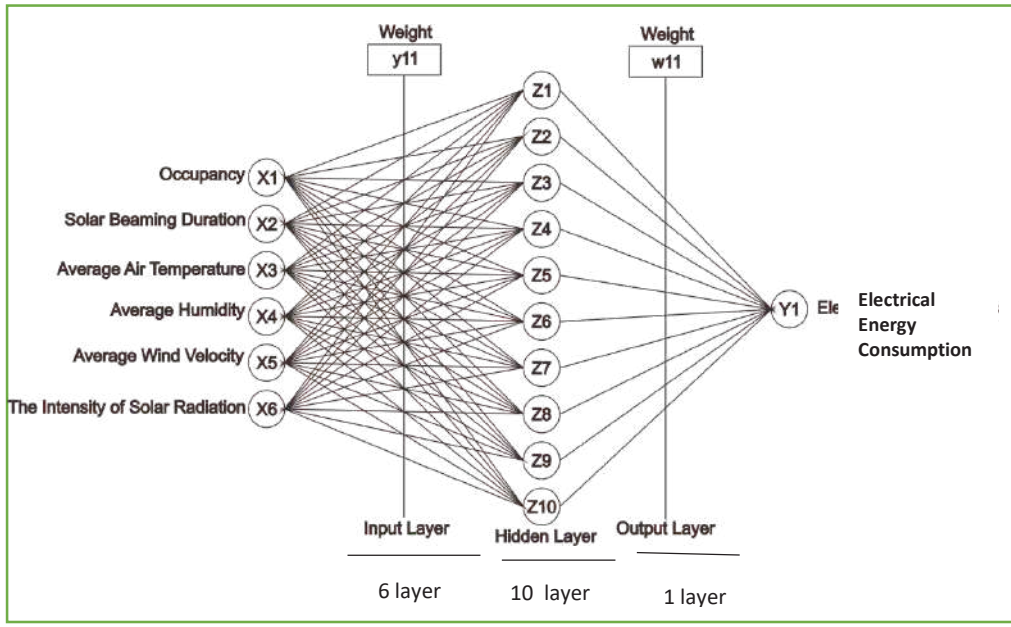


(b)

Fig. 2: (a) Consumption energy electricity prediction model; (b) Network topology.

data and 40% for testing of the total initial data. The training process used a pattern of 6 inputs, 10 hidden, and 1 output layer (Fig. 2). Therefore, the output from this training data was analyzed, and the value of Mean Square Error (MSE) was the measure of forecasting accuracy. The best MSE value (smallest error value) from several trainings was used for simulation with test data. The formation of an artificial neural network used the Feedforward Back-propagation model, and the training process used the Traingdm function. Furthermore, the analysis step in building the best architecture was determined from several parameters such as (1) Logsig activation function used to bridge the comparison between the sum of the values of all future weights and the input with a threshold value available in the Matlab toolbox (Howard 2000), (2) In this study, the best result was indicated by the epoch value of 10000. (3) the best learning result using goal performance with a value of 0.001. (4) the more hidden layers, the better the learning and the longer it takes. This research used 10 hidden layers with values of 20 and 50 to slow the learning rate, while hidden layers of less than 10 shorten the learning rate with high error values. Furthermore, (5) research conducted by Trainingdm used the Gradient Descent learning function with Momentum and Adaptive Learning Rate (GDM / Traingdm). The traingdx algorithm updates the weight according to the gradient descent method with an adaptive learning rate combined with momentum to accelerate the network learning rate. In addition, the network learning process (Train Network) within the specified epoch or error value will automatically stop.

### Model Evaluation

The method of Mean Absolute Percentage Error (MAPE) forecasting is used to determine the absolute error of each period. It is then divided by the observed value for that period and averaging the absolute percentage. Furthermore, MAPE states the percentage of error forecasting against actual results over a certain period. It is the average absolute error over a certain period multiplied by 100% to obtain a percentage result. This approach is useful when the size or magnitude of the forecast variable is important in evaluating the accuracy of the forecast. MAPE compares the weight of the error in guessing to the real value. Mathematically (Chen et al. 2007), it is given as:

$$\text{MAPE} = \sum_{t=1}^{n} \left| \frac{y_i - \hat{y}_i}{\hat{y}_i} \right| \times 100\%$$

Where:

MAPE = Mean Absolute Percentage Error

n = the number of data

y = actual yield value

$\hat{y}$ = forecast value

The resulting MAPE value has the following interpretation :

1. MAPE < 10% : highly accurate
2. 10% ≤ MAPE < 20% : good accurate
3. 20% ≤ MAPE <≤ 50% : reasonable accurate
4. MAPE 50% : inaccurate

## RESULTS AND DISCUSSION

### Electrical Energy Consumption Forecast Using BP-ANN

In the energy management and climate change program, the campus makes policies through the office of the implementing unit for conservation tasks. This was conducted by implementing energy efficiency on campus for new renewable energy, such as using solar modules to replace electricity sources from PLN (Perusahaan Listrik Negara/ (State Electricity Enterprise), automatic control applications for lighting, air conditioning, and other equipment electricity. Furthermore, it includes conducting energy audits for campus electrical systems and training employees on energy audits and electric power systems. However, the results of observations from the campus household showed a yearly increase in electricity costs. Therefore, the monthly increase and the cost of electricity consumption should be examined. This research used BP-ANN to predict errors in training since it recognizes the pattern and produces an accurate input-output relationship. It also used a feedforward back propagation algorithm with one hidden layer, and the number of neurons was developed in this BP-ANN method. In addition, several structural MLP (Multi-layer Perception) efforts have been trained and developed in Matlab software. This structure showed the number of neurons in the input, hidden, and output layers. The comparison of measured and predicted values was checked according to the Mean Average Percentage Error (MAPE) with equation (6). The results showed that the BP-ANN model achieved a significant agreement between the estimated value and the average monthly electricity consumption with MAPE, which is 9.6105% below 10% and has a high prediction accuracy (Lewis 1982, Tayman & Swanson 1999). An estimator can achieve MAPE with the structure of MLP consisting of 6, 10, and 1 neuron in the input, hidden, and output layers.

The measured or forecasted values of electrical energy consumption in green campuses are presented in Table 1.

Table 1: The results of the measurement value with the target value of electrical energy consumption using BP-ANN.

| Month | Monthly electricity consumption [kWh] | Monthly electricity consumption predicted [kWh] | Error [kWh] | Error [%] | MAPE |
|---|---|---|---|---|---|
| January | 218028,230 | 218626 | 597,7696 | 0.071142 | 0.096105 |
| February | 198498,260 | 199467 | 968,7396 | -0.01653 | |
| March | 176182,273 | 175897 | 285,273 | -0.16102 | |
| April | 267692,607 | 269987 | 2294,393 | 0.008223 | |
| May | 244261,746 | 246789 | 2527,254 | 0.009057 | |
| June | 249430,670 | 250243 | 812,3296 | 0.002911 | |
| July | 181879,404 | 178748 | 3131,404 | -0.01122 | |
| August | 209176,099 | 210239 | 1062,9 | 0.003809 | |
| September | 229160,837 | 227034 | 2126,837 | -0.00762 | |
| October | 261834,830 | 263748 | 1913,17 | 0.016856 | |
| November | 269313,258 | 269849 | 535,742 | 0.02192 | |
| December | 259735,610 | 258839 | 896,6098 | -0.00541 | |

The validity results showed that the MAPE price was below 10%. Because of that, the BP-ANN model is feasible to use to estimate electricity consumption in green campuses, as illustrated in Fig. 3.

The results of the forecasted electrical energy consumption can be presented in Table 2.

Fig. 4 shows the results of forecasting electrical energy consumption using the BP-ANN model in 2020 - 2025 in the green campus building at Universitas Negeri Semarang, Indonesia. The electricity consumption in green campuses was different every month and was quite high in February and March, then low in June, July, August, and September. It increased from October to November and then decreased in December. This finding allows managers to consider strategies for saving electricity, energy conservation, electricity system management, and support for the environment in reducing carbon emissions in the future. The relevant research (Lee & Choi 2013) shows that back-propagation neural networks have other advantages over other artificial neural networks, namely back-propagation artificial neural networks using supervised training. The neural network is supervised if the expected output is known beforehand and concludes that the accuracy of back-propagation ANN forecasts is 81.43% greater than the accuracy of multivariate discriminant analysis, which is 74.82%. The ANN model can be applied to forecast building energy consumption and is suitable for all buildings (Deb

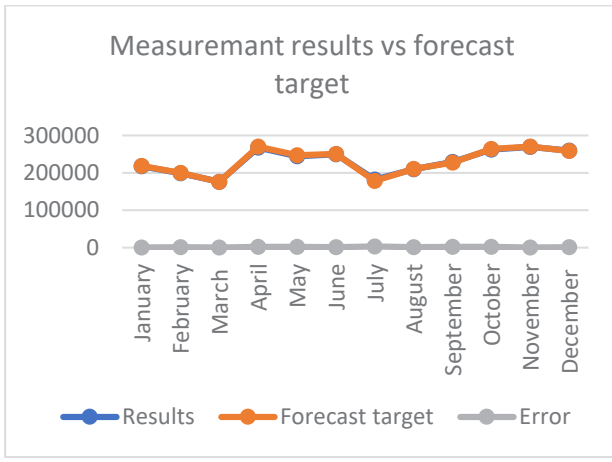


Fig. 3: Graph of validation of measurement results versus forecast targets.

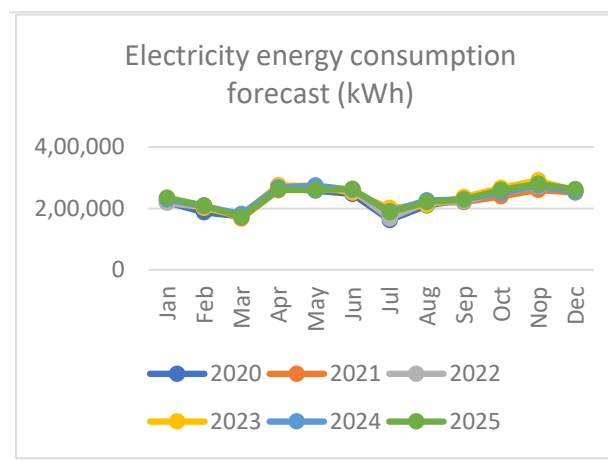


Fig. 4: Graph of electrical energy consumption forecast (kWh) in 2020-2025.

Table 2: Estimated results of electrical energy consumption (kWh) in green campuses in 2020 -2025 using the BP -ANN model.

| Month | Year | | | | | |
|---|---|---|---|---|---|---|
| | 2020 | 2021 | 2022 | 2023 | 2024 | 2025 |
| January | 221.098 | 226.678 | 218.307 | 232.259 | 229.469 | 235.049 |
| February | 187.337 | 209.939 | 204.079 | 201.289 | 206.870 | 209.660 |
| March | 174.507 | 167.811 | 178.972 | 176.182 | 181.762 | 173.391 |
| April | 264.903 | 259.322 | 273.274 | 276.064 | 267.693 | 262.113 |
| May | 258.215 | 263.795 | 261.005 | 272.166 | 274.957 | 261.005 |
| June | 246.640 | 257.802 | 260.592 | 251.105 | 260.592 | 263.382 |
| July | 162.347 | 170.718 | 167.928 | 201.412 | 190.251 | 187.460 |
| August | 209.177 | 218.106 | 220.339 | 211.968 | 225.919 | 220.339 |
| September | 229.162 | 220.791 | 223.581 | 237.533 | 229.162 | 229.162 |
| October | 250.672 | 239.511 | 253.463 | 267.414 | 251.788 | 260.997 |
| November | 263.734 | 260.944 | 272.105 | 291.637 | 274.895 | 280.476 |
| December | 257.559 | 251.978 | 260.349 | 257.559 | 254.769 | 263.140 |

Table 3: $CO_2$ emission factors for the Java-Bali electricity system in 2020-2025.

| Year | Emission Factor (EF) [$kgCO_2/kWh^{-1}$] |
|---|---|
| 2020 | 0.854 |
| 2021 | 0.854 |
| 2022 | 0.871 |
| 2023 | 0.871 |
| 2024 | 0.871 |
| 2025 | 0.759 |

$CO_2$ emissions = EF x Electricity production, given in ($kgCO_2$/kWh) per month: (Source: ESDM of Republic of Indonesia 2016)

2016, Ghedamsi 2015).

### The Relationship between Electrical Energy Consumption and $CO_2$ Emissions on Campus

The amount of $CO_2$ emissions can be determined from the equation based on the results of forecasting electricity consumption in the location:

$CO_2$ emissions = EF x Electricity production (IPCC 2006). The Emission Factor (EF) of electricity was determined from the electricity emission factor of the Java–Bali system. The factors of CO2 emissions in Java and Balli over the year are given in Table 3.

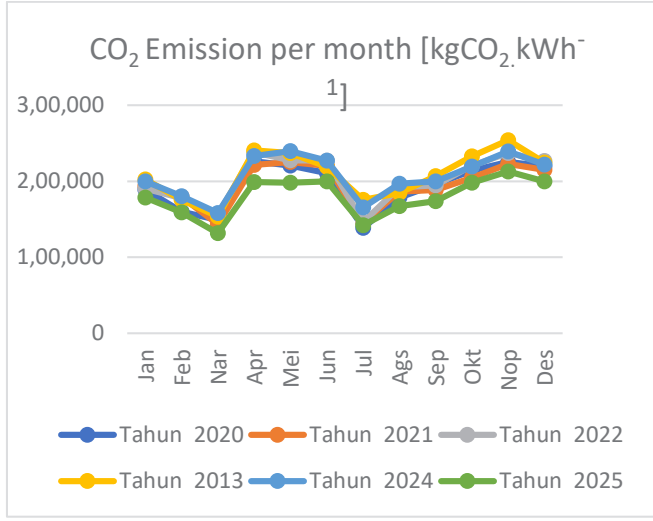


Fig. 5: Graph of the amount of $CO_2$ emissions per month ($kgCO_2.kWh^{-1}$) in 2020-2025.

Fig. 5 and Table 4 show the quantity of $CO_2$ emissions per month ($kgCO_2.kWh^{-1}$) on a green campus in 2020-2025. These predictions and calculations support policies to reduce electricity consumption and greenhouse gas emissions. The future implications of this electrical energy forecast can provide an overview of $CO_2$ emissions in green campuses. (Presekal et al. 2018, Robinson et al. 2015, Riddel et al. 2009, Babatunde et al. 2020). The estimated electrical energy demand (kWh) results affect the $CO_2$ emissions generated in 2020-2025.

## CONCLUSION

The development of sustainability policies oriented toward reducing campus electricity consumption should be prioritized. Furthermore, implementing the BP-ANN model for predicting electrical energy consumption in the State University of Semarang green campus building showed good accuracy with a MAPE value of 9.6105%. Therefore, it was "feasible" to be used as a model for forecasting electricity consumption. In addition, the makers of green campus policies can obtain information on $CO_2$ gas emissions from electrical energy consumption to investigate the amount.

Several things that require further research are related to electrical energy data during the COVID-19 pandemic to estimate electrical energy on campus and the reduction in $CO_2$ emissions due to reduced occupancy rates. Future work on the results of electrical energy forecasts in reducing CO2 emissions is one of the aspects taken into account for the achievement of SDGs in higher education institutions

## ACKNOWLEDGMENTS

The authors are grateful to DRPM DIKTI Republic Indonesia and LPPM Universitas Negeri Semarang for funding this research.

## REFERENCES

Agdas, D., Ravi S. and Srinivasan, M. 2015. Energy use assessment of educational buildings: Toward a campus-wide sustainable energy policy. Sustain. Cities Soc., 17: 15-21.

Ahmad, A.S., Hassan, M.Y. and Abdullah, M.P. 2014. A review on applications of ANN and SVM for building electrical energy consumption forecasting. Renew. Sustain. Energy Rev., 2014; 33: 102-109.

Ahmed, T., Muttaqi, K.M., Agalgaonkar, A. 2012. Climate change impacts on electricity demand in the State of New South Wales, Australia. Appl. Energy., 98: 376-383.

Amaral, A.R., Rodriguesa E., Gaspara, A.R. and Gomes, A. 2020. A review of empirical data of sustainability initiatives in university campus operations. J. Clean. Prod., 250: 119558.

Ambariyanto., Utama Y.J. and Purwanto, R. 2018 Managing campus energy: compromising between rapid needs and environmental requirement. E3S Web Conf., 31: 01003.

Amber, K.P., Aslam, M.W. and Hussain, S.K 2015. Electricity consumption forecasting models for administration buildings of the UK higher education sector. Energy Build., 90: 127-136.

Babatunde, D.E., Anozie, A. and Omoleye, J. 2020. Artificial neural network and its applications in the energy sector: An overview. Int. J. Energy Econ. Policy., 10(2): 250-264.

Babu, D., Thangarasu,V. and Ramanathan, A. 2020. Artificial neural network approach on forecasting diesel engine characteristics fuelled with waste frying oil biodiesel. Appl. Energy., 263: 114612).

Becerik-Gerber, B., Siddiqui, M.K. and Brilakis, I. 2014. Civil engineering grand challenges: opportunities for data sensing, information analysis, and knowledge discovery. J. Comp. Civil Eng., 28: 401-4013

Chen, D.S. and Jain R.C.A. 1994. Robust back-propagation learning algorithm for function approximation. IEEE Trans. Neural Netw., 5: 467-479.

Chen, R..J.C., Bloomfield, P. and Cubbage, F.W. 2007. Comparing forecasting models in tourism. J. Hospital. Tour. Res., 32: 3-21.

Deb, C. 2016. Forecasting diurnal cooling energy load for institutional buildings using Artificial Neural Networks. Energy Build., 12: 284-297.

Decree of the Minister of Energy and Mineral Resources (ESDM) of the Republic of Indonesia No. 5899 K / 20 / MEN / 2016. 2016. Ratification of The Electricity Supply Business Plan of PT Perusahaan Listrik Negara (PLN) Persero 2016 to 2025, 170-172.

Ding, Y., Wang, Q. and Wang, Z. 2019. An occupancy-based model for building electricity consumption prediction: A case study of three campus buildings in Tianjin. Energy Build., 109: 12-22.

Fang, H. and He, L. 2014. Human activity recognition based on feature selection in smart home using back-propagation algorithm. ISA Trans., 53: 1629-1638.

Farah, S. and Whaley, D. 2019. Integrating climate change into meteorological weather data for building energy simulation. Energy Build., 183: 749-760.

Fausett, L. 1994. Fundamental of Neural Networks: Architectures, Algorithms, and Applications. Prentice-Hall, New Jersey.

Ghedamsi, R. 2015. Modeling and forecasting energy consumption for residential buildings in Algeria using bottom-up approach. Energy Build., 121: 309-317.

Hashimoto, Y. and Ihara, T. 2013. Sensitivity of Electricity Consumption to Air Temperature, Air Humidity And Solar Radiation In City-Block Scale: Based on 2013 Osaka City Observation. ICUC9 - 9 th International Conference on Urban Climate Jointly with 12th Symposium on the Urban Environment, 20-24 July 2015, Toulouse, France, pp. 1-5.

Hongwei, T., Shuqin, C. and Qian, S. 2014. Development of green campus in China. J. Clean. Prod., 64: 646 – 653.

Howard, D.M.B. 2000. Neural Network Toolbox For Use with MATLAB. The MathWorks, Inc., Natick, MA, USA

Intergovernmental Panel on Climate Change (IPCC). 2006. IPCC Guidelines for National Greenhouse Gas Inventories. IPCC, Geneva, Switzerland.

Tayman, J. and Swanson, D.A. 1999. On the validity of MAPE as a measure of population forecast accuracy. Popul. Res. Policy Rev., 18(4): 299-322

Kalogirou, S.A. 2006. Artificial neural networks in energy applications in buildings. Int. J. Low Carbon Technol., 1: 201-216.

Lee, S. and Choi, W.S. 2012. A multi-industry bankruptcy prediction model using back-propagation neural network and multivariate discriminant analysis. Expert Syst. Appl., 40: 2941-2946.

Lewis, C.D. 1982. Industrial and Business Forecasting Methods: A Practical Guide to Exponential Smoothing and Curve. Butterworth Scientific, Boston.

Li, X. and Sailor, D.J. 1995. Electricity use sensitivity to climate and climate change. World Resour. Rev., 3: 334.

Li, Z., Chen, H. and Lin, B. 2019. An ANN-based fast building energy consumption prediction method for complex architectural form at the early design stage. Build. Simul., 12: 665–681.

Liu, Z., Wu, D. and Liu, Y. 2019. Accuracy analyses and model comparison of machine learning adopted in building energy consumption prediction. Energy Explor. Exploit., 37: 1426-1451.

Lupato, M. 2019. Italian TRYs: New weather data impact on building energy simulations. Energy Build., 185: 287-303.

Malik, H. and Savita. 2016. Application of artificial neural network for long-term wind speed prediction. Conf. Adv. Signal Process., 64: 217-222.

Meng, L.L., Abidin, M., Razak, A. and Dzulkifli, A. 2007. Kampus Sejahtera Kampus Lestari: The Genesis for a Sustainable Campus. Corporate & Sustainable Development Division, Universiti Sains Malaysia.

Min, H. and Chunga, E.K.R. 2014. Potential opportunities for energy conservation in existing buildings on a university campus: A field survey in Korea. Energy Build. 78: 176-182.

Moazami, A., Nik, V.M. and Carlucci, S.G. 2019. Impacts of future weather data typology on building energy performance – Investigating long-term patterns of climate change and extreme weather conditions. Appl. Energy, 238: 696-720.

Obaidellah, U.H. and Danaee, M. 2019. An application of TPB constructs on energy-saving behavioural intention among university office building occupants: a pilot study in Malaysian tropical climate. J. Hous. Built Environ., 34: 533-569.

Olawoyin, R. 2016. Application of back-propagation artificial neural network prediction model for the PAH bioremediation of polluted soil. Chemosphere, 161: 145-150.

Park, M.J. and Kang, H.T. 2007. Prediction of fatigue life for spot welds using back-propagation neural networks. Mater. Des., 28: 2577-2584.

Presekal, A., Herdiansyah, H., Harwahyu, R., Suwartha, N. and Sari, S.F. 2018. Evaluation of electricity consumption and carbon footprint of UI GreenMetric participating universities using regression analysis. E3S Web Conf., 48: 03007.

Prihanto, T. 2018. Green campus management based on conservation program in Universitas Negeri Semarang. AIP Conf. Proceed., 941: 020-024.

Qiao, R. and Liu, T. 2020. Impact of building greening on building energy consumption: A quantitative computational approach. J. Clean Prod., 246: 119020.

Riddell, W., Bhatia, K.K. and Parisi, M. 2009. Assessing carbon dioxide emissions from energy use at a university. Int. J. Sustain. High. Edu., 10: 266-278.

Robinson, O., Kemp, S. and Williams, I. 2015. Carbon management at universities: A reality check. J. Clean. Prod., 106: 109-118.

Rochester University. 2015. Sustainability home. https://www.rochester.edu/sustainability/.

Rokhman, F. and Zaenuri, X. 2020. Concept evolution of conservation. J. Phys. Conf. Ser. IOP Publ., 1567: 042-055.

Ruijiang, L., Ying, H. and Xuejie, Z. 2017. Characteristics of campus energy consumption in North China University of Science and Technology. Sci. Proced. Eng., 205: 3816-3823.

Runge, J. and Zmeureanu, R. 2019. Forecasting energy use in building using artificial neural network: A review. Energies, 12: 3254.

Safi, Y. and Bouroumi, A. 2013. Prediction of forest fires using artificial neural networks. Appl. Math. Sci., 7: 271- 286.

Sharma, A. and Nijhawan, G. 2015. Rainfall prediction using neural network. Int. J. Comp. Sci. Trends Technol., 3: 65-69.

Siregar, A.P. and Wanto, A. 2017. Analysis accuracy of artificial neural network using back-propagation algorithm in predicting process (forecasting). Int. J. Inform. Syst.Technol., 1: 34-42.

Tarigana, J., Nadiab, B., Diedan, R. and Surayana, Y. 2017. Plate recognition using back-propagation neural network and genetic algorithm. Proceed. Comp. Sci., 111: 365-372.

Wahyuningsih, M., Sudana, I..M. and Fardhyanti, D.S. 2020. Education indicator evaluation of UI Green Metric of campus sustainability of Faculty of Engineering Universitas Negeri Semarang. Int. J. Innov. Learn., 28: 12-24.

Yeo, J. and Wang Y. 2019. Estimation of energy efficiency for educational buildings in Hong Kong. J. Clean Prod., 235: 453-460.

Nature Environment and Pollution Technology
An International Quarterly Scientific Journal

p-ISSN: 0972-6268
(Print copies up to 2016)
e-ISSN: 2395-3454

Vol. 22 | No. 1 | pp. 471-476 | 2023

Original Research Paper

https://doi.org/10.46488/NEPT.2023.v22i01.045

Open Access Journal

# Concentration of Toxic Heavy Metals and Phytochemicals in a Medicinal Plant (*Asclepias fruticosa*) Collected Around Mining Areas in Brits, Pretoria

**L. L. Mugivhisa†, D. Mzimba and J. O. Olowoyo**

Department of Biology, Sefako Makgatho Health Sciences University, P.O Box 139, 0204, Pretoria, South Africa

†Corresponding author: L. L. Mugivhisa; liziwe.mugivhisa@smu.ac.za

**Nat. Env. & Poll. Tech.**
**Website: www.neptjournal.com**

*Received:* 01-08-2022
*Revised:* 12-09-2022
*Accepted:* 29-09-2022

**Key Words:**
Heavy metals
Traditional medicine
Phytochemicals
Medicinal plants
Mining areas

## ABSTRACT

The use of African traditional medicine in rural and peri-urban areas is common due to its affordability and accessibility. The study aimed to determine the levels of toxic heavy metals in the medicinal plant (*Asclepias fruticosa*) samples collected around three mining areas in Brits using ICP-OES. The phytochemical screening analysis was done to indicate the absence or presence of different phytochemicals in the medicinal plant. The results of the qualitative phytochemical analysis indicated the presence of flavonoids, alkaloids, proteins, and carbohydrates in *Asclepias fruticosa* collected from all the mining areas. The results of the heavy metals showed that the mean highest concentration for all the heavy metals was recorded for Mn from the leaves of the medicinal plants. The trend in the heavy metals accumulation was roots > leaves > stems from all the sites, and the differences were significant ($p < 0.05$). The range of heavy metals in the plant was in the range Mn (12.33 ± 2.31-85.33 ± 51.07 $\mu g.g^{-1}$), Zn (10.67 ± 0.58-60.33 ± 0.56 $\mu g.g^{-1}$), Cr (3.43 ± 0.06 -34.90 ± 0.10 $\mu g.g^{-1}$), Cu (8.67 ± 0.12-18.8 ± 1.57 $\mu g.g^{-1}$), Ni (5.67 ± 0.12-23.23 ± 1.7 $\mu g.g^{-1}$) and Pb (0.53 ± 0.013-1.59 ± 0.15 $\mu g.g^{-1}$). The values of the heavy metals Cr, Zn, and Ni in the plant exceeded the recommended limits set by WHO for human consumption. Heavy metals in the medicinal plant were accumulated in the roots and not translocated to the stems and leaves. It is therefore recommended that communities staying around the mines should be discouraged from picking and using medicinal plants growing around the mines and should be educated on the safety of medicinal plants growing around the mines.

## INTRODUCTION

The consumption of medicinal plants has been practiced since ancient times (Brima 2017) by all populations worldwide (Niaz et al. 2013). Medicinal plants have been widely used for treating, preventing, and managing diseases and most of the world's population depends on them for health benefits. About 65-80% of the world's population in marginal communities is dependent on traditional medicines and supplements as a form of primary healthcare for the treatment of several diseases in some rural communities where there is no availability or access to western medicine or where western medicine is not affordable (Dghaim et al. 2015, Kulhari et al. 2013, Kostić et al. 2011, Ekor, 2014, Annan et al. 2013, Mabona & Vuuren 2013, Olowoyo et al. 2012, Mulaudzi et al. 2017). Even though there has been an overwhelming introduction of medicinal plants in South Africa, there has not been any scientific validation of their efficacy and toxicity (Mtunzi et al. 2012).

Medicinal plants are preferable over synthetic remedies because they are believed to be natural, more effective, affordable, and original (Mulaudzi et al. 2017, Kulhari et al. 2013, Ayaz et al. 2014). However, traditional medicines may be toxic due to contaminants such as heavy metals, chemical toxins, pesticides, and microbes, which might be present in the soil, water, and air (Lajayer et al. 2017). In addition, the geography and the geochemical characteristics of the soil, the storage and transport conditions, harvesting and handling can also affect the quality and properties of traditional medicines (Aliyu et al. 2008, Dghaim et al. 2015).

According to Olowoyo et al. (2012), heavy metals are considered among medicinal plants' primary contaminants or pollutants. Most are toxic, even at low concentrations (Fahimirad & Hatami 2017). Heavy metals are assimilated into medicinal plants due to the presence of residues and the high prevalence of heavy metals in the environment (Fahimirad & Hatami 2017). The accumulation of heavy metals by medicinal plants is due to the extraction of metals soluble from the sediments, soil, and air, which are contaminated (Sarma et al. 2011). The primary source of heavy metals has been linked to environmental pollution, which includes emissions from traffic, municipal wastes,

pesticides and fertilizers, sewage sludge, industrial and mining activities (Fatima et al. 2014, Fahimirad & Hatami 2017, Kulhari et al. 2013, Rai et al. 2019, Asati et al. 2015). Pegadogenesis and weathering of parent rocks are also responsible for the non-anthropogenic origin of heavy metals resulting in their occurrence in soils (Street 2013).

Heavy metals are non-biologically degradable and have specific gravity of more than 5 $g.cm^3$ and atomic weights between 63.5–200.6 $g.mol^{-1}$ (Kulhari et al. 2013). Examples of common heavy metals are lead (Pb), copper (Cu), chromium (Cr), zinc (Zn), mercury (Hg), aluminum (Al), manganese (Mn), and cadmium (Fahimirad & Hatami 2017). Plants require certain heavy metals for uptake and growth. They can take in trace elements and heavy metals into their tissues because they can withstand toxic ions that are potentially toxic in the environment (Shirin et al. 2009, Street 2013). The concentrations and accumulation of the heavy metals vary from plant to plant found in the exact location (Niaz et al. 2013). Contamination of the environment results mainly from the toxicity, non-biodegradability, persistence, and bioaccumulative nature of the heavy metals, making them major hazardous chemicals in the environment that pose potential risks to the environment and human health (Zulkafflee et al. 2022, Malikula et al. 2021).

The majority of the curative effects of traditional medicines are a result of the presence of a minimal amount of trace metals (Shirin et al. 2009) which include elements such as Cobalt (Co), Nickel (Ni), magnesium (Mg), iron (Fe), iodine (I) and copper (Cu) which plants take up through the roots, foliar adsorption and deposition into the leaves (Kulhari et al. 2013, Nema et al. 2012). However, the levels of heavy metals in traditional medicines which are grown or collected from polluted or contaminated places are usually above the limits which are safe for human consumption resulting in traditional medicines being a crucial source of heavy metals through ingestion and consumption (Sarma et al. 2011, Glavač et al. 2017). Incidents of metal poisoning linked to the consumption of traditional medicines in South Africa are popular with magnesium (Mg), chromium (Cr), and arsenic (As) which are the most often implicated metals causing morbidity, poisoning, and mortality (Okem 2014).

Phytochemicals are bioactive compounds derived from plants that are non-nutritional and promote healing and health effects such as anti-inflammation, anti-hypertension, antioxidant, antibacterial, pain relief, and therapeutic effects (Khan et al. 2019, Khaleel 2018, Mahmood et al. 2019). Plants exposed to stress due to heavy metals exhibit different responses towards the phytochemicals, such as in the composition and the effectiveness of the medicinal plants (Street 2013, Okem 2014). Some plants can even show deviations in the production of phytochemicals with the increased levels of heavy metals contamination in medicinal plants leading to a decrease in the production of phytochemicals (Lajayer et al. 2017). Accumulating heavy metals in medicinal plants can also cause the production of phytochemicals in most species of plants (Nasim & Dhir 2010).

A synonym for *Asclepias fruticosa* is *Gomphocarpus fruticosus,* and its common English name is milkwood. The different parts of the plant are used medicinally for other purposes in various African countries. The infusion from the roots and leaves or the powder made from the leaves and roots dissolved in water is used medicinally to induce vomiting (https://uses.plantnet-project.org/en/Gomphocarpus_fruticosus; PROTA). The decoction of the plant roots and leaves can also be used to treat abdominal pains, gonorrhea, general body pain, infertility, malaria, diabetes, liver problems, asthma, diuretic, and nerve pain. The crushed leaves or dried leaves can be drunk as tea, used for skin cancer, or applied to sores, while the plant's latex is used for toothache treatment (https://uses.plantnet-project.org/en/Gomphocarpus_fruticosus; PROTA). The decoction made from the seed is used as a medicine for the treatment of cough, or the cooked roots of the plant are eaten as a vegetable (https://uses.plantnet-project.org/en/Gomphocarpus_fruticosus; PROTA).

The demand and consumption of traditional medicines and herbal products are growing globally. However, with an increase in the introduction of new developments in the market, there is also increasing recognition of concerns on the health issues of the public and their safety with regards to the consumption of traditional medicines (Ekor 2014, Nasim & Dhir 2010, Kostić et al. 2011). The consumption of medicinal plants collected around soils polluted by heavy metals must be carefully monitored and managed to reduce the levels of heavy metals in medicinal plants to protect the public from the harmful and adverse effects of the heavy metals (Nianz et al. 2013,0 Fahimirad & Hatami 2017). Hence the aim of the study was to determine the levels of heavy metals and phytochemicals in the medicinal plant *Asclepias fruticosa* growing around mining areas close to residential areas.

## MATERIALS AND METHODS

### Collection of Plant Samples

The medicinal plant, *Asclepias fruticosa,* known commonly in English as milkweed, was collected from around the three mining areas in Brits, in the North-West Province at a radius of about 50m from the mining areas (Olowoyo et al. 2015) and authenticated by a botanist in the Department of Biology

at Sefako Makgatho Health Sciences University in the north of Pretoria in South Africa. The collected plant samples were washed thoroughly with distilled water to remove superficial dust, separated into roots, leaves, and stems, dried in an oven, and then pulverized into a fine powder with a mortar and pestle. The pulverized plant samples were then stored in sample bags until they were analyzed.

**Analysis of Heavy Metals**

The collected plant samples were analyzed for the heavy metals, lead (Pb), copper (Cu), zinc (Zn), manganese (Mn), nickel (Ni), iron (Fe), and chromium (Cr) with the aid of the ICP-OES (Perkin Elmer ICP-OES Optima. 4300 DV (USA). Before analysis, 0.5 g of the dried plant samples were digested by mixing with 10.0 mL of nitric acid (HNO3,65% Merck supra pure) and 3.0 mL of HCIO4 (65% Merck supra pure). The resulting mixture was then heated up to 150°C using an oven for two hours and brought to a volume of 10.0 mL with deionized water. For quality assurance, plant samples were analyzed in triplicate. The same procedure was performed twice with a blank without plant samples with the digest of CRM042-050 containing the heavy metals to quantify any related contamination by the reagents. The subsequent solutions were analyzed for heavy metals with the aid of ICP-OES.

The translocation factors (TF) from the roots to stems and leaves to determine where the heavy metals accumulated within the different plant parts were calculated as flows: TF = conc. in the stems /conc. in the roots and TF = conc. in the leaves/conc. in the roots (Kutty & Al-Mahaqeri 2016). TF > 1 indicates that the different heavy metals were being translocated from the roots to the upper parts and that the medicinal plant is a hyperaccumulator, and TF < 1 suggests that the heavy metals were remaining in the roots and not being translocated and that the plant is not a hyperaccumulator (Kutty & Al-Mahaqeri 2016).

The mean concentrations of the heavy metals were presented as mean ± standard deviation. The tables and graphs were used to represent the results. For statistical analysis, the Analysis of Variance (ANOVA) was used to determine if there was any significant difference between the concentrations of the trace metals in the plant samples collected from the three different mines.

**Qualitative Determination of Phytochemicals**

The phytochemical screening analysis was done to indicate the absence or presence of different phytochemicals (tannins, saponins, alkaloids, and flavonoids) using standard methods as described with slight modifications (Yadav & Agarwala 2011).

The method of McGaw & Eloff (2008) was used for the plant extraction with minor modifications using Methanol, ethyl acetate, hexane, and distilled water. To obtain the plant extracts, 30.0ml of each solvent was added to 3.0 g of plant material and shaken for 30 minutes. The solution was then filtered using the Whitman No. 1 filter paper, and the filtered plant extracts were analyzed to identify the chemical constituents.

***Determination of Tannins***

About 0.5 ml of the extract solution was added to 1 mL of distilled water in a test tube to test for tannins. 2 to 3 drops of diluted ferric chloride solution were added until brownish green or blue-black color was observed

***Determination of Flavonoids***

For the presence of flavonoids, a few drops of 1% $NH_3$ were added to the extract solution in a test tube. The yellow coloration observed indicated the presence of flavonoids.

***Determination of Saponins***

About 2 mL of the extract solution was mixed with 2 mL of distilled water in a test tube and shaken thoroughly. The formation of stable foam indicated the presence of saponins.

***Determination of Alkaloids***

About 1 ml of 1% HCI was added to 3 mL of the extract solution in a test tube and treated with a few drops of Meyer's reagent. A formation of a creamy precipitate indicated the presence of alkaloids

## RESULTS AND DISCUSSION

The results in Table 1 show that from all the heavy metals investigated, the highest mean concentration recorded for all heavy metals in the roots, stems, and leaves was Mn, followed by Zn and then Cr, while the lowest mean concentration was for Pb. The concentration of Mn in the leaves, stems, and roots ranged between $12.33 \pm 2.31$ $\mu g.g^{-1}$ and $85.33 \pm 51.07$ $\mu g.g^{-1}$. The trend of Mn accumulation in *Asclepias fruticosa* from around the mining areas was: roots > leaves > stems. As the World Health Organisation (WHO) recommended, the permissible limit of Mn in medicinal plants is 200 $mg.kg^{-1}$ (Niaz et al. 2013). The Mn content in the roots, stems, and leaves was within the permissible limit recommended by WHO. Even though Mn plays and essential role in the production of proteins in the human body and is crucial in reproduction, it has been associated with neurotoxicity and reduced neural activation (Barahona et al. 2022).

Zn in the medicinal plant's roots, stems, and leaves from the mining areas ranged from $10.67 \pm 0.58$ $\mu g.g^{-1}$ to $60.33 \pm 0.56$ $\mu g.g^{-1}$ (Table 1). The maximum content limit of Zn

(to 60.33 ± 0.56 μg.g$^{-1}$) was above the permissible limit of 50mg/kg in medicinal plants as recommended by the WHO (Niaz et al. 2013). Zn in the human body is crucial for the functioning of the nerves, the production of white and red blood cells, vitamin stimulation, and fertility in males (Mtunzi et al. 2012). In contrast, excess Zn causes growth retardation and impairment in reproduction (Kamunda et al. 2016). The results of Mn and Zn in the present study agree with those in Maharia et al. (2010), where the Mn and Zn in the medicinal plants collected from around the mines ranged from 36.4 mg/kg to 69.3 mg/kg and 24.9mg/kg to 49.9mg/kg respectively.

The ranges of Cu and Cr concentrations in the roots, stems, and leaves of *Asclepias fruticosa,* as shown in Table 1, were 8.67 ± 0.12 μg.g$^{-1}$ - 18.8 ± 1.57 μg.g$^{-1}$ and 3.43 ± 0.06 μg.g$^{-1}$ - 34.90 ± 0.10 μg.g$^{-1}$ respectively. The highest Cu content in the medicinal plant collected around the mines was in the roots followed by the leaves, while the stems showed the lowest concentration. The trend for the Cr content was roots > stems > leaves. The concentration levels of Cu were significantly different ($p<0.05$). The upper limit of Cu was above the permissible limit of 15mg/kg in medicinal plants, as recommended by WHO for Cu (Olowoyo et al. 2012). The maximum value of 34.90 ± 0.10μg/g for Cr was also higher than the value of 1.5mg/kg for Cr as recommended by the United States Environmental Protection Agency (Nianz et al. 2013).

The results of Cu concentrations in the current study are comparable with those in the medicinal plants which were collected from polluted areas in Nianz et al. (2013), which ranged between 3.12 mg.kg$^{-1}$ and 21.40 mg.kg$^{-1}$ while those of Cr are not comparable with those in the same study which ranged from 0.17 mg.kg$^{-1}$ to 8.00 mg.kg$^{-1}$. Cu in humans is an essential cofactor for an enzyme that is crucial for the cross-linking of collagen. It also prevents the osteoclast's activity even though it excessively decreases lipids' metabolism (Skrajnowska et al. 2022). Cr in excess can contribute to skin allergies, bronchial asthma, cancer, problems in reproduction and development, and may even lead to death (Shekhawat et al. 2015).

From all the heavy metals determined in *Asclepias fruticosa* collected around the mines, the lowest values were for Pb, which ranged between 0.53 ± 0.013 μg.g$^{-1}$ and 1.59 ± 0.15 μg.g$^{-1}$ followed by Ni, which ranged from 5.67 ± 0.12 μg.g$^{-1}$ to 23.23 ± 1.7 μg.g$^{-1}$. The highest Pb and Ni concentrations were in the roots, followed by the stems, while the leaves showed the lowest values of Pb and Ni contents. All the measured values were below the recommended limit of 10mg/kg for Pb, while the upper limit of Ni was above the recommended permissible limit of 10 mg.kg$^{-1}$ (Annan et al. 2013, Okem 2014).

The results of Pb in the present study are not in agreement with those in Nawab et al. (2015), which were found in medicinal plants collected from around mine-affected areas and ranged between 3.66 mg.kg$^{-1}$ and 11.6 mg.kg$^{-1}$ in the shoots while in the shoots Pb was in the 2.00 mg.kg$^{-1}$ – 7.00 mg.kg$^{-1}$. In Kutty & Al-Mahaqeri (2016), the highest value of 9.79 ± 0.13 $\mu$g/g$^{-1}$ was determined in a medicinal plant around abandoned mining areas compared to the highest value of 1.59 ± 0.15 $\mu$g/g$^{-1}$ in the current study. The results of Ni in the present study did not compare with those in Maharia et al. (2010), where the levels of the medicinal plants collected from around the Copper mines ranged between 3.09mg/kg and 9.01mg/kg. High levels of Pb in humans can result in abnormal hemoglobin levels and size in red blood cells (Sithole et al. 2016) and cause health problems such as neurological disorders, anemia, hyperactivity, and changes in enzymes (Nawab et al. 2015) while elevated levels Ni can cause blindness, increased levels of cholesterol in the serum and sugar in the blood (Mugivhisa & Olowoyo 2017).

Table 2 shows that all the heavy metals were not translocated from the roots to the stems and leaves of

Table 1: The heavy metal concentration in the roots & stems of *Asclepias fruticosa* harvested from around the three mining areas in Brits.

| Mine | Plant part | Heavy metals concentration [μg.g$^{-1}$] | | | | | |
|---|---|---|---|---|---|---|---|
| | | Cr | Mn | Ni | Cu | Zn | Pb |
| Mine 1 | Roots | 25.67 ± 0.31 | 44.33 ± 0.58 | 12.47 ± 0.06 | 17.73 ± 0.06 | 59.00 ± 0.00 | 0.83 ± 0.00 |
| | Stems | 11.87 ± 0.23 | 36.67 ± 0.58 | 8.93 ± 0.05 | 11.97 ± 0.21 | 22.33 ± 0.58 | 0.81 ± 0.00 |
| | Leaves | 4.10 ± 0.10 | 52.33 ± 2.31 | 5.67 ± 0.12 | 12.33 ± 0.15 | 28.67 ± 0.57 | 0.53 ± 0.013 |
| Mine 2 | Roots | 27.53 ± 2.58 | 85.33 ± 51.07 | 23.23 ± 1.7 | 18.8 ± 1.57 | 51.00 ± 4.58 | 1.59 ± 0.15 |
| | Stems | 3.43 ± 0.06 | 12.33 ± 0.58 | 8.07 ± 0.21 | 8.67 ± 0.12 | 10.67 ± 0.58 | 1.00 ± 0.00 |
| | Leaves | 17.27 ± 6.87 | 39.67 ± 0.587 | 9.97 ± 0.15 | 9.7 ± 0.100 | 19.33 ± 0.58 | 0.78 ± 0.06 |
| Mine 3 | Roots | 34.90 ± 0.10 | 77.67 ± 0.58 | 10.57 ± 0.06 | 16.03 ± 0.40 | 39.33 ± 1.16 | 1.00 ± 0.00 |
| | Stems | 33.30 ± 0.17 | 64.00 ± 0.00 | 8.87 ± 0.12 | 11.90 ± 0.17 | 60.33 ± 0.56 | 0.59 ± 0.01 |
| | Leaves | 26.63 ± 0,93 | 75.33 ± 2.52 | 8.7 ± 0.20 | 10.47 ± 0.40 | 23.33 ± 0.58 | 0.55 ± 0.02 |

Table 2: Translocation factor (TF) values for the stems and leaves in *Asclepias fruticosa* collected from the different mining areas.

| Heavy metal | Mine 1 | | Mine 2 | | Mine 3 | |
|---|---|---|---|---|---|---|
| | Stems | Leaves | Stems | Leaves | Stems | Leaves |
| Cr | 0.46 | 0.16 | 0.12 | 0.63 | 0.95 | 0.76 |
| Mn | 0.83 | 1.18 | 0.14 | 0.46 | 0.82 | 0.97 |
| Ni | 0.72 | 0.45 | 0.35 | 0.43 | 0.84 | 0.82 |
| Cu | 0.68 | 0.70 | 0.46 | 0.52 | 0.74 | 0.65 |
| Zn | 0.38 | 0.49 | 0.21 | 0.38 | 1.53 | 0.59 |
| Pb | 0.98 | 0.64 | 0.63 | 0.49 | 0.59 | 0.55 |

Table 3. Phytochemical screening of *Asclepias fruticosa* collected from the mines.

| Phytochemical | Mine 1 | | | | Mine 2 | | | | Mine 3 | | | |
|---|---|---|---|---|---|---|---|---|---|---|---|---|
| | Ethyl acetate | Hex-ane | Methanol | Distilled water | Ethyl acetate | Hex-ane | Metha-nol | Distilled water | Ethyl acetate | Hex-ane | Metha-nol | Distilled water |
| Tannins | + | - | - | + | + | - | - | + | + | - | - | + |
| Saponins | - | + | + | + | - | - | + | + | - | + | + | + |
| Flavonoids | + | + | + | + | + | + | - | + | + | + | + | + |
| Alkaloids | + | + | + | + | + | + | + | - | + | + | + | + |
| Proteins | + | + | + | + | + | + | + | + | + | + | + | + |
| Carbohydrates | + | + | + | + | + | + | + | + | + | + | + | + |

*Asclepias fruticosa* (TF < 1) except for Mn and Zn, which were translocated from the roots to the leaves and stems and hyperaccumulated (TF > 1) by the medicinal plant which was collected around mine one and mine two respectively.

The results of the qualitative phytochemical analysis, as shown in Table 3, indicated the presence of flavonoids, alkaloids, proteins, and carbohydrates in *Asclepias fruticosa* collected from all the mining areas in all the fractions of the solvents except for Methanol and distilled water. The tannins were only in Ethyl acetate and Methanol extracts, whereas saponins were not present in ethyl acetate extract

## CONCLUSION

The phytochemicals flavonoids, alkaloids, proteins, and carbohydrates were present in the medicinal plant. The upper limits of the majority of the heavy metals (Zn, Cu, Cr, and Ni) in the *Asclepias fruticosa* were above the allowable limits as set by WHO and the United States Environmental Protection Agency for medicinal plants and edible plants and exceeded the safe and recommended limits for human consumption except for Mn and Pb. The heavy metals were mostly accumulated in the roots of the medicinal plant and not taken to the aerial parts. Recommendations are that communities should be discouraged from using medicinal plants growing around mines, and communities should be educated on the dangers of consuming medicinal plants growing around mines. More similar studies can be done on other medicinal plants growing around the mines or other polluted areas to determine the levels of the heavy metals in the medicinal plants and regular monitoring of the heavy metals in medicinal plants should be encouraged in all communities making use of such plants for health purposes.

## REFERENCES

Aliyu, A.B., Oshanimi, J.A., Ibrahim, A.M., Musa, H.A. and Oyewale, A.O. 2008. Phytochemical analyses and mineral elements composition of some medicinal plants of Northern Nigeria. Niger. J. Pharm. Sci., 7(1): 119-125.

Annan, K., Dickson, R.A., Amponsah, I.K. and Kwesi, N.I. 2013. The heavy metal contents of some selected medicinal plants sampled from different geographical locations. Pharmacogn. Res., 5(2): 539. https://doi: 10.4103/0974-8490.110539

Asati, A., Pichhode, M. and Nikhil, K. 2015. Effect of heavy metals on plants: An overview. Int. J. Appl. Innov. Eng. Manag., 5(3): 56-66.

Ayaz, M., Junaid, M., Subhan, F., Ullah, F., Sadiq, A., Ahmad, S., Imran, M., Kamal, Z., Hussain, S. and Shah, S.M. 2014. Heavy metals analysis, phytochemical, phytotoxic, and anthelmintic investigations of crude methanolic extract, subsequent fractions, and crude saponins from *Polygonum hydropiper* L. BMC Compl. Altern. Med., 14(465): 11651.

Barahona, A.J., Bursac, Z., Veledar, E., Lucchini, R., Tieu, K. and Richardson, J.R. 2022. Relationship of blood and urinary manganese levels with cognitive function in elderly individuals in the united states by race/ethnicity, NHANES 2011-2014. Toxics, 10: 40191. https://doi.org/ 10.3390/toxics10040191

Brima, E.I. 2017. Toxic elements in different medicinal plants and their impact on human health. Int. J. Environ. Res. Public Health., 4: 1209. https://doi.org/10.3390/ijerph14101209

Dghaim, R., Al Khatib, S., Rasool, H. and Khan, A.M. 2015. Determination of heavy metals concentration in traditional herbs commonly consumed in the United Arab Emirates. J. Environ. Res. Public Health., 6: 878. https://doi.org/10.1155/2015/973878.

Ekor, M. 2014. The growing use of herbal medicine: issues relating to adverse reactions and challenges in monitoring safety. Front. Pharmacol., 10(4): 177. https://doi. 10.3389/fphar.2013.00177.

Fahimirad, S. and Hatami, M. 2017. Heavy Metal-Mediated Changes in Growth and Phytochemicals of Edible and Medicinal Plants. In Ghorbanpour, M. and Varma, A. (eds.), Medicinal Plants and Environmental Challenges, Springer, Cham, https://doi.org/10.1007/978-3-319-68717-9_11

Fatima, G.X., Sowmya K.V., Rahul R.S., Shanmughanathan, S. and Chamundeeswari, D. 2014. Preliminary phytochemical screening and heavy metal analysis by atomic absorption spectroscopy of a marketed polyherbal churna. Am. J. Drug Deliv. Ther., 61: 510

Glavač, N.K., Djogo, S., Ražić, S., Kreft, S. and Veber, M. 2017. Accumulation of heavy metals from soil in medicinal plants. Arh. Hig. Rada. Toksikol., 68: 236-244. https://doi:10.1515/aiht-2017-68-2990.

Kamunda, C., Mathuthu, M. and Madhuku, M. 2016. Health risk assessment of heavy metals in soils from witwatersrand gold mining basin, South Africa. Int. J. Environ. Res. Public Health., 13(7): 663. https://doi:10.3390/ijerph13070663

Khaleel, S.M.J. 2018. Studying the Heavy Metals Composition and the Impact of Different Common Solvents on the Extraction Efficiency of Phytochemical Secondary Metabolites from the Leaves of *Ziziphus spina-christi* Grown in Jordan. Pak. J. Nutr., 17(8): 392-398. https://doi.103923/pjn.2018.392.398.

Khan, W., Subhan, S., Shams, S.D., Afridi, S.G., Ullah, R., Shahat, A.A. and Alqahtani, A.S. 2019. Antioxidant Potential, Phytochemicals Composition, and Metal Contents of *Datura alba*. Biomed. Res. Int., https://doi.org/10.1155/2019/2403718.

Kostić, D., Mitić, S., Zarubica, A., Mitić, M., Veličković, J. and Randjelović, S. 2011. Content of trace metals in medicinal plants and their extracts. Hem. Ind., 65(2): 165-170. https://doi: 10.2298/HEMIND101005075K.

Kulhari, A., Sheorayan, A., Bajar, S., Sarkar, S., Chaudhury, A. and Kalia, R.K. 2013. Investigation of heavy metals in frequently utilized medicinal plants collected from environmentally diverse locations of northwestern India. SpringerPlus, 2: 676.

Kutty, A.A. and Al-Mahaqeri, S.A. 2016. An investigation of the levels and distribution of selected heavy metals in sediments and plant species within the vicinity of ex-iron mine in Bukit Besi. J. Chem., 15: 147. https://doi.org/10.1155/2016/2096147.

Lajayer, B.A., Ghorbanpour, M. and Nikabadi, S. 2017. Metals in contaminated environment: destiny of secondary metabolite biosynthesis, oxidative status and phyto-extraction in medicinal plants. Ecotoxicol. Environ. Saf., 2 (145): 377-390. https://doi: 10.1016/j.ecoenv.2017.07.035.

Mabona, U. and Van Vuuren, S.F. 2013. Southern African medicinal plants used to treat skin diseases. S. Afr. J. Bot., 87: 175-193. https://doi.org/10.1016/j.sajb.2013.04.002.

Maharia, R.S., Dutta, R.K., Acharya, R. and Reddy, A.V.R. 2010. Heavy metal bioaccumulation in selected medicinal plants collected from Khetri Copper Mines and comparison with those collected from fertile soil in Haridwar, India. J. Environ. Sci. Health B, 45(2): 174-181. https://doi: 10.1080/03601230903472249.

Mahmood, N., Nazir, R., Khan, M., Iqbal, R. and Adnan, M. 2019. Phytochemical screening, antibacterial activity and heavy metal analysis of ethnomedicinal recipes and their sources used against infectious diseases. Plants, 8: 454. https://doi.org/10.3390/plants8110454.

Malikula, R.S., Kaonga, C.C., Mapoma, H.W.T., Thulu, F.G.D. and Chiipa, P. 2021. Heavy metals and nutrients loads in water, soil, and crops irrigated with effluent from WWTPs in Blantyre City, Malawi. Water, 14: 121. https://doi.org/10.3390/w14010121.

McGaw, L.J., and Eloff, J.N., 2008. Ethnoveterinary use of Southern African plants and scientific evaluation of their medicinal properties. J. Ethnopharmacol. 119: 559-574.

Mtunzi, F., Nkwe, J., Modise, J., Sipamla, A. and Dikio, E. 2012. Phytochemical analysis and heavy metals composition of some medicinal plants products in South African Markets. J. Nat. Prod., 5: 21-26.

Mugivhisa, L.L. and Olowoyo, J.O. 2017. Accumulation pattern of trace metals in *Spinacia oleracea* harvested from soil treated with urine in comparison with other soil amendments in Pretoria, South Africa. Int. J. Recycl. Org. Waste Agric., 6: 133-141. https://doi:10.1007/s40093-017-0161-y

Mulaudzi, R.B., Tshikalange, T.E., Olowoyo, J.O., Amoo, S.O. and Du Plooy, C.P. 2017. Antimicrobial activity, cytotoxicity evaluation and heavy metal content of five commonly used South African herbal mixtures. S. Afr. J. Bot., 112: 314-318. https://doi.org/10.1016/j.sajb.2017.06.024.

Nasim, S.A. and Dhir, B. 2010. Heavy metals alter the potency of medicinal plants. Rev. Environ. Contam. Toxicol., 203: 139-49. https://doi:10.1007/978-1-4419-1352-4_5.

Nawab, J., Khan, S., Shah, M.T., Oamar, Z., Din, I., Mahmood, O., Gul, N. and Huang, Q. 2015. Contamination of soil, medicinal, and fodder plants with lead and cadmium present in mine-affected areas, Northern Pakistan. Environ. Monit. Assess., 187: 605. https://doi.10.1007/s10661-015-4807-9.

Nema, N.K., Maity, N., Sarkar, B. and Mukherjee1, P.K 2012. Determination of trace and heavy metals in some commonly used medicinal herbs in Ayurveda. Toxicol. Ind. Health., 30(10): 964-968. https://doi:10.1177/0748233712468015.

Niaz, A., Ullah, N., Rehman, A., Ahmad, I., Ikhlaq, M. and Rehman, H.U. 2013. Pollution based study of heavy metals in some selected medicinal plants by dry digestion method. Int. J. Pharm. Sci., 4(2): 545.

Okem, A. 2014. Heavy Metals in South African Medicinal Plants with Reference to Safety, Efficacy and Quality. University of KwaZulu-Natal, Pietermaritzburg, South Africa.

Olowoyo, J.O., Mugivhisa, L.L. and Busa, N.G. 2015. Trace metals in soil and plants around a cement factory in Pretoria. South Africa. Pol. J. Environ. Stud., 24(5): 2087-2093.

Olowoyo, J.O., Okedeyi, O.O., Mkolo, N.M., Lion, G.N. and Mdakane, S.T.R. 2012. Uptake and translocation of heavy metals by medicinal plants growing around a waste dump site in Pretoria, South Africa. S. Afr. J. Bot., 78: 116-121. https://doi.org/10.1016/j.sajb.2011.05.010.

Rai, P.K., Lee, S.S., Zhang, M., Tsang, Y.F. and Kim, K. 2019. Heavy metals in food crops: Health risks, fate, mechanisms, and management. Environ. Int., 125: 365-385.

Sarma, H., Deka, S., Deka, H. and Saikia, R.R. 2011. Accumulation of heavy metals in selected medicinal plants. Rev. Environ. Contam. Toxicol., 214: 63-86. doi:10.1007/978-1-4614-0668-6_4.

Shekhawat, K., Chatterjee, S. and Joshi, B. 2015. Chromium toxicity and its health hazards. Int. J. Adv. Res., 3(7): 167-172.

Shirin, K., Imad, S., Shafiq, S. and Fatima, K. 2009. Determination of major and trace elements in the indigenous medicinal plant *Withania somnifera* and their possible correlation with therapeutic activity. J. Saudi Chem. Soc., 14: 97-100.

Sithole, S.C., Mugivhisa, L.L., Amoo, S.O. and Olowoyo, J.O. 2016. Pattern and concentrations of trace metals in mushrooms harvested from trace metal-polluted soils in Pretoria, South Africa. S. Afr. J. Bot., 108: 315-320. https://doi.org/10.1016/j.sajb.2016.08.010

Skrajnowska, D., Jagielska, A., Ruszczyńnska, A., Idkowiak, J. and Bobrowska-Korczak, B. 2022. Effect of copper and selenium supplementation on the level of elements in rats' femurs under neoplastic conditions. Nutrients, 14: 1285. https://doi.org/10.3390/nu14061285

Street, R.A. 2013. Heavy metals in medicinal plant products-An African perspective. S. Afr. J. Bot., 82: 67-74. https://doi.org/10.1016/j.sajb.2012.07.013.

Yadav, R.N.S. and Agarwala, M. 2011. Phytochemical analysis of some medicinal plants. J. Phytol., 3: 10-14.

Zulkafflee, N.S., Redzuan, N.A.M., Nematbakhsh, S., Selamat, J., Ismail, M.R., Praveena, S.M., Lee, S.Y. and Razis, A.F.A. 2022. Heavy metal contamination in *Oryza sativa* L. at the Eastern Region of Malaysia and its risk assessment. Int. J. Environ. Res. Public Health, 19: 739. https://doi.org/10.3390/ijerph19020739.

Nature Environment and Pollution Technology
An International Quarterly Scientific Journal

p-ISSN: 0972-6268
(Print copies up to 2016)
e-ISSN: 2395-3454

Vol. 22 | No. 1 | pp. 477-487 | 2023

Original Research Paper

https://doi.org/10.46488/NEPT.2023.v22i01.046

Open Access Journal

# Sustainable Green Approach of Silica Nanoparticle Synthesis Using an Agro-waste Rice Husk

**Mikhlesh Kumari*, Kulbir Singh*(**), Paramjeet Dhull*, Rajesh Kumar Lohchab*† and A. K. Haritash*****

*Department of Environmental Science & Engineering, Guru Jambheshwar University of Science & Technology, Hisar, Haryana, India

**Department of Civil Engineering, M.M. Engineering College, Maharishi Markandeshwar (Deemed to be University), Mullana-Ambala-133207, India

***Department of Environmental Engineering, Delhi Technological University, Shahbad, Daulatpur, Delhi-110042, India

†Corresponding author: Rajesh Kumar Lohchab; rajeshlohchab@gmail.com

**Nat. Env. & Poll. Tech.**
**Website: www.neptjournal.com**

*Received:* 10-08-2022
*Revised:* 03-10-2022
*Accepted:* 04-10-2022

**Key Words:**
Silica nanoparticle
Biogenic
Agricultural waste
Rice husk ash

## ABSTRACT

Agro-waste can provide a non-metallic, environmentally friendly bio-precursor for the production of green silica nanoparticles. To manufacture silica nanoparticles from rice husk, biogenic silica nanoparticles were generated using an alkaline precipitation approach. Rice husk as a source of silica nanoparticles is environmentally and economically valuable because it is a plentiful lower price agricultural derivative that can be used to help with waste management. During the synthesis process, the dose of rice husk ash was used at 5 g at pH 7, alkali dose concentration of 0.5 M, reaction period of 3.5 h, and temperature of 90°C that produced maximum silica nanoparticles with a yield of 88.5%. To optimize the silica nanoparticle production from rice husk ash Box Behnken Design (BBD) a subcategory of the response surface methodology (RSM) was accomplished. BBD model was successfully matched, as evidenced by the high correlation values of adjusted $R^2$ 0.9989 and predicted $R^2$ 0.9977. Silica nanoparticles' amorphous form generated from rice husk ash is indicated by XRD analysis 2Θ peak at 22.12° and UV-Vis Spectroscopy absorbance peak at 312 nm. The amorphous shape of silica is amorphous and crystalline defined through XRD. nanoparticles generated from rice husk ash is indicated by FESEM analysis and EDX analysis, confirming that the $SiO_2$ elemental configuration comprises the highest concentration of Si and O. The existence of a siloxane group in the produced compound was revealed by FTIR spectra stretching vibrations at 803.69 and 1089.05 $cm^{-1}$

## INTRODUCTION

Rice is among the greatest crops cultivated around the world since it is one of the most important food varieties and a supplier of nourishment for individuals. In contrast to 2020, the estimated global rice production has increased from 513.2 million tons to 519.7 million tons in 2021 (FAO 2021). As a result of generation and refining in the industry of agriculture, rice husk accounts for the major residue. Due to its characteristics like lignin, cellulose, hemicellulose content, hard surface, a small quantity of proteins, and high silicon quantity, rice husk can't be bacterial decomposed easily and is also insoluble in water (Soltani et al. 2015). In many countries, mostly rice husk has pointlessly burned and it is responsible for the air pollution problem. Additionally, composting of rice husk generates a huge quantity of methane. Rice husk contains approximately 20% of rice in weight ratio and incineration of these rice husks under 500-700°C of controlled temperature can generate ash and also amorphous silica (Kang et al. 2019). As compared to other crops, silica act as a unique crop residue in rice (Setiawan & Chiang 2021). The silica-separated rice husk is eco-accommodating as a result of its procurement from natural items and affordable because of the low-cost raw substance value.

The development of silica dioxide nanoparticles has drawn gigantic consideration in the world of science and technology in light of their broad use in different fields like biomedical fields, drug delivery systems, pesticides degradation, thermal insulators, humidity sensors, and electronic devices (Bharti et al. 2015, Bapat et al. 2016, Nazeran & Moghaddas 2017, Chong et al. 2018, Kano et al. 2019). According to previous studies, $SiO_2$ nanoparticles have been synthesized using natural resources like rice husk, marine sponges and diatom, coal fly ash, sand, and sugarcane bagasse (Sankar et al. 2018, Falk et al. 2019, Aphane et al. 2020, Ismail et al. 2021). One of these natural

resources that are easily accessible in huge amounts is a byproduct of rice. There are different methods of silica nanoparticles synthesis like biotransformation method, microwave synthesis, thermal decomposition technique, laser ablation, chemical precipitation, plasma-assisted aerosol precipitation, sol-gel method, vapor-phase reaction, sonochemical synthesis, mechano-chemical method, hydrothermal synthesis, precipitation method, and pyrolysis, etc. (Krishna et al. 2021). Due to some environmental and technical problems like harsh experimental conditions, costly chemicals, and long-time and complex technologies in all these above syntheses, they are not environment friendly and economical to produce silica nanoparticles, thus, it is intriguing to build up flexible and elective techniques for acquiring nano silica from such biomass. There is a solution approach to a vital field of nanotechnology's potential applications for the present innovation. Furthermore, because the reuse of biomass assets has the potential to be extremely beneficial for eco-companion nanotechnology and nanoscience, the production of $SiO_2$ nanoparticles from rice husk has been extensively researched utilizing several exploratory methodologies. Chemical reaction techniques such as hydrothermal synthesis, acid-alkali leaching, microwave, combustion synthesis, precipitation, sonochemical, pyrolysis, and sol-gel are popular methods for producing $SiO_2$ nanoparticles from rice husk (Dubey et al. 2015, Sankar et al. 2016, Gao et al. 2017, Peres et al. 2018, Sankar et al. 2018, Almeida et al. 2019, Bui et al. 2020). When involving the biomass asset, rice husk is used to create silica as a siliceous substance at an unimaginable pace of gig tons/year, since rice husk contains an amorphous form of silica 90% (Hossain et al. 2018). After reviewing the literature, we found a persuasive and straightforward procedure for producing bio-created silica from a variety of rice husk sources. We used a rapid sonochemical method to demonstrate the properties of amorphous silica nanoparticles obtained from brown rice husk, which is one of the simplest methods for obtaining excellent silica of high quality from siliceous biomass reserves. The surface-to-volume ratio and microstructural size of silica oxide nanoparticles can be easily regulated by adjusting the sonication period throughout the sonochemical process. The optical, textural, morphological, and structural aspects of rice husk-derived silica oxide nanoparticles were investigated, as well as the impacts of sonochemical procedure duration on the objective properties (Sankar et al.2018). Because of the foregoing, rice husk is regarded as the greatest economically significant silica source.

Subsequently, we present a simple technique for synthesizing biogenic silica nanoparticles of high purity from rice husk and evaluated their biocompatible qualities. The silica nanoparticle was well characterized by different methods like X-Ray Diffraction, UV-VIS spectroscopy, Fourier Transform Infrared, Field Emission Scanning Electron Microscopy, and Energy Dispersive X-Ray. Silica nanoparticles have been made synthetically by various methods involving substance reductants.

## MATERIALS AND METHODS

### Material

For this study, rice husk (RH) was taken as a raw material from a rice mill. An analytical-grade chemical was used to make the nanoparticles.

### Process of Silica Nanoparticles Synthesis

To remove dust and soil, rice husk was cleaned thoroughly with tap water adhering to it until the water was clear. The pH was then neutralized by washing it with distilled water. The rice husk was then rinsed and dried out in the sunlight for two days before being dried for 3 h at 90°C. The dried rice husk was ground into flour. The dried rice husk was then ignited at 600°C for 4 h to generate a grey powder of rice husk ash (RHA). A 500 mL NaOH (0.5M) solution was used to disperse the rice husk ash. For dissolving silica, stirring was done with a magnetic stirrer at 200 rpm for 3.5 h at a particular temperature of 90°C to form a solution of sodium silicate. Whatman no. 41 filter paper was used to filter the resultant solution. The filtrate from the sodium silicate solution was permitted to cool to room temperature. To generate silica precipitation, with regular stirring the sodium silicate solution was titrated with $H_2SO_4$ acid solution to pH 7. The solution was then agitated for one day before being aged for two days to let the silica gel to develop. Finally, using distilled water, the gel-containing solution was filtered, fragmented, and washed, yielding a fresh silica gel that was lyophilized overnight to get rid of water. For further characterization, the produced $SiO_2$ nanoparticles are stored in vacuum desiccators. Fig. 1 represents an alkali-based silica extraction process.

$$SiO_2 + 2NaOH \rightarrow Na_2SO_3 + H_2O$$
$$Na_2SiO_3 + H_2SO_4 \rightarrow SiO_2.H_2O + Na_2SO_4$$

### Optimization and Characterization of Silica Nanoparticles

For value addition, silica production from rice husk using alkali digestion was precisely carried out at optimum pH, alkali dose concentration, digestion time, temperature, and adsorbent concentration.

Optimization has a lengthy history of research, notably in the subject of operational analysis, which has resulted in

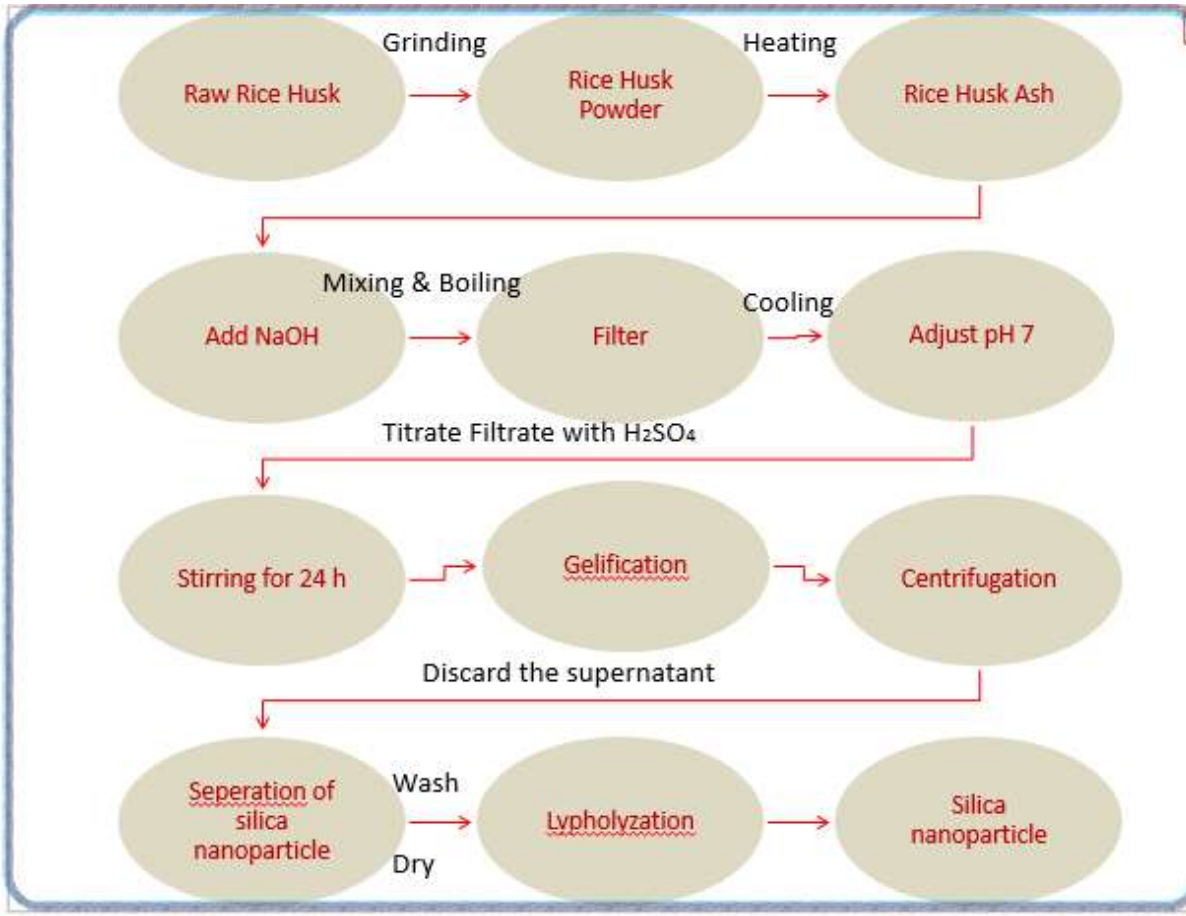


Fig. 1: Extraction process of silica nanoparticles from rice husk.

a plethora of methodologies. The influence of interaction among the elements is overlooked in traditional single-factor time testing because the experimenter modifies a single factor while keeping the other factors constant. Response surface methodology is a systematic analytical strategy for investigating the correlations between design features and responses to gain better overall knowledge with the fewest possible experiments (Cheng et al.2015). The Box Behnken generates designs that have favorable statistical features, allowing the quadratic model to be used. Response surface methodology optimizes processes and products by using quantitative data in an experimental design to discover and simultaneously solve multivariate equations. (Li et al. 2019).

The standard RSM, the Box–Behnken design model, for optimization, was built using Design Expert software 13. The optimum pH, NaOH concentration, temperature, time, and raw material dose were determined using a five-variable Box Behnken design. The design was chosen because it meets the majority of the requirements for silica nanoparticle production optimization. The fundamental goal of response surface methodology is to find the process's optimum practical conditions that meet the operating criteria. There were 46 experiments in the quadratic model's Box Behnken design (BBD). The design variables of BBD for silica nanoparticle production include pH (2-12), NaOH concentration (0.3-0.8 M), Temperature (40-130°C), time (2-5 h), and raw material dose (3-8 gm). To characterize the connection between independent variables and their observed responses, the equation employed was a quadratic polynomial (Cheng et al. 2015). The following is the model equation:

$$Y_{Pred} = \beta_0 + \sum_{i=1}^{n} \beta_i x_i + \sum_{i=1}^{n-1} \sum_{j=1}^{n} \beta_{ij} x_i x_j + \sum_{i=1}^{n} \beta_{ii} x_i^2 + e \quad \ldots(1)$$

Where, $Y_{pred}$ is the approximation value of the reactive variable, $\beta_0$ is constant, $\beta_i$, $\beta_{ii}$, $\beta_{ij}$ are the linear, quadratic, and interaction constants of the regression coefficients, and $x_i$ and $x_j$ are the independent variables in the form of coded values and e is the residual error. The consequences of the silica nanoparticle manufacturing were analyzed us-

ing model graphs and analysis of variance (ANOVA) like three-dimensional graphs, expected vs actual value plots, and contour plots.

The properties of the Silica nanoparticles like functional groups, phase identification, surface topography, size analysis, determining elemental composition and absorbance were determined using Scanning Electron Microscopy (JSM-7610F Plus, JEOL Japan), X-Ray Diffraction (Rigaku Miniflex-II Diffractometer, Japan), Energy Dispersive X-Ray Analysis (EDX), UV-Vis Spectroscopy (Shimadzu) and Fourier Transform Infrared (Spectrum Two, Perkin Elmer).

### Optimization of Silica Nanoparticles Synthesis

**Effect of pH:** The influence of pH on silica extraction was studied from pH 2 to pH 10 using 5 gm rice husk ash dissolving in 0.5 M NaOH solution at 100°C for 4 hours. Silica extraction productivity improved when the pH was raised from 2 to 7, which was 29.56% to 88.5% (Fig. 2(a)). Further increases in pH did not lead to a significant increase in silica nanoparticle yield. The results show that the optimum pH of 7 results in a dose for getting the maximum output of silica nanoparticles from rice husk ash. This optimum pH for silica synthesis was 7. Similar findings were made by Yang et al. (2019) of China in their ing vestigation on mesoporous silica aerogels.

**Effect of alkali dose:** To study the NaOH concentration effect on the digestion of 5 g rice husk ash to manufacture silica nanoparticles varying dose of alkali was studied at pH 7 for 4 hours at 100°C. When the NaOH concentration was elevated from 0.3 M to 0.5 M, the silica elimination rose from 40.6 % to 88.5 %. (Fig. 2(b)). Further rise in the alkali dose did not result in a substantial increase in the production of silica nanoparticles. As a result, in the given digestion conditions, the optimum dose of NaOH concentration for silica extraction was found as 0.5 M. In their research, Ghorbani et al. (2015), of Iran study on silica nanoparticles, employed a similar NaOH concentration and observed similar results.

### Effect of Digestion Time

The influence of processing time on silica extraction was studied for 5 grams of rice husk ash at pH 7, 0.5 M NaOH, and 100°C digesting temperature over time intervals ranging from 0.5 to 6 hours. It has been detected that the silica production was elevated from 16.91 % to 88.45 % when the digestion period was increased from 0.5 to 3.5 hours [Fig. 2(c)]. However, increasing the duration beyond 3.5 hours there was no considerable increase in silica nanoparticle extraction, hence 3.5 hours was considered to be the ideal reaction time for rice husk ash working dose aforementioned specified digestion states for silica extraction. According to Yang et al. (2019), in a China study on mesoporous silica aerogels, the optimal time was 4 hours since there was no significant extraction after that.

**Effect of temperature:** To study the influence of digestion temperature ranging from 30°C to 150°C on silica extraction from rice husk ash (5 gm) in 0.5 M NaOH solution at pH 7, with a digestion time of 3.5 hours. The silica extraction efficiency escalated from 14.8 % to 88.45% when the digestion temperature was elevated from 30°C to 90°C (Fig. 2(d)). However, an increase in the temperature did not result in a substantial increase in nanoparticle extraction. The optimum temperature for extraction of silica nanoparticles was found 90°C. Manaa (2015) from Egypt's study on silica products also noted comparable outcomes.

**Raw material dose:** A variable dose of 2 gm to 10 gm of rice husk ash was used to extract silica nanoparticles while keeping the alkali dose constant at 0.5 M NaOH and a digestion period of 3.5 hours at 90°C. As shown in Fig. 2(e), the raw dose concentration increasing from 2 to 5 gm increased the silica extraction from 54.8% to 88.5 %. Though, raising it after 5 gm did not yield a remarkable rise in silica nanoparticle extraction. As a consequence, a 5 g dose of rice husk ash was discovered to be ideal for the largest yield of silica nanoparticles. Ghorbani et al. (2015) revealed a 5.0 g optimum dose of rice husk ash in their research.

### RSM-BBD Analysis

Design Expert Software 13 was used to analyze the data performance for regression analysis. The encoded versions of a second-order polynomial equation, Eq. (2), that reveals silica nanoparticle production is shown below:

Silica Production (%)

$$Y_{Pred} = +89.17 + 26\,A + 6.38\,B + 10.63\,C + 2.56\,D + 2.56\,E + 2.00\,AB + 2.00\,AC + 2.50\,AD + 0.0000\,AE - 4.25\,BC - 1.75\,BD - 1.50\,B - +1.25\,CD - 1.0000\,CE + 2.75\,DE - 31.29\,A^2 - 4.29\,B^2 - 6.79C^2 - 2.37\,D^2 - 1.04E^2 \quad \ldots(2)$$

Fisher's F-test was accustomed to determining the arithmetical significance of the polynomial equation. Table 1 shows the study of data variability for the response surface quadratic model. Table 1 also includes the regression coefficients for the quadratic, linear, intercept, and interaction factors of the model. The p-values of the model terms were used to determine their significance. An F-test revealed that the model was extremely effective, with a Fvalue of 2122.78 and a p-value < 0.0001. The "lack-of-fit" F-value of 3.81

and p-value of 0.0716 suggested that the "lack-of-fit" was insignificant in comparison to the pure error.

In Predicted vs. Actual (Fig. 3), Contour (Fig. 4), and 3D response-surface (Fig. 5) plots show the kind of interactions between the five studied variables, as well as the relationship between experimental levels and responses of each variable.

## Characterization of Silica Nanoparticles

**Fourier transform infra-red (FTIR) spectroscopy:** Fig. 6 shows the FTIR spectrum of silica dioxide nanoparticles. Specifically, the Si-O-Si vibration peak could be seen. The bending vibration, asymmetric stretching vibration, and symmetric stretching vibration are assigned to the transmittance peaks of Si-O-Si at 469.49 $cm^{-1}$, 1089.05 $cm^{-1}$, and 803.69 $cm^{-1}$, correspondingly (Mohd et al. 2017, Nandiyanto et al. 2016, Wibowo et al. 2017). The silica surfaces produced a broad peak at 3149.79 $cm^{-1}$ due to the hydroxyl stretching vibration produced by the remaining adsorbed water and the silanol group vibration. (Chen et al. 2014). The H-O-H bond in molecular water is liable for the bending vibration, the band saw at roughly 1626.26 $cm^{-1}$ (Chen et al. 2014). The carboxyl side groups show a symmetric stretching peak at 1406.01 $cm^{-1}$ (Sarkar et al.2014). As in charged amines ($C=NH^+$), the 2359.78 $cm^{-1}$ band exhibits $NH^+$ stretching (Lade et al. 2015). The findings are consistent with previous research on silica nanoparticles (Ghorbani et al. 2015, Manna 2015).

**X-Ray powder diffraction:** The $SiO_2$ nanoparticles XRD patterns made from rice husk ash shown in Fig. 7. The broad peak in the XRD pattern of rice husk ash at 22.12° established the amorphous nature of silica (Wibowo et al. 2017), which is appropriate for the formation of sodium silicate solution, however sharp peaks at 31.37°, 45.16°, 55.99°, and 75.02° specify the silica nanoparticles crystalline nature (Wahab et al. 2019). As a result of these XRD peaks, it was concluded

Table 1: Analysis of variance for response surface quadratic model.

| Source | Sum of Squares | df | Mean Square | F-value | p-value | |
|---|---|---|---|---|---|---|
| Model | 22996.83 | 20 | 1149.84 | 2122.78 | < 0.0001 | significant |
| A-pH | 10816.00 | 1 | 10816.00 | 19968.00 | < 0.0001 | |
| B-NaOH Concentration | 650.25 | 1 | 650.25 | 1200.46 | < 0.0001 | |
| C-Temperature | 1806.25 | 1 | 1806.25 | 3334.62 | < 0.0001 | |
| D-Time | 105.06 | 1 | 105.06 | 193.96 | < 0.0001 | |
| E-Raw Material Dose | 105.06 | 1 | 105.06 | 193.96 | < 0.0001 | |
| AB | 16.00 | 1 | 16.00 | 29.54 | < 0.0001 | |
| AC | 16.00 | 1 | 16.00 | 29.54 | < 0.0001 | |
| AD | 25.00 | 1 | 25.00 | 46.15 | < 0.0001 | |
| AE | 0.0000 | 1 | 0.0000 | 0.0000 | 1.0000 | |
| BC | 72.25 | 1 | 72.25 | 133.38 | < 0.0001 | |
| BD | 12.25 | 1 | 12.25 | 22.62 | < 0.0001 | |
| BE | 9.00 | 1 | 9.00 | 16.62 | 0.0004 | |
| CD | 6.25 | 1 | 6.25 | 11.54 | 0.0023 | |
| CE | 4.00 | 1 | 4.00 | 7.38 | 0.0118 | |
| DE | 30.25 | 1 | 30.25 | 55.85 | < 0.0001 | |
| $A^2$ | 8545.47 | 1 | 8545.47 | 15776.25 | < 0.0001 | |
| $B^2$ | 160.74 | 1 | 160.74 | 296.76 | < 0.0001 | |
| $C^2$ | 402.56 | 1 | 402.56 | 743.19 | < 0.0001 | |
| $D^2$ | 49.23 | 1 | 49.23 | 90.88 | < 0.0001 | |
| $E^2$ | 9.47 | 1 | 9.47 | 17.48 | 0.0003 | |
| Residual | 13.54 | 25 | 0.5417 | | | |
| Lack of Fit | 12.71 | 20 | 0.6354 | 3.81 | 0.0716 | not significant |
| Pure Error | 0.8333 | 5 | 0.1667 | | | |
| Cor Total | 23010.37 | 45 | | | | |

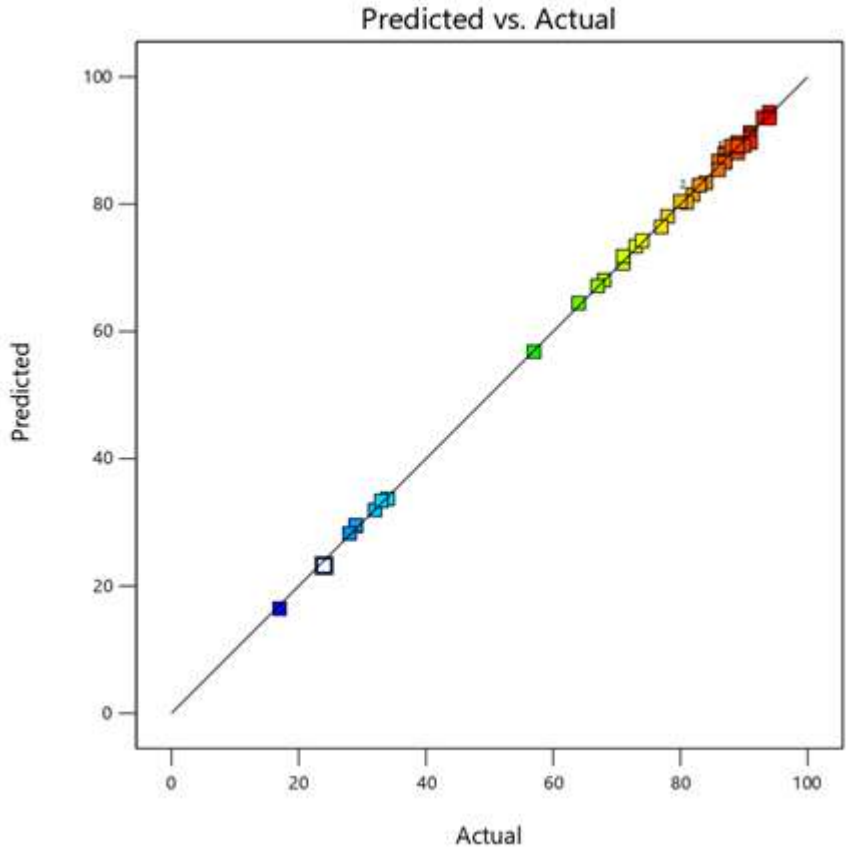


Fig. 3: Predicted vs. Actual plots.

that the rice husk contains a mixture of crystalline and amorphous silica phases. It was obvious that no other material impurities were present based on the peak positions of the observed spectra (Wahab et al. 2019). The creation of an amorphous form of silica nanoparticles has varied applications in our daily lives and adds to the beneficial effect (Raut & Panthi 2019). Peaks in the XRD pattern of silica nanoparticles generated by alkaline precipitation from rice husk ash are amorphous and contain a small proportion of crystalline silica (Wahab et al. 2019).

**Scanning electron microscope (SEM) and EDX analysis:** Scanning electron microscope images reveal the spherical shape structure of silica nanoparticles (Fig. 8). The silica nanoparticles produced were approximately 61.87 nm in size. A small portion of the generated $SiO_2$ particles formed an aggregation of $SiO_2$ nanoparticles, according to the findings. As a result, amorphous silica nanoparticles were discovered in nature, as seen in Fig. 8. Ahmad et al. (2017) also made similar observations.

EDX confirmed the chemical configuration of silica nanoparticles. The strongest peaks are displayed by oxygen and silica existent in silica nanoparticles, indicating that $SiO_2$ nanoparticles are generated. The non-appearance of other elements indicated that extensive washing with water had eliminated most of the soluble ions. During the thermal decomposition of rice husk, metal contaminants have also been from the rice husk transported along with the volatiles. Akhayere et al. (2019), reported similar results for synthetic silica in their elemental analysis.

**UV-visible spectroscopy:** The absorption band edge of silica nanoparticles by UV-visible spectroscopy was analyzed between 200 and 700 nm and a major adsorption band has been discovered at 312 nm with an absorbance of 1.91 (Fig. 9). The absorbance of nanoparticles is strongly influenced by wavelength and sample amount. The presence of silica nanoparticles is indicated by these observations, which lead to a Si-O-Si link. Patil et al. (2018) reported comparable findings.

## CONCLUSIONS

The percentage yield of nano silica produced from rice husk ash at 600°C was 88.5%. The surface response approach using

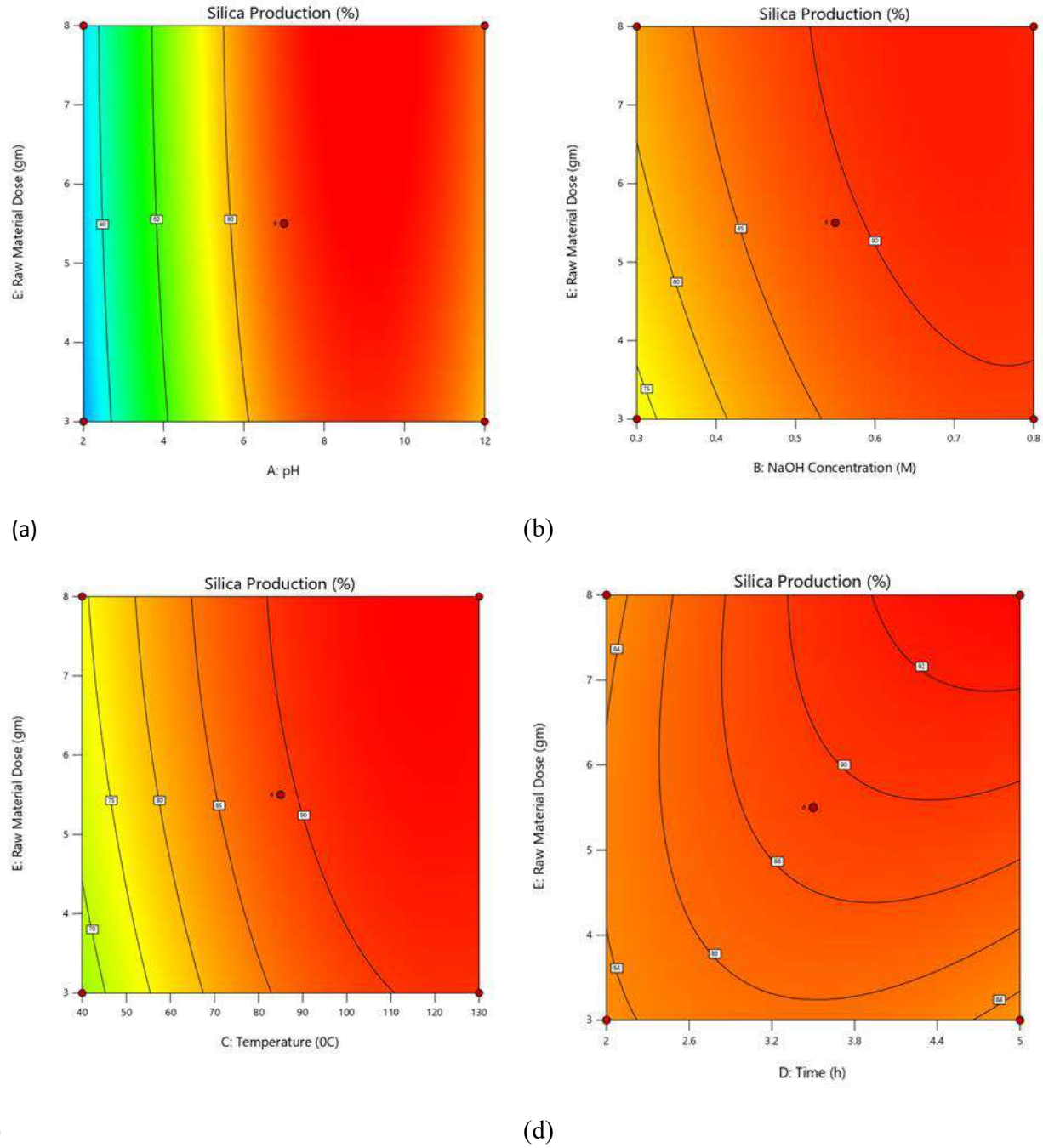


Fig. 4: Contour plots showing the interaction between (a) pH vs. raw material dose (b) NaOH concentration vs. raw material dose (c) Temperature vs raw material dose (d) Time vs. raw material dose.

the BBD model was successfully matched, as evidenced by the high correlation values of Adjusted $R^2$ 0.9989 and Predicted $R^2$ 0.9977. FESEM analysis of nano-silica particles from rice husk ash has shown its agglomeration form, with a particle diameter of 61.87 nm. The form of the particles was observed to be consistent. The presence of a significant broad peak at 22.12 on the XRD spectrum suggested that the nano-silica made from rice husk ash was mainly amorphous. The existence of hydrogen-linked groups siloxane and silanol in silica was established by FTIR data. The occurrence of O and Si in the ultimate formation, $SiO_2$ nanoparticles, was confirmed by EDX analysis. Biosynthesis

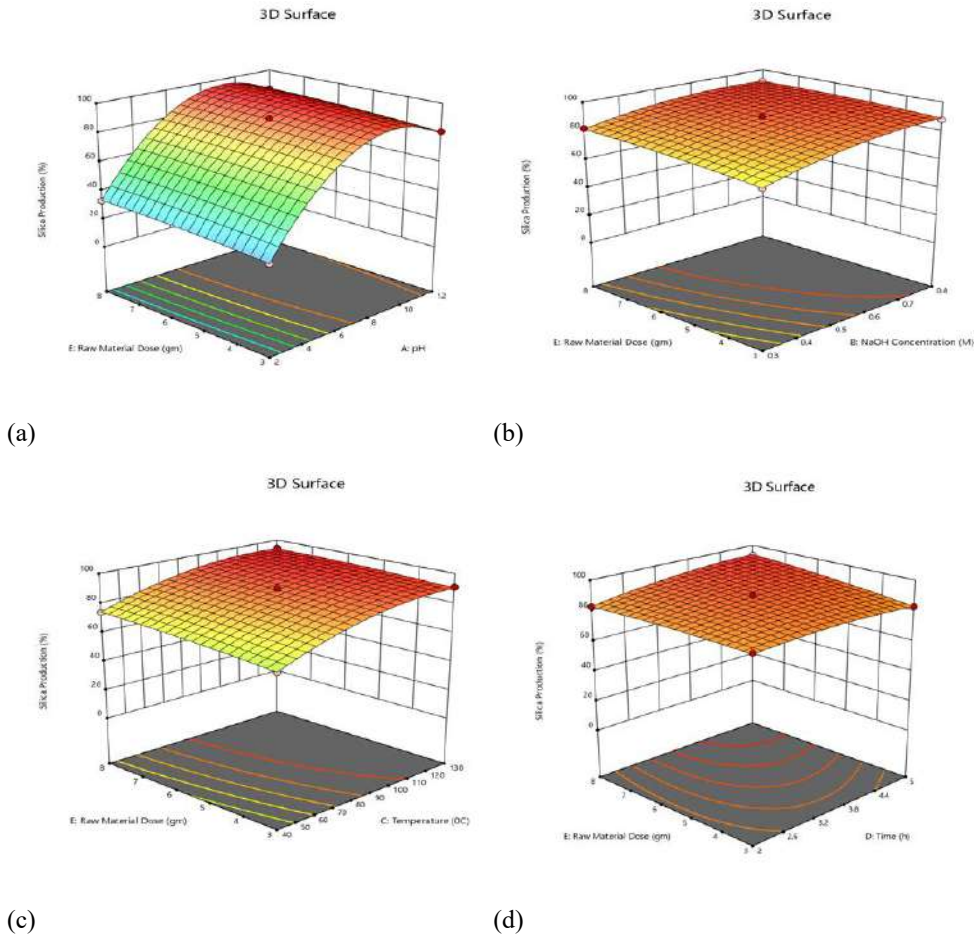


Fig. 5: 3D Response surface plots showing the interaction between (a) pH vs. raw material dose (b) NaOH concentration vs. raw material dose (c) Temperature vs. raw material dose (d) Time vs. raw material dose.

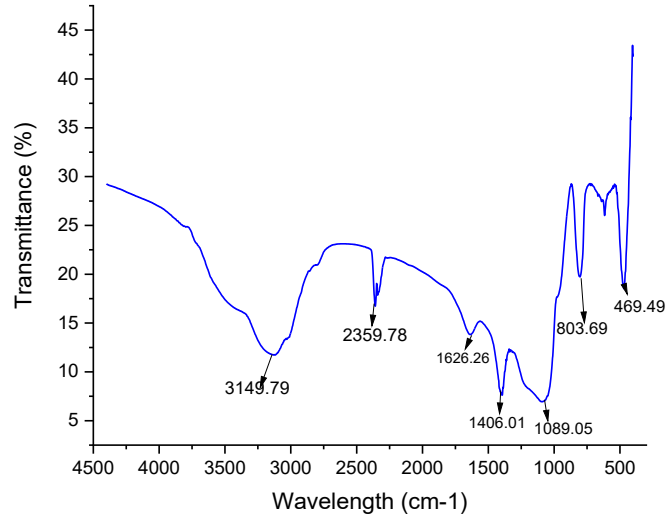


Fig. 6: FT-IR spectra $SiO_2$ nanoparticles prepared from rice husk.

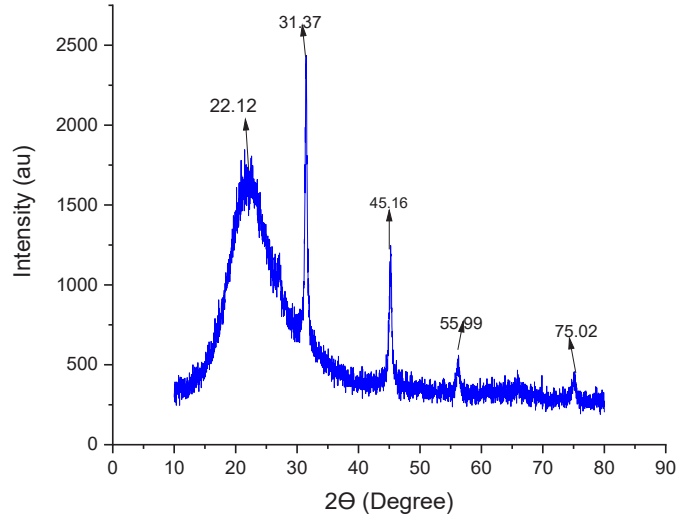


Fig. 7: XRD of $SiO_2$ nanoparticles prepared from rice husk.

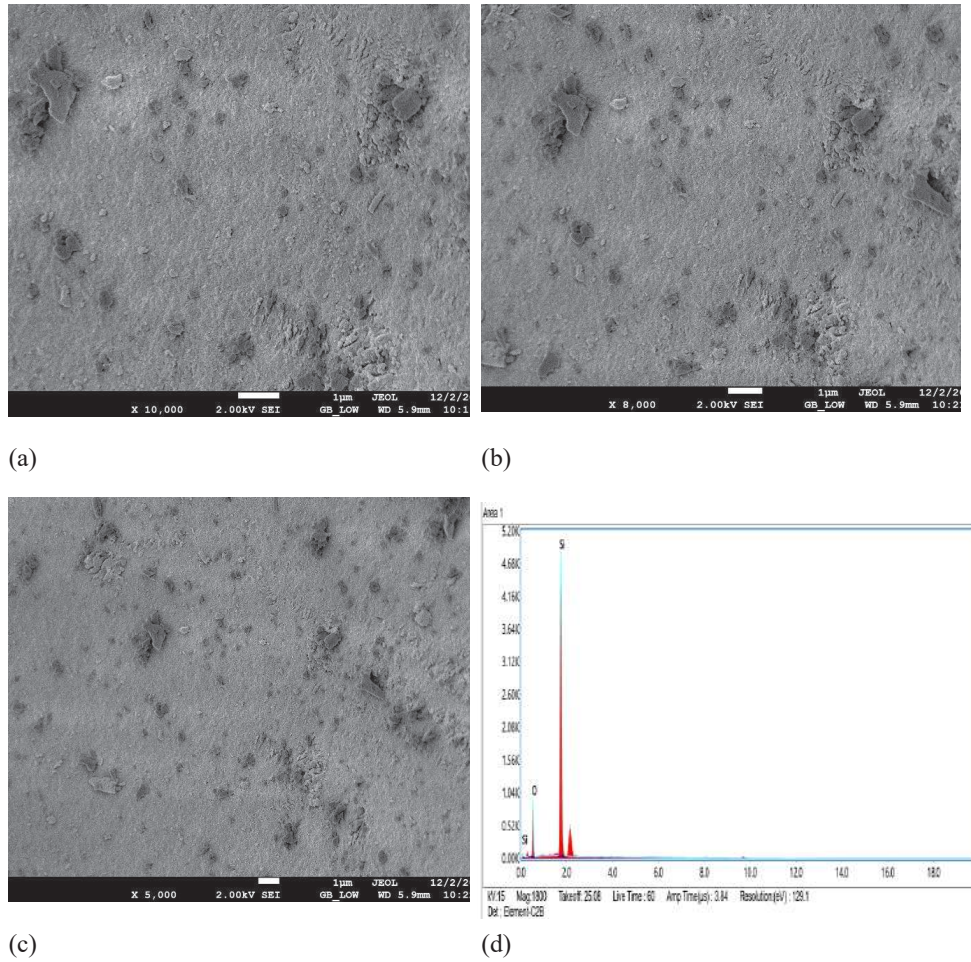


Fig. 8: (a) SEM images taken with 1 **µm** (10,000) index (b) SEM images taken with 1 **µm** (8,000) index (c) SEM images taken with 1 **µ**m (5,000) index (d) EDX of $SiO_2$ nanoparticles.

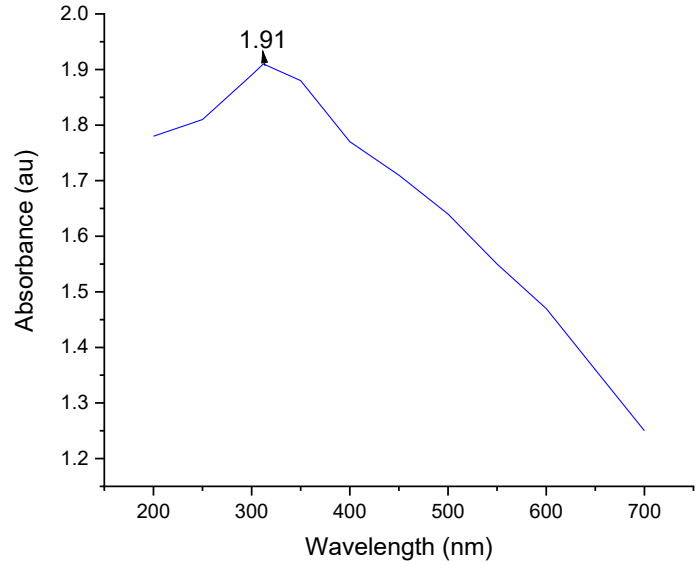


Fig. 9: UV-Visible Spectroscopy of $SiO_2$ nanoparticles procured from rice husk.

of silica nanoparticles using rice husk is an environmentally favorable, cost-effective green synthesis method. Rice husk as an origin of silica nanoparticles has a beneficial economic and environmental influence because it is a plentiful lower valuable agronomic by-product that can help with agro-waste clearance. In industry and agriculture, biosynthesized silica nanoparticles can be employed for a variety of applications.

## ACKNOWLEDGMENTS

The authors express their gratitude to the Department of Environmental Science & Engineering and Central Instrumentation Laboratory, Guru Jambheswar University of Science & Technology, Hisar, for their support and productivity grants.

## REFERENCES

Ahmad, I., Siddiqui, W. A. and Ahmad, T. 2017. Synthesis, characterization of silica nanoparticles and adsorption removal of $Cu^{2+}$ ions in aqueous solution. Int. J. Emerg. Technol. Adv. Eng., 7(8): 439-445.

Akhayere, E., Kavaz, D. and Vaseashta, A. 2019. Synthesizing nano silica nanoparticles from barley grain waste: effect of temperature on mechanical properties. Pol. J. Environ. Stud., 28(4): 2513-2521.

Almeida, S. R., Elicker, C., Vieira, B. M., Cabral, T. H., Silva, A. F., Sanches Filho, P. J., Raubach, C. M., Hartwig, C. A., Mesko, M. F., Moreira, M. L. and Cava, S. 2019. Black $SiO_2$ nanoparticles obtained by pyrolysis of rice husk. Dyes Pigm., 164: 272-278.

Aphane, M. E., Doucet, F. J., Kruger, R. A., Petrik, L., and van der Merwe, E. M. 2020. Preparation of sodium silicate solutions and silica nanoparticles from south african coal fly ash. Waste Biomass Valorization, 8)11): 4403-4417.

Bapat, G., Labade, C., Chaudhari, A. and Zinjarde, S. 2016. Silica nanoparticle based techniques for extraction, detection, and degradation of pesticides. Adv. Colloid Interface Sci., 237: 1-14.

Bharti, C., Nagaich, U., Pal, A. K. and Gulati, N. 2015. Mesoporous silica nanoparticles in target drug delivery system: A review. Int. J. Pharm. Investig., 5: 124-133.

Bui, T. M. A., Nguyen, T. V., Nguyen, T. M., Hoang, T. H., Nguyen, T. T. H., Lai, T. H., Tran, T. N., Nguyen, V. H., Hoang, V. H., Le, T. L., Tran, D. L., Dang, T. C., Vu, T. Q. and Nguyen-T. P. 2020. Investigation of crosslinking, mechanical properties and weathering stability of acrylic polyurethane coating reinforced by $SiO_2$ nanoparticles issued from rice husk ash. Mater. Chem. Phys., 241: 122445.

Chen, X., Jiang, J., Yan, F., Tian, S. and Li, K. 2014. A novel low temperature vapor phase hydrolysis method for the production of nano-structured silica materials using silicon tetrachloride. RSC Adv., 4: 8703-8710.

Cheng, Z., Zhang, L., Guo, X., Jiang, X. and Liu, R. 2015. Removal of lissamine rhodamine B and acid orange 10 from aqueous solution using activated carbon/surfactant: process optimization, kinetics and equilibrium. J. Taiwan Inst. Chem. Eng., 47: 149-159.

Chong, M. Y., Numan, A., Liew, C. W., Ng, H. M., Ramesh, K. and Ramesh, S. 2018. Enhancing the performance of green solid-state electric double-layer capacitor incorporated with fumed silica nanoparticles. J. Phys. Chem. Solids., 117: 194-203.

Dubey, R. S., Rajesh, Y. B. R. D. and More, M. A. 2015. Synthesis and characterization of $SiO_2$ nanoparticles via sol-gel method for industrial applications. Mater. Today: Proc., 3579-3575 :2.

Falk, G., Shinhe, G. P., Teixeira, L. B., Moraes, E. G. and de Oliveira, A. N. 2019. Synthesis of silica nanoparticles from sugarcane bagasse ash and nano-silicon via magnesiothermic reactions. Ceram. Int., 45(17): 21618-21624.

FAO Statistics on rice production 2021. https://www.fao.org/worldfoodsituation/csdb/en/

Gao, M., Ma, Q., Lin, Q., Chang, J. and Ma, H. 2017. A novel approach to extract $SiO_2$ from fly ash and its considerable adsorption properties. Mater. Des., 116: 666-675.

Ghorbani, F., Sanati, A. M. and Maleki, M. 2015. Production of silica nanoparticles from rice husk as agricultural waste by environmental friendly technique. Environ. Stud. Persian Gulf., 2: 56-65.

Hossain, S. S., Mathur, L. and Roy, P. K. 2018. Rice husk/rice husk ash as an alternative source of silica in ceramics: A review. J. Asian Ceram. Soc., 6: 299-313.

Ismail, A., Saputri, L. N. M. Z., Dwiatmoko, A. A., Susanto, B. H. and Nasikin, M. 2021. A facile approach to synthesis of silica nanoparticles from silica sand and their application as superhydrophobic material. J. Asian Ceram. Soc., 9(2): 665-672.

Kang, S. H., Hong, S. G. and Moon, J. 2019. The use of rice husk ash as reactive filler in ultra-high performance concrete. Cem. Concr. Res., 115: 389-400.

Kano, S., Yamamoto, A., Ishikawa, A. and Fujii, M. 2019. Respiratory rate on exercise measured by nanoparticle-based humidity sensor. In: 41st Annual International Conference of the IEEE Engineering in Medicine and Biology Society (EMBC), pp. 3567-3570.

Krishna, J., Perumal, A. S., Khan, I., Chelliah, R., Wei, S., Swamidoss, C. M. A., Oh, D. H. and Bharathiraja, B. 2021. Synthesis of nanomaterials for biofuel and bioenergy applications. In: Nanomaterials: Application in Biofuels and Bioenergy Production Systems, Academic Press Publishers, pp. 97-165.

Lade, H., Govindwar, S. and Paul, D. 2015. Mineralization and detoxification of the carcinogenic azo dye Congo red and real textile effluent by a polyurethane foam immobilized microbial consortium in an upflow column bioreactor. Int. J. Environ. Res. Public Health., 12: 6894-6918.

Li, H., van den Driesche, S., Bunge, F., Yang, B. and Vellekoop, M. J. 2019. Optimization of on-chip bacterial culture conditions using the Box-Behnken design response surface methodology for faster drug susceptibility screening. Talanta, 194: 627-633.

Manaa, A. 2015. Extraction of highly pure silica from local rice straw and activation on the of the left carbon for chromium (VI) adsorption. Indian J. Chem. Technol., 10: 242-251.

Mohd, N. K., Wee, N. N. A. N. and Azmi, A. A. 2017. Green synthesis of silica nanoparticles using sugarcane bagasse. AIP Conference Proceedings, **1885**(1): 020123. AIP Publishing LLC.

Nandiyanto, A. B. D., Rahman, T., Fadhlulloh, M. A., Abdullah, A. G., Hamidah, I. and Mulyanti, B. 2016. Synthesis of silica particles from rice straw waste using a simple extraction method. IOP Conference Series: Materials Science and Engineering, **128**(1): 012040.

Nazeran, N. and Moghaddas, J. 2017. Synthesis and characterization of silica aerogel reinforced rigid polyurethane foam for thermal insulation application. J. Non-Cryst. Solids., 461: 1-11.

Patil, N. B., Sharanagouda, H., Doddagoudar, S. R., Ramachandra, C. T. and Ramappa, K. T. 2018. Biosynthesis and Characterization of Silica Nanoparticles from Rice (*Oryza sativa* L.) Husk. Int. J. Curr. Microbiol. Appl. Sci., 7: 2298-2306.

Peres, E. C., Slaviero, J. C., Cunha, A. M., Hosseini–Bandegharaei, A. and Dotto, G. L. 2018. Microwave synthesis of silica nanoparticles and its application for methylene blue adsorption. J. Environ. Chem. Eng., 6: 649-659.

Priya, T. R., Nelson, A. R. L. E., Ravichandran, K. and Antony, U. 2019. Nutritional and functional properties of coloured rice varieties of South India: a review. J. Ethn. Foods., 6: 1-11.

Raut, B. K. and Panthi, K. P. 2019. Extraction of silica nanoparticles from rice husk ash (RHA) and study of its application in making composites. J. Nepal Chem. Soc., 40: 67-72.

Sankar, S., Kaur, N., Lee, S. and Kim, D. Y. 2018. Rapid sonochemical synthesis of spherical silica nanoparticles derived from brown rice husk. Ceram. Int., 44: 8720-8724.

Sankar, S., Sharma, S. K. and Kim, D. Y. 2016. Synthesis and characterization of mesoporous SiO2 nanoparticles synthesized from biogenic rice husk ash for optoelectronic applications. Int. J. Eng. Sci., **8-353 :17.**

Sarkar, J., Ghosh, M., Mukherjee, A., Chattopadhyay, D. and Acharya, K. 2014. Biosynthesis and safety evaluation of ZnO nanoparticles. Bioprocess Biosyst. Eng., 37: 165-171.

Setiawan, W. K. and Chiang, K. Y. 2021. Crop residues as potential sustainable precursors for developing silica materials: a review. Waste Biomass Valorization., 12: 2207-2236.

Soltani, N., Bahrami, A., Pech-Canul, M. I. and González, L. A. 2015. Review on the physicochemical treatments of rice husk for production of advanced materials. Chem. Eng. J., 264, 899-935.

Wahab, R., Khan, F., Gupta, A., Wiggers, H., Saquib, Q., Faisal, M. and Ansari, S. M. 2019. Microwave plasma-assisted silicon nanoparticles: cytotoxic, molecular, and numerical responses against cancer cells. RSC Adv., 9: 13336-13347.

Wibowo, E. A. P., Arzanto, A. W., Maulana, K. D., Hardyanti, I. S., Septyaningsih, H. D. and Nuni W. N. 2017. Preparation and characterization of silica nanoparticles from rice straw ash and its application as fertilizer. J. Chem. Pharm. Res., 9: 193-199.

Yang, R., Wang, X., Zhang, Y., Mao, H., Lan, P. and Zhou, D. 2019. Facile synthesis of mesoporous silica aerogels from rice straw ash-based biosilica via freeze-drying. Bioresources., 14: 87-98.

Nature Environment and Pollution Technology
An International Quarterly Scientific Journal

p-ISSN: 0972-6268
(Print copies up to 2016)
e-ISSN: 2395-3454

Vol. 22 | No. 1 | pp. 489-496 | 2023

Original Research Paper

https://doi.org/10.46488/NEPT.2023.v22i01.047

Open Access Journal

# Study on Effectiveness of Intervention of a Vertical Flow Constructed Wetland in between Septic Tank and Soak Pit for the Treatment of Septic Tank Effluent

**S. Suresh*, P. Sharma*, R. R. Yaragal* and S. Mutnuri*†**

*Water Sanitation and Hygiene Laboratory, Department of Biological Sciences, BITS Pilani, K.K. Birla Goa Campus, NH 17B, Zuarinagar, Goa-403726, India

†Corresponding author: S. Mutnuri; srikanth@goa.bits-pilani.ac.in

**Nat. Env. & Poll. Tech.**
**Website: www.neptjournal.com**

*Received:* 16-07-2022
*Revised:* 06-10-2022
*Accepted:* 18-10-2022

**Key Words:**
Vertical flow constructed wetland
Septic tank
Soak pit
Wastewater treatment

## ABSTRACT

Septage comprises the solid and liquid constituents of any primary treatment system, including a Septic Tank. In this study, the wastewater collected from a septic tank is passed through a partially converted anaerobic filter, and a vertical flow constructed wetland (VFCW) before being sent to a soak pit. The main objective of this case study was to check the effectiveness of incorporating a VFCW between a septic tank and a soak pit to bring down the consequences created due to effluent seepage from soak pits to the groundwater. Conventionally, the effluent gets directly passed to soak pits after primary onsite treatment in the septic tank. The soak pit walls made of porous materials allow the gradual seepage of final effluent into the ground, polluting the groundwater reserves. We analyzed the septic tank effluent from 60 households wherein the effluent was let off into the soak pits. The various parameters analyzed with their averages were 393.83 ± 293.41 $mg.L^{-1}$ for COD, 151.48 ± 94.37 $mg.L^{-1}$ for BOD, 30.81 ± 13.05 $mg.L^{-1}$ for $NO_3^-$, 23.35 ± 13.54 $mg.L^{-1}$ for $PO_4^{3-}$, 7.35 ± 0.31 for pH, 184.05 ± 163.20 $mg.L^{-1}$ for TSS, 3.05 x $10^7$± ٢٫٠٤ x $10^8$ $CFU.100mL^{-1}$ for TC. Therefore, it is certain that the final effluent being sent into soak pits after primary treatment does not meet the Central Pollution Control Board (CPCB) discharge standards. In this case study, we were able to obtain final effluent values after VFCW treatment as 55.72 $mg.L^{-1}$ for COD, 12.12 $mg.L^{-1}$ for BOD, 10.2 $mg.L^{-1}$ for $NO_3^-$, 3.74 $mg.L^{-1}$ for $PO_4^{3-}$, 7.41 for pH, 8.37 $mg.L^{-1}$ for TSS, 379.27 $mg.L^{-1}$ for TS and 51.9 $CFU.100mL^{-1}$ for TC. With this case study, we were able to resolve this impediment by bringing down the values of all the parameters considered while analyzing under the limits of discharge standards set by CPCB. The removal efficiency of COD, BOD, $NO_3^-$, $PO_4^{3-}$, pH, TSS, and TC after wetland was found to be 89.46%, 88.051, 63.484, 44.37%, 3.41%, 98.47%, 97.71%, 97.19% respectively. The study has proven that with the introduction of another decentralized treatment system between a septic tank and soak pit, it is safe to dispose of the effluent into soak pits, thereby reducing the chances of groundwater pollution considerably.

## INTRODUCTION

The concept of sanitation remits the idea of being clean for oneself and considering their immediate surroundings (Nurudeen & Toyin 2020). With the object of providing this and various other goals, the United Nations introduced 8 Millennium Development Goals (MDG) in 2000 to be achieved by 2015 and later replaced it with Sustainable Development Goals in 2015 (SDG) with 17 agendas to be fulfilled by 2030 which had a clear targeted goal for sanitation and especially hygiene. Joint Monitoring Programme (JMP) by World Health Organization (WHO)/ United Nations Children's Fund (UNICEF) was established to provide guidelines and to compare the progress of MDGs across countries and later revised to WHO/UNICEF Joint Programme for Water Supply, Sanitation, and Hygiene by 2017 with regards to 2030 agenda (Jong & Vijge 2021).

According to Central Pollution Control Board (CPCB), India will need 1.5 trillion cubic meters of water to meet the water demand by 2030 (CPCB ENVIS Letters 2021). Based on Niti Aayog's report in 2018, the per capita water availability is disputed to deplete to 1465 cubic meters by 2025 from 1544 cubic meters, which was available in 2011 and 1816 cubic meters in 2001. To meet the water demand, Recycling and Reusing wastewater can be beneficial alternatives to reduce the stress on the water reserve that is available today (Matto et al. 2019). Sanitation and water availability being a merit good, the Indian government has brought forward specific key policy initiatives and programs in accordance with that, like the Flagship program Namami Gange Program in 2014, Jawaharlal Nehru National Urban Renewal Mission (JNNURM) in 2005, National Urban Sanitation Policy (NUSP) in 2008, Swachh Bharat Mission (SBM) in 2014 and National Policy on Fecal Sludge

and Septage Management (NPFSSM) in 2017 for Urban Sanitation (Kapur 2021). Out of all the policies, the policy that garnered the maximum attention among the public was SBM. SBM consists of Phase 1 with significant objectives of making India Open Defecation Free (ODF), uprooting Manual Scavenging, and bringing about specific behavioral changes regarding some already existing sanitary practices, whereas Phase 2 gave importance to maintaining the ODF status achieved in phase 1 and to improve the lives of sanitation workers and the management of solid and liquid waste (Bhattacharya et al. 2018).

Even though in phase 1 access to safe sanitation was provided, it is also required to make sure that safe and proper Containment, Collection, Transportation (If on-site treatment is not possible), Treatment, and Resource recovery or Safe disposal is made systematically to maintain sanitation (Peal et al. 2020, Schrecongost et al. 2020). In developing countries like India and other countries, certain complications can arise due to the transportation of waste collected to a far-off treatment facility either through sewers or vacuum trucks or manually if there is no provision for a treatment plant present nearby. There are chances of waste getting dumped elsewhere into the environment rather than being taken to the treatment facility (Mehta et al. 2019). Thereby untreated waste will lead to more trouble if left unattended. If treatment is not done effectively, the usage or disposal of the end product will also be unhygienic and can create disorders in humans (Reymond et al. 2020). As a solution to all of this inconvenience, onsite treatment of waste can be considered. One such treatment technology is the usage of septic tanks and soak pits and the sanitary facility available (Strande 2014).

A septic tank acts as a sedimentation tank where settling settleable solids happens and a digestion tank where some magnitude of anaerobic digestion happens (Ergas et al. 2021). Thereby, there is a slight destruction in solids occurring along with a reduction in sludge concentration, little pathogen reduction, and release of Carbon dioxide ($CO_2$), Methane ($CH_4$), and Hydrogen sulfide ($H_2S$) gases. A septic tank usually comprises two chambers with a sludge layer, a clear zone with effluent, and a scum layer found inside (Adegoke & Stenstrom, 2019). From these chambers, effluent will be passed onto soak pits, typically in circular dimensions provided with inner linings and filled with brick ballasts and loose stones. The effluent in soak pits will gradually leach out through the porous walls of the soak pits in time. Since proper and complete treatment is not done inside the septic tanks, the effluent leached out from the soak pit pores will join the groundwater reserves or any other drinking water source present in the proximity to contaminate the water body (Ergas et al. 2021). There are a lot of disadvantages due to the percolation of the effluent from soak pits. Besides cross-contamination, leachate can also affect the soil properties that it comes in contact with without treatment. The leachate is unhygienic, and since total oxidation of organic matter is not completed properly, upon introduction to air, it will become offensive and produce a foul smell (Mahajan n.d). Since countries like India largely depend upon septic tanks and soak pits for onsite treatment technologies, it is vital to have a treatment system between the septic tank stage and soak pit in highly congested areas to avoid this condition (Forbis-Stokes et al. 2021).

To detect the impact of soak pits on the environment, a survey was conducted by collecting Septic tank effluent from 60 different locations in Goa, and inlet characteristics of the wastewater were done. After screening this data, we were able to arrive at the conclusion that an immense amount of pollution is directly passed onto the soak pits and, from there, eventually, to the ground. Since Laterite is the major soil type in Goa with very little retention capacity, the leachate from the soak pits will seep into the groundwater reserve and pollute the groundwater table, unfitting for the environment's well-being. So, it was essential to find an alternative to this condition by introducing a treatment system between the septic tank and the soak pit. VFCW was selected as the intermediate treatment system as it is cheap and would require significantly less operation as it is a passive system. The main objective of the case study was to find the effectiveness of introducing a partial anaerobic filter inside the septic tank chamber and a VFCW before disposing of the effluent from the septic tank chamber into soak pits. The case study aimed to bring down the values of physico-chemical parameters used for analyzing wastewater samples to the standard limits set forward for Sewage Treatment Plants of India by CPCB (Central Pollution Control Board 2008) and globally by the US EPA (Environmental Protection Agency) (US-EPA 1994).

## MATERIALS AND METHODS

### Characterization of Wastewater from Septic Tank

With regards to the characterization of wastewater in septic tanks, 60 different locations in Goa were selected, and surveys were conducted. From the locations, septic tank wastewater samples were collected. The samples obtained in this survey were analyzed for all the physico-chemical parameters of wastewater in the Water Sanitation and Hygiene Lab in BITS Pilani K K Birla Goa Campus, Goa. The supplementary file contains data regarding the locations of sample collection and parameter values obtained after analysis.

**Construction of the Setup**

The system consists of a septic tank comprising three chambers. The third chamber is partially converted into an anaerobic filter, a vertical flow constructed wetland (VFCW), a disinfection tank, and a soak pit. Cement Concrete walls were used to construct all the chambers in the setup. The septic tank was constructed with dimensions 5×2×2 m, and the length of the three compartments was provided as 2 m, 2 m, and 1m, respectively. In the Anaerobic filter in the third compartment of the Septic tank, 20-40 mm gravel was added up to a height of 1m from the bottom of the chamber. VFCW was constructed as a second-stage wetland with the dimensions 2×2×2 m, comprising three layers of sand and gravel. From the top, 0- 40 mm sand was provided to a height of 40 cm, followed by 4-10 mm sized gravel for a height of 15-20 cm, and finally, for the third layer, 10-20 mm sized gravel was given for the height of 20 cm (Yadav et al. 2018). Aeration pipes were provided at the bottom of the wetland to maintain passive ventilation. Out of the 2m depth provided for VFCW, 20 cm at the top is utilized by plants in the wetland, and the bottom 20 cm is occupied by the aeration pipes leaving 1.6 m of the anaerobic zone. Dimensions for the Disinfection tank were designated as 1x2x2 m. The soak pit was filled with loose stones of size 20-40 mm for a height of 2 m. the pictorial representation of the setup is shown in Fig. 1.

**Working of the Setup**

The system was constructed and implemented in July 2021 and was left operational till January 2022 so that the system gets acclimatized to the treatment conditions. From January 2022, monitoring of the system was initiated; collection and

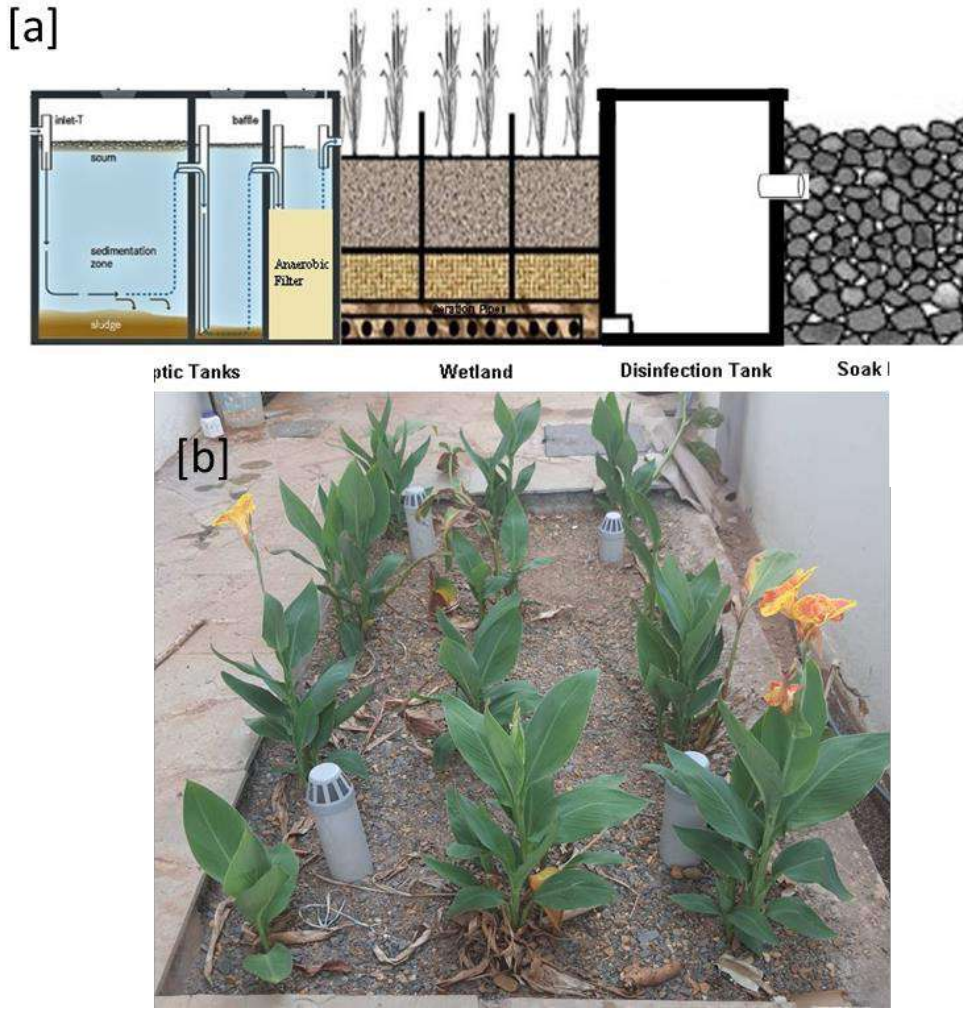


Fig. 1: [a] Design of the treatment system after the septic tank and [b] Real-time picture of the setup.

analysis of samples were started along with it. The system was operated manually and treated 1$m^3$ of raw wastewater per day. Wastewater enters the first chamber of the septic tank system, where the inlet pipe is placed to the bottom and moves towards the rest of the chambers by the up flow. In the third chamber of the septic tank, wastewater will flow through an anaerobic filter placed at the center of the chamber, extending up to the bottom. From this chamber, wastewater will move onto the VFCW from the bottom to the top by vertical flow at 1.8 m and pass onto the disinfection tank where chlorination was done. Once the residual total coliform was removed, treated effluent was circulated for gardening, and the leftover effluent was then deposited into the soak pit.

### Analytical Methodology

Samples were collected from three collection points; the initial model was the raw wastewater before providing any treatment, the second sample was generated after anaerobic filtration, and the third sample was collected after the wetland treatment. Once collected, all three sampling points were analyzed for Chemical Oxygen Demand (COD), Biochemical Oxygen Demand (BOD), Turbidity, pH, Nitrates ($NO_3^-$), Ortho-Phosphate ($PO_4^{3-}$), Total Solids (TS), Total Suspended Solids (TSS) and Total Coliforms (TC). For COD and $PO_4^{3-}$, analysis was done using Standard Operating Procedures mentioned in APHA (APHA, WEF 2005). For the analysis of $NO_3^-$, Spectroquant® Prove 100 Spectrophotometer was used with the Spectroquant® cell test kits. Oakton-PC 450 pH meter was used for the study of pH. For calculating TSS and TS, a Hot air oven and weighing balance were used, and for TSS, filter paper of pore size 1.45 microns was used.

### Location of the Setup

This work was carried out near Bogmallo, South Goa, Goa, India, and the location coordinates are 15.3556314°, 73.8490873°.

## RESULTS AND DISCUSSION

### Wastewater Characteristics

Table 1 represents the results obtained after performing various analyses on the septic tank wastewater samples collected from 60 locations in Goa. After treatment in the septic tank, the average values of parameters obtained with the relative standard deviation were 393.83 ± 293.41 mg.$L^{-1}$, 151.43 ± 94.37 mg.$L^{-1}$, 30.81 ± 13.05 mg.$L^{-1}$, 23.35 ± 13.54 mg.$L^{-1}$, 7.35 ± 0.31, 184.05 ± 163.20 mg.$L^{-1}$, 3.05x$10^7$ ± 2.04x$10^8$ CFU.100mL$^{-1}$ for the parameters COD, BOD, $NO_3^-$, $PO_4^{3-}$, pH, TSS, TC respectively. The standard limits set by CPCB for the safe discharge of treated wastewater for COD, BOD, $NO_3^-$, $PO_4^{3-}$, pH, TSS, and TC are less than 50 mg.$L^{-1}$, less than 10 mg.$L^{-1}$, less than 10 mg.$L^{-1}$, less than 5 mg.$L^{-1}$, 6.5 - 9.0, less than 20 mg.$L^{-1}$, less than 100 CFU.100 mL$^{-1}$ respectively (Central Pollution Control Board 2008). Based on the values obtained after analysis compared to the standard limits, it is evident that the treatment is insufficient, and all the values are well above the limits set by the CPCB. From these values, it can be concluded that a huge amount of pollution is being transferred into the soak pits without adequate treatment (Schellenberg et al. 2020). This argument clarifies the need to introduce an efficient treatment system after the septic tank before the effluent is sent to the soak pits.

Table 1: Characteristics of the septic tank wastewater collected from 60 different points in Goa.

| Parameters | Values obtained |
|---|---|
| COD [mg.$L^{-1}$] | 393.83 ± 293.41 |
| BOD [mg.$L^{-1}$] | 151.48 ± 94.37 |
| $NO^{3-}$ [mg.$L^{-1}$] | 30.81 ± 13.05 |
| $PO_4^{3-}$ [mg.$L^{-1}$] | 23.35 ± 13.54 |
| pH | 7.35 ± 0.31 |
| TSS [mg.$L^{-1}$] | 184.05 ± 163.20 |
| TC [CFU.100mL$^{-1}$] | 3.05 x $10^7$ ± 2.04 × $10^8$ |

As illustrated in Table 2, the values obtained after analysis of the samples collected from the constructed new setup are shown. The average COD value with its corresponding standard deviation for raw wastewater was 529.21 ± 84.83 mg.$L^{-1}$; after complete treatment, the value obtained was 55.72 ± 7.68 mg.$L^{-1}$. From this, it can be inferred that the treatment was working. With the introduction of wetland, the system brought down the COD value from 248.07 mg.$L^{-1}$ obtained after the anaerobic filter to 55.72 mg.$L^{-1}$ after wetland treatment, which is around the CPCB standard limit 50 mg.$L^{-1}$ provided for COD. BOD's value varied from 101.48 ± 11.26 mg.$L^{-1}$ to 12.126 ± 3.145 mg.$L^{-1}$ after complete treatment. Here it can be observed that in VFCW treatment, the BOD value was reduced to 12.126 mg.$L^{-1}$, which is around the limit of BOD set by CPCB. When considering the values of $NO_3^-$ it can be seen that the values reduced from 27.93 ± 2.38 mg.$L^{-1}$ for raw wastewater to 10.2 ± 1.31 mg.$L^{-1}$ after VFCW. After wetland treatment, the $NO_3^-$ value is 10.2, around the standard limit for $NO_3^-$ set by CPCB. Generally, it is found that while using VFCW, there is a hike in nitrate values (Yaragal & Mutnuri 2021). While considering the values obtained, we can infer that this system was able to overcome the drawback of an increase in nitrate with the introduction of VFCW. For the values obtained for $PO_4^{3-}$ also, we can observe a considerable

Table 2: Characteristics of the wastewater samples collected from the system constructed.

| Parameters | Domestic wastewater | After anaerobic chamber | After VFCW |
|---|---|---|---|
| COD [mg.L$^{-1}$] | 529.21 ± 84.83 | 248.07 ± 29.54 | 55.77 ± 2.68 |
| BOD [mg.L$^{-1}$] | 101.48 ± 11.26 | 49.63 ± 4.55 | 12.12 ± 3.14 |
| $NO_3^-$ [mg.L$^{-1}$] | 27.93 ± 2.38 | 17.76 ± 0.86 | 10.2 ± 1.31 |
| $PO_4^{3-}$ [mg.L$^{-1}$] | 6.73 ± 1.62 | 4.98 ± 1.21 | 3.74 ± 0.69 |
| pH | 7.16 ± 0.10 | 7.39 ± 0.073 | 7.41 ± 0.35 |
| TSS [mg.L$^{-1}$] | 549.2 ± 109.55 | 69.48 ± 16.22 | 8.37 ± 2.30 |
| TS [mg.L$^{-1}$] | 16595.46 ± 2119.30 | 3692.37 ± 610.50 | 379.27 ± 32.96 |
| TC [CFU.100 mL$^{-1}$] | 1852.8 ± 500.66 | 805.5 ± 95.48 | 51.90 ± 12.16 |

decrease in values after wetland treatment as 6.73 ± 1.62 mg.L$^{-1}$ to 3.74 ± 0.69 mg.L$^{-1}$ after VFCW, and we can see that the final effluent has $PO_4^{3-}$ value as 3.745 which is under the standard limit 5 mg.L$^{-1}$ for $PO_3^{4-}$ set by CPCB. In the case of pH, we can observe the values 7.165 ± 0.10 changing to 7.41±0.35 after complete treatment, and the pH value of sample 7.41 is in the limit of the effluent discharge standard for the pH ranges from 6.5-9.0. TSS values differ from 549.2 ± 109.55 m.L$^{-1}$ to 8.37 ± 2.30 mg.L$^{-1}$ after VFCW. It can be deduced that upon treatment, the system was able to cut down the concentration of TSS from 549.2 mg.L$^{-1}$ to 8.37 mg.L$^{-1}$, which is under the CPCB standard limit of 20 mg.L$^{-1}$. From the TS values observed, we can conclude that there is a substantial reduction in the values mentioned in the initial raw sample, which is 16595.46 ± 2119.30 mg.L$^{-1}$ to the final effluent after VFCW with 379.27 ± 32.96 mg.L$^{-1}$. Even if good quality treatment happens after VFCW, the final value obtained for TS is still higher. It can also be noticed that there is a good quality treatment for pathogen reduction with TC varying from 1852.8 ± 500.66 CFU.100 mL$^{-1}$ to 51.90 ± 12.16 CFU.100 mL$^{-1}$ after VFCW which is well under the CPCB standard limit of 100 CFU.100 mL$^{-1}$ (Central Pollution Control Board 2008). After all the analysis, it can be concluded that the introduction of wetlands has a positive impact in lowering the values of the wastewater sample to the standard limits set forth by the CPCB. Accordingly, we can assume that the values of all the parameters around the CPCB limit after wetland treatment, and the final effluent can be reused after disinfection and sent to soak pits. Even if there is a percolation of leachate from the soak pits in time, there won't be any groundwater pollution since the physicochemical parameters remaining after disinfection will be under the limits.

Table 3 shows the removal efficiency of the system after the series of treatments. It can be seen that there is a considerable reduction of 89.469% (+), 88.051% (+), 63.484% (+), 44.378% (+), 3.419% (-), 98.475% (+), 97.714% (+), 97.198% (+) for COD, BOD, $NO_3^-$, $PO_4^{3-}$, pH, TSS, TC respectively in which positive sign (+) represents the reduction in parameter values after wetland treatment and negative sign (-) represents the increase in the parameter values. Fig. 2 explains the weekly variation in physicochemical parameters.

From the graphical observation of COD, we can deduce that the raw wastewater sample produced COD values around 529.11 mg.L$^{-1}$ varying from a maximum of 677.84 mg.L$^{-1}$ to a minimum of 429.82 mg.L$^{-1}$. A higher COD level generally indicates a higher quantity of oxidizable organic matter in the sample (Burns 2021). After Septic tank treatment, the values obtained were around 248.07 mg.L$^{-1,}$ differing from 304.54 mg.L$^{-1}$ to 213.782 mg.L$^{-1}$. The reduction in COD values from raw wastewater to the final treated wastewater can be associated with anaerobic digestion and sedimentation in the septic tank (Adegoke & Stenstrom 2019). After VFCW, the COD values obtained were around an average value of 55.72 mg.L$^{-1}$ ranging from 67.89 mg.L$^{-1}$ to 42.87 mg.L$^{-1}$ and the accelerated decrease in COD value observed was also supplemented by the partial aeration provided below the wetland (Tang & Huang 2008). In accordance with the COD values, we can see a similar reduction in BOD values averaging at 101.482 mg.L$^{-1}$ without treatment ranging from 121.54 to 85.57 mg.L$^{-1}$, 49.636 mg.L$^{-1}$ after anaerobic filter varying

Table 3: Percentage reduction occurring in each parameter after complete treatment.

| Parameters | Per cent reduction |
|---|---|
| COD [mg.L$^{-1}$] | 89.46% |
| BOD [mg.L$^{-1}$] | 88.05% |
| $NO_3^-$ [mg.L$^{-1}$] | 63.48% |
| $PO_4^{3-}$ [mg.L$^{-1}$] | 44.37% |
| pH | -3.41% |
| TSS [mg.L$^{-1}$] | 98.47% |
| TS [mg.L$^{-1}$] | 97.71% |
| TC [CFU.100mL$^{-1}$] | 97.19% |

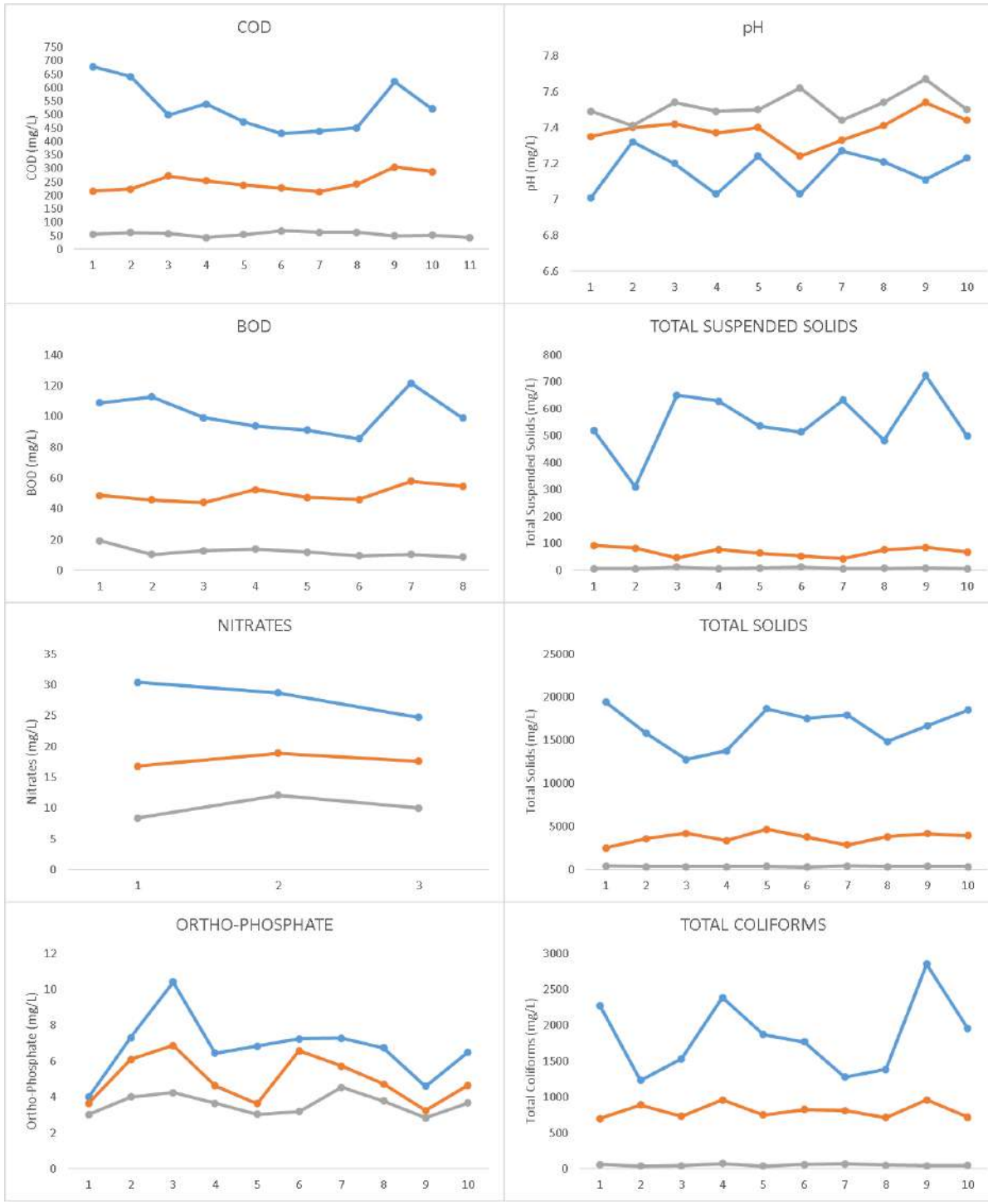


Fig. 2: Graphical representation of variation in physic-chemical parameters after each stage of treatment.
The blue line indicates the inlet wastewater, orange line indicates the wastewater after anaerobic filter and the grey line indicates the wastewater characteristics after VFCW

within 57.86 to 44.08 mg.$L^{-1}$ and 12.126 mg.$L^{-1}$ after VFCW treatment with maximum and minimum values 13.79 to 8.74 mg.$L^{-1}$. The high BOD value of raw wastewater indicates that the oxygen required to decompose biodegradable organic matter is high. The lesser value of BOD for samples after VFCW treatment shows that the oxygen required for organic matter decomposition is significantly less. This validates the fact that proper treatment of wastewater is happening in the system with the introduction of wetlands.

In the case of $NO_3^-$, average values obtained were 27.93 mg.$L^{-1}$ for raw wastewater with a minimum of 30.4 mg.$L^{-1}$ to a maximum of 24.7 mg.$L^{-1}$, 17.76 mg.$L^{-1}$ after treatment in an anaerobic filter ranging from 18.9 to 16.8 mg.$L^{-1}$, 10.2 mg.$L^{-1}$ after VFCW treatment varying from12.1 to 10 mg.$L^{-1}$. There is enough reduction in nitrate values after the septic tank and anaerobic filter, indicating that some of the nitrates got reduced in the chamber. The decrease in nitrate value after VFCW treatment is because of the larger anaerobic zone of size 1.8m provided in the VFCW and the anaerobic filter provided in the septic tank. For $PO_4^{3-}$ analysis, raw wastewater gave an average value of 6.73 mg.$L^{-1}$ with 10.39 mg.$L^{-1}$ as the maximum and 3.99 mg.$L^{-1}$ as the minimum. Sample after anaerobic treatment produced 4.98 mg.$L^{-1}$ ranging from 6.86 to 3.25 mg.$L^{-1}$, and after complete treatment, the value was reduced to 3.745 mg.$L^{-1}$ varying from 4.53 to 2.83 mg.$L^{-1}$. The reduction in $PO_4^{3-}$ after wetland can be considered as due to the uptake by plants. We can observe pH values of 7.165 with limits from 7.32 to 7.01 for raw wastewater, 7.39 ranging from 7.54 to 7.24 for the sample after the anaerobic filter, and 7.41 as average with maximum and minimum varying from 7.67 to 7.44 for the sample after VFCW.

In the case of TSS, we can see that the maximum and minimum value ranges obtained for raw wastewater are from 723 to 310 mg.$L^{-1}$ with 549.2 mg.$L^{-1}$ as average, which is at a high. The sample after the anaerobic filter produced a TSS value of the average of 69.48 mg.$L^{-1}$ ranging from 93.33 to 43 mg.$L^{-1}$ whereas the sample after VFCW had a value of 8.37 mg.$L^{-1}$ as average with maximum and minimum varying from 6.5 to 13 mg.$L^{-1}$. The higher reduction of TSS occurring in the septic tank is due to the sedimentation of most of the settleable solids in the chambers. For the analysis of TS, we can observe that for raw wastewater, an average of 16595.46 mg.$L^{-1}$ with ranges of at19435.93 to 12765.88 mg.$L^{-1}$ was obtained. The average TS value for the sample after the anaerobic filter was 3692.37 mg.$L^{-1}$, with maximum and minimum changing from 4665.45 to 2507.66 mg.$L^{-1}$. After complete treatment, the final effluent sample showed an average TS value of 379.27 mg.$L^{-1}$ with ranges within 430 to 323.75 mg.$L^{-1}$. There is a considerable decrease in Total coliforms after the septic tank and anaerobic filter as well as after wetland treatment with average values at 1852.8 CFU.100 $mL^{-1}$ for raw wastewater with ranges from 2850 to 1230 CFU.100 $mL^{-1}$, 805.5 CFU.100 $mL^{-1}$ for sample after anaerobic filter varying from 960 to 700 CFU.100 $mL^{-1}$ and 51.909 CFU.100 $mL^{-1}$ for the sample collected after complete treatment in VFCW with maximum value 75 CFU.100 $mL^{-1}$ to a minimum of 37 CFU.100 $mL^{-1}$. Reduction of total coliforms happening in the septic tank due to the help of the bacteria present that will decompose the organic matter current once the organic matter gets settled (Holt 2011).

## CONCLUSIONS

Based on the results obtained by the physicochemical analysis of parameters at different stages of the treatment system, it can be concluded that the introduction of another on-site wastewater treatment system, such as a VFCW between the septic tank and soak pit, showed better treatment of the septic tank effluent. The final effluent obtained after VFCW met the standards set by CPCB (Central Pollution Control Board 2008). The removal efficiency of parameters COD, BOD, $NO_3^-$, $PO_4^{3-}$, pH, TSS, and TC after wetland was found to be 89.469%, 88.051%, 63.484%, 44.378%, 3.419%, 98.475%, 97.714%, 97.198% respectively. We can infer from the values obtained for removal efficiency that the treatment is positive and satisfactory. The final effluent values were 55.727 mg.$L^{-1}$ for COD, 12.126 mg.$L^{-1}$ for BOD, 10.2 mg.$L^{-1}$ for $NO_3^-$, 3.745 mg.$L^{-1}$ for $PO_4^{3-}$, 7.41 for pH, 8.373 mg.$L^{-1}$ for TSS, 379.27 mg.$L^{-1}$ for TS and 51.909 CFU.100 $mL^{-1}$ for TC. The final effluent values being around the Effluent Discharge standards by CPCB, our study was able to show that the effluent after wetland treatment in the system was safe enough to be circulated for reuse or to be sent to a soak pit after disinfection. The aim of the case study was thus achieved by introducing an alternate treatment system like VFCW between a septic tank and a soak pit. VFCW being less expensive and requiring less maintenance, it is a better and cheap alternate treatment addition to the conventional septic tank–soak pit system used in India and does not require any skill for maintenance.

## ACKNOWLEDGEMENTS

The authors are thankful to BITS Pilani K K Birla Goa Campus for providing all the facilities to carry out this work. We are also grateful to the Water Sanitation and Hygiene laboratory for providing facilities to conduct the analysis. We thank Mutnuri family for allowing us to conduct experiments on their premises.

## REFERENCES

Adegoke, A.A. and Stenstrom, T.A. 2019. Septic Systems: Global Water Pathogen Project (GWPP). UNESCO, Paris, France

APHA; WEF 2005. Standard methods for the examination of water and wastewater. American Public Health Association, American Water Works Association, Water Environment Federation.

Bhattacharya, S., Sharma, D. and Sharma, P. 2018. Swachh Bharat Mission: an integrative approach to attain public health in India. Int. J. Environ. Health, 16: 1-17.

Burns, T. 2021. How to Reduce COD in Water. https://www.bioprocessh2o.com/blog/cod

Central Pollution Control Board 2008. Guidelines for Water Quality Management. CPCB, New Delhi.

CPCB ENVIS Letter 2021. Wastewater Generation and Treatment: Domestic Sewage Urbanisation and Wastewater Management in India.

Ergas, S. J., Amador, J. and Boyer, T. F. 2021. Onsite and decentralized wastewater management systems. J. Sustain. Water Built Environ., 9: 1-3.

Forbis-Stokes, A.A., Kalimuthu, A., Ravindran, J. and Deshusses, M.A. 2021. Technical evaluation and optimization of a mobile septage treatment unit. J. Environ. Manag., 5: 1-9.

Holt, K. 2011. Septic Systems: Total Fecal Coliform. Retrieved from https://www.aero-stream.com/septic-systems-total-fecal-coliform-ii/. Access date: 09-05-2022

Jong, E.D. and Vijge, M.J. 2021. From millennium to sustainable development goals: Evolving discourses and their reflection in policy coherence for development. Earth Syst. Govern., 16: 1-12.

Kapur, D. 2021. Swachh Bharat Mission 2: Why Centralised Sanitation Will Not Address Urban Problems. Retrieved from https://www.downtoearth.org.in/blog/waste/swachh-bharat-mission-2-why-centralised-sanitation-will-not-address-urban-problems-77562. Access date: 09-05-2022

Mahajan, B. Soak Pit, Soakage Pit, Soak Pit Design, Soak Pit Meaning, Leach Pit, Advantages & Disadvantages of Soak Pit. Retrieved from Civiconcepts: https://civiconcepts.com/blog/soak-pit. Access date: 09-05-2022

Matto, M., Singhal, S. and Prasad, J. 2019. Decentralised Wastewater Solutions the Need of the hour for India. Retrieved from https://www.downtoearth.org.in/blog/water/decentralised-wastewater-solutions-the-need-of-the-hour-for-india-67218. Access date: 09-05-2022

Mehta, M., Mehta, D. and Yadav, U. 2019. Citywide inclusive sanitation through scheduled desludging services: Emerging Experience from India. Front. Environ. Sci., 7: 61-73.

Nurudeen, A.S. and Toyin, A. 2020. Knowledge of personal hygiene among undergraduates. J. Health Educ., 5: 71-83.

Peal, A.E., Ahilan, S., Ban, R., Blackett, I., Hawkins, P., Schoebitz, L. and Veses, O. 2020. Estimating safely managed sanitation in urban areas; lessons learned from a global implementation of excreta-flow diagrams. Front. Environ. Sci., 8: 1-13.

Reymond, P., Chandragiri, R. and Ulrich, L. 2020. Governance arrangements for the scaling up of small-scale wastewater treatment and reuse systems: Lessons from India. Front. Environ. Sci., 14: 8-16.

Schellenberg, T., Subramanian, V., Ganeshan, G., Tompkins, D. and Pradeep, R. 2020. Wastewater discharge standards in the evolving context of urban sustainability: The case of India. Front. Environ. Sci., 16: 36-43.

Schrecongost, A., Pedi, D., Rosenbiim, J.W., Shrestha, R. and Ban, R. 2020. Citywide inclusive sanitation: A public service approach for reaching the urban sanitation SDGs. Front. Environ. Sci., 6: 149-158.

Strande, L. 2014. Faecal Sludge Management: Systems Approach for Implementation and Operation. IWAP, London.

Talekar, G.V., Sharma, P.Y., Clauwaert, P., Rabaey, K. and Mutnuri, S. 2018. Sanitation of blackwater via sequential wetland and electrochemical treatment. Nature Part. J., 4:1-9.

Tang, X. and Huang, S.S. 2008. Nutrient removal in pilot-scale constructed wetlands treating eutrophic river water: Assessment of plants, intermittent artificial aeration, and polyhedron hollow polypropylene balls. Water Air Soil Pollut., 197: 61-73.

US EPA. 1994. Decentralized Systems Technology Factsheet Septage Treatment/ Disposal. US EPA, 1-7.

Yadav, A., Chazarenc, F. and Mutnuri, S. 2018. Development of the "French system" vertical flow constructed wetland to treat raw domestic wastewater in India. Ecol. Eng., 23: 88-93.

Yaragal, R.R. and Mutnuri, S. 2021. Nitrates removal using ion exchange resin: Batch, continuous column, and pilot-scale studies. Int. J. Environ. Sci. Technol., 4: 1-16.

Nature Environment and Pollution Technology
An International Quarterly Scientific Journal

p-ISSN: 0972-6268
(Print copies up to 2016)
e-ISSN: 2395-3454

Vol. 22 | No. 1 | pp. 497-502 | 2023

Original Research Paper

https://doi.org/10.46488/NEPT.2023.v22i01.048

Open Access Journal

# Performance of Alum Coagulation and Adsorption on Removing Organic Matter and *E. coli*

**E. N. Hidayah*†, O. H. Cahyonugroho* and N. A. Fauziyah****
*Department of Environmental Engineering, Universitas Pembangunan Nasional Veteran Jawa Timur, Indonesia
**Department of Chemical Engineering, Universitas Pembangunan Nasional Veteran Jawa Timur, Indonesia
†Corresponding author: E.N. Hidayah; euisnh.tl@upnjatim.ac.id

**Nat. Env. & Poll. Tech.**
**Website: www.neptjournal.com**

*Received:* 07-08-2022
*Revised:* 17-09-2022
*Accepted:* 29-09-2022

**Key Words:**
Organic matter
*E. coli*
Coagulation
Adsorption
Chlorination

## ABSTRACT

Surface water is the primary resource for raw water in drinking water treatment processes. Therefore, the presence of microorganisms, bacteria, and viruses should be the main focus in drinking water treatment, in addition to natural organic matter, which is composed of organic carbon groups derived from aquatic biota as well as organic material, organic matter from industrial and domestic waste. This study applied coagulation-flocculation followed by adsorption as the advanced treatment with activated carbon for removing organic matter and bacteria simultaneously to know each process's performance. The results indicated that all treatment processes have a good performance for removing dissolved organic matter in water with efficient removal of 28.35%-70.75% of TOC concentration and 26.75%-55.95% of $UV_{254}$ concentration. Further, the selected processes demonstrated a high percentage of removal of *E. coli*, about 65.35%-96.43%. However, the effect of chlorination impacted the increasing THMs concentration up to 36.32%, while the other processes could remove THMs concentration 17.25%-51.08%. Overall, this study conjectures that all treatment processes simultaneously perform well for removing dissolved organic matter, THMs, and *E. coli*. However, chlorination should be managed to control the formation of THMs due to the remaining organic matter in water.

## INTRODUCTION

Surface water contains diverse pollutants and biological activities that humans and industries generate. One of the primary pollutants is organic matter, known as natural organic matter (NOM), which is composed of organic carbon groups derived from plants or aquatic biota, as well as organic material and organic matter from industrial and domestic waste. Characterization of the organic matter revealed that organic matter is composed of various molecular weight fractions, aromatic, aliphatic, hydrophobic/hydrophilic, and humus/non-humus (Sillanpää et al. 2015). Surface water is the primary resource for raw water in drinking water treatment processes. Therefore, drinking water treatment should focus on microorganisms, bacteria, and viruses. Numerous microorganisms and bacteria have been identified as the most dangerous pathogens, capable of causing diarrhea, diseases, and death (Edzwald & Tobiason 2011). In developing countries, *Escherichia coli* (*E. coli*) is one of the most common causes of many bacterial infections, including gastroenteritis (Owoseni et al. 2017).

Nevertheless, surface water is used as raw water for the production of clean and drinking water. The most applicable clean and drinking water technologies are coagulation-flocculation, sedimentation, filtration, and disinfection. However, it has limitations in treating all parameters to meet the quality standards optimally, especially to fill the requirement for the lowest concentration of organic matter and bacteria or viruses concentration simultaneously (Chen et al. 2021).

The most commonly used clean water treatment technology to set aside the content of viruses and bacteria is a chlorine disinfection process because cheap and chlorine is relatively stable. It means that chlorine residual remains in the distribution system, preventing the regrowth of viruses and microorganisms (Edzwald & Tobiason 2011). However, chlorine is very reactive and quickly reacts with organic and inorganic materials contained in water. Reaction chlorine on the organic matter can cause the formation of disinfectant by-products (DBPs), namely trihalomethanes (THMs) and haloacetic acids (HAAs), which are carcinogenic and harmful to human health (Bond et al. 2009, Hidayah et al. 2017). Some issue related to the formation of DBPs is increasing chlorine dosage to eliminate viruses and bacteria in production water. In contrast, the treated water still contains dissolved organic matter (DOM). Therefore, it will

trigger an increase in carcinogenic compounds in drinking water (Bond et al. 2009, Hidayah et al. 2016).

Regarding natural organic matter (NOM) removal, generally, the most common and economically feasible standard processes for removing NOM and drinking water parameters are considered coagulation and flocculation, sedimentation, and sedimentation and filtration. The most widely used coagulant is an alum and iron-based coagulant, which has been reported to be consistently more effective in removing NOM (Uyak & Toroz 2007, Matilainen et al. 2010). Coagulation-flocculation has primarily been used in waterworks companies and is typically applied before further treatments. The other treatment process is the application of advanced treatment of adsorption by using activated carbon, charcoal, and diverse biosorbent. Activated carbon is a suitable adsorbent due to its ability to bind with various molecules (Han et al. 2015, Azad et al. 2020). In addition, activated carbon has been found that can be used to remove bacteria and bacteria toxins, in addition to developing the water quality used for consumption purposes.

Furthermore, the active part of adsorbents can remove organic matter in the water (Karanfil et al. 1999, Han et al. 2015) and remove pathogens (Naka et al. 2001). This study applied coagulation-flocculation followed by adsorption as the advanced treatment with activated carbon to remove organic matter and bacteria simultaneously. This study aimed to know the concentration of THMs and *E. coli* under post-treatment of adsorption only and adsorption followed by chlorination.

## MATERIALS AND METHODS

The primary source of raw water for water treatment, Kali Surabaya in Surabaya City, provided the source water for this study. The raw water sample was taken in May 2022. This study was conducted under four treatments: alum, adsorption with activated carbon, coagulation-adsorption, and coagulation-adsorption-chlorination. The first treatment, alum ($Al_2(SO_4)_3.18H_2O$, Merck, Germany), was used as a coagulant with various dosages of 10 to 60 $mg.L^{-1}$ with intervals of 10 $mg.L^{-1}$. Jar test equipment was used for flash mixing for 3 min at 100 rpm, slow mixing for 15 min at 35 rpm, and then settling for 15 min. The second treatment, powder-activated carbon (PAC), was used as an adsorbent with various dosages of 10 to 60 $mg.L^{-1}$ with an interval of 10 $mg.L^{-1}$ under slow mixing for 60 min at 35 rpm. In the third treatment, the optimum alum dosage from the first treatment was applied in coagulation, followed by adsorption with the optimum adsorbent dosage at the second treatment. The treated water from the third treatment was injected with 10 $mg.L^{-1}$ $Na(OCl)_2$ (Merck Germany) as a disinfectant solution with 30 min contact time, or it was the fourth treatment. All treated samples from each treatment were collected and filtered through 0.45 m filter paper (cellulose acetate) before being subjected to additional analysis, which included dissolved organic matter in terms of total organic carbon (TOC) and ultraviolet absorbance at 254 nm wavelength ($UV_{254}$); THMs, and *E. coli*. The TOC and $UV_{254}$ analyses followed Standard Methods and procedures. (APHA AWWA & WEF 2012). TOC was determined using the combustion-infrared method with a total organic carbon analyzer Model TOC Analyzer 5000A Shimadzu, and $UV_{254}$ was determined with a Carry 100 Bio UV-Visible Spectrophotometer with a 1 cm quartz cell. THMs were determined using gas chromatography and headspace-solid-phase microextraction (HS-SPME, 85 m carboxy/polydimethylsiloxane fiber). The DPD ferrous method was used to measure residual chlorine (APHA AWWA & WEF 2012). The Most Probability Number (MPN) test was used to determine the amount of *E. coli* in all treated samples. The MPN is an estimated number of individual bacteria with a 95% confidence interval, with a unit per 100 mL or gram.

## RESULTS AND DISCUSSION

Fig. 1 explains the performance of coagulation, adsorption, and its combination processes for removing organic matter. The graph shows the percentage change of each treatment's TOC concentration and $UV_{254}$ concentration. Firstly, the results present the maximum efficiency of each treatment process for TOC concentration, that is, 28.35% removal in alum coagulation, 46.85% removal in adsorption of activated carbon, 63.25% removal in alum coagulation followed by adsorption with activated carbon, and 70.75% removal in alum coagulation combined with adsorption with activated carbon followed by chlorination. This result indicated that all treatment processes effectively remove dissolved organic matter in water. Coagulation is the primary process in all water and wastewater treatment (Sillanpää et al. 2015, Hidayah et al. 2017). Previous studies have revealed the efficiency of coagulation up to 50% in removing dissolved organic matter, which depends on the treated water's characteristics (Aslam et al. 2013, Hidayah et al. 2016). Adsorption is an advanced treatment for removing pollutants such as heavy metals, particulates, organic matter, etc. Several kinds of research have demonstrated adsorption performance with activated carbon as an adsorbent for removing dissolved organic matter up to 30% (Han et al. 2015). The capacity and characteristics of the adsorbent, as well as the capacity and characteristics of activated carbon, determine the efficiency of the adsorption process (Karanfil et al. 1999). Adsorption with activated carbon demonstrated

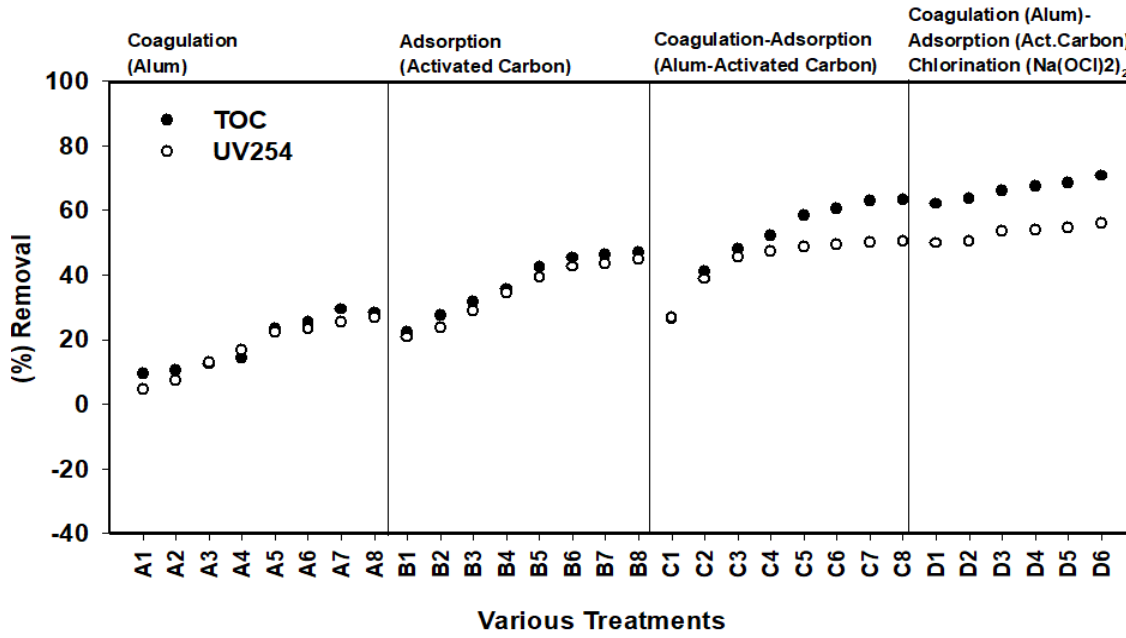


Fig. 1: The efficiency removal of various treatments for removing dissolved organic matter in water.

a high removal of hydrophilic and low molecular weight of dissolved organic matter (Velten et al. 2011).

Secondly, alum coagulation and adsorption with activated carbon have a better efficient removal than alum coagulation. Another combination, coagulation-adsorption-chlorination, performed a similar result to the coagulation-adsorption processes. It indicates that post-chlorination had an insignificant effect on the removal of dissolved organic matter. Chlorination could remove dissolved organic matter through various mechanisms, such as transformation, oxidation, and polymerization. The mechanism of chlorination on microorganisms is to inactivate a microorganism by damaging its cell membrane, and chlorine can be involved in the cell and alter cell respiration and disrupt DNA activities (Bond et al. 2009, Mazhar et al. 2020). Chlorination of organic matter can destroy the organic coating on the particle's surface, causing the zeta potential to change. Oxidation will strengthen the bond between particles and their adsorbed organics, lowering the molecular weight of organic matter.

Furthermore, oxidative polymerization of dissolved organic matter may result in particle aggregation via bridging reactions (Xie et al. 2016). Due to organic being transformed into lower molecular weight, the TOC analyzer and $UV_{254}$ could not detect the lower molecular weight organic compounds. According to previous studies, HPSEC with UVD/OCD revealed the changing molecular weight organic after chlorination (Hidayah et al. 2017) and the changing of fluorophores properties as detected by FEEMs (Han et al. 2015).

Third, $UV_{254}$ concentration decreased to 26.75% removal in alum coagulation, 44.85% removal in adsorption of activated carbon, 50.32% removal in alum coagulation, followed by adsorption with adsorption activated carbon, and 55.95% removal in alum coagulation combined with adsorption with activated carbon followed by chlorination. The changing of $UV_{254}$ concentration demonstrated that these selected processes could remove aromatic dissolved organic matter composed of saturated carbon double bonds. Fourth, comparing the percentage removal of TOC concentration and $UV_{254}$ concentration results in higher removal of TOC concentration than $UV_{254}$ concentration. $UV_{254}$ represents aromatic dissolved organic carbon, while TOC explains all types of dissolved organic carbon. It means a higher removal of TOC indicates a removal of the other kind of dissolved organic carbon instead of an aromatic compound, such as aliphatic non-aromatic. The removal difference between TOC concentration and $UV_{254}$ concentration in alum coagulation was lower than the removal difference in alum coagulation combined with adsorption with activated carbon followed by chlorination. These results follow the performance of each treatment, which mentioned that alum coagulation has a good performance for the removal of aromatic and less for non-aromatic compounds (Aslam et al. 2013, Hidayah et al. 2016). Adsorption has been well known to remove low molecular weight organic compounds,

hydrophilic and non-aromatic compounds (Velten et al. 2011, Azad et al. 2020), and it was related to a higher removal difference between TOC concentration and $UV_{254}$ concentration in adsorption with activated carbon followed by chlorination (Azad et al. 2020).

Fig. 2 presents the changing THMs and *E. coli* concentrations in each treatment process. THMs decreased up to 17.25% in alum coagulation, adsorption with activated carbon removed 35.32% THMs concentration, and a higher removal up to 51.08% in alum coagulation followed by adsorption with activated carbon. However, alum coagulation, adsorption, and chlorination increased THMs concentration by about 36.32%. This result shows compliance with the removal of TOC and $UV_{254}$ concentration, as shown in Fig.1. The selected processes, except chlorination, are potentially carried out to remove dissolved organic matter. It is well known that organic matters are the precursor for the formation of disinfectant by-products, such as THMs and HAAs. There is contradictory information regarding dissolved organic matter fractions are the most important precursors of THMs and HAAs.

Regarding hydrophobicity or hydrophilicity, it has been proposed that the hydrophilic fraction is a more critical precursor of THMs than HAAs. According to the humic compound, a humic substance fraction is a significant precursor for HAAs, while an aliphatic biopolymer fraction is a primary precursor for THMs. The characteristic organic matter with high molecular weight and hydrophobic was the primary source of THM precursors.

In contrast, the low molecular weight components were more significant DHAA (dihaloacetic acids) precursors than THAA (trihaloacetic acids) (Wang et al. 2013, Hidayah et al. 2016). Increasing THMs concentration indicates the formation of by-product compounds due to disinfections reacting with the organic matter in treated water. The higher chlorination dosage caused a higher formation of by-product compounds. In addition, the dominant mechanism of the reaction of chemical biocides with NOMs and other constituents in water is different. Therefore, the type and level of the resultant DBPs are expected to differ (Mazhar et al. 2020, Hidayah et al. 2017). Factors such as oxidant concentration, pH, organic matter characteristics, temperature, bromide existence, and precursor reactivity may affect DBPs formations. Therefore, water work companies have been looking for alternative disinfection processes, especially using chemical compounds, reducing the formation and discharge of DBPs. The most recently used chemical biocide is chlorine dioxide ($ClO_2$) (Edzwald & Tobiason 2011, Postigo et al. 2021).

Secondly, Fig. 2 shows the *E. coli* concentration gradually reduced up to 65.35% in coagulation, 70.32% in adsorption, 90% in coagulation-adsorption, and 96.43% in coagulation-adsorption-chlorination. The trend of *E. coli* reduction in those treatment processes follows the THMs reduction, except in coagulation-adsorption-chlorination. Treatment processes without chemical chlorination resulted in an inline reduction between THMs concentration and *E. coli* concentration. The reduction of THMs concentration

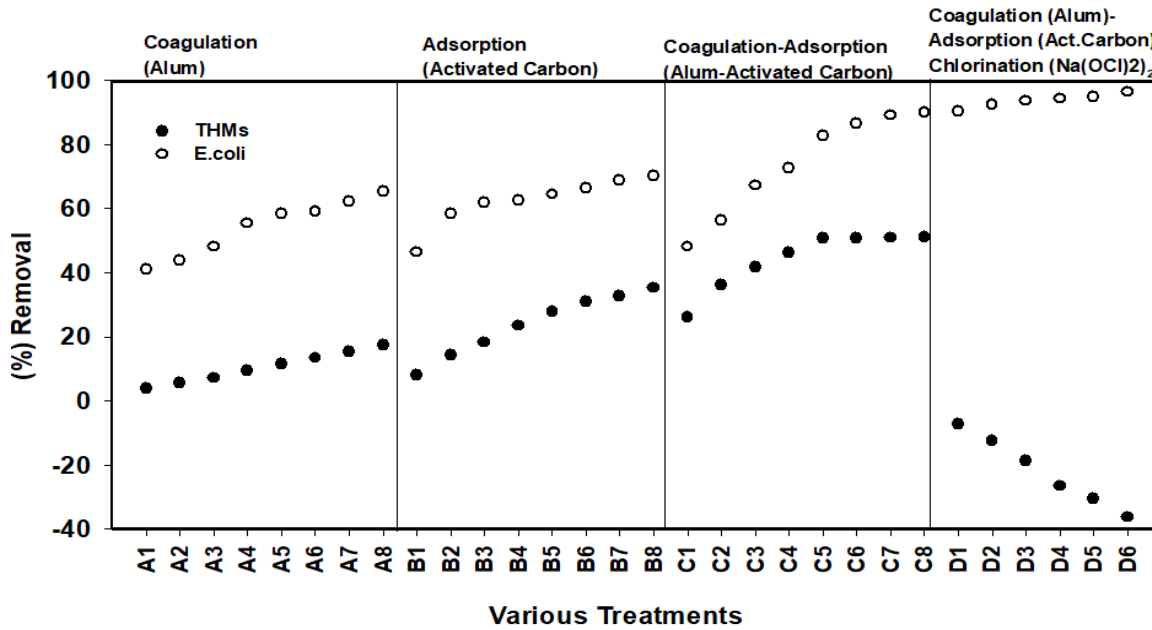


Fig. 2: The efficient removal of various treatments for removing the THMs formation and *E. coli*.

is lower than *E. coli* concentration removal, probably due to THMs indicating the existence of organic matters as precursors of DBPs formations (Mazhar et al. 2020). A higher reduction of *E. coli* through those selected processes is probably due to the power of each mechanism applied. Several mechanisms explain the coagulation of particles and organic substances, including precipitation, charge neutralization, adsorption, bridge aggregation, and sweep-flocculation. The coagulant develops the chemical and physical properties of flocs, especially on the particle bridging, increasing settling velocity.

Further, the cells are more easily taken into flocs, resulting in a greater density, particle size, strength, and settleable flocs. Furthermore, in addition, to charge neutralization, the surface charge of the microorganism is an important factor in the removal of microorganisms during the coagulation process (Aslam et al. 2013). Several studies mentioned the removal of microorganisms and viruses from water by coagulation, flocculation, and sedimentation (Shin & Sobsey 2015, Chen et al. 2013, Swiatlo et al. 2002) because it is most likely due to microorganisms having a negative charge. Microorganisms contain pyruvate, acidic sugars, or phosphate in different serotype capsular polysaccharides, with additional contributions from cell surface structures, which caused the negative charge (Swiatlo et al. 2002). The internal surface area of activated carbon may affect *E. coli* removal, mainly activated carbon with a large area of its pore. The activated carbon has various pore sizes and shapes due to it has complex network inside. Therefore, the high capacity adsorption indicates that the internal pores provide a vast internal surface area for activated carbon. However, in some cases, the activated carbon has low binding capacity because activated carbon does not possess pores of sufficient diameter for those bacteria (Chandy & Sharma 1998, Naka et al. 2001. Li et al. 2013). Combining coagulation followed by adsorption has given a higher efficiency removal of *E. coli* because *E. coli* was continuously removed into two different processes (Chen et al. 2021). Further, the robust chlorination process provides a higher removal of *E. coli* because chlorine is a potential oxidant that destroys the microorganism's nucleic acids and cell membranes, such as the effectiveness of chlorination for *E. coli* inactivation (Edzwald & Tobiason 2011).

## CONCLUSIONS

This study presents the performance of alum coagulation, adsorption with activated carbon, alum coagulation followed by adsorption, and the effect of chlorination after the coagulation and adsorption in removing dissolved organic matter as parameters TOC and $UV_{254}$ and in removing *E. coli* and THMs as one of the DBPs potentials. The efficiency performance of those treatment processes shows various percentage removal, such as 28.35%-70.75% of TOC concentration, 26.75%-55.95% of $UV_{254}$ concentration, 65.35%-96.43% of *E. coli* concentration, 17.25%-51.08% of THMs concentration. Regarding dissolved organic carbon, combining alum coagulation and adsorption with activated carbon has a better efficiency removal than alum coagulation only. At the same time, coagulation-adsorption-chlorination performed a similar result to coagulation-adsorption processes. It indicates that post-chlorination had an insignificant effect on the removal of dissolved organic matter. Treatment processes without chemical chlorination resulted in an inline reduction between THMs concentration and *E. coli* concentration. Chlorination affected the increase of THMs formation up to 36.32% due to the reactivity of chlorine with dissolved organic matter. The removal difference between TOC concentration and $UV_{254}$ concentration in alum coagulation was lower than the removal difference in alum coagulation combined with adsorption with activated carbon followed by chlorination.

## ACKNOWLEDGMENTS

This study was a part of the Primary University Flagship Research (PDUPT) scheme Basic Research (PD), which the Directorate of Research supports, Technology, and Community Services, Directorate General of Higher Education, Research, and Technology, Ministry of Education, Culture, Research, and Technology in the Year 2022, SP DIPA-023.17.1.690523/2022 2nd revised date April 22nd, 2022

## REFERENCES

APHA, AWWA and WEF 2012. Standard Methods for the Examination of Water and Wastewaters. Twenty-First edition. American Public Health Association, Washington, D.C.

Aslam, Z., Chow, C.W.K., Murshed, F., van Leeuwen, J., Drikas, M. and Wang, D. 2013. Variation in character and treatability of organics in river water: an assessment by HPAC and alum coagulation. Sep. Purif. Technol., 120: 162-171.

Azad, M.S., Azhari, S. and Hassan, M.S. 2020. Removal of methylene blue, Escherichia coli, and Pseudomonas aeruginosa by adsorption of activated carbon produced from moringa oleifera bark. Malay. J. Sci. Health Technol., 7: 29-39

Bond, T., Henriet, O., Golan, E.H., Parsons, S.A. and Jefferson, B. 2009. Disinfection by-product formation behavior of natural organic matter surrogates. Environmental Science and Technology, 43:5982-5989.

Chandy, T. and Sharma, C.P. 1998. Activated charcoal microcapsules and their applications. J. Biomater. Appl., 13(2):128-157

Chen, L., Deng, Y., Dong, S., Wang, H., Li, P., Zhang, H. and Chu, W. 2021. The occurrence and control waterborne viruses in drinking water treatment: A review. Chemosphere, 281: 1-11.

Edzwald, J.K. and Tobiason, J.E. 2011. Chemical principles, source water composition, and watershed protection. In Edward, J.K. (ed.), Water

Quality & Treatment: A Handbook on Drinking Water. AWWA McGraw-Hill, New York, pp. 1-76.

Han, Q., Yan, H., Zhang, F., Xue, N., Wang, Y., Chu, Y. and Gao, B. 2015. Trihalomethanes (THMs) precursor fractions removal by coagulation and adsorption for bio-treated municipal wastewater: Molecular weight, hydrophobicity/hydrophily, and fluorescence. J. Hazard. Mater., 297: 119-126.

Hidayah, E.N., Yeh, H.H. and Chou, Y.C. 2016. Using HPSEC to identify NOM fraction removal and the correlation with disinfection by-product precursors. Water Sci. Technol. Water Supply, 16(2): 305-313.

Hidayah, E.N., Yeh, H.H. and Chou, Y.C. 2017. Comparison between HPSEC-OCD and FEEMs for assessing DBPs formation in water. J. Environ. Sci. Health Part A, 52(4): 391-402.

Karanfil, T., Kitis, M., Kilduff, J.E. and Wigton, A. 1999. Role of granular activated carbon surface chemistry on the adsorption of organic compounds natural organic matter. Environ. Sci. Technol., 33(18): 3225-3233.

Li, D., Zeng, S., Gu, A.Z., He, M. and Shi, H. 2013. Inactivation, reactivation, and regrowth of indigenous bacteria in reclaimed water after chlorine disinfection of a municipal wastewater treatment plant. J. Environ. Sci., 25:1319–1325.

Matilainen, A., Vepsäläinen, M., and Silanpää, M. 2010. Natural organic matter removal by coagulation during drinking water treatment: a review. Adv. Coll. Interf. Sci., 159: 189-197.

Mazhar, M.A., Khan, N.A., Ahmed, S., Khan, A.H., Hussain, A., Rahisuddin, Changani, F., Yousefi, M., Ahmadi, S. and Vambol, V. 2021. Chlorination disinfection by-products in municipal drinking water: A review. J. Clean. Prod., 16: 273.

Naka, K., Watarai, S., Tana, Inoue, K., Kodama, Y., Oguma, K., Yasuda, T. and Kodama, H. 2001. Adsorption effect of activated charcoal on enterohemorrhagic Escherichia coli. J. Veter. Med. Sci., 63(3): 281-285

Owoseni M.C., Olaniran, A.O. and Okoh, A.I. 2017. Chlorine tolerance and inactivation of Escherichia coli recovered from wastewater treatment plants in the eastern cape, south Africa. Appl. Sci., 7(8): 810-825.

Postigo, C., Solsona, R.G., Batista, M.F.H., Ferrero, P.G., Alygizakis, N., Ahrens, L. and Wiberg, K. 2021. A step forward in detecting by-products of anthropogenic organic micropollutants in chlorinated water. Trends Environ. Anal. Chem., 32: 116-125.

Shin, G.A. and Sobsey, M.D. 2015. Removal of norovirus from water by coagulation, flocculation, and sedimentation processes. Water Supply, 15(1): 158-163.

Sillanpää, M., Metsämuuronen, S. and Mänttäri, M. 2015. Membranes. In: Silaanpää, M. (eds.), Natural Organic Matter in Water: Characterization and Treatment Method, Butterworth-Heinemann, Oxford, pp. 113-157.

Swiatlo, E., Champlin, F.R. and Holman, S.C. 2002. Contribution of choline-binding proteins to cell surface properties of streptococcus pneumonia. Infect. Immun., 70(1): 412-415.

Uyak, V. and Toroz, I. 2007. Disinfection by-product precursors reduction by various coagulation techniques in Istanbul water supplies. J. Hazard. Mater., 141(1): 320-328.

Velten, S., Detlef, R.U.K., Traber, J., Kaiser, H.P., Guntena, U., Boller, M. and Meylan, S. 2011. Characterization of natural organic matter adsorption in granular activated carbon adsorbers. Water Res., 45: 3951-3959.

Wang, D.S., Zhao, Y.M., Yan, M.Q. and Chow, C.W.K. 2013. Removal of DBP precursors in micro-polluted source waters: A comparative study on the enhanced coagulation behavior. Sep. Purif. Technol., 118: 271-278.

Xie, P., Chen, Y., Ma, J., Zhang, X., Zou, J. and Wang Z. 2016. A mini-review of peroxidation to improve coagulation. Chemosphere, 155: 550-563.

Nature Environment and Pollution Technology
An International Quarterly Scientific Journal

p-ISSN: 0972-6268
(Print copies up to 2016)
e-ISSN: 2395-3454

Vol. 22 | No. 1 | pp. 503-509 | 2023

Original Research Paper

https://doi.org/10.46488/NEPT.2023.v22i01.049

Open Access Journal

# Statistical Model for Tube Settler Clarifier at Different Operational Conditions

**Abdulmuhsin S. Shihab*†** and **Aladdin M. Ahmad****
*Environmental Research Centre, Mosul University, Mosul, Iraq
**Department of Civil Engineering, College of Engineering, Mosul University, Mosul, Iraq
† Corresponding author: Abdulmuhsin S. Shihab; mss_qzz@uomosul.edu.iq

**Nat. Env. & Poll. Tech.**
**Website: www.neptjournal.com**

*Received:* 15-08-2022
*Revised:* 01-10-2022
*Accepted:* 16-10-2022

**Key Words:**
Tube settler
Surface loading rate
Tube inclination angle
Statistical model
Regression analysis
High rate sedimentation

## ABSTRACT

The present study aimed to find a relationship between turbidity removal percent in tube settler clarifier and independent variables (tube inclination, alum dosage, and surface loading rate) by constructing a statistical model and categorizing these explanatory variables according to their impact on turbidity removal percentage. A pilot scale of tube settlers was designed and fabricated to conduct the experiments. It consisted of a coagulation and flocculation basin, pre-tube settler chamber, and tube settler. Alum was used to coagulate the Tigris river raw water at different dosages. After flocculation, water is transferred to the pre-tube settler chamber and flows through the tube settler. It consists of four tubes of square section, 4 centimeters in diameter, with the flexibility of changing tube length and inclination angle to obtain different levels of surface loading rate. More than 120 experiments were conducted, and the results were analyzed statistically. A regression model was found with a coefficient of determination of 0.802 between turbidity removal percentage as a dependent variable and each tube inclination, alum dosage, and surface loading rate as independent variables. The model is considered good as the model's relationship between actual and predicted values has a slope of one and a constant near zero. Surface loading rate has the highest effect on turbidity removal percentage with 4.44 times that of inclination angle and 2.5 times for the optimum alum dosage model. The study concluded that the linear model is suitable to represent the performance of tube settlers at optimum alum dosage.

## INTRODUCTION

Removing suspended particles by sedimentation is one of the most widely used in water clarification. It is a physical process used after coagulation and flocculation. The conventional sedimentation in water treatment plants includes rectangular or circular tanks with a depth of 4.6 to 4.9 meters or greater and a detention time of more than 2 hours (Randtke & Horsley 2012, Davis 2010). Hazen recognized in the previous century that the removal of settleable particles was independent of detention time and basin depth. At the same time, it was a function of the surface overflow rate (Shammas & Wang 2015).

Numerous sedimentation techniques have been developed to decrease detention time and increase water production. Of these techniques is tube settlers, an application of high-rate sedimentation theory (Gurjar et al. 2017). It depends on reducing the distance traveled by particles until they are deposited. Tube settler consists of small tubes with a square or circular, or hexagonal cross-section of 5 cm and a length of 60-120 cm (Davis 2010). The tubes may be adjusted at an angle of 45 to 60 degrees with the horizon to increase the effective settling area and to achieve self-cleaning of sludge from the tubes (Balwan et al. 2016).

Additionally, tube settler has the advantage of occupying a small space to create it. It can be fabricated and worked indoors, which may decrease the problems caused by algal growth, clogging related to blowing debris accumulation, and odor control (Qasim 2017). In addition, tube settlers and plate settlers can be used to upgrade conventional sedimentation basins (Shammas & Wang 2015). In Ethiopia, Ballcha (2015) found that applying tube settlers can provide better performance than conventional sedimentation by 35.3% and increase water production by 34.5%. Furthermore, many studies found that tube settler clarifiers were more efficient in removing turbidity than other sedimentation systems (Fouad et al. 2016, Wang et al. 2020).

The present water treatment plants in Mosul city/Iraq, use conventional deep sedimentation tanks to remove suspended solids. With the population increase and the

**ORCID details of the authors:**

**Abdulmuhsin S. Shihab**
https://orcid.org/0000-0003-0827-9950

town's expansion, there is a need to increase water production and improve the performance of sedimentation tanks. The research aimed to investigate the performance of inclined tube settlers by constructing a statistical model and analyzing the independent variables' effect and weight on the removal efficiency and with respect to others.

## MATERIALS AND METHODS

A pilot scale system was designed and fabricated at the Al-Ayssar water treatment plant in Mosul city, Iraq. Transparent plastic and glass were used in the construction of the model. It consisted of a coagulation-flocculation basin, fixed head basin, pre-tube settler chamber, and tube settlers (Fig. 1). Coagulation-flocculation unit has a volume of 40 L, equipped with a variable speed mechanical mixer (vertical shaft and blades) for fast and slow stirring. It was fed with raw water from the Tigris river by a pump connected with the inlet of the water treatment plant. Raw water turbidity ranged from 20 to 29 NTU. The coagulant dosage was added to raw water manually in this basin and mixed by the mechanical mixer. Coagulation was conducted after alum addition, followed by flocculation at velocity gradients of 1000 $sec^{-1}$ and 80 $sec^{-1,}$ respectively. After that, the flocculated water flows to the fixed head basin until it is filled to the specified level. Subsequently, the flocculated water flows to the "pre-tube settler chamber" (inlet) equipped with a baffle to prevent the turbulence of flocs. The flow was controlled at 1 L per minute. This unit is connected from the top by four squared tubes of 4 cm in length. These tubes have variable lengths

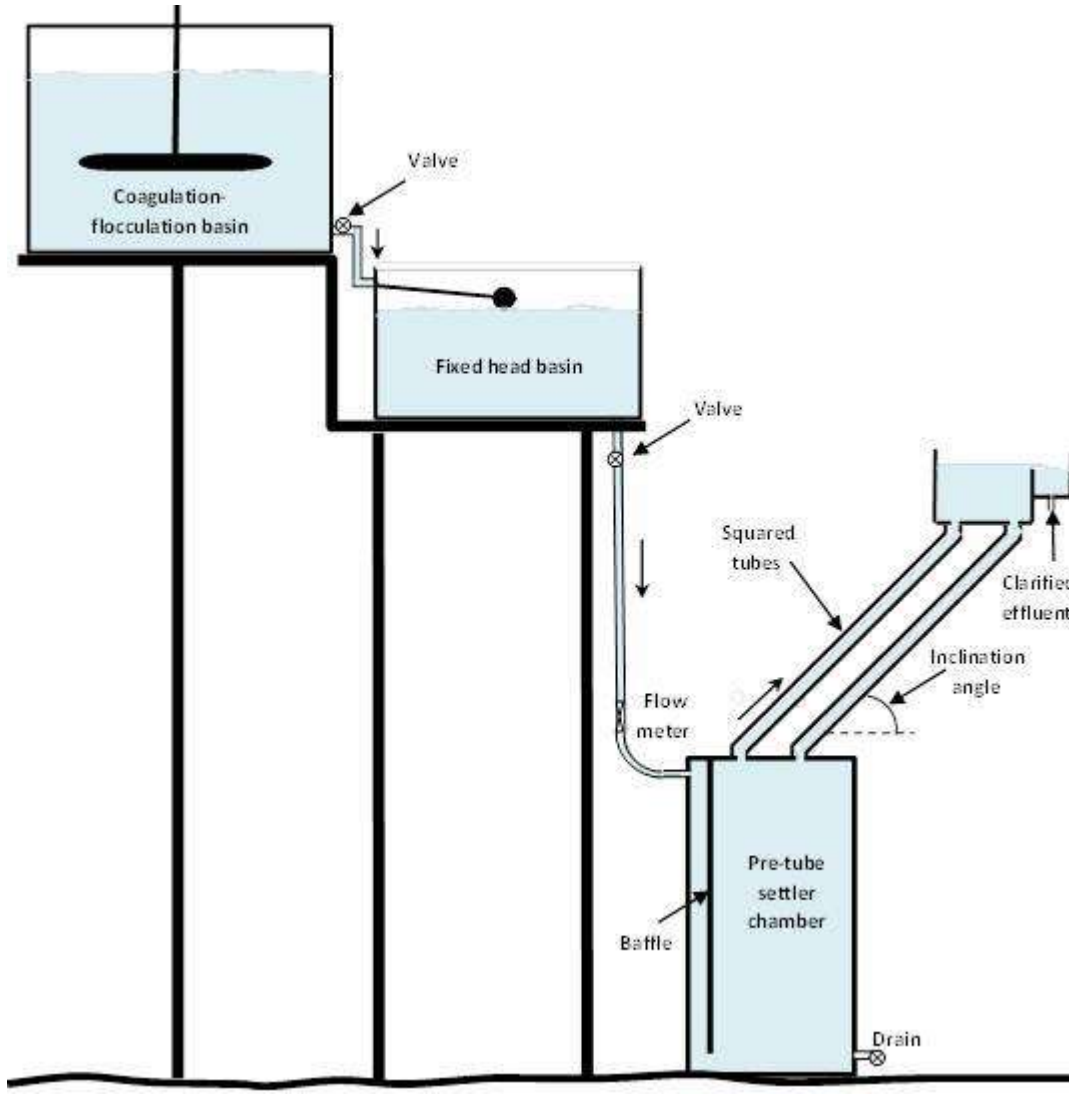


Fig. 1: Schematic diagram of the pilot scale of tube settler apparatus.

(40, 60, 80, 100, and 120 cm) and inclination angles (30, 40, 50, 60, and 70 degrees). As these units are lower than the fixed head basin, the flocculated water rises in the tubes and flows upward till it reaches the top and flows to the outlet unit. Influent and effluent samples were collected and tested for turbidity to find the system's efficiency.

Depending on the tubes lengths and inclination angles, the surface loading rate (SLR) was calculated according to equations (1) and (2) (Brandt et al. 2017):

$$SLR = C * K * \frac{V_o}{L_r} \quad ...(1)$$

SLR = surface loading rate

C = constant = $8.64 * 10^2$

$$K = S_c * \frac{L_r}{Sin\theta + L_r\, Cos\theta} \quad ...(2)$$

$S_c$ = shape factor (for square $S_c$ = 11/8)

$V_o$ = flow velocity in the tube

$L_r$ = relative length = L/d

L = length of the tube, d = diameter of the tube

θ = tube inclination angle

### Statistical Analysis

The results were analyzed statistically using SPSS 26. Simple regression (linear model) was used to find the relationship between turbidity removal percentage and SLR, while a quadratic model was used for the relationship with alum. Multiple linear regression was used to find a model between turbidity removal percentage as the dependent variable and each tube's inclination angle, alum dosage, and SLR as independent variables. Another model was found for turbidity removal percentage at optimum alum dosage as the dependent variable versus tube inclination angle and SLR as independent variables using multiple linear regression. The models were evaluated using the Coefficient of determination ($R^2$). In addition, correlate predicted versus observed values and compare slope and intercept against a 1:1 line (Pineiro et al. 2008). The significance of the model was found according to F-test. In addition, a t-test was used for the significance of the independent variable. The weight of each variable in the model was found according to standardized coefficients or β-weight.

## RESULTS AND DISCUSSION

The effect of tube inclination on the efficiency of the tube settler is explained in Fig. 2. As the tube inclination angle increased, the turbidity removal percentage also increased to 60 degrees, and the trend reversed. As tube inclination grew, the self-cleaning efficiency of settled solids became more efficient. In addition, increasing the inclination angle gives the sliding settled flocs a chance to collide with the rising particles in the tube to form larger settleable ones

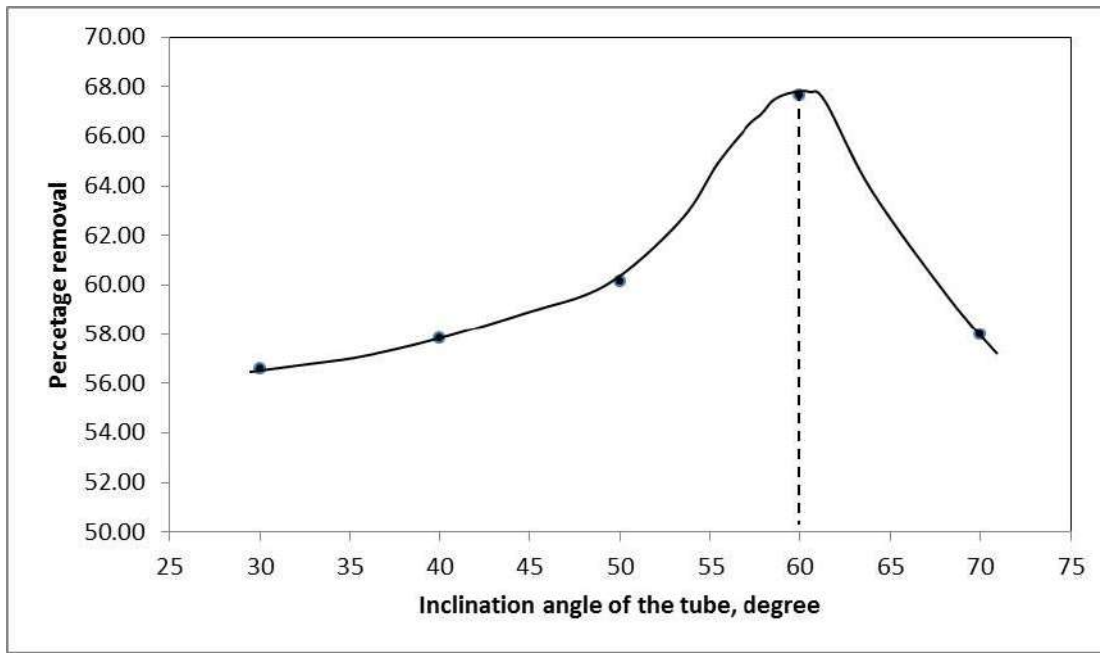


Fig. 2: Effect of the inclination angle of the tube settler on effluent turbidity.

(Al-Dulaimi & Racoviteanu 2019). Furthermore, increasing the inclination angle will decrease SLR, which in turn will improve the efficiency of the clarifier, as stated by Faraji et al. (2013). More increase in inclination angle over 60 degrees leads the tube settler to lose its characteristics as a shallow depth settler.

An inverse relationship was observed for the surface loading rate (SLR) relationship with turbidity removal percentage (Fig. 3). As SLR increases, the velocity of flow increases, which decreases the chance of particles settling and lowering turbidity removal percentage. These results coincided with the results of Al-Dulaimi & Racoviteanu

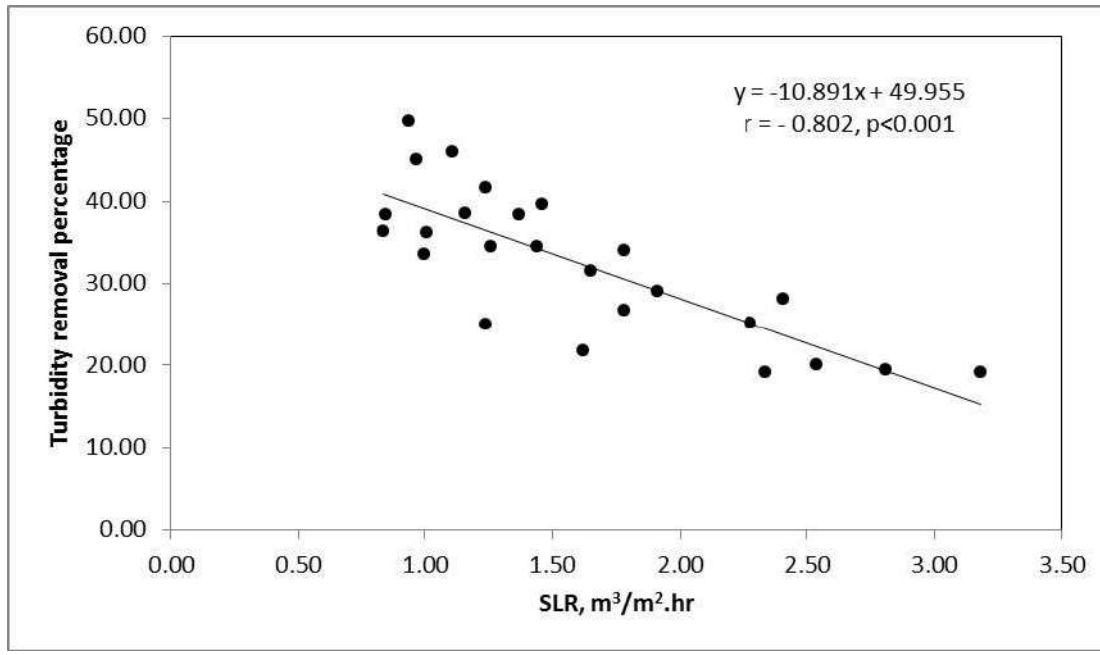


Fig. 3: Relationship between surface loading rate and turbidity removal percentage in tube settler.

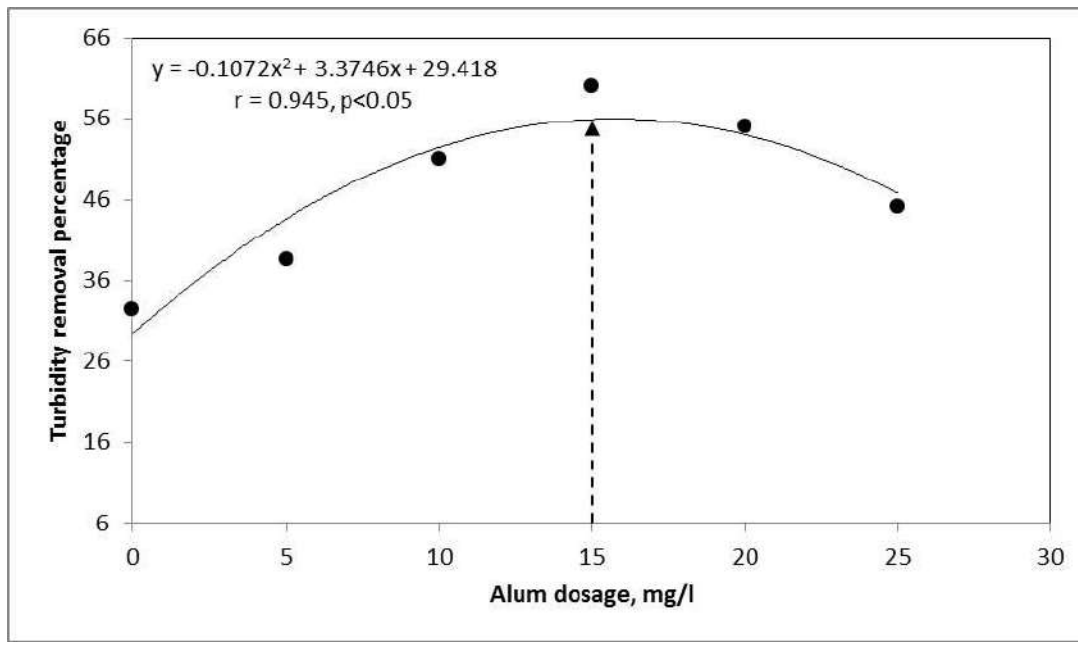


Fig. 4: Relationship between alum dosage and turbidity removal percentage in the tube settler.

Table 1: Regression analysis results for turbidity removal percentage in tube settler versus independent variables.

| Variable | Coefficient | SE | β-weight | t-value | p-value |
|---|---|---|---|---|---|
| Constant | 53.69 | 2.395 | | | |
| Inclination angle (degree) | 0.142 | 0.039 | 0.142 | 3.64 | <0.001 |
| Alum dosage [mg.L$^{-1}$] | 0.695 | 0.064 | 0.419 | 10.91 | <0.001 |
| SLR [m$^3$.m$^{-2}$.hr$^{-1}$] | -13.96 | 0.861 | -0.631 | 16.21 | <0.001 |

$R^2$ = 0.564, p < 0.001, dependent variable = turbidity removal percent, SE = Standard error, $R^2$ = Coefficient of determination.

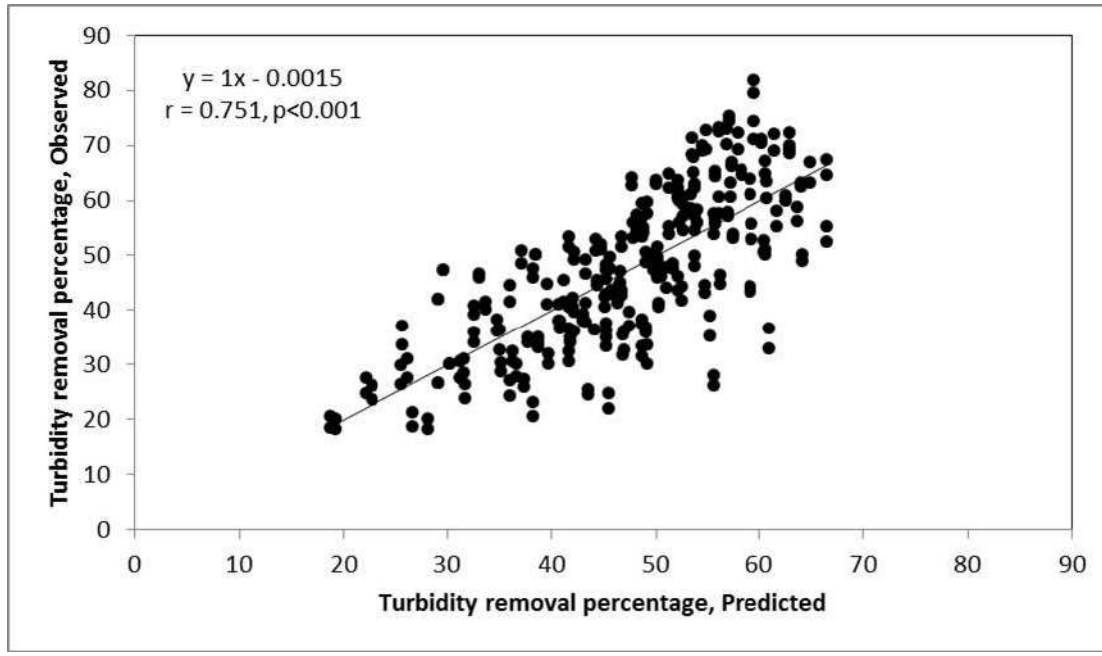


Fig. 5: Observed versus predicted turbidity removal percentage for the statistical mode.

(2018), Lekhak & Amatya (2021), and Oli et al. (2021). Additionally, this relationship was statistically significant (p < 0.001) with a correlation coefficient of 0.802. The increase in SLR by one unit exhibits a 10.89% decrease in turbidity removal (Fig. 3).

Alum dosage was correlated significantly with turbidity removal percentage in the tube settler (p < 0.05). The quadratic relationship between them was more suitable with a correlation coefficient of 0.945 (Fig. 4). The optimum alum dosage was recorded with 15 mg.L$^{-1}$ for a maximum turbidity removal percentage of 56% as a mean for 20-29 NTU influent. On the other hand, alum over-dozing leads to charge reversal and destabilizing of particles, which will decrease turbidity removal percentage (Saritha et al. 2017).

The linear model results show a significant effect of the studied parameters on turbidity removal percentage at p < 0.001 (Table 1). Independent variables were responsible for 56.4% of the variation in turbidity removal percentage. Inclination angle and alum dosage directly correlate with turbidity removal percentage versus inverse relationship for SLR. According to standardized coefficients (β-weight), SLR has the highest effect on turbidity removal percentage variation among the other independent parameters. It has 4.44 (0.631/0.142) times the impact of tube inclination angle, which agrees with the results of Al-Dulaimi and Racoviteanu (2018), while it has only 1.51 times the effect of alum dosage (Table 1). On the other hand, alum dosage has a 2.95-time tube inclination angle effect on turbidity removal percentage variation.

The relationship between observed and predicted turbidity removal percentage values of tube settlers was evaluated as good as it has a slope of 1 (Fig. 5) and a constant near zero (0.0015) (Pineiro et al. 2008).

The statistical model for turbidity removal percentage in the tube settler for optimum alum dosage shows that the inclination angle of the tube settler and SLR were responsible for 81.9% ($R^2$) of the variation in the dependent variable with significance (p < 0.001). The effect of SLR was more

Table 2: Regression analysis results for turbidity removal percentage at optimum alum dosage in tube settler versus independent variables.

| Variable | Coefficient | SE | β-weight | t-value | p-value |
|---|---|---|---|---|---|
| Constant | 71.416 | 2.648 | | | |
| Inclination angle | 0.238 | 0.046 | 0.327 | 5.20 | <0.001 |
| SLR | -14.47 | 1.010 | -0.902 | 14.33 | <0.001 |

$R^2 = 0.819$, $p < 0.001$, dependent variable = percent removal, for optimum alum dose 15 $mg.L^{-1}$. $R^2$ = Coefficient of determination.

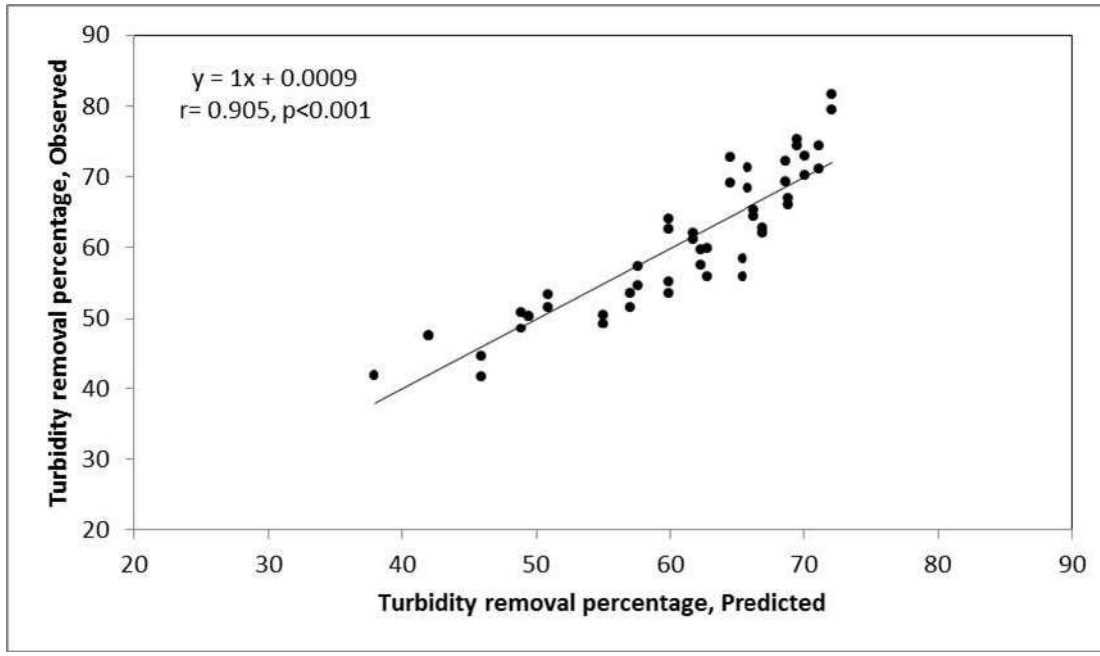


Fig. 6: Observed versus predicted turbidity removal percentage for optimum alum dosage 15 $mg.L^{-1}$.

than 2.5 (0.902/0.327) times that of the inclination angle of the tube (Table 2). This means that the weight of SLR relative to tube inclination angle decreased from 4.44 to 2.5 at optimum alum dosage.

The relationship between observed and predicted turbidity removal percentage at optimum alum dosage of tube settler was evaluated as good also as it has a slope of 1 (Fig. 6) and a constant near zero (0.0009) (Pineiro et al. 2008).

## CONCLUSIONS

1. Surface loading rate (SLR) has the highest effect on the efficiency of the tube settler, among other parameters.
2. The tube settler inclination angle of 60 degrees produced the best turbidity removal at optimum alum dosage.
3. The surface loading rate has more than 2.5 times the effect of inclination angle on the response turbidity removal percentage in tube settler.
4. The linear model is suitable to represent the performance of the tube settler at optimum alum dosage.
5. The increase in the length of the sedimentation tube in the tube settler improved the performance of the settler as SLR decreased.

## ACKNOWLEDGEMENT

The author is very grateful to Mosul University/ Environmental Research Center for funding this work and providing the facilities that helped improve the quality of this work.

## REFERENCES

Al-Dulaimi, S.M.S. and Racovitaenu, G. 2018. Performance of the tube settler clarification at different inclination angles and variable flow rate. Math. Modell. Civ. Eng., 14(2): 13-25.

Al-Dulaimi, S.M.S. and Racovitaenu, G. 2019. The efficiency of tube settler on removal of coagulated particles. E3S Web Conf., 85: 07012. https://doi.org/10.1051/e3sconf/20198507012

Ballcha, O.B. 2015. The Application of High Rate Tube Settler: The Case of Legadadi Water Supply Treatment Plant. M.Sc. Thesis, Addis Ababa

Institute of Technology School of Civil and Environmental Engineering, Addis Ababa University, pp 68. http://213.55.95.56

Balwan, K., Mujawar, A., Bhabuje, B. and Karake, M. 2016. Study of the effect of length and inclination of tube settler on the effluent quality. Int. J. Innov. Res. Adv. Eng., 3(1): 36-40.

Brandt, M.J., Johnson, K.M., Elphinston, A.J. and Ratnayaka, D.D. 2017. Twort's Water Supply. Seventh edition. Elsevier Ltd., Amsterdam, pp. 932.

Davis, M.L. 2010. Water and Wastewater Engineering: Design Principles and Practice. Second edition. McGraw-Hill Education, New York, pp.1344.

Faraji, A., Asadollafardi, G. and Shevidi, A. 2013. A pilot study for the application of one- and two-stage tube settlers as a secondary clarifier for wastewater treatment. Int. J. Civ. Eng., 11(4): 272-280.

Fouad, H.A., Elhefny, R.M. and Marei, A.I. 2016. Evaluating the use of tube settlers and lamella plates in increasing the efficiency of sedimentation tanks. J. Appl. Life Sci. Int., 7(4): 1-8.

Gurjar, A., Bhorkar, M., Bhole, A.G. and Baitule, P. 2017. Performance study of tube settlers module. Int. J. Eng. Res. Appl., 7(3): 52-55.

Lekhak, B. and Amatya, I.M. 2021. Kinetics of suspended solids removal in tube settler. J. Innov. Eng. Educ., 4(2): 81-84.

Oli, H.R., Amatya, I.M. and Khatri, N.R. 2021. Use of tube settler for the removal of inorganic suspended particles present in water. Glob. Sci. J., 9(3): 1240-1243.

Pineiro, G., Perelmanb, S., Guerschmanb, J.P. and Parueloa, J.M. 2008. How to evaluate models: Observed vs. predicted or predicted vs. observed? Ecol. Modell., 216: 316-322.

Qasim, S.R. 2017. Wastewater Treatment Plants: Planning, Design, and Operation. Second edition. CRC Press, Boca Raton, Florida, pp.1128.

Randtke, S.J. and Horsley M.B. (eds.). 2012. Water Treatment Plant Design. Fifth edition. McGraw-Hill Co., New York, pp.1376.

Saritha, V., Srinivas, N. and Srikanth Vuppala N.V. 2017. Analysis and optimization of coagulation and flocculation process. App. Water Sci., 7: 451-460.

Shammas, N.K. and Wang, L.K. 2015. Water Engineering: Hydraulics, Distribution, and Treatment. Fifth edition. John Wiley and Sons, New Jersey, pp. 832.

Wang, K., Li, Y., Ren, S. and Yang, P. 2020. A case study on settling process in inclined-tube gravity sedimentation tank for drip irrigation with the yellow river water. Water, 12(6): 1685.

Nature Environment and Pollution Technology
An International Quarterly Scientific Journal

p-ISSN: 0972-6268
(Print copies up to 2016)
e-ISSN: 2395-3454

Vol. 22 | No. 1 | pp. 511-516 | 2023

Original Research Paper

https://doi.org/10.46488/NEPT.2023.v22i01.050

Open Access Journal

# Evaluation of Biomass Solid Waste as Raw Material for Preparation of Asphalt Mixture

**He Tao*†, Hongming Liu*, Jie Yang** and Tao Sun***

*The Zhengzhou University of Aeronautics, School of Civil Engineering and Architecture, Zhengzhou, 450000, China

**Department of Ecology and Environment of Henan Province, Zhengzhou, 450000, China

†Corresponding author: He Tao; 54757050@qq.com

**Nat. Env. & Poll. Tech.**
**Website: www.neptjournal.com**

*Received:* 11-05-2022
*Revised:* 15-07-2022
*Accepted:* 18-07-2022

**Key Words:**
Bio-asphalt
Straw fiber
Asphalt mixture
Road performance

## ABSTRACT

At present, the resource utilization of solid waste in China is facing prominent problems such as high production intensity, insufficient utilization, and low added value of products. The preparation of biomass composites from biomass solid waste and plastic solid waste reduces not only environmental pollution and energy consumption but also promotes the high-value utilization of solid waste. So, the characterization and preparation experiments of samples with two different biomass are carried out. The wheat straw fiber and corn straw fiber were added into the bio-asphalt mixture with the content of 0.1%, 0.2%, 0.3%, and 0.4%, respectively, with the content of 9% and 12% bio-heavy oil. The physical properties and rheological properties of asphalt were analyzed and evaluated by three indexes and a dynamic shear rheological test. Through the rutting test and immersion Marshall test, high-temperature performance and biological asphalt mixture's water stability were evaluated. The results show that straw fiber can improve bio-asphalt mixture's road performance, especially the performance of high-temperature rutting. When the fiber content of bio-asphalt with 9% bio-heavy oil content is 0.3%, the physical properties and rheological properties of bio-asphalt are the best. Corn straw fiber's influence on bio-asphalt mixture was better than that of wheat straw fiber.

## INTRODUCTION

The development of the circular economy is to reduce raw material consumption and carbon emissions from the source and the whole process. It is an important path and support to achieving carbon peak and carbon neutralization. To improve the processing and utilization level of renewable resources, there is an urgent need to break through several key common technologies of green recycling in the fields of comprehensive utilization of bulk solid wastes and high-quality recycling of renewable resources. At present, China's urban and rural areas produce 6.3 billion tons of organic waste such as agricultural waste and urban waste every year, which are largely treated by landfill and incineration, and the energy utilization rate is less than 5%. Therefore, improving the resource utilization level of waste has significant environmental, social, and economic benefits. Adopting innovative technology to improve the resource utilization level of waste, while controlling pollution, and transforming waste into high-value-added resources and products, in line with the concept of circular economy, is an important research direction to solve waste pollution. In this paper, typical biomass solid waste is used as raw material to prepare asphalt mixture to improve the resource utilization level of biomass solid waste. In recent years, scholars have done a lot of research on the application of waste biomass to road asphalt materials (Hill et al. 2013, Fini 2013, Yang et al. 2014, Zhang et al. 2014, Gai et al. 2015.

Yang et al. (2003) found that the porous structure of lignin fibers can improve its absorptivity to asphalt, showing high residual stability and improving water damage resistance. At the same time, fiber adsorption increases the bonding ability of asphalt and plays a role in reinforcement in asphalt concrete, and the lubricating ability is weakened. Therefore, the anti-rutting performance of the fiber-asphalt mixture is improved, and it is pointed out that the fiber-asphalt has a good application prospect. Peng (2005) also added lignin fibers into the asphalt mixture. It showed that when the optimum dosage is 0.25% to 0.4%, the adsorption capacity of the mixture to asphalt increased slightly due to the increase of the specific surface area of the fiber after pretreatment, and it also better mechanical properties and stronger water stability in the Marshall test and water stability test. The fiber skeleton network composed of complex interlaced wood fibers increases the

strength and stiffness, elasticity deformation restorability, and tensile strength of the mixture, and improves low-temperature crack resistance and the high-temperature anti-rutting resistance of the mixture greatly. Based on an understanding of the basic technical properties of cotton stalk fiber, Lei et al. (2016) studied the proportioning design of cotton stalk fiber AC-13 and SMA-13 asphalt mixture. Ma et al. (2020) evaluated the effects of modified KTLG2 and KTLF1 composite fibers on the road performance of asphalt mixtures. The test results showed that cotton straw fiber improved low-temperature crack resistance and the high-temperature performance of the asphalt mixture significantly, and the composite fiber's water stability greatly improved. Lv (2001) pointed out that the type of fiber will affect the properties of the asphalt concrete mixture, but wood fiber will only increase the amount of asphalt in the SMA-type mixture, and cannot play a role in internal reinforcement. Gao et al. (2008) incorporated basalt fiber and lignin fiber into SMA asphalt mixtures and measured the performance of the two fiber asphalt mixtures through the Cantabro abrasion test, leakage test, water stability, and rutting test. The results showed that basalt fiber can significantly improve asphalt concrete's water stability and was better than lignin fiber, but significantly worse than basalt fiber in terms of bonding and tackifying effect. Because lignin fiber has a large specific surface area, its adsorption capacity and strength to asphalt are better than those of basalt fiber. Fu and Chang (2020) used a composite reinforcing agent composed of high polymer and lignin fiber to improve the asphalt mixture's road performance and prepared three graded asphalt mixtures of AC-13, AC-16, and AC-20. The results showed that when the optimal dosage of the composite reinforcing agent is 1.0%, the improvement effect of the high and low-temperature performance is remarkable.

Above all, scholars have made some achievements in the study of bio-asphalt and fiber-asphalt mixtures respectively, but there are few studies on bio-asphalt fiber-asphalt mixtures. So, this paper adopts bio-asphalt with bio-heavy oil accounting for 9% and 12% of the matrix asphalt respectively. The mixing ratio is designed through the AC-13 type mineral grading, and the wheat straw and corn straw fibers with the mineral mass fraction of 0.2%, 0.3%, and 0.4% are added respectively. Bio-asphalt's physical and rheological properties are analyzed and evaluated through three major indexes and dynamic shear rheological tests. Through the rutting test and water immersion Marshall test, the high-temperature performance and biological asphalt's water stability as an asphalt mixture are evaluated. These provide the bio-asphalt straw fiber asphalt mixture's application as a reference.

## MATERIALS AND METHODS

### The Raw and Processed Materials

#### *The Matrix Asphalt*

The test selects 70# asphalt as the research object (after this referred to as matrix asphalt), and the technical index of asphalt is shown in Table 1.

#### *Biomass Heavy Oil*

In the experiment, waste biomass, including wheat and corn straw is used as raw material to undergo high-temperature cracking in a high-temperature cracking furnace. And then the waste is obtained by distillation, oxidation, and other treatment processes. It is solid, black, and brown and lighter than traditional petroleum asphalt at room temperature. The technical index of bio-heavy oil is shown in Table 2.

Table 1: Technical index of asphalt.

| Technical indicators | Technical requirements | Test results |
|---|---|---|
| Penetration [25°C, 5s, 100 g]/[0.1 mm] | 60~80 | 62 |
| penetration index PI | -1.5 ~ + 1.0 | -1.27 |
| Softening point [°C] | ≥ 46 | 47.1 |
| Ductility [10°C, 5 cm.min$^{-1}$] | ≥ 15 | 36 |
| Ductility [15°C, 5 cm.min$^{-1}$]] | ≥ 100 | > 100 |
| Residues after TFOT | | |
| Weight changing [%] | -0.8 ~ + 0.8 | -0.158 |
| Residual needle penetration ratio (25°C), [%] | ≥ 61 | 61.4 |
| Residual ductility [10°C] | ≥6 | 6.3 |

Table 2: The technical index of bio-heavy oil.

| Technical indicators | Density [g.cm$^{-3}$] | Lighting [$^{o}$C] | Viscosity [Pa.s$^{-1}$] |
|---|---|---|---|
| Test result | 0.899 | 240 | 121 |

Table 3: The oil absorption result of fiber.

| Fiber type | Fiber [mass.g$^{-1}$] | Mixture [mass.g$^{-1}$] | oil absorption rate [%] |
|---|---|---|---|
| Wheat straw | 10.0 | 14.87 | 48.7 |
| Corn stover | 10.0 | 14.21 | 42.1 |

Table 4: Mass heat loss percentage of fiber under constant temperature heating.

| Temperature [°C] Fiber type | 120 | 140 | 160 | 180 |
|---|---|---|---|---|
| Wheat straw | 6.2 | 7.4 | 8.1 | 8.3 |
| Corn stover | 5.4 | 6.3 | 7.5 | 7.6 |

### Basic Technical Properties of Straw Fiber

In the experiment, wheat and corn straws were selected, and fiber materials were obtained by mechanical crushing, and then dried and screened. According to the test standard, the average length of the fiber satisfies is <6mm, the oil absorption rate is >5%, and the pH is between 6.5 and 8.5. The oil absorption and heat resistance of the two fibers were evaluated by the dropping test and the constant temperature heating test, respectively.

### Oil Absorption

Using the dropping test, we weighed 10 g of the asphalt, put it on the mesh basket, and then, slowly poured the molten asphalt, and placed it at 160°C for 30 min. Then we weighed the fiber and asphalt mixture to determine the oil absorption rate. The oil absorption results of the two kinds of straw fibers are shown in Table 3.

### Heat Resistance

Using the constant temperature heating test, the two fibers were set in an oven for 2 h at 50°C, and 10 g of the two samples were weighed and set in an oven at 120°C, 140°C, 160C, and 180°C for 5 h. By measuring the absorption of two kinds of straw, the mass heat loss percentage of fiber under constant temperature heating is shown in Table 4.

The oil absorption and heat resistance of the fiber meets the requirements.

### Technology Properties of Aggregate

Thick and fine matrix materials are all from limestone, and the ore powder is finely ground limestone. After testing, all indicators meet the specification's requirements. Fig. 1 shows the AC-13 asphalt mixture gradation.

### Preparation of Bio-Asphalt

Heat the matrix asphalt to the molten state, and the biomass heavy oil was mixed into the matrix asphalt according to 9% and 12% proportion of the total matrix asphalt at 130°C and 2000 R/min, and prepare the biological asphalt after mixing for 20 min under the action of the high-speed shear instrument.

### Test Method

#### *Physical Property Test*

The basic physical characteristics of asphalt are represented by its three indexes, ductility, penetration, and softening point, which also indicate its flexibility, temperature sensitivity, heat resistance, and other characteristics. The test is conducted to determine the ductility, penetration degree, and the composite modified asphalt's softening point according to the Test Rules for Highway Engineering Asphalt and Asphalt Mixture (JTG E20-2011).

#### *Dynamic Shear Rheological Test*

To analyze asphalt's dynamic viscoelasticity, the instrument model MCR302&CR102 dynamic shear rheological instrument is selected for the test. The shear rheological test was carried out in the temperature control mode, where the loading frequency was 1.59 Hz, the temperature was controlled between 40 and 80°C, the type of the parallel plate is PP25, and the spindle is 1 mm.

#### *Pavement Performance Tests*

According to the asphalt mixture's design method, the Test Rules for Highway Engineering Asphalt and Asphalt Mixture (JTG E20-2011), Marshall test, rutting test, and immersion Marshall test are carried out to evaluate asphalt mixture's road performance.

## RESULTS AND DISCUSSION

### Physical Performance

The ductility and penetration of bio-asphalt are higher

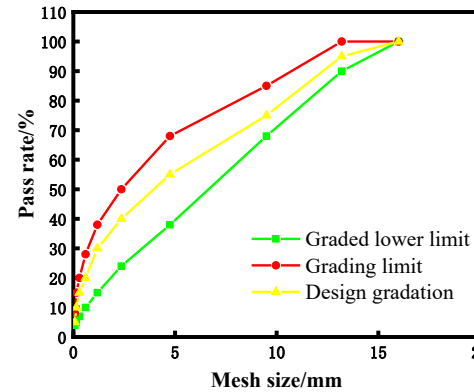


Fig. 1: Marshall grading.

Table 5: Physical performance test results.

| Technical indicators Heavy oil content [%] | Penetration [25°C, 5 s, 100 g]/[0.1 mm] | Softening point [°C] | Ductility [10°C, 5cm. $mm^{-1}$] |
|---|---|---|---|
| 9% | 11.78 | 49.3 | 121 |
| 12% | 12.05 | 45 | 133 |

compared to matrix asphalt, as shown in Table 5's three key indexes. It shows that bio-asphalt's low-temperature performance is significantly better than that of matrix asphalt. The main reason is that with the addition of the light components in heavy oil, the asphalt becomes softer gradually, but the high-temperature performance and shear failure resistance are weakened. Considering the utilization rate and performance of bio-heavy oil, two levels of bio-asphalt of 9% and 12% were finally selected to prepare the asphalt mixture.

## Rheology Performance

As shown in Fig. 2, with the temperature's increasing, the asphalt's fluidity rises, and the composite shear modulus of the three asphalts decreases. The variation trends of the three asphalt phase angles are the same, and the viscoelastic properties of the bio-asphalt with 9% heavy oil content are more similar. As shown in Fig. 3, the rutting resistance of 12% bio-asphalt is worse than that of matrix asphalt, and the rutting resistance of 9% bio-asphalt is a little stronger than that of matrix asphalt.

## Pavement Performance

Bio-asphalt with 9% and 12% bio-heavy oil content was comprehensively selected from the aspects of utilization and performance. The asphalt mixture's optimum oil-to-stone ratio is 5.2% to laboratory experiments' results. Under the above conditions, wheat and corn straw fiber were added at 0.2%, 0.3%, and 0.4% of the total mass of aggregate and mineral powder, respectively, and the road performance test was carried out.

## Marshall Test

Fig. 4 and Fig. 5 show Marshall stability and flow values results. When the level of bio-asphalt was the same, the stability of the mixture gradually improved with the increase of wheat and corn straw fiber content. If the fiber content is the same, the effect of the two types of fibers on the stability and flow value is close to the same, but the corn stover fiber is slightly stronger than the wheat stover fiber. The addition of straw fibers forms a stiffening structure inside, which enhances the bearing capacity of the bio-asphalt mixture. The flow value of 0.3% fiber content becomes

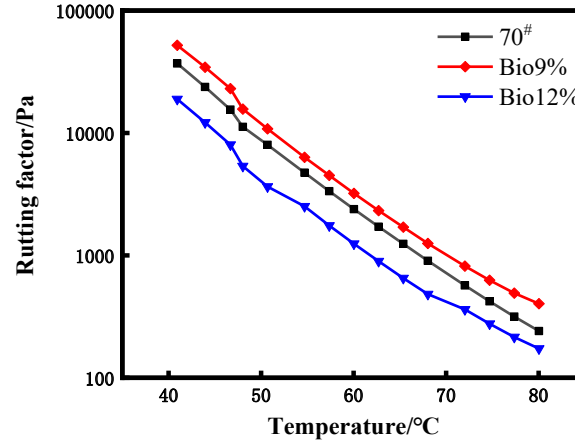


Fig. 3: Relationship between rutting factor and temperature.

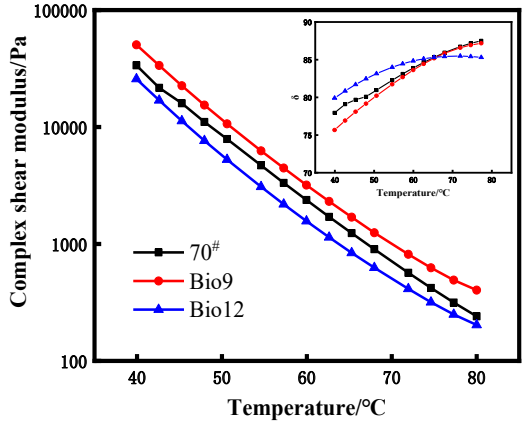


Fig. 2: Relationship between complex shear modulus, δ, and temperature.

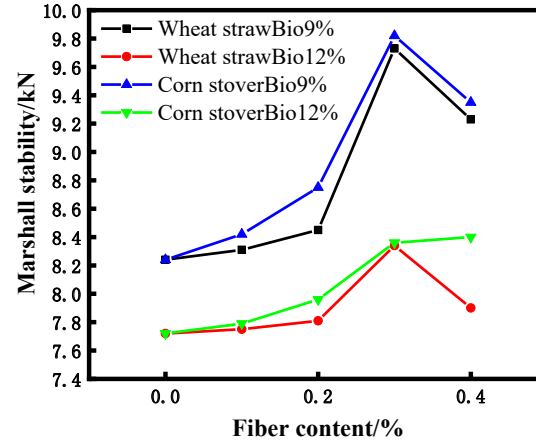


Fig. 4: Marshall stability test results (kN).

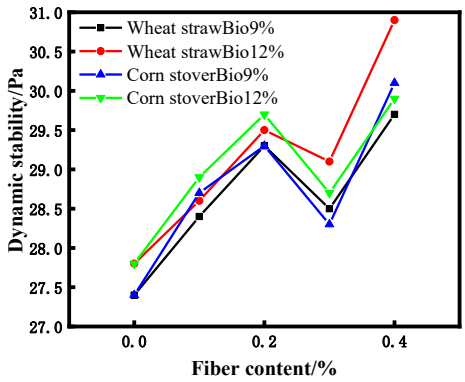


Fig. 5: Flow value test results (0.1mm).

smaller, which may be due to the strong adsorption of fiber to asphalt, which enhances the deformation resistance of the bio-asphalt mixture. While the fiber content is 0.4%, the Marshall stability decreases, and the flow value increases. It shows that the breaking strength of the asphalt mixture under high-temperature conditions decreases, and the deformation increases during failure. This conclusion is consistent with the article (Ma et al. 2019).

## Rutting Test

According to JTG E20-2011, the mixture's high-temperature performance was evaluated by the rutting test. As shown in Fig. 6 and Fig. 7, with the fiber content's rise, the bio-asphalt's dynamic stability at the same level is enhanced, the relative deformation is also gradually reduced, and the rutting resistance of the mixture is enhanced. Among them, under the condition of 9% heavy oil level bio-asphalt, 0.3% and 0.4% wheat straw fiber content can improve the dynamic stability of the mixture by 14.6%, 16.2%, 22.3%, and 20.3%. Under the condition of 12% heavy oil level bio-asphalt, 0.3%, 0.4% wheat straw fiber content can improve the mixture's dynamic stability by 24.3%, 26.2%, and 39.6%. Although the fiber improves the dynamic stability of the bio-asphalt mixture with 12% bio-heavy oil content significantly, its overall value is low. This indicates that the two kinds of straw fibers can enhance the asphalt mixture's high-temperature performance and make up for the poor high-temperature performance of bio-asphalt. This conclusion is consistent with the optimal result of 0.3% fiber content in Li et al. (2019). There are two main reasons why straw fiber can improve high-temperature stability. First, the presence of fibers will adsorb "free asphalt", which increases the "structural asphalt" in the mixture. Structural asphalt binds aggregates in the mixture to form skeleton support, which enhances the ability of asphalt pavement to resist deformation. Second, the corn stalk fibers obtained by crushing and extraction are of different lengths, dispersed in the mixture to build a network constitution, and overlapped with each other. When the pavement is under load, the fiber can play the role of transmitting the load and preventing the structural damage caused by the stress concentration (Li et al. 2019).

## Immersion Marshall test

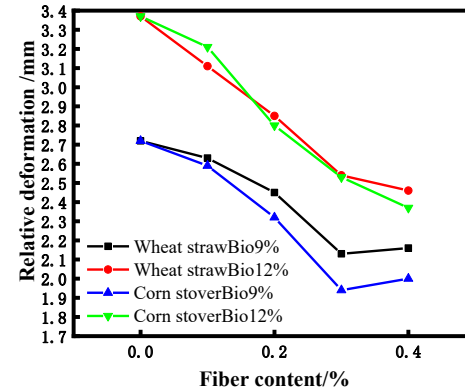


Fig. 7: Relationship between relative deformation and fiber content.

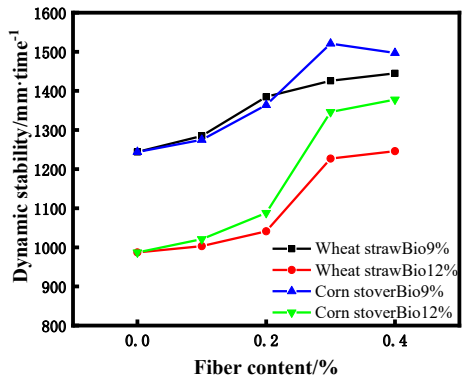


Fig. 6: Relationship between dynamic stability and fiber content.

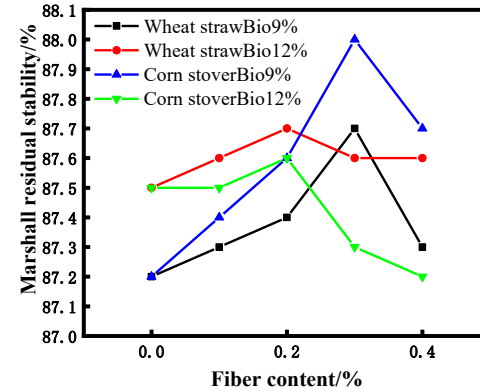


Fig. 8: Relationship between immersion Marshall test and fiber content.

The water immersion residual stability of the Marshall specimen is calculated by the the following formula and the results are shown in Fig. 8.

$$MS_0 = MS_1/MS$$

In the formula:

$MS_0$ - Specimen immersion residual stability (%)

$MS_1$ - Immersion residual stability in 48h (kN)

$MS$ - Immersion residual stability in 30 min

Bio-heavy oil significantly improves the asphalt mixture's water stability, and the straw fibers' addition can also improve asphalt mixtures' water stability. However, fiber content above 0.3% will make the bio-asphalt mixture's water stability worse. The conclusion that the bio-asphalt mixture's water stability is enhanced is consistent with Zhu et al. (2020). The bio-asphalt mixture with 9% bio-heavy oil content has the largest residual stability value when the corn stover fiber content is 0.3%. This indicates that corn stalk fiber's water stability enhancement effect on bio-asphalt mixture is better than that of wheat stalk fiber.

## CONCLUSION

Taking biomass solid waste as the main raw material, this paper develops high value-added green biomass asphalt mixture, realizes the high-value utilization of solid waste, reduces solid waste environmental pollution and energy consumption, and gives full play to the negative carbon effect of biomass, which is conducive to the national goal of carbon peak and carbon neutralization. The conclusions of this paper are as follows:

(1) Considering the physical properties and rheological properties of bio-asphalt, the bio-asphalt's high-temperature performance is poor, and its mixture cannot meet the requirements of road use. However, the addition of straw fibers can improve the bio-asphalt mixture's road performance, especially the high-temperature rutting resistance. Combining the effects of two kinds of straw fibers on the high-temperature performance and bio-asphalt mixture's water stability, the effect of corn straw fiber on the bio-asphalt mixture's road performance is greater than that of wheat straw fiber.

(2) Considering the performance of bio-asphalt and straw fiber mixture's road performance, it is suggested that the content of bio-heavy oil should be about 9% and the content of corn straw fiber between 0.3% and 0.4%.

## REFERENCES

Fini, E.H. 2013. Synthesis and characterization of bio-modified rubber (BMR) Asphalt: sustainable waste management solution for scrap tire and swine manure. J. Environ. Eng., 139(12): 1454-1461.

Fu, Z. and Chang, X.R. 2020. Effect of polymer-lignin fiber composite enhancer on the performance of asphalt mixture. J. Xi'an Technol. Univ., 40(3): 266-272.

Gai, C., Zhang, Y. and Chen, W.T. 2015. Characterization of aqueous phase from the hydrothermal liquefaction of Chlorella pyrenoidosa. Bioresour. Technol., 184: 328-335.

Gao, D.Y., Tang, Y.J. and Li, H.G. 2008. Influence of fiber on SMA Road performance J. Build. Mater., 11(6): 741-745.

Hill, B., Oldham, D. and Behnia, B. 2013. Low-temperature performance characterization of biomodified asphalt mixtures that contain reclaimed asphalt pavement. Transp. Res. Record, 2371(1): 49-57.

Lei, T., Li, Z. and Liu, K.P. 2016. Road performance of cotton straw fiber asphalt mixture. Highway, 7(7): 59-63.

Li, Z.X., Chen, Y.S. and Zhou, J.B. 2019. Analysis of road performance and fiber mechanism for corn stalk fiber asphalt mixture. China J. Highway Transp., 32(2): 47-58.

Lv, W. 2001. Design principle and method of asphalt mixture. Tongji University Press, Shanghai

Ma, F., Li, Y.B. and Fu, Z. 2020. Study on road performance of composite fiber asphalt mixture. J. Henan Polytech. Univ. Nat. Sci., 39(1): 157-163.

Ma, F., Pan, J. and Fu, Z. 2019. Determination of optimum fiber content in fiber asphalt mixture. J. Henan Polytech. Univ. Nat. Sci., 38(5): 138-145

Peng, B. 2005. Application of methyl cellulose in bituminous mixture. J. Xi'an Univ. Arch. Technol., Nat. Sci., 37(1): 104-107.

Yang, H., Yuan, H.W. and Hao, P.W. 2003. Study on pavement performance of asphalt mixture with fiber. J. Highway Transport. Res. Dev., 20(4): 10-11

Yang, X., You, Z. and Dai, Q. 2014. Mechanical performance of asphalt mixtures modified by bio-oils derived from waste wood resources. Constr. Build. Mater., 51: 424-431.

Zhang, Z.J., Li, H.Y. and Zhu, J. 2014. Review and perspective on waste biomass liquefaction for bio-fuel. Environ. Pollut. Contr., (3): 87.

Zhu, W.Q., Zeng, M.L., Wu, G.R. and Xia, Y.L. 2020. Performance of bio-asphalt and rock-asphalt co-modified asphalt mixture. J. Highway Transp Res. Dev., 37(9):1-7.

Nature Environment and Pollution Technology
An International Quarterly Scientific Journal

p-ISSN: 0972-6268
(Print copies up to 2016)
e-ISSN: 2395-3454

Vol. 22 | No. 1 | pp. 517-522 | 2023

Original Research Paper

https://doi.org/10.46488/NEPT.2023.v22i01.051

Open Access Journal

# Use of Ground Glass Waste as Aggregate Filler in Concrete

**A. S. Pasana*† , M. E. Loretero* and M. B. Giduquio***
*School of Engineering, University of San Carlos, Talamban Campus, Cebu City 6000, Philippines
†Corresponding author: A .S. Pasana; aspasana16@gmail.com

**Nat. Env. & Poll. Tech.**
**Website: www.neptjournal.com**

*Received:* 27-05-2022
*Revised:* 19-07-2022
*Accepted:* 21-07-2022

**Key Words:**
Waste glass
Concrete
Mechanical properties
Densified concrete mix

## ABSTRACT

The disposal of the huge volume of glass waste is one of the significant environmental issues that need to be addressed. One of the efficient ways to solve this problem is to incorporate ground glass waste in concrete mixtures. However, its inherent surface smoothness and microcracks within the glass particle harm the hardened properties of concrete. Minimizing the particle size and controlling the amount of cement in the mixture can reduce the adverse effect of using glass in concrete. This study utilized ground glass waste (850 μm) as aggregate filler in a concrete mix. More specifically, this study investigated the effect of paste volume (Vp) on the properties of fresh and hardened concrete with ground glass waste as aggregate filler. Based on the test results, ground glass waste as aggregate filler negatively affects the workability of fresh concrete, but increasing the amount of paste can mitigate it. Vp values in terms of void volume (Vv) in the aggregates of 1.6Vv and 1.8Vv achieved satisfactory consistency of fresh concrete. In addition, the concrete compressive strength increased when increasing Vp. The test results have shown that ground glass waste has the potential to be utilized as aggregate filler in concrete mixtures.

## INTRODUCTION

In the coming ten years, it is anticipated that glass manufacturing will increase steadily worldwide. Construction industries already accounted for $81.9 billion in 2015 and forecast a compound annual growth rate of 7.6% from 2016 to 2022 (Precient & Strategic Intelligence 2021). Consequently, this increasing demand for glass products also entails a growing volume of generated glass waste. Though used glass can be utilized in producing a new glass, the recycling process is limited by the production cost and impurities or mixed colors (Shi & Zheng 2007). For example, in the Philippines, only around 48.5% of post-consumer waste glass bottles were reutilized (National Solid Waste Commission 2018). Since glass cannot be decomposed or incinerated, a considerable volume of cullet occupies high-valued land space, which may potentially cause environmental issues.

The hardness and nonbiodegradability properties of glass make it a suitable aggregate substitute for concrete (Rashad 2014, Jamshidi et al. 2016, Gahoi & Kansal 2016, Afshinnia & Rangaraju 2015). In addition, recycling glass waste as an aggregate substitute in concrete may be one of the most practical options because it can be used in large quantities with low-quality requirements and has a potentially broader scope of application (Shi & Zheng 2007).

Despite the promising application of glass waste in concrete production, the proportion of glass waste incorporated in concrete should be appropriately considered. Based on Park et al. (2004), concrete compaction in concrete specimens was degraded as the glass waste amount was increased, resulting in a decreased slump, increased air content, and consequently reduced concrete density (Topcu & Canbaz 2004). This effect was mainly attributed to the shape irregularity of waste glass with particle size generally larger than 600 μm. In addition, concrete compressive strength reduces as the quantity of waste glass increases because adherence between waste glass and cement paste cannot be fully achieved (Topçu & Canbaz 2004) due to the inherent smooth surface of glass particles. Another concern about using glass waste as an aggregate substitute is the potential alkali-silica reaction (ASR), which may result in undesirable expansion and cracking in concrete (Khan & Sarker 2019). However, some studies (Zhu et al. 2009, Lee et al. 2011) have shown that ASR expansion decreased with decreasing glass particle size. Maraghechi et al. (2012) explained that ASR occurred within interior cracks of glass particles originating from glass crushing and not on the glass-paste interface. Based on the scanning electron microscope (SEM) images, ASR was only observed between cracks larger than 2 μm in ground glass waste with particle sizes larger than 1.18 mm. In addition, controlling cement type and content and aggregates' size can mitigate ASR-related issues (Penacho et al. 2014).

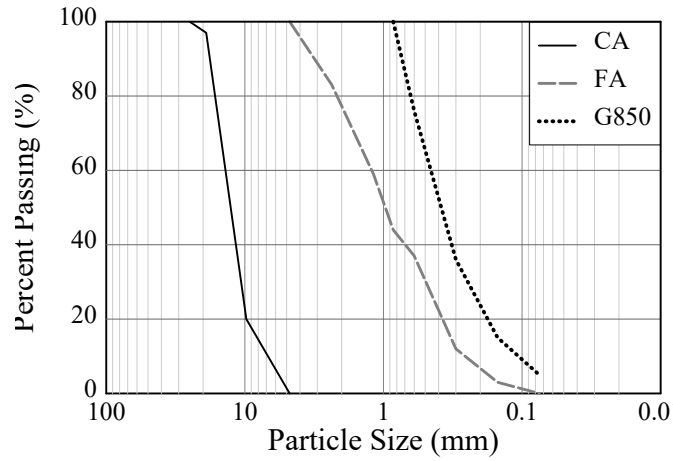


Fig. 1. Particle size distribution.

The particle packing method introduced by Tasi et al. (2006) essentially controls the amount of cement needed in a concrete mix. Successively filling voids within aggregates of coarser particle size with relatively smaller ones effectively reduces the void to be filled by the cement paste, leading to an increase in mixture density. Workability is controlled by adjusting paste volume or applying a superplasticizer.

Most studies related to particle packing utilize fly ash as a micro filler. This study evaluates the applicability of glass waste as aggregate micro filler in normal-strength concrete. It mainly focuses on the effect of paste volume on the workability and compressive strength of concrete with ground glass waste.

## MATERIALS AND METHODS

### Materials and Characterization

The glass waste used in this study was sourced from a local jalousie window fabricator. The glass waste was washed, air-dried, and ground using a hammer mill. The ground glass waste was then sieved using an 850-μm sieve. Glass particles passing an 850-μm sieve, referred to as G850, were used. The particle size was smaller than 1.18 mm to avoid ASR-related issues (Maraghechi et al. 2012). G850 had a specific gravity of 2.50 and a fineness modulus of 1.73. The particle size distribution of G850 is presented in Fig. 1.

The coarse aggregates (CA) used in this study were crushed river gravel with a specific gravity of 2.40, water absorption of 2.31%, and a fineness modulus of 6.80. Fine aggregates (FA) were river sand with a specific gravity of 2.46, water absorption of 2.31%, and a fineness modulus of 3.00. Particle size distributions of CA and FA are also presented in Fig. 1. The cement used was a Type-1 Portland with a specific gravity of 3.11.

### Aggregate Proportioning

The proportion of aggregates was obtained based on the maximum particle packing density per Tasi et al. (2006). Coarse aggregates were increasingly blended with fine aggregates, and corresponding dry-rodded densities of the blends with different fine-to-coarse aggregate ratios were determined per ASTM International C29/C29M-17 (2017). This process was continued until an apparent drop in density was obtained. The fine-to-coarse aggregate ratio corresponding to the maximum dry-rodded density was then obtained using quadratic regression and was used as a constant fine-to-coarse aggregate ratio. Then, the fine and coarse aggregates were increasingly blended with G850. Finally, the glass-fine-coarse aggregate proportion corresponding to the maximum dry-rodded density of the blend was obtained using the same process mentioned above. The final aggregate proportion by mass was 45.5% coarse aggregate, 47.6% fine aggregate, and 6.9% G850, with a dry-rodded density of 1874.1 kg.m$^{-3}$ of the mixture.

### Concrete Mix Design

Ideally, the paste volume ($V_p$) - or the amount of cement paste - needed is equivalent to the volume of void ($V_v$) in the aggregates. However, in the actual case, $V_p$ is always higher than $V_v$ to account for the additional paste necessary for lubrication to facilitate better consistency of the concrete mix.

In this study, the proportion of aggregates was based on the maximum dry-rodded density obtained in the particle packing procedure described above and common to all specimens. A constant water-to-cement ratio (w/c) of 0.54 by mass was used to proportion the cement paste. This w/c ratio was based on the recommended value per ACI Committee 211 (1991) for non-air-entrained concrete with specified concrete strength of 30 MPa. The main parameter

Table 1: Mix proportions per cubic meter of concrete.

| Specimen | CA [kg] | FA [kg] | G850 [kg] | Cement [kg] | Water [kg] |
|---|---|---|---|---|---|
| G-1.2Vv | 815 | 853 | 124 | 307 | 166 |
| G-1.4Vv | 780 | 817 | 119 | 343 | 185 |
| G-1.6Vv | 749 | 784 | 114 | 376 | 203 |
| G-1.8Vv | 720 | 753 | 110 | 406 | 219 |
| G-2.0Vv | 693 | 725 | 106 | 435 | 235 |
| C-1.6Vv | 803 | 840 | 0 | 376 | 203 |

of this study was the $V_p$ in terms of the $V_v$ of the aggregates. Initially, the study considered five $V_p$ values ranging from 1.2Vv to 2.0Vv. However, the concrete mix with $1.2V_v$ was relatively drier and not workable, and concrete with $2.0V_v$ was observed to have severe segregation during the trial mix. Hence, only three $V_p$ values ($1.4V_v$, $1.6V_v$, and $1.8V_v$) were used in this study. The mix proportions of the specimens are summarized in Table 1 based on a cubic meter of concrete mix. In Table 1, the samples are labeled as follows: the first alphabetic character refers to the presence of G850 in the mixture (G for with G850 and C for conventional mix without G850); the following symbols after the hyphen correspond to the paste volume. Another concrete mix, C-1.6Vv, without G850, was added as a conventional mix, and its amount of cement paste was similar to G-1.6Vv. The FA-CA ratio was constant in all concrete mixtures, but the total mass of aggregates (CA+FA) in C-1.6Vv was similar to that in G-1.6Vv (CA+FA+G850). It should be noted that the paste volume in C-1.6Vv did not necessarily correspond to the 1.6Vv, but rather, it was the intention of this study to maintain the amount of paste in the concrete mix in both specimens for direct comparison. The paste volume of C-1.6Vv was around 1.42Vv, lower than that of G-1.6Vv because of the larger Vv compared to concrete mixtures with G850.

### Preparation and Testing of Samples

One batch of the concrete mix was used for each mix proportion. Test specimens were prepared following ASTM International C192/C192M-19 (2019). The concrete constituent materials were blended using a conventional 1-bagger mixer. The slump of the fresh concrete was obtained as per ASTM International C143/C143M-15 (2015). For each concrete mix, nine 100 mm x 200 mm concrete cylinder samples were cast per ASTM International C192/192M-19 (2019). These nine concrete cylinder samples included three sets of 3 specimens for 7-, 28- and 56-day strengths. The mold's opening was covered with plastic wrap to minimize evaporation loss. After 24 h, the concrete specimens were demolded and cured in potable water at room temperature. The samples were tested for compressive strength at 7, 28, and 56 days.

## RESULTS AND DISCUSSION

### Workability

Specimen G-1.2Vv was observed to be relatively drier and unworkable. A closer look at the aggregate particles revealed that a significant portion remained uncoated with paste. The amount of paste in specimen G-1.2Vv was essentially not sufficient. The slump was not determined for this concrete mix and was not cast for the compression test. At a paste volume of 1.4Vv, the paste amount seemed sufficient to coat the aggregates but not enough to provide lubrication between particles in specimen G-1.4Vv. The concrete was essentially very stiff and had a slump of zero. Aggregates in specimen G-1.6Vv were essentially coated with cement, and the amount of cement paste seemed sufficient to provide better consistency in the concrete mix. It had a slump of 30 mm, which was well within the desired value for structural application. When increasing the paste volume of 1.8Vv, the slump value of specimen G-1.8Vv increased to 70 mm without visible segregation of aggregates. However, the concrete mix showed significant segregation and bleeding in specimen G-2.0Vv (with a paste volume of 2.0Vv). During the slump test, the fresh concrete collapsed. Apparent segregation of aggregate particles was observed, and the cement paste flowed outward freely. No concrete cylinder samples were prepared for this concrete mix. Based on the test results, the slump of fresh concrete with G850 increased as the paste volume increased. However, the amount of paste volume should be limited to avoid bleeding and segregation. These observations were similar to the findings of Ling and Kwan (2015) that, beyond a certain point, increasing paste volume in concrete decreased the dimensional stability of concrete.

Specimen C-1.6Vv was relatively easier to mix compared to specimen G-1.6Vv. Qualitatively, with a slump of 40 mm, the consistency of the fresh concrete of specimen C-1.6Vv was relatively better than that of specimen G-1.6Vv. It should be noted that in terms of Vv, the paste volume in specimen C-1.6Vv was only around 1.42Vv. With similar Vp in terms of Vv, C-1.6Vv was essentially more workable at a fresh concrete state, which indicated that the addition of glass negatively affected the consistency of concrete. This adverse impact

might be attributed to the irregularity of glass particles which could increase frictional resistance between particles due to the interlocking of particles (Jamshidi et al. 2016). In addition, the increased surface area of aggregates due to other smaller particles in G850 had also increased the demand for the paste to bind the particles together and for lubrication.

The amount of paste in the concrete mix directly influenced the workability of the fresh concrete. It should be noted that the idea of maximizing the packing density of aggregates will result in the reduction of the void and, consequently, the paste required to coat the aggregates. However, fresh concrete should be workable enough to facilitate better compaction, which can directly affect hardened concrete properties. Based on the concrete mixtures with G850 in this study, paste volume should be within 1.6Vv and 1.8Vv to ensure satisfactory fresh concrete consistency and avoid segregation and bleeding.

## Compressive Strength

The compressive strengths of the specimens are summarized in Table 2 and presented in Fig. 2. The 7-day strengths of the specimens had at least 21 MPa, roughly 70% of their respective 28-day strengths, and increased gradually in the later age. Among the specimens with G850, G-1.4Vv had the lowest strength. This result might be attributed to the stiff fresh concrete characteristics, which led to poor compaction in preparing concrete cylinder specimens. Concrete compressive strength increased as the paste volume increased. This strength increase could be associated with the better compaction of fresh concrete mixtures with higher paste volume.

Compared to specimen C-1.6Vv with conventional concrete mix, specimen G-1.4Vv with similar Vp in Vv had slightly lower strength. However, similar strengths were observed in both specimens, C-1.6Vv and G-1.6Vv, which have similar paste amounts by mass. Though not significant, G-1.8Vv had the highest compressive strength among the specimens considered in this study. This result implies that concrete specimens would have comparable strength provided the amount of cement paste is sufficient to be workable and the water-to-cement ratio is similar.

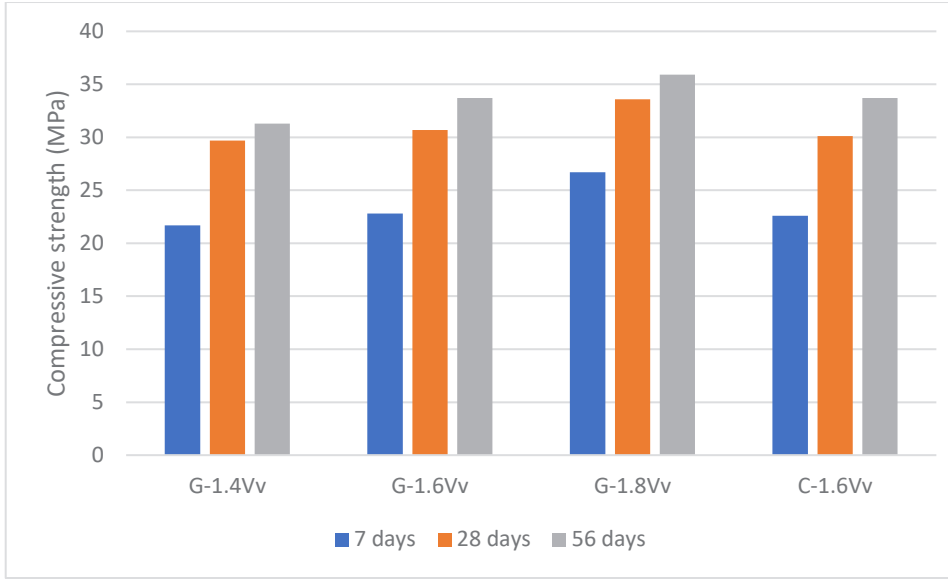


Fig. 2. The compressive strength of the glass-filled concretes at various paste volumes.

Table 2: Concrete compressive strength and cement efficiency index.

| Specimen | Compressive Strength [MPa] | | | Cement Strength Efficiency [kPa.kg$^{-1}$] | | |
|---|---|---|---|---|---|---|
| | 7-day | 28-day | 56-day | 7-day | 28-day | 56-day |
| G-1.4Vv | 21.7 | 29.7 | 31.3 | 63.3 | 86.9 | 91.5 |
| G-1.6Vv | 22.8 | 30.7 | 33.7 | 60.9 | 81.7 | 89.8 |
| G-1.8Vv | 26.7 | 33.6 | 35.9 | 65.8 | 82.7 | 88.4 |
| C-1.6Vv | 22.6 | 30.1 | 33.7 | 60.3 | 80.1 | 89.9 |

The incorporation of G850 in the concrete mixture provides economic and environmental incentives. Furthermore, considering that all specimens had comparable strengths compared to C-1.6Vv, G850 could be used as aggregate filler in the formulation of structural concrete. Based on the concrete mix proportions considered in this study, G850 can potentially replace about 7 percent of the aggregates by mass.

### Cement Strength Efficiency

The strength efficiency of cement on all the concretes is summarized in Table 2 and presented in Fig. 3. The values denote the yielded compressive strength per one-kilogram cement. Since this adhesive powder is the most expensive concrete-making-materials, these data would serve as a cost-benefit analysis. Likewise, the data assess the carbon footprint, wherein the more efficient the powder, the lesser carbon dioxide generated. As observed, a clear relationship between the values and PV prevails at a later period. Specifically, at 56 days, G-1.4Vp (with the least PV) achieved a higher value by 1.9% than G-1.6Vp and 3.6% than G-1.8Vp. Hence, the less paste, the more efficient. Also, G-1.6Vp (with filler) had higher efficiency than its control (C-1.6Vp) by 1.0% at seven days and 1.9% at 28 days, but both were equivalent at 56 days. This finding demonstrates that G850 did not reduce the strength efficiency of cement and, therefore, can lessen the required dosage of sand, gravel, and cement.

## CONCLUSION

This paper explored the possible use of 850-μm glass as an aggregate supplement. The investigation centered on the optimum packing density of the glass-sand-gravel mixture and the concrete's workability and compressive strength at various water-cement paste volumes. Based on the findings, the following conclusions were drawn:

- In packing density, the optimum ratios by weight were 51.1:48.9 for sand-gravel and 6.9:47.6:45.5 for glass-sand-gravel, indicating that an optimum mixture contains more fine particles. The glass lowered the voids volume by around 6.9% and increased the density by about 1.77%. The voids reduction corresponds to a saving of water-cement paste.
- In concrete mix design, the volumetric paste increment by 0.2Vp relatively reduced the aggregates content by about 3.95% or 62 kg per one-cubic-meter concrete. The incorporation of glass saves around 6.7% of sand and gravel at a fixed amount of paste.
- The workability improved by increasing paste volume to 1.8Vp: zero-slump for 1.4Vp, 30 mm for 1.6Vp, and 70 mm for 1.8Vp. The 1.2Vp was insufficient to coat the aggregates, while 2.0Vp resulted in slump failure. However, the workability was reduced with the incorporation of glass.
- In compression, all the glass concretes reached the required design strength (30 MPa), and the fortification improved as paste volume was increased up to 1.8Vp. This finding indicates the suitability of glass aggregate at various paste volumes.
- The compressive-strength efficiency of cement negatively correlates with paste volume: the lesser the

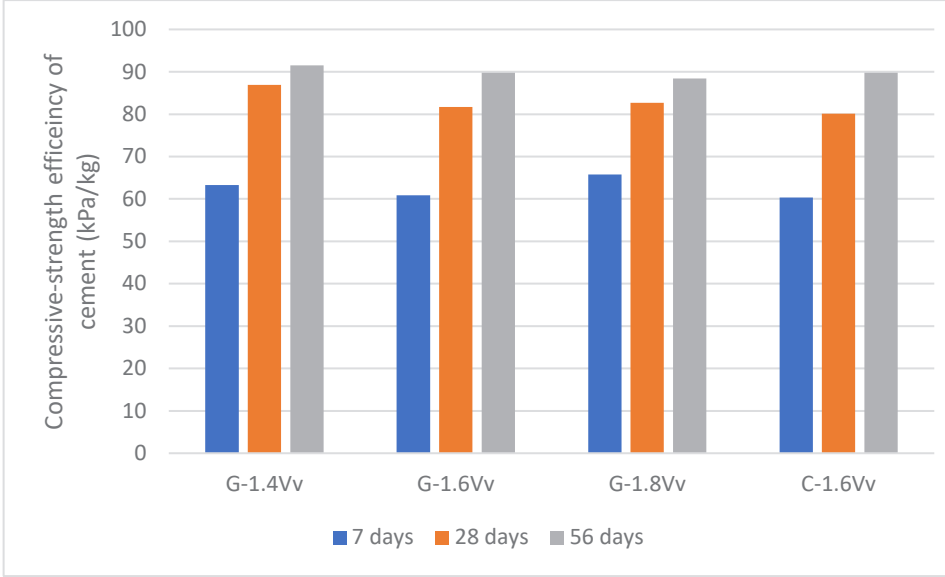


Fig. 3: The compressive-strength efficiency of cement at various paste volumes.

paste, the more efficient the cement. This efficiency is not negatively affected by G850, which supports the suitability of glass waste in concrete production.

Overall, recycling can reduce the amount of sand, gravel, and cement. This finding can promote glass utilization in concrete production, generating economic and environmental incentives in both glass and concrete contexts. In particular, it can solve the waste disposal crisis of the glass industry, particularly the jalousie window enterprises; likewise, it can free the existing dumpsite for other uses.

## ACKNOWLEDGEMENT

This research was supported by the Commission on Higher Education, the University of San Carlos, and the Visayas State University.

## REFERENCES:

ACI Committee 211. 1991. Standard Practice for Selecting Proportions for Normal, Heavyweight, and Mass Concrete. American Concrete Institute, Michigan, US.

ASTM International C29/C29M-17. 2017. Standard Test Method for Bulk Density ("Unit Weight") and Voids in Aggregate. ASTM, West Conshohocken.

ASTM International C143/C143M-15. 2015. Standard test method for the slump of hydraulic-cement concrete. Annual Book of ASTM Standards. ASTM, West Conshohocken

ASTM International C192/C192M-19 2019. Making and Curing Concrete Test Specimens in the Laboratory. ASTM, West Conshohocken.

Afshinnia, K. and Rangaraju, P.R. 2015. Influence of fineness of ground recycled glass on mitigation of alkali-silica reaction in mortars. Constr. Build, Mater., 81: 257-267.

Gahoi, K. and Kansal, R. 2016. Effect of waste glass powder on properties of concrete: A literature review. Int. J. Sci. Res., 11: 7064

Jamshidi, A., Kurumisawa, K., Nawa, T. and Igarashi, T. 2016. Performance of pavements incorporating waste glass: The current state of the art. Renew. Sustain. Energy Rev., 64: 211-236.

Khan, M.N.N. and Sarker, P.K. 2019. Alkali silica reaction of waste glass aggregate in alkali-activated fly ash and GGBFS mortars. Mater. Struct., 52(5): 93.

Lee, G., Ling, T.C., Wong, Y.L. and Poon, C.S. 2011. Effects of crushed glass cullet sizes, casting methods and pozzolanic materials on ASR of concrete blocks. Construction and Building Materials, 25(5): 2611-2618.

Ling, S.K. and Kwan, A.K.H. 2015. Adding ground sand to decrease paste volume, increase cohesiveness and improve passing ability of SCC. Constr. Build. Mater., 84: 46-53.

Maraghechi, H., Shafaatian, S.M.H., Fischer, G. and Rajabipour, F. 2012. The role of residual cracks on alkali-silica reactivity of recycled glass aggregates. Cem. Concr. Comp., 34(1): 41-47.

National Solid Waste Commission. 2018. Final Report, Volume 1. Retrieved from http://nswmc.emb.gov.ph/wp-content/uploads/2018/03/Final-Report-Volume-I.pdf

Park, S.B., Lee, B.C. and Kim, J.H. 2004. Studies on mechanical properties of concrete containing waste glass aggregate. Cem. Concr. Res., 34(12): 2181-2189.

Penacho, P., Brito, J. and Rosário Veiga, M. 2014. Physico-mechanical and performance characterization of mortars incorporating fine glass waste aggregate. Cem. Concr. Comp., 50: 47-59.

Precient & Strategic Intelligence. 2021. Global Construction Glass Market Size, Share, Development, Growth, and Demand Forecast to 2022 – Industry Insights by Type (Apparel Construction Glass and Non-Apparel Construction Glass) by Application (Industrial Protective Clothing, Defense and Firefighting Services, Transportation, Others). Retrieved from https://www.psmarketresearch.com/market-analysis/construction-glass-market

Rashad, A.M. 2014. Recycled waste glass as fine aggregate replacement in cementitious materials based on Portland cement. Constr. Build. Mater., 72: 340-357.

Shi, C. and Zheng, K. 2007. A review on the use of waste glasses in the production of cement and concrete. Resour. Conserv. Recycl., 52(2): 234-247.

Tasi, C.T., Li, L.S. and Hwang, C.L. 2006. The effect of aggregate gradation on engineering properties of high performance concrete. J. ASTM Int., 3(3): 13410.

Topçu, İ.B. and Canbaz, M. 2004. Properties of concrete containing waste glass. Cem. Concr. Research, 34(2): 267-274.

Zhu, H., Chen, W., Zhou, W. and Byars, E.A. 2009. Expansion behaviour of glass aggregates in different testing for alkali-silica reactivity. Mater. Struct., 42(4): 485-494.

Nature Environment and Pollution Technology
An International Quarterly Scientific Journal

p-ISSN: 0972-6268
(Print copies up to 2016)
e-ISSN: 2395-3454

Vol. 22 | No. 1 | pp. 523-526 | 2023

Original Research Paper

https://doi.org/10.46488/NEPT.2023.v22i01.052

Open Access Journal

# Design and Development of Smart Irrigation System Using Internet of Things (IoT) - A Case Study

**G. Sasi Kumar*†, G. Nagaraju*, D. Rohith* and A. Vasudevarao***

*Department of Mechanical Engineering, GMR Institute of Technology, Rajam, Srikakulam-532127, Andhra Pradesh, India

†Corresponding author: G. Sasi Kumar; sasikumar.g@gmrit.edu.in

**Nat. Env. & Poll. Tech.**
**Website: www.neptjournal.com**

*Received:* 17-06-2022
*Revised:* 03-08-2022
*Accepted:* 10-08-2022

**Key Words:**
Smart irrigation
Node MCU
Soil moisture sensor
Internet of things

## ABSTRACT

With India's population growing at a rapid pace, traditional agriculture will have a tough time meeting future food demands. Water availability and conservation are major concerns for farmers. This paper aims to discuss the aspects related to designing and fabricating an automatic irrigation system using the Internet of Things (IoT) which will save the farmer's time and money significantly. Human intervention in fields will be reduced. Changes in soil moisture are detected by soil moisture sensors and irrigation is automated using IoT. The proposed system is most economical for underdeveloped places because it is very cost-effective. Based on the soil moisture content, the sensor detects and sends signals to the node MCU, which activates the motor. When the plants receive enough water, the motor automatically shuts off. The user will be alerted about the soil's moisture content through his mobile phone. The proposed smart irrigation system is implemented at our campus which conserves energy and water.

## INTRODUCTION

India is a village-based country, and agriculture is critical to the country's prosperity. Agriculture in our country is reliant on the monsoons, which are in short supply. As a result, irrigation is employed in agriculture. Water is delivered to plants based on the soil type nature of irrigation. In agriculture, two things are critical: first, obtaining information about soil fertility, and second, measuring soil moisture content. Different irrigation techniques are now available, which are utilized to lessen the reliance on rain. Electrical power and on/off scheduling are the primary drivers of this strategy.

Any device integrated with electronics, software, sensors, and network connectivity to allow the objects for collecting and sharing data is considered an Internet of Things (IOT) item. It refers to a world in which everything is intelligently connected and communicated. Time and water can be saved by enabling smart watering. It saves water by automatically watering plants according to water demand. The sensors are placed to check the moisture of the soil. Using a moisture sensor, a smart autonomous irrigation system focuses on irrigating plants regularly with no human supervision.

It is critical to develop food technology production quickly to fulfill the ever-increasing need for food and the shrinking availability of food essentials. Agriculture is the only way to get this. This is a critical aspect in human societies' rising and dynamic food production demand. Agriculture is critical to the economy and growth of countries like India. Farmers utilize irrigation because of a lack of water and scarcity of land water, which results in water shortage on the planet.

## PAST STUDIES

A project is designed to empower field owners to monitor and regulate the growth of their plants in their farms. This is accomplished by utilizing a smart IoT platform and solenoid valves to control water flow using soil moisture and provide real-time surveillance to owners who are unable to visit their farms. This initiative also enables the monitoring of employees and crops to prevent losses. Anyone with a Smartphone may use it, and once set up, it requires no upkeep (Guptha et al. 2019). A smart method was used professionally capable of employing ontology to decide on sensor data values. The ontology decision and sensor information together constitute the final decision using the outcome of a machine learning algorithm (KNN). An irrigation system is designed which activates the motor ON and OFF based on variations in moisture content. Soil moisture amount is studied in this article, however, the proposed project added to an existing project by connecting IOT (Arun & Sudha

2012). A watering system developed for tunnel farming is so intelligent that it develops and applies true machine learning decision-making capability, e-architecture, and hardware specifics in the preceding section (Archana & Priya 2016). To test the proposed system's reaction, all of the sensors (temperature and humidity, light sensor, and soil moisture sensors) were deployed (Chavan & Karnade 2014). The data is communicated to the edge server via a GSM module and an Android application, and the results may be viewed by the farmer. After that, the user can operate the valve with some actuation (Kim et al. 2019). The suggested system by Al-Ali et al. (2019) uses a chip controller with integral Wi-Fi connectivity to provide the needed energy to operate. He also suggested that if high crop production is sought, irrigation systems must be constantly monitored, particularly in distant places where water is scarce. Farming operations may also encounter issues linked to the amount of energy needed to provide a decent crop yield. Energy efficiency in agriculture is examined from a variety of perspectives. Furthermore, a renewable energy source, such as a solar cell, is given to enable stand-alone functioning in the event of a utility company power outage. A wireless monitoring system interface is also being developed, which will allow remote users to check the state of a farm from the comfort of their phone or computer. A remote irrigation method built for plantation using Arduino. Water is supplied based on the change in humidity of the soil without considering the amount of soil moisture (Shwetha 2019). Considering the points from the literature review, irrigation is the science of artificially applying water to land or soil, which means that plants must be given water based on the soil type. This paper is intended to achieve the following objectives:

1. To overcome the problem of soil moisture variation for proper irrigation
2. To develop a low-cost automatic watering system using the Internet of Things.
3. To keep track of moisture levels in various environments
4. To use a mobile phone app to improve the system

## THE EXISTING SYSTEM

The farms were irrigated manually in prior irrigation technologies. It is accomplished by turning on and off the motor and examining the water level in the fields. Farmers water their crops at regular intervals despite not knowing the soil moisture content. This results in either under or over-watering, which has an impact on plant development.

A worker had to be deployed in fields to monitor plants regularly, which meant an additional fee had to be paid for plant monitoring labor. The farmer has no idea when he needs to go to the field to turn the motor On/Off during scorching sunny days or even in the middle of the night.

Due to problems in traditional irrigation technologies, crop output is reduced. Water must be supplied in sufficient quantities to allow plants to grow properly. Otherwise, crop failure will occur. As a result, the farmer loses money due to traditional irrigation methods.

## THE PROPOSED SYSTEM

The crop is automatically irrigated in this suggested smart irrigation system employing IOT by sensing the moisture amount of soil. This system is led by the Node MCU, which serves as the system's brain. Using jumper wires, the Node MCU is connected to a soil moisture sensor (SMS) and relay module. The SMS is placed in the soil and detects moisture levels before sending the data to Node MCU. The Node MCU is programmed with code that turns on and off the relay switch based on a moisture content threshold.

The moisture content value is forwarded to the user's phone. Based on the content the user will turn on the motor On/Off in his phone. When the moisture content is lower than the threshold value, the motor is turned ON and it is turned off when the moisture content goes above the threshold value. The relay switch is used to turn the motor automatically dependent on soil moisture content.

The irrigation of fields is done automatically when this method is used. Human intervention is not required in fields. As a result, the farmer can save labor charges. By implementing this technology, the proper amount of water is delivered to the fields, reducing the difficulties caused by under and over-irrigation. As a result, there is no risk of crop failure. The components of the proposed smart irrigation system are depicted in Fig. 1.

## METHODOLOGY USED

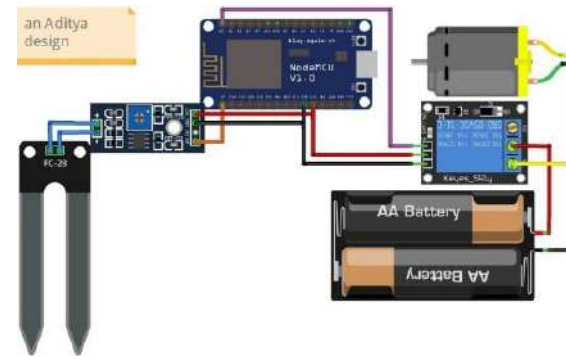


Fig. 1: Components of proposed smart irrigation system.

The design of the system produced during the project's design phase is revealed in Fig. 2, had to be properly implemented during the project's implementation. The widespread adoption of automated technology in agriculture has shown to be cost-effective. The proposed system is capable of transforming irrigation and has an impact on the commercial and industrial sectors. As a result, this project has been a system-based expert or non-expert approach to field monitoring for detecting dryness and treating the area. The food and beverage system is beneficial to the agriculture business, which is looking for smart methods to reduce costs.

## RESULTS AND DISCUSSION

The irrigation of fields is done automatically when this method is used. Human intervention is not required in fields. As a result, the farmer can save labor charges. By implementing this technology, the proper amount of water is delivered to the fields, reducing the difficulties caused by under and over-irrigation. As a result, there is no risk of crop failure. The moisture sensors detect the moisture level in the plants and delivers a signal to the operational amplifier if the moisture level is lower than desired level, causing the DC Motor pump to switch on and feed water to the appropriate field area. The system comes to a complete stop when the appropriate moisture level is reached, and the DC Motor pump is shut off. As a result, the entire system's operation has been thoroughly tested and is said to work well.

To check the effectiveness of the proposed smart irrigation the following tests are performed which are given in Table 1. It is clear from the table that the motor is turned ON when the moisture level is less and the motor is turned OFF when the required moisture level is reached.


Fig. 2: Circuit diagram of the proposed system.

Table 1: Performance test on different soils.

| S. No. | Type of soil | Moisture content (%) | Motor ON/OFF |
|---|---|---|---|
| 1 | Wet soil | 75 | OFF |
| 2 | Partially Wet soil | 55 | ON |
| 3 | Dry soil | 30 | ON |

## CONCLUSION AND FUTURE SCOPE

Agriculture networking technology is not only necessary for modern agricultural growth, but it plays a major role in future agricultural development; it will be the future path of agricultural development. After constructing the agricultural water irrigation system hardware and analyzing and researching the network hierarchy features, functionality, and corresponding software architecture of precision agriculture water irrigation systems, applying IoT to highly effective and safe agricultural production has a high influence on confirming the effective usage of water and efficiency of agricultural yield. Using the smart irrigation method, irrigation becomes simple, precise, and practical, and can be utilized in agricultural fields in the future to advance agriculture to the next level. The yield from the moisture sensor and level system has a significant impact on the output.

The proposed smart irrigation system is successfully implemented using IoT at our campus which conserves energy and water by the soil moisture content. Once the plants get sufficient water, the motor automatically stops. The user will be notified of the soil's moisture content through SMS. The effectiveness is checked and the total savings of Rs.1.5 Lakh per year are achieved by the proposed system by way of energy and water conservation. Performance test on soil moisture content using different soils (wet soil, partially wet soil and dry soil) is carried out to validate the results. The proposed system functions well and controls the water flow by turning the motor On/Off according to the moisture level.

As there is a rapid growth potential for IoT in the future, the proposed system could become more effective, faster, and cheaper. As an extension of the project, this system can be converted into a smart system that forecasts worker activities, rainfall patterns, harvest times, and animal intruders in the field, and then communicates the information using advanced technology such as IoMT, allowing agricultural systems to become self-contained and better yield.

## REFERENCES

Al-Ali, A.R., Al Nabulsi, A., Mukhopadhyay, S., Awal, M.S., Fernandes, S. and Ailabouni, K. 2019. IOT-Solar energy powered smart farm irrigation system. Journal of Electronic Science and Technology, 17(4): 3514-3528.

Archana, P. and Priya, R. 2016. Design and implementation of automatic plant watering system. International Journal of Advanced Engineering and Global Technology, 4(1): 1567-1570.

Arun, C. and Sudha, K.L. 2012. Agricultural management using wireless sensor networks-a survey. International Proceedings of Chemical, Biological and Environmental Engineering (IPCBEE), 48: 76-80.

Chavan, C.H. and Karnade, V. 2014. Wireless monitoring of soil moisture, temperature and humidity using zigbee in agriculture. International Journal of Engineering Trends and Technology, 11(10): 493-497.

Guptha, M. A., Seal, A. and Tejomurthula, B. T. 2019. Smart irrigation system using IOT. Asian Journal of Science and Technology, 10(6): 9756-9768.

Kim, Y., Evans, R.G. and Iversen, W.M. 2008. Remote sensing and control of an irrigation system using a distributed wireless sensor network. IEEE Transactions on Instrumentation and Measurement, 57(7): 1379-1387.

Shwetha 2019. Automated irrigation system using wireless sensor networks. Int. Res. J. Eng. Tech., 3(4):1586-1588.

Nature Environment and Pollution Technology
An International Quarterly Scientific Journal

p-ISSN: 0972-6268
(Print copies up to 2016)
e-ISSN: 2395-3454

Vol. 22 | No. 1 | pp. 527-533 | 2023

Original Research Paper

https://doi.org/10.46488/NEPT.2023.v22i01.053

Open Access Journal

# Radiation Risk Among Children due to Natural Radioactivity in Breakfast Cereals

**H. H. Abbas*, Shaymaa A. Kadhim*†, Shatha F. Alhous**, H. H. Hussein*, F. A. AL-Temimei* and H. A. A. Mraity***

*Department of Physics, Faculty of Science, University of Kufa, Iraq
**Department of Physics, Faculty of Education for Girls, University of Kufa, Iraq
†Corresponding author: Shaymaa A. Kadhim; shaymaa.alshebly@uokufa.edu.iq

**Nat. Env. & Poll. Tech.**
**Website: www.neptjournal.com**

*Received:* 03-08-2022
*Revised:* 15-09-2022
*Accepted:* 29-09-2022

**Key Words:**
Radioactivity
Excessive lifetime cancer risk
Annual gonadal equivalent
Breakfast cereal

## ABSTRACT

Breakfast cereal is one of the common foods for children's nutrition. It is made from sugar, barley, calcium carbonate, salt, maize, peanuts, molasses, and honey. Therefore, assessing the levels of radioactivity in breakfast cereal is essential for children's health. Gamma-ray spectrometry NaI(Tl) was used to measure the radiation hazard in ten samples collected from the Iraqi market. The corresponding radiation dose quantities and hazard indices were also calculated. The average concentrations of $^{226}Ra$, $^{232}Th$, and $^{40}K$ were found to be 18.195, 20.965, and 796.500 ($Bq.kg^{-1}$). The annual effective dose equivalent ($AEDE_{in}$), annual ingestion dose (AID), and the risk of cancer incidence (ELCR) were all seen to be within the accepted levels, except the annual gonadal equivalent dose (AGED). Radiation hazard index values (i.e., $I_\gamma$, $I_\alpha$, and $H_{in}$) were noticed to be lower than unity, except $I_\gamma$ was much higher than the internationally permissible limits for the samples of BGF5, BGF6, and BGF7 recommended by UNSCER2000. Therefore, the study findings reveal that this type of cereal can be considered a safe feeding material for children's health.

## INTRODUCTION

Natural radiation comes from many sources. One of these sources is natural radioactivity, divided into three main types: cosmic rays, radionuclides generated from cosmic rays, and radionuclides of terrestrial origin (Reedy et al. 1983). A second source is an artificial source. Ionizing radiation is a natural part of the environment in which we live, present in the Earth, buildings, food, and even in the bones of our bodies. Earth, water, air, plants, and animals contain over 40 natural radioactive elements, mainly in a non-active state. The number of artificial radioactive elements is much higher (Webber & Higbie 2003, Dolchinkov 2017). While radionuclides formed as a result of cosmic rays come from the interaction between the radionuclides of cosmic and the Earth's atmosphere. Nevertheless, the terrestrial source represents the dangerous part due to its radionuclides' direct contact with humans (Beer et al. 2012). In this context, Uranium-238 ($^{238}U$), Actinium-235 ($^{235}U$), and Thorium-232 ($^{232}Th$) are the largest naturally occurring radioactive elements in the Earth's crust that their half-lives are estimated to be at millions of years (Mernagh & Miezitis 2008).

The radioactive materials in nature differ according to location, height above sea level, the nature of the soil, and the type of dwelling. There are a large number of radionuclides that have decayed with time (Eisenbud & Gesell 1997). The radionuclides enter the body by ingestion or inhalation and emit either alpha or beta particles (Raabe 2010). Therefore, it is worth studying the radioactivity in commonly consumed foodstuffs and estimating the potential risk level to protect the consumer's health (Alhous et al. 2020). Cereal is a traditional product for evaluating cancer risk and the annual gonadal equivalent dose. Many studies have been conducted on this item of food, in which the radioactivity and risk factors were estimated. The latter may be due to the ease of preparation and storage, the long half-life, and the low cost (Changizi et al. 2013).

An example of the aforementioned studies is that the activity concentration of natural and anthropogenic radionuclides was measured for five different types of honey in Italy (Caridi et al. 2022). Another complete investigation was conducted to determine various radionuclide activities in foods ingested and evaluate dose levels in different foodstuffs in eight Sudanese states. Cereals, milk, and others for age groups 7–12 years and older than 17 years, the yearly effective dosage attributable to various foodstuffs was determined to be 2.78 $mSv.y^{-1}$ and 1.18 $mSv.y^{-1}$, respectively (Hemada 2009). A published relevant work examined the

Table 1: Information about the samples and their companies, origins, and the content of each sample.

| I.D. | The product | company | Origin | Content of each sample | Mass [g] |
|---|---|---|---|---|---|
| BGF1 | Gold corn flakes | Nestle | Turkey | Maize Semolina, sugar, Barley, Calcium Carbonate, and Salt. | 234 |
| BGF2 | Corn flakes hony and nuts | Kellogg's | Saudi Arabia | Maize, Sugar, Peanuts, Barley, Molasses, Honey, Salt. | 267 |
| BGF3 | Corn flakes | Temmy's | Egypt | Flour, Salt, Sugar, Barley, Vanillin, Calcium carbonatE170. | 287 |
| BGF4 | Semolina wheat | Alryad | U.A.E. | Soft white Semolina | 319 |
| BGF5 | Munchies cheese puff | Dena | Iraq | Wheat Flour, Sugar, vegetable, oil, cocoa powder, lecithin | 212 |
| BGF6 | Oat flakes | Skvira | Ukraine | Fat, Graisse, Carbohydrates, sugar, protein, Salt, Vitamins, Minerals | 259 |
| BGF7 | Supermi | Indomie | Indonesia | Wheat flour, edible vegetable oil, salt, acidity regulators, potassium carbonate, sodium carbonate. | 263 |
| BGF8 | Alafandi | Alfajr | Iraq | Peanut, Corn Starch, Salt, Olin, Oil Refined, Flavors, Food Allowed. | 55 |
| BGF9 | Corn flakes | Kellogg's | Turkey | Maize Semolina, sugar, Salt, Wheat Flour, blubbery, Vitamins, Minerals, | 265 |
| BGF10 | Nesquik | Nesquik | Turkey | Wheat, coco powder, Vitamins, protein | 314 |

long-lived gamma radiation emitters in the various types of pasta available in the Iraqi market. In another study, the measured $^{238}$U, $^{232}$Th, and $^{40}$K concentrations were evaluated in 20 different types of pasta (Alaboodi et al. 2020). Therefore, it is necessary to investigate this food type and calculate some important transactions related directly and significantly to children's health. The current study aims to measure the radionuclides of $^{226}$Ra, $^{232}$Th, and $^{40}$K and then evaluate the excess lifetime cancer risk and annual gonadal equivalent dose in breakfast cereals for children's food. It should be noted that this study was the first conducted to assess the radioactivity in children's breakfast cereal.

## MATERIALS AND METHODS

### Sample Collection and Preparation

Ten samples of breakfast cereals were collected from the local and imported breakfast cereals available in the Iraqi markets. The weight of each sample differs from the other due to the different sizes of breakfast cereals containers, as shown in Table 1. The samples were then ground into a powder and stored in special containers. The latter samples were held for a month to ensure the radioactive equilibrium between the uranium and thorium series and their short-lived progenies (Cochran & Masqué 2003). After that, the samples became ready for measurement. The elapsed time for measurement was determined to be 3 hours. Also, all sample measurements were conducted in the physics laboratory at the Faculty of Science, University of Kufa.

### Gamma-Ray Detection System

The radioactivity measurements were conducted using Sodium Iodide NaI (Tl) detector. Spectral data were collected and analyzed using MAESTRO-32 (A65- B32) software from ORTEC. The activity concentration of natural radionuclides $^{226}$Ra, $^{232}$Th, and $^{40}$K was calculated utilizing equation (1) (Harb et al. 2008, Adhab & Alsabari 2020, Hamza et al. 2020, Salman et al. 2020).

$$A = \frac{N_{net}}{\varepsilon . I_G . m . t} \frac{\sqrt{N_{net}}}{\varepsilon . I_G . m . t} (Bq / Kg) \quad \ldots(1)$$

where $N_{net}$ represents the net count (area under the specified energy peak after background subtraction) in (c.s$^{-1}$), $\sqrt{N_{net}}$ is the random error in (c.s$^{-1}$), ε is the efficiency of the detector, $I_G$ is the transition probability of the emitted gamma ray, $t$ refers to the time of spectrum collection from the sample (3 h), and $m$ is the mass of the sample in kg units. Through the data obtained from the aforementioned system, many variables will be calculated, as shown below.

### Representative Gamma and Alpha Index ( $I_\gamma$, $I_\alpha$)

$I_\gamma$ was used to calculate the risk arising from gamma radiation associated with radioactive natural nuclei in the studied samples and was calculated using equation (3) which depends on the activity concentrations of $^{226}$Ra, $^{232}$Th, and $^{40}$K. Its value must be less than one in order not to cause any risk to human health. An alpha index was calculated for the breakfast cereal samples using the equation below (Ziqiang et al. 1988):

$$I_\alpha = \frac{A_{Ra}}{200} \quad \ldots(2)$$

### Internal Radiation Hazard Indices ($H_{in}$ )

Internal exposure to $^{222}$Rn and its radioactive progeny, which

are harmful to the respiratory system, can be estimated using the internal hazard index. They are derived from $^{226}Ra$, $^{232}Th$ and $^{40}K$ activity concentrations (Hussain et al. 2010, Kadhim et al. 2020, 2022).

**Annual Effective Dose Equivalent ($AEDE_{in}$)**

The effective equivalent dose calculations are based on the absorbed dose rate level in the air. To perform these calculations, a conversion coefficient that relates the absorbed dose rate in the air to the effective dose equivalent and occupancy fraction must be considered. The value of the aforementioned two parameters varies in relation to climate conditions in the considered area and the mean age of the population taken in this work. Considering the UNSCEAR (2000a) report account, the conversion coefficient value was 0.7 $Sv.Gy^{-1}$ for male and female (indoor and outdoor), and a value of 0.8 for the outdoor occupancy fraction, then calculate Indoor absorbed dose $D_{in}$(nGy/h). (Absar 2014). As a result, the outdoor annual effective dose equivalent can be estimated as follows (UNSCEAR 2000a):

$$AEDE_{in}(\mu Sv.y^{-1}) = D_{in}(nGy.h^{-1}) \times 8760\ (h) \times 0.8 \times 0.7(Sv.Gy^{-1}) \times 10^{-3} \quad \ldots(3)$$

**Annual Gonadal Equivalent Dose (AGED) and Annual Ingestion Dose (AID)**

AGED was also calculated because the reproductive gland is important due to its high sensitivity to radiation (Alhous et al. 2020). The latter index is highly important in the UNSCEAR (2000b) publication (Vanmarcke 2002). Therefore, it is essential to calculate the annual gonadal equivalent dose (AGED) depending on the specific activities of $^{226}Ra$, $^{232}Th$, and $^{40}K$, in addition to the annual ingestion dose (AID.) using the following formulas, respectively (Changizi et al. 2013, Aswood et al. 2017):

$$AGED = 3.09\,A_{Ra} + 4.18\,A_{Th} + 0.314\,A_K \quad \ldots(4)$$

$$AID = A_i \times C_R \times FDC_{ING} \quad \ldots(5)$$

where $A_i$ is the total activity concentration ($Bq.kg^{-1}$) of $^{226}Ra$, $^{232}Th$, and $^{40}K$, while the C.R. is the consumption rate ($9.125\ kg.y^{-1}$) and $FDC_{ING}$ is the ingestion dose coefficient of the $^{226}Ra$, $^{232}Th$, and $^{40}K$, which are 0.28, 0.23 and 0.0062 in ($\mu Sv.Bq^{-1}$) respectively (Alhous et al. 2020, UNSCEAR 2000b).

**Excess Lifetime Cancer Risk (ELCR)**

The excess lifetime cancer risk (ELCR) is significant, and it was done using the following equation (El-Arabi 2001, Hamza et al. 2020, Aswood et al. 2022):

$$ELCR = AID \times DL \times RF \quad \ldots(6)$$

DL is the mean children's lifespan of 10 years, and R.F. is the risk factor value of 0.055 per Sievert as recommended by the ICRP (Wrixon 2008).

## RESULTS AND DISCUSSION

Table 2 presents the activity concentrations of $^{226}Ra$, $^{232}Th$, and $^{40}K$ in the breakfast cereal samples, with an average value of 18.195, 20.965, and 796.500 ($Bq.kg^{-1}$), respectively. Depending on the internationally permissible limits, the concentrations of $^{226}Ra$, and $^{232}Th$ were seen to be lower than the values reported by UNSCEAR 2000, except the specific activity of $^{40}K$ was higher than the recommended level, as shown in Fig. 1 (BGF2 (Saudi Arabia), BGF3 (Egypt) and BGF8 (Iraq). From Table 3, the average values of $AEDE_{in}$, AID., and ELCR were 0.356 $mSv.y^{-1}$, 0.136 $mSv.y^{-1}$, and $0.068*10^{-3}$, respectively. All the latter results of dosemetric parameters were less than the global permissible value, where ELCR was less than the $2.5*10^{-3}$ recommended by ICRP and WHO.

The average AGED was $393.983*10^{-3}$ $\mu Sv.y^{-1}$, this means that it is higher than the internationally accepted limit, as reproductive organs are susceptible to radiation, and the reason may be because each sample is a mixture of a group of different materials in terms of origin, cultivation, preservatives, and storage method, which may affect this rise, as shown in Fig. 2.

The results have shown that the averages of all the radiometric parameters of the studied samples in this study were 0.862, 0.091, and 0.345 for $I_{\gamma}$, $I_{\gamma,}$ and $H_{in,}$ respectively. The relationship among radiation hazard indices for the radionuclides in the studied samples has also been drawn in Fig. 3. In this work, it has been noted that the average values of all radiation hazard indices were less than the global value (Nordic), except, $I_{\gamma}$ was greater than the internationally recommended limits for samples, BGF5 (Iraq), BGF6 (Ukraine), and BGF7 (Indonesia). Table 4 presents the ratio between $^{226}Ra$ to $^{232}Th$, $^{232}Th$ to $^{226}Ra$, $^{226}Ra$ to $^{40}K$, and $^{232}Th$ - $^{40}K$ for the studied samples, where the calculated average of the ratios was (0.869, 2.700, 0.026, and 0.030) respectively.

The studied data were statistically analyzed using SPSS program version 20, as shown in Table 5. The relationship between the specific activity of $^{226}Ra$ and $AEDE_{in}$ was moderately direct and had no statistical significance. At the same time, there was a positive, high, and statistically significant direct relationship between AID and ELCR. The specific activity of $^{232}Th$ is moderately positive and had no statistical significance with $AEDE_{in}$, AID, AGED, and ELCR, respectively. The specific activity of $^{40}K$ had a very

Table 2: Activity concentration (Bq.kg$^{-1}$) of $^{226}$Ra, $^{232}$Th and $^{40}$K.

| Code of sample | Activity Concentration | | | | | |
|---|---|---|---|---|---|---|
| | $^{226}$Ra | ±SD | $^{232}$Th | ±SD | $^{40}$K | ±SD |
| BGF1 | 4.385 | ± 3.205 | 13.682 | ± 2.549 | 943.901 | ± 20.962 |
| BGF2 | 40.503 | ± 1.922 | 24.216 | ± 2.116 | 416.826 | ± 11.959 |
| BGF3 | 3.025 | ± 1.650 | 15.639 | ± 1.476 | 345.857 | ± 13.705 |
| BGF4 | 29.818 | ± 3.588 | 13.972 | ± 2.115 | 973.671 | ± 14.942 |
| BGF5 | 29.787 | ± 4.654 | 25.169 | ± 2.813 | 1117.815 | ± 21.610 |
| BGF6 | 14.477 | ± 3.505 | 25.752 | ± 2.484 | 995.727 | ± 17.867 |
| BGF7 | 27.463 | ± 3.151 | 25.838 | ± 35.863 | 926.917 | ± 17.595 |
| BGF8 | 8.109 | ± 2.225 | 17.120 | ± 1.113 | 409.328 | ± 8.582 |
| BGF9 | 2.383 | ± 2.383 | 26.117 | ± 2.428 | 990.819 | ± 18.161 |
| BGF10 | 21.997 | ± 2.765 | 22.141 | ± 1.799 | 845.043 | ± 15.032 |
| Average | 18.195 | ± 2.905 | 20.965 | ± 5.476 | 796.590 | ± 16.042 |

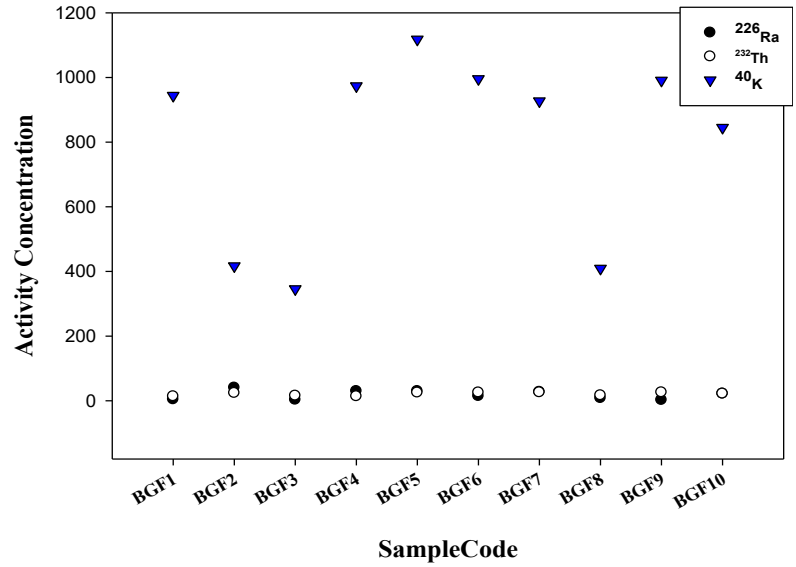


Fig. 1: Comparison of the specific activities (Bq.kg$^{-1}$) of the radionuclides in the studied samples.

Table 3: Radiological parameters dosemetric and radiation hazard indices of breakfast cereal samples.

| I.D. | AEDE [mSv.y$^{-1}$] | AID [mSv.y$^{-1}$] | ELCR*10$^{-3}$ | AGED*10$^{-3}$ [μSv.y$^{-1}$] | Radiation hazard indices < 1 | | |
|---|---|---|---|---|---|---|---|
| | | | | | I$_{\gamma}$ | I$_{\alpha}$ | H$_{in}$ |
| BGF1 | 0.329 | 0.093 | 0.047 | 367.125 | 0.795 | 0.022 | 0.273 |
| BGF2 | 0.327 | 0.178 | 0.089 | 357.262 | 0.790 | 0.203 | 0.399 |
| BGF3 | 0.169 | 0.060 | 0.030 | 183.319 | 0.407 | 0.015 | 0.149 |
| BGF4 | 0.407 | 0.161 | 0.080 | 456.271 | 0.988 | 0.149 | 0.418 |
| BGF5 | 0.494 | 0.192 | 0.096 | 548.244 | 1.195 | 0.149 | 0.491 |
| BGF6 | 0.421 | 0.147 | 0.074 | 465.035 | 1.018 | 0.072 | 0.385 |
| BGF7 | 0.438 | 0.177 | 0.088 | 483.914 | 1.059 | 0.137 | 0.441 |
| BGF8 | 0.207 | 0.080 | 0.040 | 225.149 | 0.498 | 0.041 | 0.195 |
| BGF9 | 0.388 | 0.117 | 0.058 | 427.648 | 0.938 | 0.012 | 0.320 |
| BGF10 | 0.385 | 0.150 | 0.075 | 425.863 | 0.931 | 0.110 | 0.380 |
| Average | 0.356 | 0.136 | 0.068 | 393.983 | 0.862 | 0.091 | 0.345 |

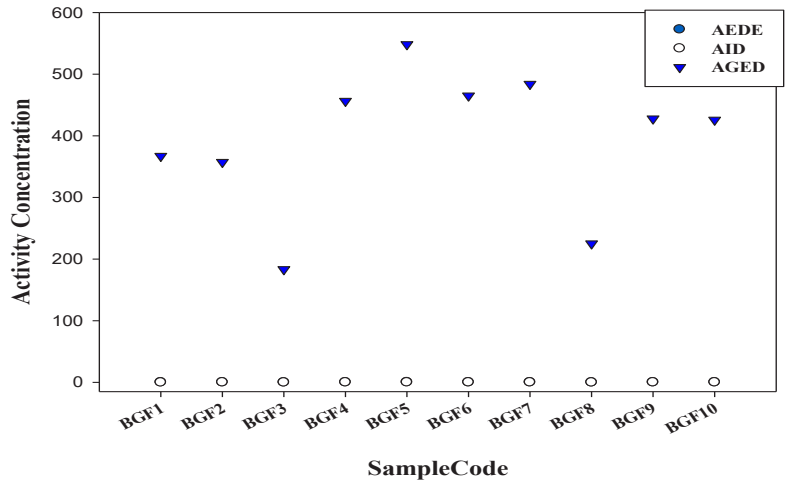


Fig. 2: Comparison of the radiation doses of radionuclides in the studied samples.

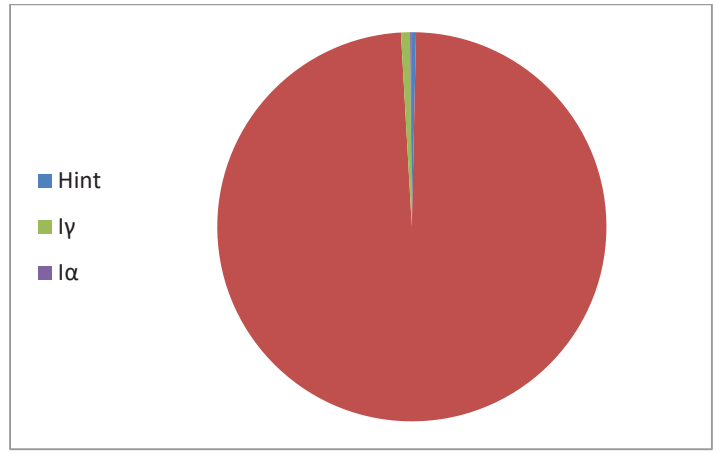


Fig. 3: Comparison of the coefficients of radiation hazard indices for the radionuclides in the studied samples.

Table 4: The ratio between the specific activity of $^{226}$Ra, $^{232}$Th, and $^{40}$K in the breakfast cereal samples.

| ID | $^{226}$Ra-$^{232}$Th | $^{232}$Th-$^{226}$Ra | $^{226}$Ra-$^{40}$K | $^{232}$Th-$^{40}$K |
|---|---|---|---|---|
| BGF1 | 0.321 | 3.120 | 0.005 | 0.014 |
| BGF2 | 1.673 | 0.598 | 0.097 | 0.058 |
| BGF3 | 0.193 | 5.169 | 0.009 | 0.045 |
| BGF4 | 2.134 | 0.469 | 0.031 | 0.014 |
| BGF5 | 1.183 | 0.845 | 0.027 | 0.023 |
| BGF6 | 0.562 | 1.779 | 0.015 | 0.026 |
| BGF7 | 1.063 | 0.941 | 0.030 | 0.028 |
| BGF8 | 0.474 | 2.111 | 0.020 | 0.042 |
| BGF9 | 0.091 | 10.960 | 0.002 | 0.026 |
| BGF10 | 0.993 | 1.007 | 0.026 | 0.026 |
| Average | 0.86 | 2.700 | 0.026 | 0.030 |
| Worldwide (Talab 2016) | 0.86 | 11.43 | - | - |

Table 5: Correlation among sample studies.

| | | $^{226}$Ra [ppm] | $^{232}$Th [ppm] | $^{40}$K [ppm] | $AEDE_{in}$ | AID | ELCR | AGED |
|---|---|---|---|---|---|---|---|---|
| $^{226}$Ra (ppm) | *P. C* | 1 | | | | | | |
| | Sig. (2-tailed) | | | | | | | |
| $^{232}$Th (ppm) | *P. C* | 0.329 | 1 | | | | | |
| | Sig. (2-tailed) | 0.354 | | | | | | |
| $^{40}$K (ppm) | *P. C* | 0.102 | 0.318 | 1 | | | | |
| | Sig. (2-tailed) | 0.779 | 0.370 | | | | | |
| $AEDE_{in}$ | P. C | 0.514 | 0.583 | 0.884** | 1 | | | |
| | Sig. (2-tailed) | 0.129 | 0.077 | 0.001 | | | | |
| AID | *P. C* | 0.879** | 0.605 | 0.512 | 0.849** | 1 | | |
| | Sig. (2-tailed) | 0.001 | 0.064 | 0.130 | 0.002 | | | |
| ELCR | *P. C* | 0.879** | 0.605 | 0.513 | 0.849** | 1.000** | 1 | |
| | Sig. (2-tailed) | 0.001 | 0.064 | 0.129 | 0.002 | .000 | | |
| AGED | *P. C* | 0.510 | 0.564 | 0.890** | 1.000** | .844** | .844** | 1 |
| | Sig. (2-tailed) | 0.132 | 0.089 | 0.001 | .000 | .002 | .002 | |

**Correlation is significant at the 0.01 level (2-tailed)

high positive relationship and was statistically significant with $AEDE_{in}$ and AGED.

In contrast, it had a moderate positive relationship without statistical significance with AID and ELCR. The annual effective dose equivalent $AEDE_{in}$ has a vital, positive, high statistical significance with AID and ELCR, with a direct relationship and very high statistical significance with AGED. The annual ingestion dose (AID) and ELCR have a direct relationship with high statistical significance, while AGED has a strong direct relationship with high statistical significance. Therefore, a solid positive direct relationship exists between ELCR and AGED with high statistical significance.

## CONCLUSIONS

In the current study, the samples demonstrate low specific activity values for radionuclides of $^{226}$Ra and $^{232}$Th, thus contributing to the low-absorbed dose rates in the air. In general, the activity of the calculated radionuclide in terrestrial sources has given a lower value than the global permissible value, with the exception of $^{40}$K. The average values of $AEDE_{in}$, AID., and ELCR, together with the radiation hazard indices, were less than the average world value. Still, the AGED was higher than 0.29 $mSv.y^{-1,}$ as mentioned in UNSCEAR (2000a, 2000b). Finally, it is considered the first study at the level of Iraq, and it must be developed in the future by studying samples of other origins.

## ACKNOWLEDGMENTS

We would like to give warm thanks and praise to the University of Kufa/Iraq for the support and facilities it provides to researchers, specifically, the laboratory of the Physics department at the Faculty of education for girls for their support.

## REFERENCES

Absar, N. 2014. Natural and anthropogenic radioactivity levels and the associated radiation hazard in the soil of Oodalia Tea Estate in the hilly region of Fatickchari in Chittagong, Bangladesh. J. Radiat. Res., 55(6): 1075-1080.

Adhab, H.G. and Alsabari, E.K. 2020. Assessment of excess lifetime cancer risk of soils samples in Maysan neighborhood adjacent to the middle Euphrates cancer center in Najaf/Iraq. I.O.P. Confe. Ser. Mater. Sci. Eng., 1419: 0123301.

Alaboodi, A.S., Inaas, A.G., Shaymaa, A.K., Shatha, F. and Khadim, B.A. 2020. Estimation of the radiation hazard indices in most types of Pasta spread in the Iraqi markets. J. Phys. Conf. Ser., 151l: 013817.

Alhous, S.F., Khadim, S.A., Alkulfi, A.A. and Kadhim, B.A. 2020. Measuring the level of Radioactive contamination of selected samples of Sugar and Salt available in the local markets in Najaf governorate/ Iraq. IOP Conf. Ser. Mater. Sci. Eng., 17: 58.

Alhous, S.F., Khadim, S.A., Alkulfi, A.A., Muhamood, A.A. and Zgair, I.A. 2020. Calculation of radioactivity levels for various soil samples of Karbala-Najaf road (Ya-Hussein)/Iraq. IOP Conf. Ser. Mater. Sci. Eng., 928: 072076.

Aswood, M.S., Alhoys, S.F. and Abdulridha, S.A. 2022. Life time cancer risk evaluation due to inhalation of radon gas in dwellings of Al-Diwaniyah Governorate, Iraq. Nat. Environ. Pollut. Technol., 21(1): 331-337.

Aswood, M.S., Jafoor, M.S. and Salih, N. 2017. Estimation of annual effective dose due to natural radioactivity in ingestion of vegetables from Cameron Highlands, Malaysia. Environ. Technol. Innov., 8: 96-102.

Beer, J., McCracken, K. and Steiger, R. 2012. Cosmogenic Radionuclides: Theory And Applications in the Terrestrial and Space Environments. Springer Science & Business Media, Cham.

Caridi, F., Venuti, V., Paldini. G., Crupi, V., Belmusto, G. and Majolino, D. 2022. The radioactivity distribution and radiation hazard in honey samples from Italian large retailers. J. Phys. Conf. Ser., 2162: 012002.

Changizi, V., Shafiei, E. and Zera, M.R 2013. Measurement of 226Ra, 232Th, 137Cs, and 40K activities of wheat and corn products in Ilam province–Iran and resultant annual ingestion radiation dose. Iran. J. Pub Health, 42(8): 903.

Cochran, J. and Masqué, 2003. Short-lived U/Th series radionuclides in the ocean: tracers for scavenging rates, export fluxes, and particle dynamics. Rev. Mineral. Geochem., 52(1): 461-492.

Dolchinkov, N.T. 2017. Sources of natural background radiation. Sec. Def. Quart., 16(3): 40-51.

Eisenbud, M. and Gesell, T.F. 1997. Environmental Radioactivity From Natural, Industrial and Military Sources: From Natural, Industrial and Military Sources, Elsevier, The Netherlands.

El-Arabi, A. 2001. Gamma spectroscopic analysis of powdered granite samples in some Eastern desert's areas. Arab J. Nucl. Sci. Appl., 34(2): 245-255.

Hamza, Z.M., Alshelbhy, S. A. and Hussein, H.H. 2020. A practical study to determine the percentage of radiation in medicinal herbs used in the Iraqi market. J. Phys. Conf. Ser., 1591: 012007

Harb, S., Kamal, A.H., Mageed, A.I.A., Abbady, A. and Rasheed, W. 2008. Concentration of U-238, U-235, Ra-226, Th-232, and K-40 for some granite samples in the eastern desert of Egypt. Environ. Phys. Conf., 19: 2180.

Hemada, H.E.F. 2009. Radioactivity levels of basic foodstuffs and dose estimates in Sudan. Master Thesis. NCL Collection, University of Khartoum, pp. 1-71.

Hussain, H.H., Hussain, R.O., Yousef, R.M. and Shamkhi Q. Natural radioactivity of some local building materials in the middle Euphrates of Iraq. J Radioanal. Nucl. Chem., 284(1): 43-47.

Kadhim, S.A., Alhous, S.F., Hussein. A.S., Hussein, H.H. and Alaboodi, A.S. 2020. Estimated the concentration of 238U, 232Th, and 40K in flour samples of Iraq markets. J. Phys. Conf. Ser., 1221: 1101251.

Kadhim, S.A., Harjan, A.H., Alhous, S.F. and AL-Khafaji, Q.S. 2022. Study of the difference between uranium concentrations in blood samples of healthy, newly infected women who took chemotherapy in Iraq, Najaf. A.I.P. Conf Proc., 222: 67044.

Mernagh, T.P. and Miezitis, Y. 2008. A review of the geochemical processes controlling the distribution of thorium in the Earth's crust and Australia's thorium resources. Citeseer, 2: 8.

Raabe, O.G. 2010. Concerning the health effects of internally deposited radionuclides. Health Phys., 98(3): 515-536.

Reedy, R.C., Arnold, J.R. and Lal, D. 1983. Cosmic-ray record in solar system matter. Science, 219(4581): 127-135.

Salman, A.Y., Kadhim, S.A., Alaboodi, A.S. and Alhous, S.F. 2020. Study the contamination of Radioactivity levels of 226Ra, 232Th, and 40K in (water) Iraq and their potential radiological risk to the human population. I.O.P. Conf S Mater Sci Eng., 928(7): 072008.

Talab, A.H.D. 2016. Evaluation of the effect of individual and demographic factors on awareness, attitude, and performance of radiographers regarding principles of radiation protection. Al Ameen J. Med. Sci., 9(2): 90-95.

UNSCEAR 2000a. Sources and Effects of Ionizing Radiation, United Nations, New York.

UNSCEAR 2000b. United Nations Scientific Committee on the Effects of Atomic Radiation. United Nations, New York.

Vanmarcke, H. 2002. UNSCEAR 2000: Sources of ionizing radiation. Ann. Belg. Ver. Stralingsbescherming, 27(2): 41-65.

Webber, W. and Higbie, P. 2003. Production of cosmogenic Be nuclei in the Earth's atmosphere by cosmic rays: Its dependence on solar modulation and the interstellar cosmic ray spectrum. J. Geophys. Res., 108(A9): 9863.

Wrixon, A.D. 2008. New ICRP recommendations. J. Radiol. Prot., 28(2): 161.

Ziqiang, P., Yin, Y. and Mingqiang, G. 1988. Natural radiation and radioactivity in China. Radiat. Prot. Dosim., 24(1-4): 29-38.

Nature Environment and Pollution Technology
An International Quarterly Scientific Journal

p-ISSN: 0972-6268
(Print copies up to 2016)
e-ISSN: 2395-3454

Vol. 22 | No. 1 | pp. 535-539 | 2023

Original Research Paper

https://doi.org/10.46488/NEPT.2023.v22i01.054

Open Access Journal

# The Study of Filamentous Fungi in Potable Water and Its Biofilm Formation in Water Pipeline System

**S. Asha and G. Sangeetha Vani†**
Department of Microbiology, Ethiraj College for Women, Chennai-600008, Tamil Nadu, India
†Corresponding author: G. Sangeetha Vani; sangeethavani_g@ethirajcollege.edu.in

**Nat. Env. & Poll. Tech.**
**Website: www.neptjournal.com**

*Received:* 05-07-2022
*Revised:* 22-08-2022
*Accepted:* 06-09-2022

**Key Words:**
Filamentous fungi
Water pipeline system
Biofilm analysis
Drinking water

## ABSTRACT

Water is essential for life and it is an inorganic constituent of living matter. Water pipeline systems are sighted as problematic in aquatic habitats in which multiple pathogens are occupied including fungi. They have rigid cell walls containing glucans and chitin. The bodies of fungi comprise filaments called hyphae. These hyphae are split into a mat of interwoven single cells made of mycelium. Fungi can pollute the drinking water system and are responsible for biofilm formation. Biofilms are complex polymers containing many times their dry weight in water. Moisture is essential for biofilm formation. The occurrence of biofilms affects the quality of drinking water. Hence, the present study is aimed at recovering the fungi from drinking water samples and their biofilm formation in the water pipeline system. Drinking water samples such as mineral water, tap water, and RO-purified water are collected from different places. Fungi such as *Aspergillus*, *Penicillium* and *Mucor* were recovered from these samples and most species belong to *Aspergillus* and *Penicillium.* Further, the biofilm formation of fungi from cast iron in the pipeline system was detected using fluorescence microscopy and fluorescent *in situ* hybridization analysis.

## INTRODUCTION

Fungi are eukaryotic and they can occur as unicellular yeast or multicellular filamentous fungi or molds (Yamaguchi et al. 2007). Fungi are widely distributed in nature and it is also present in the soil, organic material, etc. A broad range of filamentous fungi has been discovered or isolated from drinking water. Among the isolated filamentous fungi, possibly contagious, harmful, and allergenic species have also been found (Hageskal et al. 2009). The presence of fungi in drinking water can cause various fungal infections in immunocompromised patients. Mostly, *Aspergillus* and *Penicillium* species are found in water and (Grabinska-Loniewska et al. 2007) causes allergy, ear infections, lung and kidney failure, respiratory problems, and increased levels of invasive infections. Fungi invade into drinking water pipeline system through various routes which include, water treatment, insufficient stored water facilities, cracks in pipelines, main breaks, and installation (Sonigo et al. 2011, Afonso et al. 2019). Filamentous fungi have the potential to grow on surfaces, thus leading to the formation of biofilms. Biofilm is a thin layer of microorganisms adhering to the surface of the structure (Simoes & Simoes 2013). Biofilms form slimy extracellular polymeric substances (EPS), which include polysaccharides, proteins, lipids, carbohydrates, and DNA (Flemming et al. 2002). It is a collection of organic and inorganic, living and dead material present on a surface. It can alter the surrounding environment such as microbial community, pH, and aerobic and anaerobic conditions. These are established on moist surfaces such as water pipelines, food processing equipment, industrial piping, medical devices, and so on (Huq et al. 2008).

There is no conventional method for analyzing fungi in drinking water. As a consequence, diverse isolation procedures are handled. Membrane filtration techniques, spread plate techniques, and direct microscopic observations are relevant methods. High nutritional media such as Sabouraud Dextrose Agar (SDA), Dichloran Glycerol Medium Base (DG18), Corn Meal Agar (CMA), Potato Dextrose Agar (PDA), Czapek Dox Agar (CZ), Malt Extract Agar (MEA), Dichloran Rose Bengal Chloramphenicol Agar (DRBC) are widely used (Afonso et al. 2021). The morphology and etiology of filamentous fungal biofilms are distinguished by *in situ* microscopic examinations (Douterelo et al. 2016) and by using sequencing techniques, such as flow cytometry, pyrosequencing, etc. These methods are outlined to address knowledge gaps concerned to the formation of biofilms in the drinking water system. This study is one such attempt to confirm the existence of fungi in drinking water and to emphasize the importance of fungal biofilms in affecting the quality of water.

Table 1: Filamentous fungi in drinking water samples.

| Sample location | Water source | Total water samples | Isolation method | Frequent fungal species |
|---|---|---|---|---|
| Chennai | Tap water | 15 | Direct plating | *Aspergillus* sp., *Penicillium* sp. |
| Chennai | Mineral water | 15 | Direct plating | *Aspergillus* sp., *Penicillium* sp. |
| Chennai | RO purified water | 15 | Direct plating | *Aspergillus* sp., *Penicillium* sp. |

## MATERIALS AND METHODS

Water samples (45) were collected aseptically from various places in Chennai (Table 1). All the samples were stored in sterile bottles and processed on the day of the collection. The media used for the isolation of fungi are SDA (Sabouraud Dextrose Agar) and DG18 (Dichloran Glycerol Medium Base). The medium was prepared by standard procedure and autoclaved at 121°C for 15 min. The sterilized medium was flooded onto the sterile plate and allowed to solidify. 0.1 mL of the water samples was added directly and plated on the prepared medium plates. A spread plate technique was performed and plates were incubated at room temperature for one week. Fungal colonies were observed after 7 days. Each unique colony was sub-cultured on SDA and DG18 medium to obtain unique individual isolates. The preliminary identification of the fungal isolates was observed using lactophenol cotton blue (LPCB) mount staining. Macroscopic features such as size, shape, color, and appearance were studied from the fungal isolates.

Biofilm sampling has been performed using cast iron from water pipeline distribution systems. Cast iron was plated on DG18 medium and it was suspended in a sterile saline solution before being plated. The prepared DG18 medium plates were incubated at room temperature for the fungal isolates to grow. Fungal colonies that emerged after incubation were detected using fluorescence microscopy and fluorescent *in situ* hybridization (FISH) probe analysis.

## RESULTS

A total of 45 water samples were collected. Out of 45 water samples, fungi were retrieved from 20 samples (Fig. 1 to Fig. 5). The most abundant genera were identified as *Aspergillus* and *Penicillium*. The macroscopic examination was studied based on morphological characteristics and color of mycelium and the microscopic analysis was performed using lactophenol cotton blue staining (Fig. 6).

Fig. 1: *Aspergillus niger* on SDA.

Fig. 2: *Penicillium verrucosum* on DG18. medium.

Fig. 3: *Colletotrichum gloeosporioides* was grown on DG18 medium.

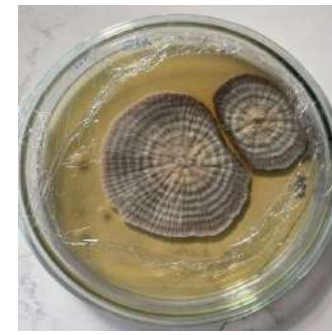

Fig. 4: *Penicillium notatum* on SDA medium.

Fig. 5: *Mucor mucedo* on DG18 medium.

### Sampling Biofilms

After incubation, fungal isolates were reclaimed from the cast iron and they were identified as *Aspergillus niger, Penicillium verrucosum,* and *Mucor mucedo* (Fig. 7).

### Biofilm Detection

For monitoring microbial biofilm formation, fluorescence microscopy was enabled. Fluorescence microscopy utilizes an elevated level of light intensity to brighten the sample (Simoes et al. 2015). Radiant objects in opposition to black backgrounds are seen better. Hence the habitual of fluorescence microscopy is vastly specific and sensitive. Morphological characters were visualized using Calcofluor White MR2 (CW) staining (Fig. 8). CW stain is an indefinite fluorochrome that is attached with chitin and cellulose accommodated in the fungal cell walls (Goncalves et al. 2006).

To confirm the filamentous structure, samples were submitted for fluorescent *in situ* hybridization (FISH) analysis. FISH is an important machinery to examine eukaryotic chromosomes and genomes in molecular biology, cytogenetics, etc. For the identification from fungal culture, the cells are fixed in the first stage. After fixation, the sample was denatured for the hybridization process. After hybridizing, the washing and mounting step proceeded. Hybrids formed between the probes and the targets can be detected using a fluorescent microscope. (Fig. 9). Filamentous fungi with biofilm formation were identified between 24 h and 48 h of FISH probe analysis. Overall, a comprehensive association between the Calcofluor White (CW) filamentous fungi in biofilm is effective for fluorescent *in situ* hybridization analysis.

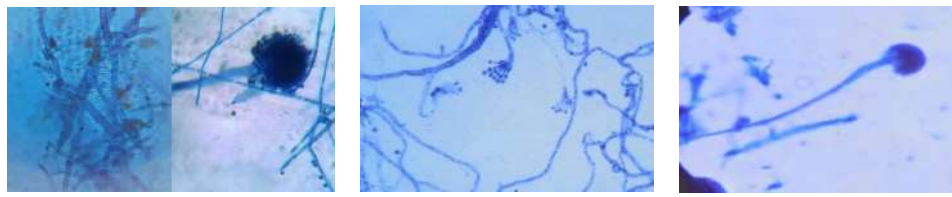

(a) (b) (c)

Fig. 6: a) *Aspergillus niger,* b) *Penicillium verrucosum,* and c) *Mucor mucedo* was microscopically observed using lactophenol cotton blue stain.

7 days of incubation. 30 days of incubation.

Fig. 7: Fungal growth on DG18 medium using cast iron.

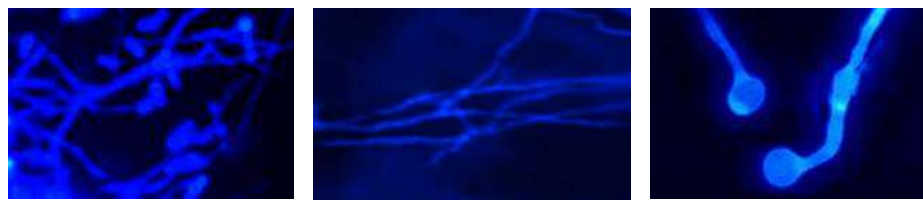

Fig. 8: Filamentous fungi structure visualized using CW staining.

## DISCUSSION

Examination of fungi in drinking water was accomplished in the least number (Nagy & Olson 1982). Most authors agreed fungi generally exist, but the importance of cleanliness and health risks are noticed to be in less number. The pervasiveness of fungi was scrutinized in 45 drinking water samples from mineral water, tap water, and RO-purified water in workplaces and residences. Mineral water was more polluted than tap water. The prevailing genera were mostly *Aspergillus* and *Penicillium spp*., and it can be considered a feasible transmission path for filamentous fungi. Fungi are eukaryotic creature and they possess unusual features which includes nourishment by heterotrophic absorption, growth of vegetative and reproductive formation (i.e., spores and hyphae), and reproduction by both sexual and asexual (Siqueira & Lima 2013). Drinking water biofilms are devised as complex infectious groups of several microbes (bacteria, protozoa, fungi, algae, and viruses), however, all are modified to develop under oligotrophic circumstances (Gonclaves et al. 2006). The laboratory investigations have also displayed that fungal hypha could facilitate bacterial assembly in the surroundings and thus establishing new bacteria. But this theory and the environmental interconnection between them will require further research. Secondary metabolites produced by fungi can provide microbial attribution in water pipes (Arvanitidou et al. 1999, Giuseppina et al. 2020). As a consequence, alterations in proper sanitization can take place and the remaining chlorine in the treated water pipeline system can be modified. The elevated popularity of *Aspergillus spp., Penicillium spp*. and *Cladosporium spp*. are considered as dark colored fungi and it gives rise to mycoses and many other causes, such as skin diseases, allergies, and transmissible infections. Moreover, the genera are also linked with the manufacture of mycotoxins. Fluorescence microscopy is commonly used to acquire information on the cell morphology of fungi. Siqueira et al., 2011, stated that Calcofluor White MR2 (CW) staining enables the vision of cell walls in fungi due to its bond between the carboxylated polysaccharide and beta (1-3), (1-4) polysaccharides in cellulose. The main heterogeneity of fungi established in this work recommends that further deliberation must be given to certain microorganisms in water distribution system analysis. The predominance of fungi in the drinking water distribution system might be difficult as they can produce spores to accumulate with one another along with distinct particles expanding their resistance to purification and they can be more resistant than bacteria.

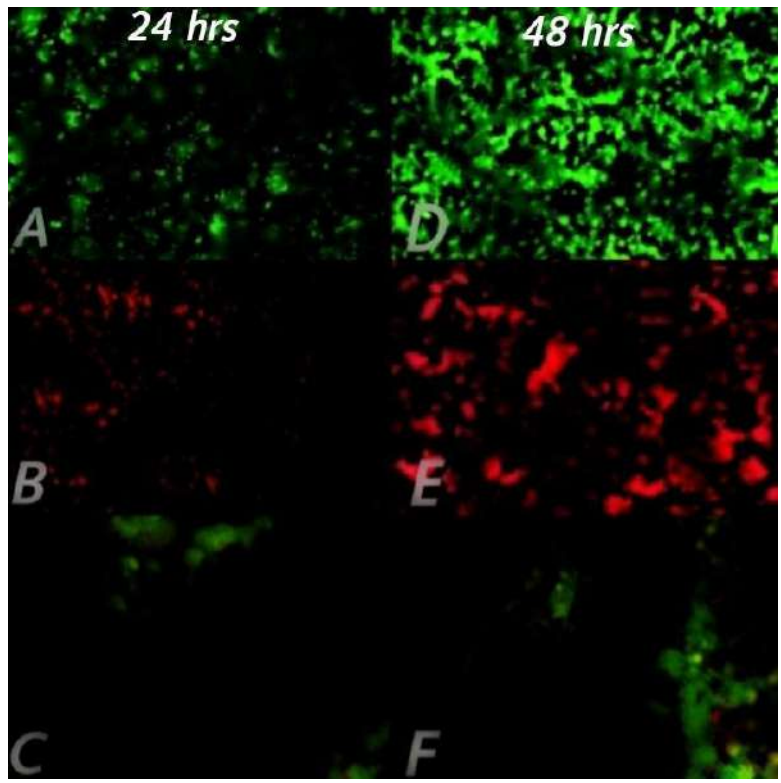


Fig. 9: Biofilm formation of filamentous fungi between 24 and 48 hrs.

## CONCLUSION

Fungi are relatively usual in drinking water pipeline systems. This work is an outline concerning the issue correlated with filamentous fungi in drinking water and its relation to the formation of biofilms. Tap water, mineral water, and RO purified water could be a reservoir for fungi, which make public health at threat. For the study of fungi-related biofilms, standard techniques are needed, similar to those that are involved in the contamination of bacteria in water. Fungal identification at the species level is laborious. Therefore, in the future new molecular and epidemiological studies also require to regulate the importance of health. At the same time, we must anxious about fungal presence in drinking water, because increasing levels of fungi can diminish the grade of water and comprise health issues (Boe-Hansen et al. 2003). Fungal species are challenging to analyze, therefore the studies on fungi in drinking water need skill and caution. To overcome the problem, sufficient treatment of water could be a result (Momba et al. 2000), and also the use of sanitizers helps in the control of biofilms. Although, once the biofilms are formed it is not easy to remove because of the reality that the EPS are counteracting sanitizers. It is necessary to identify the threshold levels of fungi from different types of water in various places (hospitals, industries, etc). In conclusion, the results show that filamentous fungi can form biofilms in the water pipeline system.

## ACKNOWLEDGEMENT

The author thanks the Department of Microbiology, Ethiraj College For Women for the support throughout the research and also the Centre for Medical Genetics to carry out Fluorescent in situ Hybridization analysis.

## REFERENCES

Afonso, T.B., Simoes, L.C. and Lima, N. 2019. *In vitro* assessment of inter-kingdom biofilm formation by bacteria and filamentous fungi isolated from a drinking water distribution system. Biofouling, 35: 1041-54.

Arvanitidou, M., Kanellou, K., Constantinides, T.C. and Katsouyannopoulous, V. 1999. The occurrence of fungi in hospital and community potable waters. Lett. Appl. Microbiol., 29:81-4.

Boe-Hansen, R., Martiny, A.C., Arwin , E. and Alberchtsen, H.J. 2003. Monitoring biofilm formation and activity in drinking water distribution networks under oligotrophic conditions. Water Sci Technol., 47: 91-97.

Douterelo, I., Jackson, M., Solomon, C. and Boxall, J. 2016. Microbial analysis of *in situ* biofilm formation in drinking water distribution systems: implications for monitoring and control of drinking water quality. Appl. Microbiol. Biotechnol., 100: 3301-3311.

Flemming, H.C., Percival, S.L. and Walker, J.T. 2002. Contamination potential of biofilms in water distribution systems. Water Sci. Technol. Water Supply, 2: 271-80.

Giuseppina, C., Giusy, D., Francesco, T., Nicola, B., Francesca, A., Carmen, C., Marco, L., Maria, T. and Montagna, O. 2020. Occurrence of fungi in potable water of hospitals. Pub. Health Threat Patho., 9: 783.

Goncalves, A.B., Paterson, R.R.M. and Lima, N. 2006. Survey and significance of filamentous fungi from tap water. Int. J. Hyg. Environ. Health, 209: 257-264.

Goncalves, A.B., Santos, I.M., Paterson, R.R.M. and Lima, N. 2006. FISH and Calcofluor staining techniques to detect *in situ* filamentous fungi biofilms in water. Rev. Iberoam. de Micol., 23: 192-196.

Grabinska-Loniewska, A., Konillowicz-Kowalska, T., Wardzynska, G. and Boryn, K. 2007. Occurrence of fungi in the water distribution system. Pol. J. Environ. Stud., 16: 539-547.

Hageskal, G., Lima, N. and Skaar, I. 2009. The study of fungi in drinking water. Mycol. Res., 133: 165-172.

Huq, A., Whitehouse, C.A., Grim, C.J., Alam, M. and Colwell, R.R. 2008. Biofilms in water, their role, and their impact on human disease transmission. Curr. Opin. Biotechnol., 19: 244-247.

Momba, M.N.B., Kfir, R., Venter, S.N. and Loete, T. 2000. An overview of biofilm formation in distribution systems and its impact on the deterioration of water quality. Water SA, 26: 59-66.

Nagy, L.A. and Olson, B.H. 1982. The occurrence of filamentous fungi in drinking water distribution systems. Can. J. Microbiol., 28: 667-671.

Simoes, L.C. and Simoes, M. 2013. Biofilms in drinking water: problems and solutions. Rsc. Adv., 3: 2520-2533.

Simoes, L.C., Simoes, M. and Lima, N. 2015. Kinetics of biofilm formation by drinking water isolated *Penicillium expansum*. Biofouling, 31(4): 349-362.

Siqueira, V.M. and Lima, N. 2013. Biofilm formation by filamentous fungi recovered from a water system. J Mycol., 9: 152.

Siqueira, V.M., Oliveira, H.M.B., Santos, C., Paterson, R.R.M., Gusmao, N.B. and Lima, N. 2011. Filamentous fungi in drinking water, particularly in relation to biofilm formation. Int. J. Environ. Res, Pub. Health, 45: 6469.

Sonigo, P., De Toni, A., Reilly, K. and Defra, N. 2011. A review of fungi in drinking water and the implications for human health. Rev. Lit. Arts Am., 33: 1-107.

Afonso, T.B., Simoes, L.C. and Lima, N. 2021. Occurrence of filamentous fungi in drinking water: their role on fungal- bacterial biofilm formation. Research in Microbiology. 172: 103791.

Yamaguchi, M.U., Rampazzo, R.C.P., Yamada-Ogatta, S.F., Nakamura, C.V., Ueda Nakamura, T. and Filho, B.P.D. 2007. Yeasts and filamentous fungi in bottled mineral water and tap water from municipal supplies. Braz. Arch. Biol. Technol., 53: 1-9.

*... Continued from inner front cover*

- The text of the manuscript should run into **Abstract, Introduction, Materials & Methods, Results, Discussion, Acknowledgement** (if any) and **References** or other suitable headings in case of reviews and theoretically oriented papers. However, short communication can be submitted in running with **Abstract and References.** The references should be in full with the title of the paper.
- The figures should preferably be made on a computer with high resolution and should be capable of withstanding a reasonable reduction with the legends provided separately outside the figures. Photographs may be black and white or colour.
- Tables should be typed separately bearing a short title, preferably in vertical form. They should be of a size, which could easily be accommodated in the page of the Journal.
- References in the text should be cited by the authors' surname and year. In case of more than one reference of the same author in the same year, add suffix a,b,c,.... to the year. For example: (Thomas 1969, Mass 1973a, 1973b, Madony et al. 1990, Abasi & Soni 1991).

## List of References

The references cited in the text should be arranged alphabetically by authors' surname in the following manner: (Note: The titles of the papers should be in running 'sentence case', while the titles of the books, reports, theses, journals, etc. should be in 'title case' with all words starting with CAPITAL letter.)

Dutta, A. and Chaudhury, M. 1991. Removal of arsenic from groundwater by lime softening with powdered coal additive. J. Water Supply Res. Techno. Aqua., 40(1) : 25-29.

Hammer, D.A. (ed.) 1989. Constructed Wetlands for Wastewater Treatment-Municipal, Industrial and Agricultural. Lewis Publishers Inc., pp. 831.

Haynes, R. J. 1986. Surface mining and wetland reclamation. In: Harper, J. and Plass, B. (eds.) New Horizons for Mined Land Reclamation. Proceedings of a National Meeting of the American Society for Surface Reclamation, Princeton, W.V.

## Submission of Papers

- The paper can be submitted by e-mail as an attachment in a single WORD file at **contact@neptjournal.com**
- The paper can also be submitted online in a single WORD file through the **online submission portal** of journal's website: **www.neptjournal.com**

## Attention

1. Any change in the authors' affiliation may please be notified at the earliest.
2. Please make all the correspondence by e-mail, and authors should always quote the manuscript number.

**Note:** In order to speed up the publication, authors are requested to correct the galley proof immediately after receipt. The galley proof must be checked with utmost care, as publishers owe no responsibility for mistakes. The papers will be put on priority for publication only after receiving the processing and publication charges.

# Nature Environment and Pollution Technology

**(Abbreviation: Nat. Env. Poll. Tech.)**

**(An International Quarterly Scientific Journal)**

Published by

**Technoscience Publications**

A-504, Bliss Avenue, Opp. SKP Campus

Balewadi, Pune-411 045, Maharashtra, India

In association with

**Technoscience Knowledge Communications**

Mira Road, Mumbai, India


For further details of the Journal, please visit the website. All the papers published on a particular subject/topic or by any particular author in the journal can be searched and accessed by typing a keyword or name of the author in the 'Search' option on the Home page of the website. All the papers containing that keyword or author will be shown on the home page from where they can be directly downloaded.

**www.neptjournal.com**




Published for Proprietor, Printer and Publisher: Mrs. T. P. Goel, A-504, Bliss Avenue, Balewadi, Pune, Maharashtra, India; Editors: Dr. P. K. Goel (Chief Editor) and Prof. K. P. Sharma